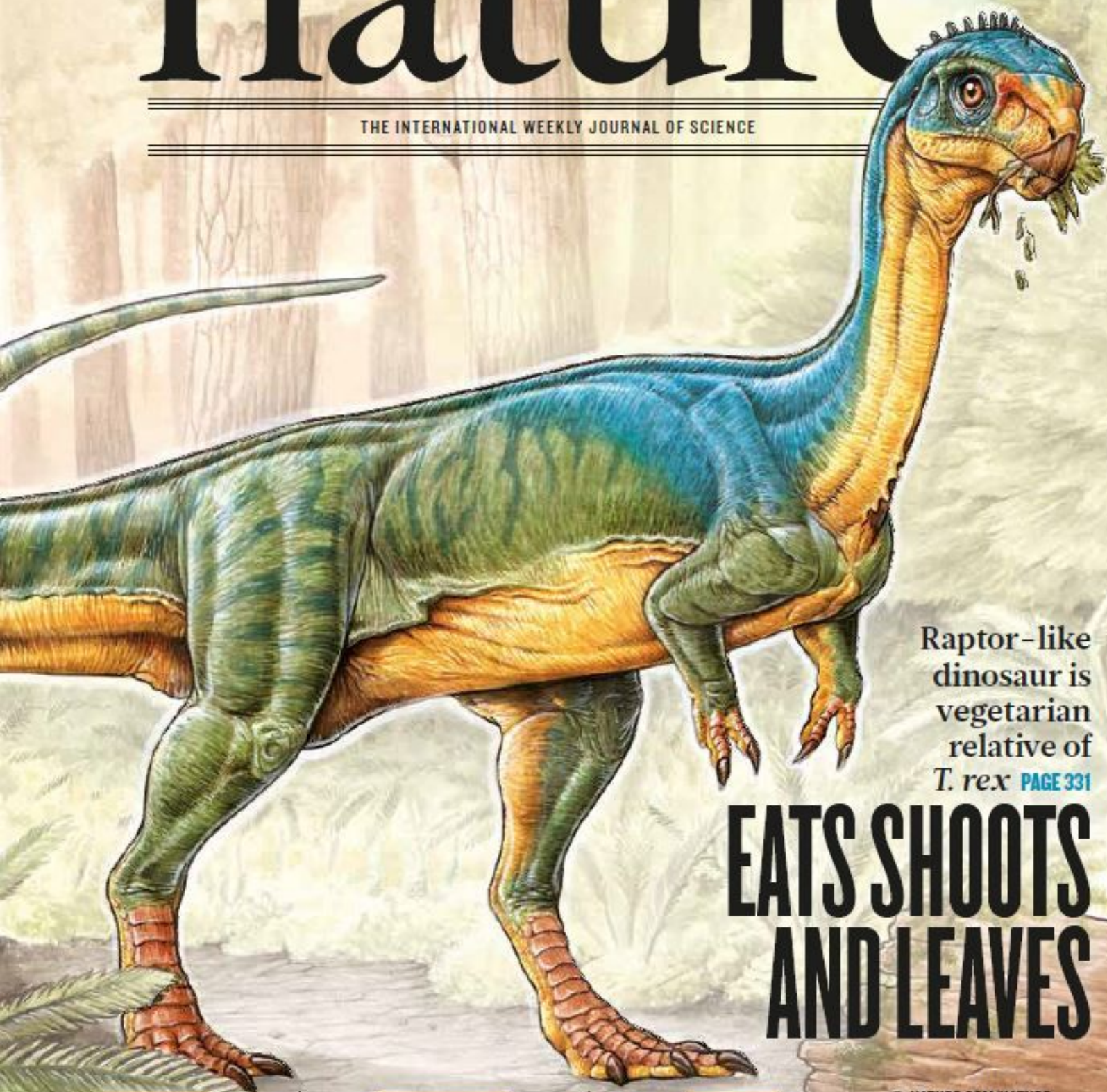


nature

THE INTERNATIONAL WEEKLY JOURNAL OF SCIENCE



Raptor-like
dinosaur is
vegetarian
relative of
T. rex **PAGE 331**

EATS SHOOTS AND LEAVES

MICROBIOLOGY

LIGHTEN THE DARKNESS

Mining microbial dark
matter for new antibiotics

PAGE 270

NATURAL HAZARDS

PREPARE FOR DISASTERS

A call for multidisciplinary
unified risk assessment

PAGE 277

ASTRONOMY

RING AROUND THE MOON

What links shooting stars to
a dusty cloud in lunar orbit?

PAGE 324

NATURE.COM/NATURE

18 June 2015 £10

Vol. 522, No. 7556



THIS WEEK



EDITORIALS

FUNDING Acknowledge that research support is a risky business **p.256**

TRIALS 'Post-normal science' could smooth clinical regulation **p.257**

CUCKOO Adult birds repeat the look-alike trick with feathers **p.258**

Sexism has no place in science

The comments about women in the laboratory made by Nobel laureate Tim Hunt are a reminder that equality in science is a battle still far from won.

Last week's incident at a meeting of science journalists in South Korea, at which the British Nobel prizewinner Tim Hunt expressed jaw-dropping and belittling sentiments about women in the laboratory, is focusing minds, once again, on how to make the most of that half of the human population in research.

All involved in science should condemn the comments, which suggested that single-sex labs might be preferable because "girls" tend to fall in love with their male colleagues and cry when criticized.

Hunt — who won the 2001 Nobel Prize in Physiology or Medicine for his work on cell division — said that his remarks were intended to be light-hearted. Following a storm on Twitter and much media coverage, he was asked to step down from various influential roles.

Some public and media analysis of the sorry story has now shifted to argument about whether the punishment fits the crime. In an interview with the *Observer* newspaper last weekend, Hunt complained that he had been "hung out to dry".

Whether or not the reaction has been fair, his comments and attitudes have become shorthand for the dismaying extent to which sexism still pervades science, and serve as a prompt to discuss the problem.

The problem is worth, once again, stating clearly. In the United States and Europe, around half of those who gain doctoral degrees in science and engineering are women — but barely one-fifth of full professors are women. Women are not invited in significant numbers to sit on the scientific advisory boards of start-up companies. A scientific conference at which half of the keynote speakers are women stands out simply because of that.

The challenge and the consequences of the lack of women in research — especially at senior levels — are expressed in many ways, with worrying persistence. Evidence suggests that too many women encounter patronizing attitudes or harassment in research contexts — whether at work, at academic conferences or in the field. Recent evidence, such as studies of mock hiring exercises, and analysis of grant success rates, authorship assignment and citation counts, suggests that discrimination against women runs deep in the psyches of both genders.

The problem is serious and long-standing. But there are plenty of ways to tackle it. *Nature* has discussed and promoted them before, and is happy to do so again. Here is a list of measures to consider afresh:

- Recognize and address unconscious bias. Graduate students given grants by the US National Institutes of Health are required to undergo ethics training. Gender-bias training for scientists, for example, would be a powerful way to help turn the tide.
- Encourage universities and research institutions to extend the deadlines for tenure or project completion for scientists (women and men) who take parental leave, and do not penalize these researchers by excluding them from annual salary rises. Many workplaces are happy

to consider and agree to such extension requests when they are made. The policy should simply be adopted across the board.

- Events organizers and others must invite female scientists to lecture, review, talk and write articles. And if the woman asked says no — for whatever reason — then ask others. This is about more than mere visibility. It can boost female participation too. Anecdotal reports suggest that women are more likely to ask questions in sessions chaired

"Too many women encounter patronizing attitudes or harassment in research contexts."

by women. After acknowledging our own bias towards male contributors, *Nature*, for example, is engaged in a continued effort to commission more women in our pages.

- Do not use vocabulary and imagery that support one gender more than another. Words matter. It is not 'political-correctness-gone-mad' to avoid defaulting to the pronouns 'him' and 'he', or to ensure that photographs and illustrations feature women.
- In communication and promotional materials, highlight women who have made key contributions to previous work, whether in your own lab or within your research discipline more broadly.
- Be aware of the importance of informal settings and social activities to workplace culture, and people's sense of their place within it. Senior scientists can, where possible, make such events inclusive.

The lot of the female scientist in most developed countries is better than it was a few decades ago — a time that forged the thinking and attitudes of many of today's senior scientists. But such attitudes continue to prevent equality. It is right to highlight and protest against examples of explicit and implicit bias — of all types — in research. And it is essential that all involved strive for better. ■

The right climate

A Republican US presidential candidate speaks on climate change, but will his party listen?

US Senator Lindsey Graham of South Carolina became the ninth contender for the Republican presidential nomination earlier this month. He is a staunch conservative who tends to vote with his party on everything from gun control to health care and foreign policy. He is also the first Republican candidate to squarely address the question of climate change — in a constructive way. During an interview on the CNN news channel on 7 June, Graham highlighted the problem and issued a welcome challenge to his fellow Republicans.

"Here's a question you need to ask everybody running as a Republican: what is the environmental policy of the Republican Party?" Graham said. "When I ask that question, I get a blank stare."

Graham could not be more correct. It has been clear for some time that climate change is a defining social, and therefore political, issue for the twenty-first century. Questions remain about what kind of impacts to expect and how best to reduce greenhouse-gas emissions, while extending the benefits of modern industry to the world's poorest citizens. But the core science is solid, and policy-makers at all levels have a responsibility to engage with it. Sadly, the Republican Party's strategy in Congress thus far has been to ignore or dodge the problem, or to deny it outright.

Fellow candidates such as senators Marco Rubio of Florida and Ted Cruz of Texas have both questioned the science of global warming or humanity's contribution to it, as has former Pennsylvania senator Rick Santorum. When the US Senate took up a pair of symbolic resolutions in January, just 15 Republicans voted in favour of an amendment declaring that human activity contributes to climate change, and only 5 were willing to support a resolution stating that the human contribution is significant.

So far, the only significant Republican engagement on climate has come in the form of opposition to regulations being imposed by the administration of President Barack Obama. Those regulations are in place for cars and trucks, and the administration is expected to finalize a rule to limit carbon pollution by the electricity sector as early as next month. Just last week, the Environmental Protection Agency released a draft "endangerment" finding that will enable the agency to regulate emissions from aeroplanes, in accordance with standards being negotiated through the International Civil Aviation Organization.

Many on the right — including Senator Graham — have argued against these regulatory efforts, and there are legitimate reasons for doing

so. Most experts agree that it would be much more effective to tackle the issue in a comprehensive way, whether through a market-based regulatory emissions scheme like that adopted in the European Union, or a simple carbon tax. An insurgent environmental faction in the Republican Party is pushing for the latter, perhaps paired with a dividend system that would make the tax revenue-neutral and offset the higher prices paid by consumers for petrol and for fossil-fuel-based electricity, as a simpler conservative solution. But before they can even think about laying out a proactive agenda, Republicans must acknowledge the problem.

"The rest of the world has moved beyond questions about whether climate change is real."

In this sense, Senator Graham's challenge is a step forward. Not only is it in line with mainstream science, but it also chimes with mainstream views within the US public.

A March survey by the Yale Project on Climate Change Communication found that 63% of Americans believe that global warming is happening and 52% think that it is mostly caused by humans; just 18% think that it is not happening, with 32% believing that it is mostly due to natural environmental factors. Also, 71% of Americans "mostly" or "somewhat" trust climate scientists, compared with 27% who mostly or somewhat distrust them. Even the corporate community that Republicans claim to represent is beginning to engage with climate change. And Pope Francis has issued his own call to action on climate change this week (see go.nature.com/l9lurz).

The rest of the world has moved beyond questions about whether climate change is real and is focused on how best to address it. There is plenty of pressure on Republicans to do the same, but the challenge to party orthodoxy ultimately needs to come from within. Senator Graham has put the problem on the Republican presidential agenda. To build momentum, he and other brave souls will now need to start talking about solutions. ■

Risky business

Funding agencies should highlight their roles as risk managers to underpin public trust.

Anyone who has helped to run an organization knows that good governance includes regular evaluation of risks — risks to employees, to security, to processes, to reputation, to financial viability — and, where these risks are considered excessive, actions to mitigate them. Risk assessments of this type need to be specific, so inevitably they are confidential.

Research funders who steward the allocation of millions or billions of dollars routinely assess and manage such risks. But they also deal with other kinds of risk — and success in those areas should not be kept quiet.

There are two types of risk management that funders should highlight: one that deals with bad risk, and the other with good.

The bad risks involve funds being wasted on inept, sloppy or downright fraudulent research. Funding agencies are usually responsible to taxpayers; it is therefore crucial that they are publicly accountable for ensuring that they support robust science. This is easily said. How can it be done? The least that the funder can do is to ensure that the institutions that it funds have procedures for tackling sloppy or dishonest research when it arises and, better still, for reducing the likelihood of such problems through appropriate scrutiny and training.

Journals tackling the challenges of reproducibility have found that measures to ensure that research is robust can be onerous for editors, referees and authors. The same will be true for funders. But if public trust in science is to be maintained, funders need to mitigate bad risks

through assessment procedures. They could, for example, ensure that claims about the statistical power of proposed experiments stand up. What is more, they need to be seen to be doing this.

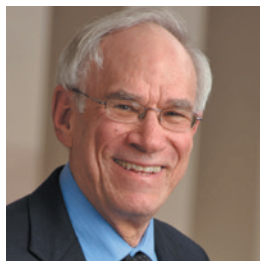
One funder that has taken these responsibilities seriously is the US National Institutes of Health. To tackle poor reproducibility in biomedical research, it has arranged discussion meetings, introduced training programmes and made its assessment of grant applications more rigorous. It has also made these initiatives highly visible: see go.nature.com/8jhvwq. Others should follow its example.

Then there are the good risks. At a meeting of the Global Research Council in Tokyo last month, funders produced a declaration of principles to address the challenges of funding scientific breakthroughs (see go.nature.com/nrlxmd). The most consistent point was that funders should feel able to take positive risks — that is, to support daring ideas that have a chance of failure. They should "encourage risk-taking and tolerate failure in research activities". And they should "provide researchers with the flexibility and intellectual space needed for serendipity". Much of this comes down to funders ensuring "the freedom of researchers in defining their topics, their methodologies and their resource allocations".

Although such boldness is not easy to implement, researchers know what the combination of great talent and bold ideas can deliver. Outsiders, including governments and taxpayers, might not appreciate the potential value of positive risk-taking. But it goes with the territory of supporting outstanding science.

It is important, therefore, that funding-agency managers empower selection committees to accept a degree of risk in supporting boldness in research, and to back researchers up when (and it will be when, not if) some of those risks do not pay off. Any funding agency that lives up to these principles should proclaim its risk-taking mission with pride. ■

➔ **NATURE.COM**
To comment online,
click on Editorials at:
go.nature.com/xhunqv



Rethink our approach to assessing risk

The 'post-normal science' framework would make regulatory decisions about research in humans more effective, says **Frederick Grinnell**.

For four years, officials in the United States have been working on modified rules to regulate research with human participants. At the heart of the issue — and one likely reason why the discussions are taking so long — is the question of risk, and how to assess it. In fact, the goal of the new rules is to more effectively link how risky a project is perceived to be for the people taking part with how it should be regulated. Hence the name: risk-based regulation.

How to assess risk in research with humans has been a persistent problem. These decisions are typically taken by institutional review boards (IRBs), but studies have shown that different boards, and indeed different members of the same IRBs, judge the risk of identical procedures in very different ways.

This variation in risk assessment contributes to multiple problems as reflected in the title of the 2011 US advanced notice of proposed rule-making: *Enhancing Protections for Research Subjects and Reducing Burden, Delay, and Ambiguity for Investigators* (see go.nature.com/x8rftth).

The current US regulatory framework known as the common rule calls for the evaluation of 'probability and magnitude of harm or discomfort'. This language implies that IRBs can make objective assessments of risk and wrongly assumes that accurate predictions about experimental outcomes will be possible. Moreover, verdicts such as 'minimal risk' and 'minor increase over minimal risk' do not distinguish whether the increase is because of the perceived extent of added risk or the uncertainty of that added risk. Two IRB members, in other words, can reach the same decision for very different reasons. This can make it harder for groups to reach a consensus.

How should we think differently about risk? A good starting point would be to ensure that the risk to humans is always considered in context and not in an abstract sense. For instance, chairs of IRBs have been shown to grade the risk of lumbar puncture in 11-year-old children without sedation differently if they are told the children are healthy or ill and have undergone the procedure previously (S. Shah *et al.* *JAMA* **291**, 476–482; 2004).

In my view, a better way to assess and discuss risk is by using a method of inquiry called post-normal science (PNS). Introduced in the 1990s, PNS was put forth as a heuristic risk-assessment framework to assist decision-making at the interface between environmental science and public policy (S. O. Funtowicz and J. R. Ravetz *Futures* **25**, 739–755; 1993). Designed to address specific scenarios, it always focuses on contextual rather than abstract risk.

Importantly, PNS makes no attempt to merge magnitude and probability of risk, which are referred to as 'decision stakes' and 'system

uncertainties' — to reflect the emphasis on value, not quantitative, judgements, which are required of regulatory groups. As an example of PNS applied to human research, the decision stakes (added risk) for a highly toxic intervention that is first undergoing testing would be higher for healthy people than for patients who have the condition under investigation. In this example, the system uncertainties (uncertainty about the occurrence of added risk) are similar for both groups.

However, the system uncertainties would be higher, say, if a procedure such as cardiac catheterization in healthy people was to be performed by a physician with little experience, compared with one with a highly successful track record. (The decision stakes, added risk, would be similar.)

Under the PNS approach, research administrators and IRB members would assess both criteria to allocate proposed research to one of three separate risk domains, which demand different levels of scrutiny and regulation.

PNS designates the lowest of these domains as 'applied science'. Research currently typically categorized as exempt or expedited has relatively low decision stakes and low system uncertainty and would fall into this domain in which the principal investigator is given the responsibility to carry out the work with minimal oversight.

As levels of decision stakes and system uncertainty rise to intermediate, proposals are placed in the second category, which in PNS is called professional consultancy. This is the domain of ongoing involvement of IRBs and the increasing importance of participant understanding of the research to give informed consent. PNS use of separate criteria would lead to clearer analysis of what makes a project

more or less risky, and help IRBs to reach decisions.

The final category, the domain of 'post-normal science', is reserved for projects for which system uncertainties are so high that they include the adequacy of the current ethical principles used to assess risk. Values, in other words, become as important as facts. Managing risk in this zone needs extended consultation with a wider community, and one that assesses social values as well as scientific facts and expertise. A recent example of science that falls into this top tier is the question of whether or not to genetically engineer human embryos.

Using PNS to assess risk in human research has received little attention so far. But it offers a more coherent approach and permits a more nuanced analysis than the current regulatory framework. It would promote the goal of risk-based regulation of human research. ■

Frederick Grinnell is a professor in the Department of Cell Biology at the UT Southwestern Medical Center, University of Texas in Dallas, Texas.
e-mail: frederick.grinnell@utsouthwestern.edu

A GOOD STARTING
POINT WOULD BE
TO ENSURE
THAT RISK IS
CONSIDERED IN
CONTEXT AND NOT AN
ABSTRACT
SENSE.

➔ **NATURE.COM**
Discuss this article
online at:
go.nature.com/vuw5su

RESEARCH HIGHLIGHTS

Selections from the
scientific literature

PRIMATOLOGY

Chimps are not averse to alcohol

Chimpanzees at a site in West Africa drink alcohol-containing sap from raffia trees — the first systematic evidence that non-human apes ingest naturally fermented food in the wild.

In Guinea, local people collect this sap by hanging containers under holes tapped near the crowns of raffia palms (*Raphia hookeri*). Kimberley Hockings at the Centre for Research in Anthropology in Lisbon and her colleagues found that the chimps dip crumpled leaves into the containers to sponge out the sweet sap, which contains about 3% ethanol.

The results suggest that the last common ancestor of African apes and humans could tolerate the consumption of ethanol.

R. Soc. Open Sci. 2, 150150 (2015)

ZOOLOGY

Cuckoo finch is a master of mimicry

Some birds use other species' nests to lay eggs that resemble those of the other species, escaping the burdens of parenthood. Now researchers have found a type of finch in Africa that also mimics how another bird looks as an adult.

The female cuckoo finch (*Anomalospiza imberbis*; pictured left) lays its eggs in



the nests of tawny-flanked prinias (*Prinia subflava*) but also strongly resembles the female of a common African species called the southern red bishop (*Euplectes orix*; pictured right). The resemblance, studied by William Feeney at the University of Cambridge, UK, and his colleagues, may have evolved initially to help cuckoo finches to sneak closer to the prinias' nests. But prinias have evolved what seems to be a countermeasure: they attack the finch and the southern red bishop with equal aggression.
Proc. R. Soc. B 282, 20150795 (2015)



HYDROLOGY

Floods used as defensive weapons

One-third of all major floods recorded in the Netherlands over the past 500 years were caused deliberately by humans to defend the territory during wartime.

Adriaan de Kraker of Free University Amsterdam trawled historical maps, land ownership documents and written accounts of flooding events in the low-lying southwest Netherlands, where three rivers flow into the North Sea. The largest floods occurred either during storm surges when sea water breached the

flood defences, or during wartime when people destroyed dikes to deter enemies such as the Spanish in the sixteenth century. The tactic was also used by both sides during the Second World War (pictured are residents of Walcheren being rescued from floods in 1945, after a sea wall was breached). Strategic flooding was not always successful in deterring the enemy, de Kraker says, and caused as much damage to land and property as natural floods did.

Hydrol. Earth Syst. Sci. 19, 2673–2684 (2015)

OPTICS

Graphene shines bright in a vacuum

Physicists have designed a 2D device that can emit bright, visible light, paving the way for ultra-thin light-emitting devices.

One-atom-thick layers of carbon called graphene can withstand the high temperatures at which they emit light. But when graphene is stuck to a surface and electricity is applied, only a small amount of light energy is released because too much energy dissipates as heat.

Young Duck Kim at Seoul National University and his colleagues got around the problem by putting a current through a piece of graphene suspended between two electrodes in a vacuum. By isolating the graphene, they were able to heat it to more than 2,500 °C and increase the level of radiation by 1,000 times compared to graphene on a substrate.

With further improvements, the device could serve as a nanoscale light emitter in ultra-thin displays, say the authors.
Nature Nanotech. <http://dx.doi.org/10.1038/nnano.2015.118> (2015)

ASSOCIATED PRESS

CLAIRE SPOTTISWOODE

ASTRONOMY

Stars seen forming in a far-off galaxy

Astronomers have seen their best glimpse yet of stars forming in the early Universe.

The ALMA radio telescope in Chile explored the SDP.81 galaxy, which is 3.6 billion parsecs (11.7 billion light years) away from Earth. Its light was magnified and distorted by the gravitational pull of another galaxy between it and Earth, but a model developed by Yoichi Tamura of the University of Tokyo and his team corrected the distortions. Their images reveal many cold clouds of dust and gas that are driving a rapid rate of star formation.

Several research teams have analysed the ALMA data to characterize other aspects of this galaxy.

Publ. Astron. Soc. Japan
<http://doi.org/5bv> (2015)

APPLIED PHYSICS

Evaporation drives engine

An engine fuelled only by water evaporation can power a miniature car and lights.

Ozgur Sahin at Columbia University in New York and his colleagues applied bacterial spores to thin plastic strips. The spores absorb and release water with changes in relative humidity, so the strips curl and straighten. The team stacked the strips and formed them into a water-containing engine so that the strips were exposed to recurring periods of high and low humidity, acting like oscillators to power the engine. When attached to a generator, the engine powered light-emitting diodes. A rotary version attached to two pairs of wheels (**pictured**, left) pushed

a 100-gram car forwards (**pictured**, right).

The engine could be used in devices in areas that have scarce electricity, the authors say.

Nature Commun. 6, 7346 (2015)

BEHAVIOURAL ECOLOGY

Angry spiders spin long-lived colonies

Animal personality can influence the lifespan of whole ecological communities.

Female *Anelosimus studiosus* spiders create large webs shared by multiple females of this species and by many other types of spider. Jonathan Pruitt and Andreas Modlmeier of the University of Pittsburgh in Pennsylvania started colonies with either two docile spiders or two aggressive ones. Docile females allowed many kinds of spider to colonize and scavenged the other spiders' prey. Aggressive ones caught their own prey and fought off competing and predatory spiders. All of the communities collapsed in the end, but those founded by aggressive females lasted up to three years longer.

Communities founded by docile spiders reached a similar destabilizing species composition to aggressive spiders' colonies, but did so at a faster rate, making the docile-founded colonies shorter lived. *J. Anim. Ecol.* <http://doi.org/5bt> (2015)

GENOME EDITING

CRISPR system controlled by light

A popular genome-editing technique has been modified so researchers can use light to control when editing occurs and in which cells.

To better control how the CRISPR-Cas9 system cuts

SOCIAL SELECTION

Popular topics on social media

Unreliable dietary data under fire

Much of the data on personal eating habits — which form the basis of many national dietary guidelines — are unreliable and misleading, according to a report in *Mayo Clinic Proceedings* that drew attention on social media. The authors argue that the widely used survey method of asking people to recall their food and drink intake is so inaccurate that any conclusions based on such data should be called into question. “Must read paper in nutrition! At what point does inaccurate data become worse than no data?” tweeted Dylan MacKay, a human-nutrition researcher at the University of Manitoba in Winnipeg, Canada. But Brenda Davy, a clinical nutritionist at Virginia Polytechnic Institute and State University in Blacksburg, writes in an accompanying editorial that whereas self-reports are imperfect, they have helped to uncover vital nutritional links, such as that between fat intake and heart disease.

Mayo Clin. Proc. <http://doi.org/5dd>; <http://doi.org/5df> (2015)



Based on data from altmetric.com. Altmetric tracks and compiles online attention around research outputs such as papers, books and data sets.

NATURE.COM
For more on popular papers:
go.nature.com/necdqh

and alters DNA sequences, Moritoshi Sato and his team at the University of Tokyo in Japan split the Cas9 DNA-cutting enzyme in two and fused each part to a protein. These proteins join together when hit with blue light, reactivating Cas9. They found that the modified enzyme could still edit the genome accurately in human cells in the lab. The frequency of edits increased with longer light exposures and no editing was seen in cells kept in the dark.

The team also shone patterns of light onto the cells and found that genome editing occurred along the same patterns. The technique could help to improve the precision of CRISPR, the authors say. *Nature Biotech.* <http://dx.doi.org/10.1038/nbt.3245> (2015)

REGENERATIVE BIOLOGY

Mammary ducts made in a dish

Cells from human mammary glands develop in the lab into structures that look and behave like milk-producing

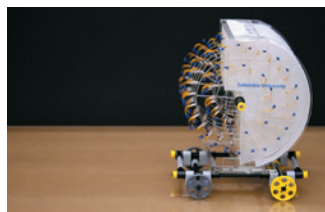
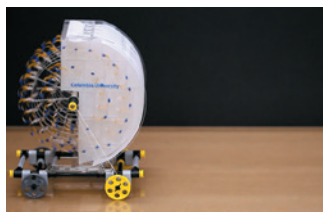
ducts in the breast.

A team led by Christina Scheel at the Helmholtz Center for Health and Environmental Research in Munich, Germany, obtained mammary gland tissue from healthy women undergoing surgery and isolated cells that line the ducts of the glands. The team suspended individual cells in a 3D flexible collagen gel, added growth factors, and found that the cells developed into structures that resembled the key functional units of the mammary gland. Some of the structures even contracted in the same way as ducts do during lactation.

Cells developed into duct-like structures only when they were grown in collagen gels that were not physically attached to the culture dish, suggesting that a flexible matrix is needed for normal growth of this tissue. *Development* <http://dx.doi.org/10.1242/dev.123554> (2015)

NATURE.COM
For the latest research published by Nature visit:
www.nature.com/latestresearch

XI CHEN



SEVEN DAYS

The news in brief

EVENTS

Comet probe wakes

Philae, the space probe that landed on a comet in November 2014, is awake. The European Space Agency (ESA) announced that it had received signals from the lander on 13 June. Philae's battery ran out just three days after it landed on 67P/Churyumov–Gerasimenko. Stuck in the shade, it was unable to charge its solar-powered battery and entered hibernation. Scientists had hoped that Philae would regain power as the comet neared the Sun. See page 263 for more.

Oil-sands petition

A group of more than 100 North American scientists released a petition calling for a moratorium on the development of Canadian oil sands. Issued on 10 June, the statement claims that crude oil from oil sands is responsible for more carbon emissions than are other transport fuels. Its use also pollutes the air and water. Continued development of the oil sands in Alberta is therefore inconsistent with efforts to reduce greenhouse-gas emissions unless it is coupled with a larger plan to address global warming, the petitioners say.

Curve honoured

The iconic 'Keeling curve', a 57-year global record of carbon dioxide in the atmosphere, was made a US National Historic Chemical Landmark on 12 June. The late Charles David Keeling, a geochemist at the Scripps Institution of Oceanography in La Jolla, California, began the CO₂ measurements in 1958 at Mauna Loa in Hawaii, and the curve has become a record of human

effects on the atmosphere. The designation is from the American Chemical Society, which has held commemoration events at the Scripps campus and the Mauna Loa site.

FACILITIES

Array amplification

The Telescope Array, a Japanese cosmic-ray observatory in Utah, will nearly quadruple in size to about 2,500 square kilometres, the University of Utah in Salt Lake City announced on 15 June. Japan pledged ¥568 million (US\$4.6 million) to add scintillation detectors, and US collaborators will seek \$1.8 million to build extra fluorescence detectors. The upgrade could take three years to complete. Researchers hope that the expansion will help them to determine the nature of an apparent 'hotspot' of ultra-high-energy cosmic rays

coming from the part of the sky near Ursa Major.

Neutrino switch

Neutrinos — subatomic particles that come in three 'flavours' — have been confirmed to switch spontaneously from muon to tau flavour. Physicists in the OPERA experiment detected five tau neutrinos in a muon neutrino beam that travelled 730 kilometres from Switzerland to the Gran Sasso underground laboratories in Italy. OPERA spokesperson Giovanni De Lellis announced on 16 June that the phenomenon has been achieved with the necessary statistical precision for it to be considered a discovery.

POLICY

Aviation emissions

The US Environmental Protection Agency issued a draft ruling on 10 June that

heavy rains. People in Tbilisi were warned to stay in their homes after various animals — including a bear and hippopotamus — escaped from the zoo after floods destroyed enclosures.



TINATIN KIGURADZE/AP

Zoo escape adds to Georgia's flood woes

Georgia declared 15 June a national day of mourning after severe flooding killed at least 12 people and led to the escape of zoo animals in Tbilisi. A further 24 people are missing after

greenhouse-gas emissions from aviation endanger human welfare. A formal finding of 'endangerment' would enable the agency to set climate regulations for aircraft under the Clean Air Act, building on similar regulations that have already been established for cars. The EPA said that it is participating in an international effort to develop carbon dioxide standards led by the International Civil Aviation Organization, which is expected to produce a set of standards in early 2016.

Emissions peak

Global energy-related emissions could peak as early as 2020, according to a report published by the International Energy Agency on 15 June. Achieving the goal would require countries to increase energy efficiency and use of renewable

energies, reduce reliance on coal, phase out fossil-fuel subsidies and reduce methane emissions from oil and gas production. The report also laid out steps to achieve a successful international climate agreement in Paris this December: negotiators must focus on an early peak in energy emissions, set up a five-year review of national targets, establish a long-term emissions goal and create a process to track progress.

PEOPLE

NIH role changes

Sally Rockey, long-time head of the extramural research programme at the US National Institutes of Health (NIH), will leave the agency in September, she announced on 11 June. Rockey, well known for her *Rock Talk* blog about NIH grants, will now head a non-profit corporation called the Foundation for Food and Agriculture Research, which seeks private donations for research (see *Nature* <http://doi.org/5dm; 2015>). On the same day, the NIH named neurologist Walter Koroshetz as director of the US National Institute of Neurological Disorders and Stroke. Koroshetz has served as the institute's interim director since October 2014.

**Nature knighthood**

The editor-in-chief of *Nature*, Philip Campbell, was among those recognized for contributions to science in the United Kingdom's 2015 Queen's birthday honours. Campbell (pictured) received a knighthood, one of the highest distinctions in UK honours system, alongside metallurgist Harshad Bhadeshia of the University of Cambridge, UK, Peter Downes, vice-chancellor of the University of Dundee, UK, and other researchers. Among those made dames were Frances Ashcroft, a diabetes researcher at the University of Oxford, UK, and Anne Glover, the former chief scientific adviser to the European Commission. See go.nature.com/gvzy22 for more.

RESEARCH

Frozen-ovary first

A healthy baby boy has been born to a woman transplanted with her own preserved

ovarian tissue, removed in childhood, researchers said on 9 June. The woman had had her right ovary removed as a consequence of treatment for sickle-cell anaemia. Tissues from it were frozen, and were transplanted back a decade later. Two years after that, the woman conceived naturally, giving birth in November 2014 (I. Demeestere *et al.* *Hum. Reprod.* <http://doi.org/5dj; 2015>). Babies have been born from frozen ovarian tissue before — but previous cases have always involved tissue taken from adults.

US chimp ruling

Biomedical research using chimpanzees in the United States may become nearly impossible, following a 12 June ruling from the US Fish and Wildlife Service (FWS) that designated the animals an endangered species. Wild chimpanzees have been on the endangered list since 1990, but until now their captive counterparts have been exempted. The FWS rule makes it illegal to harass or harm captive chimpanzees unless the research also benefits the animals in the wild. US chimpanzee research was sharply curtailed in 2013, when the US National Institutes of Health retired most of its chimps. See go.nature.com/fvkouw for more.

COMING UP

22–26 JUNE

Some 600 astrophysicists gather in Tenerife, Spain, for the annual meeting of the European Astronomical Society. go.nature.com/cnkj7g

22–26 JUNE

Pathogen detection, biosurveillance and point-of-care technologies will be discussed by leaders from government, academia and industry at the Biodefense World Summit in Bethesda, Maryland. go.nature.com/ymuyui

24–27 JUNE

The International Society for Stem Cell Research holds its annual meeting in Stockholm. More than 4,000 experts from 50 countries are expected to attend. go.nature.com/acbz3

BUSINESS

Cholesterol drugs

An emerging class of cholesterol drug has won overwhelming support from advisers to the US Food and Drug Administration (FDA). On 9 and 10 June, advisers voted in favour of recommending FDA approval for two drugs that target a protein called PCSK9, which is involved in cholesterol processing by the liver. Drugs that inhibit PCSK9 boost cholesterol uptake (see *Nature* **496**, 152–155; 2013). The two drugs — alirocumab (Praluent) from Paris-based Sanofi and evolocumab (Repatha) from Amgen of Thousand Oaks, California — are under consideration for treating a genetic condition that causes high cholesterol.

► **NATURE.COM**

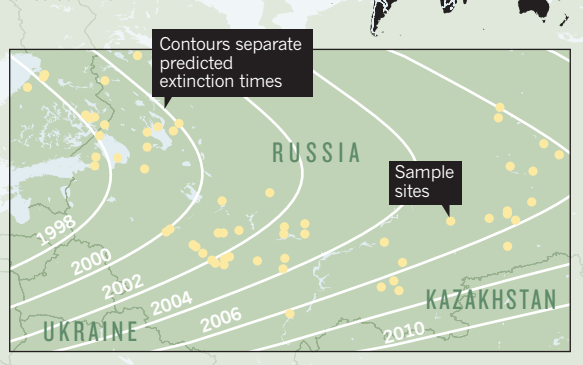
For daily news updates see: www.nature.com/news

TREND WATCH

The population of what was once one of Eurasia's most abundant songbirds has crashed. Numbers of the yellow-breasted bunting (*Emberiza aureola*) fell by 84–95% between 1980 and 2013 and its range has shrunk by 5,000 kilometres (J. Kamp *et al.* *Conserv. Biol.* <http://doi.org/5dh; 2015>). The bird is now thought to be extinct in the northwestern parts of its habitat. The authors of the study say that widespread trapping of the birds in China may be partly to blame, but that other drivers cannot be ruled out.

BIRD EXTINCTIONS

The range of the yellow-breasted bunting has shrunk so much that the bird now seems to be extinct in many regions where it was once common.



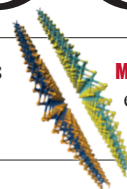
NEWS IN FOCUS

TURKEY Election result raises hopes for science autonomy **p.264**

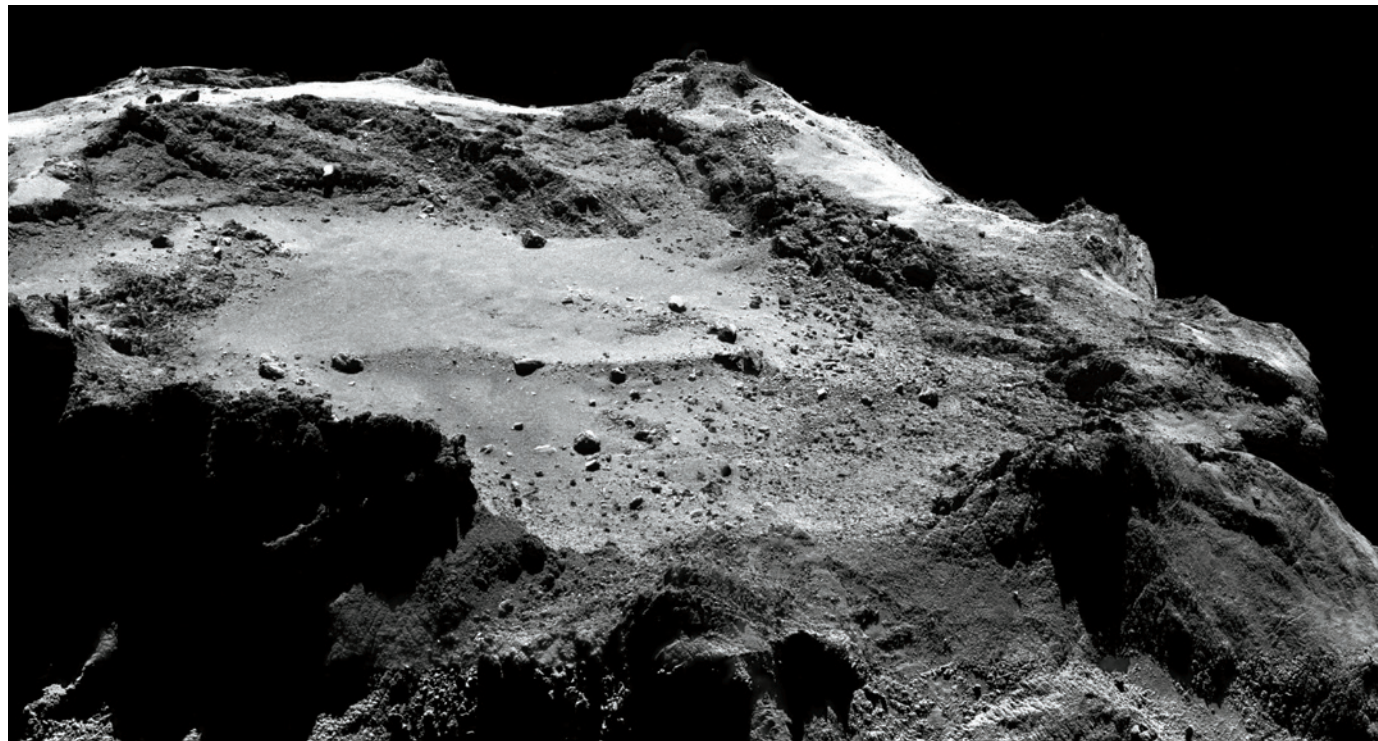
MEDICINE Anti-ageing pills pushed as bona fide drugs **p.265**

GRAPHENE Growing pains as wonder material booms **p.268**

MATERIALS After graphene, excitement over a zoo of 2D materials **p.274**



ESA/ROSETTA/MPS FOR OSIRIS TEAM MPS/UPD/LAM/IAA/SSO/INTA/UPM/DASP/IDA



Drilling the surface of comet 67P/Churyumov-Gerasimenko will be among the next tasks for the Philae lander, if it can establish a better communications link.

ROSETTA MISSION

Let the comet science begin

Philae comet lander wakes up — with enough power to do experiments.

BY ELIZABETH GIBNEY

“We all said the chance that the lander would wake up was 50:50, but actually many of us thought it was much less,” says Uwe Meierhenrich, an analytical chemist at the University of Nice Sophia Antipolis in France. He is one of a group of scientists from the Rosetta comet mission who met last week in Rome to hash out a plan should their lander, Philae, awaken from its slumber on the surface of a comet. Not a peep had been heard from Philae since its battery ran out seven months ago, three days after a historic landing on comet 67P/Churyumov-Gerasimenko.

The doubters were in for a surprise. Days

later, at 22:28 Central European Standard Time on 13 June, the European Space Agency (ESA) received a signal from Philae.

Scientists had hoped that as the comet neared the Sun, the craft's solar panels would provide it with enough power to wake, but they also feared that the cold might prevent a reboot. The incoming data show that not only is Philae awake, but also that its prognosis is better than anyone had hoped. “Both temperature- and power-wise we are in a really good state,” says lander manager Stephan Ulamec of the German Aerospace Centre (DLR) near Cologne.

The Rosetta scientists are itching to begin experiments. But first the communication link — which depends on a direct line-of-sight between the lander and the Rosetta mothership

currently orbiting the comet — has to improve. As *Nature* went to press, the communication bursts had been just a few minutes long, compared with three-hour stints in November, and were often interrupted, suggesting that Philae is not in the orientation that scientists had predicted. It might be that the lander has moved a little, says Meierhenrich. But Ulamec reckons that the predictions — used to align Rosetta's antenna — were “slightly wrong” to begin with.

The team is piecing together how to shift Rosetta's orbit to better align the two craft, something ESA plans to do on 17 June. “By the end of the week we really should be getting better, longer communication slots,” says Ulamec.

Philae's 24 watts of available power is a “good amount”, says Koen Geurts, a member of ▶

► the landing team at the DLR. “It’s more than enough to communicate and to do science activities.” And the lander’s reported operating temperature of -35°C should be warm enough for the team to attempt turning on the battery. “Then we are not relying on the short window when the lander is illuminated,” he adds. “We can do more things.”

HOMING IN

Assuming that the instruments have survived the cold, the first experiments will measure the comet’s magnetic and electric fields and temperature, says Ulamec. Next, Philae will start up its cameras, which were last deployed when Philae landed. “The surface might have changed, and we might see different features due to changing illumination,” says Ulamec.

The CONSERT radar instrument, which is designed to probe the comet’s interior, will be used to pinpoint Philae’s exact location: although scientists knew that Philae had landed in November, they do not know exactly where it ended up, because it bounced twice.

Eventually, Philae should deploy its drill to get samples from the comet’s crust, says Meierhenrich, who is a co-investigator on Philae’s chemical analyser, COSAC.

With enough sunlight to recharge its battery, Philae has potentially more power and more operating time than before hibernation, meaning that it should now be able to do more-complex experiments. For example, it could use an infrared microscope to examine samples before they are chemically analysed, to verify that its drill did scoop something up.

“We couldn’t do this in the first science phase; we had to run the most simple system we could,” says Meierhenrich.

The comet is now a very different environment from when Philae landed, with a much stronger outpouring of gas and dust. For Philae, the change of seasons is double-edged: there will be more particles in the atmosphere for the lander to ‘sniff’, says Ulamec, but the particles pose a danger to Rosetta’s navigation systems, and will continue to intensify until August, when the comet will be closest to the Sun. To avoid damage, Rosetta might need to retreat to such a distance that it would no longer be able to communicate with Philae on the surface. But once the comet rounds the Sun in September, Rosetta could come back in closer and let Philae phone home again. ■



Recep Tayyip Erdoğan meets students days after the party he co-founded lost its parliamentary majority.

stripping public science organizations of their autonomy; allowing the teaching of creationism and astrology; and, most recently, a ban on social scientists interviewing political refugees.

Many of the policies that scientists object to were pushed by Recep Tayyip Erdoğan, who was prime minister between 2003 and 2014 and is now president. Although the AKP remains the largest party in parliament, it now needs a coalition partner to form a government.

“With more pluralism in the parliament there are more prospects that some of the new rules imposed during the last years could be unpicked,” says Ali Alpar, an astrophysicist from Sabancı University in Istanbul.

Turkish academics have never been entirely free, but the AKP has escalated government interference. For example, as in many European countries, university faculty members in Turkey vote for their rectors. However, the centralized higher-education council YÖK then compiles a final shortlist, from which Turkey’s president selects the winner. The AKP had promised to abolish the unpopular council but ended up using YÖK to promote its own ideology: most Turkish rectors are now AKP sympathizers.

In the latest round of appointments in April, Erdoğan caused consternation at Istanbul University by selecting historian Mahmut Ak as rector, instead of the left-leaning psychiatrist Raşit Tükel, who won most of the faculty’s votes and the favour of almost 14,500 people who petitioned Erdoğan to pick Tükel.

The People’s Democratic Party (HDP), a coalition of anti-nationalist, environmentalist and other leftist movements, won 13% of the vote in the election. It will use its influence in parliament to prioritize the freeing of academia from state control and to push for the abolition of YÖK, says Gençay Gürsoy, a neurologist who won a seat in the new parliament for the HDP.

“I can’t tell you how we will celebrate if YÖK is finally abolished,” says Esra Mungan, a psychologist at Boğaziçi University in Istanbul and a member of the HDP advisory council.

TURKEY

Election results delight scientists

Turkish researchers hope that a more pluralistic parliament will put an end to interference and slipping standards.

BY ALISON ABBOTT

Scientists in Turkey are euphoric after a 7 June election that stripped the mildly Islamic and increasingly repressive Justice and Development Party (AKP) of its

absolute parliamentary majority.

They hope that Turkey’s next parliament will reverse the creeping restrictions on academic freedom and the seeping away of scientific standards that have been a feature of the AKP’s 12 years of political domination. These include

"We are going to dance in the streets."

The AKP's grip on science extends beyond YÖK. In 2005, Erdoğan began to place political loyalists in top posts at Turkey's research-funding agency TÜBİTAK, which had previously enjoyed a degree of autonomy. Many of them were from the Gülen movement — a transnational religious and social organization. Scientists say that research funds were no longer distributed according to merit and that the agency has seemed to be anti-evolution. In 2009, TÜBİTAK removed a portrait of Charles Darwin from a cover of a government-backed science magazine and sacked the editor (see *Nature* 458, 259; 2009). Under the AKP, which turned Turkey from a constitutionally secular nation to one where religion is state-sponsored, creationism is often taught in schools and debated in universities. (The AKP fell out with the Gülenists in 2013 and purged them from TÜBİTAK, leaving it in chaos.)

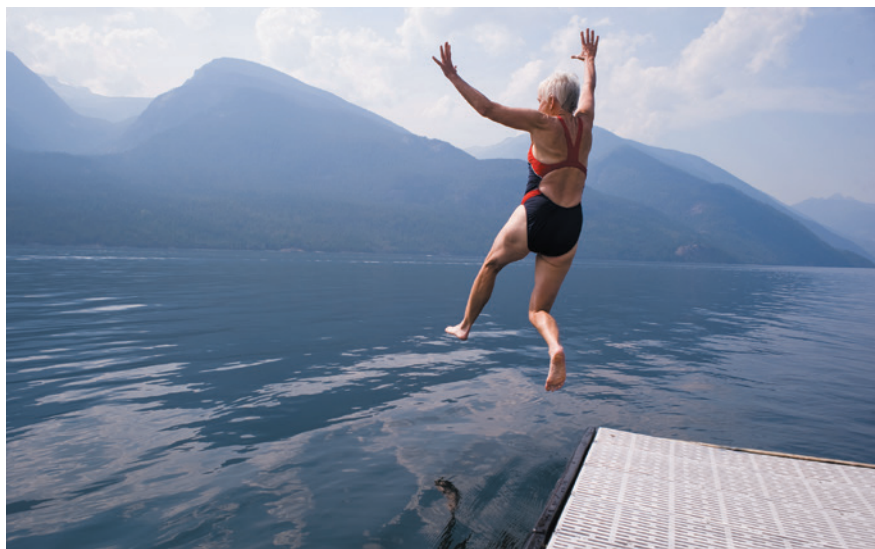
In 2011, the science ministry assumed control of the Turkish Academy of Sciences, TÜBA. It decreed that TÜBİTAK and YÖK would appoint two-thirds of TÜBA's members, who would then elect the remaining one-third. Most of TÜBA's original members resigned in protest and launched another national academy, Bilim Akademisi, which has regularly challenged science standards.

Earlier this month, the academy, of which Alpar is president, identified two universities that had approved theses and certificates in astrology, and called on YÖK not to allow such unscientific practices. It also contested a government order forbidding university researchers from interviewing refugees without government supervision. The academy argued that the government's claim that the interviews would infringe data-protection laws was invalid.

Until a new government forms, the AKP remains in charge. It irked scientists further on 11 June by appointing Ahmet Arif Ergin as head of TÜBİTAK. "It is extremely undemocratic and inappropriate for a caretaker government to make such an important political appointment," says Mungan.

But the election results have brought hope. "You can't imagine what a relief it has been in scientific circles — the one-man rule had looked unstoppable, but now it is over," says Şevket Ruacan, a pathologist at Koç University in Istanbul and a former TÜBİTAK board member. Change will take time, he says, "but conservative religious influences may now be reduced in education and it may become possible to reduce the political influences in scientific matters".

At least Turkish scientists have not wanted for funding. Research spending has more than trebled since Erdoğan came to power — a result of his now-stalled endeavour for Turkey to be admitted to the European Union. Some major infrastructures have been developed, including the ambitious €60-million (US\$68-million) Izmir Biomedicine & Genome Center, due to open in September. ■



Researchers hope to find drugs that extend a person's healthy years.

CLINICAL RESEARCH

Ageing pushed as treatable condition

Regulators asked to consider innovative trial design.

BY ERIKA CHECK HAYDEN

Doctors and scientists want drug regulators and research funding agencies to consider medicines that delay ageing-related disease as legitimate drugs. Such treatments have a physiological basis, researchers say, and could extend a person's healthy years by slowing down the processes that underlie common diseases of ageing — making them worthy of government approval. On 24 June, researchers will meet with regulators from the US Food and Drug Administration (FDA) to make the case for a clinical trial designed to show the validity of the approach.

Current treatments for diseases related to ageing "just exchange one disease for another", says physician Nir Barzilai of the Albert Einstein College of Medicine in New York. That is because people treated for one age-related disease often go on to die from another relatively soon thereafter. "What we want to show is that if we delay ageing, that's the best way to delay disease."

Barzilai and other researchers plan to test that notion in a clinical trial called Targeting Aging with Metformin, or TAME. They will give the drug metformin to thousands of people who already have one or two of three conditions — cancer, heart disease or cognitive impairment — or are at risk of

them. People with type 2 diabetes cannot be enrolled because metformin is already used to treat that disease. The participants will then be monitored to see whether the medication forestalls the illnesses they do not already have, as well as diabetes and death.

On 24 June, researchers will try to convince FDA officials that if the trial succeeds, they will have proved that a drug can delay ageing. That would set a precedent that ageing is a disorder that can be treated with medicines, and perhaps spur progress and funding for ageing research.

"What we're trying to do is increase health span, not look for eternal life."

During a meeting on 27 May at the US National Institute on Aging (NIA) in Bethesda, Maryland, Robert Temple, deputy director for clinical science at the FDA's Center for Drug Evaluation and Research, indicated that the agency is open to the idea.

Barzilai and his colleagues eschew claims of a quest for immortality, because they think that such assertions have led to a perception that the field is frivolous and irresponsible. "The perception is that we are all looking for a fountain of youth," says Stephanie Lederman, executive director of the American Federation for Aging Research in New York. "We want to avoid that; what we're trying to do is increase health span, not look for eternal life." ►

► Ageing research has hit bumps in the past decade, as companies marketing drugs touted to prolong life have gone bust (see *Nature* **464**, 480–481; 2010). But organizers of the TAME trial think that the field is now in a better position because animal studies have shown that some drugs and lifestyle practices can extend life by targeting physiological pathways¹.

For instance, the NIA-sponsored Interventions Testing Program, in which investigators at three sites are systematically trialling candidate age-delay treatments, has shown that a handful of interventions convincingly and reproducibly prolong the lives of various strains of mice. Those include cutting down on calorie intake and taking a drug called rapamycin that is used to prevent rejection of transplanted organs.

And researchers from the Novartis Institutes for Biomedical Research in Cambridge, Massachusetts, reported in December that elderly people develop a stronger immune response to an influenza vaccination if they also take a rapamycin-like drug². Rapamycin, which acts on a biological pathway involved in cell growth, is now seen as one of the most promising drugs for delaying ageing, but given over long periods of time it also suppresses the immune system.

SAFETY FIRST

The TAME test is for metformin, which suppresses glucose production by the liver and increases sensitivity to insulin. The drug has been used for more than 60 years and is safe and prolongs healthy life and lifespan in worms³ and in some mouse strains¹. Data also suggest that it could delay heart disease, cancer, cognitive decline and death in people with diabetes⁴. Plans call for the trial to enrol 3,000 people aged 70–80 years at roughly 15 centres around the United States. The trial will take 5–7 years and cost US\$50 million, Barzilai estimates, although it does not yet have funding.

Matt Kaeberlein at the University of Washington, Seattle, who is running a trial of rapamycin in elderly dogs, says that the concept behind Barzilai's trial is sound. Even though other drugs might be more effective at delaying ageing in animal studies, he says, the many years of experience with metformin in people, combined with data suggesting that it impacts the ageing process in people, make it a good candidate for a first clinical trial in the field.

"It's a smart way to engage the FDA in a discussion about recognizing ageing as an indication that is appropriate for clinical trials," Kaeberlein says. ■

1. Miller, R. A. *et al.* *J. Gerontol A Biol. Sci. Med. Sci.* **66A**, 191–201 (2010).
2. Mannick, J. B. *et al.* *Sci. Transl. Med.* **268**, 268ral179 (2014).
3. Onken, B. & Driscoll, M. *PLoS ONE* **5**, e8758 (2010).
4. Bannister, C. A. *et al.* *Diabetes Obes. Metab.* **16**, 1165–1173 (2014).



Infrared technologies are subject to tight restrictions because of their military applications.

TECHNOLOGY

US 'export rules' threaten research

Proposed updates to national–security regulations would restrict collaboration with foreign scientists and industry.

BY ALEXANDRA WITZE

The US government is considering policy changes that could dramatically affect how researchers handle equipment and information that have national-security implications. Among other impacts, scientists would need to reconsider what they can discuss with graduate students from other countries, or when travelling abroad on work trips.

One set of rules would affect technologies such as infrared detectors, which are commonly used for environmental and other types of monitoring but can fall under military restrictions because of their night-vision capabilities. Another set of proposed rules would revise the government definition of "fundamental research" in ways that could affect any scientist who

collaborates with industrial partners.

The proposals are part of a long-running effort to overhaul Byzantine regulations that seek to prevent certain information and technologies from reaching countries perceived to be hostile by the United States. These 'export control' rules can create a major — even perilous — headache for US researchers. In 2012, a plasma engineer at the University of Tennessee in Knoxville began serving a four-year jail sentence for violating these rules by working with graduate students from China and Iran while on a US Air Force contract.

Public-comment periods on the proposed rules close on 6 July and 3 August, and science groups are trying to raise awareness of what is at stake. "Once the rules get put in place, it's very hard to dial back if you find them overly aggressive," says Gregory Quarles, a physicist

MOISES SAMAN/MAGNUM

and board member of the Optical Society, a professional organization in Washington DC that is encouraging its members to study the rules and weigh in with any concerns.

Export control covers both physical equipment that leaves the United States — such as spacecraft components on their way to a launch site, or a laptop computer carrying sensitive information to a conference — and information conveyed to someone from another country. There are two parallel lists that describe which items are controlled, one maintained by the US Department of State and the other by the Department of Commerce. Over the past five years, regulators have been working to relax the system, moving some items from the restrictive state-department list — commonly known as ITAR, for International Traffic in Arms Regulations — to the less tightly controlled commerce-department list. But they have left some of the hardest topics for last.

On 5 May, the departments released the first set of long-awaited proposals for regulating the category that includes sensors and night-vision equipment. Many researchers hoped these would loosen current regulations that they say have impeded research, but that does not seem to be the case. The rules specify performance parameters, such as wavelengths for infrared cameras, that would continue to restrict commercially available sensors that are popular

with many researchers for environmental, medical and other applications.

At the University of Rochester in New York, astronomer Judith Pipher develops infrared detectors to observe the cosmos, which are regulated under ITAR because military night-vision goggles also use infrared sensors. Astronomical sensors detect radiation that is one million times less intense than that detected by

“We’ve heard from at least a few institutions that this will totally stifle their ability to work with industry.”

the military, but neither the current nor the proposed rules take that into account. “I don’t think this particular reform is going to get us there,” says Pipher, who, before she acquired US citizenship, was once

barred from seeing data gathered by infrared instruments that her team was testing. The second set of proposed rules could have wider-reaching consequences. It aims to harmonize state and commerce department definitions of terms such as “fundamental research” and “public domain”.

In general, the rules state that information developed through fundamental research is considered to be in the public domain and not subject to ITAR controls. But one newly added phrase says that if the research is subject

to proprietary review before being published, such as by a company that sponsored the work, then it falls under ITAR.

“We’ve heard from at least a few institutions that this will totally stifle their ability to work with industry,” says Tobin Smith, vice-president for policy at the Association of American Universities in Washington DC.

Any university researcher who has a contract or sponsored research agreement with a company could face a huge load of paperwork. “It will fundamentally change the way we do business,” says Elizabeth Peloso, associate vice-president and associate vice-provost for research services at the University of Pennsylvania in Philadelphia.

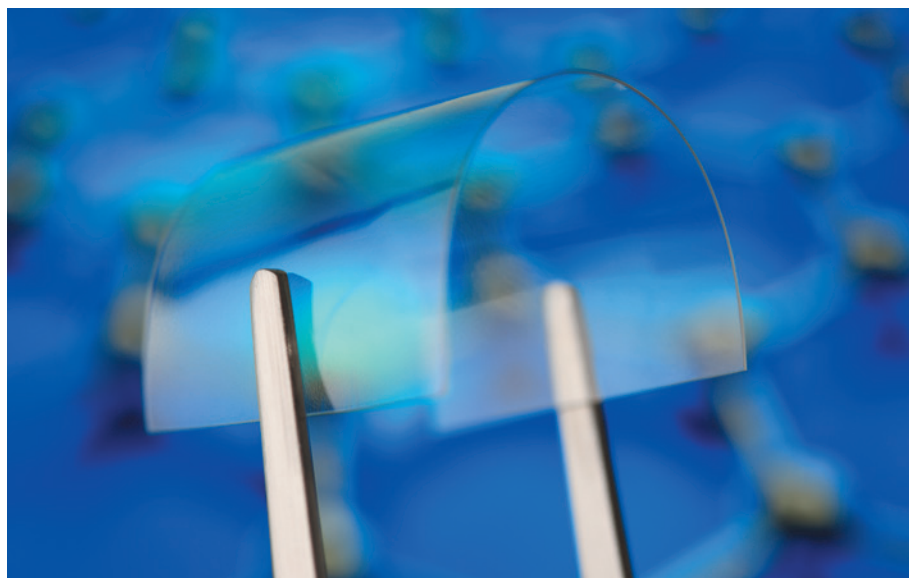
The new rules would add some needed changes, she adds, such as clarifying that a US researcher can e-mail data to a collaborator elsewhere in the world, as long as those data are encrypted.

After the comment periods close, the state and commerce departments will either issue another round of interim rules for more feedback, or publish whatever final regulations they decide on.

“You asked for reforms, so now you got it,” says Kevin Wolf, who oversees the export control reform effort at the commerce department. “If you’re an export nerd, now is an exciting time.” ■

Graphene booms in factories but lacks a killer app

Although the wonder material is being made in record volume, commercial success is elusive.



Graphene films can be used as transparent electrodes for touchscreens.

BY MARK PELOW

The city of Manchester, UK, is gearing up for a graphene jamboree. Graphene Week 2015, which kicks off on 22 June, is sure to delight its more than 600 attendees with a conference and celebrations of the 'wonder material'. Graphene's commercial future, however, is much less certain.

The atom-thin flakes of carbon are being produced in record volume and have found their way into a handful of eye-catching gizmos. But experts fret that graphene production far exceeds requirements, and that the material offers only marginal benefits over incumbent technologies in many of its target applications.

"There's a heck of a lot of production capacity and not much demand, because we just haven't

seen any compelling technologies coming through," says Ross Kozarsky, a senior analyst at market-intelligence company Lux Research, who is based in San Francisco, California.

This mirrors the trajectory of carbon nanotubes, which were once touted as transformative but have so far failed to make a significant commercial impact. "Graphene looks much closer to the next carbon nanotube than the next silicon," says Kozarsky. In a 2014 report, Lux predicted that the global market for graphene would be worth US\$349 million by 2025; by comparison, the University of Manchester estimates that graphene has already attracted \$2.4 billion for research (see 'Market growth').

Some scientists are growing frustrated that companies are not lining up outside their offices begging to use the material, says Helena

Theander, innovation deputy at the European Union's €1-billion (US\$1.1-billion) Graphene Flagship research programme, which was set up in 2013 to usher graphene from the lab to the marketplace within a decade.

Researchers have been in thrall to graphene's properties ever since the material was first isolated by the University of Manchester's Andre Geim and Konstantin Novoselov (K. S. Novoselov *et al. Science* **306**, 666–669; 2004) — who won the 2010 Nobel Prize in Physics for their work. Graphene is transparent and flexible, yet very strong; electrons zoom through it; and it conducts heat ten times better than copper. Enthusiasts expect these qualities to propel graphene into dozens of commercial applications, from flexible electronics to strong, lightweight composites.

GRAPHENE GLUT

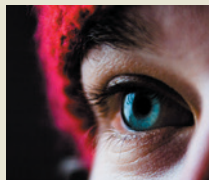
This has sparked a graphene-making frenzy, particularly in China (see 'Manufacturing fever'), where the government has poured investment into some half a dozen 'graphene industry parks', which host research institutes and business incubators side by side. Manufacturers enjoy reduced infrastructure costs, and are not expected to repay government grants. The graphene mass-produced in China falls broadly into two categories: thin films that can be used as transparent electrodes for touchscreens, for example, replacing the brittle indium tin oxide (ITO) used today; and nanoplatelets, stacks of graphene flakes that form a black powder targeted at applications such as battery electrodes, in which their high surface area may help to store more charge.

Products are starting to appear. Last year, AWIT in Wuxi, China, brought 2,000 graphene-touchscreen phones to market, and in March, Galaxy Microsystems of Shenzhen,

VINCENZO LOMBARDO/GETTY


**MORE
ONLINE**

TOP STORY



Can the human eye detect a single photon?
go.nature.com/syqcae

MORE NEWS

- The image detective who roots out manuscript flaws go.nature.com/n8ibch
- Vaccine hope for post-traumatic stress go.nature.com/rxjjpe
- How gravity prevents quantum superposition on large scales go.nature.com/5cqyhz

NATURE PODCAST



Positive memories help depression, plant intelligence, and measuring the mass of exoplanets
nature.com/nature/podcast

GABE ROGEL/AURORA CORBIS

China, released 30,000 phones that use graphene in their touchscreens, cases and batteries (see 'Batteries and phones rule'). But Kozarsky says that some nanoplatelet producers are selling their product at below cost to offload their surplus. And although graphene-film factories have quoted impressive-sounding figures on capacity, these are sometimes used as a "marketing tool", says Guocai Dong, vice-dean of the JiangNan Graphene Research Institute, which is in the Changzhou graphene park. "Most of the capacity is not used," he says.

One reason for the mismatch is that graphene films still do not beat ITO on price. The films are grown on hot copper foil from a feedstock of methane gas mixed with hydrogen, in a process called chemical vapour deposition (CVD). Dong says that heating the foil, maintaining clean rooms and separating graphene from the foil tend to push the final cost above 400 yuan (US\$64) per square metre, about twice what it needs to be to compete with ITO. And although graphene's flexibility could add value to wearable devices, the wonder material will have to beat off other pretenders to ITO's throne, including silver-nanowire meshes, which have been in development for longer.

A new approach to manufacturing is needed to depress costs further, says Xuesong Li, who helped to develop the copper-foil CVD method (X. Li *et al.* *Science*, **324**, 1312–1314; 2009). Last year, Li founded LasLumin, a company in New York City that aims to slash graphene manufacturing costs by using feedstocks that are easier to handle than the potentially explosive mixture of methane and hydrogen. Graphene films may find more-profitable applications in innovative chemical sensors, rather than in taking on an established material such as ITO, he adds.

FROM LAB TO MARKET

China also dominates the graphene patent landscape (see 'Patent kings'). SIO Grafen, an innovation programme in Gothenburg, Sweden, that supports industrial graphene development, reported in March that Chinese entities hold 45% of all graphene patents granted in the seven categories that it surveyed. That is more than twice the share of China's nearest rival, the United States. However, most of the Chinese patents are registered nationally rather than globally, and they tend to be cited less often than the US ones, suggesting that they may not have much impact on graphene's long-term commercial development.

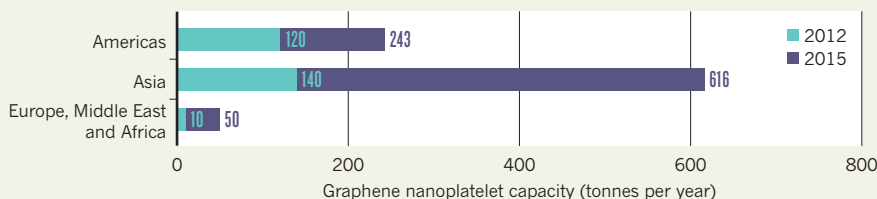
Enter the Graphene Flagship, which plans to focus on quality and innovation. With that in mind, Theander has run seven Graphene Connect workshops to introduce small and medium-sized companies to graphene researchers, and will host another during Graphene Week. But she says it is too soon for concrete results: "Growing trust and new relationships takes time, so I imagine it will take a couple of years until we have true success stories."

A similar approach has proved successful

THE GRAPHENE COUNT

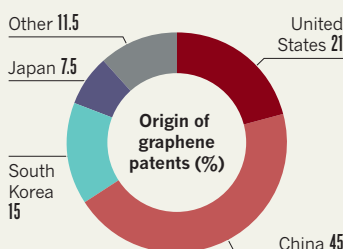
Manufacturing fever

Graphene production capacity has exploded in Asia, driven mainly by China.

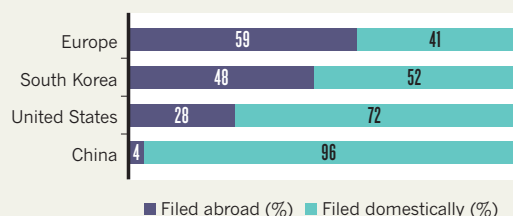


Patent kings

China dominates the graphene patent landscape in key fields, but its patents are overwhelmingly domestic and may have little global impact.

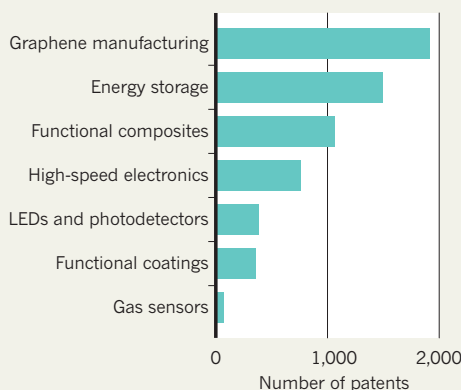


Where patents are filed



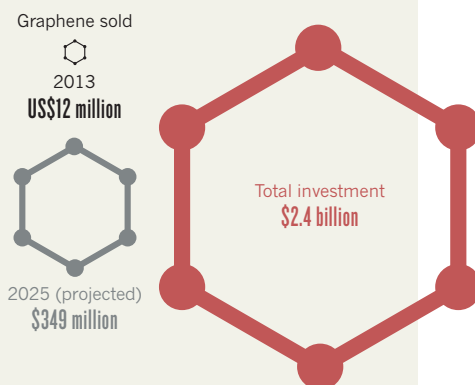
Batteries and phones rule

The most patents filed for graphene applications concern energy storage and composite materials.



Market growth

Investment committed to graphene research so far dwarfs even the raw material's projected sales in 2025.



at the University of Manchester's National Graphene Institute (NGI), says its business director, James Baker. The NGI has almost 40 industrial partners who have funded work at the university; the biggest, BGT Materials in Manchester, has a subsidiary called Graphene Lighting that unveiled a 'graphene light bulb' in March. The bulb is actually a conventional light-emitting diode (LED) coated with a transparent film of graphene that draws off heat more effectively than conventional metal components, improving the efficiency and longevity of the LED. The company hopes that the bulb will go on sale in the next few months.

Meanwhile, Baker notes, multinational sports-equipment company Head has unveiled a range of tennis rackets that are strengthened by a dash of graphene in their frames.

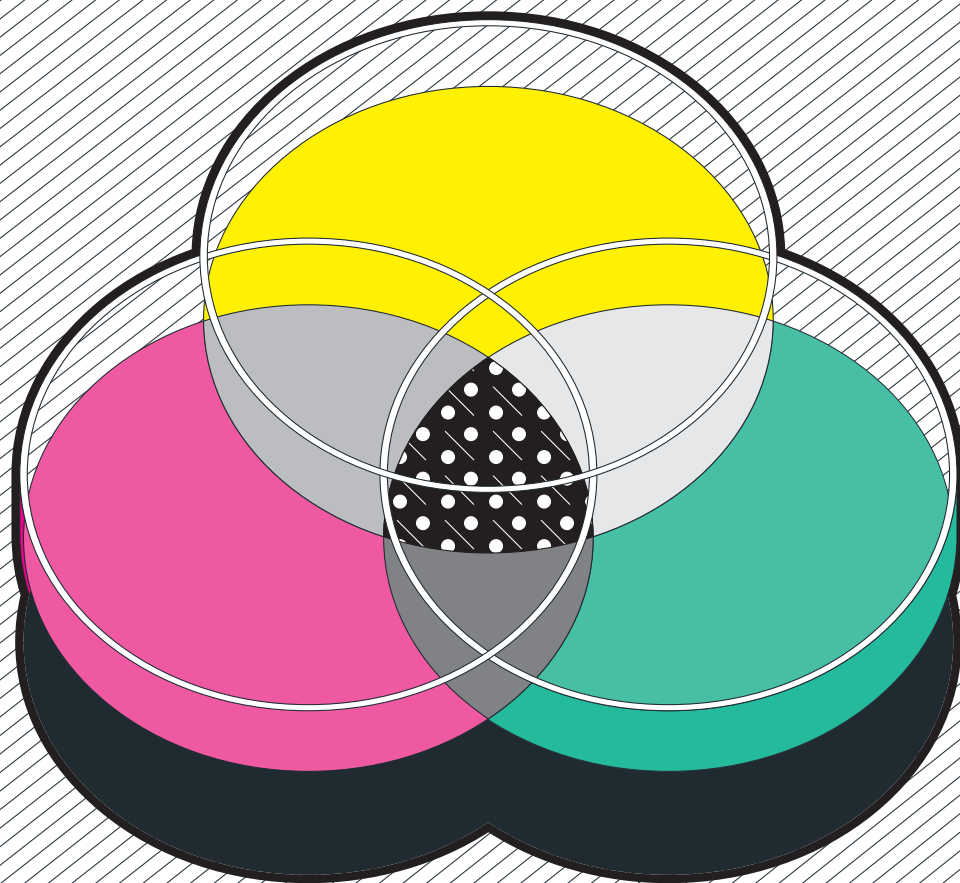
Such niche applications are a start, but if graphene is to fulfil the commercial potential anticipated by projects such as the Graphene

Flagship, it will need to find a role in which it dramatically and reliably outperforms existing technologies at a reasonable cost.

Baker believes that the answer lies in creating devices that rely on a combination of graphene's properties — flexible electronics, for example — or that could have a transformative global impact, such as in membranes that desalinate water. But it is early days, he says: "There are so many potential applications that it's difficult to see what will be the killer app." ■ SEE NEWS FEATURE P.274 AND BOOKS & ARTS P.284

CORRECTION

The News story 'Start-ups fight for a place in Boston's biotech hub' (*Nature* **522**, 138–139; 2015) misstated prices for lab and office space in Kendall Square; the figures reflect annual rather than monthly rents.



ILLUSTRATIONS BY THOMAS POROSTOCKY

MINING THE MICROBIAL DARK MATTER

Microbiologists are finding new ways to explore the vast universe of unknown microbes in the hunt for antibiotics.

BY CORIE LOK

The first time Robert Heinzen tried to get *Coxiella burnetii* to grow by itself, he failed miserably. The bacterium, which causes an influenza-like illness called Q fever, normally divides only inside the cells it infects — forcing researchers to grow it in mammalian tissue and hampering their efforts to investigate the microbe. When Heinzen tried to find a different way to culture it during his time as a postdoc in the early 1990s, he emerged with only half a book of scribbled notes.

But the problem kept nagging at him until 2003, when the *C. burnetii* genome was sequenced¹ and he was starting a lab at the US National Institutes of Health's Rocky Mountain Laboratories in Hamilton, Montana. Heinzen thought that the genome could offer important clues to the bacterium's metabolism and growth. Even so, it took his postdoc Anders Omsland almost four years of systematically testing hundreds of combinations of culture conditions to come up with the perfect recipe for cultivating the microbe outside cells². "When he showed me the cultures, I thought, it's got to be a contaminant," Heinzen recalls. But several more months of work confirmed their success.

Coxiella burnetii is still in the minority. An estimated 85–99% of bacteria and archaea

cannot yet be grown in the lab, drastically limiting scientists' knowledge of microbial life and holding back the search for new antibiotics, which tend to be derived from bacteria. That search is becoming more urgent as resistance to existing drugs surges: last month, the World Health Organization approved a global plan to combat antibiotic resistance, and a review panel appointed by the UK government called for a £1.3-billion (US\$2-billion) investment from the global drug industry to revitalize antibiotic research. To find new drugs, researchers say that they need alternative ways to investigate the array of uncultured organisms — the mysterious dark matter of the microbial world.

Scientists are already taking steps towards this goal. Advances in cultivation methods and other technologies have helped them to grow previously unculturable microbes, and improved DNA sequencing and bioinformatics are allowing them to examine some microbes without needing to grow them at all. The work has uncovered a breathtaking amount of microbial diversity in samples ranging from soil to permafrost, marine sponges, hydrothermal vents and the crevices of the human body. Some of the discoveries are already pointing to possible antibiotics — and scientists say that they are only just scratching the surface.

"There is, for sure, high potential for more biodiversity to be discovered," says Ute Hentschel, a marine microbiologist at the University of Würzburg in Germany. "If you look for more, you'll find more."

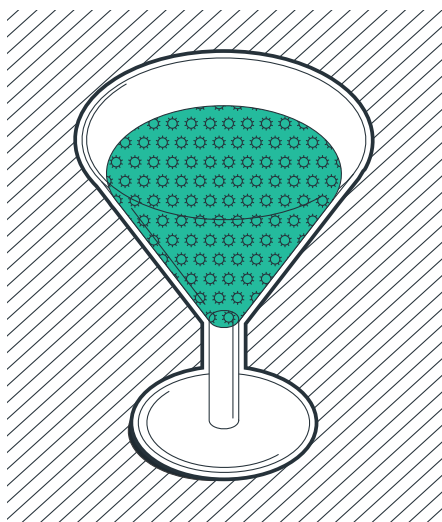
CULTURE COCKTAIL

Conventionally, biologists have studied microbes by growing pure cultures of a species in fairly standard sets of nutrients. The trouble is that bacteria do not live like that in nature: they inhabit a huge range of environments, usually alongside other organisms, and scientists have struggled to recreate those conditions. But as Heinzen and Omsland showed with their studies on *C. burnetii*, genetic sequences can throw open a door.

Omsland used sequencing to compare the genes expressed when the bacteria were growing successfully inside host cells with those expressed when they were struggling to grow alone. He found a suite of genes involved in protein synthesis that were less active in the struggling microbes, a hint that adding amino acids and peptides to the growth medium might help the bacterium to thrive. But even when Omsland managed to increase the bacterium's protein synthesis 13-fold, it still would not divide².

The final clue came from genes suggesting that *C. burnetii* could survive in low-oxygen environments. When the team placed the microbe in 5% oxygen or less, they finally saw it grow. "That was the critical finding," says Heinzen. "It wasn't a nutrient, it was an environmental factor."

Since adopting the new 'axenic' or



"THAT WAS THE CRITICAL FINDING. IT WASN'T A NUTRIENT, IT WAS AN ENVIRONMENTAL FACTOR."

host-cell-free culture technique, the *C. burnetii* field has expanded. By selectively turning genes on and off, researchers have learned about how the bacterium interacts with host cells to infect them and divide. "The ability to grow *Coxiella* axenically has, without any exaggeration, completely revolutionized this field of study," says Hayley Newton, a microbiologist and *Coxiella* researcher at the

University of Melbourne in Australia. The bacterium is highly transmissible through air and is considered a possible biothreat. Heinzen's lab is now working on making strains in which key virulence genes have been inactivated, in the hope that they might be useful in developing vaccines.

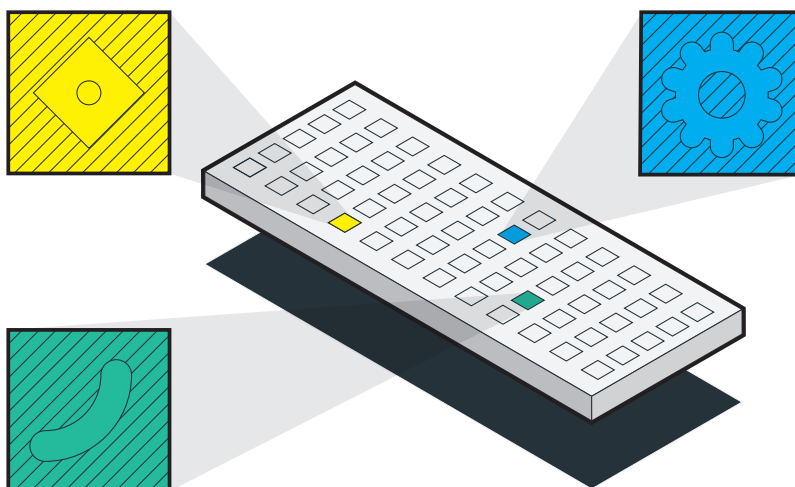
Researchers are now designing culture systems for other microbes that grow only inside cells. Omsland, now at Washington State University in Pullman, has developed a cell-free culture system for *Chlamydia trachomatis*³, the pathogen behind one of the most common sexually transmitted diseases. He has not yet coaxed *Chlamydia* to divide in his medium, but "I was born optimistic," he says — and his success with *C. burnetii* fuels his hope.

MINIATURIZED CULTURES

One way to speed up the process of finding a culture recipe is to use microfluidic chips — devices with thousands of tiny wells connected by channels that make it possible to run many experiments in parallel. After using this method to cultivate a new microbe⁴, Rustem Ismagilov at the California Institute of Technology in Pasadena and his collaborators even named the bacterium isolate microfluidicus 1.

Ismagilov was already working on microfluidics when, in 2012, a group of microbiologists issued a list of 'most wanted' taxa — a call to the research community to grow and sequence microbes that were relatively common in the human body, were distantly related to already-sequenced organisms and had eluded all attempts at cultivation⁵.

Ismagilov and his team answered the call with a device that holds 3,200 nanolitre-sized wells and that can fit in the palm of a hand. They scraped samples from the gut lining of a healthy volunteer, and then diluted them so that no more than one cell would end up in each well. By filling so many wells, the researchers increased the chances that their target organism — a human-gut microbe in



the *Oscillibacter* genus — would find its way into at least a few of them. The team used about ten chips to test various conditions, and looked for growth of the microbe by checking its DNA for a key marker gene.

They managed to find their bacterium, and then grow it to larger amounts in Petri dishes. It was one of the first members of the wanted list to be cultivated. Further genetic study revealed that isolate microfluidicus 1 was not actually part of the *Oscillibacter* genus; it had been classified incorrectly and was actually part of a new, related group that the team is now working to characterize.

A key ingredient for growing this bacterium, the team found, was a dash of fluid that had been extracted from the volunteer's intestine. Being able to stretch the use of such a precious sample across thousands of experiments is an important advantage of the microfluidics approach, says Ismagilov. Another is that each starting cell does not have to compete with other species. "Microfluidics allows us to identify culture conditions efficiently and then increase our chances that our target will grow," he says.

Xiaoxia Nina Lin, a chemical engineer at the University of Michigan in Ann Arbor, is using microfluidics to hunt down members of the most-wanted list in human faecal samples. Microbes normally live in complex communities and often rely on other species, so Lin is trying to dissect those relationships by putting two, three or four cells together in myriad combinations on a chip, and working out who is dependent on whom. "It's a good engineering approach," says Vincent Young, an infectious-disease researcher at the University of Michigan who is helping Lin to obtain clinical samples. "You can quickly reduce the complexity."

NATURE'S INCUBATOR

When Slava Epstein and Kim Lewis started to collaborate 15 years ago, they realized that they might not need to coax recalcitrant microbes into growing in the lab. If a bacterium already grows happily in its natural environment, they reasoned, then why not just cultivate it there? So the two microbiologists, from Northeastern University in Boston, Massachusetts, started working on a simple device that they could stick in the ground. They called it the iChip.

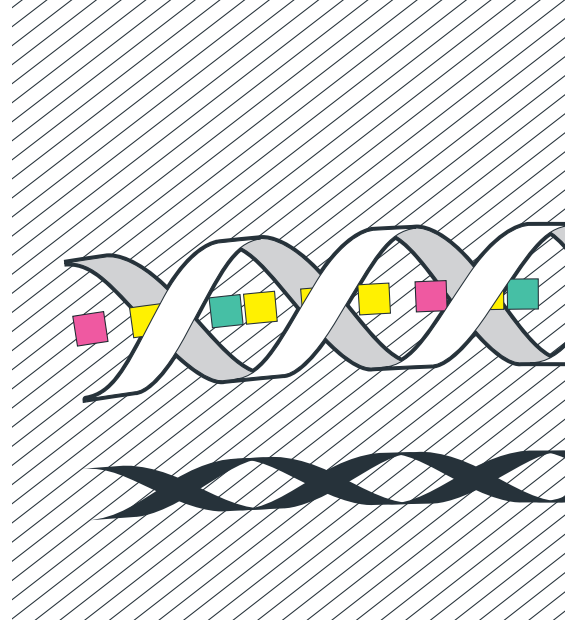
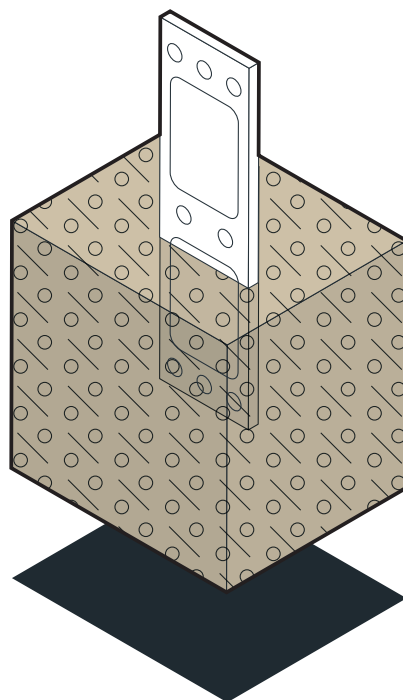
The approach paid off earlier this year, when Lewis, Epstein and scientists from their start-up company NovoBiotic Pharmaceuticals in Cambridge, Massachusetts, reported that they had used the iChip to isolate a new bacterial species from soil⁶. The thumb-sized device is less sophisticated than a microfluidics chip: it consists of 384 tiny wells that were filled with samples of soil that have been mixed with agar and diluted to ensure that only one cell ends up in each chamber. The chip is sealed with a membrane that traps the bacteria but allows molecules to diffuse back and forth, and was planted in a grassy field in Maine — the same

soil from which the sample had been taken.

After a month, the researchers transferred colonies from the chip to Petri dishes in the lab, took extracts from them and screened those for antibiotic activity. They had grown 10,000 types of bacterium — many more than if they had just put the soil sample on an agar plate. They homed in on a new species that they called *Eleftheria terrae*⁶ and found that the bacterium produces an antibiotic, called teixobactin, that kills various human pathogens in the lab, including drug-resistant strains of *Staphylococcus aureus*. "To me that's a phenomenal result, that they can find really neat new molecules from groups of organisms that pharma largely hasn't focused on," says Sean Brady, a chemical biologist at Rockefeller University in New York.

But what generated headlines was the discovery that other bacteria did not develop resistance to teixobactin⁶, as they do to most other antibiotics. That is because teixobactin binds to molecules that have important roles in cell-wall synthesis; bacteria are not known to modify these molecules to evade the effects of antibiotics. The clincher, Lewis says, is that although *E. terrae* is inherently resistant to the teixobactin, it does not seem to have resistance genes that could be transferred easily to other bacteria. This does not mean that resistance will never emerge, but that it could take 20 or 30 years.

The NovoBiotic team went on to grow larger quantities of the bacterium. It is now generating grams of the drug using a fermenter, doing extensive preclinical testing of this and other drug candidates, and seeking more leads from uncultivated microbes in soil and marine samples. Epstein is using the iChip to culture new microbes from soil and water in Greenland,



and says that he has received more than 200 requests this year for the device and advice on how to use it.

DON'T CULTURE, SEQUENCE

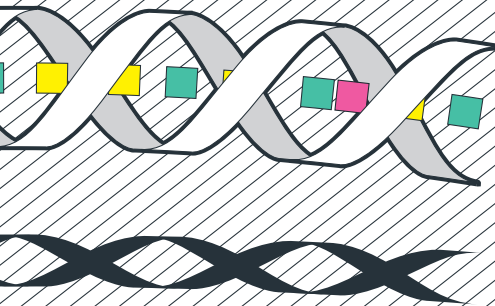
Despite these successes, culturing microbes is still a complicated, hit-and-miss affair, so many researchers are bypassing it altogether and instead learning what they can from DNA. Advances in sequencing methods mean that scientists can now analyse genomes from individual uncultured microbial cells — rather than, as before, typically sequencing a community of many different types of microbe en masse and then trying to piece the sequences back together.

Tanja Woyke at the US Department of Energy's Joint Genome Institute in Walnut Creek, California, first got interested in single-cell sequencing not long after the key discovery ten years ago that an enzyme from a bacteria-infecting virus could be used to make many copies of a bacterial cell's genome⁷. Woyke wanted to use the tools to fill out the microbial tree of life.

She and her group collected samples from nine different habitats, including sediment from a Nevada hot spring and water near a Pacific hydrothermal vent. They isolated some 200 cells, sequenced the genome of each one and classified the cells into more than 20 new lineages that do not have any cultivated representatives⁸. "They were the first to really take single-cell genomics to the next level, in terms of the number of sequences and single cells analysed," says Hentschel.

Last year, Jörn Piel of the Swiss Federal Institute of Technology in Zurich and his colleagues reported that they had used single-cell sequencing and other techniques to identify uncultured bacteria in marine sponges⁹. These filter-feeding creatures have long been of interest to scientists because they produce a rich set of chemicals with anticancer, antibiotic and other medicinal properties. They also harbour dense microbial communities that contribute up to 40% of the sponge's mass and were suspected to be the source of these chemicals. But the members of those communities had not been cultured.

Piel and his group focused on the sponge



“THEY WERE THE FIRST TO REALLY TAKE SINGLE-CELL GENOMICS TO THE NEXT LEVEL.”

Theonella swinhoei, which harbours about 1,000 types of bacterium and generates dozens of known bioactive compounds. In 2011, they started to sequence DNA from individual bacterial cells isolated from sponge samples and looked for two gene clusters known to be involved in the production of biologically active molecules. They found these genes in a bacterium called *Entotheonella*⁹.

What was most surprising to Piel, however, was that this one organism was responsible for nearly all of the bioactive compounds linked to the sponge — something that became clear when sequence data showed that the bacterium harboured all the necessary genes. When Piel received the key data from his collaborators, “I

almost fell out of my chair,” he says; it was the first evidence that an uncultivated microbe can be such a ‘talented’ producer of bioactive chemicals. “The ability to create many distinct compounds in a single strain, this is not that common,” he says.

Piel’s lab is now trying to engineer gene clusters from *Entotheonella* into a culturable organism such as *Escherichia coli* so that the host can churn out the compounds, something that is not likely to be easy given that biosynthetic genes can be large. He is also mining the genomes of microbes in sponges from Japan, Papua New Guinea and Israel in search of other bacterial super-producers.

GENE PROSPECTING

Michael Fischbach, a biochemist at the University of California, San Francisco, has developed a different way to analyse microbial sequences: rather than isolating single cells, he sifts through the growing banks of bacterial genomic data.

Fischbach and his group developed a machine-learning algorithm that is trained to recognize key patterns associated with bacterial genes that synthesize interesting molecules such as antibiotics. Then they let it loose on a large set of bacterial genomes to look for new gene clusters with similar features.

Their targets included bacteria from soils and oceans, which are known to harbour an incredible diversity of microbes. But the algorithm generated a surprising number of hits from microbes that live on or in the human body, known collectively as the human microbiota. Fischbach was both excited and intimidated when he got the first results. Excited, because the bioactive compounds made by the microbiota were largely uncharted territory, and could have important roles in human health and disease. Intimidated because Fischbach mostly worked on microorganisms in soil.

Still, Fischbach decided to take the plunge, and has since switched his entire lab’s focus to the human microbiome. Using an improved version of the algorithm, his team went prospecting in the genomes of almost 2,500 organisms in the human body¹⁰, and found more than

14,000 biosynthetic gene clusters. “It has been remarkably easy to find interesting molecules from the human microbiome,” says Fischbach. “It’s so easy that I can tell it has nothing to do with our ability to find them, it’s more that there’s just a lot to find.”

The group narrowed down the list to more than 3,000 common gene clusters, and found that one generated an antibiotic, lactocillin, made by a microbe commonly found in the vagina. It is one of only a handful of bioactive chemicals isolated from the human microbiota. Lactocillin blocks the growth of common vaginal pathogens such as *S. aureus*, but not of other bacteria that normally inhabit the vagina. Fischbach is now generating the molecules from the gene clusters he is finding, solving their structures, and working with collaborators to learn more about their function.

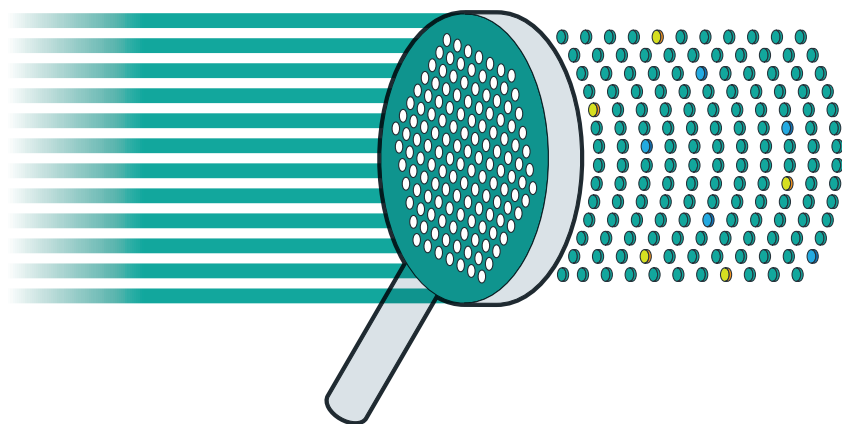
The natural-products field has tended to focus on soil and marine microorganisms rather than on human ones, says Gerry Wright, a chemical biologist at McMaster University in Hamilton, Canada. “I think it’s a great idea to look at those genes and clusters,” he says. However, turning such compounds into usable drugs will require a lot of preclinical work, says Wright. “Just by looking at a molecule, it’s almost impossible to tell whether it’s going to be suitable as a drug.” And even if it seems promising, the barriers to commercializing a new antibiotic are high (see M. Woolhouse and J. Farrar *Nature* **509**, 555–557; 2014).

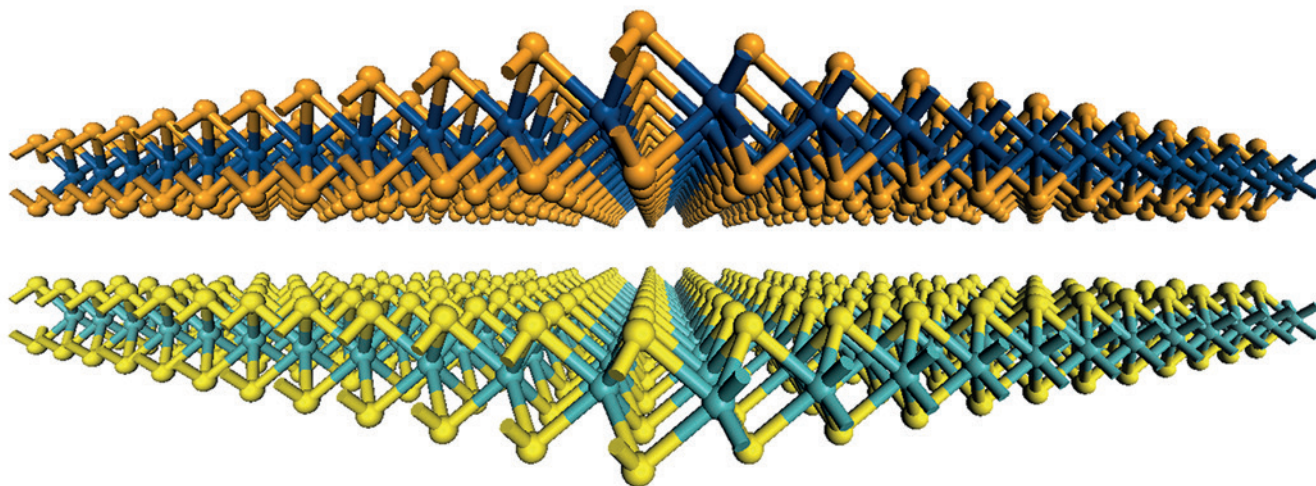
But Lewis takes hope from the recent progress. With all the burgeoning efforts to culture and analyse uncultured microbes, he is already imagining what could be discovered if such efforts were scaled up. He hopes to see a level of drug discovery to match that in the Waksman era, the time in the 1940s and 1950s when Nobel-prizewinning microbiologist Selman Waksman discovered more than 20 antibiotics by systematically screening thousands of soil microbes for their ability to block the growth of other bacteria.

“The fact that we’re finding compounds with such remarkably interesting modes of action that we haven’t seen before, that’s the most interesting part,” says Lewis. “We’ve scratched only a tiny part of Mother Earth.” ■

Corie Lok is Nature’s Research Highlights editor.

1. Seshadri, R. *et al. Proc. Natl Acad. Sci. USA* **100**, 5455–5460 (2003).
2. Omsland, A. *et al. Proc. Natl Acad. Sci. USA* **106**, 4430–4434 (2009).
3. Omsland, A., Sager, J., Nair, V., Sturdevant, D. E. & Hackstadt, T. *Proc. Natl Acad. Sci. USA* **109**, 19781–19785 (2012).
4. Ma, L. *et al. Proc. Natl Acad. Sci. USA* **111**, 9768–9773 (2014).
5. Fodor, A. A. *et al. PLoS ONE* **7**, e41294 (2012).
6. Ling, L. L. *et al. Nature* **517**, 455–459 (2015).
7. Raghunathan, A. *et al. Appl. Environ. Microbiol.* **71**, 3342–3347 (2005).
8. Rinke, C. *et al. Nature* **499**, 431–437 (2013).
9. Wilson, M. C. *et al. Nature* **506**, 58–62 (2014).
10. Donia, M. S. *et al. Cell* **158**, 1402–1414 (2014).





SOURCE: H. TERRONES ET AL. SCIENCE 341, 1549 (2013)

2D OR NOT 2D

A wave of innovative flat materials is following in the wake of graphene — but the most exciting applications could come from stacking them into 3D devices.

BY ELIZABETH GIBNEY

Physicists have used almost every superlative they can think of to describe graphene. This gossamer, one-atom-thick sheet of carbon is flexible, transparent, stronger than steel, more conductive than copper and so thin that it is effectively two-dimensional (2D). No sooner was it isolated in 2004 than it became an obsession for researchers around the world.

But not for Andras Kis. As miraculous as graphene was, says Kis, “I felt there had to be more than carbon.” So in 2008, when he got the chance to start his own research group in nanoscale electronics at the Swiss Federal Institute of Technology in Lausanne (EPFL), Kis focused his efforts on a class of super-flat materials that had been languishing in graphene’s shadow.

These materials had an ungainly name — transition-metal dichalcogenides (TMDCs) — but a 2D form that was quite simple. A single sheet of transition-metal atoms such as molybdenum or tungsten was sandwiched between equally thin layers of chalcogens: elements, such as sulfur and selenium, that lie below oxygen in the periodic table. TMDCs were almost as thin, transparent and flexible as graphene,

says Kis, but “somehow they got a reputation as not that interesting. I thought they deserved a second chance.”

He was right. Work by his team and a handful of others soon showed that different combinations of the basic ingredients could produce TMDCs with a wide range of electronic and optical properties. Unlike graphene, for example, many TMDCs are semiconductors, meaning that they have the potential to be made into molecular-scale digital processors that are much more energy efficient than anything possible with silicon.

Within a few years, laboratories around the world had joined the 2D quest. “At first it was one, then two or three, and suddenly it became whole zoo of 2D materials,” says Kis. From a scattering of publications in 2008, 2D TMDCs alone now generate six publications each day. Physicists think that there may be around 500 2D materials, including not just graphene and TMDCs, but also single layers of metal oxides, and single-element materials such as silicene and phosphorene. “If you want a 2D material with a given set of properties,” says Jonathan Coleman, a physicist at Trinity College Dublin, “you will find one.”

Ironically, one of the most exciting frontiers in 2D materials is

Stacks of multiple kinds of flat materials can exploit the best properties of each.

stacking them into structures that are still very thin, but definitely 3D. By taking advantage of the vastly different properties of various super-flat materials, it should be possible to build entire digital circuits out of atomically thick components, creating previously unimagined devices. Applications are already being touted in fields from energy harvesting to quantum communications — even though physicists are just beginning to learn the materials' potential.

"Each one is like a Lego brick," says Kis. "If you put them together, maybe you can build something completely new."

ADVENTURES IN FLATLAND

A material that is just a few atoms thick can have very different fundamental properties from a material made of the same molecules in solid form. "Even if the bulk material is an old one, if you can get it into 2D form it opens up new opportunities," says Yuanbo Zhang, an experimental condensed-matter physicist at Fudan University in Shanghai, China.

Carbon is the classic example, as physicists Andre Geim and Konstantin Novoselov found in 2004 when they first reported isolating graphene¹ in their laboratory at the University of Manchester, UK. Their technique was almost absurdly simple. The basic step is to press a strip of sticky tape onto a flake of graphite, then peel it off, bringing with it a few of the atom-thick layers that make up the bulk material. By repeating this process until they had single layers — which many theorists had said could not exist in isolation — Geim and Novoselov were able to start investigating graphene's remarkable properties. Their work won them the 2010 Nobel Prize in Physics.

Physicists were soon hurrying to exploit those properties for applications ranging from flexible screens to energy storage (see page 268). Unfortunately, graphene proved to be a poor fit for digital electronics. The ideal material for that application is a semiconductor — a material that does not conduct electricity unless its electrons are boosted with a certain amount of energy from heat, light or an external voltage. The amount of energy needed varies with the material, and is known as the band gap. Turning the material's conductivity on and off creates the 1s and 0s of the digital world. But graphene in its pure form does not have a band gap — it conducts all the time.

Still, Geim and Novoselov's success in making graphene spurred them, Kis and many others to start investigating alternative 2D materials that could have a band gap². They began with TMDCs, which had been studied in bulk form since the 1960s. By 2010, Kis's team had built its first single-layer transistor³ from the TMDC molybdenum disulfide (MoS_2 ; see 'Flat-pack assembly'), speculating that such devices could one day offer flexible electronics whose small component size and low voltage requirements would mean that they consumed much less power than conventional silicon transistors. Being semiconducting was not their only advantage. Studies in 2010 showed that MoS_2 could both absorb and emit light^{4,5} efficiently, making it — and probably other TMDCs — attractive for use in solar cells and photodetectors.

A single layer of TMDCs can capture more than 10% of incoming photons, an incredible figure for a material three atoms thick, says Bernhard Urbaszek, a physicist at the Physics and Chemistry of Nano-Objects Laboratory in Toulouse, France. This also helps them in another task: converting light into electricity. When an incoming photon hits the three-layer crystal, it boosts an electron past the band gap, allowing it to move through an external circuit. Each freed electron leaves behind a kind of empty space in the crystal — a positively charged 'hole' where an electron ought to be. Apply a voltage, and these holes and electrons circulate in opposite directions to produce a net flow of electric current.

This process can also be reversed to turn electricity into light. If electrons and holes are injected into the TMDC from an outside circuit;

when they meet, they recombine and give up their energy as photons.

This ability to convert light to electricity and vice versa makes TMDCs promising candidates for applications that involve transmitting information using light, as well as for use in tiny, low-power light sources and even lasers. This year, four different teams demonstrated the ultimate control over light emission, showing that the TMDC tungsten diselenide (WSe_2) could absorb and release individual photons^{6–9}. Quantum cryptography and communications, which encode information in one photon at a time, need emitters like this, where you "press a button and get a photon now", says Urbaszek. Existing single-photon emitters are often made of bulk semiconductors, but 2D materials could prove smaller and easier to integrate with other devices. Their emitters are necessarily on the surface, which could also make them more efficient and easier to control.

Even as researchers were getting to grips with TMDCs, theorists were seeking other materials that could be engineered in two dimensions. One obvious candidate was silicon, which sits right below carbon in the periodic table, forms chemical bonds in a similar way, has a natural band gap and is already widely used in the electronics industry. Calculations suggested that, unlike graphene, a sheet of atomically thick silicon would have a ridged structure that could be squashed and stretched to create a tunable band gap. But like graphene, this 'silicene' would be a much faster conductor of electrons than most TMDCs.

Unfortunately, theory also suggested that a 2D sheet of silicene would be highly reactive and completely unstable in air. Nor could it be ripped from a crystal like other 2D materials: natural silicon exists only in a 3D form analogous to a diamond crystal, with nothing resembling the layered sheets of carbon found in graphite.

"People said it was insane and would never work," says Guy Le Lay, a physicist at Aix-Marseille University in France. But Le Lay, who had been growing metals on silicon surfaces for years, saw a way to make silicene by doing the reverse — growing atomically thin sheets of silicon on metal. And in 2012 he reported success¹⁰: he had grown layers of silicene on silver, which has an atomic structure that matches the 2D material perfectly (see *Nature* **495**, 152–153; 2013).

Buoyed by that effort, Le Lay and others have since moved down the carbon column of the periodic table. Last year, he demonstrated a similar technique to grow a 2D mesh of germanium atoms — germanene — on a substrate of gold¹¹. His next target is stanene: a 2D lattice of tin atoms. Stanene should have a band gap larger than either silicene and germanene, which would allow its devices to work at higher temperatures and voltages. And it is predicted to carry charges only on its outside edges, so

it should conduct with super efficiency. But Le Lay has competition. Although no one has yet reported growing stanene successfully, research groups in China are rumoured to be close.

ELEMENTAL SHIFT

Others are exploring different parts of the periodic table. Zhang's team and another led by Peide Ye at Purdue University in West Lafayette, Indiana, last year described^{12,13} stripping 2D layers of phosphorene from black phosphorus, a bulk form of the element that has been studied for a century. Like graphene, phosphorene conducts electrons swiftly. But unlike graphene, it has a natural band gap — and it is more stable than silicene.

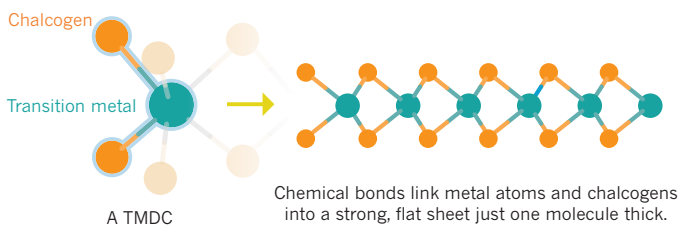
Phosphorene has enjoyed a meteoric rise. At the 2013 meeting of the American Physical Society, it was the subject of a single talk by members of Zhang's group; by 2015, the meeting had three entire sessions devoted to it. But like its fellow pure-element 2D materials, phosphorene reacts very strongly with oxygen and water. If it is to last longer than a few hours, it needs to be sandwiched between layers of other materials. This natural instability makes fabricating devices with the 'enes' difficult; Le Lay estimates that around 80% of the papers about them are still theoretical.

Nonetheless, both Zhang and Ye succeeded in making phosphorene transistors. This year, the first transistor from silicene emerged¹⁴,

**"PEOPLE SAID
IT WAS INSANE
AND WOULD
NEVER WORK."**

FLAT-PACK ASSEMBLY

Transition-metal dichalcogenide (TMDC) crystals contain one transition-metal atom (green) for every two chalcogen atoms (orange). Some 40 such TMDCs — mostly those made with the metals highlighted in dark green in the periodic table — can be split into 2D layers that are flexible, transparent and excellent conductors of electricity. Some are also semiconductors.



H																	He
Li	Be											B	C	N	O	F	Ne
Na	Mg											Al	Si	P	S	Cl	Ar
K	Ca	Sc	Ti	V	Cr	Mn	Fe	Co	Ni	Cu	Zn	Ga	Ge	As	Se	Br	Kr
Rb	Sr	Y	Zr	Nb	Mo	Tc	Ru	Rh	Pd	Ag	Cd	In	Sn	Sb	Te	I	Xe
Cs	Ba	Ln	Hf	Ta	W	Re	Os	Ir	Pt	Au	Hg	Tl	Pb	Bi	Po	At	Rn
Fr	Ra	An	Rf	Db	Sg	Bh	Hs	Mt	Ds	Rg							
		La	Ce	Pr	Nd	Pm	Sm	Eu	Gd	Tb	Dy	Ho	Er	Tm	Yb	Lu	
		Ac	Th	Pa	U	Np	Pu	Am	Cm	Bk	Cf	Es	Fm	Md	No	Lr	

although it survived for only a few minutes. Still, Le Lay is optimistic that these issues are not insurmountable. Just two years ago, he points out, Geim and other physicists were saying that a silicene transistor could not be made with current technology. "So it's always dangerous to predict the future," laughs Le Lay.

THE NEXT DIMENSION

Even as some physicists search for new 2D materials and try to understand their properties, others are already sandwiching them together. “Instead of trying to pick one and say this is the best, maybe the best thing to do is to combine them in such a way that all their different advantages are properly utilized,” says Kis.

This could mean stacking components made of different 2D materials to make tiny, dense 3D circuits. Materials could also be layered inside components — something that chip designers already do when they grow layers of different semiconductors on top of one another to make devices such as the lasers inside DVD players. In standard devices, this is tricky: each layer has to chemically bond with the next, and only certain combinations can be matched. Otherwise, the strain between the different crystal lattices in each layer makes bonding impossible. With 2D materials, that problem goes away: the atoms in each layer bond only very weakly to the neighbouring sheets, so the strain is minimal. Many layers of semiconductors, insulators and conductors can be stacked to form complex devices known generically as van der Waals heterostructures, after the weak bonds that bind the layers.

Already, for example, graphene has been used alongside MoS₂ and WSe₂ to create the junctions at the heart of solar cells¹⁵ and photo-detectors¹⁶, exploiting the semiconductor's abilities to absorb photons and graphene's swift ability to carry the freed electrons away. In February this year, Novoselov and his team reversed the solar-cell concept to make a light-emitting diode¹⁷ from MoS₂ and other TMDCs between graphene electrodes. By selecting different TMDCs, the team could choose the wavelength of the photons released.

Better still, sandwiching together different 2D layers can allow physicists to fine-tune their devices. Although the bonds between layers are

weak, the close proximity of their atoms means that they can affect each other's properties in subtle ways, says Wang Yao, a physicist at the University of Hong Kong. Stacking order, spacing and orientation all control device behaviour. "Modelling this gives theorists like me a headache, but the new physical properties are definitely there," says Yao.

Even graphene can get a leg up from other 2D materials, says Marco Polini, a physicist at the National Enterprise for Nanoscience and Nanotechnology (NEST) in Pisa, Italy. His team has been working on devices in which graphene is sandwiched between 2D layers of the insulator boron nitride¹⁸. When laser light is focused on the device, it gets compressed and channelled through the graphene layer, much more than in devices that sandwich graphene between bulk materials. In principle, this could provide a way for information to be carried between chips using photons rather than electricity. That, says Polini, could mean faster and more efficient communications within the chips.

PRACTICAL PREDICTIONS

The current buzz around 2D materials is reminiscent of the excitement about graphene in 2005, says physicist Jari Kinnaret of Chalmers University of Technology in Gothenburg, Sweden, who heads the European Union's Graphene Flagship — a programme that also studies other 2D materials. But Kinnaret cautions that it could take two decades to really assess the potential of these materials. “The initial studies on 2D materials are focusing a lot on their electronic properties, because these are close to physicists’ hearts,” says Kinnaret. “But I think that the applications, if and when they come, are likely to be in a completely unpredicted area.”

Materials that look good in the lab are not always those that make it out into the real world. One major issue facing all 2D materials is how to produce uniform, defect-free layers cheaply. The sticky-tape method works well for TMDCs and phosphorene, but is too time-consuming to scale up. It is also expensive to make bulk black phosphorus, because it involves subjecting naturally occurring white phosphorus to extreme pressure. No one has yet perfected the process of growing single sheets of 2D materials from scratch, let alone the layered structures that physicists find so promising. “It took a long time to make our heterostructures,” says Xiaodong Xu, a physicist at the University of Washington in Seattle. “How can we speed that up or make it automatic? There is a lot of work to do.”

Such practical considerations could prevent 2D materials from living up to their early promise. "There have been many rushes like this, and some have turned out to be fads," says Kis. "But I think the sheer number of materials and different properties should make sure something comes out of this." Meanwhile, the zoo is expanding, says Coleman. Arsenene, a heavier cousin to phosphorene, is already on researcher's minds.

"As people start to branch out, they are discovering new materials that have these wonderful properties," says Coleman. "The most exciting 2D material is probably one that hasn't been made yet." ■ [SEE BOOKS & ARTS P.284](#)

Elizabeth Gibney is a reporter for Nature in London.

1. Novoselov, K. S. *et al. Science* **306**, 666–669 (2004).
2. Novoselov, K. S. *et al. Proc. Natl Acad. Sci. USA* **102**, 10451–10453 (2005).
3. Radisavljevic, B., Radenovic, A., Brivio, J., Giacometti, V. & Kis A. *Nature Nanotechnol.* **6**, 147–150 (2011).
4. Mak, K. F., Lee, C., Hone, J., Shan, J. & Heinz, T. F. *Phys. Rev. Lett.* **105**, 136805 (2010).
5. Splendiani, A. *et al. Nano Lett.* **10**, 1271–1275 (2010).
6. Srivastava, A. *et al. Nature Nanotechnol.* **10**, 491–496 (2015).
7. He, Y.-M. *et al. Nature Nanotechnol.* **10**, 497–502 (2015).
8. Koperski, M. *et al. Nature Nanotechnol.* **10**, 503–506 (2015).
9. Chakraborty, C., Kinnischtzke, L., Goodfellow, K. M., Beams, R. & Vamivakas, A. N. *Nature Nanotechnol.* **10**, 507–511 (2015).
10. Vogt, P. *et al. Phys. Rev. Lett.* **108**, 155501 (2012).
11. Dávila, M. E., Xian, L., Cahangirov, S., Rubio, A. & Le Lay, G. N. *J. Phys.* **16**, 095002 (2014).
12. Li, L. *et al. Nature Nanotechnol.* **9**, 372–377 (2014).
13. Liu, H. *et al. ACS Nano* **8**, 4033–4041 (2014).
14. Tao, L. *et al. Nature Nanotechnol.* **10**, 227–231 (2015).
15. Lee, C.-H. *et al. Nature Nanotechnol.* **9**, 676–681 (2014).
16. Zhang, W. *et al. Sci. Rep.* **4**, 3826 (2014).
17. Withers, F. *et al. Nature Mater.* **14**, 301–306 (2015).
18. Woessner, A. *et al. Nature Mater.* **4**, 421–425 (2015).

COMMENT

CLIMATE Four ways China could turn its emissions around by 2030 **p.279**



PLANTS Three books debate plant-sensing renaissance **p.282**

MUSIC A composer and a materials scientist collaborate to make *Graphene Suite* **p.284**

CONSERVATION More tigers plus more people equals more conflicts **p.287**

TURJOY CHOWDHURY/NURPHOTO/CORBIS



This year's deadly earthquakes in Nepal killed more than 8,000 people and reduced thousands of buildings to rubble.

Pool knowledge to stem losses from disasters

Public awareness, rigorous risk research and aligned targets will help policy-makers to increase resilience against natural hazards, say **Susan L. Cutter** and colleagues.

In April and May, two massive earthquakes in Nepal killed more than 8,400 people, injured 20,000 and reduced 300,000 houses to rubble. In March, Cyclone Pam destroyed homes, schools, infrastructure and livelihoods on the Pacific island of Vanuatu, affecting half the population, including 82,000 children. Both nations will take years to recover.

The number and severity of disasters is increasing (see 'Catastrophic rise'). Annual global economic losses from geophysical, hydro-meteorological and climatological events could almost double from their 2005 levels by 2030 to exceed US\$300 billion if the past decade's trend continues. The figures

may worsen as climate change, globalization, technological change, urbanization and political and economic instability put more people and assets at risk.

Improved disaster-risk management and resilience is essential for sustainable societies¹. But the science of natural hazards is too fragmented to influence policy effectively. Seismologists, for example, had long warned in specialist journals that Nepal's Kathmandu region was due a large earthquake. Local politicians did not strengthen construction codes, reinforce old buildings or inform the population about potential risks. Had such measures been implemented — as they have in Japan, California and Chile — the death toll would

have been lower (see 'Three lessons yet to be learned'). Similarly, structures in flood-prone areas can be elevated; those in cyclone zones wind-proofed; and the public educated about such possibilities.

Sadly, hazard mitigation is not a vote-winner. It pits long-range investments against short-term political cycles — even though it is cheaper to prevent losses than to rebuild after them^{2,3}. Reinforcing the levees of New Orleans, Louisiana, against hurricane storm surges would have cost ten times less than rebuilding neighbourhoods after Hurricane Katrina. It is more politically expedient to respond afterwards when constituents are demanding assistance. Public awareness ►

► of the scale of disaster risks is hindered by the breadth and complexity of research, spanning the natural, social and health sciences, law, humanities and engineering.

In March, governments met under the auspices of the United Nations in Sendai, Japan, to negotiate an international agreement to reverse the rising trend of disaster losses. Unlike previous voluntary agreements, the Sendai Framework for Disaster Risk Reduction 2015–2030 has set measureable targets. One goal is to lower average death rates and economic losses in 2020–30 relative to 2005–15 (by what percentage is not specified).

For the Sendai agreement to succeed, an open and comprehensive source of vetted information on disaster-risk reduction is needed. It would provide evidence for monitoring progress towards the goals. We call on the scientific community to set up an international assessment process to feed such information into disaster policy and practice.

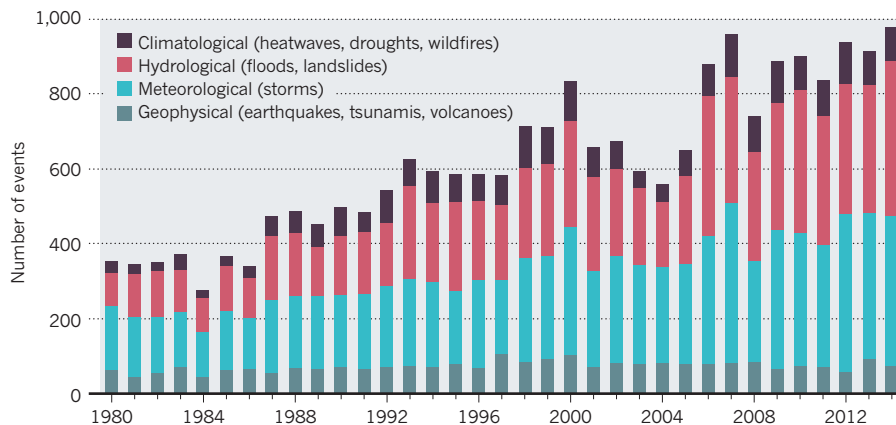
SPLINTERED APPROACH

The community of disaster-risk researchers is small and splintered into disciplines that are focused on single natural hazards. Only recently have seismologists worked with geodesists to determine how changes in Earth's shape and gravity field apply loads to faults⁴. Disaster-medicine researchers rarely meet public-health professionals or read social-science journals⁵. Local or indigenous knowledge and the on-the-ground experiences of emergency managers and humanitarian agencies are often excluded.

Governments need holistic solutions, not incremental proposals that solve one aspect but ignore wider ramifications. A move towards integrated disaster-risk research — bringing together disciplines to focus on particular problems and social needs — is filling this void⁶. But lack of a critical overview of

CATASTROPHIC RISE

The number of disasters caused by natural events has more than doubled since 1980.



SOURCE: MUNICHRE/NATCATSERVICE

what is known about disaster risk leaves politicians without guidance.

This is why early political efforts to reduce disaster losses foundered. The UN designated the 1990s as the International Decade for Natural Disaster Reduction, and in 1999 created the UN Office for Disaster Risk Reduction (UNISDR) to coordinate national efforts. In the absence of a legally binding treaty with targets, and consequences for not achieving them, UNISDR has been largely limited to promoting risk awareness and facilitating institutional development.

In 2005, some 168 countries signed up to the Hyogo Framework for Action (HFA), pledging to reduce disaster losses by 2015. Again, this did not occur. Of the ten costliest disasters between 1980 and 2014, those that happened after the agreement were more than four times as expensive as those in the decade before. Increased vulnerability and exposure account for some of the increase — but not all.

At least 35 nations, including Colombia, Brazil and India, now include disaster risk

and reduction in their development strategies. Most do not. Many financial donors view disasters as interruptions in development, not as risks that need to be managed. Disaster-risk-assessment reports are too broad to guide municipalities and nations. For example, UNISDR's Global Assessment Reports or the World Economic Forum's Global Risks reports provide global and thematic overviews, often consider risks qualitatively rather than quantitatively, and neglect the collective impacts of personal choices such as whether to purchase insurance or relocate⁷.

The Sendai framework calls on governments to do four things: understand disaster risk; strengthen risk governance to manage risks across all sectors; invest in risk-reduction measures that promote resilience; and enhance disaster preparedness and responses so that nations "build back better" in their recovery. It tasks research networks with focusing on the root causes of disasters and probable emergent risks; supporting action by local communities and authorities; and engaging policy-makers.

HAZARD PREPARATION

Three lessons yet to be learned

Build well to save life and property. At least since the 1755 Great Lisbon earthquake, scientists and politicians have known that it is not earthquakes that kill people, but the resultant building collapse. Still, construction in hazard-prone regions frequently flouts standard building codes.

Invest in pre-disaster mitigation.

Spending 5–10% of the funds necessary for recovery after a disaster on mitigation saves lives and resources². Yet few nations bother. The estimated cost of protecting New Orleans, Louisiana, against hurricanes and flooding, for example, was US\$14 billion before Hurricane Katrina in

2005; the total losses actually incurred that year were \$125 billion.

Be prepared. Emergency-management plans should be practised long before a disaster occurs. Preparedness also entails warning systems, education, awareness raising and risk communication. Most poor countries do not do this. For example, when Typhoon Haiyan approached the Philippines in 2013, had the local emergency managers communicated to residents that a tsunami was coming — instead of issuing a warning using the scientifically correct term 'storm surge' — more locals would have evacuated coastal areas.

REVIEW MECHANISM

A coherent science-based assessment process for disaster-risk reduction should be created to provide sound knowledge to inform decision-making, and to assist governments worldwide in setting policies and goals and to identify research gaps. By taking an integrated approach, such an assessment would go beyond previous proposals for international panels on natural hazards and disasters⁸.

Disaster-risk reports should identify what is known and where there are gaps in our knowledge. They must summarize information relevant to the Sendai targets. And they should examine the root causes of vulnerabilities and exposure, the potential socioeconomic impacts of natural hazards and the ways to reduce (if not prevent) human and economic losses. Finally, such an assessment should provide a mechanism for knowledge transfer from research to practice, ensuring

that the science is useful, usable and used⁹.

A high-level, transdisciplinary body of international experts in disaster-risk reduction should be established by national governments and international organizations dealing with disaster risks, with input from various sectors and civil society. Such a body would have the reach and influence — from local communities, businesses and governments — to raise people's awareness. The same findings presented by an independent scientist or article would not.

The main practical difficulties will be in incorporating the field's diverse information and practices into an assessment, and demonstrating to policy-makers that it need not take an extreme event to cause catastrophic human consequences¹⁰. Government support for the process will be essential. Synergies must be found by combining and consolidating disaster-risk reduction efforts across UN institutions.

Disaster-risk management, climate change and sustainable development targets will need to be aligned. For example, there should be a coordinated assessment of the state of knowledge in disaster risk and its utility for supporting the UN Sustainable Development Goals and the UN Framework Convention on Climate Change.

Knowledge transfer will make community-based resilience efforts possible. Illuminating findings, best practices and state-of-the-art modelling must become part of the evidence-based strategy for disaster-risk reduction. ■

Susan L. Cutter is professor of geography at the University of South Carolina in Columbia, USA. **Alik Ismail-Zadeh** is a senior scientist in applied geosciences at the Karlsruhe Institute of Technology, Karlsruhe, Germany, and at the Russian Academy of Sciences, Moscow, Russia. **Irasema Alcántara-Ayala, Orhan Altan, Daniel N. Baker, Salvano Briceño, Harsh Gupta, Ailsa Holloway, David Johnston, Gordon A. McBean, Yujiro Ogawa, Douglas Paton, Emma Porio, Rainer K. Silbereisen, Kuniyoshi Takeuchi, Giovanni B. Valsecchi, Coleen Vogel, Guoxiong Wu.** e-mail: scutter@sc.edu

1. Cutter, S. L. *Chall. Sustain.* **1**, 72–79 (2014).
2. Ismail-Zadeh, A. & Takeuchi, K. *Nat. Hazard.* **42**, 459–467 (2007).
3. Palmer, L. *Nature Clim. Change* **3**, 857–858 (2013).
4. Ismail-Zadeh, A. in *Extreme Natural Hazards, Disaster Risks and Societal Implications* (eds Ismail-Zadeh, A. et al.) 47–60 (Cambridge Univ. Press, 2014).
5. Gall, M., Nguyen, K. H. & Cutter, S. L. *Int. J. Disast. Risk Reduct.* **12**, 255–267 (2015).
6. McBean, G. A. *Curr. Opin. Environ. Sustain.* **4**, 122–127 (2012).
7. Erisman, J. W., Brasseur, G., Ciais, P., van Eekeren, N. & Theis, T. L. *Nature* **519**, 151–153 (2015).
8. Burton, I. *Environ. Hazard.* **3**, 139–141 (2001).
9. Boaz, A. & Hayden, C. *Evaluation* **8**, 440–453 (2002).
10. Cutter, S. L. *J. Extrem. Events* **1**, 1–4 (2014).

Full author affiliations accompany this article online at go.nature.com/fihq6v



Fossil-fuel factories are demolished in China's Hebei province.

Steps to China's carbon peak

Regional targets and improved market mechanisms could enable the nation's carbon dioxide emissions to peak by 2030, say **Zhu Liu** and colleagues.

In 2013, China released one-quarter of the global total of carbon dioxide for the year, and 1.5 times that released by the United States. It is the world's leading emitter of the gas. Without mitigation, China's CO₂ emissions will rise by more than 50% in the next 15 years. Last November, in a joint announcement with the United States, China pledged that its CO₂ emissions will peak by 2030. Existing policies are insufficient to make that happen.

China has a two-pronged strategy for tackling climate change — increasing energy efficiency in manufacturing, and controlling regional emissions through targets. This approach has been effective: we calculate that CO₂ emissions per unit gross

domestic product (GDP) fell by 28.5% between 2005 and 2013. This is equivalent to a saving of more than 2.5 gigatonnes of CO₂ (half of US total emissions). A fledgling domestic carbon-emissions-trading scheme (ETS) has slowed CO₂ emissions growth by 2–3% in the seven provinces or cities in which it has been piloted.

But rapid economic growth, especially the building of infrastructure, has more than offset these reductions. Total national CO₂ emissions grew by 7% each year between 2005 and 2013, although growth of emissions is slowing in cities such as Beijing and Shanghai as advanced technologies and cleaner energy sources are increasingly being used.

Curbing this growth will need a ►

► decrease in projected emissions between 2015 and 2035 that is almost equivalent to the total global CO₂ emissions in 2013 — 30 gigatonnes (see ‘Carbon crunch’). This challenging goal is within reach if China keeps its annual growth in emissions below 2%, rolls out a national carbon-trading system and obtains 30% of its energy from renewables and natural gas by around 2035. China’s per capita emissions in 2030 would then mirror those of the European Union (EU) in 2013 (a little under 8 tonnes of CO₂ per person).

We propose four steps for China to hit this ambitious target. It must strengthen regional emissions targets; improve the reporting and verification of emissions data; enhance the regulation and supervision of a nationwide emissions-trading market; and incentivize the uptake of green technologies, especially in underdeveloped regions.

Set regional emissions targets. A single target will not be suitable for all of China’s 30 provinces and autonomous regions, which have different energy-source mixes, uses and economic development needs. Peak emissions targets need to be designed for each region such that the national total falls by 2030.

Wealthy cities such as Beijing, Tianjin and Shanghai, which have reversed emissions growth since 2011, could cap their emissions and set and adjust reduction targets at five-year intervals. Developed coastal provinces, such as Guangdong, Zhejiang and Jiangsu, that have benefited from the pilot ETS since 2010 should pledge more-aggressive and earlier peak targets — for example, reducing carbon emissions per capita to below those of the EU before 2030 or even 2020. Emissions in underdeveloped regions such as Shanxi province and the Ningxia and Xinjiang autonomous regions could be allowed to peak after 2030 to leave room for more infrastructure construction.

Fossil-fuel use needs to be curtailed first. The country’s ambitious plan to cap national coal consumption in 2015 at 3.9 gigatonnes must be met. Beijing and Tianjin are required to halve their coal consumption by 2017 to meet mandated air-quality requirements. All conventional coal-fired plants in Beijing will be converted to gas by the end of 2015 and an extra 13 billion cubic metres of natural gas from western China and 12 billion cubic metres from other countries are being piped to Beijing and the surrounding cities. Smaller cities and other regions, too, must reduce their coal use.

China can strengthen technology-driven improvements in emission intensity (CO₂ emissions per unit of GDP), especially in the less developed regions. But loopholes also need to be closed. For instance, two-thirds of regions achieved their 2002–09 intensity-reduction targets by enlarging the scale of

production¹, which increased national emissions by 50% (ref. 2). To end this practice, emission-intensity targets should be supplemented by indicators of physical emissions efficiency, for example, emissions per unit of steel production. Such indicators are easier to monitor and verify and can be used to measure the efficiency of sectors, as well as of individual factories.

Air-quality indicators, such as particulate concentrations, should be integrated with emissions targets. Duplicate investments and work plans are common, with China’s National Development and Reform Commission (NDRC) in charge of climate-change mitigation and the Ministry of Environment responsible for air-pollution abatement. Better coordination between departments and a set of joint emissions-control measures — managed by one agency — are needed.

Emissions targets must be decoupled from GDP. Criteria by which local and provincial leaders are evaluated for career promotion should include energy efficiency and pollution-abatement targets, rather than measures of economic development. Otherwise, greater growth will always trump environmental sustainability.

Ensure transparent emissions monitoring, reporting and verification. Data sets for China’s total carbon emissions, especially those generated by regions and sectors, are not always reliable. Official national emissions totals have differed from self-reported provincial statistics by 20%. And in sectoral data sets, factories may overstate their emissions to make it easier for them to achieve reduction targets³. Also, the average carbon content of China’s coal is not accurately known, given the variation in the quality of coal used across different regions.

As a first step, the Chinese Academy of Sciences is coordinating a national investigation of major emissions sources and sinks that should be complete by the end of this year⁴. This should be expanded to include private and small-scale enterprises, which tend to use inefficient and dirty technologies. Small boilers, for example, consume about 10% of China’s coal and are one of the main sources of air pollution in Beijing.

The compilation and reporting of local emissions data are coordinated by regional environmental-protection departments, which also issue environmental certificates for firms and construction projects. This conflict of interest sometimes leads to data manipulation and bribery; each

year, hundreds of government officers are investigated.

The government needs to set up an independent agency to monitor and verify emissions data for regions, sectors and companies. The regulator would establish baseline emissions inventories and verify reductions through spot inspections, modelling and the installation of tamper-proof monitoring equipment.

Monitoring by third parties — the public, the media and non-governmental organizations (NGOs) — needs to be encouraged. Environmental laws and regulations must offer citizens the right to know emissions figures and the right to sue an agency or company if information has been concealed or manipulated.

State-owned projects should make information available to the public by publishing it online, as is done with Beijing’s air-quality data. More web portals should be established to show the improvement, or lack of it, in pollution reduction over time. Examples include the Air Quality Index map (see go.nature.com/82gvyn), run by a Beijing-based NGO, and the pollution map produced by the non-profit Institute of Public and Environmental Affairs in Beijing, which displays real-time emissions information for more than 6,000 large-scale enterprises in China (see go.nature.com/vb6uht). Such efforts will enable government regulators and citizens’ groups to ‘name and shame’ companies that do not adhere to environmental regulations.

Expand carbon trading nationwide. China’s pilot ETS traded nearly 14 megatonnes of CO₂ in 2013. This is less than 0.5% of the national total, but the scheme is still the second largest in the world, after that of the EU. Starting in 2016–17 (ref. 5), the NDRC intends to extend the scheme to all 30 Chinese provinces, making China the world’s largest carbon market. In the pilot ETS, each participant set its own cap and decided which sectors it would cover. For example, transport is included only in Shanghai’s ETS. Each also determined how compliance is measured. Hubei province targets enterprises consuming more than 60,000 tonnes of coal-equivalent per year, a threshold six times that of Guangdong.

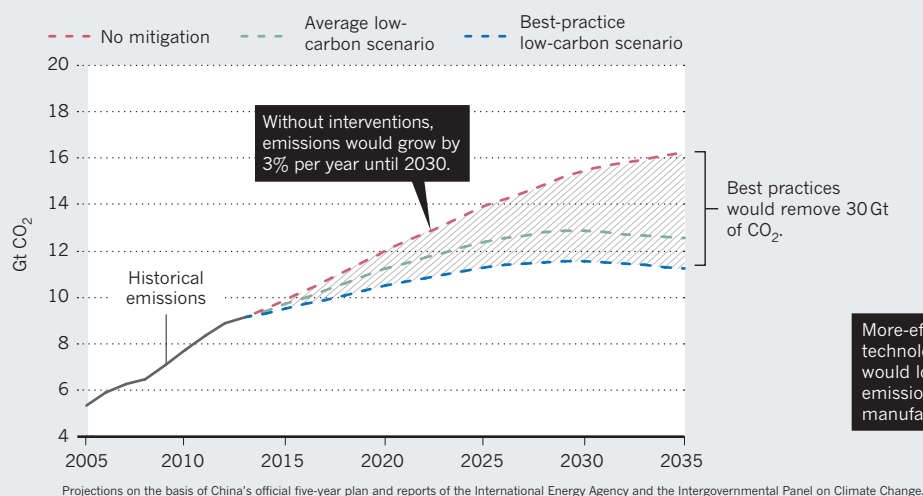
In the expanded scheme, a national emissions cap must be set and central government should develop standards and a timeline to unify cap criteria across the country. The first step should be to introduce a national ETS for the top six CO₂-emitting industries — power generation, ferrous and non-ferrous metallurgy, construction, chemicals production and aviation services — to be extended later to others. Regulations and laws are needed that mandate emissions caps for certain enterprises and encourage emissions trading. Accounting and tax

“China produced 60% of the world’s solar photovoltaic cells in 2014, yet less than 5% were installed domestically.”

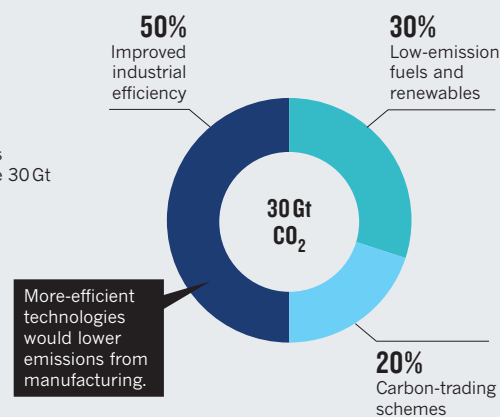
CARBON CRUNCH

China's carbon dioxide emissions will grow beyond the year 2030 unless it adopts strict low-carbon measures. Greater production efficiency, use of renewable energies and natural gas, and nationwide emissions-trading schemes can allow emissions to peak by 2030, and reduce national CO₂ emissions by 30 gigatonnes (Gt) by 2035.

1 Projected emissions, with and without mitigation



2 Carbon-saving strategies



treatments need to be clarified.

A cascading management framework of carbon trading needs to be established, with provincial ETs exchanges linked to higher-level, regional exchanges. For example, Beijing's exchange could coordinate provincial exchanges across northern China.

Market mechanisms should also be introduced to the energy-supply system. First, the monopoly of electricity and energy supply by major state-owned companies must be broken to encourage innovation and improved efficiency. PetroChina and Sinopec, the two main state-owned oil companies, together account for 80% of the national oil supply and 10% of the nation's total carbon emissions.

Second, an energy-supply market needs to be set up to allow prices to respond to demand and incentives. The price for energy delivered to the grid is now controlled by the government and is largely static. This creates barriers to the connection of power from renewable sources: low-carbon electricity is sold at a higher price than electricity generated from fossil fuels. Subsidies for fossil fuels, such as the contract price of coal sold to power plants, need to be removed so that renewables and low-carbon energy technology can be competitive. A carbon tax — starting low and ratcheting up over the next decade — on certain emissions-intensive sectors, such as transport, that are susceptible to a change in behaviour would slow the growth in fossil-fuel consumption.

Advance green technology in under-developed areas. Government incentives have stimulated double-digit growth

in renewable-energy technologies in the past decade. The 'green-energy' industry will contribute 2% of GDP (45,000 billion yuan) to the economy by the end of 2015. Yet the nation's focus is still on manufacturing rather than implementation. China manufactured wind-power capacity equivalent to 114,763 megawatts in 2014 (half of the world's added capacity for the year), but only one-third of that operates in the country. China also produced 60% of the world's solar photovoltaic cells in 2014, yet less than 5% of these panels were installed domestically.

Incentives should be targeted to domestic consumers of renewable energy and eco-products, instead of encouraging production for the global market. Low-carbon technologies should be targeted especially at power production in China's underdeveloped and poor regions. These regions provide power and goods for others and stand to gain most from generation efficiency and development.

In 2010, for example, the emission factor (CO₂ emissions per kilowatt-hour of electricity generated) of coal-fired thermal power plants in Inner Mongolia was 20% higher than that of power plants in Guangdong on the south coast⁵. Yet one-third of the power generated by Inner Mongolia is exported to the east-coast regions⁶. Poor central and western provinces should instead exploit their vast land areas for solar and wind farms.

Regional grid construction and integrated technologies should be encouraged. China is a world leader in ultra-high-voltage transmission technology. This will be essential

for linking areas generating renewable electricity, mainly in the west, to the large coastal cities. Initiatives to develop 'smart' electricity grids and high-speed connections would save energy through improving electricity distribution. Mass-transit systems and regional rail expansion would similarly reduce emissions from road traffic and construction.

We call on China's leaders to be bold and create a low-carbon economy that will benefit the country and the globe. ■

Zhu Liu is at the Institute of Applied Ecology, Chinese Academy of Sciences, Shenyang, China. **Dabo Guan** is at the School of International Development, University of East Anglia, Norwich, UK. **Scott Moore, Henry Lee and Z.L.** are at the John F. Kennedy School of Government, Harvard University, Cambridge, Massachusetts, USA. **Jun Su** is at the School of Public Policy and Management, Tsinghua University, Beijing, China. **Qiang Zhang and D.G.** are at the Center for Earth System Science, Tsinghua University, Beijing, China. e-mails: dabo.guan@uea.ac.uk; liuzhu@iae.ac.cn

1. Guan, D. et al. *Nature Clim. Change* **4**, 1017–1023 (2014).
2. Liu, Z., Geng, Y., Lindner, S. & Guan, D. *Energy* **45**, 1059–1068 (2012).
3. Guan, D., Liu, Z., Geng, Y., Lindner, S. & Hubacek, K. *Nature Clim. Change* **2**, 672–675 (2012).
4. Jiao, L. & Stone, R. *Science* **334**, 886–887 (2011).
5. National Development and Reform Commission of China. *Interim Plan for Carbon Trading in China* (NDRC, 2014).
6. Feng, K. *Proc. Natl Acad. Sci. USA* **110**, 11654–11659 (2013).



Plants regulate important processes such as photosynthesis through pores called stomata.

PLANT SCIENCE

Rediscovering the bush telegraph

Ian T. Baldwin assesses three books on the rich array of plant behaviours, from sensing to communication.

The food writer Michael Pollan, author of *The Omnivore's Dilemma* (Penguin, 2006) among others, wrote an article in *The New Yorker* in 2013 exploring why terms such as intelligence, memory and even behaviour have been contentious for plant scientists. His thesis boils down to a divide in

biology that allows zoologists to use anthropomorphic terms, but denies the privilege to plant scientists. Pollan allies himself with a small band of intrepid researchers crusading against the “cerebrocentric” view that permits behaviour only to organisms with brains. He tells of collateral damage from

Leaf Defence

EDWARD E. FARMER
Oxford Univ. Press: 2014.

Plant Sensing and Communication

RICHARD KARBAN
Univ. Chicago Press: 2015.

Plant Behaviour and Intelligence

ANTHONY TREWAVAS
Oxford Univ. Press: 2014.

sensationalist treatments that exaggerate plant-science findings, and of glimmers of a new sensitivity towards all life.

Pollan identifies an interesting story about the development of an emerging scientific field, and the baggage that scientists bring to their work. The idea that plants are ‘smarter’ than their immobility suggests is now supported by rigorous experimentation and fieldwork that are uncovering the genes and chemicals that mediate plants’ environmental intelligence. We know now that much of a plant’s rich behavioural repertoire is hard to observe because it is played out in a chemical arena. Plants overcome the constraints of immobility mainly by harnessing their prowess as synthetic organic chemists. For instance, floral scents contain compounds that attract pollinating animals and repel flower-eating ones. Nectar is a brew of nutrients and toxins that optimize the behaviour of pollinators. Much of the relevant literature is now synthesized in three books by leading researchers in the field: Edward Farmer’s *Leaf Defence*, Anthony Trewavas’s *Plant Behaviour and Intelligence* and Richard Karban’s *Plant Sensing and Communication*.

RESEARCH RENAISSANCE

The research is essentially a rediscovery. Between the eighteenth and the twentieth centuries, Erasmus Darwin, Charles Darwin and botanists Wilhelm Pfeffer and Jagadish Chandra Bose published books that brim with observations on plant behaviour. Charles Darwin’s 1880 *The Power of Movement in Plants*, for instance, incorporates insights from his experiments on how exposure to light drives bending in grasses, which laid the foundation for the discovery of the hormones responsible for plant movement. If they were alive today, these scientists would wonder what all the fuss is about.

The study of plant defences was revived in 1959, when entomologist Gottfried Fraenkel published the landmark article ‘The raison d’être of secondary plant substances’ (*G. S. Fraenkel Science* **129**, 1466–1470; 1959), building on original insights by nineteenth-century botanist C. Ernst Stahl.

Fraenkel argued that plants’ awesome diversity of secondary metabolites such as toxic alkaloids and aromatic terpenoids evolved primarily to thwart herbivores. He ushered in the modern era of chemical

ecology, including an exuberance of theory to explain these metabolites' patterns of accumulation. Much of the theorizing came from zoologists, who applied paradigms from animal-behaviour studies to plants, often without deeper understanding of how plants function as organisms. The plant-biology community had little patience for this, being at the time focused on understanding mechanisms of plant growth under controlled laboratory conditions, developing *Arabidopsis* as a model plant and embracing molecular biology. After reading Farmer, Karban and Trewavas's books, I felt that the prevailing scientific opinion that plants are mere autotrophic growth machines has perhaps as much to do with the divorce between molecular and organismic approaches as with the botany-zoology divide.

Leaf Defence considers why plants have or lack leaves, and why leaves evolved to have particular traits. Because leaves dominate most plants' above-ground biomass, herbivores usually home in on them, a circumstance that has shaped leaves' chemistry, physics, morphology and development. Plants, meanwhile, eat sunlight with their leaves. So to fathom leaf evolution, it is important to understand both herbivores' digestive tracts and the dynamics of solar radiation.

Farmer works on jasmonates, a fatty-acid-based signalling system that activates many of plants' defences against herbivores. *Leaf Defence* provides an excellent review of the rapidly evolving literature in this field. The only disappointment is that books do not evolve as rapidly even as the literature from the author's own lab. Farmer's book was written before his laboratory reported a landmark discovery: a molecular link between jasmonate signalling and electrical signalling induced by herbivore attack (S. A. R. Mousavi *et al.* *Nature* **500**, 422–426; 2013).

Farmer weaves his compelling narrative from hard-core molecular research on mechanisms of perception of herbivore attack and defence responses, to more speculative inferences about how leaf colour and escape to rocky outcrops help plants to survive the relentless interests of herbivores. He highlights the lack of evidence for some sensationalist stories of plant-plant signalling, such as one about signalling between South African acacia trees about impending attacks from antelopes. And of the three books, *Leaf Defence* is the only one to include structures of plant chemicals.

The plant 'behaviour' debate described by Pollan is the starting point for the other two books. In *Plant Sensing and Communication*, Karban, a behavioural ecologist and entomologist, discusses environmental elements to which plants are thought to

respond, such as light and sound. Karban, who featured prominently in Pollan's article, largely avoids political melodrama, instead providing clear working definitions of some of the contentious vocabulary: communication, eavesdropping, learning and memory. His summaries of plants' sensory abilities — such as the cues and signals that they use to adjust to the environment — retain an evolutionary perspective. And he branches out into areas such as mate choice, for example detailing how plants selectively breed with specific fathers represented in a mixed pollen load.

Karban's research interests overlap with mine; we even work on the same species (coyote tobacco, *Nicotiana attenuata*). Although he is a gifted writer and synthesizer, Karban's review of the research on the mechanisms of plant perception and response is not well served by his lack of familiarity with the techniques that uncover them. Issues that he identifies as central unsolved problems (such as whether the volatile 'alarm calls' of plants protect against herbivores and increase fitness under real-world conditions) have been solved and published. The unrealistic experimental designs so common in the early literature are frequently reported uncritically. In discussing the complicated process of demonstrating an adaptation, Karban does not mention the genes responsible for the expression of traits such as shade avoidance, or the advantages offered in this area by cheap sequencing. So I recommend *Plant Sensing and Communication* to those who want a low-calorie introduction and a deeper consideration of the concepts, but the primary literature is better for understanding the mechanisms.

BOTANICAL MECHANICS

Trewavas, by contrast, moves effortlessly from mechanistic research to invigorating insights into real-world plant behaviour. *Plant Behaviour and Intelligence* is a wild ride, covering ground from the origins of life to intelligent nutrient-foraging behaviour in the roots of higher plants. Trewavas's five decades of research into plants' molecular biology and physiology, and their evolution as self-organizing systems, make him fully 'phytomorphized'. He thinks like a plant, effortlessly calling on specific traits to look at how plants solve problems in similar ways to social insects — from siphonogamy (in which pollen tubes carry sperm cells to egg cells) to highly dispersed sensory systems. He celebrates behaviour in plants while avoiding "animal envy". At 76, Trewavas may have written his last book — but it is one that encapsulates his life's work beautifully.

Plant Behaviour and Intelligence is also peppered with references to classics in the field, and takes inspiration from the geneticist Barbara McClintock's "feeling for the



Charles Darwin systematically investigated plant behaviour in the late nineteenth century.

organism", which she derived from her long study of maize (corn) and discovery of 'jumping genes', or transposons. Trewavas and Farmer share a deep understanding of how plants function, mechanistically and biochemically, and this anchors their forays into how plants work in the real world. This grounding in mechanism may prove to be the key to convincing a scientific community sensitized to the gap between populist hype and the data on plant behaviour.

Plant biology is emerging from its *Arabidopsis*-in-the-laboratory phase. Researchers need to understand the natural-history context of such models before plant behaviours can be sensibly scrutinized in the functional (natural) context. The infusion of ideas from behavioural ecology between 1950 and 1990 revived the field, but it now needs balance. The mental constructs that ecologists bring to experimentation on plant function, such as the cost-benefit paradigm applied to resource allocation, are of limited value when they are unmoored from the mechanisms that anchor these phenotypes. These three books suggest that the way forward may be through a return to the observational skills that allowed the great researchers of the twentieth century to become phytomorphized. ■

Ian T. Baldwin is the founding director of the Max Planck Institute for Chemical Ecology in Jena, Germany.
e-mail: baldwin@ice.mpg.de

► **NATURE.COM**

To hear more about Anthony Trewavas, visit: go.nature.com/awtxv



Cinzia Casiraghi (left) and Sara Lowes collaborated to create the *Graphene Suite*.

Q&A Cinzia Casiraghi & Sara Lowes

Maestros of graphene

Composer Sara Lowes has teamed up with materials scientist Cinzia Casiraghi at the University of Manchester, UK. The result, Lowes' six-part *Graphene Suite*, premieres next week at the Graphene Week 2015 conference in Manchester, part of the European Union's decade-long, €1-billion (US\$1.1-billion) Graphene Flagship research programme. Lowes and Casiraghi talk crotchets, carbon chemistry and the commonalities between women in science and women in music.

How did you come to work together?

SL: The idea came from Brighter Sound, a cultural organization in Manchester that wanted to explore the common ground between the creative processes in music and in science, particularly graphene. To be given something I know nothing about and to use that to create a piece is fascinating. The brief was for a female musician to do this, because composition is a hugely male-dominated profession.

CC: That is one of the similarities between science and composition: there are not enough good role models for women. The issues are the same, whether it is in science, music or any other field. I am a member of the University of Manchester school of chemistry's Athena SWAN committee, which supports women in science, so I was very keen to collaborate with Sara.

Was it difficult to span the cultures of music and science?

SL: Composing music is like science in that you start with an idea and ask, 'I wonder what would happen if ...?' Cinzia and I met for the first time in summer 2014. She talked about her job, we met her colleagues in the chemistry and physics departments, and she showed me around a clean room. I had never been in a university science department before, and I kept feeling frustrated that people outside science do not know anything about it. Science is part of everything around us; it is part of our world.

CC: Collaboration is an important part of my research, which is often multidisciplinary. And although I work on graphene now, I come from a completely different scientific

Graphene Suite
25–28 June 2015,
Manchester, UK.
<http://go.nature.com/5damsw>

background — nuclear engineering — so it is quite natural for me to find connections between fields that you might think do not have anything in common. Collaboration helps us to see problems from different points of view, to find solutions or develop projects in a new direction.

Do you ever worry that graphene will not live up to expectations?

CC: Yes. I started my research career on carbon nanostructures, and I saw a couple of those — nanotubes and fullerenes — just dying along the way. But graphene is a little bit different. Ten years ago we were dealing with tiny pieces of graphene, hardly visible under the microscope, so it was difficult and time-consuming to produce and process the material. Now we have centimetre-sized graphene sheets, graphene inks and many other types of 2D crystal. So I am more optimistic about graphene than other carbon nanostructures.

How did you begin to shape the music?

SL: The first thing I looked at was graphene's molecular structure — the hexagonal honeycomb pattern — so I used the number six a lot in the music. It is a six-movement piece, the parts that are about graphene itself are in six-eight time, and I have tried to interpret the hexagon structure musically in one of the movements.

And how will it work in performance?

SL: Some of the audio will come from data on graphene that we have turned into waves, so we can play them as sound. Each movement is four to five minutes long. Some parts are orchestral; others will be played by my band. The classical element — a string quartet, with oboe and trumpet in some places — reflects the history of Manchester, its scientific achievements. The modern element — drums, bass, guitar and keyboard — represents the idea that this is a really forward-looking time, and that graphene is a wonderful discovery. The first movement is a journey representing 'science at work': the long hours, the commitment and the frustrations. The second movement goes on to the moment of discovery, the sheer excitement of it. The third is all the hard work that happens once that discovery has taken place. Another is dedicated to women — it has a noble, keep-on-going attitude.

What are your hopes for the *Graphene Suite*?

SL: I hope that it will help to shine a spotlight on the spaces that are available for women in science and composition. We are both passionate about making sure that that is a legacy of the project. ■

INTERVIEW BY MARK PELOW

This interview has been edited for length and clarity.

Correspondence

Factor people into tiger conservation

Tiger populations in India and Nepal have increased by almost one-third and two-thirds, respectively, over the past 5 years. But for these countries to achieve their goal of doubling their combined tiger numbers to more than 3,600 by 2022, they must take the human population into account as well.

India is projected to become the world's most populous nation by 2028, with around 1.45 billion people. This will place further pressure on tiger habitats such as those in Arunachal Pradesh and Uttarakhand, where hydropower projects are planned.

Local village populations are unlikely to cooperate with tiger conservation efforts while the animals continue to take livestock and kill humans (N. H. Carter *et al.* *Ambio* **43**, 125–137; 2014). In India alone, tigers killed 822 people between 1990 and 2009 (N. P. S. Chauhan *Julius Kühn Arch.* <http://doi.org/46k>; 2011).

It is crucial for the Indian and Nepalese governments to install protection for villagers against tigers and to provide them with incentives to participate in tiger conservation. Improved management of existing reserves and more conservation areas are also a priority.

Achyut Aryal* *Massey University, Auckland, New Zealand.*

a.aryal@massey.ac.nz

**On behalf of 5 correspondents (see go.nature.com/cr4jli for full list).*

Healthy diet sustains the environment too

The idea that dietary recommendations for humans are compatible with an environmentally sustainable food system is supported by a 2015 report from the US National Academy of Sciences (go.nature.com/t2ovdt).

The implication that dietary

recommendations should take the environmental impact of food production into account caused controversy earlier this year. Parts of the US government and the food industry accused the federal Dietary Guidelines Advisory Committee of going beyond its remit in advocating a more plant-based diet that would be better for sustainability as well as human health (see go.nature.com/lcwj6i).

Scientists, policy-makers and other stakeholders must move beyond considering health, environmental, social and economic effects in isolation. In recognizing the need to address the food system's complexities and its competing demands and trade-offs, the National Academy of Sciences' report has already been the subject of briefings to Congress and US governmental agencies.

Malden Nesheim *Cornell University, Ithaca, New York, USA.*

Patrick J. Stover *Cornell University, Ithaca, New York; and American Society for Nutrition, Bethesda, Maryland, USA.*

Maria Oria *The National Academies, Washington DC, USA.* *pjs13@cornell.edu*

Beware climate neo-scepticism

We coin 'neo-scepticism' as a term to describe an emerging science-policy argument that opposes major efforts to mitigate climate change. Neo-sceptics do not deny anthropogenic global warming, but minimize its projected effects and see mitigation efforts as unjustifiable (see, for example, S. E. Koonin *Wall Street Journal* 19 September 2014; J. Curry *Wall Street Journal* 9 October 2014).

Neo-sceptic arguments emphasize well-known uncertainties in climate science, particularly over predicted temperature changes. This diverts attention from the risks of events with extreme biological and economic consequences and from the risks of 'tipping points'

with large, nonlinear responses.

Neo-sceptics recognize the importance of policy decisions — who should do what, when, and at what cost, for example. However, they project an ironic certainty in advising the postponement of serious mitigation efforts until confidence intervals for climate projections are narrowed.

Physicists, biologists and social scientists should be focusing more on risks, rather than simply pursuing more-precise estimates of physical parameters that are not linearly related to the most worrisome hazards. Society does not demand certainty to cope with other high-consequence risks, such as those relating to public health, airline safety, terrorism, and natural or technological disasters.

John H. Perkins* *The Evergreen State College, Kensington, California, USA.*

perkinsj@evergreen.edu

**On behalf of 4 correspondents (see go.nature.com/mg7ugf for full list).*

Chinese scientists are sharing data

We cannot agree with Zheng Wan's view that it is getting harder for scientists in China to access high-quality public data (*Nature* **520**, 587; 2015). There are still technical issues to be resolved, but the trend is towards a greater amount of open data — not less.

The Chinese government has established several national data infrastructures over the past few years that are publicly accessible. These include the National Science and Technology Infrastructures organization (www.esience.gov.cn), which has been sharing data since 2009 in fields such as Earth systems, marine science, meteorology, agriculture, forestry, medicine and health. One of its 23 projects is the National Specimen Information Infrastructure (www.nsii.org.cn), launched in 2013, which currently archives data from more than 10.5 million

biological, mineral, rock and fossil specimens.

The degree and success of data sharing also rely on individual scientists' attitudes and practices. Many researchers — including some who are publicly funded in China — unfortunately often resist sharing data, actively or passively. They should instead take more responsibility for cultivating a sustainable, 'bottom-up' culture of sharing.

Xiaolei Huang *Fujian*

Agriculture and Forestry University, Fuzhou, China.

Keping Ma *Institute of Botany, Chinese Academy of Sciences, Beijing, China.*

huangxl@fafu.edu.cn

Star academics in favour of divestment

Your portrayal of the campus carbon-divestment movement could have provided a more balanced account of the controversy (*Nature* **521**, 16–17; 2015). The strongest resistance to this movement is found not among faculty members, but in the boardrooms of the managing corporations.

As for the former, our own group, Harvard Faculty for Divestment (harvardfacultydivest.com), has grown in less than a year to more than 250 names, and includes several renowned climate scientists and Nobel laureates, as well as members of every school in the Harvard community.

James Recht *Harvard Medical School, Boston, Massachusetts, USA.*

james_recht@hms.harvard.edu

CORRECTION

In the Outlook article 'Wild bees: Lone rangers' (*Nature* **521**, S62–S63; 2015), entomologist Jordi Bosch was incorrectly affiliated with the University of Barcelona; his affiliation should have read the Autonomous University of Barcelona.

ASTRONOMY

A Mars-sized exoplanet

Analysis of Kepler data has yielded the smallest known mass for an exoplanet orbiting a normal star. Its mass and size are similar to those of Mars, setting a benchmark for the properties of exoplanets smaller than Earth. [SEE LETTER P.321](#)

GREGORY LAUGHLIN

With a mass one-tenth that of Earth's, half its diameter, and a residual gleam of long-lost habitability, Mars has an outsized hold on our imagination. On page 321 of this issue, Jontof-Hutter *et al.*¹ report the discovery of Kepler-138 b — an alien world that has a mass, a radius and perhaps an overall composition very similar to those of Mars. In contrast to warm Earth or cold Mars, however, this planet is baking hot because of its proximity to its host star. The current exoplanet census is dominated by planets a few times the size of Earth and on orbits close to their stars, and so our Solar System — with its four small inner planets — seems somewhat marginalized. The detection of such a small exoplanet in a tight orbit could help to clarify how we fit into the big picture.

NASA's successful Kepler space observatory made the observations that enabled the detection of this low-mass world. Between 2009 and 2013, Kepler monitored more than 150,000 stars in a patch of sky just above the mid-plane of the Milky Way, and recorded the periodic diminutions in brightness that occur when planets with appropriately aligned orbits transit (pass in front of) their parent stars². At the last count, more than 4,600 candidate planets had been identified in the data returned by the Kepler mission³. Although the bulk of these prospective worlds have radii 2–4 times that of Earth's and display a bewildering range of compositions, more than 500 candidates have radii smaller than Earth's. The race is on to elevate these candidates to confirmed planetary detections⁴.

Observations of repeating dips in the brightness of a host star, each dip having identical depth and duration, might seem to constitute fail-safe evidence of an orbiting planet. There is, however, a host of potential false alarms that can compromise a detection, notably the possibility that a background, eclipsing binary star registers on the same detector pixel as the candidate planet's host star, so that periodic eclipses in the distant system can mimic planetary transits of the target star⁵. So far, more than 1,000 of Kepler's planets have been vetted and confirmed, but the process of follow-up evaluation (especially for the low-mass

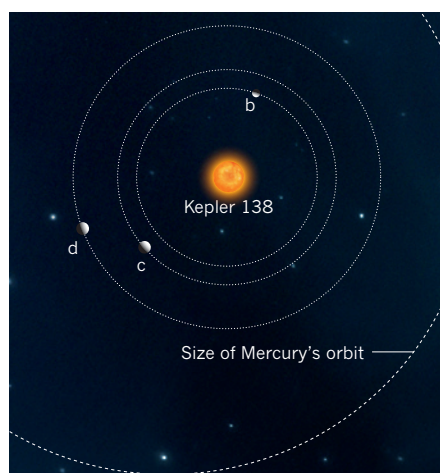


Figure 1 | The planetary system Kepler-138.

The graphic depicts the orbital architecture of an exoplanet system discovered by the Kepler space observatory. Jontof-Hutter *et al.*¹ report the sizes and masses of planets Kepler-138 b, Kepler-138 c and Kepler-138 d. Kepler-138 b, on a 10.3-day orbit, has the smallest measured mass of any transiting exoplanet — it has a size and mass similar to those of Mars. Kepler-138 c and Kepler-138 d are slightly larger than Earth and have orbital periods of 13.8 days and 23.1 days, respectively. The orbits are drawn relative to the size of Mercury's 88-day orbit.

worlds) will continue for decades.

Transit detections provide an estimate of a planet's size, but they give no information about its mass. For massive transiting planets, masses can be estimated by Doppler spectroscopic monitoring of the host star's velocity variations along the line of sight of the observation. This option, however, is unavailable for a planet such as Kepler-138 b, which is too small to induce detectable wobbles in the host star's motion⁶.

During the nineteenth century, Mars presented a similar challenge to astronomers who were trying to estimate its mass. In 1877, the discovery of the planet's tiny satellites (Phobos and Deimos) allowed the mass of Mars to be determined accurately and directly. Earlier estimates, however, beginning with the efforts of Jean Baptiste Joseph Delambre in 1806, were obtained by carefully accounting for Mars's gravitational influence on other planets in the Solar System, and calculating their effects on the precisely measurable daily

location of the Sun. By 1850, refinements of this technique had narrowed the Martian mass estimate to within 20% of its true value⁷.

Jontof-Hutter and colleagues have drawn from the same time-tested notebook of dynamical astronomy to deduce the mass of Kepler-138 b. The planet is part of a system (Fig. 1) that contains two additional transiting planets, Kepler-138 c and Kepler-138 d, which have periods of 13.8 and 23.1 days, respectively, and radii slightly larger than that of Earth. The inner planet pairing between 138 b and 138 c has an orbital-period ratio of nearly 4:3, whereas the outer pairing between 138 c and 138 d has a ratio near 5:3. Because the period ratios are almost exact ratios of integers, this enables the gravitational distortions of the orbit of one planet by the other planets to gradually ebb and flow, producing observable departures from expected strict regularity in the transit times. Measurements of the planets' transit timing variations constitute a nonlinear, computationally intensive inverse problem, the solution of which has allowed the authors to deduce the masses of all three planets.

The radii of known exoplanets generally display surprisingly little correlation with their masses, especially for planets that are somewhat more massive than Earth. Jontof-Hutter *et al.* report a mass of around 0.07 Earth masses for Kepler-138 b, imbuing it with a bulk density of about 3 grams per cubic centimetre — consistent with a purely rocky composition roughly akin to that of Mars. The planet's mass is similar to, but somewhat less than that of Mars (by contrast, its surface temperature is much higher). Whether we are probing an outlier world, or whether the authors' discovery points to an important trend among low-mass planets — whereby smaller radii exhibit strong positive correlation with smaller masses — is as yet unclear.

The derivation of dynamical properties from transit measurements requires timing data with split-second precision, and so the mass and density of Kepler-138 b both have large uncertainties, of a factor of about two. The prime drivers of the uncertainty are the relatively low number of planetary transits that have been observed and the timing precision. These can be improved both with longer observation campaigns and, eventually,

with space missions capable of observing at intervals shorter than Kepler's 1-minute limit. The European Space Agency's PLATO (Planetary Transits and Oscillations of Stars) mission planned for the mid-2020s, for example, will be able to monitor the brightest transit-bearing stars at a temporal resolution of 2.5 seconds.

Kepler-138 b orbits a red dwarf star, the mass, radius, chemical composition and space motion of which are close to those of the 'average' star in the Milky Way. The Kepler-138 planetary system also seems to be unexceptional when placed in its galactic context. The Kepler mission has demonstrated that it is extremely common for stars to harbour multiple planets with orbital periods of less than 100 days and masses of lower than 20 Earth masses. By contrast, the reaches of the Solar System interior to Mercury, which has an 88-day orbit, are completely

empty. It is imperative to improve our understanding of how our system's architecture and evolution fit into the overall census — the authors' study is a step towards that goal.

A pressing question is whether planets such as those orbiting Kepler-138 formed *in situ*, or whether they accumulated in colder, distant regions of the protoplanetary disk before migrating inwards. Short-period, low-mass planets that cannot retain hydrogen atmospheres, and the densities of which are similar to mixtures of rock and ice, present evidence in favour of inward migration from cold regions. This is because planets with an icy bulk cannot have formed close to their star. Additional, increasingly accurate mass and radius measurements, both for Kepler-138 b and for other small exoplanets, will be facilitated soon by NASA's TESS (Transiting Exoplanet Survey

Satellite) mission⁸, scheduled for 2017, and will help to provide an answer. ■

Gregory Laughlin is in the Department of Astronomy and Astrophysics, University of California at Santa Cruz, Santa Cruz, California 95064, USA.
e-mail: laughlin@ucolick.org

1. Jontof-Hutter, D., Rowe, J. F., Lissauer, J. J., Fabrycky, D. C. & Ford, E. B. *Nature* **522**, 321–323 (2015).
2. Borucki, W. *et al.* *Science* **327**, 977–980 (2010).
3. <http://exoplanetarchive.ipac.caltech.edu/index.html>
4. Marcy, G. W. *et al.* *Astrophys. J. Suppl. Ser.* **210**, 20 (2014).
5. Gautier, T. N. III *et al.* Preprint at <http://arxiv.org/abs/1001.0352> (2010).
6. Fischer, D. A. *et al.* in *Protostars and Planets VI* (eds Beuther, H. *et al.*) 715–737 (Univ. Arizona Press, 2014).
7. Grant, R. *History of Physical Astronomy* (Bohn, 1852).
8. Ricker, G. *et al.* *J. Astron. Telesc. Instrum. Syst.* **1**, 014003 (2014).

CELL BIOLOGY

Receptors for selective recycling

Two studies show that the engulfment of certain intracellular membranous structures by vesicles called autophagosomes regulates the structures' degradation in a selective, receptor-protein-mediated manner. SEE LETTERS P.354 & P.359

DAVID C. RUBINSZTEIN

Autophagy — the internal digestion of parts of a cell — is an evolutionarily conserved pathway for recycling damaged or unwanted cellular components. Although the process was initially thought to involve degradation *en masse* of cytoplasmic contents, evidence has emerged¹ to suggest that individual components can be selectively isolated in preparation for autophagy. Two complementary papers in

this issue^{2,3} identify specific receptor proteins in yeast and mammalian cells that enable the selective degradation of an organelle called the endoplasmic reticulum (ER).

During autophagy, cup-shaped double-membrane structures called phagophores develop into spherical structures called autophagosomes, which engulf cytoplasmic components destined for autophagic degradation. Autophagosomes fuse with vesicles called lysosomes, which degrade and then recycle

the engulfed components (Fig. 1). Selective autophagy of certain bacteria, aggregation-prone proteins and organelles such as mitochondria seems to be mediated by autophagy receptor proteins. These bind to protein components of the phagophore and autophagosome, such as Atg8 in yeast and its equivalent in mammals, LC3, through interactions with LC3-interacting domains (called Atg8-binding pockets and LIR domains in yeast and mammals, respectively)¹.

The ER, which directs proteins towards the plasma membrane for secretion or residency, can also be degraded through autophagy (a process called ER-phagy)⁴. It has not previously been possible to test whether ER-phagy is required for health, although in animal models it seems to protect against α_1 -antitrypsin deficiency, a condition in which a toxic form of the α_1 -antitrypsin protein accumulates in the ER and causes liver damage⁵. But is ER-phagy merely part of bulk autophagy, or does some cellular machinery enable the preferential selection of ER into autophagosomes, as has been previously hypothesized⁶?

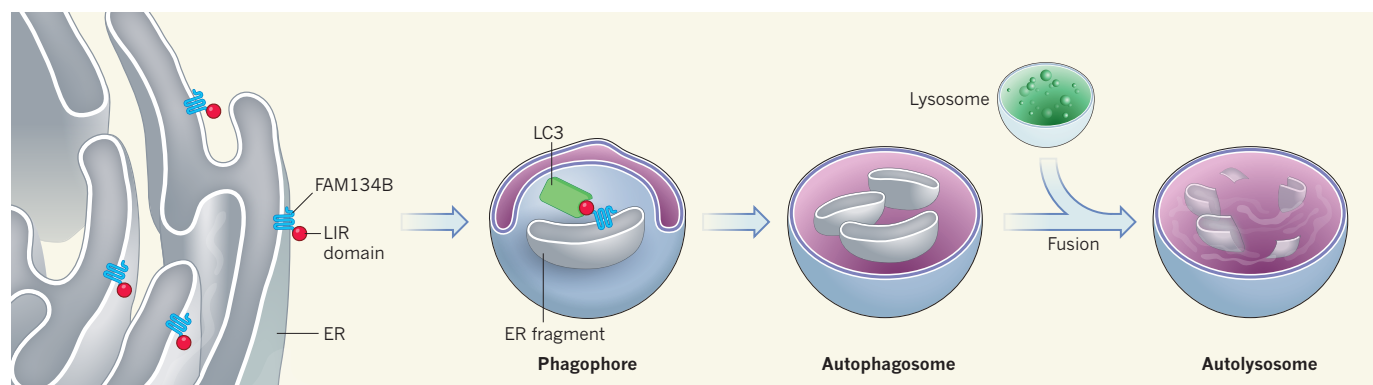


Figure 1 | Selective cellular recycling. During an intracellular recycling process called autophagy, structures called phagophores form structures called autophagosomes, which engulf damaged or unwanted intracellular components before fusing with lysosomes to form autolysosomes that degrade their contents. Khaminets *et al.*³ report that, in mammals, the receptor

protein FAM134B mediates autophagy of an organelle called the endoplasmic reticulum (ER). ER-bound FAM134B interacts with a protein called LC3 in phagophores through an LIR domain, leading to engulfment of ER fragments by autophagosomes. Mochida *et al.*² report that Atg39 and Atg40 have equivalent roles in yeast (not shown).

The current studies provide robust support for this hypothesis. The key starting point for both groups was the identification of autophagy receptors that interact with the ER and with autophagosomes, which they achieved by searching for proteins that physically interact with LC3 or Atg8. Khaminets *et al.*³ (page 354) report that FAM134B, which has an LIR domain and a reticulon domain that binds to and fragments the ER, interacts with LC3 in mammalian cells. In yeast, Mochida *et al.*² (page 359) demonstrate that Atg39 and Atg40 (which seems to be a counterpart of FAM134B), interact with Atg8 and the ER. The groups report that loss of Atg39, Atg40 or FAM134B impedes autophagy-dependent degradation of the ER, but does not affect bulk autophagy. Furthermore, mutant forms of the proteins that do not bind to the phagophore and autophagosome are ineffective in ER-phagy.

Mochida *et al.* showed that Atg40 is associated with the cytoplasmic ER and the ER close to the plasma membrane and seems to be involved in their degradation. By contrast, Atg39 is associated with the ER that surrounds the nucleus. Atg39 regulates degradation of both this nuclear envelope and some nuclear constituents — a previously unidentified form of selective autophagy that the authors call nucleophagy. It will be interesting to determine whether nucleophagy occurs in mammalian cells, and to define when the process occurs, which components are degraded, and why it is required. For instance, nucleophagy might contribute to the breakdown of the nuclear envelope that occurs when cells divide. Nucleophagy could also theoretically be responsible for quality control and repair of damaged nuclear membranes. This could be tested by investigating whether impaired nucleophagy results in the accumulation of malfunctioning pores in the nuclear envelope and compromised segregation of nuclear and cytoplasmic contents.

Khaminets and colleagues provide data suggesting that FAM134B helps to fragment the ER into 'bite-sized' pieces that can be readily incorporated into autophagosomes. This model is analogous with the hypothesis⁷ that the division of mitochondria enables their own sequestration and degradation through autophagy. The role of FAM134B is of particular interest, because it is mutated in a human disorder of the sensory nerves in which pain perception is impaired, resulting in ulceration of the hands and feet⁸. Khaminets *et al.* report that mice lacking FAM134B have similar sensory defects to those seen in the human disorder. In these mice, ER accumulates in the cell bodies of pain-sensing neurons before any morphological abnormalities are apparent, raising the interesting possibility that these neurons may be particularly vulnerable to defective ER-phagy.

The suggestion that ER-phagy might be required for cellular health is supported by

Mochida and colleagues' observation that Atg39-deficient yeast are more sensitive than wild-type cells to the stress of nitrogen starvation. However, the possibility cannot be ruled out that sensory abnormalities are mediated by autophagy-independent roles of FAM134B. If the sensory abnormalities observed in mice are directly due to the increase in ER volume, future studies should be able to determine whether the defects are caused by the toxic effects of the uncleared organelles, or whether the increased ER volume affects cellular signalling and neurotransmission.

The two complementary studies^{2,3} have identified seemingly analogous systems for regulating ER degradation through autophagy, which will lead to a deeper understanding of the process. Goals for the future include understanding the relevance of the ER-phagy machinery to maintenance of the nucleus in mammalian cells, investigating the consequences of impaired or excessive ER-phagy, and defining how the process is regulated. The activities of many autophagy receptors can be modulated by post-translational modifications such as phosphorylation¹, and it will be interesting to find out whether such mechanisms are pertinent to ER-phagy. The idea that the activity of receptors involved in ER-phagy can be regulated is supported by Mochida and colleagues' observation that levels of Atg39 and Atg40 increase when cells are treated with the drug rapamycin,

which induces some of the signalling changes associated with nitrogen starvation.

Finally, it remains to be seen whether there is any specificity to which parts of the ER and nuclear envelope are cleared by selective autophagy. If there is, what is selected and why? It will be important to discover whether ER-phagy is indiscriminate, or whether the receptors target damaged ER in the way that damaged mitochondria are preferentially degraded by mitophagy and intracellular pathogens by xenophagy⁹. ■

David C. Rubinsztein is in the Department of Medical Genetics, University of Cambridge, Cambridge Institute for Medical Research, Cambridge CB2 0XY, UK.
e-mail: dcr1000@cam.ac.uk

1. Stolz, A., Ernst, A. & Dikic, I. *Nature Cell Biol.* **16**, 495–501 (2014).
2. Mochida, K. *et al.* *Nature* **522**, 359–362 (2015).
3. Khaminets, A. *et al.* *Nature* **522**, 354–358 (2015).
4. Bernales, S., Schuck, S. & Walter, P. *Autophagy* **3**, 285–287 (2007).
5. Hidvegi, T. *et al.* *Science* **329**, 229–232 (2010).
6. Kamimoto, T. *et al.* *J. Biol. Chem.* **281**, 4467–4476 (2006).
7. Twig, G. *et al.* *EMBO J.* **27**, 433–446 (2008).
8. Kurth, I. *et al.* *Nature Genet.* **41**, 1179–1181 (2009).
9. Randow, F. & Youle, R. J. *Cell Host Microbe* **15**, 403–411 (2014).

This article was published online on 3 June 2015.

MATERIALS SCIENCE

Round the bend with microwaves

Simulations reveal that microwaves propagating through a waveguide can travel around sharp bends in the device without being reflected. The finding might open the way to technologies that exploit this uncommon phenomenon.

SUNIL MITTAL & MOHAMMAD HAFEZI

Like any synthetic structure, photonic systems do not always perform according to expectations. Fabrication errors can give rise to defects that affect the propagation of electromagnetic waves — from radio to optical wavelengths — through the wave-carrying medium, causing undesired effects. For example, structural defects introduce noise in the medium's properties that can, in extreme cases, completely block photon transmission. Efforts are therefore under way to engineer systems whose topology (rather than shape) governs photon transport, making them immune to such effects. These efforts rely on results^{1,2} showing that, as photonic systems undergo a certain type of continuous

deformation, their properties remain intact and photon transport becomes topologically protected. Writing in *Physical Review Letters*, Ma *et al.*³ demonstrate this theoretically for a waveguide design. Their system could enable the topologically protected transport of microwave photons, which would be able to travel around sharp corners without being reflected backwards.

In the early 1980s, physicists realized that certain physical properties of electronic systems are entirely dictated by the topology of the material concerned⁴. A hallmark discovery was that, in the presence of a strong magnetic field, the transverse electrical conductance of a material becomes quantized (the quantum Hall effect). In materials that exhibit this phenomenon, conduction is remarkably

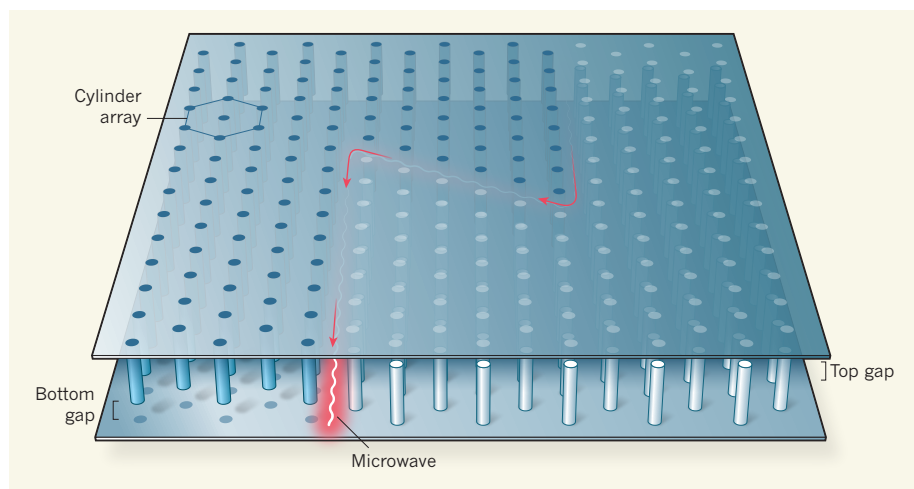


Figure 1 | Reflection-free microwave propagation in a waveguide. Ma *et al.*³ have simulated the propagation of microwaves in a metawaveguide. The proposed device contains a hexagonal array of metal cylinders displaying an asymmetry along the cylinder axis — a gap between one end of the cylinders and the enclosing metal plate. The two sections shown are joined together such that the position of the gap is inverted between them (on the left the gap is at the bottom, whereas on the right it is at the top). This configuration allows microwaves to travel along the bent interface between the two sections with negligible backward reflection at the two 120° turns.

robust against defects and disorder.

The electronic states in the interior of such systems become localized so that the bulk of the material becomes an insulator. By contrast, the boundary of the material supports extended one-way circulating electronic states, known as chiral edge states, that mediate conduction. The system's topology determines whether edge states occur; materials that allow them are called topological insulators. A remarkable property of edge states is that they allow electrical current to route around disorders, with no backscattering of electrons.

It was initially thought that topological insulators could be generated only in the presence of a magnetic field, which specifically breaks the time-reversal symmetry of the system. However, in 2005, Charles Kane and Eugene Mele showed⁵ that similar topologically robust properties can be achieved through spin–orbit coupling of electrons — that is, coupling of the electrons' orbital angular momentum with their spin angular momentum — while preserving the system's time-reversal symmetry. This opened up a wider range of systems that can have topologically protected states. Since then, topological insulators have attracted great interest, both for their intriguing fundamental properties and for their potential application in quantum computation.

Photonic systems can exhibit topological features analogous to those of electronic systems^{6–8}. Ma *et al.* simulate a system that acts like a topological insulator for microwave radiation. The authors consider a device called a parallel-plate metawaveguide, which consists of an array of centimetre-scale metallic cylinders arranged in a hexagonal lattice, bounded on either side by metal plates (Fig. 1). For microwaves that have wavelengths of about

15 cm, this array constitutes a 'metamaterial' in which the refractive index varies on a scale comparable to the wavelengths of microwaves.

The metawaveguide supports two decoupled polarization modes of the microwaves' electromagnetic fields — the transverse electric (TE) and transverse magnetic (TM) modes. These can propagate only in a plane perpendicular to the cylinder axis. The hexagonal geometry of the cylinder lattice causes the emergence of Dirac cones in the metawaveguide's energy-band structure — cone-shaped bands that meet at their tips. At the tips of the Dirac cones, the TE and TM modes have the same energy, and the velocity with which the wave envelopes propagate is constant near this point.

Ma and colleagues show that introducing an asymmetry in the metawaveguide's geometry, in the form of a gap between the cylinder array and one of the enclosing plates, couples the TE and TM modes. This change in the array's configuration modifies the energy-band structure of the device, causing a bandgap to open up between the Dirac cones. The resulting bandgap has non-trivial topological properties analogous to those described by the electronic Kane–Mele model. In other words, the metawaveguide becomes a photonic analogue of a topological insulator. Here, symmetric and antisymmetric combinations of the TE and TM modes, which are time-reversed counterparts, constitute a pseudo-spin, and the asymmetry induces spin–orbit interaction.

In further simulations, Ma *et al.* show that if two such metawaveguides are coupled to each other in a configuration of opposing topological indices — for example, such that the position of the gap at the tips of the metal cylinders is inverted between the two devices — the interface between them displays intriguing

properties. Specifically, the authors observe topologically protected edge states of opposing chirality (handedness), which propagate in opposite directions along the interface. They show how these states can be excited by placing a suitably polarized electric or magnetic dipole inside the gap of the metawaveguide that is adjacent to the interface. For example, a left-polarized dipole excites microwaves that always propagate in the backward direction, whereas a right-polarized dipole excites forward-only waves. These waves are immune to backscattering and can take sharp turns along the interface. The authors' simulations demonstrate this for an interface bent by 120°.

However, these edge states are not robust against all types of disorder. For example, a disorder that flips the pseudo-spin of a state can couple a forward-propagating state to a backward-propagating one, destroying the edge states' protection against backscattering. This is analogous to the effect of magnetic impurities in materials exhibiting the 'quantum spin Hall effect' against which edge states are not protected. In the wavelength domain applicable to telecommunications (about 1,550 nm), the effects of such pseudo-spin flips are negligible⁹, but it is not known whether the effect is also small in the microwave domain. Future work may clarify this.

An experimental realization of the effects modelled in Ma and colleagues' work would open up new ways to engineer electromagnetic structures that would benefit from topological protection^{10,11}. For example, one could explore designs for microwave devices such as waveguides, filters, antennas and amplifiers that would make the devices insensitive to design defects and that could have applications in telecommunications technology. ■

Sunil Mittal and Mohammad Hafezi are in the Department of Electrical and Computer Engineering, IREAP, Joint Quantum Institute, University of Maryland, College Park, Maryland 20742, USA.
e-mail: hafezi@umd.edu

1. Haldane, F. D. M. & Raghu, S. *Phys. Rev. Lett.* **100**, 013904 (2008).
2. Hafezi, M., Demler, E. A., Lukin, M. D. & Taylor, J. M. *Nature Phys.* **7**, 907–912 (2011).
3. Ma, T., Khanikaev, A. B., Mousavi, S. H. & Shvets, G. *Phys. Rev. Lett.* **114**, 127401 (2015).
4. Thouless, D. J., Kohmoto, M., Nightingale, M. P. & den Nijs, M. *Phys. Rev. Lett.* **49**, 405–408 (1982).
5. Kane, C. L. & Mele, E. J. *Phys. Rev. Lett.* **95**, 226801 (2005).
6. Wang, Z., Chong, Y., Joannopoulos, J. D. & Soljačić, M. *Nature* **461**, 772–775 (2009).
7. Hafezi, M., Mittal, S., Fan, J., Migdall, A. & Taylor, J. M. *Nature Photon.* **7**, 1001–1005 (2013).
8. Rechtsman, M. C. *et al.* *Nature* **496**, 196–200 (2013).
9. Mittal, S. *et al.* *Phys. Rev. Lett.* **113**, 087403 (2014).
10. Jia, N., Owens, C., Sommer, A., Schuster, D. & Simon, J. Preprint at <http://arxiv.org/abs/1309.0878> (2015).
11. Chen, W.-J. *et al.* *Nature Commun.* **5**, 5782; <http://dx.doi.org/10.1038/ncomms6782> (2014).

This article was published online on 3 June 2015.

The power of positivity

Stimulating neurons in the brain's hippocampus that are normally activated by pleasurable experiences protects mice from the depressive consequences of stress. [SEE LETTER P.335](#)

ALEX DRANOVSKY & E. DAVID LEONARDO

Our ability to construct a personal narrative and to establish a sense of identity depends on our recollection of past events, the most significant of which are inevitably associated with emotions. Understanding how emotion-laden memories affect behaviour forms the bedrock of psychotherapy treatments, but the biology of this process is poorly understood. On page 335 of this issue, Ramirez *et al.*¹ shed light on the subject, demonstrating that depressive-like stress responses in mice can be acutely suppressed through artificial reactivation of a small population of neurons that had previously been activated by a positive experience.

Understanding how memories are stored in the brain has been the subject of intensive research², much of which has focused on the hippocampus — an elongated structure in the brain's temporal lobe that is essential for forming long-term memories and regulating responses to stress. The hippocampus contributes to the generation of cellular representations of experiences through the activation of ensembles of neurons. In mice, ensembles in a hippocampal subregion called the dentate gyrus can be genetically tagged with light-sensitive molecules while being activated by an experience³. Subsequent experimental reactivation of the ensembles using pulses of light causes the animals to behave in a way that suggests they are recalling the original experience⁴. As a result, these neuronal ensembles are

thought to constitute the physical substrate of memory, called an engram.

Ramirez *et al.* used a previously described system⁴ to selectively express light-sensitive molecules in a subset of mouse dentate-gyrus cells while the cells were being activated by experiences, tagging them for optical reactivation at a later time. The authors tagged these cells in male mice under three conditions: a rewarding experience, in which the mice were placed in a cage with a female; a neutral experience, in which they were placed in an empty cage; or a negative experience, in which they were immobilized, leading to stress. The animals were subsequently exposed to stress for 10 consecutive days, which induced increased anxiety and depression-related behaviours such as passivity and decreased preference for enjoyable activities (anhedonia).

The investigators found that the depression-like behaviours seen in animals that had been subjected to this stressing could be reversed by optically reactivating dentate-gyrus neurons tagged during the positive experience, whereas activation of neutral- or negative-tagged neurons did not have this effect (Fig. 1).

Repeated exposure to positive imagery has been used in attempts to battle the symptoms of human depression⁵. Could repeated activation of a positive engram provide enduring protection from the depression-like consequences of stress in mice? Ramirez and colleagues found that when they reactivated the positive engram every day for five days in previously stressed animals, passivity and

anhedonia were reversed on day six. Importantly, animals exposed to the positive experience itself for five days after the repeated stress did not show this enduring protection. Moreover, the decreased production of new neurons that is routinely observed following stress was reversed by repeated engram stimulation, but not by the repeated positive experience.

Ramirez and colleagues' provocative results raise several questions relevant to stress-related disorders in humans. Both anxiety and depression are associated with repeated exposure to stress, and the two disorders often occur together. However, acutely activating the dentate-gyrus engram in mice primarily reversed depression-associated behaviours. Might an engram that can affect anxiety be found elsewhere in the hippocampus or other regions of the brain?

Because a single reactivation of the positive engram did not relieve anxiety, the authors did not investigate the effects of repeated engram stimulation on this trait. But although fast-acting treatments for depression and anxiety differ, chronic treatments for the two conditions overlap. Could repeated activation of the positive engram, unlike the single intervention, prevent anxiety-associated manifestations of stress? Finally, it will be interesting to investigate the other side of the coin — whether reactivation of traumatic memories is sufficient to cause stress-related disease. A first step to exploring this avenue in mice would be to test whether reactivating an ensemble of dentate-gyrus neurons tagged by negative experiences could cause anxiety or depression-like behaviours.

Why is reactivating an engram of a positive experience a more effective stress-reliever than the experience itself? We are left wondering whether the repeated recall of positive memories will result in resilience to adversity. It is intriguing to speculate that nostalgia serves a similar stress-reducing purpose in humans^{4,6}. Perhaps an experience itself results simply in memory storage, whereas its recollection activates a neuronal network associated with reward, thereby changing behaviour.

If, as has been suggested⁷, stress results in a cognitive bias against rewarding associations, then reactivation of a 'positive' engram laid down in an animal or human that was previously stressed would not combat the consequences of later stress — a hypothesis that could easily be tested in the authors' animals. In support of this suggestion, Ramirez *et al.* found that inhibiting a component of the reward neuronal circuitry while activating a positive engram interfered with the antidepressant properties of reactivating that engram. Consistent with this, a study⁸ of people with depression suggests that, unlike healthy individuals, they cannot improve their mood by recalling positive memories. So the ability to remember your way to happiness may be a normal regulatory process that is disrupted in depression. ■

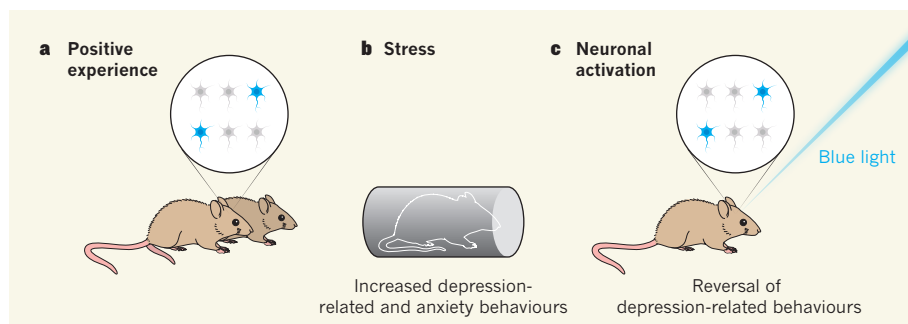


Figure 1 | Light-induced stress relief. **a**, Ramirez *et al.*¹ genetically tagged neurons in the dentate-gyrus region of the brains of male mice while the neurons were being activated (indicated in blue) by the positive experience of being in a cage with a female, or by a negative or a neutral experience (not shown). **b**, The mice were subsequently subjected to repeated immobilization, causing stress that led to anxiety and depression-related behaviours. **c**, The depression-like behaviours associated with stress could be reversed by reactivating the positive-tagged neurons with pulses of blue light, but reactivating the neutral- or negative-tagged neurons did not have this affect.

Alex Dranovsky and E. David Leonardo are in the Department of Psychiatry, Division of Integrative Neuroscience, Columbia University, New York, New York 10032, USA, and at the New York State Psychiatric Institute. e-mails: ad722@cumc.columbia.edu ;

el367@cumc.columbia.edu

1. Ramirez, S. *et al.* *Nature* **522**, 335–339 (2015).
2. Squire, L. R. *Neurobiol. Learn. Mem.* **82**, 171–177 (2004).
3. Ramirez, S., Tonegawa, S. & Liu, X. *Front. Behav. Neurosci.* **7**, 226 (2014).

4. Liu, X. *et al.* *Nature* **484**, 381–385 (2012).
5. Blackwell, S. E. *et al.* *Clin. Psychol. Sci.* **3**, 91–111 (2015).
6. Cheung, W.-Y. *et al.* *Pers. Soc. Psychol. Bull.* **39**, 1484–1496 (2013).
7. Harding, E. J., Paul, E. S. & Mendl, M. *Nature* **427**, 312 (2004).
8. Joorman, J., Siemer, M. & Gotlib, I. H. *J. Abnorm. Psychol.* **116**, 484–490 (2007).

GLOBAL WARMING

Growing feedback from ocean carbon to climate

The finding that feedbacks between the ocean's carbon cycle and climate may become larger than terrestrial carbon–climate feedbacks has implications for the socio-economic effects of today's fossil-fuel emissions.

FORTUNAT JOOS

Global warming reduces the uptake of carbon dioxide by the ocean and the land biosphere. This allows more human-caused CO₂ to remain in the atmosphere, where it causes more global warming — an amplifying climate–carbon feedback. The amplifying feedbacks associated with carbon in vegetation and soils are conventionally thought to be several times larger than those associated with carbon in the ocean. Writing in *Global Biogeochemical Cycles*, Randerson *et al.*¹ report that this idea needs to be revisited and refined: in the long term, the ocean will have a larger role than land in climate–carbon coupling.

The authors combined results from long-term simulations using an Earth-system model — specifically the Community Earth System Model (CESM)² — with an established analysis³ of feedbacks in the carbon–climate system. They ran the model up to the year 2300 using contrasting set-ups in which the greenhouse-gas forcing of CO₂ was turned on or off. They report that the ocean carbon–climate feedback (measured as the difference in the amount of carbon cumulatively taken up by the ocean for the set-up that accounts for forcing from all the main anthropogenic emissions, including CO₂, and for the set-up that omits such forcing) is 3% for 1999 and increases to a staggering 23% by 2300. Surprisingly, the ocean–climate feedback becomes larger than the land–climate feedback beyond 2100 (Fig. 1).

This apparent conflict with the conventional view of a smaller ocean than land feedback⁴ results from differences in timescales. Most carbon cycles through plants and soils within decades, whereas it takes centuries to transport

carbon from the sea surface to the deep ocean. Land carbon–climate feedbacks are therefore larger in the near term than marine ones, but this situation will reverse in the long run.

Ocean carbon uptake is primarily a physico-chemical process in which the rate-limiting step is the transport of water from the surface to the deep, and in which the reaction of CO₂ with water releases hydrogen ions, causing ocean acidification⁵. Randerson and co-workers report that warming decreases the solubility of CO₂ in water, reduces the density of surface waters and slows the overturning circulation (the movement of surface water from high latitudes to the deep ocean, compensated for by rising waters from other latitudes). These effects reduce the overall uptake capacity of the ocean for, and the

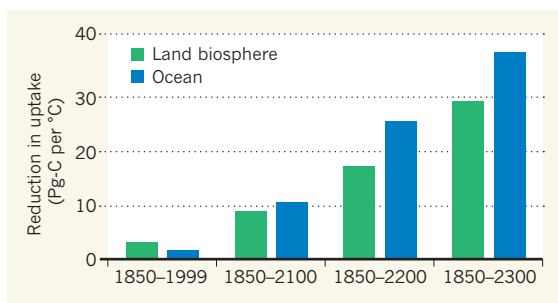


Figure 1 | Feedback between climate and the carbon cycle. Randerson *et al.*¹ have used a computational model to show that the ocean's contribution to feedback between climate and the carbon cycle increases considerably over time, and exceeds contributions from land by the year 2100. The bar chart shows, for different periods, the reduction in the uptake of anthropogenic carbon (measured in petagrams of carbon; 1 petagram is 10¹⁵ grams) by the ocean and the land biosphere that is attributable to climate change, per increase in global mean surface air temperature of 1 °C. The authors computed these sensitivities from differences in cumulative carbon flux and global mean surface air temperature between a simulation in which CO₂ influences climate and another in which the direct influence of CO₂ on global warming is suppressed.

surface-to-deep transport of, anthropogenic carbon. The magnitude of the ocean–climate feedback reported by the researchers, and the main proposed feedback mechanisms — including a near-collapse of the Atlantic overturning circulation and a small role for marine biological processes — are consistent with the findings of earlier studies (see ref. 6, for example) that used models with simpler ocean dynamics than those in the CESM.

On land, the authors find that a loss of carbon results from increased rates of soil-carbon decomposition due to warming. This dominates the stimulation of plant productivity caused by increased moisture and growing-season length at high latitudes. In addition, human land use reduces the amount of carbon in vegetation in their scenario, further limiting the potential amplifying feedback between land carbon and climate.

The representation of biogeochemical processes in the CESM is advanced, but many feedbacks to those processes are uncertain or not represented. These include⁷ the impacts of ocean acidification, warming, increased levels of dissolved CO₂ and a potential increase in the volume of low-oxygen zones on marine ecosystems, biological productivity, the production of the greenhouse gas nitrous oxide, the export of biogenic particles from the surface to the deep ocean, and their sinking velocity and decomposition rate. On land, thawing of permafrost carbon may lead to the release of CO₂ (ref. 8) and methane⁴, processes not accounted for in the version of the CESM used by the authors. More work is needed to address changes in the extent of wetlands and peatlands in model projections, and to better quantify emissions of methane, nitrous oxide and organic compounds from the land biosphere, because these changes and emissions all contribute to climate forcing⁹.

Data for past variations in CO₂ levels and climate can help us to avoid relying exclusively on models to project future trends. Although palaeoclimatic information cannot be directly used to assess how climate change affects the flow of anthropogenic carbon, it does reveal how the natural carbon cycle alters. Palaeoclimatic data document that the ratio of the change in atmospheric CO₂ concentration to the change in global mean surface air temperature is increasing with the timescale of climatic variations, and that the increase of CO₂ on decade-to-century timescales

is probably less than 20 parts per million for each degree of warming¹⁰.

Further constraints on carbon–climate interactions arise from isotope data that allow terrestrial and oceanic greenhouse-gas sources to be disentangled. Carbon isotope data show that decadal CO₂ variations during the past millennium were predominantly driven by land-carbon variations¹¹, consistent with Randerson and colleagues' finding of a small near-term marine feedback. But isotope data for nitrous oxide question the assumption made in the CESM that nitrogen availability strongly limits plant growth. These data show that the land source of nitrous oxide increased during the last deglaciation, which implies that nitrogen flow through the land biosphere increased and that nitrogen limitation was small¹². A long-standing research challenge is to develop Earth system models that perform seamless simulations from the past to the future, consistently integrating palaeoclimatic and modern instrumental information in projections.

Randerson and colleagues' work highlights another research front. The marine carbon–climate feedback increases in proportion to ocean-heat content in their model. Researchers would benefit from observational and modelling studies in which spatial and temporal variations of physical and biogeochemical parameters, such as temperature, carbon and nutrients, are analysed jointly to draw a more complete and self-consistent picture of the changing ocean. Biogeochemical variables are particularly sensitive indicators of change, but ocean physics governs both carbon and heat uptake — and therefore sea-level rise, climate change and their impacts.

The current study acts as a timely reminder of several policy-relevant findings, ahead of the conference to be held by the United Nations Framework Convention on Climate Change in Paris this December. First, the larger the amplifying carbon–climate feedback is, the more stringent will emission reductions have to be to stabilize climate at any given level. Second, shifting the peak in carbon emissions to after 2100 imposes on future generations not only the burden of implementing a carbon-free economy, but also global warming of about 10 °C above preindustrial temperatures¹.

Third, carbon emitted today will change our environment irreversibly for many generations to come, and these changes increase hand in hand with cumulative carbon emissions¹³. Sea level and the ocean's acidity and carbon and heat content — and the associated adverse effects — will continue to increase long after atmospheric CO₂ levels have stabilized, underscoring the need for near-term emission reduction. Finally, carbon-emission reductions are urgently needed if we are to limit global warming and ocean acidification to moderate levels. Any delay will narrow and eventually

close the currently available window to meet stringent climate targets¹⁴. ■

Fortunat Joos is in the Division of Climate and Environmental Physics, Physics Institute and the Oeschger Centre for Climate Change Research, University of Bern, Bern CH-3012, Switzerland.

e-mail: joos@climate.unibe.ch

1. Randerson, J. T. *et al.* *Glob. Biogeochem. Cycles* <http://dx.doi.org/10.1002/2014gb005079> (2015).
2. Hurrell, J. W. *et al.* *Bull. Am. Meteorol. Soc.* **94**, 1339–1360 (2013).
3. Friedlingstein, P. *et al.* *J. Clim.* **19**, 3337–3353 (2006).
4. Ciais, P. *et al.* in *Climate Change 2013: The Physical Science Basis. Contribution of Working Group I to the*

Fifth Assessment Report of the Intergovernmental Panel on Climate Change (eds Stocker, T. F. *et al.*) 465–570 (Cambridge Univ. Press, 2013).

5. Orr, J. C. *et al.* *Nature* **437**, 681–686 (2005).
6. Joos, F., Plattner, G. K., Stocker, T. F., Marchal, O. & Schmittner, A. *Science* **284**, 464–467 (1999).
7. Heinze, C. *et al.* *Earth Syst. Dyn.* **6**, 327–358 (2015).
8. Koven, C. D., Lawrence, D. M. & Riley, W. J. *Proc. Natl Acad. Sci. USA* **112**, 3752–3757 (2015).
9. Stocker, B. D. *et al.* *Nature Clim. Change* **3**, 666–672 (2013).
10. Heimann, M. *Nova Acta Leopoldina* **NF 121**, 97–99 (2015).
11. Bauska, T. K. *et al.* *Nature Geosci.* **8**, 383–387 (2015).
12. Schilt, A. *et al.* *Nature* **516**, 234–237 (2014).
13. Steinacher, M., Joos, F. & Stocker, T. F. *Nature* **499**, 197–201 (2013).
14. Stocker, T. F. *Science* **339**, 280–282 (2013).

NEURODEGENERATION

Aggregates feel the strain

Aggregates of α -synuclein protein can form in various cell types and cause different neurodegenerative disorders. The existence of strains with distinct structural conformations might explain this variability. [SEE LETTER P.340](#)

SEUNG-JAE LEE & ELIEZER MASLIAH

Parkinson's disease, dementia with Lewy bodies and multiple system atrophy are devastating, progressive, age-related neurodegenerative disorders that are characterized by the accumulation of clumps of α -synuclein protein in brain cells¹. These diseases, dubbed synucleinopathies, can be differentiated from one another by the distinct anatomical patterns and cell types in which α -synuclein is deposited². On page 340 of this issue, Peelaerts *et al.*³ propose that different 'strains' of α -synuclein, which adopt different structural conformations, might explain this variability.

According to current models, deposits of α -synuclein are first laid down in the synaptic connections between neurons during the early stages of synucleinopathy⁴. Deposition later spreads to other sites: to neuronal cell bodies, where they form aggregates called Lewy bodies; to neuronal projections called axons and dendrites, forming aggregates called Lewy neurites; and to cells known as oligodendrocytes that support and insulate axons, forming aggregates called glial cytoplasmic inclusions (GCIs)⁵.

These GCIs are the predominant deposits in people with multiple system atrophy². Lewy bodies and Lewy neurites are characteristic of both Parkinson's disease and dementia with Lewy bodies — although the patterns in which the proteins spread vary between these two diseases. Furthermore, patterns of α -synuclein deposition, and consequently clinical

symptoms, can vary between individual cases of the same disease⁵. But the reasons underlying this variability have remained unclear.

Synucleinopathies have several features in common with prion diseases, which are neurodegenerative diseases caused by the accumulation of misfolded prion protein in the brain. For example, the symptoms, biological abnormalities and incubation times of both types of disease are variable. In prion diseases, variability between individuals depends on the conformation adopted by aggregates of prion protein. Aggregates of a specific conformation are thought to propagate throughout the brain by inducing normal prion proteins to clump together into misfolded aggregates of the same conformation — a concept known as 'seeded aggregation'. Evidence suggests⁶ that aggregates of α -synuclein and other neurodegeneration-associated proteins spread through brain cells in a similar way, which might explain the varied patterns in which deposition spreads.

In support of this hypothesis, two distinct aggregates of α -synuclein, fibrils and ribbons, have been characterized⁷. These aggregates faithfully propagate their structural features through seeding, and induce different abnormalities in cultured cells. Following up on these findings, Peelaerts *et al.* investigated whether ribbons and fibrils are genuine protein strains by testing whether they cause different symptoms and biological changes in animals. The authors injected rat brains with four different types of α -synuclein: ribbons; fibrils; homogenized brain samples from mice

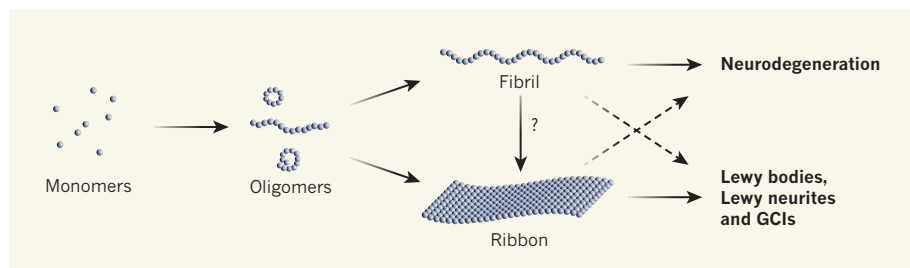


Figure 1 | Structural variability and disease. The protein α -synuclein can adopt different structural conformations. Monomers of the protein interact with each other to form complexes called oligomers, which in turn are converted into either fibrils or ribbons. Furthermore, it is possible that fibrils are converted into ribbons. Peelaerts *et al.*³ report that the different conformations have different properties: fibrils primarily cause neurodegeneration and behavioural defects when injected into the brains of rats, whereas ribbons mostly cause the accumulation of protein aggregates called Lewy bodies, Lewy neurites and glial cytoplasmic inclusions (GCIs). Structures are not to scale.

that produce a human α -synuclein aggregate; and short strings of abnormal α -synuclein protein called oligomers, which might give rise to the more complex ribbon and fibril structures⁸. They then analysed α -synuclein deposition in these animals.

Ribbons caused more deposition than other types of α -synuclein. By contrast, and consistent with a study in mice⁹, fibrils more potently promoted other hallmarks of neurodegenerative disease, such as degeneration of dopamine axons in the striatum region of the brain and deficits in motor function. Fibrils were more stable than ribbons, which generated structures resembling Lewy bodies and Lewy neurites. These findings indicate that the aggregates induced by ribbons and fibrils are indeed distinct. When they injected ribbons into rats that had been engineered to produce too much α -synuclein, Peelaerts *et al.* observed the generation of GCIs, but inoculation with fibrils did not have this effect. Together, these results suggest that different synucleinopathies are defined by different strains of α -synuclein aggregate (Fig. 1).

The researchers also demonstrated that intravenous inoculations of aggregates that had been preformed *in vitro* led to the deposition of α -synuclein in the central nervous system of animals. Blood contains relatively large amounts of α -synuclein¹⁰, so this result suggests that, if changes in this peripheral system affect conformations of α -synuclein, this could translate into specific neuronal abnormalities.

Peelaerts and colleagues' study has several implications. First, neurodegeneration and behavioural deficits seem to be associated primarily with fibrils, whereas the formation of Lewy bodies, Lewy neurites and GCIs is associated more with ribbons. Second, the distinct patterns of α -synuclein deposition observed after cerebral inoculations of fibrils and ribbons suggest that different strains of aggregate are the explanation for the variability of synucleinopathies. Third, strains might not have to be generated in the central nervous system, or even in neurons, but instead could be transported there after

being generated in the periphery.

Despite Peelaerts and colleagues' findings, and advances made by other groups¹¹, it remains to be definitively proved that injected aggregates can amplify through seeding. An alternative explanation is that the injected aggregates lead to changes such as inflammation in the microenvironment of the brain region into which they are injected, and that this could eventually result in distinct abnormalities. Synucleinopathies are accompanied by brain inflammation in humans, and the authors showed that injecting different α -synuclein aggregates caused brain inflammation to different extents. *In vitro* amplification and structural characterization of the amplified aggregates from brain tissues could provide the much-needed proof of aggregate seeding¹². Whether ribbons or fibrils are sustained if brain tissue from the infected animal is injected into another animal also needs further validation to confirm that these aggregates are indeed strains.

Can strains generated in the blood induce α -synuclein aggregation in the brain and cause

neurodegeneration? Peelaerts and colleagues' results indicate that this is a possibility. The study also suggests that the blood of people with Parkinson's disease, dementia with Lewy bodies or multiple system atrophy might contain specific strains of α -synuclein that can serve as biomarkers for these diseases.

The results raise the question of whether α -synuclein pathology can be transmitted between humans through blood. So far, there is no evidence for such a phenomenon, but future studies should address this question. ■

Seung-Jae Lee is at the Neuroscience Research Institute, Department of Medicine, Seoul National University College of Medicine, Seoul 110-799, Korea. **Eliezer Masliah** is in the Department of Pathology and Neurosciences, University of California, San Diego, La Jolla, California 92093, USA.
e-mails: sjlee66@snu.ac.kr; emasliah@ucsd.edu

1. Lashuel, H. A., Overk, C. R., Oueslati, A. & Masliah, E. *Nature Rev. Neurosci.* **14**, 38–48 (2013).
2. Brück, D., Wenning, G. K., Stefanova, N. & Fellner, L. *Neurobiol. Dis.* <http://dx.doi.org/10.1016/j.nbd.2015.03.003> (2015).
3. Peelaerts, W. *et al. Nature* **522**, 340–344 (2015).
4. Kramer, M. L. & Schultz-Schaeffer, W. J. *J. Neurosci.* **27**, 1405–1410 (2007).
5. Kim, W. S., Kågedal, K. & Halliday, G. M. *Alz. Res. Ther.* **6**, 73 (2014).
6. Brettschneider, J., Del Tredici, K., Lee, V. M.-Y. & Trojanowski, J. Q. *Nature Rev. Neurosci.* **16**, 109–120 (2015).
7. Bousset, L. *et al. Nature Commun.* **4**, 2575 (2013).
8. Lashuel, H. A., LaBrenz, S. R., Woo, L., Serpell, L. C. & Kelly, J. W. *J. Am. Chem. Soc.* **122**, 5262–5277 (2000).
9. Luk, K. C. *et al. Science* **338**, 949–953 (2012).
10. Mollenhauer, B., El-Agnaf, O. M. A., Marcus, K., Trenkwalder, C. & Schlossmacher, M. G. *Biomark. Med.* **4**, 683–699 (2010).
11. Lee, H.-J., Bae, E.-J. & Lee, S.-J. *Nature Rev. Neurol.* **10**, 92–98 (2014).
12. Lu, J.-X. *et al. Cell* **154**, 1257–1268 (2013).

This article was published online on 10 June 2015.

INORGANIC CHEMISTRY

Peculiar boron startles again

Boron's unusual properties inspired big advances in chemistry. A compound in which boron binds two carbon monoxide molecules reveals another oddity — the element forms bonds similar to those of transition metals. SEE LETTER P.327

GERNOT FRENKING

Transition-metal compounds take part in a wide range of reactions and catalytic cycles as a result of the metals' abilities to form complexes with several ligands through a process known as donor–acceptor

bonding. Many transition metals can bind several carbonyl ligands (carbon monoxide molecules). By contrast, the main-group elements — those found in groups 1, 2 and 13 to 18 of the periodic table, excluding hydrogen — were for a long time thought not to be able to form complexes that bind more than one

carbonyl. Writing on page 327, Braunschweig *et al.*¹ report the synthesis of a compound, known as a borylene adduct, in which an atom of the main-group element boron carries two carbonyl ligands, and which has remarkable similarities to transition-metal carbonyl complexes. This provides striking evidence of donor–acceptor bonding in the chemistry of main-group elements.

Boron forms compounds in which the element exhibits bonding patterns and reactivities not found for other elements. Indeed, two Nobel prizes for chemistry have been awarded for discoveries involving this property of boron. In 1976, William Lipscomb received the award for his work on the structure of boranes (boron–hydrogen compounds), which illuminated problems of chemical bonding². Three years later, Herbert Brown was recognized for his research into organoboron compounds (sharing the prize with Georg Wittig for his related groundbreaking discoveries in the area of phosphorus chemistry)³. A third Nobel prize may also be partly ascribed to discoveries in boron chemistry: in 2010, Akira Suzuki received the chemistry award for his studies of a carbon–carbon bond-forming reaction that uses boron compounds, together with Richard Heck and Ei-ichi Negishi for their work on other carbon–carbon bond-forming reactions⁴.

What makes boron compounds so peculiar? Boron atoms have three valence electrons, which can create three bonds by forming pairs with electrons from monovalent groups (R). The resulting borane (BR₃) molecules thus have six valence electrons at the boron atom. This is two electrons short of a full valence shell of eight electrons, the number required to give a stable molecule according to the octet rule for main-group atoms. Boranes are therefore Lewis acids, compounds characterized by a ‘vacancy’ in the valence shell — an absence of a pair of electrons. This vacancy is associated with an empty molecular orbital at the boron atom (Fig. 1a).

Lewis acids typically bind strongly to Lewis bases such as amines (NR₃), in which the nitrogen atom has a ‘lone pair’ of electrons in a molecular orbital. The vacancy in the valence shell of Lewis acids can be filled by the lone-pair molecular orbital of Lewis bases, yielding a donor–acceptor bond (Fig. 1b). The resulting compounds are well known to chemists.

In 2012, a theoretical study⁵ suggested that boron could take part in a different kind of chemical bonding that exhibits an unusual type of donor–acceptor interaction. This involves borylene compounds (BR), in which one boron electron is engaged in a B–R bond and the remaining two electrons form a lone-pair orbital (Fig. 1c). This electronic structure leaves two vacant molecular orbitals at boron. In other words, the borylene is a double Lewis acid (it has two vacancies), but also

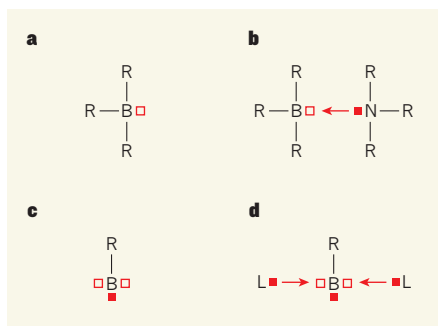


Figure 1 | The electronic structure of boron compounds. **a**, Borane compounds, BR₃, have a ‘vacancy’ — an absence of a pair of electrons (empty square) — in their shell of valence electrons. R represents any group that can donate a single atom for bond formation. **b**, Lewis bases, such as tertiary amines (NR₃), have a ‘lone pair’ of electrons (filled square), which they can donate to BR₃ to fill the vacancy, forming a complex. **c**, Borylene compounds have two vacancies and a lone pair. **d**, Borylene complexes can therefore form when two Lewis-base ligands (L) donate their lone pairs to the borylene. Braunschweig *et al.*¹ report a borylene complex in which the boron atom binds two carbon monoxide ligands.

a Lewis base (one lone-pair molecular orbital). Such borylene species could be stabilized by donor–acceptor interactions with two Lewis bases, forming complexes in which the boron atom retains its lone-pair orbital (Fig. 1d). This bonding situation was proposed for a (BR)L₂ molecule⁶ in which L is a cyclic(alkyl)(amino) carbene (CAAC) ligand — a very strong Lewis base⁷.

The theoretical study⁵ predicted that the analogous carbonyl complex (in which L is CO) would possess donor–acceptor bonds that are weaker than those of the CAAC complex, but strong enough to be synthesized. Braunschweig *et al.* have now verified that prediction by making the borylene dicarbonyl complex (BR)(CO)₂, in which R is a bulky substituent. The authors also report unusual geometries and reactivities of related borylene complexes in which L is an isocyanate ligand, CNR.

The researchers observe that the structure and reactivity of (BR)(CO)₂ mimics the typical behaviour of transition-metal carbonyl complexes, which is unheard of in the chemistry of main-group elements. For example, when the team irradiated the complex with light, free BR was generated, and it immediately reacted with available substrates. Furthermore, the B–CO bonds in the dicarbonyl complex are significantly shorter than that of a related compound⁸ in which one of the CO ligands has been replaced by CAAC. The shorter bonds indicate strong π backdonation — a process in which the boron atom’s lone pair of electrons is donated to vacant molecular orbitals (known as π^* orbitals) of the CO ligands, and which is a typical feature of transition-metal carbonyl complexes.

The isolation of the remarkably stable

dicarbonyl complex (BR)(CO)₂ also casts light on a controversy about the nature of bonding in compounds in which a main-group atom forms fewer bonds to other atoms than is normal^{9–11} (low-valent compounds). The boron complexes (BR)L₂ have the same electronic structure as the carbon compounds CL₂. For example, carbon suboxide was reported¹² in 1906, and was first thought to be a linear molecule containing sequential double bonds (O=C=C=C=O). But later experiments¹³ showed that the molecule is bent at 156° at the central carbon atom. It was therefore proposed¹⁴ that the compound is a complex of a bare carbon atom with two carbonyl ligands, C(CO)₂, and thus exemplifies a previously unrecognized class of compounds called carbones, in which carbon is in the zero oxidation state. Further examples have since been synthesized^{15,16}. The isolation of (BR)(CO)₂ shows that related boron compounds are also quite stable, and helps to support the argument that carbones are complexes of bare carbon atoms with ligands.

The synthesis of Braunschweig and colleagues’ dicarbonyl complex is just the starting point for further experimental and theoretical work in the field of low-valent boron complexes, and it will build a bridge between the chemistry of main-group compounds and that of transition-metal complexes. Considering the ubiquitous use of transition-metal compounds as catalysts in industrially important reactions, the authors’ findings might also open up fresh opportunities in applied chemistry. ■

Gernot Frenking is at the Fachbereich Chemie, Philipps-Universität Marburg, Hans-Meerwein-Strasse, Marburg 35039, Germany. e-mail: frenking@chemie.uni-marburg.de

- Braunschweig, H. *et al.* *Nature* **522**, 327–330 (2015).
- www.nobelprize.org/nobel_prizes/chemistry/laureates/1976/
- www.nobelprize.org/nobel_prizes/chemistry/laureates/1979/
- www.nobelprize.org/nobel_prizes/chemistry/laureates/2010/
- Celik, M. A., Sure, R., Klein, S., Kinjo, R., Bertrand, G. & Frenking, G. *Chem. Eur. J.* **18**, 5676–5692 (2012).
- Kinjo, R., Donnadieu, B., Celik, M. A., Frenking, G. & Bertrand, G. *Science* **333**, 610–613 (2011).
- Soleilhavoup, M. & Bertrand, G. *Acc. Chem. Res.* **48**, 256–266 (2015).
- Dahcheh, F., Martin, D., Stephan, D. W. & Bertrand, G. *Angew. Chem. Int. Edn* **53**, 13159–13163 (2014).
- Himmel, D., Krossing, I. & Schnepf, A. *Angew. Chem. Int. Edn* **53**, 370–374 (2014).
- Frenking, G. *Angew. Chem. Int. Edn* **53**, 6040–6046 (2014).
- Himmel, D., Krossing, I. & Schnepf, A. *Angew. Chem. Int. Edn* **53**, 6047–6048 (2014).
- Diels, O. & Wolf, B. *Ber. Dt. Chem. Ges.* **39**, 689–697 (1906).
- Jensen, P. & Johns, J. W. C. *J. Mol. Spectrosc.* **118**, 248–266 (1986).
- Tonner, R. & Frenking, G. *Pure Appl. Chem.* **81**, 597–611 (2009).
- Dyker, C. A., Lavallo, V., Donnadieu, B. & Bertrand, G. *Angew. Chem. Int. Edn* **47**, 3206–3209 (2008).
- Fürstner, A., Alcarazo, M., Goddard, R. & Lehmann, C. W. *Angew. Chem. Int. Edn* **47**, 3210–3214 (2008).

Pacific western boundary currents and their roles in climate

Dunxin Hu¹, Lixin Wu², Wenju Cai^{2,3}, Alex Sen Gupta⁴, Alexandre Ganachaud⁵, Bo Qiu⁶, Arnold L. Gordon⁷, Xiaopei Lin², Zhaohui Chen², Shijian Hu¹, Guojian Wang³, Qingye Wang¹, Janet Sprintall⁸, Tangdong Qu⁹, Yuji Kashino¹⁰, Fan Wang¹ & William S. Kessler¹¹

Pacific Ocean western boundary currents and the interlinked equatorial Pacific circulation system were among the first currents of these types to be explored by pioneering oceanographers. The widely accepted but poorly quantified importance of these currents—in processes such as the El Niño/Southern Oscillation, the Pacific Decadal Oscillation and the Indonesian Throughflow—has triggered renewed interest. Ongoing efforts are seeking to understand the heat and mass balances of the equatorial Pacific, and possible changes associated with greenhouse-gas-induced climate change. Only a concerted international effort will close the observational, theoretical and technical gaps currently limiting a robust answer to these elusive questions.

Western boundary currents (WBCs) are swift, narrow oceanic currents found in all major oceanic gyres. Within the Pacific Ocean, the subtropical gyre WBCs are the Kuroshio Current in the Northern Hemisphere, and the East Australian Current (EAC) in the Southern Hemisphere (Fig. 1a). The Pacific low-latitude, tropical belt WBCs include the Mindanao Current in the Northern Hemisphere and the New Guinea Coastal Undercurrent (NGCUC) south of the Equator, both of which are directly connected to the equatorial Pacific circulation system. Much of modern wind-driven ocean circulation theory was derived from a quest to understand these Pacific Ocean currents. Knowledge of the effect of the Earth's rotation on WBCs, and of the Ekman transport (see Box 1), led to ground-breaking advances: that wind stress (Fig. 1b) is a driving agent of ocean currents, but it is the horizontal gradient rather than the absolute strength that is important; that latitudinal gradients in the effect of Earth's rotation on the horizontal motion cause a flow intensification towards the west of the ocean basins; and that the Pacific wind-forced ocean currents include the equatorial current system, the low-latitude and subtropical WBCs.

Impacts of the Pacific WBCs on the global ocean circulation and climate variability are manifold. First, in winter, the subtropical WBCs are associated with the largest supply of heat and moisture into the atmosphere in the Pacific basin, and are coupled to North Pacific storm tracks¹. As cold and dry air comes into contact with the warm water carried poleward by the subtropical WBCs, heat and moisture are extracted from the surface. Second, the Indonesian Throughflow (ITF), the only low-latitude inter-ocean current, flows from the Pacific to the Indian Ocean. The throughflow plays a role in the return branch of the global thermohaline circulation². The ITF sources its water mostly from the North Pacific Ocean via the Mindanao Current with the remainder sourced from the South Pacific Ocean via the New Guinea Coastal Current (NGCC), implicating these Pacific WBCs as important players in the global climate system. Third, the Pacific is home to the

El Niño/Southern Oscillation (ENSO), the most prominent source of global climate variability on interannual timescales, which severely disrupts global weather patterns, affecting ecosystems, agriculture, tropical cyclones, drought, bushfires, floods and other extreme weather events worldwide³. The Pacific low-latitude WBCs are agents for transporting mass into the equatorial Pacific, therefore critically influencing the Western Pacific Warm Pool (a region of sea surface temperatures (SSTs) warmer than 28.5 °C) and the life cycle of ENSO, as well as the East Asian monsoon and the Indian/Southeast Asian monsoon. Finally, the EAC, through its outflow to the Indian Ocean, participates in the Southern Hemisphere supergyre circulation that links the three subtropical gyres^{4–6}, providing a subtropical gateway for the Pacific's influence on global climate.

Research and observations over the past 15 years have enabled a string of advances in our understanding of the structure of individual components of the Pacific WBCs, interactions amongst them, and their climatic impacts. In particular, several multi-national programmes are underway. Included in these are the Northwestern Pacific Ocean Circulation and Climate Experiment⁷, the Southwest Pacific Ocean Circulation and Climate Experiment⁸, and the ITF monitoring programme⁹, providing an intensive observational focus in Pacific low-latitude regions. These process studies, together with targeted modelling and recent advances in broad-scale sampling of ocean temperature and salinity, upper oceanic currents, winds, precipitation and sea surface heights, as well as satellite retrievals, have led to a significant advance in our understanding of the physical structure and dynamics of the Pacific WBCs, and their possible changes under greenhouse warming.

Here we review the current state of understanding of the structure and variability of the Pacific WBCs, their climatic impacts, and how they may be affected by greenhouse warming. We show that the entire Pacific WBC system moves northwards or southwards concurrently, on seasonal and interannual timescales. The climatic impacts of the Pacific

¹Key Laboratory of Ocean Circulation and Waves, Institute of Oceanology, Chinese Academy of Sciences, Qingdao 266071, China. ²Physical Oceanography Laboratory, Qingdao Collaborative Innovation Center of Marine Science and Technology, Ocean University of China, Qingdao 266003, China. ³CSIRO Oceans and Atmosphere Flagship, Aspendale, Victoria 3195, Australia. ⁴Australian Research Council (ARC) Centre of Excellence for Climate System Science, Mathews Building, The University of New South Wales, Sydney 2052, Australia. ⁵Institut de Recherche pour le Développement (IRD), UMR5566-LEGOS, UPS (OMP-PCA), 31400 Toulouse, France. ⁶Department of Oceanography, University of Hawaii at Manoa, 1000 Pope Road, Honolulu, Hawaii 96822, USA. ⁷Lamont-Doherty Earth Observatory, Earth Institute at Columbia University, Palisades, New York 10964, USA. ⁸Scripps Institution of Oceanography, 9500 Gilman Drive, La Jolla, California 92037, USA. ⁹IPRC, Department of Oceanography, SOEST, University of Hawaii, Honolulu, Hawaii 96822, USA. ¹⁰Center for Earth Information Science and Technology, Japan Agency for Marine-Earth Science and Technology (JAMSTEC) 3173-25 Showa-machi Kanazawa-ku, Yokohama 236-0001, Japan. ¹¹NOAA/Pacific Marine Environmental Laboratory, Seattle, Washington 98115, USA.

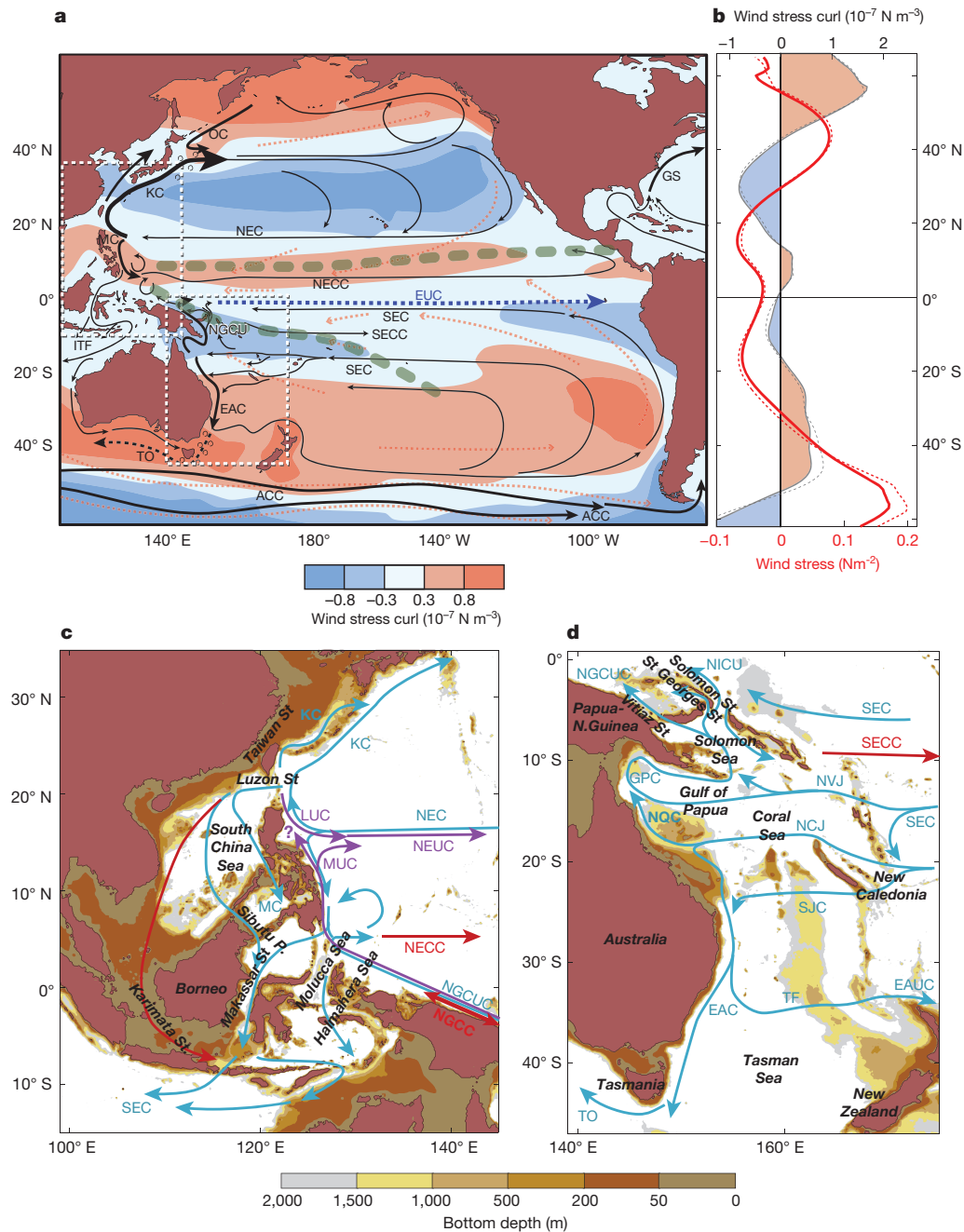


Figure 1 | Pacific Ocean circulation and boundary currents. **a**, Schematic of major currents and observed surface wind vectors (orange dashed lines) and wind stress curl (shading: positive curl in red; negative in blue). The Intertropical Convergence Zone and the South Pacific Convergence Zone are indicated by thick grey-dashed lines. Red and blue shading in the Southern Hemisphere corresponds to anticyclonic and cyclonic curls, respectively, and vice versa in the Northern Hemisphere. **b**, Pacific zonally averaged zonal wind stress (grey curve) and wind stress curl (red curve) for the present day (solid lines) and the latter half of the twenty-first century (dashed lines). Projected changes are calculated as the multi-model mean difference between 2050–2100 future winds under RCP8.5 and 1900–2000 historical winds. OC, Oyashio Current; KC, Kuroshio Current; NEC, North Equatorial Current; MC, Mindanao Current; NECC, North Equatorial Counter Current; NEC, North Equatorial Current; EUC, Equatorial Undercurrent; NGCUC, New Guinea Coastal Undercurrent; ITF, Indonesian Throughflow; SECC, South Equatorial Counter Current; SEC, South

Equatorial Current; EAC, East Australian Current; TO, Tasman Outflow; ACC, Antarctic Circumpolar Current; GS, Gulf Stream. **c**, **d**, Topographic and boundary current systems in the Northwest Pacific (**c**) and Southwest Pacific (**d**), as indicated by the dashed white boxes in **a**. Depths shallower than 2,000 m are colour-shaded. Grey shading indicates depths shallower than 50 m. The main currents, integrated from 1,000 m to the surface, are indicated by light blue arrows; the red curved arrow indicates the ‘freshwater plug’; red straight arrows indicate the main surface-trapped counter currents; purple arrows indicate undercurrents; question mark indicates uncertainty in flow path. Panel **c** is adapted from ref. 8 (John Wiley and Sons). LUC, Luzon Undercurrent; MUC, Mindanao Undercurrent; NGCC, New Guinea Coastal Current; NEUC, North Equatorial Undercurrent; NICU, New Ireland Coastal Current; NVJ, North Vanuatu Jet; NCJ, North Caledonia Jet; SCJ, South Caledonia Jet; NQC, North Queensland Current; GPC, Gulf of Papua Current; TF, Tasman Front; EAUC, East Auckland Current; TO, Tasman Outflow.

WBCs are far-reaching, and are exerted in many ways, including through interactions with the South China Sea circulation, the Tropical Pacific Warm Pool, and the ITF; through longevity of SST anomalies along the WBCs and their feedback to the atmosphere; and

through contribution to the global thermohaline circulation. Under greenhouse warming, the response of Pacific WBCs is uncertain, although changes are not expected to resemble anomalies associated with climate variability.

BOX 1

Processes associated with the Pacific surface WBCs

Ekman transport and oceanic currents. In the tropical Pacific, the main currents, westward flowing over the upper ocean, are forced by the easterly trade winds. In the first few tens of metres of water depth, immediately away from the Equator, deflection by the rotation of the Earth occurs to the right in the Northern Hemisphere, and left in the Southern Hemisphere. This 'Coriolis' force causes 'Ekman transport', whereby tropical surface waters move poleward in both hemispheres. Likewise, poleward of 25° N and 25° S, the prevailing westerly winds induce Ekman transports towards the Equator, generating a convergence between 15°–30° N and 15°–30° S, with high sea levels around 10°–15° N and 10°–15° S, respectively. The sea-level slope drives two broad geostrophic westward flows: the North Equatorial Current (NEC) and the South Equatorial Current (SEC).

Bifurcation and WBCs. Upon approaching the western boundaries, equatorial currents split into two branches: equatorward low-latitude WBCs; and poleward subtropical WBCs. In the Pacific, the NEC bifurcates into the equatorward Mindanao Current and the poleward Kuroshio Current, and the SEC bifurcates into the equatorward Gulf of Papua Current and poleward East Australia Current (EAC).

Rossby wave adjustment. The above ocean wind–current relationship assumes a steady wind forcing the ocean for a long time. Winds vary on the large scale, and the ocean adjusts by generating large-scale anomalies that move in the form of oceanic Rossby waves. Such waves propagate along the thermocline, a boundary between the warm upper layer and the cold deeper part of the ocean, and always propagate westward because of the latitudinal gradient of the tangential speed of the Earth's rotation.

Wind stress curl. It is not the absolute magnitude of the wind stress but rather its curl (the horizontal gradient of the stress) that forces the north–south transport of the interior ocean. At some locations, the curl is reduced to zero and there is no north–south transport (although there might be flows at depth which cancel when summed up). Lines along which the curl is zero provide natural boundaries that separate circulation into gyres. Such lines in subtropical latitudes are often used as an approximation to locate the bifurcation latitude.

Kuroshio Extension. At some latitude, the Kuroshio Current separates from the coast and flows eastward into the ocean interior. At this eastward excursion, the Kuroshio Extension has some of the largest air–sea fluxes found across the North Pacific basin. It is a region with a great quantity of latent, sensible, and net surface heat loss, and is co-located with the Pacific storm track.

Tasman Front and Tasman Outflow. In the South Pacific, part of the EAC separates from the coast and veers eastward as the Tasman Front; the residual continues southward passing through the Tasman Sea. A portion of the Tasman Front attaches to the northern coast of New Zealand, forming the East Auckland Current. The portion flowing through the Tasman Sea reaches Tasmania and turns westward into the eastern Indian Ocean as Tasman Outflow.

Structure of the Pacific WBC system

Driven by the large-scale pattern of wind stress curl (see Box 1), the Pacific WBC system is characterized by the unique presence of two intense equatorward WBCs—the Mindanao Current and the NGCUC. These serve as subtropical-to-tropical oceanic pathways that modulate the mass and heat balances of the Western Pacific Warm Pool, and the ventilation of the equatorial Pacific thermocline. As such, low-latitude WBCs are a part of the life cycle of ENSO and Pacific decadal variability^{10,11}.

The Mindanao Current and the NGCUC originate at the bifurcations of zonal currents arriving at the western boundaries: the westward-flowing

North Equatorial Current (NEC) in the North Pacific, and the South Equatorial Current (SEC) in the South Pacific. Upon reaching the Philippine coast, the NEC bifurcates to feed the poleward Kuroshio Current¹² and the equatorward Mindanao Current¹³ (Fig. 1c). In a similar manner, the westward-flowing SEC bifurcates at the Australian coast into the northward-flowing Gulf of Papua Current¹⁴ and southward-flowing EAC¹⁵. The Gulf of Papua Current feeds the NGCUC, which exits through narrow straits at the northern boundary of the Solomon Sea¹⁶, connecting the South Pacific to the Equator and the ITF (Fig. 1c, d).

The convergence of the Mindanao Current and NGCUC near the Equator (Fig. 2) feeds the Western Pacific Warm Pool, the surface to lower thermocline of the ITF¹⁷, and the eastward-flowing Equatorial Undercurrent (EUC)¹⁸. In this way, the two low-latitude WBCs together with the strong mixing in the Indonesian Seas largely determine the water mass characteristics of the Pacific equatorial current systems and of the ITF¹⁸. Also involved in the mass balance of the Western Pacific are counter currents, which are associated with the Intertropical Convergence Zone and the South Pacific Convergence Zone, the two prominent rainbands in the Pacific. These convergence zones themselves, together with local winds they have altered and the associated wind stress curl, produce two eastward-flowing, surface-intensified counter currents, known as the North Equatorial Counter Current¹⁹ and the South Equatorial Counter Current²⁰ (Fig. 1a).

The Pacific low-latitude current system has a rich vertical structure, and over the years there has been conflicting evidence as to the nature of some currents^{21–29}. In both hemispheres, the bifurcation latitude increases with depth. For example, the long-term average NEC bifurcation latitude is approximately 14° N at the surface, but 20° N at a depth of 1,000 m. The Luzon Undercurrent^{22,23}, observed beneath the Kuroshio, with a core at depths around 650 m near 18° N, intensifies towards the south before turning to the east to feed the North Equatorial Undercurrent. By contrast, despite the suggestion of a northward-flowing Mindanao Undercurrent with a centre at around 600 m (refs 21, 24–26; Fig. 2a), debate persisted as to whether it is transient in nature²⁷, a quasi-permanent flow but affected by thermocline variability²⁸, or a subthermocline eddy²⁹. The presence of the undercurrent at depths below 400 m has been confirmed by recent measurements (Fig. 2a; ref. 25).

In the South Pacific, the range of the SEC bifurcation latitudes as a function of depth is large, varying between 13° and 25° S. The surface SEC flow turns southward feeding the EAC, while the subsurface flow, the Great Barrier Reef Undercurrent (part of the Gulf of Papua Current system), veers northward feeding the NGCUC^{20–32}. The Great Barrier Reef Undercurrent, the South Pacific counterpart of the Luzon Undercurrent, has been linked to the basin-scale circulation of the subtropical gyre that contracts poleward with depth³³. The NGCUC was recently measured³¹ as a strong, permanent undercurrent against the coast of Papua New Guinea (Fig. 2b), with its core at about 400 m carrying the bulk of the South Pacific low-latitude WBC transport that splits in the different Solomon Sea straits then flows towards the Equator or the ITF⁸.

Because the seasonal wind stress curl variability that controls the bifurcation latitude is due to seasonal movement of trade winds, the NEC and SEC bifurcations move synchronously and in the same meridional direction on seasonal timescales. At the surface, the NEC bifurcation latitude moves from 15° N in boreal summer, to 17° N in boreal winter³⁴, in conjunction with the seasonal reversal of the South East Asia monsoon. This seasonal movement is accompanied by a stronger NEC leading to both a stronger Mindanao Current and Kuroshio Current when the bifurcation occurs at lower latitudes in boreal summer, increasing the tropical water injection into the North Pacific subtropical gyre¹³. As such, the NEC, the Mindanao Current and the Kuroshio Current transport east of Luzon are all at their seasonal maximum during boreal summer (June–July) when bifurcation occurs at the southernmost latitude^{34,35} but minimum during boreal winter (November–December) when bifurcation occurs at the northernmost

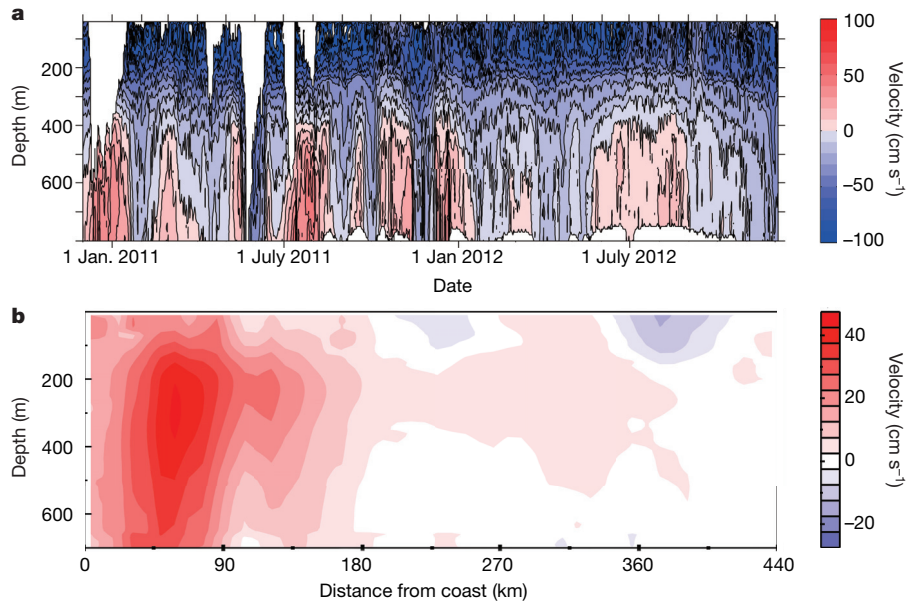


Figure 2 | Characteristics of the two equatorward low-latitude WBCs in the tropical Pacific. Such WBCs are a unique feature of the Pacific Ocean.

a, Moored current meter data at 8° N, 127° E showing evolution of meridional velocities, the Mindanao Current (blue, negative values) and its undercurrent (red, positive values) from boreal winter 2010 to boreal winter 2012, adapted from ref. 26 (John Wiley and Sons). Shown are daily ADCP data smoothed by a three-day running mean filter. Moorings were anchored in 6,100 m deep water, with two 75K RDI ADCP current meters at ~400 m scanning up and down,

respectively. The current meters move vertically in the water column, as strong currents interact with the mooring system. **b**, Velocity section across the South Solomon Sea, from a compilation of glider observations adapted from ref. 31 (AMS). Units are cm s^{-1} . Red shading indicates equatorward flow, and blue poleward flow. The NGCUC is characterized by a strong core, centred at about 400 m, against the coast of Papua New Guinea, to the left of the section. The x -axis represents an equivalent eastward distance from the coast of Papua New Guinea.

latitude. The SEC bifurcation shifts northward towards the Equator in austral summer (November–December), and is southernmost in austral winter (June–July)¹⁵. When the SEC is closer to the Equator, its transport strengthens, feeding more water into both the EAC and the NGCUC¹⁵. The EAC attains a maximum transport (up to 36 Sv; $1 \text{ Sv} = 10^6 \text{ m}^3 \text{ s}^{-1}$) and extends furthest poleward in austral summer with a large Tasman Outflow into the Indian Ocean. In austral winter, the EAC transport weakens (to 27 Sv), and much of this veers eastward as the Tasman Front (Fig. 1d; ref. 36).

Consistent with dynamical argument, observations have shown that the South Pacific subtropical gyre and the Tasman Outflow south of Australia are part of a system of nested anticyclonic gyres encompassing the entire Southern Hemisphere subtropics, connecting the Atlantic, Indian and Pacific basins to the global thermohaline circulation^{4–6,37,38}. The Atlantic and Indian Oceans are connected south of Africa by a westward Agulhas leakage and the eastward South Atlantic Current³⁸, while the Pacific and Indian Oceans are connected south of Tasmania by the westward Tasman Outflow^{4,5,37}, a narrow boundary flow of the western Pacific gyre that turns westward around the south of Tasmania and ‘leaks’ to the Indian Ocean basin⁴. Tasman leakage occurs primarily as a subsurface or intermediate water circulation⁶, in contrast to the ITF route that largely occurs in the upper 300 m. The linkage of the Tasman leakage to the supergyre provides a mechanism whereby Antarctic Intermediate Water, which transits to the southwest Pacific, is distributed between the ocean basins before it spreads northward into the Pacific, Indian and Atlantic oceans^{5,6}.

Variability of the Pacific WBCs

Pacific WBCs are subject to strong variability on intraseasonal^{26,27,39}, interannual^{30,40–44}, decadal and longer timescales^{42,43}. However, as a result of possible eddy aliasing^{30,44}, and the discrete short-term nature of *in situ* surveys that may be difficult to place in an appropriate climate context, there is large uncertainty in the volume transport estimate of these WBCs. For example, the Mindanao Current transport ranges from 13 to 39 Sv depending on the study^{12,27,41}.

The NEC bifurcation latitude and its partitioning into the Mindanao Current and the Kuroshio Current are affected by many factors, including local monsoonal winds and buoyancy fluxes, and remote forcing from the Pacific interior and North Pacific along the western boundary^{35,40}. The main forcing, though, is ENSO. The response of the WBCs to ENSO, in turn, influences the life cycle of ENSO. As an El Niño develops, the entire Pacific circulation system ‘breathes’ together, bifurcating at a more northerly latitude (Fig. 3a, b), as manifested through a positive correlation of ENSO with the north and south bifurcation latitudes. Accompanying the more northerly bifurcation are a stronger NEC and North Equatorial Counter Current, a stronger Mindanao Current, a more intense EUC at its westernmost part, but a weaker Kuroshio Current and ITF^{28,30,40} (Fig. 3a). To the south, the NGCUC intensifies during, or several months after, the peak of an El Niño³⁰, and the surface southward NGCC disappears and turns northwards (Fig. 3b), as occurred from July to February during the 1997–98 extreme El Niño⁴⁵. Although the EAC transport displays variability on interannual timescales, only a weak ENSO signal is evident in observations³⁶.

The responses of the Mindanao Current and the NGCUC to ENSO as described above are integral to the ENSO discharge/recharge cycle⁴⁶. The increased equatorward WBC transport during an El Niño creates a strong confluence of relatively cooler water in the tropical western Pacific, and constitutes a compensatory flow for the associated discharge of the equatorial Pacific warm water, conducted in the interior Pacific through the Sverdrup process, whereby mass is pumped out of the equatorial west Pacific in response to wind forcing.

Recent observations revealed a rich spatial structure and a large response of the SEC transport to ENSO^{30–32}. Variability of the NGCUC inflow to the Solomon Sea can reach 100% of the mean transport, with the changes mainly occurring in the upper 250 m. During an El Niño event, the SEC transport between New Caledonia and the Solomon Islands increases^{21,31,32}, particularly in the North Vanuatu Jet, with an enhanced transport entering the Solomon Sea (Fig. 3b). This leads to an increased equatorward mass transport through the Solomon Strait and

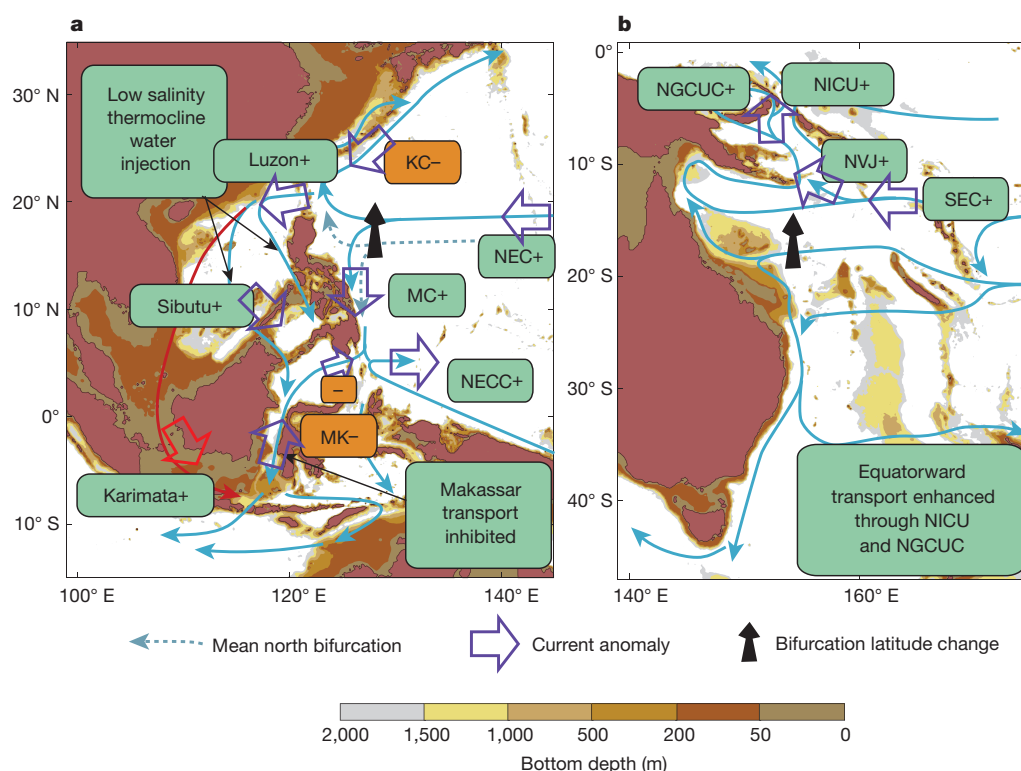


Figure 3 | Impact of El Niño on the Pacific WBC system. **a, b,** During an El Niño, the bifurcation moves north in both the Northern (**a**) and the Southern (**b**) Hemispheres, as indicated by the black arrows. The ocean depth is indicated as on Fig. 1c, d. Increasing (green boxes) and decreasing (orange boxes) flow anomalies during El Niño are indicated. Some currents are enhanced, while others are weakened, as indicated by the anomalies (large dark blue/red arrows). From the developing phase to approximately three-to-four months before the peak of an El Niño, the Kuroshio Current (KC) decreases while the Mindanao Current increases. The ITF weakens as the Pacific-Indian pressure

gradient reduces. The South China Sea Throughflow intensifies, setting up a freshwater plug. Towards the peak of an El Niño, equatorward transport enhances through NICU and NGCUC. LUC, Luzon Undercurrent; MUC, Mindanao Undercurrent; NGCC, New Guinea Coastal Current; NEUC, North Equatorial Undercurrent; NICU, New Ireland Coastal Current; NVJ, North Vanuatu Jet; NCJ, North Caledonia Jet; SCJ, South Caledonia Jet; NQC, North Queensland Current; GPC, Gulf of Papua Current; TF, Tasman Front; EAUC, East Auckland Current; TO, Tasman Outflow.

through the New Ireland Coastal Undercurrent, in addition to the increased transport via the Vitiaz Strait^{45,47} (see Fig. 3b). The transport of heat and salt through the Solomon Sea can change by up to a factor of two between extreme El Niño and La Niña conditions⁴⁷.

Connections between the Pacific WBCs and the ITF are complex, particularly when ENSO is considered. Synthesis of observational data and model simulations indicates that the depth and velocity of the ITF core vary with ENSO, with the ITF slowing and shoaling during El Niño events⁴⁸. Modelling and observational studies indicate that, on average, the proportion of the ITF water derived from the North and South Pacific depends sensitively on ENSO phases. Climatologically, approximately 80% of the ITF originates from the North Pacific and 20% from the South Pacific via the NGCUC^{48–50}. As a La Niña develops, the ITF increases due to stronger easterly trade winds, which induces a pressure gradient between the West Pacific and the eastern Indian Ocean. Climate models suggest a greater amount of ITF water originates from the South Pacific during La Niña compared to during El Niño⁴⁹. During the development of La Niña, a seasonal and ENSO-dependent inflow from the Luzon Strait to the Indonesian Seas forced by large-scale winds in the Pacific, called the South China Sea Throughflow⁵¹, weakens. Further, the Mindanao Current transport decreases, though a greater portion of this current goes into the ITF at the expense of the North Equatorial Counter Current⁵⁰.

Interactions between the Pacific WBCs and the Pacific Decadal Oscillation (PDO) occur on decadal timescales in a manner somewhat different to the interannual timescales for ENSO, particularly in the North Pacific^{42,43}. The post-1990 cold PDO phase is linked to a southward shift of the NEC bifurcation latitude, and a strengthened NEC and

North Equatorial Counter Current, as a result of intensified easterlies over the Western Pacific^{42,43}. Both the Kuroshio Current and the Mindanao Current have also strengthened, inconsistent with ENSO-induced changes, which would imply a decreased Mindanao Current. In the Southern Hemisphere, observations and ocean reanalysis suggest that a cold phase of the PDO is associated with a deeper southward EAC extension³⁶, while the Tasman Front weakens, which suggests that there is a gating between these two currents⁵². In the two decades before 1993, the PDO was in a warm phase, whereby the trade winds across the tropical Pacific were weaker, consistent with a weaker atmospheric Walker circulation⁵³. In response, the NEC and its counter currents were also weaker and shifted northward^{42,43}.

Multidecadal fluctuations can also modulate the interannual relationship between ENSO and the NEC bifurcation latitude, such that the relationship between ENSO and the northwestern Pacific WBCs is non-stationary^{13,43}. The NEC mean bifurcation latitude is situated further to the south during a cold PDO phase, and from this more southward position the NEC bifurcation latitude can ‘jump’ a considerable distance to the north during an El Niño. As such, interannual NEC bifurcation variability is more strongly correlated to the Niño-3.4 index during the cold phase of the PDO. Thus, the bifurcation latitude of the NEC which is determined by wind forcing in the 12°–14° N band also contains variability not solely represented by the Niño-3.4 index⁴².

Interactions with climate

The Pacific WBCs interact with physical climate on synoptic, interannual and long-term climate scales, and such interactions are better understood for the North Pacific than for the South Pacific. In boreal winter, strong advection of warm water by the Kuroshio Current into regions of

colder air temperatures, such as the Kuroshio/Oyashio extension region, results in large losses of latent and sensible heat to the atmosphere^{54,55}. This heat loss triggers oceanic and atmospheric deep convection, and fuels storms for their recurrent development, while contributing to the formation of mode waters⁵⁵. In the mixed water region north of the Kuroshio Extension, turbulent heat fluxes of more than 600 W m^{-2} are observed during wintertime northerly wind events⁵⁶, where the contrast between the WBC warm core and adjacent waters gives rise to particularly large SST gradients: more than 10°C over 200 km across the Oyashio Front. The presence of such oceanic fronts can generate atmospheric instability, and increased vertical momentum exchange, as well as winds induced by changes in air density^{57,58}. This tends to exert a positive feedback, whereby larger turbulent heat fluxes from the ocean to the atmosphere over the warm core of the current generate even stronger winds^{57,58}. Atmospheric eddy heat fluxes associated with synoptic systems act to reduce the sharp meridional air temperature gradients¹, but the large thermal inertia of the ocean mixed-layer and oceanic advection rapidly restore the SST front and the air temperature gradient⁵⁹. An impact of the warm water maintained in this manner is that typhoons tend to strengthen as they pass over the warm core of the Kuroshio Current⁶⁰. During summer time, heat and moisture supply from the warm Kuroshio, though less than in winter, is effective in retaining the convectively unstable stratification of low-level northwesterly monsoonal airflow from the tropics, enhancing the convective heavy rainfall along the Kuroshio⁶¹.

Beyond synoptic scales, the North Pacific WBCs exert a considerable impact on Asia summer monsoons^{62,63}. One such impact is on the South China Sea summer monsoon, which marks the commencement of the Asia summer monsoon. In post-La Niña boreal spring and early summer, the western tropical Pacific heat content is anomalously high, as a part of the heat recharge associated with stronger trade winds. In association with a stronger Walker circulation, convection over the eastern Indian Ocean and the Western Pacific remains strong, resulting in stronger-than-normal westerlies over the tropical Indian Ocean delivering the crucial moisture source favourable for the South China Sea summer monsoon⁶³. Consequently, the South China Sea summer monsoon commences earlier than normal, leading to droughts along the middle-lower Yangtze River basin and floods in southern and northern China⁶¹. Thus, the heat content of the Western Pacific Warm Pool can be a predictor of the South China Sea summer monsoon onset and strength, with a high heat content associated with an early onset and strong intensity⁶³. Conversely, in the late boreal spring-early summer after an El Niño, when the warm pool is still cooler than normal, the South China Sea monsoon takes place later than normal, causing floods along the middle-lower Yangtze River basin and drought in southern and northern China⁶³. A similar link exists between the Australian summer monsoon and ENSO via SST anomalies in the central and Western Pacific⁶⁴; however, the timing is different. The Australian summer monsoon tends to be weakened, concurrently, by an El Niño, and strengthened by a La Niña.

Interactions between the North Pacific WBCs and the South China Sea Throughflow⁶⁵ on seasonal and interannual timescales constitute another source of climatic influence. During the boreal winter, when the northwest monsoon prevails over the Indonesian Seas, or during El Niño periods, the wind drives buoyant, low-salinity surface water derived from the South China Sea via the Karimata Strait (Fig. 1c) into the southern Makassar Strait⁶⁵ and from the Sibutu Passage into the northern Makassar Strait⁵⁰. This creates an anomalous pressure gradient in the surface layer of the Makassar Strait (red curved arrow, Fig. 1c) that inhibits the warm surface water from the Mindanao Current from entering into the ITF. This surface-layer 'freshwater plug', originally due to heavy rainfall and large runoff from Southeast Asia, inhibits the Pacific warm surface water from flowing southward into the Indian Ocean, leading to a reduced, cooler ITF in the Makassar Strait during December–January and during El Niño, and inducing a cooler upper Indian Ocean, which may in turn weaken the Asian monsoon⁶⁵. During

the boreal summer, when winds in the Indonesian Seas reverse to the southeast monsoon, or during La Niña periods, the obstructing pressure gradient is reduced, reducing the impact of the freshwater plug, supporting an earlier and stronger South China Sea monsoon in the late spring, or early summer after a La Niña event⁵⁰.

Variations in the North Pacific WBCs also exert a climatic impact through the longevity of SST anomalies they generate^{54,55,66–70}, influencing the large-scale atmospheric circulation and storm-track activities, particularly near the multiple fronts of the WBC extension^{1,71,72}. These extension fronts are fertile grounds for strong SST variability. Because of the strong horizontal gradients, a slight frontal movement can lead to a large change in SSTs and is an effective process for generating SST variability^{66,69}. Frontal movement can be generated by intrinsic variability of the WBCs as well as by remote ocean and atmosphere forcing via extratropical ocean Rossby waves^{67–70}. The Kuroshio Extension fronts, for example, are strongly influenced by large-scale changes in the subtropical gyre driven by wind stress changes across the North Pacific^{42,73}, and by ENSO-induced basin-scale wind stress curl anomalies through atmospheric teleconnections^{67,68}, emanating from the tropical Pacific, remotely forcing SST variability in the Kuroshio Extension region via oceanic Rossby waves^{73,74}.

The longevity of SST anomalies along the Kuroshio Extension can be further enhanced by processes that either maintain or reinforce the anomalies^{75–80}. For example, in boreal summer, the North Pacific Ocean cools the warm moist air advected from the south, inducing the formation of low-level stratus and fog within the boundary layer on the northern sides of the Kuroshio Extension fronts^{75,76}. These clouds (in particular low clouds) reduce solar insolation because of their high albedo, in turn maintaining low SSTs^{76,77}. This positive 'cloud–SST feedback' acts to reinforce cold SST anomalies, and can enhance and prolong summertime cold SST anomalies near the North Pacific subarctic front zone⁷⁸. In boreal winter, through anomalous geostrophic heat advection, the axial migration of the Kuroshio Current and the associated frontal movement generate subsurface temperature anomalies that can persist over multiple years. Shoaling of the North Pacific mixed layer in boreal spring and deepening in autumn results in mid-latitude SST anomalies recurring from one winter to the next without persisting through the intervening summer^{79,80}. This 're-emergence mechanism' operates when SST anomalies spread throughout the deep winter mixed layer, but remain beneath the mixed layer in spring, isolated from the 'damping' surface fluxes. When the mixed-layer deepens again in the following autumn, the temperature anomalies are brought out into the surface layer and influence SST⁸⁰. Along the Kuroshio Extension, advection by the mean currents transports these anomalies by as much as 4,000 km over the course of a year^{79,80}. These processes are favourable for decadal SST variability such that it is particularly strong along such fronts^{55,69,81}.

Climatic impacts of the EAC are less well understood, but there is suggestion of an influence on Australian and New Zealand climates. Weaker EAC transport is linked to anomalous cool conditions in New Zealand⁸², and a stronger EAC is shown to promote rainfall along the east Australia coast⁸³. However, little is known about the impact of the EAC on, for example, storm tracks or atmospheric circulations.

The Pacific WBCs exert substantial influence on timescales longer than decadal, and on climate remote from the Pacific regions, through their linkage to the Southern Hemisphere supergyre circulation via the Tasman Outflow^{4–6,38} and the ITF^{9,48,84–87}. The Tasman Outflow influences downstream ocean climate through intermediate-depth water⁴, but the influence through the ITF is conducted through the upper 300 m (ref. 9). Increased transport within the warmer upper layer of the ITF modifies the heat budget of the Indian Ocean^{84,85} as well as the residence time of tropical Indian Ocean waters⁸⁶, thermocline depth and SST patterns⁸⁷. Further downstream, the ITF feeds the Agulhas leakage, and ultimately provides an important heat source for supporting the global thermohaline circulation².

Observed changes and future projection

Over the past century, there has been direct and indirect evidence supporting changes having occurred in the subtropical gyres. For example, there appears to be a synchronous surface ocean warming along the path of all subtropical WBCs that is two-to-three times greater than the global mean⁸⁸. The enhanced warming is associated with a poleward shift and/or intensification of global subtropical WBCs in conjunction with a systematic change in winds over both hemispheres. Specifically, the zero-curl line shifted poleward in the North Pacific, the North Atlantic and the South Atlantic Oceans; in the South Pacific and South Indian Oceans, high-latitude westerly winds strengthened while mid-latitude southeasterly trade winds weakened^{5,37}, consistent with a positive trend of the Southern Annular Mode^{5,38}, leading to accelerated warming and an intensified supergyre.

Over the past 60 years, there has been a synchronous long-term southward shift of the NEC and the SEC bifurcations⁸⁹ in the tropical Pacific (Fig. 4a, b), similar to their synchronous movement on inter-annual timescales. Over the 60-year period, the overall long-term southward shift of the NEC is modulated by a slight northward migration from 1970 to 1992 (ref. 90) and a southward shift in the post-2000 period, associated with the warm and cold PDO phases, respectively. The long-term southward shift of the latitude of the NEC bifurcation suggests a strengthening Kuroshio Current, consistent with the observed accelerated warming (Fig. 4a). By contrast, the southward shift of the SEC bifurcation has no bearing on the transport partition, but is accompanied by a substantial southward extension of the EAC^{5,37}. The relative importance of greenhouse warming and decadal variability for the North Pacific changes is difficult to quantify. However, about two-thirds of the poleward intensification of the Southern Hemisphere supergyre circulation, including the southward EAC extension and the strengthening of the Tasman Outflow^{91,92}, has been attributed to wind changes induced by Antarctic ozone depletion⁹³, and one-third to increasing atmospheric CO₂ (refs 91–93).

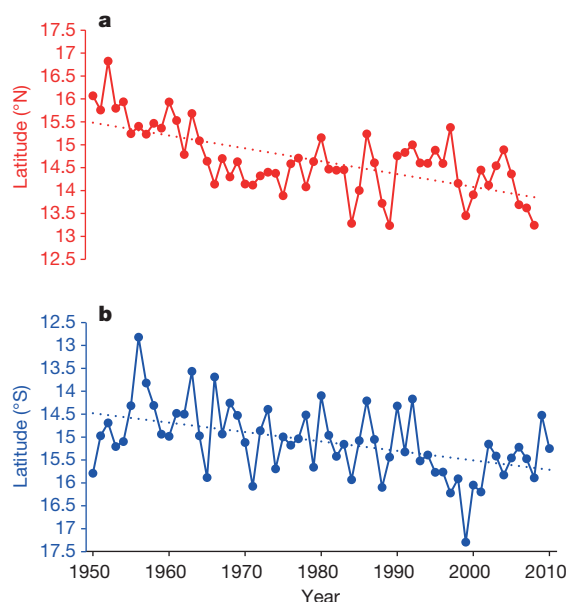


Figure 4 | Trend in the bifurcation latitude of the North and South Equatorial Currents. **a, b,** Time series of annual mean NEC bifurcation latitude integrated over the upper 381 m (**a**; red curve, adapted from ref. 90 (John Wiley and Sons)), and of SEC bifurcation latitudes integrated over the upper 200 m (**b**; blue line, adapted from ref. 89 (John Wiley and Sons)), based on SODA version 2.2.4. The bifurcation in each layer of SODA data is defined as where the meridional velocity averaged within a 2° longitude band off the Philippine/Australian coast is zero. Correlation between the NEC bifurcation latitude and Niño-3.4 is $r = 0.55$, and between the SEC bifurcation latitude and Niño-3.4 is $r = 0.40$, both statistically significant above the 95% confidence level. Both trend lines are above the 95% confidence level.

Projected changes in the Pacific WBCs depend on emission scenarios of greenhouse gases. Antarctic ozone is projected to recover by around the middle of this century, providing a mechanism to offset the impacts of a projected continuous increase in CO₂. As such, climate models under the business-as-usual emission scenario, which currently matches the observed emission rates, simulate no further trend in the Southern Hemisphere westerly winds before 2045, but an acceleration in the post-2045 period⁹⁴. In the following two paragraphs, we discuss projected changes averaged over the 2050–2100 period referenced to the mean conditions over the twentieth century, under this emission scenario.

Climate models consistently indicate that the Tasman Outflow transport will continue to increase (from ~2 Sv in the twentieth century to ~6 Sv over 2050–2100) and that the latitude of maximum EAC transport will shift further south (~1.5° latitude over 2050–2100; ref. 94); however, the projected EAC maximum transport shows little change (Fig. 5). In the North Pacific, the Kuroshio Current is projected to weaken at its origin by approximately 10%, although the maximum Kuroshio transport shows little change. The EUC tends to strengthen in the eastern and central Pacific (Fig. 5) and become shallower, particularly in the west^{95,96}. This tendency for strengthening occurs despite a weakening of the equatorial trade winds⁵³. The projected EUC intensification is driven by a projected strengthening of the NGCUC that results from a wind stress curl change that is negative, associated with a weakening of the equatorial trade winds and a strengthening of the southeasterly trade winds⁹⁶. A strengthening of the NGCUC supporting a strong EUC is consistent with a present-day observation that much of the NGCUC transport goes to support the EUC⁹⁷, although the range in model projections is rather large.

Both the Mindanao Current and the ITF are projected to weaken (Fig. 5). The reduced ITF is not fully accounted for by the projected wind-induced changes through Sverdrup dynamics that exclude an influence from upwelling deep water. This exclusion is an invalid assumption because such upwelling is important on timescales relevant for climate change. It is conceivable that a projected slowdown of the global thermohaline circulation⁹⁸ would drive a weakening in upwelling of deep water in the South Pacific, contributing to the projected ITF decrease, and following the notion that the ITF is in part supported by the upwelled deep water associated with the compensating flow for the global thermohaline circulation².

Uncertain outcome

There is little doubt that the mean climate over the Pacific will continue to change in the coming century owing to past and future emissions of greenhouse gases. Climate models suggest that the tropical trade winds are likely to weaken⁵³, and that the southern mid-latitude westerlies are likely to undergo a poleward shift and intensification^{91–94}, and contribute to the intensification of the WBCs, although changes in North Pacific winds are less clear⁹⁹. These changes, together with a projected weakening in the global thermohaline circulation⁹⁸, may simultaneously affect the Pacific WBCs. Further, such changes may not resemble anomalies associated with variability on interannual or inter-decadal timescales⁹⁶.

Although climate models agree on many aspects of the projected future changes, such as the weakening of the NEC and the NECC and the strengthening of the NGCUC and the NQC, the simulation of WBCs is generally poor because these coarse-resolution simulations do not resolve the terrain of marginal seas, complex flow structure of WBCs, bathymetry and eddies. Certain aspects of future change in high-resolution models remain consistent with the lower-resolution models¹⁰⁰, but uncertainty in projected changes remains high. Another challenge is the lack of information about the flow structure and amplitude of the low-latitude Pacific WBCs in the real world, necessary for benchmarking climate models. For example, despite an extensive observational campaign, the ITF mass budget is not closed; the estimated outflow exceeds the inflow by ~2 Sv (ref. 9). It is unknown whether a contribution from the NGCUC through the Molucca and Halmahera Seas might account for the discrepancy. This mass imbalance is linked to many long-standing issues, including whether Antarctic Intermediate Water, through the NGCUC and the Mindanao

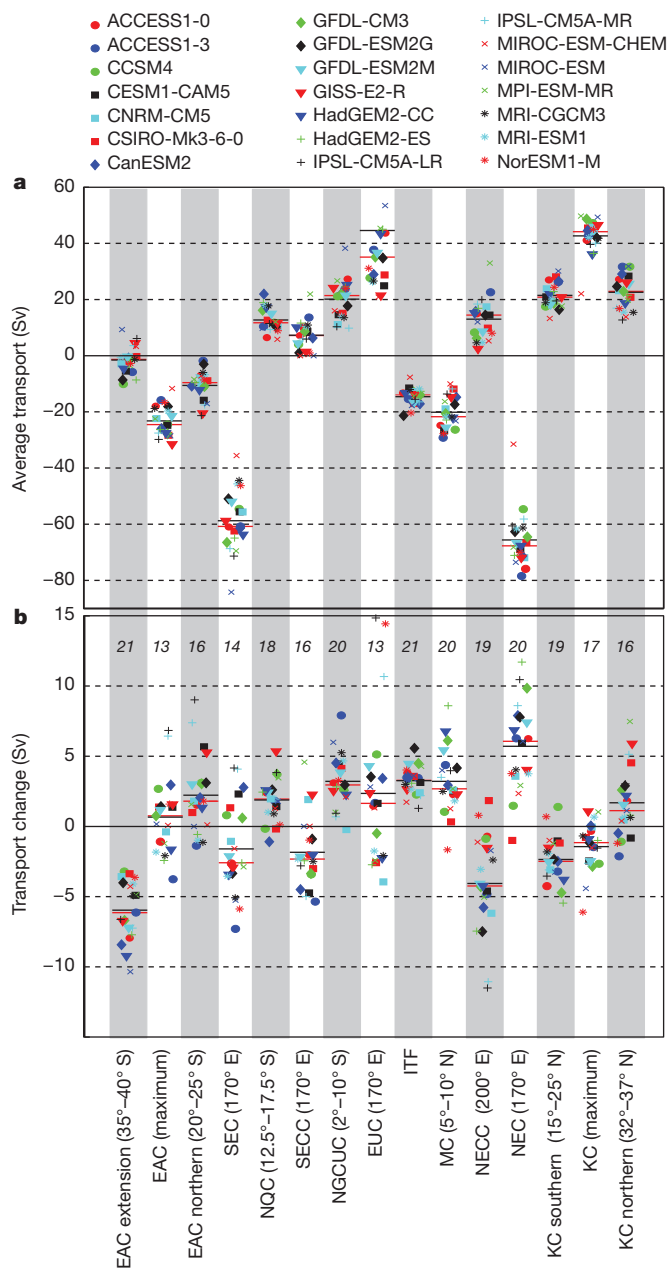


Figure 5 | Modelled transports of annual-mean Pacific WBCs and their projected changes. **a**, Historical mean transport averaged over the twentieth century (positive values indicate northward, and negative, southward transports), and **b**, projected change from the historical mean, averaged over the 2050–2100 period under RCP8.5, for selected Pacific currents (listed at bottom). Positive changes of positive mean transport indicate strengthening, and vice versa. Shown are individual models (markers; see key at top), multi-model mean (horizontal black lines) and multi-model medians (horizontal red lines). Values at the top of each column in **b** indicate the number of models (out of a total of 21) that agree on the sign of the change. Based on a binomial distribution, agreement of 13, 14, 15 and 16 models (out of 21) corresponds to significance levels of 81%, 90.5%, 96% and 99%, respectively. Mean EUC transports for IPSL-CM5A-MR/LR and CNRM-CM5 are greater than 90 Sv, and are not shown in **a**.

Undercurrent, reaches east of the Luzon northern tip¹⁹, or directs eastward between 10°–12° N under the NEC^{24,28}. Without such ground-truth information, our confidence in model performance will remain low.

With a sustained community effort, our understanding of the Pacific WBCs and their impacts will continue to improve. The ultimate goal is to produce a reliable projection of the Pacific WBCs and their climatic impacts that is consistent with our physical theoretical understanding,

as well as with what observations show. To this end, coordinated observations, studies of processes, and modelling should be bolstered. Our models need to resolve the complex terrain of marginal seas and the detailed structure of the WBCs, together with bathymetry, mesoscale eddies, and other currently unresolved processes, especially turbulent mixing. An international WBC intermodel comparison project may offer a good avenue for a substantial advance. These modelling efforts need to be supported by a coordinated observation system integrating high-density mooring arrays across all Pacific WBCs, satellite observations, Argo floats and platforms that enable near-coast measurements, to provide a three-dimensional picture of the coast-to-deep-water WBC structure. In the meantime, we need to combine all sources of information to make reliable predictions of variability and robust assessments of the response of the Pacific WBCs to greenhouse warming and the associated climatic impacts.

Received 13 August 2014; accepted 8 April 2015.

- Nakamura, H., Sampe, T., Tanimoto, Y. & Shimpo, A. Observed associations among stormtracks, jet streams and midlatitude oceanic fronts. *AGU Geophys. Monogr. Ser.* **147**, 329–346 (2004).
- Gordon, A. L. Inter-ocean exchange of thermocline water. *J. Geophys. Res.* **91**, 5037–5046 (1986).
- Cai, W. *et al.* More extreme swings of the South Pacific convergence zone due to greenhouse warming. *Nature* **488**, 365–369 (2012).
- Ridgway, K. R. & Dunn, J. R. Observational evidence for a Southern Hemisphere oceanic supergyre. *Geophys. Res. Lett.* **34**, L13612 (2007).
- Cai, W. Antarctic ozone depletion causes an intensification of the Southern Ocean super-gyre circulation. *Geophys. Res. Lett.* **33**, L03712 (2006).
- Speich, S., Blanke, B. & Cai, W. Atlantic meridional overturning circulation and the Southern Hemisphere supergyre. *Geophys. Res. Lett.* **34**, L23614 (2007).
- Hu, D. *et al.* Northwestern Pacific Ocean Circulation and Climate Experiment (NPOCE) Science/Implementation Plan (China Ocean Press, 2011).
- Details of NPOCE, outlining its goal and scope with a comprehensive literature review on ocean circulation and climate in the northwestern Pacific Ocean.**
- Ganachaud, A. S. *et al.* The Southwest Pacific Ocean Circulation and Climate Experiment (SPICE). *J. Geophys. Res.* **119**, 2642–2657 (2014).
- Gordon, A. L. *et al.* The Indonesian Throughflow during 2004–2006 as observed by the INSTANT program. *Dyn. Atmos. Oceans* **50**, 115–128 (2010).
- McCreary, J. P. & Lu, P. On the interaction between the subtropical and the equatorial ocean circulations: the subtropical cell. *J. Phys. Oceanogr.* **24**, 466–497 (1994).
- Gu, D. F. & Philander, S. G. H. Interdecadal climate fluctuations that depend on exchanges between the tropics and extratropics. *Science* **275**, 805–807 (1997).
- Stommel, H. & Yoshida, K. (eds) *Kuroshio – Its Physical Aspects* (Univ. Tokyo Press, 1972).
- Gordon, A. L., Flament, P., Villanoy, C. & Centurioni, L. The nascent Kuroshio of Lamón Bay. *J. Geophys. Res.* **119**, 4251–4263 (2014).
- Burridge, D. Naming a western boundary current from Australia to the Solomon Sea. *CLIVAR Newsl. Exchanges* **58**, 28, <http://www.clivar.org/node/238> (2012).
- Kessler, W. S. & Gourdeau, L. The annual cycle of circulation of the south-west subtropical Pacific, analysed in an ocean GCM. *J. Phys. Oceanogr.* **37**, 1610–1627 (2007).
- Lindstrom, E. *et al.* The western equatorial Pacific Ocean circulation study. *Nature* **330**, 533–537 (1987).
- Gordon, A. L. & Fine, R. Pathways of water between the Pacific and Indian oceans in the Indonesian seas. *Nature* **379**, 146–149 (1996).
- Fine, R. A., Lukas, R., Bingham, F. M., Warner, M. J. & Gammon, R. H. The western equatorial Pacific is a water mass crossroads. *J. Geophys. Res.* **99**, 25063–25080 (1994).
- Johnson, G., Sloyan, B., Kessler, W. & McTaggart, K. Direct measurements of upper ocean currents and water properties across the tropical Pacific during the 1990s. *Prog. Oceanogr.* **52**, 31–61 (2002).
- Gouriou, Y. & Toole, J. Mean circulation of the upper layers of the western equatorial Pacific Ocean. *J. Geophys. Res.* **98**, 22495–22520 (1993).
- Hu, D. & Cui, M. The western boundary current of the Pacific and its role in the climate. *Chin. J. Oceanology Limnol.* **9**, 1–14 (1991).
- Qu, T., Kagimoto, T. & Yamagata, T. A subsurface countercurrent along the east coast of Luzon. *Deep Sea Res. Part I* **44**, 413–423 (1997).
- Hu, D. *et al.* Direct measurements of the Luzon Undercurrent. *J. Phys. Oceanogr.* **43**, 1417–1425 (2013).
- Lukas, R. *et al.* Observations of the Mindanao Current during the Western Equatorial Pacific Ocean Circulation study (WEPOCS). *J. Geophys. Res.* **96**, 7089–7104 (1991).
- Qu, T. & Lindstrom, E. J. Northward Intrusion of Antarctic Intermediate Water in the Western Pacific. *J. Phys. Oceanogr.* **34**, 2104–2118 (2004).
- Zhang, L., Hu, D., Hu, S., Wang, F. & Yuan, D. Mindanao Current/Undercurrent measured by a subsurface mooring. *J. Geophys. Res. Oceans* **119**, 3617–3628 (2014).

Confirms the existence of the Mindanao Undercurrent and reveals its strong 60–80-day variability using observations spanning two years.

27. Wijffels, S., Firing, E. & Toole, J. The mean structure and variability of the Mindanao Current at 8°N. *J. Geophys. Res.* **100**, 18421–18435 (1995).
28. Kashino, Y., Ishida, A. & Kuroda, Y. Variability of the Mindanao Current: mooring observation results. *Geophys. Res. Lett.* **32**, L18611 (2005).
29. Firing, E., Kashino, Y. & Hacker, P. Energetic subthermocline currents observed east of Mindanao. *Deep Sea Res. Part II* **52**, 605–613 (2005).
30. Kessler, W. S. & Cravatte, S. ENSO and short-term variability of the south equatorial current entering the Coral Sea. *J. Phys. Oceanogr.* **43**, 956–969 (2013).
31. Davis, R. E., Kessler, W. S. & Sherman, J. T. Gliders measure western boundary current transport from the South Pacific to the equator. *J. Phys. Oceanogr.* **42**, 2001–2013 (2012).
32. Gasparin, F., Ganachaud, A., Maes, C., Marin, F. & Eldin, G. Oceanic transports through the Solomon Sea: the bend of the New Guinea Coastal Undercurrent. *Geophys. Res. Lett.* **39**, L15608 (2012).
- A hydrographic survey across the southern Solomon Sea allows a complete estimate of the NGCU transports down to 2,000 m, as well as counter currents, inflows and outflows between the Solomon and Coral Seas.**
33. Qu, T. & Lindstrom, E. A climatological interpretation of the circulation in the western South Pacific. *J. Phys. Oceanogr.* **32**, 2492–2508 (2002).
34. Qu, T. & Lukas, R. The bifurcation of the North Equatorial Current in the Pacific. *J. Phys. Oceanogr.* **33**, 5–18 (2003).
- First report of the findings of vertical distribution and seasonal variation of the NEC bifurcation, with strong relevance to seasonal variation of the South China Sea throughflow in the Luzon Strait found by later studies.**
35. Qiu, B. & Lukas, R. Seasonal and interannual variability of the North Equatorial Current, the Mindanao Current and the Kuroshio along the Pacific western boundary. *J. Geophys. Res.* **101**, 12315–12330 (1996).
36. Ridgway, K. R. Long term trend and decadal variability of the southward penetration of the East Australia Current. *Geophys. Res. Lett.* **34**, L13613 (2007).
37. Roemmich, D. et al. Decadal spinup of the South Pacific Subtropical Gyre. *J. Phys. Oceanogr.* **37**, 162–173 (2007).
38. Beal, L. M. On the role of the Agulhas system in ocean circulation and climate. *Nature* **472**, 429–436 (2011).
39. Qiu, B., Mao, M. & Kashino, Y. Intraseasonal variability in the Indo-Pacific throughflow and the regions surrounding the Indonesian seas. *J. Phys. Oceanogr.* **29**, 1599–1618 (1999).
40. Kim, Y. et al. Seasonal and interannual variations of the North Equatorial Current bifurcation in a high-resolution OGCM. *J. Geophys. Res.* **109**, C03040 (2004).
41. Kashino, Y. et al. Observations of the North Equatorial Current, Mindanao Current, and the Kuroshio Current system during the 2006/7 El Niño and 2007/08 La Niña. *J. Oceanogr.* **65**, 325–333 (2009).
42. Qiu, B. & Chen, S. Interannual-to-decadal variability in the bifurcation of the north equatorial current off the Philippines. *J. Phys. Oceanogr.* **40**, 2525–2538 (2010).
- Shows a decadal modulation in the characteristics of the NEC bifurcation, which is determined by wind forcing in the 12°–14° N band that contains variability not fully representable by the Niño-3.4 index.**
43. Wu, C.-R. Interannual modulation of the Pacific Decadal Oscillation (PDO) on the low-latitude western North Pacific. *Prog. Oceanogr.* **110**, 49–58 (2013).
44. Qiu, B., Kessler, W. S. & Chen, S. Source of the 70-day mesoscale eddy variability in the Coral Sea and North Fiji Basin. *J. Phys. Oceanogr.* **39**, 404–420 (2009).
45. Ueki, I., Kashino, Y. & Kuroda, Y. Observation of current variations off the New Guinea coast including the 1997–1998 El Niño period and their relationship with Sverdrup transport. *J. Geophys. Res.* **108** (C7), 3243 (2003).
46. Jin, F. F. An equatorial ocean recharge paradigm for ENSO. Part I: conceptual model. *J. Atmos. Sci.* **54**, 811–829 (1997).
47. Melet, A., Gourdeau, L., Verron, J. & Djath, B. Solomon Sea circulation and water mass modifications: response at ENSO timescales. *Ocean Dyn.* **63**, 1–19 (2013).
48. Sprintall, J. et al. The Indonesian seas and their role in the coupled ocean–climate system. *Nature Geosci.* **7**, 487–492 (2014).
- Reports recent progress in our understanding of oceanography in the Indonesian Seas and their climatic impact through variations with ENSO, focusing on ocean heat content, sea level, winds and precipitation in the tropical Indian Ocean region.**
49. van Sebille, E. et al. Pacific-to-Indian Ocean connectivity: Tasman leakage, Indonesian Throughflow, and the role of ENSO. *J. Geophys. Res. Oceans* **119**, 1365–1382 (2014).
50. Gordon, A. L. et al. South China Sea throughflow impact on the Indonesian throughflow. *Geophys. Res. Lett.* **39**, L11602 (2012).
51. Qu, T., Yan, D. & Hideharu, S. South China Sea throughflow: a heat and freshwater conveyor. *Geophys. Res. Lett.* **33**, L23617 (2006).
52. Hill, K. L., Rintoul, S. R., Ridgway, K. R. & Oke, P. R. Decadal changes in the South Pacific western boundary current system revealed in observations and ocean state estimates. *J. Geophys. Res.* **116**, C01009 (2011).
53. Vecchi, G. A. et al. Weakening of tropical Pacific atmospheric circulation due to anthropogenic forcing. *Nature* **441**, 73–76 (2006).
54. Kelly, K. A. et al. Western boundary currents and frontal air–sea interaction: Gulf Stream and Kuroshio Extension. *J. Clim.* **23**, 5644–5667 (2010).
55. Kwon, Y. O. et al. Role of the Gulf Stream and Kuroshio–Oyashio systems in large-scale atmosphere–ocean interaction: a review. *J. Clim.* **23**, 3249–3281 (2010).
56. Konda, M. H., Ichikawa, H., Tomita, H. & Cronin, M. F. Surface heat flux variations across the Kuroshio Extension as observed by surface flux buoys. *J. Clim.* **23**, 5206–5221 (2010).
57. Chelton, D. B., Schlax, M., Freilich, M. & Milliff, R. Satellite measurements reveal persistent small-scale features in ocean winds. *Science* **303**, 978–983 (2004).
58. Tokinaga, H. et al. Ocean frontal effects on the vertical development of clouds over the western North Pacific: *in situ* and satellite observations. *J. Clim.* **22**, 4241–4260 (2009).
59. Hotta, D. & Nakamura, H. On the significance of the sensible heat supply from the ocean in the maintenance of the mean baroclinicity along storm tracks. *J. Clim.* **24**, 3377–3401 (2011).
60. Wu, C.-R. et al. Air–sea interaction between tropical cyclone Nari and Kuroshio. *Geophys. Res. Lett.* **35**, L12605 (2008).
61. Sasaki, n., Minobe, S., Asai, T. & Inatsu, M. Influence of the Kuroshio in the East China Sea on the early summer (baidu) rain. *J. Clim.* **25**, 6627–6645 (2012).
62. Huang, R. & Li, W. Influence of the heat source anomaly over the tropical western Pacific on the subtropical high over East Asia and its physical mechanism. *Chinese J. Atmos. Sci.* **14**, 95–107 (1988).
63. Feng, J. & Hu, D. How much does heat content of the western tropical Pacific Ocean modulate the South China Sea summer monsoon onset in the last four decades? *J. Geophys. Res. Oceans* **119**, 4029 (2014).
64. Holland, G. J. Interannual variability of the Australian summer monsoon at Darwin: 1952–82. *Mon. Weath. Rev.* **114**, 594–604 (1986).
65. Gordon, A. L., Susanto, R. D. & Vranes, K. Cool Indonesian throughflow as a consequence of restricted surface layer flow. *Nature* **425**, 824–828 (2003).
- Shows that a stronger low-salinity South China Sea throughflow during boreal winter sets up a gradient, which limits the Mindanao Current inflow into the Indonesian Seas and thus leads to cold surface water in the Indonesian Seas.**
66. Seager, R., Kushnir, Y., Naik, N. H., Cane, M. A. & Miller, J. Wind-driven shifts in the latitude of the Kuroshio–Oyashio Extension and generation of SST anomalies on decadal timescales. *J. Clim.* **14**, 4249–4265 (2001).
67. Lau, N.-C. & Nath, M. J. Impact of ENSO on SST variability in the North Pacific and North Atlantic: seasonal dependence and role of extratropical sea–air coupling. *J. Clim.* **14**, 2846–2866 (2001).
68. Alexander, M. A. The atmospheric bridge: the influence of ENSO teleconnections on air–sea interaction over the global oceans. *J. Clim.* **15**, 2205–2231 (2002).
69. Nakamura, H. & Kazmin, A. S. Decadal changes in the North Pacific oceanic frontal zones as revealed in ship and satellite observations. *J. Geophys. Res.* **108**, 3078 (2003).
70. Taguchi, B. et al. Decadal variability of the Kuroshio Extension: observations and an eddy-resolving model hindcast. *J. Clim.* **20**, 2357–2377 (2007).
71. Frankignoul, C. & Sennéchal, N. Observed influence of North Pacific SST anomalies on the atmospheric circulation. *J. Clim.* **20**, 592–606 (2007).
72. Taguchi, B., Nakamura, H., Nonaka, M. & Xie, S.-P. Influences of the Kuroshio/Oyashio Extensions on air–sea heat exchanges and storm-track activity as revealed in regional atmospheric model simulations for the 2003/04 cold season. *J. Clim.* **22**, 6536–6560 (2009).
73. Taguchi, B., Xie, S.-P., Mitsudera, H. & Kubokawa, A. Response of the Kuroshio Extension to Rossby waves associated with the 1970s climate regime shift in a high-resolution ocean model. *J. Clim.* **18**, 2979–2995 (2005).
74. Liu, Z. & Alexander, M. Atmospheric bridge, oceanic tunnel and global climatic teleconnections. *Rev. Geophys.* **45**, RG2005 (2007).
75. Tokinaga, H. et al. Atmospheric sounding over the winter Kuroshio Extension: effect of surface stability on atmospheric boundary layer structure. *Geophys. Res. Lett.* **33**, L04703 (2006).
76. Norris, J. R. & Leovy, C. B. Interannual variability in stratiform cloudiness and sea surface temperature. *J. Clim.* **7**, 1915–1925 (1994).
77. Klein, S. A., Hartmann, D. L. & Norris, J. R. On the relationships among low-cloud structure, sea surface temperature and atmospheric circulation in the summertime northeast Pacific. *J. Clim.* **8**, 1140–1155 (1995).
78. Park, S., Alexander, M. A. & Deser, C. The impact of cloud radiative feedback, remote ENSO forcing, and entrainment on the persistence of North Pacific sea surface temperature anomalies. *J. Clim.* **19**, 6243–6261 (2006).
79. Alexander, M. A. & Deser, C. A mechanism for the recurrence of wintertime midlatitude SST anomalies. *J. Phys. Oceanogr.* **25**, 122–137 (1995).
80. Sugimoto, S. & Hanawa, K. Remote reemergence areas of winter sea surface temperature anomalies in the North Pacific. *Geophys. Res. Lett.* **32**, L01606 (2005).
81. Nakamura, H. & Yamagata, T. In *Beyond El Niño: Decadal and Interdecadal Climate Variability* (ed. Navarra, A.) 49–72 (Springer, 1999).
82. Sprintall, J., Roemmich, D., Stanton, B. & Bailey, R. Regional climate variability and ocean heat transport in the southwest Pacific Ocean. *J. Geophys. Res.* **100**, 15865–15871 (1995).
83. Shi, G., Ribbe, J., Cai, W. & Cowan, T. An interpretation of Australian rainfall projections. *Geophys. Res. Lett.* **35**, L02702 (2008).
84. Godfrey, S. The effect of the Indonesian Throughflow on ocean circulation and heat exchange with the atmosphere: A review. *J. Geophys. Res. Oceans* **101**, 12217–12237 (1996).
85. Vranes, K., Gordon, A. L. & Field, A. The heat transport of the Indonesian throughflow and implications for the Indian Ocean heat budget. *Deep Sea Res. Part II* **49**, 1391–1410 (2002).
86. Gordon, A. L. Oceanography of the Indonesian Seas and their throughflow. *Oceanography (Wash. D.C.)* **18**, 14–27 (2005).
87. Song, Q., Gordon, A. L. & Visbeck, M. Spreading of the Indonesian throughflow in the Indian Ocean. *J. Phys. Oceanogr.* **34**, 772–792 (2004).
88. Wu, L. et al. Enhanced warming over the global subtropical western boundary current. *Nature Clim. Change* **2**, 161–166 (2012).
- Demonstrates synchronized enhanced warming along subtropical WBCs and emphasizes the important roles played by the WBCs in global climate change.**
89. Zhai, F., Hu, D., Wang, Q. & Wang, F. Long-term trend of Pacific South Equatorial Current bifurcation. *Geophys. Res. Lett.* **41**, 3172–3180 (2014).
90. Chen, Z. & Wu, L. Long-term change of the Pacific North Equatorial Current bifurcation in SODA. *J. Geophys. Res.* **117**, C06016 (2012).

91. Cai, W. & Cowan, T. Trends in Southern Hemisphere circulation in IPCC AR4 models over 1950–1999: ozone-depletion vs greenhouse forcing. *J. Clim.* **20**, 681–693 (2007).
92. Cai, W., Shi, G., Cowan, T., Bi, D. & Ribbe, J. The response of the Southern Annular Mode, the East Australian Current, and the southern mid-latitude ocean circulation to global warming. *Geophys. Res. Lett.* **32**, L23706 (2005).
93. Thompson, D. W. J. *et al.* Signatures of the Antarctic ozone hole in Southern Hemisphere surface climate change. *Nature Geosci.* **4**, 741–749 (2011).
94. Wang, G., Cai, W. & Purich, A. Trends in Southern Hemisphere wind driven circulation in CMIP5 models over the 21st century: ozone recovery versus greenhouse forcing. *J. Geophys. Res. Oceans* **119**, 2974–2986 (2014).
95. Ganachaud, A. *et al.* Projected changes in the tropical Pacific Ocean of importance to tuna fisheries. *Clim. Change* **119**, 163–179 (2013).
Presents global warming projections showing a shift in the Pacific winds and surface temperatures that affect oceanic currents and vertical ocean structure, enhancing stratification and increasing the extent of the warm pool with consequences for tuna habitat.
96. Sen Gupta, A., Ganachaud, A., McGregor, S., Brown, J. N. & Muir, L. Drivers of the projected changes to the Pacific Ocean equatorial circulation. *Geophys. Res. Lett.* **39**, L09605 (2012).
97. Grenier, M., Jeandel, C. & Cravatte, S. From the subtropics to the equator in the Southwest Pacific: continental material fluxes quantified using neodymium data along modelled thermocline water pathways. *J. Geophys. Res. Oceans* **119**, 3948–3966 (2014).
98. Gregory, J. M. *et al.* A model intercomparison of changes in the Atlantic thermohaline circulation in response to increasing atmospheric CO₂ concentration. *Geophys. Res. Lett.* **32**, L12703 (2005).
99. Li, W., Li, L., Ting, M. & Liu, Y. Intensification of Northern Hemisphere subtropical highs in a warming climate. *Nature Geosci.* **5**, 830–834 (2012).
100. Oliver, E. C. J. & Holbrook, N. J. Extending our understanding of South Pacific gyre “spin-up”: modeling the East Australian Current in a future climate. *J. Geophys. Res. Oceans* **119**, 2788–2805 (2014).
Shows that an increase in the EAC extension of 4–5 Sv by 2060 simulated by a high-resolution model closely matches results from a low-resolution climate model.

Acknowledgements W.C. and G.W. are supported by the Australian Climate Change Science Program, a CSIRO Office of the Chief Executive Science Leader award, and CSIRO Office of the Chief Executive postdoctoral awards. L.W., Z.C. and X.L. are supported by projects (41130859, 41490640, 41306001) of the National Science Foundation of China (NSFC), and a project (2013CB956200) of the National Basic Research Program of China (MOST). D.H. is supported by CAS Program XDA 11010101, and NSFC Grants 41330963 and 41421005. S.H. is supported by NSFC Grant 41406016. Q.W. is supported by MOST Grant 2013CB956202. F.W. is supported by MOST Grant 2012CB417401 and NSFC/Shangdong Grant U1406401. A.G. is supported by CNRS/INSU/LEFE project MoorSPICE. This is PMEL Contribution Number 4207, and Lamont-Doherty Earth Observatory Contribution Number 7875. J.S. is supported by the National Aeronautics and Space Administration (NASA) under award no. NNX13AO38G. Y.K. is supported by the Tropical Ocean Climate Study of Japan Agency for Marine-Earth Science and Technology. This is a contribution to the CLIVAR SPICE and NPOCE programmes. We thank A. Purich and T. Cowan for their comments before submission. We acknowledge the World Climate Research Programme's Working Group on Coupled Modelling, and we thank the climate modelling groups for producing and making available their model output. The US Department of Energy's Program for Climate Model Diagnosis and Intercomparison provides coordinating support and led the development of software infrastructure in partnership with the Global Organization for Earth System Science Portals.

Author Contributions D.H., L.W. and W.C. conceived the study. L.W., W.C. and D.H. determined the scope. W.C. wrote the draft of the paper and finalized the manuscript with help from G.W. A.S.G. conducted model output analysis for future projections and plotted Fig. 5. A.G., A.S.G. and W.C. constructed the schematic of Figs 1 and 3. Z.C. generated Fig. 4. All authors contributed to interpreting results, discussion of the associated dynamics and improvement of this paper.

Author Information Reprints and permissions information is available at www.nature.com/reprints. The authors declare no competing financial interests. Readers are welcome to comment on the online version of the paper. Correspondence and requests for materials should be addressed to W.C. (wenju.cai@csiro.au) or L.W. (lxwu@ouc.edu.cn).

Hippocampal–prefrontal input supports spatial encoding in working memory

Timothy Spellman¹, Mattia Rigotti^{2,3,4}, Susanne E. Ahmari^{5,6}, Stefano Fusi^{2,7}, Joseph A. Gogos^{1,2} & Joshua A. Gordon^{8,9}

Spatial working memory, the caching of behaviourally relevant spatial cues on a timescale of seconds, is a fundamental constituent of cognition. Although the prefrontal cortex and hippocampus are known to contribute jointly to successful spatial working memory, the anatomical pathway and temporal window for the interaction of these structures critical to spatial working memory has not yet been established. Here we find that direct hippocampal–prefrontal afferents are critical for encoding, but not for maintenance or retrieval, of spatial cues in mice. These cues are represented by the activity of individual prefrontal units in a manner that is dependent on hippocampal input only during the cue–encoding phase of a spatial working memory task. Successful encoding of these cues appears to be mediated by gamma–frequency synchrony between the two structures. These findings indicate a critical role for the direct hippocampal–prefrontal afferent pathway in the continuous updating of task-related spatial information during spatial working memory.

Spatial working memory (SWM) is an essential feature of goal-directed action. Locating a resource, a threat, or even oneself within a dynamic or unfamiliar environment requires a cached representation of relevant spatial features that must be continuously updated, preserved and applied as needed to the execution of adaptive behaviours¹. Despite long-standing interest in the neurobiological underpinnings of SWM, its multiple cognitive components, distributed anatomical constituents and distinct temporal phases have rendered its underlying circuit mechanisms elusive^{2–6}. Nevertheless, an extensive body of work supports the idea that the prefrontal cortex (PFC) has a central role in the successful execution of tasks requiring SWM⁷. Moreover, the joint contribution of the medial prefrontal cortex (mPFC) and hippocampus (HPC) supports successful SWM in rodents^{8–12}. It remains unclear, however, which phase(s) of SWM (encoding, maintenance, and/or retrieval) require the joint participation of the HPC and mPFC, what behaviourally relevant information is conveyed between the two structures, and through which anatomical pathway(s) they interact.

Direct HPC–mPFC connectivity is confined to a unidirectional projection from the CA1/subiculum of the ventral-most two-thirds of the hippocampus (vHPC)^{13–15}. Cells in both the vHPC and mPFC exhibit location-specific firing^{16–19}, and damage to the vHPC disrupts goal-related activity in the mPFC¹⁶, suggesting that the direct vHPC–mPFC projection may transmit critical location information during SWM tasks.

We used a rodent delayed non-match-to-place (DNMTP) task, known to require activity in the vHPC and mPFC, to test the role of vHPC–mPFC afferents in SWM. We applied a projection-specific, optogenetic silencing approach that afforded anatomical and temporal precision. Inhibiting vHPC–mPFC direct input disrupted encoding, but not maintenance or retrieval, of location cues necessary for task performance. Furthermore, we found that goal-selective firing in the mPFC was dependent on vHPC direct input exclusively during the encoding phase of each trial. Finally, we found evidence suggesting

that the transmission of task-critical information through the vHPC–mPFC pathway is mediated by the synchronization of mPFC units to gamma oscillations in the vHPC. Together, these findings suggest that the direct vHPC–mPFC pathway enables the encoding of salient spatial cues during SWM performance.

Optogenetic inhibition of vHPC terminals

To interfere specifically with vHPC–mPFC inputs, a projection-specific targeting approach was used. An adeno-associated virus vector (AAV2/5) engineered to express fluorescently labelled archaerhodopsin (eArch3.0–enhanced yellow fluorescent protein (eYFP))^{20,21} was targeted to subfield CA1 of the vHPC in mice (Methods). Robust expression was seen in the dendrites and axons of the vHPC and in projection axons in the mPFC (Fig. 1a).

Arch-mediated hyperpolarization of distal axon terminals disrupted synaptic transmission *in vivo* without affecting spontaneous vHPC firing. The effect of terminal illumination on synaptic transmission was measured in acutely anaesthetized mice. Electrical stimuli were delivered via a bipolar stimulating electrode to ventral CA1 in both Arch-expressing (Arch⁺) mice and Arch-negative controls (Arch[−]). Postsynaptic multi-unit responses were observed in the mPFC (Fig. 1b). Light pulses delivered to the mPFC on interleaved trials reduced the evoked response by ~40% for Arch⁺ animals but not Arch[−] animals (Fig. 1b, c). To measure the effects of terminal illumination on vHPC cell bodies, mice were implanted with optical-fibre-coupled stereotrodes in the vHPC and optical fibres in the mPFC. In the awake, resting state, light pulses delivered to the vHPC reduced local spontaneous multi-unit activity by ~50% (Fig. 1d), while illumination of terminal fields in the mPFC had no effect on multi-unit activity in the vHPC (Fig. 1e). These experiments demonstrated successful and specific inhibition of terminals *in vivo*, an approach that was then applied to a behavioural paradigm to examine what role the vHPC–mPFC projection has in spatial working memory.

¹Department of Physiology and Cellular Biophysics, Columbia University, 630 West 168th Street, New York, New York 10032, USA. ²Department of Neuroscience, Columbia University, 1051 Riverside Drive, New York, New York 10032, USA. ³IBM T. J. Watson Research Center, 1101 Kitchawan Road, Yorktown Heights, New York 10598, USA. ⁴Italian Academy for Advanced Studies in America, Columbia University, 1161 Amsterdam Avenue, New York, New York 10032, USA. ⁵Translational Neuroscience Program, Department of Psychiatry, University of Pittsburgh, 450 Technology Drive, Pittsburgh, Pennsylvania 15219, USA. ⁶Center for Neuroscience and Center for the Neural Basis of Cognition, University of Pittsburgh, 200 Lothrop Drive, Pittsburgh, Pennsylvania 15261, USA. ⁷Kavli Institute for Brain Sciences, Columbia University, 1051 Riverside Drive, New York, New York 10032, USA. ⁸Department of Psychiatry, Columbia University, 1051 Riverside Drive, New York, New York 10032, USA. ⁹Division of Integrative Neuroscience, New York State Psychiatric Institute, 1051 Riverside Drive, New York, New York 10032, USA.

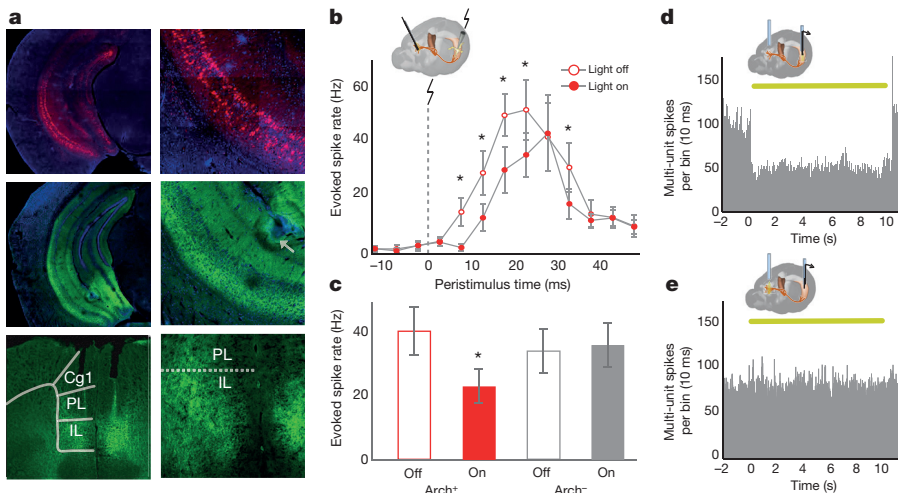


Figure 1 | Optogenetic inhibition of vHPC–mPFC terminals *in vivo*. **a**, Expression of Arch (middle row, green) and mCherry (top row, red) in ventral CA1. Arrow, lesion marking electrode location. Bottom row, Arch in terminals in the prelimbic (PL) and infralimbic (IL) mPFC. Cg1, anterior cingulate cortex. Original magnifications, $\times 2$ (left), $\times 20$ (right). **b**, mPFC multi-unit responses to vHPC stimulation in Arch⁺ mice. $n = 16$ sites from 3 animals, ANOVA $F = 5.6$, $P = 0.02$ for light effect, $*P < 0.05$, post-hoc t -test. Baseline rate = 6.1 ± 0.14 Hz. **c**, Group mean evoked mPFC spike rate summed across 5–40 ms post-stimulus. ANOVA $F = 31.4$, $P = 4 \times 10^{-6}$ for virus-by-light interaction; $n = 16$ sites from 3 mice, $t = 6.68$, $P = 0.0004$; $n = 17$ sites from 3 mice, $t = 1.57$, $P = 0.3$, for Arch⁺ and Arch[−] mice, respectively. **d**, **e**, Multi-unit activity traces from vHPC of Arch⁺ mice during somatic (**d**) and terminal field (**e**) illumination *in vivo*. Yellow bar, light on (throughout). Error bars show \pm standard error of the mean (s.e.m.).

Terminal inhibition impairs encoding

To assay working memory performance, a T-maze DNMT task was employed. In this task, each trial is divided into three phases (Fig. 2a). In the sample phase, one of two goal locations is blocked by a wall, and the mouse is directed towards a food reward in the open location; during this phase the animal must encode the location of the sample goal. In the delay phase, the mouse returns to the start box and must maintain the sample goal in working memory during a variable delay (Methods). In the choice phase, the wall is removed, and the mouse must select the previously closed arm to receive a second reward. After successful task acquisition, light was delivered to vHPC–mPFC terminal fields in Arch⁺ and Arch[−] mice during the entire trial (Entire Trial condition), the sample phase only (Sample Light), or the choice phase only (Choice Light). Trial types were randomly interleaved.

In Arch⁺ but not Arch[−] mice, performance was impaired in Entire Trial and Sample Light conditions; Choice Light did not result in a statistically significant impairment (Fig. 2b). These data raised the possibility that vHPC–mPFC input is critical for the encoding of location cues associated with the sample goal but may not be required for the retrieval of such cues.

This native version of the T-maze task, however, is not optimized to discriminate between encoding and retrieval of the sample goal location, as the animal could begin forming a motor action plan (that is, ‘go into the opposite arm’) any time after it encounters the sample goal. To segregate better the encoding, maintenance, and retrieval phases within each trial, a modified, four-goal T-maze was constructed (Fig. 2c). Here, as in the two-goal task, a single goal was made available for retrieval of the sample reward. During the choice run, the sample goal and one of the other three arms were open. This design

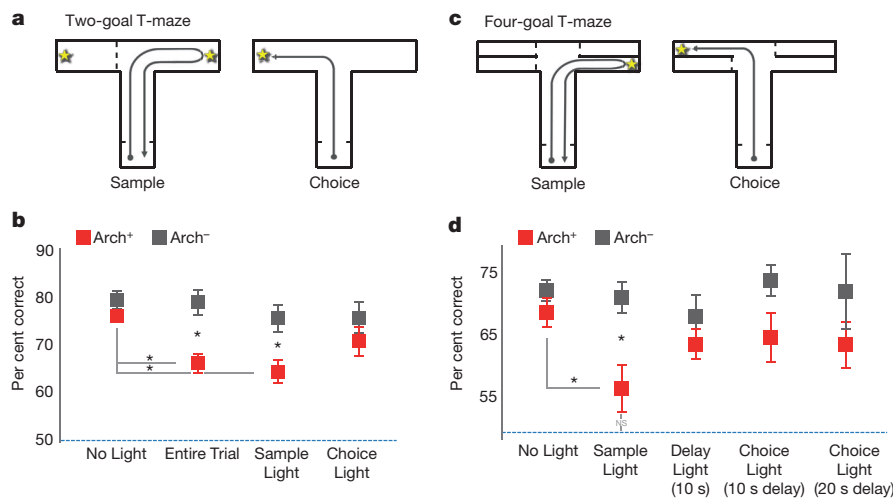


Figure 2 | Inhibition of vHPC–mPFC terminals impairs encoding. **a**, Two-goal DNMT task. **b**, Effect of mPFC illumination on performance in the two-goal task differed by trial phase and virus type (ANOVA, virus-by-light interaction, $F = 5.92$, $P = 0.02$). Post-hoc tests revealed effects of Entire Trial ($t = 3.96$, $P = 0.002$) and Sample Light ($t = 2.98$, $P = 0.011$) but not Choice Light ($t = 1.1$, $P = 0.29$) conditions in Arch⁺ ($n = 8$) versus Arch[−] ($n = 6$) animals. Entire Trial and Sample Light but not Choice Light performance differed from the No Light condition in Arch⁺ ($t = 4.9$, $P = 0.002$, Entire Trial; $t = 4.5$, $P = 0.003$, Sample Light; $t = 1.7$, $P = 0.125$, Choice Light) but not Arch[−] animals ($t = 0.18$, $P = 0.87$; $t = 1.1$, $P = 0.3$; $t = 1.3$, $P = 0.25$,

respectively). **c**, Four-goal DNMT task. **d**, Effect of illumination of mPFC terminal fields on performance in the four-goal task (Arch⁺, $n = 7$ Arch[−], $n = 6$, ANOVA $F = 3.1$, $P = 0.03$ for virus-by-light interaction). Impairment was restricted to Sample Light trials ($t = 3.1$, $P = 0.0093$; and $t = 1.1$, $P = 0.29$; $t = 1.0$, $P = 0.34$; $t = 1.91$, $P = 0.08$; $t = 1.2$, $P = 0.24$, for No Light, Delay Light, Choice Light 10 s and Choice Light 20 s, respectively). No Light and Sample Light performance were significantly reduced in Arch⁺ ($t = 2.5$, $P = 0.04$) but not Arch[−] mice ($t = 0.35$, $P = 0.73$). Performance of Arch⁺ mice during Sample Light runs was not significantly above chance ($t = 1.9$, $P = 0.11$). NS, not significant. Error bars show s.e.m.

prevents the mouse from formulating a spatially directed action plan until the choice phase, when, at the end of its centre arm run, it is presented with two of the four goals as options (Supplementary Video). Thus, selection of the choice goal was temporally restricted to the choice phase, separating out encoding from retrieval.

Again, performance was impaired in the Sample Light condition, confirming the requirement for vHPC–mPFC input during encoding (Fig. 2d). In the Choice Light condition (repeated here with either 10 or 20 s delays), a slight trend towards impairment did not reach significance, and post-hoc power analysis revealed that an n of 37 animals per group would have been required to detect a paired difference given the observed effect size. There was also no significant impairment with terminal illumination during the delay period (Delay Light; Fig. 2d). Although we cannot conclusively rule out an effect of terminal inhibition during choice, these experiments indicate that input from the vHPC to the mPFC is critical for encoding of spatial cues.

Effect on spatial representation in mPFC

The behavioural findings suggested that task-related spatial locations may be represented by firing rates in the mPFC in a vHPC-input-dependent manner. Therefore, recordings of multiple single units were obtained from the prelimbic region of the mPFC in mice performing the four-goal task (Extended Data Fig. 1). A total of 792 well-isolated single units were obtained from 9 mice. Forty-four per cent of mPFC single units displayed selectivity for one or both spatial dimensions that distinguished goal arms (left/right, back/front), and/or their interaction, as assayed by two-way analysis of variance (ANOVA) (Extended Data Fig. 2a–d). Given the inhomogeneous and distributed nature of the representation of spatial information among recorded mPFC units, a maximum margin linear classifier²² was used to decode the sample goal location from binned population firing rate vectors and to quantify the strength and reliability of the neural representation (Fig. 3). The classifier was cross-validated by training on data from half the trials and testing the model's performance on data from the remainder (see Methods).

The sample goal was decoded from spike histograms aligned to multiple trial events (Fig. 3a). Sample goal identity was decoded from the mPFC population at accuracies well above chance from the time

the animals entered the T-intersection, and peaked at 96% upon arrival at the reward port in the sample goal (Fig. 3b).

Sample goal representation at goal arrival time was then assessed during inhibition of vHPC input by training the model on firing rates from non-Sample Light trials (No Light, Delay Light and Choice Light trials combined) and testing on rates from Sample Light trials. For Arch[−] animals, the sample goal was decoded equally well with or without mPFC illumination, while in Arch⁺ animals accuracy was reduced to chance by mPFC illumination (Fig. 3c). This result demonstrates that vHPC input is critical for the representation of the sample goal among mPFC units during encoding.

To assess the impact of terminal inhibition on encoding of non-spatial, task-relevant cues, the same classifier was trained to decode the task phase (sample versus choice) at the time the start-box doors opened immediately before running down the centre arm. Because this epoch was behaviourally equivalent in sample and choice runs, an accurate representation of the task phase at this time point must rely upon a memory of the preceding task phase. Task phase was decoded with near perfect accuracy (0.98) at the time bin corresponding with the opening of the doors, revealing a memory trace for the preceding task phase (Fig. 3d). When the decoder was trained on firing rates from this epoch in No Light trials and tested on choice runs from Sample Light trials, model accuracy was not affected (Fig. 3e), suggesting that vHPC–mPFC terminal inhibition does not generally interfere with the encoding of task-relevant information.

The finding of vHPC-input-dependent location coding in the mPFC leaves open the question of how vHPC input influences mPFC neurons. Overall firing rates of mPFC units were unaffected by terminal illumination in both Arch[−] and Arch⁺ animals, whether all were considered together (Fig. 4a) or putative pyramidal cells and interneurons were separately classified on the basis of waveform features (Extended Data Fig. 4). Nonetheless, consistent effects of vHPC inputs might be revealed by a finer-grained analysis.

Each unit's preferred goal (that is, the goal in which firing rate was most different from the mean rate across the other three goals) was identified using weights generated by the classifier (Methods). Although this separation criterion allowed for the possibility that any given unit might represent location by an increase or decrease in rate, the difference was observed as an elevation in mean firing rate

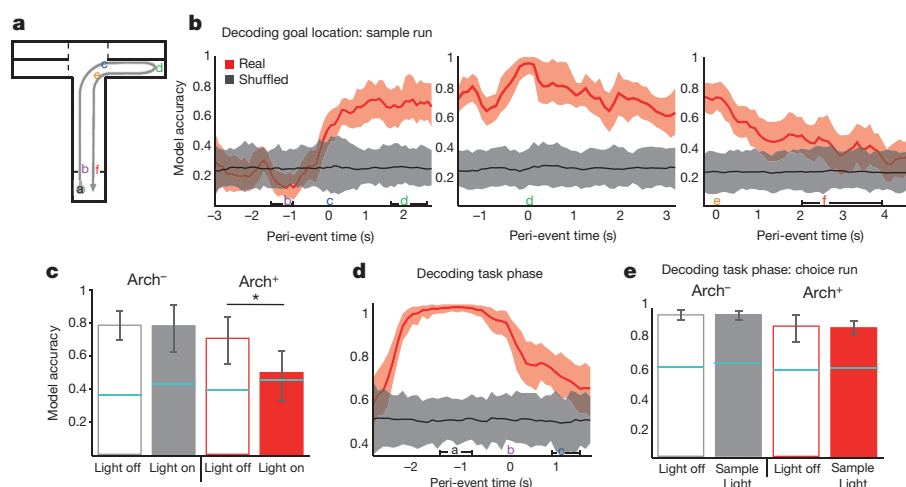


Figure 3 | mPFC units require vHPC input to encode location but not task phase. **a**, Schematic of sample run. **b**, Accuracy of goal decoding during sample run with light off. Solid lines, mean decoder accuracy; shaded areas, 95% confidence intervals. $n = 727$ units from 9 mice. **c**, Decoding accuracy for sample goal upon arrival at the reward port (location 'd' in **a**) in the presence (filled bars) and absence (open bars) of illumination of vHPC–mPFC terminals (269 units from 4 Arch⁺ mice, 285 units from 5 Arch[−] mice; $n = 100$ permutations; ANOVA $F = 1,978$, $P = 5 \times 10^{-5}$ for virus-by-light interaction;

$t = 0.48$, $P = 0.64$ for Arch[−]; $*t = 161.2$, $P = 1.2 \times 10^{-121}$ for Arch⁺). Error bars represent 95% confidence intervals; blue lines represent upper bounds of 95% confidence intervals for shuffled data. **d**, Decoding of task phase (sample versus choice) as a function of time relative to departure from the start box. Conventions as in **b** (792 units from 9 mice). **e**, Decoding of task phase at door opening (location 'a' in **a**) as a function of trial type (ANOVA, $F = 1.94$, $P = 0.17$ for virus-by-light interaction). Error bars show s.e.m.

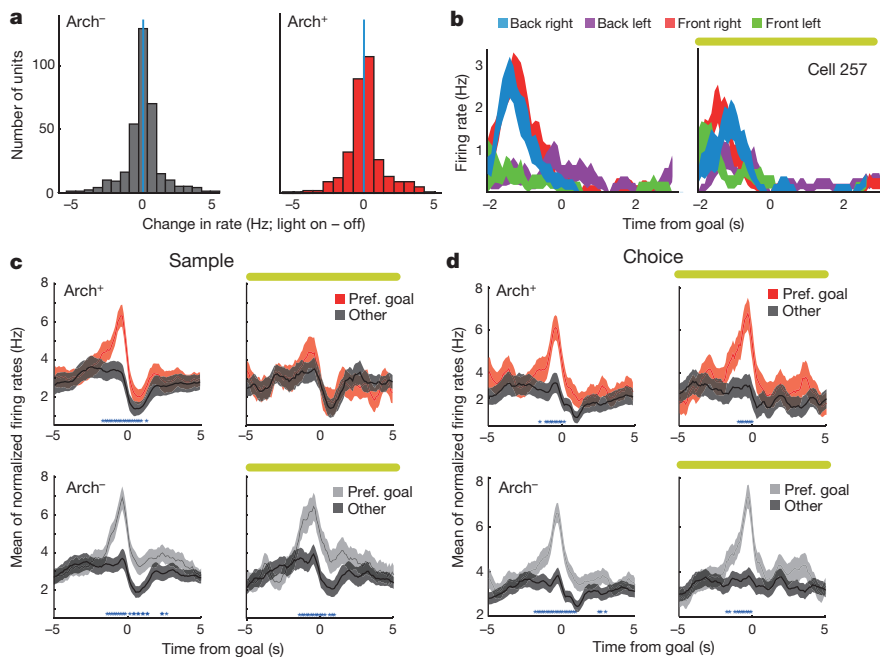


Figure 4 | Location selectivity requires vHPC input during encoding but not retrieval.

a, Differences in firing rate with terminal illumination ($n = 433$ units, sign rank $z = -0.23$, $P = 0.82$; $n = 359$, $z = -0.97$, $P = 0.33$, for Arch⁺ and Arch⁻ animals, respectively). **b**, Mean binned spike rates for an example mPFC unit from an Arch⁺ animal, aligned to arrival at each of the four sample goals (colour coded) without (left) or with (right) terminal illumination. **c**, Peri-event firing rates during the sample phase for all location-selective units as they approach the preferred (Pref.; red/grey) and non-preferred (Other; black) goals (blue asterisks, time points with Bonferroni-corrected significance) during light on (right) and light off (left) trials. $n = 67$ units from 7 Arch⁺ mice, and 78 units from 6 Arch⁻ mice. **d**, Same as **c**, but during the choice phase. $n = 145$ units from 7 Arch⁻ mice, and 77 units from 6 Arch⁺ mice.

relative to other goals, when averaged across all units (Extended Data Fig. 5), and especially those units with high goal selectivity (Fig. 4b–d). The effect in Sample Light conditions was striking. Inhibition of terminals during the sample phase prevented the increase in firing rate that occurred in units' preferred goals, without affecting baseline rates (Fig. 4c, top). The same results were obtained when including all units in the analysis (Extended Data Fig. 5). These results reveal an excitatory role for vHPC input in the location-selective firing rate enhancement seen in mPFC units.

To address whether direct vHPC input is necessary for all mPFC spatial representations, firing rate in preferred and non-preferred goals was examined during choice runs. As in sample runs, firing rate for highly goal-selective units during choice runs was also higher in the preferred goal than in non-preferred goals. However, unlike in sample runs, this elevation was unaffected by vHPC–mPFC terminal inhibition (Fig. 4d). In this finding, physiology mirrored the behavioural result, indicating that goal selectivity after encoding is no longer dependent on vHPC input.

vHPC gamma organizes mPFC spike timing

Activity in distant brain regions can be coordinated by gamma oscillations²³, and long-range gamma synchrony in both the cortex and hippocampus has been linked to spatial learning and memory^{24,25}. Therefore, long-range synchrony was quantified using the magnitude (pairwise phase consistency²⁶ (PPC)) and significance (Rayleigh's test⁹) of phase non-uniformity of spike times in one brain region relative to local field potential (LFP) oscillations in another. To determine the temporal directionality of synchronous activity, lag analysis was performed, in which phase-locking was calculated at various temporal shifts; preferential phase-locking at a non-zero lag indicates a predictive relationship between oscillatory phase and spike timing.

A subset of mPFC units were significantly phase-locked to vHPC gamma (Fig. 5b, c), and the percentage of significantly phase-locked units was greatest at lags in which vHPC gamma preceded mPFC spiking (Fig. 5c). Moreover, the mean strength of mPFC unit phase-locking to vHPC gamma was maximal at lags in which vHPC led (Fig. 5d–f). These findings suggest the possibility that gamma-frequency inputs from the vHPC influence mPFC spike timing. Consistent with this suggestion, inhibition of vHPC–mPFC terminals reduced the overall strength of gamma phase-locking (Fig. 5g, h), indicating that the observed synchrony is mediated by direct

vHPC–mPFC input. Importantly, this directionality was specific to gamma oscillations, as lag analysis of phase-locking in the theta range revealed an opposite directionality; mPFC led vHPC (but not dorsal hippocampus (dHPC)) activity in the theta range, and theta synchrony was unaffected by terminal inhibition (Extended Data Fig. 7).

vHPC–mPFC gamma synchrony correlated with behaviour in two key ways. PPC values were higher during sample than choice runs, demonstrating that stronger gamma phase-locking is associated with the encoding phase of the trial (Fig. 5i). Additionally, phase-locking was stronger during sample runs of correct trials than of incorrect trials (Fig. 5j), suggesting that it may support effective encoding of location cues.

Discussion

We leveraged a temporally precise, projection-specific manipulation to test the role of the vHPC–mPFC afferent pathway in spatial working memory. We found that direct vHPC–mPFC input is essential for successful encoding of task-related cues, both behaviourally and at the level of neural representation within the mPFC. vHPC–mPFC gamma synchrony correlated with successful cue encoding and was also disrupted by vHPC terminal inhibition. These findings point to a role for the vHPC–mPFC afferent pathway as a conduit for the updating of task-critical location cues.

The finding of a dependence of task performance on vHPC input only during sample runs, replicated across both behavioural paradigms used in this study, provides a strong argument for the importance of vHPC–mPFC afferent input during the trial phase in which relevant spatial cues are encoded. The role of vHPC–mPFC input in encoding goal location is further supported by the effect of terminal inhibition on the neural representation of goal location in the mPFC. Moreover, while contemporaneous location was robustly represented as a goal-selective enhancement of firing in preferred goals during both sample and choice runs, this representation depended on vHPC input only during the sample run. Here the physiology agrees with the behavioural observation that vHPC–mPFC input is critical for encoding, not retrieval, of task-relevant location cues.

Interestingly, we find no evidence of retrospective location coding in mPFC activity (Fig. 3 and Extended Data Fig. 3). Within the parameters of this study, this argues against persistent firing within mPFC neurons as a means of maintaining the stimulus representation between encoding and retrieval. Previously, retrospective and pro-

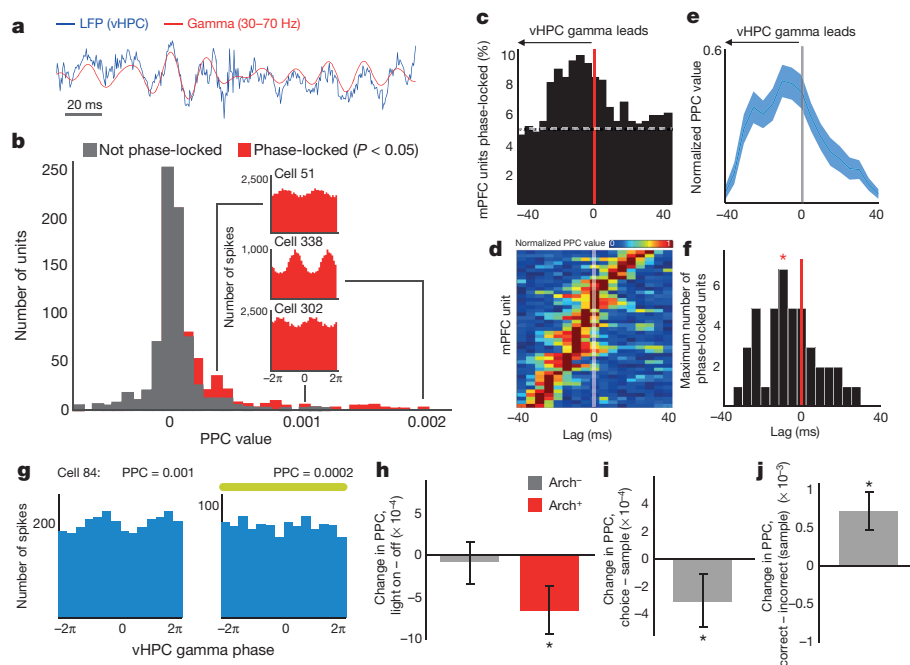


Figure 5 | Task-dependent modulation of mPFC spiking by vHPC gamma.

a, Example raw and gamma-filtered vHPC LFP. **b**, Distribution of phase-locking values for all units from spikes recorded at all times, coloured by significance (Rayleigh's test, $P < 0.05$). Insets, vHPC gamma phase histograms from example mPFC units (Cell 51: $z = -3.24$, $P < 0.001$, PPC = 0.0003; Cell 338: $z < -6$, $P < 0.0001$, PPC = 0.002; Cell 324: $z = -2.8$, $P = 0.002$, PPC = 0.001). **c**, Percentage of mPFC units significantly phase-locked to vHPC gamma across a range of lags. Dashed line, chance. **d**, Pseudocolour plot of normalized PPC values, sorted by lag of maximal phase-locking, for mPFC units with Bonferroni-corrected significance ($P < 0.0029$). **e**, Mean normalized PPC value

by lag. **f**, Distribution of lags at peak phase-locking strength; shifted towards a vHPC lead ($n = 43$ units, sign rank, $z = -2.2$, $P = 0.014$). Asterisk indicates mean lag. **g**, Distribution of gamma phases for spikes from an example mPFC unit from an Arch⁺ animal during all light off runs (Rayleigh's $P = 0.03$) and light on runs (Rayleigh's $P = 0.3$). **h–j**, Change in phase-locking comparing light on versus off ($n = 140$ units from 7 Arch⁺ mice, $z = -3.9$, $P = 8.7 \times 10^{-5}$; and $n = 222$ units from 6 Arch⁻ mice, $z = -1.83$, $P = 0.07$) (**h**); choice versus sample phases ($n = 458$ units, $z = -3.2$, $P = 0.0016$) (**i**); and correct versus incorrect trials ($n = 270$ units, $z = -4.2$, $P = 3.5 \times 10^{-5}$) (**j**). Significance by sign rank. Error bars shows s.e.m.

spective location representations have been seen in mPFC cells of rodents during delays in spatial alternation tasks in which past and future location are intertwined^{27,28}, while in primates there is ample evidence for stimulus-specific delay-period firing in the dorsolateral PFC^{29,30}. The primate dorsolateral PFC is functionally analogous to, but anatomically distinct from, the rodent prelimbic region of the mPFC^{30,31}. But retrospective place firing has been shown to be absent in the rodent mPFC when past and future location are independent¹⁷. While the delays used here were relatively brief (10–20 s), multiple previous studies have demonstrated a requirement for the mPFC at similar delays^{11,32–35}.

The combined results that vHPC–mPFC input is necessary only during cue encoding, that the mPFC lacks retrospective location representation during maintenance and retrieval, and that the mPFC representation of contemporaneous location during retrieval is not dependent on direct vHPC input, suggest that the mPFC processes sample goal location transiently and that some downstream structure(s) may maintain the information thereafter. Likely candidate structures would include the dHPC and the thalamic nucleus reuniens. We cannot, however, rule out the possibility that retrospective location is persistently represented in the mPFC in a form not detectable using the analytic techniques presented here, such as in temporary changes in synaptic weights, or transient reactivation that is too brief to be reliably decoded from binned spike histograms.

We find that vHPC–mPFC gamma synchrony is correlated with successful location encoding, and that inhibition of this input disrupts long-range gamma-frequency but not theta-frequency synchrony. vHPC gamma oscillations entrain local output in a phase-coherent manner (Extended Data Fig. 6), which influences mPFC spiking at putatively monosynaptic delays. These findings demonstrate that entrainment of mPFC spikes to vHPC gamma oscillations is a physio-

logical signature of task-critical long-range signal propagation. This phenomenon is subtle—at the lag with the greatest phase-locking, fewer than 10% of mPFC units were significantly phase-locked to vHPC gamma. Nevertheless, the observed correlation between vHPC–mPFC gamma synchrony and successful encoding suggests that gamma synchrony could be a behaviourally relevant marker of effective long-range functional connectivity²⁵.

The finding that mPFC theta activity leads vHPC theta, and that theta synchrony between the two structures did not appear to depend upon vHPC–mPFC afferents, ran counter to our initial hypotheses. Previous work had shown that dHPC theta leads mPFC theta^{10,36}, theta waves travel from the dHPC to vHPC^{37,38}, and silencing of vHPC activity affects dHPC–mPFC theta synchrony³⁹, supporting the idea that the vHPC theta-patterned activity might directly entrain mPFC theta. The current findings regarding theta synchrony suggest that there may be an alternative explanation for the previous finding of reduced dHPC–mPFC synchrony with vHPC silencing. It is possible that pharmacological inactivation of vHPC affected downstream targets in the dHPC, disrupting dHPC theta activity and thus dHPC–mPFC theta synchrony. This possibility is supported by the finding that vHPC silencing with muscimol reduces dHPC theta power³⁹.

Our findings point to a role for the vHPC–mPFC afferent pathway as a conduit for the updating of task-critical location cues, extending previous work that implicates the vHPC and mPFC in contextual learning to short timescales^{40–42}. Future work in this area should seek to implicate intermediary and/or upstream structures in the transmission of theta-patterned activity between the HPC and mPFC, to determine what (if any) role the mPFC has in maintenance and/or retrieval of task-related cues, and to identify which of the other major inputs to the mPFC serve to mediate the performance of spatial working memory.

Online Content Methods, along with any additional Extended Data display items and Source Data, are available in the online version of the paper; references unique to these sections appear only in the online paper.

Received 29 November 2014; accepted 25 March 2015.

Published online 8 June 2015.

1. Baddeley, A. & Hitch, G. in *Recent Advances in Learning and Motivation* Vol. 8 (ed. Bower, G. A.) 47–90 (Academic, 1974).
2. Klauer, K. C. & Zhao, Z. Double dissociations in visual and spatial short-term memory. *J. Exp. Psychol. Gen.* **133**, 355–381 (2004).
3. Andrade, J. *Working Memory in Perspective* (Psychology Press, 2001).
4. Miyake, A. & Shah, P. *Models of Working Memory: Mechanisms of Active Maintenance and Executive Control* (Cambridge Univ. Press, 1999).
5. Baddeley, A. Working memory: looking back and looking forward. *Nature Rev. Neurosci.* **4**, 829–839 (2003).
6. de Zubicaray, G. I., McMahon, K., Wilson, S. J. & Muthiah, S. Brain activity during the encoding, retention, and retrieval of stimulus representations. *Learn. Mem.* **8**, 243–251 (2001).
7. Curtis, C. E. & D'Esposito, M. The effects of prefrontal lesions on working memory performance and theory. *Cogn. Affect. Behav. Neurosci.* **4**, 528–539 (2004).
8. Hyman, J. M., Zilli, E. A., Paley, A. M. & Hasselmo, M. E. Working memory performance correlates with prefrontal-hippocampal theta interactions but not with prefrontal neuron firing rates. *Front. Integr. Neurosci.* **4**, 2 (2010).
9. Jones, M. W. & Wilson, M. A. Theta rhythms coordinate hippocampal-prefrontal interactions in a spatial working memory task. *PLoS Biol.* **3**, e402 (2005).
10. Sigurdsson, T., Stark, K. L., Karayiorgou, M., Gogos, J. A. & Gordon, J. A. Impaired hippocampal-prefrontal synchrony in a genetic mouse model of schizophrenia. *Nature* **464**, 763–767 (2010).
11. Lee, I. & Kesner, R. P. Time-dependent relationship between the dorsal hippocampus and the prefrontal cortex in spatial memory. *J. Neurosci.* **23**, 1517–1523 (2003).
12. Wang, G. W. & Cai, J. X. Disconnection of the hippocampal-prefrontal cortical circuits impairs spatial working memory performance in rats. *Behav. Brain Res.* **175**, 329–336 (2006).
13. Hoover, W. B. & Vertes, R. P. Anatomical analysis of afferent projections to the medial prefrontal cortex in the rat. *Brain Struct. Funct.* **212**, 149–179 (2007).
14. Jay, T. M. & Witter, M. P. Distribution of hippocampal CA1 and subicular afferents in the prefrontal cortex of the rat studied by means of anterograde transport of Phaseolus vulgaris-leucoagglutinin. *J. Comp. Neurol.* **313**, 574–586 (1991).
15. Oh, S. W. A mesoscale connectome of the mouse brain. *Nature* **508**, 207–214 (2014).
16. Burton, B. G., Hok, V., Save, E. & Poucet, B. Lesion of the ventral and intermediate hippocampus abolishes anticipatory activity in the medial prefrontal cortex of the rat. *Behav. Brain Res.* **199**, 222–234 (2009).
17. Jung, M. W., Qin, Y., McNaughton, B. A. & Barnes, C. L. Firing characteristics of deep layer neurons in prefrontal cortex in rats performing spatial working memory tasks. *Cereb. Cortex* **8**, 437–450 (1998).
18. Kjelstrup, K. B. *et al.* Finite scale of spatial representation in the hippocampus. *Science* **321**, 140–143 (2008).
19. Royer, S., Sirota, A., Patel, J. & Buzsáki, G. Distinct representations and theta dynamics in dorsal and ventral hippocampus. *J. Neurosci.* **30**, 1777–1787 (2010).
20. Chow, B. Y. *et al.* High-performance genetically targetable optical neural silencing by light-driven proton pumps. *Nature* **463**, 98–102 (2010).
21. Gradinaru, V. *et al.* Molecular and cellular approaches for diversifying and extending optogenetics. *Cell* **141**, 154–165 (2010).
22. Rigotti, M. *et al.* The importance of mixed selectivity in complex cognitive tasks. *Nature* **497**, 585–590 (2013).
23. Engel, A. K., König, P., Kreiter, A. K. & Singer, W. Interhemispheric synchronization of oscillatory neuronal responses in cat visual cortex. *Science* **252**, 1177–1179 (1991).
24. Carr, M. F., Karlsson, M. P. & Frank, L. M. Transient slow gamma synchrony underlies hippocampal memory replay. *Neuron* **75**, 700–713 (2012).
25. Yamamoto, J., Suh, J., Takeuchi, D. & Tonegawa, S. Successful execution of working memory linked to synchronized high-frequency gamma oscillations. *Cell* **157**, 845–857 (2014).
26. Vinck, M., van Wingerden, M., Womelsdorf, T., Fries, P. & Pennartz, C. The pairwise phase consistency: a bias-free measure of rhythmic neuronal synchronization. *Neuroimage* **51**, 112–122 (2010).
27. Baeg, E. H. *et al.* Dynamics of population code for working memory in the prefrontal cortex. *Neuron* **40**, 177–188 (2003).
28. Horst, N. K. & Laubach, M. Working with memory: evidence for a role for the medial prefrontal cortex in performance monitoring during spatial delayed alternation. *J. Neurophysiol.* **108**, 3276–3288 (2012).
29. Funahashi, S., Bruce, C. & Goldman-Rakic, P. Mnemonic coding of visual space in the monkey's dorsolateral prefrontal cortex. *J. Neurophysiol.* **61**, 331–349 (1989).
30. Goldman-Rakic, P. S. Cellular basis of working memory. *Neuron* **14**, 477–485 (1995).
31. Seamans, J. K., Lapish, C. C. & Durstewitz, D. Comparing the prefrontal cortex of rats and primates: insights from electrophysiology. *Neurotox. Res.* **14**, 249–262 (2008).
32. Rogers, D. C. *et al.* Photothrombotic lesions of the frontal cortex impair the performance of the delayed non-matching to position task by rats. *Behav. Brain Res.* **49**, 231–235 (1992).
33. Shaw, C. & Aggleton, J. The effects of fornix and medial prefrontal lesions on delayed non-matching-to-sample by rats. *Behav. Brain Res.* **54**, 91–102 (1993).
34. Sloan, H. L., Good, M. & Dunnett, S. B. Double dissociation between hippocampal and prefrontal lesions on an operant delayed matching task and a water maze reference memory task. *Behav. Brain Res.* **171**, 116–126 (2006).
35. Izaki, Y., Takita, M. & Akema, T. Specific role of the posterior dorsal hippocampus-prefrontal cortex in short-term working memory. *Eur. J. Neurosci.* **27**, 3029–3034 (2008).
36. Siapas, A. G., Lubenov, E. V. & Wilson, M. A. Prefrontal phase locking to hippocampal theta oscillations. *Neuron* **46**, 141–151 (2005).
37. Lubenov, E. V. & Siapas, A. G. Hippocampal theta oscillations are travelling waves. *Nature* **459**, 534–539 (2009).
38. Patel, J., Fujisawa, S., Berényi, A., Royer, S. & Buzsáki, G. Traveling theta waves along the entire septotemporal axis of the hippocampus. *Neuron* **75**, 410–417 (2012).
39. O'Neill, P. K., Gordon, J. A. & Sigurdsson, T. Theta oscillations in the medial prefrontal cortex are modulated by spatial working memory and synchronize with the hippocampus through its ventral subregion. *J. Neurosci.* **33**, 14211–14224 (2013).
40. Ruediger, S., Spirig, D., Donato, F. & Caroni, P. Goal-oriented searching mediated by ventral hippocampus early in trial-and-error learning. *Nature Neurosci.* **15**, 1563–1571 (2012).
41. Fanselow, M. A. & Dong, H. W. Are the dorsal and ventral hippocampus functionally distinct structures? *Neuron* **65**, 7–19 (2010).
42. Komorowski, R. W. *et al.* Ventral hippocampal neurons are shaped by experience to represent behaviorally relevant contexts. *J. Neurosci.* **33**, 8079–8087 (2013).

Supplementary Information is available in the online version of the paper.

Acknowledgements The authors would like to thank M. Topiwala for technical assistance, M. Kheirbek for advice and assistance with the design of fibre optics, and M. Shapiro for advice with regards to designing the four-arm T-maze. This work was supported by grants from the National Institutes of Health (MH096274 and MH081968), the Hope for Depression Research Foundation, the International Mental Health Research Organization, the Gatsby Charitable Foundation and the Swartz Foundation.

Author Contributions T.S., J. A. Gogos and J. A. Gordon designed the experiments. T.S. performed the experiments and analysed the data. M.R. and S.F. developed the linear classifier, adapted it for use with the T-maze data set, and provided guidance on its implementation. S.E.A. participated in the design of optogenetic experiments. T.S., S.F., J. A. Gogos and J. A. Gordon interpreted the results. T.S. and J. A. Gordon wrote the paper.

Author Information Reprints and permissions information is available at www.nature.com/reprints. The authors declare no competing financial interests. Readers are welcome to comment on the online version of the paper. Correspondence and requests for materials should be addressed to J. A. Gordon (jg343@columbia.edu).

METHODS

Subjects. Male C57BL/6 mice (Jackson Labs) were used for all experiments, aged 8–12 weeks at first use. Mice were housed in a New York State Psychiatric Institute satellite facility and were maintained on a 12-h light–dark cycle. Except when food-restricted for the purpose of behavioural training and testing, all mice were given *ad libitum* access to food and water. Pre-surgical mice were group-housed with littermates, while mice with chronic recording implants were singly housed in divided cages with visual, auditory and olfactory contact with another implanted mouse. Six mice were used in the acute anaesthetized experiment (3 Arch⁺, 3 Arch[−]), 14 in the two-goal T-maze experiment (8 Arch⁺, 6 Arch[−]), and 13 in the four-goal T-maze experiment (7 Arch⁺, 6 Arch[−]). The effect size for behavioural impairment in the Arch⁺ group in the four-goal experiment was 1.48, and the probability of observing a significant effect (statistical power) was 90% for an *N* of 7, 83% for an *N* of 6 (Arch⁺ and Arch[−] group sizes, respectively). Mice were randomized to a given viral type. All procedures were approved by Columbia University and the New York State Psychiatric Institute Institutional Animal Care and Use Committees.

Surgical preparation. Animals were placed inside a flow box and anaesthetized with isoflurane gas (2%) until sedated, at which point they were placed in a stereotax and maintained on 0.5% isoflurane for the duration of the surgery. Craniotomies were made bilaterally above the mPFC, dHPC and vHPC (coordinates below), and skull screws placed over the cerebellum and olfactory bulb served as ground and reference, respectively. In the acute anaesthetized experiment, surgical depth was maintained with isoflurane for the duration of the experiment.

Viral transduction. AAV2/5 of titre exceeding 10^{12} vg ml (K. Deisseroth via UNC Vector Core and UPenn Vector Core) was used to package the virus. In the acute stimulation/silencing experiment and the two-goal T-maze experiment, a CamKII α -eArch3.0-eYFP sequence was used to express the opsin and CamKII α -mCherry was used as an opsin-negative control. For the four-goal experiment, hSyn-eArch-eYFP and hSyn-eYFP were used for opsin and control, respectively. The hSynapsin promoter was chosen for the four-goal experiment to account for possible long-range GABAergic vHPC–mPFC projections and to avoid potential toxicity effects resulting from opsin expression under the stronger CamKII α promoter. Virus was targeted to multiple targets within the stratum pyramidale of ventral CA1 (two mediolateral rows at anteroposterior (AP) 2.95 and 3.25, with sites at mediolateral (ML)/dorsoventral (DV): 2.65/4.5, 3.0/4.3, 3.35/3.9, 3.7/3.3–2.9. An additional row was made at AP 3.1, with ML/DV sites at 2.8/1.55 and 3.15/1.7. All coordinates are reported in mm, all AP and ML coordinates are with respect to bregma, DV coordinates with respect to brain surface. A 200 nl bolus was delivered to each site via glass micropipette (20–40 μ M diameter) at a rate of 100 nl min^{−1} continuous infusion, with a wait time of 5 min between infusion and retraction.

Electrode and fibre implantation. LFPs were recorded using 50- μ M-diameter tungsten wire, while spikes and LFPs were recorded using stereotrodes (mPFC) and tetrodes (vHPC) made from 13- μ M-diameter tungsten fine wire. For the two-goal T-maze experiment, stereotrodes were coupled to ferrule-bound optical fibres (Thorlabs, 200- μ M-diameter core, 0.39 NA) positioned 300–500 μ M dorsal to the stereotrode tips, which were arrayed semi-circularly around the lateral edge of the fibre. Fibre-coupled stereotrode bundles were then implanted bilaterally in the mPFC (1.8 mm anterior, 0.4 mm lateral, 1.4 mm ventral), while LFP wires were implanted bilaterally in the dHPC (1.85 mm posterior, 1.25 mm lateral, 1.45 mm ventral) and the vHPC (3.1 mm posterior, 3.0 mm lateral, 3.9 mm ventral). For the four-goal experiment, 9 of the 13 animals were implanted as described earlier, while 4 animals (2 Arch⁺ and 2 Arch[−]) were instead implanted with tetrodes over the vHPC (3.7 mm ventral), which were advanced until spikes with putative pyramidal-cell waveforms were detected (Extended Data Fig. 4). mPFC optical fibres in these 4 animals were coupled to stationary bilateral LFP wires. All movable microdrives were advanced at a rate of 40 μ M per day across all recording days. Recording sites were histologically confirmed by visual examination of electrothermolytic lesions made before killing and perfusing implanted animals. Lesions were induced by passing current through an electrode at each implanted site (50 μ A, 20 s). Perfused and fixed tissue was then sectioned, and DNA was stained using 4',6'-diamidino-2-phenylindole (DAPI) Fluoromount-G mounting medium (Southern Biotech). vHPC LFP wires used for phase-locking analysis were located in the stratum pyramidale, stratum radiatum or stratum lacunosum-moleculare of ventral CA1; no differences in gamma power, peak frequency or synchrony with mPFC units were seen for the different laminar locations.

Recording and spike sorting. Recordings were amplified, band-pass filtered (1–1,000 Hz LFPs, 600–6,000 Hz spikes), and digitized using the Neuralynx Digital Lynx system. LFPs were collected at a rate of 2 kHz, while spikes were detected by online thresholding and collected at 32 kHz. Units were initially clustered using Klustakwik (Ken Harris), sorted according to the first two principal components,

voltage peak and energy from each channel. Clusters were then accepted, merged or eliminated based on visual inspection of feature segregation, waveform distinctiveness and uniformity, stability across recording session, and inter-spike interval distribution.

Behavioural training. Mice undergoing behavioural testing were given 5 weeks to recover from surgery and allow for expression and transport of the opsins, at which time they were placed on a food-restricted diet consisting of 1.5–2.5 g of food per day as needed to maintain 85% of their post-recovery bodyweight. The researcher responsible for training and running the mice was blinded as to viral group by another laboratory member, who randomly assigned opsin and control viruses. Mice were then given 2 days of habituation to the maze, which consisted of 10 min free exploration and foraging (plugged into optical fibres and recording tether) with all doors open, followed by 5 min of interleaved laser light pulses in the start box with doors closed (5–10 s on, 30 s off, 5 min). On the subsequent 2 days mice underwent behavioural shaping consisting of 10 min of running to baited goal arms in alternating directions. Mice then underwent training on the T-maze task until criterion performance (consisting of 70% correct trials on 2 out of 3 consecutive days) was achieved, in the absence of illumination. All animals that underwent successful surgeries met criterion. Inter-trial delay was 20 s. On the two-goal experiment, reward consisted of dustless pellets (Bio-Serv). Also in the two-goal experiment only, to minimize across-session performance drift and ceiling effects, intra-trial delay was adjusted according to the preceding day's performance, beginning at 10 s and progressively increasing delay by an additional 5 s following days on which performance was above 80% (as in ref. 12). For the four-goal experiment, reward consisted of sweetened condensed milk (~50 μ l, 3:1 dilution). To allow for direct comparison of delay within animals in this task, intra-trial delay was fixed at 10 s, with the addition of a single session of 20 s delays as the final session for each animal. Light stimulation was 532 nm, 10 mW in all cases. Task performance was lower when sample and choice goals matched in the left/right dimension than when they differed (*n* = 13 mice; mean = 0.65 ± 0.01 and 0.71 ± 0.02 , respectively; *t* = −3.91, *P* = 0.001), but performance on these trials remained above chance (*t* = 4.0×10^3 , *P* = 3.1×10^{-38}).

Statistics. All effects presented as statistically significant exceeded an α -threshold of 0.05. All independence tests were two-tailed. All independence testing of paired values (that is, changes across conditions) used paired *t*-tests or (where stated) signed rank tests. All ANOVA tests involving multiple observations per subject/unit (every figure except Extended Data Fig. 2d) were done as repeated measures group-by-condition tests. All *t*-tests and rank tests performed with more than two groups were done post-hoc to ANOVA tests except where Bonferroni correction for multiple comparisons is specifically cited.

Spike analysis using a linear classifier. A maximum margin linear classifier was used to decode sample goal location from binned population firing rate vectors and to quantify the strength and reliability of the neural representation. This type of classifier had the advantage of integrating comparisons between each pair of goal locations into a single inference, thus capturing all possible schemes of location discrimination in a way that can be applied across a diverse neural population. Matlab scripts are available for sharing upon request.

Analyses were performed on all units for which there was at least one training and one testing trial per condition.

Analysis using the population decoder was performed on binned spike vectors (500 ms bins, 100 ms increments) of all recorded units from sessions with at least two trials for each feature class under consideration. As in previous work with spike data from the PFC, we therefore took advantage of the accumulated data to decode task-relevant features by treating all units as a single, pseudosimultaneously recorded population⁴³. This approach assumes equivalent spike statistics across animals and recording sessions, and ignores potential contributions to population coding from correlated spike variability that would be observed if all units were indeed simultaneously recorded⁴⁴.

Model training was performed using constrained quadratic programming^{45,46} that employed a maximal margin perceptron^{46–48}. The training samples to this algorithm are generated by averaging the recorded spike counts within the relevant conditions that need to be decoded, and across a specified training set of trials. This procedure gives a mean activity vector per condition, in which each component of the vector represents the trial-averaged activity of a given neuron at a given condition. The quadratic programming procedure then aims at finding a set of readout weights that maximally separate the mean activity vectors corresponding to the conditions that have to be discriminated. Multi-class discrimination problems are reduced to a set of binary discrimination problems involving all pairwise combinations of conditions⁴⁹.

The model was then tested by cross-validating its performance on a test set of recorded trials. Given a task condition, a test vector is generated by sampling its components from the distribution of spike counts recorded from the corresponding neuron during the test trials. At each test phase 100 test vectors per condition

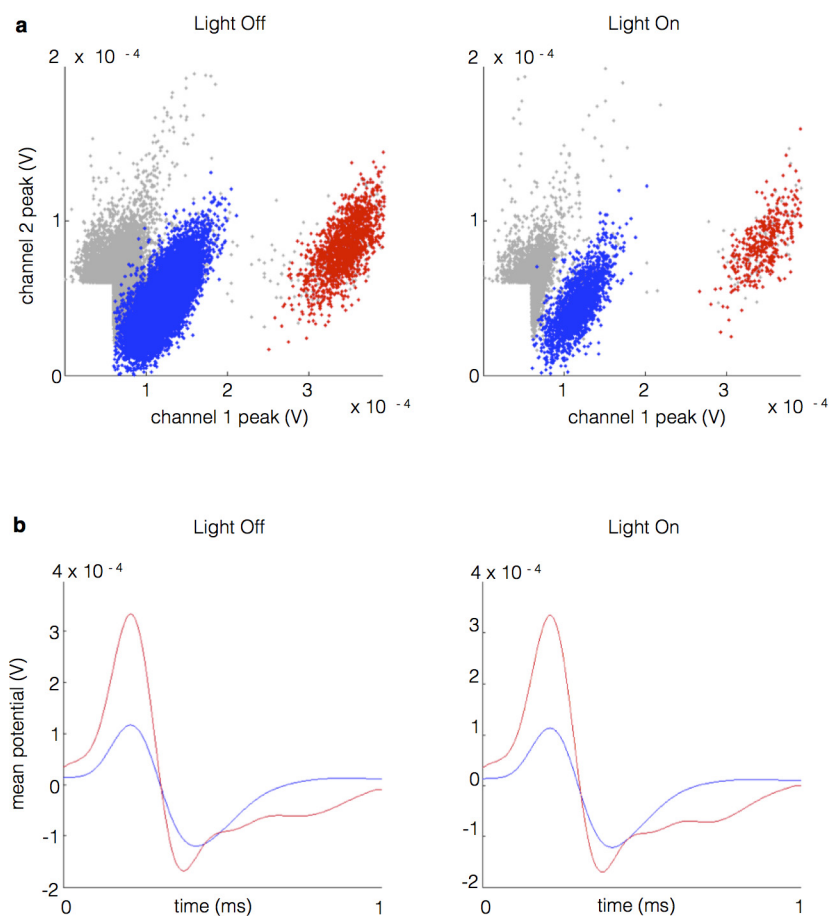
are randomly resampled with replacement, and the performance of the model is quantified as the average accuracy in classifying them. For each time bin, model training and testing was performed 100 times (at which point estimates of model accuracy approached asymptote) on non-overlapping subsets of trials (half of trials to train, half to test, random subsampling without replacement), with subsets constrained to include at least one trial corresponding with each feature class under consideration. For training and testing across separate trial conditions (Fig. 4), the same trial number requirement was applied across training and testing sets to ensure equal population sizes and equal representation of feature classes in the two trial sets.

For identification of each unit's preferred goal, absolute values of model weights for each goal's three binary classifications (comparison with each other goal) were summed, and the goal with the highest summed value was judged to be the preferred goal. To segregate units with high and low goal selectivity, the absolute model weights for all six binary classifications (each goal-goal comparison) were summed; units in the upper and lower quintiles were judged to have high and low goal selectivity, respectively.

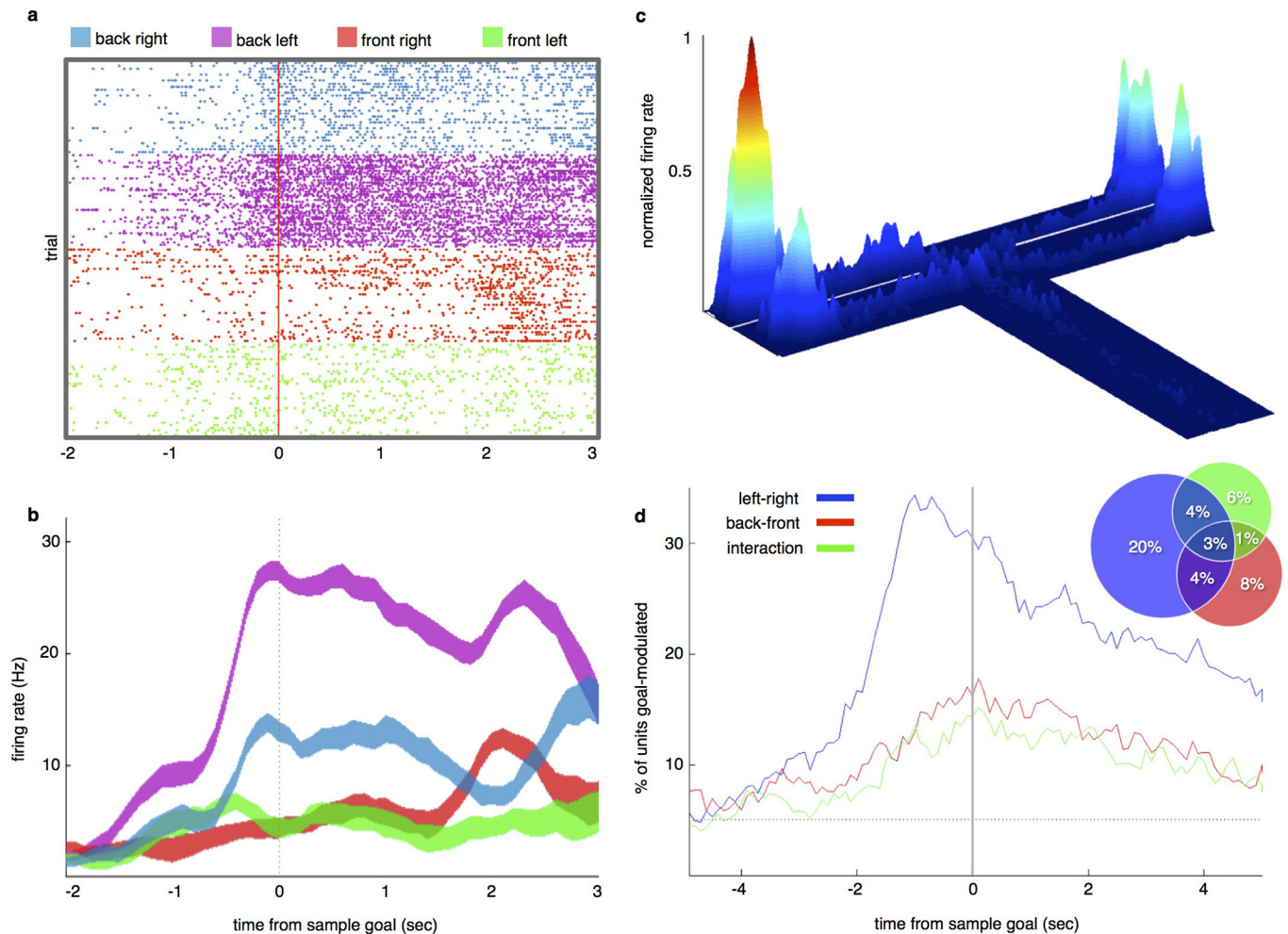
Phase-locking analysis. Phase-locking of spikes to the oscillatory phase of LFPs was performed using pairwise phase consistency, which, unlike other commonly used measures of phase-locking, is unbiased by spike number²⁶. Nevertheless, to ensure a representative estimate of spike phase, we set a threshold of 100 spikes for

all analysis; in comparisons of phase-locking across conditions (Fig. 5h–j and Extended Data Fig. 7h), only units that fired 100 spikes in each condition were included. LFP signal was digitally band-pass filtered (4–12 Hz for theta, 30–70 Hz for gamma) using a zero-phase-delay filter (filter provided by K. Harris and G. Buzsaki, order = sample frequency). The phase component was calculated by a Hilbert transform, and a corresponding phase was assigned to each spike.

43. Meyers, E. M., Freedman, D. J., Kreiman, G., Miller, E. K. & Poggio, T. Dynamic population coding of category information in inferior temporal and prefrontal cortex. *J. Neurophysiol.* **100**, 1407–1419 (2008).
44. Abbott, L. F. & Dayan, P. The effect of correlated variability on the accuracy of a population code. *Neural Comput.* **11**, 91–101 (1999).
45. Barak, O. & Rigotti, M. A simple derivation of a bound on the perceptron margin using singular value decomposition. *Neural Comput.* **23**, 1935–1943 (2011).
46. Anlauf, J. K. & Biehl, M. The AdaTron: an adaptive perceptron algorithm. *Europhys. Lett.* **10**, 687–692 (1989).
47. Rosenblatt, F. *Principles of Neurodynamics: Perceptrons and the Theory of Brain Mechanisms* (Spartan, 1962).
48. Krauth, W. & Mezard, M. Learning algorithms with optimal stability in neural networks. *J. Phys. A Math. Gen.* **20**, L745–L752 (1987).
49. Dietterich, T. G. & Ghulum, B. Error-correcting output codes: a general method for improving multiclass inductive learning programs. *Proc. AAAI* **91**, 572–577 (1991).

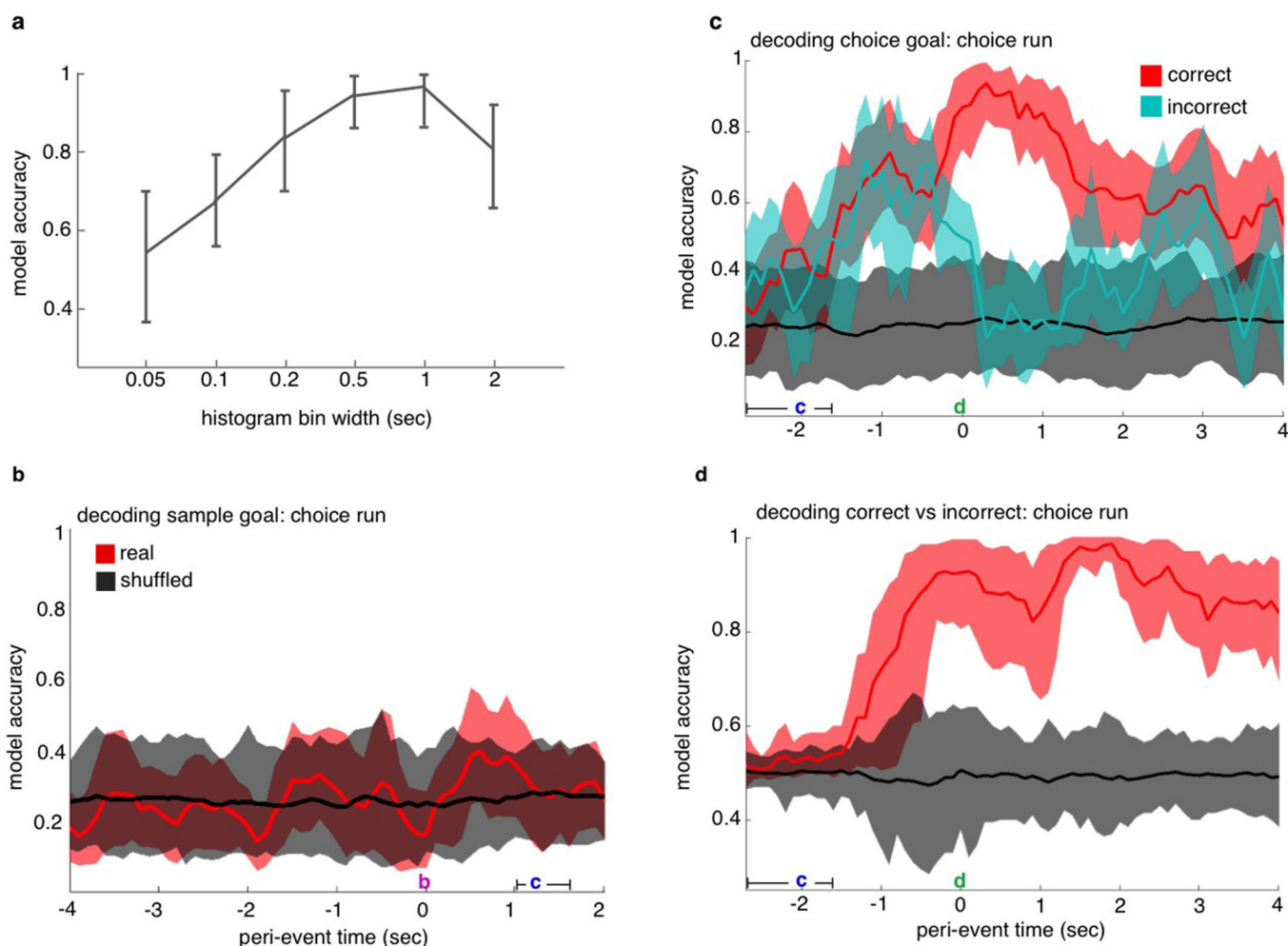


Extended Data Figure 1 | Individual mPFC units clustered from fibre-coupled stereotrodes. **a**, Multiple individual units clustered from stereotrode recordings in the mPFC in the absence and presence of illumination. **b**, Mean waveforms of extracellular potentials from example units in **a**.



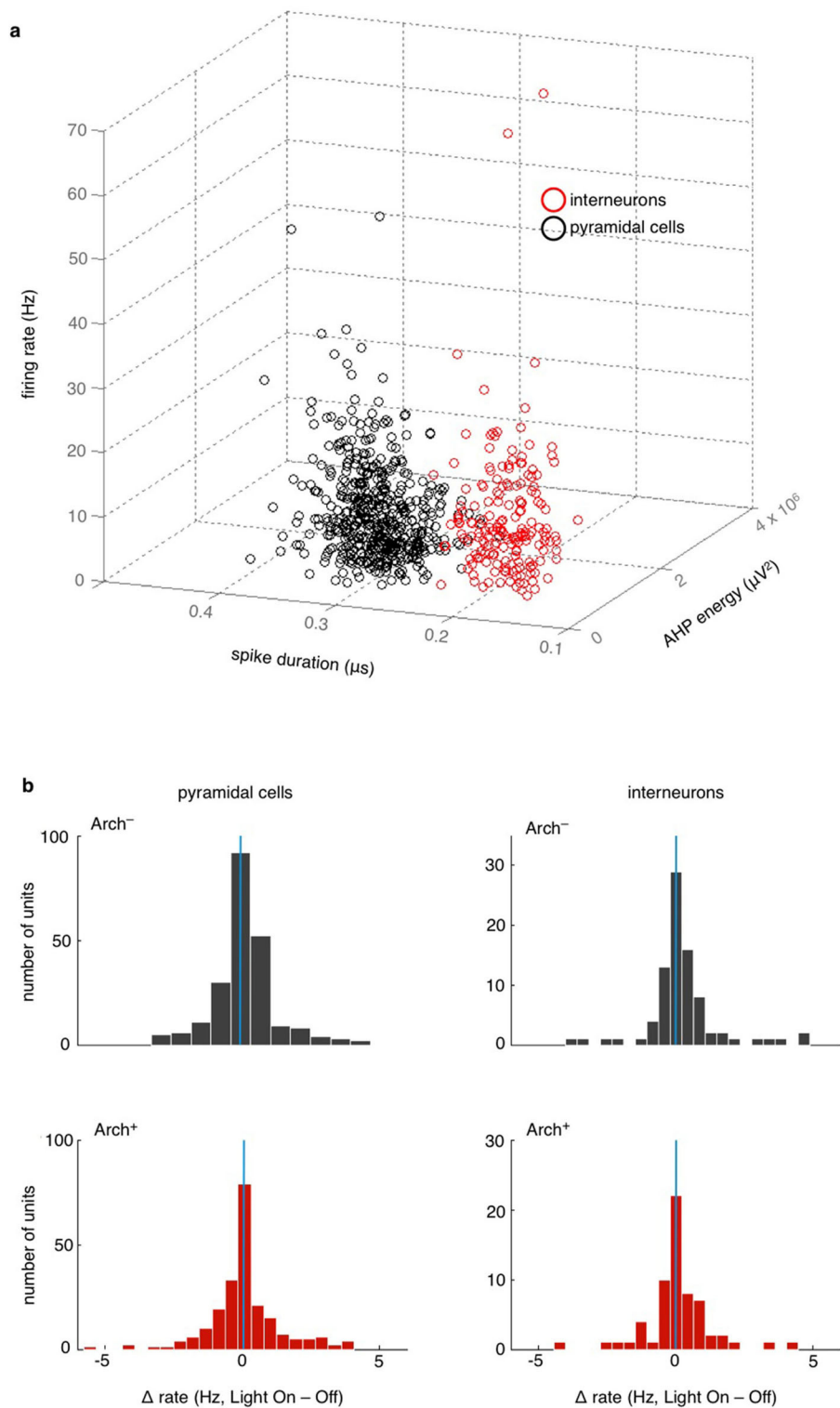
Extended Data Figure 2 | mPFC cells encode goal location both categorically and globally. **a**, A raster plot of spikes fired by an example single unit across trials, sorted by sample goal, temporally aligned to arrival at sample goal. **b**, Traces of firing rates averaged across trials by sample goal location, for the unit from **a**. This unit shows location selectivity, firing preferentially in the back left goal. Traces are mean \pm s.e.m. **c**, Spatial map of firing rates for the same unit for the full recording session. Goal-selective units tended to fire more at the preferred goal than at the other goals, and more

at all goals than in the rest of the environment. **d**, Percentage of units that were goal-selective as a function of time from sample goal, according to two-way repeated measures ANOVAs performed on binned spike rates. Units were identified as having selectivity for left/right (blue), back/front (red), and/or combined spatial dimensions (green). Dashed line represents chance ($P = 0.05$). Inset, percentage of units having each type and/or combination of selectivity at time zero (arrival at sample goal). Percentages are out of 792 recorded units.



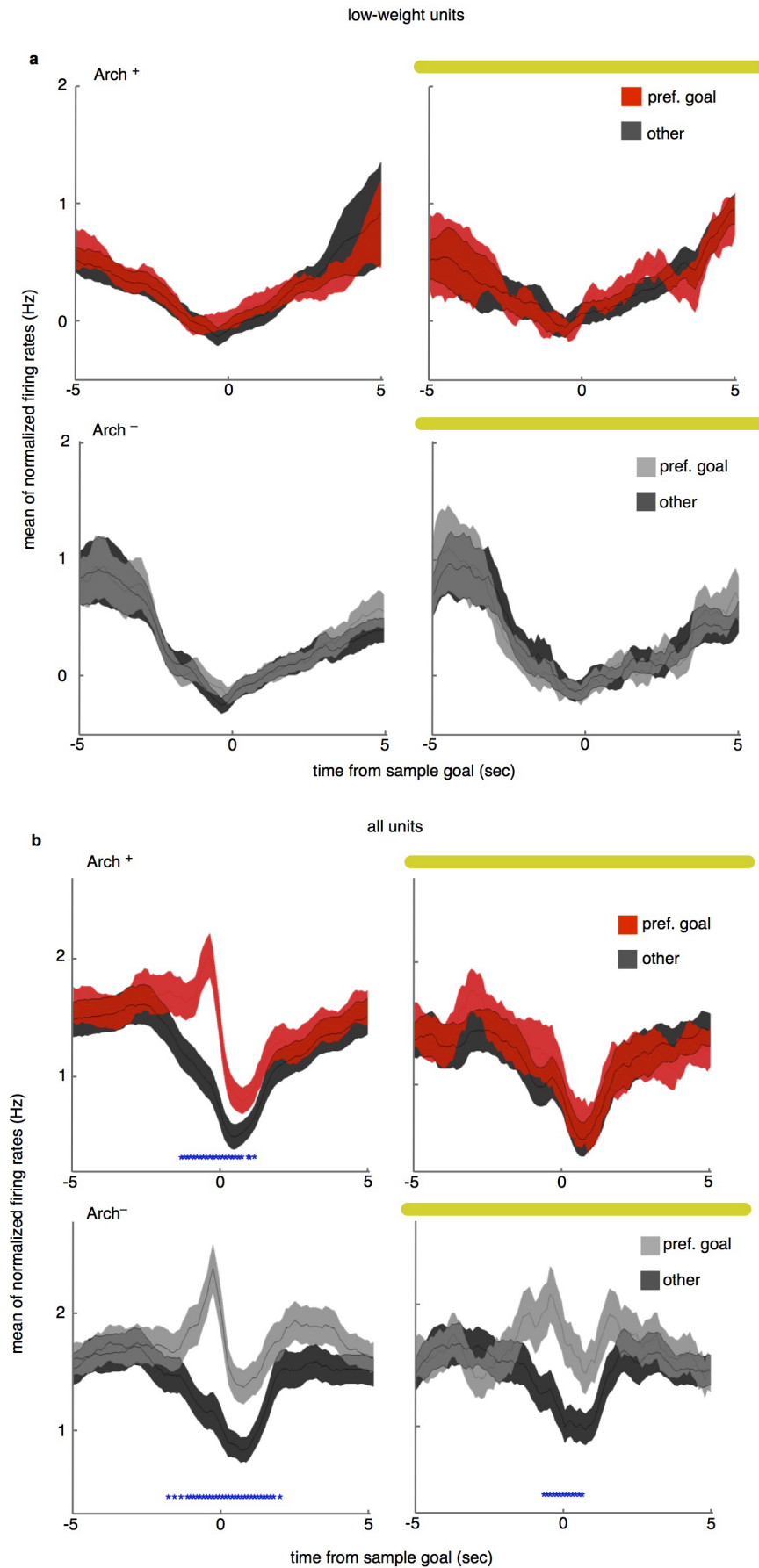
Extended Data Figure 3 | mPFC units represent choice goal location, not sample goal location, during choice runs. **a**, Model accuracy at the time bin corresponding with arrival at the sample goal port during the four-goal task was highest for spike histograms with time bins of 500 ms and 1,000 ms. Five-hundred-millisecond time bins were used for spike analyses. **b**, Decoding sample goal location during subsequent choice run during the four-goal task. Using the linear decoder, previously visited location was not detectable above chance accuracy. Ten- and twenty-second delay trials were combined. **c**, Decoding choice goal during choice run, correct versus incorrect trials during the four-goal task. Location decoded for this analysis was chosen goal (that is,

the mouse's current location) rather than correct goal. Model accuracy reached 0.93 upon arrival at the goal on correct trials. On incorrect trials, model accuracy exceeded chance during goal approach but dropped to chance levels upon reaching the goal. Ten- and twenty-second delay trials were combined. **d**, Decoding choice accuracy (correct versus incorrect) during choice trials. Model accuracy peaked at 0.99 at 1.9 s after arrival at the goal. **b–d**, Histograms were aligned to departure from start box. Ten- and twenty-second delay trials were combined. Data show mean \pm 95% confidence intervals for **b** and **d**; s.e.m. for **c** and **e**.



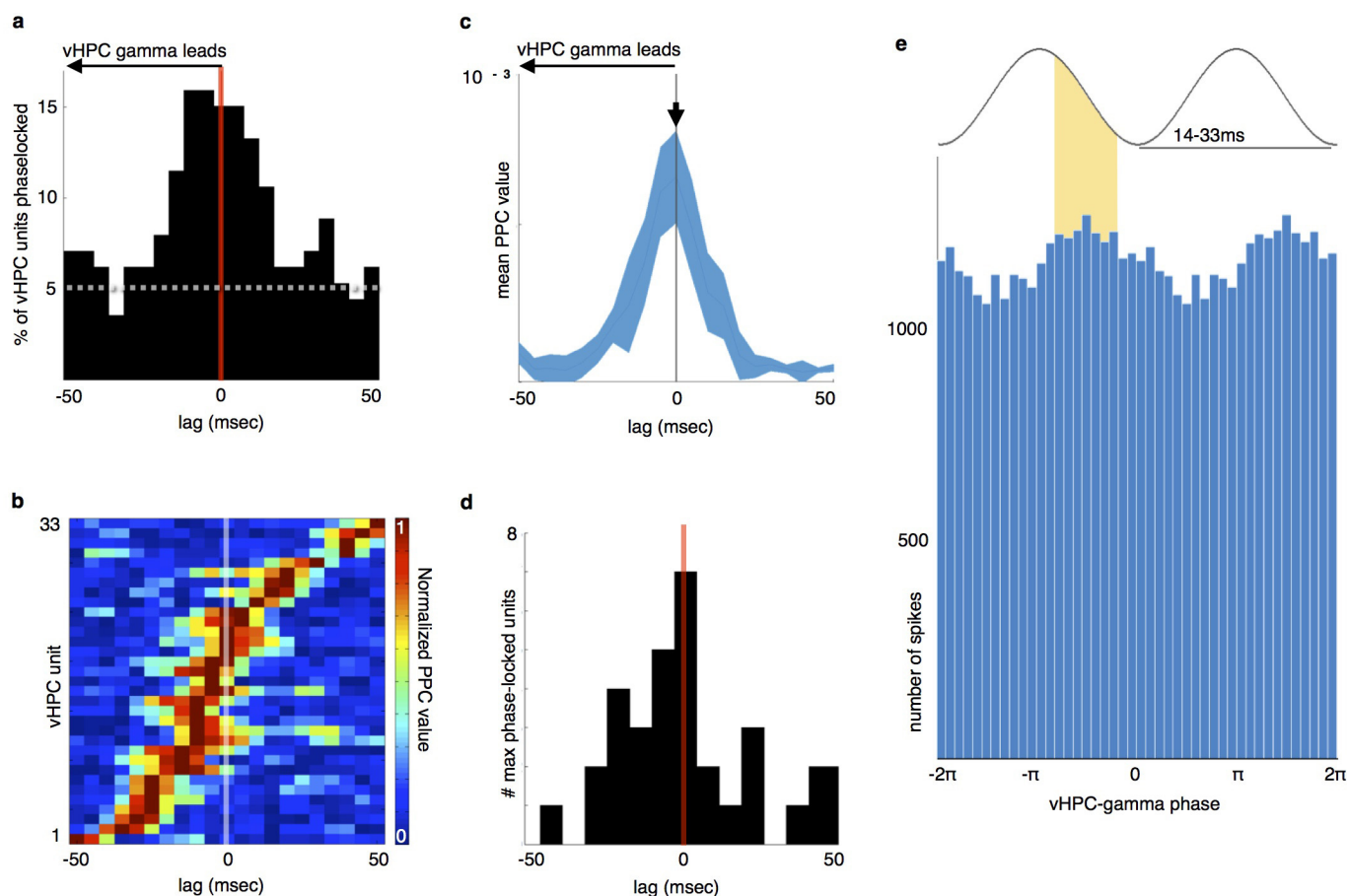
Extended Data Figure 4 | vHPC–mPFC terminal inhibition does not alter mPFC spike rate. **a**, Waveform features used to separate putative cell types. Spike duration was defined as the peak-to-trough time, while afterhyperpolarization (AHP) energy was taken as the area over the curve after the second zero-crossing. Spike duration yielded the clearest separation.

b, Putative fast-spiking (FS) and non-FS cells, sorted by spike width, showed no effect of terminal illumination on spike rate (Arch⁻ non-FS: sign rank $z = -1.7$, $P = 0.095$; Arch⁻ FS: $z = -1.6$, $P = 0.11$; Arch⁺ non-FS: $z = -2.7$, $P = 0.79$; Arch⁺ FS: $z = -0.49$, $P = 0.62$).



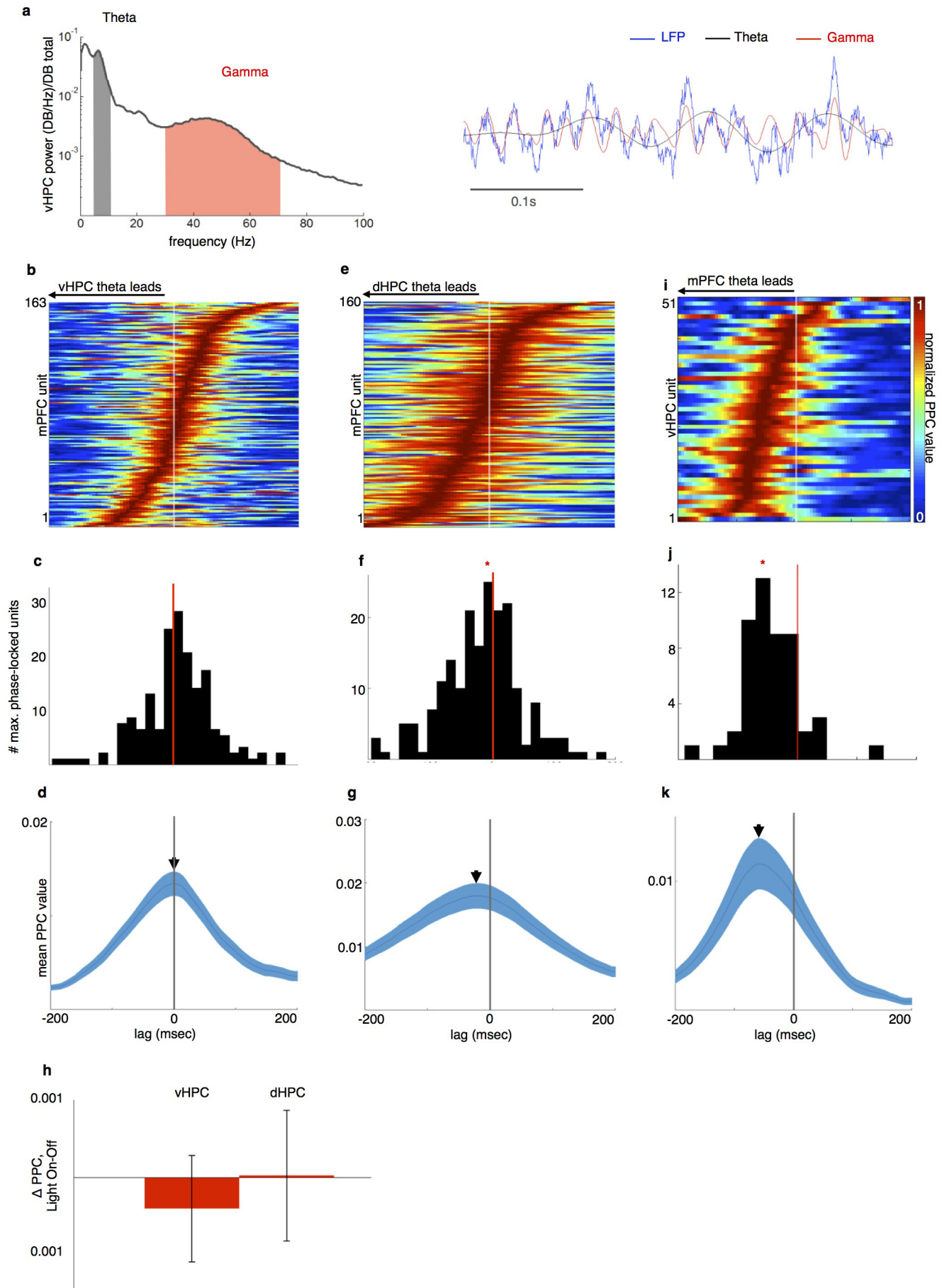
Extended Data Figure 5 | Effect of mPFC illumination on goal-selective firing in the mPFC. **a**, Low-weighted units, as identified using the classifier, show no difference in firing between the goal with the highest weight relative to the other goals. In the sample goal these units fire at rates not different than their session mean rates. Traces indicate mean \pm s.e.m. of normalized firing rate (bin FR – session FR). **b**, Terminal inhibition eliminates firing rate differences in preferred (Pref.) versus non-preferred (Other) goal during

encoding across all units. On sample runs with no light, units from both Arch[−] (bottom left) and Arch⁺ animals (top left) had elevated firing rates in preferred goal relative to non-preferred goal (red asterisks mark time points with Bonferroni-corrected significance). In Sample Light runs, units from Arch[−] animals maintain elevated firing in the preferred goal (bottom right), while units from Arch⁺ animals show no significant firing rate difference (top right; $N = 358$ Arch[−] units, 325 Arch⁺ units, sign rank $P < 0.0005$).



Extended Data Figure 6 | vHPC gamma modulates vHPC output. **a**, vHPC units phase-lock maximally to the vHPC gamma rhythm at a lag of zero (P value from Rayleigh's test < 0.05 , dashed line indicates chance rate). **b**, Normalized PPC values, sorted by lag of maximal phase-locking, for significantly phase-locked vHPC units. Units with Bonferroni-corrected significance within the -40 to 40 ms lag window (Rayleigh test, $P < 0.0029$) were included. **c**, Mean normalized PPC value for the population shown in **b**. Shading is s.e.m. **d**, Histogram of units with maximum PPC value at each lag.

Units maximally phase-locked at a lag of zero, with no net difference from zero across the population. **e**, vHPC units share a common preferred gamma phase. Pooled spikes from significantly phase-locked vHPC units were modulated by vHPC gamma phase at zero-lag ($N = 26,303$ spikes, Rayleigh's $z = 17.6$, $P = 2.2 \times 10^{-8}$, PPC value = 0.002), with peak spiking in the descending phase of the gamma cycle. (Note that spikes and LFPs were both recorded from stereotrodes in the stratum pyramidale and that this gamma phase would probably differ from that recorded in SLM, as in Fig. 5).



Extended Data Figure 7 | mPFC theta activity follows dHPC and leads vHPC during the task. **a**, Example vHPC LFP (blue, right) and spectrogram (left) demonstrating robust theta (grey, 4–12 Hz) and gamma (red, 30–70 Hz) components during all runs towards goals. **b**, Pseudocolour plot of relative strength of mPFC unit phase-locking to vHPC theta at lags from –200 ms to 200 ms, for units with Bonferroni-corrected significance in at least one lag. Warmer colours indicate stronger phase-locking. **c**, Distribution of lags at peak phase-locking strength for significantly phase-locked mPFC units. Distribution centred at 0 ($N = 189$ units, $z = 2.05$, $P = 0.98$). **d**, Mean \pm s.e.m. PPC value of mPFC units and vHPC theta, as a function of lag. **e–g**, Phase-locking of

mPFC units to dHPC theta as a function of lag, as in **b–d**. Distribution of lags at peak phase-locking is significantly shifted towards a dHPC lead ($N = 160$ units, sign rank $z = -4.4$, $P = 6 \times 10^{-6}$). **h**, No difference in strength of phase-locking of mPFC units to vHPC (left) and dHPC (right) theta in light on versus light off trials. Mean and s.e.m. shown for each ($N = 140$ units, sign rank $z = -1.3$, $P = 0.2$; $z = -1.4$, $P = 0.12$). **i–k**, Phase-locking of vHPC units to mPFC theta as a function of lag, as in **b–d**. Distribution of lags at peak phase-locking is significantly shifted towards an mPFC lead ($N = 51$ units, $z = -5.03$, $P = 2.4 \times 10^{-7}$).

A novel multiple-stage antimalarial agent that inhibits protein synthesis

Beatriz Baragaña¹, Irene Hallyburton¹, Marcus C. S. Lee^{2†}, Neil R. Norcross¹, Raffaella Grimaldi¹, Thomas D. Otto³, William R. Proto³, Andrew M. Blagborough⁴, Stephan Meister⁵, Grennady Wirjanata⁶, Andrea Ruecker⁴, Leanna M. Upton⁴, Tara S. Abraham², Mariana J. Almeida², Anupam Pradhan⁷, Achim Porzelle¹, María Santos Martínez⁸, Judith M. Bolscher⁹, Andrew Woodland¹, Suzanne Norval¹, Fabio Zuccotto¹, John Thomas¹, Frederick Simeons¹, Laste Stojanovski¹, Maria Osuna-Cabello¹, Paddy M. Brock⁴, Tom S. Churcher⁴, Katarzyna A. Sala⁴, Sara E. Zakutansky⁴, Maria Belén Jiménez-Díaz⁸, Laura Maria Sanz⁸, Jennifer Riley¹, Rajshekhar Basak², Michael Campbell¹⁰, Vicky M. Avery¹¹, Robert W. Sauerwein⁹, Koen J. Dechering⁹, Rintis Noviyanti¹², Brice Campo¹³, Julie A. Frearson¹, Iñigo Angulo-Barturen⁸, Santiago Ferrer-Bazaga⁸, Francisco Javier Gamo⁸, Paul G. Wyatt¹, Didier Leroy¹³, Peter Siegl¹³, Michael J. Delves⁴, Dennis E. Kyle⁷, Sergio Wittlin¹⁴, Jutta Marfurt⁶, Ric N. Price^{6,15}, Robert E. Sinden⁴, Elizabeth A. Winzeler⁵, Susan A. Charman¹⁰, Lidiya Bebrevska¹³, David W. Gray¹, Simon Campbell¹³, Alan H. Fairlamb¹, Paul A. Willis¹³, Julian C. Rayner³, David A. Fidock^{2,16}, Kevin D. Read¹ & Ian H. Gilbert¹

There is an urgent need for new drugs to treat malaria, with broad therapeutic potential and novel modes of action, to widen the scope of treatment and to overcome emerging drug resistance. Here we describe the discovery of DDD107498, a compound with a potent and novel spectrum of antimalarial activity against multiple life-cycle stages of the *Plasmodium* parasite, with good pharmacokinetic properties and an acceptable safety profile. DDD107498 demonstrates potential to address a variety of clinical needs, including single-dose treatment, transmission blocking and chemoprotection. DDD107498 was developed from a screening programme against blood-stage malaria parasites; its molecular target has been identified as translation elongation factor 2 (eEF2), which is responsible for the GTP-dependent translocation of the ribosome along messenger RNA, and is essential for protein synthesis. This discovery of eEF2 as a viable antimalarial drug target opens up new possibilities for drug discovery.

The World Health Organization estimates that there were approximately 200 million clinical cases and 584,000 deaths from malaria in 2013, predominantly among children and pregnant women in sub-Saharan Africa¹. The malaria parasite has developed resistance to many of the current drugs, including emerging resistance to the core artemisinin component of artemisinin-based combination therapies that constitute current first-line therapies². To support the current treatment and eradication agenda³, there are several requirements for new antimalarials: novel modes of action with no cross-resistance to current drugs; single-dose cures; activity against both the asexual blood stages that cause disease and the gametocytes responsible for transmission; compounds that prevent infection (chemoprotective agents); and compounds that clear *Plasmodium vivax* hypnozoites from the liver (anti-relapse agents)⁴.

Discovery of a novel antimalarial

A phenotypic screen of the Dundee protein kinase scaffold library⁵ (then 4,731 compounds) was performed against the blood stage of the multi-drug-sensitive *Plasmodium falciparum* 3D7 strain. A compound series from this screen, based on a 2,6-disubstituted quinoline-4-carboxamide scaffold, had sub-micromolar potency against

the parasites, but suffered from poor physicochemical properties. Chemical optimization (Fig. 1 and Extended Data Fig. 1) led to DDD107498 with improved physicochemical properties (Tables 1 and 2 in Supplementary Methods) and a 100-fold increase in potency. The key stages involved were replacing the bromine with a fluorine atom to reduce molecular mass and lipophilicity; replacing the 3-pyridyl substituent with an ethyl-pyrrolidine group; and addition of a morpholine group via a methylene spacer. Initial cost-of-goods estimates and likely human dose projections suggest a low cost (approximately US\$1 per treatment), which is important, given that most of the patient population is living in poverty.

Blood-stage activity and developability

DDD107498 showed excellent activity against 3D7 parasites: 50% effective inhibitory concentration (EC₅₀) = 1.0 nM (95% confidence interval (CI) 0.8–1.2 nM); EC₉₀ = 2.4 nM (95% CI 2.0–2.9 nM); EC₉₉ = 5.9 nM (95% CI 4.5–7.6 nM), (*n* = 39). It was also almost equally active against several drug-resistant strains (Extended Data Fig. 2a)⁶. Furthermore, DDD107498 was more potent than artesunate in *ex vivo* assays against a range of clinical isolates of both *P. falciparum* (median EC₅₀ = 0.81 nM (range 0.29–3.29 nM), *n* = 44) and

¹Drug Discovery Unit, Division of Biological Chemistry and Drug Discovery, College of Life Sciences, University of Dundee, Dundee DD1 5EH, UK. ²Department of Microbiology and Immunology, Columbia University College of Physicians and Surgeons, New York, New York 10032, USA. ³Malaria Programme, Wellcome Trust Sanger Institute, Wellcome Trust Genome Campus, Cambridge CB10 1SA, UK.

⁴Department of Life Sciences, Imperial College, London SW7 2AZ, UK. ⁵University of California, San Diego, School of Medicine, 9500 Gilman Drive 0760, La Jolla, California 92093, USA. ⁶Global Health and Tropical Medicine Division, Menzies School of Health Research, Charles Darwin University, PO Box 41096, Casuarina, Darwin, Northern Territory 0811, Australia. ⁷Department of Global Health, College of Public Health University of South Florida, 3720 Spectrum Boulevard, Suite 304, Tampa, Florida 33612, USA. ⁸GlaxoSmithKline, Tres Cantos Medicines Development Campus-Diseases of the Developing World, Severo Ochoa 2, Tres Cantos 28760, Madrid, Spain. ⁹TropiQ Health Sciences, Geert Grooteplein 28, Huispost 268, 6525 GA Nijmegen, The Netherlands. ¹⁰Centre for Drug Candidate Optimisation, Monash University, 381 Royal Parade, Parkville, Victoria 3052, Australia. ¹¹Eskitis Institute, Brisbane Innovation Park, Nathan Campus, Griffith University, Queensland 4111, Australia.

¹²Malaria Pathogenesis Laboratory, Eijkman Institute for Molecular Biology, Jalan Diponegoro 69, 10430 Jakarta, Indonesia. ¹³Medicines for Malaria Venture, PO Box 1826, 20 route de Pre-Bois, 1215 Geneva 15, Switzerland. ¹⁴Swiss Tropical and Public Health Institute, Socinstrasse 57, 4051 Basel, Switzerland. ¹⁵Centre for Tropical Medicine and Global Health, Nuffield Department of Medicine, University of Oxford, Oxford OX3 7LJ, UK. ¹⁶Division of Infectious Diseases, Department of Medicine, Columbia University College of Physicians and Surgeons, New York, New York 10032, USA.

[†]Present address: Wellcome Trust Sanger Institute, Wellcome Trust Genome Campus, Hinxton, Cambridge CB10 1SA, UK.

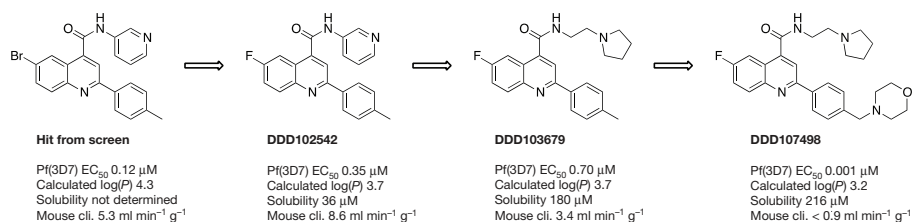


Figure 1 | Chemical evolution of DDD107498 from the phenotypic hit. Calculated log(P), calculated log(partition coefficient); Solubility, solubility in water; Mouse cli., intrinsic clearance in mouse liver microsomes.

P. vivax (median EC₅₀ = 0.51 nM (range 0.25–1.39 nM), *n* = 28) collected from patients with malaria from southern Papua, Indonesia, a region where high-grade multidrug-resistant malaria is endemic for both species (Extended Data Fig. 2b)^{7,8}. In contrast, the compound was not toxic to human cells (MRC5 and Hep-G2 cells) at much higher concentrations (>20,000-fold selectivity; Extended Data Fig. 2c).

DDD107498 showed good drug-like properties: metabolic stability when incubated with hepatic microsomes or hepatocytes from several species; good solubility in a range of different media; and low protein binding (Tables 1 and 2 in Supplementary Methods). DDD107498 displayed excellent pharmacokinetic properties in preclinical species, including good oral bioavailability (an important prerequisite for use in resource-poor settings) and long plasma half-life (important for single-dose treatment and chemoprotection) (Extended Data Table 1a).

DDD107498 was very active in several mouse models of malaria, with comparable or greater efficacy than current antimalarials (Extended Data Table 1b). DDD107498 had a 90% reduction in parasitaemia (ED₉₀) of 0.57 mg per kg (body weight) after a single oral dose in mice infected with the rodent parasite *Plasmodium berghei*. Efficacy was also tested in NOD-*scid* IL-2R_{null} mice engrafted with human erythrocytes and infected with *P. falciparum* strain 3D7^{0087/N9} (Fig. 2a)⁹. When orally dosed daily for 4 days, the ED₉₀ on day 7 after infection was 0.95 mg per kg per day. Blood sampling from the infected SCID (severe combined immunodeficiency) mice suggested a minimum parasitocidal concentration for DDD107498 of 10–13 ng ml⁻¹ for asexual blood-stage infections.

The effects of DDD107498 on circulating parasites in the SCID mouse model could be observed in one replication cycle (48 h) and led to trophozoites with condensed cytoplasm (Extended Data Fig. 3). Stage specificity studies using synchronized cultures showed that, at a concentration of 4 nM for 24 h, DDD107498 led to (1) from the ring stage, formation of abnormal trophozoites; (2) from the trophozoite stage, prevention of schizont formation with a 50% reduction in parasites, indicative of cidal activity; and (3) from the schizont stage, prevention of ring formation with a 98% reduction in parasites, indicative of cidal activity (Extended Data Fig. 3b, c).

DDD107498 showed a similar parasite killing profile both *in vitro* (Fig. 2b, c) and *in vivo* (Fig. 2a), which is supportive of a common mode of action in cellular and animal models of disease. Using a parasite reduction rate assay¹⁰ there was a lag of about 24–48 h, during which time the effects of the compounds were reversible following wash-out. Rapid killing occurred after parasites had been exposed to DDD107498 for more than 48 h (Fig. 2b, c).

All these experiments suggest for the blood-stage form that treatment with DDD107498 prevented development of trophozoites and schizonts and, at least in the case of schizonts, caused rapid killing. Any ring-stage parasites only developed as far as abnormal trophozoites, which appeared to survive for about 48 h under drug pressure, but were then killed.

In safety studies, DDD107498 showed no clinically relevant inhibition of any of the major human cytochrome P450 (CYP) isoforms and

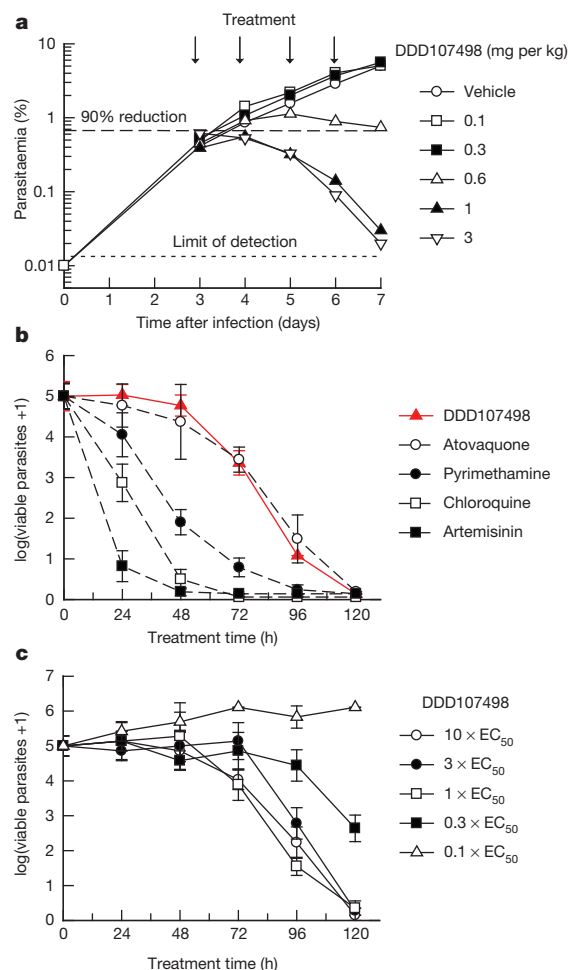


Figure 2 | Efficacy studies and parasite killing rate. **a**, *In vivo* activity against *P. falciparum* in NOD-*scid* IL-2R_{null} mice. Six mice were used, each serially sampled. The variability of cytometry for repeated acquisitions of a sample is less than 2–3%. The percentage of parasitaemia was calculated by acquiring a minimum number of 500 parasitized erythrocytes. An independent experiment with three further mice was performed to confirm the ED₉₀. **b**, Determination of the *in vitro* killing rate of DDD107498. The *in vitro* parasite reduction rate assay was used to determine onset of action and rate of killing as previously described¹⁰. *P. falciparum* was exposed to DDD107498 at a concentration corresponding to 10 × EC₅₀. The number of viable parasites at each time point was determined as described¹⁰. Four independent serial dilutions were done with each sample to correct for experimental variation; error bars, s.d. Previous results reported on standard antimalarials tested at 10 × EC₅₀ using the same conditions are shown for comparison¹⁰. **c**, The *in vitro* parasite reduction rate assay was used to determine the minimal concentration of compound needed for achieving maximal killing effects. Parasites were exposed to DDD107498 at concentrations of 0.1, 0.3, 1, 3 and 10 × EC₅₀ using conditions described above. Error bars, s.d. Concentrations of DDD107498 of 1 × EC₅₀ are sufficient to produce maximal killing effects on treated parasites.

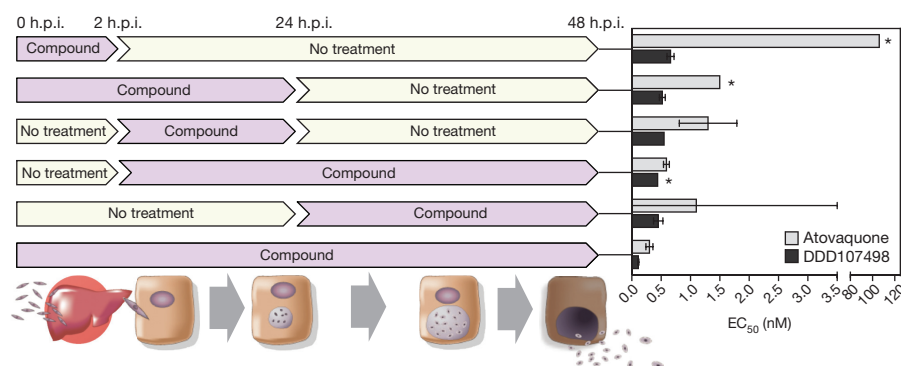


Figure 3 | *In vitro* activity of DDD107498 against *P. berghei* liver stages. Each experiment was the average of four technical replicates; h.p.i., hours post-infection. Bars, 95% CI. *More than one curve fitting possible.

CYP450 induction risk was low (Table 3 in Supplementary Methods), indicating a low risk of clinical drug–drug interactions. DDD107498 is non-mutagenic and has very weak inhibitory potencies on I_{Kr} (hERG) and other ion channels, indicating a very low risk for adverse cardiovascular activity. Given its potency, long half-life observed in preclinical species, and safety margins from a rat 7-day toxicology study, DDD107498 has potential both for single-dose treatment and for once-weekly chemoprotection¹¹.

Activity against other life-cycle stages

Intra-hepatocytic parasites (liver schizont stages) are the first stage of human infection after injection of sporozoites by anopheline mosquitoes. Compounds active against this stage have potential for use in chemoprotection. DDD107498 showed an $EC_{50} \approx 1$ nM against the liver schizont forms of *P. berghei* and *Plasmodium yoelii*¹². DDD107498 was active when dosed for only 2 h during the initial infection (hepatocyte invasion) of the liver cells (Fig. 3). In contrast, atovaquone (clinically used for chemoprotection in combination with proguanil) had a much reduced activity during this period ($EC_{50} \approx 106$ nM versus 0.3 nM for continuous treatment). Further, DDD107498 showed equivalent potency against the *P. berghei* liver stage when added after initial infection had been established (Fig. 3). This suggests that intermittent treatment may be sufficient for chemoprotection. To assess chemoprotective potential *in vivo*, mice were treated with DDD107498 2 h before being infected with luciferase-expressing *P. berghei* sporozoites (Extended Data Fig. 4). At a dose of 3 mg per kg, DDD107498 was fully curative with no sign of parasitaemia after 30 days. Thus, DDD107498 demonstrates potent chemoprotection using *in vitro* and *in vivo* models, where blood sampling from the mice during the experiment suggests a minimum parasitocidal concentration of 15–20 ng ml^{−1}.

The parasite erythrocytic form differentiates into the asymptomatic male and female gametocytes (stages I–V) within the human host. Mature stage V gametocytes are infective to mosquitoes, but are not eliminated by the majority of current antimalarial agents, and remain circulating in the human bloodstream for up to 3 weeks, long after the disappearance of clinical symptoms of malaria^{13,14}. After ingestion by the mosquito, gametocytes differentiate into gametes. DDD107498 potently inhibited both male and female gamete formation from the gametocyte stage at similar concentrations (1.8 nM (95% CI 1.6–2.1 nM) and 1.2 nM (95% CI 0.8–1.6 nM) respectively; Extended Data Fig. 5), indicating that it is an extremely potent inhibitor of the functional viability of both male and female mature gametocytes¹⁵. In line with this, DDD107498 blocked transmission, as determined by the standard membrane feeding assay. In this assay, parasite cultures containing *P. falciparum* stage V gametocytes were exposed to compound for 24 h before mosquito feeding. DDD107498 blocked subsequent oocyst development in the mosquito (measured

after 7 days) with an EC_{50} of 1.8 nM. At a baseline oocyst intensity of 27 oocysts per mosquito in the DMSO controls, prevalence of infection was inhibited, with an EC_{50} of 3.7 nM, as measured by the number of infected mosquitoes. Repeating the standard membrane feeding assay in which DDD107498 was added at the moment of mosquito feeding gave an EC_{50} of 10 nM, indicating potent activity against the parasite sexual stages that develop in the mosquito midgut (Extended Data Fig. 5)¹⁶.

A *P. berghei* mouse-to-mouse^{17,18} model was additionally used to examine transmission blockade. Mice were infected with *P. berghei* (PbGFPCON507)¹⁹, and then treated orally with compound 24 h before mosquitoes took a direct blood meal¹⁷. After a 3 mg per kg dose of DDD107498, a 90.7% reduction in infected mosquitoes and a 98.8% reduction in oocysts per midgut was observed at day 10 compared with mosquitoes fed on untreated mice (Extended Data Fig. 6). A corresponding reduction in sporozoite intensity and prevalence was observed (93.8% and 88.6% respectively). Mosquitoes previously fed on infected, drug-treated mice were allowed to feed on uninfected mice¹⁷. Testing a range of mosquito biting rates, we observed a mean reduction of 89.5% (95% CI 71.4–100) in the number of mice that developed blood-stage infection compared with mice bitten by mosquitoes that had fed on non-drug-treated infected mice. The overall effectiveness of an intervention over a round of transmission (from mouse to mosquito to mouse) can be quantified by estimating its ability to reduce the basic reproductive number (R_0). This has been termed the ‘effect size’ of an intervention. By fitting data from the mouse-to-mouse assay to a chain binomial model we can estimate the effect size of the intervention¹⁷, assessing the ability of DDD107498 usage to reduce the basic reproductive number R_0 (assuming 100% coverage). Our results estimate an effect size of 90.5% (95% CI 78.3–94.2), suggesting that DDD107498 is capable of acting as a potent transmission-blocking drug over multiple transmission settings within a field context¹⁸. The combination of these key *in vitro* and *in vivo* assays demonstrates the very strong potential of DDD107498 for blocking transmission; importantly, the required doses are likely to be similar to those required for treatment of blood-stage malaria.

DDD107498 targets PfeEF2

To determine the molecular target for DDD107498, asexual blood-stage *P. falciparum* were cultured in the presence of DDD107498 at $5 \times EC_{50}$, until parasites became resistant (Extended Data Table 2)²⁰. Resistance was obtained in the 3D7 (drug-sensitive) and 7G8 and Dd2 (multi-drug-resistant) strains, with minimum inocula of 10^7 , 10^7 and 10^6 parasites respectively. Genomic DNA was extracted from resistant lines and whole-genome sequencing of ten drug-resistant lines identified shared mutations in one gene, which were not present in the parental lines: Pf3D7_1451100 (Supplementary Data 1). This gene

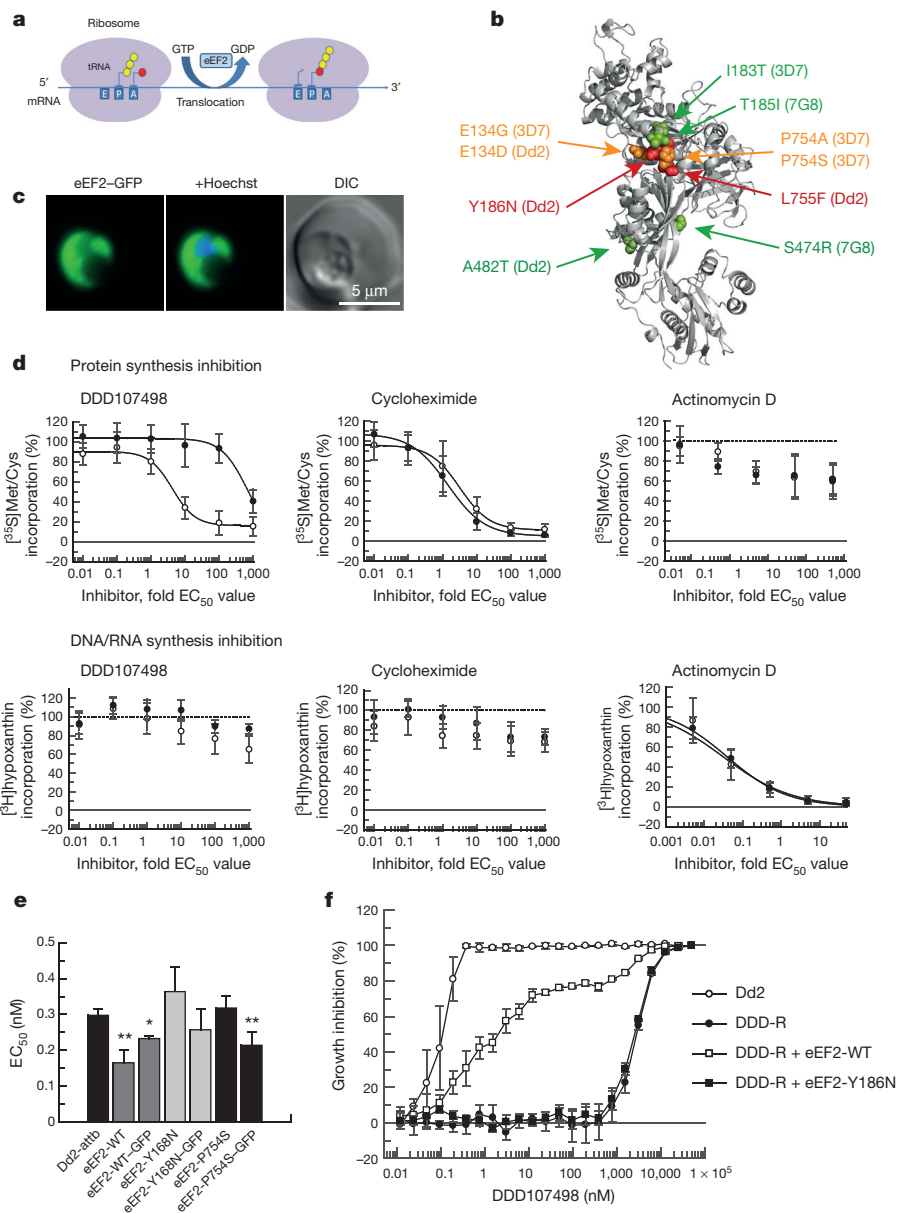


Figure 4 | DDD107498 targets protein synthesis via eEF2. **a**, eEF2 promotes the GTP-dependent translocation of the ribosome along messenger RNA during protein synthesis. **b**, Homology model of *P. falciparum* eEF2. The mapped mutations from each strain are colour coded by EC₅₀ fold (red, high; amber, moderate; green, low). **c**, Live-cell imaging of *P. falciparum* expressing an extra copy of eEF2 (WT) fused to GFP. The image is representative of more than 50 parasites visualized on two independent occasions. **d**, Protein and DNA/RNA synthesis were evaluated by measuring the incorporation of [³⁵S]Met/Cys (upper panel) and [³H]hypoxanthine (lower panel) into asynchronous 3D7 wild-type (open circles) and 3D7 DDD107498-resistant lines (eEF2-E134A/P754A) (filled circles) after incubation for 40 min with

DDD107498, cycloheximide or actinomycin D. Radiolabelled incorporation, measured as counts per minute, was normalized as the percentage of incorporation against inhibitor concentration (means ± s.d.; *n* = 3 independent experiments, each run in duplicate). **e**, The EC₅₀ values for transfectants against DDD107498 (means ± s.d.; *n* = 4–7 independent experiments, each run in duplicate). Statistical significance was determined by the Mann–Whitney *U*-test: **P* < 0.05; ***P* < 0.01. **f**, DDD107498-resistant line (eEF2-Y186N) transfected episomally with plasmids expressing either WT eEF2 or eEF2-Y186N (means ± s.d.; *n* = 3 independent experiments, each run in duplicate).

encodes *P. falciparum* translation elongation factor 2 (PfeEF2). Three lines had two single nucleotide polymorphisms in PfeEF2, with a mixture of wild-type (WT) and mutant reads at each position (Supplementary Data 2), suggesting that these lines were mixtures of two clones, each with independent mutations in PfeEF2. Single nucleotide polymorphisms were confirmed by Sanger sequencing and nine validated mutations in PfeEF2 clustered in three regions of the encoded protein. In two cases identical single nucleotide polymorphisms were identified in two independent lines, indicating mutations in functionally important residues that were acquired independently in separate selection experiments. The fact that resistance

to DDD107498 can be associated with multiple independent mutations is in keeping with observations from both artemisinin and other antimalarial compounds in development^{21–23}.

eEF2 is one of several essential elongation factors required in eukaryotic protein synthesis, by mediating GTP-dependent translocation of the ribosome along messenger RNA (mRNA) (Fig. 4a)²⁴. Yeast eEF2 is the target of the antifungal compound sordarin^{25,26}. Sordarin is selective for the *Saccharomyces cerevisiae* eEF2 over mammalian eEF2 *in vitro*, demonstrating that although protein synthesis in eukaryotes is conserved, it is possible to obtain selective inhibitors, despite the relatively high homology (67.2% identity) between the yeast and

human eEF2 (Extended Data Fig. 7)^{25,27}. In keeping with the potential for selectivity, DDD107498 is not toxic to mammalian cells (Extended Data Fig. 2c). The PfeEF2 mutations associated with resistance mapped to several areas on the surface of a homology model of the protein (on the basis of the structure of *S. cerevisiae* eEF2 with no ligands bound²⁸), with the mutations giving the highest degree of resistance clustering together (Fig. 4b). A DDD107498 binding pocket could not be elucidated through these modelling studies.

We confirmed that brief pre-incubation with DDD107498 specifically inhibited *P. falciparum* protein synthesis, by measuring short-term incorporation of [³⁵S]-labelled methionine and cysteine ([³⁵S]Met/Cys) in WT and DDD107498-resistant 3D7 *P. falciparum* parasites (Fig. 4d)²¹. Cycloheximide (a protein synthesis inhibitor) and DDD107498 both prevented [³⁵S]Met/Cys incorporation into WT *P. falciparum* 3D7, whereas actinomycin D (an inhibitor of RNA transcription) had minimal effect. Notably, DDD107498 was 100-fold less effective at inhibiting protein synthesis in DDD107498-resistant 3D7 than WT parasites, whereas cycloheximide prevented [³⁵S]Met/Cys incorporation equally in resistant and WT lines. DDD107498 and cycloheximide had minimal effects on DNA/RNA biosynthesis both in sensitive and in drug-resistant parasites (measured by incorporation of [³H]-labelled hypoxanthine), demonstrating specificity. In contrast, actinomycin D caused a marked dose-dependent reduction in [³H] incorporation.

To confirm that PfeEF2 is the target for DDD107498, we integrated transgenes expressing either WT PfeEF2 or resistance-associated alleles of PfeEF2 (Y186N, observed in mutant Dd2; and P754S, observed in mutant 3D7) using attPxattB integrase-mediated recombination^{21,29}. These transfectants also express endogenous PfeEF2. Imaging of green fluorescent protein (GFP)-fusions of PfeEF2 showed cytoplasmic localization (Fig. 4c), indicating that DDD107498 inhibits protein synthesis in the cytoplasm as opposed to the apicoplast³⁰, the site of action of tetracycline and azithromycin.

Dose-response assays with DDD107498 showed a similar inhibition profile between PfeEF2 transgene-expressing lines and the WT Dd2 strain, indicating that the endogenous WT PfeEF2 has a dominant effect in these experiments (Fig. 4e). This may be due to stable complex formation between the ribosome, WT PfeEF2 and DDD107498, resulting in ribosome stalling, which would explain why in mixed populations the WT PfeEF2 is dominant. For example in bacteria, fusidic acid binds to the complex between EF-G and the ribosome, preventing dissociation and blocking protein translation³¹.

To determine whether WT PfeEF2 was dominant in poisoning translation, we introduced episomal plasmids encoding WT or Y186N mutant PfeEF2 into the resistant PfeEF2 Y186N line (Fig. 4f). Plasmid-borne PfeEF2-Y186N had no effect on sensitivity to DDD107498 (EC₅₀ ≈ 3,100 nM), whereas WT PfeEF2 restored sensitivity (EC₅₀ = 2 nM). This demonstrated a dominant effect of WT PfeEF2 on parasite susceptibility and confirmed that PfeEF2 is the primary molecular target of the compound. We note that the shallow slope observed for the WT PfeEF2 transfected line is probably a result of heterogeneous episomal plasmid copy number seen with episomally transformed parasite lines²⁹. Structural studies will be required to define precisely how DDD107498 interacts with eEF2 and the ribosome.

Resistance has been reported for all clinical antimalarials, including artemisinins². While the correlation between the rate of resistance generation in laboratory and clinical settings for antimalarials is not fully understood, it is important to evaluate the risk of all new antimalarials both in preclinical and in clinical studies. In our studies, the minimum inoculum for generating resistance to DDD107498 is within acceptable limits³². Furthermore, selected resistant Dd2 lines revealed impaired growth rates in the absence of drug pressure compared with WT Dd2 (Extended Data Fig. 8); moreover the higher the resistance, the greater the fitness defect. Importantly genome sequences from 1,685 clinical isolates of *P. falciparum* from 17 countries^{23,33} reveal

a high degree of PfeEF2 sequence conservation in the field. The sole non-synonymous single nucleotide polymorphism (T16S) identified was unique to West Africa (allele frequency of 0.002) and is in a PfeEF2 domain distinct from mutations associated with *in vitro* resistance to DDD107498.

Conclusion

DDD107498 represents a promising prospect for development as an antimalarial agent, with a potent activity profile against multiple life-cycle stages (sub-10 nM), a novel mode of action and excellent drug-like properties. It has potential for single-dose treatment, which has major implications for ensuring patient compliance and practical deployment. Its complementary activity on the sexual stages of the parasite has potential to reduce transmission and its action on the liver stage suggests a possible role in chemoprotection. Chemoprotection and transmission-blocking properties are fundamental to the goal of eliminating and eradicating malaria, for which the high potency and long half-life of DDD107498 are well suited.

Owing to general concerns about the emergence of resistance, all antimalarials are developed as combination therapies, a strategy shown to improve efficacy and reduce the development of drug resistance. In terms of treatment of the erythrocytic stage, DDD107498 fulfils the criteria as a long-duration partner to complete the clearance of blood-stage parasites¹¹. Therefore, it should be combined with a fast-acting compound, ideally with a pharmacological duration of action as close to DDD107498 as possible. This would reduce the initial level of infection, with the prolonged activity of DDD107498 eliminating the remaining parasites¹¹.

Inhibition of protein synthesis by DDD107498 through PfeEF2, which is expressed in multiple life-cycle stages³⁴, provides mechanistic support for the observed broad-spectrum profile. This highlights PfeEF2 as a novel drug target in malaria, and implies that inhibition of protein synthesis is an effective intervention for achieving multi-stage activity in *Plasmodium*. DDD107498 has now been progressed into advanced non-clinical development, with the aim of entering into human clinical trials.

Received 10 October 2014; accepted 7 April 2015.

- World Health Organization. *World Malaria Report 2014* (World Health Organization, 2014).
- Ariey, F. *et al.* A molecular marker of artemisinin-resistant *Plasmodium falciparum* malaria. *Nature* **505**, 50–55 (2014).
- Alonso, P. L. *et al.* A research agenda for malaria eradication: drugs. *PLoS Med.* **8**, e1000402 (2011).
- Wells, T. N. C. & Gutteridge, W. E. in *Neglected Diseases and Drug Discovery* (eds Palmer, M. J. & Wells, T. N. C.) Ch. 1 1–32 (Royal Society of Chemistry, 2012).
- Brenk, R. *et al.* Lessons learnt from assembling screening libraries for drug discovery for neglected diseases. *ChemMedChem* **3**, 435–444 (2008).
- Delves, M. *et al.* The activities of current antimalarial drugs on the life cycle stages of *Plasmodium*: a comparative study with human and rodent parasites. *PLoS Med.* **9**, e1001169 (2012).
- Russell, B. *et al.* Determinants of *in vitro* drug susceptibility testing of *Plasmodium vivax*. *Antimicrob. Agents Chemother.* **52**, 1040–1045 (2008).
- Karyana, M. *et al.* Malaria morbidity in Papua Indonesia, an area with multidrug resistant *Plasmodium vivax* and *Plasmodium falciparum*. *Malar. J.* **7**, 148 (2008).
- Angulo-Barturen, I. *et al.* A murine model of falciparum-malaria by *in vivo* selection of competent strains in non-myelodepleted mice engrafted with human erythrocytes. *PLoS ONE* **3**, e2252 (2008).
- Sanz, L. M. *et al.* *P. falciparum* *in vitro* killing rates allow to discriminate between different antimalarial mode-of-action. *PLoS ONE* **7**, e30949 (2012).
- Burrows, J. N., van Huijsduijnen, R. H., Mohrle, J. J., Oeuvray, C. & Wells, T. N. Designing the next generation of medicines for malaria control and eradication. *Malar. J.* **12**, 187 (2013).
- Meister, S. *et al.* Imaging of *Plasmodium* liver stages to drive next-generation antimalarial drug discovery. *Science* **334**, 1372–1377 (2011).
- Adjalley, S. H. *et al.* Quantitative assessment of *Plasmodium falciparum* sexual development reveals potent transmission-blocking activity by methylene blue. *Proc. Natl Acad. Sci. USA* **108**, E1214–E1223 (2011).
- Bousema, T. & Drakeley, C. Epidemiology and infectivity of *Plasmodium falciparum* and *Plasmodium vivax* gametocytes in relation to malaria control and elimination. *Clin. Microbiol. Rev.* **24**, 377–410 (2011).
- Delves, M. J. *et al.* Male and female *Plasmodium falciparum* mature gametocytes show different responses to antimalarial drugs. *Antimicrob. Agents Chemother.* **57**, 3268–3274 (2013).

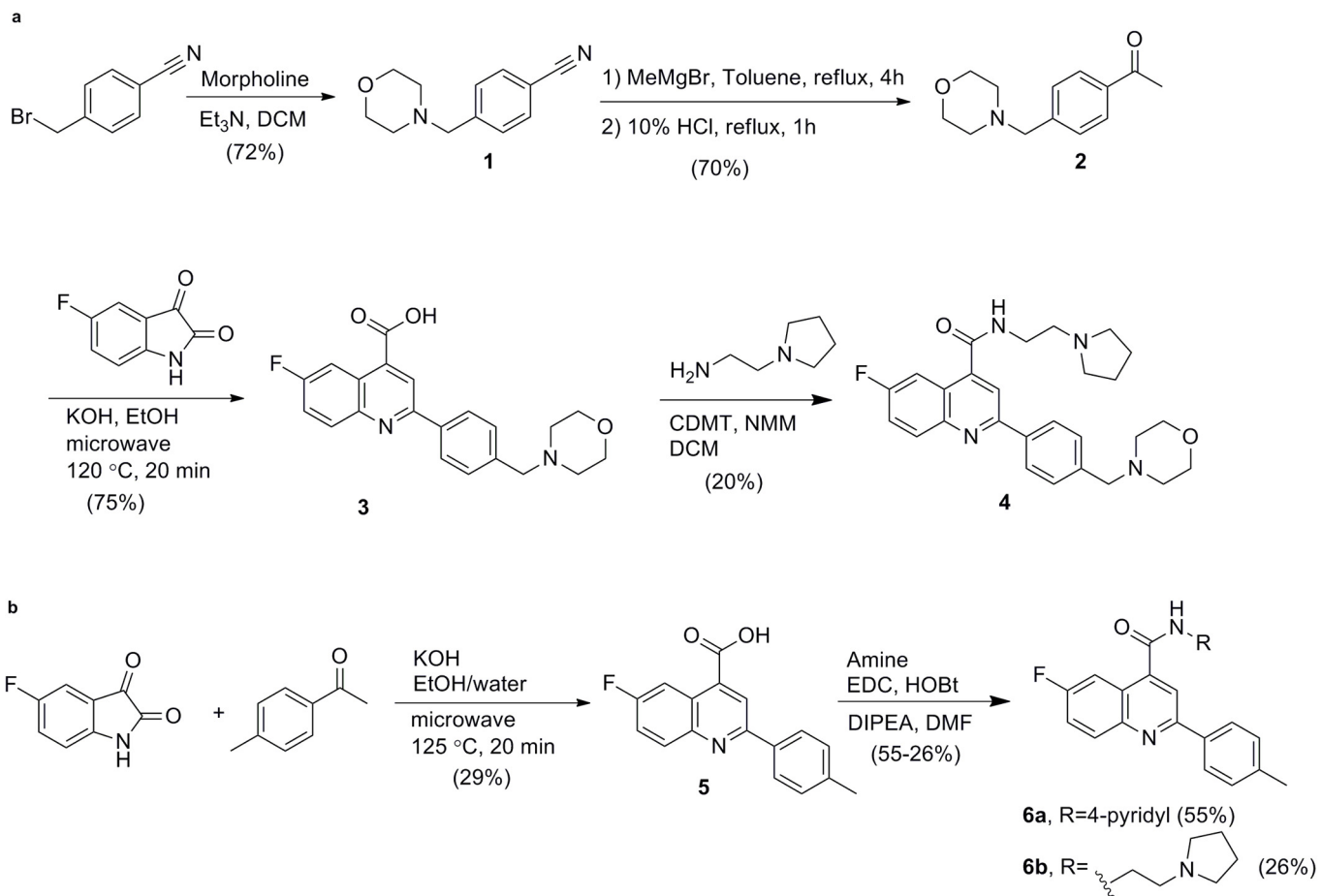
16. Delves, M. J. *et al.* A high-throughput assay for the identification of malarial transmission-blocking drugs and vaccines. *Int. J. Parasitol.* **42**, 999–1006 (2012).
17. Blagborough, A. M. *et al.* Transmission-blocking interventions eliminate malaria from laboratory populations. *Nature Commun.* **4**, 1812 (2013).
18. Upton, L. M. *et al.* Lead clinical and preclinical antimalarial drugs can significantly reduce sporozoite transmission to vertebrate populations. *Antimicrob. Agents Chemother.* **59**, 490–497 (2015).
19. Janse, C. J. *et al.* High efficiency transfection of *Plasmodium berghei* facilitates novel selection procedures. *Mol. Biochem. Parasitol.* **145**, 60–70 (2006).
20. Flannery, E. L., Fidock, D. A. & Winzeler, E. A. Using genetic methods to define the targets of compounds with antimalarial activity. *J. Med. Chem.* **56**, 7761–7771 (2013).
21. Rottman, M. *et al.* Spiroindolones, a potent compound class for the treatment of malaria. *Science* **329**, 1175–1180 (2010).
22. McNamara, C. W. *et al.* Targeting *Plasmodium* PI(4)K to eliminate malaria. *Nature* **504**, 248–253 (2013).
23. Miotto, O. *et al.* Multiple populations of artemisinin-resistant *Plasmodium falciparum* in Cambodia. *Nature Genet.* **45**, 648–655 (2013).
24. Jorgensen, R., Merrill, A. R. & Andersen, G. R. The life and death of translation elongation factor 2. *Biochem. Soc. Trans.* **34**, 1–6 (2006).
25. Justice, M. C. *et al.* Elongation factor 2 as a novel target for selective inhibition of fungal protein synthesis. *J. Biol. Chem.* **273**, 3148–3151 (1998).
26. Capa, L., Mendoza, A., Lavandera, J. L., de las Heras, F. G. & Garcia-Bustos, J. F. Translation elongation factor 2 is part of the target for a new family of antifungals. *Antimicrob. Agents Chemother.* **42**, 2694–2699 (1998).
27. Shastri, M. *et al.* Species-specific inhibition of fungal protein synthesis by sordarin: identification of a sordarin-specificity region in eukaryotic elongation factor 2. *Microbiology* **147**, 383–390 (2001).
28. Jorgensen, R. *et al.* Two crystal structures demonstrate large conformational changes in the eukaryotic ribosomal translocase. *Nature Struct. Biol.* **10**, 379–385 (2003).
29. Nkrumah, L. J. *et al.* Efficient site-specific integration in *Plasmodium falciparum* chromosomes mediated by mycobacteriophage Bxb1 integrase. *Nature Methods* **3**, 615–621 (2006).
30. Biswas, S. *et al.* Interaction of apicoplast-encoded elongation factor (EF) EF-Tu with nuclear-encoded EF-Ts mediates translation in the *Plasmodium falciparum* plastid. *Int. J. Parasitol.* **41**, 417–427 (2011).
31. Cox, G. *et al.* Ribosome clearance by FusB-type proteins mediates resistance to the antibiotic fusidic acid. *Proc. Natl Acad. Sci. USA* **109**, 2102–2107 (2012).
32. Ding, X. C., Ubben, D. & Wells, T. N. A framework for assessing the risk of resistance for anti-malarials in development. *Malar. J.* **11**, 292 (2012).
33. Manske, M. *et al.* Analysis of *Plasmodium falciparum* diversity in natural infections by deep sequencing. *Nature* **487**, 375–379 (2012).
34. Florens, L. *et al.* A proteomic view of the *Plasmodium falciparum* life cycle. *Nature* **419**, 520–526 (2002).
35. Jiménez-Díaz, M. B. *et al.* Quantitative measurement of *Plasmodium*-infected erythrocytes in murine models of malaria by flow cytometry using bidimensional assessment of SYTO-16 fluorescence. *Cytometry A* **75**, 225–235 (2009).
36. Charman, S. A. *et al.* Synthetic ozonide drug candidate OZ439 offers new hope for a single-dose cure of uncomplicated malaria. *Proc. Natl Acad. Sci. USA* **108**, 4400–4405 (2011).

Supplementary Information is available in the online version of the paper.

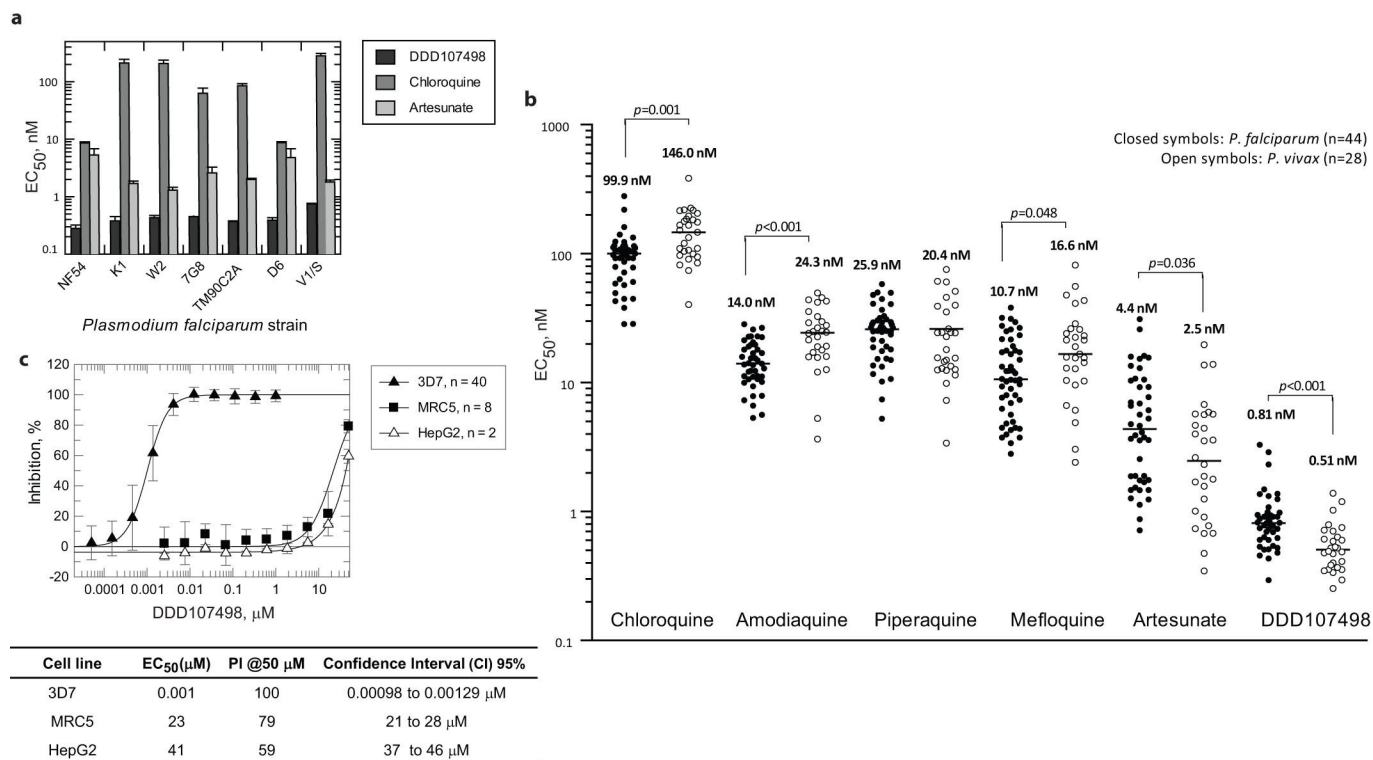
Acknowledgements This work was supported by grants from Medicines for Malaria Venture, the Wellcome Trust (100476 (I.H.G., A.H.F.), 091625 (R.N.P.) and 098051 (J.C.R., W.P., T.D.O.)), the Bill and Melinda Gates Foundation (OPP1043501 (M.D., R.S.)), the National Institutes of Health (R01 AI103058 to E.A.W. and D.A.F.) and the European Union (EVI-Malaria (T.D.O.)). Drug Discovery Unit infrastructure was supported by the European Regional Development Fund 2007–2013 and UK Research Partnership Investment Fund awards to M. Ferguson, whom we also thank for continued support. We thank C. Sibley for discussions. We acknowledge the East Scotland Blood Transfusion Service, Ninewells Hospital, Dundee, for erythrocyte supply to Dundee. We thank L. D. Shultz and The Jackson Laboratory for providing access to non-obese diabetic SCID IL2R γ null mice through their collaboration with the GlaxoSmithKline Tres Cantos Medicines Development Campus. The following are acknowledged for technical assistance: all members of the Drug Discovery Unit (Dundee), M. Berriman, J. Kamber, E. Kenangalem, A. LaCrue, O. Montagnat, J. Rini Poespoprodjo, M. Sanders, S. Sax, C. Scheurer, L. Trianty, M. Tunnicliffe (detailed in Supplementary Information).

Author Contributions The author contributions are detailed in the Supplementary Information.

Author Information Reprints and permissions information is available at www.nature.com/reprints. The authors declare competing financial interests: details are available in the online version of the paper. Readers are welcome to comment on the online version of the paper. Correspondence and requests for materials should be addressed to I.H.G. (i.h.gilbert@dundee.ac.uk) or K.D.R. (k.read@dundee.ac.uk).

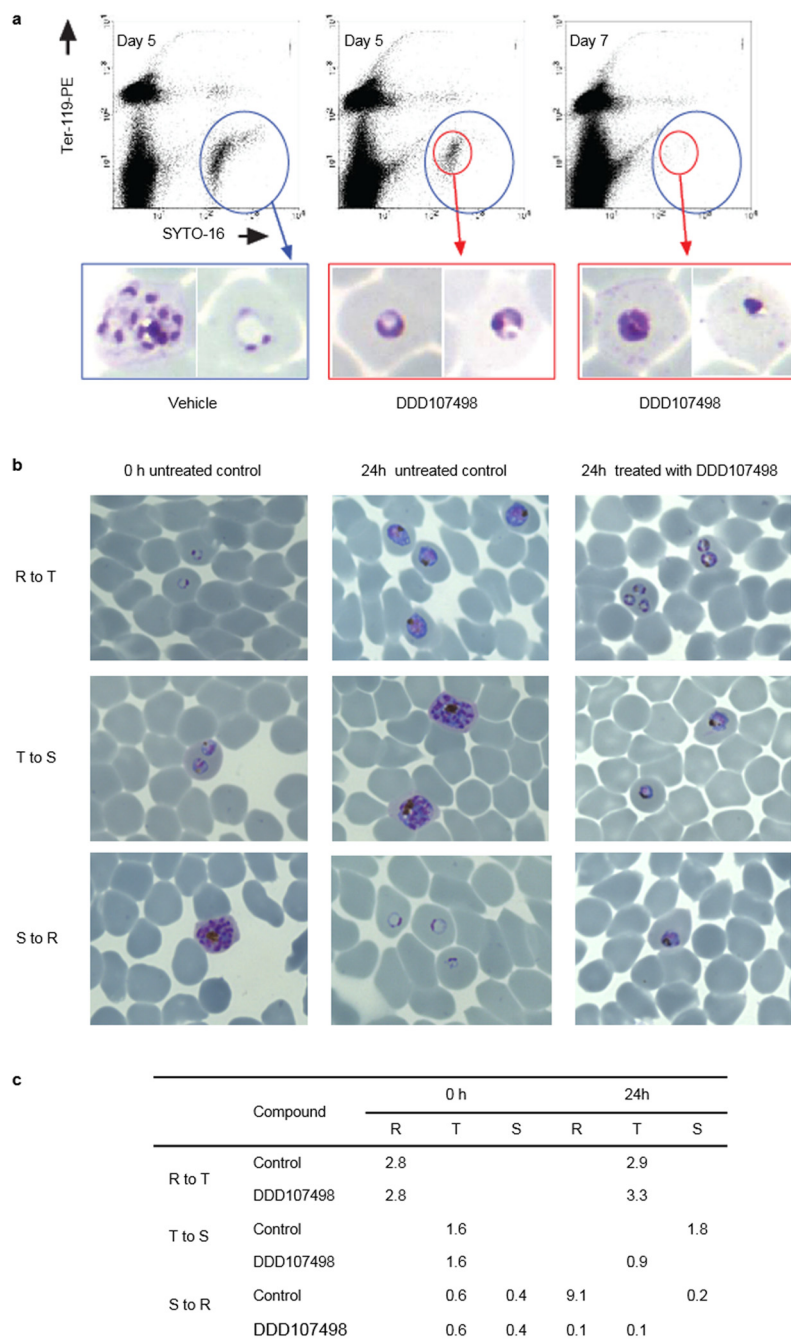


Extended Data Figure 1 | Synthetic methodology. **a**, Synthesis of DDD107498 (4). **b**, Synthesis of DDD102542 (6a) and DDD103679 (6b).



Extended Data Figure 2 | In vitro activity. **a**, *In vitro* activity against a panel of resistant and sensitive strains of *P. falciparum*. CQ, chloroquine; PYR, pyrimethamine; CYC, cycloguanil; QUI, quinine; SUL, sulfadoxine; MFQ, mefloquine. Resistance as follows: K1 (CQ, SUL, PYR, CYC); W2 (CQ, SUL, PYR, CYC); 7G8 (CQ, PYR, CYC); TM90C2A (CQ, PYR, MFQ, CYC); D6 (MFQ); V1/S (CQ, SUL, PYR, CYC). Data are the means \pm s.d. of $n = 3$

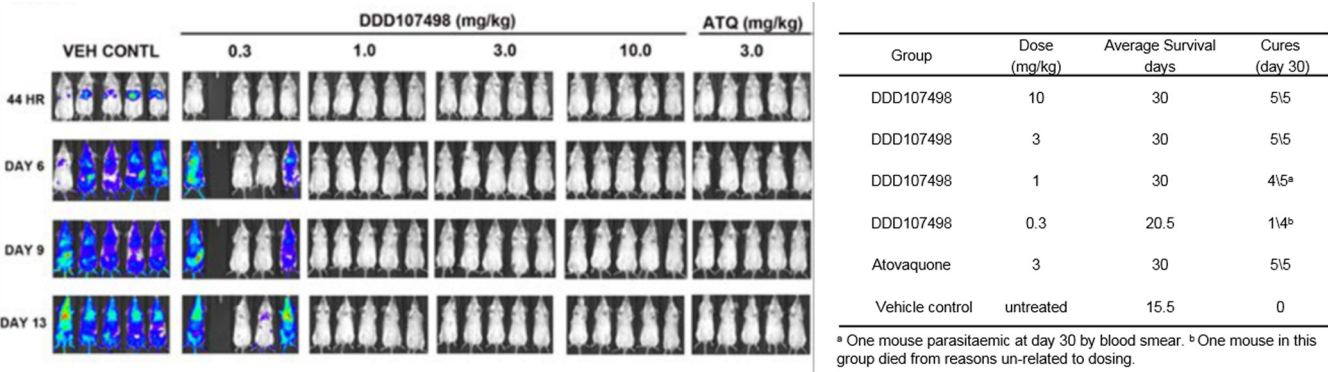
independent [^3H]hypoxanthine incorporation experiments (each run in duplicate). **b**, *Ex vivo* activity against *P. falciparum* and *P. vivax* clinical isolates from Papua (Indonesia). The lines on the scatter plots represent the median value for each drug. **c**, Effect of DDD107498 on *P. falciparum* 3D7, HepG2 and MRC5 cells. Data are the means \pm s.d. of n reported independent experiments.



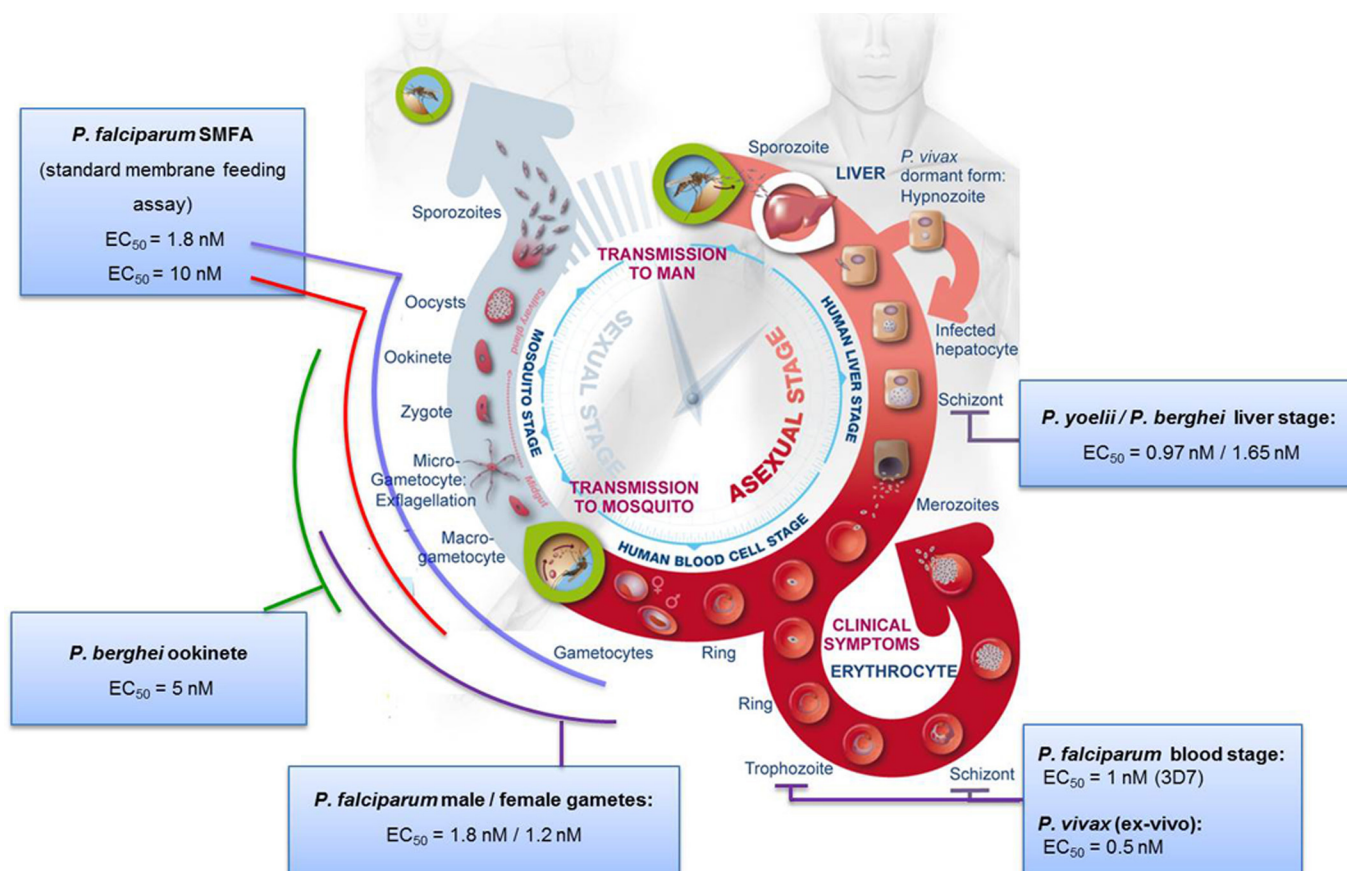
Extended Data Figure 3 | Effect of DDD107498 on parasite morphology.

a, Phenotype of *P. falciparum* in peripheral blood of NOD-*scid* IL-2R^{-null} mice engrafted with human erythrocytes. Blood samples were taken at days 5 and 7 of the assay (one and two asexual cycles, respectively) after the start of treatment with vehicle or DDD107498 at day 3. The bi-dimensional flow cytometry plots measure the murine (Ter-119-PE⁺) and human (Ter-119-PE⁻) erythrocytes, and the presence of nucleic acids (infected SYTO-16⁺ events). The blue circles indicate the region of infected erythrocytes. Vehicle-treated mice showed a characteristic pattern of staining with SYTO-16 (ref. 35), which correlated with the presence of healthy rings, trophozoites and schizonts in blood smears. Conversely, mice treated with DDD107498 at 50 mg per kg showed only trophozoites with condensed cytoplasm and some pyknotic cells at day 5 (red circle in flow cytometry plot and corresponding blood smears). By day 7, few infected erythrocytes were detected by flow cytometry and blood smears revealed parasites with a similar morphology to those at day 5. This suggests that trophozoites are the most sensitive population since the cycle is interrupted

at this stage. The images displayed are taken from a mouse with high levels of parasitaemia. At least 50 parasites were counted per sample screened in the microscope. Of these, four photographs of representative parasite phenotypes were selected to represent the morphology of the most prevalent phenotype. Thus, this is a qualitative assessment. **b**, Stage specificity assays using synchronized cultures. For morphological analysis of antimalarial drug action, thin blood smears were prepared, fixed and stained with Giemsa followed by examination with an upright microscope using an oil-immersion lens ($\times 100$). For parasitaemia determination, a total number of 1,000 red blood cells (corresponding to five microscopic fields) were counted. R to T, abnormal trophozoites observed after exposure for 24 h of synchronized rings to DDD107498. T to S, trophozoites do not develop into schizonts after exposure for 24 h to DDD107498. S to R, no ring stages are observed 24 h after treatment of schizonts with DDD107498. **c**, Percentage parasitaemia in the red blood cells. R, ring stage; T, trophozoite; S, schizont.



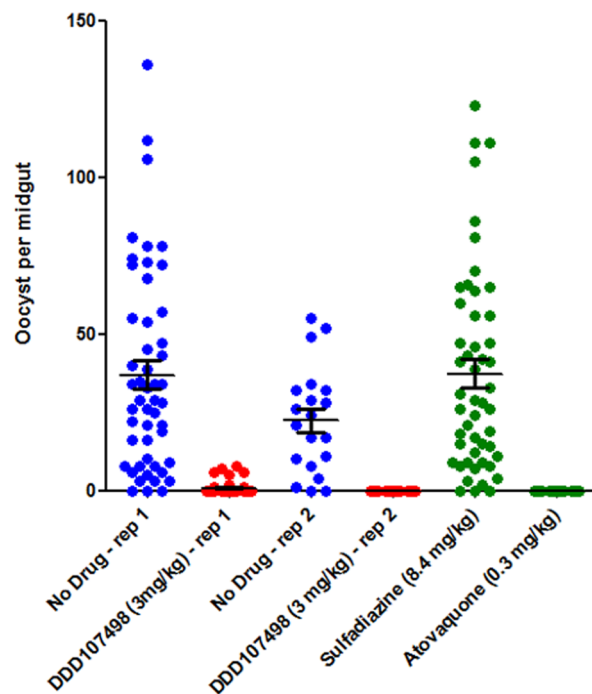
Extended Data Figure 4 | Prophylactic activity of DDD107498 against sporozoite challenge. *P. berghei* (luciferase) sporozoite *in vivo* mouse model of chemoprotection. A dose of 3 mg per kg was fully protective. Data are the mean of $n = 5$ experiments.



Extended Data Figure 5 | DDD107498 *in vitro* activity on the different life-cycle stages of *Plasmodium* spp. For comparator data with known antimalarials, see figure 5 in ref. 6. DDD107498 also showed potent activity *in*

vitro against *P. berghei* ookinetes¹⁶ (5.0 nM (95% CI 4.4–5.7 nM)), confirming that if DDD107498 was taken up during a blood meal, it could continue to kill parasites within the mosquito.

a



Intensity:	36.9	0.78	22.5	0	37.3	0
Prevalence:	94%	22%	90%	0%	94%	0%

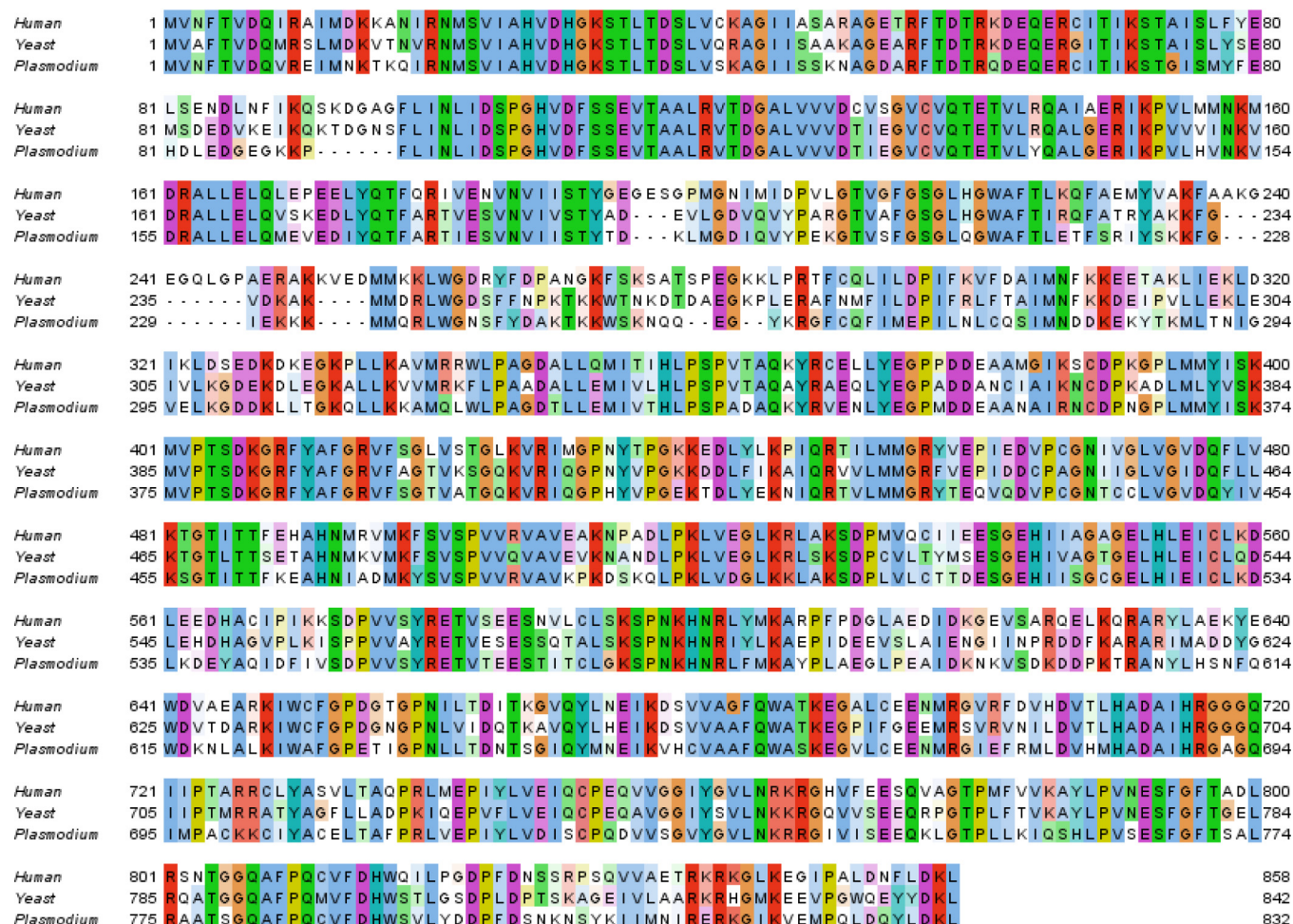
b

Effect on transmission to the mosquito host			
TB effect- oocyst intensity (%) (95% CIs)	TB effect- oocyst prevalence (%) (95% CIs)	TB effect- sporozoite intensity (%) (95% CIs)	TB effect- sporozoite prevalence (%) (95% CIs)
98.8% (98.1-99.3)	90.7% (72.9-97.2)	93.8% (88.7-96.6)	88.6% (78.3-94.2)
Effect on subsequent transmission to the vertebrate host			
Inhibition in infection of naïve mice (%) (95% CIs)	Inhibition of parasitemia in infected mice (day 10 post-bite)		Effect size (95% CI)
89.5% (71.4-100)	22.6%		90.5% (78.3-94.2)

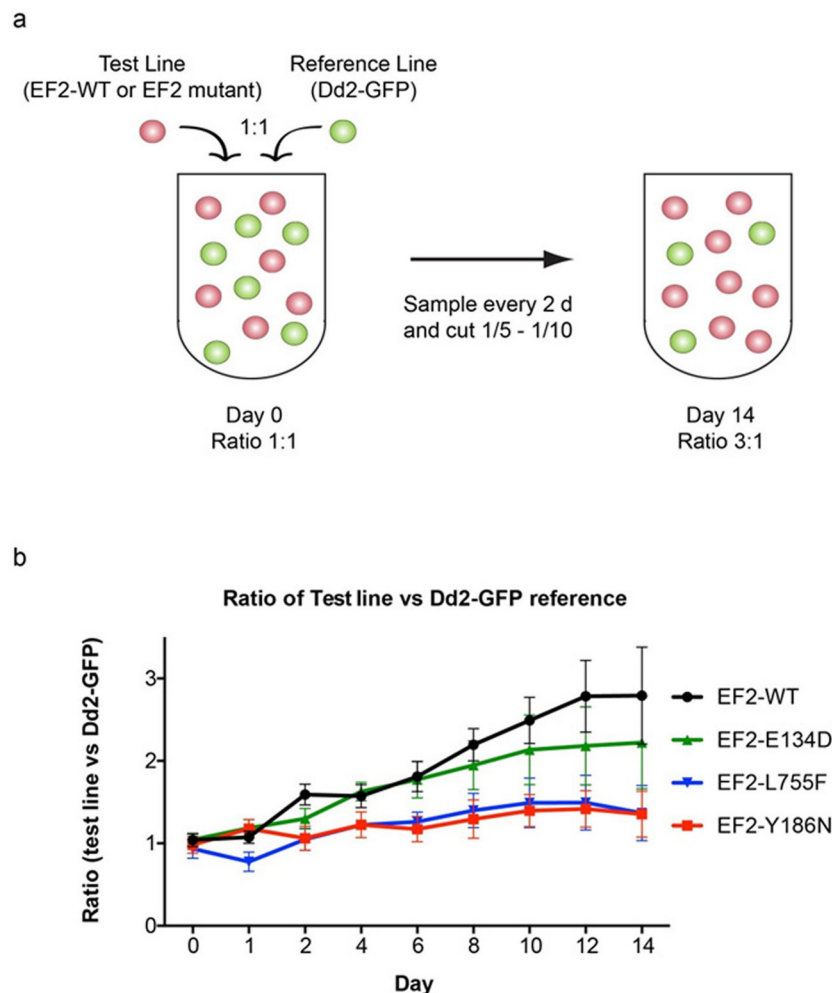
Extended Data Figure 6 | *In vivo P. berghei* mouse-to-mouse assay.

a, Impact of DDD107498 treatment on *in vivo* mosquito infection. Mice infected with *P. berghei* (PbGFPCON507 clone 1)¹⁹ were dosed orally with DDD107489 at 3 mg per kg, atovaquone at 0.3 mg per kg, sulphadiazine at 8.4 mg per kg, or were not drug treated (negative control). After 24 h, populations of treated mice ($n = 5$) were exposed to 500 female *Anopheles stephensi* mosquitoes, and oocyst intensity and infection prevalence in the mosquito midgut was measured 10 days after feeding. Individual data points represent the number of oocysts found in individual mosquitoes. Two replicates were performed. Sulphadiazine (8.4 mg per kg, intraperitoneally) and atovaquone (0.3 mg per kg, intraperitoneally) were used as negative and positive transmission-blocking drug controls, respectively. Horizontal bars represent mean intensity of infection, and error bars s.e.m., within individual mosquito populations. **b**, Impact of treatment with DDD107498 over a complete transmission cycle *in vivo*. After drug treatment of infected mice and mosquito

feeds, surviving potentially infectious mosquitoes were allowed to blood-feed on naïve mice at a range of transmission settings (biting rates of 2, 5 and 10 bites per naïve mouse) to assess the ability of drug treatment to reduce the number of new malarial cases after mosquito bite. Efficacy is expressed as the following: (1) impact on the mosquito population—expressed as reduction in both oocyst and sporozoite intensity and prevalence; (2) impact on subsequent transmission to new naïve vertebrate hosts—expressed as reduction in infection of naïve mice (reduction in number of new malarial cases after mosquito bite) and inhibition of subsequent parasitaemia (day 10 after bite) in mice that do become infected; (3) effect size generated—by fitting the data achieved within this assay to a chain-binomial model we could assess the ability of DDD107498 to reduce R_0 (assuming 100% coverage). If R_0 is reduced to <1 , transmission is unsustainable and elimination will occur. Values of 95% CIs are shown in brackets. Efficacy is calculated in comparison with no-drug controls. TB, transmission blocking.



Extended Data Figure 7 | ClustalWS alignment of eEF2 sequences from human, yeast and *Plasmodium* (*P. falciparum*). Alignment made using Jalview ClustalX default colouring.



Extended Data Figure 8 | Fitness phenotypes of DDD107498-resistant parasite lines. Unmarked Dd2- and DDD107498-selected parasites with various levels of resistance were assessed for growth in a competition assay, relative to a Dd2-GFP reference line. **a**, Equal numbers of unmarked test lines were mixed with the Dd2-GFP reference, in triplicate wells, and the ratio of non-fluorescent and fluorescent cells assessed by flow cytometry over time. At day 0, all lines had a 1:1 ratio with the Dd2-GFP reference. Increased growth of the test line over the Dd2-GFP reference, which has a slower growth rate than unmarked WT Dd2, would result in an increased ratio of test:Dd2-GFP.

b, Growth assay of four different test lines: (1) WT Dd2, (2) EF2-E134D, (3) EF2-L755F and (4) EF2-Y186N, relative to Dd2-GFP. A faster growth rate of WT Dd2 (DDD107498 IC_{50} 0.14 nM) relative to the fluorescent Dd2-GFP line is reflected in an increased ratio over time. The low-level resistant line EF2-E134D (IC_{50} 5.8 nM) did not attain a WT growth rate, and the high-level resistant lines EF2-L755F (IC_{50} 660 nM) and EF2-Y186N (3,100 nM) were further impaired. Means \pm s.d.; $n = 4$ independent experiments, each run in triplicate.

Extended Data Table 1 | Pharmacokinetics and rodent efficacy of DDD107498

a						
	Mouse		Rat		Dog	
Intravenous	1 mg/kg		1 mg/kg		1 mg/kg	
Cl (ml/min/g)	12		18		30	
V _{dss} (L/kg)	15		15		30	
T _½ (h)	16		10		13	
Oral	3 mg/kg		5 mg/kg		3 mg/kg	
C _{max} (ng/ml)	90		180		27	
T _{max} (h)	1		4		4	
T _½ (h)	19		18		20	
F%	74		84		46	

b						
Compound	30 mg/kg		10 mg/kg		3 mg/kg	
	Activity %	Survival days	Activity %	Survival days	Activity %	Survival days
Chloroquine [§]	99.9	10	99.5	7	83	7
Mefloquine [§]	99.6	22	95	16	<40	7
Artemether	98	7	89	6	59	6
Dihydroartemisinin	99	7	97	6	61	7
Artesunate [§]	92	9	75	6	<40	6
DDD107498	99.1	23	99.0	14	99	9

a. *In vivo* pharmacokinetic parameters in preclinical species ($n = 3$, all species). **b.** Oral *in vivo* single-dose efficacy of antimalarial drugs and DDD107498 in the murine *P. berghei* model. Data are the means of $n = 3$ for DDD107498 and $n \geq 5$ for the reference compounds. [§]Data from ref. 36.

Extended Data Table 2 | Summary of resistance selection experiments with DDD107498

Strain	Pressure (nM)	Pressure (x IC ₉₀)	Inoculum *						MIR	EC ₅₀ shift (inoculum) [†]
			Number of positive cultures (day of recrudescence)							
			10 ⁴	10 ⁵	10 ⁶	10 ⁷	10 ⁸	10 ⁹		
Dd2	1.25	2.7	ND	ND	2 (13, 41)	3 (13, 13, 15)	3 (13, 13, 16)	3 (29/29/29)	ND	2315 (10 ⁹) 7 (10 ⁸) 4810 (10 ⁸)
Dd2	1.25	2.7	0	0	0	3 (20, 22, 22)	ND	ND	10 ⁷	13 (10 ⁷)
Dd2	1.25	2.7	ND	0	1 (39)	ND	ND	ND	10 ⁶	5567 (10 ⁸)
7G8	1.25	3.1	ND	ND	0	3 (25, 25, 47)	1 (25)	3 (15, 15, 15)	10 ⁷	70 (10 ⁹) 60 (10 ⁸) 82 (10 ⁷)
3D7	1.5	3.3	ND	ND	0	2 (38, 38)	2 (28, 28)	3 (20, 20, 20)	10 ⁷	19 (10 ⁹) 99 (10 ⁸) 14(10 ⁷)

* Number of positive cultures (n = 3) and day of recrudescence for each inoculum. [†]EC₅₀ fold change was determined on bulk cultures. MIR, minimum inoculum of resistance.

The mass of the Mars-sized exoplanet Kepler-138 b from transit timing

Daniel Jontof-Hutter^{1,2}, Jason F. Rowe^{2,3}, Jack J. Lissauer², Daniel C. Fabrycky⁴ & Eric B. Ford¹

Extrasolar planets that pass in front of their host star (transit) cause a temporary decrease in the apparent brightness of the star, providing a direct measure of the planet's size and orbital period. In some systems with multiple transiting planets, the times of the transits are measurably affected by the gravitational interactions between neighbouring planets^{1,2}. In favourable cases, the departures from Keplerian orbits (that is, unaffected by gravitational effects) implied by the observed transit times permit the planetary masses to be measured, which is key to determining their bulk densities³. Characterizing rocky planets is particularly difficult, because they are generally smaller and less massive than gaseous planets. Therefore, few exoplanets near the size of Earth have had their masses measured. Here we report the sizes and masses of three planets orbiting Kepler-138, a star much fainter and cooler than the Sun. We determine that the mass of the Mars-sized inner planet, Kepler-138 b, is $0.066^{+0.059}_{-0.037}$ Earth masses. Its density is $2.6^{+2.4}_{-1.5}$ grams per cubic centimetre. The middle and outer planets are both slightly larger than Earth. The middle planet's density ($6.2^{+5.8}_{-3.4}$ grams per cubic centimetre) is similar to that of Earth, and the outer planet is less than half as dense at $2.1^{+2.2}_{-1.2}$ grams per cubic centimetre, implying that it contains a greater portion of low-density components such as water and hydrogen.

NASA's Kepler mission has discovered thousands of candidate transiting exoplanets, with a wide range of planetary sizes^{4–6}. A small fraction of these planets have had their masses characterized, either by radial-velocity spectroscopy or by transit timing. The latter probes the gravitational perturbations between planets in multi-planet systems by precisely measuring transit times and fitting dynamical models to the observed transit timing variations (TTV)^{1,2}. Both radial velocity and TTV signals are larger for more massive planets and improve with greater planetary masses, although the two techniques sample different populations of exoplanets. The radial-velocity technique measures the motion of a host star induced by its planet's gravity, and hence the signal declines with increasing orbital distance.

The majority of mass measurements of planets discovered in the Kepler data set have been the results of radial velocity observations. For Kepler-discovered planets characterized as rocky by this method, the orbital periods are all less than a few days. Of the radial-velocity detections, Kepler-78 b has the lowest mass ($1.7M_{\oplus}$, where M_{\oplus} is the Earth's mass), and the shortest orbital period (0.35 days)^{7,8}.

Characterizing planets by transit timing is quite complementary to using radial velocity because transit timing is very sensitive to perturbations between planets that are closely spaced or near orbital resonances^{3,9}. We note that most systems with detected TTVs are not in resonance, but rather are near enough to resonance for the perturbations to be coherent for many orbital periods, while also far enough from resonance that the planetary conjunctions cycle around the orbit plane within the four-year Kepler baseline. For near-resonant pairs, the TTVs of neighbouring planets frequently take the form of anti-correlated sinusoids over many orbits^{10–14} or the sum of sinusoids where a planet is perturbed by two neighbours¹⁵. The majority of TTV detections have been found near first-order mean-motion resonances, such that planet pairs have an orbital period ratio near to $j:j-1$, where j is an integer. Near first-order resonances generally cause stronger TTV signals than second-order resonances, although much depends on how close the planet pairs are to resonance and how eccentric (non-circular) their orbits are, as well as the masses of the planets. Eccentricity causes the orbital speed to vary during the orbit, and the distance between the planets at conjunction to vary with the position of the conjunction.

The bulk of planets with mass characterizations from the Kepler sample using TTVs so far have orbital periods ranging from about 10 days to 100 days. These generally have low density^{15–18} and probably possess deep atmospheres, with the exception of the rocky planet Kepler-36 b¹⁹.

Kepler-138 (formerly known as KOI-314) hosts three validated transiting planets²⁰. The orbital periods of Kepler-138's three planets are given in Table 1. Kepler-138 c and Kepler-138 d orbit near a

Table 1 | Stellar and planetary parameters for the Kepler-138 system

Adopted stellar parameters					
Stellar mass, M_{\star} (0.521 ± 0.055) M_{\odot}	Stellar radius, R_{\star} (0.442 ± 0.024) R_{\odot}	Effective temperature, T_{eff} 3,841 \pm 49 K	Stellar density, ρ_{\star} 9.5 \pm 2.2 g cm ⁻³	Metallicity, [Fe/H] -0.280 \pm 0.099	log[g (cm s ⁻²)] 4.886 \pm 0.055
Dynamical modelling parameters					
Planet	Period (days)	T_0 (BJD - 2,454,900)	$e \cos \omega$	$e \sin \omega$	$(M_b/M_{\oplus}) \times (M_{\odot}/M_{\star})$
b	10.3126 ^{+0.0004} _{-0.0006}	788.4142 ^{+0.0027} _{-0.0027}	-0.011 ^{+0.096} _{-0.140}	-0.024 ^{+0.075} _{-0.135}	0.13 ^{+0.12} _{-0.08}
c	13.7813 ^{+0.0001} _{-0.0001}	786.1289 ^{+0.0005} _{-0.0005}	-0.015 ^{+0.086} _{-0.126}	-0.020 ^{+0.064} _{-0.117}	3.85 ^{+3.77} _{-2.30}
d	23.0881 ^{+0.0009} _{-0.0008}	796.6689 ^{+0.0013} _{-0.0013}	-0.037 ^{+0.060} _{-0.092}	-0.057 ^{+0.674} _{-0.387}	1.28 ^{+1.36} _{-0.78}
Adopted physical characteristics					
Planet	R_p/R_{\star}	$M_p (M_{\oplus})$	$R_p (R_{\oplus})$	Density (g cm ⁻³)	Incident flux relative to Earth
b	0.0108 ^{+0.0003} _{-0.0003}	0.066 ^{+0.059} _{-0.037}	0.522 ^{+0.032} _{-0.032}	2.6 ^{+2.4} _{-1.5}	6.81 ^{+0.84} _{-0.84}
c	0.0247 ^{+0.0005} _{-0.0005}	1.970 ^{+1.912} _{-1.120}	1.197 ^{+0.070} _{-0.070}	6.2 ^{+5.8} _{-3.4}	4.63 ^{+0.57} _{-0.57}
d	0.0251 ^{+0.0007} _{-0.0007}	0.640 ^{+0.674} _{-0.387}	1.212 ^{+0.075} _{-0.075}	2.1 ^{+2.2} _{-1.2}	2.32 ^{+0.29} _{-0.29}

¹Department of Astronomy, Pennsylvania State University, Davey Laboratory, University Park, Pennsylvania 16802, USA. ²NASA Ames Research Center, Moffett Field, California 94035, USA. ³SETI Institute, 189 North Bernardo Avenue, Mountain View, California 94043, USA. ⁴Department of Astronomy and Astrophysics, University of Chicago, 5640 South Ellis Avenue, Chicago, Illinois 60637, USA.

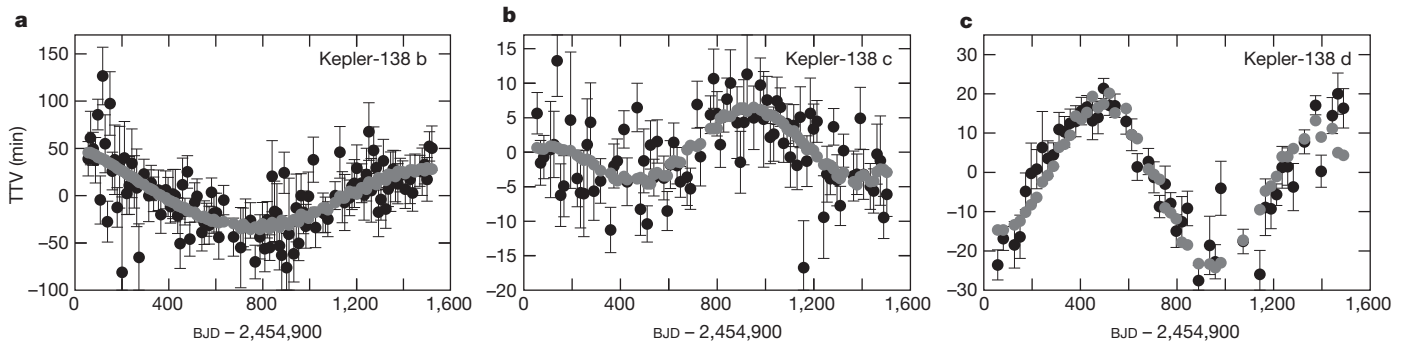


Figure 1 | Transit timing variations of the three planets orbiting Kepler-138. In black are the differences between measured transit times and a calculated linear fit to the transit times, with 1σ uncertainties shown as error bars. Grey points mark the difference between the simulated transit times based on the best-fit dynamical model and a linear fit to the transit times. **a**, TTV of Kepler-138 b; **b**, TTV of Kepler-138 c; **c**, TTV of Kepler-138 d.

second-order mean-motion resonance (5:3), while Kepler-138 b and Kepler-138 c orbit near the 4:3 first-order resonance.

Using transit times up to the fourteenth quarter of the Kepler mission, two of the three known planets orbiting Kepler-138²⁰ have been confirmed and characterized with TTVs²¹. The derived parameters in that work suggested that the outer planet, Kepler-138 d, has a density so low that it must have a substantial hydrogen/helium gaseous envelope²¹.

Using the complete Kepler data set for Kepler-138, we have detected TTVs for all three planets (see Fig. 1). We describe our procedure for measuring transit times in the Methods, and list our transit time measurements in Extended Data Table 1. TTVs are expressed as the difference between the observed transit times and the calculated linear fit to the transit times. Modelling Kepler-138 as a three-planet system, we measure the masses of all three planets, the super-Earth-sized Kepler-138 c and Kepler-138 d, as well as Kepler-138 b, which at $0.52R_{\oplus}$ is roughly the size of Mars.

We performed dynamical fits by calculating the orbits of the three planets around the star. We modelled the orbits as being co-planar, given that all three planets are transiting, that Kepler's multi-planet systems are known to have small mutual inclinations, and that we demonstrate that allowing mutual inclinations has little effect on our results for the planet masses (see Extended Data Fig. 7c).

Our model parameters for each planet are the orbital period P , the time T_0 of the first transit after our chosen epoch, the components of the eccentricity vector ($e\cos\omega$ and $e\sin\omega$, where ω is the angle between the sky plane and the orbital pericentre of the planet), and M_p/M_{\star} , the mass of the planet relative to the host star, which we express as $(M_p/M_{\oplus})(M_{\odot}/M_{\star})$ throughout, where M_{\odot} is the mass of the Sun. We perform Bayesian parameter estimation for these 15 model parameters using differential evolution Markov Chain Monte Carlo analysis. We report the properties of the star and planets in Table 1, and details of the parameter estimation algorithm, priors and statistical models in the Methods.

We measure the mass of Kepler-138 b to be $0.066^{+0.059}_{-0.037}M_{\oplus}$, where uncertainties denote the 68.3% confidence limits. The 95.4% interval spans $0.011M_{\oplus}$ to $0.170M_{\oplus}$. The robustness of this result against outlying transit times and mutual inclinations is demonstrated in the Methods.

The posterior probability for the inner planet having non-zero mass is between 99.82% and 99.91% (depending on the choice of prior for eccentricity e), that is, equivalent to a 3σ detection. This calculation is based on the Savage–Dickey density ratio for calculating the Bayes factor, which fully accounts for posterior width and shape, including asymmetries and non-Gaussianity, as described in Methods.

Kepler-138 b is by far the smallest exoplanet, both by radius and mass, to have a density measurement (see Fig. 2). Thus it opens up a new regime to physical study. It is likely to become the prototype for a class of small close-in planets that could be common. The prospect of

further constraints on this planet are excellent, because NASA's Transiting Exoplanet Survey Satellite should be able to measure transit times for the two largest planets, improving constraints on the dynamical model for all three planets. The European Space Agency's Plato mission will continue this process and ground-based measurements may also be possible. These future observations, plus more accurate stellar classification using the distance to the star measured by the European Space Agency's Gaia mission, will further improve the characterization of this system, especially the inner planet.

Our measurements of the mass and density of the small inner planet Kepler-138 b are consistent with various compositions and formation locations. If future observations imply that the planet is less dense than rock, then the only physically and cosmogonically plausible low-density constituents are water and other astrophysical ices, which could only have condensed far from the star. That would be the first definitive evidence for substantial inward orbital migration of a small planet.

For the two outer planets, Kepler-138 c and Kepler-138 d, we find a lower mass ratio between these two planets than does previous work²¹. This is not surprising, since Kepler-138 b's perturbations explain part of the TTVs observed in Kepler-138 c, which were previously attributed solely to perturbations by Kepler-138 d. Nevertheless, the mass ratios between each of these planets and their host star remains consistent with published results²¹. We find higher densities for both of these planets than does previous work, owing to our improved stellar

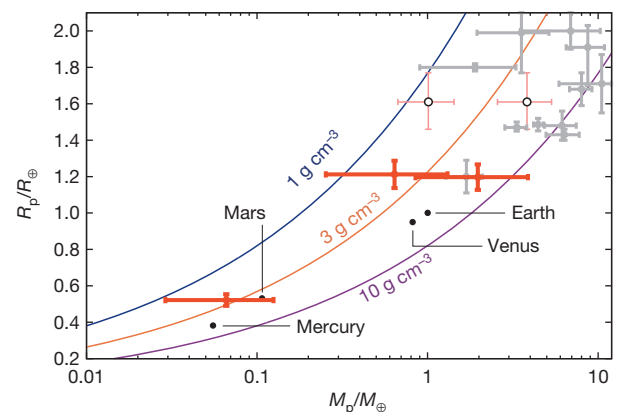


Figure 2 | Mass-radius diagram of well characterized planets smaller than 2.1 Earth radii, R_{\oplus} . Prior exoplanet characterizations and 1σ uncertainties are shown as grey points^{7–9,15,16,19,25–30}. Black points from left to right are Mercury, Mars, Venus and Earth. Red data points are our results for Kepler-138. Open circles mark previously measured masses for Kepler-138 c and Kepler-138 d²¹. Error bars mark published 1σ uncertainties for the planets of Kepler-138 and masses and radii of all other characterized exoplanets within this size range. The curves mark bulk densities of 1 g cm^{-3} , 3 g cm^{-3} and 10 g cm^{-3} .

properties, particularly the higher stellar density and consequent smaller stellar radius.

Previous estimates of the size and mass of the outer planet Kepler-138 d implied that the planet possessed a hydrogen-rich atmosphere²¹, which is difficult to explain with our current understanding of the accretion and retention of light gases from low-mass planets orbiting close to their star^{22–24}. Our new measurements could be explained by a composition of rock and water. A planet made of rock and water would be more stable against mass loss, and would imply that the planet formed at a greater distance from the star and migrated.

Online Content Methods, along with any additional Extended Data display items and Source Data, are available in the online version of the paper; references unique to these sections appear only in the online paper.

Received 9 September 2014; accepted 17 April 2015.

- Agol, E., Steffen, J., Sari, R. & Clarkson, W. On detecting terrestrial planets with timing of giant planet transits. *Mon. Not. R. Astron. Soc.* **359**, 567–579 (2005).
- Holman, M. J. & Murray, N. W. The use of transit timing to detect terrestrial-mass extrasolar planets. *Science* **307**, 1288–1291 (2005).
- Holman, M. J. *et al.* Kepler-9: a system of multiple planets transiting a Sun-like star, confirmed by timing variations. *Science* **330**, 51–54 (2010).
- Borucki, W. J. *et al.* Characteristics of planetary candidates observed by Kepler. II. Analysis of the first four months of data. *Astrophys. J.* **736**, 19–40 (2011).
- Batalha, N. M. *et al.* Planetary candidates observed by Kepler. III. Analysis of the first 16 months of data. *Astrophys. J.* **764** (Suppl.), 24–44 (2013).
- Burke, C. J. *et al.* Planetary candidates observed by Kepler IV: planet sample from Q1–Q8 (22 months). *Astrophys. J.* **770** (Suppl.), 19–30 (2014).
- Pepe, F. *et al.* An Earth-sized planet with an Earth-like density. *Nature* **503**, 377–380 (2013).
- Howard, A. W. *et al.* A rocky composition for an Earth-sized exoplanet. *Nature* **503**, 381–384 (2013).
- Cochran, W. D. *et al.* Kepler-18b, c and d: a system of three planets confirmed by transit timing variations, light curve validation, warm Spitzer photometry, and radial velocity measurements. *Astrophys. J.* **736** (Suppl.), 7–25 (2011).
- Steffen, J. H. *et al.* Transit timing observations from Kepler. III. Confirmation of four multiple planet systems by a Fourier-domain study of anticorrelated transit timing variations. *Mon. Not. R. Astron. Soc.* **421**, 2342–2354 (2012).
- Ford, E. B. *et al.* Transit timing observations from Kepler. V. Transit timing variation candidates in the first sixteen months from polynomial models. *Astrophys. J.* **756**, 185–191 (2012).
- Steffen, J. H. *et al.* Transit timing observations from Kepler. VI. Potentially interesting candidate systems from Fourier-based statistical tests. *Astrophys. J.* **756**, 186–190 (2012).
- Lithwick, Y., Xie, J. & Wu, Y. Extracting planet mass and eccentricity from TTV data. *Astrophys. J.* **761**, 122–132 (2012).
- Wu, Y. & Lithwick, Y. Density and eccentricity of Kepler planets. *Astrophys. J.* **772**, 74–86 (2013).
- Jontof-Hutter, D., Lissauer, J. J., Rowe, J. F. & Fabrycky, D. C. Kepler-79's low density planets. *Astrophys. J.* **785**, 15–18 (2014).
- Lissauer, J. J. *et al.* All six planets known to orbit Kepler-11 have low densities. *Astrophys. J.* **770**, 131–145 (2013).
- Masuda, K. Very low density planets around Kepler-51 revealed with transit timing variations and an anomaly similar to a planet-planet eclipse event. *Astrophys. J.* **783**, 53–60 (2014).
- Ofir, A., Dreizler, S., Zechmeister, M. & Husser, T.-O. An independent planet search in the Kepler dataset. II. An extremely low-density super-Earth mass planet around Kepler-87. *Astron. Astrophys.* **561**, A103 (2014).
- Carter, J. A. *et al.* Kepler-36: a pair of planets with neighboring orbits and dissimilar densities. *Science* **337**, 556–559 (2012).
- Rowe, J. F. *et al.* Validation of Kepler's multiple planet candidates. III. Light curve analysis and announcement of hundreds of new multi-planet systems. *Astrophys. J.* **784**, 45–64 (2014).
- Kipping, D. M. *et al.* The hunt for exomoons with Kepler (HEK). IV. A search for moons around eight M dwarfs. *Astrophys. J.* **784**, 28–42 (2014).
- Bodenheimer, P. & Lissauer, J. J. Accretion and evolution of ~2.5 Earth-mass planets with voluminous H/He envelopes. *Astrophys. J.* **791**, 103–134 (2014).
- Lopez, E. D. & Fortney, J. J. The role of core mass in controlling evaporation: the Kepler radius distribution and the Kepler-36 density dichotomy. *Astrophys. J.* **776**, 2–12 (2013).
- Owen, J. E. & Wu, Y. Kepler planets: a tale of evaporation. *Astrophys. J.* **775**, 105–116 (2013).
- Ferraz-Mello, S., Tadeu Dos Santos, M., Beaugé, C., Michtchenko, T. A. & Rodríguez, A. On the mass determination of super-Earths orbiting active stars: the CoRoT-7 system. *Astron. Astrophys.* **531**, A161 (2011).
- Batalha, N. M. *et al.* Kepler's first rocky planet: Kepler-10b. *Astrophys. J.* **729**, 27–47 (2011).
- Fressin, F. G. *et al.* Two Earth-sized planets orbiting Kepler-20. *Nature* **482**, 195–198 (2011).
- Gautier, T. N. III *et al.* Kepler-20: a Sun-like star with three sub-Neptune exoplanets and two Earth-size candidates. *Astrophys. J.* **749**, 15–33 (2012).
- Weiss, L. M. *et al.* The mass of KOI-94d and a relation for planet radius, mass, and incident flux. *Astrophys. J.* **768**, 14–32 (2013).
- Marcy, G. W. *et al.* Masses, radii, and orbits of small Kepler planets: the transition from gaseous to rocky planets. *Astrophys. J.* **770** (Suppl.), 20–89 (2014).

Acknowledgements D.J.-H. acknowledges support through the NASA Postdoctoral Program and funding from the Center for Exoplanets and Habitable Worlds. The Center for Exoplanets and Habitable Worlds is supported by the Pennsylvania State University, the Eberly College of Science and the Pennsylvania Space Grant Consortium. J.F.R. acknowledges NASA grant NNX14AB92G issued through the Kepler Participating Scientist Program. D.C.F. is an Alfred P. Sloan Fellow and was supported by the Kepler Participating Scientist Program award NNX14AB87G. E.B.F. was supported in part by NASA Kepler Participating Scientist Program award NNX14AN76G and NASA Exoplanet Research Program award NNX15AE21G, as well as the Center for Exoplanets and Habitable Worlds.

Author Contributions D.J.-H. led the research effort to model the TTV, constrain planetary masses, and wrote the manuscript. J.F.R. measured transit times from the Kepler data set, characterized the host star using spectral follow-up of the target and constraints from the transits and edited the manuscript. J.J.L. led the interpretation effort, assisted in the dynamical study and writing the manuscript. D.C.F. wrote the software to simulate planetary transits, assisted in interpreting results and edited the manuscript. E.B.F. assisted in the development of statistical methodologies and robustness tests for the TTV modelling and edited the manuscript.

Author Information Reprints and permissions information is available at www.nature.com/reprints. The authors declare no competing financial interests. Readers are welcome to comment on the online version of the paper. Correspondence and requests for materials should be addressed to D.J.-H. (dxj14@psu.edu).

METHODS

We have used all available short-cadence Kepler data and long-cadence data wherever short-cadence data are unavailable to complete the data set for 17 quarters. We list the transit times for each planet in Extended Data Table 1. Throughout, we express times since Barycentric Julian Day (BJD) minus 2,454,900. **Photometric transit and stellar models.** From the light curve, we filtered instrumental and astrophysical effects that are independent of planetary transits. To each segment of the photometric time series, we fitted a cubic polynomial of width 2 days, centred on the time of each measurement²⁰. We excluded measurements taken within one transit duration (defined as the time from first to last contact) of the measured centre of the transit and extrapolate the polynomial to estimate corrections during transits. This process strongly filters astrophysical signals with timescales of approximately 2 days, which could affect the shape of a planetary transit. We also excluded measurements for which the associated segment has gaps longer than 2.5 h.

We fitted the detrended Kepler light curve using a transit model for quadratic limb-darkening³¹ and non-circular Keplerian orbits. We stacked transits of each planet with corrections for the measured TTVs²⁰. To account for Kepler's observation cadence, we averaged our transit model with 11 equal spacings within the 1 min or 30 min integration window. We evaluated the photometric noise for each quarter of data to fit transit models, adopting published stellar parameters for Kepler-138³². We adopted a two-parameter quadratic model for limb-darkening with fixed coefficients (0.3576, 0.3487) appropriate for Kepler's bandpass and Kepler-138's effective temperature (T_{eff}), $\log[g]$ and metallicity $[\text{Fe}/\text{H}]$ ³³.

The light curve model parameters consist of the mean stellar density ρ_{\star} , a photometric zero point for each light curve segment, and for each planet the orbital period, time of transit, planet-to-star radius ratio, impact parameter, and eccentricity parameterized as $e\cos\omega$ and $e\sin\omega$. We determined posterior distributions of our model parameters using Markov Chain Monte Carlo techniques²⁰. Our best-fit transit models, shown in Extended Data Fig. 1, resulted in consistent estimates for ρ_{\star} from each planet.

We determined the mass and radius of Kepler-138 by fitting the spectroscopic parameters (T_{eff} , $[\text{Fe}/\text{H}]$)³² and our light curve constraints of ρ_{\star} to Dartmouth Stellar Evolution models³⁵, assuming a Gaussian probability density for each parameter³². For the Dartmouth models, we varied initial conditions of mass, age, and $[\text{Fe}/\text{H}]$ and interpolated over a grid to evaluate T_{eff} , ρ_{\star} , and $[\text{Fe}/\text{H}]$ for any set of initial conditions. We computed posteriors using Markov Chain Monte Carlo analysis to obtain stellar model-dependent posteriors on M_{\star} and R_{\star} . Table 1 lists our adopted stellar parameters. We tested the effects of eccentricity priors on our measurement of ρ_{\star} , adopting a uniform prior in eccentricity as our nominal results. We compare results with eccentricity fixed at zero in Extended Data Fig. 2. Although a uniform prior on eccentricity results in a slightly wider range of inferred radii for the star, both of these models are consistent with the spectroscopic study of Kepler-138³².

Our solution for the impact parameter of the middle planet is 0.3 ± 0.2 , much lower than the previous estimate of 0.92 ± 0.02 ²¹. The apparent U-shaped transit for Kepler-138 c (Extended Data Fig. 1) is consistent with a low impact parameter. Our measured impact parameter for Kepler-138 d is 0.810 ± 0.057 , consistent with the previous measurement²¹. Our revised impact parameters imply $\rho_{\star} = 9.0 \pm 1.9 \text{ g cm}^{-3}$, which agrees with our transit models for each planet, and with the spectroscopic study of Kepler-138³².

We find that Kepler-138 has a smaller mass and radius than previous estimates based on the absolute K-band magnitude (M_K) of the star from high-resolution Keck spectra³⁶. These relied on mass–luminosity relations³⁷ and a mass–radius relation from interferometry³⁸. However, the calibration stars used to correlate the M_K to spectral index excluded cool stars that are active. In the case of Kepler-138, the photometric time-series exhibits large (1%) variations due to starspots. These increase the risk of systematic errors in the measurement of stellar luminosity, and therefore the stellar properties derived from the mass–luminosity relation.

The time-scale for star-spot modulation, ~ 20 days, was much longer than the transit duration, and was probably dominated by two spots. We found no evidence of starspot crossings, nor did we find any TTV periodicities related to the rotation period of the star. Hence, the stellar activity is unlikely to affect our transit model or transit times.

Analytical constraints from TTV. Orbital period ratios determine how close planets are to mean motion resonance, and over what period TTVs are expected to cycle. The inner pair of planets of Kepler-138 orbit near the 4:3 resonance with an expected TTV cycle of 1,570 days, slightly longer than the 1,454-day observational baseline of Kepler-138 b's transits. We fitted a sinusoid at this periodicity to the TTVs of the inner planet, and detected a TTV amplitude of 34 ± 4 min. This permits a rough estimate for the mass¹³ of the middle planet of $(6.8 \pm 0.9)M_{\oplus} (M_{\odot}/M_{\star})$, which is close to our final measure of the mass of the middle planet.

The detection of TTVs at Kepler-138 b imply that the TTVs in Kepler-138 c have a component caused by Kepler-138 b. However, the middle planet's TTVs are the combined effect of perturbations from its two neighbours Kepler-138 b and Kepler-138 d, and the outer pair orbit near a second-order mean motion resonance for which there is no known analytical model. Hence, the masses of the inner and outermost planets cannot be estimated by fitting such a simplified sinusoidal model to the TTVs.

Detailed TTV modelling. For each set of initial conditions, we calculate the transit times of all three planets based on Newtonian gravity, using an eighth-order Dormand–Prince Runge–Kutta integrator^{15,16,39}. We compare the simulated and observed transit times for each planet assuming each observed transit time has an independent Gaussian measurement uncertainty.

We found an excess of outlying transit times to our model, where either instrumental effects or stellar activity led to a few unlikely transit times with underestimated uncertainties. Extended Data Fig. 3 shows the distribution of residuals to our best-fit TTV model compared to a Gaussian distribution, revealing these outliers. Of the 257 measured transit times, five are outliers, where for simulated transit times S , and measurement uncertainties σ_{TT} , $(O - S)/\sigma_{\text{TT}} > 3$. We removed these outliers, and used the 252 remaining measurements as our nominal data set for dynamical models. Later, we tested our results for robustness against outliers.

Performing extensive grid searches and Levenberg–Marquardt analysis, we found a single region of high posterior probability including multiple closely related local minima. To characterize the masses and orbital parameters of the three planets, we performed Bayesian parameter estimation using a differential evolution Markov Chain Monte Carlo algorithm^{40,41}. We used Metropolis–Hasting acceptance rules on 45 ‘walkers’ exploring parameter space in parallel, where for each walker, a proposal is a scaled vector between two other walkers chosen at random. Using differential evolution for the proposal steps increases the probability that proposals will be accepted, particularly for target distributions with strong correlations between model parameters.

The walkers were launched near the best-fit model found by Levenberg–Marquardt analysis. We updated the vector scale length factor every 15 generations to keep the acceptance rate near the optimum value of 0.25^{40–42} and thinned the data by recording every 20th generation in the Markov Chain. We discarded the first 50,000 generations and continued the Markov Chain for 1,250,000 additional generations.

The mean correlation between parameter values in the same Markov Chain Monte Carlo chain for a given separation in the chain begins near unity for consecutive generations, and declines for greater separations⁴³. We used this property to assess how well-mixed our Markov Chain Monte Carlo chains were. The autocorrelation length, defined as the lag between generations required for the correlation to fall below 0.5, varied between the walkers, averaging 9,000 generations for the planet-to-star mass ratio of Kepler-138 b. Hence, the mean length of the differential evolution Markov Chain Monte Carlo chains was about 139 autocorrelation lengths.

For each planet, we adopted a uniform prior in orbital period, T_0 , e , and ω . For M_p/M_{\star} , we adopted a uniform prior that allowed negative masses to enable a simple estimate for the significance of a positive mass for Kepler-138 b from the posterior samples³⁰. For Kepler-138 b, the mass is greater than zero in 99.84% of posterior samples. As a further test, we considered an alternative, more realistic, uniform prior where planetary masses are positive definite and limited to the mass of a pure iron planet (given their sizes)^{44,45}.

Posteriors for the mass ratios of each planet to the host star, and each eccentricity vector component are shown in Extended Data Fig. 4. We list 68.3%, 95.4%, and 99.7% credible intervals for all parameters in Extended Data Table 2. We also include the mass ratios between the planets and relative eccentricity vector components, which are more constrained by the data than absolute masses and eccentricities.

Orbital eccentricity. Joint posteriors for the eccentricity vector components are displayed in Extended Data Fig. 5. These show extreme correlations because a broad class of orbital parameters in which there is a precise apsidal alignment of orbits satisfies the data.

We performed long-term integrations on a subset of our posterior planet masses and orbital parameters including a wide range of eccentricities using the *HNBODY* code⁴⁶. We investigated whether long-term stability could further constrain the eccentricities. A sample of the solutions were integrated for ten million orbits and all were found to be stable. Integrating one of the best-fit solutions with high eccentricities for Kepler-138 b, Kepler-138 c and Kepler-138 d of 0.23, 0.20 and 0.18 respectively, we confirmed that the orbits were stable for over one billion years; the apsidal lock was maintained with the periaapses of all three planets closely aligned. Although rare in the Solar System, apsidal alignment has been observed and studied in the Uranian ring system^{47,48} and it has been detected in exoplanetary systems, including υ Andromedae⁴⁹, GJ 876⁵⁰ and possibly 55 Cancri⁵¹.

Significance of mass detection for Kepler-138 b. We establish the statistical significance of a non-zero mass for Kepler-138 b by computing the Bayes factor, that is, the ratio of the marginalized posterior probability for a model with the mass of planet Kepler-138 b fixed at zero relative to the marginalized posterior probability for a model where all three planets have a non-zero mass. Intuitively, the Bayes factor quantifies how much the transit timing data has increased our confidence that Kepler-138 b has a non-zero mass. When performing Bayesian model selection, it is essential to choose proper (that is, normalized) priors for any parameters not occurring in both models. For the mass of Kepler-138 b we adopt a uniform prior ranging between zero mass and the mass of an iron sphere the size of Kepler-138 b. We tested two models of iron planets as upper limits on our mass priors^{44,45}. We compute the Bayes factor using the generalized Savage–Dickey density ratio based on the posterior samples from our nominal model⁵². We find that the three-massive-planets model is strongly favoured, with the posterior probability for the three-massive-planets model equal to 99.82%⁴⁴ (99.80%⁴⁵) for our nominal model (that is, three massive planets, each with a uniform eccentricity prior) or 99.91%⁴⁴ (99.90%⁴⁵) for a model with three massive planets, each with a Rayleigh distribution ($\sigma = 0.02^{53}$) for an eccentricity prior. A more restrictive prior for the mass of Kepler-138 b would further increase the posterior probability for the three-massive-planets model.

The generalized Savage–Dickey density ratio is superior to more commonly used substitutes (such as the Akaike information criterion, AIC, or the Bayesian Information Criterion, BIC), since the Savage–Dickey density ratio provides a practical means of calculating the Bayes factor, the actual quantity of interest for rigorous Bayesian model comparison. The AIC and BIC use only the likelihood of the two best-fit models and do not account for the width or shape of the posterior probability distributions. Extended Data Fig. 4a shows that the marginal posterior for the mass of Kepler-138 b is asymmetric and non-Gaussian, so the AIC or BIC would be a particularly poor choice for our problem.

Therefore, we have computed the rigorously correct Bayes factor using the Savage–Dickey density ratio, which provides an efficient way of calculating the Bayes factor when comparing two nested models, meaning that the simpler model is equivalent to the more general model when the additional parameters (θ) take on a particular value ($\theta = \theta_0$). In our case, this occurs when $M_b = 0$. One advantage of the Savage–Dickey density ratio over computing fully marginalized likelihoods is that the Savage–Dickey density ratio can be computed from the posterior for the more general model. This is computationally practical when comparing models that differ by one to a few dimensions, since then the posterior at θ_0 can be computed from a posterior sample using a kernel density estimator. We estimate the posterior density using a Gaussian kernel density estimator with bandwidth $0.001M_\oplus(M_\star/M_\odot)$, which was found to be optimal when analysing synthetic posterior samples data. We verified that the results were insensitive to varying the choice of bandwidth by an order of magnitude.

Sensitivity analyses. We performed several tests to assess the robustness of our results to: (1) the choice of prior for eccentricity, (2) the treatment of transit time outliers, (3) the assumption of co-planarity, and (4) our algorithm. For these sensitivity analyses, we adopt our nominal prior for planet masses to allow for negative planet masses. While any such models are clearly unphysical, allowing for such models offers an efficient and intuitive means for evaluating whether the lower limit on the planet masses is robust to the above assumptions.

Choice of eccentricity prior. As noted above, our nominal model has a uniform prior in eccentricity. The joint posterior for the mass ratio of Kepler-138 b to the host star and its orbital eccentricity is shown in Extended Data Fig. 5. We show this plot with two alternative priors in eccentricity: a Rayleigh distribution with a scale length 0.1⁵⁴, and a more constrained one, consistent with Kepler’s multi-planet systems, with a scale length of 0.02⁵³. Since the data constrain the eccentricity so weakly, the choice of priors strongly affects the posteriors of eccentricity. However, the planet-to-star mass ratios were much more weakly affected by the choice of eccentricity prior, as shown in Extended Data Fig. 7a.

Because the apsidally locked solutions are long-term stable, we adopt the uniform prior as our nominal solution, and note that a more constraining prior on eccentricity results in a marginally wider posterior for mass ratio of Kepler-138 b to the star. Although, as noted above, the orbital eccentricities in the system are only weakly constrained, the relative eccentricities and mass ratios between the planets are tightly constrained by the TTVs, as shown in Extended Data Fig. 6 and Extended Data Table 2.

Transit time observation outliers. To assess the effect of residual outlying transit times, we repeated the analysis with two other sets of measured transit times, differing only in that we removed transit time residual outliers beyond (1) 4σ (leaving 254 transit times) or (2) 2.5σ (leaving 244 transit times), as opposed to our nominal data set, which excluded 3σ outliers. Extended Data Fig. 3 shows the relative frequency of residuals compared to a Gaussian. The majority of outliers are between 2.5σ and 3σ . We excluded outliers beyond 4σ from all models.

The posterior for the mass of Kepler-138 b for each of these three data sets is displayed for comparison in Extended Data Fig. 7b. Overall, the outliers have a modest effect on the measured mass ratio for Kepler-138 b to the host star. Since most of the outliers are in the transit times of Kepler-138 b, these have a small effect on our mass measurement of Kepler-138 b. Furthermore, the mass of Kepler-138 c is constrained by its effect on the transit times of both planets Kepler-138 b and Kepler-138 d. Nevertheless, we note that the inclusion of more outliers increases the skewness of the posterior for planetary mass and causes the mode of the distribution to shift to a slightly lower mass.

Assumption of co-planarity. The known low inclination dispersion amongst Kepler’s multiplanet systems makes co-planarity a reasonable assumption for TTV modelling^{13,55,56}. Furthermore, geometric considerations make multi-planet transiting less likely to be observed for systems with large mutual inclinations. Nevertheless, we tested the effect of mutual inclinations on our solutions. We performed two additional sets of simulations: (1) with the longitude of the ascending node of Kepler-138 b as a free parameter, leaving the other two planets as co-planar, and (2) with a free ascending node for Kepler-138 d. In each case, we adopted a uniform prior for the ascending node. In Extended Data Fig. 7c, we compare the posteriors for the mass ratio of Kepler-138 b to the host star with mutual inclinations to our nominal result. The nominal result gives a consistent, but slightly wider posterior than with free ascending nodes.

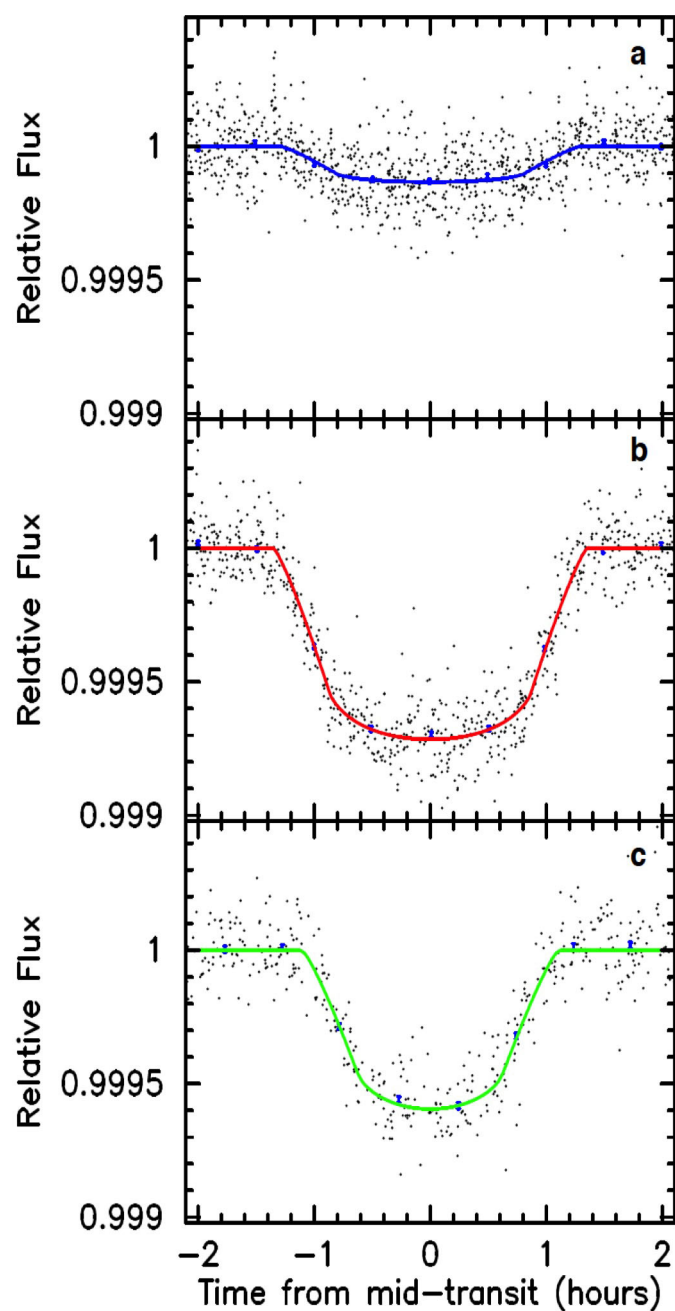
Tests with synthetic transit times. We evaluated our method by generating synthetic data sets of transit times with known planetary masses and orbital parameters to test how well the input parameters were recovered. The results are shown in Extended Data Fig. 8. We generated synthetic transit times based on the median values of each parameter from the marginal posteriors of our nominal model and added Gaussian noise to each observation with a standard deviation equal to the measured timing uncertainties. Our analysis of the simulated data results in a posterior for the mass of Kepler-138 b consistent with the true values. While the resulting posterior for the mass of Kepler-138 b shows a slightly higher mode and is less skewed than the posterior for the nominal model, the differences are comparable to the minor effects of transit timing outliers or choice of eccentricity prior. This result validates our both our transit timing method and our TTV analysis.

Additionally, we generated eight independent synthetic data sets with zero mass for Kepler-138 b and other parameters based on our nominal model (Extended Data Fig. 8). In all eight cases, the posterior probability for Kepler-138 b’s mass was insignificant, with only 16% to 86% of posterior samples having a mass greater than zero, consistent with expectations for non-detections. This is in sharp contrast to our analysis of the actual data, which results in 99.84% of the posterior yielding a positive mass for Kepler-138 b.

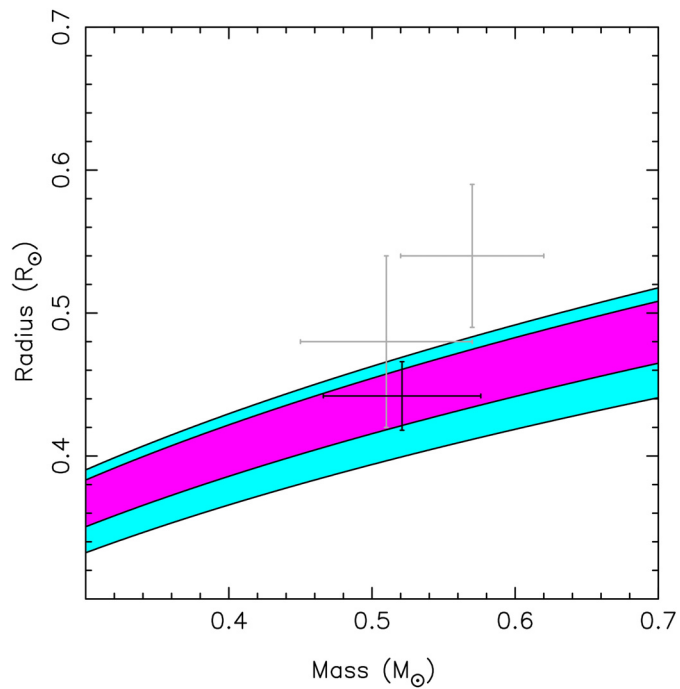
Planetary characteristics. Our adopted credible intervals in planetary mass and density were calculated by repeatedly multiplying samples from the posteriors of planet-to-star mass ratios, and M_\star . Uncertainties in planetary radii were calculated with the fractional uncertainty in the stellar radius and the uncertainty in planet-to-star radius ratio added in quadrature. Time-averaged incident flux for each planet compared to the Earth was calculated in the low eccentricity limit, although we note that if the orbits were highly eccentric, the fluxes would be marginally higher.

31. Mandel, K. & Agol, E. Analytic light curves for planetary transit searches. *Astrophys. J.* **580**, L171 (2002).
32. Muirhead, P. S. *et al.* Characterizing the cool Kepler objects of interest. New effective temperatures, metallicities, masses and radii of low-mass Kepler planet-candidate host stars. *Astrophys. J.* **750**, L37 (2012).
33. Claret, A. & Bloeman, S. Gravity and limb-darkening coefficients for the Kepler, CoRoT, Spitzer, uvby, UBVRJHK, and Sloan photometric systems. *Astron. Astrophys.* **529**, A75 (2011).
34. Seager, S. & Mallen-Ornelas, G. A unique solution of planet and star parameters from an extrasolar planet transit light curve. *Astrophys. J.* **585**, 1038–1055 (2003).
35. Dotter, A. The Dartmouth Stellar Evolution Database. *Astrophys. J.* **178** (Suppl.), 89–101 (2008).
36. Pineda, J. S., Bottom, M. & Johnson, J. A. Using high resolution optical spectra to measure intrinsic properties of low-mass stars: new properties for KOI-314 and GJ 3470. *Astrophys. J.* **767**, 28–38 (2013).
37. Delfosse, X. *et al.* Accurate masses of very low mass stars. IV. Improved mass-luminosity relations. *Astron. Astrophys.* **364**, 217–224 (2000).
38. Boyajian, T. S. *et al.* Stellar diameters and temperatures. II. Main sequence K- and M-stars. *Astrophys. J.* **757**, 112–142 (2012).
39. Lissauer, J. J. *et al.* A closely packed system of low-mass, low-density planets transiting Kepler-11. *Nature* **470**, 53–58 (2011).
40. Ter Braak, C. A Markov Chain Monte Carlo version of the genetic algorithm Differential Evolution: easy Bayesian computing for real parameter spaces. *Stat. Comput.* **16**, 239–249 (2006).
41. Nelson, B., Ford, E. B. & Payne, M. J. RUN DMC: an efficient, parallel code for analyzing radial velocity observations using N-body integrations and Differential Evolution Markov Chain Monte Carlo. *Astrophys. J.* **210** (Suppl.), 11–23 (2014).

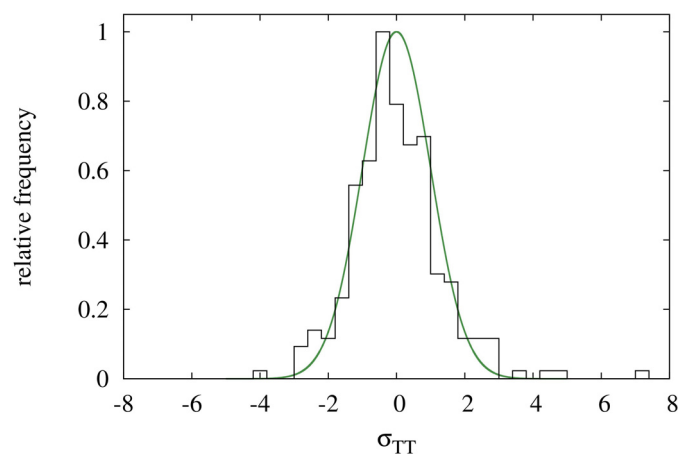
42. Ford, E. Quantifying the uncertainty in the orbits of extrasolar planets. *Astron. J.* **129**, 1706–1717 (2005).
43. Tegmark, M. *et al.* Cosmological parameters from SDSS and WMAP. *Phys. Rev. D* **69**, 103501 (2004).
44. Fortney, J. J., Marley, M. S. & Barnes, J. W. Planetary radii across five orders of magnitude in mass and stellar insolation: application to transits. *Astrophys. J.* **659**, 1661–1672 (2007).
45. Zeng, L. & Sasselov, D. A detailed model grid for solid planets from 0.1 through 100 Earth masses. *Publ. Astron. Soc. Pacif.* **125**, 227–239 (2013).
46. Rauch, K. P. & Hamilton, D. P. HNBODY: Hierarchical N-Body Symplectic Integration Package. In *Astrophysics Source Code Library* <http://ascl.net/1201.010> (2012).
47. Goldreich, P. & Tremaine, S. Precession of the epsilon ring of Uranus. *Astron. J.* **84**, 1638–1641 (1979).
48. Chiang, E. I. & Goldreich, P. Apse alignment of narrow eccentric planetary rings. *Astrophys. J.* **540**, 1084–1090 (2000).
49. Chiang, E. I., Tabachnik, S. & Tremaine, S. Apsidal alignment in Upsilon Andromedae. *Astron. J.* **122**, 1607–1615 (2001).
50. Rivera, E. J., Laughlin, G., Butler, R. P., Vogt, S. S. & Haghighipour, N. The Lick-Carnegie Exoplanet Survey. A Uranus-mass fourth planet for GJ 876 in an extrasolar Laplace configuration. *Astrophys. J.* **719**, 890–899 (2010).
51. Nelson, B. E. *et al.* The 55 Cancri planetary system: fully self-consistent N-body constraints and a dynamical analysis. *Mon. Not. R. Astron. Soc.* **441**, 442–451 (2014).
52. Verdinelli, I. & Wasserman, L. Computing Bayes factors using a generalization of the Savage-Dickey density ratio. *J. Am. Stat. Assoc.* **90**, 614–618 (1995).
53. Hadden, S. & Lithwick, Y. Densities and eccentricities of 139 Kepler planets from transit timing variations. *Astrophys. J.* **787**, 80–87 (2014).
54. Moorhead, A. V. *et al.* The distribution of transit durations for Kepler planet candidates and implications for their orbital eccentricities. *Astrophys. J.* **197** (Suppl.), 1–15 (2011).
55. Fabrycky, D. C. *et al.* Architecture of Kepler's multi-transiting systems. II. New investigations with twice as many candidates. *Astrophys. J.* **790**, 146–157 (2014).
56. Lissauer, J. J. *et al.* Architecture and dynamics of Kepler's candidate multiple transiting planet systems. *Astrophys. J.* **197**, 8–33 (2011).



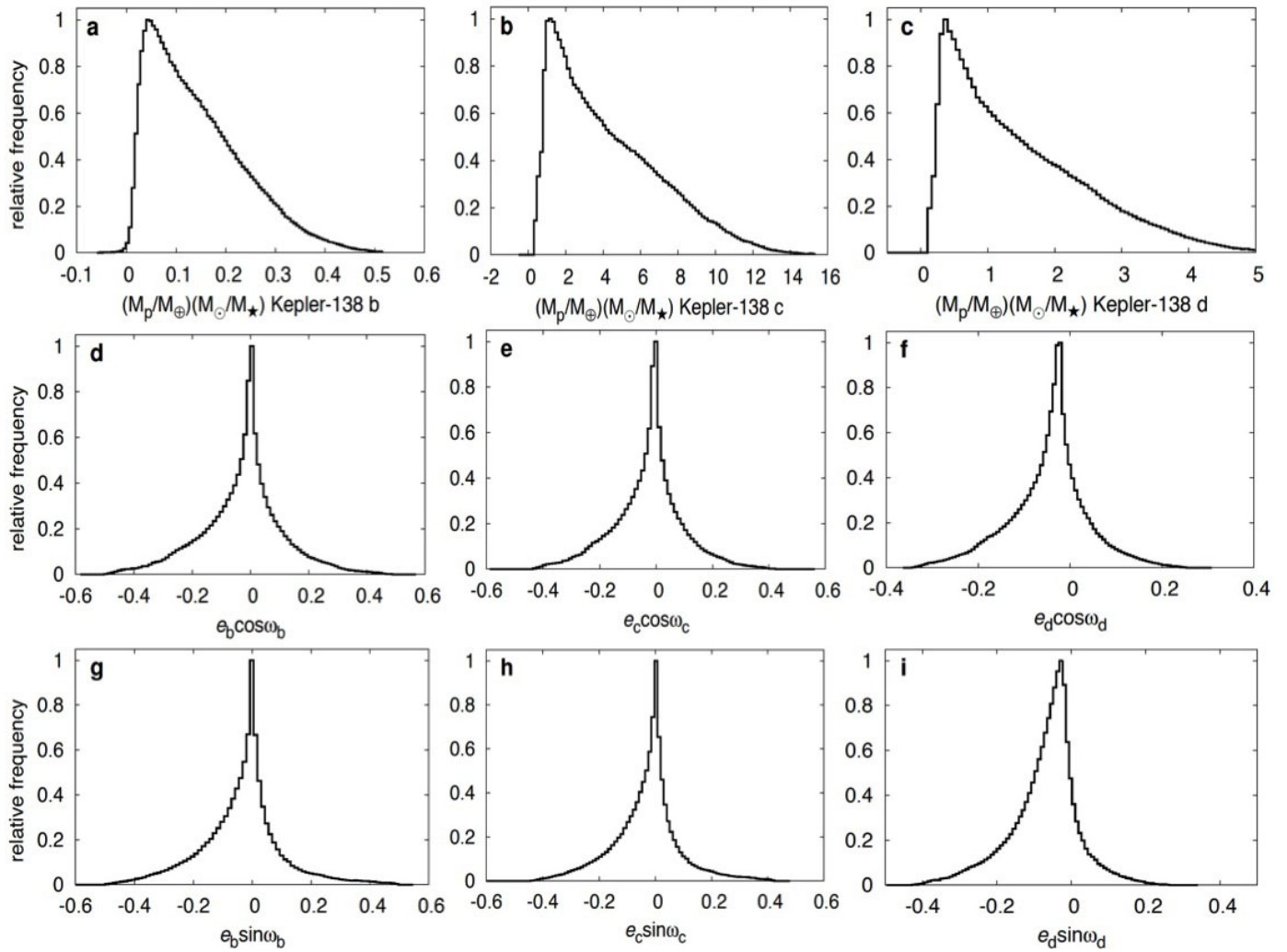
Extended Data Figure 1 | Folded light curves with corrections for observed TTV for Kepler-138. The scattered points are photometric relative fluxes and the curves are analytical models of the transit shape described in the text. a, Kepler-138 b; b, Kepler-138 c; c, Kepler-138 d.



Extended Data Figure 2 | Stellar mass and radius models using constraints on the stellar mean density inferred from the light curve. In cyan are models that adopted a uniform prior in eccentricity, and in magenta are constraints found with orbital eccentricities fixed at zero. Grey points with error bars mark stellar parameters found in the literature while the black error bars mark our adopted solution for stellar mass and radius.

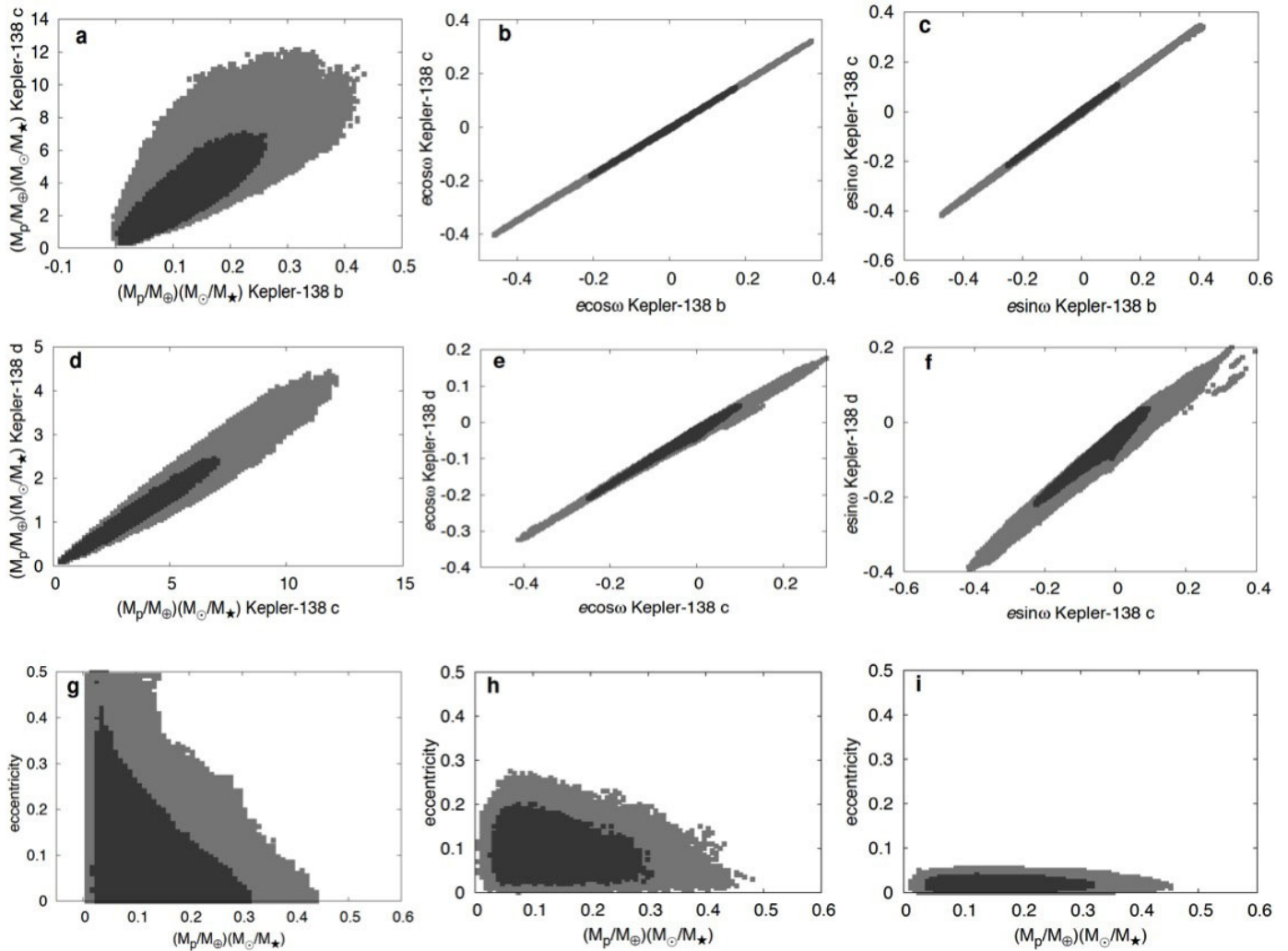


Extended Data Figure 3 | The distribution of residual normalized deviations from our best fit dynamical model to the raw transit times. The histogram marks deviations calculated as: $(O - S)/\sigma_{TT}$, where O is the observed transit time, S is the simulated transit time and σ_{TT} is the measurement uncertainty. The green curve marks a Gaussian distribution.



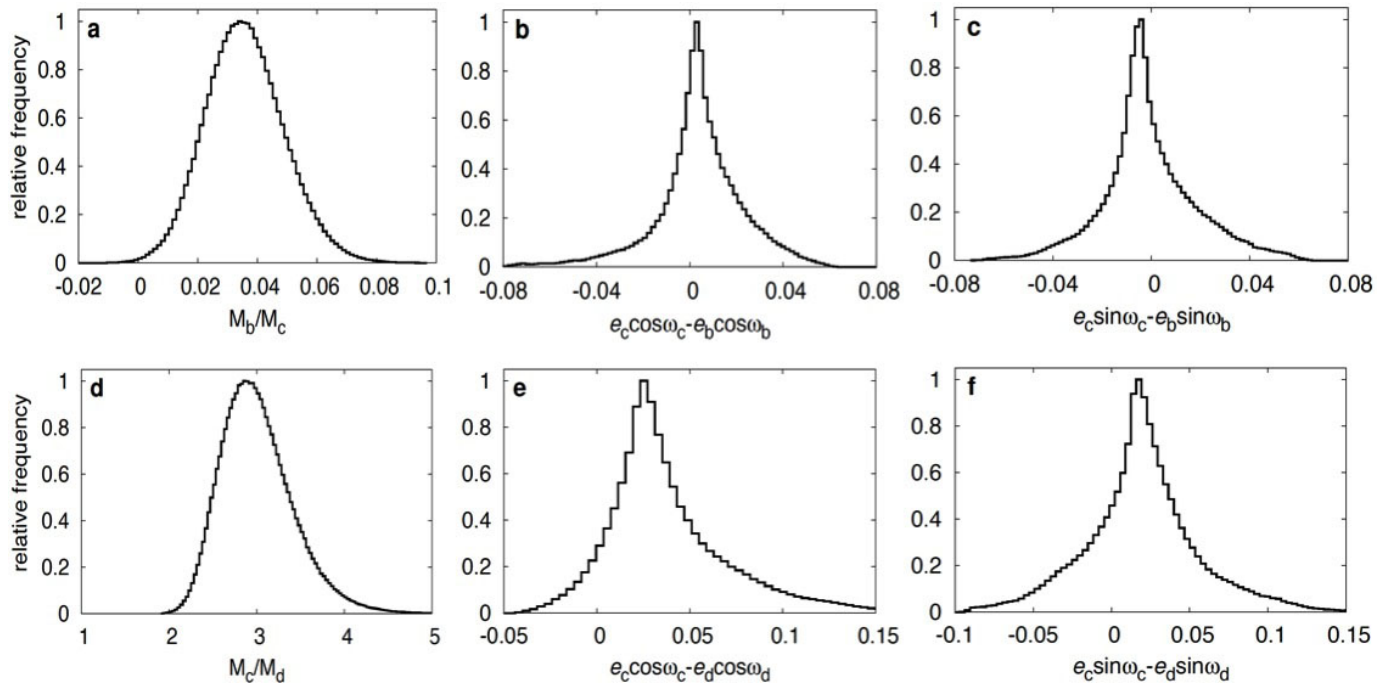
Extended Data Figure 4 | Posterior distributions for TTV model parameters. Data are shown for our nominal model. **a**, The planet-to-star mass ratio (M_p/M_\star) for Kepler-138 b; **b**, M_p/M_\star for Kepler-138 c; **c**, M_p/M_\star for Kepler-138 d. **d**, $e \cos \omega$ for Kepler-138 b; **e**, $e \cos \omega$ for Kepler-138 c; **f**, $e \cos \omega$ for

Kepler-138 d. **g**, $e \sin \omega$ for Kepler-138 b; **h**, $e \sin \omega$ for Kepler-138 c; **i**, $e \sin \omega$ for Kepler-138 d. The relative frequency for each histogram is scaled to the mode. Mass ratios are scaled to the M_\odot/M_\oplus mass ratio.



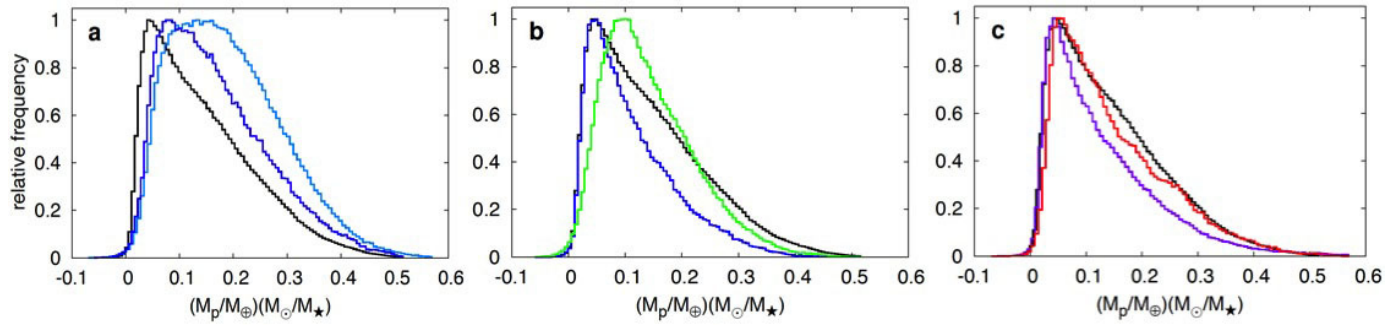
Extended Data Figure 5 | Joint posteriors of model parameters and the effects of eccentricity priors. The dark (light) grey marks the 68.3% (95.4%) credible intervals for each joint posterior. **a–c**, M_p/M_\star and eccentricity vector components for the inner and middle planets. **d–f**, M_p/M_\star and eccentricity

vector components for the middle and outer planets. Panels **g**, **h** and **i** compare Kepler-138 b's M_p/M_\star and its orbital eccentricity, for three eccentricity priors: a uniform prior on eccentricity (**g**), and models with a Rayleigh distribution of scale factor 0.1 (**h**), and 0.02 (**i**).



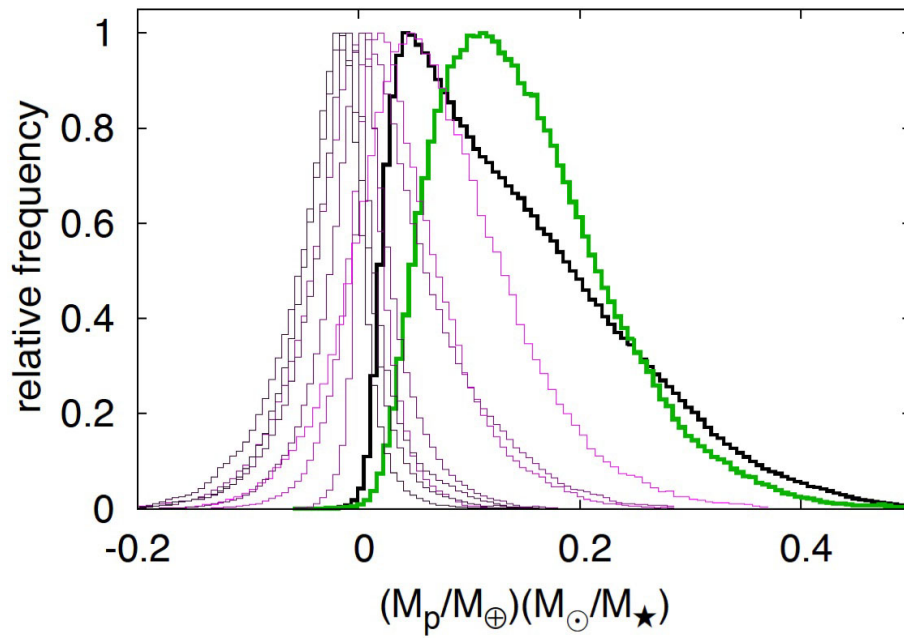
Extended Data Figure 6 | Posterior distributions for mass ratios and relative eccentricities between planets. The mass ratio of the inner and middle planets is shown in **a**, and relative eccentricity vector components—that is, the difference in $e \cos \omega$ ($e \sin \omega$) in the inner pair—are shown in **b** (**c**). The mass

ratio of the middle and outer planets are plotted in **d**, and the relative eccentricity vector components—that is, the difference in $e \cos \omega$ ($e \sin \omega$) in the outer pair—are shown in **e** (**f**).



Extended Data Figure 7 | Sensitivity tests for the effects of eccentricity prior, outlying transit times and free inclinations on the mass of Kepler-138 b relative to the host star. Panel a compares a uniform prior (black curve, our nominal posterior for all comparisons) and a Rayleigh distribution with scale

factors 0.1 (navy) and 0.02 (cyan). Panel b compares posteriors with 3σ outliers excluded (black), with two alternatives: 4σ outliers (blue) and 2.5σ outliers removed (light green). Panel c compares our nominal model with one with a free ascending node for the inner (purple) or outer (red) planet.



Extended Data Figure 8 | Validation of our method with synthetic data sets. The green curve marks the posterior for a synthetic data set generated with the same parameters as were the medians of our nominal posteriors (in Table 1). The agreement between the green and black curves validates our method and

our claim for a positive mass detection for Kepler-138 b. The magenta and purple shades are posteriors for models using data generated with zero mass for Kepler-138 b. These zero-mass synthetic models all reproduced non-detections.

Extended Data Table 1 | Transit times of Kepler-138's planets

Kepler-138 b				Kepler-138 d
56.23045±0.01261	633.73803±0.01076	1324.71431±0.01427	648.31255±0.00155	57.81311±0.00267
66.55886±0.01962	674.96352±0.01399	1335.04216±0.01297	675.87519±0.00283	80.90677±0.00212
76.86414±0.01211	705.89533±0.02944	1345.36064±0.02184	689.65512±0.00208	127.08360±0.00410
87.16890±0.01670	716.22338±0.01418	1355.68308±0.01380	717.22575±0.00237	150.17399±0.00382
97.51565±0.01126	726.53871±0.01875	1365.99107±0.01877	731.00161±0.00295	173.27102±0.00324
107.76610±0.01772	747.16800±0.01297	1376.29867±0.01476	772.34908±0.00190	196.36319±0.00534
118.17035±0.02111	757.44480±0.00921*	1386.61821±0.01230	786.13380±0.00298	219.45290±0.00346
128.43371±0.02127	767.76381±0.01237	1396.93177±0.01012	799.91135±0.00223	242.54570±0.00639
138.68975±0.01501	788.40859±0.01624	1407.23423±0.01422	813.68933±0.00227	265.63275±0.00311
149.08968±0.02329	798.73107±0.01595	1427.86777±0.01784	827.47331±0.00161	288.72239±0.00210
159.35323±0.01381	809.02624±0.01691	1438.17099±0.01347	841.25609±0.00213	311.81585±0.00301
169.67471±0.02554	819.36067±0.01339	1448.50021±0.01257	855.03878±0.00336	334.90440±0.00272
179.95288±0.01453	829.65344±0.00945	1469.12674±0.01137	882.59698±0.00361	357.99487±0.00252
190.29561±0.03001	840.01903±0.02614	1479.43924±0.01741	896.37408±0.00312	381.08423±0.00274
200.53153±0.05541	850.30643±0.02219	1489.75786±0.01432	910.15919±0.00428	404.17500±0.00242
210.92867±0.02677	860.61829±0.02166	1500.06004±0.01604	923.94511±0.00405	427.26468±0.00206
221.21582±0.01553	870.90735±0.01757	1510.39743±0.01074	951.50290±0.00319	450.35127±0.00336
231.53491±0.02127	881.21371±0.02906	1520.70942±0.01625*	979.06837±0.00273	473.44082±0.00289
241.86431±0.02522	891.58748±0.01517	Kepler-138 c	992.84600±0.00482	496.53494±0.00178
252.16382±0.01926	901.83111±0.02494	55.73273±0.00208	1006.62904±0.00238	519.62090±0.00176
262.47265±0.02855	912.16861±0.04122	69.50883±0.00225	1020.40638±0.00267	542.70985±0.00208
272.73469±0.02464	922.61657±0.01640*	83.29050±0.00217	1034.18777±0.00273	588.88500±0.00221
293.42230±0.01085	932.78055±0.02060	110.85343±0.00484	1047.97221±0.00238	611.97165±0.00281
314.03280±0.01904	943.12746±0.02492	124.63503±0.00333	1061.75267±0.00194	635.05492±0.00235
324.35524±0.01297	953.41465±0.01273	138.42452±0.00358	1075.53011±0.00193	681.23384±0.00232
334.66018±0.01269	963.76298±0.01606	152.19210±0.00315	1089.31318±0.00199	704.32004±0.00276
345.02249±0.01162*	974.06380±0.01566	165.97408±0.00308	1103.09090±0.00304	727.40385±0.00198
355.28950±0.01491	984.36675±0.01611	193.54290±0.00687	1116.87516±0.00212	750.49681±0.00318
365.58461±0.01360	994.70183±0.01800	221.09921±0.00286	1130.65224±0.00246	773.58233±0.00193
386.22924±0.01392	1015.35516±0.01660	234.87885±0.00353	1144.43817±0.00307	796.66645±0.00288
396.53721±0.01443	1025.61860±0.01477	248.65986±0.00433	1158.20412±0.00472	819.75707±0.00448
406.84333±0.01218	1056.56881±0.01466	262.44586±0.00462	1171.99592±0.00255	842.84842±0.00305
417.16572±0.01807	1066.88059±0.01294	276.22920±0.00397	1185.78181±0.00356	889.01363±0.00268
427.47777±0.01928	1077.19053±0.01288	290.00336±0.00294	1199.56134±0.00251	935.19781±0.00515
437.77623±0.01316	1088.14741±0.01024	317.56657±0.00224	1213.34319±0.00211	958.28389±0.00303
448.06880±0.01816	1108.14741±0.01024	337.56657±0.00224	1240.89572±0.00416	981.38587±0.00477
458.42534±0.01954	1128.80557±0.01898	358.90489±0.00228	1254.68113±0.00281	1073.73237±0.00217
468.71871±0.00985	1139.08576±0.01882	372.69242±0.00221	1268.46175±0.00161	1142.99351±0.00424
479.06107±0.01195	1149.39509±0.02059	386.47399±0.00224	1282.24807±0.00185	1166.09435±0.00502
489.32477±0.01240	1170.02484±0.01307	414.03936±0.00188	1296.02377±0.00257	1189.18306±0.00352
509.97820±0.01444	1180.34646±0.01704	427.81517±0.00240	1309.80228±0.00198	1212.27453±0.00191
520.29576±0.01286	1190.66161±0.01759	469.16591±0.00245	1323.58892±0.00166	1235.36836±0.00368
530.64900±0.01046*	1200.98622±0.01705	482.93674±0.00261	1364.92964±0.00252	1258.45747±0.00330
540.89551±0.01345	1221.60140±0.01428	496.72271±0.00322	1378.71091±0.00204	1281.54282±0.00419
551.21595±0.01603	1231.90599±0.01844	510.49745±0.00182	1392.49762±0.00311	1327.72877±0.00212
561.53131±0.01220	1242.23411±0.01937	524.28649±0.00244	1406.27306±0.00251	1373.91321±0.00170
571.84046±0.01392	1252.57897±0.02116	538.06429±0.00185	1433.83402±0.00231	1396.99052±0.00283
582.17781±0.01054	1262.84891±0.02335	551.84901±0.00219	1447.61464±0.00223	1443.17833±0.00318
592.47561±0.01480	1273.19155±0.01717	579.40750±0.00221	1461.39945±0.00302	1466.27118±0.00365
602.78923±0.01425	1283.49165±0.01618	593.18526±0.00196	1475.17987±0.00450	1489.35757±0.00347
613.08427±0.01595	1293.77245±0.01799	606.97103±0.00241	1488.95524±0.00212	1512.45493±0.00353*
	1304.09485±0.01510	620.75436±0.00195		
	1314.43639±0.01590	634.53308±0.00183		

All times are expressed in days since BJD 2,454,900. Estimated uncertainties give 68% confidence limits. Outliers beyond 3σ in the residuals of dynamical fits are marked with an asterisk.

Extended Data Table 2 | Confidence intervals from distributions found with differential evolution Markov Chain Monte Carlo TTV analysis.

Param. \ Conf. Int.	68.3%	95.4%	99.7 %
P (days) b	10.3126 ^{+0.0004} _{-0.0006}	^{+0.0006} _{-0.0010}	^{+0.0007} _{-0.0014}
c	13.7813 ^{+0.0001} _{-0.0001}	^{+0.0002} _{-0.0002}	^{+0.0002} _{-0.0004}
d	23.0881 ^{+0.0009} _{-0.0008}	^{+0.0016} _{-0.0012}	^{+0.0022} _{-0.0013}
T₀ b	788.4142 ^{+0.0027} _{-0.0027}	^{+0.0055} _{-0.0054}	^{+0.0084} _{-0.0081}
c	786.1289 ^{+0.0005} _{-0.0005}	^{+0.0010} _{-0.0010}	^{+0.0015} _{-0.0015}
d	796.6689 ^{+0.0013} _{-0.0013}	^{+0.0025} _{-0.0023}	^{+0.0035} _{-0.0026}
ecosω b	-0.011 ^{+0.096} _{-0.140}	^{+0.273} _{-0.300}	^{+0.383} _{-0.370}
c	-0.015 ^{+0.086} _{-0.126}	^{+0.249} _{-0.289}	^{+0.386} _{-0.390}
d	-0.037 ^{+0.060} _{-0.092}	^{+0.170} _{-0.210}	^{+0.255} _{-0.283}
esinω b	-0.024 ^{+0.075} _{-0.135}	^{+0.238} _{-0.316}	^{+0.335} _{-0.424}
c	-0.020 ^{+0.064} _{-0.117}	^{+0.205} _{-0.276}	^{+0.293} _{-0.369}
d	-0.057 ^{+0.053} _{-0.095}	^{+0.148} _{-0.226}	^{+0.239} _{-0.292}
$\frac{m_p}{m_\oplus} \frac{M_\odot}{M_*}$ b	0.129 ^{+0.121} _{-0.078}	^{+0.252} _{-0.108}	^{+0.363} _{-0.131}
c	3.846 ^{+3.771} _{-2.304}	^{+7.431} _{-3.029}	^{+10.003} _{-3.408}
d	1.282 ^{+1.362} _{-0.783}	^{+2.759} _{-1.027}	^{+3.667} _{-1.141}
M_b/M_c	0.0353 ^{+0.0136} _{-0.0125}	^{+0.0284} _{-0.0244}	^{+0.0447} _{-0.0359}
$e_c \cos \omega_c - e_b \cos \omega_b$	0.0038 ^{+0.0167} _{-0.0139}	^{+0.0389} _{-0.0487}	^{+0.0530} _{-0.0792}
$e_c \sin \omega_c - e_b \sin \omega_b$	-0.0033 ^{+0.0202} _{-0.0132}	^{+0.0469} _{-0.0379}	^{+0.0625} _{-0.0608}
$\omega_c - \omega_b$ (°)	-0.58 ^{+2.20} _{-2.41}	^{+10.66} _{-10.51}	^{+17.86} _{-16.78}
M_c/M_d	2.9586 ^{+0.4434} _{-0.3528}	^{+1.0303} _{-0.6369}	^{+1.7453} _{-0.8774}
$e_c \cos \omega_c - e_d \cos \omega_d$	0.0312 ^{+0.0391} _{-0.0205}	^{+0.1059} _{-0.0458}	^{+0.1845} _{-0.0664}
$e_c \sin \omega_c - e_d \sin \omega_d$	0.0186 ^{+0.0322} _{-0.0319}	^{+0.0874} _{-0.0750}	^{+0.1439} _{-0.1069}
$\omega_c - \omega_d$ (°)	3.31 ^{+9.11} _{-15.30}	^{+13.75} _{-20.34}	^{+14.62} _{-21.24}

We include the parameters of our dynamical fits, as well as the mass ratios and relative eccentricity vector components between the planets, which have tighter constraints than the absolute masses or eccentricity vector components.

A permanent, asymmetric dust cloud around the Moon

M. Horányi^{1,2,3}, J. R. Szalay^{1,2,3}, S. Kempf^{1,2,3}, J. Schmidt⁴, E. Grün^{1,3,5}, R. Srama⁶ & Z. Sternovsky^{1,3,7}

Interplanetary dust particles hit the surfaces of airless bodies in the Solar System, generating charged¹ and neutral² gas clouds, as well as secondary ejecta dust particles³. Gravitationally bound ejecta clouds that form dust exospheres were recognized by *in situ* dust instruments around the icy moons of Jupiter⁴ and Saturn⁵, but have hitherto not been observed near bodies with refractory regolith surfaces. High-altitude Apollo 15 and 17 observations of a 'horizon glow' indicated a putative population of high-density small dust particles near the lunar terminators^{6,7}, although later orbital observations^{8,9} yielded upper limits on the abundance of such particles that were a factor of about 10^4 lower than that necessary to produce the Apollo results. Here we report observations of a permanent, asymmetric dust cloud around the Moon, caused by impacts of high-speed cometary dust particles on eccentric orbits, as opposed to particles of asteroidal origin following near-circular paths striking the Moon at lower speeds. The density of the lunar ejecta cloud increases during the annual meteor showers, especially the Geminids, because the lunar surface is exposed to the same stream of interplanetary dust particles. We expect all airless planetary objects to be immersed in similar tenuous clouds of dust.

The Lunar Atmosphere and Dust Environment Explorer (LADEE) mission was launched on 7 September 2013. After reaching the Moon in about 30 days, it continued with an instrument checkout period of about 40 days at an altitude of 220–260 km. LADEE began its approximately 150 days of science observations at a typical altitude of 20–100 km, following a near-equatorial retrograde orbit, with a characteristic orbital speed of 1.6 km s^{-1} (ref. 10). The Lunar Dust Experiment (LDEX) began its measurements on 16 October 2013 and detected a total of approximately 140,000 dust hits during about 80 days of cumulative observation time out of 184 total days by the end of the mission on 18 April 2014. LDEX was designed to explore the ejecta cloud generated by sporadic interplanetary dust impacts, including possible intermittent density enhancements during meteoroid showers, and to search for the putative regions with high densities of $0.1\text{-}\mu\text{m}$ -scale dust particles above the terminators. The previous attempt to observe the lunar ejecta cloud by the Munich Dust Counter on board the HITEN satellite orbiting the Moon (15 February 1992 to 10 April 1993) did not succeed, owing to its distant orbit and low sensitivity¹¹.

LDEX is an impact ionization dust detector (Methods subsection 'The LDEX instrument'). When pointed in the direction of motion of the spacecraft, LDEX recorded average impact rates of about 1 and about 0.1 hits per minute of particles with impact charges of $q \geq 0.3$ and $q \geq 4 \text{ fC}$, corresponding to particles with radii of $a \gtrsim 0.3 \mu\text{m}$ and $a \gtrsim 0.7 \mu\text{m}$, respectively (Fig. 1). Approximately once a week, LDEX observed bursts of 10 to 50 particles in a single minute. Particles detected in a burst are most likely to originate from the same well-timed and well-positioned impact event that happened just minutes before their detection on the ground-track of LADEE. Several of the

yearly meteoroid showers generated sustained elevated levels of LDEX impact rates, especially those where the majority of the incoming meteoroids hit the lunar surface near the equatorial plane, greatly enhancing the probability of LADEE crossing their ejecta plumes. The Geminids generated the strongest enhancement in impact rates for ± 1.5 days centred around 14 December 2013.

The distribution of the detected impact charges remained largely independent of altitude, and throughout the entire mission it closely followed a power law: $p_q(q) \propto q^{-(1+\alpha)}$ (Fig. 2). This alone indicates that the initial mass distribution of the ejecta particles is, to a good approximation, independent of their initial speed and angular distributions (Methods subsection 'Dust ejecta clouds'), and that the number of ejecta particles generated on the surface per unit time with mass greater than m follows a power law: $N^+(>m) \propto m^{-\alpha}$. The LDEX measurements indicate $\alpha \approx 0.9$, surprisingly close to the value $\alpha_G = 0.8$ suggested by the Galileo mission at the icy moons of Jupiter¹²

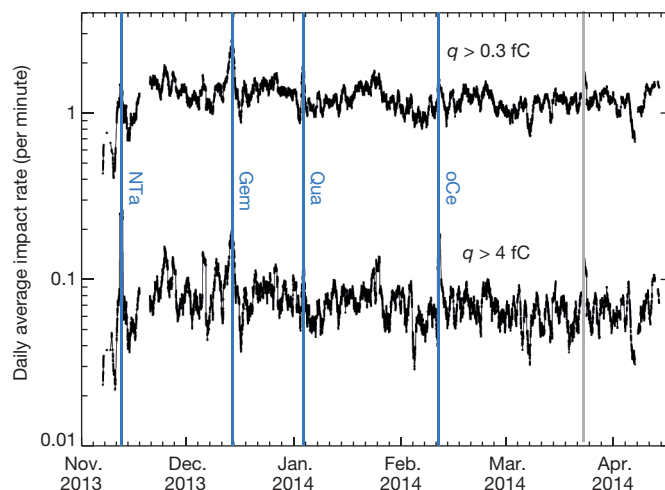


Figure 1 | Impact rates throughout the mission. The daily running average of impacts per minute of particles that generated an impact charge of $q \geq 0.3 \text{ fC}$ (radius $a \gtrsim 0.3 \mu\text{m}$) and $q \geq 4 \text{ fC}$ (radius $a \gtrsim 0.7 \mu\text{m}$) recorded by LDEX. The initial systematic increase until 20 November 2013 is due to transitions from the high-altitude checkout to the subsequent science orbits. Four of the several annual meteoroid showers generated elevated impact rates lasting several days. The labelled annual meteor showers are: the Northern Taurids (NTa); the Geminids (Gem); the Quadrantids (Qua); and the Omicron Centaurids (oCe). The observed enhancement peaking on 25 March 2014 (grey vertical line) does not coincide with any of the prominent showers. During the Leonids meteor shower around 17 November 2013, the instrument remained off due to operational constraints. From counting statistics, we determine that the daily average impact rate of particles generating a charge of at least 0.3 fC is 1.25 hits per minute and, hence, the 1σ relative error is about 2%, while for particles generating an impact charge $> 4 \text{ fC}$ the average rate is 0.08 hits per minute and, hence, the 1σ relative error is about 10%.

¹Laboratory for Atmospheric and Space Physics, University of Colorado, Boulder, Colorado 80303, USA. ²Department of Physics, University of Colorado, Boulder, Colorado 80309, USA. ³Institute for Modeling Plasma, Atmospheres, and Cosmic Dust (IMPACT), University of Colorado, Boulder, Colorado 80303, USA. ⁴Astronomy and Space Physics, University of Oulu, FI-90014 Oulu, Finland.

⁵Max-Planck-Institut für Kernphysik, D-69117 Heidelberg, Germany. ⁶Institut für Raumfahrtssysteme, Universität Stuttgart, Raumfahrtzentrum Baden-Württemberg, 70569 Stuttgart, Germany. ⁷Aerospace Engineering Sciences, University of Colorado, Boulder, Colorado 80309, USA.

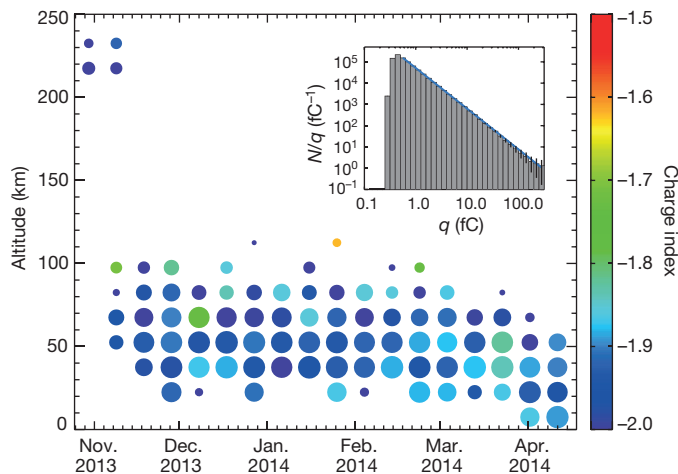


Figure 2 | Slope of the charge and mass distributions. The exponent of the power-law distributions of the impact charges $p_q(q) \propto q^{-(1+\alpha)}$ fitted to LDEX measurements as functions of altitude (15 km bins) and time (10 day bins). The colour indicates the value of the charge distribution index $-(1+\alpha)$, and the size of a circle is inversely proportional to its absolute uncertainty (largest circle: ± 0.1 ; smallest circle ± 0.5). The inset shows the impact charge distribution for all heights for the entire mission, resulting in a χ^2 minimizing fit²¹ of $\alpha = 0.910 \pm 0.003$.

and to laboratory experimental results of ejecta production from impacts¹³. The derived ejecta size distribution also represents the size distribution of the smallest lunar fines (very small particles) on the surface because most ejecta particles return to the Moon and comprise the regolith itself, unless these small particles efficiently conglomerate on the lunar surface into larger particles.

The characteristic velocities of dust particles in the cloud are of the order of hundreds of metres per second, which is small compared to typical spacecraft speeds of 1.6 km s^{-1} . Hence, with the knowledge of the spacecraft orbit and attitude, impact rates can be converted directly into particle densities as functions of time and position. This approach is expected to result in a relative error $< 20\%$, on the basis of a complete ejecta cloud model¹² (Extended Data Fig. 2). Both the derived average number density as a function of height, and the initial speed distribution match expectations only for altitudes $h \geq 50 \text{ km}$ (Extended Data Fig. 3). This indicates that, for the lunar surface, the

customary assumption of a simple power-law speed distribution with a single sharp cut-off minimum speed u_0 needs revision for speeds below about 400 m s^{-1} . At higher values the speed distribution follows a simple power law (Extended Data Table 1), as predicted by existing models¹². An ejecta plume opening cone angle of $\psi_0 \approx 30^\circ$ is consistent with our measurements, including those taken during the observed bursts of impacts. The average total mass of the dust ejecta cloud is estimated to be about 120 kg, approximately 0.5% of the neutral gas atmosphere¹⁴.

We found that the density distribution is not spherically symmetric around the Moon (Fig. 3), exhibiting a strong enhancement near the morning terminator between 5 and 7 h local time (LT), slightly canted towards the Sun from the direction of the motion of the Earth–Moon system about the Sun (6 LT). The observed anisotropy reflects the spatial and velocity distributions of the bombarding interplanetary dust particles (Extended Data Fig. 4) responsible for the generation of the ejecta clouds (Methods subsection ‘Dust production from impacts’). This observed anisotropy is in contrast to the roughly isotropic ejecta clouds engulfing the Galilean satellites, where the vast gravitational influence of Jupiter is efficiently randomizing the orbital elements of the bombarding interplanetary dust particles¹⁵. The anisotropic ejecta production is consistent with existing models of the interplanetary dust distributions near the Earth that combine *in situ* dust measurements, visible and infrared observations of the zodiacal cloud, as well as ground-based visual and radar observations of meteors in the atmosphere^{16,17}. The dust production on the lunar surface is dominated by particles of cometary origin, as opposed to slower asteroidal dust particles, which follow near-circular orbits as they migrate towards the Sun, owing to Poynting–Robertson drag¹⁸. Meteoroids that are of asteroidal origin would be able to sustain only a much weaker, more azimuthally symmetric ejecta cloud, contrary to LDEX observations.

In addition to bombardment by interplanetary dust, the exposure of airless surfaces to ultraviolet radiation and solar wind plasma flow could result in the lofting of small dust particles, owing to electrostatic charging and subsequent mobilization¹⁹. The charging processes are expected to be most efficient over the terminators, where strong localized electric fields could exist over the boundaries of lit and dark regions. High-altitude horizon glow observations near the lunar terminator suggested a population of grains, characteristically of radius $0.1 \mu\text{m}$, with a density of $n \approx 10^4 \text{ m}^{-3}$ at an altitude of $h = 10 \text{ km}$,

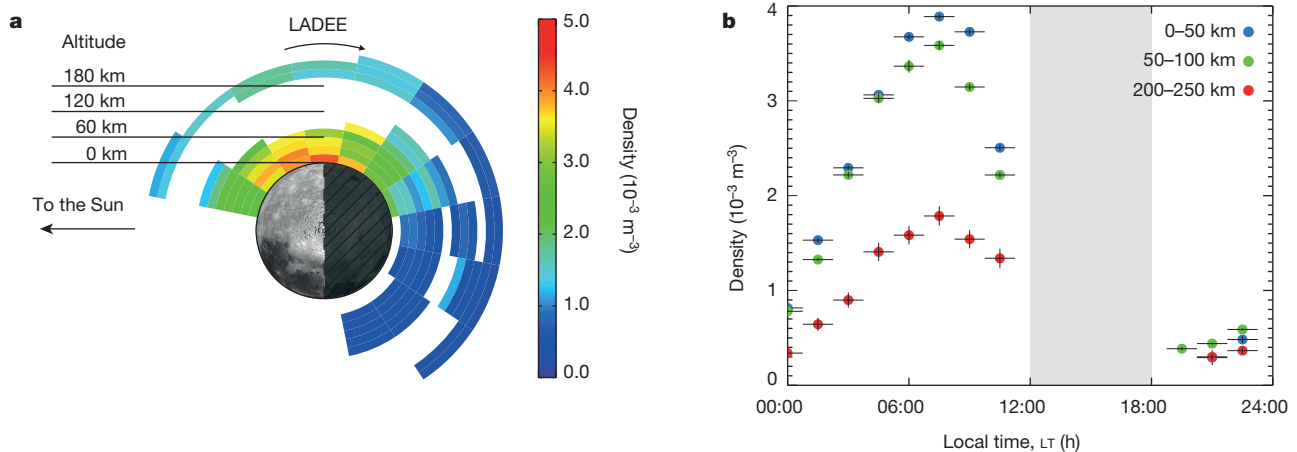


Figure 3 | Lunar dust density distribution. **a**, The top-down view of the dust density $n(a \geq 0.3 \mu\text{m})$ projected onto the lunar equatorial plane. While pointed near the direction of the motion of the spacecraft, LDEX did not make measurements between 12 and 18 LT. White colouring indicates regions where LADEE did not visit or was not set up for normal operations. **b**, The density as a

function of LT at three different altitude bins showing a persistent enhancement canted towards the Sun away from the direction of the orbital motion of the Earth–Moon system. Error bars were calculated by propagating the \sqrt{N} error through the density calculation, where N is the number of detected dust impacts.

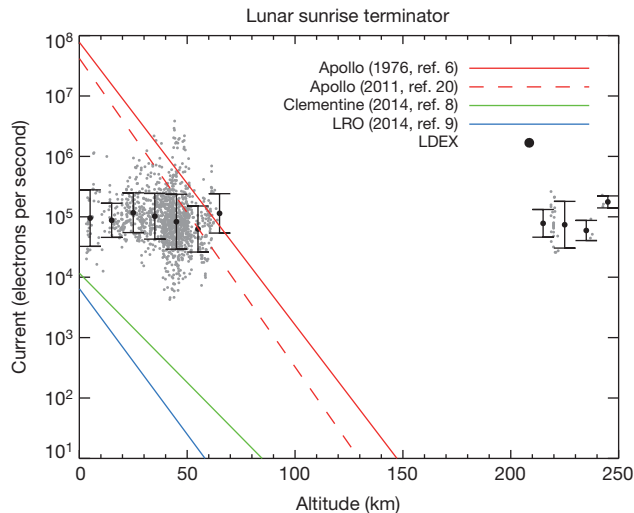


Figure 4 | LDEX current measurements. The accumulated charge collected by LDEX in $dt = 0.1$ s intervals (J_{dust}), averaged over the sunrise terminator between 5:30 and 6:30 LT. The coloured lines show the predicted value of J_{dust} based on the impacts of small particles alone using the upper limits of the dust densities estimated by remote sensing visible^{6,8,20} and ultraviolet⁹ observations. Error bars show 1σ on $\log J_{\text{dust}}$ as the current measurements are log-normally distributed. Because $J_{\text{dust}} \approx 10^5$ electrons per second is two orders of magnitude lower than the Apollo estimates near an altitude of 10 km and exhibits no altitude dependence, LDEX measurements show no evidence for the existence of the suggested relatively dense clouds of $0.1\text{-}\mu\text{m}$ -sized dust particles. LRO is the Lunar Reconnaissance Orbiter.

increasing towards the surface to $n = 5 \times 10^5 \text{ m}^{-3}$. Follow-up observations^{8,9} indicated a drastically lower upper-limit of the lofted dust densities. At an altitude of 10 km, our dust current measurements show an upper limit for the density of particles of radius $0.1 \mu\text{m}$ that is approximately two orders of magnitude below the Apollo estimates²⁰. However, the LDEX dust current measurements (Methods subsection ‘The LDEX instrument’) of $J_{\text{dust}} \approx 10^5$ electrons per second (Fig. 4) remained independent of altitude and, hence, gave no indication of the relatively dense cloud of $0.1\text{-}\mu\text{m}$ -sized dust that was inferred from the Apollo observations over the lunar terminators.

Online Content Methods, along with any additional Extended Data display items and Source Data, are available in the online version of the paper; references unique to these sections appear only in the online paper.

Received 7 October 2014; accepted 15 April 2015.

1. Auer, S. & Sitte, K. Detection technique for micrometeoroids using impact ionization. *Earth Planet. Sci. Lett.* **4**, 178–183 (1968).
2. Collette, A., Sternovsky, Z. & Horányi, M. Production of neutral gas by micrometeoroid impacts. *Icarus* **227**, 89–93 (2014).

3. Hartmann, W. K. Impact experiments: 1. Ejecta velocity distributions and related results from regolith targets. *Icarus* **63**, 69–98 (1985).
4. Krüger, H., Krivov, A., Hamilton, D. & Grün, E. Detection of an impact-generated dust cloud around ganymede. *Nature* **399**, 558–560 (1999).
5. Spahn, F. *et al.* Cassini dust measurements at Enceladus and implications for the origin of the E ring. *Science* **311**, 1416–1418 (2006).
6. McCoy, J. E. Photometric studies of light scattering above the lunar terminator from Apollo solar corona photography. *Proc. Lunar Sci. Conf.* **7**, 1087–1112 (1976).
7. Zook, H. A. & McCoy, J. E. Large scale lunar horizon glow and a high altitude lunar dust exosphere. *Geophys. Res. Lett.* **18**, 2117–2120 (1991).
8. Glenar, D. A., Stubbs, T. J., Hahn, J. M. & Wang, Y. Search for a high-altitude lunar dust exosphere using Clementine navigational star tracker measurements. *J. Geophys. Res. Planets* **119**, 2548–2567 (2014).
9. Feldman, P. D. *et al.* Upper limits for a lunar dust exosphere from far-ultraviolet spectroscopy by LRO/LAMP. *Icarus* **233**, 106–113 (2014).
10. Elphic, R. C. *et al.* The Lunar Atmosphere and Dust Environment Explorer mission. *Space Sci. Rev.* **185**, 3–25 (2014).
11. Iglseider, H., Uesugi, K. & Svedhem, H. Cosmic dust measurements in lunar orbit. *Adv. Space Res.* **17**, 177–182 (1996).
12. Krivov, A. V., Sremčević, M., Spahn, F., Dikarev, V. V. & Kholoshevnikov, K. V. Impact-generated dust clouds around planetary satellites: spherically symmetric case. *Planet. Space Sci.* **51**, 251–269 (2003).
13. Buhl, E., Sommer, F., Poelchau, M. H., Dresen, G. & Kenkmann, T. Ejecta from experimental impact craters: particle size distribution and fragmentation energy. *Icarus* **237**, 131–142 (2014).
14. Stern, S. A. The lunar atmosphere: history, status, current problems, and context. *Rev. Geophys.* **37**, 453–492 (1999).
15. Sremčević, M., Krivov, A. V., Krüger, H. & Spahn, F. Impact-generated dust clouds around planetary satellites: model versus Galileo data. *Planet. Space Sci.* **53**, 625–641 (2005).
16. McNamara, H. *et al.* Meteoroid Engineering Model (MEM): a meteoroid model for the inner Solar System. *Earth Moon Planets* **95**, 123–139 (2004).
17. Dikarev, V. *et al.* The new ESA meteoroid model. *Adv. Space Res.* **35**, 1282–1289 (2005).
18. Nesvorný, D. *et al.* Dynamical model for the zodiacal cloud and sporadic meteors. *Astrophys. J.* **743**, 129 (2011).
19. Rennilson, J. J. & Criswell, D. R. Surveyor observations of lunar horizon-glow. *Moon* **10**, 121–142 (1974).
20. Glenar, D. A., Stubbs, T. J., McCoy, J. E. & Vondrak, R. R. A reanalysis of the Apollo light scattering observations, and implications for lunar exospheric dust. *Planet. Space Sci.* **59**, 1695–1707 (2011).
21. Markwardt, C. B. in *Astronomical Data Analysis Software and Systems XVIII* (eds Bohlender, D. A., Durand, D. & Dowler, P.) *ASP Conf. Ser.* **411**, 251 (2009); preprint at <http://arxiv.org/abs/0902.2850>.

Acknowledgements The LADEE/LDEX project was supported by NASA. Tests and calibrations were done at the dust accelerator facility of the University of Colorado, supported by NASA’s Solar System Exploration Research Virtual Institute (SSERVI). We are grateful for engineering and technical support from the Laboratory for Atmospheric and Space Physics (LASP), especially from M. Lankton (project manager), S. Gagnard and D. Gathright (mission operations), and D. James (calibration).

Author Contributions M.H. was the instrument principal investigator, directed the data analysis, and was primarily responsible for writing this paper. J.R.S. developed the data analysis software. S.K. was responsible for the calibration of the instrument and contributed to the data analysis. J.S. led the modelling effort. E.G. and R.S. contributed to the analysis and interpretation of the data. Z.S. designed the instrument and contributed to the data analysis.

Author Information Reprints and permissions information is available at www.nature.com/reprints. The authors declare no competing financial interests. Readers are welcome to comment on the online version of the paper. Correspondence and requests for materials should be addressed to M.H. (horanyi@colorado.edu).

METHODS

The LDEX instrument. The Lunar Dust Experiment (LDEX) is an impact ionization dust detector, which measures both the positive and negative charges of the plasma cloud generated when a dust particle strikes its target²². The amplitude and shape of the waveforms (signal versus time) recorded from each impact are used to estimate the mass of the dust particles. The instrument has a total sensitive area of 0.01 m², which gradually decreases to zero for particles arriving from outside its dust field-of-view of $\pm 68^\circ$ off from the normal direction. LDEX is sensitive to ultraviolet; hence, its operations, in general, excluded the Sun in its optical field-of-view of $\pm 90^\circ$.

Particles below the single impact detection threshold generate a plasma cloud in the same way as larger impacts, but without triggering a full waveform capture. Their collective signal is integrated independently of the impacts of large particles. In addition to small dust particles, the integrated ion signal is also sensitive to a number of possible background contributions, most importantly ultraviolet photons scattering into the ion detector, generating photoelectrons. To identify the background contributions in the collective signal, the acceleration potential between the target and ion collector is intermittently switched from its nominal -200 V to $+30$ V, making the instrument 'blind' to dust. The contributors to the current in nominal mode (J_N) are ions from dust impacts, photoelectrons and low- and high-energy ions. In switched mode (J_S) the contributors are photoelectrons and high-energy ions. High energy in this case indicates >30 eV, as these ions can reach the microchannel plate even in switched mode. Hence, the difference $J_N - J_S$ represents the collective signal of small dust particles and low-energy ions only. Each dust particle with a radius of 0.1 μm and impact speed of 1.6 km s⁻¹ is expected to generate²³ $Q_i \approx 100e$. Their collective current is $J_{\text{dust}} \approx AvnQ_i$, where A is the detector sensitive area, v is the speed of dust particle relative to the spacecraft, and n is the density of the small particles. Hence, attributing $J_N - J_S$ to small dust particles alone allows us to set an upper limit for n . Alternatively, estimates for n from independent observations can be used to predict J_{dust} , which we can then compare to our measurements. The low-energy ion contribution may be due to back-scattered solar wind protons²⁴, energetic neutral atoms^{25,26} and the lunar ionosphere²⁷. Any contribution of low-energy ions to $J_N - J_S$ would further reduce our estimate of n .

Dust ejecta clouds. We compare the steady state, spherically symmetric model of a dust cloud¹² to the LT-averaged LDEX observations. The phase space density of dust above the surface based on a model for an impact-generated ejecta cloud can be written as^{12,28}

$$n(v, \theta, \phi; r) = \frac{N^+}{8\pi^2 R r} \frac{f_u(u(v)) f_\psi(\psi(v, \theta))}{v u(v)^2 \sin \theta \cos \psi(v, \theta)} \quad (1)$$

Here, the variables v , θ , ϕ denote the velocity vector of dust grains at a radial distance r from the Moon (lunar radius $R = 1,737$ km). The distance r is regarded as a parameter of the distribution, not a variable. Further, θ is the angle between the velocity vector and the radial direction and ϕ is the velocity azimuth angle (anti-clockwise around the radius vector). The distribution does not depend explicitly on ϕ for a spherically symmetric cloud. We retain the azimuthal dependence to perform averages over quantities that do depend on ϕ . N^+ is the total rate of grains produced on the surface. We denote by u the starting speed of ejecta on the surface and by ψ the ejection cone angle measured from the surface normal. Using the conservation of energy and angular momentum of the two-body problem we have $\psi = \psi(v, \theta)$ and $u = u(v)$. For the distribution of starting velocities, f_u , we use a power law with exponent μ (equivalent to $\gamma + 1$ in other customary notation¹²), normalized to unity in the range $u \in [u_0, \infty]$:

$$f_u(u) = \frac{\mu - 1}{u_0^{1-\mu}} u^{-\mu}$$

For the ejecta cone angles, we use a uniform distribution, f_ψ , normalized to unity in the range $\psi \in [0, \psi_0]$:

$$f_\psi(\psi) = \frac{\sin \psi}{1 - \cos \psi_0}$$

The mass distribution of the grains is uncorrelated with the velocity and is described as a power law that is normalized to the total rate of mass production in the range $m \in [m_{\min}, m_{\max}]$ (refs 12 and 18). The generalized version of equation (1) becomes

$$n(m, v, \theta, \phi; r) = \frac{M^+}{8\pi^2 R r} \frac{1 - \alpha}{m_{\max}^{1-\alpha} - m_{\min}^{1-\alpha}} m^{-(1+\alpha)} \frac{f_u(u(v)) f_\psi(\psi(v, \theta))}{v u(v)^2 \sin \theta \cos \psi(v, \theta)} \quad (2)$$

where M^+ denotes the total mass production rate that is related to N^+ as

$$N^+ = M^+ \frac{1 - \alpha}{\alpha} \frac{m_{\min}^{-\alpha} - m_{\max}^{-\alpha}}{m_{\max}^{1-\alpha} - m_{\min}^{1-\alpha}}$$

The exponent is expected^{12,30} to be in the range $0.5 \leq \alpha \leq 1$. Equation (2) gives the number of particles found at distance r from the centre of the moon in the phase space volume element $d^3v d^3r dm$.

When a grain of mass m hits the dust detector at a velocity v it produces an impact charge²⁹

$$q = cmv^\beta \quad (3)$$

The combination of equations (2) and (3) can be used to estimate the distribution of charges to be recorded by LDEX in the following manner.

Typically the LADEE spacecraft followed a nearly circular orbit around the moon with speed v_{sc} relative to the surface. The boresight of LDEX pointed in the direction of spacecraft motion (apex) so that the detector encountered dust grains of velocity \mathbf{v} at a relative velocity $\mathbf{v}_{\text{sc}} - \mathbf{v}$. The number of grains ΔN with velocity in d^3v and mass in dm , that can reach the detector during time Δt , is given by the number of such grains found in a cylindrical volume spanned by the detector surface A and the relative velocity vector (Extended Data Fig. 1)

$$\Delta N = A \Delta t d^3v dm A(\omega) \cos \omega \Theta_H(\cos \omega) n(m, v, \theta, \phi; r) |\mathbf{v} - \mathbf{v}_{\text{sc}}| \quad (4)$$

where ω is the angle between the boresight and the relative velocity vector. The Heaviside function, $\Theta_H(\cos \omega)$, guarantees that we count only grains that can enter the detector. With $A(\omega)$ we account for the fact that the effective detector area of LDEX depends on the angle ω . The effective area is maximal for $\omega = 0$, dropping to zero for $\omega = 68$ degrees (ref. 22). We evaluate $\cos \omega$ in terms of the spacecraft and dust velocities, as well as the angles ϕ , θ by noting that for a circular spacecraft orbit

$$\cos \omega = \frac{v_{\text{sc}} - v \sin \theta \cos \phi}{|\mathbf{v} - \mathbf{v}_{\text{sc}}|} \quad (5)$$

Dividing (4) by Δt we obtain the differential rate $d\gamma$ of particles that impact the detector

$$d\gamma = dv v^2 d\theta d\phi \sin \theta dm A(\omega) (v_{\text{sc}} - v \sin \theta \cos \phi) \Theta_H(v_{\text{sc}} - v \sin \theta \cos \phi) n(m, v, \theta, \phi; r) \quad (6)$$

where $A(\omega)$ is expressed with equation (5) as a function of v , θ , ϕ . We re-arrange the right-hand side of (6) into a mass and a velocity distribution as

$$d\gamma = dv d\theta d\phi dm p_m(m) p(v, \theta, \phi; r, \psi_0, \mu, u_0)$$

where

$$p_m(m) = M^+ \frac{1 - \alpha}{m_{\max}^{1-\alpha} - m_{\min}^{1-\alpha}} m^{-(1+\alpha)} \Theta_H(m - m_{\min}) \Theta_H(m_{\max} - m) \quad (7)$$

and

$$p(v, \theta, \phi; r, \psi_0, \mu, u_0) = \frac{A(\omega)}{8\pi^2 R r} (v_{\text{sc}} - v \sin \theta \cos \phi) \Theta_H(v_{\text{sc}} - v \sin \theta \cos \phi) v^{\frac{f_u(u(v)) f_\psi(\psi(v, \theta))}{u(v)^2 \cos \psi(v, \theta)}}$$

We define

$$p_v(v) = \int_0^\pi d\theta \int_0^{2\pi} d\phi p(v, \theta, \phi; r, \psi_0, \mu, u_0)$$

Using equation (3) we can then $\pi \pi$ express the model prediction for the distribution of charges detected by LDEX as

$$p_q(q) = \int d\gamma \delta(q - mc v^\beta) = \int_0^\infty dm p_m(m) \int_0^\infty dv p_v(v) \delta(q - mc v^\beta) = \int_0^\infty dv \frac{p_v(v)}{c v^\beta} p_m\left(\frac{q}{c v^\beta}\right)$$

Inserting equation (7) and sorting terms gives

$$p_q(q) = \frac{M^+}{m_{\max}} \frac{1 - \alpha}{1 - \left(\frac{m_{\min}}{m_{\max}}\right)^{1-\alpha}} \frac{1}{q} \left(\frac{cm_{\max}}{q}\right)^\alpha \int_{v_{\min}(q)}^{v_{\max}(q)} dv p_v(v) v^{2\beta} \quad (8)$$

where the boundaries

$$v_{\min}(q) = \left(\frac{q}{cm_{\max}} \right)^{1/\beta}, \quad v_{\max} = \left(\frac{q}{cm_{\min}} \right)^{1/\beta}$$

follow from the normalization of the mass distribution, equation (7).

Evaluating $p_v(v)$ shows that the integral in equation (8) depends only weakly on the charge q via the boundaries. Quantitatively,

$$0.13 < \frac{\int_{v_{\min}(q)}^{v_{\max}(q)} dv p_v(v) v^{2\beta}}{\int_0^{\infty} dv p_v(v) v^{2\beta}} < 0.23$$

when changing q from 0.1 fC to 1,000 fC. Therefore, the distribution $p_q(q)$ is dominated by far by the power law, so that we expect to see

$$p_q(q) \propto q^{-(1+\alpha)}$$

in the data. Hence, measuring the exponent of the impact charge distribution yields the exponent of the mass distribution of the particles recorded by LDEX.

Dust production from impacts. Extended Data Fig. 3 and Extended Data Table 1 were generated assuming that the LT-averaged ejecta cloud is spherically symmetric to determine the bulk properties of the cloud and allow for direct comparison with previous studies^{12,30}. Here we address the anisotropic nature of the dust influx to the lunar surface. To this end we replace the single global dust mass production M^+ with an LT- and time (t)-dependent function of mass production per unit surface area $M^+(\text{LT}, t)$.

The mass flux of bombarding interplanetary dust particles with mass m and velocity v is a function of both the position on the lunar surface and time: $F(m, v, \text{LT}, t)$. A single dust particle striking a pure silica surface generates a large number of ejecta particles with a total mass $m^+ = mY(m, v)$, where the yield, $Y \sim m^{0.2} v^{2.5}$, is determined on the basis of laboratory experiments³¹. The mass flux of impactors is dominated by particles with characteristic mass $m_0 \approx 10^{-8}$ kg (about 100 μm in radius)³². Our detected impacts are dominated by ejecta particles generated along the ground track of the spacecraft that followed a nearly equatorial orbit. Hence, it is convenient to track the position on the lunar surface in LT, with LT = 0, 6, 12, 18 marking midnight, the dawn terminator, the sub-solar point and the dusk terminator, respectively. The mass production rate per surface area as function of LT is found by integrating the product of the interplanetary dust flux F and the yield Y around the lunar equator

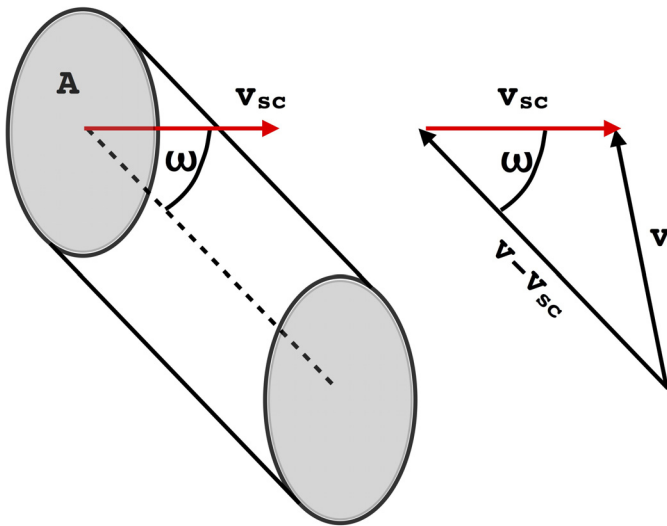
$$M^+(\text{LT}, t) = \iint F(m, v, \text{LT}, t) Y(m, v) dm dv \quad (9)$$

We evaluated equation (9) using both NASA's MEM¹⁶ and ESA's IMEM¹⁷ models, which agree well near one astronomical unit. The flux F and the predicted mass production rates $M^+(\text{LT}, t)$ are shown in Extended Data Fig. 4, and are consistent with the asymmetric dust ejecta cloud observed by LDEX. We note that the meteoroid population still remains one of the most uncertain space environment components³³.

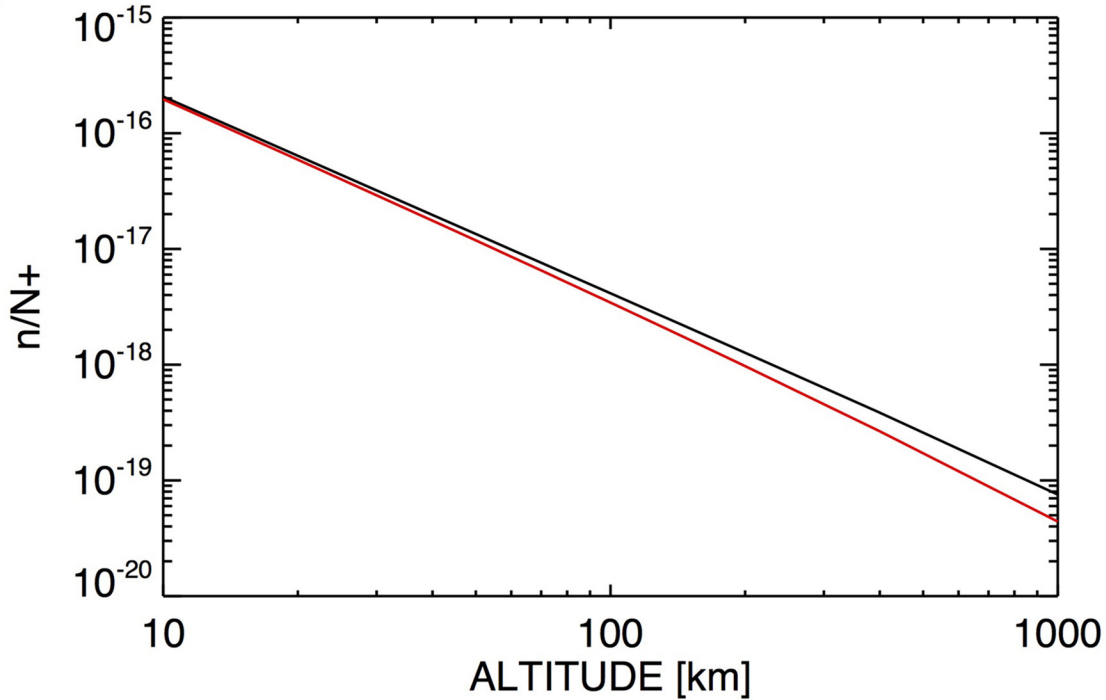
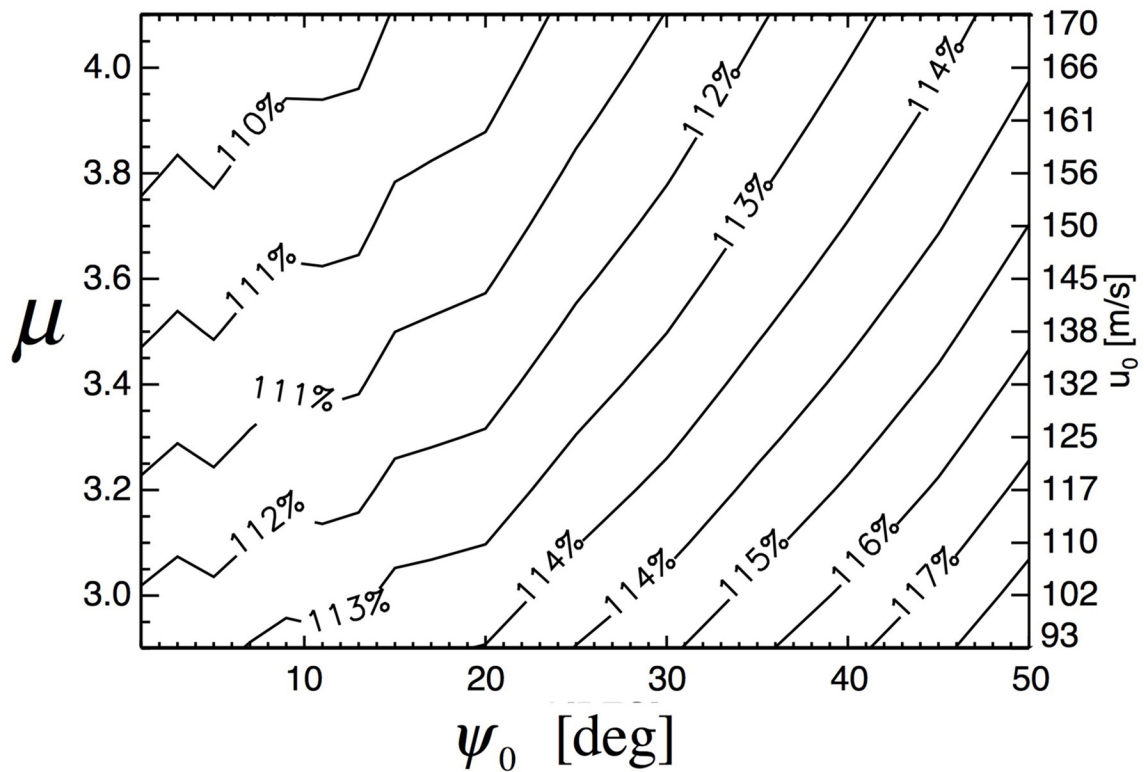
Data availability. All LDEX data are available through NASA's Planetary Data System (<http://sbn.psi.edu/pds/resource/ldex.html>).

Code availability. The code used for calculating the flux of interplanetary dust particles reaching the lunar surfaces is available upon request from NASA (<http://www.nasa.gov/offices/meo/software>).

22. Horányi, M. *et al.* The Lunar Dust Experiment (LDEX) onboard the Lunar Atmosphere and Dust Environment Explorer (LADEE) mission. *Space Sci. Rev.* **185**, 93–113 (2014).
23. Dietzel, H. *et al.* The HEOS 2 and HELIOS micrometeoroid experiments. *J. Phys. E* **6**, 209–217 (1973).
24. Saito, Y. *et al.* Solar wind proton reflection at the lunar surface: low energy ion measurement by MAP-PACE onboard SELENE (KAGUYA). *Geophys. Res. Lett.* **35**, L24205 (2008).
25. Saul, L. *et al.* Solar wind reflection from the lunar surface: the view from far and near. *Planet. Space Sci.* **84**, 1–4 (2013).
26. Allegrini, F. *et al.* Lunar energetic neutral atom (ENA) spectra measured by the interstellar boundary explorer (IBEX). *Planet. Space Sci.* **85**, 232–242 (2013).
27. Poppe, A. R., Halekas, J. S., Szalay, J. R., Horányi, M. & Delory, G. T. Model-data comparisons of LADEE/LDEX observations of low-energy lunar dayside ions. *Lunar Planet. Sci. Conf. Abstr.* **45**, 1393 (2014).
28. Sremčević, M., Krivov, A. V. & Spahn, F. Impact-generated dust clouds around planetary satellites: asymmetry effects. *Planet. Space Sci.* **51**, 455–471 (2003).
29. Auer, S. in *Interplanetary Dust* (eds Grün, E., Gustafson, B., Dermott, S. & Fechtig, H.) 387–438 (Springer, 2001).
30. Krüger, H., Krivov, A. V. & Grün, E. A dust cloud of Ganymede maintained by hypervelocity impacts of interplanetary micrometeoroids. *Planet. Space Sci.* **48**, 1457–1471 (2000).
31. Koschny, D. & Grün, E. Impacts into ice-silicate mixtures: ejecta mass and size distributions. *Icarus* **154**, 402–411 (2001).
32. Grün, E., Zook, H. A., Fechtig, H. & Giese, R. H. Collisional balance of the meteoritic complex. *Icarus* **62**, 244–272 (1985).
33. Drolshagen, G. *Comparison of Meteoroid Models*. IADC Report No. 24.1 (Inter-Agency Space Debris Coordination Committee, 2009).

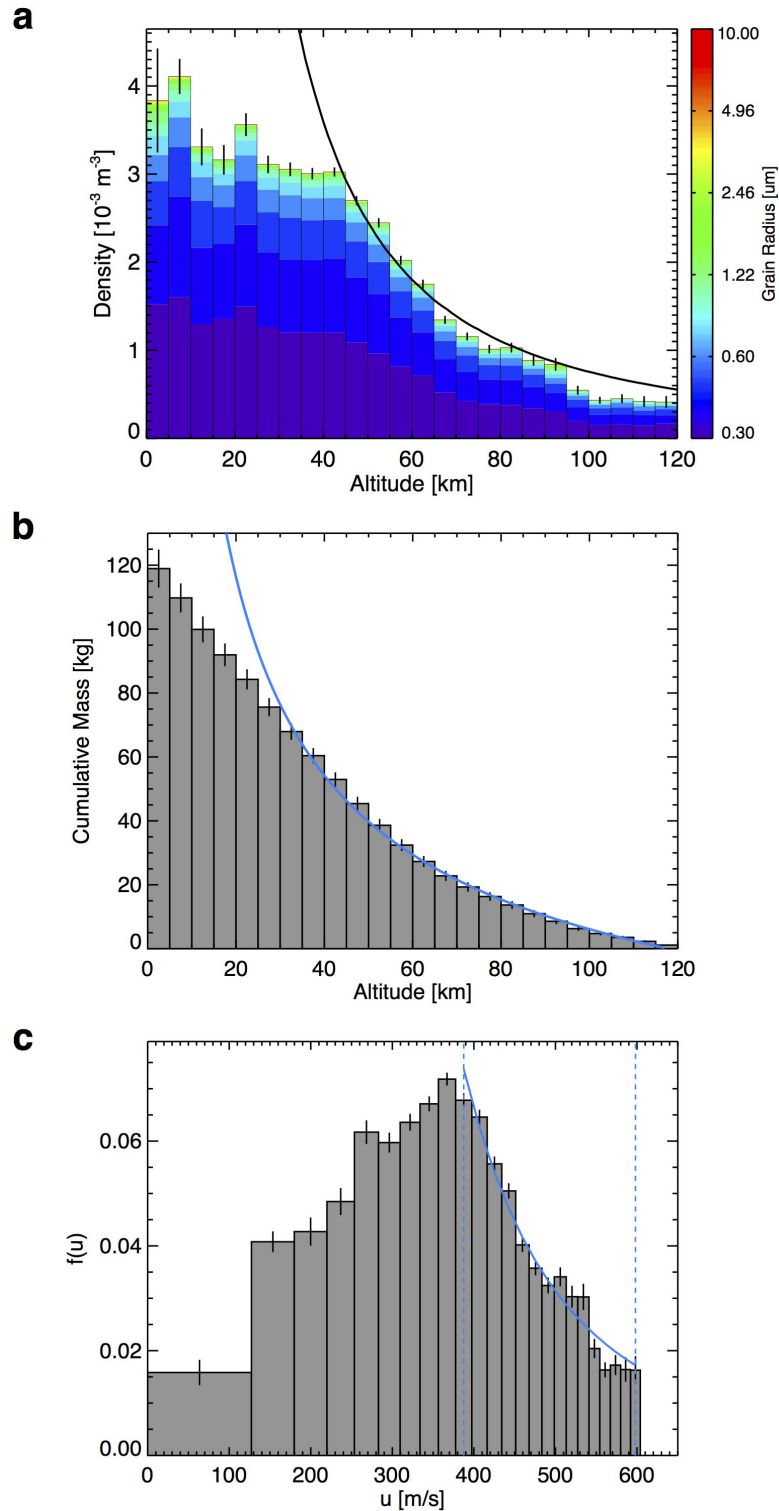


Extended Data Figure 1 | Detection geometry. A particle of velocity \mathbf{v} is recorded by a detector of sensitive area A . The surface normal of the detector area points along the velocity vector of the spacecraft \mathbf{v}_{sc} . The particle enters the instrument with an angle ω measured between the instrument boresight and the relative velocity vector of the particle $\mathbf{v}_{sc} - \mathbf{v}$.

a**b**

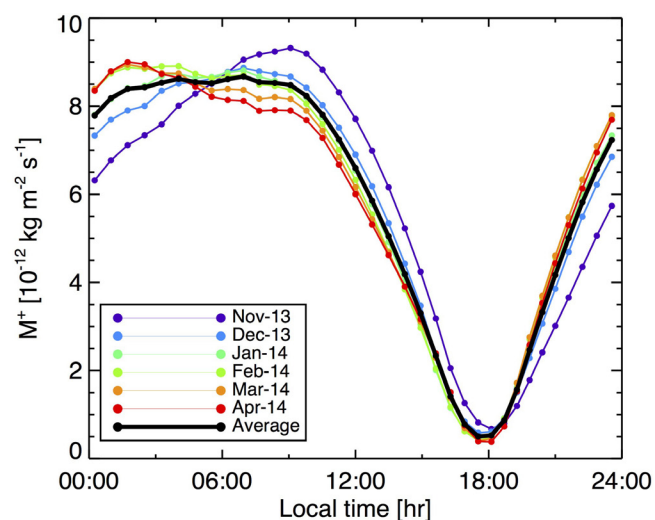
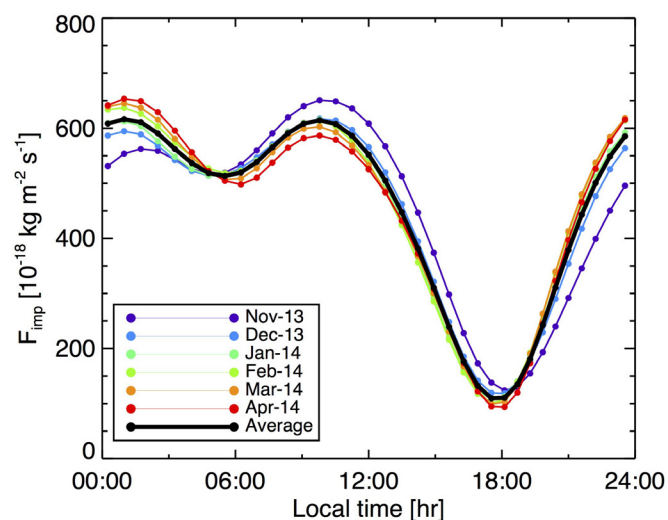
Extended Data Figure 2 | Systematic approximation error and its dependence on ejection parameters. **a**, The calculated density for a standard set of parameters listed in Extended Data Table 1 for the model ejecta cloud¹² as function of altitude (black line) normalized to the production rate N^+ . The density is recalculated using $n = \gamma/(A v_{sc})$ (red line), the approach taken in this paper to infer the dust density from the measured impact rates γ , indicating an

underestimate of $<20\%$ for altitudes below 100 km. **b**, Contour plot of the ratio of the 'true' model density over the recalculated density at the altitude $h = 50$ km, as a function of the opening cone angle of the ejecta plume ψ_0 and the exponent of the power-law initial-speed distribution μ , appropriately setting the minimum speed u_0 , while keeping the maximum speed constant at $2v_{escape}$, maintaining a constant total kinetic energy of the ejecta particles.



Extended Data Figure 3 | Comparison of observed and modelled cloud properties. **a**, The dust density $n(h)$ of the lunar ejecta cloud as function of altitude and size (colour scale). The continuous black line shows the model prediction¹² using the best-fit parameters listed in Extended Data Table 1. **b**, The cumulative dust mass in the lunar exosphere. The continuous blue line shows the ejecta model prediction (Extended Data Table 1). **c**, The initial

normalized vertical velocity distribution $f(u)$ calculated from $n(h)$ using energy conservation. The continuous line shows $f(u) \propto u^{-3.4 \pm 0.1}$ matched to the data at $u \geq 400$ m s⁻¹ (altitude $h \approx 50$ km). Error bars were calculated by propagating the \sqrt{N} error through the various calculations, where N is the number of detected dust impacts.



Extended Data Figure 4 | Modelled flux and mass production in the lunar equatorial plane. **a**, The calculated flux of interplanetary dust particles F_{imp} reaching the lunar equatorial region as a function of LT and t (colour coded for

monthly averages). **b**, The mass production rate, equation (9), calculated using a model for the spatial and velocity distributions of interplanetary dust particles near the Earth¹⁶, consistent with the observed asymmetric dust cloud.

Extended Data Table 1 | Parameters of the theoretical ejecta cloud model¹² for the Moon

Parameter	Definition	Value
mass distribution	$N^+(\geq m) \propto m^{-\alpha}$	$\alpha = 0.91 \pm 0.003$
smallest mass*	m_{min}	$3 \cdot 10^{-16}$ kg
largest mass**	m_{max}	10^{-8} kg
speed distribution	$f_u(u) \propto u^{-\mu}$	$\mu = 3.4 \pm 0.1$
minimum speed	u_0	130 m/s
maximum speed	$u_{max} = 2 \cdot v_{escape}$	4.8 km/s
impactor speed	v_{imp}	20 km/s
ratio of ejecta/impactor kinetic energy	K_e/K_i	20%
ratio of ejecta/impactor mass	Y	1000
initial velocity maximum cone angle	ψ_0	30°

*radius $a_{min} = 0.3 \mu\text{m}$; ** $a_{max} = 100 \mu\text{m}$

These parameters form a consistent set, and are not independent of each other³⁰.

Multiple complexation of CO and related ligands to a main-group element

Holger Braunschweig¹, Rian D. Dewhurst¹, Florian Hupp¹, Marco Nutz¹, Krzysztof Radacki¹, Christopher W. Tate¹, Alfredo Vargas² & Qing Ye¹

The ability of an atom or molecular fragment to bind multiple carbon monoxide (CO) molecules to form multicarbonyl adducts is a fundamental trait of transition metals. Transition-metal carbonyl complexes are vital to industry, appear naturally in the active sites of a number of enzymes (such as hydrogenases), are promising therapeutic agents¹, and have even been observed in interstellar dust clouds². Despite the wealth of established transition-metal multicarbonyl complexes³, no elements outside groups 4 to 12 of the periodic table have yet been shown to react directly with two or more CO units to form stable multicarbonyl adducts. Here we present the synthesis of a borylene dicarbonyl complex, the first multicarbonyl complex of a main-group element prepared using CO. The compound is additionally stable towards ambient air and moisture. The synthetic strategy used—liberation of a borylene ligand from a transition metal using donor ligands—is broadly applicable, leading to a number of unprecedented monovalent boron species with different Lewis basic groups. The similarity of these compounds to conventional transition-metal carbonyl complexes is demonstrated by photolytic liberation of CO and subsequent intramolecular carbon–carbon bond activation.

The ubiquity and utility of transition-metal carbonyl complexes can be attributed partly to CO's combination of high-lying filled and low-lying vacant orbitals, which allows it to take advantage of the versatile *d*-orbital arrangement of transition metals and thus engage in synergic σ bonding and π backbonding. In contrast, surprisingly few non-*d*-block elements form monoadducts with CO; they include a handful of complexes of uranium⁴, phosphorus⁵, boranes (BR₃)⁶, polyboranes⁷, and certain carbenes⁸. Only two multicarbonyls of the elements of the *s* and *p* blocks have been crystallographically characterized^{9,10}: carbon suboxide (OCCC O) and the cation in the salt [OCNCO]⁺[Sb₃F₁₆][−]. However, neither can be prepared by carbonylation of the central atom with CO itself.

The relatively recent realization that low-valent main-group species can act as synthetic mimics of transition-metal species has led to a flourishing area of chemistry centred around their synthesis and use as reagents for small-molecule activation^{11–18}. Double Lewis-base adducts of main-group elements have recently attracted theoretical interest in the literature with the development of the concept of ‘carbones’, twofold Lewis adducts of a single carbon atom of the form L→C←L (where L is a Lewis base)^{19,20}. In a similar manner, the synthesis of twofold base adducts of monovalent boron extended this concept to elements beyond carbon^{21–24}, and more recently analogous ‘-ones’ of heavier group 14 elements have also been realized²⁵. This rethinking of the bonding in main-group compounds in terms of bonding between a Lewis donor and a Lewis acceptor has recently spurred heated debate in the literature^{26–28}.

While earlier reports on carbon suboxide and its cationic nitrogen analogue presume a cumulenec (O = C = E = C = O) (where E is C or N) structure^{9,10}, Frenking and co-workers have suggested that these compounds might be better considered as Lewis adducts (OC→E←CO). In contrast, they predicted that the hypothetical

borylene dicarbonyl HB(CO)₂ would contain much more E→CO π backbonding than in the carbon and nitrogen dicarbonyls (when E is boron, π backbonding is 33.8% of the total bonding energy, whereas it is 5.2% and 10.0% for nitrogen and carbon, respectively)²⁰, making the boron analogue much more akin to transition-metal bis(CO) counterparts. Frenking and co-workers²⁰ additionally made the prediction that “substituted homologues [of HB(CO)₂] with bulky groups at boron which protect the boron atom from electrophilic attack might also be stable enough to become isolated.” Here we prove this prediction to be correct by the synthesis of a remarkably air-stable, neutral and crystalline borylene dicarbonyl, related monovalent boron compounds, and the reactivity thereof.

Stirring a CO-saturated benzene solution of the terminal borylene²⁹ complex [(OC)₅Mo(BTp)] (compound **1b**, where Tp is 2,6-di(2,4,6-triisopropylphenyl)) at reflux for 18 h resulted in a colour change from yellow to blue. After removal of molybdenum hexacarbonyl by fractional crystallization from toluene, blue crystals were obtained (compound **2**, see Fig. 1; note that the monovalent boron compounds **2–4** and **8** are depicted in both conventional covalent forms and Lewis donor/acceptor forms in this figure, according to the conflicting ideas set out in the aforementioned debate on the existence of dative bonds in main-group compounds^{26–28}). This compound showed a strongly upfield-shifted ¹¹B nuclear magnetic resonance (NMR) signal (δ −32.2) compared to that of the precursor **1b** (δ 155) and signals corresponding to the Tp fragment in the ¹H NMR spectrum. The two strong bands in the carbonyl region of its infrared spectrum (at 1,942 cm^{−1} and 2,060 cm^{−1}) are also reminiscent of the symmetrical and unsymmetrical stretches of transition-metal *cis*-dicarbonyl complexes. The crystallographically determined molecular structure of **2** (Fig. 2a) confirmed the dicarbonylation of the boron atom and the presence of a borylene dicarbonyl, with two essentially linear B–C–O axes (the B–C–O angles are 173.9(1)° and 174.2(2)°). The C–O distances in **2** (1.150(2) Å and 1.152(2) Å) are within the range of C=O bonds in crystallographically characterized ketenes³ (1.13–1.18 Å), indicating a lower bond order of the CO units than in free carbon monoxide and a substantial amount of π -electron delocalization across the five-atom OCBCO unit. The B–C bonds of **2** (1.473(3) Å and 1.475(3) Å) are furthermore distinct from those of borane carbonyls (R₃B←CO; typical B–C distances³ are 1.6–1.7 Å), which feature markedly longer B–C distances indicative of single bonds. A related, structurally characterized borylene monocarbonyl has recently been reported²⁴, containing a much more localized B–C≡O unit (the C–O bond length is 1.091(3) Å; that for B–C is 1.529(5) Å), making it thus more reminiscent of the aforementioned family of borane carbonyl adducts. The large structural differences between **2** and borane carbonyl adducts (including the compound of ref. 24) suggests that **2** is the first compound in which a boron atom binds CO with strong π backbonding from the boron to the CO, as is observed in traditional transition-metal carbonyl complexes, thus revealing boron's ability in this case to act as a transition-metal mimic. As a test of its stability to air and moisture,

¹Institut für Anorganische Chemie, Julius-Maximilians-Universität Würzburg, Am Hubland, 97074 Würzburg, Germany. ²Department of Chemistry, School of Life Sciences, University of Sussex, Brighton BN1 9QJ, Sussex, UK.

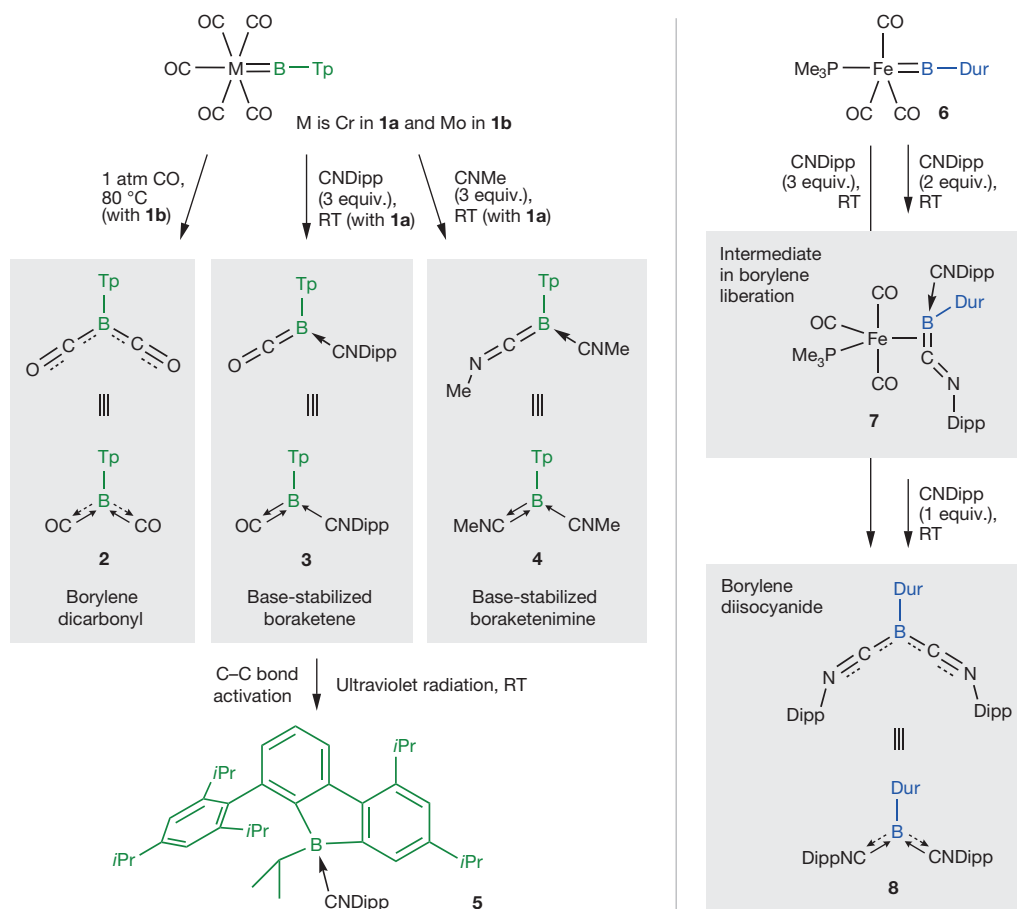


Figure 1 | Synthesis and reactivity of bis(CO), bis(isonitrile) and mixed adducts of boron. Note that in solution, compound 4 adopts a borylene isocyanide form akin to compound 8. Tp is 2,6-di(2,4,6-triisopropylphenyl)-

phenyl. Dur is 2,3,5,6-tetramethylphenyl. Dipp is 2,6-diisopropylphenyl. RT, room temperature.

a solid sample of **2** was kept in an ambient atmosphere for five days, after which time its blue colour remained unchanged and a ^1H NMR spectrum of this sample indicated approximately 30% decomposition.

Treatment of terminal borylene complex $[(\text{OC})_5\text{Cr}(\text{BTp})]$ (**1a**) with 2,6-diisopropylphenylisocyanide (DippNC) at room temperature led to a similarly high-field signal in its ^{11}B NMR spectrum ($\delta -28.4$) and the isolation of blue crystals. However, ^1H and ^{13}C NMR spectroscopy and single-crystal X-ray crystallography (Fig. 2a) indicated that this compound (**3**, Fig. 1) was the product of monocarbonylation of the boron atom (presumably via migration from the $\text{M}(\text{CO})_5$ fragment), with concomitant addition of one isocyanide. Compound **3**, while sharing a similar $\text{L} \rightarrow \text{B}(\text{R})(\text{CO})$ connectivity to the aforementioned borylene monocarbonyl of ref. 24, differs dramatically in terms of delocalization of the boron atom with the CO unit, having much longer C–O bonds (1.161(3) Å) and much shorter B–C bonds (1.464(4) Å). The slightly bent isocyanide CNC unit in **3** ($162.5(2)^\circ$) also indicates weak delocalization over the BCN unit. The ability of **3** to act like a ‘masked’ free borylene was indicated by its behaviour under photolytic conditions for four days, after which colourless crystals (**5**, Fig. 1) were isolated. Compound **5**, a conventional isocyanide-borane adduct, is the product of decarbonylation and formal borylene insertion into a carbon–carbon bond of the terphenyl substituent Tp. Such C–C bond insertions are hallmarks of reactive (free) borylene chemistry³⁰, the formation of which can be envisaged via photolytic decarbonylation of **5**. The ability of **3** to photolytically liberate CO and break strong element–element bonds further reinforces its comparison with transition-metal carbonyl complexes, for which this is a key reactivity motif.

Alternatively, addition of three molar equivalents of methylisocyanide to terminal borylene complex **1a** led to the isolation of red crystals

(**4**, Fig. 1) that showed a ^{11}B NMR signal ($\delta -18.8$) to slightly lower field than those of **2** and **3**. The ^1H NMR spectrum of **4** indicated the existence of two equivalent methylisocyanide units in the compound; however, in the solid state this equivalence does not persist. The crystallographically determined molecular structure of **4** (Fig. 2a) shows the compound to be effectively an isocyanide-stabilized boraketenimine, wherein one DippNC group adopts a linear, non-BC-delocalized arrangement (C–N–C angle is $171.2(2)^\circ$), while the other adopts a bent, imine-like geometry (C–N–C angle is $126.5(1)^\circ$). In a similar manner, addition of three molar equivalents of DippNC to the terminal iron borylene complex $[(\text{OC})_3(\text{Me}_3\text{P})\text{Fe}(\text{BDur})]$ (**6**; where Dur is 2,3,5,6-tetramethylphenyl) led to isolation of an analytically pure red oil (**8**, Fig. 1). Multinuclear NMR spectroscopy and single-crystal X-ray crystallography of **8** (Fig. 2a) indicated the presence of a borylene bis(isonitrile) similar to **4**, but in which the isonitriles are more geometrically equivalent. When borylene **6** was treated with only two molar equivalents of DippNC, a 73% yield of an iron-containing complex (**7**, Fig. 1) was obtained that showed extensive ^{31}P – ^{13}C and ^{31}P – ^1H coupling in the ^{13}C and ^1H NMR spectra, respectively, and a ^{31}P NMR signal at $\delta 11.55$. A ^{11}B NMR signal of **7** was found at $\delta -37.5$, to even higher field than those of the formally monovalent boron compounds **2**–**4** and **8**. The crystallographically determined molecular structure of **7** showed this compound to be effectively a complex of **8** with the zero-valent $[\text{Fe}(\text{CO})_3(\text{PMe}_3)]$ fragment, bound as a base-stabilized boraketenimine in a π fashion through one B=C bond. The CNC unit of the Fe-bound DippNC group of **7** is bent (at $128.1(2)^\circ$) and imine-like. The presumed role of complex **7** as an intermediate in the borylene liberation that leads to **8** was confirmed

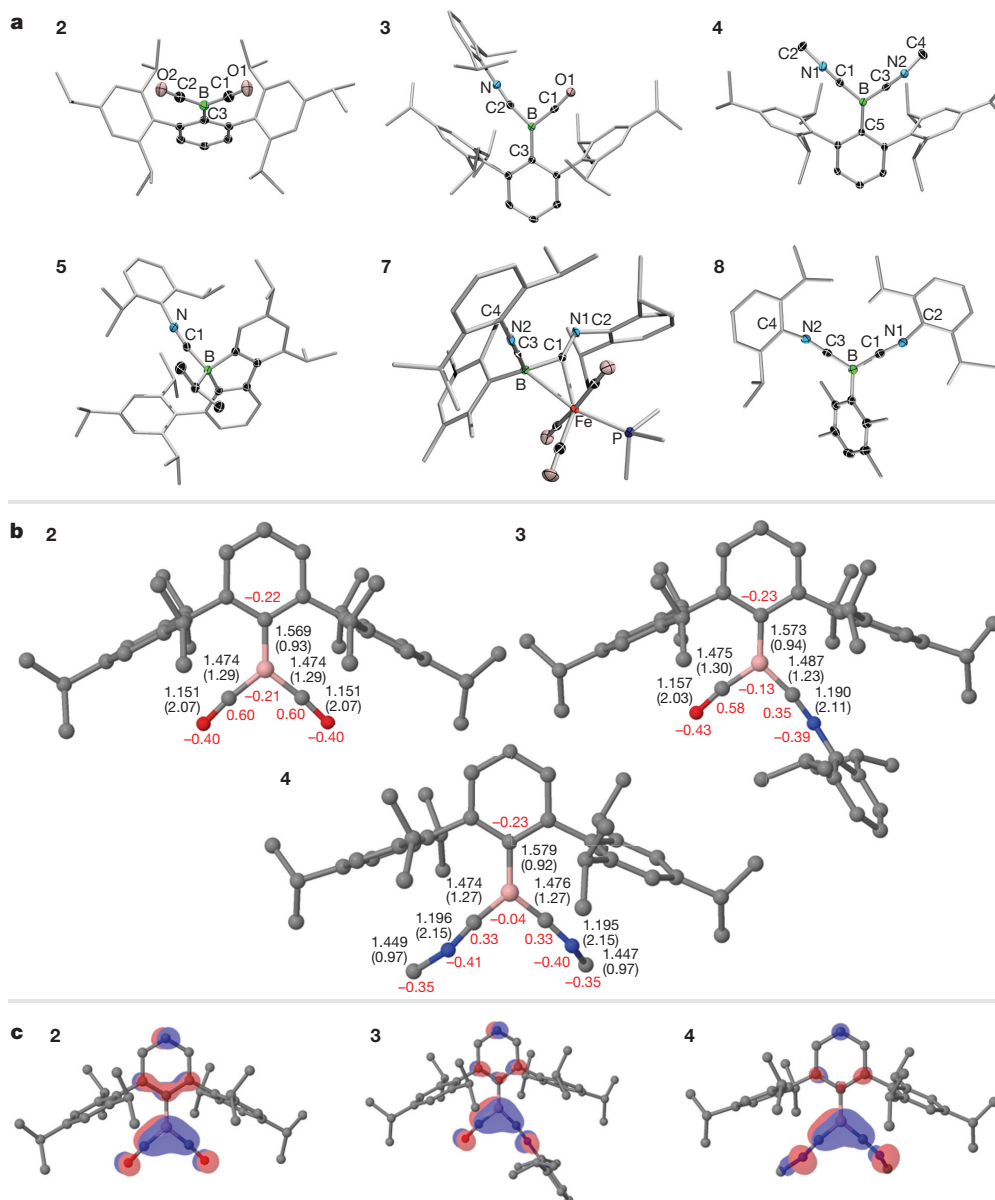


Figure 2 | Crystallographic and computational results on the molecules prepared herein. **a**, Molecular structures of 2–5, 7 and 8 as derived from single-crystal X-ray crystallography. Thermal ellipsoids in the structures represent the 50% probability level. For clarity, hydrogen atoms and some thermal ellipsoids have been removed. Selected bond lengths and angles are given as follows. For 2: B–C1 1.475(3) Å, C1–O1 1.152(2) Å, B–C2 1.473(3) Å, C2–O2 1.150(2) Å and B–C3 1.571(3) Å. For 3: B–C1 1.466(3) Å, C1–O1 1.159(2) Å, B–C2 1.485(3) Å, C2–N 1.177(2) Å and B–C3 1.574(2) Å. For 4: B–C1 1.504(2) Å, C1–N1 1.153(2) Å, B–C3 1.450(2) Å, C3–N2 1.210(2) Å, B–C5 1.569(2) Å, C1–N1–C2 171.2(2)° and C3–N2–C4 126.5(1)°. For 5: B–C1

1.584(2) Å and C1–N 1.146(2) Å. For 7: B–Fe 2.265(3) Å, C1–Fe 2.046(3) Å, B–C1 1.546(4) Å, C1–N1 1.247(3) Å, B–C3 1.518(4) Å, C3–N2 1.154(3) Å, B–C1–N1 141.7(3)°, and C1–N1–C2 128.1(2)°. For 8: B–C1 1.472(3) Å, C1–N1 1.187(2) Å, B–C3 1.469(3) Å, C3–N2 1.186(2) Å, B–C5 1.590(3) Å, C1–N1–C2 149.9(2)° and C3–N2–C4 145.2(2)°. **b**, Computed geometries of 2–4. Interatomic distances (in Å) are given in black, Wiberg bond indices in parentheses, and natural charges in red. **c**, Computed HOMOs of compounds 2–4, where red and blue indicate different phases of the wavefunction.

by the addition of a further equivalent of DippNC, furnishing **8** quantitatively, as judged by NMR spectroscopy.

Kohn–Sham density functional theory calculations at the B3LYP/6-311G* level were also performed on 2–4 (see Supplementary Figs 28 and 29). Although the natural charges at the boron atoms of 2–4 are all negative, they become more neutral as the number of carbonyls is decreased (2: –0.21; 3: –0.13; 4: –0.04, Fig. 2b). However, the calculated distances between the boron atoms and the *sp*-hybridized carbon atoms of all three compounds do not vary much (1.474–1.487 Å), and nor do the corresponding Wiberg bond indices, which are without exception greater than unity (1.23–1.30) and reflect the extensive boron-to-ligand

backbonding in these molecules. Analysis of the frontier orbitals of 2–4 (Fig. 2c) indicates in all cases that the highest occupied molecular orbital (HOMO) level consists of three-centre π bonding interactions between the boron atom and the attached (carbonyl and/or isocyanide) groups. This backbonding from the boron atom's filled *p* orbital into the π^* orbitals of the 'ligands' is reminiscent of the well known metal-to-carbon π backbonding seen in transition-metal carbonyl complexes.

Received 4 March; accepted 23 April 2015.

1. Simpson, P. V. & Schatzschneider, U. in *Inorganic Chemical Biology: Principles, Techniques and Applications* (ed. Gasser, G.) Ch.10, 309–340 (Wiley, 2014).

2. Tielens, A. G. G. M., Wooden, D. H., Allamandola, L. J., Bregman, J. & Witteborn, F. C. The infrared spectrum of the galactic center and the composition of interstellar dust. *Astrophys. J.* **461**, 210–222 (1996).
3. The Cambridge Crystallographic Database. http://www.ccdc.cam.ac.uk/data_request/cif, Version 5.35 (Cambridge Crystallographic Data Centre, November 2013).
4. Parry, J., Carmona, E., Coles, S. & Hursthouse, M. Synthesis and single crystal X-ray diffraction study on the first isolable carbonyl complex of an actinide, $(C_5Me_4H)_3U(CO)$. *J. Am. Chem. Soc.* **117**, 2649–2650 (1995).
5. Puschmann, F. F. et al. Phosphination of carbon monoxide: a simple synthesis of sodium phosphathynolate (NaOCP). *Angew. Chem. Int. Ed.* **50**, 8420–8423 (2011).
6. Finze, M. et al. Tris(trifluoromethyl)borane carbonyl, $(CF_3)_3BCO$ —synthesis, physical, chemical and spectroscopic properties, gas phase, and solid state structure. *J. Am. Chem. Soc.* **124**, 15385–15398 (2002).
7. Glöckner, J. D., Rathke, J. W. & Schaeffer, R. Some reactions of triborane(7) and the structure of triborane(7)-carbonyl. *Inorg. Chem.* **12**, 2175–2178 (1973).
8. Lavallo, V., Canac, Y., Donnadieu, B., Schoeller, W. W. & Bertrand, G. CO fixation to stable acyclic and cyclic alkyl amino carbenes: stable amino ketenes with a small HOMO–LUMO gap. *Angew. Chem. Int. Ed.* **45**, 3488–3491 (2006).
9. Ellern, A., Drews, T. & Seppelt, K. The structure of carbon suboxide, C_3O_2 , in the solid state. *Z. Anorg. Allg. Chem.* **627**, 73–76 (2001).
10. Bernhardt, I., Drews, T. & Seppelt, K. Isolation and structure of the $OCNCO^+$ ion. *Angew. Chem. Int. Ed.* **38**, 2232–2233 (1999).
11. Power, P. P. Main-group elements as transition metals. *Nature* **463**, 171–177 (2010).
12. Martin, D., Soleilhavoup, M. & Bertrand, G. Stable singlet carbenes as mimics for transition metal centers. *Chem. Sci.* **2**, 389–399 (2011).
13. Braunschweig, H. et al. Ambient-temperature isolation of a compound with a boron–boron triple bond. *Science* **336**, 1420–1422 (2012).
14. Wang, Y. & Robinson, G. H. Carbene-stabilized main group diatomic allotropes. *Dalton Trans.* **41**, 337–345 (2012).
15. Khan, S., Sen, S. S. & Roesky, H. W. Activation of phosphorus by group 14 elements in low oxidation states. *Chem. Commun.* **48**, 2169–2179 (2012).
16. Braunschweig, H. et al. Metal-free binding and coupling of carbon monoxide at a boron–boron triple bond. *Nature Chem.* **5**, 1025–1028 (2013).
17. Spikes, G. H., Fettingner, J. C. & Power, P. P. Facile activation of dihydrogen by an unsaturated heavier main group compound. *J. Am. Chem. Soc.* **127**, 12232–12233 (2005).
18. Frey, G. D., Lavallo, V., Donnadieu, B., Schoeller, W. W. & Bertrand, G. Facile splitting of hydrogen and ammonia by nucleophilic activation at a single carbon center. *Science* **316**, 439–441 (2007).
19. Tonner, R. & Frenking, G. $C(NHC)_2$: divalent carbon(0) compounds with N-heterocyclic carbene ligands—theoretical evidence for a class of molecules with promising chemical properties. *Angew. Chem. Int. Ed.* **46**, 8695–8698 (2007).
20. Celik, M. A. et al. Borylene complexes $(BH)L_2$ and nitrogen cation complexes $(N^+)L_2$: isoelectronic homologues of carbon CL_2 . *Chemistry* **18**, 5676–5692 (2012).
21. Kinjo, R., Donnadieu, B., Celik, M. A., Frenking, G. & Bertrand, G. Synthesis and characterization of a neutral tricoordinate organoboron isoelectronic with amines. *Science* **333**, 610–613 (2011).
22. Ruiz, D. A., Melaimi, M. & Bertrand, G. An efficient synthetic route to stable bis(carbene)borylenes $[(L_1)(L_2)BH]$. *Chem. Commun.* **50**, 7837–7839 (2014).
23. Kong, L., Li, Y., Ganguly, R., Vidovic, D. & Kinjo, R. Isolation of a bis(oxazol-2-ylidene)–phenylborylene adduct and its reactivity as a boron-centered nucleophile. *Angew. Chem. Int. Ed.* **53**, 9280–9283 (2014).
24. Dahcheh, F., Martin, D., Stephan, D. W. & Bertrand, G. Synthesis and reactivity of a CAAC–aminoborylene adduct: a hetero-allene or an organoboron isoelectronic with singlet carbenes. *Angew. Chem. Int. Ed.* **53**, 13159–13163 (2014).
25. Mondal, K. C. et al. A stable singlet biradicaloid siladiborane: $(L)_2Si$. *Angew. Chem. Int. Ed.* **52**, 2963–2967 (2013).
26. Himmel, D., Krossing, I. & Schnepf, A. Dative bonds in main-group compounds: a case for fewer arrows! *Angew. Chem. Int. Ed.* **53**, 370–374 (2014).
27. Frenking, G. Dative bonds in main-group compounds: a case for more arrows! *Angew. Chem. Int. Ed.* **53**, 6040–6046 (2014).
28. Himmel, D., Krossing, I. & Schnepf, A. Dative or not dative? *Angew. Chem. Int. Ed.* **53**, 6047–6048 (2014).
29. Braunschweig, H., Dewhurst, R. D. & Schneider, A. Electron-precise coordination modes of boron-centered ligands. *Chem. Rev.* **110**, 3924–3957 (2010).
30. Grigsby, W. J. & Power, P. P. Isolation and reduction of sterically encumbered arylboron dihalides: novel boranediyl insertion into C–C σ -bonds. *J. Am. Chem. Soc.* **118**, 7981–7988 (1996).

Supplementary Information is available in the online version of the paper.

Acknowledgements This work was supported by a European Research Council Advanced Grant to H.B.

Author Contributions H.B. conceived and supervised the study. C.W.T., M.N. and Q.Y. performed the synthetic studies. F.H. and K.R. performed the single-crystal X-ray diffraction studies. A.V. performed the computational experiments. R.D.D. wrote the manuscript with input from all authors. All authors analysed the results and commented on the manuscript.

Author Information Crystallographic data have been deposited with the Cambridge Crystallographic Data Center as supplementary publication numbers CCDC 1049463–1049468. These data can be obtained free of charge from The Cambridge Crystallographic Data Centre at http://www.ccdc.cam.ac.uk/data_request/cif. Reprints and permissions information is available at www.nature.com/reprints. The authors declare no competing financial interests. Readers are welcome to comment on the online version of the paper. Correspondence and requests for materials should be addressed to H.B. (h.braunschweig@uni-wuerzburg.de).

An enigmatic plant-eating theropod from the Late Jurassic period of Chile

Fernando E. Novas^{1,2}, Leonardo Salgado^{1,3,4}, Manuel Suárez⁵, Federico L. Agnolín^{2,6}, Martín D. Ezcurra⁷, Nicolás R. Chimento², Rita de la Cruz⁸, Marcelo P. Isasi^{1,2}, Alexander O. Vargas⁹ & David Rubilar-Rogers^{9,10}

Theropod dinosaurs were the dominant predators in most Mesozoic era terrestrial ecosystems¹. Early theropod evolution is currently interpreted as the diversification of various carnivorous and cursorial taxa, whereas the acquisition of herbivorism, together with the secondary loss of cursorial adaptations, occurred much later among advanced coelurosaurian theropods^{1,2}. A new, bizarre herbivorous basal tetanuran from the Upper Jurassic of Chile challenges this conception. The new dinosaur was discovered at Aysén, a fossil locality in the Upper Jurassic Toqui Formation of southern Chile (General Carrera Lake)^{3,4}. The site yielded abundant and exquisitely preserved three-dimensional skeletons of small archosaurs. Several articulated individuals of *Chilesaurus* at different ontogenetic stages have been collected, as well as less abundant basal crocodyliforms, and fragmentary remains of sauropod dinosaurs (diplodocids and titanosaurs).

Theropoda Marsh, 1881

Tetanurae Gauthier, 1986

Chilesaurus diegosuarezi gen. et sp. nov.

Etymology. In reference to Chile, and honoring Diego Suárez, who at the age of 7, discovered the first bone remains in the Toqui Formation. **Holotype.** Servicio Nacional de Geología y Minería, Chile (SNGM)-1935 consists of a nearly complete, articulated skeleton, approximately 1.6 m long (Fig. 1, Supplementary Information and Extended Data Fig. 1). Holotype specimen was skeletally immature at the time of its death, as evidenced by the incomplete fusion of neurocentral sutures. This ontogenetic inference agrees with the size of the holotype, which represents 50% the length of the larger specimen SNGM-1888 (ref. 3). **Paratypes.** Postcranial skeletons of four individuals, corresponding to different ontogenetic stages, ranging approximately from 1.2 to 3.2 m in total length (Extended Data Table 1). Several specimens referred to as indeterminate theropods and tetanurans previously³ are here referred to as *Chilesaurus diegosuarezi*.

Locality and horizon. Central Patagonian Cordillera, Aysén (Chile; approximately 46°S); Toqui Formation^{3,4}, Tithonian, latest Jurassic.

Diagnosis. *Chilesaurus* differs from other dinosaurs in the following combination of autapomorphies: premaxilla short and deep, with prominent plate-like postnasal process; teeth leaf-shaped, being finely denticulate only on the crown apex of erupting teeth; coracoid subquadrangular in side view and with transversely thick margins; manual digit II with short pre-ungual phalanges; manual digit III atrophied; iliac blade with posterodorsal prominence; ischiadic peduncle of ilium robust; supracetabular crest absent; pubis fully retroverted; pubic shaft rod-like and distally unexpanded; femoral mediodistal crest absent; tibia without fibular crest. In addition, *Chilesaurus* shows the

following unique combination of characters: dentary deeper anteriorly than posteriorly; cervicals with septate and paired pleurocoels; pubic apron transversely narrow; ischia connected through a proximodistally extended medial lamina ('ischial apron'); femoral greater trochanter anteroposteriorly expanded; astragalar ascending process lower than astragalar body; calcaneum subtriangular in distal view; metatarsal I robust, elongate, and proximally compressed transversely; metatarsal II transversely wider than the other metatarsals; pedal digit I large.

Isolated skull material (including premaxilla, maxillae, frontals, postorbital, squamosal, basicranium, ectopterygoid and dentary; Extended Data Fig. 2), suggests a proportionally small head for *Chilesaurus*. The premaxilla is short and deep, with a rugose rostral margin that suggests a ramphotheca (Fig. 2). Frontals are elongate and narrow and participate extensively in the orbital margin. The basi-sphenoidal recess is deep. The dentary is short and deep, with a downturned symphyseal region but a straight alveolar margin. Dentary teeth are tall, leaf-shaped, and procumbent, with small serrations restricted to the crown apex (Fig. 2).

Cervical vertebrae are long and low, forming a slender neck. Cervical and anterior dorsal vertebrae possess a pair of septate pleurocoels, which are absent posterior to the pectoral region (Fig. 1g). 'Pectoral' vertebrae bear prominent hypapophyses.

The scapular blade (Extended Data Fig. 3) is elongate and slightly anteroposteriorly expanded distally, as in basal averostrans⁵. The coracoid is subquadrangular and lacks theropod characteristics such as the posteroventral process and biceps tuberosity¹. It is notably thick transversely, contrasting with the delicate anterodorsal and dorsal margins of most dinosaurs. The limb bones are stout, as in sauropodomorphs, and forelimb length is 56% that of hind limbs. The humerus is proximodistally short and transversely wide (Extended Data Fig. 3). The single proximal carpal is large, with a transversely convex proximal articular surface. Metacarpals I–III are present, but only manual digits I and II are well developed (Fig. 1d–f). Metacarpal I is stout, and phalanx 1–I is short and strongly twisted along its main axis, as in basal sauropodomorphs⁶. The ungual of digit I is shorter than metacarpal II and less curved than most basal tetanurans^{5,7}. Metacarpal II is the longest, and its digit presents strongly shortened pre-ungual phalanges, as in some ceratosaurs⁸. Metacarpal III is much more slender than in basal theropods, and its digit comprises a single minute phalanx.

The ilium is dolichoiliac, typical for Theropoda¹ (Fig. 1b). The pubic pedicle is elongate (as in sauropods, ornithischians and therizinosaurs^{2,9}), and the ischiadic peduncle is bulbous, as in ornithischians and alvarezsaurid coelurosaurs¹⁰. A prominent supratrochanteric process is present on the posterodorsal corner of the ilium, similar to those of sauropods, therizinosaurs, paravians, and some ornithischians^{11–13}. The acetabular roof is transversely narrow and a supracetabular crest

¹Conicet, Museo Argentino de Ciencias Naturales "B. Rivadavia", Av. Ángel Gallardo 470 (C1405DJR), Buenos Aires, Argentina. ²Museo Argentino de Ciencias Naturales "B. Rivadavia", Av. Ángel Gallardo 470 (C1405DJR), Buenos Aires, Argentina. ³Conicet, Instituto de Investigación en Paleobiología y Geología, Universidad Nacional de Río Negro, General Roca 1242, General Roca (8332), Río Negro, Argentina. ⁴Instituto de Investigación en Paleobiología y Geología, Universidad Nacional de Río Negro, General Roca 1242, General Roca (8332), Río Negro, Argentina. ⁵Universidad Andres Bello, Geología, Facultad de Ingeniería, Sazie 2315, Santiago, Chile. ⁶Fundación de Historia Natural Félix de Azara, Universidad Maimónides, Hidalgo 775 (C1405BDB), Buenos Aires, Argentina. ⁷School of Geography, Earth and Environmental Sciences, University of Birmingham, Birmingham B15 2TT, UK. ⁸Servicio Nacional de Geología y Minería, Avenida Santa María 0104, Santiago 8330177, Chile. ⁹Red Paleontológica U-Chile, Laboratorio de Ontogenia y Filogenia, Departamento de Biología, Facultad de Ciencias, Universidad de Chile, Santiago 7800003, Chile. ¹⁰Área Paleontología, Museo Nacional de Historia Natural de Chile, casilla 787, Santiago, Chile.

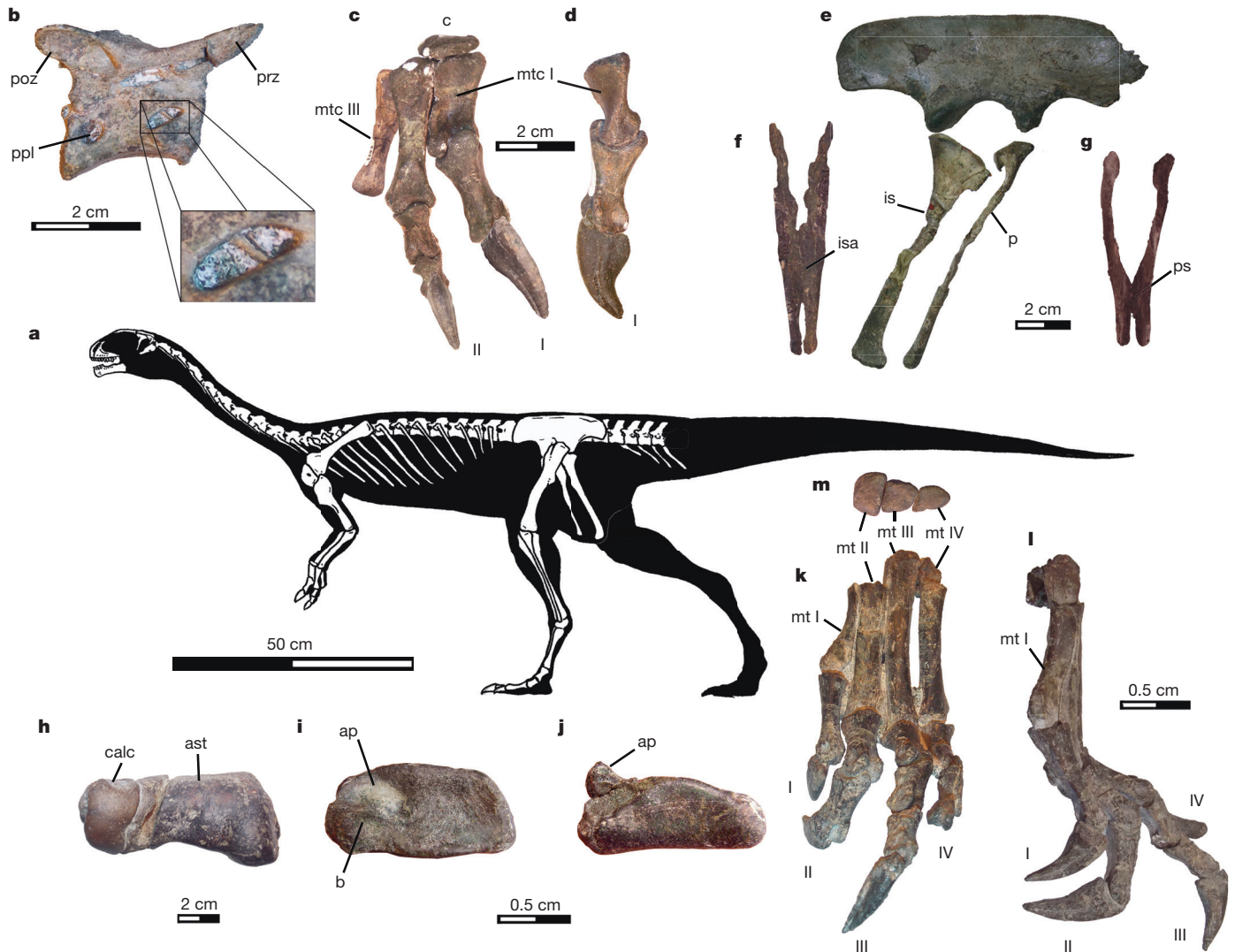


Figure 1 | Skeletal anatomy of *Chilesaurus diegosuarezi* gen. et sp. nov. **a**, Reconstructed skeleton (SNGM-1935). **b**, Fourth cervical vertebra (SNGM-1935) in right lateral view, with a close-up of tabicated anterior pleurocoel. **c**, **d**, Composite reconstruction of right hand (carpals, metacarpals, and non-ungual phalanges of digits I and II) are from specimen SNGM-1935; ungual phalanges I and II are from specimen SNGM-1887; metacarpal III is from specimen SNGM-1887 in dorsal (**c**) and medial (**d**) views. **e**, Pelvic girdle (SNGM-1936) in right lateral view. **f**, Articulated ischia (SNGM-1936) in

posterior view. **g**, Articulated pubes (SNGM-1936) in anterior view. **h**, Proximal tarsals (SNGM-1888) in distal view. **i**, **j**, Left astragalus (SNGM-1936) in proximal (**i**) and anterior (**j**) views. **k–m**, Left pes (SNGM-1937) in dorsal (**k**), medial (**l**) and proximal (**m**) views. ap, ascending process; ast, astragalus; b, basin; c, carpal; calc, calcaneum; ia, ischiadic apron; is, ischium; mtc, metacarpal; p, pubis; poz, postzygapophysis; pps, posterior pleurocoel; prz, prezygapophysis; ps, pubic symphysis; I, II, III, IV, digits first to fourth.

is absent, as occurs in derived coelurosaur and ornithomorphs^{1,11,13}. The pubis (Fig. 1b, c) closely resembles that of basal ornithischians, therizinosaurs and dromaeosaurid paravians in being fully retroverted, with a reduced proximal end bearing a posteriorly open obturator notch^{1,2}. The pubic apron is transversely narrow and the pubis has a rod-like shaft. It is distally unexpanded with a rounded contour, sharply contrasting with the prominent distal ‘foot’ of other theropods¹. The ischium (Fig. 1a, b) is proximally expanded and lacks an obturator process. Notably, both ischia are connected through a proximodistally extended medial lamina (ischial apron), a feature reported in some megalosauroids¹⁴.

The femur is robust (Extended Data Fig. 4). The greater trochanter is anteroposteriorly expanded, similar to coelurosaur. The anterior trochanter is wing-like and proximally projected, and the fourth trochanter is semicircular. The distal third of the femur resembles sauropodomorphs in that it lacks distinctive theropod features, such as an anteromedial elliptical muscle scar, a mediolateral crest and its associated medial adductor fossa. The cnemial crest of tibia (Extended Data Fig. 4) is rounded in lateral view, as in basal sauropodomorphs and

basal ornithischians, and differs from the subtriangular crest present in most basal theropods^{1,15}. As in sauropodomorphs, and unlike most theropods, the proximal end of the tibia lacks a fibular crest¹. Like theropods, the distal end of the tibia is anteroposteriorly compressed with a laterally extending malleolus, more transversely expanded than in coelophysoids, but less than in tetanurans¹. The fibula lacks a proximomedial pocket and iliofibular tubercle. The tarsus (Fig. 1k–m) resembles basal saurischians¹⁶. The astragalar ascending process is low and broad, unlike tetanurans, in which it is laminar, tall, and transversely wide^{1,6,17}. The proximal astragalar surface possesses a deep, well-defined basin posterior to the ascending process, as in basal dinosaurs. As in early saurischians (for example, *Herrerasaurus*, basal sauropodomorphs), the calcaneum of *Chilesaurus* is transversely wide and subtriangular in distal view, rather than rectangular and disc-shaped as in theropods^{1,16,17}. The foot is wide and proximodistally short (Fig. 1h–j). The proximal half of metatarsal I is transversely compressed but anteroposteriorly expanded, unlike most theropods, in which it tapers proximally. Metatarsal I of *Chilesaurus* represents more than 50% of the length of metatarsal II, in contrast with

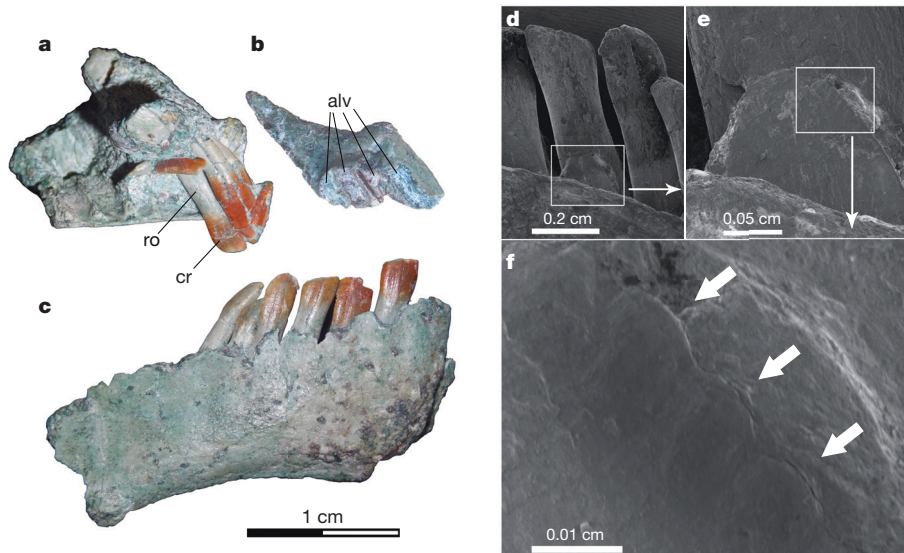


Figure 2 | Selected cranial bones and teeth of *Chilesaurus diegosuarezi* gen. et sp. nov. (SNGM-1935). **a**, Partial right (?) maxilla in lateral view. **b**, Left premaxilla in medial view. **c**, Right dentary in lateral view. **d**, Details of dentary

teeth in lingual view. **e**, Crown of unerupted dentary tooth. **f**, Detail of the carina of an unerupted tooth (arrows indicate denticle positions). alv, alveoli; cr, crown tooth; ro, root tooth.

most other theropods (25–33%)^{1,17}. Metatarsal III is the longest, but metatarsal II is the thickest, as in basal sauropodomorphs. Digit I is large, only slightly shorter than digit II, approaching the tetradactyl condition of early sauropodomorphs, ornithischians¹⁸ and derived therizinosaurs².

The bizarre anatomy of *Chilesaurus* raises interesting questions about its phylogenetic relationships. We scored *Chilesaurus* into four

different integrative archosauriform, theropod and sauropodomorph data sets^{9,19–21}. Remarkably, all these analyses placed *Chilesaurus* as a member of Theropoda, near the origin of tetanurans⁵ (Fig. 3a), dismissing conceivable positions near Therizinosaurs, Sauropodomorpha or Ornithischia. The theropodan position of *Chilesaurus* is supported by pleurocoels in cervical and anterior dorsal vertebrae; hypapophyses on ‘pectoral’ vertebrae; preacetabular process of ilium

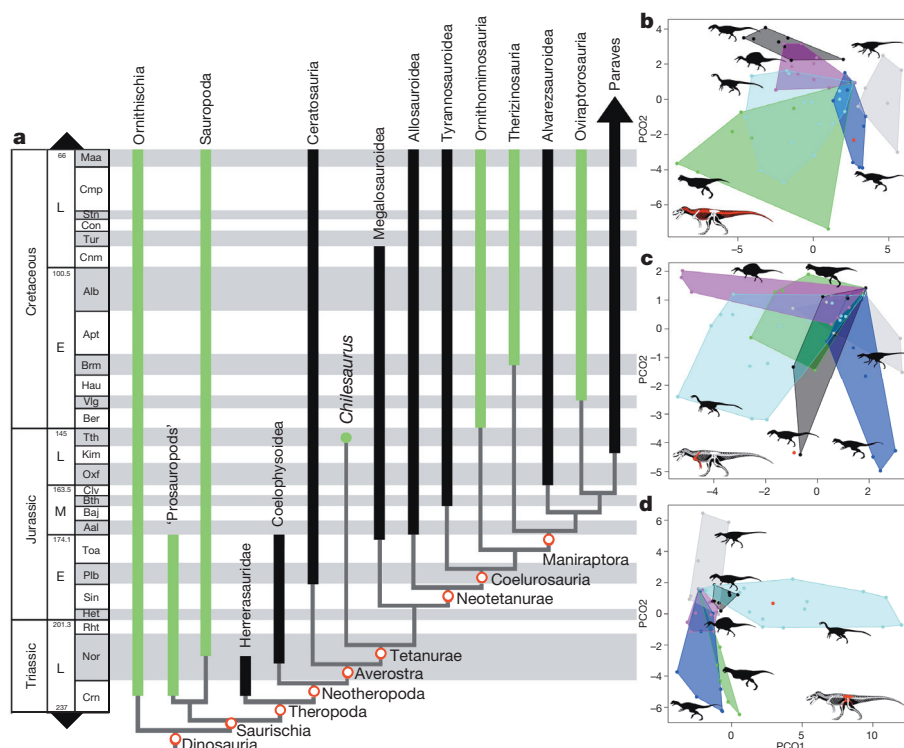


Figure 3 | Phylogenetic relationships of *Chilesaurus diegosuarezi* gen. et sp. nov. among main dinosaur clades and its plots in the theropod morphospaces. **a**, Time-calibrated simplified strict consensus tree, in which the green bars indicate herbivorous dinosaur lineages²⁸. E, Early; L, Late; M, Middle. Aal, Aalenian; Alb, Albian; Apt, Aptian; Baj, Bajocian; Ber, Berriasian; Brm, Barremian; Bth, Bathonian; Clv, Callovian; Crn, Carnian; Cmp, Campanian; Cnm, Cenomanian; Con, Coniacian; Hau, Hauterivian; Het,

Hettangian; Kim, Kimmeridgian; Maa, Maastrichtian; Nor, Norian; Oxf, Oxfordian; Plb, Pliensbachian; Rh, Rhaetian; Sin, Sinemurian; Stn, Santonian; Tth, Tithonian; Toa, Toarcian; Tur, Turonian; Vlg, Valanginian. Numbers indicate millions of years ago. **b–d**, *Chilesaurus diegosuarezi* gen. et sp. nov. plotted in the theropod morphospace (principal coordinate (PCO)1 versus PCO2) based on axial skeleton (**b**); scapular girdle and forelimb (**c**); and pelvic girdle (**d**). Red dots in **b–d** indicate the position of *Chilesaurus*.

dorsoventrally expanded; femoral fourth trochanter semicircular; and tibia distally expanded and with lateral malleolus extending strongly laterally. Tetanuran affinities are supported by scapular blade elongate and strap-like; distal carpal semilunate; and manual digit III reduced (Supplementary Information). For a basal tetanuran, *Chilesaurus* possesses a number of surprisingly plesiomorphic traits on the hindlimbs, especially in the ankle and foot, which resemble basal sauropodomorphs^{7,9,12}. These features are here considered as secondary reversals that might be related to a less-cursorial mode of locomotion. Furthermore, derived features of the dentary and teeth shared by *Chilesaurus*, sauropodomorphs and therizinosaurs are interpreted as homoplasies related to herbivorous habits^{22–25}. In this context, pubic retroversion of *Chilesaurus* may be related to an increased gut capacity for processing plant material²⁵.

The discovery of *Chilesaurus* lends support to the interpretation^{22,23} that dietary diversification towards herbivory was more commonplace among basal theropods than previously thought. Independent evolution of herbivory has been recognized for several major coelurosaurian subclades²³, but for just a single probable example outside Coelurosauria (that is, the toothless ceratosaurian *Limusaurus*^{26,27}). *Chilesaurus* expands the list of non-coelurosaurian theropods that shifted their diet from carnivore to herbivore.

Chilesaurus represents an extreme case of mosaic evolution among dinosaurs, owing to the presence of dental, cranial and postcranial features that are homoplastic with multiple disparate groups. Using quantitative morphospace analysis, we explored morphospace occupation of different skeletal regions in *Chilesaurus* with respect to a variety of avian and non-avian theropods. This shows that *Chilesaurus* has a ceratosaur-like axial skeleton, a 'basal tetanuran' forelimb and scapular girdle, a coelurosaur-like pelvis, and a tetanuran-like hindlimb (Fig. 3b–d and Extended Data Fig. 5). General ankle and foot construction does not group with any theropod clade, probably as a result of the characters shared by *Chilesaurus*, sauropodomorphs and herrerasaurids.

Chilesaurus is the numerically dominant taxon in the Aysén tetrapod fossil assemblage, and represents an unusual case of a theropod having the palaeoecological role of a preeminent small-to-medium sized herbivore in a Jurassic ecosystem. This is in sharp contrast with other Late Jurassic dinosaur assemblages (for example, Tendaguru and Morrison formations^{11,27}), in which ornithischian dinosaurs are the most abundant small-to-medium sized herbivores. Available evidence indicates that *Chilesaurus* is a unique dinosaur lineage known only from southern South America, suggesting an outstanding case of endemism among otherwise relatively cosmopolitan worldwide Jurassic dinosaur faunas²⁸.

Chilesaurus illustrates how much relevant data on the early diversification of major dinosaur clades remain unknown. It also provides an important cautionary benchmark in our attempts to gain a reliable view of the overall evolutionary history of Dinosauria.

Online Content Methods, along with any additional Extended Data display items and Source Data, are available in the online version of the paper; references unique to these sections appear only in the online paper.

Received 19 September 2014; accepted 10 February 2015.

Published online 27 April; corrected online 17 June 2015 (see full-text HTML version for details).

1. Rauhut, O. W. M. The interrelationships and evolution of basal theropod dinosaurs. *Spec. Pap. Palaeont.* **69**, 1–213 (2003).
2. Paul, G. S. The segnosaurian dinosaurs: relics of the prosauropod–ornithischian transition? *J. Vert. Paleont.* **4**, 507–515 (1984).
3. Salgado, L., De La Cruz, R., Suárez, M., Gasparini, Z. & Fernández, M. First Late Jurassic dinosaur bones from Chile. *J. Vert. Paleont.* **28**, 529–534 (2008).

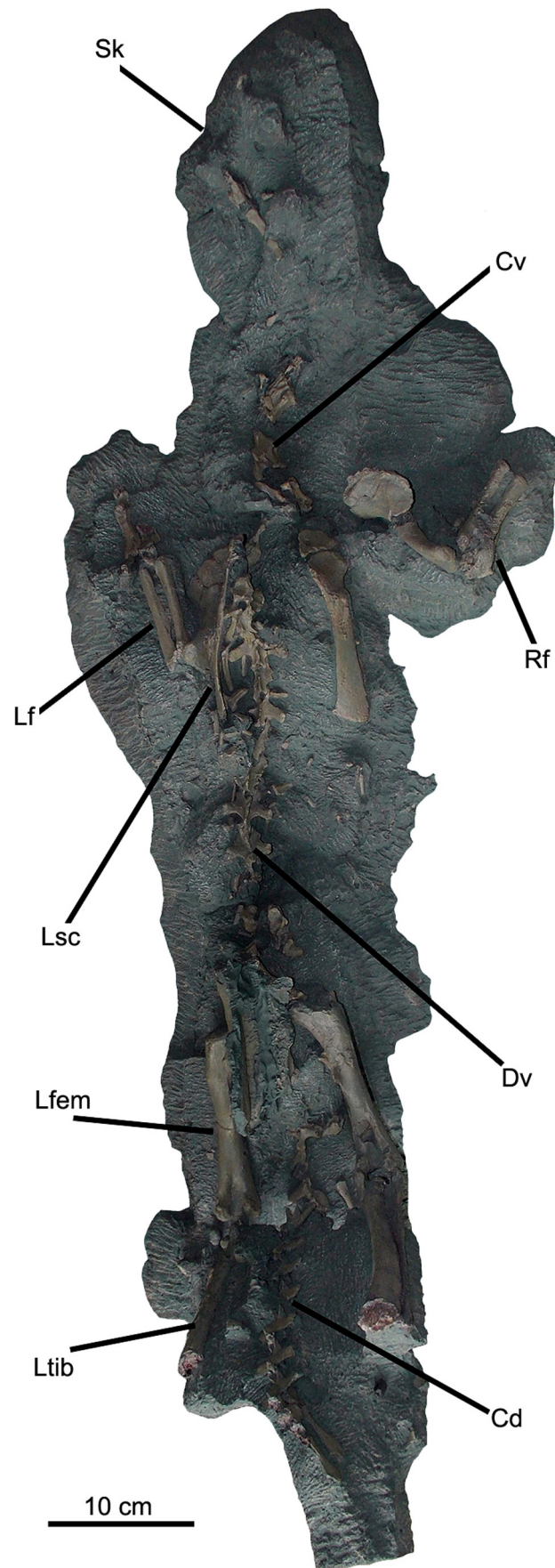
4. De la Cruz, R. & Suárez, M. Geología del área de Puerto Guadal–Puerto Sánchez, región de Aysén del General Carlos Ibáñez del Campo, escala 1:100.000 [in Spanish]. *Carta Geológica de Chile* **95**, 1–117 (2006).
5. Madsen, J. H. *Allosaurus fragilis*: a revised osteology. *Utah Geol. Min. Surv. Bull.* **109**, 1–163 (1976).
6. Martínez, R. N. et al. A basal dinosaur from the dawn of the Dinosaur Era in Southwestern Pangaea. *Science* **331**, 206–210 (2011).
7. Lautenschlager, S. Morphological and functional diversity in therizinosaurs claws and the implications for theropod claw evolution. *Proc. R. Soc. Lond. B* **281**, 1471–1473 (2014).
8. Bonaparte, J. F. The Gondwanan theropod families Abelisauridae and Noasauridae. *Hist. Biol.* **5**, 1–25 (1991).
9. Otero, A. & Pol, D. Postcranial anatomy and phylogenetic relationships of *Mussaurus patagonicus* (Dinosauria, Sauropodomorpha). *J. Vert. Paleont.* **33**, 1138–1168 (2013).
10. Novas, F. E. Alvarezsauridae, Cretaceous basal birds from Patagonia and Mongolia. *Mem. Queensl. Mus.* **39**, 675–702 (1996).
11. Weishampel, D. B., Dodson, P., Osmólska, H. & Hilton, R. P. *The Dinosauria* 2nd edn (Univ. of California Press, 2004).
12. Yates, A. M. A new species of the primitive dinosaur *Thecodontosaurus* (Saurischia: Sauropodomorpha) and its implications for the systematics of early dinosaurs. *J. Syst. Palaeontology* **1**, 1–42 (2003).
13. Hutchinson, J. R. The evolution of pelvic osteology and soft tissues on the line to extant birds (Neornithes). *Zool. J. Linn. Soc. London* **131**, 123–168 (2001).
14. Sadleir, R., Barrett, P. M. & Powell, H. P. The anatomy and systematics of *Eustreptospondylus oxoniensis*, a theropod dinosaur from the Middle Jurassic of Oxfordshire, England. *Mon. Palaeont. Soc. London* **160**, 1–82 (2008).
15. Novas, F. E. Dinosaur monophyly. *J. Vertebr. Paleontol.* **16**, 723–741 (1996).
16. Novas, F. E. The tibia and tarsus in Herrerasauridae (Dinosauria, incertae sedis) and the origin and evolution of the dinosaurian tarsus. *J. Paleontol.* **63**, 677–690 (1989).
17. Zanno, L. E. Osteology of *Falcarius utahensis*: characterizing the anatomy of basal therizinosaurs. *Zool. J. Linn. Soc.* **158**, 196–230 (2010).
18. Galton, P. M. The ornithischian dinosaur *Hypsilophodon* from the Wealden of the Isle of Wight. *Bull. Brit. Mus. Geol. London* **25**, 1–152 (1974).
19. Smith, N. D. et al. *Megaraptor* (Dinosauria: Tetanurae) in Australia; evidence for faunal interchange between eastern and western Gondwana during the Early Cretaceous. *Proc. R. Soc. Lond. B* **275**, 2085–2093 (2008).
20. Nesbitt, S. J. et al. A complete skeleton of a Late Triassic saurischian and the early evolution of dinosaurs. *Science* **326**, 1530–1533 (2009).
21. Carrano, M. T., Benson, R. B. J. & Sampson, S. D. The phylogeny of Tetanurae (Dinosauria: Theropoda). *J. Syst. Paleontol.* **10**, 211–300 (2012).
22. Zanno, L. E., Gillette, D. D., Albright, L. B. & Titus, A. L. A new North American therizinosaurid and the role of herbivory in “predatory” dinosaur evolution. *Proc. R. Soc. Lond. B* **276**, 3505–3511 (2009).
23. Zanno, L. E. & Makovicky, P. J. Herbivorous ecomorphology and specialization patterns in theropod dinosaur evolution. *Proc. Natl Acad. Sci. USA* **108**, 232–237 (2011).
24. Norman, D. B. & Weishampel, D. B. in *Biomechanics and Evolution* (eds Rayner, J. M. V. & Wootton, R. J.) 161–181 (Cambridge Univ. Press, 1991).
25. Barrett, D. P. The diet of ostrich dinosaurs (Theropoda: Ornithomimosauria). *Palaeontology* **48**, 347–358 (2005).
26. Xu, X. et al. A Jurassic ceratosaur from China helps clarify avian digital homologies. *Nature* **459**, 940–944 (2009).
27. Barrett, P. M. Paleobiology of herbivorous dinosaurs. *Annu. Rev. Earth Planet. Sci.* **42**, 207–230 (2014).
28. Ezcurra, M. D. & Agnolín, F. L. A new global palaeobiogeographical model for the late Mesozoic and early Tertiary. *Syst. Biol.* **61**, 553–566 (2012).

Supplementary Information is available in the online version of the paper.

Acknowledgements We thank P. Barrett, A. Milner and R. Butler for comments on early versions of this manuscript. We are grateful to C. Alsina, M. Milani, R. Stoll and M. Aranciaga for field assistance and technical preparation of *Chilesaurus* specimens. G. Lio executed the silhouette of *Chilesaurus* in Fig. 1. C. Burke offered support to conduct fieldwork and technical preparation of the specimens. We are indebted to the Agencia Nacional de Promoción Científica y Tecnológica (PICT 2010-066 to F.E.N.) and the Fondo Nacional de Desarrollo Científico y Tecnológico (no. 1121140 and 1030162 to M.S.) for continuing financial assistance.

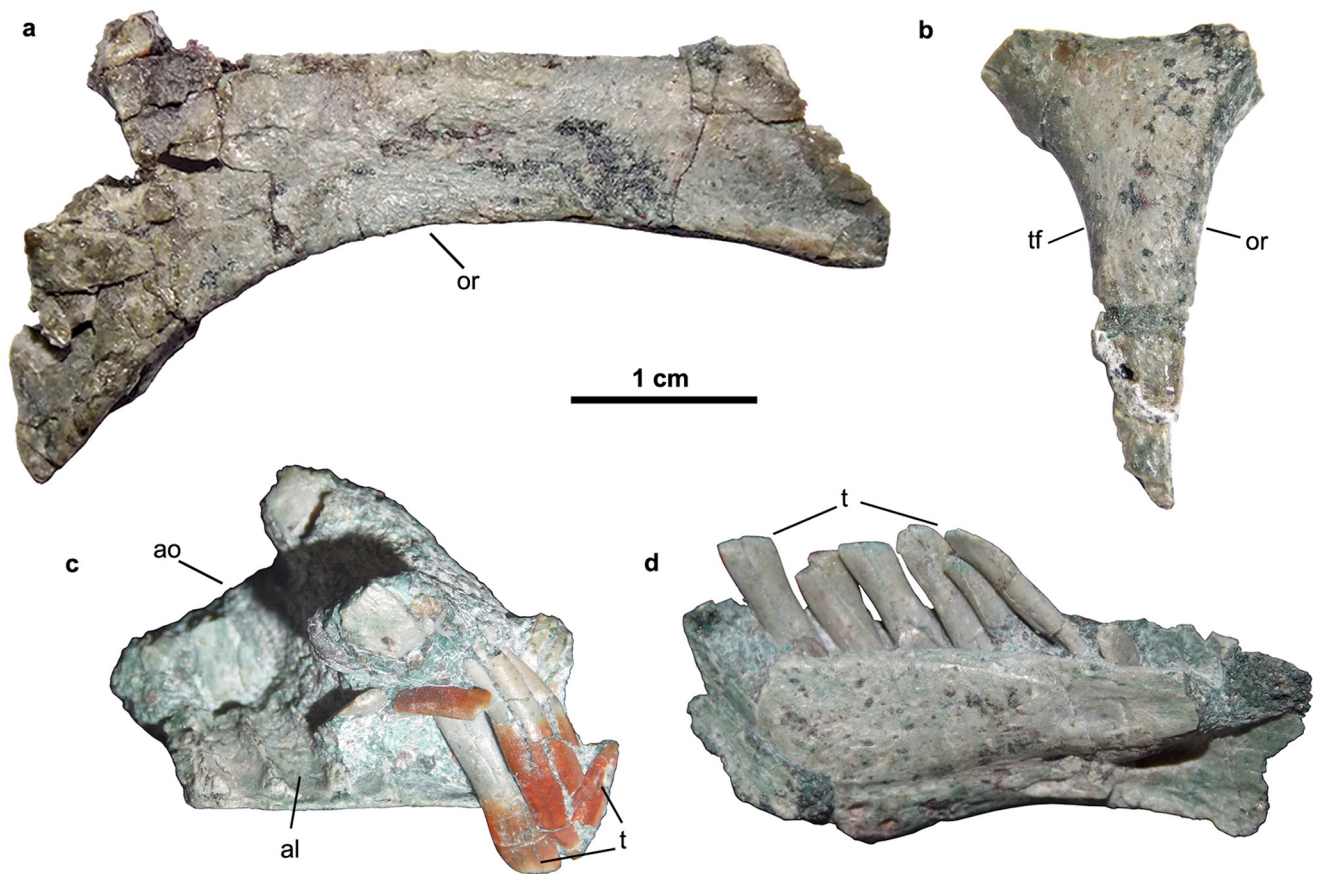
Author Contributions F.E.N., L.S., M.S., F.L.A., M.D.E., N.R.C., A.O.V. and D.R.-R. designed the study, collected data, performed the comparative and analytical work, and wrote the paper. R.d.I.C. and M.P.I. collected data and contributed to the writing and discussion.

Author Information Data have been deposited in ZooBank under Life Science Identifier (LSID) urn:lsid:zoobank.org:act:7B6DE8C7-C78D-48C0-B818-65C454AEFB58. Reprints and permissions information is available at www.nature.com/reprints. The authors declare no competing financial interests. Readers are welcome to comment on the online version of the paper. Correspondence and requests for materials should be addressed to F.E.N. (fernovas@yahoo.com.ar).



Extended Data Figure 1 | Holotype of *Chilesaurus diegosuarezi* gen. et sp. nov. (SNGM-1935) as it was found in the field. Cd, caudal vertebrae; Cv,

cervical vertebrae; Dv, dorsal vertebrae; Lf, left forelimb; Lfem, left femur; Lsc, left scapulocoracoid; Ltib, left tibia; Rf, right forelimb; Sk, skull.



Extended Data Figure 2 | Selected skull bones of *Chilesaurus diegosuarezi* gen. et sp. nov. (SNGM-1935; holotype). **a**, Right frontal in dorsal view; **b**, right postorbital in lateral view; **c**, incomplete right (?) maxilla in lateral view;

d, right dentary in medial view. al, alveolus; ao, antorbital opening; or, orbital rim; t, teeth; tf, lower temporal fossa rim.



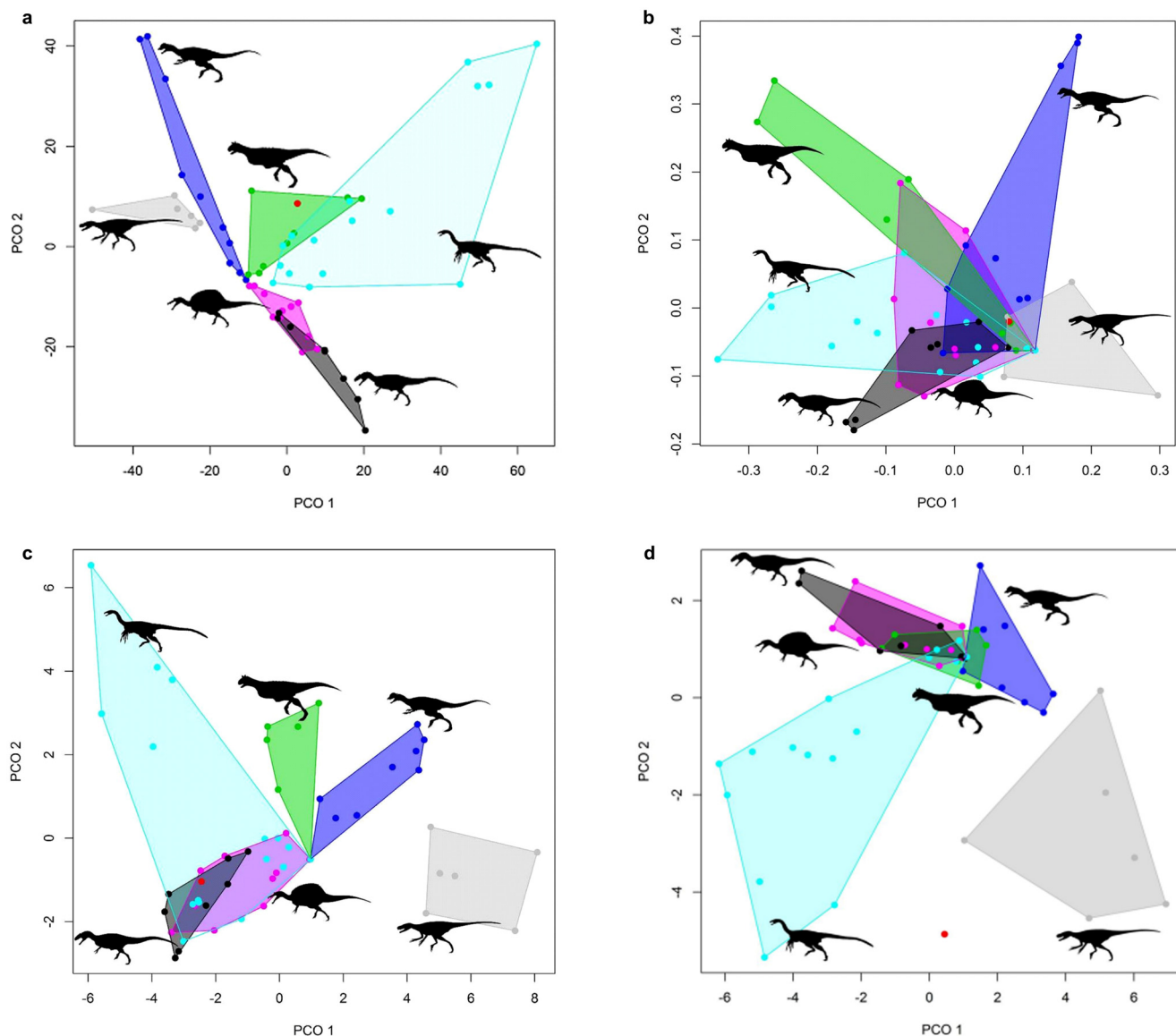
Extended Data Figure 3 | Scapular girdle and selected forelimb bones of *Chilesaurus diegosuarezi* gen. et sp. nov. **a, b**, Left scapula and coracoid (SNGM-1938) in lateral (**a**) and posterior (**b**) views. **c**, Left humerus (SNGM-

1938) in anterior view; **d**, left radius (SNGM-1935, holotype) in lateral view; and **e**, left ulna (SNGM-1935, holotype) in lateral view. cf, coracoid foramen; dp, deltopectoral crest; gl, glenoid cavity; ol, olecranon process.



Extended Data Figure 4 | Selected hindlimb elements of *Chilesaurus diegosuarezi* gen. et sp. nov. **a, b**, Right femur (SNGM-1935) in anterior (a) and lateral (b) views. **c–e**, Articulated right tibia and fibula (SNGM-1935) in

posterior (c), medial (d) and proximal (e) views. at, anterior trochanter; cn, cnemial crest; f, fibula; fh, femoral head; 4t, fourth trochanter; gt, greater trochanter; ic, inner condyle; oc, outer condyle; t, tibia; tfc, tibiofibular crest.



Extended Data Figure 5 | Bivariate plots showing the results of the morphospace occupation analysis of *Chilesaurus diegosuarezi* gen. et sp. nov. based on characters of different regions of the skeleton, taken from the modified data matrix and the first and second axes of the principal coordinate analysis. a–d, Bivariate plots using all the characters (a), cranial characters (b), hindlimb zeugopodium and stylopodium characters (c), and

tarsal and pedal characters (d). The convex hulls represent different dinosauriform groups rather than statistically distinct clusters. Light grey polygon, non-neotheropod dinosauriforms; blue polygon, non-averostran neotheropods; green polygon, ceratosaurs; pink polygon, megalosauroids; dark grey polygon, allosauroids; light blue polygon, coelurosaurs; red dot, *Chilesaurus*.

Extended Data Table 1 | Selected postcranial measurements of three specimens of *Chilesaurus diegosuarezi* gen. et sp. nov.

Specimens Bones	SNGM-1935	SNGM-1937	SNGM-1936
Scapula	116.3	-	-
Radius	68.8	64.0	-
Humerus	97.8	-	-
Metacarpal III	26.7	21.7	-
Iliac blade	116.9	-	-
Pubis	95.7	-	97.7
Ischium	101.2	-	101.6
Femur	142.4	-	114.6
Tibia	144.4	114.6	-
Metatarsal I	-	31.4	-
Metatarsal II	-	50.9	-
Metatarsal III	-	71.1	-

Measurements are in mm. All the values represent maximum measurable lengths. Maximum deviation of the digital calliper equals 0.02 mm but measurements were rounded to the nearest 0.1 mm.

Activating positive memory engrams suppresses depression-like behaviour

Steve Ramirez¹, Xu Liu[‡], Christopher J. MacDonald¹, Anthony Moffa¹, Joanne Zhou¹, Roger L. Redondo^{1,2} & Susumu Tonegawa^{1,2}

Stress is considered a potent environmental risk factor for many behavioural abnormalities, including anxiety and mood disorders^{1,2}. Animal models can exhibit limited but quantifiable behavioural impairments resulting from chronic stress, including deficits in motivation, abnormal responses to behavioural challenges, and anhedonia^{3–5}. The hippocampus is thought to negatively regulate the stress response and to mediate various cognitive and mnemonic aspects of stress-induced impairments^{2,3,5}, although the neuronal underpinnings sufficient to support behavioural improvements are largely unknown. Here we acutely rescue stress-induced depression-related behaviours in mice by optogenetically reactivating dentate gyrus cells that were previously active during a positive experience. A brain-wide histological investigation, coupled with pharmacological and projection-specific optogenetic blockade experiments, identified glutamatergic activity in the hippocampus–amygdala–nucleus accumbens pathway as a candidate circuit supporting the acute rescue. Finally, chronically reactivating hippocampal cells associated with a positive memory resulted in the rescue of stress-induced behavioural impairments and neurogenesis at time points beyond the light stimulation. Together, our data suggest that activating positive memories artificially is sufficient to suppress depression-like behaviours and point to dentate gyrus engram cells as potential therapeutic nodes for intervening with maladaptive behavioural states.

Our recent studies have demonstrated that dentate gyrus cells that express c-Fos during fear or reward conditioning define an active neural population that is sufficient to elicit both aversive and appetitive responses, and that the mnemonic output elicited by these artificially reactivated cells can be updated with new information^{6–8}. These findings raise the possibility of alleviating stress-induced behavioural impairments via a defined set of dentate gyrus cells that are active during a positive experience. Indeed, how positive episodes interact with psychiatric-disease-related behavioural states, including depression-related impairments, at the neuronal and systems level remains largely unknown, despite the promising cognitive treatments available in humans⁹.

To address this issue, we used our recently developed method that enables labelling and manipulation of memory engram cells (see Methods)^{6–8}. Exposing animals that were taken off doxycycline to a naturally rewarding experience⁸ (that is, exposure to a female mouse in a modified home cage, hereafter referred to as a ‘positive experience’ and further validated in Extended Data Fig. 1), a neutral context (hereafter referred to as a ‘neutral experience’), or a single bout of immobilization stress (hereafter referred to as a ‘negative experience’) all elicited comparable levels of ChR2–mCherry expression in the dentate gyrus (Extended Data Fig. 2a–e).

As shown in Fig. 1a, mice were split into six groups (see Methods). After 10 days of chronic immobilization stress (CIS) (Extended Data Fig. 2f) or in a home cage, all groups were put through the open field test (OFT) and elevated plus maze test (EPMT) as measures of anxiety-like behaviours, as well as the tail suspension test (TST) as a measure of

active/passive escape behaviour in response to a challenging situation, and the sucrose preference test (SPT) for anhedonia^{10–14}. In unstressed animals, optogenetic reactivation of cells previously active during a positive experience did not significantly change anxiety-related measures, time spent struggling, or preference for sucrose compared to unstressed mCherry controls (Fig. 1b–e). In the stressed groups, the CIS paradigm elicited a robust decrease in time struggling and preference for sucrose, as well as increased anxiogenic responses, consistent with previous reports^{13,14} (Fig. 1b–e).

However, optically reactivating dentate gyrus cells that were previously active during a positive experience, but not a neutral or a negative experience, in stressed animals acutely increased time struggling and sucrose preference to levels that matched the unstressed group’s behaviour (Fig. 1b, c). Additionally, optical reactivation of dentate gyrus cells associated with a positive experience decreased the latency to feed in a novelty-suppressed feeding test (NSFT)¹⁴ (Extended Data Fig. 3a) without affecting hunger or satiety (Extended Data Fig. 3b). Once again, the CIS paradigm had an anxiogenic effect across all groups, and all groups failed to show light-induced behavioural changes in the OFT or EPMT (Fig. 1d, e). Similarly, total distance travelled was consistent across groups (Extended Data Fig. 4c). Taken together, these data argue that reactivating dentate gyrus cells labelled by a positive experience is sufficient to acutely reverse the behavioural effects of stress in the TST, SPT and NSFT.

To identify potential neural loci that mediate the light-induced reversal of the stress-induced behaviours observed in our experiments, all subjects first underwent the CIS protocol and then were exposed to the TST while dentate gyrus cells previously active during a positive experience were optically reactivated. We then performed a brain-wide mapping of c-Fos expression in areas activated by this treatment (Fig. 2a).

Optical reactivation of dentate gyrus cells labelled by a positive experience correlated with a robust increase of c-Fos expression in several brain areas, including the nucleus accumbens (NAcc) shell, lateral septum, basolateral amygdala (BLA), central amygdala, as well as the dorsomedial, ventromedial, and lateral hypothalamus (Fig. 2b–i and Extended Data Fig. 5a, b), but not in the medial prefrontal cortex (mPFC) (Fig. 2j–m) or in several other loci (Extended Data Fig. 5c–e). Furthermore, we monitored single-unit activity in the BLA of mice while simultaneously activating dentate gyrus positive memory-*engram* cells with blue light and found that ~8% of cells (9/106; *n* = 3 mice) had excitatory (8/9 cells) or inhibitory (1/9 cells) responses (Extended Data Fig. 4a). A parallel set of experiments in which unstressed animals received optical stimulation of dentate gyrus cells revealed mostly similar patterns of c-Fos expression (Extended Data Fig. 6).

The NAcc has been heavily implicated in stress responses, mood disorders, and processing natural rewards^{2,5,10–12,15–20}. Moreover, pathophysiological dysfunction of the NAcc in response to various stressors has been implicated in anhedonia and reward conditioning^{17–20}. Our within-subject experiments revealed that, in the TST, the behavioural

¹RIKEN-MIT Center for Neural Circuit Genetics at the Picower Institute for Learning and Memory, Department of Biology and Department of Brain and Cognitive Sciences, Massachusetts Institute of Technology, Cambridge, Massachusetts 02139, USA. ²Howard Hughes Medical Institute, Massachusetts Institute of Technology, Cambridge, Massachusetts 02139, USA. [‡]Deceased.

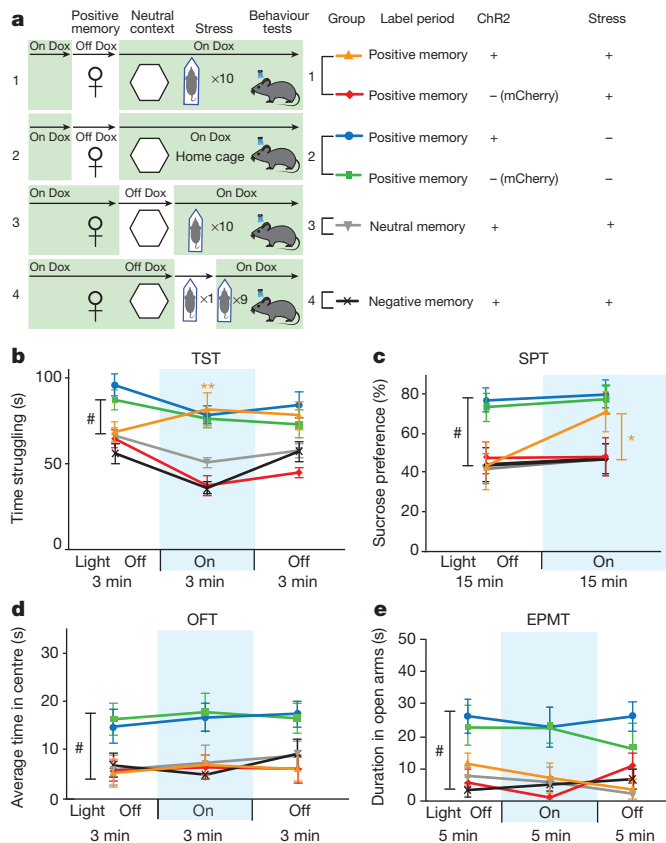


Figure 1 | Activating positive memory engrams rescues depression-related behaviour. **a**, Behaviour schedule and groups used. Dox, doxycycline.

Female symbols represent exposure to a female conspecific, white hexagons represent neutral contexts, and mice in the 'stress' condition are depicted undergoing an immobilization protocol. **b-e**, Optical reactivation of dentate gyrus cells that were previously active during a positive experience significantly increases time struggling in the tail suspension test (**b**) and preference for sucrose (**c**), but does not have a significant effect in anxiety-like behaviour in the open field test (**d**) or elevated plus maze test (**e**). A two-way analysis of variance (ANOVA) with repeated measures revealed a group-by-light epoch interaction in the TST ($F_{5,294} = 21.20$, $P < 0.001$) or SPT ($F_{5,196} = 6.20$, $P < 0.001$) followed by Bonferroni post hoc tests, which revealed significant increases in struggling or preference for sucrose in the positive memory plus stress group. # $P < 0.01$. # used to denote significant differences between the four stressed groups ($n = 18$ per group) versus the two non-stressed groups ($n = 16$ per group); * $P < 0.05$, ** $P < 0.01$ (orange asterisks used to denote significant differences between the stress plus positive memory group versus the other three stressed groups). Data are means \pm s.e.m.

effects of optically reactivating dentate gyrus cells labelled by a positive experience were blocked in the group of mice that concurrently received the glutamate receptor antagonists NBQX and AP5 in the NAcc, but not in the group that received saline, without altering basal locomotion (Extended Data Fig. 4b, c). Blocking dopaminergic activity yielded a similar blockade of the dentate gyrus light-induced effects (Extended Data Fig. 7a).

The BLA is known to have robust glutamatergic inputs to the NAcc¹⁹, and previous studies have implicated BLA projections to the NAcc in enabling reward-seeking behaviour¹⁹. We therefore investigated whether the hippocampus (dentate gyrus)-BLA-NAcc functional pathway is crucial for the real-time light-induced rescue of depression-related behaviour. Our transgenic mice were bilaterally injected with TRE-ArchT-eGFP into the BLA to allow for activity-dependent ArchT-eGFP labelling of axonal terminals from the BLA to the NAcc in response to a positive experience²¹ (Fig. 3a, b). Optic fibres were bilaterally placed over the NAcc and the dentate gyrus to allow for real-time inhibition of these terminals originating from ~18% (Fig. 3c)

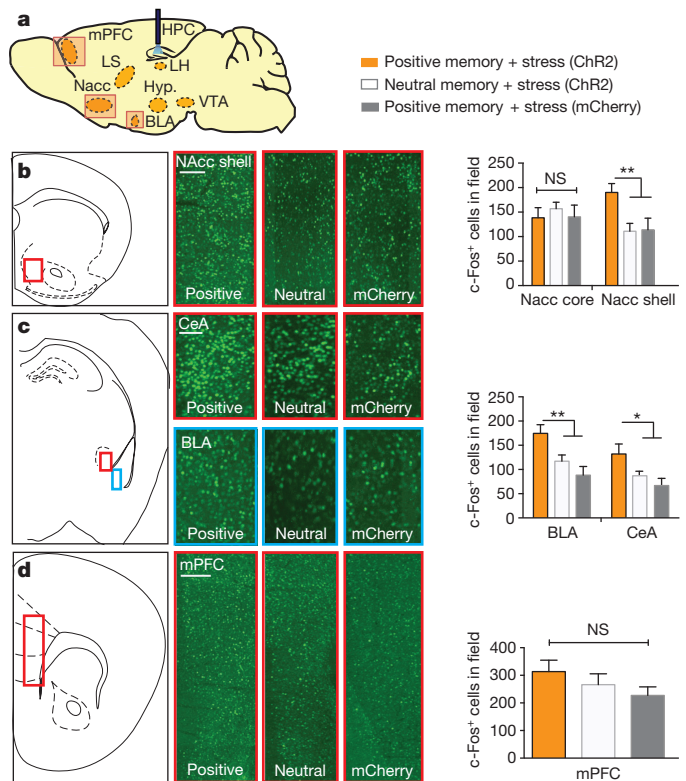
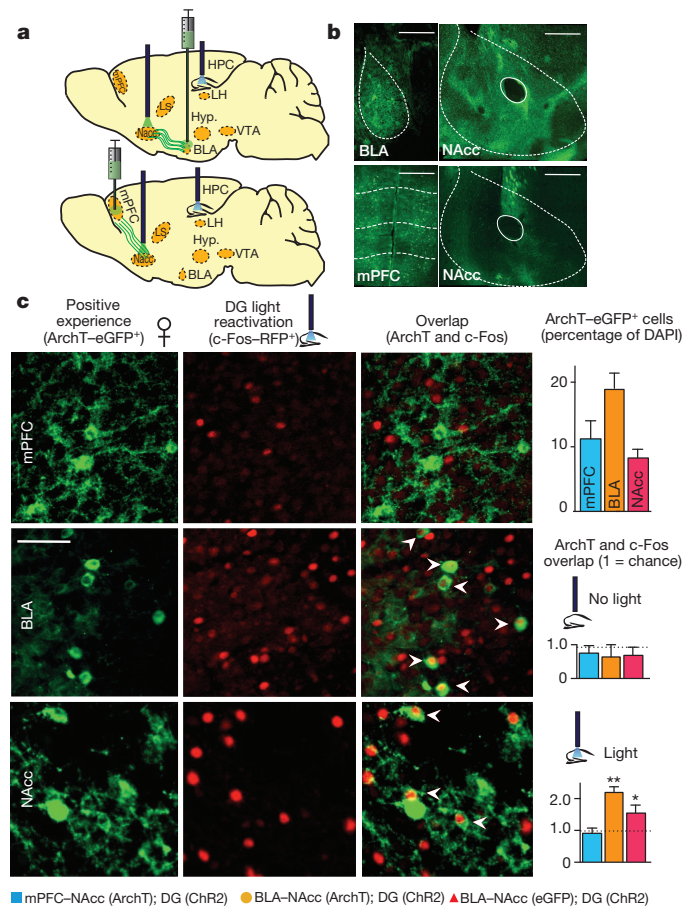


Figure 2 | Positive memory reactivation increases c-Fos expression in the nucleus accumbens shell and the amygdala. **a**, Brain diagram illustrating target areas analysed. **b-d**, Activation of a positive memory, but not a neutral memory or mCherry only, in the dentate gyrus during the TST elicits robust c-Fos expression in the nucleus accumbens shell (**b**), basolateral amygdala, and central amygdala (**c**), but not in the medial prefrontal cortex (**d**). For histological data, a one-way ANOVA followed by a Bonferroni post hoc test revealed a significant increase of c-Fos expression in the positive memory plus stress group relative to controls in the NAcc and amygdala, but not the mPFC (NAcc shell, $F_{2,30} = 15.2$, $P < 0.01$; BLA, $F_{2,30} = 11.71$, $P < 0.01$; central amygdala, $F_{2,30} = 11.45$, $P < 0.05$; mPFC, $F_{2,30} = 1.33$, $P = 0.294$. $n = 6$ animals per group, 3–5 slices per animal). NS, not significant; * $P < 0.05$, ** $P < 0.01$. Data are means \pm s.e.m. Scale bars correspond to 100 μ m. HPC, hippocampus; LH, lateral habenula; LS, lateral septum; Hyp., hypothalamus.

of BLA neurons and simultaneous activation of ChR2-mCherry-positive dentate gyrus cells, respectively, in stressed mice. At the neuronal level, light-induced reactivation of dentate gyrus cells previously activated by a positive experience also reactivated BLA⁸ and NAcc¹⁸, but not mPFC, cells (that is, endogenous c-Fos⁺ cells, red) previously activated by the same positive experience (that is, ArchT-eGFP⁺ cells, green) (Fig. 3c). These results suggest that the dentate gyrus engram cells are functionally connected to BLA engram cells and NAcc engram cells. At the behavioural level, inhibition of BLA terminals onto the NAcc blocked the dentate gyrus light-induced rescue in both the TST and SPT (Fig. 3d–g). Within the same behavioural session for the TST, and across 2 days for the SPT, when ArchT-mediated inhibition was released (that is, the green light was turned off), the rescue effects of reactivating dentate gyrus cells previously active during a positive experience were rapidly observed in all groups (Fig. 3d–g). ArchT-mediated inhibition of BLA-NAcc terminals alone did not negatively affect behaviour in the TST or SPT beyond the levels of the stressed animals (Fig. 3d–g insets). The specificity of the hippocampus (dentate gyrus)-BLA-NAcc pathway for the rescue was supported by an analogous experiment conducted with bilateral injections of TRE-ArchT-eGFP into the mPFC. Although the mPFC is also known to provide robust glutamatergic input to the NAcc¹⁹, the induction of c-Fos expression in this area upon optogenetic activation of dentate gyrus cells associated with a positive experience was not significantly higher

than that observed with a neutral experience (Fig. 2m), and mPFC cells reactivated by dentate gyrus cell reactivation was at chance level (Fig. 3c). Correspondingly, inhibition of terminals originating from ~12% of the mPFC (Fig. 3c) onto the NAcc did not block the dentate gyrus light-induced rescue in either the TST or SPT (Fig. 3d–g). Moreover, inhibition of BLA, but not mPFC, terminals onto the NAcc partially inhibited the dentate-gyrus-mediated, light-induced increase of c-Fos⁺ cells observed in the NAcc shell (Fig. 3h), supporting the conclusion that the hippocampal (dentate gyrus)–BLA–NAcc pathway of positive engrams plays a crucial role in the rescue of depression-related behavioural phenotypes.



Recent meta-analyses have suggested that treating psychiatric disorders through prescribed medication or cognitive interventions are capable of producing symptom remission when administered chronically²⁰, though the neural underpinnings inducing and correlating with long-lasting rescues are poorly understood^{20,22,23}. The aforementioned acute intervention did not induce enduring behavioural changes (Extended Data Fig. 7b). We therefore investigated whether chronic reactivation of dentate gyrus engram cells could attenuate depression-related behaviours in a manner that outlasted acute optical stimulation following the protocol depicted in Fig. 4a (Methods). A group in which dentate gyrus cells associated with a positive experience were optically reactivated across 5 days, but not 1-day or no stimulation groups, showed a reversal of the stress-induced behavioural deficits measured in the TST and SPT that was not significantly different from an unstressed control group (Fig. 4b, c). A group in which dentate gyrus cells associated with a neutral experience were optically reactivated across 5 days did not show such effects, nor did a group that was exposed to a natural social reward for 5 days (Fig. 4b–d). Histological analyses revealed decreased levels of neurogenesis as measured both by the polysialylated neuronal cell adhesion molecule (PSA-NCAM) and doublecortin (DCX)—often considered markers of developing and migrating neurons^{24,25}—in all stressed groups except for the positive experience and 5-day stimulation group, and the unstressed control group (Fig. 4d and Extended Data Fig. 8). This increase in adult-born neurons positively correlated with the degree to which each group preferred sucrose in the SPT (Extended Data Fig. 9a); moreover, performance levels on the SPT and TST positively correlated with one another on an animal-by-animal basis (Extended Data Fig. 9b).

Our data demonstrate that the depression-related readouts of active/passive coping-like behaviour and anhedonia, as measured in the TST and SPT, respectively, can be ameliorated by activating cells in the hippocampus associated with a positive memory, while anxiety-related behaviours measured by the OFT and EPMT remained unchanged. Differential regulation of depression- and anxiety-related behaviour could have been achieved by leveraging the functional

Figure 3 | The antidepressant effects of an optically activated positive memory require real-time terminal activity from the BLA to the NAcc.

a, Brain diagram illustrating target areas manipulated. **b**, Representative coronal slices showing TRE–ArchT–eGFP-positive cells in the BLA or mPFC, as well as their corresponding terminals in the NAcc. Scale bars: BLA and mPFC, 500 μ m; NAcc, 200 μ m. **c**, Animals were taken off Dox and initially exposed to a positive experience, which caused labelling of corresponding BLA (~18%), mPFC (~12%), or NAcc (~9%) cells with eGFP derived from AAV₉–TRE–ArchT–eGFP (green, halo-like expression). Light-activation of a positive memory engram in the dentate gyrus (DG) preferentially reactivated the BLA and NAcc shell cells, as measured by endogenous c-Fos expression (red, nucleus-localized), that were originally labelled by the same positive experience, while groups with no light stimulation showed levels of overlap not significantly different from chance. Arrowheads indicate double-stained cells. Scale bar, 5 μ m. **d–g**, ArchT-mediated inhibition of BLA, but not mPFC, terminals in the NAcc prevents the dentate-gyrus-mediated light-induced increases in struggling (d, e) or preference for sucrose (f, g), while inhibition of BLA terminals in the NAcc without dentate gyrus stimulation does not affect behaviour (insets). **h**, ArchT-mediated inhibition of BLA, but not mPFC, terminals prevents the dentate-gyrus-mediated light-induced increase of c-Fos expression in the NAcc. For behavioural data, a two-way ANOVA with repeated measures followed by a Bonferroni post hoc test revealed a group-by-light epoch interaction and significant ArchT-mediated attenuation of struggling in the TST (d: $F_{2,99} = 7.30$, $P < 0.001$; e: $F_{2,99} = 6.61$, $P < 0.01$) or preference for sucrose water in the SPT (f: $F_{2,66} = 10.66$, $P < 0.01$). $n = 12$ per behavioural group. * $P < 0.05$, ** $P < 0.01$, *** $P < 0.001$; orange asterisks used to denote significant differences between the stress plus positive memory group versus all other groups. For histological data, one-sample t -tests against chance overlap were performed ($n = 4$ per group, 3–5 slices per animal). NS, not significant. HPC, hippocampus; LH, lateral habenula; LS, lateral septum; Hyp., hypothalamus. Data are means \pm s.e.m.

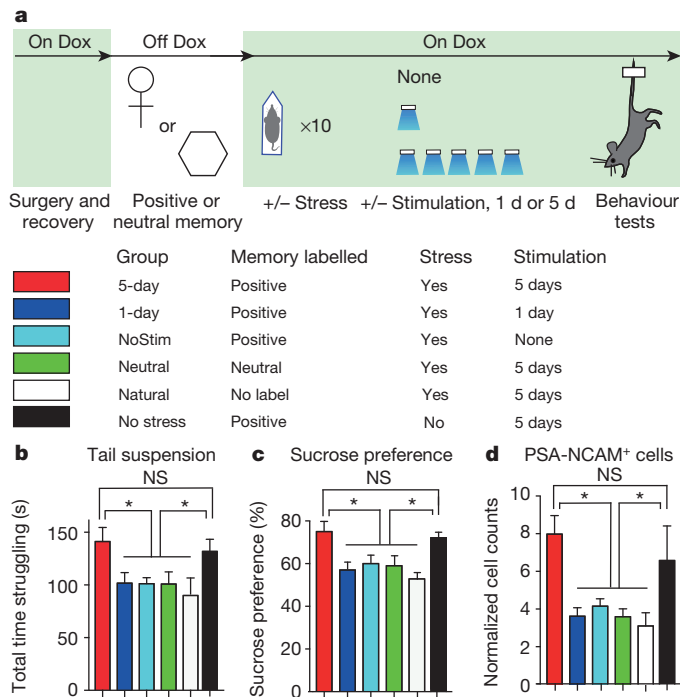


Figure 4 | Chronic activation of a positive memory elicits a long-lasting rescue of depression-related behaviour. **a**, Behavioural schedule and groups used. NoStim, no stimulation. Female symbols represent exposure to a female conspecific, white hexagons represent neutral contexts, and mice in the 'stress' condition are depicted undergoing an immobilization protocol. **b**, **c**, Animals in which a positive memory was reactivated twice a day for 5 days showed increased struggling in a 6-min tail suspension test ($F_{5,78} = 3.34$, $P < 0.05$) (**b**) and increased preference for sucrose measured over 24 h ($F_{5,84} = 6.25$, $P < 0.01$) (**c**). **d**, The 5-day positive memory stimulation group showed a significant increase of adult newborn cells in the dentate gyrus as measured by PSA-NCAM⁺ cells ($F_{5,72} = 4.65$, $P < 0.01$; see Extended Data Fig. 8 for doublecortin data and PSA-NCAM images). For these data (**b–d**), a one-way ANOVA revealed a significant interaction of the experimental-group factor and stimulation-condition factor and was followed by a Bonferroni post hoc test. $n = 14$ per TST behavioural group, $n = 15$ per SPT behavioural group, $n = 5$ slices per animal for data appearing in **d**. * $P < 0.05$. Data are means \pm s.e.m.

segregation present along the hippocampus dorsal–ventral axis; for instance, activation of ventral hippocampal dentate gyrus engram cells could reveal heterogeneous, behaviourally relevant roles in the emotional regulation of anxiety and stress responses that our dorsal hippocampus manipulations presumably did not access^{26,27}. To that end, we speculate that, at the engram level, the circuitry sufficient to modulate anxiety-related behaviour relies more heavily on a synaptic dialogue within the amygdala, its bidirectional connections with the ventral hippocampus, and its effects on downstream mesolimbic and cortical structures^{10,11,26,27}.

Depression is diagnosed as a constellation of heterogeneous symptoms; their complex aetiology and pathophysiology underscore the varied responses to currently available treatments. While most psychopharmacological treatments take weeks to achieve effects, other alternative treatments such as deep-brain stimulation and the NMDA antagonist ketamine have been reported to have rapid effects in a subset of patients²⁸. In rodents, optogenetic stimulation of mPFC neurons, mPFC to raphe projections, and ventral tegmental dopaminergic neurons achieved a rapid reversal of stress-induced maladaptive behaviours^{4,10,11}. We speculate that our acute behavioural changes reflect the degree to which directly stimulating positive-memory-engram-bearing cells might bypass the plasticity that normally takes antidepressants weeks or months to achieve, thereby temporarily suppressing the depression-like state. In support, we observed that

the effects of optically stimulating a positive memory are contingent on active glutamatergic projections from the amygdala to the NAcc in real time, as well as intra-NAcc dopamine activity¹⁸. Our data dovetail with this circuit's proposed role of relaying BLA stimulus-reward associations to a ventral striatal motor-limbic interface. This interface is thought to be capable of coalescing such information with motivational states and finally translating such activity into behaviourally relevant outputs^{5,17–19}.

Moreover, our chronic stimulation data reveal that repeatedly activating dentate gyrus engram cells associated with a positive experience elicits an enduring reversal of stress-induced behavioural abnormalities and an increase in neurogenesis. While future experiments are required to identify the causal link between chronically reactivated positive memory engrams and the corresponding rescue of behaviours, many tantalizing hypotheses surface, including a normalization of VTA firing rates²⁹, epigenetic and differential modification of effector proteins (for example, CREB, BDNF) in areas upstream and downstream of the hippocampus³⁰, and a reversal of neural atrophy in areas such as CA3 and mPFC or hypertrophy in BLA²⁶. The aforementioned molecular and homeostatic mechanisms—in addition to our observed increase of adult-born neurons in the 5-day stimulation group—could be partly realized in a hormone- or neuromodulator-mediated manner (Extended Data Fig. 5). Finally, our data demonstrate that exposing stressed subjects to a natural positive experience repeatedly is not effective, while repeated direct reactivations of dentate gyrus engram cells associated with a previously acquired positive memory is effective (Fig. 4b–d). We speculate that invasively stimulating these dentate gyrus cells is effective in activating both the internal contextual representation associated with a positive experience as well as associated downstream areas, while exposure to natural exogenous positive cues may not be able to access similar neural pathways in subjects displaying depression-like symptoms such as passive behaviour in challenging situations and anhedonia (Fig. 4b–d).

Collectively, the data described here build a novel experimental bridge between memory engrams in the brain and animal models of psychiatric disorders. We propose that direct activation of dentate gyrus engram cells associated with a positive memory offers a potential therapeutic node for alleviating a subset of depression-related behaviours and, more generally, that directly activating endogenous neuronal processes may be an effective means to correct maladaptive behaviours.

Online Content Methods, along with any additional Extended Data display items and Source Data, are available in the online version of the paper; references unique to these sections appear only in the online paper.

Received 14 October 2014; accepted 1 May 2015.

- Caspi, A. *et al.* Influence of life stress on depression: moderation by a polymorphism in the 5-HTT gene. *Science* **301**, 386–389 (2003).
- Pittenger, C. & Duman, R. S. Stress, depression, and neuroplasticity: a convergence of mechanisms. *Neuropsychopharmacology* **33**, 88–109 (2008).
- Hyman, S. E. Revitalizing psychiatric therapeutics. *Neuropsychopharmacology* **39**, 220–229 (2014).
- Covington, H. E. III *et al.* Antidepressant effect of optogenetic stimulation of the medial prefrontal cortex. *J. Neurosci.* **30**, 16082–16090 (2010).
- Russo, S. J. & Nestler, E. J. The brain reward circuitry in mood disorders. *Nature Rev. Neurosci.* **14**, 609–625 (2013).
- Liu, X. *et al.* Optogenetic stimulation of a hippocampal engram activates fear memory recall. *Nature* **484**, 381–385 (2012).
- Ramirez, S. *et al.* Creating a false memory in the hippocampus. *Science* **341**, 387–391 (2013).
- Redondo, R. L. *et al.* Bidirectional switch of the valence associated with a hippocampal contextual memory engram. *Nature* **513**, 426–430 (2014).
- Seligman, M. E. P., Rashid, T. & Parks, A. C. Positive psychotherapy. *Am. Psychol.* **61**, 774–788 (2006).
- Tye, K. M. *et al.* Dopamine neurons modulate neural encoding and expression of depression-related behaviour. *Nature* **493**, 537–541 (2013).
- Warden, M. R. *et al.* A prefrontal cortex-brainstem neuronal projection that controls response to behavioural challenge. *Nature* **492**, 428–432 (2012).
- Deisseroth, K. Circuit dynamics of adaptive and maladaptive behaviour. *Nature* **505**, 309–317 (2014).

13. Lim, B. K., Huang, K. W., Grueter, B. A., Rothwell, P. E. & Malenka, R. C. Anhedonia requires MC4R-mediated synaptic adaptations in nucleus accumbens. *Nature* **487**, 183–189 (2012).
14. Snyder, J. S., Soumier, A., Brewer, M., Pickel, J. & Cameron, H. A. Adult hippocampal neurogenesis buffers stress responses and depressive behaviour. *Nature* **476**, 458–461 (2011).
15. Lammel, S. *et al.* Input-specific control of reward and aversion in the ventral tegmental area. *Nature* **491**, 212–217 (2012).
16. Dölen, G., Darvishzadeh, A., Huang, K. W. & Malenka, R. C. Social reward requires coordinated activity of nucleus accumbens oxytocin and serotonin. *Nature* **501**, 179–184 (2013).
17. Schlaepfer, T. E. *et al.* Deep brain stimulation to reward circuitry alleviates anhedonia in refractory major depression. *Neuropsychopharmacology* **33**, 368–377 (2008).
18. Xiu, J. *et al.* Visualizing an emotional valence map in the limbic forebrain by TAI-FISH. *Nature Neurosci.* **17**, 1552–1559 (2014).
19. Stuber, G. D. *et al.* Excitatory transmission from the amygdala to nucleus accumbens facilitates reward seeking. *Nature* **475**, 377–380 (2011).
20. DeRubeis, R. J., Siegle, G. J. & Hollon, S. D. Cognitive therapy versus medication. *Nature Rev. Neurosci.* **9**, 788–796 (2008).
21. Han, X. *et al.* A high-light sensitivity optical neural silencer: development and application to optogenetic control of non-human primate cortex. *Front. Syst. Neurosci.* **5**, 18 (2011).
22. Brody, A. L. *et al.* Regional brain metabolic changes in patients with major depression treated with either paroxetine or interpersonal therapy. *Arch. Gen. Psychiatry* **58**, 631–640 (2001).
23. Airan, R. D. *et al.* High-speed imaging reveals neurophysiological links to behavior in an animal model of depression. *Science* **317**, 819–823 (2007).
24. Seki, T. & Arai, Y. Highly polysialylated neural cell adhesion molecule (NCAM-H) is expressed by newly generated granule cells in the dentate gyrus of the adult rat. *J. Neurosci.* **13**, 2351–2358 (1993).
25. Santarelli, L. *et al.* Requirement of hippocampal neurogenesis for the behavioral effects of antidepressants. *Science* **301**, 805–809 (2003).
26. Roozendaal, B., McEwen, B. S. & Chattarji, S. Stress, memory and the amygdala. *Nature Rev. Neurosci.* **10**, 423–433 (2009).
27. Felix-Ortiz, A. C. *et al.* BLA to vHPC inputs modulate anxiety-related behaviors. *Neuron* **79**, 658–664 (2013).
28. Berman, R. M. *et al.* Antidepressant effects of ketamine in depressed patients. *Biol. Psychiatry* **47**, 351–354 (2000).
29. Friedman, A. K. *et al.* Enhancing depression mechanisms in midbrain dopamine neurons achieves homeostatic resilience. *Science* **344**, 313–319 (2014).
30. Tsankova, N., Renthal, W., Kumar, A. & Nestler, E. J. Epigenetic regulation in psychiatric disorders. *Nature Rev. Neurosci.* **8**, 355–367 (2007).

Acknowledgements We thank B. Chen, D. S. Roy, and J. Kim for help with the experiments, T. J. Ryan and T. Kitamura for the TRE-ArchT-eGFP construct, J. Sarinana and E. Hueske for comments and extensive discussions on the manuscript, and all the members of the Tonegawa laboratory for their support. We dedicate this study to the memory of Xu Liu, who made major contributions to memory engram research. This work was supported by RIKEN Brain Science Institute and Howard Hughes Medical Institute.

Author Contributions S.R., X.L., C.M., A.M., J.Z., R.L.R. and S.T. contributed to the study design. S.R., X.L., A.M., J.Z., C.M. and R.L.R. contributed to the data collection and interpretation. X.L. cloned all constructs. S.R., X.L., C.M., J.Z. and A.M. conducted the surgeries, behaviour experiments, and histological analyses. S.R., X.L. and S.T. wrote the paper. All authors discussed and commented on the manuscript.

Author Information Reprints and permissions information is available at www.nature.com/reprints. The authors declare no competing financial interests. Readers are welcome to comment on the online version of the paper. Correspondence and requests for materials should be addressed to S.T. (tonegawa@mit.edu).

METHODS

Subjects. The *c-fos-tTA* mice were generated by crossing TetTag³¹ mice with C57BL/6J mice and selecting for those carrying the *c-fos-tTA* transgene. Littermates were housed together before surgery and received food and water *ad libitum*. All mice were raised on a diet containing 40 mg kg⁻¹ doxycycline (Dox) for a minimum of 1 week before receiving surgery at age 12–16 weeks. Post-operation, mice were individually housed in a quiet home cage with a reverse 12 h light–dark cycle, given food and water *ad libitum*, and allowed to recover for a minimum of 2–3 weeks before experimentation. All animals were taken off Dox for an undisturbed 42 h to open a time window of activity-dependent labelling. In our system, the promoter of *c-Fos*—an immediately early gene often used as a marker of recent neural activity—is engineered to drive the expression of the tetracycline transactivator (tTA), which in its protein form binds to the tetracycline response element (TRE). Subsequently, the activated TRE drives the light-responsive channelrhodopsin-2 (ChR2). Importantly, the expression of ChR2 only occurs in the absence of doxycycline (Dox) from the animal's diet, thus permitting inducible expression of ChR2 in correspondingly active cells.

Each group of male mice was exposed to all three subsequent treatments for 2 hours and randomly assigned which experience would occur while off Dox; a negative experience (that is, a single bout of immobilization stress, see below), a naturally rewarding experience (that is, exposure to a female conspecific while in a modified home cage, as previously reported³³), and a neutral experience (that is, exposure to a conditioning chamber). For female exposure, single-caged male mice were moved to a behaviour room distinct from the housing room and with dim lighting conditions. Next, the cage tops were removed and a 4-sided (31 × 25 × 30 cm) white box was placed over the home cage, after which a female mouse was introduced to the home cage. Importantly, this modification to the home cage during female exposure ensured similar levels of dentate gyrus labelling as the neutral and negative memory exposure groups (Extended Data Fig. 2). Each group was taken off Dox only during one of the aforementioned treatments and placed back on Dox immediately afterwards. The subjects were age-matched and split into two groups: a stressed group and a non-stressed group. Non-stressed animals remained in their home cages before experimentation. Stressed animals underwent 2–3 h of chronic immobilization stress (CIS) each day for ten consecutive days before behavioural testing using Mouse DecapiCone disposable restrainers. All procedures relating to mouse care and treatment conformed to the institutional and National Institutes of Health guidelines for the Care and Use of Laboratory Animals. Sample sizes were chosen on the basis of previous studies^{32–34}; variance was similar between groups for all metrics measured. No statistical methods were used to predetermine sample size.

Virus constructs and packaging. The pAAV₉-TRE-ChR2-mCherry and pAAV₉-TRE-mCherry plasmids were constructed as previously reported³³. The pAAV₉-TRE-ArchT-eGFP was constructed by replacing the *ChR2-eYFP* fusion gene in the pAAV₉-TRE-ChR2-eYFP plasmid from Liu *et al.*³⁴ with a fusion gene of *ArchT-eGFP* from Han *et al.*³⁵. These plasmids were used to generate AAV₉ viruses by the Gene Therapy Center and Vector Core at the University of Massachusetts Medical School. Viral titrations were 8 × 10¹² genome copy per ml for AAV₉-TRE-ChR2-mCherry, 1.4 × 10¹³ genome copy per ml for AAV₉-TRE-mCherry, and 0.75 to 1.5 × 10¹³ genome copy per ml for AAV₉-TRE-ArchT-eGFP.

Stereotactic injection, cannulation, and fibre optic implants. All surgeries were performed under stereotaxic guidance and subsequent coordinates are given relative to bregma. Animals were anaesthetized using 500 mg kg⁻¹ Avertin before receiving bilateral craniotomies using a 0.5 mm diameter drill bit at −2.2 mm anteroposterior (AP), ±1.3 mm mediolateral (ML) for dentate gyrus injections. All mice were injected with 0.15 µl of AAV9 virus at a controlled rate of 0.6 µl min⁻¹ using a mineral oil-filled glass micropipette joined by a microelectrode holder (MPH6S; WPI) to a 10 µl Hamilton microsyringe (701LT; Hamilton) in a microsyringe pump (UMP3; WPI). The needle was slowly lowered to the target site at −2.0 mm dorsoventral (DV). The micropipette remained at the target site for another 5 minutes post-injection before being slowly withdrawn. A bilateral optical fibre implant (200 µm core diameter; Doric Lenses) was lowered above the injection site (−1.6 mm DV for dentate gyrus) and three jewellery screws were secured into the skull at the anterior and posterior edges of the surgical site to anchor the implant. For mice used in pharmacological manipulations, bilateral guide cannula (PlasticsOne) were implanted above the NAcc (+1.2 mm AP; ±0.5 mm ML; −3.25 mm DV). Mice used in the BLA-to-NAcc or mPFC-to-NAcc experiments received bilateral injections (0.2 µl to 0.3 µl) of TRE-ArchT-eGFP or TRE-eGFP into the BLA (−1.46 mm AP; ±3.20 mm ML; −4.80 mm DV), NAcc (+1.2 mm AP; ±0.50 mm ML; −4.3 mm DV), or the mPFC (+1.70 mm AP; ±0.35 mm ML; −2.70 mm DV). These mice were then injected with TRE-ChR2-mCherry into the dentate gyrus and received bilateral optic fibre implantation as described above (Doric Lenses), as well as bilateral optic fibre implantation over the NAcc (+1.2 mm AP; ±0.50 mm ML; −3.70 mm DV).

Layers of adhesive cement (C&B Metabond) followed by dental cement (Teets cold cure; A-M Systems) were spread over the surgical site and protective cap to secure the optical fibre implant. The protective cap was made from the top portion of a black polypropylene microcentrifuge tube. Mice received intraperitoneal injections of 1.5 mg kg⁻¹ analgesics and were placed on heating pads throughout the procedure until recovery from anaesthesia. Histological studies were used to verify fibre placements and viral injection sites. Only data from mice with opsin or fluorophore expression restricted to the dentate gyrus, BLA or mPFC were used for histological, behavioural and statistical analyses.

Pharmacological infusion of glutamate or dopamine receptor antagonists. Glutamate antagonists were bilaterally infused into the NAcc as follows: 0.2 µl per hemisphere of NBQX at a concentration of 22.3 mM to antagonize AMPA (α-amino-3-hydroxy-5-methyl-4-isoxazole propionic acid) receptors and 0.2 µl per hemisphere of AP5 at a concentration of 38.04 mM to antagonize NMDA (N-methyl-D-aspartate) receptors. Dopamine receptor antagonists were bilaterally infused into the NAcc as follows: 0.2 µl SCH23390 at a concentration of 6.16 mM to antagonize D1-like receptors and 0.2 µl raclopride at a concentration of 2.89 mM to antagonize D2-like receptors. A 26-gauge stainless steel double internal cannula (PlasticsOne) was used to bilaterally infuse each drug; the internal cannula was connected with a microsyringe pump by a PE20 tube to control the injection rate at 100 nl min⁻¹. The injection cannula was left connected for 5 min before removal to allow for diffusion. Finally, all behaviour was performed 20 min following drug infusion.

Immunohistochemistry. Mice were overdosed with 750–1000 mg kg⁻¹ Avertin and perfused transcardially with cold PBS, followed by 4% paraformaldehyde (PFA) in PBS. Extracted brains were kept in 4% PFA at 4 °C overnight, then transferred to PBS. A vibratome was used to recover 50-µm coronal slices in cold PBS. Slices were washed with PBS-T (PBS + 0.2% Triton X-100), then incubated with PBS-T + 5% normal goat serum at 4 °C for 1 h for blocking. For immunostaining, slices were incubated with one or more primary antibodies (1:1000 dilution) at 4 °C for 24 h (600-401-379 Rockland; A10262, Invitrogen; SC-52, Santa Cruz). Three washes of PBS-T for 10 min each were performed on the slices before 1 h incubation with secondary antibody at 1:200 dilution (A11039, Invitrogen; A21429, Invitrogen). Slices were washed three more times in PBS-T for 10 min each, stained with 4',6-diamidino-2-phenylindole (DAPI; 1:10,000 dilution) to label cell nuclei and mounted with Vectashield H-1200 onto microscope slides.

Behavioural assays. All behaviour assays were conducted during the light cycle of the day (7:00–19:00) on animals 12–16 weeks old. Mice were handled for 3–5 days, 2 min per day, before all behavioural experiments.

Tail suspension test. Fibre optic implants on experimental mice were plugged into a patch cord before the tail suspension test. Each subject was hung by its tail from a bar 40 cm from the ground with a single piece of autoclave tape. The animal was positioned such that it had no contact with other objects. Immediately after positioning, video recordings of the animal's movements were taken (Noldus by Ethovision). Blue light stimulation was given at 20 Hz, 15 ms pulse width, ~15–20 mW. For behavioural data appearing in Fig. 1, all mice were exposed to a 9 min tail suspension test with light stimulation occurring at minutes 3–5, inclusive; for histological data appearing in Fig. 2, all mice were exposed to a 6 min tail suspension test with light stimulation occurring throughout the entire session using the same stimulation parameters described above. For data appearing in Fig. 3, all animals were given a 9 min tail suspension test once a day for 2 days to assess the effects of ArchT inhibition on BLA or mPFC terminals in the NAcc while simultaneously activating ChR2-positive cells in the dentate gyrus. For half of the subjects, on day 1, ArchT-mediated inhibition occurred during minutes 3–5, inclusive, using constant green light at ~25 mW; dentate gyrus stimulation occurred from minutes 3–8, inclusive. For the other half, ArchT-mediated inhibition occurred during minutes 6–8, inclusive; and dentate gyrus stimulation occurred from minutes 3–8, inclusive. The treatments occurring on days 1 and 2 were counterbalanced within and across groups. A separate cohort of animals were used for the data appearing in the insets of Fig. 3d–g. These groups contained TRE-ChR2-mCherry in the dentate gyrus, as well as bilateral optic fibres over the dentate gyrus, and TRE-ArchT-eGFP in the BLA, as well as optic fibres over the NAcc to inhibit BLA terminals during the appropriate light-on epochs in the TST and SPT. These cohorts, too, were counterbalanced across sessions and only received green light over the NAcc for 3 min during the TST or 15 min during the SPT. For the *c-Fos* counts appearing in Fig. 3h, all groups underwent a 6 min tail suspension test with blue light delivered to the dentate gyrus and green light delivered to the NAcc throughout the entirety of the session. These groups were sacrificed 1.5 h later for histological analyses. For data appearing in Fig. 4, mice were exposed to a 6 min tail suspension test without light stimulation. An experimenter blind to each mouse condition and light treatment scored all the tail

suspension videos by measuring the total time in seconds that each mouse spent struggling throughout the protocol.

Sucrose preference test. A Med Associates operant chamber—equipped with photolickometers placed on two separate corners of the chamber—was used to count the number of licks made by the mice on lick spouts with direct access to 2% sucrose water solution or water alone. All animals undergoing the sucrose preference protocol were water-restricted for 36 h before each habituation session. These sessions consisted of first plugging the optic fibres on the water-deprived mice to a corresponding patch cord and exposing the mice to the operant chamber, which contained bottles filled only with water. Each exposure occurred on three separate days for 30 min per day. The three habituation sessions occurred interspersed throughout the 10-day chronic immobilization stress protocol (that is, on days 1, 4 and 7 of stress) at least 6 h before or after the stress protocol. In pilot experiments, ~90% of water-deprived animals failed to sample both photolickometers in the operant chamber even after multiple 30-min habituation sessions (data not shown); to address this issue, a glove box was inserted on its side in the operant chamber such that each subject had a narrow ~10 cm corridor to explore and find each lick spout. With this modification, >90% of animals found both lick spouts during the first and subsequent habituation sessions. Upon completing a habituation session, mice were given water only when 2 h of being placed back into the home cage had elapsed. On the test day (that is, the day on which optical stimulation occurred), the location of each sucrose or water bottle in the chamber was counterbalanced between animal chambers. A 30 min protocol—15 min light off, 15 min light on—was used on all animals. The first 15 min were used to detect the baseline preference; blue light stimulation at 20 Hz, 15 ms pulse width, ~15–20 mW, occurred during the second 15 min epoch to detect light-induced changes in preference. For data appearing in Fig. 3, water-deprived animals were exposed to the same 30-min protocol on two separate days. On day 1, after the first 15-min epoch, half of the animals received constant green light stimulation at ~15 mW (as previously reported³⁶) over the NAcc while simultaneously receiving blue light stimulation over the dentate gyrus; the other half received only blue light stimulation over the dentate gyrus. On day 2, the treatments were reversed in a counter-balanced manner. Data was only collected in animals that licked at both spouts in the first 15-min interval; animals that did not discover both lick spouts (as evidenced by licking only one spout during the first 15-min interval) were not given light stimulation, the experiment was terminated early, and the test was repeated the following day. Sucrose preferences were calculated as follows:

$$\frac{\text{total number of licks to sucrose spout}}{\text{total number of licks to sucrose spout} + \text{total number of licks to water spout}} \times 100.$$

For the sucrose preference data appearing in Fig. 4, mice were first habituated to two water bottles for 2 days in their home cages. On day 3, two water bottles containing either 2% sucrose or water were placed into the cages in a counter-balanced manner and left undisturbed for 24 h. Sucrose preferences were calculated as follows:

$$\frac{\Delta \text{weight of sucrose water}}{\Delta \text{weight of sucrose water} + \Delta \text{weight of water}} \times 100.$$

Open field test. An open, metal chamber (Accuscan system) with transparent, plastic walls was used for the open field test. Implanted mice were plugged into a patch cord, individually placed into the chamber, and allowed to explore freely for 12 min. An automated video-tracking system (Ethovision by Noldus) was used to track the amount of time spent in the centre of the chamber compared to the edges, as well as the total distance travelled across a session. Light stimulation, as described above, was given during minutes 3–5 and 9–11, inclusive.

Elevated plus maze test. Implanted animals were plugged into a corresponding patch cord before the beginning of the session and subsequently placed in an elevated plus maze. Two pieces of plastic (30 cm long, 5 cm wide) formed the two arms of the maze that intersected at right angles. One arm was enclosed with plastic black walls, and the other arm was open with no walls. The structure was elevated 60 cm above the floor and mice were placed one at a time at the intersection of the maze facing into an arm with walls to start a trial. Video tracking software (Ethovision by Noldus) was used to track the amount of time the mice spent in the enclosed versus the open arms of the maze throughout a 15-min session. Optical stimulation occurred only during the second 5-min epoch using the same stimulation parameters as noted above.

Novelty-suppressed feeding. The novelty suppressed feeding paradigm was performed as previously described³⁷. In brief, food was removed from the subjects' home cages 24 h before testing. The next day, mice were placed for 10 min in an open field apparatus containing bedding with a food pellet at the centre on a 1 cm² elevated platform. Light stimulation using the parameters described above occurred throughout the entire session. All behaviour was videotaped (Ethovision by Noldus) and latency to feed was scored offline by an experimenter

blind to the experimental conditions for each mouse. Once placed back into their home cages, mice were given a single food pellet, which was weighed before and after a 5-min test to measure for motivation/hunger effects on feeding behaviour compared to feeding in a novel environment.

5-day stimulation protocol. For data appearing in Fig. 4, animals were first split into six groups: a group in which dentate gyrus cells previously active during a positive experience were reactivated twice a day for 5 days (5-day group) after the CIS protocol, a group in which such stimulation occurred twice a day for 1 day (1-day group) after the CIS protocol, a group in which no stimulation was delivered (NoStim group) after the CIS protocol, a group in which dentate gyrus cells previously active during a neutral experience were reactivated twice a day for 5 days (Neutral group) after the CIS protocol, a group that did not receive the CIS stress protocol but still had dentate gyrus cells previously active during a positive experience reactivated twice a day for 5 days (NoStress group), and finally, a group that was exposed to a natural social reward (that is, female mouse) twice a day for 5 days (Natural group). Optical stimulation first occurred at 10:00 for 15 min (blue laser, 20 Hz, 15 ms pulse width, ~15–20 mW) as animals explored an operant chamber, and then again at 15:00 for 15 min using the same conditions. The same behavioural schedule was performed for the Natural group. All groups were exposed for an equal amount of time to each chamber, plugged into a corresponding patch cord, and optical stimulation occurred only in the appropriate groups. Each chamber contained dim lighting, white plastic floors, and no artificial odorants. One day after the final stimulation, all groups were exposed to a 6 min tail suspension or 24 h sucrose preference test as described above.

Object–female association. Twenty-four wild-type B6 mice were divided in two groups (neutral-object group, that is, control group, and female-object group, that is, experimental group ($n = 12$ per group)). The learning and testing phases were conducted on the same day, 6 h apart. In the learning phase, all mice spent 30 min in their home cage in the middle of a well-lit room with the lid of the cage and metal grid holding water and food removed and a 30 cm tall white rectangular frame placed around the home cage to prevent mice from escaping. All the boxes contained one target object (counterbalanced objects within and between groups: empty methanol bottle or cryostat liquid bottle (sealed)). After 3 min exploring the target object, a wild-type female b6 mouse (age 9 to 16 weeks) was introduced in the boxes of the experimental mice and remained there for the next 27 min). The control mice did not experience a female mouse and only experienced the object. After a total of 30 min from the beginning of the learning phase, the object and female mouse were removed and the male mice returned to their holding rooms. In the testing phase, mice were placed in a rectangular arena (70 × 25 × 30 cm) with white floors. A video camera resides above the testing chamber where the locations of the subjects were tracked and recorded using Noldus EthoVision XT video tracking software. Two zones (left and right) on either end of the box (30 × 30 cm) as well as a neutral zone in the centre of the box (10 cm) were denoted as part of the arena settings. Mice were introduced in the neutral zone of the empty arena and allowed to explore freely for 3 min. The tracking software monitored which of the two zones each individual mouse preferred. After 3 min, the experimenter introduced two objects (empty methanol bottle or cryostat liquid bottle (sealed)) and placed them in the middle of the left and right zones. For each mouse, one of the objects was the same as the one experienced during training (target object in target zone) and was placed in the least preferred zone. The other object was novel (novel side) and placed in the preferred side. During minutes 6 to 9, objects were absent from the arena. During minutes 9 to 12, the objects were reintroduced in the same positions as minutes 3 to 6.

Cell counting. The number of mCherry or c-Fos immunoreactive neurons in the dentate gyrus and downstream areas were counted to measure the number of active cells during defined behavioural tasks in 3–5 coronal slices (spaced 160 μm from each other) per mouse. Only slices that showed accurate bilateral injections in the dentate gyrus were selected for counting. Fluorescence images were acquired using a microscope with a ×20/0.50 NA objective. All animals were sacrificed 90 min post-assay or optical stimulation for immunohistochemical analyses. The number of c-Fos-positive cells in a set region of interest (0.5 mm² per brain area analysed) were quantified with ImageJ and averaged within each animal. Background autofluorescence was accounted for by applying an equal cut-off threshold to all images by an experimenter blind to experimental conditions. To calculate the percentage of BLA, mPFC, or NAcc cells expressing ArchT–eGFP in Fig. 3c, we counted the number of GFP-positive cells and divided by the total number of DAPI-positive cells in each region. Statistical chance was calculated by multiplying the observed percentage of ArchT–GFP-single-positive cells by the observed percentage of c-Fos-single-positive cells; overlaps over chance were calculated as observed overlap divided by chance overlap:

$$\frac{\text{GFP}^+ \times \text{c-Fos}^+}{\text{DAPI}} \div \text{chance overlap}.$$

A one-way ANOVA followed by Tukey's multiple comparisons or one-sample *t*-tests were used to analyse data and later graphed using Microsoft Excel with the Statplus plug-in or Prism.

Neurogenesis. After all the behaviour tests, on the 15th day since the first day of light stimulation, the mice were overdosed with Avertin and perfused transcardially with cold phosphate buffer saline (PBS), followed by 4% paraformaldehyde (PFA) in PBS. Brains were extracted from the skulls and kept in 4% PFA at 4 °C overnight. Coronal slices 50-µm thick were taken using a vibratome and collected in cold PBS. For immunostaining, each slice was placed in PBST (PBS + 0.2% Triton X-100) with 5% normal goat serum for 1 h and then incubated with primary antibody at 4 °C for 24 h (1:250 mouse anti-PSA-NCAM, Millipore; 1:500 doublecortin, AB2253, Millipore). Slices then underwent three wash steps for 10 min each in PBST, followed by a 1 h incubation period with secondary antibody (PSA-NCAM: 1:250 AlexaFluor488 anti-mouse, Invitrogen; Doublecortin: 1:300 A21435, Invitrogen). Slices were then incubated for 15 min with 4',6-diamidino-2-phenylindole (DAPI; 1:10,000) and underwent three more wash steps of 10 min each in PBST, followed by mounting and coverslipping on microscope slides. Images were taken using a Zeiss Axio Imager2 microscope. PSA-NCAM⁺ or doublecortin⁺ cells in the dentate gyrus granule cell layer were counted and normalized to the area of the granule cell layer for each brain slice using ImageJ by a researcher blind to the identities of each animal. After all the data were collected, the identities of each animal were revealed and the data were assigned back into each group for statistical analysis.

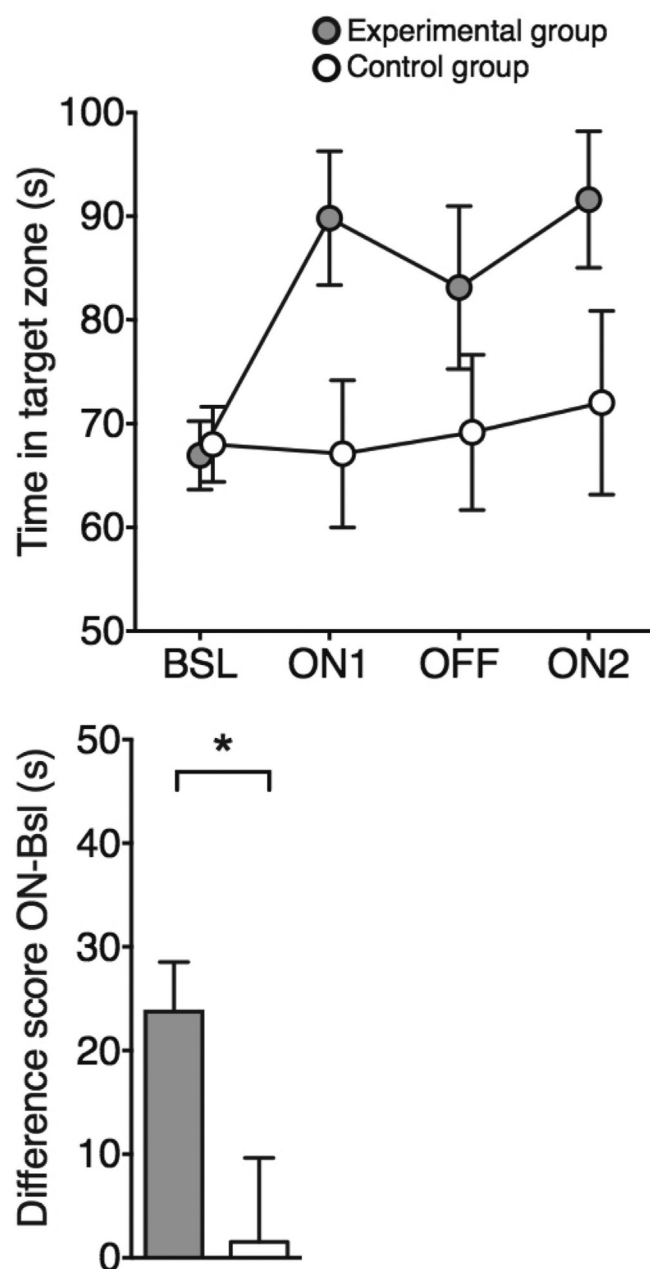
In vivo electrophysiology. As described above, three mice were first bilaterally injected with an AAV₉-TRE-ChR2-mCherry virus into the dentate gyrus followed by lowering a bilateral optic fibre implant into position and cementing it to the skull. Following 10 days for recovery and viral expression, in a separate surgery, mice were chronically implanted with a hyperdrive that housed six independently moveable tetrodes targeting the BLA. To accommodate the optic fibre implant cemented on the skull, the AP coordinate for the hyperdrive was adjusted slightly (centred at AP = −0.85 mm) and implanted at a ~15° angle. The electrical signal recorded from the tips of the tetrodes was referenced to a common skull screw over the cerebellum and differentially filtered for single unit activity (200 Hz to 8 kHz) and local field potentials (1–200 Hz). The amplified signal from each wire is digitized at 40 kHz and monitored with an Omniplex system (Plexon). Action potentials from single neurons were isolated off-line using time-amplitude window discrimination through Offline Sorter (Plexon). Putative single units were isolated by visualizing combinations of waveform features (square root of the power, peak–valley, valley, peak, principal components, and time-stamps) extracted from wires composing a single tetrode. The average firing rate for isolated neurons was 2.25 Hz ± 4.14 Hz (mean ± s.d.; range 0.01–30.15 Hz). However, the firing rate distribution was highly rightward skewed (median: 0.81 Hz) and more than half of the neurons (62%; 66/106) had firing rates under 1 Hz. After the last recording session, small lesions were made near the tips of each tetrode by passing current (30 µA for ~10 s) and mice were transcardially perfused and brains extracted for histology using standard procedures.

Recording and light stimulation protocol. Each mouse had two recording sessions that occurred on two different days separated by 72 h. Mice were first placed

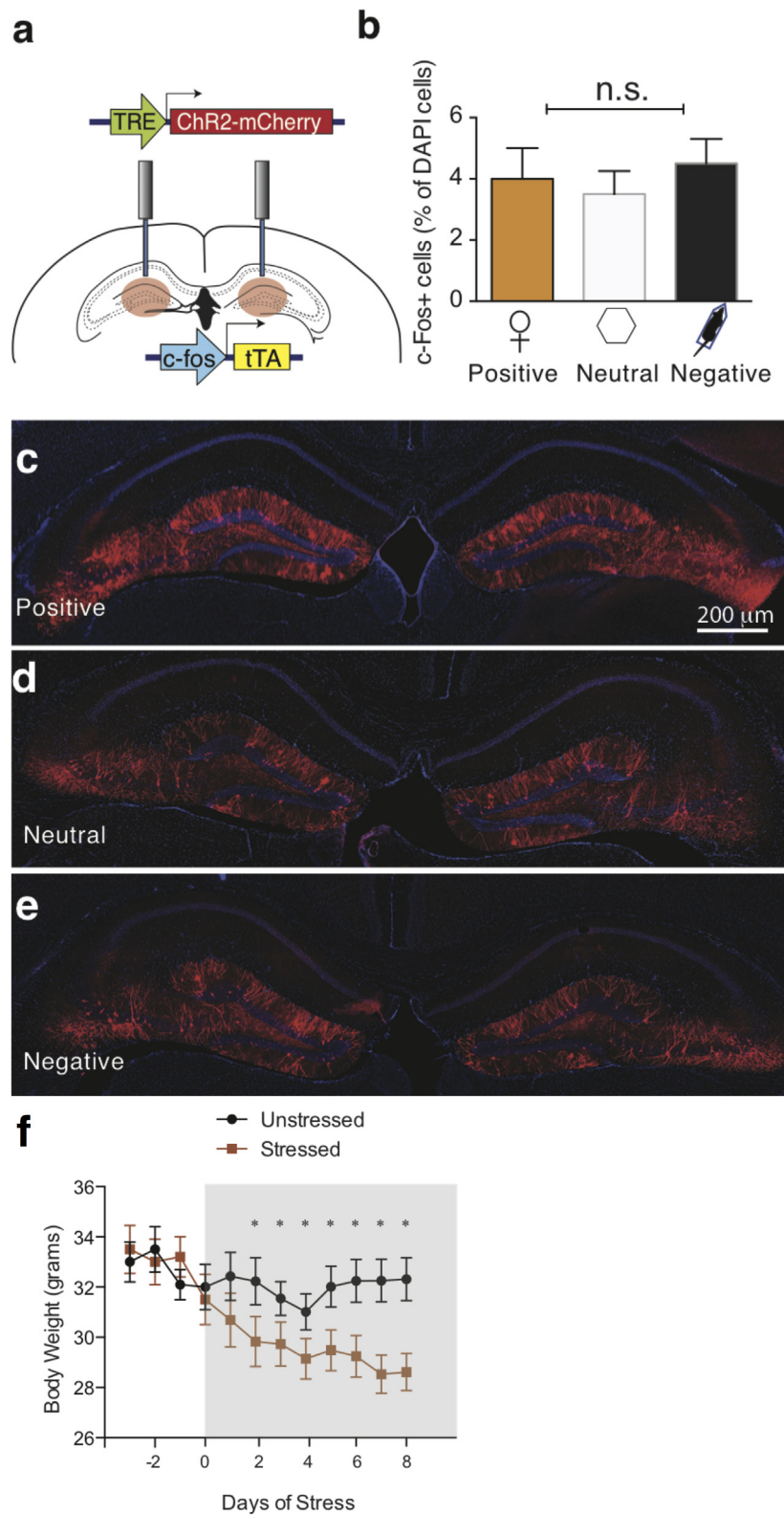
into a small recording chamber. In a single recording session, mice were first bilaterally stimulated in the dentate gyrus with blue light (450 nm; Doric Lenses) for 10 s over 15 such trials in total. As a control, the blue light was replaced with red light (640 nm; Doric Lenses) and the mice were given twelve 10-s trials under this condition. The power output for the blue and red lights emitted from the tips of each patch cord was adjusted to 15–18 mW as measured with a standard photometer (Thor Labs). The blue and red lasers were powered using a laser diode driver (Doric Lenses) triggered by transistor–transistor logic (TTL) pulses emitted from a digital I/O card, and these events were also time-stamped and recorded in the Omniplex system. The recording session lasted ~20 min and each tetrode was lowered ~0.25 mm after the first recording session.

Electrophysiological data analysis. Spiking activity was analysed using commercial (Neuroexplorer, NEX Technologies) and custom-made software in Matlab (R2014B). To visualize each neuron's trial-averaged activity for the blue and red light stimulation period, a peristimulus time histogram (PSTH) with 100-ms time bins was generated with activity time locked to the onset of the blue or red light, and then smoothed with a Gaussian kernel ($\theta = 127$ ms). In order to confirm a response during blue or red light stimulation period, 99% confidence intervals were constructed for the trial-averaged activity using a baseline 2.5 s period of spiking activity before the onset of each light under the assumption of Poisson spiking statistics (for example, Neuroexplorer, NEX Technologies). A neuron was considered to have a response for a particular light stimulation condition if trial averaged activity exceeded the upper (excitatory) or lower (inhibitory) bound of the 99% confidence interval. We considered neurons activated from dentate gyrus stimulation when a neural response was confirmed for the blue light condition but not the red light condition. For each neuron identified as such, we *z*-scored neural activity depicted in the blue and red light PSTH, then identified the maximum trial-averaged *z*-score value from the 2.5 s baseline (Pre) and during blue or red light stimulation (Post). The Pre and Post maximum *z*-score values for the blue and red light stimulation period was compared using paired *t*-tests (Fig. 2p).

31. Reijmers, L. G., Perkins, B. L., Matsuo, N. & Mayford, M. Localization of a stable neural correlate of associative memory. *Science* **317**, 1230–1233 (2007).
32. Redondo, R. L. *et al.* Bidirectional switch of the valence associated with a hippocampal contextual memory engram. *Nature* **513**, 426–430 (2014).
33. Ramirez, S. *et al.* Creating a false memory in the hippocampus. *Science* **341**, 387–391 (2013).
34. Liu, X. *et al.* Optogenetic stimulation of a hippocampal engram activates fear memory recall. *Nature* **484**, 381–385 (2012).
35. Han, X. *et al.* A high-light sensitivity optical neural silencer: development and application to optogenetic control of non-human primate cortex. *Front. Syst. Neurosci.* **5**, 18 (2011).
36. Huff, M. L., Miller, R. L., Deisseroth, K., Moorman, D. E. & LaLumiere, R. T. Posttraining optogenetic manipulations of basolateral amygdala activity modulate consolidation of inhibitory avoidance memory in rats. *Proc. Natl Acad. Sci. USA* **110**, 3597–3602 (2013).
37. Snyder, J. S., Soumier, A., Brewer, M., Pickel, J. & Cameron, H. A. Adult hippocampal neurogenesis buffers stress responses and depressive behaviour. *Nature* **476**, 458–461 (2011).

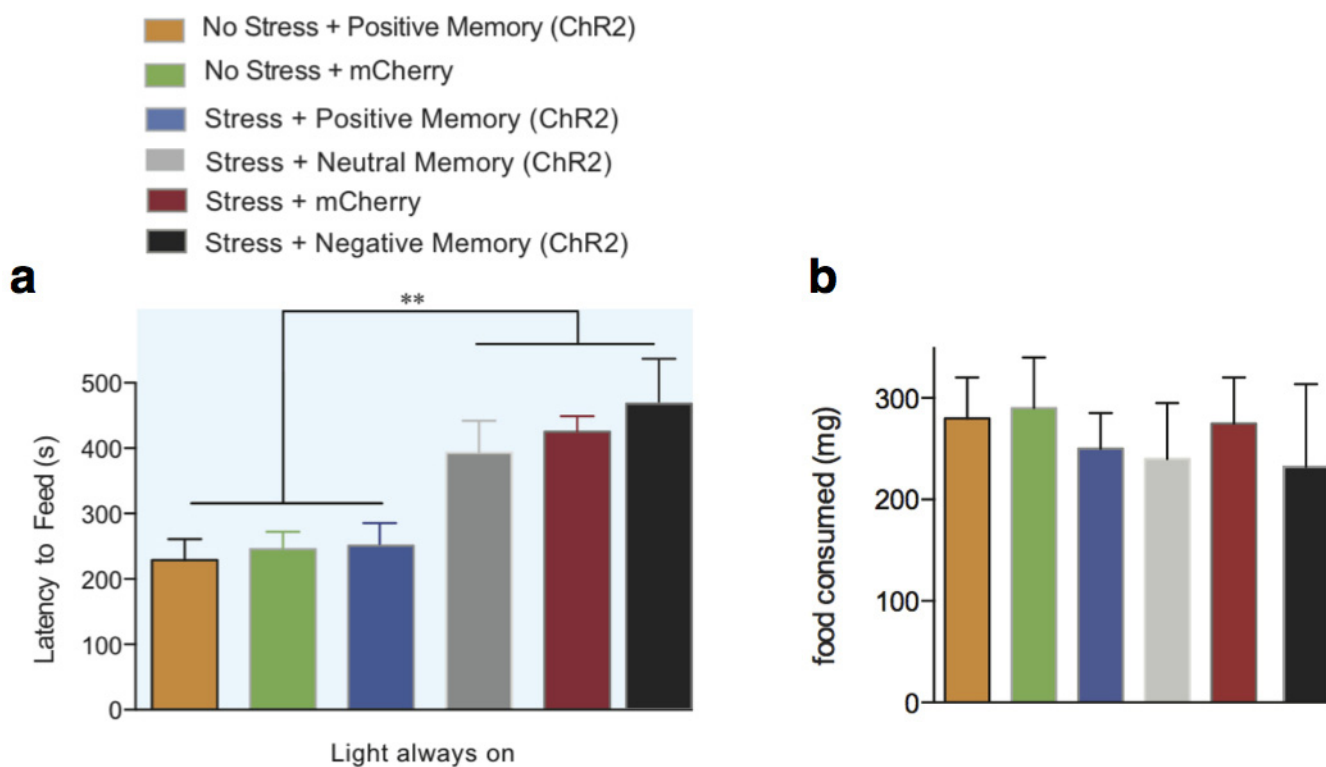


Extended Data Figure 1 | Male mice spend more time around an object associated with females. Top, Time spent in the target zone where the object associated with females is introduced in the ON phases. Female-object paired mice (experimental group) spend more time in the target zone during the ON phases than the neutral-object paired mice (control group; two-way ANOVA with multiple comparisons, ON1 $t_{88} = 2.41$; $P < 0.05$, ON2 $t_{88} = 2.08$; $P < 0.05$). Bottom, Difference score (average of ON phases – baseline (Bsl)) also shows the increased preference for the target zone in the female-object group compared to neutral-object group ($t_{22} = 2.37$; $*P < 0.05$). $n = 12$ per group. See the Methods section for detailed methods.



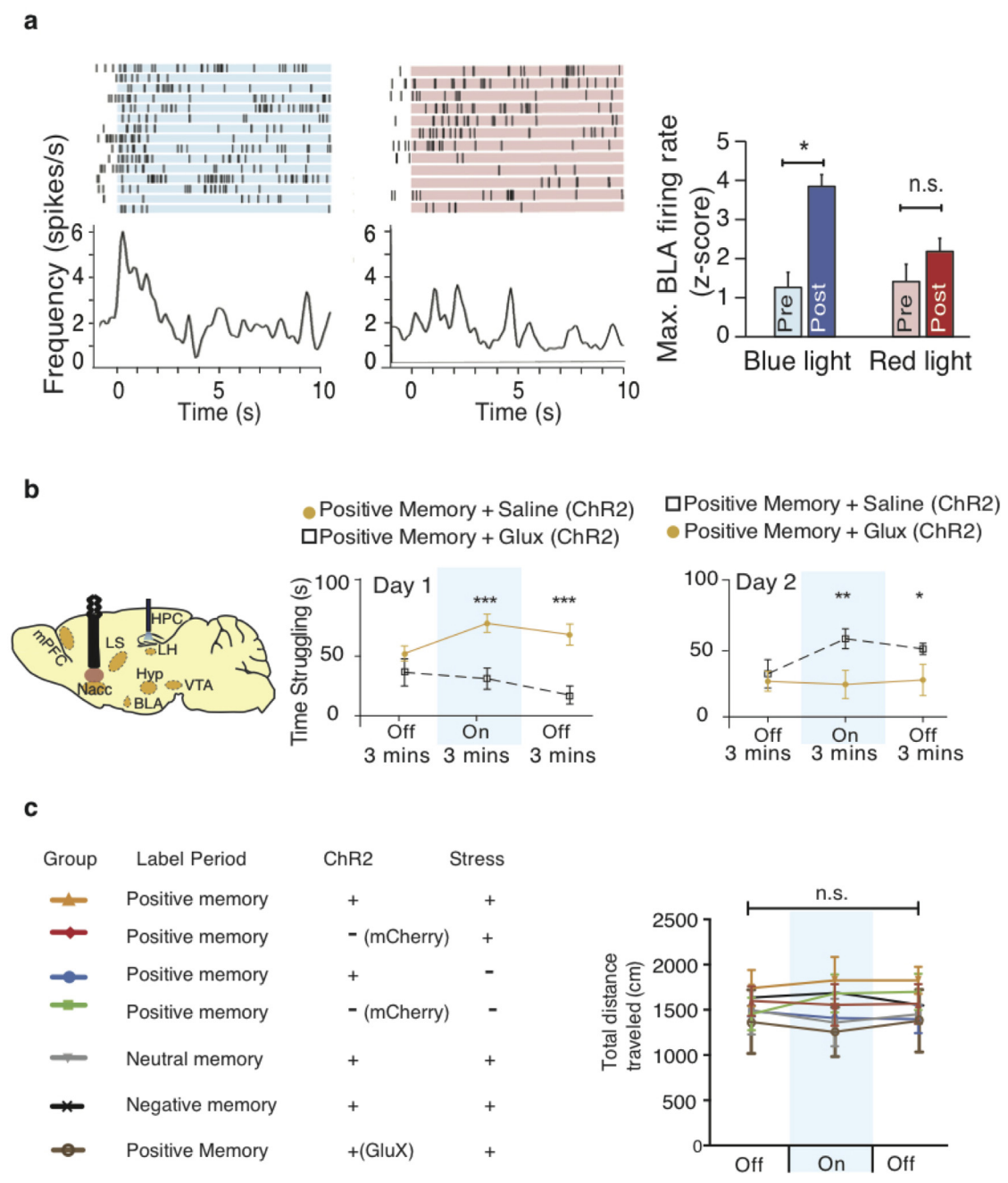
Extended Data Figure 2 | Positive, neutral, or negative experiences label a similar proportion of dentate gyrus cells with ChR2; stress prevents weight gain over 10 days. **a**, The c-Fos mice were bilaterally injected with AAV₉-TRE-ChR2-mCherry and implanted with optical fibres targeting the dentate gyrus. **b–e**, Histological quantifications reveal that, while off Dox, a similar proportion of dentate gyrus cells are labelled by ChR2-mCherry in response to a positive (**c**), neutral (**d**), or negative (**e**) experience. All animals

were sacrificed a day after completing the CIS protocol. One-way ANOVA followed by Bonferroni post hoc test, $P > 0.05$, n.s., not significant. **f**, Animals were chronically immobilized for 10 days, during which they lost a significant amount of weight compared to an unstressed group (one-way ANOVA followed by Bonferroni post hoc test, $*P < 0.05$, $n = 9$ per group). Data are means \pm s.e.m.



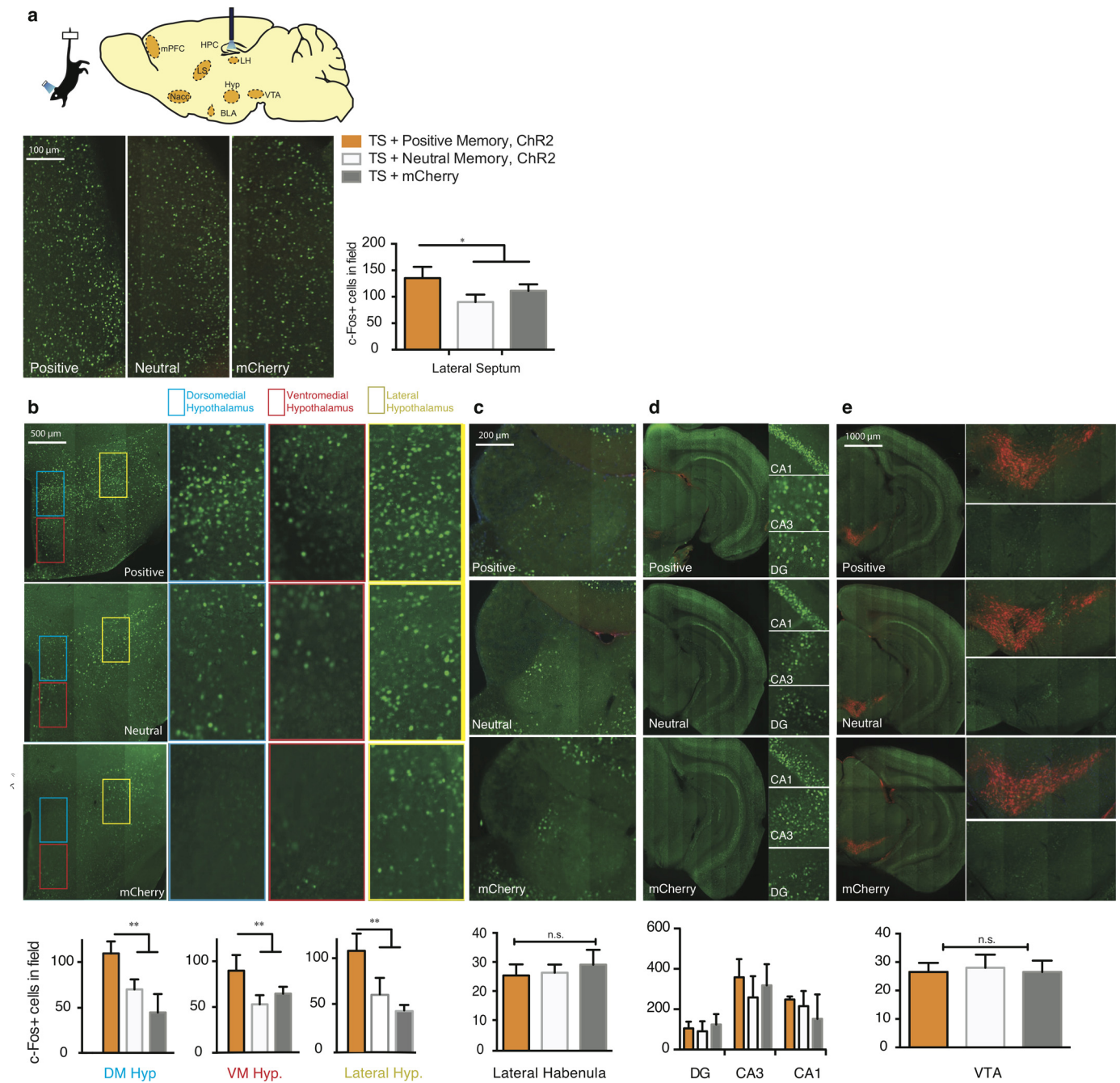
Extended Data Figure 3 | Reactivation of a positive memory decreases latency to feed in a novelty suppressed feeding paradigm. **a**, All groups were food deprived for 24 h and then underwent a novelty-suppressed feeding protocol. While chronic immobilization increased the latency to feed, light-reactivation of a positive memory significantly decreased the latency to feed

at levels that matched the unstressed groups. **b**, Upon completion of the novelty suppressed feeding test, all groups were returned to their home cage and food intake was measured after 5 min (one-way ANOVA followed by Bonferroni post hoc test, $**P < 0.01$, $n = 16$ per group). Data are means \pm s.e.m.



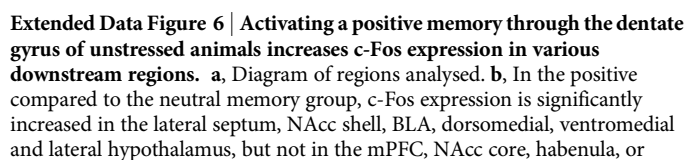
Extended Data Figure 4 | Activation of a positive memory elicits BLA spiking activity, requires NAcc glutamatergic activity in the tail suspension test, but does not alter locomotor activity in the open field test. **a**, Raster plots and peri-stimulus time histograms (PSTH) illustrating a transient excitatory response from a single BLA neuron out of the nine neurons responsive to dentate gyrus positive memory activation during 10 s of blue light stimulation, but not in response to 10 s of red light as a control. Blue bar plots on the right illustrate maximum BLA neural firing rate before (Pre) and after (Post) blue light stimulation in the dentate gyrus (paired t -test, $t_7 = 6.91$, $*P = 0.023$). Red bar plots show the maximum neural activity for the same neurons after red light stimulation in the dentate gyrus that serves as a control (paired t -test, $t_7 = 1.62$, $P = 0.15$). **b**, Brain diagram illustrating target areas

manipulated. Within-subjects experiments revealed that glutamatergic antagonists (GluX), but not saline, in the accumbens shell blocked the light-induced effects of a positive memory in stressed subjects. For behavioural data, a two-way ANOVA with repeated measures followed by a Bonferroni post hoc test revealed a group-by-light epoch interaction on day 1 ($F_{1,90} = 28.39$, $P < 0.001$; $n = 16$ per group) and day 2 of testing ($F_{1,90} = 8.28$, $P < 0.01$). Data are means \pm s.e.m. **c**, All groups failed to show significant changes in locomotor activity within a session of open field exploration during either light off or light on epochs, though any trends towards decreases in locomotion are consistent with stress-induced behavioural impairments. $*P < 0.05$, $**P < 0.01$, $***P < 0.001$.



Extended Data Figure 5 | Activating a positive memory in the dentate gyrus produces an increase in c-Fos expression in the lateral septum and hypothalamus, but not the lateral habenula, ventral hippocampus, or VTA. **a**, Diagram of regions analysed. **b**, **c**, c-Fos expression significantly increased in the lateral septum (**b**) and subregions of the hypothalamus including the dorsomedial (DM), ventromedial (VM), and lateral hypothalamus (**c**) in the positive memory group but not in a group in which a neutral memory was

stimulated or in a group expressing mCherry alone. **c–e**, c-Fos expression did not significantly increase in the lateral habenula (**c**), various ventral hippocampus subregions (**d**), or VTA, identified by tyrosine hydroxylase staining (red) stainings in the images expanded on the right (**e**) (one-way ANOVA followed by Bonferroni post hoc test $*P < 0.05$, $**P < 0.01$, $n = 5$ animals per group, 3–5 slices per animal). TS, tail suspension. Data are means \pm s.e.m.

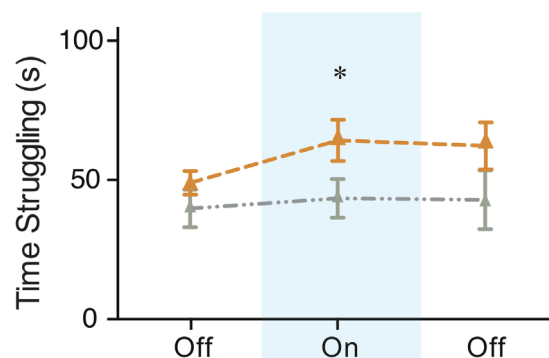


©2015 Macmillan Publishers Limited. All rights reserved

a

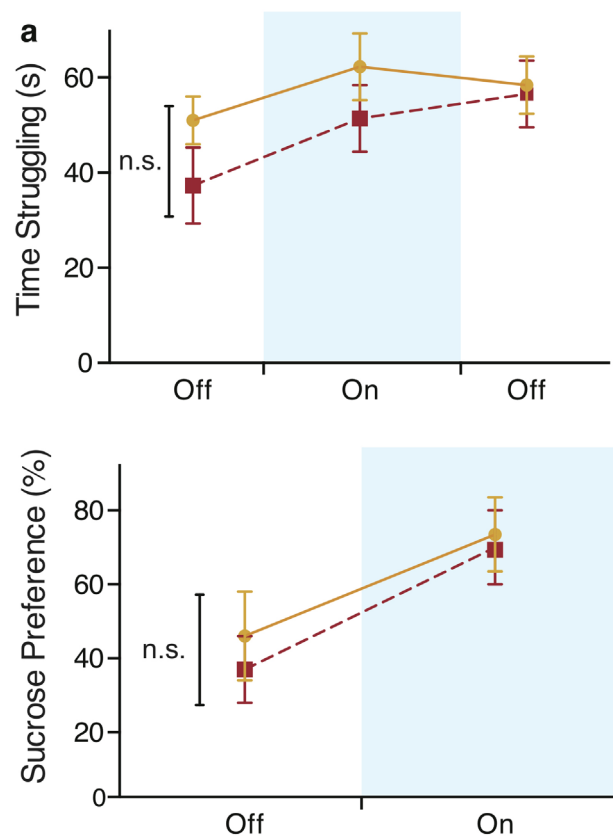
▲ Positive Memory + Stress + DAX, (ChR2): Day 1

▲ Positive Memory + Stress + Saline, (ChR2): Day 2

**b**

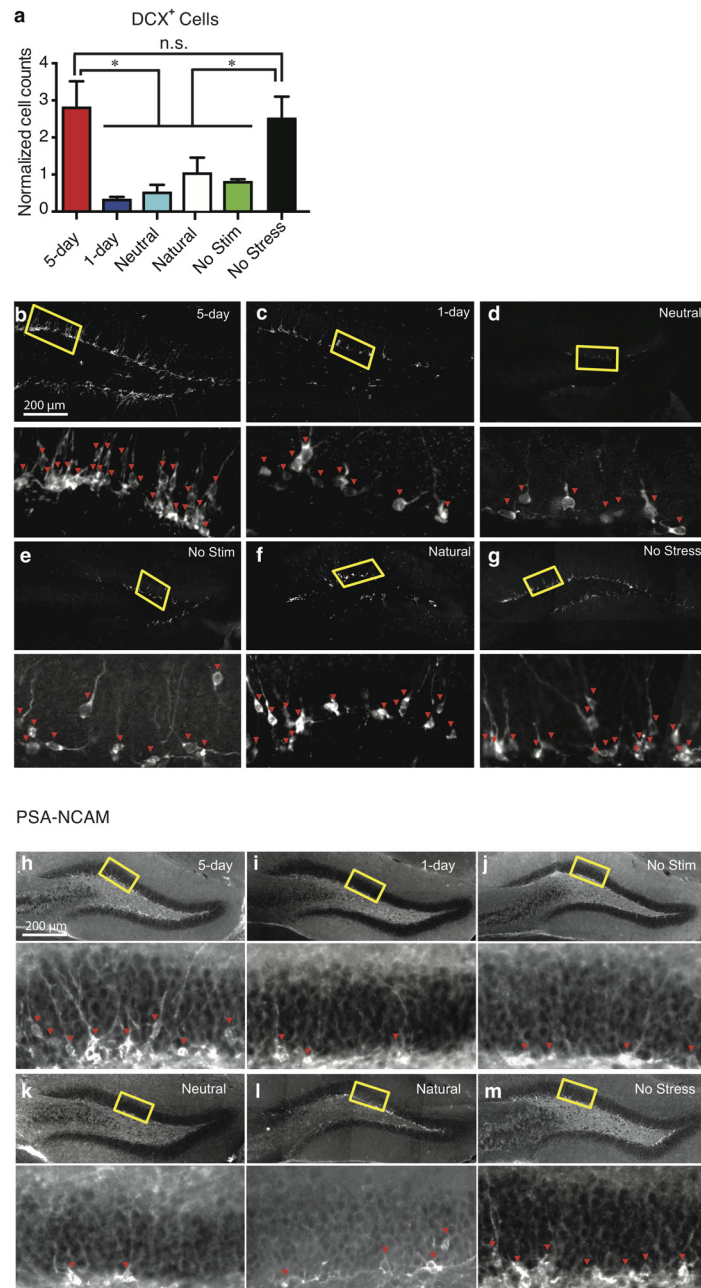
● Day 1: Stress + Positive Memory (ChR2)

■ Day 2: Stress + Positive Memory (ChR2)



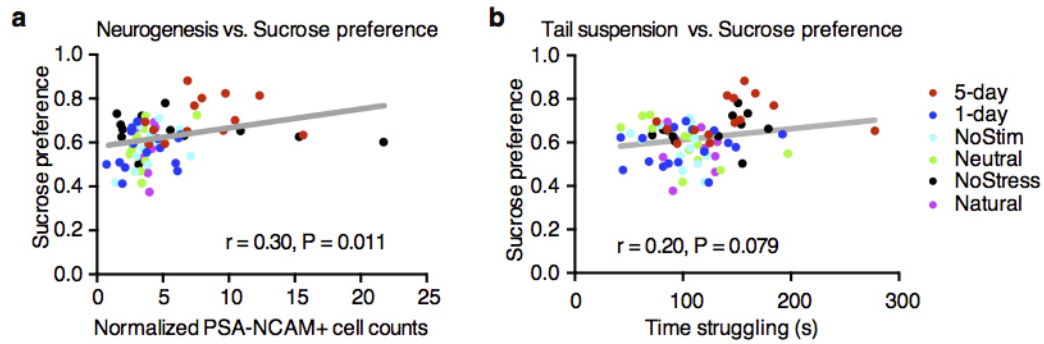
Extended Data Figure 7 | Dopamine receptor antagonists block the light-induced effects of positive memory activation; a single session of activating a positive memory in the dentate gyrus does not produce long-lasting antidepressant-like effects. **a**, Administration of a cocktail of dopamine receptor antagonists (DAX) prevented the light-induced increases in struggling during the tail suspension test. When animals were tested again on day 2 and infused with saline, the behavioural effects of optically reactivating a positive

memory were observed (two-way ANOVA with repeated measures followed by Bonferroni post hoc test, $*P < 0.05$, $n = 9$ per group). **b**, Animals in which a positive memory was optically activated during the tail suspension test or sucrose preference test showed acute increases in time struggling or preference for sucrose; this change in behaviour did not persist when tested again on day 2 (within subjects ANOVA followed by Bonferroni post hoc test), $n = 9$. n.s., not significant. Data are means \pm s.e.m.



Extended Data Figure 8 | Chronic activation of a positive memory prevents stress-induced decreases in neurogenesis. **a**, The 5-day positive memory stimulation group showed a significant increase of adult newborn cells in the dentate gyrus as measured by doublecortin (DCX)-positive cells (one-way ANOVA followed by Bonferroni post hoc test, $F_{5,72} = 7.634$, $P < 0.01$) relative to control groups. **b–g**, Representative images of DCX-positive cells in the

dentate gyrus for the 5-day (**b**), 1-day (**c**), neutral (**d**), no stimulation (**e**), natural (**f**), and no stress (**g**) groups. **h–m**, Representative PSA-NCAM images corresponding to data appearing in Fig. 4d. $n = 5$ slices per animal, 13 animals per group for data appearing in **a**. * $P < 0.05$, n.s., not significant. Data are means \pm s.e.m.



Extended Data Figure 9 | Behavioural and neuronal correlations.

a, Performance levels in the SPT and the number of adult-born neurons as measured by PSA-NCAM are positively correlated on an animal-by-animal

basis. **b**, Performance levels between the TST and SPT show strong positive correlation trends on an animal-by-animal basis. $n = 14$ per TST behavioural group, $n = 15$ per SPT behavioural group.

α -Synuclein strains cause distinct synucleinopathies after local and systemic administration

W. Peelaerts¹, L. Bousset², A. Van der Perren¹, A. Moskalyuk³, R. Pulizzi³, M. Giugliano^{3,4,5,6}, C. Van den Haute^{1,7}, R. Melki² & V. Baekelandt¹

Misfolded protein aggregates represent a continuum with overlapping features in neurodegenerative diseases, but differences in protein components and affected brain regions¹. The molecular hallmark of synucleinopathies such as Parkinson's disease, dementia with Lewy bodies and multiple system atrophy are megadalton α -synuclein-rich deposits suggestive of one molecular event causing distinct disease phenotypes. Glial α -synuclein (α -SYN) filamentous deposits are prominent in multiple system atrophy and neuronal α -SYN inclusions are found in Parkinson's disease and dementia with Lewy bodies². The discovery of α -SYN assemblies with different structural characteristics or 'strains' has led to the hypothesis that strains could account for the different clinicopathological traits within synucleinopathies^{3,4}. In this study we show that α -SYN strain conformation and seeding propensity lead to distinct histopathological and behavioural phenotypes. We assess the properties of structurally well-defined α -SYN assemblies (oligomers, ribbons and fibrils) after injection in rat brain. We prove that α -SYN strains amplify *in vivo*. Fibrils seem to be the major toxic strain, resulting in progressive motor impairment and cell death, whereas ribbons cause a distinct histopathological phenotype displaying Parkinson's disease and multiple system atrophy traits. Additionally, we show that α -SYN assemblies cross the blood-brain barrier and distribute to the central nervous system after intravenous injection. Our results demonstrate that distinct α -SYN strains display differential seeding capacities, inducing strain-specific pathology and neurotoxic phenotypes.

The discovery that Lewy bodies spread within the nervous system^{5,6} led to the demonstration that fibrillar assemblies seed soluble α -SYN and spread between cells in cellular and animal models⁷. The most widely accepted paradigm postulates that pre-fibrillar oligomers, as opposed to mature fibrils, represent the neurotoxic entities in Parkinson's disease^{8,9}. Although a direct quantitative *in vivo* comparison of the neurotoxic potential of different α -SYN assemblies is lacking, recent evidence indicates that fibrillar α -SYN toxicity is significantly greater than that of pre-fibrillar precursors^{4,10}. Studies with inoculation of recombinant fibrils or pathogenic brain lysates in rodent brain triggered α -SYN pathology with varying efficiencies and moderate neuronal loss^{11,12}. In contrast, recombinant adeno-associated viral vector-mediated (rAAV) overexpression of α -SYN in rodent and primate brain induces time-dependent robust behavioural impairment and dopaminergic neurodegeneration^{13,14}. In this study, we compared the *in vivo* properties of α -SYN oligomers and two distinct α -SYN strains ('fibrils' and 'ribbons') (Extended Data Fig. 1a–e)⁴, by inoculation of highly purified and structurally characterized recombinant human α -SYN preparations in rat substantia nigra in absence and presence of rAAV-mediated human α -SYN overexpression.

To assess α -SYN uptake and spreading in a detailed and quantitative way, we fluorescently labelled all α -SYN assemblies (Extended Data

Fig. 1f–h). First, we applied *ex vivo* fluorescent tomography to visualize spreading of α -SYN in whole brain after inoculating 10 μ g of α -SYN assemblies (Fig. 1a and Supplementary Table 1). Reconstructed images of the fluorescence volume after 20 min and 7 days showed that α -SYN oligomers spread more efficiently than fibrils, ribbons and free fluorophore (Fig. 1b). Subsequent histological analysis revealed that all assemblies were taken up in dopaminergic neurons, spread over the arborizing striatal dopaminergic axons and were transmitted transsynaptically in a time-dependent manner (Extended Data Fig. 2a–g). These results build upon previous findings that the α -SYN oligomers disseminate more efficiently than higher molecular weight assemblies after intracerebral inoculation^{15,16}.

The reason why certain Lewy body-bearing regions are subject to neurodegeneration and others not, remains incompletely understood. The fact that patients with Parkinson's disease, dementia with Lewy bodies, and multiple system atrophy present variable striatonigral pathology is also confounding. We therefore assessed whether α -SYN oligomers, fibrils and ribbons translate their distinctive structural and biochemical properties into motor behavioural and neurotoxic phenotypes. Four months after nigral injection of ribbons or fibrils, Lewy body- and Lewy neurite-like inclusions formed essentially in dopaminergic neurons. These juxta-, peri-, nuclear and filamentous inclusions stained positive for α -SYN phosphorylated at Ser129 (P α -SYN), resembling the situation in Lewy body/Lewy neurite pathology-associated inclusions (Fig. 1c–f and Extended Data Fig. 3). P α -SYN inclusions were considerably more abundant for α -SYN ribbons compared to fibrils with a predominant Lewy neurite-like filamentous phenotype staining positive for the aggresome marker SQSTM1 (also known as p62; Fig. 1e–g). Injection of α -SYN oligomers and brain homogenate from aged 18-month transgenic mouse expressing mutant human α -SYN(A30P) did not result in detectable P α -SYN accumulation. Combined rAAV-mediated α -SYN overexpression with ribbons and fibrils inoculation lead to increased P α -SYN⁺ cells (Extended Data Fig. 4). Remarkably, and only after combined rAAV-mediated α -SYN overexpression with α -SYN ribbons inoculation, a second but sparse α -SYN phosphorylation pattern was observed in oligodendroglial cells (Fig. 1h, i).

In terms of neurotoxicity, nigral inoculation of brain homogenate, oligomers, fibrils and ribbons did not induce detectable dopaminergic cell death until the final time point of 120 days (Fig. 2a, b). In contrast, sole rAAV-mediated α -SYN overexpression (control) led to 27% cell loss of tyrosine hydroxylase-positive neurons and 32% striatal dopaminergic axonal loss (Fig. 2c, d). Combined rAAV- α -SYN overexpression with inoculation of brain homogenate, α -SYN oligomers, fibrils or ribbons accelerated tyrosine hydroxylase-positive cell death (Fig. 2c–e) and severely reduced striatal dopaminergic nerve terminal volume by 61% and 43% for α -SYN fibrils and brain homogenate, respectively. Combined rAAV- α -SYN overexpression and inoculation of α -SYN

¹KU Leuven, Laboratory for Neurobiology and Gene Therapy, Department of Neurosciences, 3000 Leuven, Belgium. ²Paris-Saclay Institute of Neuroscience, CNRS, Avenue de la Terrasse, 91198 Gif-sur-Yvette, France. ³Theoretical Neurobiology & Neuroengineering Laboratory, Department of Biomedical Sciences, University of Antwerp, 2610 Antwerp, Belgium. ⁴Department of Computer Science, University of Sheffield, S1 4DP Sheffield, UK. ⁵Brain Mind Institute, Swiss Federal Institute of Technology of Lausanne, 1015 Lausanne, Switzerland. ⁶Neuro-Electronics Research Flanders (NERF), 3001 Leuven, Belgium. ⁷KU Leuven, Leuven Viral Vector Core, 3000 Leuven, Belgium.

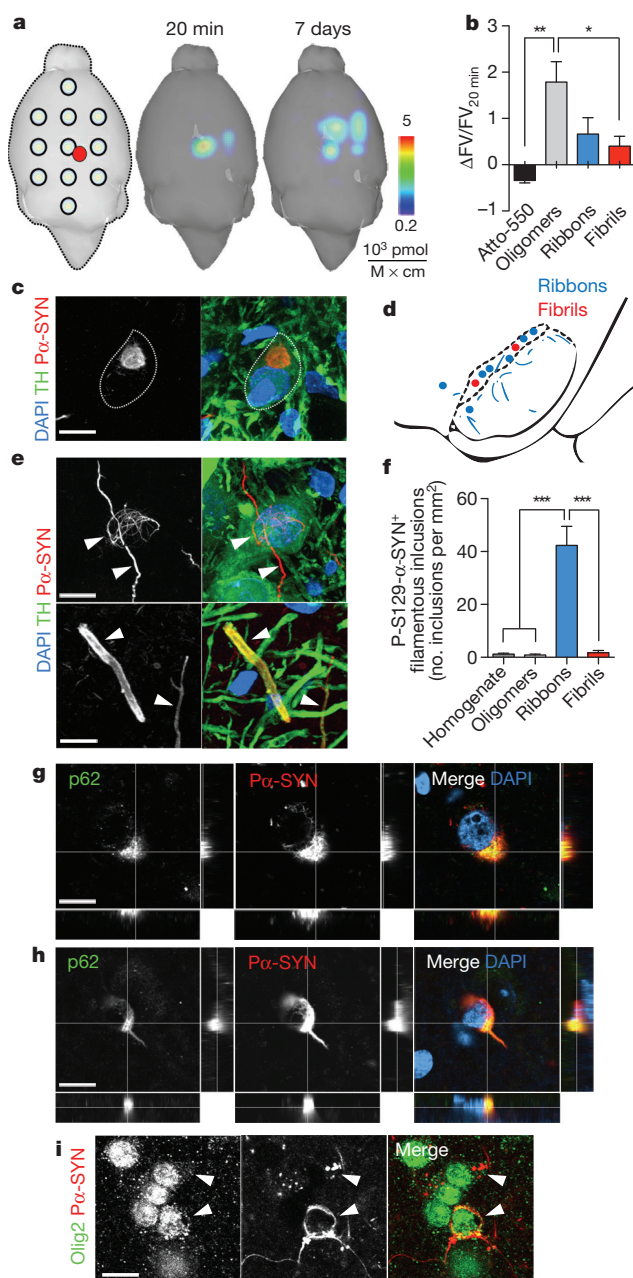


Figure 1 | α -SYN assemblies spread, but only strains cause Lewy-like pathology after injection in rat substantia nigra. **a**, *Ex vivo* macroscopic imaging of atto-550 labelled α -SYN after nigral inoculation (red injection spot) by reconstructing 11 separate excitation spots into a macroscopic 3D map allowing the visualization of α -SYN spread. Representative image of fluorescently labelled oligomeric α -SYN distribution after 20 min and 7 days is shown. **b**, Quantification of change in α -SYN fluorescent volume (ΔFV) between 20 min and 7 days as a measure for α -SYN spreading. Oligomers show a significant increase in spreading (1.78 ± 0.44 s.e.m.) compared to free dye (-0.34 ± 0.06 s.e.m.) and α -SYN fibrils (0.40 ± 0.21 s.e.m.) (** $P < 0.01$, * $P < 0.05$ for one-way ANOVA with Tukey's post-hoc analysis, $n = 3$). **c**, After 4 months Lewy-like pathology is observed in dopaminergic neurons after inoculation of α -SYN strains (fibrils and ribbons). **d**, Schematic overview of Lewy body- and Lewy neurite-like inclusions in substantia nigra for ribbons and fibrils. **e**, Lewy neurite-like threads and club-shaped inclusions (upper and lower panel, respectively) show abundant inclusions for ribbons quantified in **f** (** $P < 0.001$ for one-way ANOVA with Tukey's post-hoc analysis, $n = 4$). **g–i**, Confocal images with z-axis show phosphorylated inclusions in dopaminergic neurons colocalizing with the ubiquitin binding protein p62 (**g**), whereas only ribbons result in GCI's in the presence of elevated α -SYN levels after combined rAAV-driven α -SYN overexpression (**h**), further indicated by the oligodendroglial lineage marker Olig2 (**i**). Scale bars, 10 μ m.

oligomers and ribbons did not yield additional tyrosine hydroxylase fibre loss (Fig. 2d). Assessment of spontaneous forepaw use with the cylinder test revealed a consistent significant motor deficit from 60 days onwards upon injection of α -SYN fibrils (Fig. 2f). Combined rAAV-mediated α -SYN overexpression with α -SYN assemblies inoculation further aggravated motor deficits (Fig. 2g). These findings demonstrate that introduction of seeds under conditions where α -SYN is expressed at higher levels greatly enhances neurodegeneration in a strain-dependent manner. Thus, although ribbon inoculation induced more pronounced Lewy body/Lewy neurite-like inclusions (Fig. 1c–f), fibrils imposed the largest neurotoxic burden on the striatonigral pathway (Fig. 2h).

The observation of a behavioural phenotype after inoculation of pure α -SYN strains in the absence of dopaminergic degeneration indicated that this functional deficit was not a downstream effect of dopaminergic cell death. Recent studies in cellular models, α -SYN transgenic animals and patients with incidental Lewy body disease, Parkinson's disease and dementia with Lewy bodies have shown neuronal dysfunction and motor abnormalities before overt neurodegeneration and Lewy body/Lewy neurite pathology^{17–19}. We therefore employed cellular electrophysiology to study the impact of α -SYN assemblies on neuronal and synaptic physiology. Endogenous α/β -SYN is calculated to be over 40 μ M within the rat synaptosome²⁰. Four days exposure of rat primary cortical cultures to 1 μ M of α -SYN assemblies left passive and excitable electrical membrane properties unaltered in single neurons, as recorded intracellularly by patch-clamp (Extended Data Fig. 5a–e). Instead, significant effects were observed on synaptic physiology. The frequency of occurrence of spontaneous bursts of action potentials revealed a direct substantial decrease after exposure to α -SYN assemblies (Fig. 2i, j). Further evidence was obtained via substrate-integrated microelectrode arrays (MEAs) allowing simultaneous extracellular monitoring of the spontaneous neuronal network electrical activity from 59 independent microelectrodes. The spontaneous firing of cortical neurons self-organizes *ex vivo* as episodic network-wide epochs of action potential synchrony, offering an indirect indicator of (dys)functional glutamatergic synaptic transmission. Exposure to low concentrations of different α -SYN assemblies revealed an increase in the average inter-spike intervals, which was significant for fibrils and oligomers (Fig. 2k, l).

Taken together, these data indicate that different α -SYN assemblies can affect neurotransmission after acute exposure, but only fibrillar α -SYN exhibited perpetual behavioural and aggravated neurotoxic phenotypes *in vivo*. To further investigate this, we assessed the capacities of α -SYN oligomers, ribbons and fibrils to seed endogenous α -SYN and to propagate, leading to long-term functional effects. We inoculated 40 μ g of α -SYN assemblies divided over 3 injection sites in rat striatum in combination with rAAV- α -SYN overexpression (Fig. 3a) or not (Extended Data Fig. 6). Large amounts of sarkosyl-insoluble rodent α -SYN were detected after 60 days throughout the striatonigral pathway for ribbons and fibrils (Fig. 3a and Extended Data Fig. 6), although the inoculated human α -SYN was undetected after sarkosyl extraction in animals injected only with α -SYN assemblies (Extended Data Fig. 7). This implies that exogenous α -SYN strains seed the assembly of endogenous α -SYN, overcoming the species barrier. In addition, the proteinase K resistance of sarkosyl-insoluble α -SYN extracted from the brains of animals overexpressing α -SYN inoculated with either ribbons or fibrils differed (Fig. 3b). Fibrils exhibited a higher resistance compared to ribbons, reflecting the capacity of each strain to amplify in a specific manner *in vivo* (Fig. 3b and Extended Data Figs 6 and 7). Hence, fibrils possess the highest capacity to translate their neuropathological potential from a defined structural to a wide spatiotemporal level.

α -SYN knockout animals show no robust pathology, possibly because of functional redundancy (β - and γ -SYN isoforms)²¹. The remarkable capacity of α -SYN strains to persist and act as seeds by imprinting their intrinsic structures, causing synaptic defects, is

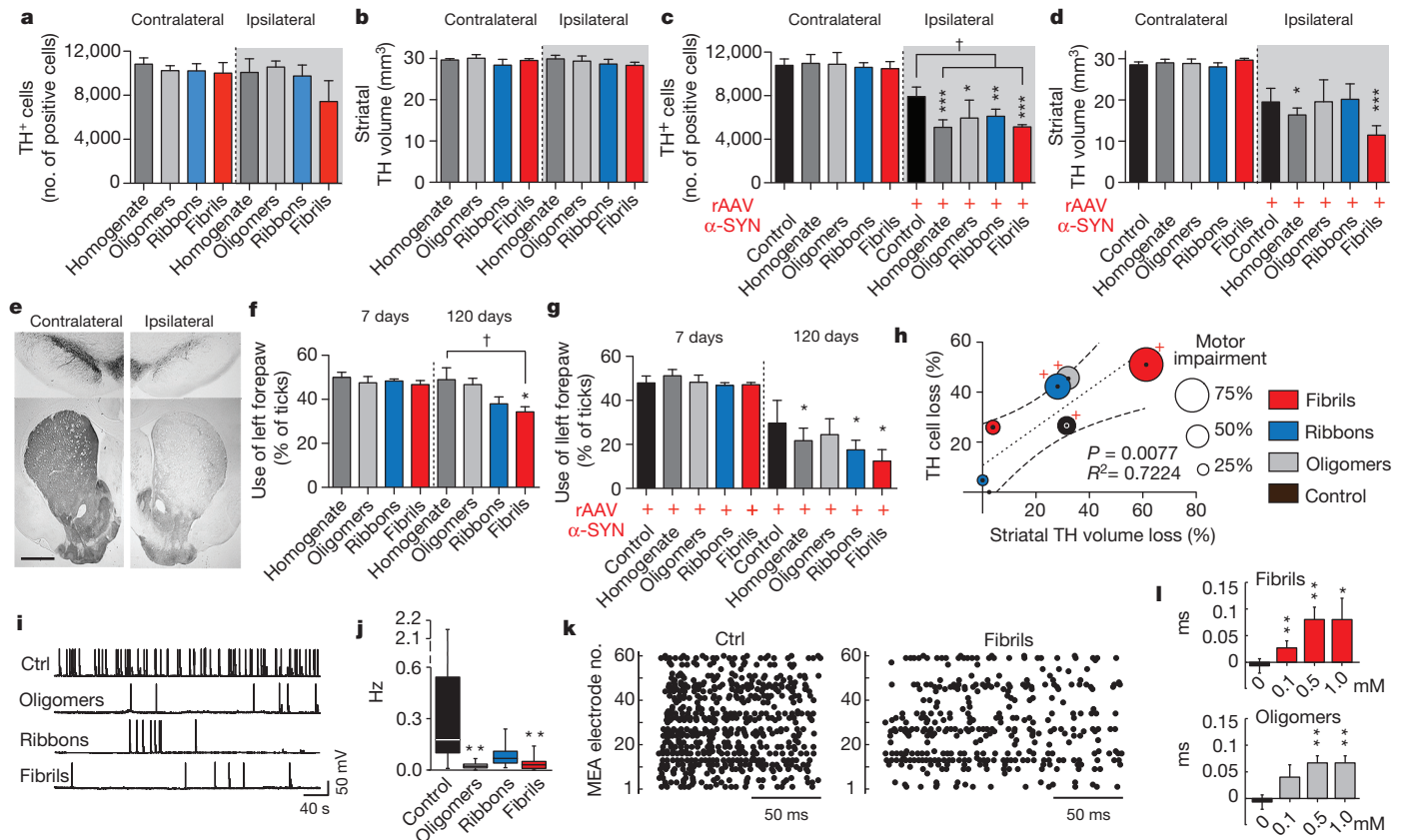


Figure 2 | α-SYN fibrils are the major toxic strain *in vivo* and cause synaptic impairment. **a, b**, Stereological quantification of tyrosine hydroxylase-positive (TH⁺) cells and striatal TH volume shows no significant cell or axonal loss after nigral injection of different α-SYN assemblies. **c, d**, Significant loss of dopaminergic cells and projecting axons is observed upon inoculation of fibrils and brain homogenate with rAAV-driven α-SYN overexpression (one-way ANOVA with Tukey's post-hoc analysis versus contralateral side *** $P < 0.001$, ** $P < 0.01$, * $P < 0.05$; or Dunnett's post-hoc analysis versus control condition † $P < 0.05$; s.e.m, $n = 4$). **e**, Representative image of TH staining in substantia nigra and striatum after co-injection of α-SYN fibrils and rAAV-driven α-SYN overexpression after 4 months. Scale bar, 1,000 μm. **f**, Impaired motor behaviour after inoculation of α-SYN fibrils (** $P < 0.01$, * $P < 0.05$, one-sample t -test for a hypothetical value of 50% with Bonferroni post-hoc analysis; † $P < 0.05$ for one-way ANOVA with Tukey's post-hoc analysis; s.e.m, $n = 4$) and **g**, increased decline of motor behaviour after combined α-SYN assemblies inoculation and rAAV-driven α-SYN

overexpression. **h**, Schematic overview indicating neurotoxic effects induced by different α-SYN strains with fibrils exhibiting the largest neurotoxic potential. Red plus (+) indicates data obtained upon rAAV-driven α-SYN overexpression. **i–l**, Reduced spontaneous collective firing in 4-week-old primary rat cortical neurons indicates synaptic impairment. **i**, Whole-cell patch-clamp intracellular recordings in single neurons revealed a progressive reduction of the rate of spontaneous emission of APs, quantified in **j** (* $P < 0.05$, ** $P < 0.01$, Wilcoxon rank sum test, $n = 32$ cells). **k**, Representative raster plot of spontaneous action potential firing and the effect of fibrils on network-wide spontaneous episodic synchronization of neuronal action potentials. **l**, Significant lengthening of the average inter-spike intervals during the episodes of synchronization was observed across increasing concentrations of fibrils and oligomers ($n = 9$ cultures). No significant changes occurred during the entire incubation time in the total number of microelectrodes detecting spontaneous action potentials, indicating normal cell viability.

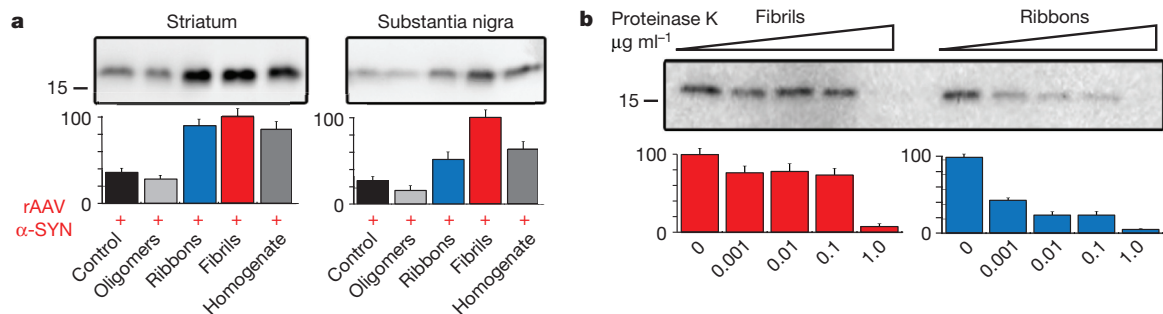


Figure 3 | α-SYN assemblies propagate in a strain-dependent manner. **a**, Sarkosyl-insoluble α-SYN is detected in striatum and substantia nigra after striatal inoculation of brain homogenate, oligomers, ribbons and fibrils in combination with rAAV-driven α-SYN overexpression. **b**, Degradation of Sarkosyl-insoluble α-SYN in brain extracts from fibrils and ribbons inoculated animals with rAAV-driven α-SYN overexpression by increasing proteinase

K concentrations. The results reveal that each strain imprints its intrinsic structure to endogenous α-SYN. Western blot analysis was performed using the monoclonal anti-α-SYN antibody clone 42. The data correspond to the mean and associated standard error calculated from 3 independent measurements from 2 biological replicates.

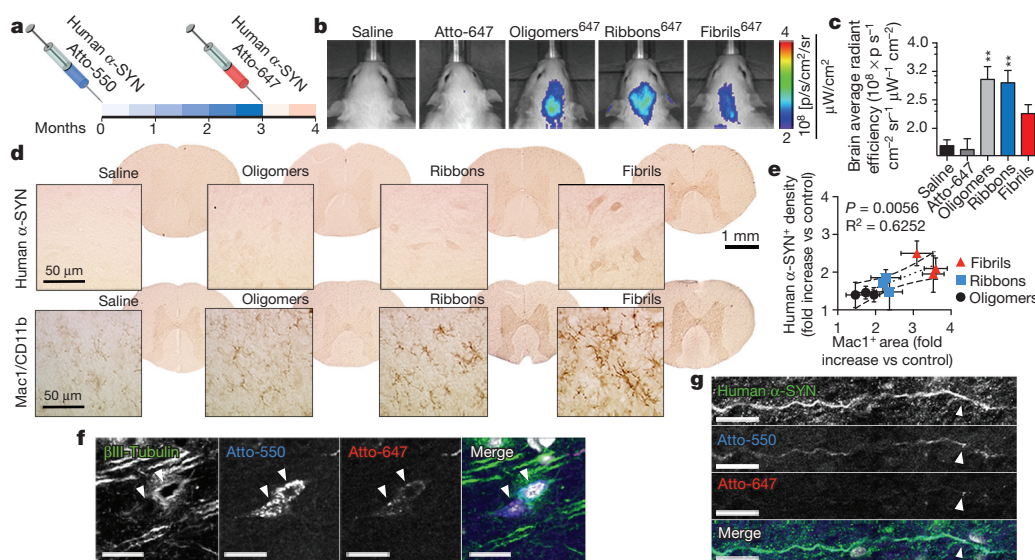


Figure 4 | α -SYN strains cross the blood–brain barrier after systemic administration. **a**, α -SYN oligomers, ribbons and fibrils were intravenously injected every two weeks during 4 months in rat tail vein. **b**, Epifluorescent imaging reveals a fluorescent atto-647 signal originating from the brain region for α -SYN oligomers, ribbons and fibrils 4 months after the initial injection. **c**, Fluorescent yield is significantly higher for ribbons and oligomers compared to control conditions (** $P < 0.01$, * $P < 0.05$, one-way ANOVA with Dunnett's post-hoc analysis versus control condition). **d**, Overview panel of human

α -SYN deposits and microglial activation (Mac1/CD11b staining) in thoracic spinal segment at low and high magnification. **e**, Quantification of α -SYN density in the spinal cord (cervical, thoracic and lumbosacral segments) shows a strong correlation between α -SYN density and microglial activation. **f**, Intravenous injection of α -SYN fibrils for 4 months results in α -SYN inclusions in cortical neurons labelled with the neuron-specific marker β III-tubulin. **g**, Confocal analysis of spinal cord reveals human α -SYN deposits labelled with the atto-550 and atto-647 markers. Scale bars, 20 μm .

evidence for a gain-of-toxic function. α -SYN fibrils can multiply by simple elongation with addition of monomers at their ends or by breakage creating additional nuclei^{22,23}. This growth process appears strain-dependent, making strains the crucial pathogenic factor. Indeed, several months after nigral injection and in sharp contrast to all other assemblies, α -SYN fibrils were detectable in striatal dopaminergic axons (Extended Data Fig. 8). Therefore, and although all α -SYN assemblies might have a role during pathogenesis, fibrillar α -SYN exhibited the largest neurotoxic potential accompanied by disease-specific hallmarks at long-term (overview in Supplementary Table 2).

In early stages of neurodegeneration pathological changes are often localized in defined brain areas, whereas at later stages neuronal dysfunction and associated protein aggregates are widespread. Oligomeric prion proteins invade the central nervous system acutely after crossing the blood–brain barrier or chronically via the splenic-nerve route²⁴. To assess whether α -SYN assemblies cross the blood–brain barrier, or behave in a similar manner, we repeatedly injected α -SYN oligomers, ribbons and fibrils intravenously on a two-weekly basis during 4 months using two fluorescent labels, providing additional temporal resolution (Fig. 4a). No rAAV- α -SYN was used in these experiments. The red-shifted fluorescent label allowed epifluorescence imaging of the injected α -SYN strains in live animals. At the final time point we observed a striking, localized fluorescent signal originating from the brain for α -SYN oligomers, ribbons and fibrils, but not for control animals injected with saline or the free atto-647 label (Fig. 4b, c). Immunohistochemical staining revealed α -SYN deposits in the central nervous system for ribbons and fibrils (Fig. 4d, e and Extended Data Fig. 9) but only diffuse staining for oligomers (Fig. 4d, Extended Data Fig. 10 a–f). This could indicate that α -SYN oligomers might either diffuse to a higher extent because of their molecular mass or are partly washed out during perfusion, while α -SYN fibrils and ribbons remain in place after crossing the blood–brain barrier. Detailed histological analysis showed an accumulation of atto-550- and atto-647-labelled human α -SYN fibrils in cortical neurons (Fig. 4f) and in spinal cord (Fig. 4g). This pattern was accompanied with microglial activation,

which was most pronounced for fibrils throughout the spinal cord, and with redistribution of the early neuronal injury marker GAP43 (Fig. 4d, e and Extended Data Fig. 10g). These observations demonstrate that, in this experimental setup, the spread of α -SYN assemblies is not restricted to the intracerebral route but extends beyond the central nervous system.

The findings that α -SYN spread after intramuscular and gastric injection^{25,26}, and the demonstration of systemic spread we make here are striking. The contribution of these routes to α -SYN assemblies spread and associated pathology deserves further investigation. In contrast to rapidly transmitted oligomers, the *in vivo* behaviour of slowly amplifying α -SYN strains may provide a basis for the observed heterogeneity in synucleinopathies and its slow but relentless pattern of spreading. This underlines the need for therapeutic strategies aimed at changing the surface properties of α -SYN assemblies either using epitope- or strain-specific antibodies or molecular chaperone-derived peptides²⁷ to interfere with the propagation of disease-associated α -SYN assemblies.

Online Content Methods, along with any additional Extended Data display items and Source Data, are available in the online version of the paper; references unique to these sections appear only in the online paper.

Received 28 March 2014; accepted 1 May 2015.

Published online 10 June 2015.

- Lee, S. J., Desplats, P., Sigurdson, C., Tsigelny, I. & Masliah, E. Cell-to-cell transmission of non-prion protein aggregates. *Nature Rev. Neurol.* **6**, 702–706 (2010).
- Goedert, M., Clavaguera, F. & Tolnay, M. The propagation of prion-like protein inclusions in neurodegenerative diseases. *Trends Neurosci.* **33**, 317–325 (2010).
- Guo, J. L. et al. Distinct α -synuclein strains differentially promote tau inclusions in neurons. *Cell* **154**, 103–117 (2013).
- Bousset, L. et al. Structural and functional characterization of two alpha-synuclein strains. *Nat. Commun.* **4**, 2575 (2013).
- Li, J. Y. et al. Lewy bodies in grafted neurons in subjects with Parkinson's disease suggest host-to-graft disease propagation. *Nature Med.* **14**, 501–503 (2008).
- Kordower, J. H., Chu, Y., Hauser, R. A., Freeman, T. B. & Olanow, C. W. Lewy body-like pathology in long-term embryonic nigral transplants in Parkinson's disease. *Nature Med.* **14**, 504–506 (2008).
- Lee, H. J., Bae, E. J. & Lee, S. J. Extracellular α -synuclein—a novel and crucial factor in Lewy body diseases. *Nature Rev. Neurol.* **10**, 92–98 (2014).

8. Conway, K. A. *et al.* Acceleration of oligomerization, not fibrillization, is a shared property of both alpha-synuclein mutations linked to early-onset Parkinson's disease: implications for pathogenesis and therapy. *Proc. Natl Acad. Sci. USA* **97**, 571–576 (2000).
9. Winner, B. *et al.* *In vivo* demonstration that alpha-synuclein oligomers are toxic. *Proc. Natl Acad. Sci. USA* **108**, 4194–4199 (2011).
10. Pieri, L., Madiona, K., Bousset, L. & Melki, R. Fibrillar alpha-synuclein and huntingtin exon 1 assemblies are toxic to the cells. *Biophys. J.* **102**, 2894–2905 (2012).
11. Luk, K. C. *et al.* Pathological alpha-synuclein transmission initiates Parkinson-like neurodegeneration in nontransgenic mice. *Science* **338**, 949–953 (2012).
12. Sacino, A. N. *et al.* Induction of CNS alpha-synuclein pathology by fibrillar and non-amyloidogenic recombinant alpha-synuclein. *Acta Neuropathol. Commun.* **1**, 38 (2013).
13. Ulusoy, A., Decressac, M., Kirik, D. & Bjorklund, A. Viral vector-mediated overexpression of alpha-synuclein as a progressive model of Parkinson's disease. *Prog. Brain Res.* **184**, 89–111 (2010).
14. Van der Perren, A. *et al.* Longitudinal follow-up and characterization of a robust rat model for Parkinson's disease based on overexpression of alpha-synuclein with adeno-associated viral vectors. *Neurobiol. Aging* **36**, 1543–1558 (2015).
15. Rey, N. L., Petit, G. H., Bousset, L., Melki, R. & Brundin, P. Transfer of human alpha-synuclein from the olfactory bulb to interconnected brain regions in mice. *Acta Neuropathol.* **126**, 555–573 (2013).
16. Reyes, J. F. *et al.* Alpha-synuclein transfers from neurons to oligodendrocytes. *Glia* **62**, 387–398 (2014).
17. Janežic, S. *et al.* Deficits in dopaminergic transmission precede neuron loss and dysfunction in a new Parkinson model. *Proc. Natl Acad. Sci. USA* **110**, E4016–E4025 (2013).
18. Milber, J. M. *et al.* Lewy pathology is not the first sign of degeneration in vulnerable neurons in Parkinson disease. *Neurology* **79**, 2307–2314 (2012).
19. Kramer, M. L. & Schulz-Schaeffer, W. J. Presynaptic alpha-synuclein aggregates, not Lewy bodies, cause neurodegeneration in dementia with Lewy bodies. *J. Neurosci.* **27**, 1405–1410 (2007).
20. Wilhelm, B. G. *et al.* Composition of isolated synaptic boutons reveals the amounts of vesicle trafficking proteins. *Science* **344**, 1023–1028 (2014).
21. Greten-Harrison, B. *et al.* $\alpha\beta\gamma$ -Synuclein triple knockout mice reveal age-dependent neuronal dysfunction. *Proc. Natl Acad. Sci. USA* **107**, 19573–19578 (2010).
22. Buell, A. K. *et al.* Solution conditions determine the relative importance of nucleation and growth processes in alpha-synuclein aggregation. *Proc. Natl Acad. Sci. USA* **111**, 7671–7676 (2014).
23. Brundin, P., Melki, R. & Kopito, R. Prion-like transmission of protein aggregates in neurodegenerative diseases. *Nature Rev. Mol. Cell Biol.* **11**, 301–307 (2010).
24. Mabbott, N. A. & MacPherson, G. G. Prions and their lethal journey to the brain. *Nature Rev. Microbiol.* **4**, 201–211 (2006).
25. Sacino, A. N. *et al.* Intramuscular injection of alpha-synuclein induces CNS alpha-synuclein pathology and a rapid-onset motor phenotype in transgenic mice. *Proc. Natl Acad. Sci. USA* **111**, 10732–10737 (2014).
26. Holmqvist, S. *et al.* Direct evidence of Parkinson pathology spread from the gastrointestinal tract to the brain in rats. *Acta Neuropathol.* **128**, 805–820 (2014).
27. Redeker, V., Pemberton, S., Bienvenut, W., Bousset, L. & Melki, R. Identification of protein interfaces between alpha-synuclein, the principal component of Lewy bodies in Parkinson disease, and the molecular chaperones human Hsc70 and the yeast Ssa1p. *J. Biol. Chem.* **287**, 32630–32639 (2012).

Supplementary Information is available in the online version of the paper.

Acknowledgements We thank J. Van Asselbergs and C. van Heijningen for their technical assistance and Z. Debyser for revising the manuscript. We thank J. Hofkens and C. David for the use of the CLSM and V. Redeker for assessing the number of atto dyes bound to α -SYN by mass spectrometry. The authors thank the Leuven Viral Vector Core (LVVC) for the rAAV vector construction, optimization and production. M.G., R.P., and A.M. thank M. Wijnants and D. Van Dyck for their excellent technical assistance. Research was funded by the FWO-Vlaanderen (G.0768.10, G.0927.14 and PhD fellowship to W.P.), the IWT-Vlaanderen (IWT SBO/80020 Neuro-TARGET, SBO/110068 OPTOBRAIN and SBO/130065 MIRIAD), the FP7 RTD projects MEFOPA (HEALTH-2009-241791) and INMiND (HEALTH-F2-2011-278850), the KU Leuven (OT/08/052A, OT/14/120, IMIR PF/10/017), the Agence Nationale de la Recherche (ANR-09-MNPS-013-01 and ANR-11-BSV8-021-01), the Centre National de la Recherche Scientifique, a 'Coup d'Élan à la Recherche Française' award from Fondation Bettencourt Schueller, the EC-FP7 (Marie Curie Initial Training Network "NAMASEN", grant n. 264872, the ICT-FET projects "ENLIGHTENMENT" and "BRAINLEAP", grants no. 284801 and 306502), and the Belgian Science Policy Office (grant no. IUAP-VII/20). The authors declare that there is no actual or potential conflict of interest.

Author Contributions W.P. designed and conducted *in vivo* experiments. L.B. generated α -SYN assemblies and performed characterization of α -SYN strains. A.V.P. conducted *in vivo* experiments. C.V.H. was responsible for viral vector production. R.M. co-designed the study. V.B. was responsible for the overall design and coordination of the study. M.G., R.P., and A.M. conducted intracellular and extracellular *in vitro* experiments and analysed the electrophysiological recordings. W.P., V.B. and R.M. prepared the manuscript.

Author Information Reprints and permissions information is available at www.nature.com/reprints. The authors declare no competing financial interests. Readers are welcome to comment on the online version of the paper. Correspondence and requests for materials should be addressed to V.B. (veerle.baekelandt@med.kuleuven.be) or R.M. (ronald.melki@lebs.cnrs-gif.fr).

METHODS

Production and purification of recombinant α -SYN and rAAV- α -SYN. Recombinant α -SYN production was performed as previously described⁴. Vector production and purification was performed as previously described²⁸. The plasmids include the constructs for the AAV2/7 serotype, the AAV transfer plasmid encoding the human A53T mutant α -synuclein transgene under the control of the ubiquitous CMVie enhanced synapsin1 promoter and the pAdvDeltaF6 adenoviral helper plasmid. Real-time PCR analysis was used for genomic copy determination.

Endotoxin detection. Protein endotoxin detection was performed using LAL Chromogenic Endotoxin Quantitation Kit (ThermoFisher catalogue no. 88282) following the manufacturer's instruction. Briefly, 10 μ g of α -SYN monomers, fibrils, ribbons and unbound Atto-550 were dissolved in 50 μ l of endotoxin-free water provided in the kit and distributed in a 96-well microplate. The LAL reagent was added next and the plate was incubated 10 min at 37 °C in a thermomixer (Eppendorf, Germany). The chromogenic reagent was next added and the incubation further extended 6 min. The reaction was arrested with 25% acetic acid. Absorbance at 405 nm was measured using a Flexstation microplate reader (FlexStation, Molecular Devices). Protein endotoxin units are presented in Extended Data Fig. 1.

rAAV- α -SYN vector endotoxin detection was performed using LAL bacterial endotoxin test (Endosafe-PTSTM, Charles River) following the manufacturer instruction. Briefly, rAAV α -SYN vector was loaded in the sample reservoir, mixed with the LAL reagent and combined with the chromogenic substrate. The Optical density was measured and analysed against an internally achieved standard curve. The measurements were performed in quadruple. Endotoxin units were determined to be 0.0000114 endotoxin unit per injection.

Generation and labelling of α -SYN assemblies. α -SYN fibrils and ribbons were generated as previously described⁴. Oligomeric α -SYN was generated by incubating monomeric α -SYN 4 °C for 7 days. Oligomeric α -SYN was separated from monomeric α -SYN by size exclusion chromatography using a Superose6 HR10/30 column (GE Healthcare) equilibrated in phosphate buffered saline (PBS) buffer.

α -SYN assemblies in PBS were labelled by addition of 2 molar excess of the aminoreactive fluorescent dye atto-550 or atto-647 (ATTO-Tech GmbH). Labelling was performed following the manufacturer's recommendations. Unreacted dye was removed by size exclusion chromatography or three cycles of sedimentation and suspension in PBS for oligomers or fibrils and ribbons, respectively. The amount of incorporated dye was assessed by mass spectrometry. The samples were de-salted (with 5% acetonitrile, 0.1% trifluoroacetic acid (TFA)) and eluted from a C18 reversed-phase Zip-Tip (Millipore, Billerica, MA, USA) in 50% acetonitrile, 0.1% TFA. Peptide samples were mixed in a ratio of 1:5 to 1:20 (v/v) with sinapinic acid (10 mg ml⁻¹) in 50% acetonitrile and 0.1% TFA and spotted (0.5 μ l) on a stainless steel MALDI target (Opti-TOF; Applied Biosystems). MALDI-TOF-TOF MS spectra were acquired with a MALDI-TOF-TOF 5800 mass spectrometer (Applied Biosystems) using linear mode acquisition. External calibration was performed using unmodified WT α -SYN. Acquisition and data analysis were performed using the Data Explorer software from Applied Biosystems.

The nature of all α -SYN assemblies used was routinely assessed using a Jeol 1400 (Jeol Ltd, Peabody, MA) Transmission Electron Microscope (TEM) after adsorption of the samples onto carbon-coated 200-mesh grids and negative staining with 1% uranyl acetate. The images were acquired with a Gatan Orius CCD camera (Gatan).

Stereotactic injections. All animal experiments were carried out in accordance with the European Communities Council Directive of 24 November 1986 (86/609/EEC) and approved by the Bioethical Committee of the KU Leuven (Belgium). Young adult female Wistar rats (Janvier, France) weighing about 200–250 g were housed under a normal 12 h light/dark cycle with free access to pelleted food and tap water. All surgical procedures were performed using aseptic techniques and ketamine (60 mg per kg intraperitoneally, Ketalar, Pfizer, Belgium) and medetomidine (0.4 mg per kg, Dormitor, Pfizer) anaesthesia. Following anaesthesia the rodents were placed in a stereotactic head frame (Stoelting, IL, USA). Injections were performed with a 30-gauge needle and a 10- μ l Hamilton syringe. After making a midline incision of the scalp, a burr hole was drilled in the appropriate location for the substantia nigra (single injections) or striatum (triple injections) at the right site of the skull. Stereotactic coordinates, dose and concentration of α -SYN protein and rAAV- α -SYN vectors are described in Supplementary Table 1. Brain homogenate was extracted from 18 month old Thy-1 A30P transgenic mice²⁹ as described previously³⁰ adjusted to a total amount of 10 μ g. Supplemented viral titres were diluted to 3.0×10^{10} genome copies per ml A53T α -SYN rAAV2/7. **Fluorescent imaging.** Epifluorescent images and fluorescent tomography were performed using the IVIS Spectrum *in vivo* imaging system (Caliper, PerkinElmer, version 4.3.1). Anaesthesia was induced in an induction chamber

with 3% isoflurane in 100% oxygen at a flow rate of 1 l min⁻¹ and maintained in the IVIS with a 1.5% mixture at 0.5 l min⁻¹. Rats were injected with 500 μ l saline supplemented with 10 μ g of fluorescently labelled α -SYN protein intravenously in the tail vein. Subsequently, they were placed in the prone position in the IVIS and epifluorescent images of atto-647 α -SYN labelled proteins were acquired at the final time point. Atto-550 α -SYN labelled proteins could not be imaged due to high autofluorescent background levels in live animals. Each frame depicts the fluorescent image as a pseudocolour image superimposed on the grey-scale photographic image. The data are reported on a logarithmic scale as the fluorescent yield or fluorescence emission radiance per incident excitation intensity (p s⁻¹ cm⁻² sr⁻¹ μ W⁻¹ cm⁻²) from a 2 cm² circular region of interest around the head.

Fluorescent tomography *ex vivo* images of α -SYN spreading were acquired by merging 11 distinct and predefined transillumination excitation sources of perfused and fixed rat brain. A small illumination spot is scanned over a predefined grid resulting in distinct illumination foci. The excitation source was positioned below the brain with the delivery of a concentrated excitation light beam and observed by a detector located above the object. Superimposing surface topography and fluorescent signal results in fluorescent tomography providing a 3D reconstruction of atto-550-tagged α -SYN fluorescent volume. Emitted fluorescent light propagation is calculated through diffusion approximation allowing the reconstruction of the fluorescent source in 3D. 3D reconstruction is presented as voxels with fluorescent intensity profile for each condition and is mapped to a 3D brain atlas. Fluorescence yield is expressed in units of pmol M⁻¹ cm⁻¹. A threshold % value was set to keep the minimum count of pixels above 200 to exclude background pixels from the reconstruction. The accuracy of reconstruction was checked for all samples by comparing the measured light diffusion pattern with the simulated light diffusion pattern. If the % error between these two has a near-zero % difference, the reconstruction was considered successful and used for spatial measurements.

Behavioural testing. The cylinder test was used to measure asymmetry in spontaneous forelimb use. Contacts made by each forepaw with the wall of 20 cm-wide clear glass cylinder were scored from the videotapes by an observer blinded to the animal's identity. Between 20 and 30 wall touches per animal (contacts with fully extended digits executed with the forelimb ipsilateral and contralateral to the lesion) were counted. The number of impaired forelimb contacts was expressed as a percentage of total forelimb contacts. Non-lesioned control rats should score around 50% in this test. No habituation of the animals to the testing cylinder was allowed before video recording. An investigator blind to different groups performed all the analyses.

Histology. Rats were euthanized with an overdose of sodium pentobarbital (60 mg per kg intraperitoneally, Nembutal, Ceva Santé, Belgium) followed by intracardial perfusion with 4% paraformaldehyde in PBS. After postfixation overnight, 50 μ m thick coronal brain sections were made with a vibrating microtome (HM 650V, Microm, Germany). IHC was performed as previously described³¹ using antibodies summarized in Supplementary Table 3. For spinal cord staining, commercial TNB blocking buffer (Perkin Elmer) was added to all incubation steps to minimize background staining in 50 μ m vibratome sections.

For fluorescent double or triple staining, sections were rinsed three times in PBS and incubated overnight in the dark in PBS-0.1% Triton X-100 and 0.1% sodium azide, 10% donkey or goat serum and antibodies summarized in Supplementary Table 3. After rinsing, the sections were incubated in the dark for 2 h in fluorochrome-conjugated secondary antibodies. After being rinsed and mounted, the sections were coverslipped with Mowiol. Fluorescent staining was visualized by confocal microscopy (Fluoview 1000, Olympus). Reconstructed 3D images from z-stack tiles were imaged using an Olympus confocal laser-scanning microscope and rendered into the complete neuronal reconstructions by tiling the entire set of z-stacks using Imaris software.

Stereological quantification. The number of TH-positive cells and α -SYN-positive cells in the substantia nigra was determined by stereological measurements using the optical fractionator method in a computerized system as described before³² (StereoInvestigator; MicroBright-Field, Magdeburg, Germany). Every fifth section throughout the entire substantia nigra was analysed, with a total of seven sections for each animal. The coefficients of error, calculated according to the procedure of Schmitz and Hof as estimates of precision³³ varied between 0.05 and 0.10. The volume of α -SYN expression in the brain and the substantia nigra was determined by the Cavalieri method. Every fifth section covering the entire extent of the substantia nigra, with a total of seven sections for each animal, was included in the counting procedure. The coefficients of error varied between 0.05 and 0.14. We quantified both the injected and non-injected substantia nigra (internal control), no cell loss was observed in the non-injected side. An investigator blind to different groups performed all the analyses.

Sarkosyl extraction. Unfixed brains were dissected to isolate substantia nigra and striatum from both hemispheres and frozen in liquid nitrogen. Brain samples were weighted and homogenized at 10% (w/v) in PBS buffer supplemented with phosphatase inhibitor cocktail (sigma P5726 and P0044) and protease inhibitors (Roche Complete EDTA free). Sarkosyl was added to 1%. 250 μ l were centrifuged at 1,000g for 30 min to remove cell debris. The supernatants (200 μ l) were further centrifuged at 200,000g for 60 min at 20 °C in an Optima MAX-XP Ultracentrifuge (Beckman). The pellets were washed with PBS-1% Sarkosyl, and resuspended in 200 μ l of PBS buffer.

Proteinase K digestion, SDS-, native-PAGE and western blot analysis. Sarkosyl insoluble fractions containing α -SYN were incubated at 25 °C with proteinase K (0.001, 0.01, 0.1, 1 μ g ml⁻¹) (Roche) for 30 min. Aliquots were mixed v/v with denaturing buffer (50 mM Tris-HCl, pH 6.8, 4% SDS, 2% β -mercaptoethanol, 12% glycerol and 0.01% bromophenol blue) and heated at 90 °C to arrest immediately the cleavage reaction. After incubation for 10 min at 90 °C, the samples were processed to monitor the time course of α -SYN cleavage by SDS-PAGE (15% polyacrylamide gels) followed by western blotting and detection with Clone42 monoclonal antibody (BD Bioscience ref. 610787) or anti-phospho-Ser 129 α -SYN antibody. For native-PAGE, sarkosyl insoluble fractions subjected or not to PK treatment were supplemented with Triton X-100 (0.2%, v/v) β -mercaptoethanol (2%), glycerol (12%) and bromophenol blue (0.01%) and loaded on 15% native-PAGE. The samples were transferred to nitrocellulose membranes and probed with D37A6 or Syn 211 anti-rodent and human α -SYN antibodies (Supplementary Table 3).

Electrophysiology and MEA recordings. Primary cortical cultures were obtained from postnatal Wistar rats, employing standard methods³⁴. Briefly, after mechanical and enzymatic dissociation of the cerebral cortices of postnatal day 0 (P0) pups, cells were plated at a final density of ~ 1.500 mm⁻² on glass coverslips and of 6.500 mm⁻² on commercial microelectrode arrays (MEAs; Multichannel Systems GmbH, Reutlingen, Germany). Individual MEAs incorporated 59 substrate microelectrodes made of indium titanium nitrate, featuring a diameter of 30 μ m and an electrical impedance of ~ 100 k Ω at 1 kHz. The inter-electrode spacing was 200 μ m, and the microelectrodes arranged in a regular 8 \times 8 layout that covered an area of ~ 2.56 mm². MEAs and coverslips were coated overnight with polyethyleneimine 0.1% (w/v) in millQ water at room temperature, before cell seeding. Seeded MEAs and coverslips were maintained under sterile conditions at 37 °C under 5% CO₂ atmosphere with 100% relative humidity for several weeks.

Patch-clamp intracellular recordings were performed 22–23 days after plating, from neurons cultured under control conditions (that is, 1 μ M bovine serum albumin) or incubated for 3–4 days with 1 μ M α -SYN (that is, as ribbons, fibrils, oligomers). Patch-clamp recordings were made from the cell somata under the whole-cell configuration using an Axon Multiclamp 700B Amplifier (Molecular Devices LLC, Sunnyvale, CA, US), employing both current-clamp and voltage-clamp modes. Patch electrodes were pulled from thick-walled borosilicate glass capillaries (1BF150, World Precision Instruments, Hitchin, UK) by a horizontal puller (P97, Sutter, Novato, US) to a resistance of 6–7 M Ω . Electrodes were filled with an intracellular solution containing (in mM): 135 K-gluconate, 10 KCl, 10 HEPES, 0.2 EGTA, 4 Mg-ATP, 0.4 Na₃GTP, and 14 Na₂-phosphocreatine (pH 7.3, titrated with KOH). All recordings were obtained at 34 °C and replacing the culture medium by an artificial cerebrospinal fluid, constantly perfused at a rate of 1 ml min⁻¹ and containing (in mM): 145 NaCl, 4 KCl, 2 Na-pyruvate, 5 HEPES, 5 glucose, 2 CaCl₂, and 1 MgCl₂ (pH adjusted to 7.4 with NaOH). Voltage and current traces were sampled at 15 kHz, analog to digital converted at 16 bits, and stored on a PC employing the software LCG³⁵. Data were analysed off-line,

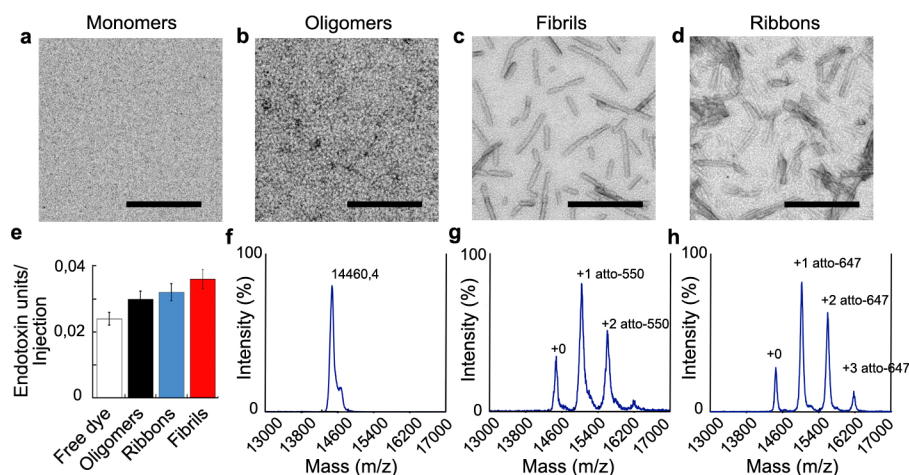
employing custom scripts written in MATLAB (The MathWorks, Natick, US) or Excel (Microsoft, USA).

Extracellular recordings experiments were performed 15–20 days after plating, and continued until day 28, from neurons cultured over MEAs under control conditions (that is, 1 μ M bovine serum albumin) or incubated for up to 10 days with 1 μ M α -SYN (that is, as ribbons, fibrils, oligomers). Recordings were performed by a MEA1060BC amplifier, (Multichannel Systems GmbH, Reutlingen, Germany) inside an electronic-friendly incubator, maintaining 37 °C, 5% CO₂, and 100% relative humidity. This allowed us to monitor simultaneously, chronically, and non-invasively the neuronal electrical activity from up to 60 locations within the very same culture. MEA recordings were analysed off-line by QSpokeTools³⁶. Briefly, the extracellular electric fields were monitored from the 59 independent electrodes in each MEAs were sampled at 25 kHz per channel, 1,200 \times amplified, bandpass-filtered (200–3,000 Hz), and digitally recorded for 30 min every day, up to 6 days following the bath application of α -SYN, dissolved in culture medium with distinct concentrations (that is, 0.1, 0.5, and 1 μ M). Simple spike-sorting, based on spike-shape peak polarity, was performed. Epochs of spontaneous synchronized firing across the MEAs electrodes were identified over 25 ms bins by standard procedures³⁶, and their features were extracted from each recording session.

Statistical analysis. Results are expressed as means \pm standard error of the mean. Normality of data was assessed with the Lilliefors test. Statistical significance was assessed using one-way ANOVA followed by Dunnett's or Tukey's post-hoc test and column statistics followed by Bonferroni's post-hoc test. Null hypothesis was rejected if the *P* value was below 0.5. Statistical significance level was set as follows: * if *P* < 0.05, ** if *P* < 0.01, *** if *P* < 0.001. In case of improper fitting of data by a normal distribution, median and interquartile range were used for data representation, and Wilcoxon rank sum test was used for analysis.

No statistical methods were used to predetermine sample size. Randomization was not applied because all animals (acquired via commercial animal lab, Janvier) used in this study were similar for age, sex and strain background.

28. Van der Perren, A. *et al.* Efficient and stable transduction of dopaminergic neurons in rat substantia nigra by rAAV 2/1, 2/2, 2/5, 2/6.2, 2/7, 2/8 and 2/9. *Gene Ther.* **18**, 517–527 (2011).
29. Kahle, P. J. *et al.* Selective insolubility of alpha-synuclein in human Lewy body diseases is recapitulated in a transgenic mouse model. *Am. J. Pathol.* **159**, 2215–2225 (2001).
30. Luk, K. C. *et al.* Intracerebral inoculation of pathological alpha-synuclein initiates a rapidly progressive neurodegenerative alpha-synucleinopathy in mice. *J. Exp. Med.* **209**, 975–986 (2012).
31. Oliveras-Salv , M. *et al.* rAAV2/7 vector-mediated overexpression of alpha-synuclein in mouse substantia nigra induces protein aggregation and progressive dose-dependent neurodegeneration. *Mol. Neurodegener.* **8**, 44 (2013).
32. Baekelandt, V. *et al.* Characterization of lentiviral vector-mediated gene transfer in adult mouse brain. *Hum. Gene Ther.* **13**, 841–853 (2002).
33. Schmitz, C. & Hof, P. R. Design-based stereology in neuroscience. *Neuroscience* **130**, 813–831 (2005).
34. Reinartz, S., Biro, I., Gal, A., Giugliano, M. & Marom, S. Synaptic dynamics contribute to long-term single neuron response fluctuations. *Front. Neural Circuits* **8**, 71 (2014).
35. Linaro, D., Couto, J. & Giugliano, M. Command-line cellular electrophysiology for conventional and real-time closed-loop experiments. *J. Neurosci. Methods* **230**, 5–19 (2014).
36. Mahmud, M., Pulizzi, R., Vasilaki, E. & Giugliano, M. QSpoke tools: a generic framework for parallel batch preprocessing of extracellular neuronal signals recorded by substrate microelectrode arrays. *Front. Neuroinform.* **8**, 26 (2014).

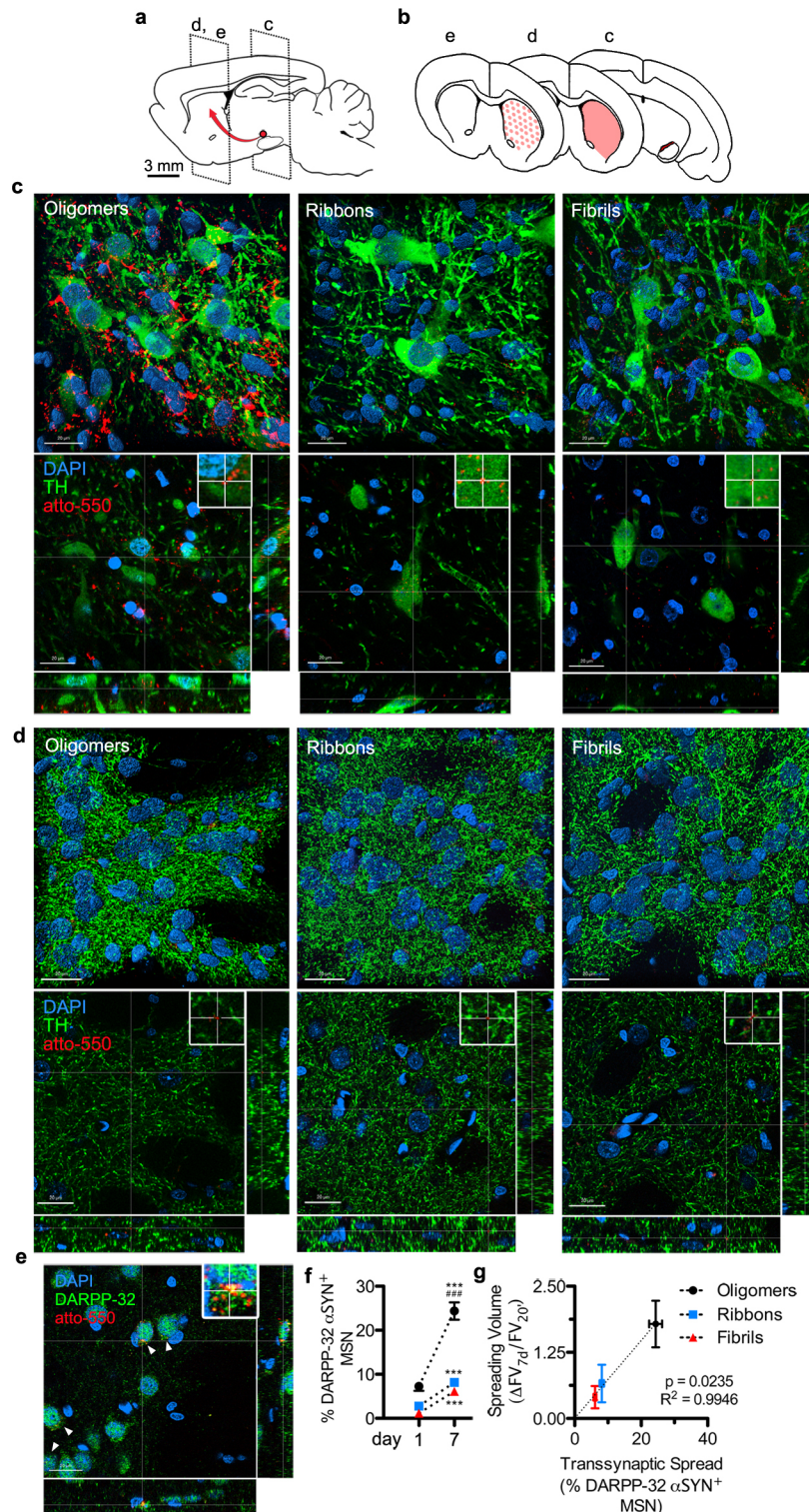


Extended Data Figure 1 | Characterization of α -SYN assemblies.

a–d, Electron micrographs of α -SYN monomers (**a**), oligomers (**b**), fibrils (**c**) and ribbons (**d**) used throughout this study. The scale bars represent 200 nm. **e**, Quantification of endotoxin amounts in different recombinant α -SYN preparations used throughout this study. Endotoxin levels were below

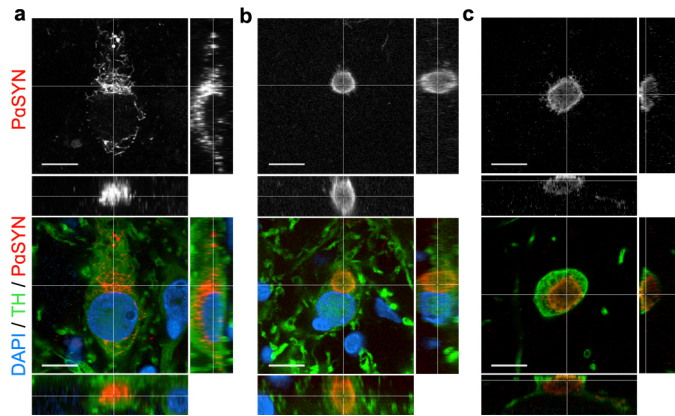
0.05 units per injection for all conditions. **f–h**, Mass spectrometry analysis of covalently labelled fluorescent wild-type (WT) α -SYN by MALDI-TOF.

f, Unlabelled WT α -SYN (theoretical mass 14,460.1 Da); **g**, atto-550 WT α -SYN (average molecular ratio 1 atto molecule per α -SYN molecule) and **h**, atto-647 WT α -SYN (average molecular ratio 1 atto molecule per α -SYN molecule).

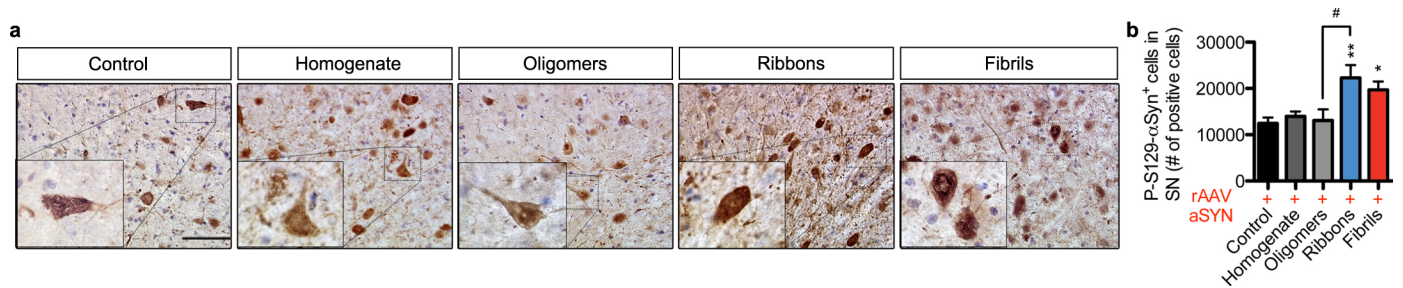


Extended Data Figure 2 | Trans-synaptic spreading of fluorescently labelled α -SYN in rat striatum. α -SYN assemblies were injected in rat substantia nigra (red injection spot) and were allowed to spread for 7 days to the striatum. Sagittal and coronal views are depicted in **a** and **b**, respectively. Representative confocal images of α -SYN spreading in **c**, dopaminergic neurons and **d**, striatal dopaminergic axons for α -SYN oligomers, ribbons and fibrils after 7 days. Reconstructed images from z-stack tiles of the dopaminergic neurons and axons in striatum were rendered into complete axonal reconstructions by tiling the entire set of z-stacks. Scale bar is 20 μ m. The rectangle identifying Atto-550-tagged α -SYN is shown at a higher magnification in upper right corner of sections in lower panels. **e**, Representative confocal image of recombinant oligomeric Atto-550 labelled α -SYN uptake in medium spiny neurons (MSN)

after injection in substantia nigra. White arrows indicate positive inclusions. **f**, Quantification of fluorescently labelled α -SYN DARPP-32⁺ MSN. Uptake is measured after 1 and 7 days for oligomers ($n_{1 \text{ day}} = 1,674$, $n_{7 \text{ days}} = 2,118$, $n_{\text{animals}} = 3$), ribbons ($n_{1 \text{ day}} = 2,152$, $n_{7 \text{ days}} = 1,968$, $n_{\text{animals}} = 3$) and fibrils ($n_{1 \text{ day}} = 1,223$, $n_{7 \text{ days}} = 1,486$, $n_{\text{animals}} = 3$). Oligomers show increased uptake rates compared to ribbons and fibrils ($***P < 0.001$, $**P < 0.01$, one-way ANOVA with Dunnett's multiple comparison test for 7 day time point) and increases over time ($***P < 0.001$, one-way ANOVA with Tukey's multiple comparison test). Error bars indicate s.e.m., scale bars indicate 20 μ m. **g**, Correlation of spreading volume and trans-synaptic spread at 7 days. Oligomers show the highest spreading capacity compared to fibrils and ribbons using two independent techniques and experiments.

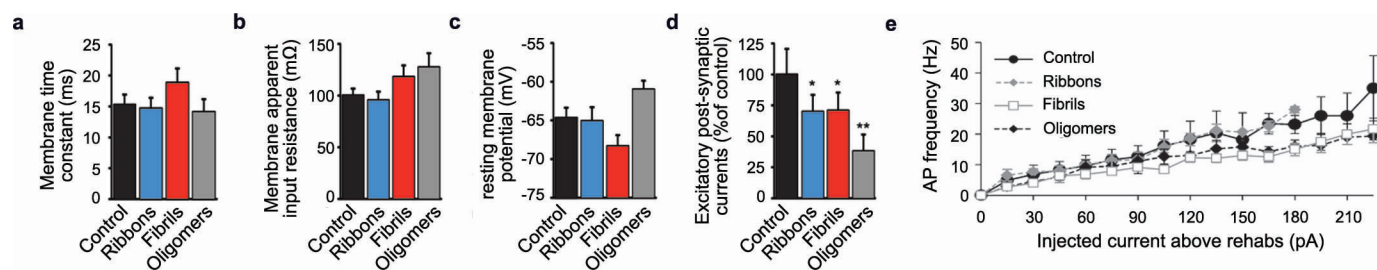


Extended Data Figure 3 | Histopathological hallmarks after nigral inoculation of α -SYN strains. a–c, Immunofluorescent staining in substantia nigra shows a, granular cytoplasmic, b, intracytoplasmic and c, nuclear P α -SYN inclusions in dopaminergic neurons. Reconstructed images from z-stack tiles were rendered into complete reconstructions by tiling the entire set of z-stacks. Scale bars indicate 20 μ m.



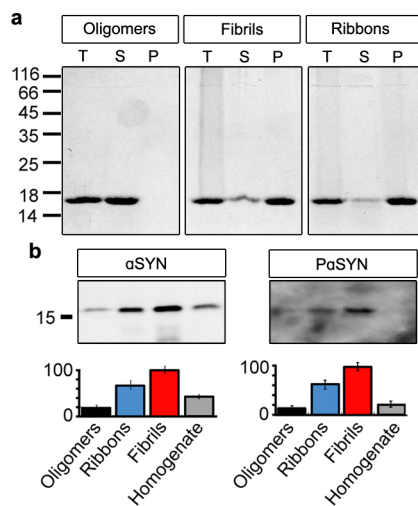
Extended Data Figure 4 | Phosphorylation pattern of different α -SYN assemblies upon rAAV-driven α -SYN overexpression. **a**, Inoculation of ribbons and fibrils result in increased amount of phosphorylated α -SYN cells in substantia nigra. Scale bar, 50 μ m. **b**, Animals where α -SYN overexpression is rAAV-driven yield a total of 12,426 \pm 1,288 cells with phosphorylated α -SYN (s.e.m, n = 4). A significant increase of cells with

phosphorylated α -SYN is observed upon injection of ribbons and fibrils, to 22,254 cells \pm 2,800 (s.e.m, n = 4) and 19,690 cells \pm 1,803 (s.e.m, n = 4), respectively (** P < 0.01, * P < 0.05, one-way ANOVA with Dunnett's multiple comparison test versus control, # P < 0.05, one-way ANOVA with Tukey's multiple comparison test).

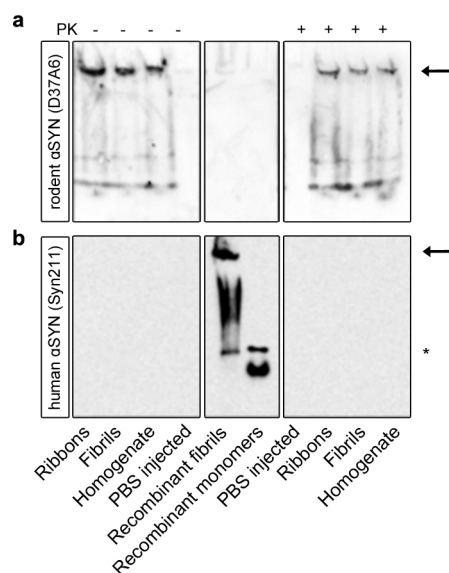


Extended Data Figure 5 | Intracellular and extracellular electrophysiological recordings of early effects of α -SYN assemblies on the electrical properties of single neurons. Rat primary cortical neurons, cultured *ex vivo* for over 4 weeks, displayed no significant alterations of the intrinsic electrical phenotype after exposure for 3–4 days to 1 μ M of α -SYN assemblies. This was characterized by means of intracellular recordings, and analysed in current-

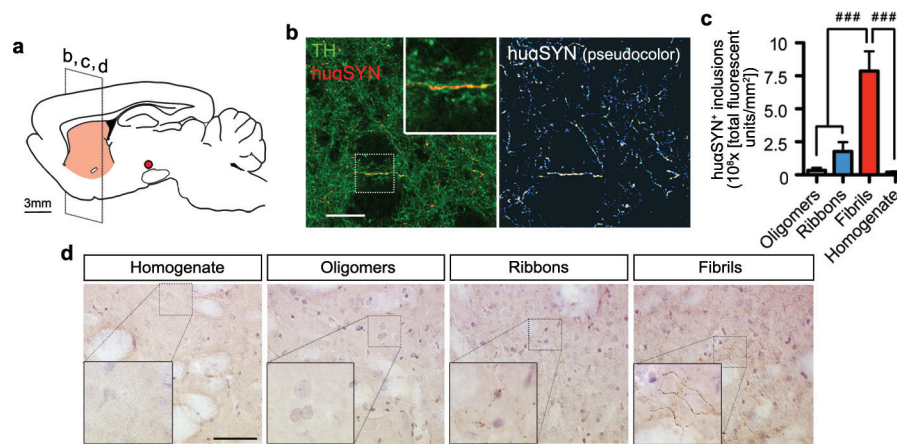
clamp in terms of membrane passive properties ($n = 32$ cells), **a**, as membrane time constant, **b**, membrane apparent input resistance, **c**, resting membrane potential and **e**, as evoked excitable responses ($n = 30$ cells). By the same technique, the amplitude of **d**, excitatory spontaneous post-synaptic currents (PSCs) revealed a significant downregulation, recorded under voltage-clamp ($n = 32$ cells).



Extended Data Figure 6 | α -SYN strains propagate after intracerebral inoculation. **a**, Preformed α -SYN fibrils and ribbons resist 1% sarkosyl treatment and are pelleted upon sedimentation at 200,000g for 60 min at 25 °C *in vitro*. (T, total; S, Soluble; P, Pellet) **b**, Fibrils resist 1% sarkosyl treatment and persist more after striatal injections than ribbons or oligomers. Sarkosyl-insoluble α -SYN from animals inoculated fibrils or ribbons is phosphorylated. Mean and associated standard error was calculated from 3 independent quantifications of the intensities made using ImageJ on samples from two independent experiments.

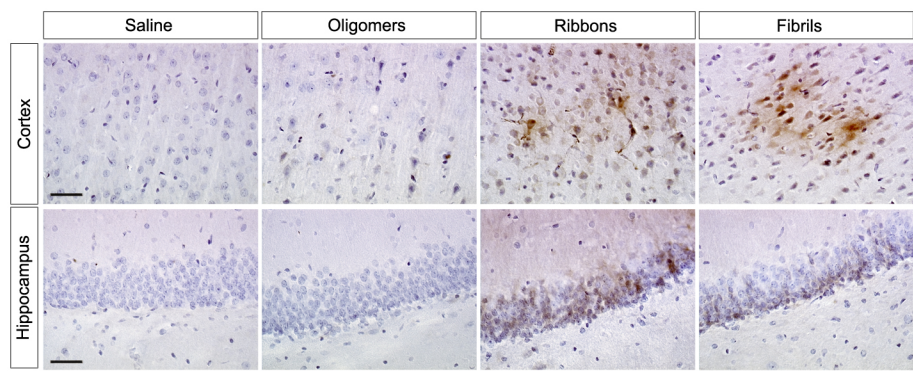


Extended Data Figure 7 | α -SYN strains recruit rodent α -SYN. Seeding of endogenous α -SYN in rat brain by exogenous human ribbons, fibrils or diseased rat brain homogenates. PBS was inoculated to the control animal. The nature of α -SYN assemblies was assessed by western blot following native PAGE separation prior (–) or after (+) proteinase K ($76 \text{ ng } \mu\text{l}^{-1}$) treatment. **a**, Staining with rat-specific antibody (D37A6) detects endogenous α -SYN and **b**, staining with human-specific antibody (Syn211) detects exogenous injected α -SYN on a duplicate blot. Arrows indicate fibrillar α -SYN at the bottom of the gel well. The non specific band (*) is recognized by the secondary antibody. Representative image from 3 independent experiments is shown.



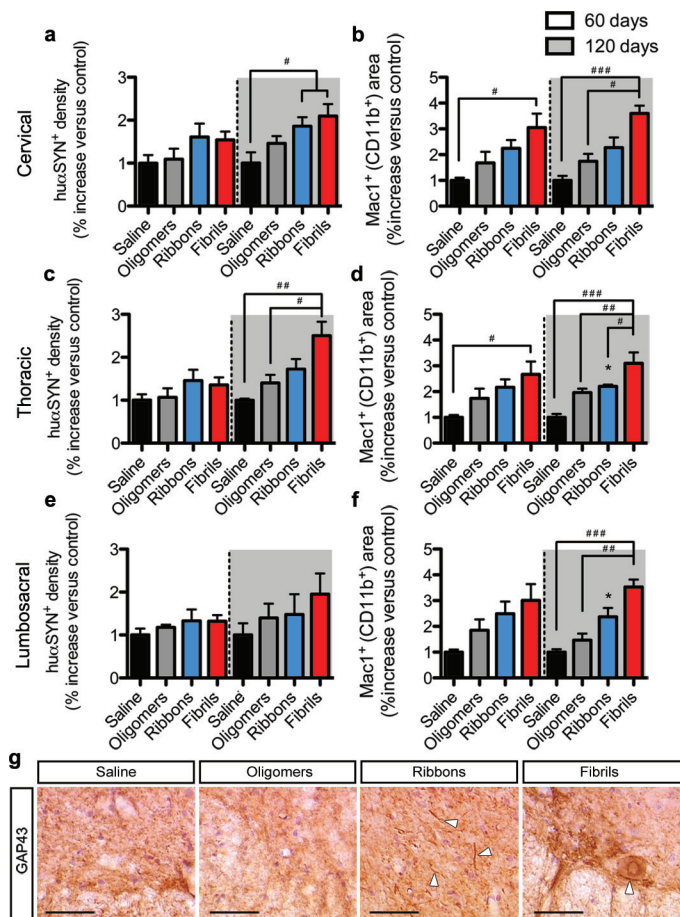
Extended Data Figure 8 | α -SYN fibrils persist months after intracerebral inoculation. **a**, α -SYN assemblies were injected in rat substantia nigra (red injection spot) and assessed 4 months later in striatum. **b**, Immunohistochemical analysis of rat striatum reveals clear human α -SYN⁺ inclusions colocalizing with dopaminergic axons. Representative image of fibrils is shown with detailed image in right upper corner. Right panel shows pseudocolour image of only human α -SYN. Scale bar indicates 30 μ m. **c**, Quantification of different α -SYN strains in rat striatum by means of total fluorescent units.

Fibrils appear to persist to a much higher extent compared to ribbons (****P* < 0.001, one-way ANOVA with Tukey's multiple comparison test, *n* = 4). Oligomers and brain homogenate show very low immunofluorescent staining for human-specific α -SYN. **d**, Fibrils appear as axonal inclusions and are abundantly present in striatum in contrast to ribbons after nigral injection. Oligomers and brain homogenate are not detected using the same human-specific antibody Syn211. Scale bar indicates 40 μ m.



Extended Data Figure 9 | α -SYN ribbons and fibrils spread across the central nervous system after intravenous administration. Overview of human α -SYN (Syn211) inclusions in different areas of the central nervous

system after intravenous injection of α -SYN oligomers, ribbons and fibrils. Scale bars indicate 50 μ m.



Extended Data Figure 10 | Intravenous injection of α -SYN strains leads to increased microglial response and distinct histopathological hallmarks in the spinal cord. Quantification of human α -SYN (hu α -SYN) density and Mac1/CD11b microglial response following intravenous administration of a saline solution or α -SYN oligomers, ribbons or fibrils in **a**, **b**, cervical, **c**, **d**, thoracic and **e**, **f**, lumbosacral segments ($^{**}P < 0.05$, one-way ANOVA with Dunnett's multiple comparison test versus control, $^{***}P < 0.001$, $^{*}P < 0.01$, $^{*}P < 0.05$, one-way ANOVA with Tukey's multiple comparison test, $n = 4$). Error bars indicate s.e.m., white boxes and grey boxes indicate 60 and 120 days after intravenous injections, respectively. **g**, Immunohistochemical staining for growth associated protein 43 (GAP43), an early injury marker, shows a filamentous distribution for α -SYN ribbons and cellular distribution for α -SYN fibrils (white arrow heads). Scale bars indicate 50 μ m.

IL-17-producing $\gamma\delta$ T cells and neutrophils conspire to promote breast cancer metastasis

Seth B. Coffelt¹, Kelly Kersten^{1*}, Chris W. Doornebal^{1*}, Jorieke Weiden¹, Kim Vrijland¹, Cheei-Sing Hau¹, Niels J. M. Verstegen¹, Metamia Ciampricotti¹, Lukas J. A. C. Hawinkels^{2,3}, Jos Jonkers⁴ & Karin E. de Visser¹

Metastatic disease remains the primary cause of death for patients with breast cancer. The different steps of the metastatic cascade rely on reciprocal interactions between cancer cells and their micro-environment. Within this local microenvironment and in distant organs, immune cells and their mediators are known to facilitate metastasis formation^{1,2}. However, the precise contribution of tumour-induced systemic inflammation to metastasis and the mechanisms regulating systemic inflammation are poorly understood. Here we show that tumours maximize their chance of metastasizing by evoking a systemic inflammatory cascade in mouse models of spontaneous breast cancer metastasis. We mechanistically demonstrate that interleukin (IL)-1 β elicits IL-17 expression from gamma delta ($\gamma\delta$) T cells, resulting in systemic, granulocyte colony-stimulating factor (G-CSF)-dependent expansion and polarization of neutrophils in mice bearing mammary tumours. Tumour-induced neutrophils acquire the ability to suppress cytotoxic T lymphocytes carrying the CD8 antigen, which limit the establishment of metastases. Neutralization of IL-17 or G-CSF and absence of $\gamma\delta$ T cells prevents neutrophil accumulation and downregulates the T-cell-suppressive phenotype of neutrophils. Moreover, the absence of $\gamma\delta$ T cells or neutrophils profoundly reduces pulmonary and lymph node metastases without influencing primary tumour progression. Our data indicate that targeting this novel cancer-cell-initiated domino effect within the immune system—the $\gamma\delta$ T cell/IL-17/neutrophil axis—represents a new strategy to inhibit metastatic disease.

In patients with breast cancer, increased neutrophil abundance predicts worsened metastasis-specific survival^{3,4}. Currently, the role of neutrophils in metastasis is controversial, since both pro- and anti-metastatic functions have been described^{5–7}. We found a profound systemic expansion of neutrophils in mammary tumour-bearing *K14cre; Cdh1^{F/F}; Trp53^{F/F}* (KEP) mice⁸, compared with wild-type (WT) littermates (Extended Data Fig. 1a, b). Neutrophils, defined as CD45⁺ CD11b⁺ Ly6G⁺ Ly6C⁺ F4/80[–] cells, accumulated throughout every organ examined (Extended Data Fig. 1c, d). We also investigated our recently described KEP-based model of spontaneous breast cancer metastasis⁹ (Fig. 1a), where systemic neutrophil expansion was observed as well (Fig. 1b and Extended Data Fig. 1e, f). Neutrophil expansion was tumour-induced, because surgical removal of the primary tumour resulted in their immediate reduction (Extended Data Fig. 1g).

To determine the functional significance of neutrophils in metastasis, neutrophils were depleted using anti-Ly6G antibodies (Extended Data Fig. 2a–c). Treatment was initiated when tumours were palpable and continued until mice developed overt metastatic disease. Neutrophil depletion did not influence tumour growth (Extended Data Fig. 2d), tumour histopathology (Extended Data Fig. 2e) or microvessel density (Extended Data Fig. 2e, f). In contrast, neutrophil depletion resulted in significant reduction in both pulmonary and lymph node metastasis

(Fig. 1c). These data indicate that neutrophils assist the spread of cancer cells to multiple locations.

Next, we evaluated the role of neutrophils in different phases of the metastatic cascade. Neutrophils were depleted during primary tumour growth (early phase) or after removal of the primary tumour (late phase) (Fig. 1a). Interestingly, neutrophil depletion decreased multi-organ metastasis in the early phase, but not the late phase (Fig. 1d). Metastatic nodule size was not affected (Extended Data Fig. 2g), suggesting that neutrophils facilitate multi-organ metastasis during the early steps of the metastatic cascade.

To understand the mechanism by which neutrophils facilitate metastasis, their phenotype was investigated. Previous reports identified the haematopoietic stem cell marker cKIT on pro-metastatic myeloid cells^{6,10–12}, and CD11b⁺ VEGFR1⁺ cells have been implicated in the pre-metastatic niche^{10,13,14}. A greater proportion of neutrophils from tumour-bearing KEP mice expressed cKIT, while both neutrophils and monocytes from WT and KEP mice expressed VEGFR1 (Extended Data Fig. 3a, b). In the metastasis model, cKIT⁺ neutrophils also expanded systemically, as tumours grew larger (Extended Data Fig. 3c) and reduced to baseline levels after tumour resection (Extended Data Fig. 3d). Nuclear morphological analysis revealed characteristics of immature cells¹⁵, including banded, circular and non-segmented nuclei, whereas most WT neutrophils appeared hyper-segmented (Extended Data Fig. 3e), suggesting that KEP mammary tumours promote the release of immature neutrophils into circulation.

Next-generation RNA sequencing (RNA-seq) was performed on circulating neutrophils from WT and tumour-bearing KEP mice, revealing 100 differentially expressed genes (Extended Data Fig. 4a and Extended Data Table 1). Several genes upregulated in neutrophils from KEP mice, including *Prok2* (also known as *Bv8*), *S100a8* and *S100a9* (Fig. 2a), have previously been linked to metastasis^{6,14}. *Nos2*, the gene encoding inducible nitric oxide synthase (iNOS), was the most strongly upregulated gene, by more than 150-fold (Fig. 2a). Because iNOS suppresses T cells^{16–18}, we hypothesized that neutrophils promote metastasis via immunosuppression. Indeed, neutrophils from KEP mice inhibited the CD3/CD28-induced proliferation of naive splenic CD8⁺ T cells *ex vivo* compared with WT neutrophils, and an iNOS inhibitor reversed this effect (Fig. 2b and Extended Data Fig. 4b). In lungs of control and neutrophil-depleted tumour-bearing mice, the proportions of CD8⁺ T cells did not differ (Extended Data Fig. 4c). However, the effector phenotype of CD8⁺ T cells was markedly enhanced upon neutrophil depletion, as evidenced by a significantly greater proportion of CD62L[–] CD44⁺ and interferon- γ ⁺ (IFN- γ ⁺) cells (Fig. 2c and Extended Data Fig. 4d, e). To establish further a mechanistic link between neutrophils and CD8⁺ T cell activity, we depleted both cell populations in the metastasis model. Combined depletion of neutrophils and CD8⁺ T cells reversed the metastasis phenotype of neutrophil depletion alone

¹Division of Immunology, Netherlands Cancer Institute, Plesmanlaan 121, Amsterdam, 1066 CX, The Netherlands. ²Department of Molecular Cell Biology, Leiden University Medical Center, Albinusdreef 2, Leiden, 2300 RC, The Netherlands. ³Centre for Biomedical Genetics, Leiden University Medical Center, Albinusdreef 2, Leiden, 2300 RC, The Netherlands. ⁴Division of Molecular Pathology, Netherlands Cancer Institute, Plesmanlaan 121, Amsterdam, 1066 CX, The Netherlands.

*These authors contributed equally to this work.

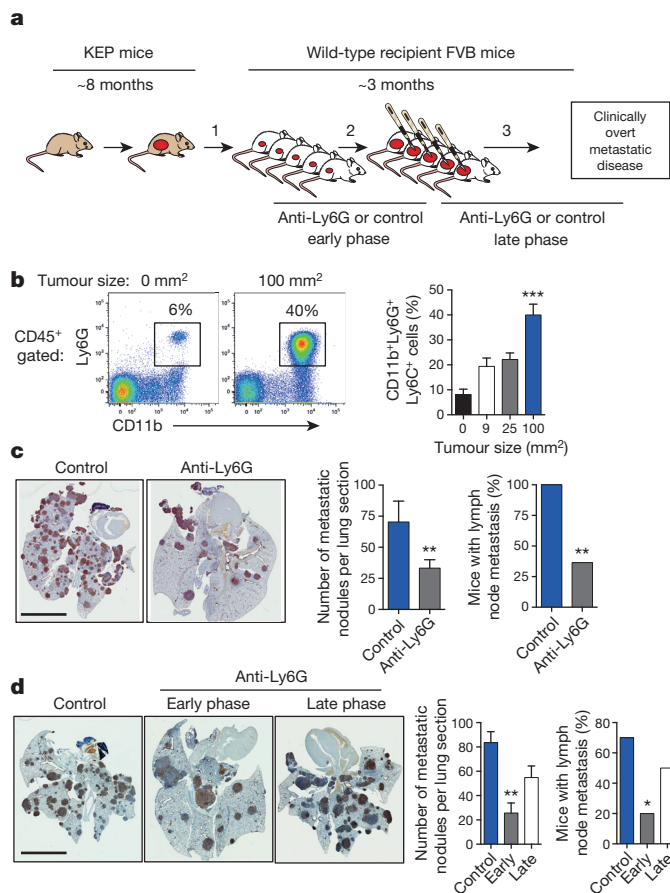


Figure 1 | Neutrophils promote breast cancer metastasis. **a**, Spontaneous metastasis model. Tumour fragments from KEP mice are orthotopically transplanted into WT female FVB/N recipient mice (designated by 1), allowed to proliferate (2), then surgically resected (3)⁹. Metastases develop in 100% of recipient mice. Antibody-mediated depletion experiments were performed in three ways: from palpable tumours to metastasis-related death (continuous treatment), during primary tumour growth (early phase) or after surgery until metastasis-related death (late phase). **b**, Neutrophil proportions in lungs at the indicated tumour size ($n = 6, 5, 6$ and 8 mice for $0, 25$ and 100 mm^2 , respectively; Kruskal–Wallis test followed by post-hoc Dunn’s test). **c, d**, Images of cytokeratin 8-stained lung sections, quantification of lung metastases and incidence of metastasis in lymph nodes. Neutrophils were depleted continuously until metastasis-related death in **c** ($n = 11$ mice per group; Mann–Whitney U -test and Fisher’s exact test) or depleted during the early or late phases in **d** ($n = 9$ control, 11 early phase, 14 late phase; Kruskal–Wallis test followed by post-hoc Dunn’s test and Fisher’s exact test). Data in **d** are representative of two independent experiments. All data are mean \pm s.e.m. * $P < 0.05$, ** $P < 0.01$, *** $P < 0.001$. Scale bars, 6 mm .

(Fig. 2d), without affecting primary tumour growth (Extended Data Fig. 4f). Depletion of CD8⁺ T cells alone did not alter tumour growth or multi-organ metastasis (data not shown). These data suggest that neutrophils facilitate cancer cell spread by suppressing CD8⁺ T cells. As such, neutrophils in the KEP model can be categorized as a subpopulation of myeloid-derived suppressor cells¹⁵.

We then asked how mammary tumours induce systemic neutrophil expansion. Cytokine profile comparison of WT mammary glands and KEP mammary tumours showed that granulocyte–macrophage colony-stimulating factor (GM-CSF) and G-CSF levels—two key regulators of neutrophil biology¹⁹—were not significantly increased in KEP tumours (Extended Data Fig. 5a, b). However, expression of IL-1 β , IL-6 and IL-12p40, a subunit of IL-23, was increased (Extended Data Fig. 5a, b). These cytokines are known to stimulate IL-17 from lymphocytes^{20–23}.

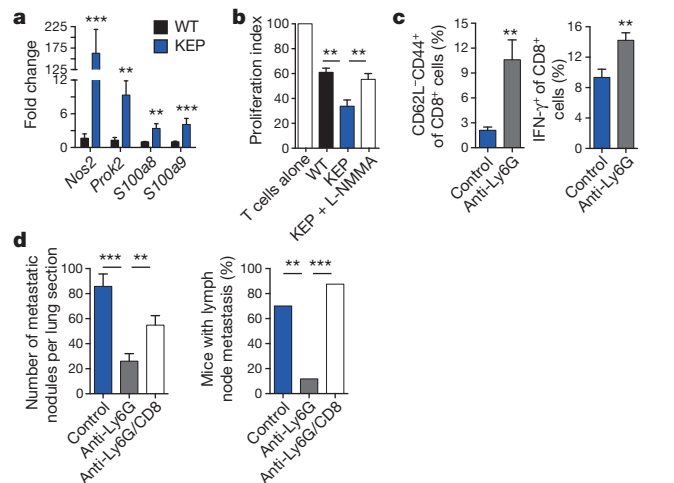


Figure 2 | Neutrophils suppress CD8⁺ T cell activation to facilitate metastasis. **a**, Gene expression in circulating neutrophils ($n = 5$ WT, 10 KEP mice). **b**, Circulating neutrophils from either WT ($n = 7$) or tumour-bearing KEP mice ($n = 8$) were incubated with CFSE-labelled splenic CD8⁺ T cells from WT mice and CD3/CD28 stimulation beads. The iNOS inhibitor L-NMMA was added where indicated ($n = 8$). After 48 h , CD8⁺ T cell proliferation was measured. **c**, CD8⁺ T cell activation status in lungs of transplanted tumour-bearing control and neutrophil-depleted mice ($n = 6$ per group). **d**, Quantification of lung metastases and incidence of lymph node metastasis following neutrophil and CD8⁺ T cell depletion ($n = 11$ control, 16 anti-Ly6G, 8 anti-Ly6G/CD8; Kruskal–Wallis test followed by post-hoc Dunn’s test and Fisher’s exact test). All data are mean \pm s.e.m. * $P < 0.05$, ** $P < 0.01$, *** $P < 0.001$.

In inflammatory diseases such as psoriasis, lymphocyte-derived IL-17 regulates neutrophil expansion via systemic induction of G-CSF^{21,22,24}. We hypothesized that the same inflammatory cascade is important in breast cancer metastasis. Indeed, serum levels of IL-17A and G-CSF were higher in tumour-bearing KEP mice than in WT mice (Fig. 3a). Neutralization of IL-17A in tumour-bearing KEP mice decreased G-CSF serum levels, while G-CSF blockade did not affect IL-17A levels (Fig. 3a), indicating that IL-17 is upstream of G-CSF. Inhibition of either cytokine reduced circulating neutrophils, lowered cKIT⁺ neutrophil proportions (Fig. 3b) and reversed neutrophil phenotype (Fig. 3c). Injection of recombinant G-CSF to anti-IL-17-treated tumour-bearing KEP mice overcame the effects of anti-IL-17 treatment (Extended Data Fig. 5c–e). Additionally, treatment of WT mice with recombinant G-CSF resulted in neutrophil expansion, increased presence of cKIT⁺ neutrophil proportions and changed neutrophil phenotype (Extended Data Fig. 5c–e). These data demonstrate a requirement for the IL-17/G-CSF signalling cascade in both neutrophil expansion and phenotype.

Next, we determined the source of IL-17. As T cells are known to produce IL-17 (refs 20, 21, 23), splenic CD3⁺ T cells were analysed using a T cell-specific gene expression array. This analysis validated upregulation of IL-17-related cytokines in T cells from tumour-bearing KEP mice (Extended Data Fig. 5f). We then asked whether lymphocytes are the only source of IL-17 and whether they drive metastasis. KEP mice were crossed with *Rag1*^{−/−} mice, which lack T and B cells. Tumour initiation, proliferation and histology were the same between KEP;*Rag1*^{+/−} and KEP;*Rag1*^{−/−} mice (Extended Data Fig. 6a and data not shown). However, KEP;*Rag1*^{−/−} mice exhibited lower levels of IL-17A and G-CSF in serum (Fig. 3d), decreased neutrophil counts (Fig. 3e) and altered neutrophil phenotype (Fig. 3f). Transforming growth factor β 1 (TGF- β 1) levels were unchanged between KEP;*Rag1*^{+/−} and KEP;*Rag1*^{−/−} mice (Extended Data Fig. 6b), suggesting that, unlike other models²⁵, TGF- β plays a lesser role in modulating neutrophil phenotype than IL-17-induced G-CSF. Importantly, KEP;*Rag1*^{−/−} mice displayed less pulmonary and lymph node metastases (Fig. 3g). The metastasis phenotype in KEP;*Rag1*^{−/−} mice was validated in the metastasis model

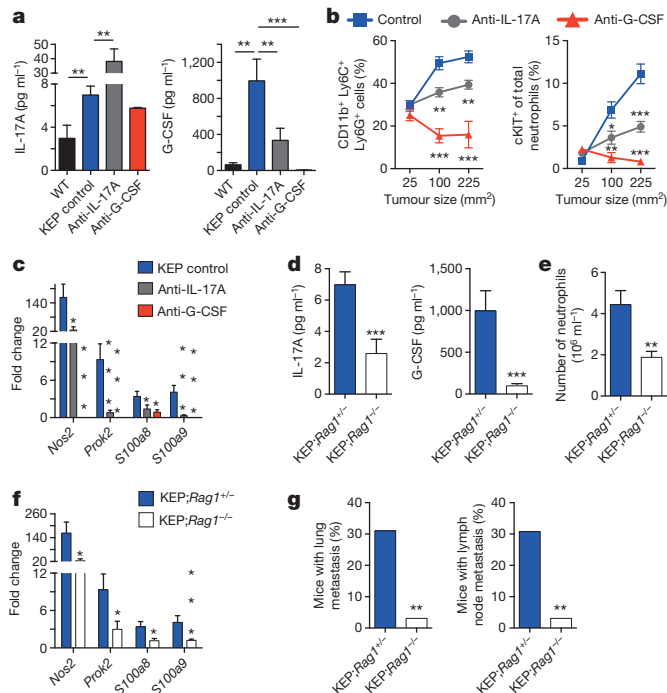


Figure 3 | Lymphocyte-derived IL-17 is required for G-CSF-induced neutrophil expansion and phenotype. **a**, Cytokine levels in serum of WT ($n = 5$), tumour-bearing KEP mice ($n = 9$) and anti-IL-17- ($n = 7$) or anti-G-CSF-treated KEP mice ($n = 6$). **b**, Proportions of circulating neutrophils and cKIT-expressing neutrophils in KEP mice during primary tumour growth ($n = 9$ control, 8 anti-IL-17, 6 anti-G-CSF). **c**, Gene expression in circulating neutrophils from tumour-bearing KEP control mice ($n = 9$), anti-IL-17- ($n = 6$) or anti-G-CSF-treated KEP mice ($n = 6$). **d**, Cytokine levels in serum of tumour-bearing KEP;*Rag1*^{+/−} ($n = 9$) and KEP;*Rag1*^{−/−} mice ($n = 7$). **e**, Absolute blood neutrophil counts in tumour-bearing KEP;*Rag1*^{+/−} mice ($n = 8$) or KEP;*Rag1*^{−/−} mice ($n = 5$). **f**, Gene expression in circulating neutrophils from KEP;*Rag1*^{+/−} ($n = 10$) and KEP;*Rag1*^{−/−} mice ($n = 8$). **g**, Percentage of tumour-bearing mice with lung or lymph node metastasis ($n = 50$ KEP;*Rag1*^{+/−}, 32 KEP;*Rag1*^{−/−} mice). All data are mean + s.e.m. * $P < 0.05$, ** $P < 0.01$, *** $P < 0.001$ as determined by Mann–Whitney *U*-test or Fisher's exact test.

where *Rag1*^{−/−} mice were recipients of transplanted KEP tumour fragments, resulting in reduced pulmonary metastasis (Extended Data Fig. 6c). Thus, IL-17-producing lymphocytes drive neutrophil accumulation, phenotype and metastasis.

Direct *ex vivo* intracellular cytokine staining was performed to determine which T lymphocyte subset produces IL-17. Both CD4⁺ T cells and $\gamma\delta$ T cells expressed IL-17A (Fig. 4a), and both IL-17-producing subpopulations were increased in various organs of tumour-bearing KEP mice compared with WT mice (Fig. 4b and Extended Data Fig. 7a). In primary tumours, the abundance of $\gamma\delta$ and CD4⁺ T cells was too low (<0.2% and <2% of all live cells, respectively) to assess IL-17 expression reliably. $\gamma\delta$ T cells exhibited higher IL-17A levels than CD4⁺ T cells (Fig. 4a and Extended Data Fig. 7b). Both cell populations were depleted to determine their functional importance. CD4⁺ T cell depletion lowered cKIT⁺ neutrophils, but failed to influence total neutrophil expansion, IL-17A or G-CSF levels (Extended Data Fig. 7c–e). Conversely, depletion of $\gamma\delta$ T cells decreased IL-17A and G-CSF serum levels (Fig. 4c), reduced circulating neutrophils, lowered cKIT⁺ neutrophil proportions (Fig. 4d and Extended Data Fig. 7c) and reversed neutrophil phenotype (Fig. 4e). These data indicate that IL-17-producing $\gamma\delta$ T cells promote neutrophil expansion and phenotypic alterations. IL-17-producing $\gamma\delta$ T cells in tumour-bearing KEP mice were CD27[−], mostly V γ 4⁺, and a proportion expressed CCR6, IL-1R1 and ROR- γ t (Extended Data Fig. 8a, b) similar to other inflammatory diseases²¹.

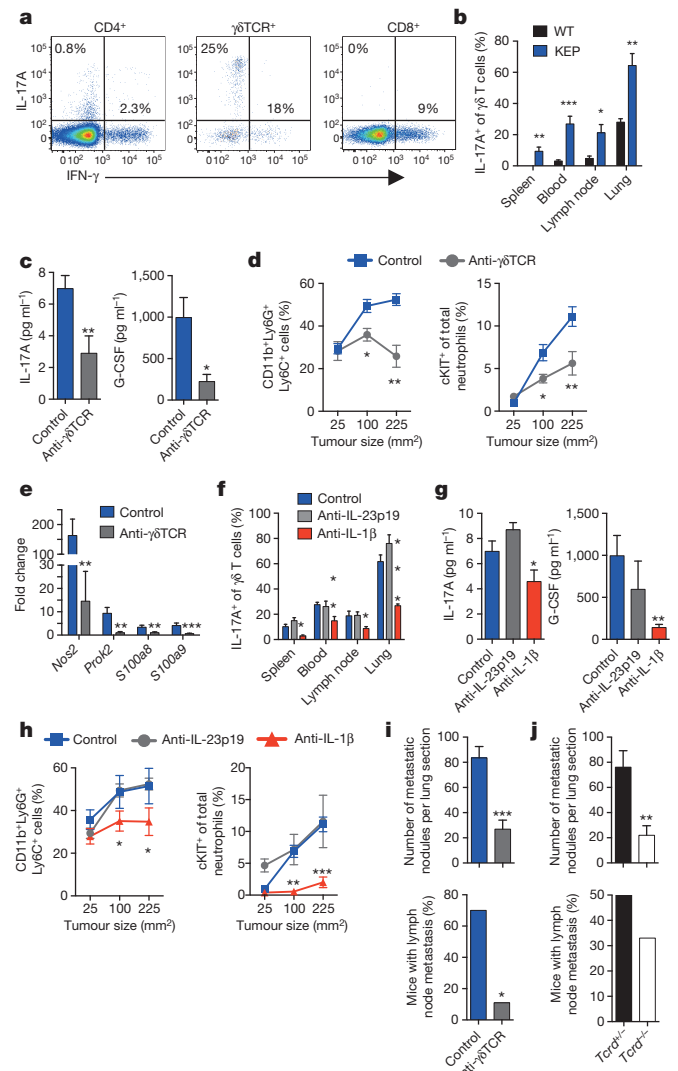


Figure 4 | IL-1 β -activated, IL-17-producing $\gamma\delta$ T cells regulate neutrophil expansion, neutrophil phenotype and metastasis. **a**, Intracellular staining within circulating T cells of tumour-bearing KEP mice. **b**, Proportion of IL-17A-producing $\gamma\delta$ T cells (WT, $n = 5$; KEP, $n = 6$). **c**, Cytokine levels in serum of control ($n = 10$) and anti- $\gamma\delta$ TCR-treated ($n = 7$) KEP mice. **d**, Proportions of circulating neutrophils and cKIT-expressing neutrophils in KEP mice during primary tumour growth ($n = 8$ per group). **e**, Gene expression in circulating neutrophils from tumour-bearing KEP control mice ($n = 10$) and anti- $\gamma\delta$ TCR-treated KEP mice ($n = 6$). **f**, Proportion of IL-17A-producing $\gamma\delta$ T cells in tumour-bearing mice ($n = 6$ KEP control, 5 anti-IL-23p19, 5 anti-IL-1 β). **g**, Cytokine levels in serum ($n = 9$ KEP control, 5 anti-IL-23p19, 6 anti-IL-1 β). **h**, Proportions of circulating neutrophils and cKIT-expressing neutrophils in KEP mice during primary tumour growth ($n = 9$ control, 5 anti-IL-23p19, 5 anti-IL-1 β). **i**, **j**, Quantification of lung metastases and incidence of lymph node metastasis in the metastasis model ($n = 10$ control, 9 anti- $\gamma\delta$ TCR-treated mice; $n = 9$ per group *Tcrd*^{+/−} and *Tcrd*^{−/−} mice). All data are mean + s.e.m. * $P < 0.05$, ** $P < 0.01$, *** $P < 0.001$ as determined by Mann–Whitney *U*-test or Fisher's exact test.

We then asked how KEP mammary tumours activate IL-17-producing $\gamma\delta$ T cells. On the basis of literature^{20–23} and cytokine analysis (Extended Data Fig. 5a, b), we focused on IL-23 and IL-1 β . IL-17A expression by $\gamma\delta$ T cells, G-CSF serum levels and neutrophil expansion was decreased by neutralization of IL-1 β , but unaffected by inhibition of IL-23 (Fig. 4f–h). Macrophages were the most abundant IL-1 β -expressing cell type in KEP tumours (Extended Data Fig. 8c, d). These data provide a mechanistic link between mammary tumours and $\gamma\delta$ T cells.

Depletion of $\gamma\delta$ T cells in the early phase of the metastasis model did not affect tumour histopathology, microvessel density or primary tumour

growth (Extended Data Fig. 8e and data not shown). Importantly, however, pulmonary and lymph node metastases were significantly decreased in $\gamma\delta$ T cell-depleted mice (Fig. 4i). These data were validated with *Tcrd*^{-/-} mice, which lack $\gamma\delta$ T cells. KEP tumour fragments were orthotopically transplanted into *Tcrd*^{+/-} and *Tcrd*^{-/-} mice and resected after outgrowth. Genetic elimination of $\gamma\delta$ T cells also resulted in a significant reduction in pulmonary metastasis (Fig. 4j) without affecting primary tumour growth (Extended Data Fig. 8f). These data confirm a pro-metastatic role for $\gamma\delta$ T cells.

In summary, we show that mammary tumour-induced, IL-17-producing $\gamma\delta$ T cells drive systemic expansion and polarization of neutrophils towards a CD8⁺ T cell-suppressive phenotype and subsequent metastasis formation in distant organs (Extended Data Fig. 9). The importance of neutrophils during the early steps of the metastatic cascade and the upregulation of *Prok2*, *S100a8* and *S100a9* in neutrophils suggest that neutrophils may help to establish the pre-metastatic niche^{6,10,14}; however, the role of these neutrophil-derived factors and others remains to be established in the KEP model. In patients with breast cancer, independent clinical studies consistently point towards a pro-metastatic role for neutrophils, $\gamma\delta$ T cells and IL-17 (refs 3, 4, 26–29). Here, we establish a mechanistic connection between these independent clinical observations. In infection and inflammatory disorders, the $\gamma\delta$ T cell/IL-17/neutrophil axis drives disease pathogenesis^{21,23,30}. We now demonstrate that this targetable pathway also perpetuates breast cancer metastasis.

Online Content Methods, along with any additional Extended Data display items and Source Data, are available in the online version of the paper; references unique to these sections appear only in the online paper.

Received 11 April 2014; accepted 4 February 2015.

Published online 30 March; corrected online 17 June 2015 (see full-text HTML version for details).

- Quail, D. F. & Joyce, J. A. Microenvironmental regulation of tumor progression and metastasis. *Nature Med.* **19**, 1423–1437 (2013).
- McAllister, S. S. & Weinberg, R. A. The tumour-induced systemic environment as a critical regulator of cancer progression and metastasis. *Nature Cell Biol.* **16**, 717–727 (2014).
- Noh, H., Eomm, M. & Han, A. Usefulness of pretreatment neutrophil to lymphocyte ratio in predicting disease-specific survival in breast cancer patients. *J. Breast Cancer* **16**, 55–59 (2013).
- Azab, B. *et al.* Usefulness of the neutrophil-to-lymphocyte ratio in predicting short- and long-term mortality in breast cancer patients. *Ann. Surg. Oncol.* **19**, 217–224 (2012).
- Granot, Z. *et al.* Tumor entrained neutrophils inhibit seeding in the premetastatic lung. *Cancer Cell* **20**, 300–314 (2011).
- Kowanetz, M. *et al.* Granulocyte-colony stimulating factor promotes lung metastasis through mobilization of Ly6G+Ly6C+ granulocytes. *Proc. Natl Acad. Sci. USA* **107**, 21248–21255 (2010).
- Bald, T. *et al.* Ultraviolet-radiation-induced inflammation promotes angiogenesis and metastasis in melanoma. *Nature* **507**, 109–113 (2014).
- Derkse, P. W. *et al.* Somatic inactivation of E-cadherin and p53 in mice leads to metastatic lobular mammary carcinoma through induction of anoikis resistance and angiogenesis. *Cancer Cell* **10**, 437–449 (2006).
- Doornebal, C. W. *et al.* A preclinical mouse model of invasive lobular breast cancer metastasis. *Cancer Res.* **73**, 353–363 (2013).
- Kaplan, R. N. *et al.* VEGFR1-positive haematopoietic bone marrow progenitors initiate the pre-metastatic niche. *Nature* **438**, 820–827 (2005).
- Erler, J. T. *et al.* Hypoxia-induced lysyl oxidase is a critical mediator of bone marrow cell recruitment to form the premetastatic niche. *Cancer Cell* **15**, 35–44 (2009).
- Kuonen, F. *et al.* Inhibition of the Kit ligand/c-Kit axis attenuates metastasis in a mouse model mimicking local breast cancer relapse after radiotherapy. *Clin. Cancer Res.* **18**, 4365–4374 (2012).
- Hiratsuka, S. *et al.* MMP9 induction by vascular endothelial growth factor receptor-1 is involved in lung-specific metastasis. *Cancer Cell* **2**, 289–300 (2002).
- Hiratsuka, S., Watanabe, A., Aburatani, H. & Maru, Y. Tumour-mediated upregulation of chemoattractants and recruitment of myeloid cells predetermines lung metastasis. *Nature Cell Biol.* **8**, 1369–1375 (2006).
- Pillay, J., Tak, T., Kamp, V. M. & Koenderman, L. Immune suppression by neutrophils and granulocytic myeloid-derived suppressor cells: similarities and differences. *Cell. Mol. Life Sci.* **70**, 3813–3827 (2013).
- Mazzoni, A. *et al.* Myeloid suppressor lines inhibit T cell responses by an NO-dependent mechanism. *J. Immunol.* **168**, 689–695 (2002).
- Young, M. R., Wright, M. A., Matthews, J. P., Malik, I. & Prechel, M. Suppression of T cell proliferation by tumor-induced granulocyte-macrophage progenitor cells producing transforming growth factor- β and nitric oxide. *J. Immunol.* **156**, 1916–1922 (1996).
- Lejeune, P. *et al.* Nitric oxide involvement in tumor-induced immunosuppression. *J. Immunol.* **152**, 5077–5083 (1994).
- Hamilton, J. A. & Achuthan, A. Colony stimulating factors and myeloid cell biology in health and disease. *Trends Immunol.* **34**, 81–89 (2013).
- Chung, Y. *et al.* Critical regulation of early Th17 cell differentiation by interleukin-1 signaling. *Immunity* **30**, 576–587 (2009).
- Cai, Y. *et al.* Pivotal role of dermal IL-17-producing $\gamma\delta$ T cells in skin inflammation. *Immunity* **35**, 596–610 (2011).
- Mei, J. *et al.* Cxcr2 and Cxcl5 regulate the IL-17/G-CSF axis and neutrophil homeostasis in mice. *J. Clin. Invest.* **122**, 974–986 (2012).
- Sutton, C. E. *et al.* Interleukin-1 and IL-23 induce innate IL-17 production from gamma delta T cells, amplifying Th17 responses and autoimmunity. *Immunity* **31**, 331–341 (2009).
- Schwarzenberger, P. *et al.* Requirement of endogenous stem cell factor and granulocyte-colony-stimulating factor for IL-17-mediated granulopoiesis. *J. Immunol.* **164**, 4783–4789 (2000).
- Fridlender, Z. G. *et al.* Polarization of tumor-associated neutrophil phenotype by TGF- β : “N1” versus “N2” TAN. *Cancer Cell* **16**, 183–194 (2009).
- Han, Y. *et al.* Prognostic value of chemotherapy-induced neutropenia in early-stage breast cancer. *Breast Cancer Res. Treat.* **131**, 483–490 (2012).
- Ma, C. *et al.* Tumor-infiltrating $\gamma\delta$ T lymphocytes predict clinical outcome in human breast cancer. *J. Immunol.* **189**, 5029–5036 (2012).
- Novitskiy, S. V. *et al.* TGF- β receptor II loss promotes mammary carcinoma progression by Th17 dependent mechanisms. *Cancer Discov.* **1**, 430–441 (2011).
- Chen, W. C. *et al.* Interleukin-17-producing cell infiltration in the breast cancer tumour microenvironment is a poor prognostic factor. *Histopathology* **63**, 225–233 (2013).
- Sutherland, T. E. *et al.* Chitinase-like proteins promote IL-17-mediated neutrophilia in a tradeoff between nematode killing and host damage. *Nature Immunol.* **15**, 1116–1125 (2014).

Acknowledgements This work was supported by a Marie Curie Intra-European Fellowship to S.B.C. (BMDCMET 275610); a European Research Council Consolidator award (INFLAMET 615300) to K.E.d.V.; grants from the Dutch Cancer Society to K.E.d.V. and J.J. (2011-5004); Worldwide Cancer Research (AICR 11-0677) to K.E.d.V.; the Netherlands Organization for Scientific Research NWO VIDI (917.96.307) to K.E.d.V.; and a Dutch Cancer Society/Bas Mulder Award to L.J.A.C.H. (UL2011-5051). We thank J. Borst, T. Schumacher and J. Coquet for discussions. We thank the core facilities at the Netherlands Cancer Institute. We thank L. Coussens for *Rag1*^{-/-} mice and A. Hayday for *Tcrd*^{-/-} mice. We thank C. Ries and K. Wartha for technical assistance.

Author Contributions S.B.C., J.J. and K.E.d.V. conceived the ideas and designed the experiments. S.B.C., C.W.D., K.K., J.W., C.H., K.V., N.J.V., M.C., L.J.A.C.H. and K.E.d.V. performed the experiments. S.B.C., C.W.D., K.K., J.W., C.H., K.V., N.J.V., L.J.A.C.H. and K.E.d.V. analysed the data. S.B.C., K.K. and K.E.d.V. wrote the paper.

Author Information RNA-seq data have been deposited in the Gene Expression Omnibus (GEO) under accession number GSE55633. Reprints and permissions information is available at www.nature.com/reprints. The authors declare no competing financial interests. Readers are welcome to comment on the online version of the paper. Correspondence and requests for materials should be addressed to K.E.d.V. (k.d.visser@nki.nl).

METHODS

Mice. The generation and characterization of *K14cre;Cdh1^{fl/fl};Trp53^{fl/fl}* (KEP) mice—a conditional model of invasive lobular breast cancer—has been described⁸. KEP mice were backcrossed onto the FVB/N background. KEP mice were crossed with *Rag1^{-/-}* mice (FVB/N; a gift from L. Coussens)³¹ to generate KEP;*Rag1^{+/-}* and KEP;*Rag1^{-/-}* mice³². The onset of mammary tumour formation was monitored twice weekly by palpation and calliper measurements starting at 4 months of age. *Tcrd^{-/-}* mice on the FVB/N background were a gift from A. Hayday³³. The spontaneous metastasis model has also been described⁹. Briefly, this model is based on the orthotopic transplantation of KEP tumour pieces into 10- to 12-week-old female recipient FVB/N mice, *Rag1^{-/-}* mice, *Tcrd^{+/-}* or *Tcrd^{-/-}* mice. These tumour pieces are allowed to grow out, then surgically removed at 100 mm², after which 100% of mice develop overt metastatic disease.

To deplete immune cells or neutralize cytokines, mice were injected intraperitoneally with an initial 400 µg followed by 100 µg thrice weekly for anti-Ly6G (clone 1A8; BioXCell), 200 µg twice weekly for anti-CD8 (clone 2.43; BioXCell) or 100 µg twice weekly for anti-γδTCR (clone GL3; purified by the NK1 protein facility). For cytokine neutralization experiments, KEP mice were injected intraperitoneally with 50 µg twice weekly for anti-IL-17A (clone 17F3; BioXCell), 50 µg thrice weekly for anti-G-CSF (clone 67604; R&D Systems), 50 µg twice weekly anti-IL-23p19 (clone G23-8; eBioscience) or 50 µg twice weekly anti-IL-1β (clone B122; BioXCell). Control mice received equal amounts of isotype control antibodies or equal volumes of PBS. Where indicated, WT and KEP mice were injected intraperitoneally with 5 µg rG-CSF (Peprotech) for four consecutive days and were killed on the fifth day. Tumour-bearing KEP mice injected with rG-CSF received anti-IL-17 at the same schedule as above. Antibody injections began when KEP mammary tumours reached 25 mm² until death at 225 mm², or transplanted tumours reached 9 mm² where indicated until surgery at 100 mm². Three independent KEP donor tumours were tested in neutrophil depletion experiments resulting in the same outcome. One of these donor tumours was used throughout the remainder of the study. Blood samples were taken before and during antibody injections for flow cytometry analyses. Animals were randomized before beginning the treatment schedule. Mice were kept in individually ventilated and open cages, and food and water were provided *ad libitum*. Animal experiments were approved by the Animal Ethics Committee of the Netherlands Cancer Institute and performed in accordance with institutional, national and European guidelines for Animal Care and Use.

Immunohistochemistry. Formalin-fixed tissues were processed by routine procedures. Haematoxylin and eosin staining was performed as described⁹. Citrate antigen retrieval was used for all staining procedures. Neutrophils were detected using either anti-Ly6B (clone 7/4; Cedarlane) or anti-Ly6G (clone 1A8; BD Biosciences), when primary tumours reached 100 mm². Quantitative analysis of neutrophil abundance was performed by counting cells in five high-power (×40) fields of view (FOV) per tissue. Metastases were detected using anti-cytokeratin 8 (clone Troma 1; Developmental Studies Hybridoma Bank, University of Iowa). In the metastasis model, the total number of cytokeratin 8⁺ nodules was scored in one lung section of each animal. The size of each nodule was measured using ImageJ, then represented as arbitrary units. Lymph node metastases were scored as positive or negative on the basis of the presence of cytokeratin 8⁺ metastases. Mice that developed overt metastatic disease (that is, respiratory distress or 225 mm² axillary lymph node metastasis) were included in the analysis; mice that were killed as a result of local recurrence were excluded. Vimentin, E-cadherin and CD34 staining was performed as previously described⁹ and scored independently by two blinded researchers. Microvessel density was scored by averaging the total number of blood vessels from five fields of view for each tumour section. For metastasis quantification in *K14cre;Cdh1^{fl/fl};Trp53^{fl/fl};Rag1^{+/-}* and *K14cre;Cdh1^{fl/fl};Trp53^{fl/fl};Rag1^{-/-}* mice, single lung or lymph node sections were scored as positive or negative on the basis of the presence of cytokeratin 8⁺ metastases. Stained slides were digitally processed using the Aperio ScanScope and captured using ImageScope software version 11.0.2. Brightness and contrast for representative images were adjusted equally among groups.

Flow cytometry and intracellular staining. Tissues were collected in ice-cold PBS. Blood samples were collected in tubes containing heparin. Tumours and lungs were mechanically chopped using a McIlwain tissue chopper (Mickle Laboratory Engineering). Tumours were digested for 1 h at 37 °C in 3 mg ml⁻¹ collagenase type A (Roche) and 25 µg ml⁻¹ DNase (Sigma) in serum-free DMEM medium. Lungs were digested for 30 min at 37 °C in 100 µg ml⁻¹ Liberase TM (Roche). Enzyme activity was neutralized by addition of cold DMEM/8% FCS and suspension was dispersed through a 70 µm cell strainer. Spleen, lymph nodes and liver were mashed through a 70 µm cell strainer. All single-cell suspensions were treated with NH₄Cl erythrocyte lysis buffer. Cells were stained with directly conjugated antibodies (listed below) for 30 min at 4 °C in the dark in PBS/1% BSA. 7AAD (1:20; eBioscience) or Fixable Viability Dye eFluor 780 (1:1,000; eBioscience) was added to exclude dead cells. For intracellular staining, single-cell suspensions were stimulated in IMDM

containing 8% FCS, 100 IU ml⁻¹ penicillin, 100 µg ml⁻¹ streptomycin, 0.5% β-mercaptoethanol, 50 ng ml⁻¹ PMA, 1 µM ionomycin and (1:1,000) Golgi-Plug (BD Biosciences) for 3 h at 37 °C. Surface antigens were stained first, followed by fixation and permeabilization using the Cytofix/Cytoperm kit (BD Biosciences), then staining of intracellular proteins. All experiments were performed using a BD LSRII flow cytometer using Diva software. Data analyses used FlowJo Software version 9.7.1. Median fluorescence intensity of IL-17A expression was calculated after gating on IL-17⁺ cells within individual T cell subsets.

All antibodies were purchased from eBioscience, except Ly6G-AlexaFluor 700, CCR6 and Vγ1 from BioLegend, and VEGFR1, CCR2, IL-23R and IL-1R1 from R&D Systems. The following antibodies were used in these experiments.

Myeloid panel: CD45-eFluor 605NC (1:50; clone 30-F11), CD11b-eFluor 650NC (1:400; clone M1/70), Ly6G-AlexaFluor 700 (1:400; clone 1A8), Ly6C-eFluor 450 (1:400; clone HK1.4), F4/80-APC-eFluor 780 (1:200; clone BM8), VEGFR1-APC (1:50; clone 141522), cKIT (1:400; clone 2B8), CCR2-PE (1:50; clone 475301), CXCR4-PerCP-eFluor 710 (1:400; clone 2B11), CD49d-FITC (1:400; clone R1-2) or Gr1-FITC (1:400; clone RB6-8C5), 7AAD.

Lymphoid panel I: CD45-eFluor 605NC (1:50; clone 30-F11), CD11b-eFluor 650NC (1:400; clone M1/70), CD3-PE-Cy7 (1:200; clone 145-2C11), CD4-APC-eFluor 780 (1:200; clone GK1.5), CD8-PerCP-eFluor 710 (1:400; clone 53-6.7), γδTCR-FITC (1:400; clone GL3), CD49b-APC (1:400; clone DX5), IL-17A-PE (1:200; clone eBio17B7), IFNγ-eFluor 450 (1:200; clone XMG1.2), 7AAD.

Lymphoid panel II: CD45-eFluor 605NC (1:50; clone 30-F11), CD11b-APC-eFluor 780 (1:200; clone M1/70), CD3-PE-Cy7 (1:200; clone 145-2C11), CD4-APC-eFluor 780 (1:200; clone GK1.5), CD8-PerCP-eFluor 710 (1:400; clone 53-6.7), γδTCR-PE (1:400; clone GL3), CD49b-APC (1:400; clone DX5), CD62L-AlexaFluor 700 (1:400; clone MEL-14), CD44-FITC (1:400; clone IM7), IFNγ-eFluor 450 (1:200; clone XMG1.2), CD19-APC-eFluor 780 (1:200; clone eBio1D3), Fixable Viability Dye eFluor 780.

γδ T cell phenotyping panel I: CD45-eFluor 605NC (1:50; clone 30-F11), CD11b-APC-eFluor 780 (1:200; clone M1/70), CD3-PerCP-eFluor 710 (1:200; clone 145-2C11), CD4-APC-eFluor 780 (1:200; clone GK1.5), γδTCR-PE (1:400; clone GL3), CD19-APC-eFluor 780 (1:200; clone eBio1D3), CD27-PE-Cy7 (1:200; clone LG.7F9), IL-1R1-FITC (1:25; clone 129304), CCR6-Brilliant Violet 421 (1:200; clone 29-2L17), IL-23R-AlexaFluor 700 (1:25; clone 753317), RORγt-APC (1:100; clone B2D), Fixable Viability Dye eFluor 780.

γδ T cell phenotyping panel II: CD45-eFluor 605NC (1:50; clone 30-F11), CD11b-APC-eFluor 780 (1:200; clone M1/70), CD4-APC-eFluor 780 (1:200; clone GK1.5), γδTCR-PE (1:400; clone GL3), CD19-APC-eFluor 780 (1:200; clone eBio1D3), CD27-PE-Cy7 (1:200; clone LG.7F9), Vγ1-FITC (1:100; clone 2.11), Vγ4-PerCP-eFluor 710 (1:100; clone UC3-10A6), IFNγ-eFluor 450 (1:200; clone XMG1.2), IL-17A-APC (1:200; clone eBio17B7), Fixable Viability Dye eFluor 780.

White blood cell counts. Total white blood cell numbers were measured on a haematology analyser (Becton Dickinson). Neutrophil numbers were then calculated on the basis of the percentage of CD11b⁺Ly6G⁺Ly6C⁺ cells.

Giemsa staining. Blood was collected by tail vein puncture in heparin-coated tubes. Red blood cells were lysed with NH₄Cl lysis buffer. White blood cells were smeared onto glass slides then stained with decreasing concentrations of Wright-Giemsa solution.

RNA-seq. Ly6G⁺ neutrophils were isolated by magnetic column (Miltenyi) from blood of mice. KEP mice with mammary tumours around 225 mm² in size and age-matched WT mice were used. Purity of isolated neutrophils was validated by flow cytometry and only samples greater than 90% purity were used. RNA was isolated using Trizol and then treated with DNase I (Invitrogen). Samples were put over a Qiagen RNeasy column for cleanup. RNA quality was confirmed with a 2100 Bioanalyzer from Agilent. RNA-Seq libraries were prepared using the reagents provided in the Illumina TruSeq RNA Sample Preparation Kit, following the manufacturer's protocol. Libraries were PCR amplified for 12 cycles and sequenced on an Illumina HiSeq 2000 System with TruSeq reagent kits and software, generating paired-end 51 base-pair reads. Sequence reads were aligned to the mouse reference genome (National Center for Biotechnology Information build 37) using TopHat. HTSeq-count was then used to generate a list of the total number of uniquely mapped reads for each gene and sample. Sequence reads were normalized to 10 million reads per sample and log₂ transformed with the formula, log₂((expression gene $X \div$ library size)10⁶ + 1), where the library size was the sum of all expression values per sample. To determine which genes were differentially expressed between samples, the R package Limma was used. Absolute gene expressions were used as input and genes with no expression in any sample were removed from the data set. Voom was used to transform the count data to log₂ counts per million and estimation of the variance. The *P* value was set to a cut-off of 0.05, resulting in 100 significant, differentially expressed genes. Unsupervised clustering was performed on these 100 genes and the data were transformed into a heat-map.

Real-time PCR. Neutrophil RNA was extracted as above then converted to complementary DNA (cDNA) with an AMV reverse transcriptase using Oligo(dT) primers (Invitrogen). cDNA (20 ng per well) was analysed by SYBR green real-time PCR with 500 nM primers using a LightCycler 480 thermocycler (Roche). β -actin was used as a reference gene. The following primer sequences were used for each gene: *Nos2* forward 5'-GTTCTCAGCCCAACAATACAAGA-3', reverse 5'-GTGGACGGGTCGATGTCAC-3'; *Prok2* forward 5'-CTTCGCCCTTCTTCTTTCCT-3', reverse 5'-GCATGTGCTGTGCTGTGTCAGT-3'; *S100a8* forward 5'-TGAGCAACCTCATTGATGTCTACC-3', reverse 5'-ATGCCACACCCACTTTTATCACC-3'; *S100a9* forward 5'-GAAGAAAGAGAAGAGAAATGAAGCC-3'; reverse 5'-CTTTGCCATCAGCATCATACACTCC-3'; *Il1b* forward 5'-CAACCACAAGTGATATTCTCCATG-3', reverse 5'-GATCCACACTCTCCAGCTGCA-3'; *Actb* forward 5'-CCTCATGAAGATCCTGACCGA-3', reverse 5'-TTTGATGTCACGCACGATTTC-3'. Fold change was calculated using the formula $2^{-(\Delta C_t - \bar{X}[\Delta C_t; WT])}$.

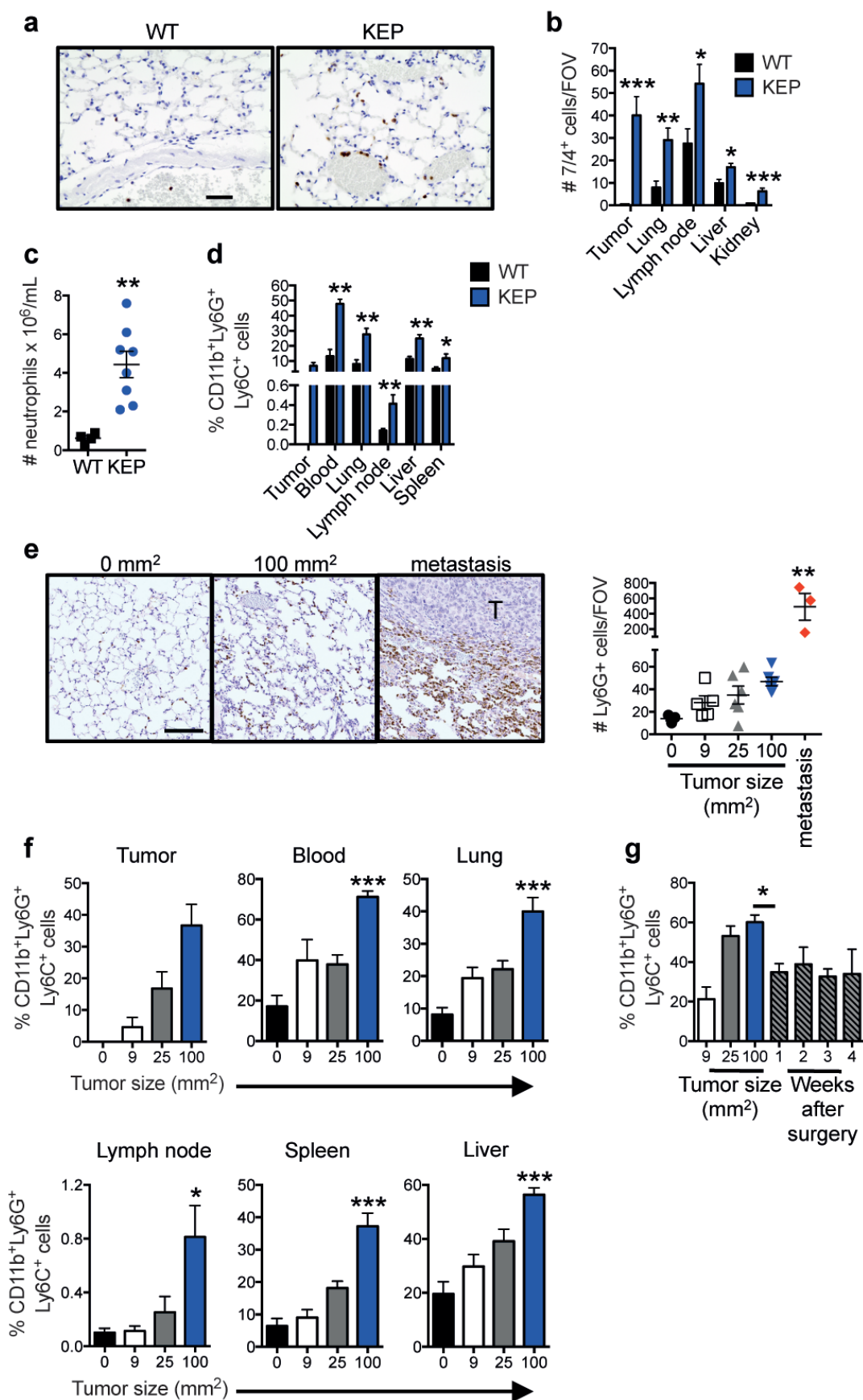
T cell proliferation assay. Blood neutrophils from WT mice and splenic CD8⁺ T cells from WT mice were isolated by magnetic column (Miltenyi). Blood neutrophils from KEP mice with mammary tumours around 225 mm² in size were also used. CD8⁺ T cells were labelled with Cell Trace CFSE following the manufacturer's instructions (Invitrogen). Equal numbers of cells (2×10^5) were co-cultured in a 96-well flat bottom plate. CD3/CD28 Dynabeads (Invitrogen) were added according to manufacturer's instruction, and the iNOS inhibitor, L-NMMA (Sigma), was added at 0.5 mM where indicated. After 48 h, T cell proliferation was evaluated on a BD LSRII flow cytometer using Diva software using the following antibodies: CD8a-PE (1:600; clone 53-6.7), CD11b-APC (1:400; clone M1/70), Ly6C-eFluor 450 (1:400; clone HK1.4), Ly6G-AlexaFluor 700 (1:400; clone 1A8) and 7AAD viability marker. Data analyses used FlowJo Software version 9.7.1. Proliferation index was calculated using the formula (percentage of proliferated, co-cultured CD8⁺ T cells)/(percentage of proliferated CD8⁺ T cells without co-culture) \times 100, for each replicate experiment.

Cytokine analysis. Multiplex quantification of cytokines and chemokines in mammary glands and tumours was performed using the premixed 24-plex Bio-Plex Pro Mouse Cytokine Assay (Bio-Rad) according to the manufacturer's recommendations. Protein lysates were prepared as previously described³⁴. Unsupervised clustering was performed on normalized, median-centred data then converted to a heat-map using Genesis software. For IL-17A and G-CSF serum levels, BD Cytometric Bead Arrays were used as directed and analysed on a Cyan flow cytometer with Summit software (Beckman Coulter). Data analyses used FlowJo Software version 9.7.1. For TGF- β 1, a DuoSet ELISA kit was purchased from R&D Systems and performed according to the manufacturer's instructions.

PCR array. The spleens of three WT or KEP mammary tumour-bearing mice were pooled and labelled with anti-CD3 antibodies. CD3⁺ T cells were sorted using a BD FACSaria II. RNA was isolated with Trizol as above. Gene expression differences were analysed using a mouse T cell-specific PCR array from Qiagen according to their instructions and software. Genes exhibiting a threefold change were considered biologically relevant.

Statistical analysis. Data analyses used GraphPad Prism version 7. Applied analyses are indicated in corresponding legends. No statistical methods were used to predetermine sample sizes. Sample sizes were based on previous experience with the models^{9,32,34}. Differences with $P < 0.05$ were considered statistically significant.

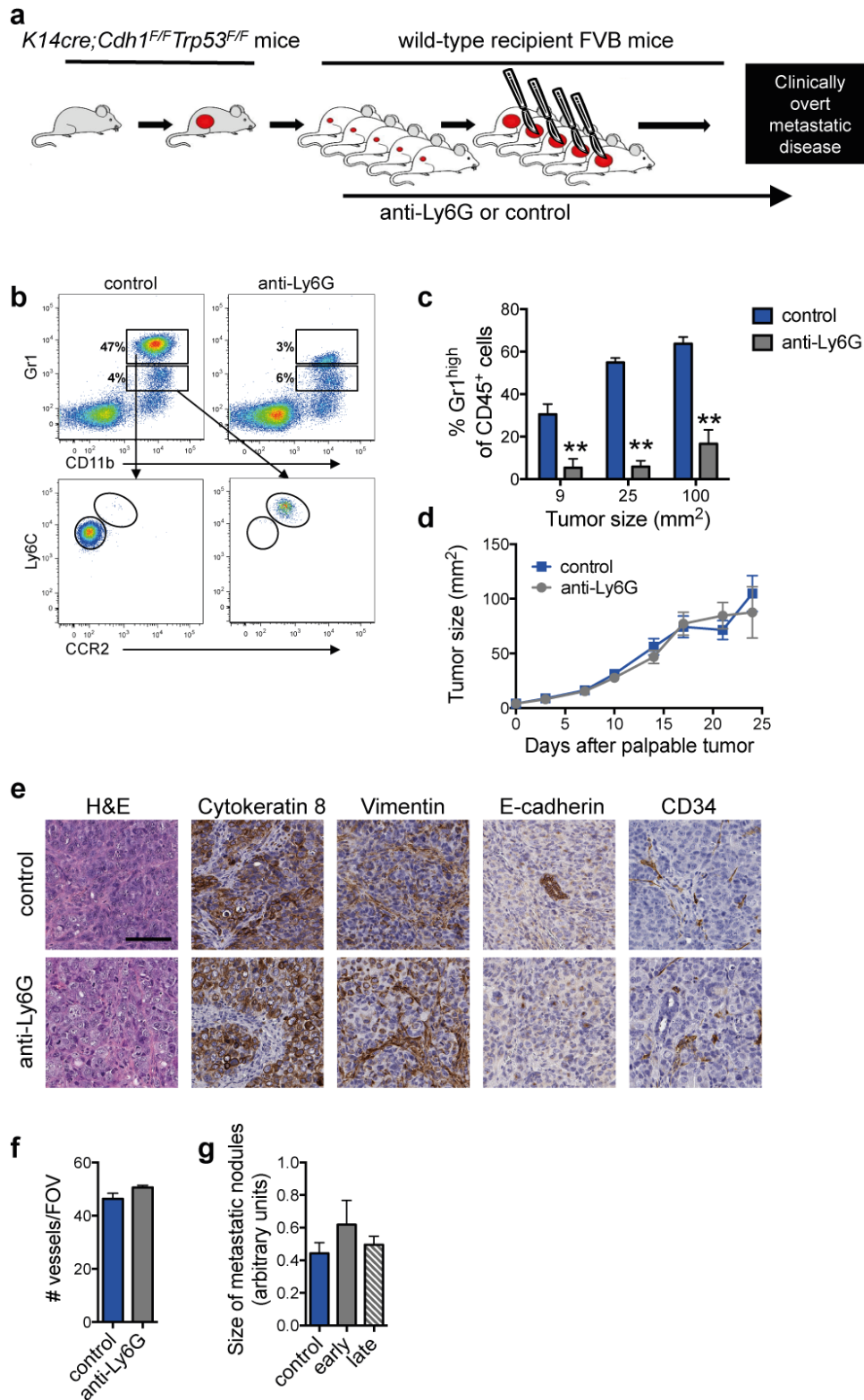
31. de Visser, K. E., Korets, L. V. & Coussens, L. M. De novo carcinogenesis promoted by chronic inflammation is B lymphocyte dependent. *Cancer Cell* **7**, 411–423 (2005).
32. Ciampicotti, M., Hau, C. S., Doornebal, C. W., Jonkers, J. & de Visser, K. E. Chemotherapy response of spontaneous mammary tumors is independent of the adaptive immune system. *Nature Med.* **18**, 344–346 (2012).
33. Girardi, M. *et al.* Regulation of cutaneous malignancy by $\gamma\delta$ T cells. *Science* **294**, 605–609 (2001).
34. Ciampicotti, M. *et al.* Development of metastatic HER2⁺ breast cancer is independent of the adaptive immune system. *J. Pathol.* **224**, 56–66 (2011).



Extended Data Figure 1 | Systemic neutrophil expansion and accumulation in mammary tumour-bearing KEP mice and the metastasis model.

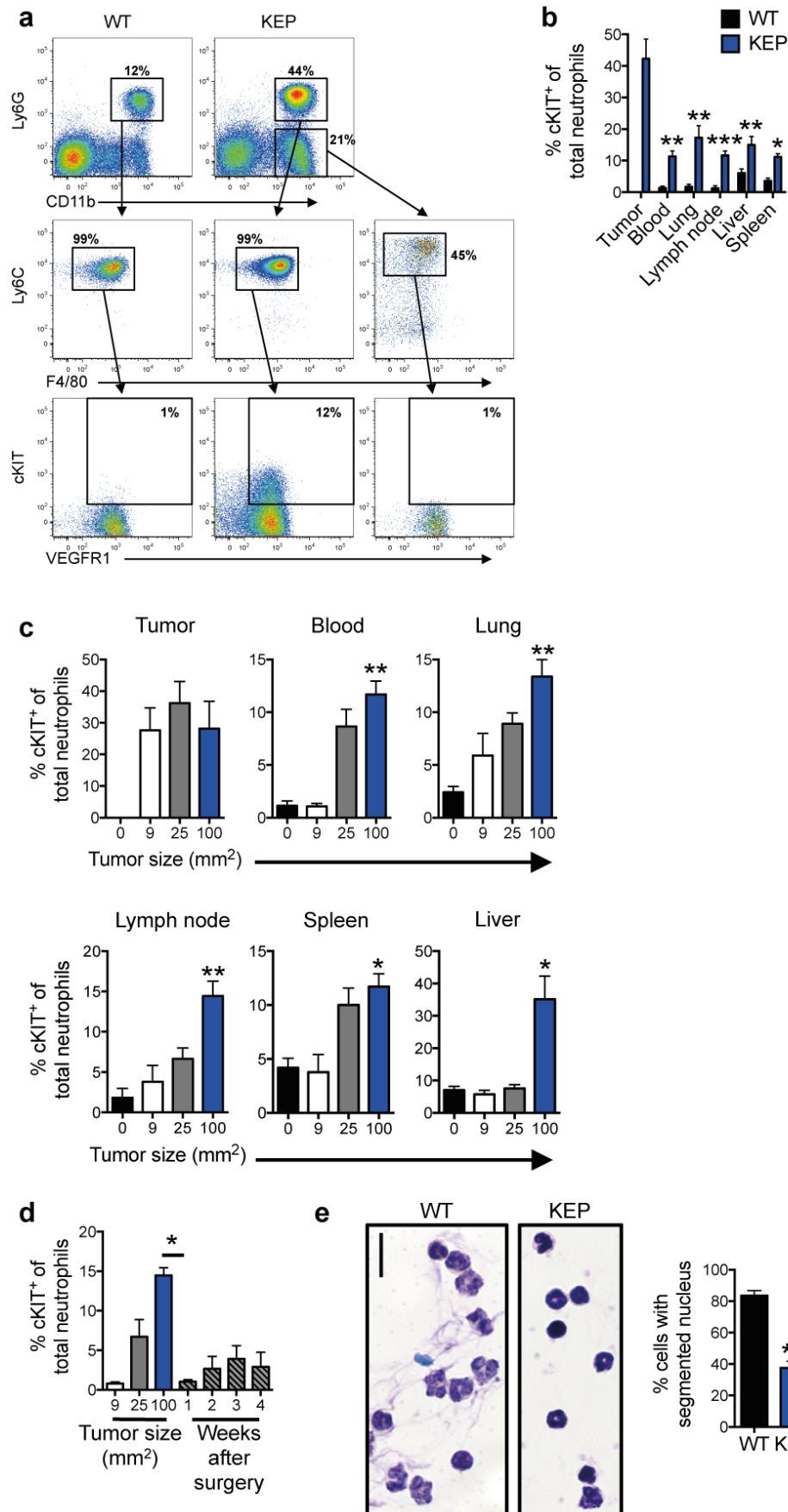
a, Representative images of neutrophils identified by the 7/4 antibody in lung sections in WT or KEP mice. Scale bar, 50 μm . **b**, Quantification of neutrophil accumulation per field of view (FOV) in various organs by immunohistochemistry using the 7/4 antibody ($n = 6$ WT, 9 KEP mice). **c**, Absolute neutrophil counts in blood of WT and tumour-bearing KEP mice ($n = 4$ WT, 8 KEP). **d**, Quantification of neutrophil accumulation in various organs determined by flow cytometry and gated on CD45⁺ cells. Neutrophils were not detectable in WT mammary glands ($n = 5$ WT, 7 KEP mice). **e**, Representative images of Ly6G-stained lung sections and quantification of neutrophil accumulation in the metastasis model. Data were generated from mock-transplanted, non-tumour-bearing mice (0 mm²), or

tumour-transplanted recipient mice killed when tumours reached the tumour size shown or when mice exhibited signs of respiratory distress due to pulmonary metastasis. For quantification in lungs with metastases, neutrophils residing inside metastases were excluded. *T*, pulmonary metastatic lesion. Scale bar, 100 μm ($n = 3, 5, 5, 6, 6$ and 3 mice for 0, 9, 25, 100 mm² and metastasis respectively). **f**, Kinetics of neutrophil accumulation in various organs of the metastasis model by flow cytometry after gating on CD45⁺ cells. Recipient mice transplanted with KEP tumour pieces were killed at the tumour size shown ($n = 6, 5, 6$, and 7 mice for 0, 9, 25, 100 mm² respectively). **g**, Kinetics of neutrophil proportions in blood (gated on CD45⁺ cells), before and after surgical removal of their primary tumour ($n = 5$). All data are mean + s.e.m. * $P < 0.05$, ** $P < 0.01$, *** $P < 0.001$ as determined by Mann–Whitney *U*-test or Kruskal–Wallis test followed by post-hoc Dunn's test.



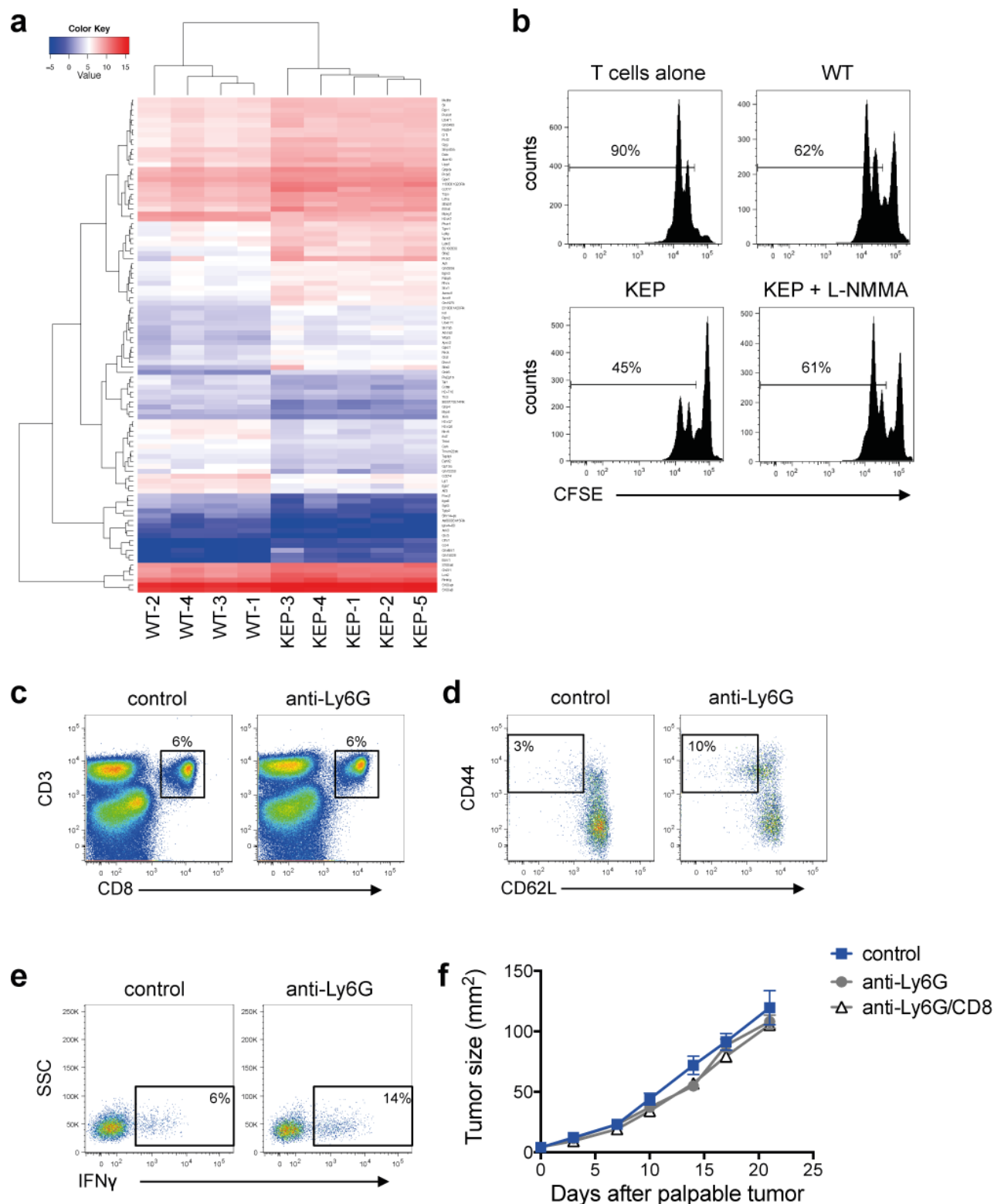
Extended Data Figure 2 | Neutrophil depletion does not affect primary tumour or metastatic nodule growth. **a**, Schematic illustration of the neutrophil depletion experiment in the spontaneous metastasis model. **b**, Representative dot plots of neutrophils gated on CD45⁺ cells in blood of control and anti-Ly6G-treated recipient mice. The Gr1 antibody was used here to avoid false-negative results since the anti-Ly6G depleting antibody may mask the Ly6G epitope. CD11b⁺Gr1^{high} cells were Ly6C⁺CCR2⁻, indicating that these cells were neutrophils. CD11b⁺Gr1^{low} cells that were Ly6C⁺ and CCR2⁺ represented the monocytic fraction. **c**, Quantification of neutrophil depletion in blood of control and anti-Ly6G-treated recipient mice at the

tumour size indicated ($n = 8$ control, 5 anti-Ly6G; $**P < 0.01$ as determined by Mann-Whitney U -test). **d**, Primary tumour growth kinetics of mice treated as indicated ($n = 12$ control, 14 anti-Ly6G). **e**, Representative images of primary tumours in the metastasis model treated as shown and stained with haematoxylin and eosin, cytokeratin 8, vimentin, E-cadherin and CD34. Scale bar, 100 μ m. **f**, Quantification of blood vessels per field of view (FOV) in control and neutrophil-depleted mice by anti-CD34 immunohistochemistry ($n = 10$). **g**, Quantification of pulmonary metastatic nodule size in control and neutrophil-depleted mice ($n = 9$ control, 11 early phase, 14 late phase mice). All data are mean + s.e.m.



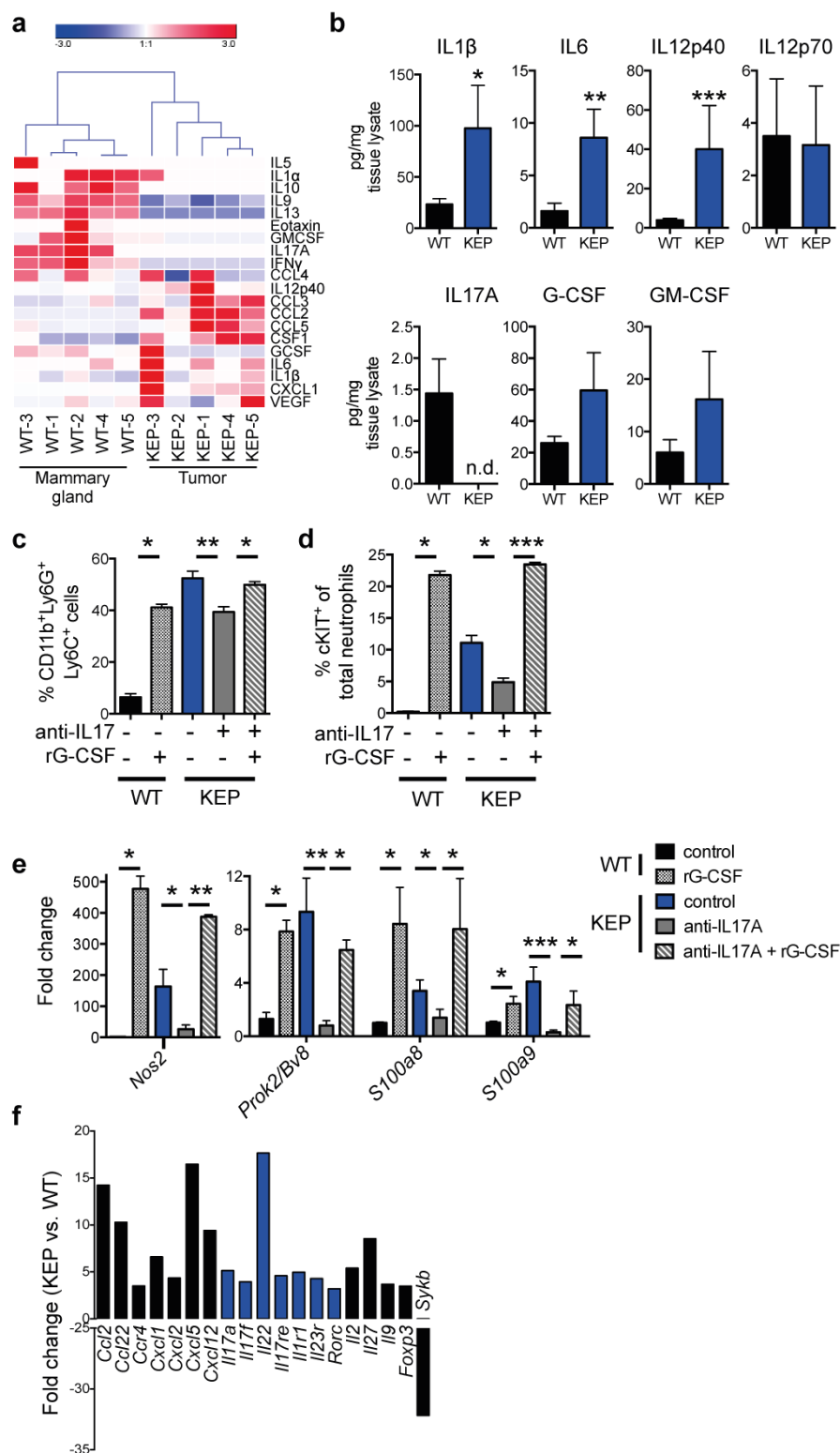
Extended Data Figure 3 | Subpopulations of neutrophils in mammary tumour-bearing mice are immature. **a**, Gating strategy for identification of neutrophils (CD45⁺CD11b⁺Ly6G⁺Ly6C⁺F4/80⁻ cells), cKIT⁺ neutrophils and monocytes (CD45⁺CD11b⁺Ly6G⁻Ly6C⁺F4/80⁻ cells) by flow cytometry. Blood cells from WT and tumour-bearing KEP mice are shown here. **b**, Quantification of cKIT⁺ neutrophil accumulation in various organs determined by flow cytometry after gating on CD45⁺CD11b⁺Ly6G⁺Ly6C⁺F4/80⁻ cells. cKIT⁺ neutrophils were not detectable in WT mammary glands ($n = 5$ WT, 7 KEP; Mann–Whitney U -test). **c**, cKIT⁺ neutrophil proportions in various organs of the metastasis model as determined by flow cytometry after gating on CD45⁺CD11b⁺Ly6G⁺Ly6C⁺F4/80⁻ cells. Mice were killed at the tumour size

shown ($n = 5, 5, 5$, and 8 mice for 0, 9, 25, 100 mm² respectively; Kruskal–Wallis test followed by post-hoc Dunn’s test). **d**, Kinetics of cKIT⁺ neutrophil proportions in blood (gated on CD45⁺CD11b⁺Ly6G⁺Ly6C⁺F4/80⁻ cells), before and after surgical removal of the primary tumour ($n = 5$ per group; Mann–Whitney U -test). **e**, Representative images and quantification of neutrophil nuclear morphology. Ly6G⁺ cells were isolated from blood of WT and tumour-bearing KEP mice then assessed by Giemsa stain. Hyper-segmented cells were considered mature, whereas all other cells were considered immature. Scale bar, 10 μ m. ($n = 6$ WT, 5 KEP mice; Mann–Whitney U -test). All data are mean + s.e.m. * $P < 0.05$, ** $P < 0.01$, *** $P < 0.001$.



Extended Data Figure 4 | Neutrophils influence the function and phenotype of CD8⁺ T cells. **a**, Unsupervised hierarchical clustering of RNA-Seq analysis depicting 100 differentially expressed genes between circulating neutrophils from WT and tumour-bearing KEP mice. *P* value (0.05) was used as cutoff (*n* = 4 WT, 5 KEP mice). See also Extended Data Table 1 for top 50 genes ranked by fold change. **b**, Circulating neutrophils from either WT or tumour-bearing KEP mice were incubated with CFSE-labelled splenic CD8⁺ T cells from WT mice and CD3/CD28 stimulation beads. The iNOS inhibitor, L-NMMA, was added where indicated. After 48 h, CD8⁺ T cell proliferation was measured by flow cytometry. **c**, Dot plots depicting live

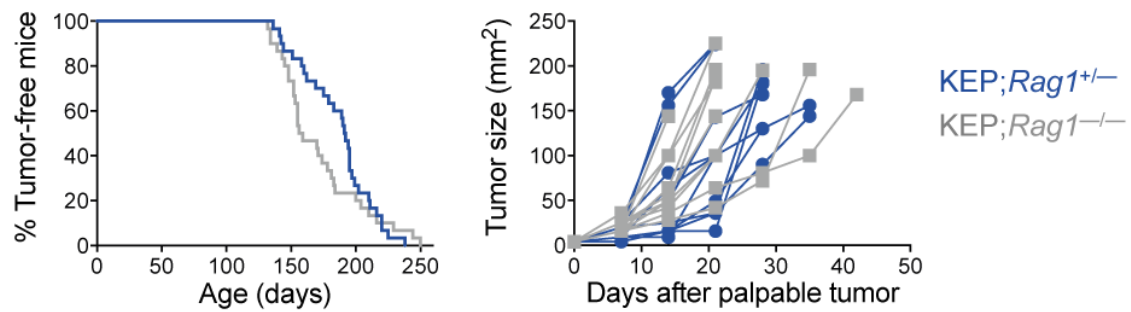
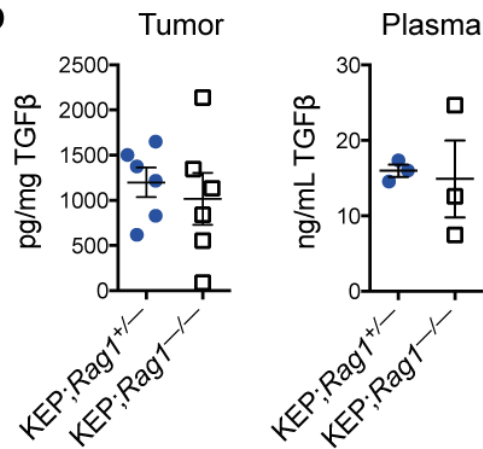
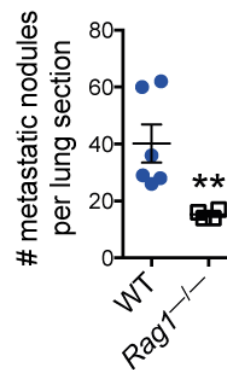
cell-gated CD8⁺ T cell proportions in lungs of mice in control and neutrophil-depleted mice, killed when transplanted tumours reached 100 mm². **d**, Dot plots of effector CD8⁺ T cell (CD62L⁺ CD44⁺) proportions in lungs of transplanted mammary tumour-bearing mice that were killed when tumours reached 100 mm². **e**, IFN-γ expression by CD8⁺ T cells in lungs of transplanted mammary tumour-bearing mice that were killed when tumours reached 100 mm². **f**, Tumour growth kinetics in neutrophil-depleted or combined neutrophil- and CD8⁺ T-cell-depleted, mammary tumour-transplanted recipient mice, compared with control (*n* = 13 control, 21 anti-Ly6G, 14 anti-Ly6G/CD8). Data are mean + s.e.m.



Extended Data Figure 5 | Cytokine expression levels in tumours and T cells, and their effects on neutrophils.

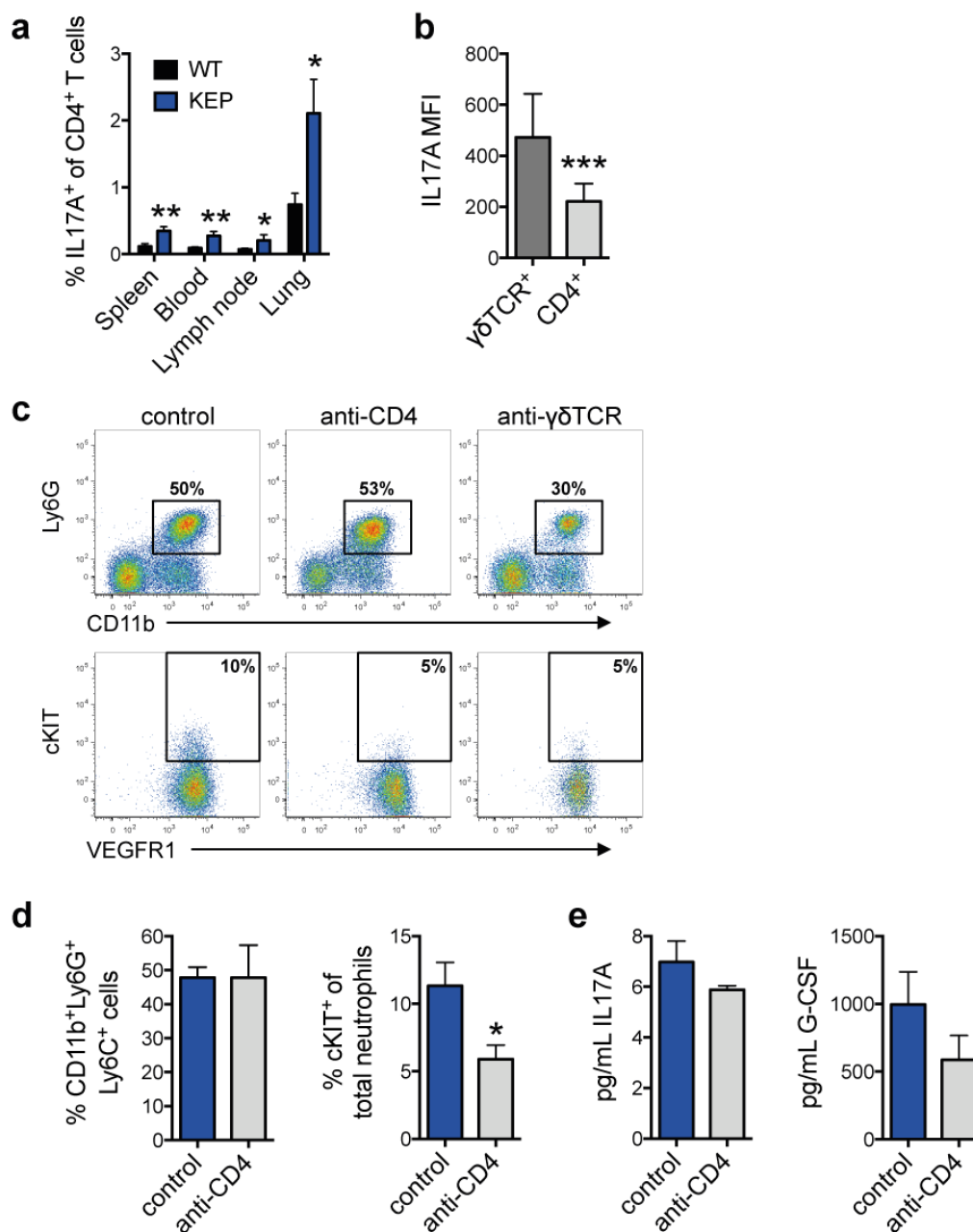
a, Unsupervised clustering of cytokine expression analysis in WT mammary glands and KEP tumours. Protein lysates were prepared as previously described from whole tissue³⁴ and analysed for expression of various cytokines by Luminex-based assay ($n = 5$ per group). **b**, Protein levels of indicated cytokines in WT mammary glands and KEP tumours, determined by Luminex-based cytokine profiling; n.d., not detectable ($n = 10$ per group; Mann-Whitney *U*-test). **c**, **d**, Quantification of neutrophil and cKIT⁺ neutrophil accumulation in blood as determined by flow cytometry and gated on CD45⁺ cells. WT ($n = 4$) or tumour-bearing KEP mice ($n = 8$) were treated with anti-IL-17 ($n = 8$) and/or recombinant G-CSF

(rG-CSF; $n = 4$) where indicated (Mann-Whitney *U*-test or Kruskal-Wallis test followed by post-hoc Dunn's test). **e**, Gene expression in circulating neutrophils from WT control ($n = 5$), rG-CSF-treated WT mice ($n = 4$), KEP control ($n = 10$), anti-IL-17-treated ($n = 6$), anti-IL-17 + rG-CSF-treated KEP mice ($n = 4$; Mann-Whitney *U*-test or Kruskal-Wallis test followed by post-hoc Dunn's test). **f**, Spleens of three WT mice and three KEP mice were pooled and CD3⁺ T cells were isolated. These cells were analysed by a real-time PCR array containing 86 different genes. Gene expression changes greater than threefold are shown. Members of the IL-17 signalling pathway are depicted in blue. * $P < 0.05$, ** $P < 0.01$, *** $P < 0.001$. All data are mean \pm s.e.m.

a**b****c**

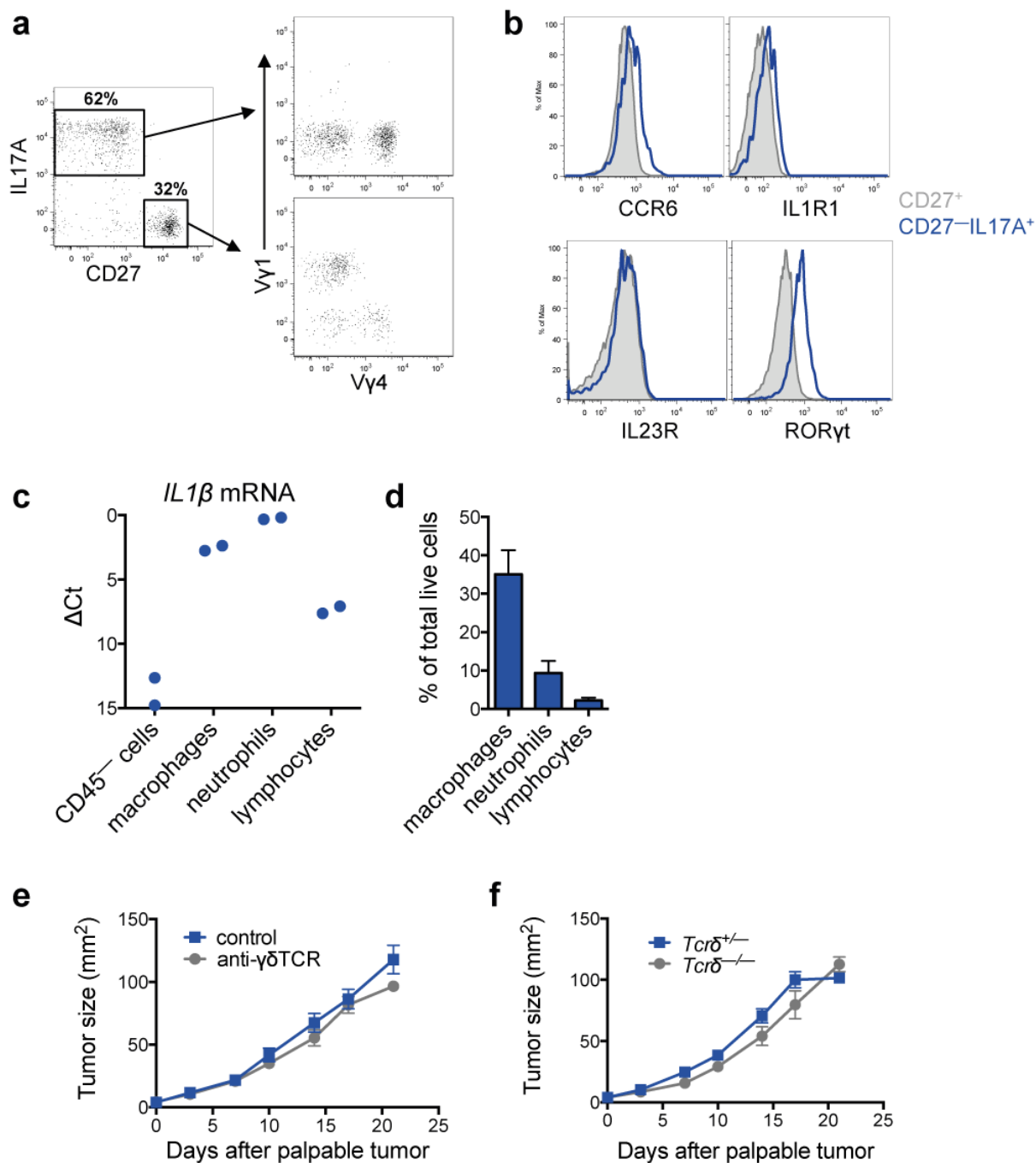
Extended Data Figure 6 | Absence of the adaptive immune system reduces metastasis. **a**, Graphic representation of mammary tumour latency (left) and tumour growth (right) in lymphocyte-proficient KEP;*Rag1*^{+/-} and lymphocyte-deficient KEP;*Rag1*^{-/-} mice ($n = 30$ per group left panel, 10 mice per group right panel). **b**, Levels of TGF-β1 in mammary tumours and the

plasma of tumour-bearing mice ($n = 6$ tumour, 3 plasma). **c**, Quantification of metastatic burden in lungs of recipient WT or *Rag1*^{-/-} mice that were transplanted with KEP mammary tumour fragments and underwent surgical removal of the primary tumour ($n = 6$ WT, 4 *Rag1*^{-/-} mice; $**P < 0.01$, Mann-Whitney *U*-test). Data are mean + s.e.m.



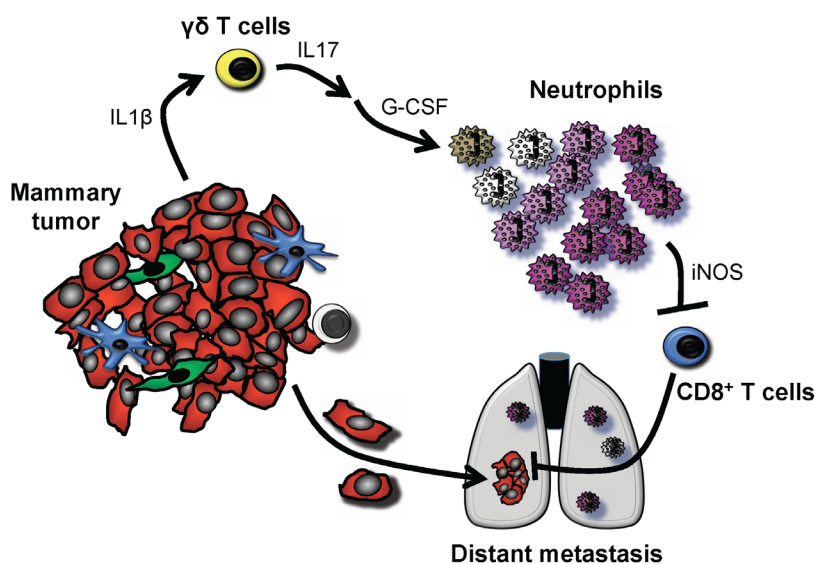
Extended Data Figure 7 | Depletion of CD4⁺ T cells does not affect systemic cytokine levels or neutrophil expansion. **a**, The proportion of IL-17A⁺ cells among CD4⁺ T cells in organs of WT and tumour-bearing KEP mice ($n = 6$ per group; Mann-Whitney U -test). **b**, Median fluorescence intensity of IL-17A expression in circulating $\gamma\delta$ and CD4⁺ T cells from tumour-bearing KEP mice, as determined by flow cytometry ($n = 11$ per group; Wilcoxon matched-pairs test). **c**, Representative dot plots depicting

total neutrophil and cKIT⁺ proportions in blood of control, anti-CD4- and anti- $\gamma\delta$ TCR-treated tumour-bearing KEP mice. **d**, Quantification of total neutrophil and cKIT⁺ neutrophil proportions in blood of control and anti-CD4-treated tumour-bearing KEP mice ($n = 7$ per group; Mann-Whitney U -test). **e**, Serum levels of IL-17A and G-CSF in control and anti-CD4-treated tumour-bearing KEP mice ($n = 10$ control, 6 anti-CD4; Mann-Whitney U -test). * $P < 0.05$, ** $P < 0.01$. All data are mean + s.e.m.



Extended Data Figure 8 | γδ T cell phenotype in KEP mice and their lack of influence on tumour growth in the metastasis model. **a**, γδ T cells from lungs of tumour-bearing KEP mice were analysed by flow cytometry for IL-17, CD27, Vγ1 and Vγ4 expression. Two major populations of γδ T cells were observed including IL-17⁺CD27⁻ and IL-17⁻CD27⁺ cells. **b**, Representative histograms of CCR6, IL-1R1, IL-23R and RORγt expression in IL-17⁺CD27⁻ and IL-17⁻CD27⁺ γδ T cell populations shown in **a**. **c**, *Il1β* gene expression in various cell populations isolated from transplanted KEP tumours. Tumours from three mice were pooled to form one group. CD45⁻ cells (which

include cancer cells, endothelial cells and fibroblasts), CD45⁺CD11b⁺F4/80⁺ macrophages, CD45⁺CD11b⁺Ly6G⁺ neutrophils and CD45⁺CD11b⁻ lymphocytes were sorted from two pooled groups. Real-time PCR was performed on individual cell populations for *Il1β* expression. Relative expression among different cells is shown. **d**, Graphic representation of immune cell proportions in KEP tumours (n = 4). **e**, Primary tumour growth kinetics of control and γδ T cell-depleted tumour transplant recipient mice (n = 13 per group). **f**, Growth kinetics of primary tumours transplanted into *Tcrδ*^{+/-} (n = 10) and *Tcrδ*^{-/-} mice (n = 6). All data are mean ± s.e.m.



Extended Data Figure 9 | The $\gamma\delta$ T cell/IL-17/neutrophil axis promotes breast cancer metastasis. Mammary tumours evoke a systemic inflammatory cascade that is initiated by IL-1 β production. Tumour-derived IL-1 β activates $\gamma\delta$ T cells to produce IL-17. Increased systemic IL-17 levels lead to upregulation of G-CSF, which subsequently causes neutrophil expansion and

alteration of neutrophil phenotype. These phenotypically altered neutrophils produce iNOS that suppresses the activity of anti-tumour CD8 $^{+}$ T cells. As a result of this systemic inflammatory cascade, the chance that disseminated cancer cells can establish metastases in distant organs is maximized.

Extended Data Table 1 | The top 50 most differentially expressed genes between neutrophils from WT and KEP mice

Gene ID	Gene name	Ensembl gene ID	fold change	p value
<i>Nos2</i>	nitric oxide synthase 2, inducible	ENSMUSG00000020826	31.5	0.345
<i>Car4</i>	carbonic anhydrase 4	ENSMUSG00000000805	25.5	0.111
<i>Lipg</i>	lipase, endothelial	ENSMUSG00000053846	24.6	0.128
<i>Gm11430</i>	predicted gene 11430	ENSMUSG00000080927	16.7	0.292
<i>Gm6551</i>	predicted gene 6551	ENSMUSG00000078100	14.2	0.039
<i>Stfa3</i>	stefin A3	ENSMUSG00000054905	14.1	0.047
<i>Pvrl2</i>	poliovirus receptor-related 2	ENSMUSG00000062300	13.8	0.143
<i>Gm16748</i>	predicted gene, 16748	ENSMUSG00000085308	13.5	0.087
<i>Prok2</i>	prokineticin 2	ENSMUSG00000030069	12.3	0.024
<i>Esm1</i>	endothelial cell-specific molecule 1	ENSMUSG00000042379	12.1	0.010
<i>Ano2</i>	anoctamin 2	ENSMUSG00000038115	10.6	0.138
<i>Saa1</i>	serum amyloid A 1	ENSMUSG00000074115	10.1	0.192
<i>Nov</i>	nephroblastoma overexpressed gene	ENSMUSG00000037362	9.6	0.295
<i>Gpr15</i>	G protein-coupled receptor 15	ENSMUSG00000047293	9.5	0.204
<i>Ggt1</i>	gamma-glutamyltransferase 1	ENSMUSG00000006345	9.3	0.076
<i>Cish</i>	cytokine inducible SH2-containing protein	ENSMUSG00000032578	9.1	0.217
<i>Stfa2</i>	stefin A2	ENSMUSG00000022902	8.9	0.020
<i>Gm14028</i>	predicted gene 14028	ENSMUSG00000082339	8.4	0.036
<i>Stfa1</i>	stefin A1	ENSMUSG00000071562	7.5	0.087
<i>Cfhr1</i>	complement factor H-related 1	ENSMUSG00000057037	7.1	0.029
<i>Ms4a3</i>	membrane-spanning 4-domains, subfamily A, member 3	ENSMUSG000000024681	6.8	0.177
<i>Kit</i>	kit oncogene	ENSMUSG00000005672	6.8	0.085
<i>Jph3</i>	junctophilin 3	ENSMUSG00000025318	6.8	0.076
<i>Cnnm2</i>	cyclin M2	ENSMUSG00000064105	6.6	0.128
<i>Gnb5</i>	guanine nucleotide binding protein (G protein), beta 5	ENSMUSG000000032192	6.4	0.004
<i>Alox12</i>	arachidonate 12-lipoxygenase	ENSMUSG00000000320	-11.2	0.103
<i>Slfn14-ps</i>	schlafen family member 14, pseudogene	ENSMUSG000000082101	-11.2	0.049
<i>Gm6634</i>	predicted gene 6634	ENSMUSG000000086538	-11.3	0.139
<i>Syt13</i>	synaptotagmin XIII	ENSMUSG000000027220	-11.4	0.213
<i>Tsc22d1</i>	TSC22 domain family, member 1	ENSMUSG000000022010	-11.4	0.107
<i>Gm10419</i>	predicted gene 10419	ENSMUSG000000072769	-11.5	0.231
<i>Sh3bgrl2</i>	SH3 domain binding glutamic acid-rich protein like 2	ENSMUSG000000032261	-11.6	0.117
<i>Fhl1</i>	four and a half LIM domains 1	ENSMUSG000000023092	-11.9	0.131
<i>Trpc6</i>	transient receptor potential cation channel, subfamily C, member 6	ENSMUSG000000031997	-11.9	0.076
<i>Ctla2a</i>	cytotoxic T lymphocyte-associated protein 2 alpha	ENSMUSG000000044258	-12.0	0.107
<i>Csgalnact1</i>	chondroitin sulfate N-acetylgalactosaminyltransferase 1	ENSMUSG000000036356	-12.2	0.156
<i>Gng11</i>	guanine nucleotide binding protein (G protein), gamma 11	ENSMUSG000000032766	-12.2	0.123
<i>2610109H07Rik</i>	RIKEN cDNA 2610109H07 gene	ENSMUSG000000029005	-12.3	0.195
<i>Nrgn</i>	neurogranin	ENSMUSG000000053310	-12.5	0.087
<i>Gm11274</i>	predicted gene 11274	ENSMUSG000000085331	-12.6	0.101
<i>Peg10</i>	paternally expressed 10	ENSMUSG000000092035	-13.1	0.177
<i>Angpt1</i>	angiopoietin 1	ENSMUSG000000022309	-13.6	0.168
<i>Plp1</i>	proteolipid protein (myelin) 1	ENSMUSG000000031425	-13.6	0.132
<i>Dlg2</i>	discs, large homolog 2 (Drosophila)	ENSMUSG000000052572	-14.6	0.080
<i>Syt14</i>	synaptotagmin-like 4	ENSMUSG000000031255	-14.6	0.138
<i>Mpl</i>	myeloproliferative leukemia virus oncogene	ENSMUSG000000006389	-15.6	0.197
<i>Mras</i>	muscle and microspikes RAS	ENSMUSG000000032470	-15.7	0.053
<i>Gp6</i>	glycoprotein 6 (platelet)	ENSMUSG000000078810	-15.9	0.215
<i>Cd226</i>	CD226 antigen	ENSMUSG000000034028	-18.4	0.134
<i>Bean1</i>	brain expressed, associated with Nedd4, 1	ENSMUSG000000031872	-19.2	0.053

MET is required for the recruitment of anti-tumoural neutrophils

Veronica Finisguerra^{1,2}, Giusy Di Conza^{1,2}, Mario Di Matteo^{1,2}, Jens Serneels^{1,2}, Sandra Costa^{1,2,3,4}, A. A. Roger Thompson⁵, Els Wauters^{6,7,8}, Sarah Walmsley^{5†}, Hans Prenen⁹, Zvi Granot¹⁰, Andrea Casazza^{1,2} & Massimiliano Mazzone^{1,2}

Mutations or amplification of the *MET* proto-oncogene are involved in the pathogenesis of several tumours^{1–4}, which rely on the constitutive engagement of this pathway for their growth and survival^{1,5}. However, *MET* is expressed not only by cancer cells but also by tumour-associated stromal cells, although its precise role in this compartment is not well characterized^{6–11}. Here we show that *MET* is required for neutrophil chemoattraction and cytotoxicity in response to its ligand hepatocyte growth factor (HGF). *Met* deletion in mouse neutrophils enhances tumour growth and metastasis. This phenotype correlates with reduced neutrophil infiltration to both the primary tumour and metastatic sites. Similarly, *Met* is necessary for neutrophil transudation during colitis, skin rash or peritonitis. Mechanistically, *Met* is induced by tumour-derived tumour necrosis factor (TNF)- α or other inflammatory stimuli in both mouse and human neutrophils. This induction is instrumental for neutrophil transmigration across an activated endothelium and for inducible nitric oxide synthase production upon HGF stimulation. Consequently, HGF/*MET*-dependent nitric oxide release by neutrophils promotes cancer cell killing, which abates tumour growth and metastasis. After systemic administration of a *MET* kinase inhibitor, we prove that the therapeutic benefit of *MET* targeting in cancer cells is partly countered by the pro-tumoural effect arising from *MET* blockade in neutrophils. Our work identifies an unprecedented role of *MET* in neutrophils, suggests a potential ‘Achilles’ heel’ of *MET*-targeted therapies in cancer, and supports the rationale for evaluating anti-*MET* drugs in certain inflammatory diseases.

To ensure *Met* deletion in the immune system only, we took advantage of the Tie2:Cre deleter that excises floxed genes in both bone marrow and endothelial cells¹², and we reconstituted lethally irradiated C57BL/6 wild-type (WT) mice with bone marrow cells from Tie2;*Met*^{wt/wt} (WT) or Tie2;*Met*^{fl/fl} (knockout (KO)) mice (Extended Data Fig. 2a), producing WT→WT or KO→WT mice, respectively. Compared to WT→WT controls, both growth and metastatic burden of subcutaneous LLC lung carcinomas were boosted in KO→WT mice (Fig. 1a–g), with reduced tumour apoptosis and necrosis, increased proliferation, but comparable vessel parameters and hypoxia (Extended Data Fig. 2b–r). A similar induction in tumour growth and metastasis was observed in non-irradiated KO versus WT mice (Extended Data Fig. 2s–u), but tumour growth, as well as the vascular features, were comparable in WT→WT versus WT→KO chimaeras, displaying *Met* deletion in endothelial cells only (Extended Data Fig. 2o–r, v). Thus, *Met* deletion in immune cells favours cancer growth and metastasis.

Blood counts and percentage of circulating blood cell subsets did not change in WT→WT and KO→WT mice, either at baseline or upon

LLC tumour engraftment (Extended Data Fig. 3a–e and Extended Data Tables 1, 2). Notably, KO→WT mice displayed reduced numbers of tumour-infiltrating CD45⁺ leukocytes and, among all the different subpopulations, only Ly6G⁺ tumour-associated neutrophils (TANs) were strongly reduced in KO→WT versus WT→WT mice at any time point (Fig. 1h–j and Extended Data Fig. 3f–k). Similarly, lungs from KO→WT tumour-bearing mice contained fewer CD45⁺ leukocytes with decreased Ly6G⁺ neutrophil infiltration, whereas the number of F4/80⁺ macrophages was comparable (Fig. 1k–m and Extended Data Fig. 3l, m). Furthermore, reconstitution of *Met* in neutrophils only¹³ (Extended Data Fig. 4a, b) was sufficient to rescue their recruitment and to hinder tumour growth and metastasis in KO→WT mice (Fig. 1n–q). Vice versa, restricted deletion of *Met* in neutrophils (Mrp8;*Met*^{fl/fl}) by the neutrophil-specific Mrp8:Cre line¹³ (Extended Data Fig. 4c, d) led to enhanced tumour growth and dissemination, and marked TAN reduction, as in KO→WT chimaeras (Fig. 1r–u and Extended Data Fig. 4e). These results indicate that *MET* is required for recruiting anti-tumoural neutrophils.

To extend our findings to other tumour types, we proved that *Met* deletion in the haematopoietic system increased the growth of (1) orthotopic T241 fibrosarcomas and B16F10 melanomas, (2) spontaneous mammary tumours in MMTV-PyMT⁺ transgenic mice, (3) H-Ras(G12V)- and c-Myc-driven hepatocellular carcinomas (HCCs), and (4) chemically induced colorectal cancers (CRCs) (Fig. 2a–j and Extended Data Fig. 5a, b). Furthermore, lung colonization of B16F10 melanoma cells (from either the primary tumour or after cancer cell intravenous injection) and of MMTV-PyMT⁺ breast tumours was boosted in *Met* KO chimaeras (Fig. 2k, l and Extended Data Fig. 5c). In all these tumour types, *Met* KO TANs were fewer than WT TANs (Fig. 2m and Extended Data Fig. 5d, e). Interestingly, during chronic bowel inflammation (preceding CRC formation), neutrophil but not macrophage infiltration of the colon was also abated by haematopoietic *Met* deletion, but this reduction did not impinge on colitis severity (Extended Data Fig. 5f–i). B16F10 melanomas and HCCs displayed enhanced tumour growth (and metastasization) as well as reduced TAN infiltration in Mrp8;*Met*^{fl/fl} versus Mrp8;*Met*^{wt/wt} mice (Fig. 2n–q). Conversely, orthotopic Panc02 carcinomas grew and metastasized similarly in both WT→WT and KO→WT mice, and TAN infiltration did not change (Extended Data Fig. 5j–l). However, these tumours produced little HGF compared to LLC tumours (Extended Data Fig. 5m, n). In general, plasma and intratumour HGF did not differ between genotypes (Extended Data Fig. 5o, p). In sum, *Met* deficiency in neutrophils promotes the progression of different (HGF-secreting) tumours.

Systemic treatment of WT mice carrying B16F10 melanomas (which are dependent on *MET*¹⁴) with three different *MET* tyrosine-kinase

¹Laboratory of Molecular Oncology and Angiogenesis, Vesalius Research Center, VIB, Leuven B3000, Belgium. ²Laboratory of Molecular Oncology and Angiogenesis, Vesalius Research Center, Department of Oncology, KU Leuven, Leuven B3000, Belgium. ³Life and Health Sciences Research Institute (ICVS), School of Health Sciences, University of Minho, 4710-057 Braga, Portugal. ⁴ICVS/3B's - PT Government Associate Laboratory, 4710-057 Braga/Guimarães, Portugal. ⁵Department of Infection and Immunity, University of Sheffield, Sheffield S10 2RX, UK. ⁶Respiratory Division, University Hospital Gasthuisberg, Leuven B3000, Belgium. ⁷Laboratory of Translational Genetics, Vesalius Research Center, VIB, Leuven B3000, Belgium. ⁸Laboratory of Translational Genetics, Vesalius Research Center, Department of Oncology, KU Leuven, Leuven B3000, Belgium. ⁹Digestive Oncology Unit, University Hospital Gasthuisberg, Department of Oncology, KU Leuven, Leuven B3000, Belgium. ¹⁰Department of Developmental Biology and Cancer Research, The Institute for Medical Research Israel-Canada, The Hebrew University, Jerusalem 91 120, Israel. [†]Present address: MRC/University of Edinburgh Centre for Inflammation Research, The Queen's Medical Research Institute, University of Edinburgh, Edinburgh EH16 4JT, UK.

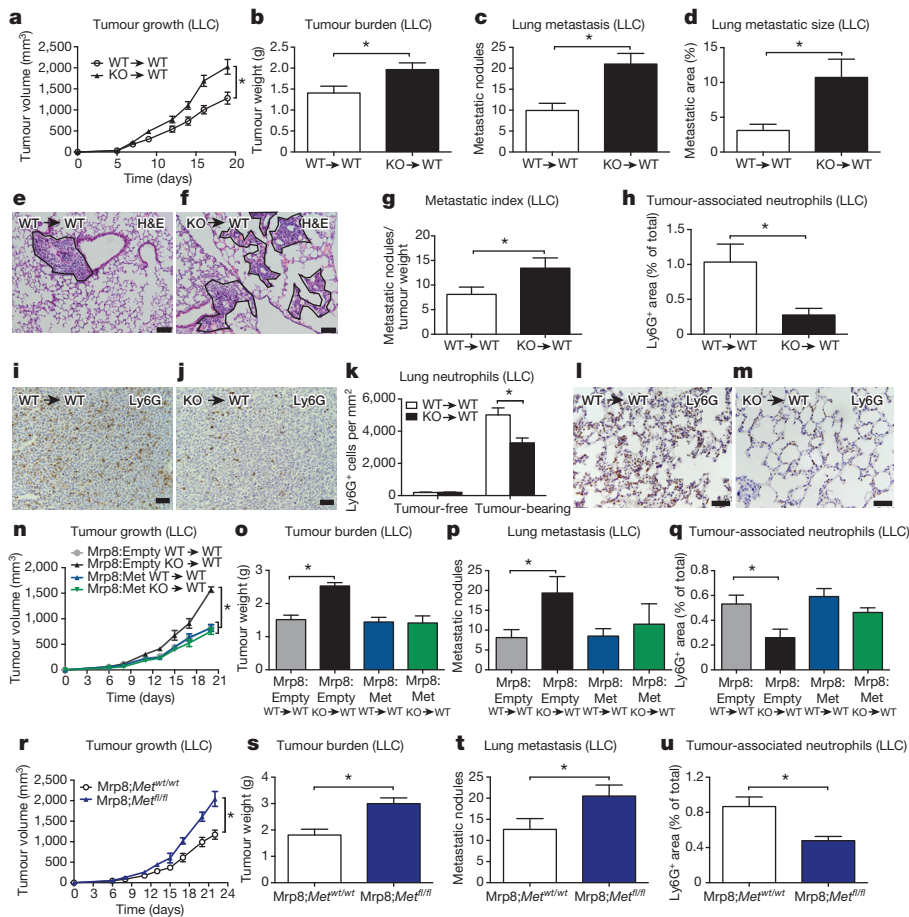


Figure 1 | *Met* deficiency inhibits neutrophil recruitment to tumour and metastatic site. **a–g**, LLC tumour growth (**a**), weight (**b**), lung macrometastases (**c**), metastatic area (**d**), representative images of haematoxylin and eosin (H&E)-stained lung sections (**e**, **f**), and metastatic index (**g**) in WT→WT and KO→WT chimaeras. Data combine three independent experiments; total mice: WT→WT, 23; KO→WT, 26. **h–m**, Neutrophil quantification and representative images on Ly6G-stained LLC tumour sections (**h–j**) or on lung sections from tumour-free and tumour-bearing mice (**k**) represented in **l**, **m**. Data in **h** are representative of four independent experiments (6 mice per condition per experiment). Data in **k** combine three independent experiments; total mice: tumour-free, 10 per condition; tumour-bearing, 15 per condition. **n–q**, LLC tumour growth (**n**), tumour weight (**o**), lung macrometastases (**p**), and TAN quantification (**q**) in WT→WT and KO→WT control chimaeras (Mrp8:Empty) or upon neutrophil-specific *Met* reconstitution (Mrp8:Met). Data combine two independent experiments; total mice, 10 per condition. **r–u**, LLC tumour growth (**r**), tumour weight (**s**), lung macrometastases (**t**), and TAN quantification (**u**) upon neutrophil-specific *Met* deletion (Mrp8:Met^{fl/fl}) and in controls (Mrp8:Met^{wt/wt}). Data combine two independent experiments; total mice, 13 per condition. **P* < 0.05. Scale bars: 100 μm (**e**, **f**); 50 μm (**i**, **j**, **l**, **m**). Graphs show mean ± standard error of the mean (s.e.m.).

inhibitors (PF-04217903, INCB28060 and JNJ-38877605), strongly reduced TAN recruitment (Extended Data Fig. 5q). We then compared MET silencing in cancer cells versus systemic MET inhibition. Systemic administration of PF-04217903 decreased the weight and volume of B16F10 melanomas by 36% and 54%, respectively. Instead, MET knockdown in cancer cells only, led to 58% and 75% inhibition of tumour growth and volume (Fig. 2r, s and Extended Data Fig. 5r). However, the combination of these two strategies was not synergistic but dampened tumour inhibition to the same level as observed with PF-04217903 alone (Fig. 2r, s). TAN inhibition by PF-04217903 was comparable in both *Met*-silenced and scrambled B16F10 melanomas (Fig. 2t). These data unveil how the therapeutic benefit of systemic MET inhibition is partly blunted by the blockade of anti-tumoural neutrophils.

To date, MET expression in neutrophils has been poorly documented¹¹. We thus measured MET levels in circulating or tumour-infiltrating neutrophils. Circulating Ly6G⁺ cells from healthy mice expressed low MET, but these levels were increased in circulating neutrophils from LLC-tumour-bearing mice and even further in TANs (Fig. 3a, b and Extended Data Fig. 6a). Similarly, neutrophils isolated from non-small-cell lung tumours displayed much higher MET levels than in the healthy tissue (Fig. 3c).

Co-culture with interleukin (IL)-1α pre-activated endothelium as well as stimulation with tumour- or cancer-cell-conditioned medium (TCM or CCM, respectively) promoted MET expression in both mouse and human neutrophils (Fig. 3d–g). In a biased approach^{15–17}, we found that TNF-α and lipopolysaccharide (LPS) (but not IL-1α, HGF, or hypoxia) induced MET expression in both mouse and human neutrophils (Fig. 3h and Extended Data Fig. 6b–e; data not shown). TNF-α-mediated MET induction required TNFR1 and subsequent nuclear factor (NF)-κB activation (Fig. 3i–k). TNF-α alone was not able to trigger either MET

phosphorylation or HGF release in neutrophils (Extended Data Fig. 6f–h).

Silencing of endothelial-cell-borne TNF-α (which is 250-fold increased upon stimulation with IL-1α; Extended Data Fig. 6i), knock-out of neutrophil-borne TNFR1 (but not of TNFR2), and pharmacological blockade of TNF-α with the TNF-α-trap Enbrel, prevented MET induction in mouse or human neutrophils upon co-culture with activated endothelial cells or exposure to TCM/CCM (Fig. 3l and Extended Data Fig. 6j–m). Finally, systemic administration of Enbrel in LLC-tumour-bearing mice diminished MET expression in neutrophils as well, resulting in their reduced recruitment to the tumour (Fig. 3m, n). Although MET is scarcely expressed in naive neutrophils, it is strongly induced by inflammatory stimuli.

Mechanistically, impaired TAN accumulation after *Met* inactivation was not due to cell death as assessed in LLC tumours and in culture, both at baseline and under LPS stimulation, with or without HGF (Extended Data Fig. 7a–e), but rather to a defect in neutrophil recruitment from the blood. Indeed, also in the case of acute inflammation, *Met* KO neutrophils displayed reduced exudation to the skin or to the peritoneal cavity (Fig. 4a–d and Extended Data Fig. 8a, b). Macrophage and lymphocyte recruitment did not change (Fig. 4d and Extended Data Fig. 8c, d). Vice versa, recombinant HGF recruited WT neutrophils inside subcutaneous air pouches with similar efficacy to the neutrophil chemoattractant CXCL1 (Fig. 4e and Extended Data Fig. 8e). In contrast, *Met* KO neutrophils did not migrate towards HGF, although their response to CXCL1 was preserved (Fig. 4e and Extended Data Fig. 8e). Mirroring this approach, an anti-HGF blocking antibody¹⁸ prevented neutrophil infiltration to tumours and inflamed skin (Fig. 4f).

We then tested the relevance of MET for neutrophil migration. Stimulation of WT neutrophils with HGF promoted their adhesion and chemotaxis through an activated endothelium whereas *Met* KO

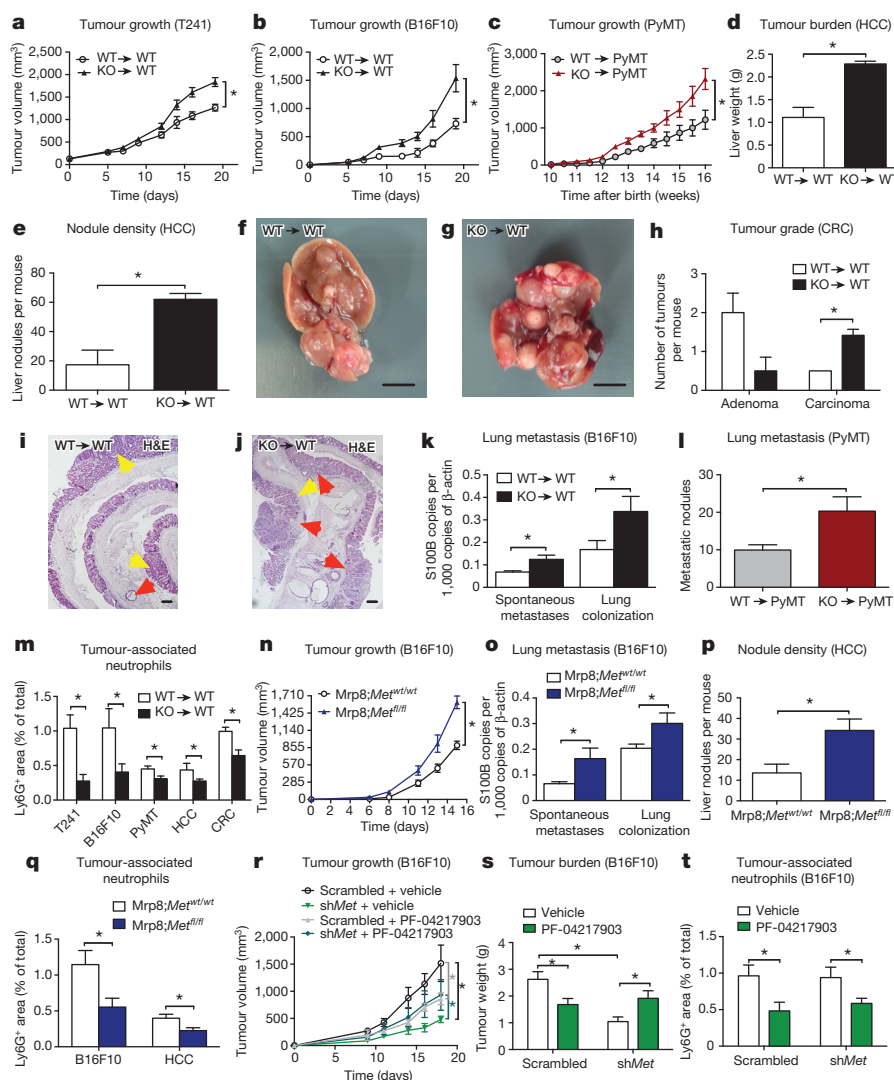


Figure 2 | *Met* deficiency in haematopoietic cells fosters progression of several tumour types. **a–c**, Growth of T241 fibrosarcomas (**a**), B16F10 melanomas (**b**) and PyMT-driven breast tumours (**c**). Data in **a**, **b** combine two independent experiments; total mice, 14 per condition (**a**); 8 per condition (**b**). Data in **c** combine three independent experiments; total mice: WT→PyMT, 13; KO→PyMT, 16. **d–g**, Liver weight (**d**), nodules (**e**), and images (**f**, **g**) after H-Ras(G12V)/c-Myc-driven HCC ($n = 4$ mice per condition). **h–j**, Quantification (**h**) on H&E-stained bowel sections (**i**, **j**) of colon adenomas (yellow arrowheads) and carcinomas (red arrowheads) after administration of azoxymethane (AOM) and dextran sodium sulfate (DSS). Data combine two independent experiments; total mice, 10 per condition. **k**, Spontaneous lung metastases from B16F10 tumours or lung colonization after B16F10 intravenous injection. Data combine two independent experiments; total mice, 8 per condition. **l**, Lung macrometastases from PyMT tumours. Data combine three independent experiments; total mice:

WT→PyMT, 13; KO→PyMT, 16. **m**, TAN quantification in T241, B16F10, PyMT, HCC and CRC tumour tissues. Total mice: T241 and CRC, 10 per condition; B16F10, 8 per condition, combining two experiments; WT→PyMT, 13; KO→PyMT, 16, combining three experiments; HCC, 4 per condition (one experiment). **n**, **o**, B16F10 tumour growth (**n**), spontaneous metastases and lung colonization (**o**) in Mrp8;Met^{wt/wt} and Mrp8;Met^{fl/fl} mice. Data combine two independent experiments; total mice: Mrp8;Met^{wt/wt}, 12; Mrp8;Met^{fl/fl}, 8. **p**, Liver nodules in Mrp8;Met^{wt/wt} and Mrp8;Met^{fl/fl} HCC-bearing mice. Total mice, 7 per condition. **q**, TAN quantification in B16F10 tumours (total mice, 8 per condition) or HCCs (total mice, 7 per condition). **r–t**, Tumour growth (**r**), weight (**s**) and TANs in short hairpin RNA (shRNA) *Met*-silenced (shMet) and scrambled B16F10 tumours after PF-04217903 or vehicle treatment. Data combine two independent experiments (total mice, 11 per condition for scramble; 14 per condition for shMet). * $P < 0.05$. Scale bars: 0.5 cm (**f**, **g**); 200 μ m (**i**, **j**). Graphs show mean \pm s.e.m.

neutrophils (displaying an 85% reduction in MET protein levels compared to WT; Extended Data Fig. 2a) completely lost this response (Fig. 4g, h and Extended Data Fig. 8f). In line with this, TCM (containing 2.6 ± 0.3 ng ml⁻¹ HGF) promoted transendothelial migration of WT neutrophils, but its effect was 43% lower on *Met* KO neutrophils (Fig. 4i). Upon HGF neutralization, WT neutrophils responded to TCM only partially, as did *Met* KO neutrophils (Fig. 4i). Neither HGF nor TCM influenced neutrophil behaviour on non-activated endothelial cells or bare membranes (Extended Data Fig. 8f–h). Hence, HGF-mediated MET activation is required for neutrophil transendothelial migration to the inflammatory site.

Once migrated inside the tumour, N1 or N2 neutrophils can inhibit or favour tumour progression, respectively¹⁹. Among the N1 and N2 genes, only the expression of the N1 marker inducible nitric oxide synthase (*Nos2*, also known as *iNos*) was lower in *Met* KO versus WT TANs but similar in macrophages (Fig. 4j and Extended Data Fig. 8i). Compared to WT→WT mice, tumours harvested from KO→WT mice displayed reduced nitric oxide (NO) production and 3-nitrotyrosine (3NT) formation, a sign of NO-mediated cell damage (Fig. 4k–n). *In vitro*, *Met* KO TANs had lower cancer-cell-killing capacity than WT TANs; iNOS inhibition by N^G-monomethyl-L-arginine (L-NMMA) blunted this difference (Fig. 4o and Extended Data Fig. 8j).

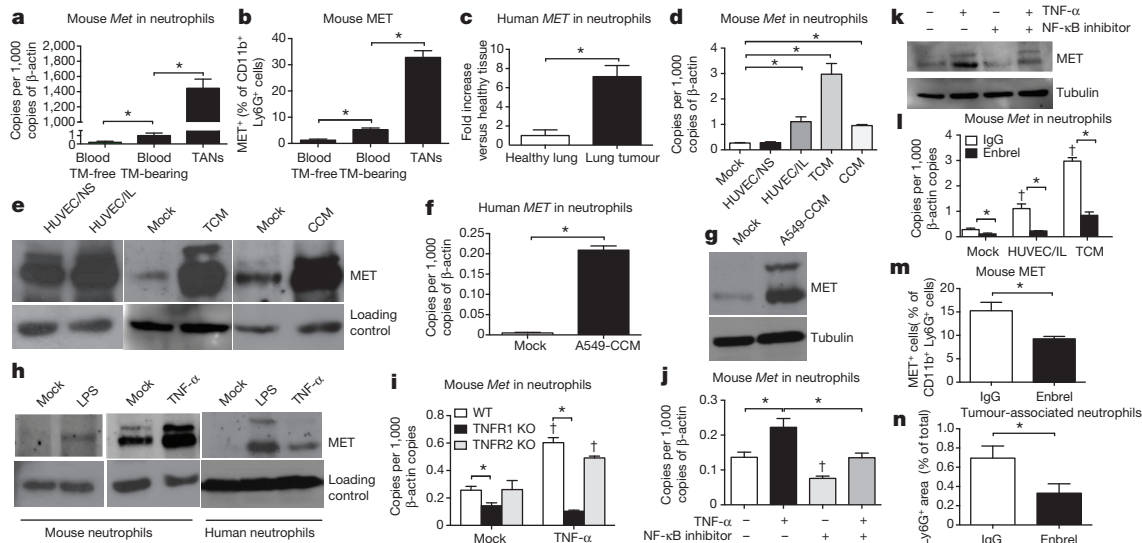


Figure 3 | *MET* expression in neutrophils is induced by tumour-derived soluble factors. **a**, **b**, Quantitative polymerase chain reaction with reverse transcription (qRT-PCR) (**a**) and fluorescence-activated cell sorting (FACS) (**b**) analysis for *MET* in blood neutrophils from tumour (TM)-free or LLC-tumour-bearing mice and in TANs. **c**, qRT-PCR for *MET* in human neutrophils from lung cancer versus healthy tissue. $n = 4$ patients. **d**, **e**, *MET* expression by qRT-PCR (**d**) and western blot (**e**) in circulating neutrophils from tumour-free mice after co-culture with unstimulated (HUVEC/NS) or IL-1 α -pre-stimulated (HUVEC/IL) human umbilical vein endothelial cells (HUVECs), or after stimulation with TCM or CCM. **f**, **g**, qRT-PCR (**f**) or western blot (**g**) for *MET* in circulating human neutrophils after stimulation with A549-CCM. **h**, Western blot for *MET* and human neutrophils after LPS or TNF- α stimulation. **i**, qRT-PCR for *Met* in WT, TNFR1 KO or

TNFR2 KO mouse neutrophils after TNF- α stimulation. **j**, **k**, qRT-PCR (**j**) and western blot (**k**) for *MET* in mouse neutrophils after TNF- α stimulation with or without NF- κ B inhibitor. **l**, qRT-PCR for *Met* in mouse neutrophils co-cultured with HUVEC/IL or stimulated with TCM in the presence or absence of Enbrel. **m**, **n**, FACS for *MET* in TANs (**m**) and immunohistochemistry for Ly6G (**n**) in LLC tumours after Enbrel. Data combine two independent experiments; total mice, 5 per condition. All data in **a**, **b**, **d**, **f**, **i**, **j**, **l** are representative of two independent experiments using four biological replicates per condition per experiment. All western blots were repeated three times on independent biological replicates. Full western blot images are shown in Supplementary Fig. 1. Loading control in **e**, **h** displays tubulin or actin according to Supplementary Fig. 1. * $P < 0.05$; † $P < 0.05$ versus mock (**i**, **l**) or versus untreated (**j**). Graphs show mean \pm s.e.m.

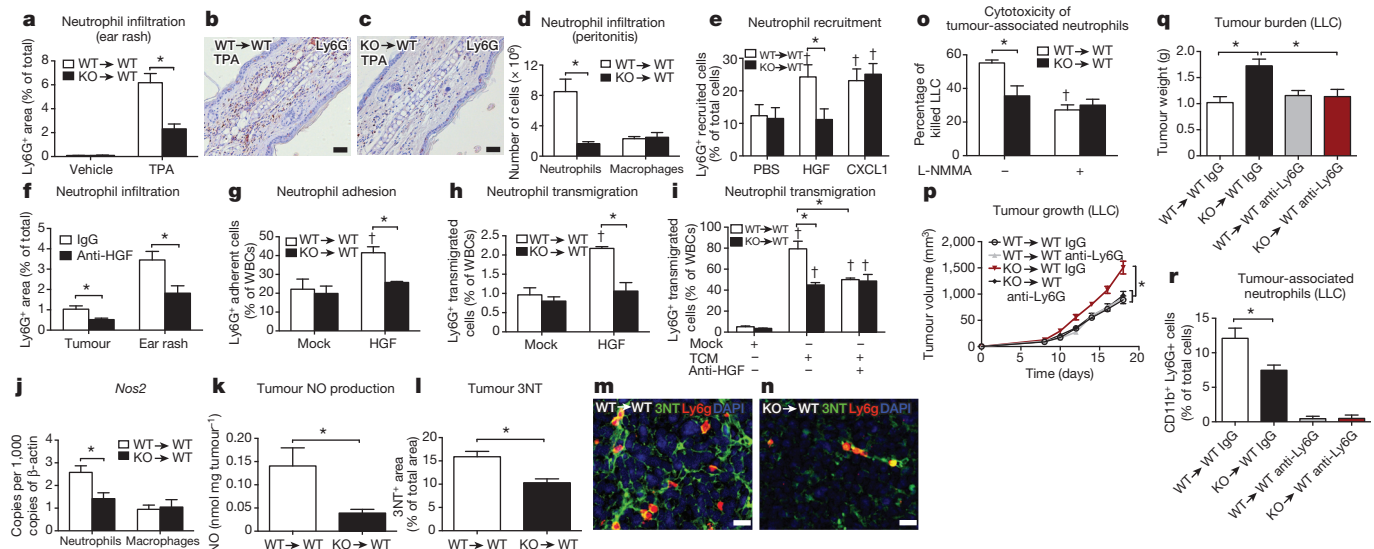


Figure 4 | *MET* is required for neutrophil transendothelial migration and cytotoxicity. **a**–**c**, Neutrophil quantification (**a**) on 12-*O*-tetradecanoylphorbol-13-acetate (TPA)-painted ear skin (**b**, **c**). Data combine two independent experiments; total mice: 10 per condition for vehicle; 14 per condition for TPA. **d**, FACS analysis for Ly6G⁺ neutrophils or F4/80⁺ macrophages on peritoneal lavages after zymosan-induced peritonitis. Data are representative of two independent experiments using 4 mice per condition per experiment. **e**, FACS analysis for neutrophil recruitment towards HGF or CXCL1 in air pouch assays. Data combine three independent experiments; total mice: 10 per condition. **f**, Ly6G infiltration in LLC tumours or in TPA-painted ear skin after anti-HGF. Data combine two independent experiments; total mice: IgG, 11; anti-HGF, 6. **g**–**i**, Neutrophil adhesion to HUVEC/IL (**g**) and transendothelial migration in response to HGF (**h**) or TCM with or without anti-HGF (**i**). Data in **g**–**i** are representative of three independent experiments

using three biological replicates per condition per experiment. WBCs, white blood cells. **j**, **k**, qRT-PCR for *Nos2* in LLC-tumour-associated neutrophils or macrophages (**j**) and tumour-derived NO production (**k**). **l**–**n**, Quantification (**l**) and representative images (**m**, **n**) of 3NT and Ly6G co-stained LLC tumour sections. DAPI, 4',6-diamidino-2-phenylindole. Data in **j**–**n** combine two independent experiments; total mice: 8 per condition. **o**, TAN cytotoxicity against LLC cells with or without L-NMMA. Data are representative of four independent experiments using three biological replicates per condition per experiment. **p**–**r**, LLC tumour growth (**p**), weight (**q**) and TANs (**r**) after neutrophil-depleting anti-Ly6G treatment. Data combine two independent experiments; total mice: 16 per condition. * $P < 0.05$; † $P < 0.05$ versus PBS (**e**), versus mock (**g**–**i**), and versus WT \rightarrow WT untreated (**o**). Scale bars: 100 μ m (**b**, **c**); 20 μ m (**m**, **n**). Graphs show mean \pm s.e.m.

HGF-stimulated WT but not *Met* KO neutrophils displayed enhanced NO release and cytotoxicity, which was abated by L-NMMA (Extended Data Fig. 8k, l).

We then hypothesized that HGF/MET pathway is key for anti-tumoural neutrophils only. Neutrophil depletion in WT→WT chimaeras did not affect LLC tumour growth, implying that in this tumour model anti-tumoural and pro-tumoural neutrophils are in balance (Fig. 4p–r). The same treatment in KO→WT mice reduced tumour growth by 34% (Fig. 4p–r), indicating that *Met* deletion inhibits recruitment and activation of cytotoxic, but not of pro-tumoural neutrophils, which are instead blocked by the anti-Ly6G antibody (Fig. 4r and Extended Data Fig. 8m).

In sum, we demonstrate that MET is induced by inflammatory stimuli. This receptor is then required for neutrophil extravasation to inflamed tissues. Extravasated neutrophils respond to HGF by producing cytotoxic nitric oxide (Extended Data Fig. 1). All these steps restrain non-specific immune reactions to the inflammatory site, preventing damage of healthy organs.

These findings highlight a double-edged role of MET in cancer: on the one hand, in MET-addicted tumours, this pathway is vital for the cell cycle and survival²; on the other hand, it promotes anti-tumorigenic activities in neutrophils. Thus, alternative approaches targeting MET on cancer cells only, and trials guided by new patient selection strategies will be important to maximize the efficacy of MET inhibition in oncological diseases^{3,4,20}.

Finally, given the fact that MET-inhibiting drugs are not associated with overt toxicity¹, MET-targeted therapies might ameliorate the symptoms of inflammatory disorders in which neutrophils are important for disease pathogenesis²¹.

Online Content Methods, along with any additional Extended Data display items and Source Data, are available in the online version of the paper; references unique to these sections appear only in the online paper.

Received 13 June 2013; accepted 13 March 2015.

Published online 18 May 2015.

- Gherardi, E., Birchmeier, W., Birchmeier, C. & Vande Woude, G. Targeting MET in cancer: rationale and progress. *Nature Rev. Cancer* **12**, 89–103 (2012).
- Bertotti, A. *et al.* Only a subset of Met-activated pathways are required to sustain oncogene addiction. *Sci. Signal.* **2**, ra80 (2009).
- Lennerz, J. K. *et al.* MET amplification identifies a small and aggressive subgroup of esophagogastric adenocarcinoma with evidence of responsiveness to crizotinib. *J. Clin. Oncol.* **29**, 4803–4810 (2011).
- Choueiri, T. K. *et al.* Phase II and biomarker study of the dual MET/VEGFR2 inhibitor foretinib in patients with papillary renal cell carcinoma. *J. Clin. Oncol.* **31**, 181–186 (2013).
- Comoglio, P. M., Giordano, S. & Trusolino, L. Drug development of MET inhibitors: targeting oncogene addiction and expedience. *Nature Rev. Drug Discov.* **7**, 504–516 (2008).
- Bussolino, F. *et al.* Hepatocyte growth factor is a potent angiogenic factor which stimulates endothelial cell motility and growth. *J. Cell Biol.* **119**, 629–641 (1992).
- Liu, Y. *et al.* Hepatocyte growth factor and c-Met expression in pericytes: implications for atherosclerotic plaque development. *J. Pathol.* **212**, 12–19 (2007).
- Chen, Q., DeFrances, M. C. & Zarnegar, R. Induction of met proto-oncogene (hepatocyte growth factor receptor) expression during human monocyte-macrophage differentiation. *Cell Growth Differ.* **7**, 821–832 (1996).
- Baek, J. H., Birchmeier, C., Zenke, M. & Hieronymus, T. The HGF receptor/Met tyrosine kinase is a key regulator of dendritic cell migration in skin immunity. *J. Immunol.* **189**, 1699–1707 (2012).
- Adams, D. H. *et al.* Hepatocyte growth factor and macrophage inflammatory protein 1β: structurally distinct cytokines that induce rapid cytoskeletal changes and subset-preferential migration in T cells. *Proc. Natl Acad. Sci. USA* **91**, 7144–7148 (1994).
- Tesio, M. *et al.* Enhanced c-Met activity promotes G-CSF-induced mobilization of hematopoietic progenitor cells via ROS signaling. *Blood* **117**, 419–428 (2011).
- Takeda, Y. *et al.* Macrophage skewing by Phd2 haploinsufficiency prevents ischaemia by inducing arteriogenesis. *Nature* **479**, 122–126 (2011).
- Elliott, E. R. *et al.* Deletion of Syk in neutrophils prevents immune complex arthritis. *J. Immunol.* **187**, 4319–4330 (2011).
- Kishi, Y. *et al.* Systemic NK4 gene therapy inhibits tumor growth and metastasis of melanoma and lung carcinoma in syngeneic mouse tumor models. *Cancer Sci.* **100**, 1351–1358 (2009).
- Pennacchietti, S. *et al.* Hypoxia promotes invasive growth by transcriptional activation of the met protooncogene. *Cancer Cell* **3**, 347–361 (2003).
- Moghul, A. *et al.* Modulation of c-MET proto-oncogene (HGF receptor) mRNA abundance by cytokines and hormones: evidence for rapid decay of the 8 kb c-MET transcript. *Oncogene* **9**, 2045–2052 (1994).
- Dai, J. Y., DeFrances, M. C., Zou, C., Johnson, C. J. & Zarnegar, R. The Met protooncogene is a transcriptional target of NFκB: implications for cell survival. *J. Cell. Biochem.* **107**, 1222–1236 (2009).
- Suga, H. *et al.* IFATS collection: fibroblast growth factor-2-induced hepatocyte growth factor secretion by adipose-derived stromal cells inhibits postinjury fibrogenesis through a c-Jun N-terminal kinase-dependent mechanism. *Stem Cells* **27**, 238–249 (2009).
- Fridlender, Z. G. & Albelda, S. M. Tumor-associated neutrophils: friend or foe? *Carcinogenesis* **33**, 949–955 (2012).
- Garber, K. MET inhibitors start on road to recovery. *Nature Rev. Drug Discov.* **13**, 563–565 (2014).
- Wright, H. L., Moots, R. J., Bucknall, R. C. & Edwards, S. W. Neutrophil function in inflammation and inflammatory diseases. *Rheumatology* **49**, 1618–1631 (2010).

Supplementary Information is available in the online version of the paper.

Acknowledgements The authors thank: R. Stirparo, M. Mambretti and Y. Jönsson for technical assistance; G. Serini, L. Trusolino and P. Bruhns for comments; and E. Radaelli for valuable advice on histological analyses. V.F. and G.D.C. were supported by grants from the Fonds Wetenschappelijk Onderzoek (FWO), A.C. by the Fondazione Umberto Veronesi. S.W. is supported by a Wellcome Trust Senior Clinical Fellowship Award. M.M. is supported by a European Research Council starting grant.

Author Contributions V.F. performed experimental design, all experiments, data acquisition and interpretation. G.D.C. performed *in vitro* assays and measured tumour experiments. M.D.M. performed ELISA assays, and designed and performed cloning strategies. J.S. performed all the bone marrow transplantations and *in vivo* tumour experiments. A.A.R.T. and S.W. performed neutrophil isolations and peritonitis assays. Z.G. provided the *Mrp8* promoter. S.C. performed tumour experiments and skin rash assays *in vivo*. E.W. provided clinical samples. H.P. provided data interpretation on the CRC and HCC models. A.C. performed experimental design, mouse tumour experiments, analysis of histological stainings and FACS, data acquisition and interpretation. M.M. performed experimental design, data analysis, conducted scientific direction and wrote the manuscript.

Author Information Reprints and permissions information is available at www.nature.com/reprints. The authors declare no competing financial interests. Readers are welcome to comment on the online version of the paper. Correspondence and requests for materials should be addressed to M.M. (massimiliano.mazzone@vib-kuleuven.be) or A.C. (andrea.casazza@vib-kuleuven.be).

METHODS

Animals. The *Met* floxed mice, a gift from S. S. Thorgeirsson, were backcrossed in a C57BL/6 background. The Tie2:Cre and MMTV-PyMT transgenic lines were obtained from our mouse facility. The Mrp8:Cre mice were a gift from C. A. Lowell and P. Bruhns^{13,22–26}. C57BL/6 mice were purchased from Harlan. TNFR1 KO mice and TNFR2 KO mice were a gift from C. Libert. The *Met* floxed mice were intercrossed for at least two generations with Tie2:Cre or Mrp8:Cre in order to obtain *Met*^{fl/fl} Cre-negative (WT) or *Met*^{fl/fl} Cre-positive (KO) littermates for the specific promoter. All the experimental procedures were approved by the Institutional Animal Care and Research Advisory Committee of the KU Leuven. In all the experiments, mice were gender and age matched (within an age range between 6 and 10 weeks).

Cell lines. Murine Lewis lung carcinoma cells (LLC), melanoma B16F10, and human non-small-cell lung carcinoma A549 cells were obtained from the American Type Culture Collection (ATCC); the murine pancreatic tumour cell line Panc02 and the murine fibrosarcoma cell line T241 were gifts from U. Cavallaro and L. Claesson-Welsh, respectively. LLC, B16F10, A549 and T241 cells were cultured in DMEM (Gibco) supplemented with 2 mM glutamine, 100 units ml⁻¹ penicillin, 100 µg ml⁻¹ streptomycin and containing 10% FBS (DMEM 10% FBS). Panc02 cells were cultured in RPMI (Gibco) supplemented with 2 mM glutamine, 100 units ml⁻¹ penicillin, 100 µg ml⁻¹ streptomycin and containing 10% FBS. All these murine tumour cell lines are syngeneic in a C57BL/6 background, allowing implantation in *Met* conditional knockout mice or chimaeras. HUVECs were isolated from human umbilical cords and maintained in M199 (Invitrogen) supplemented with 20% FBS, 2 mM glutamine, 100 units ml⁻¹ penicillin, 100 µg ml⁻¹ streptomycin, 0.15% heparin, 20 µg ml⁻¹ ECGS (M199 complete). 0.1% pork gelatin was used to favour the adhesion of HUVECs to the flask bottom. All cells were maintained in a humidified incubator in 5% CO₂ and 95% air at 37 °C. Three or four different shRNA lentiviral vectors (Sigma) were used to silence *Met* in LLC, B16F10 or T241 cells (LLC sh*Met*, B16F10 sh*Met* or T241 sh*Met*; see later), or to silence *TNFA* in HUVECs (HUVEC sh*TNFA*). Scramble lentiviral vectors were used as control. Transduced cells were selected with 8 µg ml⁻¹ puromycin. All cancer cell lines and primary HUVECs underwent mycoplasma testing before their use. Negative mycoplasma contamination status was verified using LookOut Mycoplasma PCR Kit (Sigma) and MycoAlert Mycoplasma Detection Kit plus Assay Control (Lonza). Panc02 and T241 cells were both authenticated by Idexx BioResearch. All cells were passaged in the laboratory for no longer than 6 months after receipt. Supplementary Table 1 lists the sequences of all the shRNA constructs used in this study.

Bone marrow transplantation and blood cell count. Recipient 6-week-old female mice were lethally irradiated (9.5 Gy) and then intravenously injected with 10⁷ bone marrow cells from WT or KO mice 16 h later. Experiments were initiated 5 weeks after bone marrow reconstitution. Blood cell count was determined using a haemocytometer on peripheral blood collected by retro-orbital bleeding.

Haematopoietic stem/progenitor cell transduction. For MET overexpression or reconstitution in WT or *Met* KO neutrophils, respectively, lineage-negative haematopoietic stem/progenitor cells (HSPCs) were enriched with the mouse haematopoietic progenitor enrichment kit (Stem Cell Technologies) and checked for purity by FACS according to the manufacturer's protocol. 1 × 10⁶ cells ml⁻¹ were pre-stimulated for 5 h with stem span serum-free medium (Stem Cell Technologies) supplemented with IL-3 (20 ng ml⁻¹), SCF (100 ng ml⁻¹), TPO (100 ng ml⁻¹) and FLT-3L (100 ng ml⁻¹) (Promega), and transduced with 1 × 10⁸ transducing units (TU) ml⁻¹ of a lentiviral vector expressing mouse *Met* under the promoter of the human gene *S100A8* (Mrp8:Met), which has been engineered for neutrophil-specific transcriptional targeting, or an empty vector (Mrp8:Empty) as control. Briefly, the promoter driving *Met* expression in neutrophils only corresponds to a 3.6 kb DNA fragment encompassing the natural 5' and 3' regulatory regions but deleted of its exon coding sequences. Hence, *Met* is under the control of the 5' and 3' untranslated regions of the human *S100A8* gene and other proximal *cis* regulatory sequences present in the surrogate DNA fragment^{13,22–26}. Ten hours after the first viral transduction, cells received a second round of their respective lentiviral vector; 7 h later 1 × 10⁶ cells were injected via tail vein in lethally irradiated C57BL/6 recipient mice. A fraction of transduced HSPCs were cultured and collected after 9 days to measure the number of integrated vector copies per cell genome (vector copy number (VCN)) by qPCR using custom TaqMan assays specific for HIV *gag* sequences (Applied Biosystems), as previously described²⁷. Standard curves for HIV *gag* (contained by both Mrp8:Empty and Mrp8:Met lentiviral vectors) were obtained from the corresponding plasmids. Fifty nanograms of genomic DNA from each sample were subjected to qPCR in quadruplicate using an ABI Prism 7500 Fast Real-Time PCR System (Applied Biosystems). VCN was determined comparing the amplification signal on the genomic DNA with the standard curve consisting of serial dilutions over a 6 log range (slope, approximately -3.3; intercept, approximately 35; efficiency percent-

age, approximately 100). Average copies per cell genome were calculated taking into account that one murine diploid genome = 5.92 pg. The results of this analysis are shown in Supplementary Table 2.

Tumour models. 2 × 10⁶ LLC or 1 × 10⁶ B16F10 cells were injected subcutaneously while 2 × 10⁶ T241 cells were injected intradermally in a volume of 200 µl PBS. Tumour volumes were measured three times a week with a calliper. At end stage, tumours were weighed and collected for histological examination or FACS analysis. MMTV-PyMT⁺ spontaneous breast tumours were measured 10 weeks after birth (6 weeks after bone marrow transplantation), three times a week, and mice were killed at week 16. Lung metastases were contrasted by intratracheal injection of a 15% India ink solution, by H&E staining on lung paraffin sections, or detected by qRT-PCR for the melanoma-specific gene *S100B* in the models involving B16F10 cells. For orthotopic pancreatic tumour growth, mice were anaesthetized with isoflurane, the stomach exteriorized via abdominal midline incision, and 1 × 10⁶ Panc02 tumour cells in 30 µl PBS were injected into the head of the pancreas using a 29-gauge needle. A successful intrapancreatic injection of tumour cells was identified by the appearance of a fluid bleb without intraperitoneal leakage. Mice displaying peritoneal leakage were immediately killed and excluded from the analysis. At day 12, primary tumours were removed and weighed. Enlarged lymph nodes were counted under a stereoscopic microscope. For the chemically induced colorectal cancer model, body-weight-matched mice received one intraperitoneal injection of 10 mg kg⁻¹ of azoxymethane (AOM) followed by 3 cycles of 7 days of 1.5% (cycle I) or 1.7% (cycle II–III) dextran sodium sulphate (DSS) in drinking water, starting from the day of AOM injection²⁸. After 160 days, the colon was collected and prepared for histological evaluation with the 'Swiss roll' technique²⁹. For the oncogene-driven hepatocellular carcinoma model, mice received a 1:1 molar ratio (3 µg total DNA) of piggyBac transposons encoding for *c-Myc* and *H-Ras*^{G12V} oncogenes, driven by the PGK promoter, together with the hyperactive piggyBac transposase-encoding plasmid³⁰. DNA solutions containing transposon/transposase plasmids were diluted in 2 ml of Ringer's solution and hydrodynamically delivered in 7 s through the tail vein. Mice were killed 24 weeks after the hydrodynamic injection.

Lung colonization assay. In the experimental metastasis assays, 0.5 × 10⁶ B16F10 cells were injected in the tail vein and lungs were collected after 12 days. To quantify pulmonary seeding, lungs were homogenized in Trizol (Ambion) and RNA was purified with the RNeasy Mini kit (Ambion) according to manufacturer's instructions. The expression of the melanocyte-specific gene *S100B* was measured as a readout of lung colonization by qRT-PCR following reverse transcription to complementary DNA with the QuantiTect Reverse Transcription kit (Qiagen).

Mice treatments. To induce chronic colitis, mice received 3 cycles of 7 days of 1.5% (cycle I) or 1.7% (cycle II–III) DSS in drinking water; 2 weeks after the last DSS cycle, the colon was collected and prepared for histological evaluation as described earlier²⁹. For *in vivo* MET inhibition, B16F10 tumour-bearing mice received 40 mg kg⁻¹ PF-04217903 (AbMole Bioscience) or the corresponding vehicle (0.5% methylcellulose in saline) via oral gavage every day once a day starting from day 2 after tumour injection and twice a day from day 11 until the end of the experiment; alternatively mice were treated with 50 mg kg⁻¹ INCB28060 (AbMole Bioscience) or 50 mg kg⁻¹ JNJ-38877605 (Selleckchem). For TNF-α inhibition *in vivo*, LLC tumour-bearing mice were randomized for comparable tumour volumes at the end stage and intraperitoneally (i.p.) injected with 10 mg kg⁻¹ of Enbrel or human IgG in PBS, 3 and 1 day before tumour collection. For HGF inhibition *in vivo*, LLC tumour-bearing mice were randomized when average tumour volume was 300 mm³ and i.p. injected with 0.2 mg per mouse of anti-HGF blocking antibody (AF-2207, R&D^{18,31}) or goat IgG in PBS. Tumours were collected 20 h later for histological analysis; 12-*O*-tetradecanoylphorbol-13-acetate (TPA) ear painting was done 5 h after antibodies administration and ears were collected 15 h later. For neutrophil depletion, mice were treated with 50 µg per 20 g body weight of rat anti-mouse Ly6G antibody (clone 1A8, BioXCell) or rat IgG every second day starting from day 4 after LLC tumour injection and every day from day 12 after tumour injection until the end of the experiment. Efficiency of neutrophil depletion was assessed by FACS in blood and tumours.

TPA model of acute skin inflammation. Phorbol ester TPA was used to induce acute skin inflammation as described previously³². Briefly, TPA (2.5 µg in 20 µl acetone per mouse) was topically applied on the ear skin of anaesthetized mice. The contralateral ear was painted with acetone alone as vehicle control. Mice were killed after 24 h and ears were collected in 2% PFA for histological analysis.

Zymosan-mediated acute peritonitis model. To induce acute peritonitis, zymosan A (Sigma) was prepared at 2 mg ml⁻¹ in sterile PBS. Four hours after i.p. injection of 0.1 mg zymosan A per mouse, inflammatory exudates were harvested by peritoneal lavage with 2 ml PBS. Cells were counted with a Burkert chamber and stained for Ly6G (1A8) and F4/80 (BM8) for FACS analysis.

Air pouch assay. To create subcutaneous air pouches, bone marrow transplanted chimaeric mice or Mrp8;Met^{fl/fl} or Mrp8;Met^{wt/wt} mice were injected with 3 ml of sterile air by dorsal subcutaneous injection with a butterfly 23 G needle on day 0 and on day 3. On day 6, 200 ng per mouse of murine CXCL1 or HGF dissolved in 0.5 ml PBS-Heparin (15 U ml⁻¹) or PBS-Heparin (15 U ml⁻¹) as control, were injected in the newly formed dorsal camera. After 4 h, inflammatory cells were harvested by washing the pouch with 5 ml of PBS. Cells were stained for Ly6G (1A8), washed and resuspended in PBS 0.1% BSA with unlabelled counting beads and quantified by FACS.

Mouse white blood cell isolation. Blood was collected from the retro-orbital vein in 10% heparin. For the isolation of white blood cells (WBCs), the blood was diluted in 1.25% dextran in saline to allow the sedimentation of red blood cells (RBCs). After 30 min, the erythrocyte-poor upper layer was collected and washed in PBS 0.1% BSA. The remaining RBCs were lysed in a hypotonic solution of 0.2% NaCl for 30 s and brought in isotonic condition with 1.6% NaCl and 0.1% glucose. WBCs were washed in PBS 0.1% BSA, counted and resuspended accordingly with the experimental setting.

Mouse blood neutrophil isolation. Blood was collected from the retro-orbital vein in 10% heparin and diluted in an equal volume of PBS 0.5% BSA. Up to 5 ml of diluted blood was layered on top of a discontinuous gradient of Histopaque 1119 (4 ml) and Histopaque 1077 (5 ml) from Sigma. The gradient was centrifuged for 30 min at 700g with the brake off. The neutrophil layer between the Histopaque 1077 and 1119 was collected and washed in PBS 0.5% BSA. RBC lysis was performed as described earlier. Neutrophils were washed in PBS 0.5% BSA, counted and resuspended according to the experimental condition. Alternatively, blood was sedimented in a saline solution containing 1.25% dextran and neutrophils were negatively selected with magnetic beads³³. Neutrophil purity, as assessed by the hemocytometer, was always higher than 93%.

Bone marrow neutrophil and mononuclear cell isolation. To reach reasonable amounts of protein, all the western blot analyses in mice were performed on neutrophils isolated from bone marrows. Mice were killed by cervical dislocation. Femurs and tibias were collected in cold sterile Hank balanced salt solution (HBSS; Invitrogen) and flushed with HBSS 0.25% BSA. Cells were layered on top of a discontinuous gradient of Percoll 81%, 62%, 55%, freshly prepared and centrifuged for 30 min at 2,000g with the brake off. Monocytes were collected at the interface between the bone marrow cells and the layer of Percoll 55%, whereas neutrophils were collected at the interface between Percoll 55% and 62%. Cells were washed in HBSS 0.25% BSA and RBC lysis was performed as described earlier. Neutrophils (or monocytes) were washed again, counted and resuspended according to the experimental setting. Neutrophil (or monocyte) purity, as assessed using a haemocytometer, was higher than 87%.

FACS analysis and flow sorting of blood or tumour-associated cells. Blood was collected in 10% heparin, incubated for 15 min with Mouse BD Fc Block (2.4G2, BD Pharmingen) 1:100 and stained for 20 min at room temperature. After RBC lysis, cells were washed and resuspended in FACS buffer (PBS containing 2% FBS and 2 mM EDTA). Tumours were minced in RPMI medium containing 0.1% collagenase type I and 0.2% dispase type I (Gibco) for 30 min at 37 °C and passed through a 70 and 40 µm cell strainer. After RBC lysis, cells were resuspended in FACS buffer. Lungs were collected after 7 min of transcardial perfusion with saline and processed as for the tumours. Single-cell suspensions were incubated for 15 min at 4 °C with Mouse BD Fc Block 1:100 in FACS buffer. The antibodies were added directly in the blocking solution in the appropriate combinations (as indicated in the figure legends). CD45 (30F-11), CD11b (M1/70), Ly6G (1A8), CD45R (RA3-6B2), CD3 (17A2), CD4 (RM4-5), IgE (R35-72), CD49b (DX5), Ly6C (AL-21) (all from BD Pharmingen), F4/80 (BM8), CD115 (AF598), MHCII (M5/114.15-12) (all from eBioscience), were used 1:200 for 2 × 10⁶ in 100 µl; Siglec-F (E50-2440, BD Pharmingen) was diluted 1:750. In all the stainings 7AAD (BD Pharmingen) was used to gate out dead cells. For intra-tumour proliferation, 1 mg of BrdU was i.p. injected in each mouse 4 h before tumour collection and cell proliferation was quantified on single-cell suspensions with the FITC BrdU Flow Kit (BD Bioscience) according to the manufacturer's protocol. Tumour apoptosis was assessed by staining single-cell suspensions for the apoptotic marker AnnexinV (1:40, BD Bioscience), excluding 7AAD-positive cells. For TAN apoptosis, tumour single-cell suspensions were gated for CD11b (M1/70) and Ly6G (1A8); AnnexinV and 7AAD were used to distinguish apoptotic or dead neutrophils. *In vitro* neutrophil apoptosis was performed by seeding neutrophils isolated from tumour-bearing mice at a concentration of 1 × 10⁶ per ml and stimulating them with or without LPS (1 µg ml⁻¹), alone or in combination with HGF (100 ng ml⁻¹) for 10 h at 37 °C. Cells were collected, washed and stained for AnnexinV and 7AAD. The combination of CD11b (M1/70), Ly6G (1A8) and MET (eBioscience, 1:50) was used to identify triple-positive MET-expressing neutrophils in blood or 7AAD-negative single-cell suspensions from tumours. Freshly stained samples were analysed by FACS Canto II (BD Bioscience). For tumour-associated

neutrophil sorting, the myeloid population was enriched by coating with CD11b-conjugated magnetic beads (MACS, Miltenyi Biotec), followed by separation through magnetic columns (MACS, Miltenyi Biotec), staining with Ly6G and sorting with a FACS Aria I (BD Bioscience). Cells were collected in RLT buffer (Qiagen) for RNA extraction or resuspended according to the experimental conditions.

Human neutrophil isolation. Ten millilitres of venous blood from healthy volunteers were collected in citrate-coated tubes and isolated by erythrocyte sedimentation with dextran and purification with a discontinuous plasma-Percoll gradient as already described³⁴.

Lung cancer patients. We enrolled four non-small-cell lung carcinoma patients with no previous history of oncological, chronic inflammatory, or autoimmune diseases within 10 years before this study. This patient list includes 2 males (61 and 71 years of age) and 2 females (64 and 68 years of age), of which 3 were smokers (1 T1N0M0 adenocarcinoma, 1 T2N0M0 large-cell carcinoma, 1 T3N0M0 squamous-cell carcinoma) and 1 was a non-smoker (T2N0M0 adenocarcinoma). The protocol was approved by the Ethics Committee of the University Hospitals Gasthuisberg (Leuven), and all subjects consented before study participation.

Flow sorting of neutrophils from lung cancer patients. Lung tumour biopsies or healthy tissues were minced in RPMI medium containing 0.1% collagenase type I, 0.2% dispase type I and DNase I 100 U ml⁻¹ (60 min at 37 °C), passed through a 19 G needle and passed through a 70 and 40 µm cell strainer. After RBC lysis, cells were resuspended in FACS buffer (PBS containing 2% FBS and 2 mM EDTA) and counted. The myeloid population, enriched using CD11b-conjugated magnetic beads (MACS, Miltenyi Biotec) and separated through a magnetic column (MACS, Miltenyi Biotec), was stained with anti-CD66b (G10F5, BD Pharmingen, 1:100) for 20 min at 4 °C and sorted with FACS Aria I (BD Bioscience). Cells were counted and resuspended in RLT buffer (Qiagen) for RNA extraction.

Endothelial cell isolation. Lungs were collected and a single-cell suspension was obtained as described earlier. Endothelial cells were obtained by performing a negative selection for CD45 (30F-11) and F4/80 (CI:A3-1) followed by a positive selection for CD31 (MEC 13.3) by using magnetic beads (Dynabeads, Invitrogen) according to the manufacturer's protocol.

Peritoneal macrophages. Five millilitres of sterile PBS were injected in the peritoneum of anaesthetized mice and collected after 3 min. Cells were centrifuged, washed and cultured overnight.

TCM and LLC (or A549) CCM preparation. Two grams of end-stage LLC tumour explanted from WT mice were chopped and incubated at 37 °C in 7 ml of DMEM (supplemented with 2 mM glutamine, 100 units ml⁻¹ penicillin/100 µg ml⁻¹ streptomycin) FBS-free (DMEM 0% FBS). 5 × 10⁴ LLC (or A549) were seeded in a 6-multiwell plate in DMEM 10% FBS and incubated at 37 °C. Medium alone (DMEM 0% FBS or DMEM 10% FBS, respectively) was used to prepare mock controls. After 72 h, the medium was filtered, supplemented with 2 mM glutamine and 20 mM HEPES and stored at -20 °C. TCM and mock medium (DMEM 0% FBS) were diluted 1:5 in DMEM 10% FBS; CCM and mock medium (DMEM 10% FBS) were diluted 4:5 in DMEM FBS-free.

qRT-PCR. For mRNA analysis, 1 × 10⁵ or 3 × 10⁵ mouse or human blood neutrophils, respectively, were incubated in normoxic (21% oxygen) or hypoxic (1% oxygen) conditions, or stimulated with TCM (plus 50 µg ml⁻¹ Enbrel or human IgG where indicated), CCM, A549-CCM, 100 ng ml⁻¹ of murine or human TNF-α, 50 ng ml⁻¹ LPS, or mock medium in a 96-multiwell plate for 4 h at 37 °C. For NF-κB inhibition, 0.18 × 10⁶ neutrophils were pre-treated with 10 µM 6-amino-4-(4-phenoxyphenylethylamino) quinazoline (Calbiochem) for 1 h at 37 °C and stimulated with 100 ng ml⁻¹ of murine TNF-α for 1 h at 37 °C. 2 × 10⁵ HUVECs were seeded in a 24-multiwell plate coated with 0.1% gelatin and stimulated with 5 ng ml⁻¹ IL-1α in DMEM 10% FBS for 4 h at 37 °C. Cells were washed in PBS, collected in RLT buffer (Qiagen) and kept at -80 °C. RNA was extracted with the RNeasy Micro kit (Qiagen) according to the manufacturer's instructions. Reverse transcription to cDNA was performed with the SuperScript III First Strand cDNA Synthesis Kit (Life Technologies) according to the manufacturer's protocol. Pre-made assays were purchased from Applied Biosystem, except for Nos2 that was provided by IDT. cDNA, primer/probe mix and TaqMan Fast Universal PCR Master Mix were prepared in a volume of 10 µl according to manufacturer's instructions (Applied Biosystems). Samples were loaded into an optical 96-well Fast Thermal Cycling plate (Applied Biosystems) and qRT-PCR were performed using an ABI Prism 7500 Fast Real-Time PCR System (Applied Biosystems).

ELISA. To quantify plasma, intra-tumoural, tumour-released (TCM) and neutrophil-released HGF, a murine HGF ELISA kit (R&D) was used according to manufacturer's protocols. Blood was collected from tumour-free or tumour-bearing mice and plasma was prepared according to manufacturer's instruction. TCM was prepared as described earlier. Tumour proteins were extracted in Extraction Buffer (20 M Tris HCl, 150 mM NaCl, 1% Triton X-100, 10% glycerol, 5 mM EDTA). 0.2 × 10⁶ neutrophils were cultured for 20 h in DMEM complete in

presence or absence of 100 ng ml^{-1} of murine TNF- α . Medium was collected, spun down and supernatant stored at -80°C until use. Mock medium was used as negative control. For phospho-MET quantification, 6×10^6 mouse blood neutrophils isolated from tumour-bearing mice were cultured in the presence or absence of 100 ng ml^{-1} of murine TNF- α ; 11 h later, cells were stimulated or not with 100 ng ml^{-1} of mouse HGF in the presence of 1 mM orthovanadate for 3 min at 37°C , washed in PBS supplemented with 1 mM orthovanadate and $1 \times$ phosStop (Roche) and lysed in Extraction Buffer supplemented with 1 mM orthovanadate, $2 \times$ phosStop and Complete Mini protease inhibitor cocktail (Roche) for 20 min at 4°C . After clearance, samples were quantified and the same amount of proteins was used for MET and phospho-MET detection using a sandwich ELISA. Briefly, 96-well microtitre plates (MaxiSorp, Nunc) were coated with $1 \mu\text{g ml}^{-1}$ of anti-mouse MET antibody (AF527, R&D Systems) overnight at 4°C and then incubated for 2 h at room temperature in blocking buffer (PBS, 0.1% Tween-20, 6% non-fat dry milk). The same amount of proteins per sample was diluted in blocking buffer and incubated for 2 h at room temperature on the ELISA plate. After 6 washes in PBS 0.1% Tween-20, samples were incubated for 2 h at room temperature with the mouse anti-MET (3D4, Invitrogen) or the mouse anti-phosphotyrosine (4G10, Merck Millipore) antibodies diluted 1:500 in blocking buffer, then washed 6 times in PBS 0.1% Tween-20, and incubated with goat anti-mouse immunoglobulins conjugated to horseradish peroxidase (sc-2031, Santa Cruz Biotechnology) diluted 1:500 in blocking buffer for 2 h at room temperature. Signals were developed by 15 min incubation with the 3,3',5,5'-tetramethylbenzidine (TMB) substrate solution (Promega). After stopping the reaction with H_2SO_4 , absorbance was measured at 450 nm and corrected for 630 nm with a spectrophotometer.

Western blot. To assess MET deletion, bone marrow cells, neutrophils, peritoneal macrophages, monocytes (all cultured overnight in TCM) or endothelial cells were lysed in hot Laemmli buffer (2.5% SDS, 25% Tris-HCl pH 6.8) for 10 min at 96°C , sonicated, cleared and quantified. Alternatively, 2×10^6 bone-marrow-derived neutrophils from WT mice were stimulated with TCM, CCM, 100 ng ml^{-1} of murine TNF- α (or mock medium 0% FBS or 10% FBS as control) for 20 h at 37°C . For the co-culture with HUVECs, a monolayer of HUVECs was stimulated for 4 h with 5 ng ml^{-1} IL-1 α at 37°C , and washed before neutrophil seeding. After 20 h of stimulation, neutrophils were collected using Cell Dissociation Buffer Enzyme Free PBS-Based (Gibco). Cells were washed in PBS, lysed in $15 \mu\text{l}$ of a protease inhibitor mixture and incubated for 15 min on ice. The protease inhibitor mixture was obtained by dissolving one tablet of Complete Mini protease inhibitor mixture (Roche) in 5 ml of PBS with 2 mM diisopropyl fluorophosphate (DFP; Acros Organics). After addition of an equal amount of $2 \times$ SDS sample buffer supplemented with 4% 2-mercaptoethanol, the lysates were boiled for 15 min and kept at -80°C until use. NF- κB inhibition was achieved by pre-treating 7×10^6 neutrophils with $10 \mu\text{M}$ 6-amino-4-(4-phenoxyphenylethylamino) quinazoline (Calbiochem) for 1 h at 37°C ; cells were then stimulated with murine TNF- α (100 ng ml^{-1}) for 5 h before lysis. Human MET was assessed by stimulating 3×10^7 blood neutrophils isolated from the blood of healthy volunteers with A549-CCM, 100 ng ml^{-1} human TNF- α , 50 ng ml^{-1} LPS (or mock medium 10% FBS as control) for 20 h. Cells were incubated with 2.7 mM DFP for 15 min at 4°C , collected and washed in PBS supplemented with 2.7 mM DFP and Complete Mini protease inhibitor $1 \times$, and lysed in hot Laemmli buffer at 96°C for 10 min. Cell lysates were sonicated, cleared and quantified. $6 \times$ loading buffer was added before loading on the gel. The following primary antibodies were used: mouse anti-mouse Met (3D4, Invitrogen), mouse anti-mouse β -actin (I-19, Santa Cruz), mouse anti-vinculin (hVIN-1, Sigma), rabbit anti-human MET (D1C2, Cell Signaling), horseradish peroxidase (HRP)-conjugated anti- β -tubulin (Abcam). The following secondary antibodies were used: HRP-conjugated goat anti-mouse and HRP-conjugated goat anti-rabbit (Santa Cruz). Signal was visualized by Enhanced Chemiluminescent Reagents (ECL; Invitrogen) or West Femto by Thermo Scientific according to the manufacturer's instructions.

Adhesion assay. 4×10^4 HUVECs were seeded in M199 complete in a 96-multiwell plate, previously coated with 0.1% gelatin. After 12 h, HUVECs were stimulated with 5 ng ml^{-1} IL-1 α in DMEM 10% FBS at 37°C . After 4 h the endothelial monolayer was gently washed and 2.5×10^5 WBCs were isolated indistinctly from Tie2;Met^{wt/wt} and Tie2;Met^{fl/fl} mice or from WT \rightarrow WT and KO \rightarrow WT transplanted mice, were seeded on top of it, with or without murine HGF (50 ng ml^{-1}). After 15 min non-adherent cells were washed out whereas adherent cells were detached by using a Cell Dissociation Buffer Enzyme Free PBS-Based (Gibco). Cells were stained for Ly6G (clone 1A8), washed and resuspended in PBS-BSA 0.1% with unlabelled counting beads (BD Bioscience) and quantified by FACS Canto II (BD Bioscience).

Transmigration and migration assay. For the transmigration assay, 2×10^5 HUVECs were seeded on $3 \mu\text{m}$ polycarbonate membrane (Transwell; Costar) previously coated with 0.1% gelatin in M199 complete. After 12 h, HUVECs were

stimulated for 4 h at 37°C in DMEM 10% FBS with 5 ng ml^{-1} IL-1 α and then washed. 5×10^5 WBCs isolated indistinctly from Tie2;Met^{wt/wt} and Tie2;Met^{fl/fl} mice or from WT \rightarrow WT and KO \rightarrow WT transplanted mice were seeded on top of the endothelial monolayer, while mock medium, TCM (with or without $3 \mu\text{g ml}^{-1}$ anti-HGF antibody AF-2207; R&D) or 50 ng ml^{-1} murine HGF was added in the bottom. After 2 h at 37°C , transmigrated cells were collected from the bottom chambers and from the lower side of the filter with cold PBS 0.5% EDTA. Cells were stained and Ly6G⁺ cells were quantified as described earlier. In the migration assays WBCs were seeded directly on top of $3 \mu\text{m}$ polycarbonate porous membranes.

Nitric oxide measurement by FACS. Neutrophils isolated from the blood of WT or KO LLC-tumour bearing mice were co-cultured for 4 h with LLC shMet, washed and resuspended in 20 mM HEPES-PBS, and incubated for 10 min with $5 \mu\text{M}$ DAF-FM diacetate (Molecular Probes) in the absence or presence of mouse HGF (100 ng ml^{-1}) at 37°C . Cells were then washed and analysed by FACS.

Cytotoxicity assay. LLC shMet or T241 shMet were transduced with a luciferase-expressing lentiviral vector (EX-hLUC-Lv14 from GeneCopoeia); 10^4 cells were then seeded in DMEM 10% FBS in a 96-multiwell plate. After 4 h, 0.2×10^6 neutrophils purified from the blood of tumour-bearing mice or directly from the tumours themselves, were co-cultured with the cancer cells in DMEM 2% FBS for 4 h at 37°C , with or without 100 ng ml^{-1} mouse HGF or 1 mM L-NMMA (Sigma). After washing, adherent cells were lysed in 0.2% Triton, 1 mM dithiothreitol (DTT). Luciferase signal was revealed with a microplate luminometer. The use of shMet was thought to prevent any possible confounding activity of MET on cancer cell survival and thus to restrict the effect of HGF to neutrophils only.

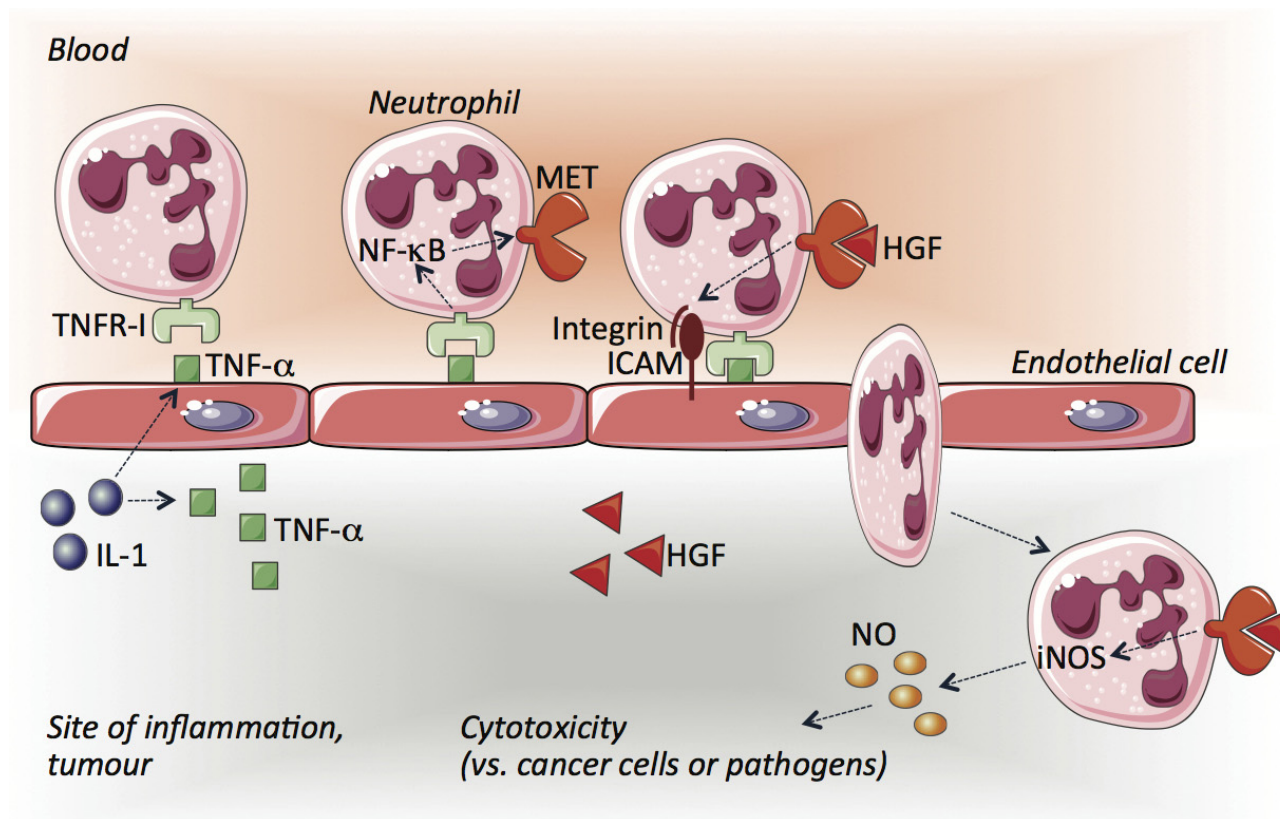
Histology and immunostainings. To obtain serial 7- μm -thick sections, tissue samples were immediately frozen in OCT compound or fixed in 2% PFA overnight at 4°C , dehydrated and embedded in paraffin. Paraffin slides were first rehydrated to proceed further with antigen retrieval in citrate solution (DAKO). Cryosections were thawed in water and fixed in 100% methanol. If necessary, 0.3% H_2O_2 was added to methanol to block endogenous peroxidases. The sections were blocked with the appropriate serum (DAKO) and incubated overnight with the following antibodies: rat anti-CD45 (30F-11, BD Pharmingen) 1:100, rat anti-Ly6G (1A8, BD Pharmingen) 1:100, rat anti-CD31 (MEC 13.3, BD Pharmingen) 1:200, rabbit anti-FITC (Serotec) 1:200, goat anti-phosphohistone H3 (Cell Signaling) 1:100, rat anti-F4/80 (CI:A3-1, Serotec) 1:100, mouse anti-NK1.1-biotin (PK136, BD Pharmingen) 1:200, rat anti-CD45R (RA3-6B2, BD Pharmingen) 1:100, rat anti-CD4 (H129.9, BD Pharmingen) 1:100, rat anti-CD8 (53-6.72, BioXCell) 1:100, hamster anti-CD11c biotin (N418, eBioscience) 1:100, mouse anti-3-nitrotyrosin (HM.11 Santa Cruz) 1:200. Appropriate secondary antibodies were used: Alexa488-or Alexa568-conjugated secondary antibodies (Molecular Probes) 1:200, HRP-labelled antibodies (DAKO) 1:100, Biotin-labelled antibodies (Jackson ImmunoResearch) 1:100. When necessary, tyramide signalling amplification (Perkin Elmer, Life Sciences) was performed according to the manufacturer's instructions. Whenever sections were stained in fluorescence, ProLong Gold mounting medium with DAPI (Invitrogen) was used. Otherwise, 3,3'-diaminobenzidine was used as a detection method followed by Harris' haematoxylin counterstaining, dehydration and mounting with DPX. Apoptotic cells were detected by the TUNEL method, using the AptoTag peroxidase *in situ* apoptosis detection kit (Millipore) according to the manufacturer's instructions. For the double staining TUNEL and Ly6G, TUNEL staining was performed as described earlier, followed by Ly6G staining by using the Vectastain ABC kit (Vector Laboratories) according to the manufacturer's instructions. Tumour necrosis and lung metastasis were evaluated by H&E staining. Necrotic area was defined as the area including necrotic cancer cells, inflammatory cells and stromal cells, compared to the total area of the field. Necrotic cells display a more glassy homogeneous appearance in the cytoplasm with increased eosinophilia, while the nuclear changes are reflected by karyolysis, pyknosis and karyorrhexis. Alternatively, the necrotic tissue was visualized by autofluorescence as previously described³⁵. Microscopic analysis was done with an Olympus BX41 microscope and Cell Sense imaging software or a Zeiss Axioplan microscope with KS300 image analysis software. The morphometric analysis was performed by acquiring 4–6 fields per section on five independent sections (at a distance of $40 \mu\text{m}$ in depth during sectioning) from the same biological tissue sample. The values in the graphs represent the average of the means of at least five samples and the standard error indicates the variability among the different samples.

Hypoxia assessment and tumour perfusion. Tumour hypoxia was detected by injection of 60 mg kg^{-1} pimonidazole into tumour-bearing mice 1 h before tumour harvesting. To detect the formation of pimonidazole adducts, tumour cryosections were immunostained with Hypoxyprobe-1-Mab1 (Hypoxyprobe kit, Chemicon) following the manufacturer's instructions. Perfused tumour vessels were counted on tumour cryosections from mice injected intravenously with 0.05 mg fluorescein isothiocyanate (FITC)-conjugated lectin (Lycopersicon esculentum; Vector Laboratories).

Tumour-derived nitric oxide production. LLC tumours were collected 8 days after injection, cut in pieces of about 5×5 mm, weighted and incubated at 37°C in a 24-multiwell plate with 800 μl of DMEM. After 24 h, the media was collected, centrifuged to remove cell debris, and NO levels were measured using the Griess reagent system kit (Promega).

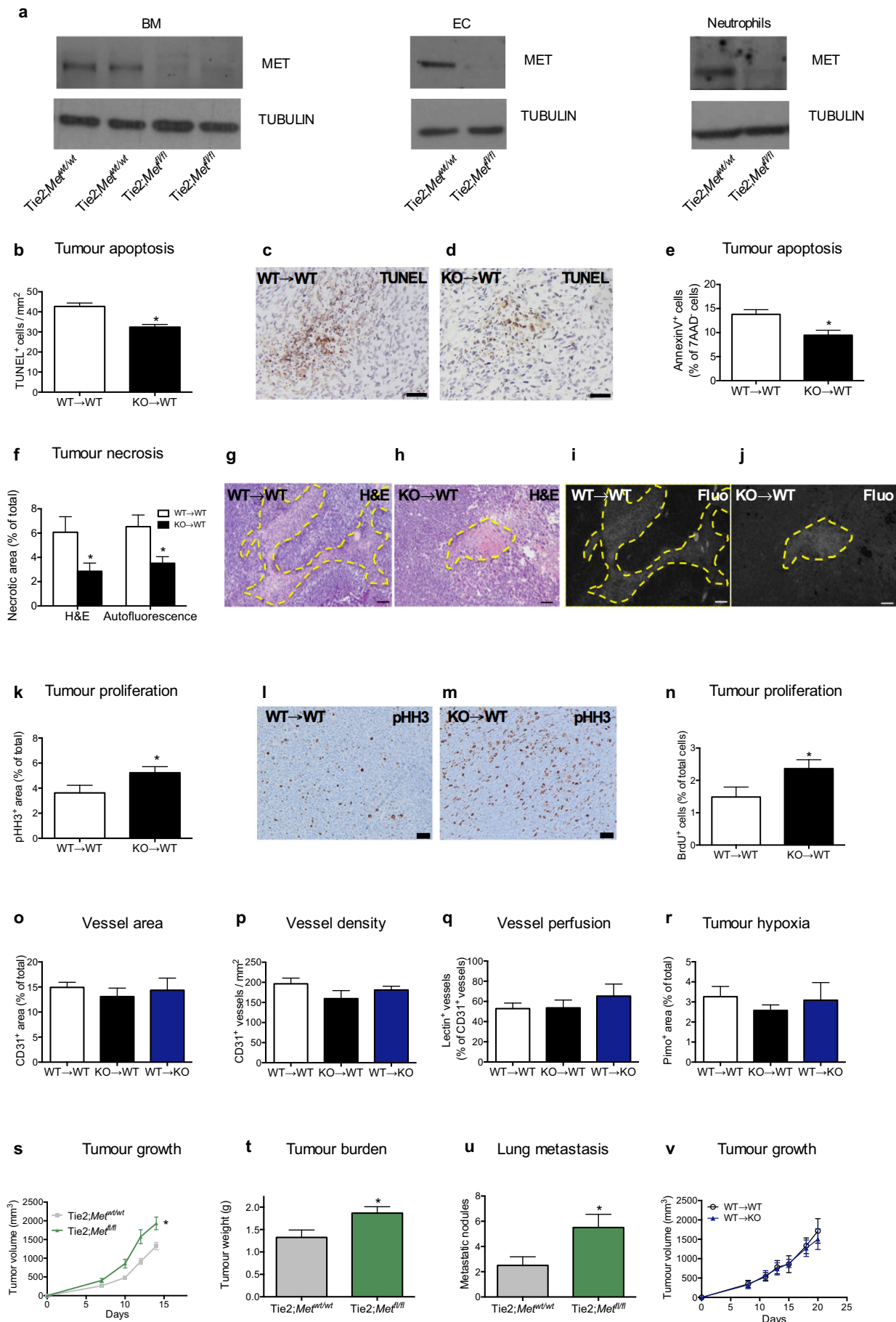
Statistics. Data entry and all analyses were performed in a blinded fashion. All statistical analyses were performed using GraphPad Prism software. Statistical significance was calculated by two-tailed unpaired *t*-test on two experimental conditions or two-way analysis of variance (ANOVA) when repeated measures were compared, with $P < 0.05$ considered statistically significant. Data were tested for normality using the D'Agostino–Pearson omnibus test (for $n > 8$) or the Kolmogorov–Smirnov test (for $n \leq 8$) and variation within each experimental group was assessed. Detection of mathematical outliers was performed using the Grubbs' test in GraphPad. Sample sizes for all experiments were chosen based on previous experiences. Independent experiments were pooled and analysed together whenever possible as detailed in figure legends. All graphs show mean values \pm s.e.m.

22. Passegué, E., Wagner, E. F. & Weissman, I. L. JunB deficiency leads to a myeloproliferative disorder arising from hematopoietic stem cells. *Cell* **119**, 431–443 (2004).
23. Van Ziffle, J. A. & Lowell, C. A. Neutrophil-specific deletion of Syk kinase results in reduced host defense to bacterial infection. *Blood* **114**, 4871–4882 (2009).
24. Abram, C. L., Roberge, G. L., Pao, L. I., Neel, B. G. & Lowell, C. A. Distinct roles for neutrophils and dendritic cells in inflammation and autoimmunity in *motheaten* mice. *Immunity* **38**, 489–501 (2013).
25. Albanesi, M. *et al.* Neutrophils mediate antibody-induced antitumor effects in mice. *Blood* **122**, 3160–3164 (2013).
26. Lagasse, E. & Clerc, R. G. Cloning and expression of two human genes encoding calcium-binding proteins that are regulated during myeloid differentiation. *Mol. Cell. Biol.* **8**, 2402–2410 (1988).
27. Hamm, A. *et al.* PHD2 regulates arteriogenic macrophages through TIE2 signalling. *EMBO Mol. Med.* **5**, 843–857 (2013).
28. Neufert, C., Becker, C. & Neurath, M. F. An inducible mouse model of colon carcinogenesis for the analysis of sporadic and inflammation-driven tumor progression. *Nature Protocols* **2**, 1998–2004 (2007).
29. Moolenbeek, C. & Ruitenberg, E. J. The “Swiss roll”: a simple technique for histological studies of the rodent intestine. *Lab. Anim.* **15**, 57–59 (1981).
30. Chen, X. & Calvisi, D. F. Hydrodynamic transfection for generation of novel mouse models for liver cancer research. *Am. J. Pathol.* **184**, 912–923 (2014).
31. Schira, J. *et al.* Significant clinical, neuropathological and behavioural recovery from acute spinal cord trauma by transplantation of a well-defined somatic stem cell from human umbilical cord blood. *Brain* **135**, 431–446 (2012).
32. Cramer, T. *et al.* HIF-1 α is essential for myeloid cell-mediated inflammation. *Cell* **112**, 645–657 (2003).
33. Cotter, M. J., Norman, K. E., Hellewell, P. G. & Ridger, V. C. A novel method for isolation of neutrophils from murine blood using negative immunomagnetic separation. *Am. J. Pathol.* **159**, 473–481 (2001).
34. Haslett, C., Guthrie, L. A., Kopaniak, M. M., Johnston, R. B. Jr & Henson, P. M. Modulation of multiple neutrophil functions by preparative methods or trace concentrations of bacterial lipopolysaccharide. *Am. J. Pathol.* **119**, 101–110 (1985).
35. Shaked, Y. *et al.* Rapid chemotherapy-induced acute endothelial progenitor cell mobilization: implications for antiangiogenic drugs as chemosensitizing agents. *Cancer Cell* **14**, 263–273 (2008).



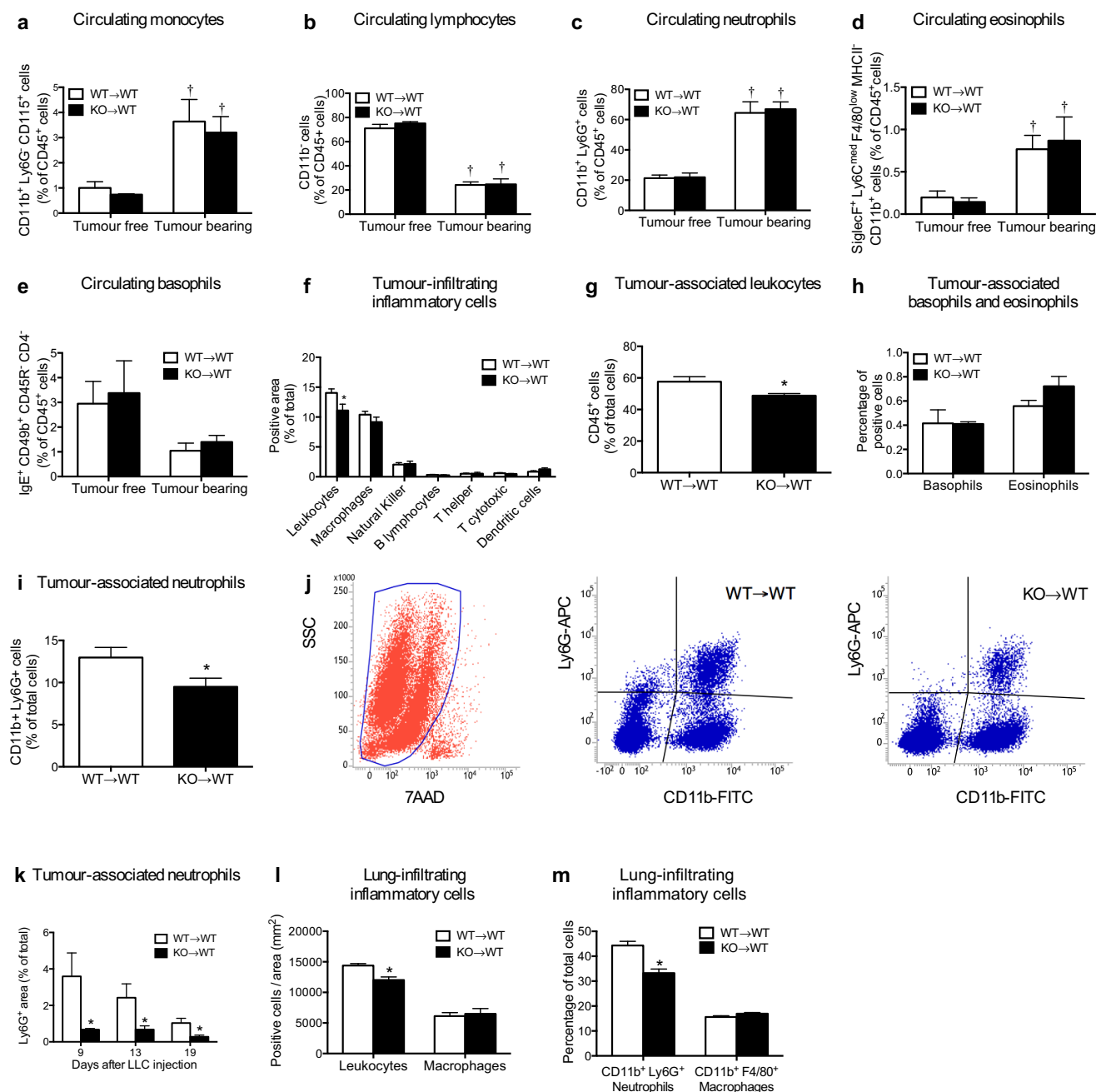
Extended Data Figure 1 | Scheme illustrating the role of MET in neutrophils. During cancer or infections, the release of cytokines such as IL-1 at the inflammatory site will promote the expression of TNF- α on the endothelium and the surrounding tissue. When circulating neutrophils encounter the activated endothelium, TNF- α will unleash NF- κ B through binding to TNFR1, which in turn will induce MET expression on the neutrophil surface. HGF, also released and proteolytically activated at the site of

inflammation, will bind to MET and stimulate the firm adhesion of neutrophils to the endothelium, probably via integrin engagement, and thus neutrophil diapedesis. Once extravasated, the HGF/MET pathway will still function on neutrophils by reinforcing their cytotoxic response through the induction of iNOS and NO production, ultimately favouring a bactericidal and tumoricidal neutrophil phenotype.



Extended Data Figure 2 | *Met* deletion in immune cells, but not in endothelial cells, fosters tumour growth. **a**, MET expression in total bone marrow (BM) cells, endothelial cells (EC) and neutrophils harvested from *Met* floxed mice intercrossed with the Tie2:Cre deleter thus generating Tie2;*Met*^{fl/fl} (KO) or Tie2;*Met*^{wt/wt} (WT) mice. Western blots are representative of three repetitions on independent biological replicates. Western blot images have been cropped for presentation. Full scan images are shown in Supplementary Fig. 1. **b–d**, Quantification (**b**) and representative images of tumour sections' TdT-mediated dUTP nick end labelling (TUNEL) stainings (**c**, **d**) from subcutaneous end-stage LLC tumours in WT→WT and KO→WT mice. Data combine two independent experiments; total *n* = 10 mice per condition. **e**, FACS quantification of AnnexinV⁺ 7AAD[−] early apoptotic tumour cells in WT→WT and KO→WT mice. Data combine two independent experiments; total *n* = 8 mice per condition. **f–j**, Tumour necrosis quantification in WT→WT and KO→WT mice (**f**), assessed by histological evaluation of H&E-stained tumour sections (**g**, **h**) and by measurement of autofluorescent tumour areas (**i**, **j**); yellow dotted lines demarcate necrosis. Data combine two independent experiments; total *n* = 10 mice per condition. **k–m**, Quantification (**k**) and representative images of tumour sections stained

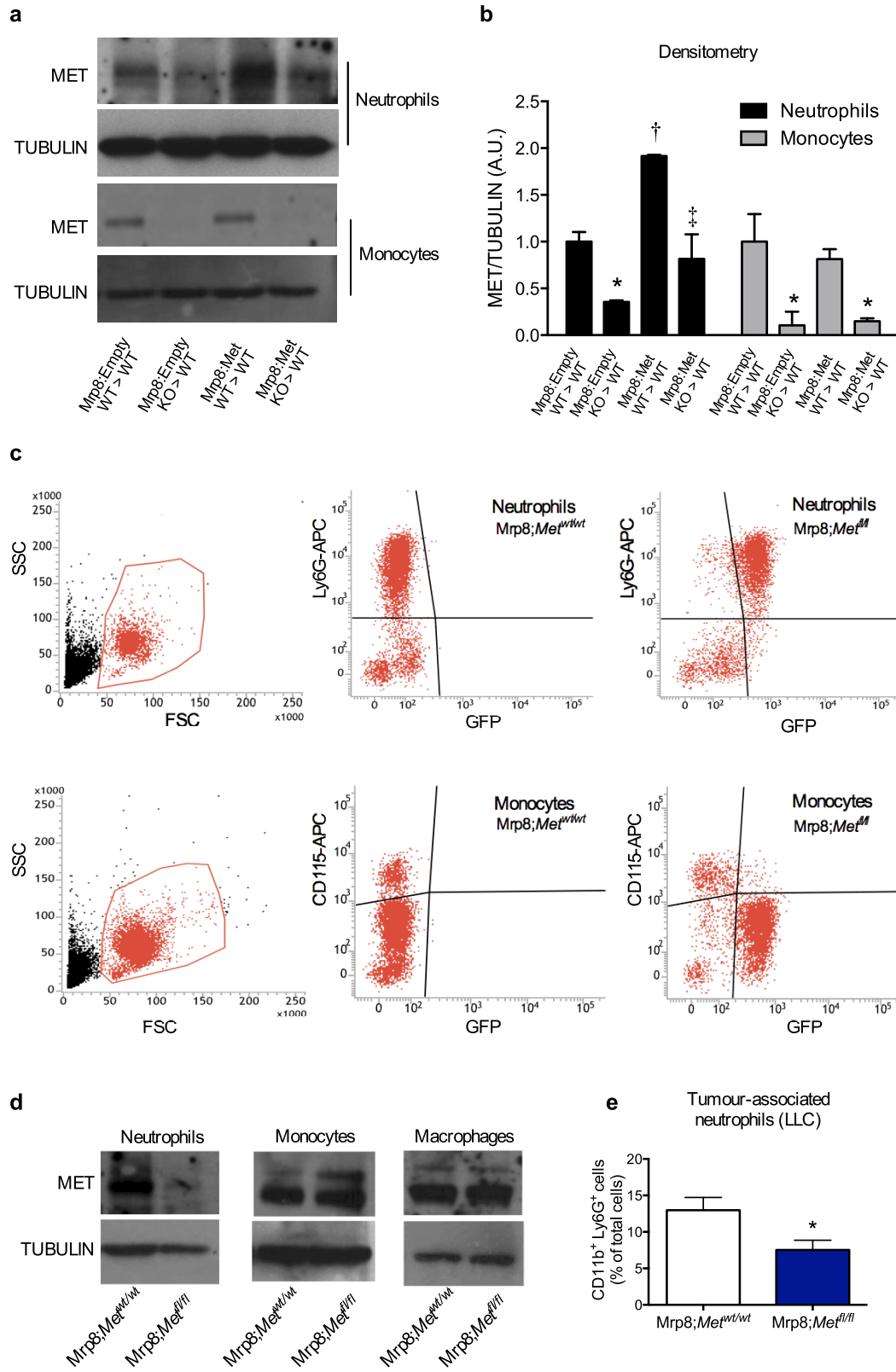
for the proliferation marker pHH3 (**l**, **m**) from subcutaneous end-stage LLC tumours in WT→WT and KO→WT mice. Data combine two independent experiments; total *n* = 10 mice per condition. **n**, FACS quantification of BrdU⁺ proliferating tumour cells in WT→WT and KO→WT mice. Data combine two independent experiments; total *n* = 10 mice per condition. **o–r**, CD31⁺ vessel area (**o**), vessel density (**p**), lectin perfusion (**q**) and hypoxic (Pimo⁺) area (**r**) in LLC subcutaneous tumours from KO→WT mice (in which the haematopoietic/immune system is knocked out for *Met*) or WT→KO mice (in which endothelial cells only are knocked out for *Met*) compared to control WT→WT mice. Data in **o–r** combine two independent experiments; total *n*: WT→WT, 12; KO→WT, 8; WT→KO, 8. **s–u**, Subcutaneous LLC tumour growth (**s**), weight (**t**) and lung metastases (**u**) in Tie2;*Met*^{fl/fl} compared to Tie2;*Met*^{wt/wt} mice. Data combine two independent experiments; total *n*: Tie2;*Met*^{wt/wt}, 12; Tie2;*Met*^{fl/fl}, 10. **v**, Subcutaneous LLC tumour growth in endothelial-cell-specific *Met* KO (WT→KO) and control (WT→WT) mice. Data combine two independent experiments; total *n* = 8 per condition. **P* < 0.05 versus WT→WT (**b**, **e**, **f**, **k**, **n**), versus Tie2;*Met*^{wt/wt} (**s–u**). Scale bars: 50 μm (**c**, **d**, **l**, **m**); 100 μm (**g–j**). All graphs show mean ± s.e.m.



Extended Data Figure 3 | Circulating and tumour-infiltrating immune cells upon *Met* deletion.

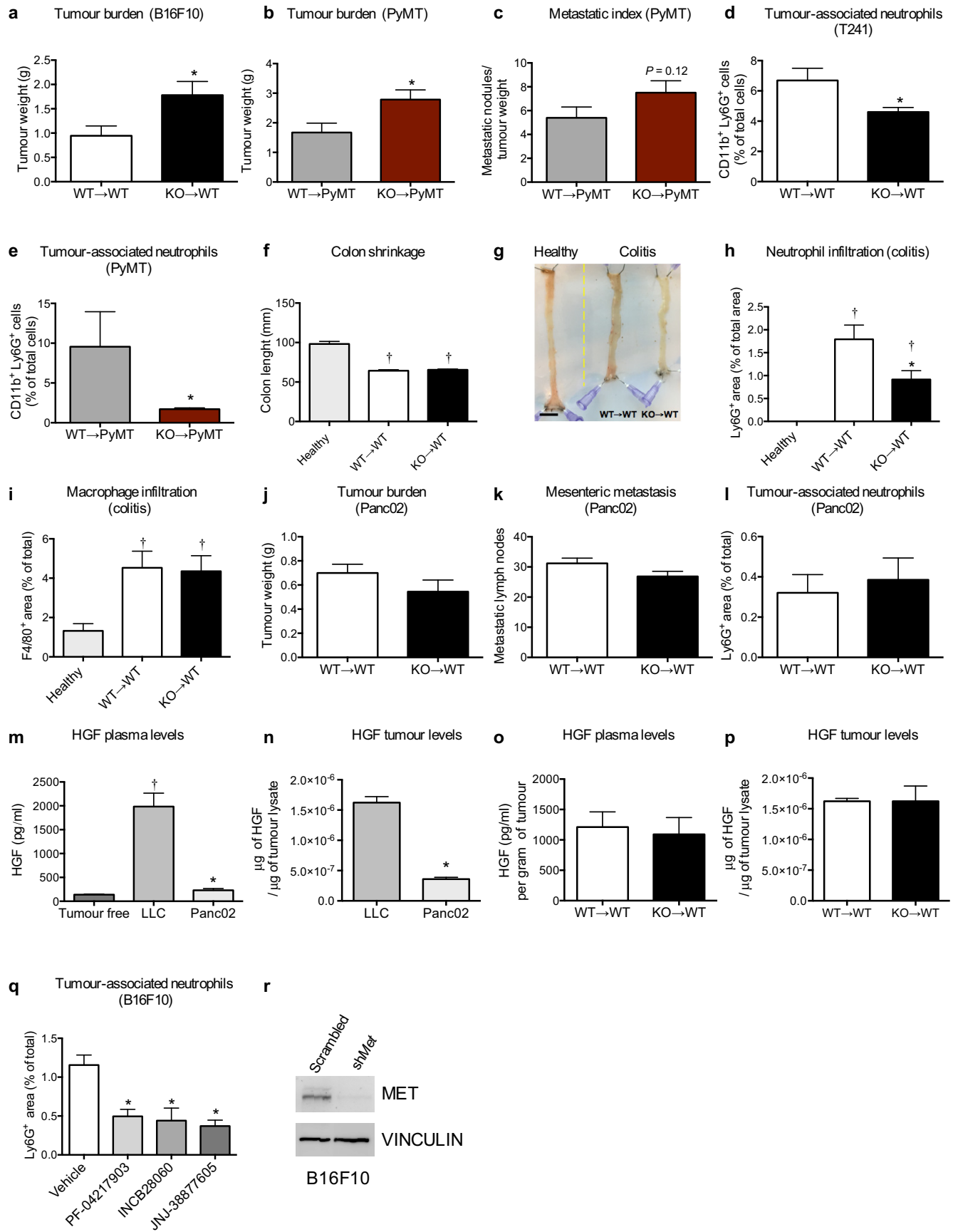
a–e, FACS analysis showing percentages of circulating monocytes (**a**), lymphocytes (**b**), neutrophils (**c**), eosinophils (**d**) and basophils (**e**) in tumour-free or in LLC-tumour-bearing WT→WT and KO→WT mice. Data combine two independent experiments; total $n = 8$ mice per condition. **f**, Quantification of LLC tumour sections stained for the pan-leukocyte marker CD45, the macrophage marker F4/80, the NK marker NK1.1, the B lymphocyte marker CD45R, the T helper cell marker CD4, the cytotoxic T cell marker CD8 and the dendritic cell marker CD11c (with exclusion of F4/80⁺ area) in WT→WT and KO→WT mice. Data combine two independent experiments; total $n = 8$ mice per condition. **g, h**, FACS quantification for tumour-associated CD45⁺ leukocytes (**g**) or CD45⁺ IgE⁺ CD49b⁺ CD4[−] CD45R[−] basophils and CD45⁺ CD11b⁺ SiglecF⁺ Ly6C^{med} F4/80^{low} MHCII[−] eosinophils (**h**) in WT→WT and KO→WT mice. Data combine two independent experiments; total $n = 8$ mice per condition. **i, j**, FACS quantification (**i**) and gating strategy (**j**) for

tumour-associated neutrophils selected from the main tumour cell population negative for 7AAD staining; tumour-associated neutrophils were then gated as CD11b and Ly6G double-positive cells. Data combine two independent experiments; total n : WT→WT, 11; KO→WT, 10. **k**, Ly6G⁺ tumour infiltration at day 9, day 13 and day 19 after LLC subcutaneous tumour injection in WT→WT and KO→WT mice. Data combine two independent experiments; total $n = 8$ mice per condition. **l**, Morphometric quantification of leukocytes and macrophages on CD45- and F480-stained lung sections, respectively, from LLC-tumour-bearing WT→WT or KO→WT mice. Data combine two independent experiments; total $n = 8$ mice per condition. **m**, FACS quantification of CD11b⁺ Ly6G⁺ neutrophils and CD11b⁺ F4/80⁺ macrophages infiltrating metastatic lungs from LLC-tumour-bearing WT→WT or KO→WT mice. Data combine two independent experiments; total $n = 8$ mice per condition. * $P < 0.05$ versus WT→WT (**f, g, i, k–m**); † $P < 0.05$ versus tumour free (**a–d**). All graphs show mean \pm s.e.m.



Extended Data Figure 4 | MET in neutrophils is required for their anti-tumour activity. **a, b**, Western blot analysis (**a**) and relative densitometric analysis (**b**) for MET expression in bone marrow neutrophils and monocytes upon reconstitution of WT recipient mice by WT or KO HSPCs transduced *in vitro* with an empty vector (Mrp8:Empty) or a vector expressing *Met* under the neutrophil-specific promoter Mrp8 (Mrp8:Met); tubulin was used as loading control. Western blots are representative of three repetitions on independent biological samples where each sample is the pool of neutrophils or monocytes isolated from three mice. Densitometric analysis was performed on these three western blots. A.U., arbitrary units. **c**, FACS analysis for green fluorescent protein (GFP) in circulating Ly6G⁺ neutrophils or CD115⁺ monocytes, harvested from the neutrophil-specific Mrp8:Cre line carrying separate expression of GFP because of an internal ribosome entry site (IRES)

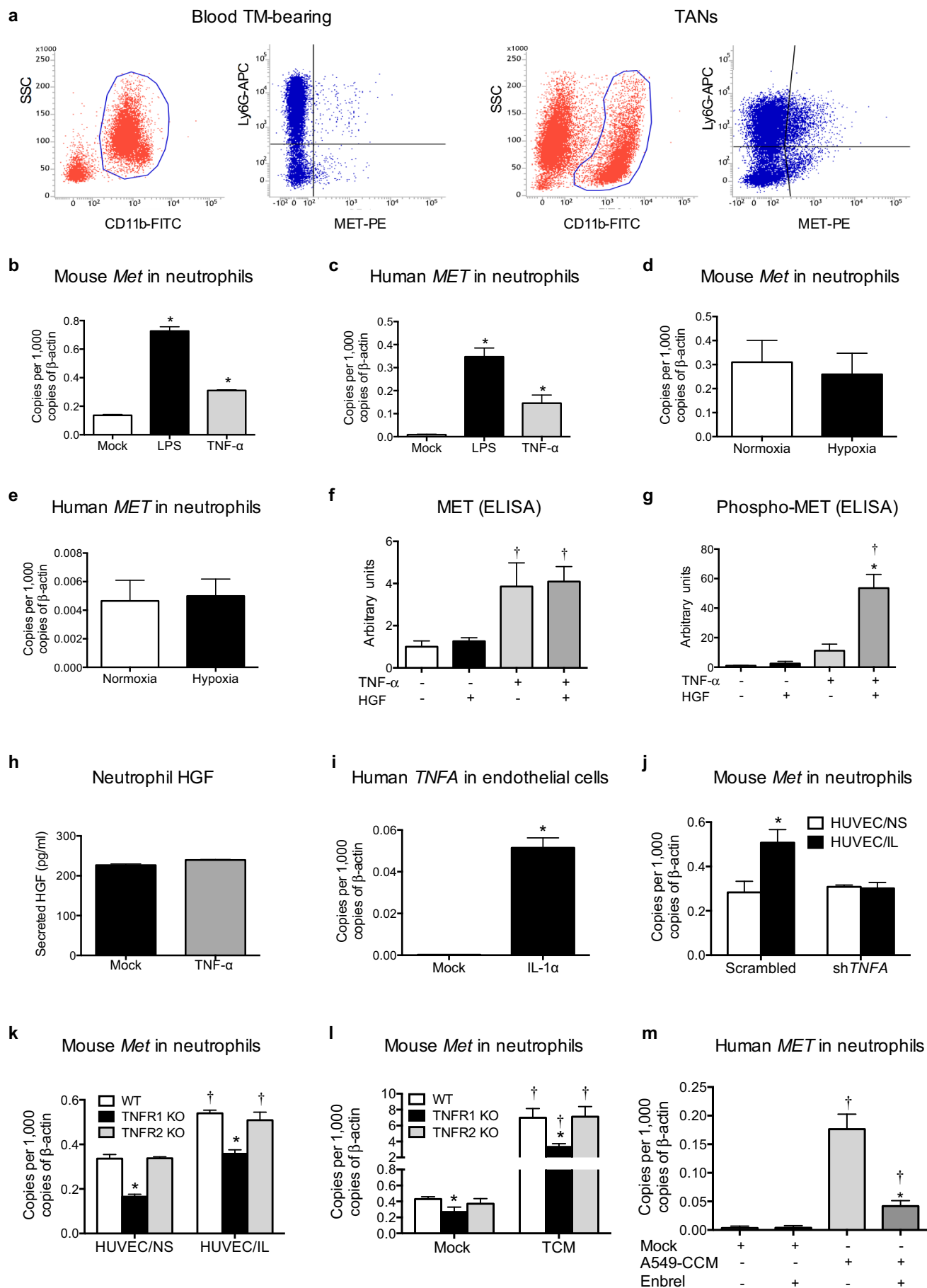
downstream the Mrp8-driven *cre* gene. Data combine two independent experiments; total *n* = 10 mice per condition. **d**, MET expression in neutrophils, monocytes and macrophages harvested from Mrp8;*Met*^{wt/wt} or Mrp8;*Met*^{fl/fl} mice. Western blots are representative of three repetitions on independent biological replicates. **e**, FACS analysis for CD11b⁺ Ly6G⁺ neutrophils in subcutaneous LLC tumours from Mrp8;*Met*^{wt/wt} or Mrp8;*Met*^{fl/fl}. Data combine two independent experiments; total *n*: Mrp8;*Met*^{wt/wt}, 10; Mrp8;*Met*^{fl/fl}, 11. Western blot images in **a, d** have been cropped for presentation. Full scan images are shown in Supplementary Fig. 1. **P* < 0.05 versus Mrp8:Empty WT→WT (**b**), versus Mrp8;*Met*^{wt/wt} (**e**); †*P* < 0.05 versus Mrp8:Empty WT→WT; ‡*P* < 0.05 versus Mrp8:Empty KO→WT. All graphs show mean ± s.e.m.



Extended Data Figure 5 | Pharmacological and genetic inhibition of MET prevents the recruitment of anti-tumoural neutrophils to several neoplastic tissues and inflammatory sites.

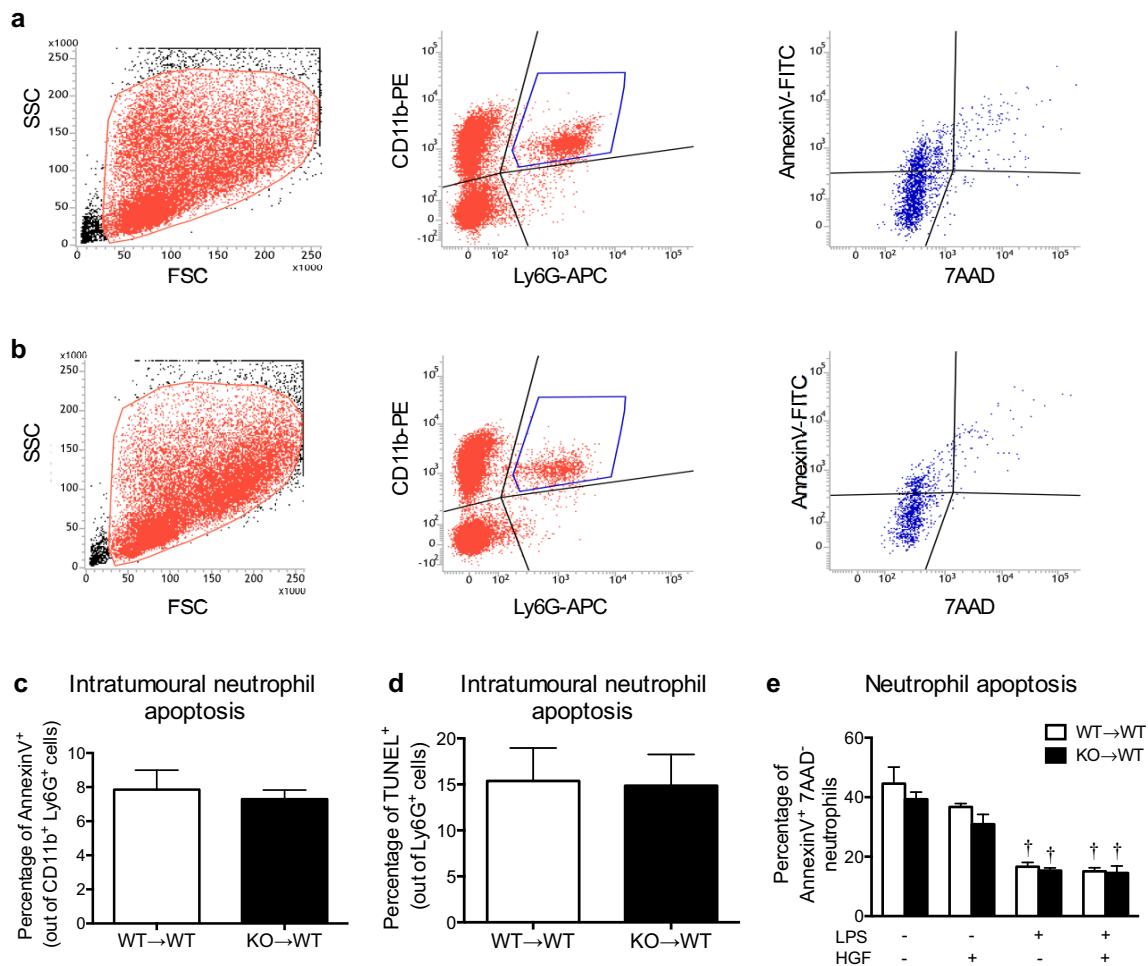
a, Tumour weight of subcutaneous B16F10 melanomas in WT→WT and KO→WT mice. Data combine two independent experiments; total n : WT→WT, 8; KO→WT, 9. **b, c**, Total tumour weight (**b**) and metastatic index (**c**) in MMTV-PyMT mice reconstituted with WT or *Met* KO bone marrow cells before tumour appearance (WT→PyMT and KO→PyMT mice, respectively). Data combine three independent experiments; total n : WT→PyMT, 13; KO→PyMT, 16. **d, e**, FACS quantification for CD11b⁺ Ly6G⁺ neutrophils in T241 tumours harvested from WT→WT or KO→WT mice (**d**) or in breast tumours spontaneously grown in WT→PyMT and KO→PyMT mice (**e**). Data combine two independent experiments; total n = 10 mice per condition (**d**) or total n = 8 mice per condition (**e**). **f–i**, Length measurement (**f**) and representative image (**g**) of the colon, as well as quantification of neutrophils (**h**) and macrophages (**i**) on bowel sections, from WT→WT and KO→WT mice upon induction of chronic colitis compared to healthy control. Data combine two independent experiments; total n : healthy, 5; WT→WT, 12; KO→WT, 15. **j, k**, Tumour weight (**j**) and metastatic mesenteric lymph nodes (**k**) 12 days after orthotopic injection of pancreatic Panc02 cancer cells in WT→WT and KO→WT mice. Data combine two independent experiments; total n = 12 per condition. **l**, Histological quantification of Ly6G⁺ infiltrates in Panc02 pancreatic tumours harvested from WT→WT and KO→WT mice. Data combine two independent

experiments; total n = 12 mice per condition. **m**, Quantification of plasma HGF in tumour (TM)-free mice, in subcutaneous LLC or orthotopic Panc02 tumour-bearing mice. Data combine two independent experiments; total n : tumour free, 10; LLC, 10; Panc02, 8 biological replicates. **n**, Quantification of HGF in subcutaneous LLC or orthotopic Panc02 tumours. Data combine two independent experiments; total n : LLC, 10; Panc02, 8 biological replicates. **o, p**, Quantification of HGF in plasma (**o**) or in subcutaneous LLC tumours (**p**) from tumour-bearing WT→WT and KO→WT mice. Data are representative of two independent experiments using 5 mice per condition per experiment. **q**, Quantification of Ly6G⁺ area on sections from B16F10 melanomas grown in C57BL/6 WT mice, daily treated with PF-04217903, INCB28060, JNJ-38877605, or vehicle as control. Data combine two independent experiments; total n : vehicle, 14; PF-04217903, 9; INCB28060, 6; JNJ-38877605, 4. **r**, Western blot analysis for MET in B16F10 melanoma cells after transduction with a lentiviral vector encoding scrambled or mouse *shMet* under a constitutive promoter; vinculin was used as loading control. Western blot is representative of three independent repetitions. Western blot images have been cropped for presentation. Full scan images are shown in Supplementary Fig. 1. * P < 0.05 versus WT→WT (**a, d, h**), versus WT→PyMT (**b, e**), versus LLC (**m, n**), versus vehicle (**q**); † P < 0.05 versus healthy (**f, h, i**), versus tumour free (**m**). Scale bar: 10 mm (**g**). All graphs show mean ± s.e.m.



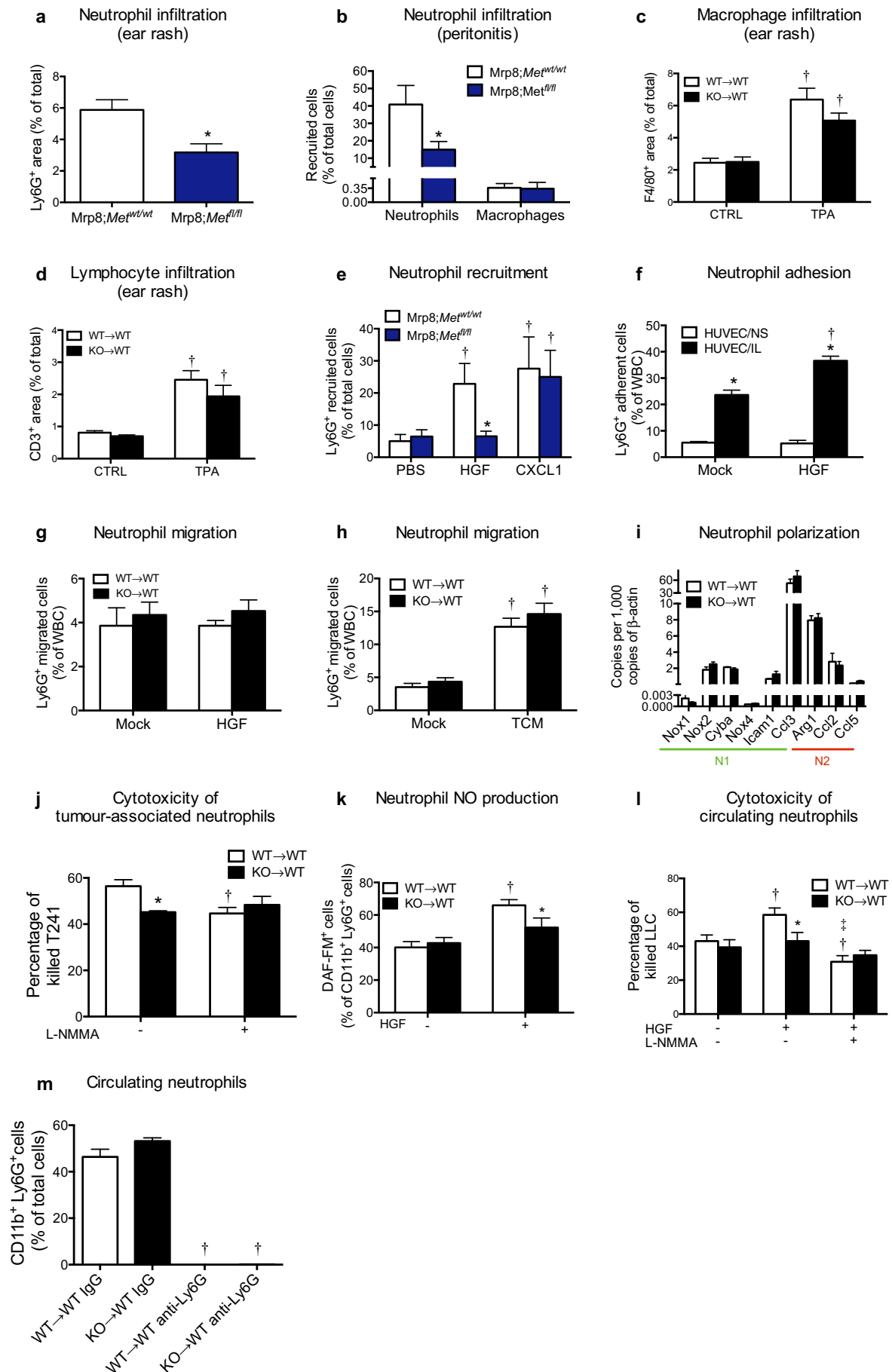
Extended Data Figure 6 | HGF is required for MET activation upon induction by TNF- α . **a**, Gating strategy related to Fig. 3b to quantify MET expression in blood neutrophils from LLC-tumour (TM)-bearing mice and in TANs, where live cells were first gated as CD11b-positive cells; this population was finally gated for Ly6G and MET to identify MET-expressing Ly6G⁺ neutrophils. **b, c**, qRT-PCR for *MET* in mouse (**b**) and human (**c**) neutrophils after LPS or TNF- α stimulation. Data are representative of three independent experiments using four biological replicates per condition per experiment. **d, e**, qRT-PCR for *MET* expression in mouse (**d**) or human (**e**) neutrophils cultured in normoxia (21% O₂) or hypoxia (1% O₂). Data combine two independent experiments; total $n = 8$ biological replicates per condition. **f, g**, ELISA for total MET (**f**) and phospho-MET (**g**) from mouse neutrophils stimulated for 3 min with mock medium or HGF after an overnight incubation with or without TNF- α . Data combine three independent experiments; total $n = 6$ biological replicates per condition. **h**, HGF release by neutrophils stimulated with mock medium or TNF- α after 20 h in culture. Data combine two independent experiments; total $n = 6$ biological replicates per condition. **i**, qRT-PCR for *TNFA* in HUVECs upon stimulation with IL-1 α compared to

mock medium. Data combine two independent experiments; total $n = 4$ biological replicates per condition. **j**, qRT-PCR for *Met* in mouse neutrophils co-cultured with HUVEC/NS or HUVEC/IL transduced with sh*TNFA* or scramble as control. Data are representative of three independent experiments in which three different shRNA sequences were used; total $n = 4$ biological replicates per condition per experiment. **k, l**, qRT-PCR for *Met* in WT, TNFR1 KO or TNFR2 KO neutrophils upon co-culture with HUVEC/NS or HUVEC/IL (**k**), or after stimulation with conditioned medium (TCM) from LLC tumours (**l**). Data are representative of two independent experiments using four biological replicates per condition per experiment. **m**, qRT-PCR for *MET* in human neutrophils stimulated with A549-CCM in the presence or absence of Enbrel or human IgG as control. Data are representative of two independent experiments using four biological replicates per condition per experiment. * $P < 0.05$ versus mock (**b, c, i**), versus TNF- α alone (**g**), versus HUVEC/NS (**j**), versus WT (**k, l**), versus A549-CCM (**m**); † $P < 0.05$ versus untreated or HGF alone (**f, g**), versus HUVEC/NS (**k**), versus mock (**l, m**). Graph shows mean \pm s.e.m.



Extended Data Figure 7 | *Met* deletion in neutrophils does not affect apoptosis. **a, b**, Gating strategy of apoptotic WT (**a**) and *Met* KO (**b**) neutrophils in LLC tumours where single-cell suspensions were first gated for physical parameters and then for CD11b and Ly6G to identify neutrophils as double-positive cells; this population was finally gated for AnnexinV and 7AAD: AnnexinV⁺ 7AAD⁻ cells display early apoptotic neutrophils whereas AnnexinV⁺ 7AAD⁺ cells display late apoptotic neutrophils. **c**, Quantification of apoptotic WT and *Met* KO tumour-associated neutrophils measured by

FACS. Data combine two independent experiments; total $n = 7$ mice per condition. **d**, Quantification of apoptotic WT and *Met* KO neutrophils on LLC tumour sections by immunohistochemistry. Data combine two independent experiments; total n : WT→WT, 7; KO→WT, 6. **e**, FACS analysis for AnnexinV and 7AAD of WT or KO neutrophils incubated for 10 h in the presence or absence of LPS and HGF, alone or in combination. Data combine two independent experiments; total $n = 6$ biological replicates per condition. † $P < 0.05$ versus untreated or HGF alone. Graph shows mean \pm s.e.m.



Extended Data Figure 8 | MET affects neither neutrophil basal migration nor polarization but it is required for neutrophil recruitment and cytotoxicity.

a, Quantification of Ly6G staining in ear sections upon phorbol ester (TPA)-induced cutaneous rash in *Mrp8;Met^{wt/wt}* and *Mrp8;Met^{fl/fl}* mice. Data combine two independent experiments; total $n = 8$ mice per condition. **b**, FACS analysis on peritoneal lavages for Ly6G⁺ neutrophils or F4/80⁺ macrophages in *Mrp8;Met^{wt/wt}* and *Mrp8;Met^{fl/fl}* mice 4 h after intraperitoneal injection of sterile zymosan A. Data are representative of two independent experiments using 5 mice per condition per experiment. **c, d**, Quantification of F4/80 (**c**) and CD3 (**d**) stainings in ear sections at baseline and upon TPA-induced cutaneous rash. Data combine two independent experiments; total n : WT→WT control (CTRL), 22; KO→WT CTRL, 15; WT→WT TPA, 23; KO→WT TPA, 15 (**c**); or total $n = 8$ mice per condition (**d**). **e**, FACS quantification of *Mrp8;Met^{wt/wt}* and *Mrp8;Met^{fl/fl}* neutrophils recruited into subcutaneous air pouches in response to HGF, CXCL1 or PBS. Data combine two independent experiments; total $n = 6$ mice per condition. **f**, FACS quantification of WT neutrophil adhesion to quiescent HUVECs (HUVEC/NS) or activated HUVECs (HUVEC/IL) in the presence or absence of HGF. Data are representative of two independent experiments using four biological replicates per condition per experiment. **g, h**, FACS quantification of WT and *Met* KO neutrophils migrated through a bare porous filter (that is, in the absence of HUVECs) towards HGF (**g**) or tumour conditioned medium (TCM) (**h**). Data are representative of two independent experiments using three biological replicates per condition per

experiment. **i**, Gene expression profile for N1 and N2 markers in neutrophils sorted from LLC tumours grown in WT→WT or KO→WT mice. Data are representative of three independent experiments using 4 mice per condition per experiment. **j**, Cytotoxicity of WT and KO tumour-associated neutrophils against T241 cells in the absence or presence of the NO synthase inhibitor L-NMMA. Data are representative of three independent experiments using three biological replicates per condition per experiment. **k**, FACS quantification of DAF-FM-positive circulating neutrophils after co-culture with LLC cancer cells as a readout of NO production in the absence or presence of HGF. Data are representative of four independent experiments using three biological replicates per condition per experiment. **l**, Quantification of LLC cancer cell killing by WT and KO neutrophils (isolated from the blood of tumour-bearing mice), stimulated with HGF alone or in the presence of L-NMMA. Data are representative of two independent experiments using $n = 12$ biological replicates per condition per experiment. **m**, Blood neutrophils in WT→WT and KO→WT mice treated with neutrophil-depleting Ly6G antibody or rat IgG as control. Data combine two independent experiments; total $n = 16$ per condition. * $P < 0.05$ versus *Mrp8;Met^{wt/wt}* (**a, b**), versus *Mrp8;Met^{wt/wt}* + HGF (**e**), versus HUVEC/NS (**f**), versus WT→WT untreated (**j**), versus WT→WT + HGF (**k, l**); † $P < 0.05$ versus CTRL (**c, d**), versus PBS (**e**), versus mock (**f, h**), versus WT→WT untreated (**j–l**), versus IgG (**m**); ‡ $P < 0.05$ versus WT→WT + HGF (**l**). All graphs show mean ± s.e.m.

Extended Data Table 1 | Blood count in Tie2;*Met*^{wt/wt} or Tie2;*Met*^{fl/fl} tumour-free mice

Tumour free	Tie2; <i>Met</i> ^{wt/wt}	Tie2; <i>Met</i> ^{fl/fl}
WBC (k/ μ l)	5.68 \pm 1.44	5.55 \pm 1.29
NEU (%)	23.03 \pm 5.45	29.67 \pm 7.88
LYM (%)	69.72 \pm 6.46	72.03 \pm 4.89
MON (%)	1.24 \pm 0.37	2.86 \pm 1.15
EOS (%)	0.12 \pm 0.05	0.17 \pm 0.12
BAS (%)	3.38 \pm 1.32	4.47 \pm 2.1
RBC (M/ μ L)	5.21 \pm 1.91	4.89 \pm 1.52
HCT (%)	71.3 \pm 3.43	60.2 \pm 13.38
MCHC (g/dl)	15.83 \pm 2.65	18.3 \pm 0.26
PLT (K/ μ L)	439.73 \pm 26.64	508 \pm 55.79

The values show the haematological parameters (mean \pm s.e.m.) in tumour-free Tie2;*Met*^{wt/wt} and Tie2;*Met*^{fl/fl} mice. Data combine two independent experiments; total $n = 10$ per condition. BAS, basophil; EOS, eosinophil; HCT, haematocrit; LYM, lymphocyte; MCHC, mean cell haemoglobin concentration; MON, monocyte; NEU, neutrophil; PLT, platelet; RBC, red blood cell; WBC, white blood cell.

Extended Data Table 2 | Blood count in WT→WT and KO→WT tumour-free or tumour-bearing mice

Tumour free	WT→WT	KO→WT
WBC (k/ μ l)	10.03 \pm 2.05	8.66 \pm 0.93
NEU (%)	9.18 \pm 2.1	10.3 \pm 3.07
LYM (%)	85.2 \pm 2.91	83.94 \pm 3.46
MON (%)	1.41 \pm 0.48	1.3 \pm 0.4
EOS (%)	0.44 \pm 0.17	0.25 \pm 0.05
BAS (%)	3.77 \pm 0.68	4.21 \pm 0.18
RBC (M/ μ L)	8.21 \pm 0.54	9.3 \pm 0.21
HCT (%)	59.86 \pm 3.52	70.16 \pm 1.67
MCHC (g/dl)	18.63 \pm 0.61	13.4 \pm 0.16
PLT (K/ μ L)	589.26 \pm 134.65	758.4 \pm 50.63
Tumour bearing	WT→WT	KO→WT
WBC (k/ μ l)	7.97 \pm 0.63	9.12 \pm 1.22
NEU (%)	44.3 \pm 0.37	53.71 \pm 7.23
LYM (%)	27.29 \pm 8.33	33.96 \pm 2.52
MON (%)	1.79 \pm 0.75	1.9 \pm 0.64
EOS (%)	0.26 \pm 0.03	0.45 \pm 0.1
BAS (%)	1.94 \pm 0.53	1.84 \pm 0.57
RBC (M/ μ L)	5.5 \pm 0.54	6.83 \pm 0.46
HCT (%)	42.13 \pm 2.93	49.43 \pm 3.47
MCHC (g/dl)	18.27 \pm 0.5	19.24 \pm 0.05
PLT (K/ μ L)	566.17 \pm 109.48	805.5 \pm 88.19

The values show the haematological parameters (mean \pm s.e.m.) in tumour-free or LLC-tumour-bearing (21 days) WT→WT and KO→WT chimaeric mice. Data combine two independent experiments; total $n = 10$ per condition. BAS, basophil; EOS, eosinophil; HCT, haematocrit; LYM, lymphocyte; MCHC, mean cell haemoglobin concentration; MON, monocyte; NEU, neutrophil; PLT, platelet; RBC, red blood cell; WBC, white blood cell.

Regulation of endoplasmic reticulum turnover by selective autophagy

Aliaksandr Khaminets^{1*}, Theresa Heinrich^{2*}, Muriel Mari^{3,4}, Paolo Grumati¹, Antje K. Huebner², Masato Akutsu⁵, Lutz Liebmann², Alexandra Stolz¹, Sandor Nietzsche⁶, Nicole Koch⁷, Mario Mauthe^{3,4}, Istvan Katona⁸, Britta Qualmann⁷, Joachim Weis⁸, Fulvio Reggiori^{3,4}, Ingo Kurth^{2§}, Christian A. Hübner^{2§} & Ivan Dikic^{1,5,9§}

The endoplasmic reticulum (ER) is the largest intracellular endomembrane system, enabling protein and lipid synthesis, ion homeostasis, quality control of newly synthesized proteins and organelle communication¹. Constant ER turnover and modulation is needed to meet different cellular requirements and autophagy has an important role in this process^{2–8}. However, its underlying regulatory mechanisms remain unexplained. Here we show that members of the FAM134B protein family are ER-resident receptors that bind to autophagy modifiers LC3 and GABARAP, and facilitate ER degradation by autophagy ('ER-phagy'). Downregulation of FAM134B protein in human cells causes an expansion of the ER, while FAM134B overexpression results in ER fragmentation and lysosomal degradation. Mutant FAM134B proteins that cause sensory neuropathy in humans⁹ are unable to act as ER-phagy receptors. Consistently, disruption of *Fam134b* in mice causes expansion of the ER, inhibits ER turnover, sensitizes cells to

stress-induced apoptotic cell death and leads to degeneration of sensory neurons. Therefore, selective ER-phagy via FAM134 proteins is indispensable for mammalian cell homeostasis and controls ER morphology and turnover in mice and humans.

Selective autophagy is a degradative pathway that controls the quality and abundance of proteins and cellular organelles and is mediated by autophagy receptors that simultaneously bind the designated target and LC3/GABARAP proteins on autophagosomal membranes^{10–12}. To identify proteins involved in selective autophagy we performed yeast two-hybrid screens using LC3B (microtubule associated protein light chain 3B; MAP1LC3B) and GATE16/GABARAPL2 (γ -aminobutyric acid receptor-associated protein-like 2) as baits¹³. Members of the reticulon-homology-domain-containing FAM134 protein family were found to be interaction partners of LC3B and GABARAPL2 and this interaction was confirmed using FAM134B as the bait (Supplementary Table 1). Also, overexpressed and endogenous FAM134B directly

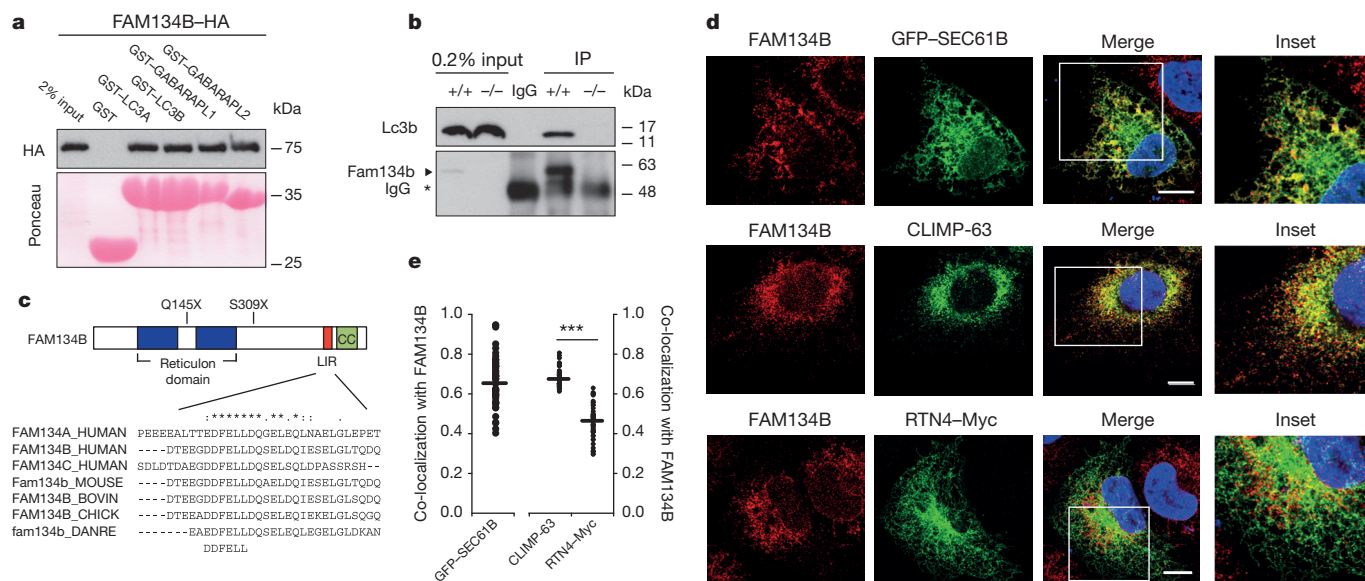


Figure 1 | FAM134B binds LC3-like modifiers and co-localizes with ER marker proteins. **a**, Overexpressed FAM134B-HA (haemagglutinin) binds GST-LC3-like modifiers. **b**, Co-immunoprecipitation (IP) of Fam134b in *Fam134b*^{+/+} and *Fam134b*^{-/-} MEFs with LC3b. **c**, Domain architecture of FAM134B and alignment of the LIR motif. Blue, reticulon domain; red, LC3-interacting region (LIR); green, coiled-coil (CC) domain; Q145X and

S309X, disease-associated stop mutations. Residues with full (*), strong (:) and weak (.) conservation are indicated. **d**, Endogenous FAM134B co-stains with ER-markers in A549 cells. Representatives of ten images are shown. Scale bar, 10 μ m. **e**, Quantification of FAM134B co-localization presented as Pearson's correlation coefficient (*r*); ****P* < 0.001, one-way ANOVA, *n* = 50 cells.

¹Institute of Biochemistry II, Goethe University School of Medicine, Theodor-Stern-Kai 7, 60590 Frankfurt am Main, Germany. ²Institute of Human Genetics, Jena University Hospital, Friedrich-Schiller-University Jena, Kollegiengasse 10, 07743 Jena, Germany. ³Department of Cell Biology, Center for Molecular Medicine, University Medical Center Utrecht, Heidelberglaan 100, 3584 CX Utrecht, The Netherlands. ⁴Department of Cell Biology, University Medical Center Utrecht, University of Groningen, Antonius Deusinglaan 1, 3713 AV Groningen, The Netherlands. ⁵Buchmann Institute for Molecular Life Sciences, Goethe University Frankfurt, Riedberg Campus, Max-von-Laue-Straße 15, 60438 Frankfurt am Main, Germany. ⁶Electron Microscopy Center, Jena University Hospital, Friedrich-Schiller-University Jena, Ziegelmühlenweg 1, 07743 Jena, Germany. ⁷Institute for Biochemistry I, Jena University Hospital, Friedrich-Schiller-University Jena, 07743 Jena, Germany. ⁸Institute of Neuropathology, RWTH Aachen University Hospital, Pauwelsstr. 30, 52074 Aachen, Germany. ⁹Institute of Immunology, School of Medicine University of Split, Mestrovicova setaliste bb, 21 000 Split, Croatia.

*These authors contributed equally to this work.

§These authors jointly supervised this work.

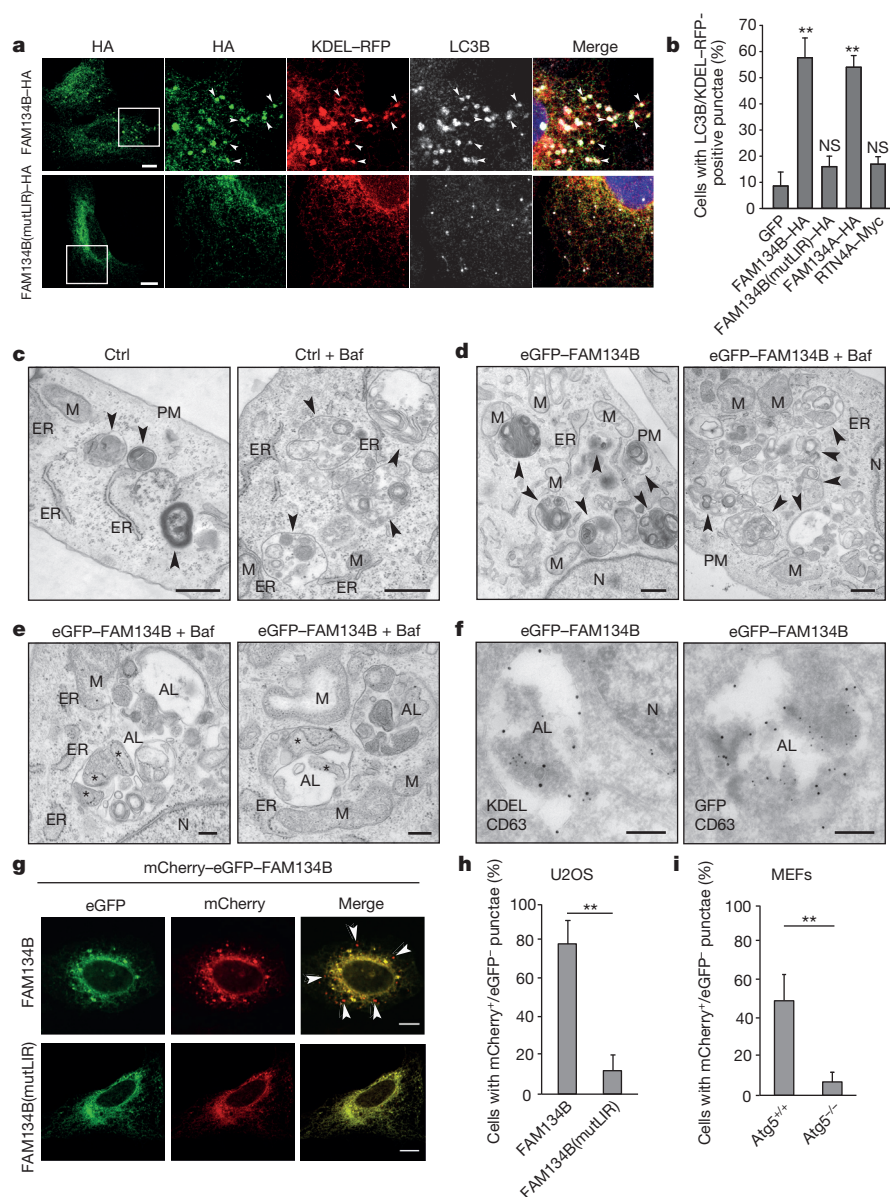


Figure 2 | FAM134B targets ER into autophagosomes. **a, b**, Stable KDEL-RFP U2OS cells transiently expressing FAM134B-HA or FAM134B(mutLIR)-HA were quantified for KDEL-RFP- and LC3B-positive punctae (arrowheads). Representatives of ten images are shown. Scale bars, 10 μ m. ** P < 0.01, one-way ANOVA, error bars indicate s.d., n = 300. NS, not significant. **c–f**, Transmission electron microscopy of U2OS control cells (Ctrl) and stable eGFP-FAM134B cells. **c, d**, Autolysosomes indicated by arrowheads. **e**, Asterisks label ER fragments inside autolysosomes. **f**, Immunogold labelling against CD63 (large dots, diameter 15 nm) and KDEL peptide or GFP (small dots, diameter 10 nm). Treatment with bafilomycin is indicated (+Baf). AL, autolysosome; M, mitochondria; N, nucleus; PM, plasma membrane. Scale bars, 500 nm (**c, d**), 200 nm (**e, f**); n = 150 cells for **c–e**, n = 100 cells for **f–h**. **g, h**, U2OS cells stably expressing mCherry-eGFP-FAM134B or mCherry-eGFP-FAM134B(mutLIR). Cells that exhibited lysosomal mCherry-positive but eGFP-negative punctae (arrowheads) were quantified. Scale bars, 10 μ m. ** P < 0.01, one-way ANOVA, error bars indicate s.d., three biological replicates. **i**, Quantification of mCherry-positive and eGFP-negative punctae in wild-type and *Atg5*^{−/−} MEFs transiently expressing mCherry-eGFP-FAM134B. ** P < 0.01, one-way ANOVA, error bars indicate s.d., n = 60 cells, three biological replicates.

interacts with LC3/GABARAP in mammalian cells (Fig. 1a, b and Extended Data Fig. 1a, b). Similar results were obtained for FAM134A and FAM134C proteins (Extended Data Fig. 1c). FAM134 proteins contain a conserved putative LC3-interacting region (LIR motif) (Fig. 1c). Substitution of amino acids of this LIR motif with alanines (DDFELL/AAAAAA; mutLIR) completely abolished the interaction of FAM134B with LC3-like modifiers, whereas deletion of the C-terminal coiled-coil domain (Δ CC) did not affect LC3 binding (Extended Data Fig. 1d). Truncated FAM134B proteins (Q145X, S309X) causing sensory neuropathy in humans⁹ lack the C-terminal LIR motif and consequently did not bind LC3-like proteins (Extended Data Fig. 1d). Moreover, the crystal structure of a LIR-motif-containing FAM134B peptide bound to LC3A further demonstrated

that amino acids F455 and L458 of FAM134B mediate the interaction with the hydrophobic pockets of LC3A (Extended Data Fig. 1e)^{14,15}. These data thus show a direct interaction of FAM134 proteins with the autophagy machinery and identify a potential novel family of autophagy receptors.

Endogenous and overexpressed FAM134B co-localized with CLIMP-63 and SEC61B, marker proteins of sheet-like cisternal ER and to a lesser extent with RTN4-positive tubular ER (Fig. 1d, e and Extended Data Fig. 2a–c). We found that both the N-terminus and the LIR-motif-containing C-terminus, which flank the reticulon homology domain of FAM134B, face the cytoplasm, suggesting a hairpin topology of the protein^{16,17} (Extended Data Fig. 2d, e). Liposome-binding assays confirmed that FAM134B binds to membranes (Extended

Data Fig. 3a) and its incubation with liposomes resulted in a reduced liposome size (Extended Data Fig. 3b, c). Neuropathy-associated proteins lacking both the coiled-coil domain and the LIR-motif (S309X) showed weaker binding to membranes but retained the ability to shape them, whereas deletion of a part of the reticulon domain (Q145X) abolished the formation of small-diameter liposomes (Extended Data Fig. 3c). These data indicate that FAM134B is capable of remodelling membranes *in vitro* via its reticulon homology domain.

Transient overexpression of FAM134B in U2OS cells stably expressing the ER marker protein KDEL-RFP led to pronounced morphological changes and fragmentation of the ER. FAM134B-positive ER fragments co-localized with LC3B and CD63-positive lysosomes (Fig. 2a–f). In contrast, the ability of FAM134B to fragment and sequester ER into LC3-positive autophagosomes was abolished upon expression of a LIR-motif-deficient FAM134B (Fig. 2a, b). Overexpression of RTN4A, another reticulon-domain-containing protein¹⁶, induced morphological ER changes, but did not lead to a formation of LC3B/KDEL-RFP-positive punctae (Fig. 2b). These observations suggest that FAM134B, through its LIR motif, acts as an ER-selective autophagy receptor. To dissect the fate of FAM134B-induced ER fragments, we performed transmission electron microscopy (Fig. 2c–f). Lysosomes and autolysosomes were more abundant in U2OS cells stably overexpressing eGFP-FAM134B compared to controls, an effect which was even more prominent upon inhibition of lysosomal degradation by bafilomycin A1 (Fig. 2c–e). Autolysosomes in bafilomycin A1-treated and eGFP-FAM134B-expressing cells showed an accumulation of ribosome-decorated ER fragments in their interior (Fig. 2e). The presence of ER-derived structures in autolysosomes was confirmed by double immunogold labelling using antibodies against the lysosomal marker CD63 and the KDEL peptide (Fig. 2f). Double labelling with CD63 and GFP antibodies proved that eGFP-FAM134B was delivered into autolysosomes (Fig. 2f). ER turnover was further investigated by monitoring the degradation of the ER-resident protein SEC61B. Increased degradation of SEC61B was observed in FAM134B-overexpressing cells but not in cells expressing FAM134B(mutLIR) (Extended Data Fig. 4a). Delivery of ER fragments into lysosomes was further confirmed in U2OS cells stably expressing FAM134B with a tandem fusion of mCherry and eGFP (mCherry-eGFP-FAM134B), as indicated by mCherry-positive but eGFP-negative punctae, owing to the higher stability of mCherry in acidic milieu¹³ (Fig. 2g, h). In contrast, only few mCherry-positive and eGFP-negative punctae were observed in cells stably expressing mCherry-eGFP-FAM134B(mutLIR) (Fig. 2g, h) or in autophagy-deficient *Atg5*^{−/−} mouse embryonic fibroblasts (MEFs) expressing wild-type mCherry-eGFP-FAM134B (Fig. 2i and Extended Data Fig. 4b). Moreover, ER fragmentation and degradation was abolished after FAM134B overexpression in *Atg5*^{−/−} MEFs (Extended Data Fig. 4c–f). These data demonstrate that FAM134B is an ER-anchored autophagy receptor that mediates ER delivery into lysosomes through sequestration into autophagosomes (ER-phagy). Notably, this mechanism is different from a recently described ER-phagy pathway in yeast that operates independently from the core autophagy machinery¹⁸.

We next performed short hairpin RNA (shRNA)-mediated *FAM134B* knockdown in U2OS cells stably expressing KDEL-RFP. FAM134B downregulation led to a striking ER expansion especially in the cell periphery (Fig. 3a–d and Extended Data Fig. 5a). Knockdown of two major autophagy regulators, *ATG5* and *BECN1*, likewise triggered a comparable phenomenon (Fig. 3e–h). The ER expansion was accompanied by an increase in both CLIMP-63-positive membranes and increased cellular levels of CLIMP-63 and TRAP α proteins (Extended Data Fig. 5b–d). Reconstitution of knockdown cells with shRNA-resistant *FAM134B* variants (wild type, mutLIR, Q145X, S309X or Δ ret (lacking the reticulon domain)) revealed that only wild-type FAM134B rescues the ER-phenotype (Fig. 3i, j). Thus, ER remodelling and turnover by FAM134B requires both the reticulon domain and LIR-mediated targeting to autophagosomes.

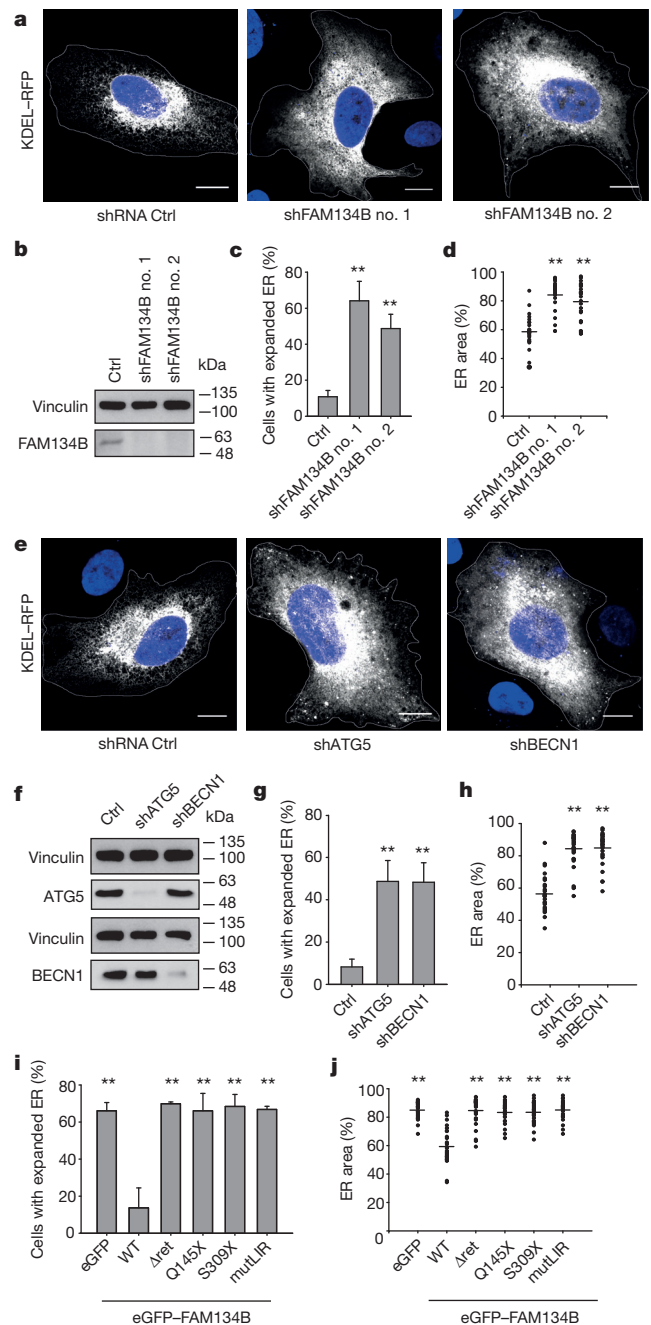


Figure 3 | FAM134B and autophagy regulate ER volume and structure.

a–d, ER expansion in cells lacking FAM134B. **a**, shRNA-mediated knockdown of *FAM134B* in U2OS cells stably expressing KDEL-RFP. Representatives of ten images are shown. Scale bars, 10 μ m. **b**, Knockdown efficiency determined by western blot. **c**, Quantification of cells with expanded ER. ****P** < 0.01, one-way ANOVA, error bars indicate s.d., *n* = 300. **d**, Quantification of ER area. ****P** < 0.0001, Mann-Whitney test, *n* = 25. **e–h**, Defective autophagy leads to ER expansion. **e**, shRNA-mediated knockdown of *ATG5* or *BECN1* in U2OS cells stably expressing KDEL-RFP. Representatives of ten images are shown. Scale bars, 10 μ m. **f**, Knockdown efficiency determined by western blot. **g**, Quantification of cells with expanded ER. ****P** < 0.01, one-way ANOVA, error bars indicate s.d., *n* = 300. **h**, Quantification of ER area. ****P** < 0.0001, Mann-Whitney test, *n* = 25. **i, j**, Rescue of ER expansion in *FAM134B*-knockdown U2OS cells after expressing shRNA-resistant FAM134B proteins. **i**, Quantification of cells with expanded ER. ****P** < 0.01, one-way ANOVA, error bars indicate s.d., *n* = 300. **j**, Quantification of ER area. ****P** < 0.0001, Mann-Whitney test, *n* = 25.

To study the consequence of *Fam134b* loss *in vivo*, we disrupted the mouse *Fam134b* gene by homologous recombination (Fig. 4a). An expanded ER and alterations of Climp-63-positive ER sheets were

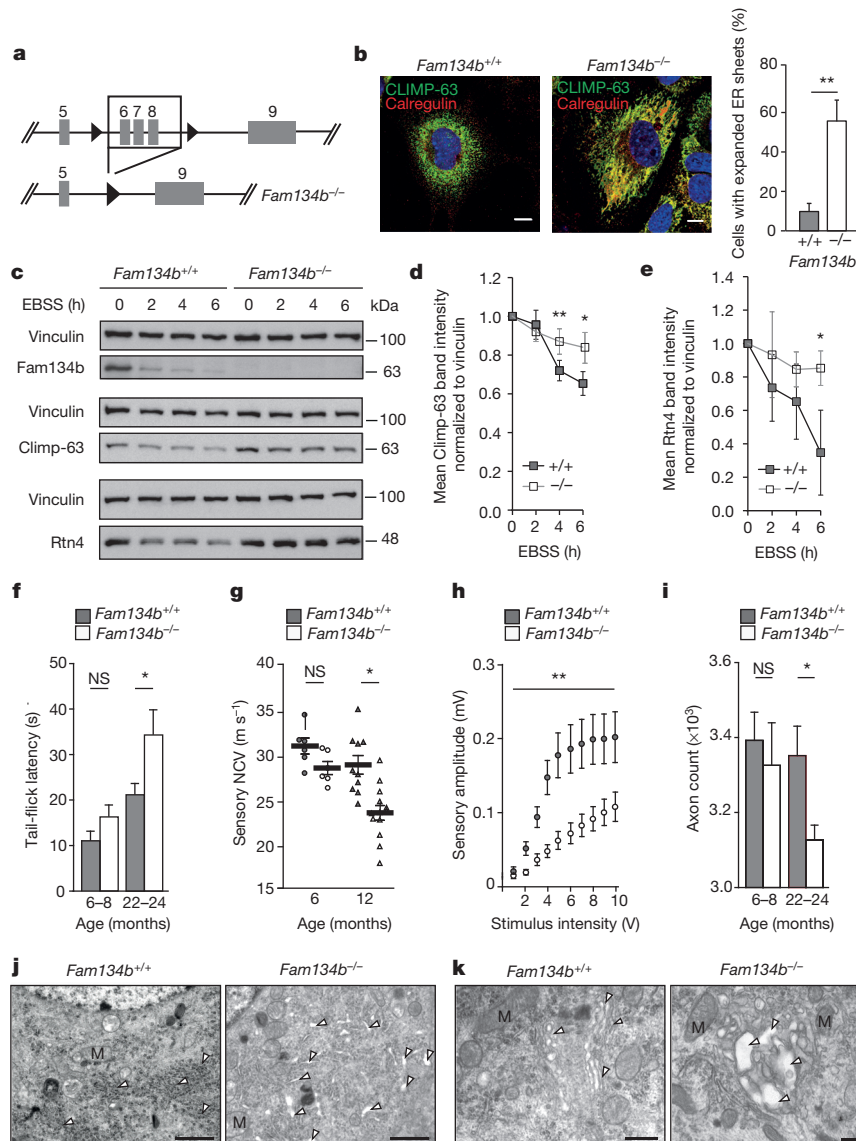


Figure 4 | Impaired selective ER turnover and sensory neuropathy in *Fam134b*^{-/-} mice. **a**, Cre-loxP-mediated deletion of exons 6–8 of *Fam134b* (loxP site, black triangle). **b**, Expanded ER in *Fam134b*^{-/-} MEFs. ***P* < 0.01, one-way ANOVA, error bars indicate s.d., *n* = 300. Representative of ten images is shown. Scale bars, 10 μ m. **c**, Protein turnover in MEFs after Earle's Balanced Salt Solution (EBSS) starvation. **d**, **e**, Densitometry of **c** normalized to vinculin in three (**d**) or four (**e**) independent experiments. **P* < 0.05, ***P* < 0.01, one-way ANOVA. **f**, Tail withdrawal latency from noxious heat stimulus (tail-flick assay, 45 °C). NS, not significant, **P* < 0.05, Mann-Whitney *U*-test, error bars indicate s.e.m. (*n* = 13 for *Fam134b*^{+/+}, *n* = 11 for *Fam134b*^{-/-}). **g**, Sensory nerve conduction velocities (NCVs) recorded from the mouse tail. **P* < 0.05, one-way ANOVA (*n* = 6 for both *Fam134b*^{+/+} and *Fam134b*^{-/-} at

6–8 months; *n* = 10 for *Fam134b*^{+/+} and *n* = 12 for *Fam134b*^{-/-} at 22–24 months). **h**, Input-output curves of sensory nerve amplitudes at 12–15 months (*n* = 13 for *Fam134b*^{+/+} and *n* = 11 for *Fam134b*^{-/-}). ***P* < 0.005, two-way ANOVA, error bars indicate s.e.m. **i**, Afferent sensory fibres cut distally to the dorsal root ganglia were quantified. (*n* = 7 for *Fam134b*^{+/+} and *n* = 7 for *Fam134b*^{-/-}). NS, not significant, **P* < 0.05, Student's *t*-test, error bars indicate s.e.m. **j**, **k**, Transmission electron microscopy images showing enlarged ER tubules and distorted Golgi cisternae in dorsal root ganglia tissue sections (45-week-old *Fam134b*^{-/-} mice). Arrowheads indicate representative examples for ER (**j**) and Golgi compartment (**k**). Scale bars: 1 μ m (**j**); 0.5 μ m (**k**). *n* = 3 animals for each genotype. M, mitochondria.

observed in MEFs isolated from *Fam134b*^{-/-} mice (Fig. 4b). However, autolysosome number, turnover of long-lived proteins, Lc3b processing and p62 degradation were unaltered in *Fam134b*^{-/-} MEFs, suggesting that although Fam134b specifically affects ER morphology and turnover via autophagy proteins, it is dispensable for basal or induced bulk autophagy and other types of selective autophagy (Extended Data Fig. 6). Of note, cytoplasmic protein aggregates that accumulated after 2 h of treatment with puromycin were removed during a 3 h recovery in both control and *Fam134b*^{-/-} MEFs (Extended Data Fig. 6m, n). Nutrient starvation has previously been shown to induce ER degradation^{5,19}, accordingly, starvation triggered rapid Fam134b degradation in MEFs (Fig. 4c and Extended Fig. 4f). To a lesser extent we observed starvation-induced degradation of other structural ER proteins includ-

ing Climp-63 and Rtn4 (Fig. 4c–e). Importantly, turnover of Climp-63 and Rtn4 was significantly impaired in *Fam134b*^{-/-} MEFs upon nutrient starvation (Fig. 4c–e), revealing that Fam134b acts as a general autophagy receptor for ER-phagy and may contribute to the dynamics of both Climp-63-positive sheets and Rtn4-enriched tubules/edges of sheets. Impaired ER turnover in *Fam134b*-deficient MEFs and A549 cells affected cell viability under various stress conditions and led to cell death by involving the mitochondrial apoptotic pathway (Extended Data Fig. 7). This, together with other reports^{20–22}, suggests that a compromised ER homeostasis undermines long-term cell survival.

Phenotypic analyses of aged *Fam134b*^{-/-} mice revealed a reduced sensitivity towards noxious heat, which indicates a loss of small nociceptive neurons (Fig. 4f). Sensory nerve conduction velocities were

reduced, and together with a severe reduction of the sensory amplitude suggested additional loss of myelinated axons (Fig. 4g, h). In line with this, sensory axon numbers of *Fam134b*^{-/-} mice were significantly reduced in aged animals (Fig. 4i). No changes of lower motor neurons were found, suggesting that neurodegeneration is restricted to peripheral sensory nerves (Extended Data Fig. 8a–f). Ultrastructural analyses of the somata of sensory neurons in tissue sections revealed ER expansions in *Fam134b*^{-/-} mice at 10 months of age, which were absent in wild-type littermates (Fig. 4j). Notably, Golgi cisternae were also dilated in 10-month-old *Fam134b*^{-/-} animals (Fig. 4k). No obvious changes in other subcellular compartments were observed. The ultrastructure of sensory neurons before phenotypic disease onset was further examined by a transmission electron microscopy approach allowing the maintenance of the neuronal architecture²³. While neurites in cultured sensory neurons from 3-month-old *Fam134b*^{+/+} and *Fam134b*^{-/-} mice were indistinguishable, the ER in the cell body was swollen in approximately 60% of *Fam134b*^{-/-} neurons (Extended Data Fig. 9). The *in vivo* data support the role of Fam134b as an ER-phagy receptor and demonstrate its relevance for sensory axon maintenance.

In summary, we show that FAM134B is essential for ER homeostasis *in vitro* and *in vivo*, and that its reticulon domain and LIR motif are both required for ER-phagy (Extended Data Fig. 10). We propose that FAM134B promotes membrane remodelling and ER scission via the membrane-bending capacity of its reticulon domain, whereas the LIR motif is necessary to target the ER fragments to autophagosomes for lysosomal degradation. A similar coordination between organelle scission and autophagosomal sequestration has been proposed for mitophagy²⁴.

Maintaining ER homeostasis via FAM134B-mediated autophagy is essential for cell survival, especially under stress conditions. This is particularly relevant *in vivo*, where FAM134B inhibition, coupled with age-associated attenuation of autophagy, could contribute to an accumulation of misfolded or aggregated proteins within the ER leading to impaired proteostasis, compromised neuronal survival, and progressive neurodegeneration. An accompanying paper identified two novel receptors for selective ER-phagy in yeast termed Atg39 and Atg40, with the latter harbouring a reticulon domain²⁵, and showed that ER-phagy is required for ER turnover and yeast cell fitness under stress conditions. Thus, our studies unveil a novel evolutionarily conserved molecular pathway that regulates the turnover and structure of the ER, and provide insight into selective autophagy in physiological organelle dynamics and pathological conditions.

Online Content Methods, along with any additional Extended Data display items and Source Data, are available in the online version of the paper; references unique to these sections appear only in the online paper.

Received 17 November 2014; accepted 24 April 2015.

Published online 3 June 2015.

- Borgese, N., Francolini, M. & Snapp, E. Endoplasmic reticulum architecture: structures in flux. *Curr. Opin. Cell Biol.* **18**, 358–364 (2006).
- Walter, P. & Ron, D. The unfolded protein response: from stress pathway to homeostatic regulation. *Science* **334**, 1081–1086 (2011).
- Schuck, S., Prinz, W. A., Thorn, K. S., Voss, C. & Walter, P. Membrane expansion alleviates endoplasmic reticulum stress independently of the unfolded protein response. *J. Cell Biol.* **187**, 525–536 (2009).
- Maiuolo, J., Bulotta, S., Verderio, C., Benfante, R. & Borgese, N. Selective activation of the transcription factor ATF6 mediates endoplasmic reticulum proliferation triggered by a membrane protein. *Proc. Natl Acad. Sci. USA* **108**, 7832–7837 (2011).
- Hamasaki, M., Noda, T., Baba, M. & Ohsumi, Y. Starvation triggers the delivery of the endoplasmic reticulum to the vacuole via autophagy in yeast. *Traffic* **6**, 56–65 (2005).
- Bernales, S., McDonald, K. L. & Walter, P. Autophagy counterbalances endoplasmic reticulum expansion during the unfolded protein response. *PLoS Biol.* **4**, e423 (2006).
- Tasdemir, E. *et al.* Cell cycle-dependent induction of autophagy, mitophagy and reticulophagy. *Cell Cycle* **6**, 2263–2267 (2007).
- Yorimitsu, T. & Klionsky, D. J. Eating the endoplasmic reticulum: quality control by autophagy. *Trends Cell Biol.* **17**, 279–285 (2007).

- Kurth, I. *et al.* Mutations in FAM134B, encoding a newly identified Golgi protein, cause severe sensory and autonomic neuropathy. *Nature Genet.* **41**, 1179–1181 (2009).
- Stolz, A., Ernst, A. & Dikic, I. Cargo recognition and trafficking in selective autophagy. *Nature Cell Biol.* **16**, 495–501 (2014).
- Weidberg, H., Shvets, E. & Elazar, Z. Biogenesis and cargo selectivity of autophagosomes. *Annu. Rev. Biochem.* **80**, 125–156 (2011).
- Rogov, V., Dotsch, V., Johansen, T. & Kirkin, V. Interactions between autophagy receptors and ubiquitin-like proteins form the molecular basis for selective autophagy. *Mol. Cell* **53**, 167–178 (2014).
- Kirkin, V. *et al.* A role for NBR1 in autophagosomal degradation of ubiquitinated substrates. *Mol. Cell* **33**, 505–516 (2009).
- Wild, P. *et al.* Phosphorylation of the autophagy receptor optineurin restricts Salmonella growth. *Science* **333**, 228–233 (2011).
- Rogov, V. V. *et al.* Structural basis for phosphorylation-triggered autophagic clearance of Salmonella. *Biochem. J.* **454**, 459–466 (2013).
- Voeltz, G. K., Prinz, W. A., Shibata, Y., Rist, J. M. & Rapoport, T. A. A class of membrane proteins shaping the tubular endoplasmic reticulum. *Cell* **124**, 573–586 (2006).
- Shibata, Y. *et al.* Mechanisms determining the morphology of the peripheral ER. *Cell* **143**, 774–788 (2010).
- Schuck, S., Gallagher, C. M. & Walter, P. ER-phagy mediates selective degradation of endoplasmic reticulum independently of the core autophagy machinery. *J. Cell Sci.* **127**, 4078–4088 (2014).
- Cebollero, E., Reggiori, F. & Kraft, C. Reticulophagy and ribophagy: regulated degradation of protein production factories. *Int. J. Cell Biol.* **2012**, 182834 (2012).
- Beetz, C. *et al.* A spastic paraplegia mouse model reveals REEP1-dependent ER shaping. *J. Clin. Invest.* **123**, 4273–4282 (2013).
- Hübner, C. A. & Kurth, I. Membrane-shaping disorders: a common pathway in axon degeneration. *Brain* **137**, 3109–3121 (2014).
- Renvoisé, B. & Blackstone, C. Emerging themes of ER organization in the development and maintenance of axons. *Curr. Opin. Neurobiol.* **20**, 531–537 (2010).
- Spoerri, P. E., Dresch, W. & Heyder, E. A simple embedding technique for monolayer neuronal cultures grown in plastic flasks. *Acta Anat.* **107**, 221–223 (1980).
- Mao, K., Wang, K., Liu, X. & Klionsky, D. J. The scaffold protein Atg11 recruits fission machinery to drive selective mitochondria degradation by autophagy. *Dev. Cell* **26**, 9–18 (2013).
- Mochida, K. *et al.* Receptor-mediated selective autophagy degrades the endoplasmic reticulum and the nucleus. *Nature* <http://dx.doi.org/10.1038/nature14506> (2015).

Supplementary Information is available in the online version of the paper.

Acknowledgements We would like to thank S. Horwitz, K. Rajalingam, C. Behrends and J. Lippincott-Schwartz for cell lines and vectors, N. Mizushima for Atg5^{-/-} and control immortalized MEFs, H.-P. Hauri and H. Farhan for vectors, and S. Giebelmann and K. Schorr for excellent technical assistance. We acknowledge D. McEwan, D. Hoeller, D. Popovic and K. Koch for critical reading of the manuscript and valuable insights. We also thank M. M. Kessels for support. This work was supported by grants from the Deutsche Forschungsgemeinschaft to I.D. (DI 931/3-1), I.K. (KU 1587/2-1, KU 1587/3-1, KU 1587/4-1), C.A.H. (HU 800/5-1, RTG 1715, HU 800/6-1, HU 800/7-1), B.Q. (QU116/6-2, RTG1715), J.W. (WE1406/13-1), the Cluster of Excellence 'Macromolecular Complexes' of the Goethe University Frankfurt (EXC115), LOEWE grant Ub-Net and LOEWE Centrum for Gene and Cell therapy Frankfurt and the European Research Council/ERC grant agreement number (250241-LineUb) to I.D. F.R. is supported by ECHO (700.59.003), ALW Open Program (821.02.017 and 822.02.014), DFG-NWO cooperation (DN82-303) and ZonMW VICI (016.130.606) grants. P.G. is supported by the 7.FP, COFUND, Goethe International Postdoc Programme GO-IN, No. 291776.

Author Contributions A.K. performed biochemical analyses, immunofluorescence and cellular localization, functional analysis and contributed to interpretation of data and manuscript writing and preparation. T.H. characterized *Fam134b*^{-/-} mice, carried out FAM134B topology analysis and contributed to manuscript preparation. M.Mar. performed transmission electron microscopy of cells and neurons in culture. P.G. performed apoptosis and autophagy analysis, and contributed to manuscript preparation and writing. A.K.H. generated the *Fam134b*^{-/-} mouse model and was involved in mouse phenotyping. M.A. performed crystal structure assay. L.L. performed the electrophysiological analysis of *Fam134b*^{-/-} mice. S.N., I. Ka. and J.W. performed transmission electron microscopy on murine tissues. A.S. performed fractionation and autophagy flux experiments. M.Mau. carried out the assay for the turnover of long-lived proteins. N.K. performed liposome assays, B.Q. supervised liposome assays. F.R., I.Ku., C.A.H. and I.D. designed the study, analysed data and wrote the manuscript. I.Ku., C.A.H. and I.D. contributed equally to the study. All the authors discussed the results and the manuscript.

Author Information Atomic coordinates of the crystal structure of FAM134B-LIR-LC3A have been deposited in the Protein Data Bank under accession number 4ZDV. Reprints and permissions information is available at www.nature.com/reprints. The authors declare no competing financial interests. Readers are welcome to comment on the online version of the paper. Correspondence and requests for materials should be addressed to I.D. (Ivan.Dikic@biochem2.de), C.A.H. (Christian.Huebner@med.uni-jena.de) or I.Ku. (Ingo.Kurth@med.uni-jena.de).

METHODS

Plasmids, antibodies and reagents. pcDNA3.1(+)-FAM134A-HA, pcDNA3.1(+)-FAM134B and pcDNA3.1(+)-FAM134C were generated by subcloning FAM134A, FAM134B and FAM134C ORFs into pcDNA3.1(+)- (Invitrogen) from pOTB7-FAM134A (MHS1011-59267), pOTB7-FAM134B (MHS1011-9199640) and pBluescript-FAM134C (MHS1010-9204031), respectively (Thermo Scientific), using HindIII and XhoI cloning sites. pcDNA3.1(+)-FAM134A-HA construct contained a 50-nucleotide N-terminal deletion that did not affect the ORF. pcDNA3.1(+)-FAM134A/B(mutLIR) (DDFELLD LIR substituted by seven alanine residues) and pcDNA3.1(+)-FAM134B DH1/2 (lacking amino acids 83–140 and 196–248) were generated by site-directed mutagenesis. pGEX4T1-hGABARAP(ΔG), pGEX4T1-hGABARAPL1(ΔG), pGEX4T1-hGABARAPL2 (GATE-16)(ΔG), pGEX4T1-hMAP1LC3A(ΔG), pGEX4T1-hMAP1LC3B(ΔG) and pGEX4T1-hMAP1LC3C(ΔG) have been described previously¹³. FAM134B was cloned into Gateway entry vector pDONR223 (Invitrogen) and then recombined further into pHage-eGFP (Invitrogen) by the gateway LR reaction (Invitrogen) to generate pHage-eGFP-FAM134B as described²⁶. pHage-eGFP-FAM134B Δret (lacking amino acids 80–250), Q145X (stop codon at position 145), S309X (stop codon at position 309), mutLIR (DDFELLD LIR motif substituted by alanine residues) and ΔCC (stop codon at position 464) were generated by site-directed mutagenesis. FAM134B and the Δret mutant were delivered into pcDNA3.1/N mCherry-eGFP and pET-60-DEST destination vectors by the Gateway LR reaction to generate mCherry-eGFP-FAM134B. pcDNA3.1/N mCherry-eGFP was generated as follows: eGFP was added to pcDNA3.1/N mCherry destination vector (Invitrogen) through PCR amplification and ligation into pcDNA3.1/N mCherry using an ApaI restriction site. To generate the FAM134B(mutLIR) double tag vector, DDFELLD LIR has been substituted with seven alanine residues. Other plasmids used in the study were peGFP-C1 (Clontech), KDEL-RFP (pmRFP-C1-KDEL-RFP, a gift from J. Lippincott-Schwartz²⁷), pcDNA3.1(+)-RTN4A (NogoA)-mycHis (a gift from S. Strittmatter²⁸), and GFP-SEC61 fusion (a gift from H.-P. Hauri and H. Farhan²⁹).

Mouse monoclonal antibodies. Anti-β-Actin (Abcam), anti-HA (Santa Cruz, sc-7392), anti-c-Myc (Santa Cruz, sc-40), anti-GFP (Santa Cruz, sc-9996), anti-LC3B (MBL, M152-3), anti-mono- and -polyubiquitinated conjugates (Enzo, BML-PW8810), anti-p62 (MBL, M162-3), anti-CLIMP-63 (Enzo, ALX-804-604), anti-LAMP1 (DSHB University of Iowa, H4A3), anti-LC3 (NanoTools, 0260-100/LC3-2G6), anti-GM130 (BD Transduction Laboratories, 610823), anti-caspase-8 (MBL, M058-3), anti-G-adaptin (BD Transduction), anti-vinculin (Sigma).

Rabbit polyclonal antibodies. Anti-LC3B (MBL, PM063), anti-p62 (Enzo, PW9860) anti-dsRed (Clontech, 632496), anti-ATG5 (Cell Signaling, 2630), anti-BECN1 (Cell Signaling, 3495), anti-CKAP4 (ProteinTech, 16686-1-AP), anti-NogoA+B (Abcam, ab47085), anti-TRAPα (Abcam, ab133238), anti-PARP (Cell Signaling, 9542), anti-caspase-9 (Cell Signaling, 9502).

Goat polyclonal antibody. Anti-Calnexin (Santa Cruz, sc-6467).

For immunoelectron microscopy analyses, sections were labelled with a monoclonal antibody anti-KDEL (Calbiochem) and a biotin-conjugated monoclonal antibody recognizing CD63 (Calbiochem).

Secondary antibodies. HRP-conjugated secondary antibodies were purchased from Santa Cruz Biotechnology; Cy3- and Cy5-conjugated antibodies were from Jackson ImmunoResearch and Alexa488-conjugated antibodies were from Invitrogen. Secondary gold-labelled rabbit anti-goat, -mouse and -biotin antibodies were purchased from Nordic MUBio, Dako and Rockland Immunochemicals Inc., respectively.

Chemicals. Bafilomycin A, MG132, CCCP and thapsigargin were purchased from Sigma. Tunicamycin was obtained from Santa Cruz while Ku-0063794 was from Axon Medchem. β-NGF was obtained from Preprotech.

Antibody generation. Antisera were raised against synthetic peptide sequences chosen on the basis of predicted antigenicity and uniqueness within the family of FAM134 proteins. Peptides were synthesized with N- or C-terminal cysteine (indicated in brackets in the amino-acid sequences given below) and coupled to the keyhole limpet hemocyanin (KLH) carrier protein. For FAM134A, rabbits were immunized against the peptide GLGPEMPKPPDVLP(C) (amino acids 503–517; NP_739561.2), for FAM134B against (C)GYTPQTDTSDDLDRP (amino acids 307–321; NP_001030023.1) and (C)LPTELKRKKQQLDSAH (amino acids 352–368; NP_001030023.1), for FAM134C against (C)AFRRRRAMSGSWE RDQ (amino acids 18–33; NP_080777.1). Resulting antisera were purified on an affinity matrix made by conjugation with the same peptide.

shRNA knockdown. Annealed oligonucleotides were cloned into pLKO.1puro³⁰ using AgeI and EcoRI cloning sites. pLKO.1 puro shRNA control was provided by D. Popovic (see ref. 31). The following pairs of oligonucleotides were used to target specified genes: FAM134B no. 1, CCGGGAGGTATCTGGACTGATAATCTCGAGATTATCAGTCCAGGATACCTCTTTTGTG and AATTCAAAAAGAGGTATCTCTGGACTGATAATCTCGAGATTATCAGTCCAGGATACCTC; FAM

134B no. 2, CCGGCACAAGGATGACAGTGAATTACTCGAGTAATTCACATGTCATCCTGTGTGTTTTG and AATTCAAAAACACAAGGATGACAGTG AATTACTCGAGTAATTCAGTGTATCCTGTGTG; ATG5, CCGGCATCTG AGTACCCGGATAATCTCGAGATTATCCGGGTAGCTCAGATGTTTTTG and AATTCAAAAACATCTGAGCTACCCGGATAATCTCGAGATTATCCG GGTAGCTCAGATG; BECN1, CCGGAAGATTGAAGACACAGGAGGCCCTC GAGGCCTCTGTGTCTTCAATCTTTTGTG and AATTCAAAAAAGAT TGAAGACACAGGAGGCCCTCGAGGCCCTCTGTGTCTTCAATCTT.

Liposome-shaping assay. The liposome-shaping assay was performed as described previously²⁰. For freeze-fracture experiments, 1 mg of liposomes was incubated with 5 μM protein in liposome buffer containing 0.3 M sucrose for 15 min at 37 °C. Small aliquots (1 to 2 μl) of vesicle suspension were freeze-fractured. The samples were examined using an EM 902 A electron microscope (Zeiss). Images were acquired using a 1k FastScan CCD camera (TVIPS). Diameters of approximately 1,600 to 2,600 liposome structures per incubation condition were determined using ImageJ software.

Liposome co-floatation assay. The liposome co-floatation assay was performed as described in ref. 20. Liposomes (150 μg) were incubated with 0.5 μM protein for 15 min at 37 °C in 0.3 M sucrose in liposome buffer (25 mM HEPES-KOH, pH 7.2; 25 mM KCl; 2.5 mM Mg-acetate; 100 mM K-glutamate) and mixed with 150 μl 75% sucrose in liposome buffer. The mixture was overlaid with 200 μl 35% sucrose and 200 μl liposome buffer and then centrifuged at 200,000g for 30 min at 28 °C. Six fractions, each containing 100 μl of eluate, were collected from top to bottom and analysed by SDS-PAGE and immunoblotting.

Cell culture. Human Embryonic Kidney 293 cells ((HEK293T) (ATCC), U2OS, A549, WT and Atg5^{-/-} MEFs³²) were maintained at 37 °C with 5% CO₂ in DMEM medium (Gibco) supplemented with 10% fetal calf serum (Gibco) and 100 U ml⁻¹ penicillin and streptomycin (Invitrogen). Starvation was conducted by incubating cells in EBSS medium (Invitrogen). Cells were treated with 10 μM KU-0063794, 200 ng ml⁻¹ bafilomycin A1, 1 μM thapsigargin and 2 μg ml⁻¹ tunicamycin for the indicated time periods. Primary MEFs were isolated from embryos and immortalized with the SV40 large T antigen. All cell lines were checked for mycoplasma presence using Venor GeM Classic mycoplasma detection kit for conventional PCR (MB Minerva biolabs). Primary sensory neurons from mice were not tested for mycoplasma due to the short duration in culture.

Generation of stable cell lines. To generate U2OS cells stably expressing KDEL-RFP, mCherry-eGFP-FAM134B and mCherry-eGFP-FAM134B(mutLIR) cells were transfected with GeneJuice (Merck), followed by selection in DMEM medium containing 600 μg ml⁻¹ geneticin (G418, Invitrogen) for 15–21 days.

U2OS cells stably expressing shRNA oligonucleotides were generated by lentiviral infection as described previously³¹. A shRNA-resistant pHage-eGFP-FAM134B variant (against shRNA FAM134B #1) was generated by site-directed mutagenesis and was stably introduced in U2OS cells via lentiviral transduction and selection in medium containing 10 μg ml⁻¹ blasticidin (Invitrogen).

Apoptosis analysis by FACS. Apoptosis assays on wild type and *Fam134b*^{-/-} MEFs were performed using Annexin V-FITC Apoptosis detection Kit (Enzo Life Sciences) according to the manufacturer's protocol. Numbers of annexin-V- and propidium-iodide-positive cells were detected using BDFACS Canto II and data were processed with FlowJo program.

Protein aggregate clearance assay. Puromycin treatment (5 μg ml⁻¹) was carried out for 2 h in wild-type and *Fam134b*^{-/-} MEFs. After treatment, cells were either fixed in 4% PFA for 10 min or washed three times with fresh medium, without puromycin, and incubated for a further 3 or 6 h prior to fixation and immunofluorescence analysis.

Subcellular fractionation. Fractionation was performed similar to ref. 33. Samples were loaded on a linear 0–20% iodaxinol gradient. Centrifugation took place in a SW28 swing-out rotor for 115 min at maximum speed (28,000 r.p.m.). After centrifugation 600-μl fractions were taken (top to bottom) and subjected to western blot analyses.

Protein expression and purification. FAM134B (450–459) and LC3A (2–120) chimera was cloned into pGEX6P1 and expressed as glutathione-S-transferase (GST) fusion proteins in *Escherichia coli* BL21 DE3. Cells were lysed by sonication in lysis buffer (25 mM Tris, 100 mM NaCl, pH 8.5), and the lysate was cleared by centrifugation. The expressed protein was purified by glutathione-Sepharose 4B, cleaved by PreScission Protease, and further purified by size-exclusion chromatography (HiLoad 16/600 Superdex 75 column, GE Healthcare Life Sciences) in 25 mM Tris, 100 mM NaCl, pH 8.5.

Crystallization, X-ray data collection and structure determination. FAM134-LIR-LC3A crystals were obtained using 8% Tacsimate (Hampton Research) pH 8.0, 20% Poly ethylene glycol 3350 as a reservoir solution by the sitting-drop vapour diffusion method at 293 K. Data were collected at Diamond Light Source beam line I03 and processed with iMOSFILM. The crystal structure of FAM134B-LIR-LC3A was determined by molecular replacement with Molrep

using the LC3A structure (Protein Data Bank ID: 3ECI) as a search model. Manual model building and refinement were done with Coot and Phenix. The final statistics of refined models are shown in Supplementary Table 2 and the atomic coordinates have been deposited in the Protein Data Bank under accession number 4ZDV.

GST pull-down. HEK293T cells were transfected with indicated constructs using GeneJuice (Merck) for 24 h. Cells were lysed in lysis buffer (50 mM HEPES, pH 7.5, 150 mM NaCl, 1 mM EDTA, 1 mM EGTA, 1% Triton X-100, 10% glycerol, 25 mM NaF supplemented with PMSF (Sigma), aprotinin (Sigma), leupeptin (Biomol), and sodium vanadate (Sigma)). Lysates were cleared by centrifugation at 12000g for 10 min, and incubated with GST-fusion-protein-loaded beads for 2 h. Beads were then washed three times in lysis buffer, resuspended in Laemmli buffer and boiled. Supernatants were loaded on SDS-PAGE.

Endogenous co-immunoprecipitation between FAM134B and LC3B. Three confluent 15-cm diameter Petri dishes of wild-type and *Fam134b*^{-/-} MEFs were harvested in 50 mM Tris/HCl (pH 8), 120 mM NaCl, 1% (v/v) NP40, complete protease inhibitor cocktail (Roche), and 1 mM PMSF. Lysates were cleared by centrifugation at 12000g for 10 min, and incubated over night at 4 °C with FAM134B primary antibody. Lysates and FAM134B antibody solutions were incubated with Protein A-Agarose beads (Roche) for 4 h at 4 °C. Beads were then washed three times in lysis buffer, resuspended in Laemmli buffer and boiled. Supernatants were loaded on SDS-PAGE.

Long-lived protein degradation assay. The turnover of long-lived proteins upon autophagy induction in wild-type and *Fam134b*-knockout MEFs was measured as previously described³⁴.

Immunofluorescence microscopy. Cells were grown on coverslips and after each experiment fixed with 4% PFA for 20 min. Cells were permeabilized with 0.1% saponin in PBS for 30 min and blocked with 5% bovin serum albumin (BSA) in PBS for 1 h. Subsequently the coverslips were incubated in a wet chamber with primary antibody solution for 2 h, washed in the permeabilizing buffer and then incubated with secondary antibody solution for 1 h. Coverslips were finally washed three times and mounted on microscope slides using the mounting medium (Molecular Probes). Fluorescence signals were captured using a LSM510 META (Zeiss) or a Leica TCS SP8 confocal laser-scanning microscope. Images were processed using ImageJ software. Co-localization was analysed using Volocity Demo software (Perkin Elmer).

Fluorescence protein protection (FPP) assay. The FPP assay was carried out with COS-7 cells transiently transfected with FAM134B-eGFP- (C-terminal eGFP tag), eGFP-FAM134B- (N-terminal eGFP tag), CD3-RFP-, or RFP-KDEL-expressing plasmids (Lipofectamine2000, Invitrogen). Twenty four hours after transfection cells were transferred to a perfusion chamber (37 °C) and kept in live-cell buffer (50 mM HEPES, 23 mM NaCl, 3 mM MgCl₂, 100 nM CaCl₂, 1 mM EGTA, 107 mM glutamate, 1 mM ATP, 2 mM DTT). Images were recorded with a 20× objective every 20 s for 10 min at an inverted microscope (Axio Observer Z.1; AxioCam MRm, Zeiss). After plasma membrane permeabilization with digitonin (18 µM, 80 s) cells were washed for 80 s with live-cell buffer. Subsequently, trypsin (1 µM) was added to the cells. ImageJ was used for fluorescence quantification measurements. Mean fluorescent values of single cells were subtracted from background fluorescence and normalized to fluorescence at the starting time point.

Protein sequence alignment. The multisequence FAM134 protein sequence alignment was generated with ClustalW using the default settings.

ER area measurements. Cells with expanded ER were visually defined if KDEL-RFP-labelled ER occupied over approximately 80% of cell area. Additionally, the ER area measurements were conducted using ImageJ as follows. Background threshold was manually defined and set for all images. Borders of each cell were drawn and the ER area was then calculated and presented as a fraction of the total cell area.

Ultrastructural analyses. For conventional TEM, U2OS cells transfected with either control or FAM134B shRNA, or overexpressing eGFP-FAM134B treated or untreated with 200 nM bafilomycinA1, were scrapped from culture flask and pelleted by centrifugation. Pellets were resuspended in 2% glutaraldehyde in 0.1 M cacodylate buffer (pH 7.4) for at least 2 h at room temperature. Fixative was replaced by cacodylate buffer and fixation was prolonged overnight. Cells were then embedded in Epon resin as previously described³⁵. Subsequently, 55-nm sections were cut and stained with uranyl acetate and lead citrate using the EM AC-20 contrasting instrument (Leica Microsystems). For the immunoelectron microscopy analyses, U2OS cells stably expressing eGFP-FAM134B and grown to 80% confluence were treated with 200 nM bafilomycin A1 for 6 h. Cells were fixed in an equal volume as the culture medium by adding a freshly prepared mix of 4% PFA and 0.4% glutaraldehyde in 0.1 M phosphate buffer (pH 7.4) for 3 h, followed by a post-fixation in 2% PFA/0.2% glutaraldehyde for 2 h at room temperature and an overnight incubation at 4 °C. Cells were then embedded for

the Tokuyasu procedure before cutting ultrathin cryo-sections and immuno-gold labelling as previously described³⁶. Cell sections were examined using an 80 kV transmission electron microscope (Jeol 1200-EX).

To preserve the neuron native morphology, a monolayer culture of dorsal root ganglia (DRG) neurons was embedded in Epon resin in their original position in 25-cm² plastic culture flasks following the flat embedding procedure³⁷. After Epon resin polymerization at high temperature, the embedded material was stripped off the plastic flask using needle-nose pliers and forceps. Small circular specimens (≤0.5 cm in diameter) of Epon-embedded material were cut using a drill bit (mounted with a rotating cutting tool) and glue onto supports for ultra-microtome. Ultrathin serial sections of 50 nm were cut parallel to the neuron monolayer using an ultra-microtome (Leica Microsystems) and transferred onto Formvar carbon-coated copper grids for staining using the EM AC-20 contrasting instruments (Leica Microsystems).

Generation of *Fam134b*-knockout mice. A 10.4-kb fragment of the 129/SvJ mouse genomic lambda phage library (Stratagene) containing exons 5 to 9 of the mouse *Fam134b* gene was subcloned into the pKO-V901 vector containing a diphtheria toxin A (DTA) cassette (Lexicon Genetics). A pgk-promoter-driven neomycin resistance cassette (neo) flanked by FRT-sites and a 5' loxP site was inserted into an EcoRV site in intron 5 of *Fam134b*. A second loxP site together with an additional 3' EcoRI site was inserted into the ClaI site of exon 8. The targeting construct was linearized and electroporated into R1 mouse embryonic stem (ES) cells. Homologous recombination was verified by Southern blot analysis of neomycin-resistant clones using EcoRI and an external 498-bp Southern probe. Correctly targeted embryonic stem cell clones were injected into C57BL/6 blastocysts to generate chimaeras. Resulting chimaeric mice were crossed with Cre-deleter mice to remove exons 6–8 of *Fam134b*. For PCR genotyping, DNA was isolated from tail biopsies by alkaline lysis and used in a single PCR mix containing the primers: F1, 5'-ACCCATAGTTCATACACTAGGC-3'; R1, 5'-CGTAACA GAGGTTGGTGAGG-3'; and F2, 5'-CATGGCAATGACATTCTCC -3'. A product size of 280 bp was obtained for the wild-type allele and a 420-bp amplicon for the knockout allele. Studies were performed in a mixed 129SvJ/C57BL/6 background in the F4 and F5 generations. Animals were chosen from the animal house database without prior inspection/pre-selection of animals. Both male and female mice were used, except for tail-flick experiments, which included only male mice. Age of the mice and sample size is given for each experiment. The experimenter was blinded to the genotype of the mice in all behavioural tests and for axon counting. Animal care and experimental procedures were performed in accordance with the guidelines established by the animal welfare committee of the State of Thuringia.

FAM134B protein expression analysis. MEFs were prepared from embryonic-day-13.5 mouse pups as described previously³⁷. Primary MEFs were harvested in 50 mM Tris/HCl (pH 8), 120 mM NaCl, 0.5% (v/v) NP40, complete protease inhibitor cocktail (Roche), and 1 mM PMSF. Homogenates were incubated on ice for 15 min and centrifuged for 30 min at 16,900g. Thirty micrograms of supernatant protein was subjected to SDS-PAGE and western blot analysis using an affinity-purified antibody against the Fam134b-specific peptide LPTELKRRK QQLDSAHR.

Recording of tail sensory nerve conduction velocities. Mice were anaesthetized and body temperature was maintained with a warming pad. Tail sensory nerve conduction velocities (TSNCVs) were recorded 30 mm proximal to the stimulation electrodes. Sensory action potentials were evoked with increasing intensity (0–10 V, increment 1 V, 50 µs duration). Electrodes with a tip diameter of 1–2 µm and an impedance of 0.1 MΩ were used (WE30030.1H10, Science Products). Signals were processed with an extracellular amplifier (EXT 02F, NPI; high-pass filter: 3 Hz, low-pass filter: 2 kHz). The sample frequency was 20 kHz. For analysis Signal 3 software (CED) was used. TSNCVs were calculated by dividing the distance by the take-off latency of five averaged sensory potentials. Amplitudes were determined from peak to peak.

Pain-related behavioural assays/tail-flick assay. Thermal stimulation (at 45 °C) was applied to the tail of adult male mice after their habituation to the test environment using the water immersion method³⁸. The time from onset of stimulation to rapid movement of the tail was recorded. Two separate determinations of tail-flick latency per mouse were recorded and averaged. Statistical comparisons of two groups of data were made using the Mann–Whitney *U*-test. The experimenter was blinded to the genotype of the mice.

Histological analysis of spinal cord and afferent sensory fibres. Murine tissue was fixed by *in vivo* perfusion of fixative solution containing 4% paraformaldehyde and 1% glutaraldehyde in PBS. The fourth lumbar DRG and spinal cord was isolated, post-fixed overnight at 4 °C in fixative and further processed for sectioning. Afferent sensory fibre bundles distal to the DRG were counted using ImageJ software. Cross-sections of the spinal cord with a thickness of 10 µm underwent

the cresyl violet staining protocol for quantification of Nissl-stained motor neuron cell bodies in the ventral horn.

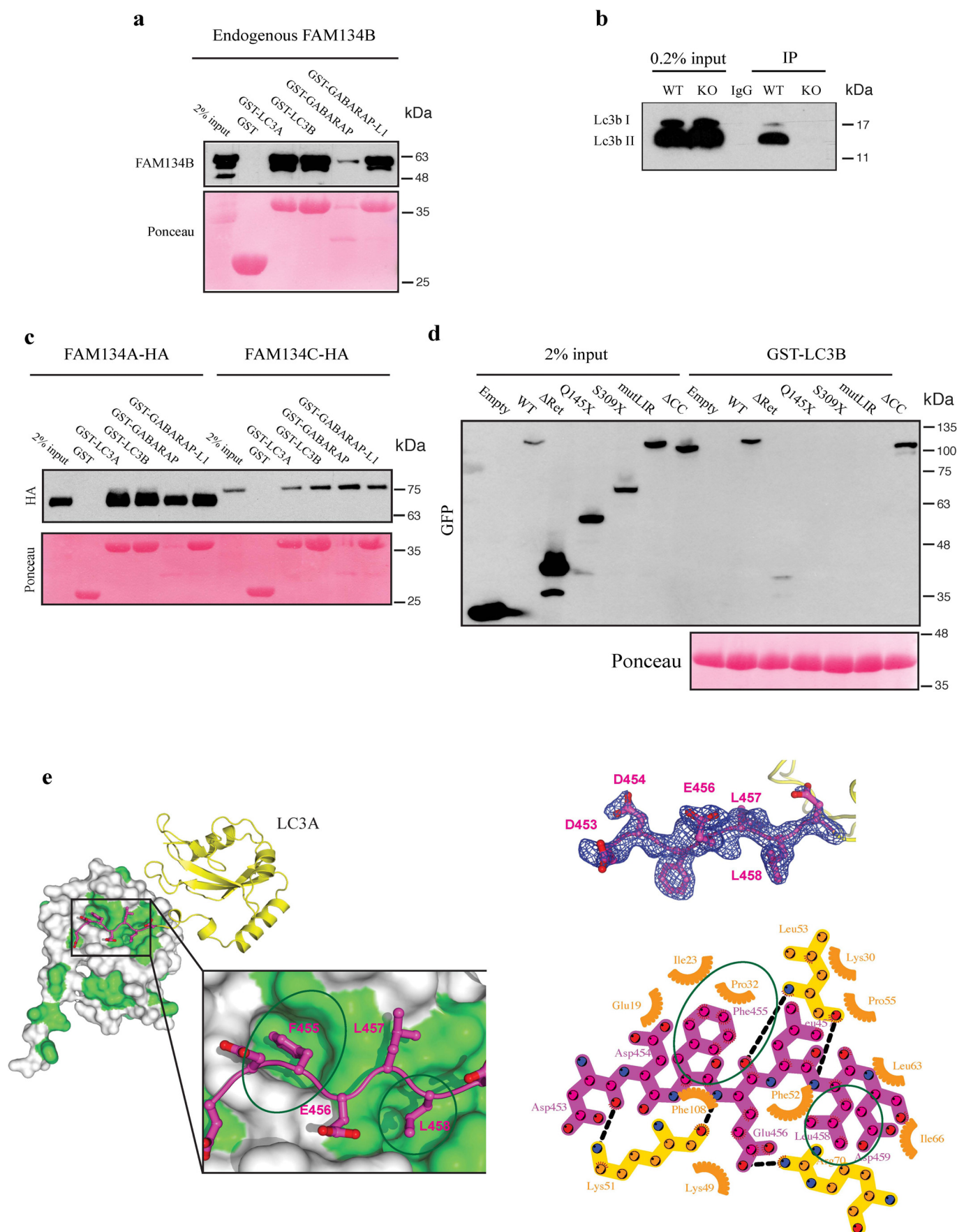
DRG cultures. Primary DRG neurons were prepared from adult mice killed via cervical dislocation. DRGs were extracted from the spinal cord and rinsed three times with Hank's buffered salt solution (HBSS) followed by an incubation in collagenase solution (3 mg ml⁻¹ solved in HBSS) for one hour at 37 °C. Activated trypsin was added to a final concentration of 0.1% and DRGs were incubated for further 10 min at 37 °C. DRGs were rinsed three times with HBSS and then dissociated by using BSA-blocked, fire-polished glass Pasteur pipettes of decreasing diameters. The single cell suspension was centrifuged for 5 min at 160g and supernatant was removed from the cell pellet. DMEM containing 10% horse serum was added to the cell pellet and again centrifuged for 5 min at 160g. The supernatant was carefully removed and cells were resuspended in Neurobasal-A medium supplemented with 2 mM L-glutamine and 2% B27. Cells were plated on poly-L-lysine coated cover slips or T25 cell culture flasks and placed at 37 °C in a 5% CO₂ atmosphere. Thirty minutes after plating, medium was replaced by fresh culture medium containing β -NGF (50 ng ml⁻¹).

Ultrastructural analysis of DRG sensory neurons and motoneurons of the spinal cord *in vivo*. Tissue of DRG and spinal cord was fixed in 4% glutaraldehyde. The tissues were post-fixed with osmium tetroxide. Ultrathin sections were treated with uranyl acetate and lead citrate and viewed with a Philips CM10 transmission electron microscope.

Statistical analysis. Data are presented as mean \pm s.e.m. or s.d. Statistical analysis of two experimental groups was performed using one-way ANOVA or parametric two-tailed Student's *t*-test after confirming a parametric distribution by Normal Q-Q plots. For non-parametric distributed data, the Mann-Whitney *U*-test was applied. If more than two groups were compared, one-way ANOVA was performed, and differences between subjects were analysed by a subsequent Bonferroni's or Tukey honest significant difference test. If necessary, two-way

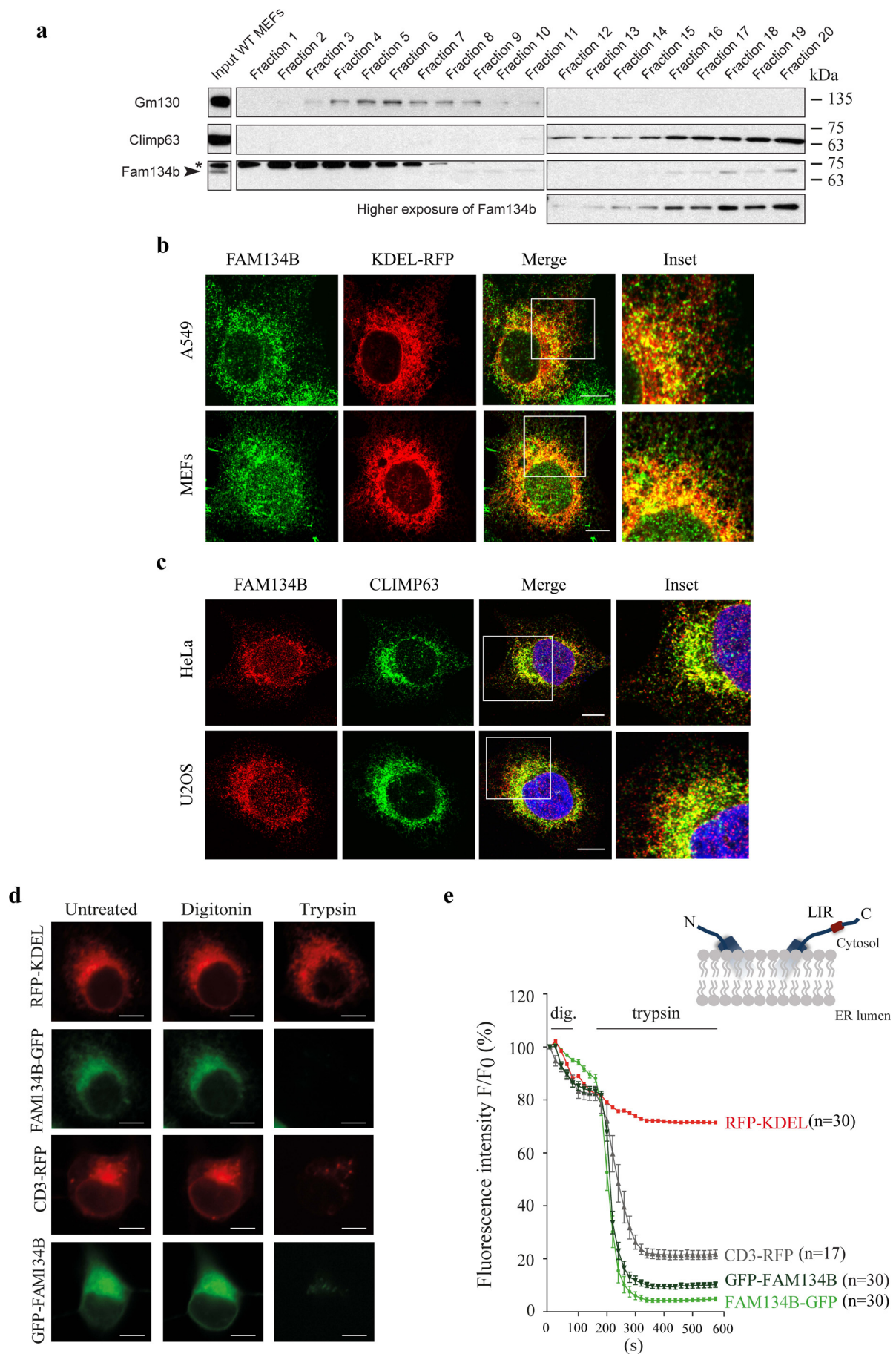
ANOVA was applied. Results were considered significant at $P < 0.05$. No statistical methods were used to predetermine sample size.

26. Behrends, C., Sowa, M. E., Gygi, S. P. & Harper, J. W. Network organization of the human autophagy system. *Nature* **466**, 68–76 (2010).
27. Altan-Bonnet, N. *et al.* Golgi inheritance in mammalian cells is mediated through endoplasmic reticulum export activities. *Mol. Biol. Cell* **17**, 990–1005 (2006).
28. GrandPré, T., Nakamura, F., Vartanian, T. & Strittmatter, S. M. Identification of the Nogo inhibitor of axon regeneration as a Reticulon protein. *Nature* **403**, 439–444 (2000).
29. Klopfenstein, D. R. *et al.* Subdomain-specific localization of CLIMP-63 (p63) in the endoplasmic reticulum is mediated by its luminal alpha-helical segment. *J. Cell Biol.* **153**, 1287–1300 (2001).
30. Stewart, S. A. *et al.* Lentivirus-delivered stable gene silencing by RNAi in primary cells. *RNA* **9**, 493–501 (2003).
31. Popovic, D. *et al.* Rab GTPase-activating proteins in autophagy: regulation of endocytic and autophagy pathways by direct binding to human ATG8 modifiers. *Mol. Cell. Biol.* **32**, 1733–1744 (2012).
32. Kuma, A. *et al.* The role of autophagy during the early neonatal starvation period. *Nature* **432**, 1032–1036 (2004).
33. Yang, M., Ellenberg, J., Bonifacino, J. S. & Weissman, A. M. The transmembrane domain of a carboxyl-terminal anchored protein determines localization to the endoplasmic reticulum. *J. Biol. Chem.* **272**, 1970–1975 (1997).
34. Chan, E. Y., Kir, S. & Tooze, S. A. siRNA screening of the kinome identifies ULK1 as a multidomain modulator of autophagy. *J. Biol. Chem.* **282**, 25464–25474 (2007).
35. Verheije, M. H. *et al.* Mouse hepatitis coronavirus RNA replication depends on GBF1-mediated ARF1 activation. *PLoS Pathog.* **4**, e1000088 (2008).
36. Slot, J. W. & Geuze, H. J. Cryosectioning and immunolabeling. *Nature Protocols* **2**, 2480–2491 (2007).
37. Khundadze, M. *et al.* A hereditary spastic paraplegia mouse model supports a role of ZFYVE26/SPASTIZIN for the endolysosomal system. *PLoS Genet.* **9**, e1003988 (2013).
38. Le Bars, D., Gozariu, M. & Cadden, S. W. Animal models of nociception. *Pharmacol. Rev.* **53**, 597–652 (2001).



Extended Data Figure 1 | FAM134 proteins bind to GST-LC3-like modifiers. **a**, A549 cell lysates were added to beads with various immobilized GST fusion proteins (GST, GST-LC3A, GST-LC3B, GST-GABARAP, GST-GABARAP-L1), followed by western blotting using an antibody against FAM134B. **b**, Co-immunoprecipitation between Fam134b and Lc3b in wild-type (WT) mouse embryonic fibroblasts (MEFs). MEFs isolated from *Fam134b*-knockout (KO) mice served as control. **c**, Interaction of FAM134A and FAM134C with LC3-like modifiers. **d**, FAM134B proteins lacking the reticulon domain (Δ ret), disease-associated truncating FAM134B variants

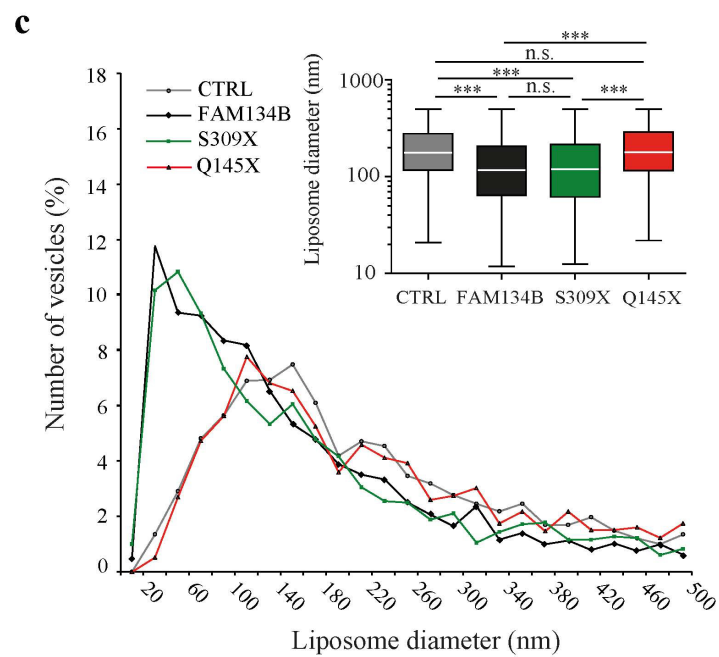
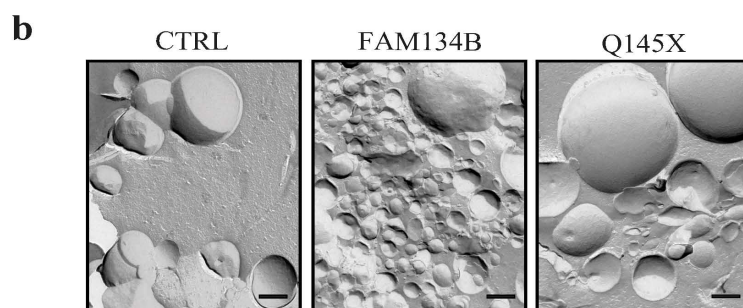
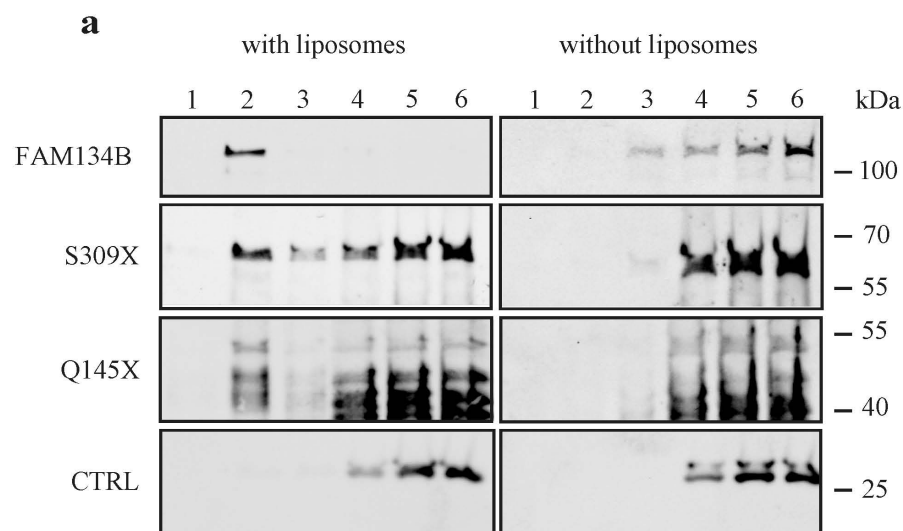
Q145X and S309X, and FAM134B with a mutated LIR-motif (mutLIR) fail to bind GST-LC3-like modifiers (LC3B) in contrast to wild-type FAM134B and FAM134B lacking the coiled-coil domain (Δ CC). **e**, Crystal structure of a FAM134B-LIR peptide interacting with LC3A. Ribbon and surface representation model of the FAM134B-LIR-LC3A interaction and crystallographic symmetry related molecule. (LIR, magenta; LC3A, yellow). $2F_o - F_c$ electron density (blue mesh) of FAM134B-LIR (amino acids 453–459), contoured at 1σ and with ball-and-stick model.



Extended Data Figure 2 | Subcellular localization and topology of endogenous FAM134B.

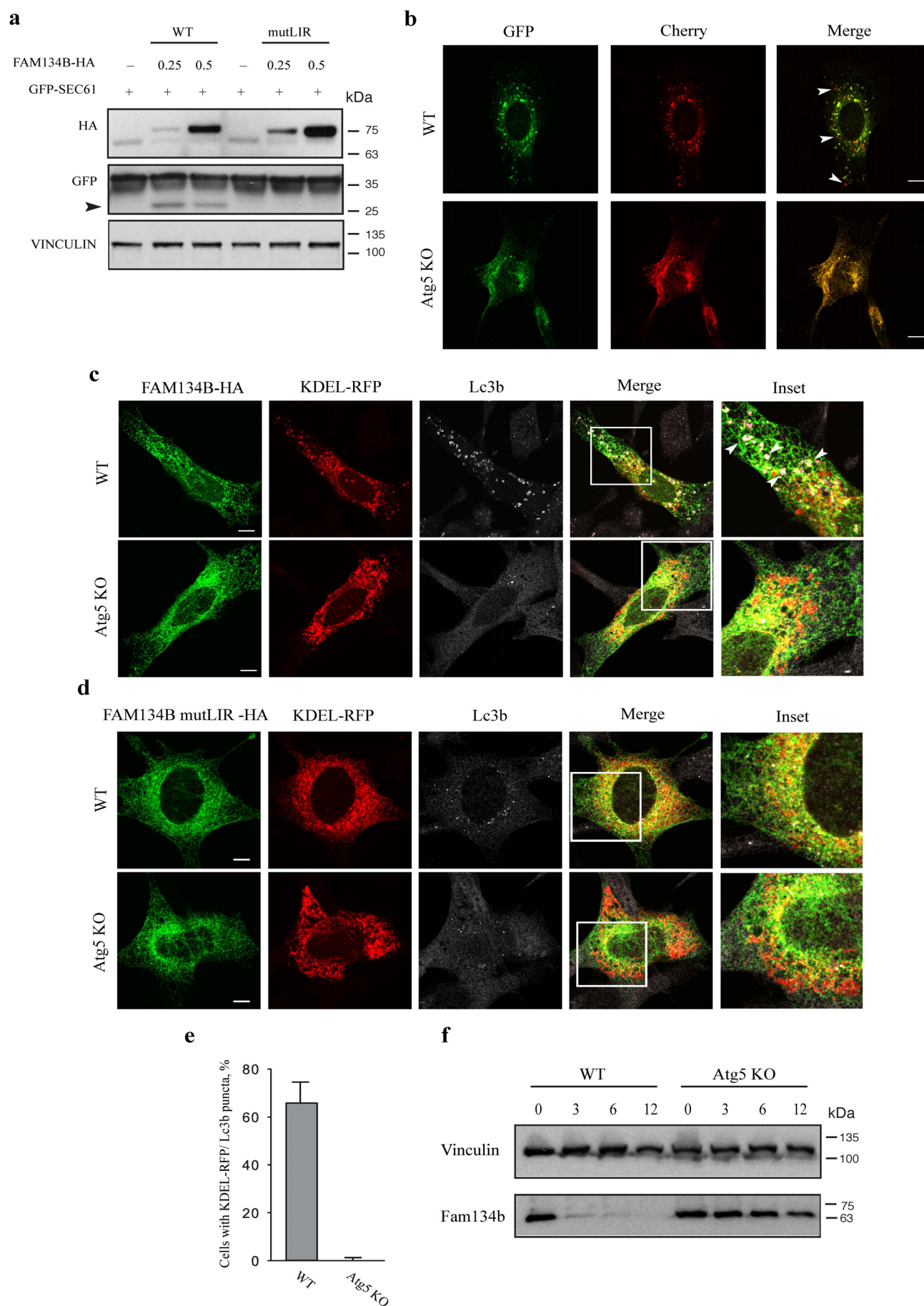
a, The post-nuclear fraction of wild-type MEF lysate was loaded on a linear Iodixanol gradient (0–20%). Fractions (top to bottom) were subjected to western blot and analysed with antibodies directed against endogenous proteins as indicated. Images are from two different gels, while the exposure time is the same. Asterik indicates non-specific band. **b**, A549 cells and MEFs were transfected with a KDEL-RFP expression plasmid for 24 h. After fixation, endogenous FAM134B was detected. FAM134B co-localizes with KDEL-RFP. Representatives of five images are shown. Scale bar, 10 μ m. **c**, HeLa and U2OS cells were fixed and stained for endogenous FAM134B and CLIMP-63. FAM134B co-localizes with CLIMP-63. Representatives of five images are shown. Scale bar, 10 μ m. **d**, FAM134B topology analysis. COS-7 cells transiently overexpressing C-terminal tagged FAM134B (FAM134B-eGFP) or N-terminal tagged FAM134B (eGFP-FAM134B) were

subjected to fluorescence protein protection (FPP) assay. COS-7 cells transfected with plasmids encoding the luminal ER peptide RFP-KDEL and C-terminal RFP-tagged CD3 (CD3-RFP) served as controls. RFP-KDEL, which localized to the ER lumen, shows fluorescence protein protection upon trypsin administration following digitonin treatment. By contrast, according to the known topology of CD3-RFP the RFP-tag faces the cytosol and as a consequence trypsin treatment abolishes protein fluorescence. Scale bar, 10 μ m. **e**, C-terminal RFP-tagged CD3 (CD3-RFP) served as control (RFP-tag faces the cytosol). A N-terminal tagged FAM134B variant was also subjected to the FPP assay. A strong decrease in fluorescence was observed for CD3-RFP, FAM134B-eGFP and eGFP-FAM134B after sequenced digitonin and trypsin treatment, but not for RFP-KDEL (n = number of cells, error bars indicate s.e.m.).



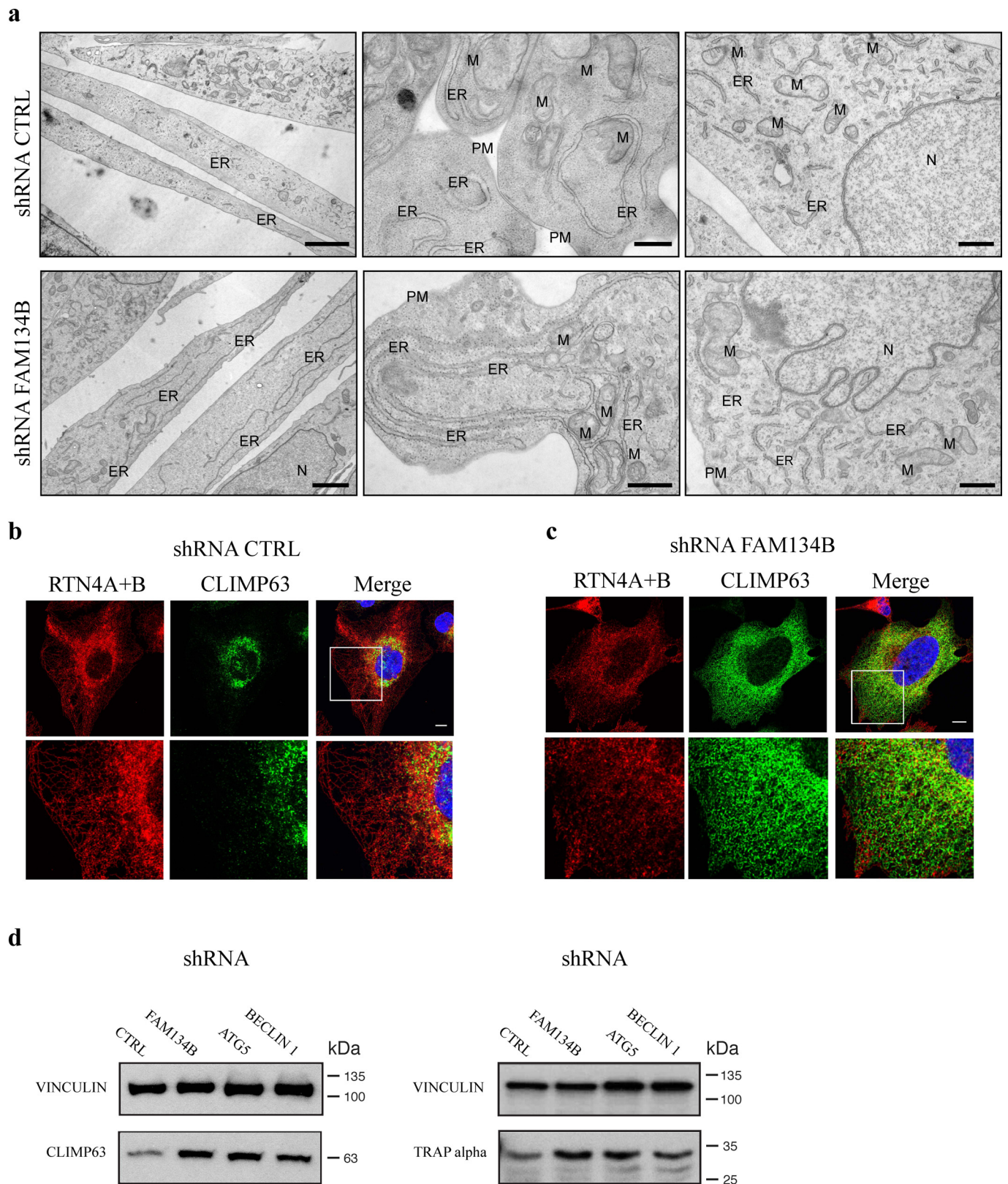
Extended Data Figure 3 | FAM134B is a membrane-shaping protein that remodels lipid bilayers. **a**, Liposome co-floatation assays. Proteins were detected using anti-GST antibodies in immunoblots of sucrose gradient fractions 1 (top) to 6 (bottom). GST–FAM134B, but not GST (Ctrl), floated with liposomes in fraction 2. Disease-related truncating mutations S309X and Q145X only partially floated with the liposome fraction. **b**, Representative transmission electron microscopy (TEM) images of freeze-fractured incubations of liposomes with recombinant GST-fusion proteins (GST–FAM134B; GST–FAM134B(Q145X); Ctrl, GST). Scale bar, 200 nm.

c, Distribution of liposome diameters observed by TEM of freeze-fractured liposome incubations. Incubation with FAM134B and S309X leads to a pronounced increase in the relative numbers of smaller structures in comparison to control (GST) and Q145X. Inset, box plots of data presented in **c**; *y* axis is logarithmic. n.s., not significant; *** $P < 0.001$ one-way ANOVA, error bars indicate s.e.m. ($n = 2,682$ for Ctrl, $n = 2,683$ for FAM134B, $n = 1,685$ for Q145X, $n = 1,612$ for S309X, $n =$ number of liposomes). Boxes contain 50% of the values; minimal, maximal, and median values are marked by vertical lines.



Extended Data Figure 4 | Fam134b determines ER degradation through autophagy. **a**, U2OS cells transiently co-transfected with 0.25 μ g of GFP-SEC61 plasmid expressing full length or mutLIR FAM134B-HA at the indicated quantities (μ g). Cell lysates were immunoblotted with antibodies against HA, GFP and vinculin. Black arrow-head indicates protein-degradation products. **b**, Wild-type (WT) and *Atg5*-knockout (KO) MEFs transiently expressing mCherry-eGFP-FAM134B were fixed and processed for immunofluorescence analysis. Cells with mCherry-positive and simultaneously GFP-negative punctae were counted in three independent experiments (biological replicates). Representative of 50 images is shown. Scale bar, 10 μ m. **c, d**, *Atg5*-knockout and control MEFs were co-transfected with plasmids expressing full-length LIR (**c**) or mutLIR (**d**) FAM134B-HA and KDEL-RFP

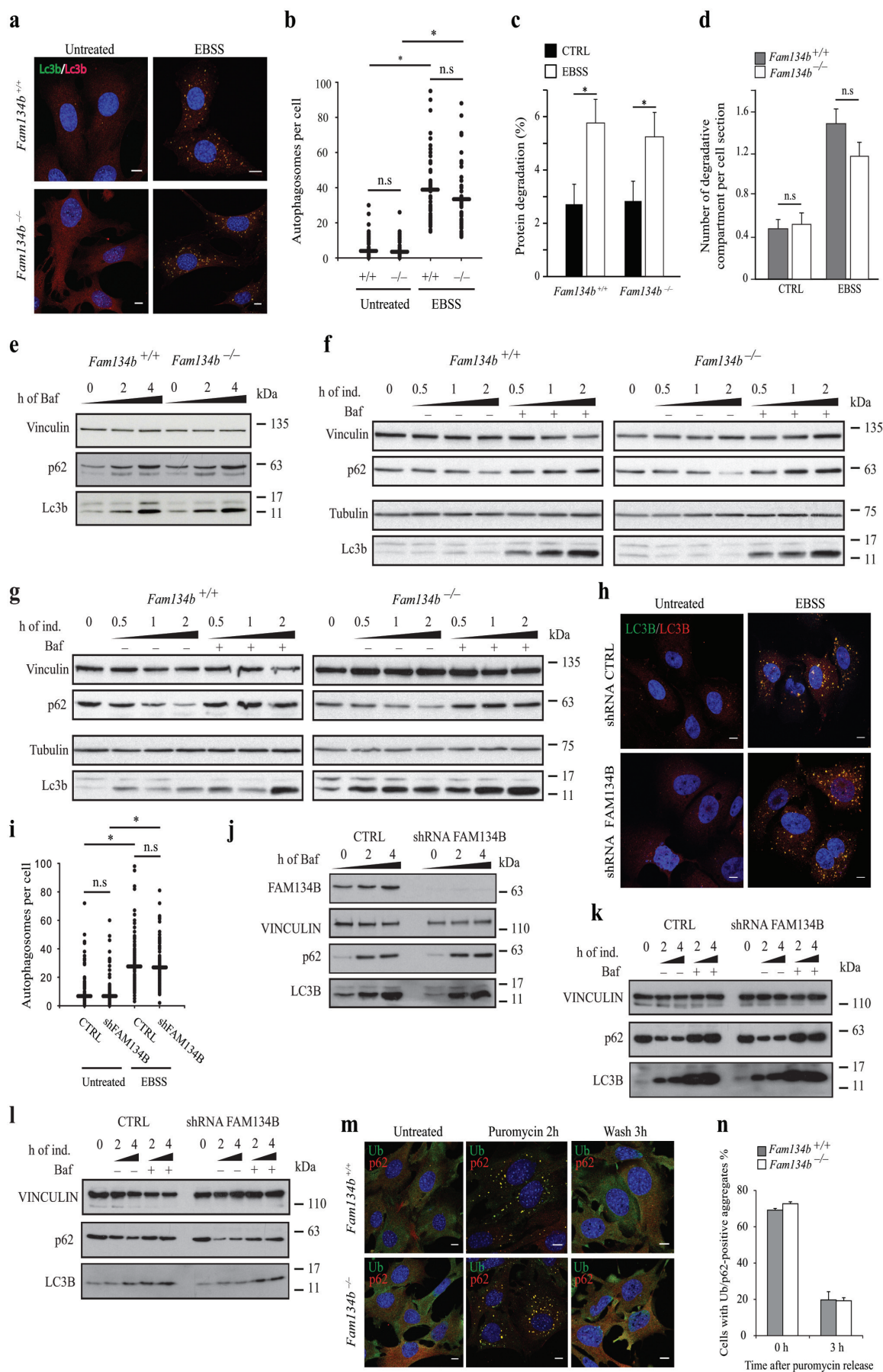
for 24 h, fixed and processed for immunofluorescence using antibodies against the HA tag and Lc3b. Overexpression of FAM134B-HA in wild-type but not in *Atg5*-knockout MEFs leads to the formation of punctae positive for both KDEL-RFP and Lc3b. Representatives of five images are shown. Scale bar, 10 μ m. **e**, Quantification of cells displaying KDEL-RFP- and Lc3b-positive punctae shown in **c** and **d**. At least 50 cells per experiment from three independent experiments (biological replicates) were quantified (error bars indicate s.d.). **f**, Fam134b is stabilized in starved *Atg5*-knockout MEFs. Wild-type and *Atg5*-knockout MEFs were starved in EBSS for the indicated periods of time. Cell lysates were processed by SDS-PAGE and western blot using antibodies against Fam134b and vinculin.



Extended Data Figure 5 | *FAM134B* knockdown causes ER expansions.

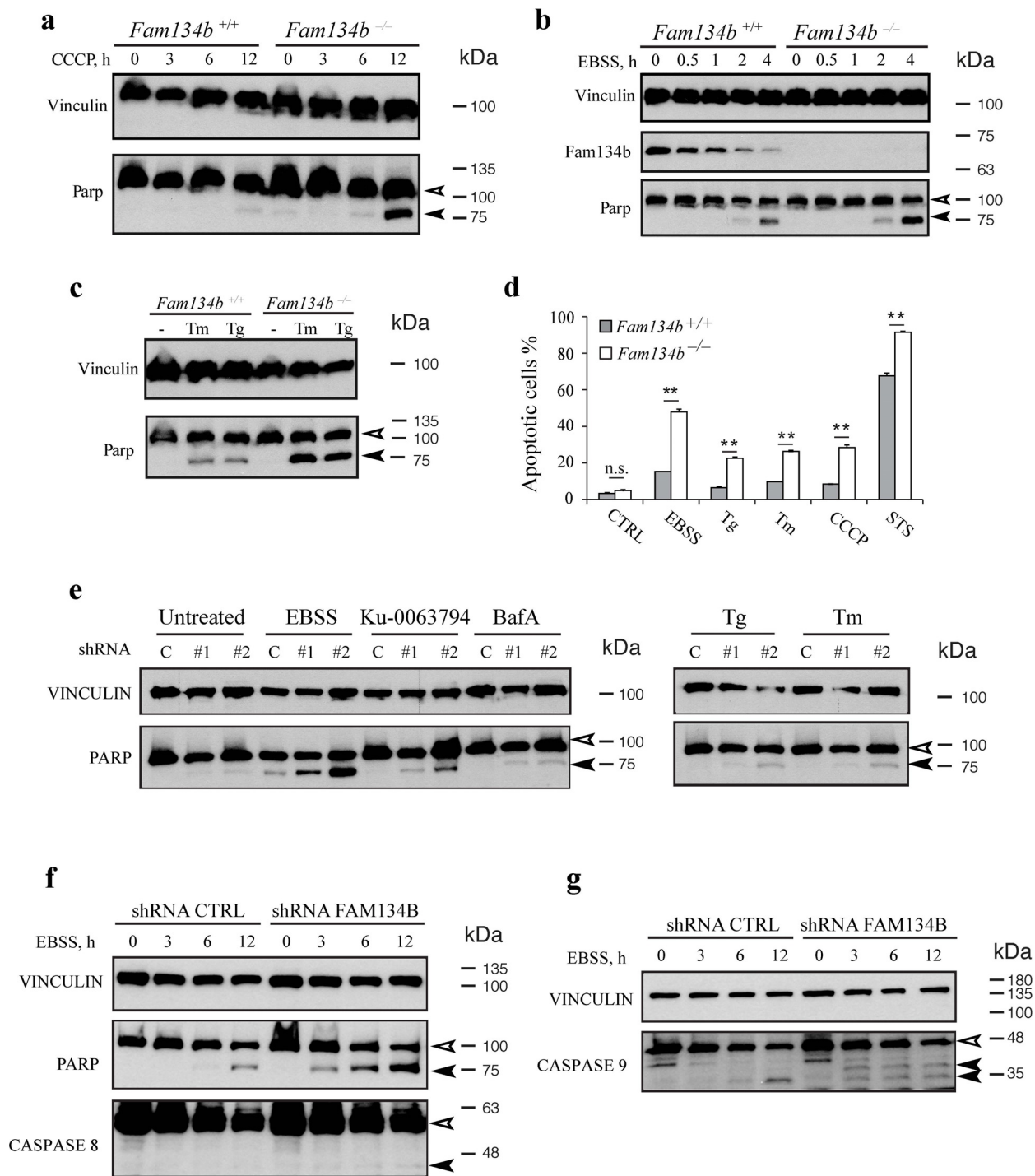
a, Ultrastructural analysis of *FAM134B*-depleted cells. Constructs expressing control shRNA or α -*FAM134B* shRNA were lentivirally delivered into U2OS cells. Cells were chemically fixed and embedded with Epon resin. Longitudinal and transversal sections and a part of the nuclear membrane is shown. *FAM134B*-depleted cells display ER expansions, particularly in the cell periphery. The membrane of the nucleus of *FAM134B*-knockdown cells also undergoes expansion. M, mitochondria; N, nucleus; PM, plasma membrane.

Scale bars, 2 μ m (left images) and 500 nm (middle and right images) ($n = 150$ cells). **b, c**, ER sheets are expanded in *FAM134B*-deficient cells. Constructs expressing control shRNA or α -*FAM134B* shRNA were lentivirally delivered in U2OS cells. After selection, cells were fixed, stained for CLIMP-63 and RTN4A and RTN4B and analysed by fluorescence microscopy. Representatives of five images are shown. Scale bar, 10 μ m. **d**, CLIMP-63 and TRAP α levels in autophagy-deficient and *FAM134B*-depleted cells.



Extended Data Figure 6 | FAM134B is not required for bulk autophagy and aggrephagy. **a**, *Fam134b*^{+/+} and *Fam134b*^{-/-} MEFs were starved in EBSS for 2 h, fixed and stained for Lc3b (using two different anti-Lc3b antibodies to enhance the signal). Representatives of five images are shown. Scale bar, 10 μ m. **b**, Lc3b-positive punctae in 50 cells per experiment from three independent experiments were counted. $*P < 0.0001$, one-way ANOVA. **c**, Long-living proteins degradation assay. For autophagy induction, cells were starved with EBSS. Protein degradation was assessed in three independent experiments in triplicate. Error bars represent s.e.m. of three independent counts (three technical replicates, $n = 20$ cells per each replicate, P value is calculated using t -test, $*P < 0.05$). **d**, Transmission electron microscopy of *Fam134b*^{+/+} and *Fam134b*^{-/-} cells. Autophagosomal/degradative compartments (that is, autophagosomes, autolysosomes and lysosomes) were counted. Quantification was performed by counting 20 cells in three different grids (three biological replicates). Error bars represent s.d., P value is calculated using t -test. **e**, Lc3b lipidation and p62 degradation was analysed in *Fam134b*^{+/+} and *Fam134b*^{-/-} MEFs treated with 200 nM bafilomycin A1 for the indicated time. **f**, **g**, For autophagy induction, cells were starved with EBSS (**f**) or treated with the chemical Ku-0063794 (10 μ M) (**g**) for the indicated periods of time.

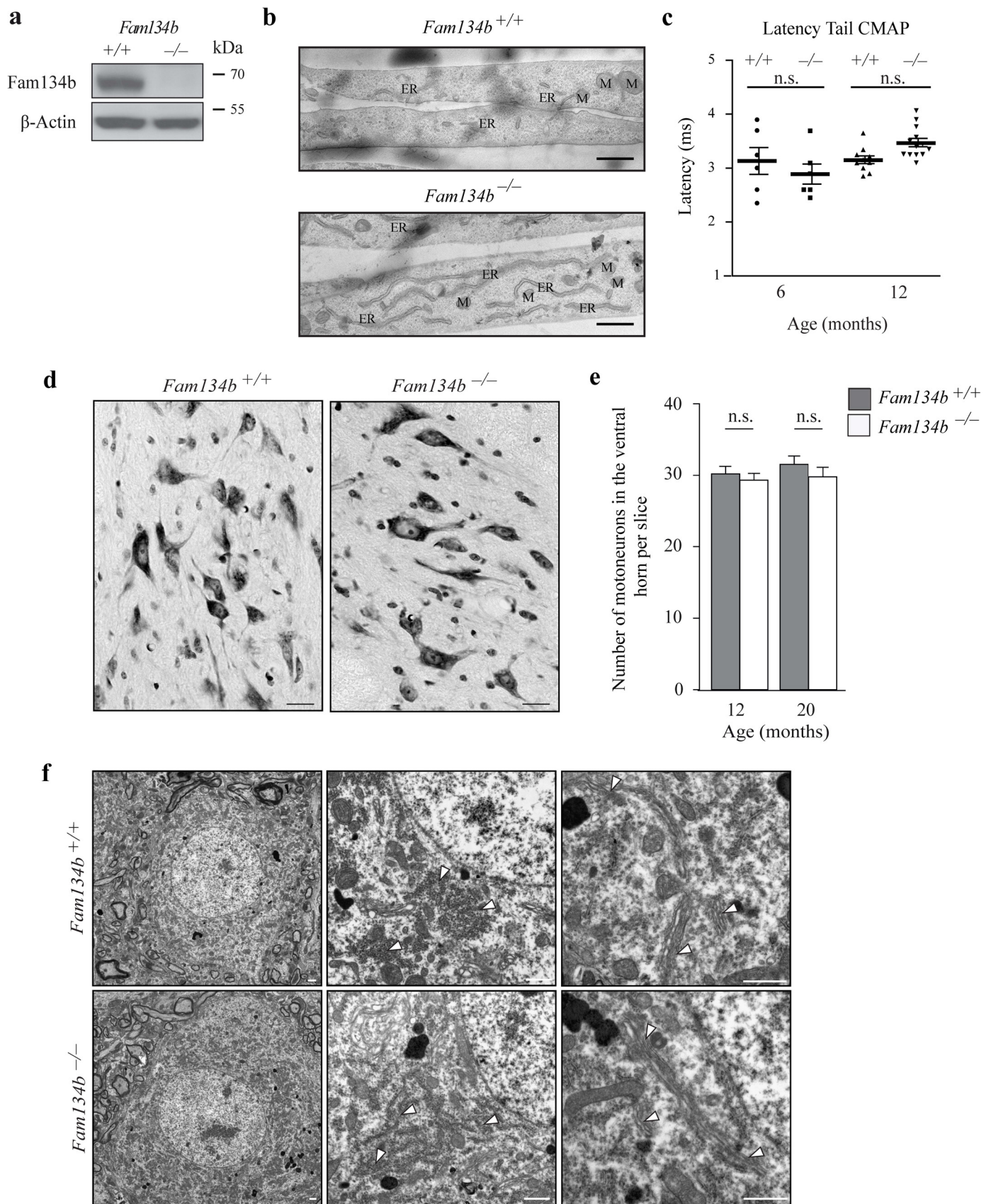
Bafilomycin A1 was added 1 h before the beginning of the treatment. **h**, Control and *FAM134B*-knockdown (shRNA-mediated) U2OS cells were starved in EBSS for 2 h, fixed and stained for LC3B (using two different anti-LC3B antibodies to enhance the signal). Representatives of five images are shown. Scale bar, 10 μ m. **i**, LC3B-positive punctae in 150 cells per experiment from three independent experiments were counted. $*P < 0.0001$, Mann-Whitney U -test. **j**, LC3B lipidation and p62 degradation were analysed in control and *FAM134B* shRNA cells treated with 200 nM bafilomycin A1 for the indicated time. **k**, **l**, For autophagy induction, cells were starved with EBSS (**k**) or treated with the chemical Ku-0063794 (10 μ M) (**l**) for the indicated periods of time. Bafilomycin A1 was added 1 h before the beginning of the treatment. **m**, *Fam134b*^{+/+} and *Fam134b*^{-/-} MEFs were either treated with 5 μ g ml⁻¹ puromycin for 2 h or treated and subsequently washed and incubated in puromycin-free medium for 3 h, fixed and stained for ubiquitin (Ub) and p62. Representatives of five images are shown. Scale bar, 10 μ m. **n**, The number of cells with Ub/p62 punctae before and after puromycin release per 100 cells per experiment was determined from three independent experiments (biological replicates). Error bars indicate s.d.



Extended Data Figure 7 | FAM134B deficiency sensitizes cells to apoptosis.

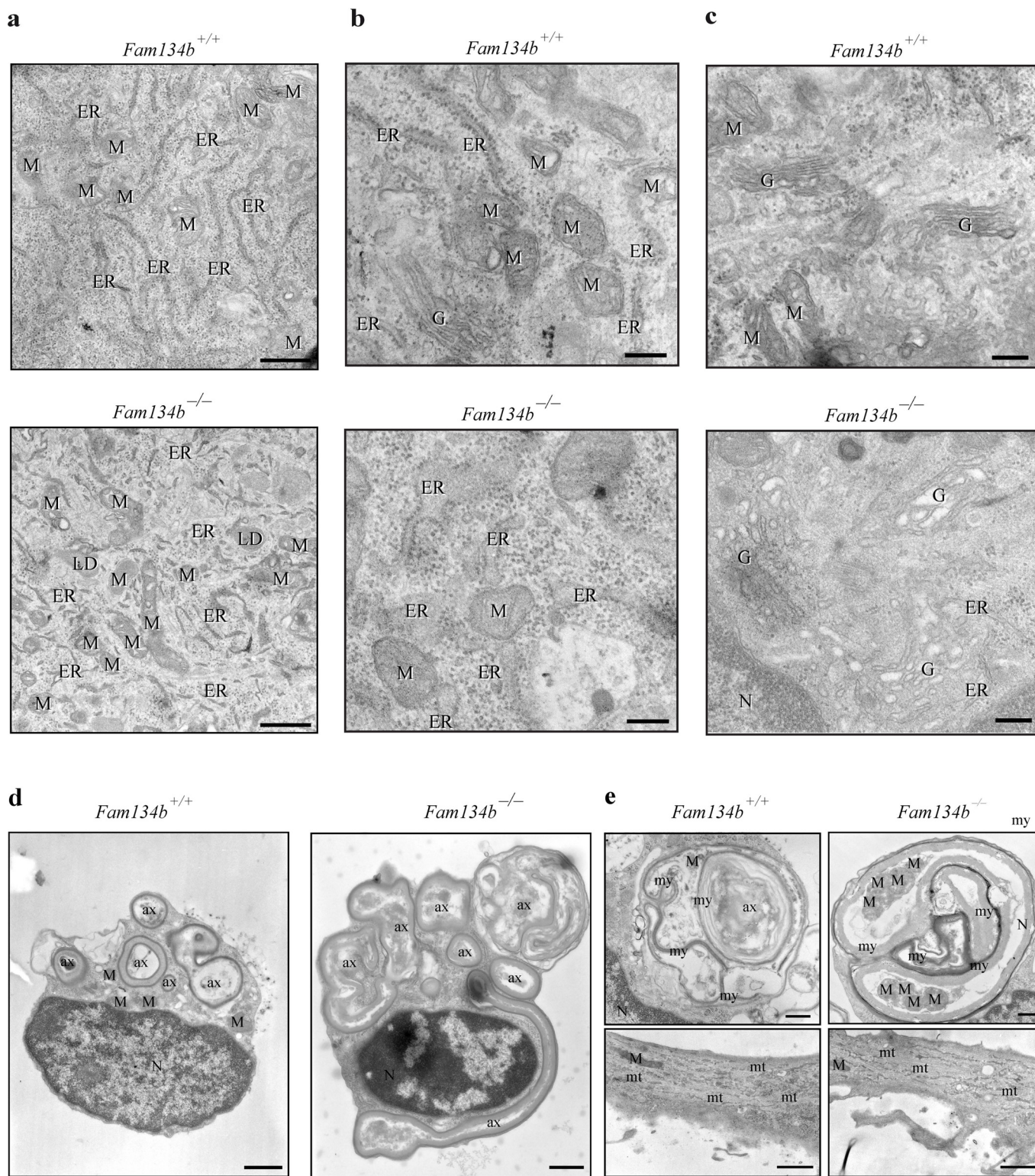
a, b, *Fam134b*^{+/+} and *Fam134b*^{-/-} MEFs were treated with 25 μ M CCCP (carbonyl cyanide 3-chlorophenylhydrazine) (**a**) or starved in EBSS (**b**) for the time indicated. Cell lysates were processed by SDS-PAGE and western blot using antibodies against vinculin, Parp and Fam134b. **c**, *Fam134b*^{+/+} and *Fam134b*^{-/-} MEFs were treated with 2 μ g ml⁻¹ tunicamycin (Tm) or 1 μ M thapsigargin (Tg) for 12 h or left untreated. Cell lysates were processed by SDS-PAGE and western blot using antibodies against vinculin and Parp. **d**, FACS analysis for annexin V and propidium iodide (PI) in *Fam134b*^{+/+} and *Fam134b*^{-/-} MEFs. Quantifications of annexin V/propidium iodide-positive cells after the indicated experimental settings (EBSS starvation for 8 h, treatment with 1 μ M thapsigargin, 2 μ g ml⁻¹ tunicamycin, 25 μ M CCCP for 12 h and 200 nM staurosporin (STS) for 6 h). Data are shown as mean \pm s.d. of two independent biological replicates; for each biological replicate two

experiments were performed and for each experiment 10,000 cells were analysed. ** $P < 0.01$, one-way ANOVA. **e**, A549 cells stably expressing control and anti-FAM134B no. 1 and no. 2 shRNAs were either starved in EBSS or treated with 10 μ M Ku-0063794, 200 ng ml⁻¹ bafilomycin A1 (BafA), 1 μ M thapsigargin or 2 μ g ml⁻¹ tunicamycin for 12 h or left untreated. Cell lysates were processed by SDS-PAGE and western blot using antibodies against vinculin and PARP. **f, g**, *FAM134B* knockdown induces apoptosis involving the mitochondrial pathway. A549 cells stably expressing control and anti-FAM134B no. 2 shRNAs were starved in EBSS for the time indicated. Cell lysates were processed by SDS-PAGE and western blot using antibodies against vinculin, PARP and caspase 8/9 (**f**) or caspase 9 (**g**). **a-c, e-g**, Filled arrowheads indicate processed PARP and caspase 8/9; empty arrowheads indicate unprocessed PARP and caspase 8/9.



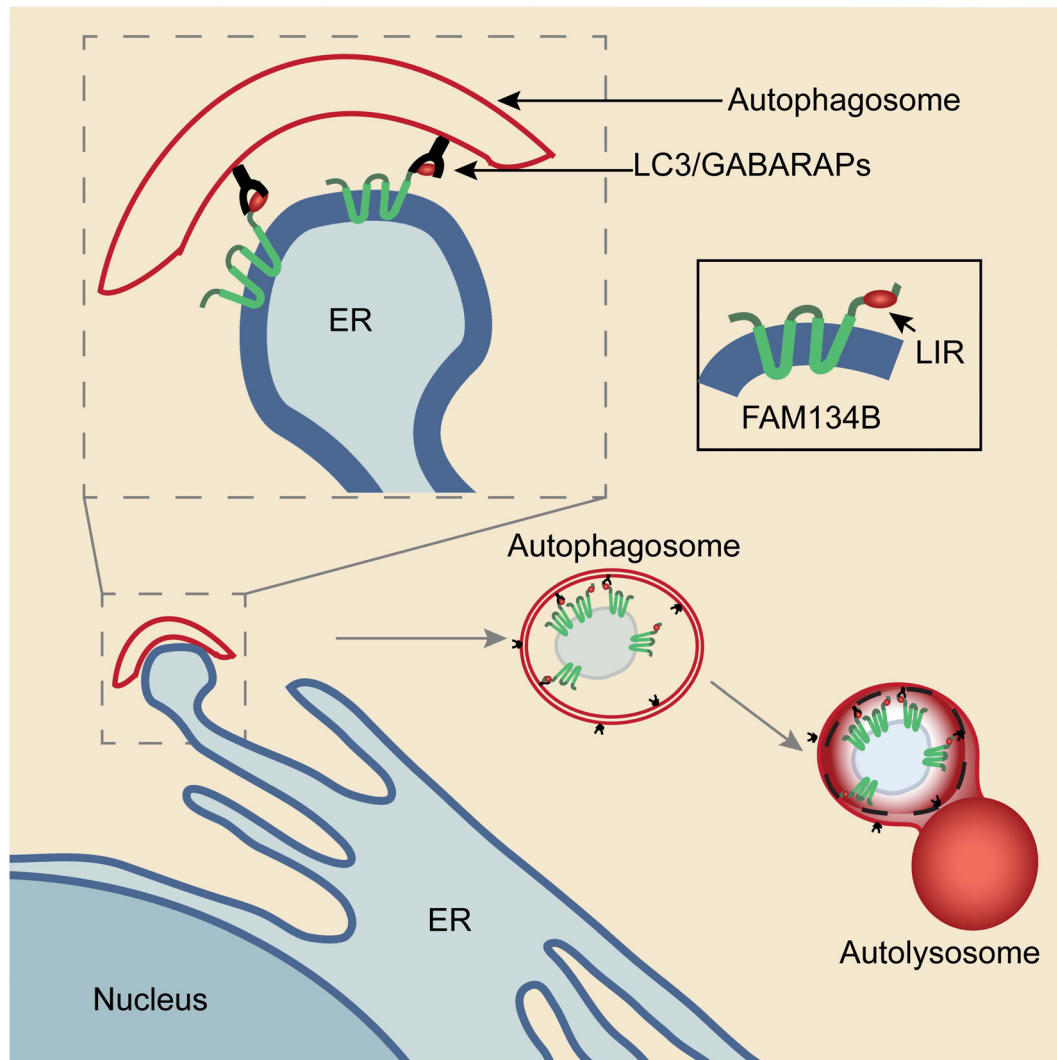
Extended Data Figure 8 | Fam134b deficiency does not affect spinal cord motor neurons. **a**, Western blot analysis of mouse embryonic tissue lysates with a Fam134b antibody. **b**, Transmission electron microscopy analysis of *Fam134b*^{+/+} and *Fam134b*^{-/-} MEFs. Cells lacking Fam134b display an expanded ER. M, mitochondria. Scale bar, 1 μ m; n = 150 cells. **c**, Compound muscle action potential (CMAP). CMAP latencies were recorded from tail nerves of wild-type (+/+) and knockout (-/-) mice at the ages indicated. No significant differences were observed between *Fam134b*^{+/+} and *Fam134b*^{-/-} mice. One-way ANOVA, error bars indicate s.e.m.; n = 6 for +/+ and -/- at 6 months; n = 10 for +/+ and n = 13 for -/- at 12 months. n.s., not significant. **d**, Motor neurons in Nissl-stained thoracic spinal cord sections (10-

μ m thick) of *Fam134b*^{+/+} and *Fam134b*^{-/-} mice. Scale bar, 20 μ m. Representatives of seven images per genotype are shown. **e**, Quantification of motor neuron cell bodies in the ventral horn. Motor neuron number was unchanged in *Fam134b*^{+/+} and *Fam134b*^{-/-} mice at an age of 12 and 20 months (n = 7 for +/+ and n = 7 for -/-). n.s., not significant, Student's *t*-test, error bars indicate s.e.m. **f**, Normal ultrastructure of motor neurons in spinal cord sections of 12-month-old mice. Arrows in the middle and right panels highlight that there were no observed alterations in ER and Golgi architecture, respectively. Scale bar, 1 μ m. Representatives of three images per genotype are shown.



Extended Data Figure 9 | Ultrastructural analysis of dorsal root ganglia neurons in *Fam134b*^{-/-} mice. **a-e**, *Ex vivo* analysis of dorsal root ganglia (DRG) neurons. DRG neurons from 3-month-old *Fam134b*^{+/+} and *Fam134b*^{-/-} littermates were cultured for 2 days before transmission electron microscopy using the flat embedding approach. **a, b**, The ultrastructural architecture of the peripheral ER as found in the DRG neuron cell body above or below the nucleus (**a**) and ER (**b**) adjacent to the nucleus of DRG neurons is shown. Scale bars: **a**, 500 nm; **b**, 200 nm. **c**, Representative examples of Golgi compartments. Scale bar, 200 nm. (*n* = 25 cells for **a-c**). **d, e**, Lateral

cross-sections of the axons recognizable by their heavy myelination around the plasma membrane and their emptiness in organelles. Panel **d** shows a bundle of axons whereas panel **e** presents a single axon. **e**, lower panels, longitudinal cross-sections of neurites, which are typically packed with microtubules and ER. ER appears as thin black stripes in these images. ax, axon; ER, endoplasmic reticulum; G, Golgi; M, mitochondrion; mt, microtubule; my, myelin; N, nucleus; LD, lipid droplet. Scale bars: **d**, 1 μm ; **e**, upper panels, 1 μm ; lower panels, 500 nm. Representatives of 25 images per genotype are shown.



Extended Data Figure 10 | Model of FAM134B function. To drive ER-phagy, FAM134B clusters at the edges of cisternal ER. Local enrichment of FAM134B LIR leads to the recruitment of autophagosomal membranes and

subsequent budding of ER-derived vesicles. Mature autophagosomes fuse with lysosomes leading to the degradation of enclosed ER fragments.

Receptor-mediated selective autophagy degrades the endoplasmic reticulum and the nucleus

Keisuke Mochida¹, Yu Oikawa², Yayoi Kimura³, Hiromi Kirisako^{1,4}, Hisashi Hirano³, Yoshinori Ohsumi² & Hitoshi Nakatogawa^{1,4}

Macroautophagy (hereafter referred to as **autophagy**) degrades various intracellular constituents to regulate a wide range of cellular functions, and is also closely linked to several human diseases^{1,2}. In selective autophagy, receptor proteins recognize degradation targets and direct their sequestration by double-membrane vesicles called autophagosomes, which transport them into lysosomes or vacuoles³. Although recent studies have shown that selective autophagy is involved in quality/quantity control of some organelles, including mitochondria and peroxisomes⁴, it remains unclear how extensively it contributes to cellular organelle homeostasis. Here we describe selective autophagy of the endoplasmic reticulum (ER) and nucleus in the yeast *Saccharomyces cerevisiae*. We identify two novel proteins, Atg39 and Atg40, as receptors specific to these pathways. Atg39 localizes to the perinuclear ER (or the nuclear envelope) and induces autophagic sequestration of part of the nucleus. Atg40 is enriched in the cortical and cytoplasmic ER, and loads these ER subdomains into autophagosomes. Atg39-dependent autophagy of the perinuclear ER/nucleus is required for cell survival under nitrogen-deprivation conditions. Atg40 is probably the functional counterpart of FAM134B, an autophagy receptor for the ER in mammals that has been implicated in sensory neuropathy⁵. Our results provide fundamental insight into the pathophysiological roles and mechanisms of 'ER-phagy' and 'nucleophagy' in other organisms.

Autophagy receptors bind to Atg8/LC3 homologues on forming autophagosomal membranes to allow membrane expansion along the surface of degradation targets^{3,6}. To understand comprehensively the physiological roles of selective autophagy, we sought to identify Atg8-binding proteins in *S. cerevisiae*, which should include unknown autophagic receptors. Among proteins detected by mass spectrometry of Atg8 immunoprecipitates, we focused on two uncharacterized proteins, Ylr312c and Yor152c, which were named Atg39 and Atg40, respectively. Atg39 and Atg40 are not homologous to each other, although both contain putative transmembrane domains (Fig. 1a). Yeast two-hybrid assays and immunoprecipitation analysis confirmed the interactions of Atg39 and Atg40 with Atg8 (Fig. 1b and Extended Data Fig. 1a, b). These interactions were weakened by mutations in the Atg8 pocket that binds to the Atg8-family-interacting motif commonly found in autophagy receptors⁶ (Extended Data Fig. 1a, c). Consistent with this, we identified Atg8-family-interacting motifs in Atg39 (W8-XX-V11) and Atg40 (Y242-XX-M245); mutations in these motifs abolished the interactions between these proteins and Atg8 (Fig. 1a, b and Extended Data Fig. 1b). In yeast, another feature of autophagy receptors is binding to Atg11, which recruits the autophagosome-formation machinery onto receptor-target complexes⁴. Our analysis suggested that Atg39 and Atg40 also interact with this protein, and also found a consensus Atg11-binding sequence⁷ in Atg39 (Fig. 1a and Extended Data Fig. 1a, d). These results suggested that Atg39 and Atg40 are bona fide autophagic receptors.

Atg39 and Atg40 were dispensable for selective autophagy pathways, which target vacuolar enzymes, mitochondria, and peroxisomes,

and non-selective autophagy also occurred normally without these proteins (Extended Data Fig. 2a–d). The protein levels of Atg39 and Atg40 markedly increased when cells were treated with rapamycin, which mimics nitrogen starvation by inactivating the TORC complex⁸ (Fig. 2a). A previous study reported that the ER is efficiently degraded via autophagy under these conditions⁹. In this study, we used the ER membrane protein Sec63 fused with GFP to monitor autophagy of the ER. Autophagic degradation of Sec63–GFP yielded vacuolar protease-resistant GFP fragments, which increased GFP fluorescence in the vacuole in fluorescence microscopy and were also detected by immunoblotting analysis (Fig. 2b, c). Our results suggested that macroautophagy of the ER induced by nitrogen deprivation or rapamycin treatment (hereafter referred to as ER-phagy, whereas a previous study also described ER stress-induced microautophagy of the ER using the same term¹⁰) involved an unknown receptor (Extended Data Fig. 3a–d). Knockout of either *ATG39* or *ATG40* partially blocked ER-phagy, and the double knockout almost completely blocked this pathway (Fig. 2b, c) (Atg1 is a protein kinase essential for autophagosome formation¹). Atg39 and Atg40 mutants deficient for binding to Atg8 or Atg11 also showed defects in ER-phagy (Extended Data Fig. 3e). In addition, in cells lacking Ypt7, a GTPase required for

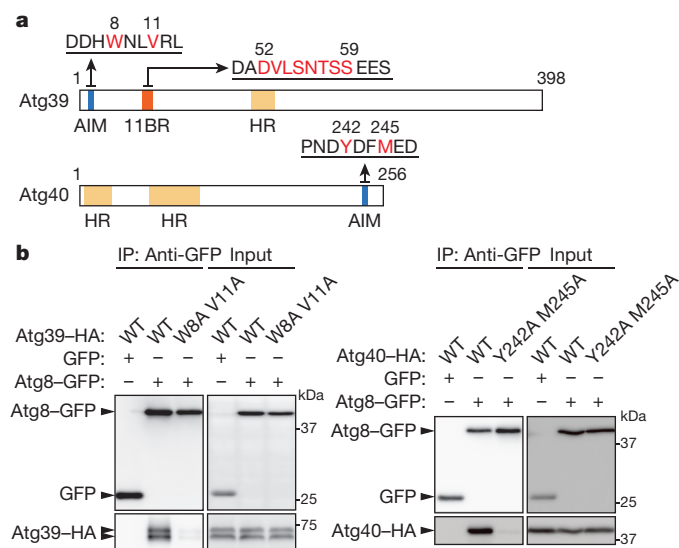


Figure 1 | Atg39 and Atg40 interact with Atg8 and Atg11. **a**, Schematic diagram of Atg39 and Atg40. AIM, Atg8-family-interacting motif; 11BR, Atg11-binding region; HR, hydrophobic region predicted to be a transmembrane domain. Alanine substitutions for red residues impair Atg39 or Atg40 binding to Atg8 or Atg11 (see Fig. 1b and Extended Data Fig. 1b, d). **b**, Lysates (input) prepared from cells treated with rapamycin for 12 h were subjected to immunoprecipitation using anti-GFP antibody, and the immunoprecipitates (IP) were analysed by immunoblotting using anti-GFP or anti-HA antibody. Representative results of three technical replicates. WT, wild type.

¹Graduate School of Bioscience and Biotechnology, Tokyo Institute of Technology, Yokohama 226-8503, Japan. ²Frontier Research Center, Tokyo Institute of Technology, Yokohama 226-8503, Japan. ³Advanced Medical Research Center, Yokohama City University, Yokohama 236-0004, Japan. ⁴CREST, Japan Science and Technology Agency, Saitama 332-0012, Japan.

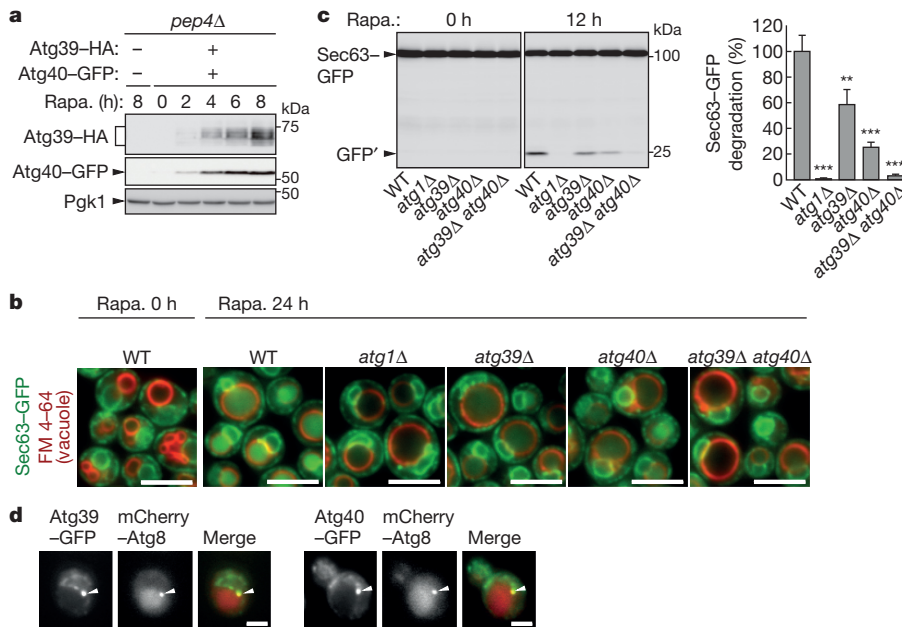


Figure 2 | Atg39 and Atg40 are receptors for ER-phagy. **a**, Immunoblotting analysis of Atg39 and Atg40. *PEP4* was disrupted to block autophagic degradation of these proteins. Pgl1, loading control; Rapa., rapamycin. Representative immunoblots of two technical replicates.

b, Fluorescence microscopy images of cells treated with rapamycin (representative of at least 100 cells). FM 4-64 stains the vacuolar membrane. **c**, Sec63-GFP degradation was analysed by immunoblotting using anti-GFP antibody. GFP', GFP fragments generated by Sec63-GFP degradation. Representative results from four technical replicates. The quantification results (see Methods) are shown as the mean \pm s.d. ($n = 4$). $^{**}P < 0.01$; $^{***}P < 0.001$ (unpaired two-tailed Student's *t*-test). **d**, Fluorescence microscopy images of cells treated with rapamycin for 3 h (representative of at least 100 cells). Arrowheads, Atg8-positive puncta of Atg39 or Atg40. Scale bars, 5 μm (**b**) and 2 μm (**d**).

autophagosome–vacuole fusion¹¹, Atg8-positive autophagosomes containing Sec63-positive ER fragments accumulated when treated with rapamycin; this accumulation was abolished by double knockout of *ATG39* and *ATG40*, although Sec63-negative autophagosomes were still observed (Extended Data Fig. 3f). Furthermore, overexpression of

these proteins stimulated ER-phagy (Extended Data Fig. 4a). Both Atg39-GFP and Atg40-GFP localized to the ER (see the next paragraph) and also formed Atg8- and Atg11-positive puncta near the vacuole, suggesting their localization to the pre-autophagosomal structure¹ (Fig. 2d and Extended Data Fig. 4b). Finally, Atg39 and

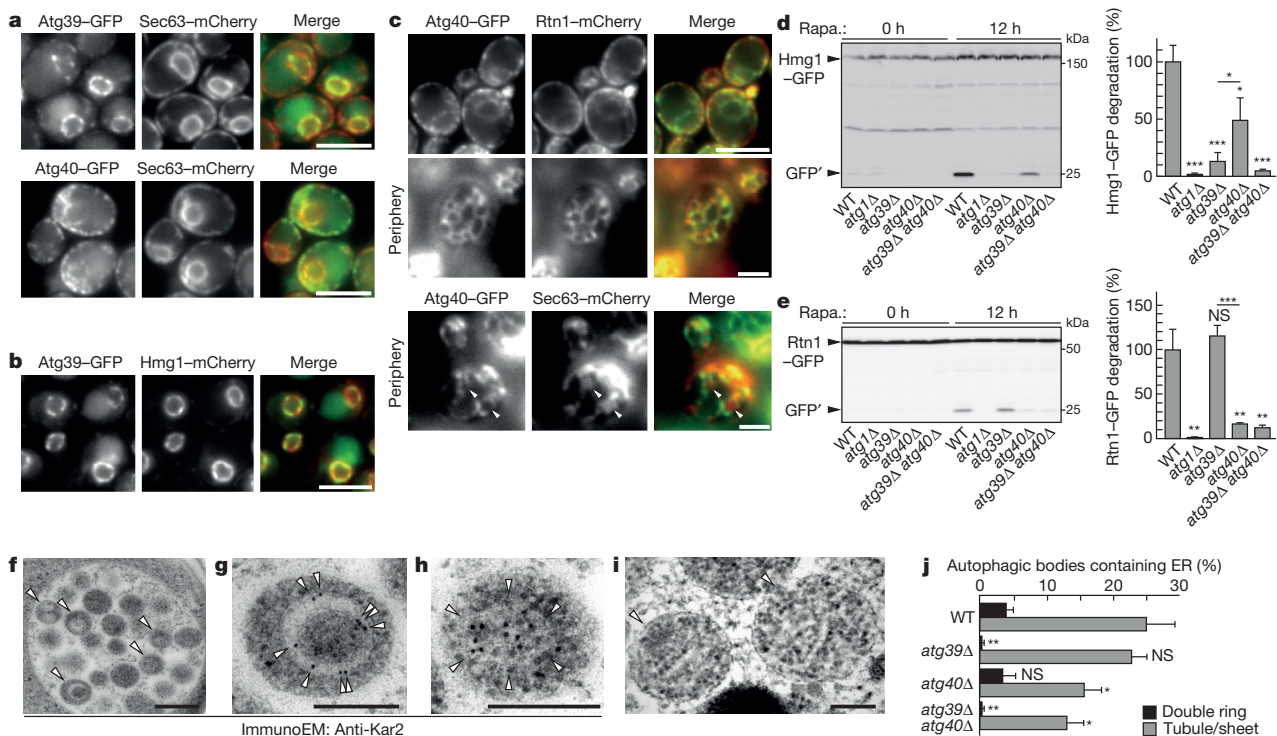


Figure 3 | Atg39 and Atg40 mediate autophagic degradation of distinct ER subdomains. **a–c**, Fluorescence microscopy images of cells treated with rapamycin for 3 h (representative of at least 100 cells). Some images were taken by focusing cell periphery (periphery). Arrowheads, Sec63-positive regions without Atg40. **d**, **e**, Degradation of Hmg1-GFP (**d**) or Rtn1-GFP (**e**). Representative results from three technical replicates. The quantification results (see Methods) are shown as the mean \pm s.d. ($n = 3$). **f–h**, Immunoelectron microscopy (ImmunoEM) images (using anti-Kar2 antibodies) of cells treated with rapamycin for 13 h (representative of at least 50 cells containing autophagic bodies). **i**, Electron microscopy (without immunogold labelling) of

cells after 12 h nitrogen starvation (representative of 14 cells containing autophagic bodies). Arrowheads, autophagic bodies containing Kar2 signals (**f**), Kar2 signals in a double-ring structure (**g**), tubules/sheets with Kar2 signals (**h**), or autophagic bodies containing tubules/sheets (**i**). **j**, In experiments described in **f–h**, autophagic bodies containing Kar2-positive double-ring structures or tubules/sheets were counted, and their percentages of total autophagic bodies are shown as the mean \pm s.d. ($n = 3$) (see Methods). Scale bars, 5 μm (**a**, **b** and **c**, top), 2 μm (**c**, middle and bottom), 500 nm (**f**), and 200 nm (**g–i**). NS, not significant; $^{*}P < 0.05$; $^{**}P < 0.01$; $^{***}P < 0.001$ (unpaired two-tailed Student's *t*-test) (**d**, **e**).

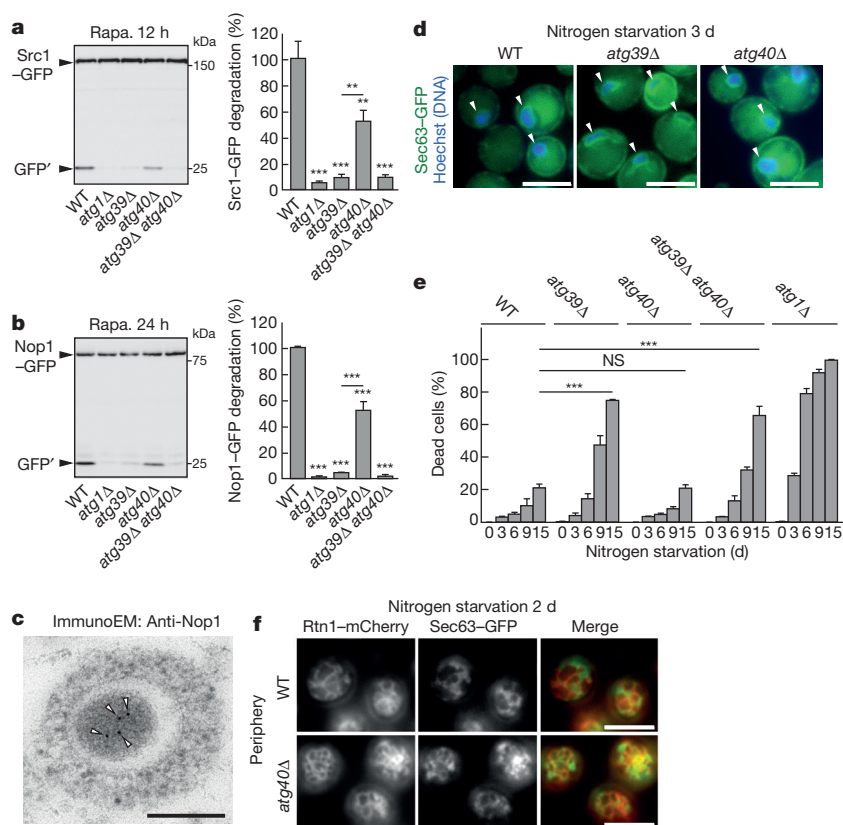


Figure 4 | Atg39-dependent degradation of nuclear components and phenotype of cells lacking Atg39 or Atg40. **a**, **b**, Degradation of Src1-GFP (**a**) or Nop1-GFP (**b**). Representative results from three technical replicates. The quantification results (see Methods) are shown as the mean \pm s.d. ($n = 3$). **c**, Immunoelectron microscopy images (using anti-Nop1 antibody) of cells treated with rapamycin for 13 h (representative of seven cells containing Nop1 signals within autophagic bodies). Arrowheads, Nop1 signals. **d**, Fluorescence microscopy images of cells after 3 days of nitrogen starvation (representative of at least 1,000 cells). Arrowheads, nuclei. **e**, The percentages of dead cells under nitrogen-starvation conditions (see Methods) are shown as the mean \pm s.d. ($n = 3$). **f**, Fluorescence microscopy images of starved cells (representative of at least 200 cells). Scale bars, 200 nm (**c**) and 5 μ m (**d**, **f**). NS, not significant; ** $P < 0.01$; *** $P < 0.001$ (unpaired two-tailed Student's *t*-test) (**a**, **b**, **e**).

Atg40 themselves were transported to the vacuole in cells undergoing ER-phagy (Extended Data Fig. 4c–e). On the basis of these results, we concluded that Atg39 and Atg40 are ER-phagy receptors.

As demonstrated by fluorescence microscopy of Sec63-mCherry (Fig. 3a), the ER in yeast consists of two distinct subdomains, the perinuclear ER (pnER) and the cortical (cell periphery) ER (cER), and these domains are connected with cytoplasmic ER (cytoER)¹². Whereas Atg39 specifically localized to the pnER, a large proportion of Atg40 resided in the cER and cytoER, although weak localization to the pnER was also observed (Fig. 3a). The pnER localization of Atg39 was confirmed by its co-localization with the pnER protein Hmg1 (Fig. 3b). We also showed that Atg40 co-localizes well with the reticulon Rtn1, which localizes to highly curved regions in ER membranes such as tubules and sheet edges¹³ but is excluded from ER sheets, in which Sec63 resides (Fig. 3c). In accordance with their characteristic localization, whereas ATG39 disruption severely impaired degradation of the pnER (Hmg1-GFP), ATG40 disruption caused a weaker defect in degradation of this subdomain (Fig. 3d and Extended Data Fig. 5). By contrast, degradation of the cER and cytoER (Rtn1-GFP) strongly depended on Atg40, but not Atg39 (Fig. 3e and Extended Data Fig. 5). These results suggest that Atg39 and Atg40 are differently involved in selective autophagy of these ER subdomains: Atg39 has a major role in pnER-phagy, whereas Atg40 is primarily responsible for cER/cytoER-phagy.

We used electron microscopy to morphologically characterize the ER sequestered into the autophagosome. Cells lacking the vacuolar protease Pep4 accumulate autophagic bodies (inner autophagosomal membrane vesicles containing sequestered material) inside the vacuole¹⁴. We immunogold-labelled the ER using antibodies against the luminal protein Kar2 and closely investigated the contents of autophagic bodies (Fig. 3f–h, j and Extended Data Fig. 6a). Autophagic bodies enclosing Kar2-positive membranes together with a part of the cytoplasm were frequently observed and categorized into two types based on their morphologies: double rings that probably represent

cross-sections of double-membrane vesicles (Fig. 3g and Extended Data Fig. 6b, c), and intricate structures that appear to be folded tubules or sheets (Fig. 3h, i and Extended Data Fig. 6d). Knockout of ATG39 or ATG40 specifically reduced autophagic bodies containing double-ring structures or those containing tubules/sheets, respectively (Fig. 3j), suggesting that double-ring structures and folded tubules/sheets are derived from the pnER and the cER/cytoER, respectively. Taken together, our results suggest that Atg39 and Atg40 have central roles in loading the pnER as double-membrane vesicles and the cER/cytoER as folded tubules/sheets, respectively, into autophagosomes (Extended Data Fig. 7).

Double-membrane vesicles derived from the pnER contained Kar2 signals in the intermembrane space (Fig. 3g), suggesting that this space had originally been the pnER lumen. The pnER is equivalent to the nuclear envelope. We hypothesized that the outer and inner membranes of double-membrane vesicles are derived from the outer and inner nuclear envelope/pnER membranes, respectively. Indeed, the inner nuclear membrane protein Src1 was also degraded in a manner similar to the outer nuclear membrane protein Hmg1 (Figs 3d and 4a and Extended Data Fig. 8a, b). This was also the case for the nucleolar protein Nop1 (Fig. 4b and Extended Data Fig. 8c). Immunoelectron microscopy detected Nop1 signals inside double-membrane vesicles, although with low frequency (Fig. 4c and Extended Data Fig. 8d). These results suggest that Atg39 directs autophagic sequestration of double-membrane vesicles derived from the nuclear envelope/pnER, which also contain some intranuclear components. Therefore, Atg39-mediated selective autophagy should also be called nucleophagy, as well as pnER-phagy (Extended Data Fig. 7). Deletion of NVJ1, which is required for microautophagy of the nucleus¹⁵, did not affect Nop1 degradation (Extended Data Fig. 8c), suggesting that Atg39-dependent nucleophagy is predominant in nucleolus degradation in our experimental conditions.

When exposed to prolonged nitrogen starvation, atg39Δ cells showed abnormal morphology in the nucleus/pnER, and lost their

viability earlier than wild-type cells (Fig. 4d, e and Extended Data Fig. 9a, b). Importantly, non-selective autophagy, which is also required for cell survival under these conditions¹⁶, occurred normally in the mutant cells (Extended Data Fig. 2a, d). In addition, *ATG39* deletion did not exaggerate starvation-induced death in cells lacking Atg1 (Extended Data Fig. 9c). Atg39 mutant cells defective in the interaction with Atg8 or Atg11 also exhibited similar phenotypes (Extended Data Fig. 9d). These results suggest that *atg39* mutants are susceptible to cell death under nitrogen-deprived conditions due to their inability to perform pnER-phagy/nucleophagy, and thus the physiological significance of this pathway. On the other hand, in *atg40Δ* cells, the cER was more densely reticulated than wild-type and *atg39Δ* cells, whereas the nucleus/pnER appeared to be normal (Fig. 4d, f and Extended Data Fig. 9e, f). However, no significant decrease in cell viability was observed in *atg40Δ* cells under nitrogen-starvation conditions (Fig. 4e); Atg40-dependent ER-phagy may be more important for cell survival or adaptation under other circumstances.

The putative transmembrane domains of Atg40 show a similarity to those of reticulon-related proteins (Extended Data Fig. 10), consistent with the observation that Atg40 favours highly curved ER regions (Fig. 3c). An accompanying paper identified the reticulon-domain-containing protein FAM134B as a mammalian ER-phagy receptor, and showed that its disruption causes progressive sensory neurodegeneration⁵. The domain architectures of Atg40 and FAM134B resemble each other (Extended Data Fig. 10). In addition, FAM134B localizes to the cytoplasmic ER network rather than the pnER⁵. These results suggest that FAM134B is the mammalian counterpart of Atg40. Atg39 homologues are found only in closely related yeast species. However, macroautophagy of the nucleus has been reported in other organisms, including mammals^{17–19}, and the molecular bases remain unclear. These organisms may possess Atg39 homologues with very low sequence similarity to the yeast protein, or non-homologous counterparts that share fundamental functions with Atg39, such as nuclear envelope localization and interaction with the autophagosome-formation machinery, as in the cases of autophagy receptors for mitochondria and protein aggregates^{4,20}.

In this study, we show that the ER and the nucleus are degraded by receptor-mediated selective autophagy. Our findings pave the way towards understanding the role of autophagy in the maintenance and regulation of ER and nuclear functions. However, several questions remain to be answered. (1) The components in the ER and the nucleus that must be degraded have not yet been identified. (2) The purpose of ER-phagy and nucleophagy under nutrient-limiting conditions, whether it is elimination of deleterious material or recycling of degradation products to provide scarce molecules, remains unknown. (3) In the context of ER-phagy, cells require two receptors to degrade different ER subdomains, but the reasons for this are unexplored. Under certain situations, cells may use only one receptor to specifically degrade the corresponding subdomain. (4) On a mechanistic level, it remains to be determined whether the generation of ER fragments and nuclear-envelope-derived vesicles is coupled with, or separated from, their sequestration into autophagosomes. (5) Whether Atg39 and Atg40 are also involved in ER fragmentation and nuclear envelope vesiculation also requires investigation. Future studies should address these important issues.

Online Content Methods, along with any additional Extended Data display items and Source Data, are available in the online version of the paper; references unique to these sections appear only in the online paper.

Received 21 November 2014; accepted 29 April 2015.

Published online 3 June 2015.

1. Nakatogawa, H., Suzuki, K., Kamada, Y. & Ohsumi, Y. Dynamics and diversity in autophagy mechanisms: lessons from yeast. *Nature Rev. Mol. Cell Biol.* **10**, 458–467 (2009).
2. Schneider, J. L. & Cuervo, A. M. Autophagy and human disease: emerging themes. *Curr. Opin. Genet. Dev.* **26**, 16–23 (2014).
3. Stolz, A., Ernst, A. & Dikic, I. Cargo recognition and trafficking in selective autophagy. *Nature Cell Biol.* **16**, 495–501 (2014).
4. Okamoto, K. Organellaphagy: eliminating cellular building blocks via selective autophagy. *J. Cell Biol.* **205**, 435–445 (2014).
5. Khaminets, A. et al. Regulation of endoplasmic reticulum turnover by selective autophagy. *Nature* <http://dx.doi.org/10.1038/nature14498> (2015).
6. Noda, N. N., Ohsumi, Y. & Inagaki, F. Atg8-family interacting motif crucial for selective autophagy. *FEBS Lett.* **584**, 1379–1385 (2010).
7. Farré, J. C., Burkenroad, A., Burnett, S. F. & Subramani, S. Phosphorylation of mitophagy and pexophagy receptors coordinates their interaction with Atg8 and Atg11. *EMBO Rep.* **14**, 441–449 (2013).
8. Noda, T. & Ohsumi, Y. Tor, a phosphatidylinositol kinase homologue, controls autophagy in yeast. *J. Biol. Chem.* **273**, 3963–3966 (1998).
9. Hamasaki, M., Noda, T., Baba, M. & Ohsumi, Y. Starvation triggers the delivery of the endoplasmic reticulum to the vacuole via autophagy in yeast. *Traffic* **6**, 56–65 (2005).
10. Schuck, S., Gallagher, C. M. & Walter, P. ER-phagy mediates selective degradation of endoplasmic reticulum independently of the core autophagy machinery. *J. Cell Sci.* **127**, 4078–4088 (2014).
11. Kirisako, T. et al. Formation process of autophagosome is traced with Apg8/Aut7p in yeast. *J. Cell Biol.* **147**, 435–446 (1999).
12. Friedman, J. R. & Voeltz, G. K. The ER in 3D: a multifunctional dynamic membrane network. *Trends Cell Biol.* **21**, 709–717 (2011).
13. Voeltz, G. K., Prinz, W. A., Shibata, Y., Rist, J. M. & Rapoport, T. A. A class of membrane proteins shaping the tubular endoplasmic reticulum. *Cell* **124**, 573–586 (2006).
14. Takeshige, K., Baba, M., Tsuboi, S., Noda, T. & Ohsumi, Y. Autophagy in yeast demonstrated with proteinase-deficient mutants and conditions for its induction. *J. Cell Biol.* **119**, 301–311 (1992).
15. Kvam, E. & Goldfarb, D. S. Nucleus-vacuole junctions and piecemeal microautophagy of the nucleus in *S. cerevisiae*. *Autophagy* **3**, 85–92 (2007).
16. Tsukada, M. & Ohsumi, Y. Isolation and characterization of autophagy-defective mutants of *Saccharomyces cerevisiae*. *FEBS Lett.* **333**, 169–174 (1993).
17. Park, Y. E. et al. Autophagic degradation of nuclear components in mammalian cells. *Autophagy* **5**, 795–804 (2009).
18. Shoji, J. Y., Kikuma, T., Arioka, M. & Kitamoto, K. Macroautophagy-mediated degradation of whole nuclei in the filamentous fungus *Aspergillus oryzae*. *PLoS ONE* **5**, e15650 (2010).
19. Mijaljica, D. & Devenish, R. Nucleophagy at a glance. *J. Cell Sci.* **126**, 4325–4330 (2013).
20. Lu, K., Psakhye, I. & Jentsch, S. Autophagic clearance of polyQ proteins mediated by ubiquitin-Atg8 adaptors of the conserved CUET protein family. *Cell* **158**, 549–563 (2014).

Supplementary Information is available in the online version of the paper.

Acknowledgements We thank the members of our laboratory for materials, discussions, and technical and secretarial support; Biomaterial Analysis Center, Technical Department at Tokyo Institute of Technology for DNA sequencing service; T. Yoshihisa and T. Endo for providing antibodies. This work was supported in part by Grants-in-Aid for Scientific Research 25111003 (to H.N.), 25711005 (to H.N.), and 23000015 (to Y.Oh.) from the Ministry of Education, Culture, Sports, Science and Technology of Japan.

Author Contributions K.M. and H.N. designed the study; K.M. performed most of the experiments with the help of H.K.; Y.Oi., Y.K. and H.H. performed mass spectrometry; K.M., Y.Oh. and H.N. analysed data. K.M. and H.N. wrote the manuscript.

Author Information Reprints and permissions information is available at www.nature.com/reprints. The authors declare no competing financial interests. Readers are welcome to comment on the online version of the paper. Correspondence and requests for materials should be addressed to H.N. (hakatogawa@bio.titech.ac.jp)

METHODS

No statistical methods were used to predetermine sample size. The experiments were not randomized. The investigators were not blinded to allocation during experiments and outcome assessment.

Yeast strains and media. Strains used in this study, derived from BY4741, BJ3505 or SEY6210 (refs 21–23), are listed in Supplementary Table 1. Gene disruption and tagging were performed by a standard PCR-based method^{24,25}. Yeast cells were grown at 30 °C in YPD medium (1% yeast extract, 2% peptone and 2% glucose) or SD+CA medium (0.17% yeast nitrogen base without amino acids and ammonium sulphate (YNB w/o aa and as), 0.5% ammonium sulphate, 0.5% casamino acid, and 2% glucose) with appropriate supplements. To induce ER-phagy and nucleophagy, cells grown to mid-log phase were treated with 200 ng ml⁻¹ rapamycin or incubated in SD-N medium (0.17% YNB w/o aa and as, and 2% glucose).

Plasmids. pRS314-ATG39-6HA, pRS314-ATG40-6HA (used in Fig. 1b and Extended Data Fig. 1b), pRS426-ATG39-6HA, and pRS426-ATG40-6HA (used in Extended Data Fig. 3e) were constructed as follows. The coding sequences of ATG39-6HA and ATG40-6HA with their own promoters were amplified by PCR using genomic DNA prepared from YKM656 and YKM658, and the pairs of the oligonucleotides SacI-ATG39pro-Fw (5'-AAAGAGCTCTGTAGTTTCAAAA ACTGTG-3')/HA-NotI-Rv (5'-AAAGCGGCCGCGCTGGCCGGGTGACCCG GCG-3') and SacI-ATG40pro-Fw (5'-AAAGAGCTCGTCTCCACGGACGT TTTCT-3')/HA-NotI-Rv, respectively. These PCR products were digested with SacI and NotI, and ligated into the single-copy vector pRS314 or the multi-copy vector pRS426 (ref. 26). pRS316-ATG39-EGFP and pRS316-ATG40-EGFP (used in Extended Data Figs 1d, 4e and 9d) were constructed similarly by inserting DNA fragments, which were obtained by PCR using genomic DNA prepared from YKM564 and YKM567, and the oligonucleotides SacI-ATG39pro-Fw/ADH1ter-XhoI-Rv (5'-AAACTCGAGCCGGTAGAGGTGTGGTCAAT-3') and SacI-ATG40pro-Fw/ADH1ter-XhoI-Rv, respectively, into pRS316. Mutations in ATG39 and ATG40 were introduced by site-directed mutagenesis using Quik Change kit (Agilent Technologies). To construct pRS316-*atg8*^{G116A}-GFP and pRS316-*atg8*^{P52A R67A G116A}-GFP (used in Fig. 1b and Extended Data Fig. 1b, c), the BamHI site was introduced immediately upstream of the stop codon of ATG8 in pRS316-ATG8 (ref. 11), and then a GFP sequence was inserted into the site, resulting in pRS316-ATG8-GFP. The mutations were introduced into this plasmid by site-directed mutagenesis to obtain the above plasmids. A control plasmid expressing GFP alone (used in Fig. 1b and Extended Data Fig. 1b, c, d) was constructed by removing the ATG8 sequence from pRS316-GFP-ATG8 (ref. 9) by site-directed mutagenesis.

Yeast two-hybrid assay. Yeast two-hybrid analysis was performed as described previously²⁷. Full-length ATG39, ATG8, *atg8*^{P52A R67A}, ATG11, and truncated *atg40* (Ser93–Asp256) were inserted into the pGAD-T7 (Clontech) or pGBD-C1 (ref. 27) plasmids. The AH109 yeast cells transformed with the generated plasmids were grown in SC medium (0.17% YNB w/o aa and as, 0.5% ammonium sulphate, 2% glucose, and appropriate supplements) lacking leucine and tryptophan, spotted on to SC (-Leu, -Trp) and SC (-Leu, -Trp, -His) agar plates, and grown at 30 °C for 2–4 days.

Immunoblotting analysis. Harvested cells were treated with 20% trichloroacetic acid on ice for 20 min, centrifuged at 15,000g for 5 min, washed with cold acetone, dried at room temperature, suspended in SDS sample buffer (100 mM Tris-HCl (pH 7.5), 2% SDS, 20 mM dithiothreitol (DTT), and 10% glycerol), and incubated at 65 °C for 10 min. Urea sample buffer (37.5 mM MOPS-NaOH (pH 6.8), 2% SDS, 100 mM DTT, and 4 M urea) was used for immunoblotting analysis of Atg39. These cells were disrupted using a FastPrep-24 (MP Biomedicals) and 0.5-mm YZB zirconia beads (Yasui Kikai). Samples were separated by SDS-PAGE, and analysed by immunoblotting using antibodies against GFP (Clontech, 632381), HA (Roche, 11867431001), Pgk1 (Invitrogen), Atg11, Ape1 (our laboratory stocks), and mCherry (gifted from T. Endo). To calculate degradation of GFP-fused proteins (%), GFP' intensity was divided by the sum of GFP' and GFP-fused full-length protein intensities, and the values relative to that in wild-type cells are shown.

Immunoprecipitation. Cells harvested by centrifugation were disrupted in IP buffer (50 mM Tris-HCl (pH 8.0), 150 mM NaCl, 5 mM EDTA, 5 mM EGTA, 50 mM NaF, and 10% glycerol) containing 2 mM phenylmethylsulfonyl fluoride (PMSF), 2× Complete protease inhibitor cocktail (Roche), 0.1× PhosSTOP phosphatase inhibitor cocktail (Roche), and 50 nM microcystin using a Multi-beads Shocker (Yasui Kikai) and 0.5-mm YZB zirconia beads. The lysates were solubi-

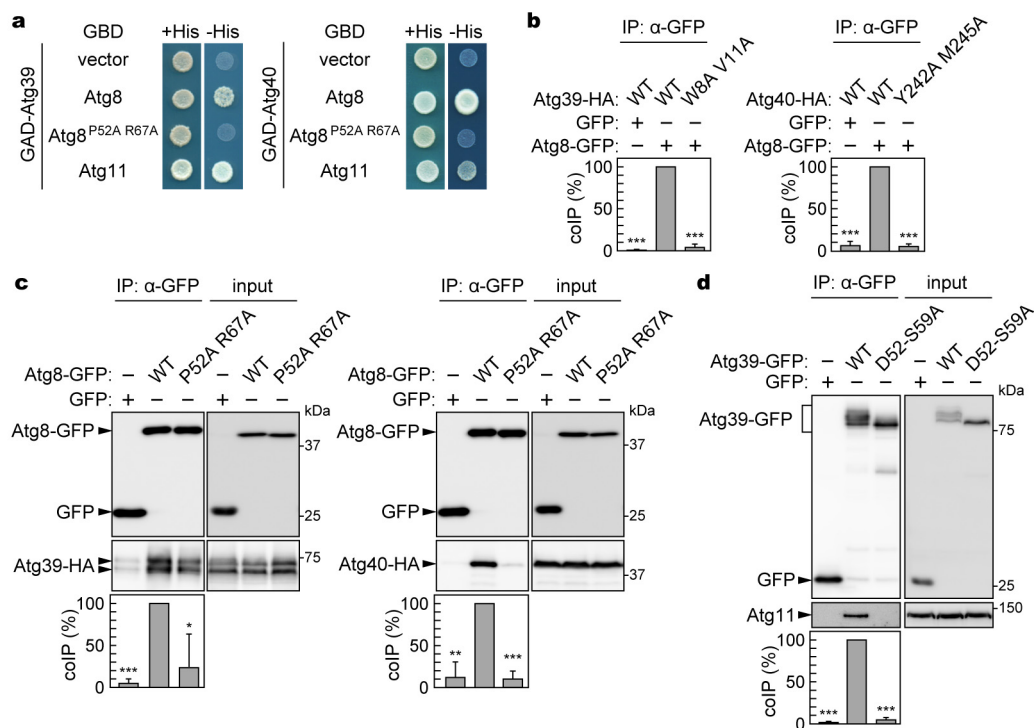
lized by rotation at 4 °C for 30 min with 0.5% Triton X-100, and then cleared by centrifugation at 15,000g for 15 min. The supernatants were incubated with GFP-Trap_M beads (ChromoTek) at 4 °C for 2 h. The beads were washed with IP buffer containing 0.3% Triton X-100 three times, and then incubated in SDS sample buffer at 65 °C for 10 min to elute bound proteins.

Fluorescence microscopy. Fluorescence microscopy was performed using an inverted fluorescence microscope (Olympus, IX81) equipped with an electron-multiplying CCD camera, a 150× objective lens, a 488-nm blue laser, a 561-nm yellow laser, and appropriate mirrors and filters, as described previously²⁸. Images shown in Fig. 4d and Extended Data Fig. 9b were obtained using a different microscope system²⁹. Vacuolar membranes and DNA were stained with 0.3 μM FM 4-64 (Invitrogen) and 0.5 μg ml⁻¹ Hoechst 33258 (Dojindo), respectively. Images were acquired using the MetaMorph software (Molecular Devices) and processed using MetaMorph and Adobe Photoshop CS6. Images shown in Extended Data Figs 3f and 9f were obtained by deconvolution of original images using AutoQuant X3. Intensities of Sec63-GFP at the periphery of cells were analysed by line scan function in Metamorph.

Electron microscopy. Electron microscopy was performed by Tokai-EMA Inc. based on rapid freezing and freeze-fixation methods. Cells were sandwiched with copper disks and quickly frozen in liquid propane at -175 °C using EM CPC (Leica). The frozen cells were treated with 2% OsO₄ and 2% distilled water in acetone (Extended Data Fig. 9a) or 0.5% tannic acid and 2% distilled water in acetone, and then with 2% OsO₄ in acetone (Fig. 3i and Extended Data Fig. 6b–d). Samples were dehydrated, and embedded in Quetol-651. Electron microscopy was performed using a transmission electron microscope (JEM-1400Plus; JEOL Ltd). For immunoelectron microscopy, frozen cells were treated with 0.2% glutaraldehyde and 2% distilled water in acetone, and embedded in LR white. Ultrathin sections were stained with anti-Kar2 antibodies (gifted from T. Endo) and anti-Nop1 antibody (GeneTex, 28F2), and secondary antibodies conjugated to 10-nm gold particles. Autophagic bodies containing Kar2-positive double-ring structures or tubules/sheets were counted in three independent experiments (more than 250 autophagic bodies were examined in each experiment).

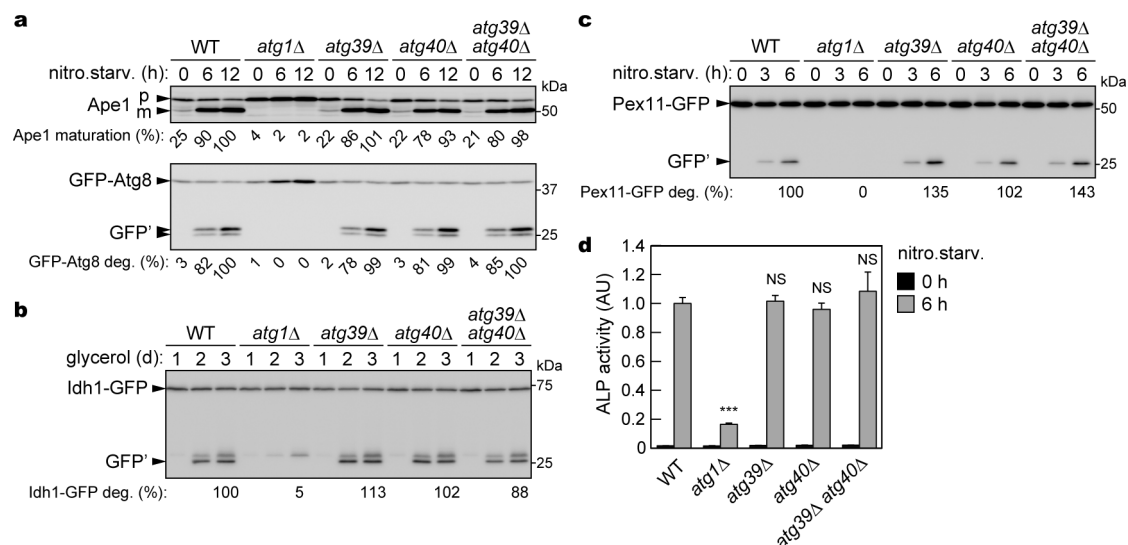
Cell viability assay. Yeast cells grown to mid-log phase (OD₆₀₀ = 1.5) in SD+CA medium with appropriate supplements were shifted to SD-N medium, and incubated for the indicated time periods. Dead cells were stained with 2.5 μg ml⁻¹ phloxine B as described previously²⁹. At least 200 cells were examined for each strain, and the proportion of phloxine B-positive cells to total cells observed under a bright field was calculated.

- Brachmann, C. B. *et al.* Designer deletion strains derived from *Saccharomyces cerevisiae* S288C: a useful set of strains and plasmids for PCR-mediated gene disruption and other applications. *Yeast* **14**, 115–132 (1998).
- Jones, E. W., Zubenko, G. S. & Parker, R. R. *PEP4* gene function is required for expression of several vacuolar hydrolases in *Saccharomyces cerevisiae*. *Genetics* **102**, 665–677 (1982).
- Robinson, J. S., Klionsky, D. J., Banta, L. M. & Emr, S. D. Protein sorting in *Saccharomyces cerevisiae*: isolation of mutants defective in the delivery and processing of multiple vacuolar hydrolases. *Mol. Cell. Biol.* **8**, 4936–4948 (1988).
- Janke, C. *et al.* A versatile toolbox for PCR-based tagging of yeast genes: new fluorescent proteins, more markers and promoter substitution cassettes. *Yeast* **21**, 947–962 (2004).
- Nakatogawa, H., Ishii, J., Asai, E. & Ohsumi, Y. Atg4 recycles inappropriately lipidated Atg8 to promote autophagosome biogenesis. *Autophagy* **8**, 177–186 (2012).
- Sikorski, R. S. & Hieter, P. A system of shuttle vectors and yeast host strains designed for efficient manipulation of DNA in *Saccharomyces cerevisiae*. *Genetics* **122**, 19–27 (1989).
- James, P., Halladay, J. & Craig, E. A. Genomic libraries and a host strain designed for highly efficient two-hybrid selection in yeast. *Genetics* **144**, 1425–1436 (1996).
- Mochida, K., Ohsumi, Y. & Nakatogawa, H. Hrr25 phosphorylates the autophagic receptor Atg34 to promote vacuolar transport of α-mannosidase under nitrogen starvation conditions. *FEBS Lett.* **588**, 3862–3869 (2014).
- Suzuki, S. W., Onodera, J. & Ohsumi, Y. Starvation induced cell death in autophagy-defective yeast mutants is caused by mitochondrial dysfunction. *PLoS ONE* **6**, e17412 (2011).
- Noda, N. N. *et al.* Structural basis of target recognition by Atg8/LC3 during selective autophagy. *Genes Cells* **13**, 1211–1218 (2008).
- Tanaka, C. *et al.* Hrr25 triggers selective autophagy-related pathways by phosphorylating receptor proteins. *J. Cell Biol.* **207**, 91–105 (2014).
- Noda, T., Matsuura, A., Wada, Y. & Ohsumi, Y. Novel system for monitoring autophagy in the yeast *Saccharomyces cerevisiae*. *Biochem. Biophys. Res. Commun.* **210**, 126–132 (1995).



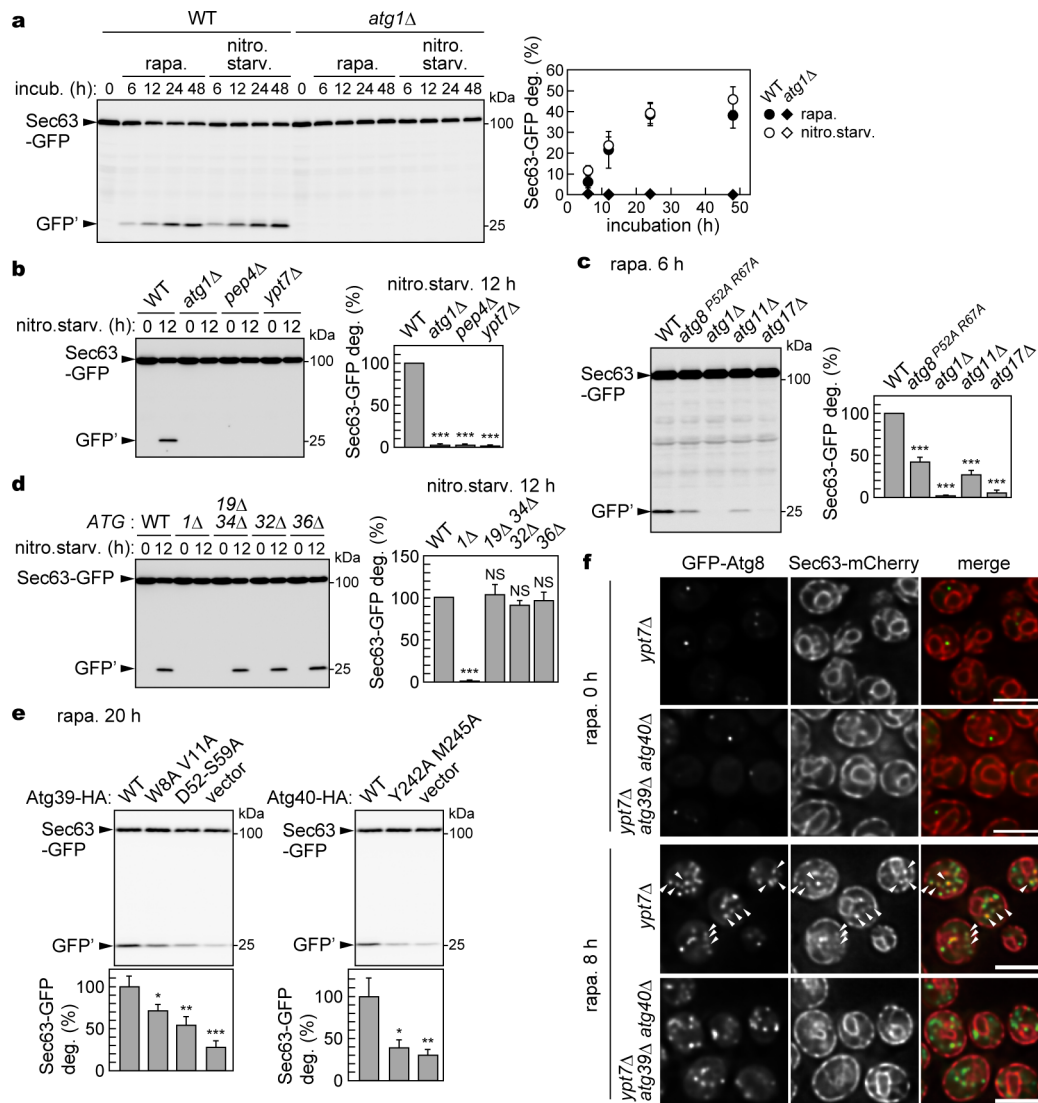
Extended Data Figure 1 | Interactions of Atg39 and Atg40 with Atg8 and Atg11. **a**, Yeast two-hybrid assay. Cells expressing proteins fused with the Gal4 activation domain (GAD) or the Gal4 DNA-binding domain (GBD) were grown on the agar plate with or without histidine (His). Representative results of two technical replicates are shown. Growth without His indicates positive interaction. The P52A R67A mutation in Atg8 weakens its binding to the Atg8-family-interacting motif (AIM)³⁰. **b**, In the experiments described in Fig. 1b, the protein band intensities were measured, and the relative ratios of co-precipitated proteins to direct targets of immunoprecipitation (coIP (%)) are shown as the mean \pm s.d. (n = 3). WT, wild type. **c**, Cells were treated with

rapamycin for 13 h, and the lysates (input) were subjected to co-immunoprecipitation analysis using anti-GFP antibody. The immunoprecipitates (IP) were analysed by immunoblotting. **c**, Co-immunoprecipitation efficiencies were calculated as described in **b**, and the results are shown as the mean \pm s.d. (n = 3). **d**, Cells treated with rapamycin for 12 h were subjected to co-immunoprecipitation analysis as described in **c**. Eight residues in the Asp52–Ser59 region in Atg39 were replaced with Ala in the D52–S59A mutant. Representative results of three technical replicates are shown (**c**, **d**). **P* < 0.05; ***P* < 0.01; ****P* < 0.001 (unpaired two-tailed Student's *t*-test) (**b**, **c**, **d**).



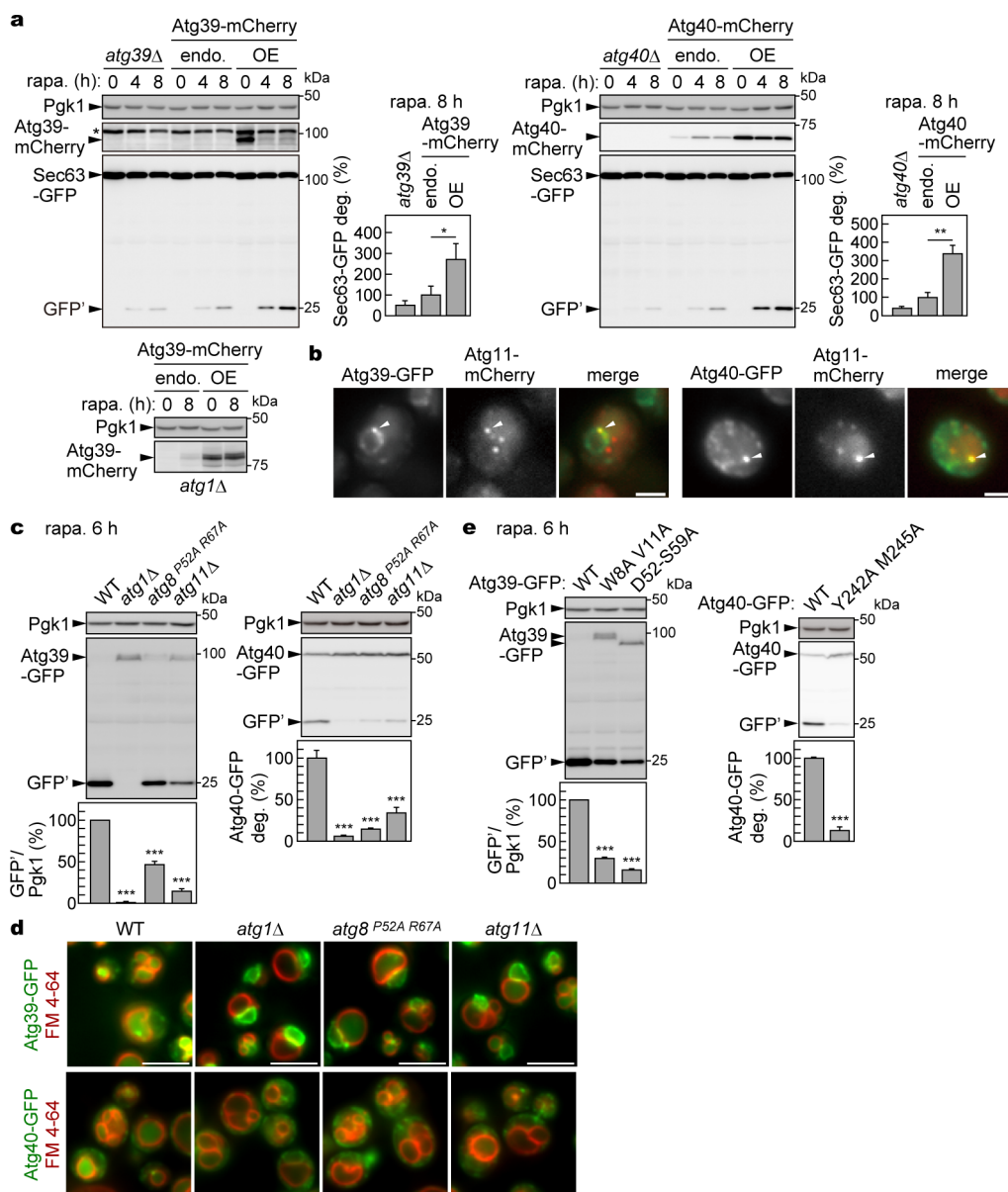
Extended Data Figure 2 | Atg39 and Atg40 are not required for the cytoplasm-to-vacuole targeting pathway, mitophagy, pexophagy, and non-selective autophagy. **a**, Cells were incubated in nitrogen starvation medium, and the processing of the proform (p) of the vacuolar aminopeptidase Ape1 into the mature form (m), which is indicative of activity of the cytoplasm-to-vacuole targeting pathway, was examined by immunoblotting using anti-Ape1 antibodies. mApe1 intensity was divided by the sum of mApe1 and pApe1 intensities, and the relative values are shown (Ape1 maturation (%)). Vacuolar degradation of GFP-Atg8, which correlates with activity of non-selective

autophagy, was also investigated. The results were quantified (see Methods), and the relative values (%) are shown. **b**, **c**, Mitophagy and pexophagy were examined as described previously³¹. Degradation of GFP-fused proteins was quantified (see Methods), and the relative values (%) are shown. Representative immunoblots of two technical replicates are presented (**a–c**). **d**, To assess bulk degradation of the cytoplasm by non-selective autophagy, a Pho8Δ60 alkaline phosphatase (ALP) assay was performed as described previously³². ALP activities are shown as the mean \pm s.d. ($n = 3$). AU, arbitrary units; NS, not significant; *** $P < 0.001$ (unpaired two-tailed Student's t -test).



Extended Data Figure 3 | The ER is degraded via selective macroautophagy under nitrogen-deprived conditions in a manner dependent on Atg39 and Atg40. **a–e**, Cells treated with rapamycin or incubated in nitrogen-starvation medium were subjected to immunoblotting analysis. Pep4 and Ypt7 are required for vacuolar lytic activity and autophagosome-vacuole fusion, respectively. Atg17 is a subunit of the Atg1 kinase complex and required for starvation-induced autophagy¹. Atg19 and Atg34 are autophagy receptors for vacuolar enzymes; Atg32 and Atg36 are those for mitochondria and peroxisomes, respectively. In **e**, *atg39Δ* or *atg40Δ* cells harbouring Atg39–HA or Atg40–HA plasmids, respectively, were analysed. Representative

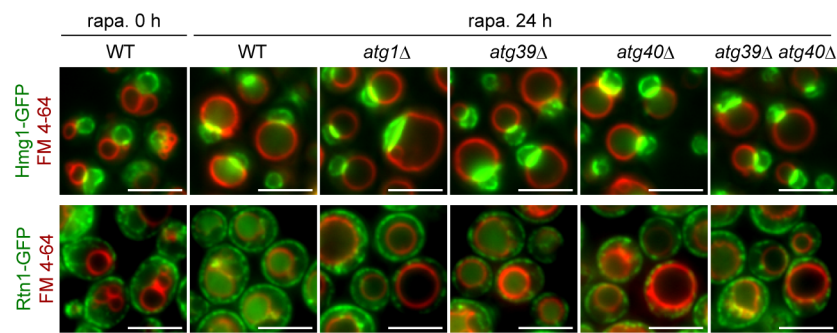
immunoblots of three (**a**, **b**, **d**, **e**) or four (**c**) technical replicates are shown. Sec63–GFP degradation (%) was quantified (see Methods), and the results are shown as the mean \pm s.d. ($n = 3$ (**b**, **d**, **e**) or 4 (**c**)). NS, not significant; * $P < 0.05$; ** $P < 0.01$; *** $P < 0.001$ (unpaired two-tailed Student's *t*-test) (**b–e**). The results in **c** and **d** showed that ER-phagy requires Atg11 and the AIM-binding ability of Atg8, but not previously characterized autophagic receptors, suggesting the existence of an unknown receptor for this pathway. **f**, Fluorescence microscopy of cells treated with or without rapamycin. Images are representative of at least 150 cells. Arrowheads, Atg8- and Sec63-positive puncta. Scale bars, 5 μ m.



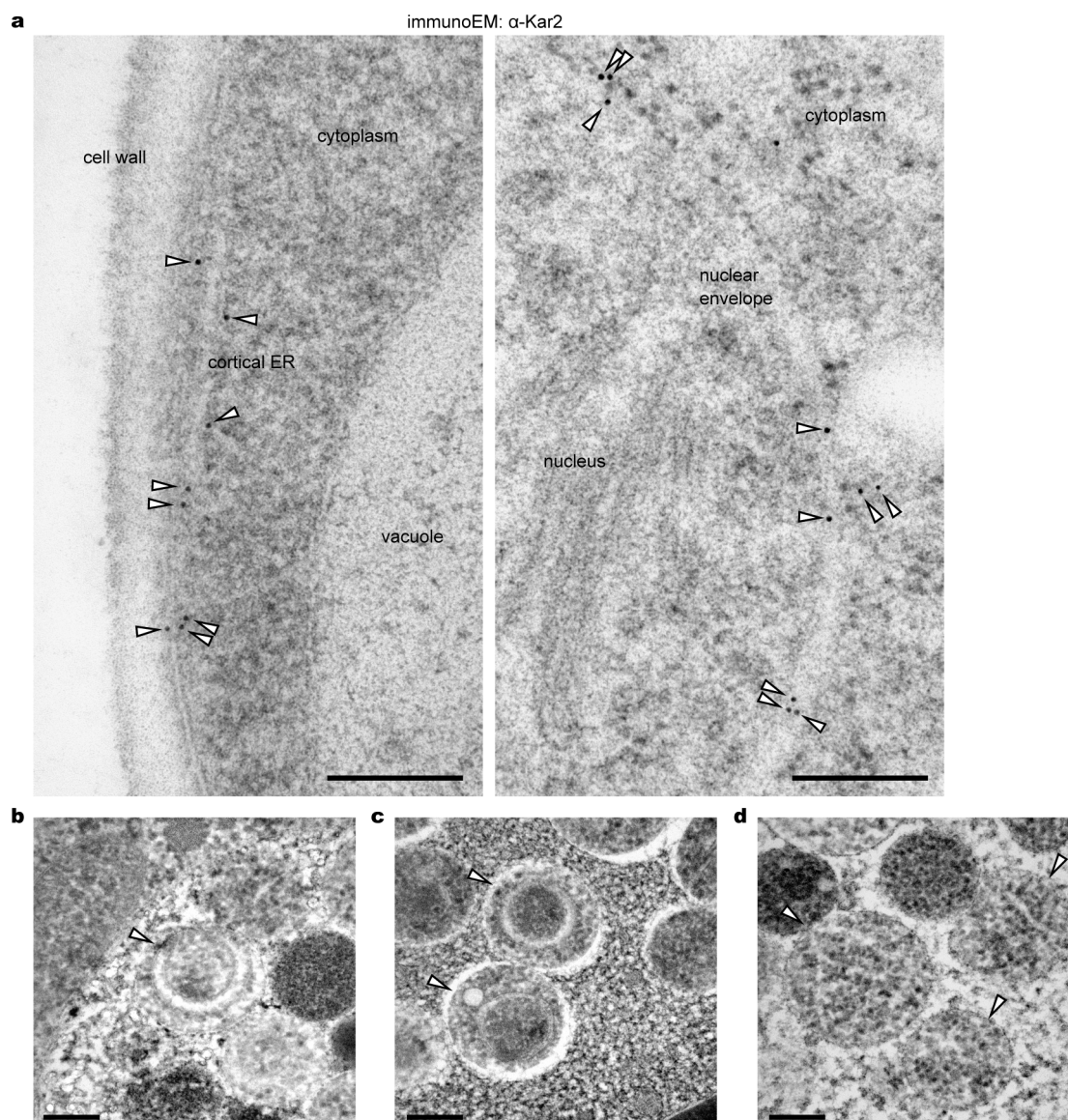
Extended Data Figure 4 | Atg39 and Atg40 function as ER-phagy receptors.

a, Atg39-mCherry or Atg40-mCherry was expressed under the endogenous promoter (endo.) or the *CUP1* promoter for overexpression (OE) in the presence of 250 μ M CuSO₄. These cells were treated with rapamycin, and degradation of Sec63-GFP was examined by immunoblotting. Pgk1 serves as a loading control. Representative immunoblots of three technical replicates are presented, and the quantification results (see Methods) are shown as the mean \pm s.d. ($n = 3$). * $P < 0.05$; ** $P < 0.01$ (unpaired two-tailed Student's *t*-test). The results for *atg1Δ* cells suggest that the rapamycin-induced decrease in Atg39-mCherry overexpressed in wild-type cells is due to its autophagic degradation. **b**, The co-localization of Atg39 or Atg40 with Atg11 in cells treated with rapamycin for 3 h was observed under a fluorescence microscope.

Images are representative of at least 100 cells. Scale bars, 2 μ m. **c–e**, Vacuolar degradation of Atg39-GFP and Atg40-GFP was examined by immunoblotting (**c, e**) and fluorescence microscopy (**d**). *atg39Δ* and *atg40Δ* cells carrying Atg39-GFP and Atg40-GFP plasmids, respectively, were examined in **e**. Representative immunoblots of three (Atg39-GFP degradation in **c, e**), or four (Atg40-GFP degradation in **c, e**) technical replicates are presented, and the quantification results are shown as the mean \pm s.d. ($n = 3$ (Atg39-GFP degradation in **c, e**) or 4 (Atg40-GFP degradation in **c, e**)). *** $P < 0.001$ (unpaired two-tailed Student's *t*-test) (**c, e**). Images are representative of at least 100 cells (**d**). Scale bars, 5 μ m. The results in **c–e** suggest that vacuolar transport of Atg39 and Atg40 requires their binding to Atg11 and Atg8.

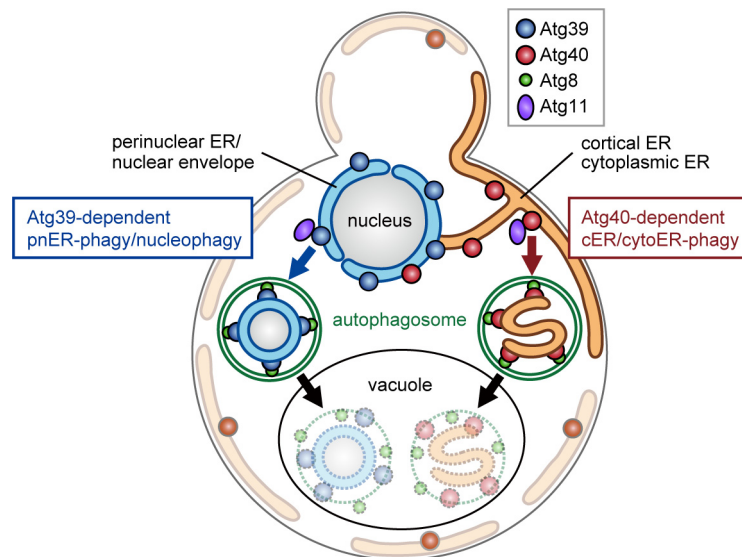


Extended Data Figure 5 | Atg39 and Atg40 are differently involved in degradation of the pnER and the cER/cytoER. Vacuolar transport of Hmg1-GFP and Rtn1-GFP was examined by fluorescence microscopy. Images are representative of at least 100 cells. Scale bars, 5 μ m.



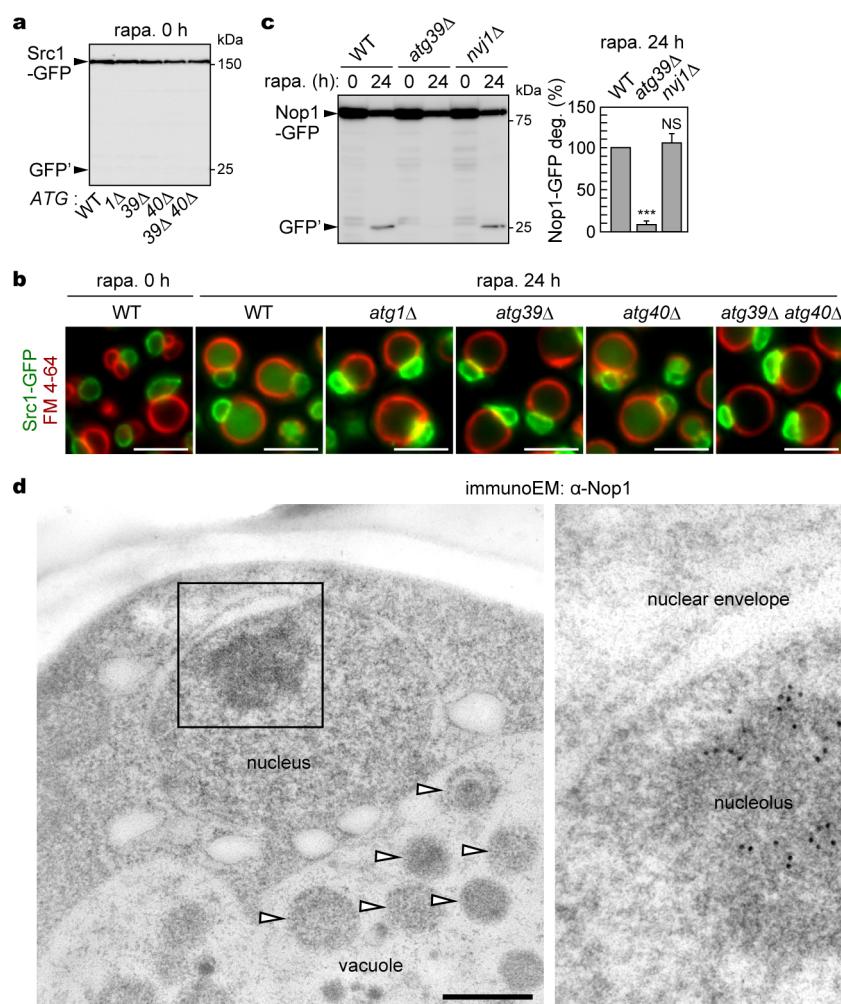
Extended Data Figure 6 | Electron microscopy of the ER sequestered into autophagic bodies. **a**, *pep4* Δ cells treated with rapamycin for 13 h were analysed by immunoelectron microscopy using anti-Kar2 antibodies. Images are representative of at least 50 cells. Arrowheads, Kar2 signals (gold particles). These images show the staining of the cortical ER (left) and the perinuclear ER/ nuclear envelope (right). **b–d**, Electron microscopy images (without

immunogold labelling) of cells incubated in nitrogen-starvation medium for 12 h (**b**, **d**) or treated with rapamycin for 12 h (**c**). Images are representative of at least 14 cells that contained autophagic bodies. Arrowheads, autophagic bodies containing double-ring structures (**b**, **c**) or those containing tubules/ sheets (**d**). Scale bars, 200 nm (**a–d**).



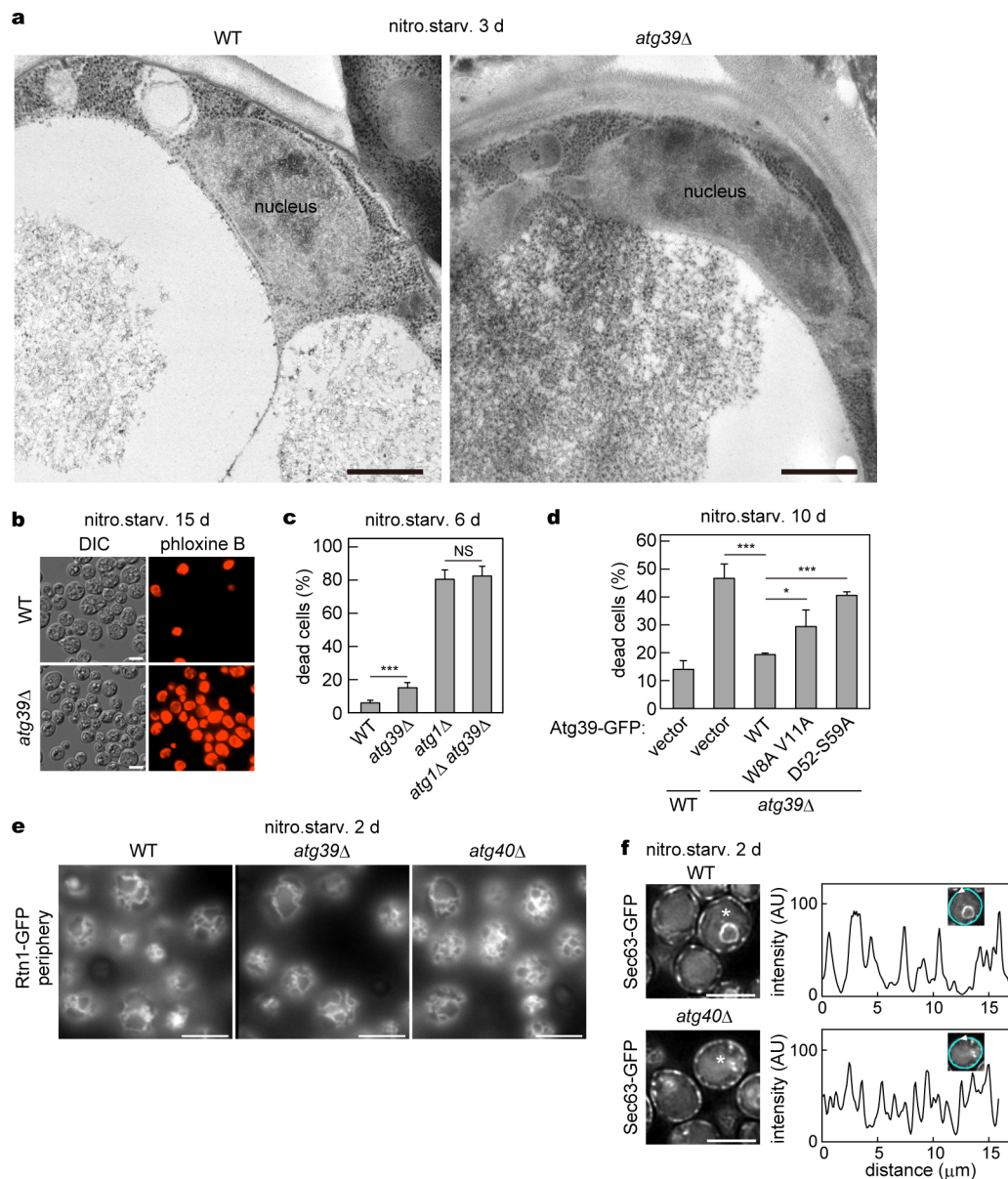
Extended Data Figure 7 | Model for Atg39- and Atg40-mediated ER-phagy and nucleophagy. Atg39 localizes to the perinuclear ER (pnER)/nuclear envelope and acts to load a part of the pnER/nucleus as double-membrane vesicles, which contain intranuclear components, into autophagosomes. Atg40 mainly localizes to highly curved regions in the cortical ER (cER) and cytoplasmic ER (cytoER), and allows sequestration of these ER domains as

folded tubules or sheets into autophagosomes. Whereas Atg39 is dispensable for cER/cytoER-phagy, Atg40 also contributes to pnER-phagy/nucleophagy. It is likely that both of these receptors interact with Atg11 to recruit the core Atg proteins that mediate autophagosome formation, and also with Atg8 to promote autophagic sequestration of the ER or a part of the nucleus.



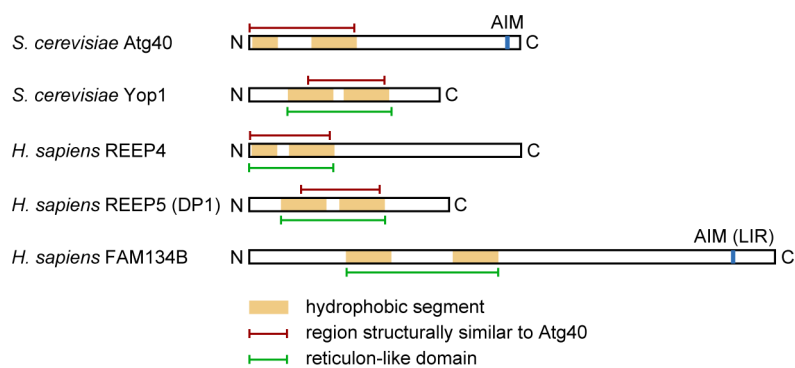
Extended Data Figure 8 | Atg39-dependent degradation of part of the nucleus. **a**, Src1-GFP degradation assay for cells before rapamycin treatment. The results for cells treated with rapamycin are shown in Fig. 4a. **b**, Vacuolar transport of Src1-GFP was examined by fluorescence microscopy. Images are representative of at least 100 cells. Scale bars, 5 μ m. **c**, Autophagic degradation of Nop1-GFP was examined by immunoblotting. Representative results of two (a) or three (c) technical replicates are shown. Nop1-GFP degradation was

quantified (see Methods), and the results are shown as the mean \pm s.d. ($n = 3$). NS, not significant; *** $P < 0.001$ (unpaired two-tailed Student's t -test). **d**, *pep4* Δ cells were treated with rapamycin for 13 h, followed by immunoelectron microscopy using anti-Nop1 antibody. Images are representative of six cells containing Nop1 signals in the nucleolus. Scale bars, 500 nm (left) and 200 nm (right). The data show that the nucleolus is specifically labelled with gold particles. Arrowheads, autophagic bodies in the vacuolar lumen.



Extended Data Figure 9 | Phenotypes of *atg39* and *atg40* mutants under nitrogen-deprived conditions. **a**, Cells were examined by electron microscopy. Images are representative of at least 14 cells. **b**, Cells were subjected to nitrogen starvation, and dead cells were stained with phloxine B. Images are representative of at least 600 cells. DIC, differential interference contrast microscopy images. **c**, Dead cells were counted (see Methods), and the results are shown as the mean \pm s.d. ($n = 6$). **d**, Wild-type or *atg39* Δ cells harbouring Atg39-GFP plasmids or the empty vector were subjected to nitrogen starvation, and dead cells were counted. The results are shown as

the mean \pm s.d. ($n = 3$). NS, not significant; * $P < 0.05$; *** $P < 0.001$ (unpaired two-tailed Student's t -test) (**c**, **d**). **e**, **f**, Cells expressing Rtn1-GFP (**e**) or Sec63-GFP (**f**) were subjected to nitrogen starvation, and the fluorescence microscopy images were taken by focusing cell periphery (**e**) or centre (**f**). Images are representative of at least 100 (**e**) or 200 (**f**) cells. In **f**, the fluorescence intensity of Sec63-GFP at the periphery of cells marked with asterisks (left) was measured along cyan lines in insets and graphically shown (right). Scale bars, 500 nm (**a**), 5 μ m (**b**, **e**, **f**).



Extended Data Figure 10 | Domain architectures of Atg40 and reticulon-related proteins. HHpred, a homology search tool based on structure prediction, identified reticulon-related proteins, Yop1 in *S. cerevisiae*, and REEP4 and REEP5 in *Homo sapiens*, as proteins similar to Atg40. Red bars,

regions structurally similar to Atg40; green bars, reticulon-like domains; orange regions, hydrophobic segments predicted by TMHMM, a membrane protein topology prediction method. LIR, LC3-interacting region.

Alternative 3' UTRs act as scaffolds to regulate membrane protein localization

Binyamin D. Berkovits¹ & Christine Mayr¹

About half of human genes use alternative cleavage and polyadenylation (ApA) to generate messenger RNA transcripts that differ in the length of their 3' untranslated regions (3' UTRs) while producing the same protein^{1–3}. Here we show in human cell lines that alternative 3' UTRs differentially regulate the localization of membrane proteins. The long 3' UTR of *CD47* enables efficient cell surface expression of CD47 protein, whereas the short 3' UTR primarily localizes CD47 protein to the endoplasmic reticulum. CD47 protein localization occurs post-translationally and independently of RNA localization. In our model of 3' UTR-dependent protein localization, the long 3' UTR of *CD47* acts as a scaffold to recruit a protein complex containing the RNA-binding protein HuR (also known as ELAVL1) and SET⁴ to the site of translation. This facilitates interaction of SET with the newly translated cytoplasmic domains of CD47 and results in subsequent translocation of CD47 to the plasma membrane via activated RAC1 (ref. 5). We also show that CD47 protein has different functions depending on whether it was generated by the short or long 3' UTR isoforms. Thus, ApA contributes to the functional diversity of the proteome without changing the amino acid sequence. 3' UTR-dependent protein localization has the potential to be a widespread trafficking mechanism for membrane proteins because HuR binds to thousands of mRNAs^{6–9}, and we show that the long 3' UTRs of *CD44*, *ITGA1* and *TNFRSF13C*, which are bound by HuR, increase surface protein expression compared to their corresponding short 3' UTRs. We propose that during translation the scaffold function of 3' UTRs facilitates binding of proteins to nascent proteins to direct their transport or function—and this role of 3' UTRs can be regulated by ApA.

Alternative 3' UTR isoform abundance was shown to be highly cell-type-specific and can change upon proliferation, differentiation and transformation^{1–3}. Alternative 3' UTR isoforms produce the same protein, but the long 3' UTRs contain additional regulatory elements that can regulate mRNA localization and protein abundance^{1,2,10}. We have discovered a new function of 3' UTRs: they can regulate protein localization independently of RNA localization.

CD47 is best known as a ubiquitous cell surface molecule that acts as a marker of self and protects cells from phagocytosis by macrophages^{11,12}. We found CD47 protein expressed on the cell surface, as well as intracellularly (Fig. 1a and Extended Data Fig. 1a–c). The *CD47* gene produces alternative 3' UTRs as determined by the 3'-end sequencing method 3'-seq and confirmed by northern blot analysis (Fig. 1b, c)³. Exclusive knockdown of the longer 3' UTR isoform by short hairpin RNAs (shRNAs) decreased CD47 surface expression without changing intracellular expression (Fig. 1d and Extended Data Fig. 1d–g). This suggests that the long 3' UTR isoform facilitates cell surface localization of CD47 protein.

To test this hypothesis, we asked whether green fluorescent protein (GFP) encoded by an mRNA containing the long (with a mutated proximal polyadenylation signal; Extended Data Fig. 1h) or the short 3' UTR of *CD47* would localize differently. To allow GFP to enter the secretory pathway, we replaced the extracellular domain (ECD) of

CD47 with GFP, while preserving the CD47 signal peptide, transmembrane domains (TMDs) and carboxy terminus, which we refer to as GFP-TM (Fig. 1e). We observed that GFP-TM encoded by an mRNA containing the long 3' UTR of *CD47* (GFP-TM-LU) localizes primarily to the cell surface whereas GFP-TM encoded by an mRNA with the short 3' UTR of *CD47* (GFP-TM-SU) localizes predominantly to the endoplasmic reticulum (Fig. 1f and Extended Data Fig. 1i). The localization results were confirmed by fluorescence-activated cell sorting (FACS) analysis, using an anti-GFP antibody on permeabilized and non-permeabilized cells to measure total and surface GFP levels, respectively (Fig. 1g). The localization step occurs at the protein level, as both the LU- and SU-containing GFP transcripts show a similar distribution near the perinuclear endoplasmic reticulum (Fig. 1h). Thus the LU isoform of *CD47* encodes information that is necessary for cell surface expression of GFP-TM protein, in a manner independent of RNA localization.

To address the mechanism of 3' UTR-dependent protein localization (UDPL; Fig. 2a), we reasoned that there must be an RNA-binding protein (RBP) that binds to the long, but not the short, 3' UTR of *CD47*. The long 3' UTR of *CD47* contains many uridine-rich elements (see later), which are potentially bound by HuR^{6–9}. HuR is known for its role in mRNA stabilization and translation activation^{7,13,14}. However, HuR knockdown by shRNAs did not affect *CD47* mRNA abundance or isoform levels, nor did it affect total CD47 protein levels (Fig. 2b, bottom, and Extended Data Figs 1d, 2a–c). But, strikingly, knockdown of HuR reduced CD47 surface expression (Fig. 2b, top, and Extended Data Fig. 2c). This suggests that for CD47, HuR mediates protein localization post-translationally.

Beyond the role of HuR as an RBP^{6–9}, HuR interacts through protein–protein interactions with SET, ANP32A and ANP32B⁴. Nuclear SET binds to histone tails and prevents acetylation¹⁵, but phosphorylated SET localizes to the cytoplasm and the surface of the endoplasmic reticulum^{5,16}. Also, SET interacts with RAC1, and active RAC1 translocates SET to the plasma membrane⁵. In our model of UDPL (Fig. 2a), HuR binds to the long 3' UTR of *CD47* and recruits SET. Upon targeting of the mRNA to the endoplasmic reticulum surface, the scaffold function of the 3' UTR results in local recruitment of SET to the site of translation. After translation of *CD47* mRNA, the ECD is located in the endoplasmic reticulum lumen, whereas its C terminus is cytoplasmic. This allows SET to interact with the newly translated C terminus and cytoplasmic domains of CD47 and to translocate CD47 to the plasma membrane via active RAC1. Transfer of SET from *CD47* mRNA to CD47 protein probably requires energy input, as has been shown for transfer of the signal peptide from the signal recognition particle to the translocation channel¹⁷. In this model of UDPL, surface expression of CD47-LU depends on SET and active RAC1. And indeed, knockdown of SET or RAC1 by shRNAs reduced surface expression of CD47 without affecting overall CD47 levels (Fig. 2b and Extended Data Fig. 2c–e).

To determine if UDPL is a more widespread phenomenon, we examined the localization of four additional transmembrane proteins that are derived from mRNAs with 3' UTR isoforms that can be bound by HuR^{6–8} (Extended Data Figs 3 and 4). *TSPAN13* has only one

¹Cancer Biology and Genetics Program, Memorial Sloan Kettering Cancer Center, 1275 York Ave, New York, New York 10065, USA.

3' UTR isoform, whereas the other three genes (*CD44*, *ITGA1* and *TNFRSF13C* (encoding the BAFF receptor, BAFFR) use ApA to generate alternative 3' UTR isoforms (Fig. 2c and Extended Data Fig. 2f)³. As was the case for *CD47*, knockdown of HuR decreased surface expression of all four proteins without changing total protein levels (Fig. 2c and Extended Data Fig. 2a, f). As was done for *CD47*, we generated GFP-fused *LU* and *SU* constructs for *CD44*, *ITGA1* and *TNFRSF13C* with their respective TMDs, C termini and 3' UTRs. For all tested genes, the longer 3' UTR increased surface localization of GFP-TM (Figs 1f–h, 2d and Extended Data Fig. 2g). This demonstrates that UDPL has the potential to be a widespread phenomenon.

The 3' UTR of *CD47* contains over 30 putative HuR-binding sites (Extended Data Fig. 3). We tested whether a 3' UTR with a few HuR-binding sites (HuR-BS) (Extended Data Fig. 3) is enough to mediate surface localization. Indeed, the uridine-rich sequence was necessary and sufficient for surface localization of GFP-TM, although it was less potent than the full-length 3' UTR of *CD47* (Fig. 2e).

Next, we investigated each step of our UDPL model in more detail. We demonstrated by RNA-immunoprecipitation that HuR binds to the HuR-BS and to the *LU* but not to the *SU* isoform of *CD47* (Fig. 3a, left). SET also associates with the long 3' UTR of *CD47*, which is dependent on HuR (Fig. 3a, right). SET or HuR overexpression was insufficient to localize GFP-TM-SU to the cell surface (Extended Data Fig. 5a, b). However, tethering of SET or HuR to the short 3' UTR isoform of *CD47* was sufficient to redirect GFP-TM localization from the endoplasmic reticulum to the plasma membrane (Fig. 3b and

Extended Data Fig. 5c, d; see Extended Data Fig. 5 for experimental details). This indicates that local recruitment of SET to the site of translation, mediated by the scaffold function of the long 3' UTR, is required for UDPL.

Furthermore, by co-immunoprecipitation we demonstrated that endogenous SET only interacts with *CD47*-LU protein, but not with *CD47*-SU protein (Fig. 3c). Since SET binds to lysine residues¹⁸, we mutated single lysines in the C terminus of *CD47*, which decreased GFP-TM surface localization by up to 37% (Extended Data Fig. 6a). Mutation of 2/5 lysines decreased it by more than 50% and deletion of the entire C terminus decreased it by 80% (GFP-TM-LUΔC; Fig. 3d and Extended Data Fig. 6b). Additional mutation of three lysines in the first cytoplasmic loop abolished surface GFP expression (GFP-TM-LUΔCL; Fig. 3d and Extended Data Fig. 6b). The reduction in surface expression is probably due to partial or complete loss of SET binding to *CD47*, as demonstrated by co-immunoprecipitation (Fig. 3e).

To test if the difference in surface localization has phenotypic consequences, we added the ECD of *CD47* to the GFP constructs (called *CD47*-LU or *CD47*-SU; Fig. 4a). Both constructs resulted in comparable overall *CD47* protein levels (Extended Data Fig. 7a). *CD47*-LU efficiently localized to the cell surface via UDPL mediated by active RAC1 (Fig. 4b, c and Extended Data Fig. 7b). Whereas GFP expressed from the GFP-TM-SU construct nearly completely localized to the endoplasmic reticulum (Fig. 1f–h), *CD47*-SU primarily localizes to the endoplasmic reticulum, but also localizes partially to the cell surface, but independently of active RAC1 (Fig. 4b, c).

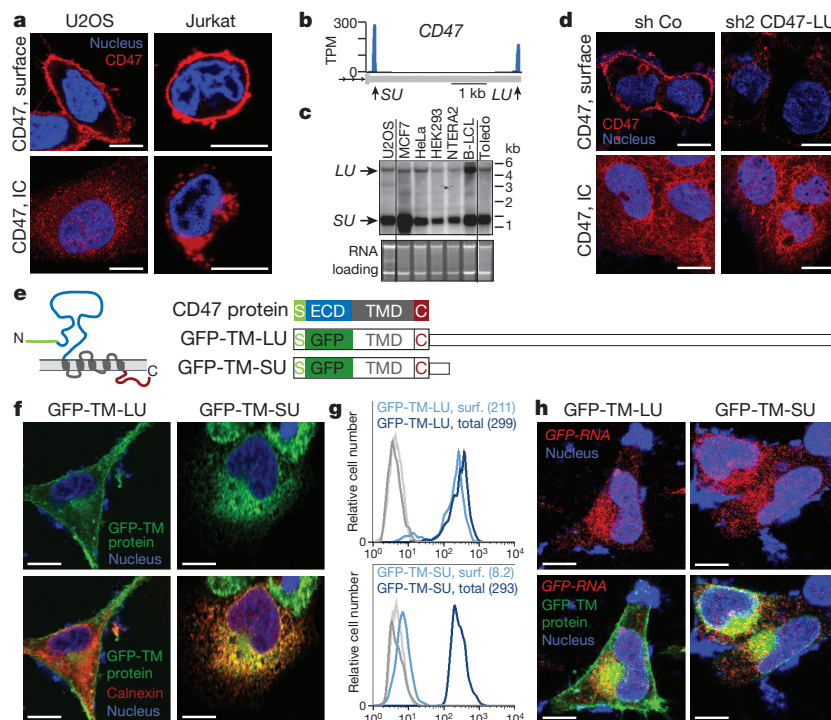


Figure 1 | The long 3' UTR of *CD47* localizes GFP-TM protein to the plasma membrane, whereas the short 3' UTR localizes it to the endoplasmic reticulum. **a**, Fluorescence confocal microscopy of endogenous *CD47* protein in non-permeabilized (top) and permeabilized (bottom) cells. IC, intracellular. **b**, 3'-seq analysis of naive B cells shows two 3' UTR isoforms of *CD47* mRNA (short 3' UTR (*SU*) and long 3' UTR (*LU*)). Shown is the last exon of the gene model. Isoform abundance shown in transcripts per million (TPM). **c**, Northern blot analysis of human cell lines confirming *CD47* mRNA isoforms from **b**. The corresponding ethidium-bromide-stained RNA gel is shown as loading control. **d**, Staining of U2OS cells as in **a** after transfection of a control shRNA (sh Co) or an shRNA against the long *CD47* 3' UTR isoform. **e**, *CD47* protein contains an N-terminal signal peptide (S; green), ECD (blue), five TMDs (grey) and a cytoplasmic C terminus (C; red). In both constructs, the

ECD was replaced with GFP and either fused with the long (GFP-TM-LU) or the short *CD47* 3' UTR (GFP-TM-SU). Constructs are drawn to scale.

f, Fluorescence confocal microscopy of fixed U2OS cells after transfection of GFP-TM-LU or GFP-TM-SU. Bottom, with additional staining of the endoplasmic reticulum with anti-calnexin. **g**, FACS analysis of GFP expression in transfected U2OS cells with (dark blue lines, detection of total expression) and without permeabilization (light blue lines, detection of surface (surf.) expression). Values for mean fluorescence intensity (MFI) are shown in parentheses. Unstained cells are shown in grey. Representative image from more than 20 experiments. **h**, RNA-fluorescence *in situ* hybridization (FISH) (red) against *GFP* in permeabilized U2OS cells after transfection of GFP-TM-LU or GFP-TM-SU. Bottom panel also shows GFP-TM protein. **a**, **d**, **f** and **h** are representative images from hundreds of cells. Scale bars, 10 μ m.

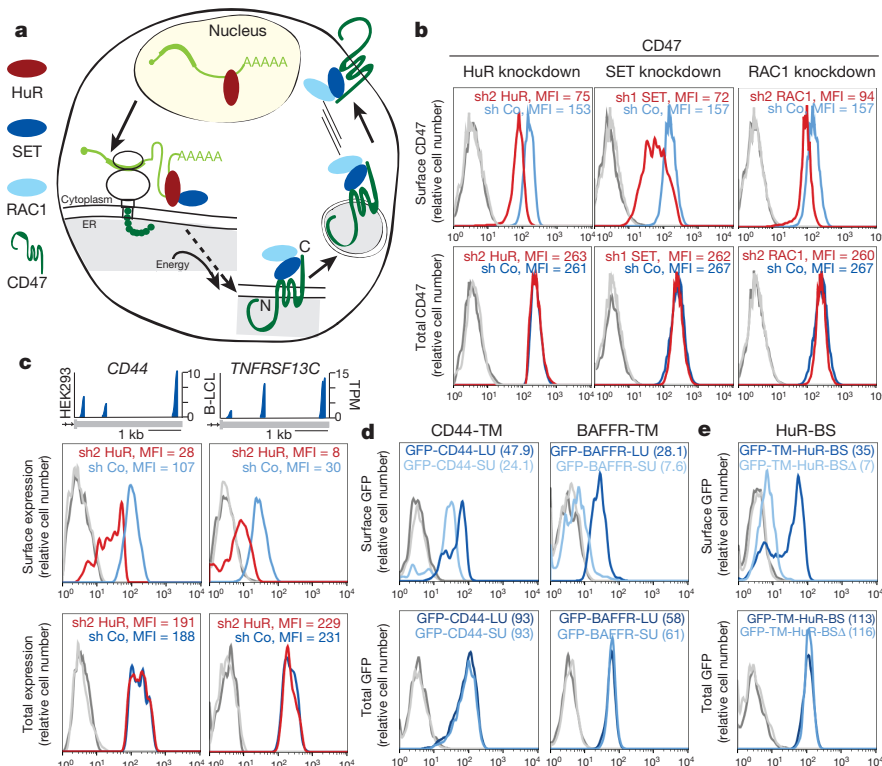


Figure 2 | 3' UTR-dependent protein localization (UDPL) depends on HuR, SET and RAC1, and mediates surface localization of membrane proteins. **a**, Model of UDPL. HuR binds to the long 3' UTR and recruits SET. During translation of *CD47* mRNA, this protein complex is targeted to the endoplasmic reticulum (ER) surface where SET binds to the newly translated cytoplasmic domains of CD47. This step probably requires energy. SET interacts with RAC1 and active RAC1 translocates SET and CD47 to the plasma membrane. **b**, FACS analysis of endogenous CD47 protein expression in HEK293 cells. Left panel is after transfection of control shRNA (sh Co) or shRNAs against HuR (shown as all GFP⁺ cells). Middle and right panels depict cells stably expressing the indicated shRNAs. Surface CD47 (top) and total CD47 protein (bottom) were measured. **c**, 3'-seq analysis for *CD44* in HEK293 cells and for *TNFRSF13C* in

We added the respective ECDs to CD44 and BAFFR, which also increased surface expression of their SU isoforms compared with their GFP-TM isoforms, but to a lesser extent than was observed for CD47 (Extended Data Fig. 7c, d). Di- or multimerization of cell surface receptor subunits, which often occurs through their ECDs, is a common strategy for overcoming endoplasmic reticulum retention, because it results in masking of endoplasmic reticulum retention signals¹⁹. We speculate that CD47-SU, CD44-SU and BAFFR-SU might use such a mechanism (although the multimerization partners are unknown) for their partial surface expression. In the case of BAFFR the ECD only increased surface expression by 1.2-fold, indicating that BAFFR strongly depends on UDPL for surface expression (Extended Data Fig. 7d). This is supported by the absence of BAFFR on B cells in Rac-deficient mice²⁰. Taken together, our data suggest that membrane proteins rely on UDPL for surface expression to varying degrees.

Cells with high CD47 surface levels are protected from phagocytosis by macrophages (Extended Data Fig. 7e)¹². To examine if the difference in surface expression of CD47-LU and CD47-SU protects cells to a different extent from phagocytosis, we used CD47-deficient Jurkat cells (called JinB8 cells²¹) and expressed similar total amounts of CD47-LU or CD47-SU (Extended Data Fig. 7a). Co-culture of these cells with macrophages demonstrated that CD47-LU fully protected the cells, whereas CD47-SU only partially protected the cells from phagocytosis (Fig. 4d).

CD47 also functions in the regulation of apoptosis²², as JinB8 cells or tissues from *Cd47*-knockout mice²³ fail to undergo apoptosis after

γ -irradiation^{24,25}. Interestingly, expression of CD47-SU in JinB8 cells restored apoptosis, but expression of CD47-LU did not affect the loss-of-apoptosis phenotype (Fig. 4e and Extended Data Fig. 7f, g). Thus, when a cell requires increased CD47 surface expression, transcriptional upregulation alone would be non-optimal as it would confer increased susceptibility to apoptosis. ApA-generated 3' UTR isoforms allow independent regulation of differentially localized and functionally distinct CD47 protein.

As the surface localization of CD47-SU is RAC1-independent, it also does not co-localize with RAC1 at the plasma membrane (Fig. 4f). In contrast, CD47-LU shows strong co-localization with RAC1 at lamellipodia (Fig. 4f). Both activated RAC1 and CD47 are necessary for efficient cell migration and activated RAC1 localizes to the leading edge of migrating cells^{25,23,26}. We show that only the expression of CD47-LU resulted in changes in cell morphology with the generation of lamellipodia at the leading edge of cells. Furthermore, CD47-LU, but not CD47-SU, resulted in increased active RAC1 (Fig. 4g), which suggests that CD47-LU may cooperate with RAC1 during cell migration. Thus, CD47 protein localized to the same cellular compartment, but produced by the SU or LU mRNA isoforms, can exert different functions. It is currently not known if other surface proteins derived from their LU or SU isoforms also have distinct biological roles.

We propose that UDPL is a widespread mechanism for surface expression of membrane proteins. All currently known components of the pathway (HuR, SET and RAC1) are ubiquitously and highly

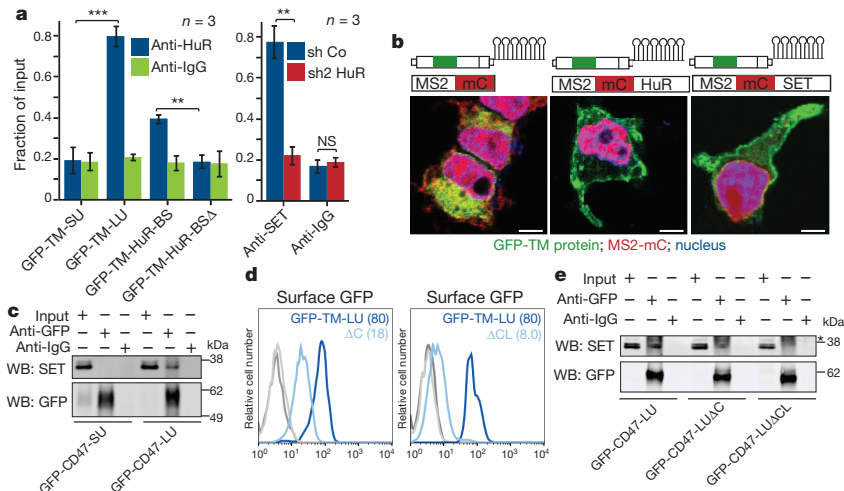


Figure 3 | Mechanism of UDPL. **a**, Left, RNA-immunoprecipitation after transfection of the indicated constructs into HEK293 cells. Protein-RNA complexes were pulled-down with anti-HuR antibody and GFP abundance was normalized to GAPDH and is shown as fraction of input. Right, RNA co-immunoprecipitation after transfection of the indicated shRNAs. Protein-RNA complexes were pulled down with anti-SET antibody and the abundance of CD47-LU was normalized to GAPDH and is shown as fraction of input. Shown is mean \pm standard deviation (s.d.), $n = 3$ biological replicates. *** $P < 0.0003$, ** $P < 0.002$, NS, not significant ($P > 0.05$), two-sided t -test for independent samples. **b**, MS2-binding sites (see Extended Data Fig. 5) were added to GFP-TM-SU and co-transfected with MS2-mC (left), MS2-mC-HuR (middle) or MS2-mC-SET (right). mC, mCherry. Fluorescence confocal microscopy of HEK293 cells after transfection of indicated constructs shows

that recruitment of HuR or SET to the short 3' UTR redirects localization of GFP protein from the endoplasmic reticulum to the cell surface. Representative images from hundreds of cells. Scale bars, 10 μ m. **c**, Co-immunoprecipitation of endogenous SET using anti-GFP antibody after transfection of CD47-SU or CD47-LU in HEK293 cells (for constructs, see Fig. 4a). Two per cent of input was loaded. WB, western blot. **d**, FACS analysis of surface GFP expression after transfection of GFP-TM-LU (dark blue line), GFP-TM-LU with a C-terminal deletion (Δ C; light blue line; left) or with destruction of both SET-binding sites (Δ C and K163A, K166A, K175A; Δ CL; light blue line, right). Shown as in Fig. 1g. Representative image from more than four experiments. **e**, Co-immunoprecipitation of endogenous SET using anti-GFP antibody after transfection of the indicated constructs. Two per cent of input was loaded. Asterisk indicates unspecific band.

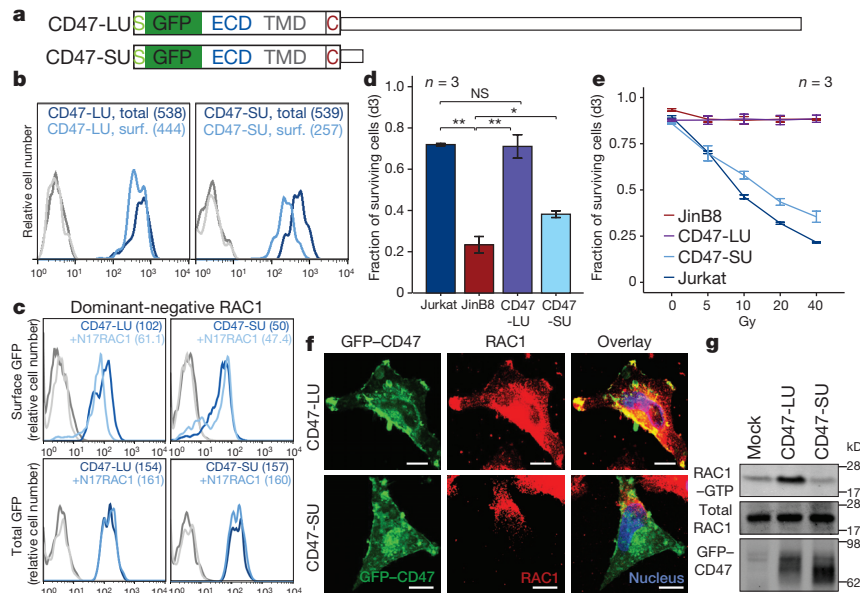


Figure 4 | CD47 protein has different functions depending on whether it was generated by the SU or LU isoform. **a**, To generate GFP-CD47, GFP was inserted in frame between the signal peptide and the rest of the CD47 open reading frame. GFP-CD47 was fused with either the long or short CD47 3' UTR, called CD47-LU and CD47-SU, respectively. **b**, FACS analysis of surface (surf.; light blue) and total (dark blue) GFP-CD47 expression in transfected JinB8 cells. Shown as in Fig. 1g. Representative images from four experiments. **c**, FACS analysis of GFP expression after transfection of CD47-LU or CD47-SU with or without co-transfection of dominant-negative RAC1 (N17RAC1). Shown as in Fig. 1g. Representative images from $n = 7$ (LU) and $n = 2$ (SU) experiments. **d**, Fraction of Mitomycin-C-treated cells that survived at day (d)3 after co-culture with macrophages is displayed for Jurkat, JinB8 (CD47^{-/-}) and the GFP⁺ JinB8 cells after nucleofection of CD47-LU

or CD47-SU. Shown is mean \pm s.d., $n = 3$ biological replicates. ** $P < 0.005$, * $P < 0.02$, NS, not significant ($P > 0.05$), two-sided t -test for independent samples. **e**, The fraction of surviving cells (TO-PRO3 negative) measured by FACS analysis at day 3 after γ -irradiation is shown for the same populations as in **d**. Shown is mean \pm s.d., $n = 3$ biological replicates of the 20% of cells with the highest GFP expression. Gy, Gray. **f**, Fluorescence confocal microscopy of permeabilized U251 cells after transfection of CD47-LU or CD47-SU co-stained with anti-RAC1 antibody. Yellow indicates co-localization. Representative images from hundreds of cells. Scale bars, 10 μ m. **g**, Immunoprecipitation of endogenous RAC1-GTP (active RAC1) in HEK293 cells after transfection of CD47-LU, CD47-SU, or empty vector. Total RAC1 and GFP-CD47 were measured from input. $n = 3$ biological replicates.

expressed (Extended Data Fig. 8a)³. UDPL requires the presence of HuR-binding sites in the 3' UTR and SET-binding sites in the cytoplasmic domains of membrane proteins (Extended Data Figs 3, 4 and 9). All candidates tested so far that met both requirements used UDPL for surface expression (Figs 1f–h, 2d, 4b and Extended Data Figs 2g, 7c). HuR-binding sites are highly abundant as HuR binds to thousands of mRNAs^{6–9}, with a third of them being membrane proteins (Extended Data Fig. 8b). Although the SET-binding motif is currently unknown, we (Fig. 3d, e and Extended Data Fig. 6) and others have shown that SET binds to positively charged amino acids in histone tails or cytoplasmic domains of membrane proteins^{18,27}. According to the positive-inside rule for integral membrane proteins, the cytoplasmic domains of membrane proteins are enriched in positively charged amino acids for topological reasons²⁸. Therefore, potential SET-binding sites in cytoplasmic domains of membrane proteins are very widespread.

So far, efforts to determine the consequences of alternative 3' UTRs have largely focused on mRNA stability and translation^{1,2,29}. We expand the known functions of 3' UTRs and show that they can act as scaffolds for RBPs that serve as adaptors to recruit effector proteins to the site of translation, which determines subcellular protein localization and function. With respect to CD47, CD44, ITGA1, TSPAN13 and BAFR, the adaptor protein is HuR and the effector protein is SET. We further speculate that the scaffold function of 3' UTRs may extend beyond the regulation of membrane proteins. RBPs could recruit other effector proteins, for example, enzymes that post-translationally modify proteins, as was shown for long non-coding RNAs³⁰. We showed here that CD47 produced by alternative 3' UTR isoforms localizes to different cellular compartments and has independent and sometimes opposite functions with respect to cell survival and cell migration. Thus, through the generation of alternative 3' UTR isoforms, ApA contributes to functional diversity of the proteome without changing the amino acid sequence.

Online Content Methods, along with any additional Extended Data display items and Source Data, are available in the online version of the paper; references unique to these sections appear only in the online paper.

Received 1 July 2014; accepted 10 February 2015.

Published online 20 April 2015.

- Sandberg, R., Neilson, J. R., Sarma, A., Sharp, P. A. & Burge, C. B. Proliferating cells express mRNAs with shortened 3' untranslated regions and fewer microRNA target sites. *Science* **320**, 1643–1647 (2008).
- Mayr, C. & Bartel, D. P. Widespread shortening of 3' UTRs by alternative cleavage and polyadenylation activates oncogenes in cancer cells. *Cell* **138**, 673–684 (2009).
- Lianoglou, S., Garg, V., Yang, J. L., Leslie, C. S. & Mayr, C. Ubiquitously transcribed genes use alternative polyadenylation to achieve tissue-specific expression. *Genes Dev.* **27**, 2380–2396 (2013).
- Brennan, C. M., Gallouzi, I. E. & Steitz, J. A. Protein ligands to HuR modulate its interaction with target mRNAs *in vivo*. *J. Cell Biol.* **151**, 1–14 (2000).
- ten Klooster, J. P., Leeuwen, I., Scheres, N., Anthony, E. C. & Hordijk, P. L. Rac1-induced cell migration requires membrane recruitment of the nuclear oncogene SET. *EMBO J.* **26**, 336–345 (2007).
- Kishore, S. *et al.* A quantitative analysis of CLIP methods for identifying binding sites of RNA-binding proteins. *Nature Methods* **8**, 559–564 (2011).
- Lebedeva, S. *et al.* Transcriptome-wide analysis of regulatory interactions of the RNA-binding protein HuR. *Mol. Cell* **43**, 340–352 (2011).
- Mukherjee, N. *et al.* Integrative regulatory mapping indicates that the RNA-binding protein HuR couples pre-mRNA processing and mRNA stability. *Mol. Cell* **43**, 327–339 (2011).
- Uren, P. J. *et al.* Genomic analyses of the RNA-binding protein Hu antigen R (HuR) identify a complex network of target genes and novel characteristics of its binding sites. *J. Biol. Chem.* **286**, 37063–37066 (2011).
- An, J. J. *et al.* Distinct role of long 3' UTR BDNF mRNA in spine morphology and synaptic plasticity in hippocampal neurons. *Cell* **134**, 175–187 (2008).
- Oldenburg, P. A. *et al.* Role of CD47 as a marker of self on red blood cells. *Science* **288**, 2051–2054 (2000).
- Jaiswal, S. *et al.* CD47 is upregulated on circulating hematopoietic stem cells and leukemia cells to avoid phagocytosis. *Cell* **138**, 271–285 (2009).
- Fan, X. C. & Steitz, J. A. Overexpression of HuR, a nuclear-cytoplasmic shuttling protein, increases the *in vivo* stability of ARE-containing mRNAs. *EMBO J.* **17**, 3448–3460 (1998).
- Mazan-Mamczarz, K. *et al.* RNA-binding protein HuR enhances p53 translation in response to ultraviolet light irradiation. *Proc. Natl Acad. Sci. USA* **100**, 8354–8359 (2003).
- Seo, S. B. *et al.* Regulation of histone acetylation and transcription by INHAT, a human cellular complex containing the set oncoprotein. *Cell* **104**, 119–130 (2001).
- Fan, Z., Beresford, P. J., Oh, D. Y., Zhang, D. & Lieberman, J. Tumor suppressor NM23-H1 is a granzyme A-activated DNase during CTL-mediated apoptosis, and the nucleosome assembly protein SET is its inhibitor. *Cell* **112**, 659–672 (2003).
- Miller, J. D., Wilhelm, H., Gierasch, L., Gilmore, R. & Walter, P. GTP binding and hydrolysis by the signal recognition particle during initiation of protein translocation. *Nature* **366**, 351–354 (1993).
- Schneider, R., Bannister, A. J., Weise, C. & Kouzarides, T. Direct binding of INHAT to H3 tails disrupted by modifications. *J. Biol. Chem.* **279**, 23859–23862 (2004).
- Zerangue, N., Schwappach, B., Jan, Y. N. & Jan, L. Y. A new ER trafficking signal regulates the subunit stoichiometry of plasma membrane K(ATP) channels. *Neuron* **22**, 537–548 (1999).
- Walmsley, M. J. *et al.* Critical roles for Rac1 and Rac2 GTPases in B cell development and signaling. *Science* **302**, 459–462 (2003).
- Reinhold, M. I., Green, J. M., Lindberg, F. P., Ticchioni, M. & Brown, E. J. Cell spreading distinguishes the mechanism of augmentation of T cell activation by integrin-associated protein/CD47 and CD28. *Int. Immunol.* **11**, 707–718 (1999).
- Lamy, L. *et al.* CD47 and the 19 kDa interacting protein-3 (BNIP3) in T cell apoptosis. *J. Biol. Chem.* **278**, 23915–23921 (2003).
- Lindberg, F. P. *et al.* Decreased resistance to bacterial infection and granulocyte defects in IAP-deficient mice. *Science* **274**, 795–798 (1996).
- Isenberg, J. S. *et al.* Thrombospondin-1 and CD47 limit cell and tissue survival of radiation injury. *Am. J. Pathol.* **173**, 1100–1112 (2008).
- Soto-Pantoja, D. R., Isenberg, J. S. & Roberts, D. D. Therapeutic targeting of CD47 to modulate tissue responses to ischemia and radiation. *J. Genet. Syndr. Gene Ther.* **2**, 1000105 (2011).
- Frazier, W. A., Isenberg, J. S., Kaur, S. & Roberts, D. D. in *UCSD Nature Molecule Pages* (University of California, San Diego, 2010).
- Avet, C. *et al.* SET protein interacts with intracellular domains of the gonadotropin-releasing hormone receptor and differentially regulates receptor signaling to cAMP and calcium in gonadotrope cells. *J. Biol. Chem.* **288**, 2641–2654 (2013).
- Nilsson, J., Persson, B. & von Heijne, G. Comparative analysis of amino acid distributions in integral membrane proteins from 107 genomes. *Proteins* **60**, 606–616 (2005).
- Lau, A. G. *et al.* Distinct 3'UTRs differentially regulate activity-dependent translation of brain-derived neurotrophic factor (BDNF). *Proc. Natl Acad. Sci. USA* **107**, 15945–15950 (2010).
- Yoon, J. H. *et al.* Scaffold function of long non-coding RNA HOTAIR in protein ubiquitination. *Nature Commun.* **4**, 2939 (2013).

Acknowledgements This work was funded by the Innovator Award of the Damon Runyon-Rachleff Cancer Foundation and the Island Outreach Foundation (DRR-24-13) and National Institutes of Health grant U01-CA164190. We thank N. Patel for help with cloning of the constructs and the members of the Mayr laboratory, specifically S.-H. Lee and E. Kallin, as well as N. Rajewsky and A. Ventura, for helpful discussions. We also thank J. Joyce, C. Haynes, A. Hall and R. Benezra for critical reading of the manuscript. The N17RAC1 construct was provided by A. Hall and the JinB8 cells by W. A. Frazier and D. D. Roberts. We thank the Molecular Cytology Core Facility (Memorial Sloan Kettering Cancer Center) for help with the confocal microscopy (funded by P30 CA008748).

Author Contributions B.D.B. designed and performed the experiments and C.M. designed the study. B.D.B. and C.M. wrote the manuscript.

Author Information Reprints and permissions information is available at www.nature.com/reprints. The authors declare no competing financial interests. Readers are welcome to comment on the online version of the paper. Correspondence and requests for materials should be addressed to C.M. (mayrc@mskcc.org).

METHODS

Cell lines. MCF7 (breast cancer), HeLa (cervical cancer), HEK293 (embryonic kidney), Caov-3 (ovarian carcinoma), NTERA2 (embryonic carcinoma) and THP-1 cells (monocytic leukaemia) were purchased from ATCC. B-LCL are Epstein Barr virus (EBV)-immortalized human B cells described earlier³. U2OS cells (sarcoma) were a gift from T. Brummelkamp, Toledo (B-cell lymphoma) cells were a gift from M. Mueschen, U251 (glioblastoma) cells were a gift from I. Mellnhoff, SHSY-5Y (neuroblastoma) cells were a gift from T. Tuschl and Jurkat (T-cell leukaemia) and JinB8 (CD47-negative Jurkat) cells were a gift from W. Frazier.

Constructs. For some of the shRNA knockdown experiments, pSUPERretropuro was modified by cloning IRES::GFP (derived from pMSCV-pig)² downstream of puromycin to obtain pSUPERretropuro containing enhanced (e)GFP (shRNA-GFP). The following DNA oligonucleotides served as shRNA precursors and were cloned into pSUPER-GFP or pSUPER. CD47-LU2F: 5'-GATCTCCCAGCTGT GTTACCGTTAAATCAAGAGATTAAACGGTAACAGCTGTTTTC-3'; CD47-LU3F: 5'-GATCCCCAGCTGTGTACCGTTAAATCAAGAGATT TAACGGTAACAGCTGTTTTC-3'; HuR2F: 5'-GATCTCCGATCAGAC CTACAGGTTTGTTCAGAGAGAACAACCTGTAGTCTGATCTTTTTC-3'; HuR3F: 5'-GATCCCCGAGGCAATTACCAGTTTCATTCAAGAGATGAAA CTGGTAATTGCCTCTTTTC-3'; HuR4F: 5'-GATCCCTCTTAAGTTTCG TAAGTTATTCAAGAGATAACTTACGAACTTAAGATTTTTC-3'; SET1F: 5'-GATCCCCCTGAAATAGACAGACTTAATTTCAAGAGAAATTAAGTCT GTCTATTTCATTTTC-3'; SET2F: 5'-GATCCCTGGTTTACTGAC CATTCTTTCAAGAGAAGAATGGTCAGTAAACAGTTTTC-3'; RAC2F: 5'-GATCCCCCTTGCCTACTGATCAGTTATTCAAGAGATAACTGATCA GTAGGCAAGTTTTC-3'; RAC3F: 5'-GATCCCCCTGCTTGGAACTT TGTATTCAAGAGATACAAAGGTTCCAAGGGACTTTTTC-3'; ControlF: 5'-GATCTCCTTCTCCGACGTGTACGTTTCAAGAGAACGTGACACG TTCGAGAATTTTTC-3'.

The sequence of shRNA1 SET and of shRNA Control were published earlier^{31,32}. The GFP fusion constructs were generated in pcDNA3.1 expression vector (Life Technologies). The short and long 3' UTRs of *CD47* were PCR-amplified from genomic DNA using Q5 High Fidelity DNA polymerase (NEB) and the primers listed later and inserted between the NotI and XbaI sites. To obtain expression of only the long 3' UTR isoform of *CD47*, the proximal polyadenylation site was mutated from AAUAAA to ACUCAA using the QuikChange Multi Site Directed Mutagenesis Kit (Agilent). The resulting plasmids were used to test qPCR primers for accuracy in measuring short to long 3' UTR isoform ratios (see later). The short 3' UTR of *CD47* used in the MS2-BS construct was cloned from the plasmid containing the long 3' UTR with the mutated proximal polyadenylation site. eGFP was PCR-amplified from pMSCV-pig and inserted upstream of each *CD47* 3' UTR (BamHI, NotI). The signal peptide of *CD47* was generated by annealing two DNA oligonucleotides that were inserted into the BamHI site. To generate the GFP-TM constructs, the sequence of the TMDs and C-terminal tail of *CD47* (the longest isoform, isoform 4; ref. 33) were cloned from Toledo cDNA and inserted downstream of eGFP (BsrGI, NotI). Isoform 4 was chosen as it is the most abundant isoform in Jurkat cells (data not shown). The two nucleotides of eGFP that occur after the BsrGI site were included in the forward primer. To generate the GFP-*CD47* constructs, the ECD, TMDs and C terminus of *CD47* were PCR-amplified from Toledo cDNA using the TM reverse primer and the CDS forward primer and inserted downstream of eGFP (BsrGI, NotI). The sequence of HuR-BS and HuR-BSA are shown in Extended Data Fig. 3 and replaced the long 3' UTR in GFP-TM-LU. The GFP constructs containing the TMDs and C termini fused to either the long or short 3' UTRs of *CD44*, *ITGA1* and *TNFRSF13C* were generated as follows. TMDs, C termini and short 3' UTRs of *CD44*, *ITGA1* and *TNFRSF13C* were cloned from Toledo, SHSY-5Y and B-LCL cDNA respectively and inserted downstream of eGFP (BsrGI, XbaI). Short 3' UTRs consisted of the first 122 nucleotides of *CD44*, the first 45 nucleotides of *ITGA1* and the first 337 nucleotides of *TNFRSF13C*. Long 3' UTRs: 3,068 nucleotides after the stop codon of *CD44* and 3,996 nucleotides after the stop codon of *ITGA1* were used. For *TNFRSF13C*, 1,221 nucleotides after the stop codon together with the last 600 nucleotides of the 3' UTR (nucleotides 2,712–3,311 after the stop codon containing the majority of HuR-binding sites) were used as long 3' UTR and were cloned from genomic DNA. To generate BAFRR-SU and -LU, the complete open reading frame of *TNFRSF13C* (without the start codon) was amplified from human B-cell cDNA and cloned using Gibson Assembly Cloning (NEB) into pcDNA3.1 vector used above downstream of eGFP. To generate CD44-SU and -LU, the open reading frame of *CD44* (without the start codon) was amplified from cDNA of the human breast cancer cell line MDA-MB231 and cloned using Gibson Assembly Cloning (NEB) into pcDNA3.1 vector used above downstream of eGFP. To generate the GFP-TM-LUΔC construct the sequence of just the TMDs of *CD47* was cloned from Toledo cDNA using the TM forward primer and TMAC reverse primer and

inserted downstream of eGFP (BsrGI, NotI). The 24 MS2-binding sites were cloned from a plasmid obtained from J. Gerst³⁴ using the primers listed later (XbaI, ApaI). The constructs in which K163, K166, K175, K290, K297 and K304 were mutated to alanines were generated using the QuikChange Multi Site Directed Mutagenesis Kit (Agilent).

CD47UTRF: 5'-ATGCGCGGCCGCGAGTGAAGTGATGGACTCCGATT-3'; CD47shortUTRR: 5'-ATGCTCTAGATGGGCAAACAACATAGATCA-3'; CD47longUTRR: 5'-ATGCTCTAGAAACACATTGGACTGATTTAAACTT-3'; GFP: 5'-ATGCGGATCCATGGTGAGCAAGGGCGA-3'; GFP: 5'-ATGCG CGGCCGCTTACTTGTACAGCTCGTCCATG-3'; SPCD47F: 5'-GATCCAT GTGGCCCCGTGTAGCGGCGCTGTTGCTGGGCTCGGCGTGTGCGGAT CAGCTG-3'; SPCD47R: 5'-GATCCAGCTGATCCGAGCAGCCGAGCC CAGCAACAGCGCCGCTACCGGGCCATG-3'; CD47TMF: 5'-ATGC TGTACAAGATTCTTATTGTTATTTTCCCAATT-3'; CD47TMR: 5'-ATGC GCGGCCGCTTATTCATCATTTCCTT-3'; CD47CDSF: 5'-ATGCT GTACAAGCAGCTACTATTAAATAAAACAA-3'; TMACR: 5'-ATGCGCGG CCGCTTATTTTCATATAAACTAGTCCAAAGTAA-3'; MS2-BSF: 5'-ATGCTC TAGAGGCCCTATATATCATGATCCTAAG-3'; MS2-BSR: 5'-ATGCGGGCC CTTTATTATGCTTGGTACCGAGCTCG-3'.

To create the MS2 fusion constructs³⁵, the pUG34-MS2-GFP-SBP plasmid was obtained from J. Gerst³⁴. SBP was replaced by either HuR, SET or a stop codon. HuR and SET were PCR-amplified from U2OS cDNA using the primers listed below (BsrGI, XbaI). The stop codon was generated by annealing two DNA oligonucleotides (BsrGI, XbaI). mCherry was PCR-amplified and replaced GFP (BamHI, BsrGI). After cloning was complete, all plasmids were sequenced to assure fidelity of the sequences.

HuR: 5'-ATGCCGTACGAGTCTAATGGTTATGAAGACCACA-3'; HuRR: 5'-ATGCTCTAGATTATTTGTGGGACTTGTGGT-3'; SET: 5'-ATGCTGT ACAAGTCGCGCGCGCGGCCAAA-3'; SETR: 5'-ATGCTCTAGATTAGT CATCTTCTCCTTCATCCTC-3'; StopF: 5'-GTACAAGTAATAAAT-3'; StopR: 5'-CTAGATTATTATTACTT-3'; mCherryF: 5'-ATGCGGATCCGTG AGCAAGGGCGAGGAG-3'; mCherryR: 5'-TTACTTGTACAGCTCGTCCA TGC-3'.

The N17RAC1 construct was provided by A. Hall³⁶.

Transfections. For transfections into U2OS, HEK293, HeLa and U251 cells Lipofectamine 2000 (Invitrogen) and for SHSY-5Y cells Xtreme reagent (Roche) was used. JinB8 and Jurkat cells were transfected using the Neon Transfection System (Invitrogen) according to the manufacturer's protocol for transfecting Jurkat cells. To account for differences in the sizes of transfected plasmids the same molar amounts were transfected. When RNA was to be extracted, the cells were grown in the presence of high amounts of puromycin (4 mg ml⁻¹) for 3 days and FACS analysis was performed to ensure that >90% of the cells were GFP⁺.

Generation of cell lines with stable expression of shRNAs. Stable cell lines were generated as described previously².

FACS analysis. For surface FACS (in order to detect surface protein expression), cells were incubated with mouse anti-CD47-PerCy5.5 (BD Biosciences, 561261), mouse anti-CD44-PE (BD Biosciences, 561858), chicken anti-GFP (Abcam, ab13970), mouse anti-ITGA1-PE (BD Biosciences, 555749), mouse anti-BAFFR-PE (BD Biosciences, 554680) or rabbit anti-TSPAN13 (Genetex, GTX52155) in FACS buffer A (0.5% FBS in PBS) for 30 min at 4 °C, and then washed twice in FACS Buffer A. For detection of GFP and TSPAN13, cells were then incubated with goat anti-chicken Alexa Fluor 568 or 633 (Invitrogen, A11041 or A21103) and goat anti-rabbit Alexa Fluor 680 (Invitrogen, A-21076), respectively, for 30 min at 4 °C, and then washed twice in FACS Buffer A. At least 30,000 cells were analysed on a BD FACSCalibur cell analyser (BD Biosciences) and FACS data were computed using the FlowJo VX software.

For intracellular FACS (in order to detect total protein expression), cells were fixed for 15 min at room temperature in fixation buffer (4% PFA, 0.02% sodium azide, and 0.1% Tween 20 in PBS), washed in FACS buffer B (0.02% sodium azide, 0.1% Tween 20 in PBS), permeabilized for 10 min at 4 °C in permeabilization buffer (0.02% sodium azide, 0.1% Tween 20 and 10% dimethyl sulfoxide in PBS), washed, re-fixed for 5 min at room temperature in fixation buffer, and washed again. Cells were incubated with the same primary and secondary antibodies as for surface FACS in FACS buffer B for 30 min at 4 °C, and then washed twice in FACS Buffer B. For live/dead analysis by FACS, cells were incubated with TO-PRO3 in FACS buffer A (0.5% FBS in PBS) for 10 min at 4 °C, and then washed twice in FACS Buffer A. Cells were analysed in the same manner as for surface FACS.

For all the GFP-expressing plasmids the 20% of cells with the highest GFP expression are shown.

Immunocytochemistry. For surface staining of CD47, cells were fixed for 15 min at room temperature in fixation buffer A (4% PFA and 0.02% sodium azide in PBS), washed with PBS, blocked for 15 min at 4 °C in 5% Normal Goat Serum

(Invitrogen, PCN5000) in PBS and then incubated with mouse anti-human CD47 (Santa Cruz, sc-59079) primary antibody for 1 h at 4 °C in PBS. After washing in PBS, donkey anti-mouse Alexa Fluor 594 (Invitrogen, A-21203) secondary antibody was incubated for 1 h at 4 °C in PBS, and during the last 10 min of incubation 4',6-diamidino-2-phenylindole (DAPI; Invitrogen, D1306) was added, followed by three washes of PBS. Mowiol mounting media (Sloan Kettering Institute, Molecular Cytology Core Facility) was used to mount the slides. Imaging was performed at the Sloan Kettering Institute Molecular Cytology Core Facility, on a Leica TCS SP5 confocal microscope, using a $\times 63$, 1.4 numerical aperture oil objective.

For intracellular staining of CD47, cells were fixed for 15 min at room temperature in fixation buffer B (4% PFA, 0.02% sodium azide, and 0.1% Tween 20 in PBS), washed in wash buffer (0.02% sodium azide, 0.1% Tween 20 in PBS), permeabilized for 10 min at 4 °C in permeabilization buffer (0.02% sodium azide, 0.1% Tween 20 and 10% dimethyl sulfoxide in PBS), washed, re-fixed for 5 min at room temperature in fixation buffer B, washed and blocked for 15 min at 4 °C in 5% Normal Goat Serum in wash buffer. Mouse anti-CD47 (Santa Cruz, sc-59079) primary antibody was incubated overnight at 4 °C in wash buffer. The strong permeabilization and overnight staining were necessary to visualize intracellular CD47, as the CD47 antibody recognizes an epitope in the ECD of CD47, which is located in the lumen of the endoplasmic reticulum. Owing to the extended treatment with a buffer containing Tween 20 the plasma membrane could no longer be visualized in these cells.

For co-staining of GFP with calnexin or RAC1, the cells were fixed for 15 min at room temperature in fixation buffer B (4% PFA, 0.02% sodium azide, and 0.1% Tween 20 in PBS), washed with wash buffer B, blocked for 15 min at 4 °C in 5% Normal Goat Serum (Invitrogen, PCN5000) in wash buffer and then incubated with rabbit anti-calnexin (Santa Cruz, sc-11397) or mouse anti-RAC1 (Abcam, ab12048) primary antibodies for 1 h at 4 °C in wash buffer. After washing, goat anti-rabbit Alexa Fluor 680 (Invitrogen, A-21076) or donkey anti-mouse Alexa Fluor 594 (Invitrogen, A-21203) secondary antibodies were incubated for 1 h at 4 °C in wash buffer, and during the last 10 min of incubation DAPI (Invitrogen, D1306) was added, followed by three washes. Mounting and imaging was performed as for the surface staining. Owing to the lack of permeabilization and short period in Tween 20, the plasma membrane was still visible. When calnexin was co-stained with endogenous CD47, the protocol for intracellular staining of CD47 was used and the plasma membrane was again not visible.

Alexa Fluor 594 and 680 were pseudo-coloured red and endogenous GFP and mCherry were imaged as they appear, without any antibody.

RNA-FISH. Custom Stellaris FISH Probes (Biosearch Technologies) were designed for the open reading frame of eGFP using the Stellaris Probe designer website, and with the assistance of Biosearch Technologies staff. The probes were conjugated to the Quasar 670 fluorochrome. Staining was carried out according to the manufacturer's protocols. Briefly, 24 h after transfection of the GFP-TM constructs cells were trypsinized and plated on Millicell EZ glass slides (Millipore) and allowed to grow overnight. Cells were washed in PBS, fixed in 4% PFA at room temperature for 10 min and permeabilized in 70% ethanol at 4 °C for 2 h. After washing, the probes were hybridized at 37 °C for 4 h, washed, incubated with DAPI at 37 °C for 30 min, washed and mounted in Mowiol mounting media. Imaging was performed as for the surface immunostaining. RNA was pseudo-coloured red, and GFP was imaged as it appears, without any antibody.

3'-seq. 3'-seq reads of naive B cells, B-LCL and HEK293 cells were analysed and visualized as described previously³.

Northern blot analysis. Northern blots were performed as previously described².

CD47 probe F: 5'-TTGATGGAGCTCTAAACAAGTCC-3'; CD47 probe R: 5'-GAATAACCAATATGGCAATGACG-3'; GFP probe F: 5'-TAAACGGCCACAAGTTCACG-3'; GFP probe R: 5'-CTTGACAGCTCGTCCATGC-3'.

Quantitative PCR. RNA was extracted using TRI Reagent (Ambion) according to the manufacturer's protocol. cDNA was synthesized using random hexamers and the TaqMan Reverse Transcription Kit (Applied Biosystems). qRT-PCR was performed using the Power SYBR Green master mix (Applied Biosystems) on a 7500 HT Fast Real-Time PCR System (Applied Biosystems). Each reaction was performed in triplicate. The experiments were performed at least three times to obtain at least three biological replicates. The following primers were used to quantify total CD47 mRNA, the long 3' UTR isoform of CD47 and GAPDH for normalization.

CD47TotalF: 5'-AGTGATGGACTCCGATTTGG-3'; CD47TotalR: 5'-GGG TCTCATAGGTGACAACCA-3'; CD47LongF: 5'-AAGAGAACTCCAGTGTT GCT-3'; CD47LongR: 5'-ACGGTAACACAGCTGTAAACA-3'; GAPDH: 5'-ACAACCTTTGGTATCGTGAAGG-3'; GAPDHR: 5'-TATTTGGCAGGTT TTTCTAGACG-3'.

To measure 3' UTR isoform expression by qRT-PCR and to take into account different affinities of primers, we generated a standard using plasmids that

contained either the short or the long 3' UTR of CD47 (see earlier). We mixed together known quantities of the two plasmids ranging from 3:1 to 1:3 of short to long 3' UTR and performed qPCR on these mixtures to test the accuracy of our primer sets. The fraction of the long 3' UTR isoform was calculated by subtracting the CT value of the long isoform from the CT value for total CD47 expression. The fraction of the long 3' UTR isoform corresponds to $2^{\Delta CT}$ difference. The fraction of the short 3' UTR isoform was obtained by subtracting the fraction of the long 3' UTR isoform from the total CD47 mRNA.

Immunoprecipitation of RNA complexes and RT-PCR. GFP-TM-LU, GFP-TM-SU, GFP-TM-HuR-BS and GFP-TM-HuR-BSA were transfected into HEK293 cells and immunoprecipitation of protein-RNA complexes was carried out as previously described³⁷. RNA-immunoprecipitations were performed with crosslinking to prevent re-association of HuR with mRNA after lysis³⁸. Briefly, cells were harvested and washed twice in cold PBS. Formaldehyde was added to a final concentration of 1% (v/v) and the cells were incubated at room temperature for 10 min. The reaction was quenched by addition of glycine to a final concentration of 0.25 M and incubated at room temperature for 5 min. After centrifugation the cell pellet was washed twice in cold PBS and resuspended in RIPA buffer (25 mM Tris-HCl (pH 7.4), 150 mM NaCl, 1% NP-40, 1% Na-deoxycholate, 0.1% SDS, 1 mM EDTA, protease inhibitor cocktail (Roche, 04693124001)). The mRNPs were solubilized by three rounds of sonication for 15 s each in a Misonix Ultrasonic Processor S-4000 at an output of 8–9 W. Insoluble material was removed by centrifugation. Lysates were pre-cleared by addition of magnetic protein A beads (Millipore, LSKMAGA10) and incubation for 30 min at 4 °C with constant mixing. The pre-cleared lysate was divided into three parts. One portion was retained for the input control and anti-HuR (Millipore, 07-1735) or IgG (Santa Cruz, sc-2025) were added to the two other portions and incubated at 4 °C for 2 h. Magnetic protein A beads (Millipore, LSKMAGA10) were added and incubated at 4 °C for 1 h. The beads were washed five times with high-stringency RIPA buffer (50 mM Tris-HCl (pH 7.4), 1 M NaCl, 1% NP-40, 1% sodium deoxycholate, 0.1% SDS and 1 mM EDTA). The crosslinking was reversed by resuspending the beads in 50 mM Tris-Cl (pH 7.0), 5 mM EDTA, 10 mM dithiothreitol (DTT) and 1% SDS, followed by incubation at 70 °C for 45 min. RNA was extracted from the beads and buffer using TRI Reagent (Ambion) according to the manufacturer's protocol, and cDNA was synthesized as previously described. qRT-PCR was carried out using primers for GAPDH (see earlier) and GFP, so as not to amplify endogenous CD47. The primers used were as follows: GFPF: 5'-TAAACGGCCACAAGTACG-3'; GFP: 5'-AAGTCGT GCTGCTTCATGTG-3'.

HEK293 cells transiently transfected with sh2 HuR or sh Co were used to assess the presence of SET on endogenous CD47 mRNA and the requirement of HuR for this association. Cells were transfected and treated with high dose puromycin for 3 days. FACS analysis was used to ensure greater than 90% of surviving cells expressed the shRNA. RNA-immunoprecipitation was carried out as described earlier, but using anti-SET (Abcam, ab181990) or IgG (Santa Cruz, sc-2025). The following primers were used for qRT-PCR of CD47-LU: CD47F: 5'-AAGAG AACTCCAGTGTGCT-3'; CD47R: 5'-ACGGTAACACAGCTGTAAACA-3'.

The obtained CT values were first normalized to GAPDH and then the fraction of input mRNA was plotted.

Western blotting. HEK293 cells stably expressing sh3 HuR, sh4 HuR, sh1 SET, sh2 SET, sh2 Rac1, sh3 Rac1 or sh Co, as well as HEK293 cells transiently transfected with sh2 HuR, CD47-SU, CD47-LU, CD47-LU+N17Rac1, CD47-LU2Km, CD47-LUAC or CD47-LUACL, were lysed in Laemmli buffer (Sigma, S3401), boiled for 7 min and then cooled on ice. Lysates were run on NuPAGE Novex 4–12% Bis-Tris Gel (Invitrogen, NP0322BOX) and transferred to PVDF membrane (Bio-rad, 162-0177). After blocking for 1 h at room temperature in Odyssey Blocking Buffer (Li-Cor, 927-40000) the following primary antibodies were used: rabbit anti-HuR (Millipore, 07-1735), rabbit anti-SET (Abcam, ab181990), mouse anti-RAC1 (Cell Signaling Technology, 8631S), mouse anti-ACTB (Sigma, A4700), rabbit anti-ACTB (Sigma, A2066), chicken anti-GFP (Abcam, ab13970), mouse anti-CD47 (Santa Cruz, sc-59079), mouse anti-CD44 (BD Bioscience, 561858), and rabbit anti-TSPAN13 (GeneTex, GTX52155). The antibodies were diluted in Odyssey Blocking Buffer containing 0.1% Tween 20 and the blots were incubated overnight at 4 °C. After four washes in PBST (PBS plus 0.1% Tween 20) the blots were incubated for 1 h at room temperature in Odyssey Blocking Buffer containing 0.1% Tween 20 and 0.01% SDS and the following secondary antibodies: donkey anti-mouse IRDye 700 (Rockland Immunochemicals, 610-730-002), donkey anti-rabbit IRDye 680 (Li-Cor Biosciences, 926-68073), donkey anti-rabbit IRDye 800 (Li-Cor Biosciences, 926-32213), donkey anti-mouse IRDye 800 (Li-Cor Biosciences, 926-32212) and rabbit anti-chicken IRDye 800 (Rockland Immunochemicals, 603-432-002). The blots were washed four times in PBST and then thoroughly soaked in PBS before imaging. Imaging was performed on

an Odyssey CLx imaging system (Li-Cor). Quantification of western blots was performed using Image J.

Co-immunoprecipitation. CD47-SU, CD47-LU, CD47-LUAC and CD47-LUACL were transfected into HEK293 cells and the cells were lysed in ice cold RIPA buffer ((25 mM Tris-HCl (pH 7.4), 150 mM NaCl, 1% NP-40, 1% Na-deoxycholate, 0.1% SDS, 1 mM EDTA, protease inhibitor cocktail (Roche, 04693124001)) for 5 min on ice. After the cells were spun down at 20,000g for 20 min the supernatant was pre-cleared as described earlier. The lysate was divided in two equal parts (a small portion was removed to be used as the input control). Anti-GFP (Invitrogen, A-6455) or IgG (Santa Cruz, sc-2025) was added to the lysates and a 1 h rocking incubation at 4 °C was performed, followed by addition of magnetic protein A beads (Millipore, LSKMAGA10) and another 1 h rocking incubation at 4 °C. After seven washes in RIPA buffer the beads were then boiled in Laemmli buffer (Sigma, S3401) for 7 min and then cooled on ice. Western blotting was carried out as described earlier. Chicken anti-GFP (Abcam, ab13970) antibody was used to confirm immunoprecipitation of GFP constructs and rabbit anti-SET (Abcam, ab181990) antibody was used to assess co-immunoprecipitation of SET protein.

Immunoprecipitation of RAC1-GTP. CD47-SU, CD47-LU and pcDNA 3.1 vector alone were transfected into HEK293 cells. The levels of RAC1-GTP were assessed using an Active Rac1 Detection Kit (Cell Signaling Technology, 8815) following the manufacturer's protocol. Briefly, cells were lysed in ice cold lysis buffer and centrifuged at 16,000g for 15 min at 4 °C. The supernatant was added to GST-PAK1-PBD and glutathione resin and incubated with rocking for 1 h at 4 °C (a small portion was removed to be used as the input control). The resin was washed three times with lysis buffer and then SDS sample buffer was added to elute the bound proteins. Western blotting was carried out as described earlier. Mouse anti-RAC1 (Cell signaling Technology, 8631S) antibody was used to detect RAC1-GTP as well as to assess total RAC1 in the samples.

Irradiation and cell survival assay. Jurkat, JinB8, and transfected JinB8 cells (24 h post-transfection) were irradiated for a total of 0, 5, 10, 20 or 40 Gy using a Shepherd Mark-1 caesium irradiator. For JinB8 or Jurkat cells transfected with CD47-LU, CD47-SU or with sh2 CD47-LU the percentage of GFP⁺ cells was determined by FACS before irradiation. Three days after γ -irradiation, cells were stained with TO-PRO3 (Sloan Kettering Institute, Flow Cytometry Core Facility) in FACS buffer A (0.5% FBS in PBS) for 10 min at 4 °C and analysed using a BD FACSCalibur cell analyser to evaluate cell survival. Per cent survival was calculated as the TO-PRO3-negative cells divided by the total number of GFP⁺ cells. Shown are mean and standard deviation of three biological replicates.

Phagocytosis assay. Human macrophages were obtained by differentiation of THP-1 cells with 25 ng ml⁻¹ phorbol 12-myristate 13-acetate (PMA; Sigma) for 3 days. On day 3, Jurkat, JinB8, or transfected JinB8 cells were treated with 10 μ g ml⁻¹ Mitomycin C for 2.5 h at 37 °C and washed three times in media. Mitomycin C treatment halts cell division and allows for a more accurate assessment of the percentage of cells that are phagocytosed. For JinB8 cells transfected

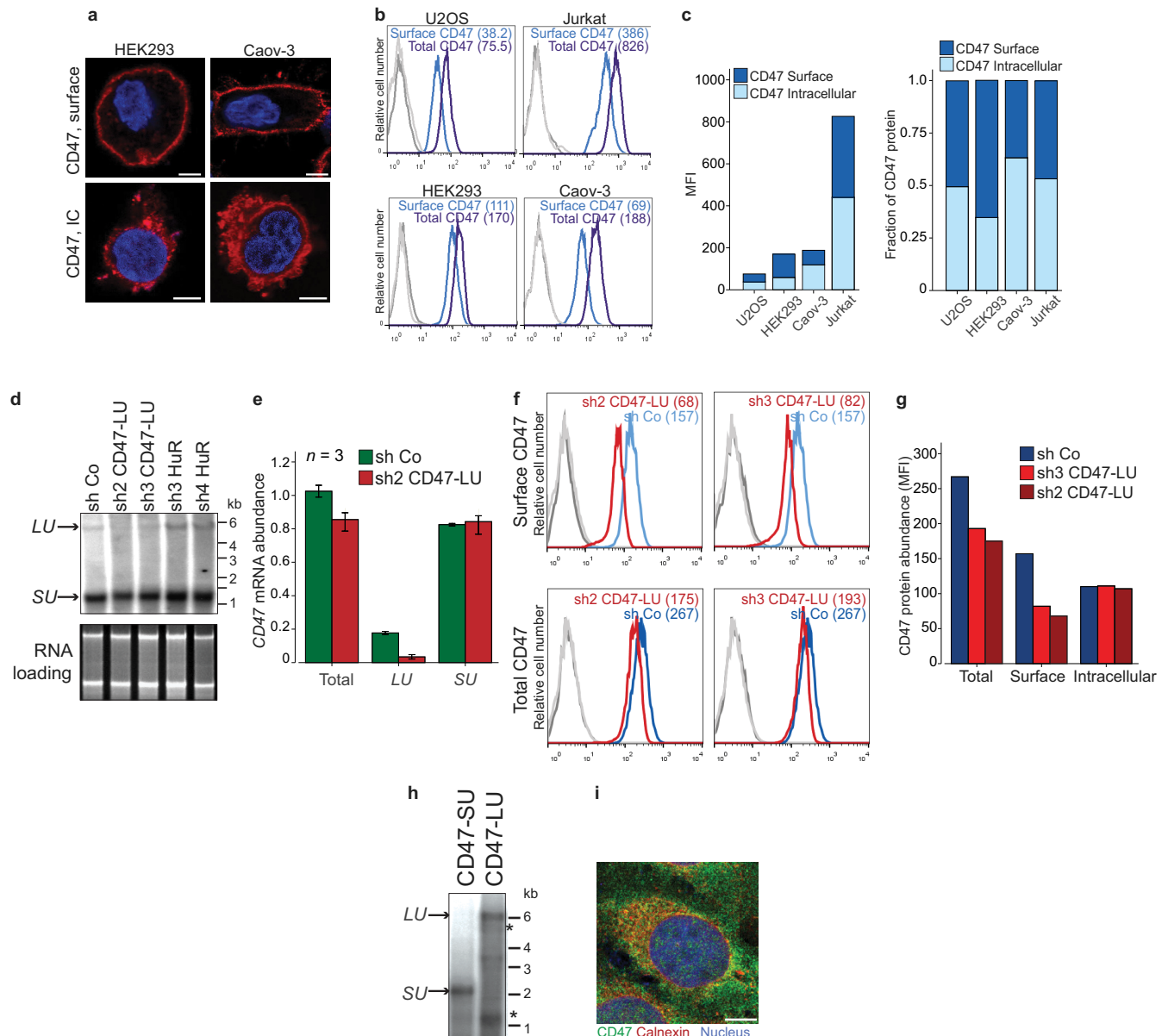
with CD47-LU or CD47-SU the percentage of GFP⁺ cells was determined by FACS before co-culture. The cells were either cultured alone or co-cultured with fully differentiated macrophages. After 3 days, cells were counted and the fraction of GFP⁺ cells was determined by FACS analysis. The fraction of surviving cells after co-culture with macrophages was normalized by the number of surviving cells without co-culture and is shown as mean and standard deviation of three independent experiments.

To demonstrate that the cells were phagocytosed, during the last 10 min of Mitomycin C treatment the cells were also labelled with carboxyfluorescein succinimidyl ester (CFSE; Invitrogen). Washing after Mitomycin C and CFSE treatment was carried out in cold media according to the manufacturer's protocol. After co-culture, CFSE uptake by macrophages was measured by FACS analysis to demonstrate that a decrease in the number of surviving cells is due to phagocytosis by macrophages.

Fraction of membrane proteins among HuR target genes. The list of HuR target genes was obtained from previous publications^{7,9}. The union of genes from both publications was analysed using gene ontology analysis³⁹ and all genes with the tag "membrane" were considered membrane proteins. This number is consistent with the number of membrane proteins obtained in yeast⁴⁰. Fisher's exact test was used to test for significance.

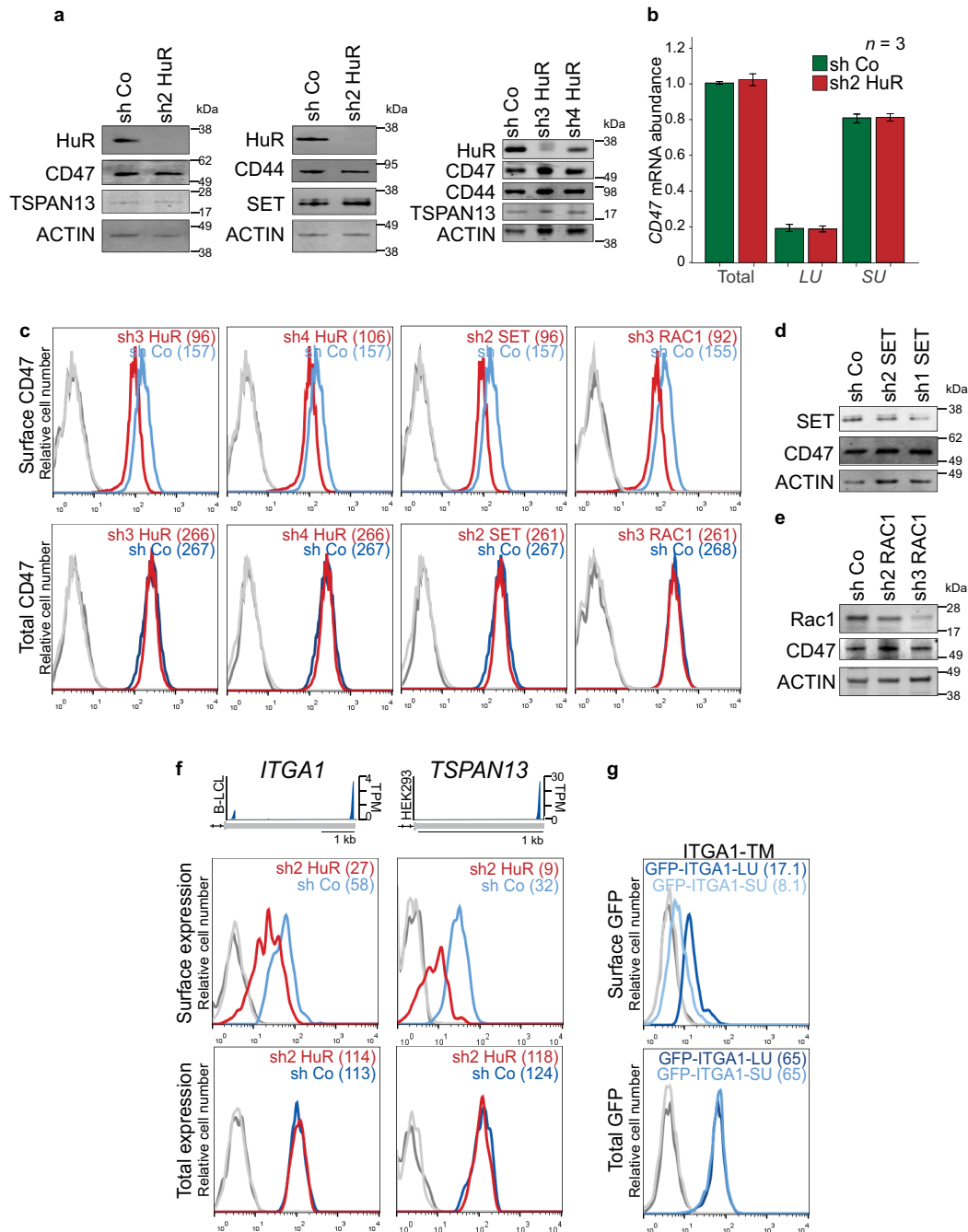
Statistical analysis. To test for significant differences between samples a two-sided *t*-test for independent samples was performed using SPSS.

31. Neviani, P. *et al.* The tumor suppressor PP2A is functionally inactivated in blast crisis CML through the inhibitory activity of the BCR/ABL-regulated SET protein. *Cancer Cell* **8**, 355–368 (2005).
32. Nho, R. S. *et al.* PTEN regulates fibroblast elimination during collagen matrix contraction. *J. Biol. Chem.* **281**, 33291–33301 (2006).
33. Reinhold, M. I. *et al.* *In vivo* expression of alternatively spliced forms of integrin-associated protein (CD47). *J. Cell Sci.* **108**, 3419–3425 (1995).
34. Slobodin, B. & Gerst, J. E. A novel mRNA affinity purification technique for the identification of interacting proteins and transcripts in ribonucleoprotein complexes. *RNA* **16**, 2277–2290 (2010).
35. Bertrand, E. *et al.* Localization of *ASH1* mRNA particles in living yeast. *Mol. Cell* **2**, 437–445 (1998).
36. Ridley, A. J., Paterson, H. F., Johnston, C. L., Diekmann, D. & Hall, A. The small GTP-binding protein rac regulates growth factor-induced membrane ruffling. *Cell* **70**, 401–410 (1992).
37. Niranjanakumari, S., Lasda, E., Brazas, R. & Garcia-Blanco, M. A. Reversible cross-linking combined with immunoprecipitation to study RNA–protein interactions *in vivo*. *Methods* **26**, 182–190 (2002).
38. Milli, S. & Steitz, J. A. Evidence for reassociation of RNA-binding proteins after cell lysis: implications for the interpretation of immunoprecipitation analyses. *RNA* **10**, 1692–1694 (2004).
39. Huang, da W., Sherman, B. T. & Lempicki, R. A. Systematic and integrative analysis of large gene lists using DAVID bioinformatics resources. *Nature Protocols* **4**, 44–57 (2009).
40. Stagljar, I. & Fields, S. Analysis of membrane protein interactions using yeast-based technologies. *Trends Biochem. Sci.* **27**, 559–563 (2002).



Extended Data Figure 1 | Expression of the long *CD47* 3' UTR isoform correlates with cell surface expression of *CD47* protein. **a**, Fluorescence confocal microscopy of cells shown as in Fig. 1a. Representative images out of hundreds of cells are shown. Scale bars, 10 μ m. **b**, FACS analysis of endogenous *CD47* expression in cells shown in Fig. 1a and **a**. Permeabilized cells show total *CD47* expression (purple) and non-permeabilized cells show surface *CD47* expression (blue). Representative histograms are shown (HEK293 cells, $n = 10$; U2OS, Jurkat cells, $n = 5$; Caov-3, $n = 3$). Unstained cells are shown in grey. **c**, Left, quantification of mean fluorescence intensity (MFI) values from **b**. Right, fraction of surface and intracellular *CD47* levels in cells lines from **b**. Intracellular *CD47* was calculated by subtracting *CD47* surface values from total *CD47* values. **d**, Northern blot of HEK293 cells stably expressing the indicated shRNAs and hybridized for *CD47*. The shRNAs against *CD47*-LU target only the long 3' UTR isoforms of *CD47*. The blot and corresponding RNA gel are shown as in Fig. 1c. **e**, Quantification of *CD47* total mRNA and

3' UTR isoform levels in U2OS cells by qRT-PCR. *GAPDH*-normalized values after transfection of sh2 *CD47*-LU or sh Co are shown as the mean \pm s.d., $n = 3$ biological replicates. The total amount of *CD47* mRNA after transfection of sh Co was set to 1. **f**, FACS analysis of endogenous *CD47* protein expression after stable expression of shRNAs against *CD47*-LU in HEK293 cells. Surface (top) and total (bottom) *CD47* expression is shown. Representative histograms out of $n = 3$ experiments are shown. Unstained cells are shown in grey. **g**, Quantification of MFI values from **f** is displayed. Intracellular *CD47* was calculated as in **b**. **h**, Northern blot of HEK293 cells after transfection of indicated constructs and hybridized against *CD47*. Mutation of the proximal polyadenylation signal in *CD47*-LU abrogates production of short 3' UTR isoforms. Asterisk indicates cross-hybridization to ribosomal RNAs. **i**, Fluorescence confocal microscopy of endogenous *CD47* and calnexin protein in permeabilized U2OS cells. Calnexin partially co-localizes with *CD47*. A representative image out of hundreds of cells is shown. Scale bars, 10 μ m.



Extended Data Figure 2 | UDPL depends on HuR, SET and RAC1 and mediates surface localization of membrane proteins. **a**, Western blot of HEK293 cells transiently transfected (left, middle) or stably expressing (right) sh Co or shRNAs against HuR. The blot shows reduced HuR protein expression after HuR knockdown, but no change in protein expression of CD47, TSPAN13, CD44 or SET. Actin was used as loading control. **b**, Quantification of *CD47* total mRNA and 3' UTR isoform levels in HEK293 cells by qRT-PCR. *GAPDH*-normalized values after transfection of sh2 HuR or sh Co are shown. Shown is the mean \pm s.d., $n = 3$ biological replicates. The total amount of *CD47* mRNA after transfection of sh Co was set to 1. **c**, FACS analysis of HEK293 cells stably expressing the indicated shRNAs. Histograms are shown as in Fig. 2b. Representative histograms from $n = 3$ experiments are shown. **d**, Western blot

of HEK293 cells stably expressing shRNAs against SET. Actin was used as loading control. The marker is shown in kDa. **e**, As in **d**, but HEK293 cells stably expressing shRNAs against RAC1 are shown. **f**, 3'-seq analysis shows 3' UTR isoform expression of *ITGA1* in B-LCL and *TSPAN13* in HEK293 cells shown as in Fig. 1b. FACS analysis of endogenous protein levels is shown as in Fig. 2c. Left panel shows *ITGA1* expression in HeLa cells and right panel shows *TSPAN13* expression in HEK293 cells. Representative histograms from $n = 2$ experiments are shown. **g**, FACS analysis of GFP after transfection of constructs containing a signal peptide and GFP fused to the TMD, C terminus and either the long 3' UTR (dark blue line) or the short 3' UTR (light blue line) of *ITGA1* in HEK293 cells. Representative histograms from $n = 3$ experiments are shown as in Fig. 2d.

CD47

[illegible]

CD44

[illegible]

HuR-BS

tttaatagggtgagcttgagagttttctttctttctgtttttttttttttttttttttgactaatttcacatgctctaa

HuR-BS Δ

tttaataggggtgagcttgagag-----gactaatttcacatgctctaa

Extended Data Figure 3 | 3' UTR isoforms that encode proteins using UDPL contain uridine-rich elements. Shown are the 3' UTR sequences of

CD47, *CD44*, HuR-BS and HuR-BSΔ. Red, ApA signals. Blue, uridine-rich elements with the potential to be HuR-binding sites.

ITGA1

[illegible]

TNFRSF13C

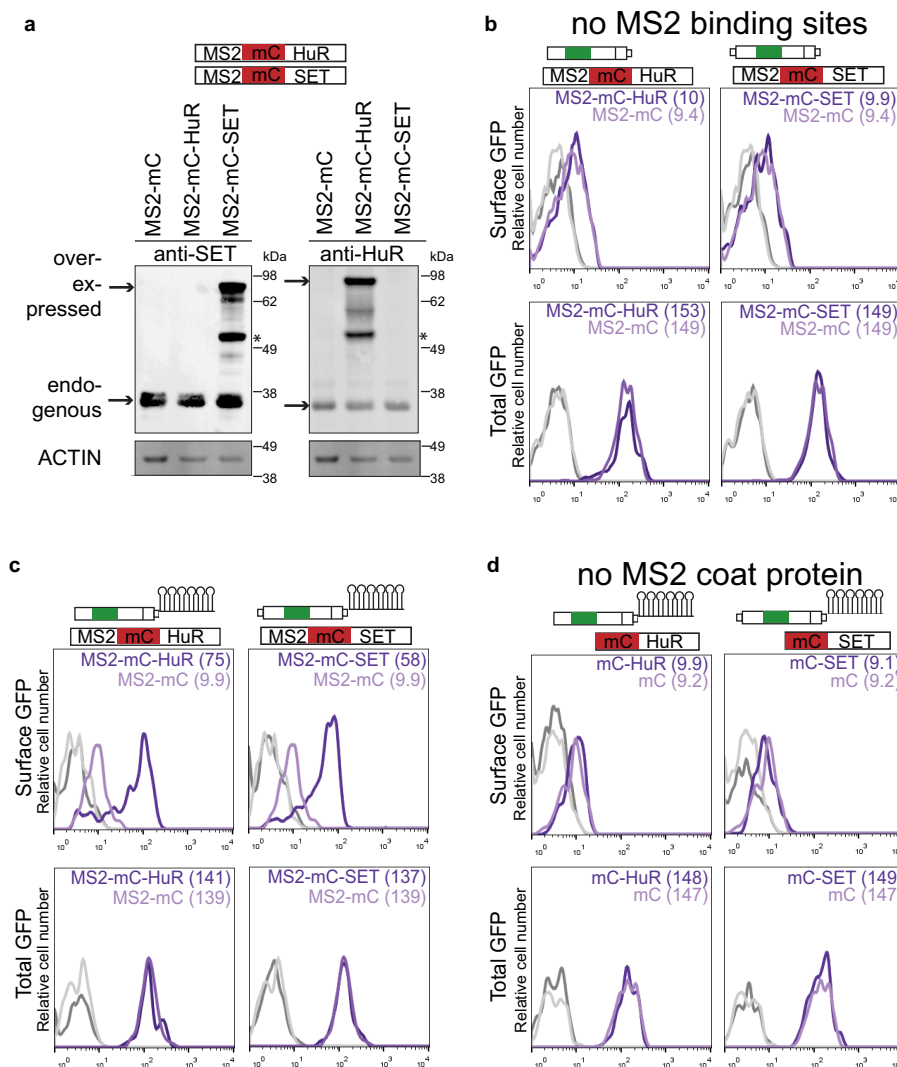
[illegible]

TSPAN13

[illegible]

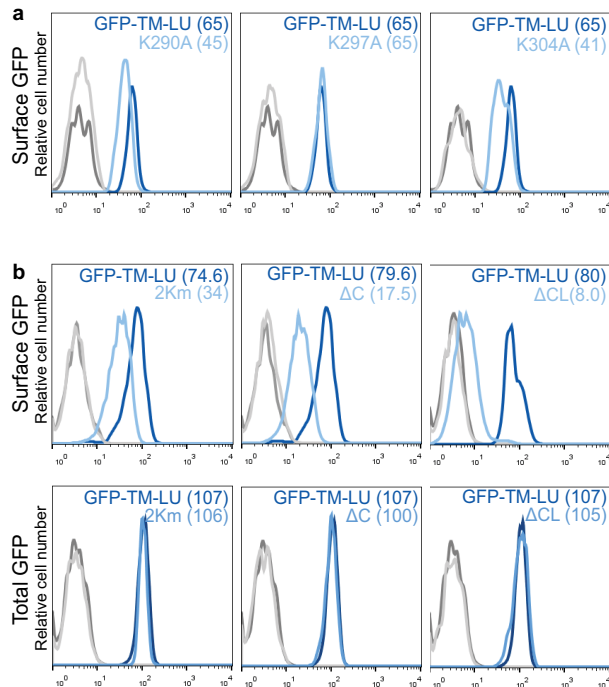
Extended Data Figure 4 | 3' UTR isoforms that encode proteins using UDPL contain uridine-rich elements. Shown are the 3' UTR sequences of

ITGA1, *TNFRSF13C* and *TSPAN13*. Red, ApA signals. Blue, uridine-rich elements with the potential to be HuR-binding sites.

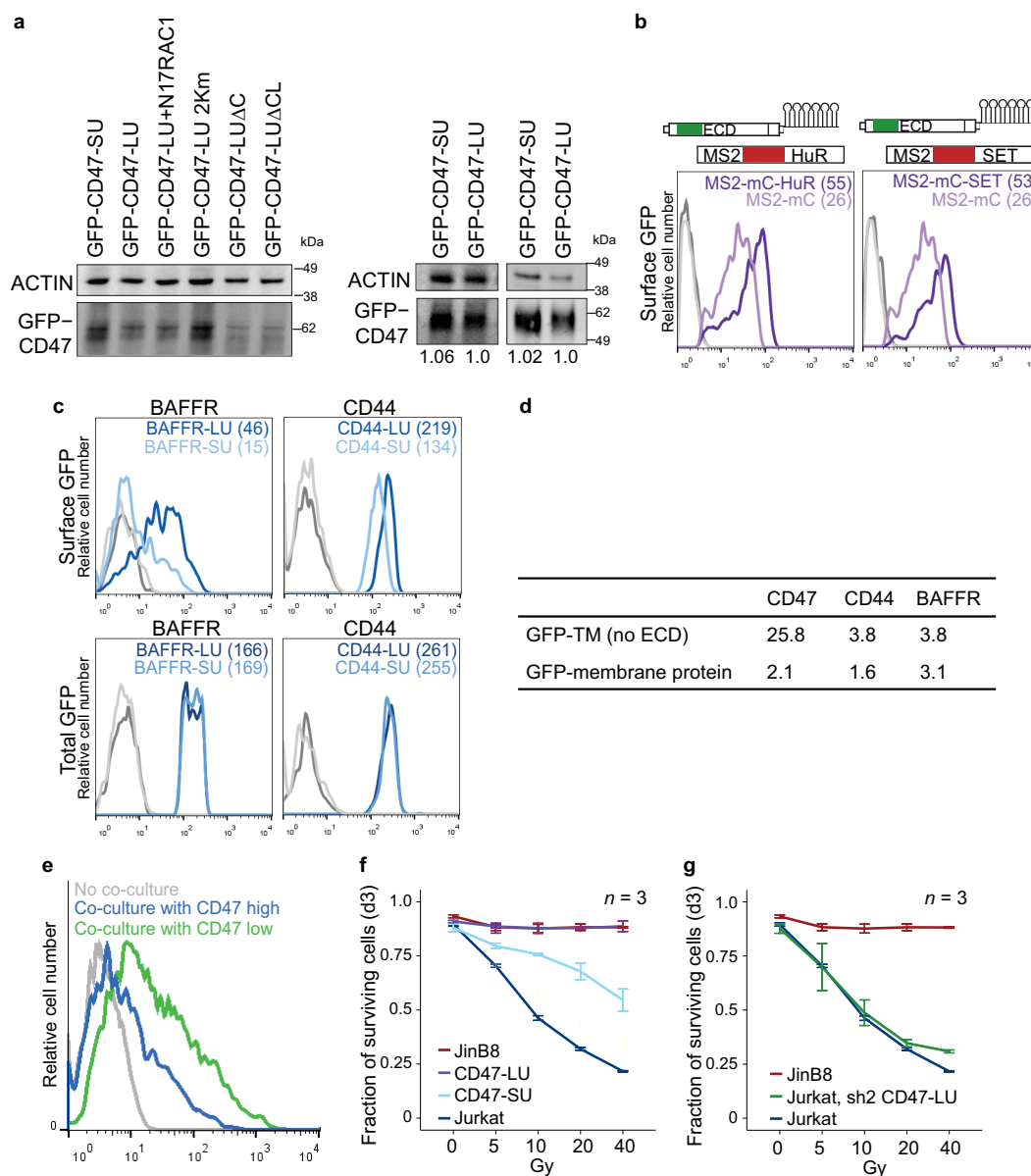


Extended Data Figure 5 | Local recruitment of SET to the site of translation is required for UDPL. **a**, Western blot of cells used in Fig. 3b shows the amount of overexpression achieved by transfection of MS2-mC-SET or MS2-mC-HuR (for constructs, see **b**). Left, anti-SET detects endogenous expression of SET as well as overexpressed SET. Right, anti-HuR detects endogenous HuR and overexpressed HuR. Actin was used as loading control. Anti-HuR and anti-SET were used on the same blot. Actin as loading control was performed once. The marker is shown in kDa. Asterisk indicates unspecific band. mC, mCherry. **b**, The top construct depicts GFP-TM-SU (Fig. 1e) and the bottom construct shows a fusion of MS2 coat protein (MS2), mC (red) and HuR or SET, respectively. Overexpression of HuR or SET compared with expression of MS2-mC alone does not change surface or total GFP expression, when co-transfected with GFP-TM-SU (without the addition of MS2-binding sites to the SU isoform) as shown by FACS analysis. Surface expression (top) and total expression (bottom) in HEK293 cells are shown. Values for MFI are shown in parentheses. Unstained cells are shown in grey. Representative histograms from $n = 2$ experiments are shown. **c**, FACS analysis of cells used in Fig. 3b. MS2-binding sites (MS2-BS, RNA stem loops) were added to GFP-TM-SU (and the proximal polyadenylation signal was mutated) to obtain GFP-TM-SU-MS2-BS. Transfection of MS2-mC-HuR (left, dark purple line) or MS2-mC-SET (right, dark purple line) increases surface GFP expression compared with

transfection of MS2-mC (light purple line), when GFP-TM-SU-MS2-BS is co-transfected. Thus, tethering of HuR or SET to the short 3' UTR of *GFP-TM* localizes GFP to the cell surface without changing total GFP expression. Histograms are shown as in **b**. Representative histograms from $n = 5$ experiments are shown. **d**, As in **c**, but tethering was impaired by omission of the MS2 coat protein. Histograms are shown as in **b**. Representative histograms from $n = 2$ experiments are shown. Summary of the tethering experiment: To tether SET or HuR to the 3' UTR (which brings it close to the site of translation through the scaffold function of the 3' UTR), we added MS2-binding sites to GFP-TM-SU **c**, MS2-binding sites are derived from the bacteriophage MS2 and form RNA stem loops. The capsid protein of MS2 (here, called MS2) specifically recognizes these MS2 stem loops. Constructs were generated containing MS2 fused to mC and then either HuR, SET or with no further coding sequence (Fig. 3b). Co-expression of these constructs with the construct containing the short UTR and MS2-binding sites results in recruitment of SET or HuR to the short 3' UTR of *GFP-TM*. The cells that express MS2 fused to only mC localize GFP to the endoplasmic reticulum, but constructs containing MS2 fusions to HuR or SET localize GFP primarily to the cell surface (Fig. 3b and Extended Data Fig. 5c). Omitting either MS2 or the MS2-binding sites from the experiment abrogates surface localization (Extended Data Fig. 5b, d).

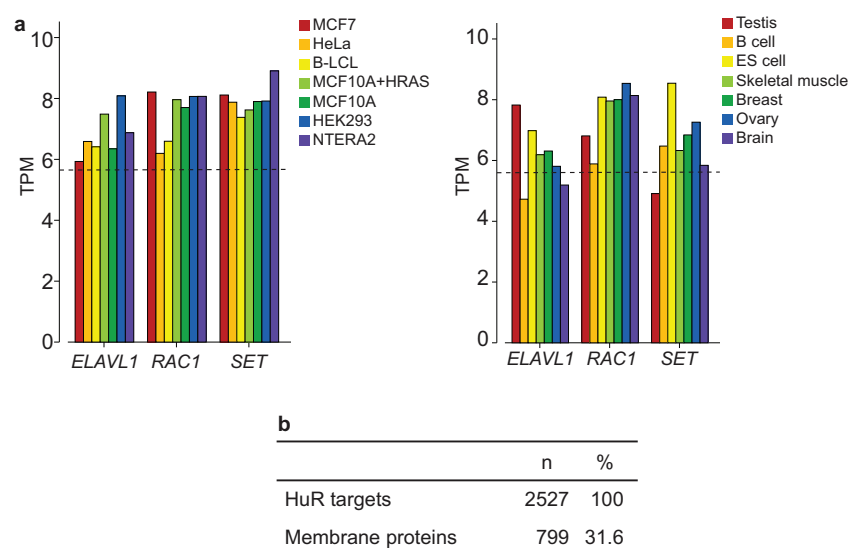


Extended Data Figure 6 | CD47 contains at least two SET-binding sites in its cytoplasmic domains. **a**, FACS analysis of surface GFP expression after transfection of GFP-TM-LU (dark blue line) and GFP-TM-LU constructs containing a single point mutation in the cytoplasmic C terminus (light blue line), K290A (left), K297A (middle), K304A (right) in HEK293 cells. Partial destruction of a single SET-binding site results in up to 37% reduction in GFP surface expression. Values for MFI are shown in parentheses. Unstained cells are shown in grey. Representative histograms from *n* = 5 experiments are shown. **b**, FACS analysis of GFP expression after transfection of GFP-TM-LU (dark blue line), GFP-TM-LU containing a mutation of the SET-binding site in the C terminus (K290A, K304A; 2Km; light blue line; left), containing a deletion of the C terminus (ΔC; light blue line; middle panel), or destruction of both SET-binding sites (ΔC combined with K163A, K166A, K175A; ΔCL; light blue line; right). Surface (top) and total (bottom) expression is shown in HEK293 cells. Values for MFI are shown in parentheses. Unstained cells are shown in grey. Representative histograms from several experiments are shown (2Km, *n* = 3; ΔC, *n* = 10; ΔCL, *n* = 4).



Extended Data Figure 7 | CD47 protein has different functions depending on whether it was generated by the SU or LU isoform. **a**, Left, western blot of HEK293 cells after transfection of the indicated constructs shows GFP-CD47 expression using an anti-GFP antibody. Actin was used as loading control. Right, as in left panel after transfection of CD47-SU and CD47-LU into HEK293 (left) or JinB8 cells (right). GFP-CD47 expression was quantified after normalization with respect to actin using Image J. Shown is the fold change in GFP-CD47 expression of CD47-SU after setting CD47-LU to 1. **b**, The experiment is similar to Fig. 3b and Extended Data Fig. 5c, but here the constructs containing the full open reading frame of CD47 were used. FACS analysis of GFP expression after transfection of CD47-SU-MS2-BS. Co-transfection of MS2-mC-HuR (left, dark purple line) or MS2-mC-SET (right, dark purple line) increases surface GFP expression compared to co-transfection of MS2-mC (light purple line). Surface expression is shown in non-permeabilized HEK293 cells. Values for MFI are shown in parentheses. Representative histograms from $n = 3$ experiments are shown. Unstained cells are shown in grey. **c**, Left, FACS analysis of GFP after transfection of constructs containing a signal peptide and GFP fused to the open reading frame of BAFFR and either the long 3' UTR (BAFFR-LU, dark blue line) or the short 3' UTR (BAFFR-SU, light blue line) in HEK293 cells. Surface (top) and total (bottom) GFP expression is shown. Values for MFI are shown in parentheses. Representative histograms from $n = 3$ experiments are shown. Unstained cells are shown in grey. Right, as in left panel but for CD44. **d**, Table showing the fold

increase in surface GFP expression mediated by the LU isoform compared with the SU isoform. Top row shows values of constructs without the ECD and bottom row shows values of constructs containing the full coding regions of the indicated proteins. The fold increase in surface GFP expression was calculated from MFI (LU)/MFI (SU). The contribution of the ECD domain for surface expression of BAFFR is 1.2-fold (3.8/3.1). **e**, FACS analysis of carboxyfluorescein succinimidyl ester (CFSE) uptake in macrophages. Macrophages were co-cultured without (grey) cells or with cells that were pre-treated with CFSE and expressed high or low amounts of surface CD47 (data not shown). The experiment shows that the macrophages phagocytose the cells depending on their CD47 surface expression levels. A representative histogram from $n = 2$ experiments is shown. **f**, The fraction of surviving cells (TO-PRO3 negative) as measured by FACS analysis at day 3 (d3) after increasing doses of γ -irradiation is shown for Jurkat, JinB8 ($CD47^{-/-}$) and the GFP⁺ fraction after nucleofection of JinB8 cells with either CD47-SU or CD47-LU. The values were obtained from the same experiment as shown in Fig. 4e, but here the values were calculated using all GFP-positive cells. Shown are the values for mean \pm s.d., $n = 3$ biological replicates. Gy, Gray. **g**, The fraction of surviving cells (TO-PRO3 negative) as measured by FACS analysis at day 3 (d3) after increasing doses of γ -irradiation is shown for Jurkat, JinB8 ($CD47^{-/-}$) and the GFP⁺ fraction after nucleofection of Jurkat cells with sh2 CD47-LU. Shown are the values for mean \pm s.d., $n = 3$ biological replicates. Gy, Gray.



Extended Data Figure 8 | HuR, SET and RAC1 are widely and highly expressed. **a**, The mRNAs of proteins necessary for UDPL are ubiquitously and highly expressed across cell lines (left) and tissues (right). Shown are values for transcripts per million (TPM). The median abundance levels of all expressed genes in the data sets are shown as dashed lines. *ELAVL1* encodes HuR. The data set from ref. 3 was analysed to obtain the TPM values. **b**, Here, ‘HuR

targets’ consist of the union of HuR targets identified previously^{7,9}. Membrane proteins consist of all the proteins that contain the tag “membrane” using gene ontology analysis. The fraction of membrane proteins found is consistent with the fraction of membrane proteins found in yeast¹⁰. Fisher’s exact test shows no enrichment or depletion of membrane proteins among the HuR targets.

CD47 150
 NILIVIFPI
 160 170 180 190 200
 FAILLFWGQF GIKTLKYRSG GMDEKTIALL VAGLVITVIV IVGAILFVPG
 210 220 230 240 250
 EYSLKNATGL GLIVTSTGIL ILLHYYVFST AIGLTSFVIA ILVIQVIAYI
 260 270 280 290 300
 LAVVGLSLCI AACIPMHGPL LISGLSILAL AQLLGLVYMK FVASNQKTIQ
 310 320
 PPRKAVEEPL NAFKESKGMM NDE

CD44
 660 670 680 690 700
 LIILASLLAL ALILAVCIAV NSRRRCGQKK KLVINSNGA VEDRKPSGLN
 710 720 730 740
 GEASKSQEMV HLVNKESSET PDQFMTADET RNLQNVDMMKI GV

ITGA1
 1150 1160 1170
 LWVILLSAF AGLLLLMLLI LALWKIGFFK RPLKKKMEK

BAFFR 80 90 100
 FG APALLGLALV LALVLVGLVS
 110 120 130 140 150
 WRRRQRRLRG ASSAEAPDGD KDAPEPLDKV IILSPGISDA TAPAWPPPGE
 160 170 180
 DPGTTPPGHS VPVPATELGS TELVTTKTAG PEQQ

TSPAN13
 10 20 30 40 50
 MVCGGFACSK NCLCALNLLY TLVSLLLIGI AAWGIGFGLI SSLRVVGVVI
 60 70 80 90 100
 AVGIFLFLIA LVGLIGAVKH HQVLLFFYMI ILLLVFIVQF SVSCACLALN
 110 120 130 140 150
 QEQQGQLLEV GWNNTASARN DIQRNLNCCG FRSVNPNDTC LASCVKSDHS
 160 170 180 190 200
 CSPCAPIIGE YAGEVLRFVG GIGLFFSFTE ILGVWLTTRY RNQKDPANP

SAFL

Extended Data Figure 9 | All tested UDPL candidates have potential SET-binding sites in their cytoplasmic domains. Shown are the amino acid sequences of the TMDs and cytoplasmic domains of the membrane proteins

studied. The TMDs are shown in green and the positively charged amino acids in the cytoplasmic domains, indicating potential SET-binding sites, are shown in red.

Synthesis and applications of RNAs with position-selective labelling and mosaic composition

Yu Liu¹, Erik Holmstrom², Jinwei Zhang³, Ping Yu⁴, Jinbu Wang¹, Marzena A. Dyba⁴, De Chen⁵, Jinfa Ying⁶, Stephen Lockett⁵, David J. Nesbitt², Adrian R. Ferré-D'Amaré³, Rui Sousa⁷, Jason R. Stagno¹ & Yun-Xing Wang¹

Knowledge of the structure and dynamics of RNA molecules is critical to understanding their many biological functions. Furthermore, synthetic RNAs have applications as therapeutics and molecular sensors. Both research and technological applications of RNA would be dramatically enhanced by methods that enable incorporation of modified or labelled nucleotides into specifically designated positions or regions of RNA. However, the synthesis of tens of milligrams of such RNAs using existing methods has been impossible. Here we develop a hybrid solid-liquid phase transcription method and automated robotic platform for the synthesis of RNAs with position-selective labelling. We demonstrate its use by successfully preparing various isotope- or fluorescently labelled versions of the 71-nucleotide aptamer domain of an adenine riboswitch¹ for nuclear magnetic resonance spectroscopy or single-molecule Förster resonance energy transfer, respectively. Those RNAs include molecules that were selectively isotope-labelled in specific loops, linkers, a helix, several discrete positions, or a single internal position, as well as RNA molecules that were fluorescently labelled in and near kissing loops. These selectively labelled RNAs have the same fold as those transcribed using conventional methods, but they greatly simplify the interpretation of NMR spectra. The single-position isotope- and fluorescently labelled RNA samples reveal multiple conformational states of the adenine riboswitch. Lastly, we describe a robotic platform and the operation that automates this technology. Our selective labelling method may be useful for studying RNA structure and dynamics and for making RNA sensors for a variety of applications including cell-biological studies, substance detection², and disease diagnostics^{3,4}.

The ability to synthesize RNAs with selectively labelled regions or positions is important for the following reasons. First, NMR is a powerful technique for probing RNA structure and dynamics, but is limited by severe signal overlap in the spectra of RNA. This could be overcome by region- or position-specific isotopic labelling of RNA so that spectral signals from critical residues could be observed without interference from the rest of the molecule. Second, Förster resonance energy transfer (FRET) experiments measure distances between fluorophores introduced site-specifically into macromolecules and have been used to study RNA structure and dynamics. Optimal placement of FRET pair fluorophores usually requires incorporation at RNA chain-internal positions and is difficult with current methods of synthesis, particularly with large RNAs. Third, position-specific incorporation of nucleotides derivatized with heavy or anomalously scattering atoms into RNA may aid crystallographic phase determination. Fourth, RNAs synthesized with modified nucleotides to enhance functionality or RNase resistance can exhibit enhanced *in vivo* efficacy⁵. Lastly, RNA aptamers, labelled with fluorophores at detection-sensitive positions, could have broad applications as sensors because of

their high affinity and specificity for a variety of substrates, including molecular cancer markers³.

Solid-phase chemical synthesis is limited to short RNAs (≤ 60 nucleotides (nt))^{6,7} and isotope-labelled versions of these chemicals are not commercially available. Solution-phase transcription with bacteriophage T7 or SP6 RNA polymerases (RNAPs) allows synthesis of longer RNAs⁸, but is limited to either uniformly labelled samples or those labelled by base type⁹. Incorporation of modified nucleotides by T7 RNAP is limited by poor processivity during initiation. However, once the RNA has been extended to at least 10 nt, elongation is highly processive^{10,11}. Elongation can be stalled by omitting the nucleoside 5'-triphosphate (NTP) required for transcription beyond a specified template position, and can be restarted by addition of the missing NTP(s)^{10,12,13}. This pause-restart method enables synthesis of RNAs with region- or position-specific modifications by using solid-phase-coupled DNA templates and limiting combinations of NTPs, so that elongation can be stopped at specific positions and restarted with a new NTP mix (Fig. 1). A similar approach has been attempted for *in vitro* peptide synthesis¹⁴. The pause-restart method has been used for mechanistic studies, although the synthesis of RNA using this method on a preparative scale has not been realized.

To achieve this, we first coupled 5'-biotinylated DNA templates to streptavidin-agarose beads (Fig. 1a)¹⁵ and then incubated them with T7 RNAP and an NTP mix lacking cytidine 5'-triphosphate (CTP)^{16,17}. This causes elongation to stall at +14, where the first CTP would otherwise be incorporated. After extensive washing with buffer, elongation was resumed by addition of a new NTP mix containing CTP. RNA synthesis can be repeatedly paused and resumed in this way to incorporate modified or labelled NTPs at desired locations (Fig. 1b). Once transcription extends past the position where specific labelling is desired, the reaction is terminated and re-initiation prevented by addition of an NTP mix without GTP, addition of heparin, which prevents reinitiation¹⁸, and a complete NTP mix, or quenching at 4 °C. The entire process can be repeated several times with the same bead-bound template to increase RNA yield. The probability of incorporating a wrong nucleotide occurs 1 in 20,000 (ref. 16). Development of the method—dubbed PLOR for position-selective labelling of RNA—is described in detail in Extended Data Figs 1 and 2. As the method requires multiple washing and NTP addition steps, we have developed a fully automated platform for performing PLOR (Fig. 1c; see Methods and Extended Data Fig. 2 for details of design and operations of the platform). We illustrate applications of this method using the 71-nt aptamer domain of an adenine riboswitch, riboA71 (Fig. 2a), which changes conformation upon binding adenine¹. The sequence of riboA71 was from *Vibrio vulnificus* with the first stem sequence modified to enhance the transcription yield^{1,19}. This adenine riboswitch controls gene expression through translational activation¹. The class of adenine riboswitches has been studied using various methods^{1,20–25}.

¹Protein-Nucleic Acid Interaction Section, Structural Biophysics Laboratory, Center for Cancer Research, National Cancer Institute, National Institutes of Health, Frederick, Maryland 21702, USA. ²JILA, National Institute of Standards and Technology and Department of Chemistry and Biochemistry, University of Colorado, Boulder, Colorado 80309, USA. ³Biochemistry and Biophysics Center, National Heart, Lung and Blood Institute, Bethesda, Maryland 20892, USA. ⁴Structural Biophysics Laboratory, Basic Science Program, Leidos Biomedical Research, Inc., Frederick National Laboratory for Cancer Research, Frederick, Maryland 21702, USA. ⁵Optical Microscopy and Analysis Laboratory, Leidos Biomedical Research, Inc., Frederick National Laboratory for Cancer Research, Frederick, Maryland 21702, USA. ⁶Laboratory of Chemical Physics, National Institute of Diabetes and Digestive and Kidney Diseases, National Institutes of Health, Bethesda, Maryland 20892, USA. ⁷Department of Biochemistry, University of Texas Health Science Center, San Antonio, Texas 78229, USA.

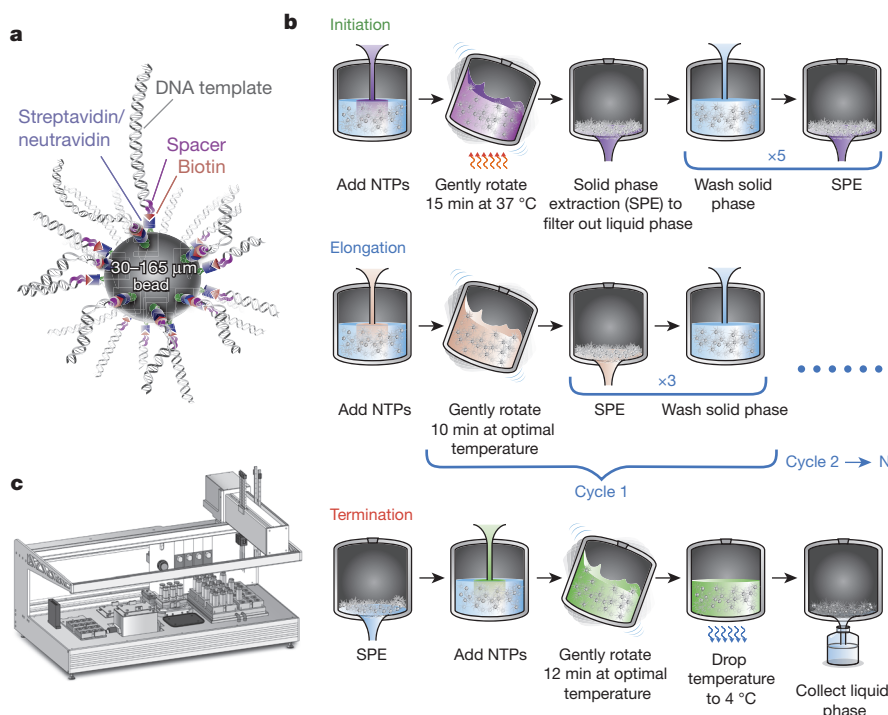


Figure 1 | The PLOR *in vitro* transcription method. **a**, Solid-phase attachment of DNA templates: 5'-biotin labelled duplex DNA templates were coupled to 30–165 μm diameter streptavidin-agarose or neutravidin-agarose beads. An 18-nt spacer was inserted between the T7 promoter and the biotin moiety to limit steric interferences with polymerase activity. **b**, Schematic

illustration of the three transcription reaction phases of the PLOR synthesis. The number of cycles, N , during the elongation phase depends on the RNA sequence and the desired labelling scheme. **c**, The robotic platform used to perform automated PLOR synthesis.

The crystal structures of the adenine-bound form of riboA71 (Protein Data Bank (PDB) accession numbers 1Y26 and 4TZX) show loops 1 and 2 in a kissing loop interaction^{1,26}. Selective labelling of these loops would allow study of their structure and dynamics in solution. Using PLOR, we synthesized RNAs in which only loop 1 (Lp1-CN) or loop 2 (Lp2-CN) was labelled with $^{13}\text{C}/^{15}\text{N}$ isotope so that only signals from those regions were observed in heteronuclear correlation spectra (Fig. 2b, c). These RNA molecules fold in the same way as those synthesized using conventional *in vitro* transcription, as illustrated by superimposing their spectra on that of the fully $^{13}\text{C}/^{15}\text{N}$ -RNA (Extended Data Figs 4 and 5). These samples could be used for detection of loop–loop interactions by recording various heteronuclear-edited/filtered nuclear Overhauser effect (NOE) spectra. We further demonstrated the utility of PLOR by $^{13}\text{C}/^{15}\text{N}$ -labelling both loops (Lp1+2-CN) (Fig. 2d), showing that the spectrum of Lp1+2-CN is consistent with the superimposition of the Lp1-CN and Lp2-CN spectra.

We also used PLOR to $^{13}\text{C}/^{15}\text{N}$ -label the linkers that connect adjacent duplexes: linker 2 (Lk2-CN) and stem 1 plus linker 1 (S1+Lk1-CN) (Fig. 2a). The use of selectively labelled RNAs greatly simplified the spectra (Fig. 2e, f), but overlaps were still present, as evidenced by the overlapping signals of A4, 5, 7, and 9 in the C8H8 region (Fig. 2f). Such overlaps are common for RNA duplexes because of similar chemical environments around the detected nuclei in the A-type duplex conformation. To overcome this, we used PLOR to generate a sample (S1+Lk1-H) in which stem 1 and linker 1 were protonated, and the rest of the molecule was deuterated (this RNA was not $^{13}\text{C}/^{15}\text{N}$ -labelled). By recording a two-dimensional NOE spectrum of S1+Lk1-H, and performing an NOE-walk in the H1'-H6/H8 region (Fig. 2g, top panel), the overlaps were partly resolved and proton chemical shifts assigned. Without partial deuteration, interpretation of this region of the spectrum would be impossible (Fig. 2g, bottom panel). With the increasing availability of high-field NMR spectrometers, the use of selectively protonated/deuterated RNA samples is

one of the most effective strategies for RNA structure determination⁹. While all labelling schemes described could, in theory, be performed using segmental labelling by ligations, such a method is impractical for placing isotope-labelled residues in multiple discrete positions. This can, however, be readily achieved using PLOR. Figure 2h shows the spectrum of another sample generated by PLOR, 4nt-CN, where only residues at positions A21, C38, U39, and G60 were $^{13}\text{C}/^{15}\text{N}$ -labelled.

RNAs may exist in multiple conformations, and while NMR is suitable for detecting such conformers^{22,27}, interpretation of data is often complicated by crowded signals. Coexistence of conformers can be unambiguously identified by monitoring a single residue at a critical structural location. It has been shown²⁸ that riboA71 thermodynamic data are best interpreted by a four-state model, and that its conformation is affected by ligand and Mg^{2+} . Inspection of the crystal structure of riboA71¹ reveals the U39 N3–H3 imino group forming a hydrogen bond with N3 of the adenine ligand (Fig. 3a). We used PLOR to incorporate a single $^1\text{H}/^{13}\text{C}/^{15}\text{N}$ -labelled uridine-5'-triphosphate (UTP) at this position (U39-CN). In the absence of adenine we detected multiple weak cross-peaks for both the H6–C6 and the N3–H3 imino groups in the ^{13}C and ^{15}N heteronuclear single-quantum correlation signals of U39, respectively, indicative of multiple conformations (Fig. 3b, c). At a 1:1 RNA:adenine ratio we detected four distinct cross-peaks (Fig. 3b, c), implying coexistence of at least four conformations of the adenine-binding pocket, in agreement with the four-state model²⁸. This type of information would be difficult to obtain unambiguously using a uniformly labelled sample, where extensive overlap and cross-peaks from other residues would obscure the weak cross-peaks associated with alternative conformations of the complex. Nevertheless, it is noteworthy to point out that a slightly different multi-state model has also been proposed on the basis of a study of an adenine riboswitch aptamer domain of a slightly different sequence using NMR and a uniformly labelled RNA sample²².

Single-molecule FRET (smFRET) is a powerful method for studying conformation change and has been used to study the adenine

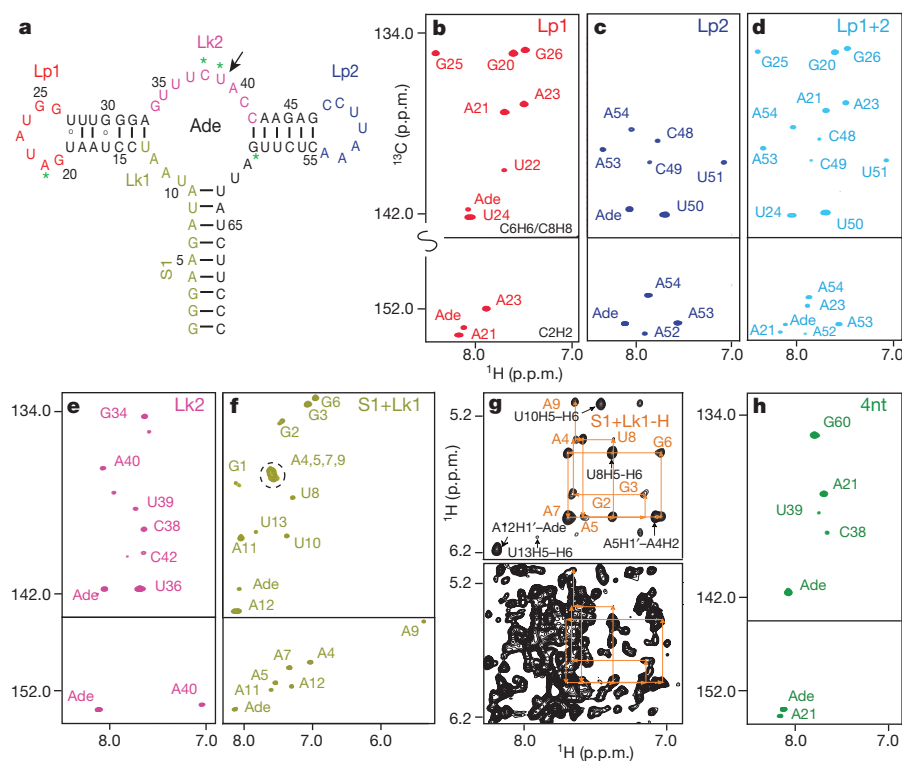


Figure 2 | PLOR isotopical labelling of a 71-nt RNA. **a**, The secondary structure of riboA71. The colour-coded sequence depicts the various regions of the RNA that were selectively labelled with $^{13}\text{C}/^{15}\text{N}$ or ^2H NTPs. PLOR was also used to label residues at four discrete positions (green asterisks), or a single residue (black arrow). **b–f**, Aromatic regions of $^1\text{H}/^{13}\text{C}$ -transverse relaxation optimized spectroscopy (TROSY) spectra of samples with $^{13}\text{C}/^{15}\text{N}$ labelling in

(b) loop1 (Lp1), (c) loop2 (Lp2), (d) Lp1 plus Lp2 (Lp1+2), (e) linker2 (Lk2), (f) stem 1 plus linker 1 (S1+Lk1), or at (h) four discrete positions (4nt). **g**, Comparison of ^1H NOE spectra. The bottom spectrum was recorded using a fully protonated sample; the top spectrum shows the same region recorded using a sample in which only the stem 1 and Lk1 were protonated.

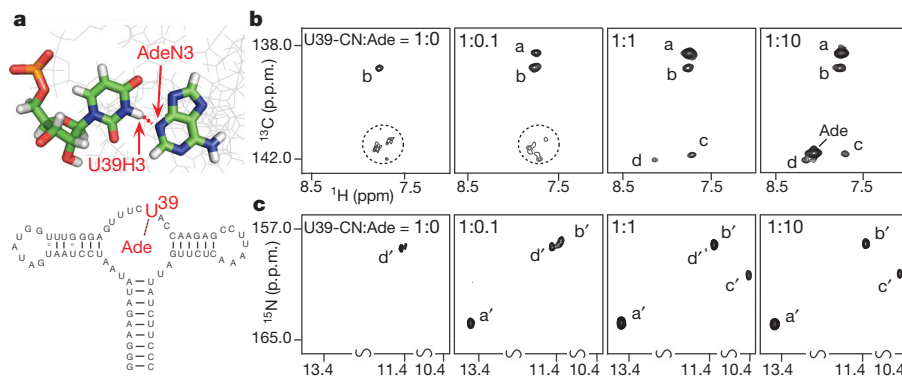


Figure 3 | Application of PLOR in dissecting the co-existence of multiple conformations using a singly labelled RNA sample. **a**, Illustration of the hydrogen bond formed between the adenine ligand and U39 in riboA71 (PDB accession number 1Y26). **b**, $^1\text{H}/^{13}\text{C}$ -TROSY and **c**, $^1\text{H}/^{15}\text{N}$ -TROSY spectra

recorded for $^{13}\text{C}/^{15}\text{N}$ -singly-labelled (U39) riboA71 titrated with adenine. Four cross-peaks in both H6–C6 (a–d) and imino (a'–d') regions are indicative of four distinct conformations at a 1:1 RNA:adenine ratio.

riboswitch^{23,24}. We illustrate that PLOR can be used to incorporate modified nucleotides tolerated by T7 RNAP. The crystal structure of adenine-bound riboA71 shows loops 1 and 2 in a kissing-loop interaction, but there is no direct information on loop–loop interactions in the absence of adenine. We used PLOR to generate U24Cy3–C55Cy5-B RNA, which contains a 3'-biotin and nucleotides tagged with fluorescent Cy3 at U24 (loop 1), and Cy5 at either U65 (stem 1) or C55 (loop 2; Cy5 was placed at the end, rather than in the middle, of loop 2 to avoid steric interference with respect to loop–loop interactions; Fig. 4a). smFRET measurements with this RNA in 0 μM adenine yield an E_{FRET} histogram (Fig. 4b) that can be approximated as the sum of

two broad Gaussian curves, indicating the presence of at least two populations of molecules with distinct loop–loop interactions. Approximately 20% of the population is in a high-FRET (~ 0.92) conformation consistent with the U24–C55 distance ($< 20 \text{ \AA}$) observed in the crystal structure. Upon addition of ligand, this conformation becomes increasingly populated (Fig. 4b, c). To further evaluate the utility of PLOR for incorporation of multiple modifications at specific sites, we imaged single U24Cy3–C55Cy5-B molecules (Fig. 4d), and not only confirmed the presence of the three RNA modifications, but also showed from the individual time traces (Fig. 4e) that adenine is not required to form the high-FRET conformation^{23,24}.

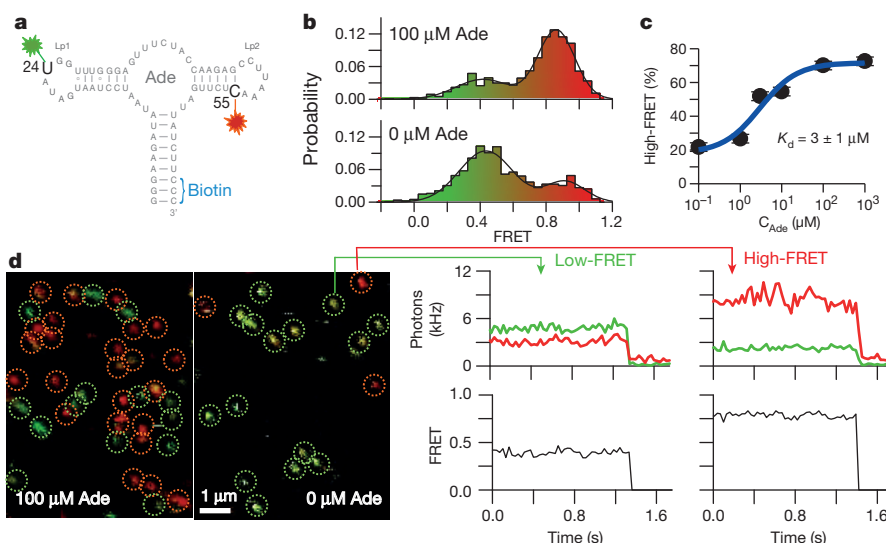


Figure 4 | Application of PLOR-generated constructs for smFRET. **a**, Secondary-structure diagram of riboA71 depicting the locations of the fluorescent labels. **b**, smFRET probability histogram for free diffusion experiments conducted in solutions containing 1 mM Mg^{2+} and either 0 or 100 μM adenine. About 1,000 fluorescent bursts were analysed for each

Adenine concentration and used to construct histograms. **c**, Ligand-binding curve for riboA71. **d**, False-colour image of surface-immobilized molecules reveals that RNA constructs contain all of the specified modifications and are able to form the high-FRET conformation. **e**, Single-step photobleaching confirms the existence of a single donor-acceptor FRET pair.

PLOR allows efficient synthesis of milligram quantities of RNA (Figs 2 and 3, Extended Data Fig. 6 and Extended Data Table 2). Both the His-tagged T7 RNAP and the DNA templates are reusable, and the same batch of bead-attached DNA templates was used for all samples generated here. The DNA templates can be produced routinely and economically in micromole quantities by PCR²⁹; all reagents are commercially available, and the technology is automated using a robotic platform. Extension of PLOR for other applications is easily envisioned. For example, variants of T7 RNAP have been developed that allow incorporation of nucleotides with modified ribose groups into RNA which can, among other useful characteristics, provide resistance to RNases for *in vivo* applications^{5,30}. PLOR may also be useful for X-ray crystallography by incorporating heavy-atom-derivatized nucleotides into the RNA at one or more desired positions for phase determination of X-ray diffraction data.

Online Content Methods, along with any additional Extended Data display items and Source Data, are available in the online version of the paper; references unique to these sections appear only in the online paper.

Received 4 November 2014; accepted 25 February 2015.

Published online 4 May 2015.

- Serganov, A. *et al.* Structural basis for discriminative regulation of gene expression by adenine- and guanine-sensing mRNAs. *Chem. Biol.* **11**, 1729–1741 (2004).
- Geiger, A., Burgstaller, P., von der Eltz, H., Roeder, A. & Famulok, M. RNA aptamers that bind L-arginine with sub-micromolar dissociation constants and high enantioselectivity. *Nucleic Acids Res.* **24**, 1029–1036 (1996).
- Mairal, T. *et al.* Aptamers: molecular tools for analytical applications. *Anal. Bioanal. Chem.* **390**, 989–1007 (2008).
- Shangguan, D. *et al.* Cell-specific aptamer probes for membrane protein elucidation in cancer cells. *J. Proteome Res.* **7**, 2133–2139 (2008).
- Wilson, C. & Keefe, A. D. Building oligonucleotide therapeutics using non-natural chemistries. *Curr. Opin. Chem. Biol.* **10**, 607–614 (2006).
- Usman, N., Ogilvie, K. K., Jiang, M. Y. & Cedergren, R. J. Automated chemical synthesis of long oligoribonucleotides using 2'-O-silylated ribonucleoside 3'-O-phosphoramidites on a controlled-pore glass support: synthesis of a 43-nucleotide sequence similar to the 3'-half molecule of an *Escherichia coli* formyl-methionine tRNA. *J. Am. Chem. Soc.* **109**, 7845–7854 (1987).
- Scaringe, S. A., Wincott, F. E. & Caruthers, M. H. Novel RNA synthesis method using 5'-O-silyl-2'-O-orthorster protection groups. *J. Am. Chem. Soc.* **120**, 11820–11821 (1998).
- Milligan, J. F., Groebe, D. R., Witherell, G. W. & Uhlenbeck, O. C. Oligoribonucleotide synthesis using T7 RNA polymerase and synthetic DNA templates. *Nucleic Acids Res.* **15**, 8783–8798 (1987).
- Lu, K., Miyazaki, Y. & Summers, M. F. Isotope labeling strategies for NMR studies of RNA. *J. Biomol. NMR* **46**, 113–125 (2010).
- Lyakhov, D. L. *et al.* Pausing and termination by bacteriophage T7 RNA polymerase. *J. Mol. Biol.* **280**, 201–213 (1998).
- Guo, Q., Nayak, D., Briebe, L. G. & Sousa, R. Major conformational changes during T7RNAP transcription initiation coincide with, and are required for, promoter release. *J. Mol. Biol.* **353**, 256–270 (2005).
- Sohn, Y., Shen, H. & Kang, C. Stepwise walking and cross-linking of RNA with elongating T7 RNA polymerase. *Methods Enzymol.* **371**, 170–179 (2003).
- Nudler, E., Gusarov, I. & Bar-Nahum, G. Methods of walking with the RNA polymerase. *Methods Enzymol.* **371**, 160–169 (2003).
- Pavlov, M. Y., Freistroffer, D. V. & Ehrenberg, M. Synthesis of region-labelled proteins for NMR studies by *in vitro* translation of column-coupled mRNAs. *Biochimie* **79**, 415–422 (1997).
- Marble, H. A. & Davis, R. H. RNA transcription from immobilized DNA templates. *Biotechnol. Prog.* **11**, 393–396 (1995).
- Huang, J., Briebe, L. G. & Sousa, R. Misincorporation by wild-type and mutant T7 RNA polymerases: identification of interactions that reduce misincorporation rates by stabilizing the catalytically incompetent open conformation. *Biochemistry* **39**, 11571–11580 (2000).
- Makarova, O. V., Makarov, E. M., Sousa, R. & Dreyfus, M. Transcribing of *Escherichia coli* genes with mutant T7 RNA polymerases: stability of lacZ mRNA inversely correlates with polymerase speed. *Proc. Natl Acad. Sci. USA* **92**, 12250–12254 (1995).
- Mentesana, P. E., Chin-Bow, S. T., Sousa, R. & McAllister, W. T. Characterization of halted T7 RNA polymerase elongation complexes reveals multiple factors that contribute to stability. *J. Mol. Biol.* **302**, 1049–1062 (2000).
- Leipply, D. & Draper, D. E. Dependence of RNA tertiary structural stability on Mg^{2+} concentration: interpretation of the Hill equation and coefficient. *Biochemistry* **49**, 1843–1853 (2010).
- Delfosse, V. *et al.* Riboswitch structure: an internal residue mimicking the purine ligand. *Nucleic Acids Res.* **38**, 2057–2068 (2010).
- Noeske, J. *et al.* An intermolecular base triple as the basis of ligand specificity and affinity in the guanine- and adenine-sensing riboswitch RNAs. *Proc. Natl Acad. Sci. USA* **102**, 1372–1377 (2005).
- Lee, M. K., Gal, M., Frydman, L. & Varani, G. Real-time multidimensional NMR follows RNA folding with second resolution. *Proc. Natl Acad. Sci. USA* **107**, 9192–9197 (2010).
- Lemay, J. F., Penedo, J. C., Tremblay, R., Lilley, D. M. & Lafontaine, D. A. Folding of the adenine riboswitch. *Chem. Biol.* **13**, 857–868 (2006).
- Dalgarno, P. A. *et al.* Single-molecule chemical denaturation of riboswitches. *Nucleic Acids Res.* **41**, 4253–4265 (2013).
- Rieder, R., Lang, K., Graber, D. & Micura, R. Ligand-induced folding of the adenosine deaminase A-riboswitch and implications on riboswitch translational control. *ChemBioChem* **8**, 896–902 (2007).
- Zhang, J. & Ferré-D'Amaré, A. R. Dramatic improvement of crystals of large RNAs by cation replacement and dehydration. *Structure* **22**, 1363–1371 (2014).
- Zhang, Q., Stelzer, A. C., Fisher, C. K. & Al-Hashimi, H. M. Visualizing spatially correlated dynamics that directs RNA conformational transitions. *Nature* **450**, 1263–1267 (2007).
- Leipply, D. & Draper, D. E. Effects of Mg^{2+} on the free energy landscape for folding a purine riboswitch RNA. *Biochemistry* **50**, 2790–2799 (2011).

29. Ferré-D'Amaré, A. R. & Doudna, J. A. Use of *cis*- and *trans*-ribozymes to remove 5' and 3' heterogeneities from milligrams of *in vitro* transcribed RNA. *Nucleic Acids Res.* **24**, 977–978 (1996).
30. Pinheiro, V. B. & Holliger, P. Towards XNA nanotechnology: new materials from synthetic genetic polymers. *Trends Biotechnol.* **32**, 321–328 (2014).

Supplementary Information is available in the online version of the paper.

Acknowledgements We thank D. E. Draper, A. Bax, A. Byrd, M. Summers, A. Rein, and J. Strathern for discussions. This work was supported in part by the Intramural Research Programs of the National Cancer Institute, the National Institute of Diabetes, Digestive and Kidney Diseases, the National Heart, Lung and Blood Institute; by the Intramural Antiviral Target Program (IATAP) of the Office of the Director, National Institutes of Health; by the 2013 Director's Challenge Innovation Award of the National Institutes of Health; by the fund from the National Cancer Institute under contract number HHSN261200800001E; by the National Science Foundation (CHE1266416, PHYS1125844); by the National Institutes of Health Molecular Biophysics Training Program (T32 GM-065103); and by the W. M. Keck Foundation, and the National Institute of Standards and Technology. The content of this publication does not

necessarily reflect the views or policies of the Department of Health and Human Services, nor does mention of trade names, commercial products, or organizations imply endorsement by the US Government.

Author Contributions Y.L. and P.Y. performed RNA synthesis and NMR experiments; E.H. and D.J.N. designed and performed smFRET experiments; J.W. contributed to chemical shift assignments; J.Z. and A.R.F. helped to design the DNA template using PCR, crystallized and determined the three-dimensional structure of the PLOR-generated riboA71; J.Y., M.A.D., D.C., and S.L. helped to characterize RNA; R.S. provided critical advice about T7-enzymatic synthesis and revised the manuscript; J.R.S. helped to characterize RNAs and revised the manuscript; Y.L., E.H., J.Z., J.R.S., and Y.-X.W. prepared figures; Y.-X.W. designed PLOR and the automated platform and wrote the manuscript. All authors discussed the results.

Author Information Structure coordinates have been deposited in Protein Data Bank under accession number 4XNR. Reprints and permissions information is available at www.nature.com/reprints. The authors declare no competing financial interests. Readers are welcome to comment on the online version of the paper. Correspondence and requests for materials should be addressed to Y.-X.W. (wangyunx@mail.nih.gov).

METHODS

No statistical methods were used to predetermine sample size.

DNA templates. Initial DNA templates used for riboA71 synthesis by the PLOR method were purchased (Avetra Bioscience). The 5'-biotinylated non-coding strand, 5'-TCTGATTTCAGTAGTCCATAATACGACTCACTATAGGGAAGATATAATCCTAATGATATGGTTGGGAGTTTCTACCAAGAGCCTTAACTCTTGATTATCTTCCC-3', was annealed to its complementary strand (the coding strand) in buffer A (40 mM Tris-HCl, 100 mM K₂SO₄, 6 mM MgSO₄, pH 8.0). An 18-nt spacer before the T7 RNAP promoter (underlined) was inserted to reduce crowding on the bead surface and potential steric hindrance to the T7 RNAP. Double-stranded DNA templates were also generated by touchdown PCR (TD-PCR) to abrogate nonspecific products³¹. The commercially synthesized DNA strands were used as templates in the TD-PCR. The forward primer contained biotin at its 5'-end and the reverse primer contained two 2'-O-methylguanosine (mG) at its 5' end to reduce non-templated nucleotide addition to transcripts³². The primer sequences were: 5'-Bio/TCTGATTTCAGTAGTCCATAATACGACTCACTATAGGGAAGATATAATCCTAATGATATGGTTGGGAGTTTCTACCAAGAGCCTTAACTCTTGATTATCTTCCC-3' (Integrated DNA Technologies), and 5'-mGmGGAAGATAATCAAGAGT TTAAGGCTC (Integrated DNA Technologies). The reagents used in the TD-PCR reactions were as follows: 0.1 µM template, 10 µM primers, 200 µM dNTPs, Taq DNA polymerase, and PCR buffer (50 mM KCl, 10 mM Tris-HCl, 2 mM MgCl₂, pH 8.4). The cycling program of the TD-PCR involved two separate phases: the touchdown phase and the PCR phase. During the touchdown phase, the annealing temperature was reduced from 75 °C to 45 °C over 20 successive cycles. Each touchdown cycle, therefore, began with melting at 95 °C for 30 s (5 min for first cycle), followed by annealing (temperature varies) for 45 s and elongation at 72 °C for 1 min. The PCR phase was a generic amplification stage of 25 cycles of 95 °C for 30 s, annealing at 50 °C for 30 s, and elongation at 72 °C for 1 min.

The DNA, 5'-TCTGATTTCAGTAGTCCATAATACGACTCACTATAGGGAAGCGGCGCAGCGCTGTCTAGCTGCGGGCATTAGACTGGAAACCTAGTCTCTTTGGGTAACCACTAAATCCGAAAGGGTGGGCTGTGGTGACCTCCG-3', and its complementary strands were used as templates in TD-PCR for turnip crinkle virus (TCV) samples. The sequences of the primers used in the TD-PCR for TCV samples were, 5'-Bio/TCTGATTTCAGTAGTCCATAATACGACTCACTA TA, and 5'-CmGGAGGGTCCACACAGC. The templates and primers were obtained from Integrated DNA Technologies.

Solid-phase attachment of DNA templates. For this study, commercial agarose beads (30–165 µm diameter), coated with either streptavidin or neutravidin (Thermo Fisher Scientific), were used as the solid-phase support. In our hands, the neutravidin-coated agarose beads appeared to have a better retention of the biotinylated DNA templates and, therefore, were used as the solid-phase support in most cases. The double-stranded DNA template (0.8 µmol) was incubated with neutravidin-coated agarose beads (8 ml) in buffer A for ~3 days at 4 °C. The bead-attached templates were washed by repeated rinsing and passing through a Pierce Centrifuge Column with a ~30 µm average pore size (Thermo) to remove non-bound DNA templates, and were stored at 4 °C. Approximately 80% of the DNA template was attached to the beads on the basis of ultraviolet-absorbance detection. The bead-attached templates were stable for an extended period, and were reused for multiple rounds of synthesis for this study.

Detailed experimental procedure for PLOR. A total of eight RiboA71 samples (Fig. 2a) with various isotopic labelling schemes were prepared using PLOR. The detailed recipes for each of the eight syntheses are provided in Extended Data Table 1, including the amounts of NTPs, which are given in molar ratios relative to the total amount of the DNA templates used in each cycle of synthesis. The NTP ratios were chosen on the basis of the number of each specific type of nucleotide in an individual segment synthesized in a particular cycle. Note that much higher ratios of NTPs were used in the initiation phase (Extended Data Table 1). This is because of the intrinsic nature of the T7 RNAP-catalysed reaction, where a large amount of abortive products are generated and relatively large amounts of NTPs are required to complete the slow initiation phase of the reaction³³. The 96-fold ratios of ATP and GTP, and 9.6-fold ratio of UTP for initiation, were optimized specifically for the adenine riboswitch RNA samples on the basis of its residue type composition. Here we use the synthesis of the ¹³C/¹⁵N-labelled Lp1-CN as an example to illustrate the PLOR procedure. T7 RNAP was mixed with DNA-attached agarose beads at 37 °C for 10 min, followed by addition of ATP, GTP, and UTP and incubation at 37 °C for 15 min with gentle rotation of the reaction vessels. The gentle mixing, as opposed to vortexing, was necessary to prevent formation of foam/bubbles by T7 in the reaction vessel. The total reaction volume was 40 ml and the concentrations of T7, DNA, ATP, GTP, and UTP were 20 µM, 20 µM, 1.92 mM, 1.92 mM, and 192 µM, respectively, in buffer B (40 mM Tris-HCl, 100 mM K₂SO₄, 6 mM MgSO₄, 10 mM DTT, pH 8.0). The reaction mixture was filtered and rinsed five times using buffer C (40 mM Tris-HCl, 6 mM MgSO₄,

pH 8.0) (Extended Data Fig. 1). In the first elongation cycle (Extended Data Fig. 1, blue), 40 µM ATP, CTP, and UTP, dissolved in buffer D (40 mM Tris-HCl, 6 mM MgSO₄, 10 mM DTT, pH 8.0), were added and the reaction was allowed to proceed for 10 min at 25 °C, followed by filtration and washing three times with buffer C. The exact concentrations of NTPs used for the remaining elongation cycles were as follows: 20 µM ¹³C/¹⁵N-ATP and 20 µM ¹³C/¹⁵N-GTP (cycle 2); 20 µM ¹³C/¹⁵N-ATP and 40 µM ¹³C/¹⁵N-UTP (cycle 3); 40 µM ¹³C/¹⁵N-GTP (cycle 4). In the termination step (Extended Data Fig. 1, red), 200 µM ATP, 220 µM CTP, 140 µM GTP, and 340 µM UTP were added to the reactor and incubated at 25 °C for ~12 min. The filtered RNA product was then collected and stored at 4 °C or -20 °C for long-term storage, and the DNA-attached agarose beads were rinsed at least five times and stored at 4 °C for future use. The final RNA products were gel-purified using 15% polyacrylamide gel electrophoresis (PAGE)-urea gels before being used for NMR data collection.

The procedure of preparing the ¹⁵N-H1-TCV³⁴ (¹⁵N-labelled at 5'-end, shown in red in Extended Data Fig. 6a) is the same as described earlier. The total reaction volume used in the ¹⁵N-H1-TCV was 30 ml, and the concentrations of T7, DNA, ¹⁵N-ATP, ¹⁵N-GTP, and ¹⁵N-CTP in the initiation were 20 µM, 20 µM, 0.64 mM, 4.8 mM, and 0.32 mM, respectively. In the first elongation cycle, 20 µM ¹⁵N-CTP, 20 µM ¹⁵N-GTP and 60 µM ¹⁵N-UTP were added in the reaction. In the termination step, 0.4 mM ATP, 0.380 mM CTP, 0.5 mM GTP, and 0.360 mM UTP were added.

NMR experiments. All NMR samples in this study were in a buffer containing 10 mM KH₂PO₄, 30 mM KCl, 2 mM MgCl₂, pH 6.8. Adenine (5 mM) was added to all riboA71 NMR samples except U39-CN. Two-dimensional ¹H/¹⁵N NOESY, ¹H/¹⁵N TROSY³⁵, and ¹H/¹³C TROSY spectra were collected at 25 °C for riboA71 and 15 °C for the 104-nt TCV RNA on Bruker spectrometers operating at a proton frequency of 850 MHz or 700 MHz and equipped with a triple-resonance cryo-probe. All spectra were processed and analysed with nmrDraw³⁶ and NMR ViewJ (One Moon Scientific). The concentrations for Lp1-CN, Lp2-CN, Lp1+2-CN, Lk2-CN, S1+Lk1-CN, 4-nt-CN, S1+Lk1-H, U39-CN, 71-nt-CN, ¹⁵N-H1-TCV, and ¹⁵N-104-nt-TCV (fully ¹⁵N-labelled TCV) were 0.5, 0.3, 0.2, 0.35, 0.4, 0.3, 0.4, 0.35, 0.5, 0.4, and 0.5 mM, respectively and the sample volumes were ~250 µl in Shigemi tubes.

Fluorescent samples generated by PLOR. Five fluorescent samples were produced by the PLOR method: U24Cy3-C55Cy5, U24Cy3-C55Cy5-B, U24Cy3-U65Cy5, U24Cy3-U65Cy5-B and U24A555-U65488-B (Extended Data Table 3). As an example, a detailed description of the U24Cy3-C55Cy5 synthesis is provided. DNA and T7 concentrations used in the preparation were 5 µM in 3 ml transcription buffer (buffer B). Then, NTPs were added as follows: 0.48 mM ATP, 0.48 mM GTP and 48 µM UTP (initiation); 10 µM ATP, 10 µM CTP and 10 µM UTP (elongation, cycle 1); 5 µM ATP and 5 µM GTP (cycle 2); 5 µM UTP (cycle 3); 5 µM ATP and 5 µM 5-aminoallyl UTP (TriLink) (cycle 4); 5 µM ATP, 30 µM GTP, and 30 µM UTP (cycle 5); 15 µM ATP, 15 µM CTP, and 5 µM UTP (cycle 6); 5 µM ATP and 10 µM GTP (cycle 7); 10 µM CTP and 10 µM UTP (cycle 8); 15 µM ATP and 5 µM Cy5-CTP (cycle 9, at 37 °C); 5 µM CTP, 5 µM GTP, and 15 µM UTP (cycle 10); 10 µM ATP, 20 µM CTP, and 25 µM UTP (termination). Cy5-CTP was from GE Healthcare. The RNA transcript was lyophilized and then dissolved in double-distilled H₂O. U24, which contained an aminoallyl group, was functionalized with Cy3 by adding a Cy3-NHS ester and 0.5 volumes of 0.3 M sodium bicarbonate buffer (pH 8.3), followed by incubation for 1 h at 37 °C, 12 h at 25 °C, and then 1 h at 37 °C. All incubations were performed in the dark. Homogeneity of dually labelled RiboA71 samples was assessed via 15% denaturing PAGE and analytical high-performance liquid chromatography before being used in free-diffusion smFRET experiments.

smFRET experimental set-up. A home-built microscope system was used to acquire all of the single-molecule fluorescence data, as recently described elsewhere³⁷. Briefly, alternating excitation³⁸ of the donor (Cy3) and acceptor (Cy5) fluorophores is achieved using pulsed-laser sources at 532 nm (20 MHz, 10 ps) and 635 nm (20 MHz, 90 ps), respectively. The interleaved pulses are directed into the back aperture of a 1.2 numerical aperture water objective, which is used in a standard epifluorescence configuration, both to focus the excitation source down to a ~250 nm diffraction limited spot and to collect the emitted fluorescence photons. The collected fluorescence is then directed out of the side-port of the microscope and focused through a 50 µm confocal pinhole, which spatially defines the detection volume. The photons are then separated by both colour (donor, acceptor) and polarization (horizontal, vertical) before being directed onto one of four single-photon avalanche photodiodes, where the arrival time of each detected photon is recorded.

Free-diffusion smFRET. After being deemed suitable, the fluorescently labelled RNA samples were diluted to a final concentration of ~100 pM in single-molecule imaging buffer (10 mM HEPES, 50 mM NaCl, 1 mM Mg²⁺, 0–1 mM Ade, 2 mM Trolox, 5 mM 3,4-protocatechuic acid (PCA), 100 nM protocatechuate

dioxygenase (PCD), pH 7.5). The PCA/PCD oxygen³⁹ and the blinking suppressant, TROLOX⁴⁰, were used together to enhance the photostability of cyanine-derived fluorophores (that is, Cy3 and Cy5).

Surface-immobilized smFRET. The selectively incorporated biotin moiety permits surface immobilization of individual fluorescently labelled nucleic acids, as recently described elsewhere³⁷. Briefly, the piezoelectric scanning stage of the experimental apparatus provides the ability to raster-scan an area of the sample (for example $15\ \mu\text{m} \times 15\ \mu\text{m}$), resulting in a false-colour image of the surface. The stage can then be used to position an individual fluorescence feature within the focus of the microscope objective, allowing continuous excitation and collection of fluorescence from a single molecule. FRET values are derived from the ratio of acceptor (A) fluorescence to the sum of both donor (D) and acceptor (A) fluorescence intensities (that is, $A/[D + A]$). These fluorescence intensities are background corrected and adjusted for various experimental artefacts such as acceptor direct excitation, donor cross-talk on the acceptor channel, and differential quantum yields of the two fluorophores⁴¹.

Crystallographic analysis. Unmodified RiboA71 RNA synthesized using PLOR (Extended Data Table 1) was crystallized as previously described^{1,26}. Briefly, for crystallization by vapour diffusion, a solution containing 700 μM RNA, 50 mM KOAc pH 6.8, 100 mM MgCl_2 , 1 mM spermine, and 5 mM adenine was mixed 1:1 (v/v) with a reservoir solution comprising 50 mM Tris-HCl pH 8.5, 100 mM KCl, 10 mM MgCl_2 , and 30% polyethylene glycol (PEG) 400. Crystals grew to maximal dimensions of $250\ \mu\text{m} \times 50\ \mu\text{m} \times 50\ \mu\text{m}$ in 1–2 weeks at 4°C and were directly flash-frozen by plunging into liquid nitrogen. The structure of the PLOR-generated riboswitch-adenine complex was solved by molecular replacement with PHASER using a published structure²⁶ (PDB accession number 4TZX) as a search model. Initial solutions were subjected to manual rebuilding⁴² interspersed with iterative rounds of rigid-body, simulated-annealing, and individual isotropic B-factor refinement using PHENIX⁴³. Refinement statistics are summarized in Extended Data Table 4. The coordinates and structure factors have been deposited in Protein Data Bank under accession number 4XNR.

Optimizing the transcription reaction. Fundamental to our method of the preparative T7-catalysed reactions is a novel stoichiometry concentration of reactants. This novel scheme is counter-intuitive to the conventional *in vitro* transcription, where multiple millimolar concentrations of NTPs are used. Various reaction conditions, including buffer conditions, NTP concentrations, reaction time, incubation temperatures, and T7 RNAP concentrations were tested in Lp2-CN synthesis to optimize the yields. Among all factors, the effects of NTP and Mg^{2+} concentrations on PLOR yields are distinctly different from those of standard solution-based *in vitro* transcription. Since the initiation phase is the least efficient of the three phases in T7 RNAP *in vitro* transcription, various conditions were tested in an attempt to improve the initiation efficiencies. We found that gentle rotation of the mixture of T7 RNAP and DNA-attached beads at 37°C for 10 min, followed by addition of NTPs dissolved in the transcription buffer and further incubation at 37°C for 15 min, resulted in a 20% increase of the final product compared with incubating all reagents simultaneously at 37°C for 15 min. Incubating the reaction at 37°C gave higher yields than incubating at 25°C , 35°C , or 40°C , as expected. Incubating the initiation reaction mixture at 37°C for 10–20 min was sufficient, but incubation for >30 min resulted in decreased yields by as much as 50%. Types of anion had little effect on the reaction yield. KCl/MgCl_2 and $\text{K}_2\text{SO}_4/\text{MgSO}_4$ were tested and the product yields were very similar (Extended Data Fig. 3b, panel II). Mg^{2+} concentration, however, affected yields dramatically and was optimal at 6 mM (Extended Data Fig. 3b, panel III). This differs from the standard transcription reaction where 20–26 mM Mg^{2+} is optimal. A series of K_2SO_4 concentrations (0, 20, 40, 60, 80, and 100 mM) was tested. Yields were similar when K_2SO_4 concentrations were between 20 and 100 mM. Transcription initiated with 100 mM K_2SO_4 had a higher yield than having no K_2SO_4 present during initiation (Extended Data Fig. 3b, panel IV). A series of different values of pH of the initiation buffer (4.0, 7.0, 7.5, 8.0, and 9.0) was also tested. As expected, the optimal pH for the initiation was between 7.5 and 8.0. We tested the impact of NTP concentrations on yields. The initiation phase requires a substantially higher NTP concentration (~ 2 mM) than the elongation phase, but this concentration is still relatively low compared with the standard transcription reactions where NTP concentrations are typically 4–6 mM. The optimal NTP concentrations for elongation using PLOR are in the micromolar range (Extended Data Table 1). This is advantageous as it means that the expensive labelled NTPs, which are used only during elongation, can be used at low concentrations to achieve a high percentage of their incorporation into the RNA. Higher NTP concentrations during elongation resulted in substantially lower yields (Extended Data Fig. 3b, panel V). The ratio of T7RNAP:DNA was tested for its effect on yield. The yield at 1:1 was similar to that at 2:1 and higher than that at 0.5:1. Higher ratios resulted in lower yields. The effect of reaction time in the termination step on yield is shown in Extended Data Fig. 3b, panel VIII.

Quantification of experimental yields. The experimental yields were measured by quantifying gel band intensities. Transcription reaction (0.2–1 μl) was loaded onto a 12% mini-PAGE gel. For quantification, 0.5, 1.0, and 1.5 pmol of pure RiboA71 samples were run as a standard. The gels were stained by Sybr Gold (Life Technologies) for 10 s, and then visualized using a Gel DocTM EZ imager (Bio-Rad). The stained gel band intensities were quantified using Image Lab 4.1 (Bio-Rad), and were used to determine the experimental yield of each synthesis product, given as a percentage relative to the amount of template used in the synthesis (Extended Data Table 2).

Estimating synthesis efficiencies. The transcription yields depend on both the reaction cycle efficiencies and the total number of cycles in the synthesis. For simplification, the average termination efficiency was taken as equal to the average elongation efficiency. The apparent efficiencies of initiation and elongation, therefore, were estimated using the equation

$$\text{Yield} = I \times E^n \quad (1)$$

where I and E are the percentage efficiencies of initiation and elongation, respectively, and n is the total number of cycles used for synthesis. As there are two unknown variables, I and E , a second equation was needed. Because the same procedures, equipment, and reagents were used to make each NMR sample, one would expect similar values for I and E among different samples. Therefore, we used a crude method to calculate the efficiencies by setting I and E of one sample equal to the I and E of another 'reference' sample, and then solving for each variable. The same reference sample, S1+Lk1-CN, was used in each calculation. For example, the Lp1-CN sample was generated using a five-cycle synthesis with an experimental yield of 30.3%. Similarly, S1+Lk1-CN was generated using a one-cycle synthesis with a yield of 40.3%. Using equation (1), then, I and E for Lp1-CN were estimated as 43.3% and 93.1%, respectively. Using this method for all RiboA71 samples, the average values for I and E were 46.0% and 87.8%, respectively (Extended Data Table 2). The 'theoretical' yields for each sample were calculated using their individual efficiencies.

Discussion of PLOR efficiency. The efficiency of the PLOR method depends heavily on a number of factors, such as the number of cycles involved in achieving a desired labelling scheme (equation (1)), the inherent initiation and elongation efficiencies for a given RNA sequence, the purity of NTPs, the efficiency of the washing/filtration cycles, the T7 RNAP quality, and the efficiency of DNA-bead attachment. For any given commercially bought NTP, the presence of other NTPs can be as high as 5%. Moreover, it is expected that some degree of cross-contamination among nucleotides occurs during synthesis as a result of carryover from one reaction cycle to the next owing to inefficient washing/filtration during solid-phase extraction. Such impurity and cross-contamination in the reaction mixture in any given cycle may result in non-synchronized transcription, where initiation or elongation may pause at non-designated positions, depending on the availability of various NTPs. In addition, sufficient quantities of all four NTPs due to contamination may lead to full-length transcripts prematurely (that is, before the designed termination phase) as well as re-initiation of transcription by recycled T7, again resulting in non-synchronized transcription. During the initiation and elongation phases, abortive and full-length transcripts generated as a result of non-synchronized transcription are removed during the washing/filtration cycles and thus do not affect the purity of the final full-length products collected at the end of the termination phase. However, highly purified NTPs and a more robust solid-phase extraction may alleviate non-synchronized transcription, thereby increasing the yield of the correctly labelled, full-length product. Leaking of DNA templates from the agarose beads may also result in lower transcription yields. The leaking is possibly due to a high off-rate of biotin binding to streptavidin beads and may be mitigated by using glass beads as the solid phase⁴⁴ or using mutant streptavidin-agarose beads with a much reduced off-rate⁴⁵.

Since it is an enzyme-catalysed reaction, there are several inherent limitations. In principle, for a given RNA sequence, the yield of the PLOR method is directly correlated to the yield of the regular *in vitro* transcription synthesis. The specific requirement for PLOR is that only three types of residue are allowed in the first 13 residues. This would probably limit the ability to label residues in the first 13 nt in the 5' end of a sequence.

Automated RNA synthesis platform. Since the PLOR process consists of repetitive steps and cycles, we designed and constructed an automated platform to perform the synthesis. This prototype RNA synthesizer (Extended Data Fig. 2) utilizes the modular liquid delivery system made by Zinsser Analytic, and is the first instrument to perform automated RNA synthesis using PLOR. The platform consists of several modules, including a rotating reaction chamber, a solid-phase extraction cube (SPEC), a pair of robotic arms, reaction vessels, four long-arm liquid transfer tips and four syringes, a six-way valve for liquid handling, and seven stations. The reaction chamber is located at the incubation station (I-station), where the reaction vessels containing reagents incubate at either 37°C (initiation)

or at 25 °C (elongation or termination). There are two reagent-stations (R-stations): one attached to a cooling unit to keep reagents at 4 °C, and another at room temperature. The reagent-addition/filter station (RF-station) has two main purposes: (1) it is where the reaction reagents are transferred to the reaction vessels, and (2) it is where solid-phase extraction is performed through the addition of buffers and nitrogen gas, and is connected to a vacuum pump for the removal of liquid waste. The wash station (W-station) washes the tips/syringes between liquid transfers. The reaction chamber cover and the SPEC are docked at the cover station (C-station) and SPEC-station, respectively, when not in use. The operation for performing the PLOR RNA synthesis is controlled by a software program with customizable input files. Certain types of information require user input to the computer based on the individual protocol, such as volumes of the various NTPs, for each cycle, to be delivered into the reaction vessels, and the number of reaction cycles. Other variables that may be changed less frequently are set as default, including the number of wash cycles, the buffer volumes used in filtration, incubation times and temperatures, the rotation rate of the reaction chamber, the movement of robotic arms, SPEC pressure and time, etc. The protocols are divided into blocks according to their purpose, and the instrument combines the blocks flexibly.

Here we describe the blocks for the automated synthesis of the LpI-CN sample.

Pre-incubation (initiation). After manual addition of the template-attached beads and T7 RNAP to the reaction vessels, which are housed in the reaction chamber at the I-station, the robotic arms seal the reaction chamber with the cover, and the chamber temperature is ramped to 37 °C with gentle rotation. After 10 min, the robotic arms remove the reactor cover and transfer it to the C-station; they then transfer the reaction vessels to the RF-station.

Reagent addition (initiation). The liquid-transfer system transfers the user-specified amounts of ATP, GTP, UTP, and transcription buffer individually from their respective stock-solution containers from the R-station (a cooling unit is used to keep all stock solutions and the transcription buffer at 4 °C) to the reaction vessels in the RF-station. The syringe tips are then rinsed three times with wash buffer at the W-station.

Incubation (initiation). The robotic arms return and seal the cover on the reaction chamber, and the reaction chamber begins gentle rotation at 37 °C for 15 min. Once the rotation stops, the robotic arms move the cover to the C-station and then the reaction vessels to the RF-station. The temperature of the reactor chamber drops back to 25 °C.

Solid-phase extraction (SPE) (initiation). The robotic arm attaches the SPEC to the top of the reaction vessels, one at a time, at the RF-station. A nitrogen flow at 80 p.s.i. is applied to the SPEC for 25 s to remove the liquid phase from the reaction vessels. The robotic arm then returns the SPEC to the SPEC-station.

Rinsing (initiation). Wash buffer is added to the reaction vessels by the liquid-transfer system, and the tips are then rinsed three times at the W-station. The reaction vessels are placed in the reactor chamber by the robotic arm, rotated for ~1 min, and then returned to the RF-station.

The SPE (initiation) and rinsing (initiation) blocks are repeated five times, followed by one more SPE (initiation) block before proceeding to the elongation steps.

Reagent addition (elongation cycle 1). This block is the same as the reagent addition (initiation) block except that the NTPs added are ATP, CTP, and UTP (see Extended Data Table 1).

Incubation (elongation cycle 1). This block is the same as the incubation (initiation) block except that the incubation is performed at 25 °C for 10 min.

SPE (elongation cycle 1) and rinsing (elongation cycle 1). These blocks are the same as SPE (initiation) and rinsing (initiation) blocks, respectively.

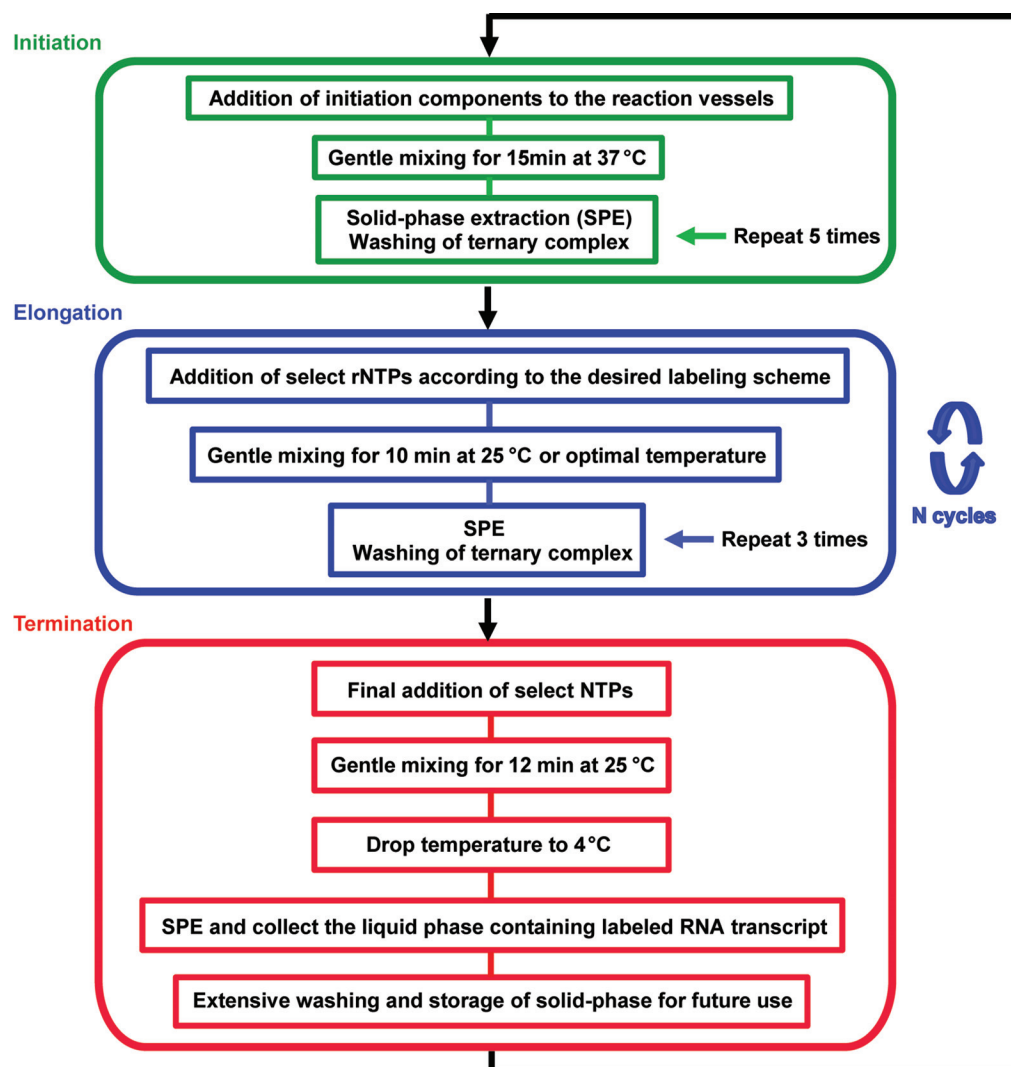
Each of the remaining cycles includes the following blocks. Reagent addition (elongation), incubation (elongation), SPE (elongation) and rinsing (elongation). The NTP additions for each cycle are listed in Extended Data Table 1.

Reagent addition (termination). This block is the same as previous reagent addition blocks except that ATP, CTP, GTP, and UTP are added.

Incubation (termination) is the same as incubation (elongation) except that the incubation time is 12 min.

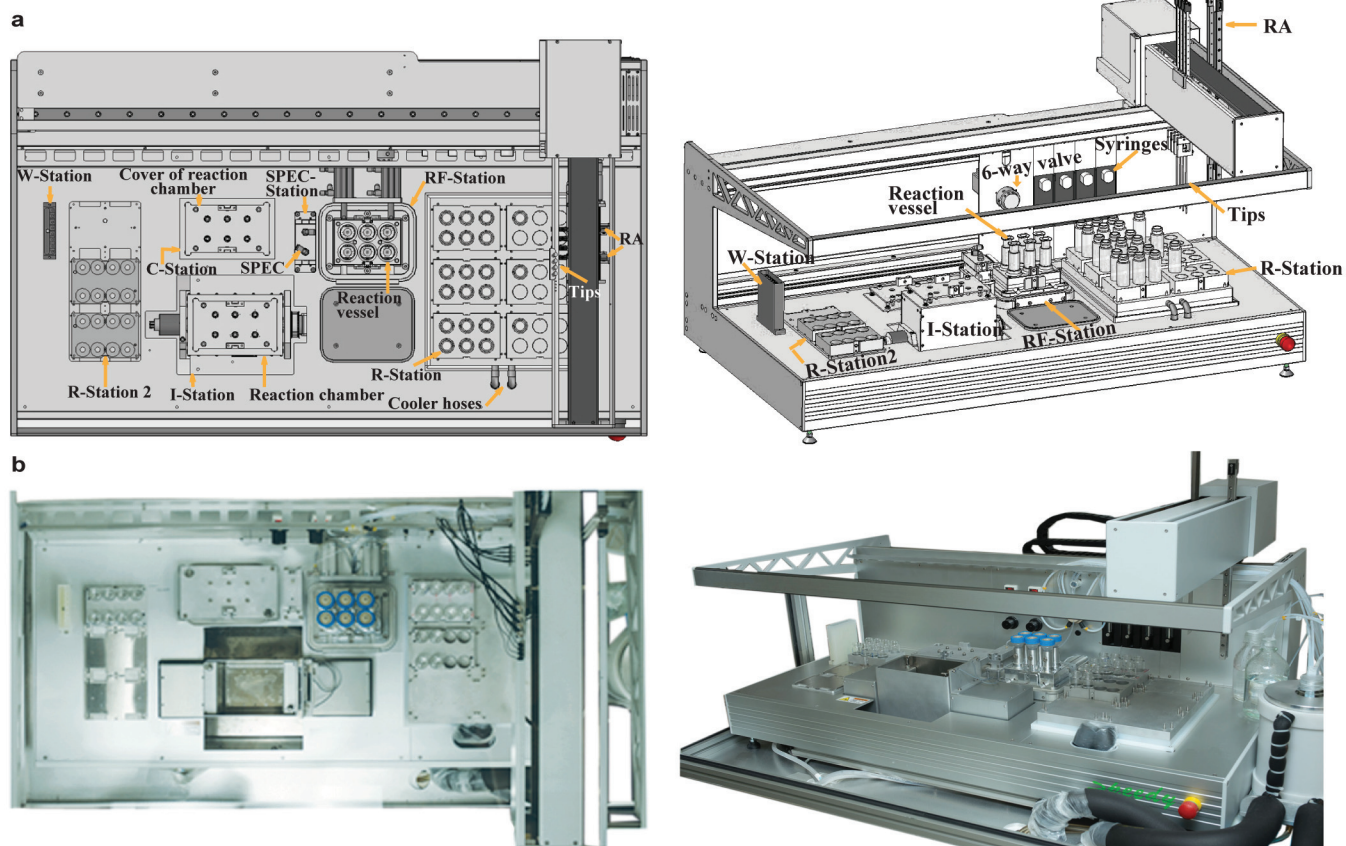
SPE (termination) and rinsing (termination). These blocks are the same as the SPE (initiation) and rinsing (initiation) blocks, respectively, except that during SPE in the termination step, the liquid removed from the reaction vessels is collected in sample containers rather than being pumped to the waste container.

31. Korbie, D. J. & Mattick, J. S. Touchdown PCR for increased specificity and sensitivity in PCR amplification. *Nature Protocols* **3**, 1452–1456 (2008).
32. Kao, C., Zheng, M. & Rüdisser, S. A simple and efficient method to reduce nontemplated nucleotide addition at the 3' terminus of RNAs transcribed by T7 RNA polymerase. *RNA* **5**, 1268–1272 (1999).
33. Mukherjee, S., Briebe, L. G. & Sousa, R. Structural transitions mediating transcription initiation by T7 RNA polymerase. *Cell* **110**, 81–91 (2002).
34. Zuo, X. *et al.* Solution structure of the cap-independent translational enhancer and ribosome-binding element in the 3' UTR of turnip crinkle virus. *Proc. Natl Acad. Sci. USA* **107**, 1385–1390 (2010).
35. Ying, J. *et al.* Measurement of ^1H - ^{15}N and ^1H - ^{13}C residual dipolar couplings in nucleic acids from TROSY intensities. *J. Biomol. NMR* **51**, 89–103 (2011).
36. Delaglio, F. *et al.* NMRPipe: a multidimensional spectral processing system based on UNIX pipes. *J. Biomol. NMR* **6**, 277–293 (1995).
37. Holmstrom, E. D. & Nesbitt, D. J. Single-molecule fluorescence resonance energy transfer studies of the human telomerase RNA pseudoknot: temperature-/urea-dependent folding kinetics and thermodynamics. *J. Phys. Chem. B* **118**, 3853–3863 (2014).
38. Kapanidis, A. N. *et al.* Alternating-laser excitation of single molecules. *Acc. Chem. Res.* **38**, 523–533 (2005).
39. Aitken, C. E., Marshall, R. A. & Puglisi, J. D. An oxygen scavenging system for improvement of dye stability in single-molecule fluorescence experiments. *Biophys. J.* **94**, 1826–1835 (2008).
40. Cordes, T., Vogelsang, J. & Tinnefeld, P. On the mechanism of Trolox as antiblinking and antibleaching reagent. *J. Am. Chem. Soc.* **131**, 5018–5019 (2009).
41. Fiore, J. L., Hodak, J. H., Piester, O., Downey, C. D. & Nesbitt, D. J. Monovalent and divalent promoted GAAA tetraloop-receptor tertiary interactions from freely diffusing single-molecule studies. *Biophys. J.* **95**, 3892–3905 (2008).
42. Emsley, P., Lohkamp, B., Scott, W. G. & Cowtan, K. Features and development of Coot. *Acta Crystallogr. D* **66**, 486–501 (2010).
43. Afonine, P. V. *et al.* Towards automated crystallographic structure refinement with phenix.refine. *Acta Crystallogr. D* **68**, 352–367 (2012).
44. Steinberg, G., Stromborg, K., Thomas, L., Barker, D. & Zhao, C. Strategies for covalent attachment of DNA to beads. *Biopolymers* **73**, 597–605 (2004).
45. Chivers, C. E. *et al.* A streptavidin variant with slower biotin dissociation and increased mechanostability. *Nature Methods* **7**, 391–393 (2010).



Extended Data Figure 1 | Synthesis algorithm for the selective labelling of RNA using the PLOR method. All samples except for fully labelled 71-nt-CN, S1+Lk1-CN, S1+Lk1-H, and ^{15}N -104-nt-TCV were synthesized following

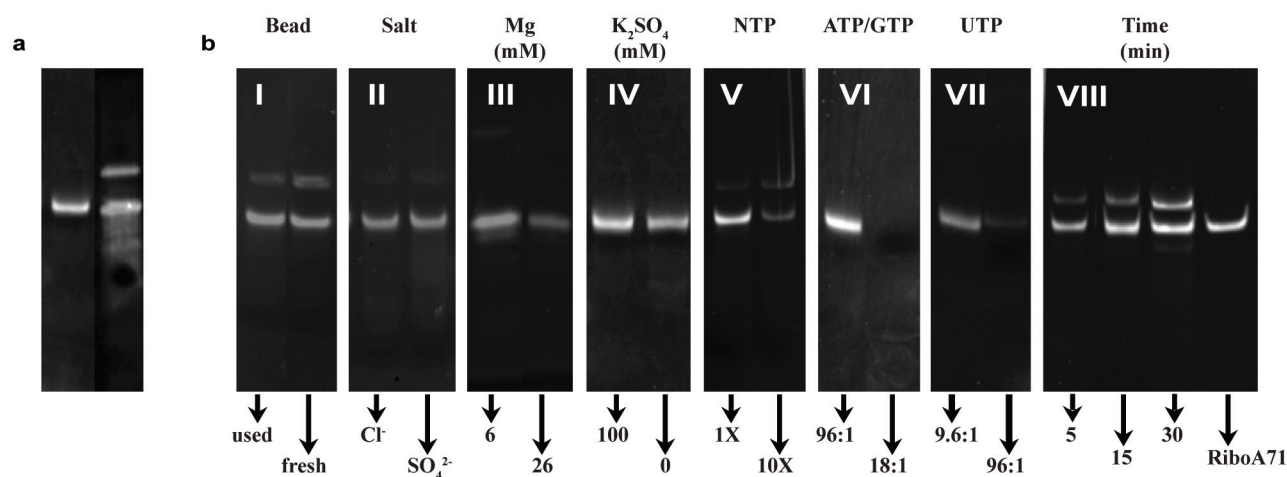
this algorithm. The initiation, elongation, and termination stages are shown in green, blue, and red, respectively. Various NTP combinations added during the elongation cycles depend on the desired labelling scheme.



Extended Data Figure 2 | Automated platform for PLOR synthesis.

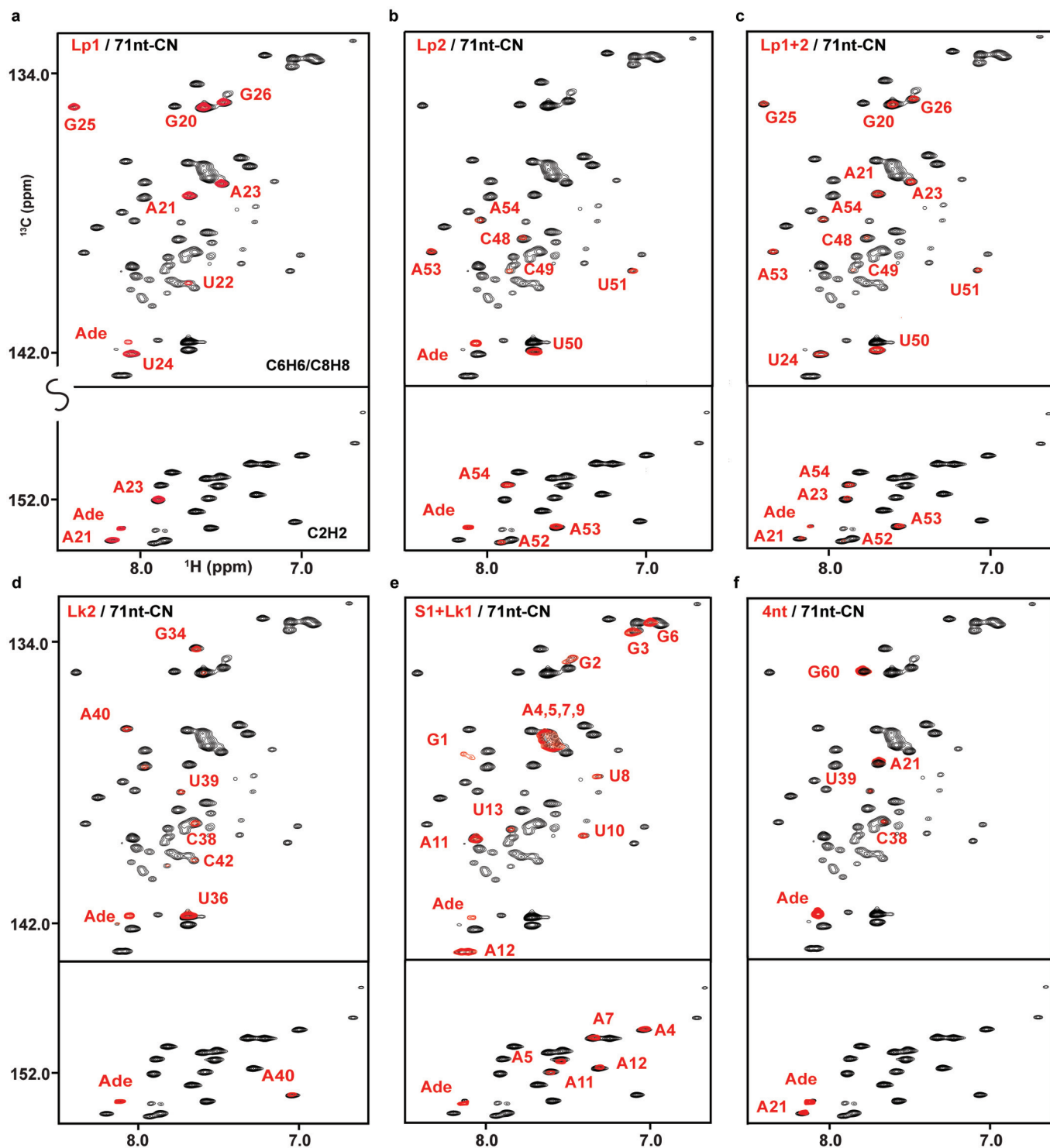
a, Diagram of the automated platform for PLOR synthesis depicting its various

parts and stations. **b**, Top-view (left) and side-view (right) photographs of the in-house automated platform.



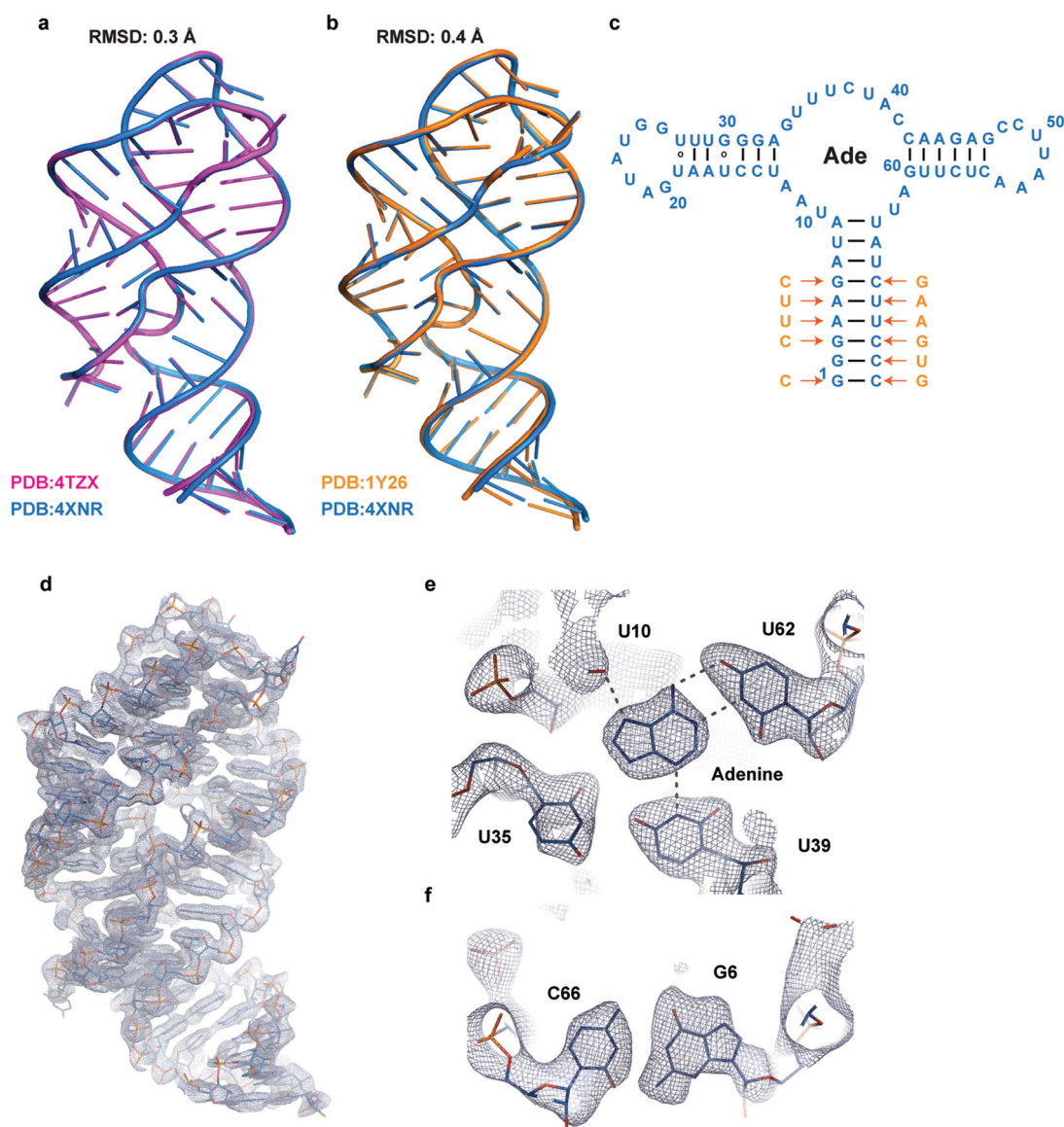
Extended Data Figure 3 | Optimization of experimental conditions for PLOR synthesis. **a**, The products of the PLOR (left) and the standard transcription methods (right). PLOR generates a pure full-length product with the desired labelling in the final step. **b**, Comparison of PLOR efficiency for Lp2-CN synthesis under various conditions: I, freshness of DNA-attached

beads; II, anion specificity; III, $[Mg^{2+}]$; IV, K_2SO_4 presence in the initiation; V, increasing NTPs ('1X' represents NTP amounts in Extended Data Table 1); VI, ratio of ATP/GTP:DNA; VII, ratio of UTP:DNA; and VIII, incubation time of the termination. The right lane contains pure RiboA71 as a control.



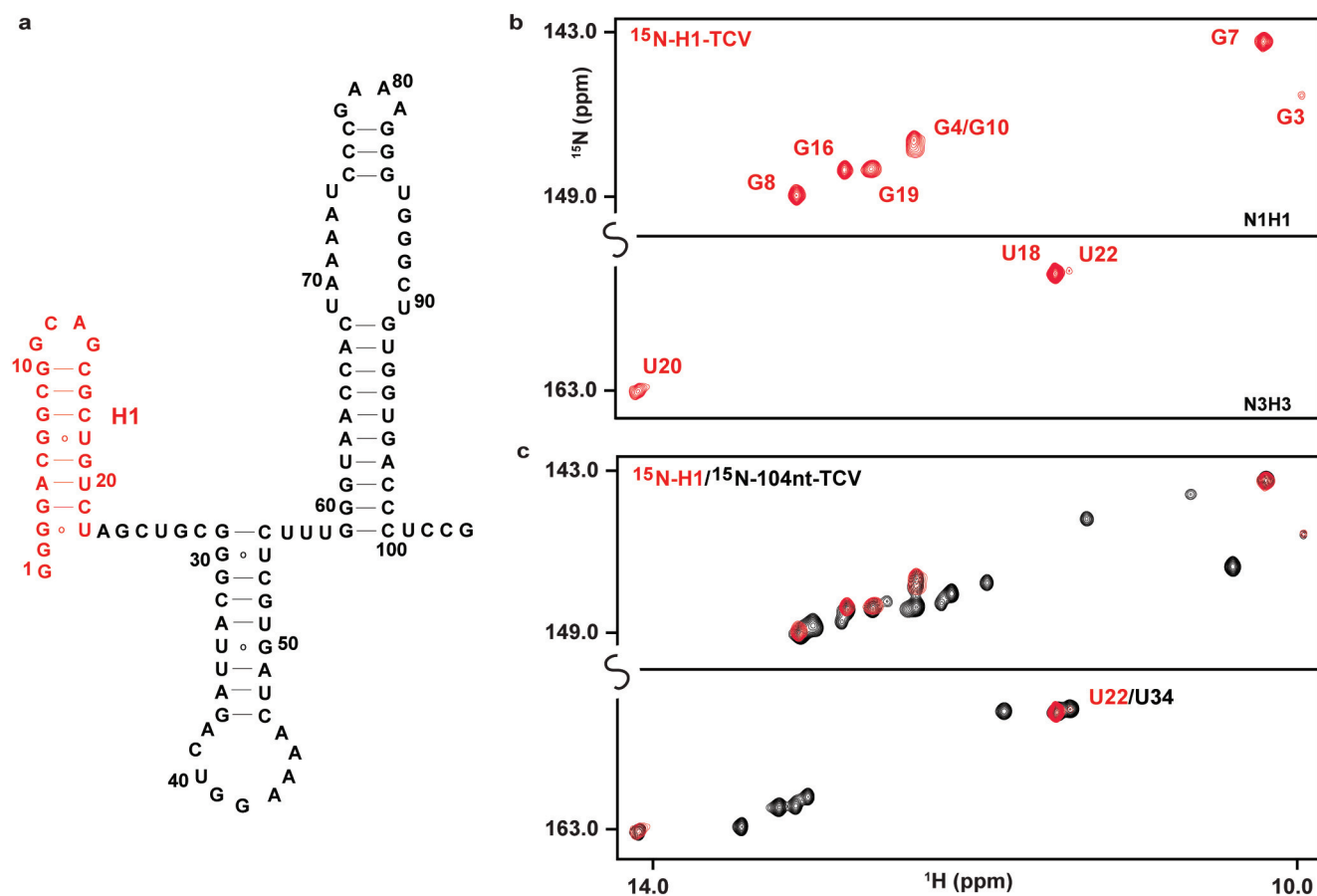
Extended Data Figure 4 | Comparison of NMR spectra of PLOR-generated and 71-nt-CN samples in adenine-bound form. Superposition of the $^1\text{H}/^{13}\text{C}$ -TROSY spectra of 71-nt-CN with Lp1-CN (a), Lp2-CN (b), Lp1+2-CN (c), Lk2-CN (d), S1+Lk1-CN (e), and 4nt-CN (f). These results indicate that

the RNAs synthesized by PLOR have the same fold as 71-nt-CN generated using the traditional solution-based transcription method and are functional as evidenced by binding of the adenine ligand.



Extended Data Figure 5 | PLOR-generated riboA71 maintains both sequence and structural fidelity. **a**, Structural superposition of the PLOR-generated riboA71 (PDB accession number 4XNR) with that of the riboA71 generated using the regular *in vitro* transcription (PDB accession number 4TZX)²⁶. The root mean squared deviation between all C1 atoms was ~ 0.3 Å. **b**, Structural superposition of the PLOR-generated riboA71 (PDB accession number 4XNR) with that of the riboA71 (PDB accession number 1Y26)¹. The root mean squared deviation between all C1 atoms was ~ 0.4 Å. **c**, Sequences and secondary structures of the RNAs in **b**. The arrows denote nucleotide sequence differences between the two ribA71 sequences. **d**, Composite

simulated anneal-omit $2|F_o| - |F_c|$ electron density of the riboA71 RNA structure (PDB accession number 4XNR) at 2.2 Å resolution calculated using the final model (1.0 s.d.). **e**, Portion of the electron density in **c** in the adenine-binding pocket unambiguously identifies the nucleobase identities of the PLOR-generated RNA, revealing no undesired sequence changes introduced by PLOR. **f**, Portion of the electron density in **c** of the G6•C66 base pair, which differs in identity between the two structures, suggesting that if there had been undesired sequence substitutions that resulted from using the PLOR method, they would have been readily detected in the crystallographic analysis.



Extended Data Figure 6 | Using PLOR to isotopically label a 104-nt RNA. **a**, Secondary structure of the 104-nt structural element in the TCV genomic RNA. The ^{15}N -H1-TCV was synthesized by the PLOR method, and the sequence in red is ^{15}N -labelled in ^{15}N -H1-TCV. **b**, ^{15}N -TROSY spectrum of

^{15}N -H1-TCV RNA. **c**, Superposition of the $^1\text{H}^{15}\text{N}$ -TROSY spectra of ^{15}N -H1-TCV with ^{15}N -104nt-TCV³⁴, indicating that the PLOR-generated selectively labelled RNA has the same fold as that generated using the regular *in vitro* transcription.

Extended Data Table 1 | PLOR recipes for the RiboA71 and TCV samples

Sample	NTP addition (NTP coefficients represent the multiples of template) *	C _{DNA} , Vol. †
Lp1-CN	Initiation: 96ATP, 96GTP, 9.6UTP; Elongation (cycle 1): 2ATP, 2CTP, 2UTP; (cycle 2): ¹³ C ¹⁵ N-ATP, ¹³ C ¹⁵ N-GTP; (cycle 3): ¹³ C ¹⁵ N-ATP, 2 ¹³ C ¹⁵ N-UTP; (cycle 4): 2 ¹³ C ¹⁵ N-GTP; Termination (cycle 5): 10ATP, 11CTP, 7GTP, 17UTP	20 μM, 40 mL
Lp2-CN	Elongation (cycle 2): 3ATP, 7GTP, 8UTP; (cycle 3): 3ATP, 3CTP, UTP; (cycle 4): ATP, 2GTP; (cycle 5): 2 ¹³ C ¹⁵ N-CTP, 2 ¹³ C ¹⁵ N-UTP; (cycle 6): 3 ¹³ C ¹⁵ N-ATP; (cycle 7): 2CTP, GTP, 3UTP; Termination (cycle 8): 2ATP, 4CTP, 5UTP	20 μM, 50 mL
Lp1+2-CN	Elongation (cycle 2): ¹³ C ¹⁵ N-ATP, ¹³ C ¹⁵ N-GTP; (cycle 3): ¹³ C ¹⁵ N-ATP, 2 ¹³ C ¹⁵ N-UTP; (cycle 4): 2 ¹³ C ¹⁵ N-GTP; (cycle 5): ATP, 4GTP, 6UTP; (cycle 6): 3ATP, 3CTP, UTP; (cycle 7): ATP, 2GTP; (cycle 8): 2 ¹³ C ¹⁵ N-CTP, 2 ¹³ C ¹⁵ N-UTP; (cycle 9): 3 ¹³ C ¹⁵ N-ATP; (cycle 10): 2CTP, GTP, 3UTP; Termination (cycle 11): 2ATP, 4CTP, 5UTP	20 μM, 50 mL
Lk2-CN	Elongation (cycle 2): ATP, GTP; (cycle 3): ATP, 2UTP; (cycle 4): 5GTP, 3UTP; (cycle 5): ATP; (cycle 6): ¹³ C ¹⁵ N-CTP, ¹³ C ¹⁵ N-GTP, 4 ¹³ C ¹⁵ N-UTP; (cycle 7): ¹³ C ¹⁵ N-ATP; (cycle 8): 2 ¹³ C ¹⁵ N-CTP; Termination (cycle 9): 8ATP, 8CTP, 3GTP, 10UTP	20 μM, 40 mL
S1+Lk1-CN	Initiation: 96 ¹³ C ¹⁵ N-ATP, 96 ¹³ C ¹⁵ N-GTP, 9.6 ¹³ C ¹⁵ N-UTP; Elongation/Termination (cycle 1): 14ATP, 13CTP, 10GTP, 21UTP	20 μM, 20 mL
4nt-CN	Elongation (cycle 2): ¹³ C ¹⁵ N-ATP, GTP; (cycle 3): 2ATP, 6GTP, 8UTP; (cycle 4): ¹³ C ¹⁵ N-CTP, ¹³ C ¹⁵ N-UTP; (cycle 5): 4ATP, 4CTP, 2GTP; (cycle 6): 3ATP, 2CTP, 5UTP; (cycle 7): ¹³ C ¹⁵ N-GTP; Termination (cycle 8): 2ATP, 4CTP, 5UTP	20 μM, 40 mL
S1+Lk1-H	Initiation: 96ATP, 96GTP, 9.6UTP; Elongation/Termination (cycle 1): 14 ² H-ATP, 13 ² H-CTP, 10 ² H-GTP, 21 ² H-UTP	20 μM, 20 mL
U39-CN	Elongation (cycle 2): 3ATP, 7GTP, 8UTP; (cycle 3): 3ATP, 3CTP, ¹³ C ¹⁵ N-UTP; (cycle 4): ATP, 2CTP, 2GTP; (cycle 5): 3ATP, 2CTP, 5UTP; (cycle 6): 2ATP, GTP, 3UTP; Termination (cycle 7): 4CTP, 2UTP	20 μM, 30 mL
RiboA71 (4XNR)	Elongation (cycle 2): 3ATP, 7GTP, 8UTP; (cycle 3): 3ATP, 3CTP, UTP; (cycle 4): ATP, 2GTP; (cycle 5): 2CTP, 2UTP; (cycle 6): 3ATP; (cycle 7): 2CTP, GTP, 3UTP; Termination (cycle 8): 2ATP, 4CTP, 5UTP	20 μM, 30 mL
¹⁵ N-H1-TCV	Initiation: 32 ¹⁵ N-ATP, 240 ¹⁵ N-GTP, 16 ¹⁵ N-CTP; Elongation (cycle 1): ¹⁵ N-CTP, ¹⁵ N-GTP, 3 ¹⁵ N-UTP; Elongation (cycle 2): 20ATP, 19CTP, 25GTP, 18UTP	20 μM, 30 mL

*The initiation and elongation (cycle 1) information are not listed if they are the same as those used in the synthesis of Lp1-CN.

†The template concentrations and total reaction volumes were listed for NMR and FRET sample synthesis.

Extended Data Table 2 | Synthesis efficiencies for the PLOR-generated NMR samples

Sample	Number of Elongation/termination cycles (<i>n</i>)	Efficiency [*]		Average Efficiency		Overall Yield	
		<i>I</i>	<i>E</i>	<i>I</i>	<i>E</i>	Calculated [†]	Experimental
Lp1-CN	5	43.3%	93.1%	46.0%	87.8%	24.0%	30.3%
Lp2-CN	8	49.0%	82.2%			16.2%	10.2%
Lp1+2-CN	11	47.0%	85.6%			11.0%	8.5%
Lk2-CN	9	44.6%	90.2%			14.3%	17.6%
S1+Lk1-CN	1	N/A	N/A			40.4%	40.3%
4nt-CN	8	47.8%	84.3%			16.2%	12.2%
S1+Lk1-H	1	N/A	N/A			40.4%	38.5%
U39-CN	7	44.2%	91.1%			18.5%	23.0%
¹⁵ N-H1-TCV	2	N/A	N/A			35.5% [‡]	32.0%

*Efficiencies, *I* and *E*, for each sample were calculated using the equation $\text{Yield} = I \times E^n$, where *I* and *E* are the initiation and elongation efficiencies, respectively, and *n* is the total number of cycles in the elongation and termination phases (see previous text on the calculations of synthesis efficiencies).

[†]These yields represent the theoretical yields for each sample based on average efficiencies, *I* and *E*, and the number of cycles.

[‡]The yield of ¹⁵N-H1-TCV is calculated by using *I* and *E* from the riboA71 system.

Extended Data Table 3 | PLOR recipes for the fluorescent-labelled RiboA71samples

Sample *	NTP addition (NTP coefficients represent the multiples of template)	[DNA], total vol. †
U24Cy3-C55Cy5	Elongation (cycle 2): ATP, GTP; (cycle 3): UTP; (cycle 4): ATP, 5-aminoallyl-UTP; (cycle 5): ATP, 6GTP, 6UTP; (cycle 6): 3ATP, 3CTP, UTP; (cycle 7): ATP, 2GTP; (cycle 8): 2CTP, 2UTP; (cycle 9, 37°C): 3ATP, Cy5-CTP; (cycle 10): CTP, GTP, 3UTP; Termination (cycle 11): 2ATP, 4CTP, 5UTP	5 μ M, 3 mL
U24Cy3-C55Cy5-B	Elongation (cycle 2): ATP, GTP; (cycle 3): UTP; (cycle 4): ATP, 5-aminoallyl-UTP; (cycle 5): ATP, 6GTP, 6UTP; (cycle 6): 3ATP, 3CTP, UTP; (cycle 7): ATP, 2GTP; (cycle 8): 2CTP, 2UTP; (cycle 9, 37°C): 3ATP, Cy5-CTP; (cycle 10): CTP, GTP, 3UTP; (cycle 11): 2ATP, 3UTP; (cycle 12): CTP; Termination (cycle 13): 2UTP, 3 biotin-11-CTP	5 μ M, 3 mL
U24Cy3-U65Cy5	Elongation (cycle 2): ATP, GTP; (cycle 3): UTP; (cycle 4): ATP, 5-aminoallyl UTP; (cycle 5): ATP, 6GTP, 6UTP; (cycle 6): 3ATP, 3CTP, UTP; (cycle 7): ATP, 2CTP, 2GTP; (cycle 8): 3ATP, 2CTP, 5UTP; (cycle 9): ATP, GTP; (cycle 10): 2UTP; (cycle 11, 37°C): ATP, Cy5-UTP; Termination (cycle 12): 4CTP, 2UTP	5 μ M, 3 mL
U24Cy3-U65Cy5-B	Elongation (cycle 2): ATP, GTP; (cycle 3): UTP; (cycle 4): ATP, 5-aminoallyl UTP; (cycle 5): ATP, 6GTP, 6UTP; (cycle 6): 3ATP, 3CTP, UTP; (cycle 7): ATP, 2CTP, 2GTP; (cycle 8): 3ATP, 2CTP, 5UTP; (cycle 9): ATP, GTP; (cycle 10): 2UTP; (cycle 11, 37°C): ATP, Cy5-UTP; (cycle 12): CTP; Termination (cycle 13): 2UTP, 3 biotin-11-CTP	5 μ M, 3 mL
U24A555-U65A488-B	Elongation (cycle 2): ATP, GTP; (cycle 3): UTP; (cycle 4): ATP, 5-aminoallyl UTP; (cycle 5): ATP, 6GTP, 6UTP; (cycle 6): 3ATP, 3CTP, UTP; (cycle 7): ATP, 2CTP, 2GTP; (cycle 8): 3ATP, 2CTP, 5UTP; (cycle 9): ATP, GTP; (cycle 10): 2UTP; (cycle 11, 37°C): ATP, Alexa488-UTP; (cycle 12): CTP; Termination (cycle 13): 2UTP, 3 biotin-11-CTP	5 μ M, 1 mL

*Cy3- and Alexa Fluor 555-labelled samples were generated by adding Cy3-NHS ester (GE Healthcare) or Alexa Fluor 555-NHS ester (Invitrogen), respectively, to a solution containing the lyophilized transcript product dissolved in double-distilled H₂O, followed by the addition of 0.5 volumes of 0.3 M sodium bicarbonate (pH 8.3). The reactions were incubated in the dark with gentle mixing for 1 h at 37 °C, 12 h at 25 °C, and then 1 h at 37 °C.

†The template concentrations and total reaction volumes were listed for NMR and FRET sample synthesis.

Extended Data Table 4 | Crystallographic statistics of data collection and refinement for the PLOR-generated riboA71 structure (PDB accession number 4XNR)

PDB Accession Code	4XNR
Data collection	
Space group	<i>P2₁2₁2</i>
Cell dimensions	
<i>a, b, c</i> (Å)	49.5 154.7 25.2
$\alpha\beta\gamma$ (°)	90, 90, 90
Resolution (Å)	41.68-2.207 (2.286-2.207)*
<i>R</i> _{merge} (%)	6.1 (103.7)
<i>I</i> / σ <i>I</i>	16.9 (1.7)
CC _{1/2}	0.999 (0.578)
Completeness (%)	100 (99)
Redundancy	6.6 (6.7)
Refinement	
Resolution (Å)	41.68-2.207 (2.286-2.207)*
No. reflections	10356 (1014)
<i>R</i> _{work} / <i>R</i> _{free} (%)	20.4 (36.6) /22.0 (37.1)
No. atoms	1582
RNA	1502
Protein	n/a
Ion	6
Water	64
Mean <i>B</i> -factors (Å ²)	65.8
RNA	66.0
Protein	n/a
Ligand/ion	79.3
Water	57.8
R.m.s. deviations	
Bond lengths (Å)	0.001
Bond angles (°)	0.27

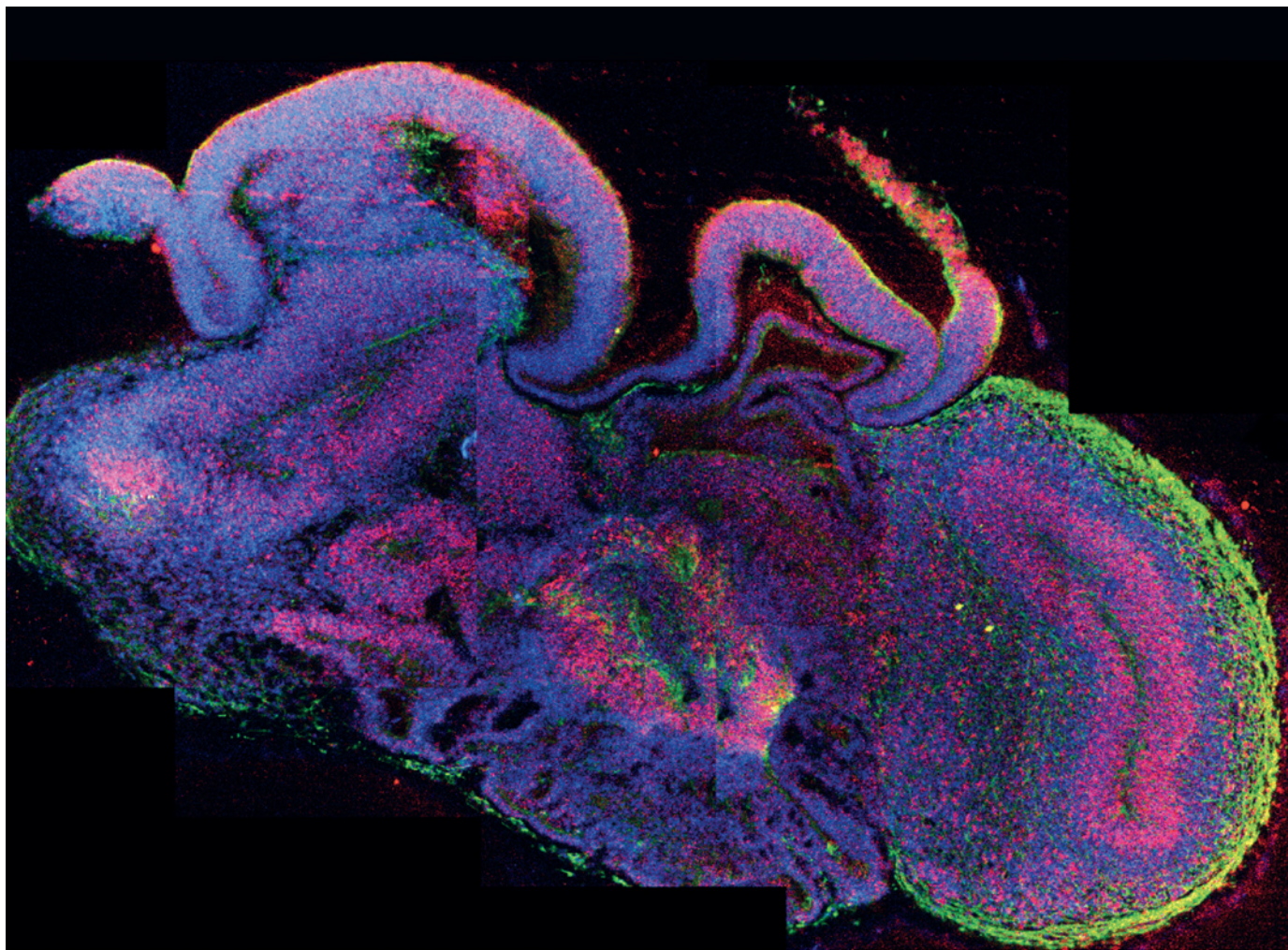
*Highest resolution shell in parenthesis.

TECHNOLOGY FEATURE

ORGANS FROM THE LAB

The body's organs are more complex than any factory. Attempts to mirror their physiology in the laboratory are getting closer to capturing their intricacies.

J. KNOBLICH, M. LANCASTER, AUSTRIAN ACAD. SCI.



Stem cells can be coaxed into forming organized clusters called organoids, such as this brain model.

BY VIVIEN MARX

In their quest to create organs in the laboratory, researchers have come a long way. Engineered tissues are already used in medical research and have even entered clinical trials. But they are much simpler than the real thing. To make a stomach, a lab might use 3D printing to create a mould that could be seeded with the appropriate cells. But without cues provided by blood flow and interactions with other tissues, the result would be simply a stomach-shaped statue, unable to digest or growl. An organ is much more than a mass of cells arranged

in a particular configuration: it also has support scaffolds, blood vessels to deliver nutrients and signal molecules, and a hierarchy of intricate control functions that can respond to internal and external cues.

All this makes it tough to build a functional, physiologically relevant organ in the lab, says Rosemarie Hunziker at the US National Institutes of Health, who manages the funding of programmes devoted to designing and building artificial organ systems.

But tissue engineers are making inroads into the problem. To try to tackle the biological complexity of organs, they can choose

from various fabrication approaches. One method is to place cells into elaborate, but still simplified models of an organ the size of a microscope slide, which can then be connected together to probe how organs interact. These miniature 'organs-on-chips' provide a unique vantage into organ function and disease, and for applications such as toxicity tests of drug candidates. An alternative approach is to foster the ability of cells to self-assemble, in the hope that they will recapitulate actual organ development and reveal insights into the process.

Whatever the strategy, researchers can start with biologically simple approaches, and ►

1

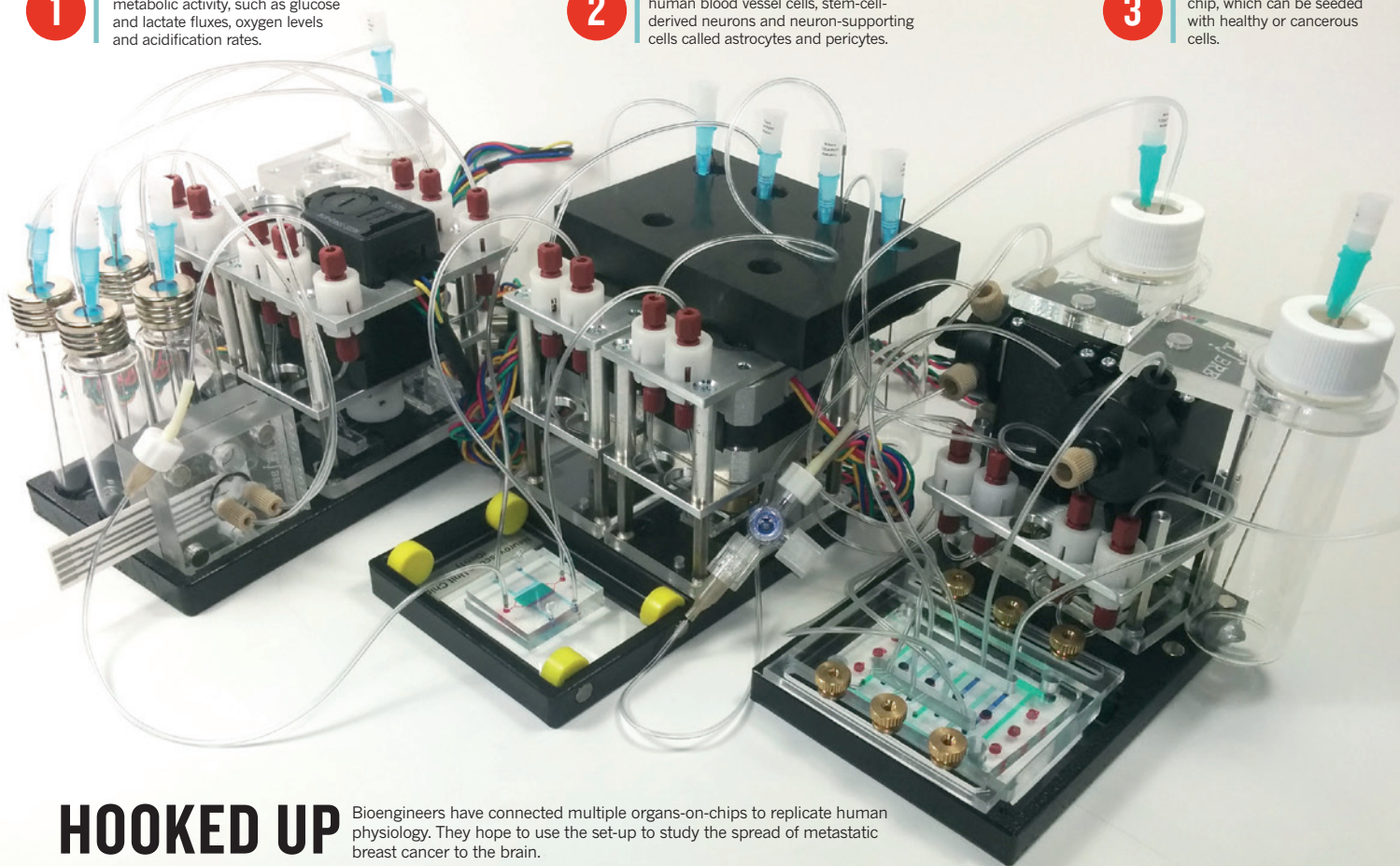
This unit measures the cells' metabolic activity, such as glucose and lactate fluxes, oxygen levels and acidification rates.

2

A brain-on-a-chip can be seeded with human blood vessel cells, stem-cell-derived neurons and neuron-supporting cells called astrocytes and pericytes.

3

A mammary-gland-on-a-chip, which can be seeded with healthy or cancerous cells.



HOOKED UP

Bioengineers have connected multiple organs-on-chips to replicate human physiology. They hope to use the set-up to study the spread of metastatic breast cancer to the brain.

► then add complexity to the model a little at a time. Just how similar an artificial version of an organ needs to be to its original depends on the questions that are being asked of it, Hunziker says. Artificial organs may look very different from their *in vivo* counterparts but nonetheless be useful for drug testing and basic research. Whether the goal is to understand an organ or to replace it, the eventual aim is an engineered system that functions as reliably as the real thing, Hunziker adds.

Researchers across the world are using these systems to address a wealth of important questions. They can, for example, help to reveal how cancer cells detach from a tumour to invade other tissues, and allow scientists to recapitulate processes in disease and development, such as what might go awry in neurodevelopmental disorders.

SYSTEMS THINKING

The most highly engineered organ models are the organs-on-chips that look the least like organs in the body. They are made using similar manufacturing techniques to those for silicon microchips in computers. First, a photosensitive material is layered onto silicon, and ultraviolet light is used to etch grooves in a desired pattern into silicone rubber. This guides the production of a 3D network of hollow tubes inside a rubbery rectangle the size of a computer memory

stick. The tubes are seeded with cells of the desired types and hooked up to pumps and an external fluid source, providing inlets and outlets through which scientists can mimic blood flow and deliver nutrients and environmental signals. Perfusion by continuously flowing liquid mirrors the dynamic environment in organs. The set-up also lets bioengineers modulate a tissue's stiffness as well as mechanical, chemical and electrical cues to reproduce the signals that cells might receive in healthy or diseased states, says John Wikswo of Vanderbilt University in Nashville, Tennessee (see 'Hooked up'). Researchers can replicate inflammation, for example, by adding the molecular messengers known as cytokines and even living immune cells into the chips' channels — they then watch the inflammatory response that is characteristic of most tissues when damaged or infected¹.

The chips are usually transparent to allow high-resolution, real-time imaging of cells, says Donald Ingber director of Harvard University's Wyss Institute for Biologically Inspired Engineering in Boston, Massachusetts. The liver, kidney, lung, intestine, fat, muscle and the blood-brain barrier have all

"The aim is an engineered system that functions as reliably as the real thing."

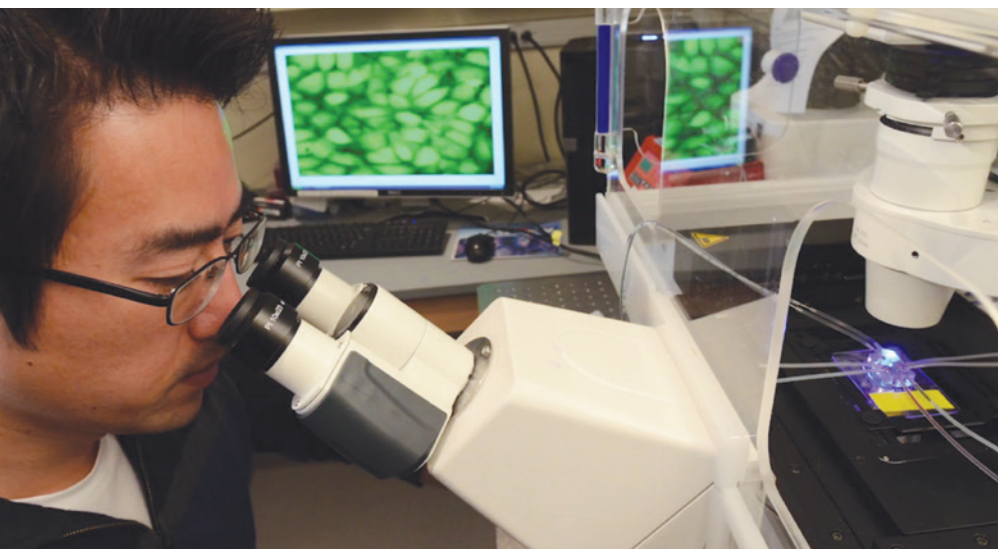
been rendered into chip form².

Now researchers are combining chips into multi-organ systems that can replicate some of the body's physiology. Gordana Vunjak-Novakovic and her team at Columbia University in New York City are building a model of the heart-liver-blood system with which to probe drug toxicity and disease. Wikswo at Vanderbilt, and his colleagues at the University of Pittsburgh, Pennsylvania, are linking organ chips together to predict the effects of potentially toxic chemicals and drugs. He believes that a liver-kidney model could identify safety problems before a drug reaches testing in humans, because these are the organs in which toxicity first becomes apparent. To emulate *in vivo* situations of health or disease, researchers can grow the appropriate cells in 3D support structures and explore their reactions to cues delivered into the system, says Wikswo.

The key to successful mimicry is attention to microstructure, says Hunziker. Careful placement of liver cells across a chip can better replicate real liver tissue, which has different zones close to and away from the main blood supply. These zones differ in the genes that are active, which results in differences in cell development and behaviour, and different responses to chemical stresses, she says.

Microscale organ systems allow experiments that cannot be done in cell cultures,

D. MARKOV, J. WIKSWO, VANDERBILT UNIV.



Dan Dongeun Huh at Harvard University's Wyss Institute tracks cellular events in a lung-on-a-chip.

animals or people, says Ingber. Organ chips lined with cells from individual patients enable the assessment of physiological differences between health and disease, and between people, in more detail and over a longer period than would be practical in people or in animal models, he says. Ingber's team has kept multi-organ chips going for more than a month. With an organ chip, it is also possible to adjust parameters to see what happens in a way that is not possible in a patient.

Several labs have formed spin-out companies to commercialize their model tissues. Emulate, in Cambridge, Massachusetts, founded by Ingber, is developing organ-on-chip systems for high-throughput drug screening and toxicity testing. The company Hepregen in Medford, Massachusetts, co-founded by bioengineer Sangeeta Bhatia at the Massachusetts Institute of Technology in Cambridge, uses the technique of 'micropatterning' to develop liver models in which different cell types are precisely placed to produce a platform that more closely mimics the complexity of the liver. These are being developed as drug-screening assays. HemoShear Therapeutics in Charlottesville, Virginia, founded by two University of Virginia scientists, has developed several organ modelling systems, including one that specifically mimics blood flow in tissues. In January, HemoShear began a collaboration with pharmaceutical company Pfizer of New York to find better ways to predict injuries to blood vessels, such as inflammation, that drug candidates might cause.

Right now, microfabrication is out of reach for many labs. However, there are some companies that offer services to make chips for labs that do not have the necessary equipment or expertise. And many universities offer microfabrication capabilities through core service centres. Meanwhile, labs at the cutting edge are working to make engineered chips better homes for living cells. One challenge is seeding cells evenly throughout the devices

and maintaining their growth within the tiny channels, says Ingber. Another is that bubbles in the system can injure the cells.

THREE-DIMENSIONAL HELP

In contrast to organs on chips, soft scaffolds seeded with cells can result in artificial organs that look much more like the real thing. This approach blends a variety of synthetic materials to make a support system. It is then seeded with cells that grow and develop throughout the scaffold and thus become arranged in the desired configuration. In one well-known example from the early days of the field, Linda Griffith at Massachusetts Institute of Technology and Charles Vacanti at Massachusetts General Hospital in Boston and their colleagues used such a scaffold implanted under the skin of a mouse to guide bovine cartilage-forming cells to grow tissue in the form of a human outer ear^{3,4}. The polymers in the scaffold degraded as the tissue formed, leaving behind the structure made of cartilage.

Today, Griffith and her team use a custom-built 3D printer to create highly intricate tissue scaffolds. A stream of photoreactive polymer spurts out of the instrument's nozzle and one layer at a time is exposed to ultraviolet light to stabilize the structure. Material is removed in an iterative process to build micrometre-scale substructure.

Scientists have also developed ways of mimicking the mechanical stimuli that seem crucial to tissue development. For example, the early development of teeth in a mammalian embryo involves embryonic cells packing closely together. To mimic this process, Ingber's lab has developed a polymer that acts like shrink-wrap at certain temperatures⁵. When the polymer is warmed to body temperature, it shrinks and compacts the cells it encloses, which activates genes responsible for tooth development. Bioengineers could potentially use this material to induce tissue development for a variety of therapies, Ingber says, because cartilage and

other internal organs (such as the lungs and kidneys) also undergo cellular compaction as they develop.

Incorporating blood flow into a model organ is particularly challenging, especially when trying to mimic the heart, which pumps rhythmically for a lifetime. Nevertheless, tissue engineers are well under way in their search for therapies to help heal injured hearts, and eventually perhaps, to find alternatives to heart transplants. Starting with a cell-sheet technology that does not incorporate a scaffold, Teruo Okano, a biomedical engineer at Tokyo Women's Medical University and his colleagues have made vascularized heart-tissue patches. The experiments start with thin layers of cells, which they can grow from a variety of cell types, including rat neonatal cardiac cells, human muscle cells and induced pluripotent stem (iPS) cells. These sheets are grown in dishes coated with a temperature-sensitive polymer. When the temperature is lowered, researchers can harvest sheets of cells that remain connected to each other without any kind of scaffold, says Okano's colleague Tatsuya Shimizu. In ongoing clinical trials, the team is evaluating 30 patients with heart problems who have received implanted tissue patches made from muscle-cell-derived sheets. These sheets secrete several types of cytokine, which promote blood-vessel formation and inhibit cell death in the patient's heart tissue. In the future, Shimizu and his colleagues hope to transplant tissues with beating cells.

But these sheets are not yet optimal. The ideal grafts need to be thick, especially because events such as heart attacks lead to thin heart tissue. The team has returned to the lab to engineer thicker patches that will be infiltrated with even

"Engineered tissues are starting to allow incisive experiments and even replacement therapies."

more blood vessels and should remain viable for longer than the previous versions. They have grown cell sheets from human iPS cells and transplanted them into rats just under the skin on their backs, building up a patch 1 millimetre thick made of 30 cell sheets⁶. After implantation, small blood vessels from the rat sprouted through the layers. By moving smaller stacks into more vascularized areas, the researchers were able to cause more and more blood vessels to grow and eventually to connect the stack directly to larger blood vessels, such as the jugular vein. The heart-muscle cells continued to beat during six months of observation.

However, similar multiple surgical interventions could not be carried out in people. So the researchers have developed a technique that relies on a gel on which they can grow multiple layers of rat-cell sheets in the lab.

One day, Okano and his team hope, it will be possible to engineer such grafts for use in

humans with severe heart failure. The general approach could also be applied to engineer tissue to mimic the liver or kidneys.

SELF-ASSEMBLY

Other teams rely even more heavily on the intrinsic ability of cells to assemble into complex structures. Stem cells grown in suspension can be coaxed to form organized clusters called organoids, and these have been made for diverse tissues, including intestine, kidney and retina. Organoids are usually much smaller than the actual organ, just a few millimetres across, and with a much simpler assortment of cells, but some teams are now making organoids with more cell types and more complex structures, and even attempting to model the most daunting organ — the brain.

In 2013, Madeline Lancaster and Juergen Knoblich at the Institute of Molecular Biotechnology of the Austrian Academy of Sciences in Vienna generated human brain-tissue organoids about the size of a lentil⁷. They started from groups of human pluripotent stem cells, which are differentiated into neural tissue. Part of the protocol is to let the biology unfold.

Under the right conditions, the differentiating cells self-organize into a tight swirl of neural tissue with multiple cell types, including radial glial stem cells that give rise to cells in the brain such as neurons. The swirls even include rudimentary brain structures such as the beginning of a forebrain and retina. “We pretty much recapitulate the formation of neural tissue in a dish, letting it develop as it does in the embryo,” says Knoblich.

These cerebral organoids have helped them to address questions that are hard to answer when growing neurons flat on the surface of a culture dish. The team studies the human neurodevelopmental disorder microcephaly, in which infants have markedly small brains. Although mice can be used to model the disorder, the animals do not show the extreme difference in brain size. But when the team reprogrammed skin cells from a patient with microcephaly into iPSC cells that developed into cerebral organoids, the resulting structures bore clear characteristics of the disease. In these organoids, the radial glial cells proliferated less and, in some regions, differentiated into neurons prematurely. Even under normal conditions, radial glial cells do not proliferate in developing mice the way they do in humans, and so human organoids are a promising way to study how these neural precursor cells might be involved in the disorder.

Lancaster and Knoblich also used organoids to assess the effects of a gene called *CDK5RAP2* that helps to guide cell division. The patient with microcephaly had a mutation in this gene that probably results in an aberrant protein. When the team introduced an undamaged protein into the organoid, some cells developed into types akin to radial glial cells, indicating that the loss of function of this gene contributes to microcephaly⁷.

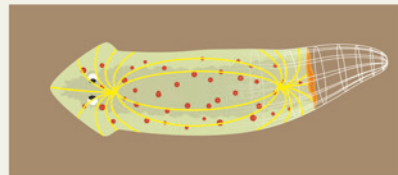
ORGAN BUILDING

Instead of replacing damaged or diseased organs, some labs have attempted to stimulate organ regeneration. Researchers have tapped into the innate chemical and bioelectric signalling of flatworms to induce the development of a second head. The regeneration occurs because the altered pattern is stored across the animal's bioelectric network.

1 An adult normal flatworm.



2 Manipulation of the worm's bioelectric network.



3 The worm is permanently altered by rewriting the memory of what should be regenerated.



There are still plenty of challenges for organoid technology. Lancaster and Knoblich point out that their organoids lack a blood supply and the interaction that neural tissue normally has with surrounding tissue. Over time, the organoids begin to die and lose resemblance to early brain tissue. The team has managed to keep them alive for as long as a year, but how useful late-stage organoids are for disease modelling remains to be seen, says Knoblich.

Another challenge is consistency, because the organoids take on different shapes from one batch to the next, he says. The lab is continuing to tinker with the growth conditions in the hope of overcoming these problems and being able to model more complex neurodevelopmental disorders.

LIKE AN EMBRYO

Bioengineers intent on building organ models can tap into the complexity of intercellular signals — the wealth of biochemical and bioelectrical messages that tell cells to differentiate, migrate, change shape or clump together to form an organ. This approach has already

been used to regenerate legs on frogs that are normally too old to naturally regrow an amputated limb. That work, led by Michael Levin, a biomedical engineer at Tufts University in Medford, Massachusetts, might translate more readily to humans than many expect: children can regenerate fingertips, but adults cannot.

To get the frogs' legs to regrow, Levin and his team chemically tinkered with the pattern of electrical charge in the limb so that it matched the bioelectrical gradient found in the limbs of young animals⁸, and this induced the cells at the tip of the amputated limb to grow. They also induced the formation of a two-headed flatworm (see ‘Organ building’). The alterations the team had made caused a permanent change in the memory of what to form, which was encoded in an electrical circuit just like memories in our brains. Levin describes the process as “manipulating information” within the tissues in ways that cause predictable, large-scale changes in growth and form. That, he says, “makes the job of growing anything much easier”.

Instead of trying to micromanage organ building, Levin believes in leveraging the body's own processes. He and his team are developing a physiological ‘phrase book’ of mathematical models and software. Scientists can use these software tools to search for factors to manipulate in their experiments, and so find ways to tell cells what tissues to build. The goal is to link data sets about genes, proteins and signalling pathways to knowledge about how organ shape and function is regulated. “These are the kinds of tools that will be indispensable as bioengineers confront the complexity barrier facing the creation of even simple organs,” says Levin.

Ultimately, the usefulness of the tool is what is important, not the specific approach that is chosen. Engineered tissues are starting to allow incisive experiments and even replacement therapies. And perfectly mirroring nature may not, in all cases, be what is needed. “What is critical is that the organ has enough complexity to accomplish its function,” says Hunziker.

Whether it be a patch for damaged hearts, a better toxicity test or an insight into a devastating brain disease, tissue engineering delivers what scientists crave: more understanding, and the potential to help people. ■

Vivien Marx is technology editor for *Nature* and *Nature Methods*

1. Wikswo, J. P. *Exp. Biol. Med.* **239**, 1061–1072 (2014).
2. Bhatia, S. & Ingber, D. E. *Nature Biotechnol.* **32**, 760–772 (2014).
3. Vacanti, C. A., Cima, L. G., Ratkowski, D., Upton, J. & Vacanti, J. P. *MRS Proc.* **252**, 367 (1991).
4. Langer, R. & Vacanti, J. P. *Science* **260**, 920–926 (1993).
5. Hashmi, B. *et al. Adv. Mater.* **26**, 3253–3257 (2014).
6. Komae, H. *et al. J. Tissue Eng. Regen. Med.* <http://dx.doi.org/10.1002/term.1995> (2015).
7. Lancaster, M. A. *et al. Nature* **501**, 373–339 (2013).
8. Mustard, J. & Levin, M. *Soft Robotics* **1**, 169–191 (2014).

CAREERS

CAREER LAUNCH Stem-cell dynamo gets his own lab before he hits thirty **p.381**

ENTREPRENEURS Scientists test their business hypotheses go.nature.com/w9c32i

NATUREJOBS For the latest career listings and advice www.naturejobs.com



COLUMN

Reset your brain

A bit of self-reflection can propel scientists into a career beyond the lab, says **Christopher Taylor**.

Last year, as I later learned, postdoctoral cancer researcher Clayton Boldt was having a bad day. Several weeks' worth of experiments had yielded little in the way of results, his cell cultures were not growing, he had mixed up his samples on a western blot, and he had no spares. As on other tough days, he began an internal pep talk: he was preparing for his future, a research career that would fulfil his love of science.

But as Boldt reviewed what was good about his work, he came to an astonishing realization: he was uncertain whether he actually wanted to pursue academic research. For the first time, he asked himself a question that occurs to almost every biomedical trainee who is considering the next stage of her or his career: 'Where do I go from here?'

In his quest to solve his dilemma, he reached out to me for guidance. As the associate director

of the Center for Professional Development & Entrepreneurship at the MD Anderson Cancer Center in Houston, Texas, I have had the opportunity to counsel hundreds of biomedical trainees who, like Boldt, find themselves questioning their commitment to academia. As I do for all in his situation, I advised Boldt to create what I call a career-exploration framework. This process involves four central steps: understand yourself, learn your options, identify any gaps in your knowledge or experience and, finally, launch your plan. Although these steps might look simplistic, each part is important and builds on the previous one.

Boldt, for instance, already knew that he enjoyed writing and talking with non-scientists about science. In 2011, he had launched a blog to pose scientific questions and topics to the online community and had begun to develop a reader base that participated in these discussions. This came up as we talked about his career-path challenges and where he saw himself after his training. So, together, we created a framework that helped him to clarify his strengths and improve his candidacy for a communications position that would dovetail with his interest in and passion for science.

Today, Boldt works as a senior communications specialist for MD Anderson. He writes opinion articles, press releases, pitch letters and blogposts in support of the institute's division of cancer prevention and population sciences. "The path out of academic research is not particularly well paved. It is certainly not something we are trained for," he says. "However, when you've found something that excites you, don't be afraid to let it guide you into the unknown."

Boldt is a good example of someone who successfully crossed the bridge from lab research into the non-academic world. Career doubts can paralyse any of the thousands of people who are pursuing PhDs and postdoc training today. By following my four-part plan, scientists can create a career-exploration framework that can help them, too, to realize a non-academic career track.

KNOW YOURSELF

The first step can be difficult — creating a personal framework requires introspection, reflection and taking a frank inventory of your life. Biomedical trainees can view this step as a way to identify their 'professional DNA': personality traits, core values, education, technical training, work experience, soft skills, accomplishments and overall life experience (see 'Map your professional DNA'). ►

► Researchers can use different methods to sketch out each of these areas. For example, taking the Myers-Briggs Type Indicator personality test (see go.nature.com/rh7koz) can help scientists to determine their preferences, strengths, weaknesses and social compatibility. Another option is to create a checklist that identifies skills that are transferable across different work settings — communication, negotiation and project-management abilities, for instance. Scientists should also make a detailed record of obligations and functions for which they are responsible in the lab.

It is important to articulate these attributes in written form because they help to sculpt the professional DNA map that will become part of the trainee's framework. Without this holistic view, it will be hard for scientists to identify gaps in their skills or experience. This information illuminates the trainee's current candidacy potential while also revealing any preferences for specific job functions, workplace settings and other specifics that they might wish to incorporate into a future position.

I have developed training exercises that aim to guide people towards such self-understanding. One of these, known as '20 words', helps scientists to start to outline their professional and personal identities and flesh out their DNA maps. They ask 8–12 people who are close to them, such as friends, family members, colleagues and supervisors, to choose 20 words to describe them. Such lists highlight positive and negative perceptions that might need to be emphasized or mitigated to potential employers during a job search. Common descriptors also measure how consistent the young scientist is across professional and personal settings. From here, scientists have a baseline from which to explore their career options.

UNDERSTAND YOUR OPTIONS

Opportunities for early-career biomedical researchers to land tenure-track academic positions are shrinking, and US federal funding remains highly competitive. This supply-demand imbalance is well documented (see go.nature.com/aq8qlu). In 2011, for instance, the US National Institutes of Health (NIH) established a workforce committee to investigate the sustainability of biomedical research. Last February, committee co-chair Sally Rockey, deputy director for extramural research at the NIH, gave a lecture at MD Anderson on the situation facing PhD graduates.

Rockey explained that in 2012, some 145,000 biomedical PhD graduates were in full-time positions in the United States, and nearly as many postdocs and graduates were in the pipeline. Although unemployment was at a low for biomedical PhDs, fewer than half of those employed full-time were doing academic research or teaching, and only a small portion had tenure-track positions.

But trainees need not despair: the biomedical enterprise is not limited to academic research

MAP YOUR PROFESSIONAL DNA

Scientists can develop a career-exploration framework to help them to identify opportunities for non-academic paths that align with their professional DNA. An example rubric might include desired job functions, workplace-environment characteristics, professional interests or specific business sectors.

Professional DNA maps a person's background, traits and talents, and will sculpt each area of the framework.

- Skills
- Abilities
- Education
- Knowledge
- Personality type
- Values
- Work style

JOB FUNCTIONS

- Project management
- Team-building
- Scientific writing
- Analytical thinking
- Collaboration development

WORKPLACE ENVIRONMENT

- Team-oriented
- Creative or innovative
- Mission-driven goals
- High ethical standards
- Contact with public

PROFESSIONAL INTERESTS

- Advancement opportunities
- Professional-growth support
- Quality mentor or supervisor
- Extracurricular activities
- International network

SUBDISCIPLINE OR SECTOR

- Biopharmaceuticals
- Devices or diagnostics
- Consulting
- Law
- Finance and investments

alone. Scientists can take advantage of their newly mapped professional DNA to find non-academic career choices that suit them. Although they typically spend years honing their scientific-research skills in a narrow discipline, many of those abilities — such as data analysis and conflict-resolution and presentation skills — are applicable in a broad range of industries and positions outside academia.

Boldt learnt the benefits of transferable skills as he prepared to embark on his new career path. "One of my biggest concerns was whether I had wasted the half decade it took to earn my PhD," he says. "I've realized, though, that my training developed skills I wasn't even aware of — perseverance, project management and communication." He notes that, beyond identifying those abilities, the other challenge for early-career scientists is to find a position in which they can continue to satisfy their love of science.

Career choices are numerous across the biomedical and bioscience enterprise, which consists of at least ten sectors: biopharmaceuticals, devices and diagnostics, consulting, law, finance and investments, government, non-profit organizations, education, health-care, and media and journalism. As scientists narrow their preferences to specific disciplines, they will become better equipped to advance to step three of the framework: addressing any holes in their background.

IDENTIFY GAPS

For this step, biomedical scientists should first research regional, national and international-trade and membership groups and associations, leading companies and the positions that exist in each of their desired sectors. Perusing these networks will allow trainees to gain an understanding of the experiences and skills that will make them competitive for a spot, and thus will flag any potential gaps in those areas that they might need to tackle.

When reading employer expectations, it is important not to focus on job titles, but rather on functions, responsibilities, work environment and aspects beyond degrees or technical skills. Different companies might use variations of titles for a role that carries the same responsibilities, so an online search for 'research scientist' could exclude positions that are equivalent in function, but different in name. Trainees seeking employment will discover that many disciplines are recruiting for similar positions; for example, the biopharma, device and diagnostics and health-care industries may all be looking for a quality-assurance specialist.

Trainees can further pinpoint gaps by examining job postings and by networking — setting up coffee chats, lunches and informational interviews with leaders and executives in a discipline of interest. It is also important to attend relevant meetings in that sector, including conferences and trade-and-industry organization conventions. The trainee's goal is to talk to employers and managers in the business to develop a clear picture of both the minimum and preferred qualifications — and to assess how her or his own skills, knowledge and experience measure up to these requirements.

Armed with this information, scientists can fill in gaps by taking advantage of internships, classroom or online courses at their institution, and Internet communities — LinkedIn, for example — that bring together members of a specific industry or discipline. Once they have solidified their competitiveness in these ways, they can start to write their applications.

LAUNCH THE PLAN

Although a PhD is essential for a scientific discipline, it is also important to recognize that one's degree — or postdoc experience — does not necessarily train one for the work world outside academia. Before launching into the career hunt, graduate students and postdocs

should keep timing in mind: those who are more than a year away from the end of their programme should continue to improve their marketability in the industry in which they will seek a job. This could include learning fundamental business principles or earning a certification of value in that sector, such as a Project Management Professional certification in health care.

Those who hope to enter the job market in the next year, however, should focus on their job search, including such factors as CV development, professional branding, interview preparation, networking and the job-application process itself.

The CV should spring from the results of the professional DNA map, and needs to highlight transferable skills and specific areas of expertise (see go.nature.com/v1nhnm). Professional branding calls for, at least, a robust LinkedIn profile that mirrors the CV and lists research projects, papers, presentations and peer recommendations. Tweeting publications and talks can also be helpful. To prepare for an interview, trainees should video themselves answering sample interview questions — examples are available at online career forums and publications (see go.nature.com/oiaoiik) — and review the footage to understand how a potential interviewer might perceive them.

Trainees should also list 10–15 professionals in their desired industry to contact for informational interviews, and use LinkedIn, company websites and other online resources. It is important to gain insight into how these professionals work and to prepare for interactions with them. Finally, applicants must remember to customize their applications and CVs to address each job advertisement, rather than using a generalized portfolio for all.

Change is difficult, especially after doing the same thing in the same environment for most of one's adult life. But making the decision to embark on a new direction is often the hardest part. Sometimes taking that different path means believing it is OK to leave academia — even though academic culture may not support that belief. Having the proper tools can reassure biomedical trainees who worry about academia's locked gates — and help them to prepare for and pursue other careers that will offer an abundance of satisfaction and success. ■

Christopher Taylor is the associate director of the Center for Professional Development & Entrepreneurship at the University of Texas MD Anderson Cancer Center in Houston, Texas.

TURNING POINT

Paul Tesar

Paul Tesar discovered a new type of mouse stem cell in 2007 and published his discovery in Nature as a graduate student at the University of Oxford, UK. The paper launched him rapidly to a professorship at Case Western Reserve University (CWRU) in Cleveland, Ohio, where he continues to drive the field forward.

How did your graduate experience shape your career pursuits?

I was part of a joint programme — the US National Institutes of Health (NIH) Oxford–Cambridge Scholars Program — and split my time working with NIH human-stem-cell biologist Ron McKay and Oxford mouse embryologist Richard Gardner. I had a great deal of independence from day one. My first publication was a solo-authored paper in the *Proceedings of the National Academies of Science* (P. Tesar *Proc. Natl Acad. Sci. USA* **102**, 8239–8244; 2005) — a feat almost unheard of today.

How crucial was the fellowship to your stem-cell discovery?

I didn't set out to discover another pluripotent state. But my 'eureka' moment came when I derived mouse embryonic stem cells with similar characteristics to human ones, including the ability to differentiate into all other tissue types, known as pluripotency (P. Tesar *et al. Nature* **448**, 196–199; 2007). It took a while to prove that there was more than one pluripotent state, but that paper triggered a frame shift in the field. Epiblast stem cells would have been discovered anyway, but drawing the NIH and Oxford research together put that revelation in our hands. So strongly do I feel that dual mentoring arrangements are fruitful, that I encourage my students to find mentors with different skill sets.

What happened after the epiblast publication?

I was looking for my next position and wanted to maintain my level of independence. I also wanted to go back to Cleveland someday, and the CWRU — where I earned my bachelor's in biology — encouraged me to return. After I explained my goals, they created a one-off position that gave me a few years of funding and my own independent lab straight away. Things went better than I could have hoped. I hired good people and published some strong papers. The next year, at 28 years old, I applied for a faculty position. It was a whirlwind experience.

How did you maintain momentum?

In 2010, I was named a New York Stem Cell Foundation Robertson Investigator, which gave



me US\$1.5 million in innovation funding. That was enough to grow my lab from 3 to 12 members and to drive our research into unexplored areas. It was such a new field that I was able to rapidly address some major questions.

Is stem-cell biology entering a 'golden age'?

People have expected much from this promising field; it is time to deliver. Stem-cell transplantations are feasible and will continue to advance — and we are learning how to control stem-cell populations to perform specific functions. For example, recently, we screened for drugs that can stimulate the generation of a brain-cell type that is typically lost in diseases such as multiple sclerosis. There has been a huge uptick in the number of stem-cell-based trials, and the results of those will guide the future.

Do you do much work at the bench?

I would love to, but I spend most of my time writing grant proposals and renewals, progress reports and paper reviews. Unfortunately, I am really there only during the holidays after I have sent everyone home. They trust me enough to grow cells.

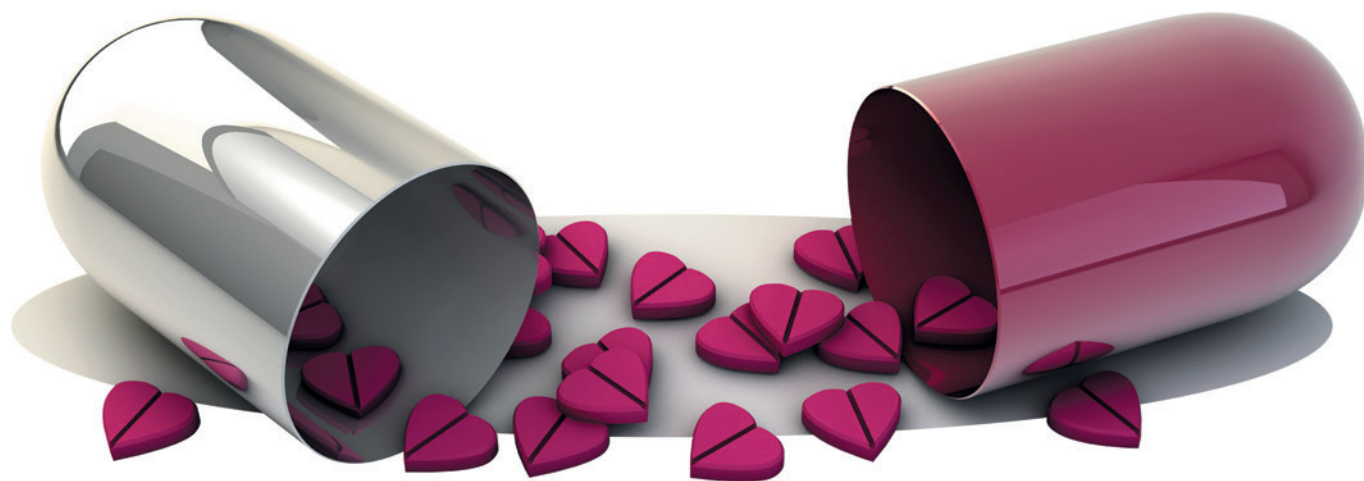
What is the best career advice that you have given or received?

They are one and the same: maintain work–life balance. The 24–7 culture of always answering e-mail and working through the night is counterproductive. I tell my students that working 12–15 hours a day does not equal a *Nature* paper; being smart about which experiments you pick will get you high-profile publications. When people are happy and stress-free, they can be creative and explore new areas. ■

INTERVIEW BY VIRGINIA GEWIN

This interview has been edited for length and clarity.

“When you’ve found something that excites you, don’t be afraid to let it guide you into the unknown.”



ALL, ALONE

Comfort comes.

BY TIM CASSFORD

It's hard to say when the voices start. It's not like they're silent one second and there the next. There's a gradual shift between the two states, I suppose. Sometimes it's only when you stop to think clearly that you notice they're there. Or that they've gone, and the world is silent again.

The pills help. I know they help and so I take them, but then everything's ok, so why am I taking any pills? Am I sick? It goes like this, round and round and round. Sometimes I wish it would end, that things would just be ok, and that would be it, finished, like a good book. But life isn't like a book, never mind a good one. It just goes on and on and on, slowly getting quieter and quieter, until it's only when someone stops to think clearly that we can see that it's gone.

So this is what I do, as often as I can remember: after I come into the house, and the doors *shush* behind me, I go and sit on the edge of the sofa bed, and I close my eyes, and I listen. Really truly listen. And I can hear the gentle *thub thub* of blood as it pulses through me. And I can hear the tiny *creak* in my neck as I move my head from side to side. I can hear the distinct hums of the refrigerator, the air conditioning, the air filters and the computer screen. The susurrus of my life. But nothing else.

The voices have stopped.

I think of the tablets, and I bite down on my thumbnail. It was healing well. I go over to the computer and I start playing some games. Messages flash up at the bottom of the screen, my online friends. Sometimes I reply to them, but not often. Everyone knows

they're not real people, only ghosts of a computer program to try to convince you that you exist, that people care for you, that your life has worth beyond your ability to contribute to the economy. Everyone knows that they're not real, but who is everyone? I try to think of the last time I saw someone in the flesh, but the memory peters out, elusive as love.

The clock on the display wall catches my eye as its numbers silently shift upwards. I used to hate the clock, resent its silent plodding. You can't get rid of the clock, only change its size and style. For a while I shrunk it down as small as it would go, but then I kept thinking it was a fly or a bug on the wall, and that was even more distracting. The last thing I need is to be seeing flies that aren't there. So now it does its impotent best to attract my attention by being inconspicuous. It's half past two. I have no idea which.

I try to do some work. I check my mail to see if my manager has noticed any change in my output, but no. There are several polite reminders noticing that I haven't taken my pills in, I count back the dates, five days now. The first few messages look like generic circulars, the tone of the last two is more pressing, more urgent. Am I sick? Do people get sick so quick?

I get up and stretch and yawn. The clock moves its hands much more gracefully. I go over to the refrigerator and take out my cold box of medication. I scan the barcode through and the pack pops open. I roll the pill out into my hand and it sticks to it awkwardly. I hadn't

realized I was sweating. I swallow the pill down and reach for the glass of water already waiting for me. There's no bitterness.

Someone once told me that drug companies would do their best to name their new medications with as many Xs, Ys and Zs in as possible. People would think they worked better if they couldn't pronounce the names. Or maybe I read it somewhere. What a world.

These pills work, everyone knows it. It's only a problem when you forget why you need them, when you're not sick; when you think you're well.

It's hard to say when the voices start. There's a shift, a gradual shift, and little by little you notice how much more comfortable everything is, like the whole world is just that much better. Like drinking hot chocolate on a crisp, cold day, or relaxing into a hot bath, or drinking a glass of fine wine, or reaching the end of a good book.

I try to remember a time before the pills came along, before they were necessary, before we all needed to hear the voices, but I can't. Maybe we spoke to each other; maybe we were each other's voices, each propping the other up. But who would do that?

When the voices come, they are a gentle whisper in my ear, a soft rustling of leaves, a faint birdsong. Gradually they take form, and I'm happy to wait. They're speaking to me. They're for me. I listen. Tears of happiness form at the corners of my eyes.

"You are loved." ■

Tim Cassford is a doctor and lives and works in West Sussex. None of the problems with the NHS are his doing. Probably.

ILLUSTRATION BY JACEY

nature

INDEX 2015

GLOBAL

NATURE, VOL. 522, NO. 7556 (JUNE 18, 2015)

COVER ART: ALISAIR MACDONALD

The Nature Index is a unique database that tracks affiliations in research publications in a select group of scientific journals. The Index can provide an indicator of high-quality research contributions from institutions, countries, regions and disciplines. In this Global Nature Index supplement, we present a snapshot of the Index for the calendar year 2014.

We have grouped countries into nine regions. The strongest performances come, not surprisingly, from North America, North & West Europe, and East & Southeast Asia. In fact, these three regions accounted for 91% of the Index's weighted fractional count (WFC), a metric that apportions credit for each article according to the affiliations of the contributing authors.

Papers from across the natural science disciplines contribute to the Nature Index: chemistry, life sciences and physical sciences each represent about one-third of the total, with earth and environmental sciences accounting for less than 10% (due to the interdisciplinary character of research, some articles count in more than one category; as a result, the total adds up to more than 100%). As the Global Overview (page S2) shows, there are some striking differences in strengths between regions. For example, North American institutions (page S4) as a group are strong contributors in the life sciences. By contrast, almost 90% of

the contribution from Central & South Asia comes in chemistry or the physical sciences.

The Index also provides insights into how scientists team up with colleagues from other regions. Contributions of researchers from regions that lack a strong scientific infrastructure often result from collaboration with better-resourced colleagues in better-resourced parts of the world. Indeed, the highest level of collaboration was found in Africa (page S28), where scientists' contributions to Nature Index papers were almost three times more likely to occur in papers with researchers from other regions than were contributions from North American scientists.

Funding is a big driver of publishing performance. For example, Israel's GDP ranks 37th globally, but it placed 17th for WFC in the 2014 Index. Much of that imbalance comes from investing in science and technology: Israel put 3.9% of its GDP into science and technology, a higher percentage than any other country.

The Nature Index 2015 Global helps us start to more deeply explore the relationships that have an impact on high-quality research output.

Mike May
Guest Editor

Herb Brody
Supplements Editor

CONTENTS

- S2 OVERVIEW**
A world of achievement in graphics
- S4 NORTH AMERICA**
Overwhelmingly dominant, but funding curtailed
- S10 NORTH & WEST EUROPE**
Strong performance from big collaborators
- S14 EAST & SOUTHEAST ASIA**
Chemistry at the fore as China's output soars
- S18 CENTRAL & EAST EUROPE**
Russia's lead unassailable despite turmoil
- S20 AUSTRALASIA & PACIFIC ISLANDS**
Funding cuts for unsettled leaders of region
- S22 WEST ASIA**
International projects promise improvements
- S24 CENTRAL & SOUTH ASIA**
Brain drain hits results as top minds lured away
- S26 LATIN AMERICA & CARIBBEAN ISLANDS**
Enormous universities yield patchy results
- S28 AFRICA**
Focus on disease, but desperate shortages
- S30 GUIDE TO THE INDEX**
How to get the most out of the data
- S34 TOP 100 COUNTRIES**
- S42 TOP INSTITUTIONS**

EDITORIAL: Herb Brody, Michelle Grayson, Mike May, Rebecca Dargie, Victoria Kitchener. **EDITORIAL SUPPORT:** Nobuko Miyairi, Larissa Kogleck. **ART & DESIGN:** Wesley Fernandes, Alisdair Macdonald, Kate Duncan, Chris Gilloch. **WEB & DATA:** Bob Edenbach, Olivier Lechevalier, Yuxin Wang, Naomi Nakahara, Masamichi Wada, Jyoti Miglani, Akiko Murakami, Takeshi Ouchi, Maxime Fontaine, Jennie Pao, Jörn Ishikawa. **PRODUCTION:** Sue Gray, Karl Smart, Ian Pope, Robert Sullivan, Chandler Gibbons. **MARKETING:** Hannah Phipps. **SALES:** Yuki Fujiwara, Janet Cen. **PROJECT MANAGER:** Anastasia Panoutsou. **ART DIRECTOR:** Kelly Buckheit Krause. **PUBLISHING:** Nick Campbell, Richard Hughes, David Swinbanks.

NATURE INDEX 2015 GLOBAL

The Nature Index 2015, a supplement to *Nature*, is produced by Nature Publishing Group, a division of Macmillan Publishers Ltd. This publication is based on data from the Nature Index, a website maintained by Nature Publishing Group and made freely available at natureindex.com.

Nature Editorial Offices
The Macmillan Building
4 Crinan Street,
London N1 9XW, UK
Tel: +44 (0)20 7833 4000
Fax: +44 (0)20 7843 4596/7

CUSTOMER SERVICES

To advertise with the Nature Index, please visit natureindex.com/support
feedback@nature.com
Copyright © 2015 Nature Publishing Group.
All rights reserved.

GLOBAL OVERVIEW

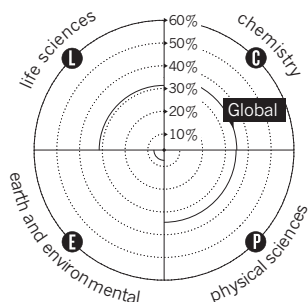
Three regions — North America, North & West Europe, and East & Southeast Asia — produced 91% of the overall 2014 output (WFC) in the Nature Index.

TO EACH THEIR OWN

Relative to its overall WFC, each region shows a unique subject distribution in the Nature Index. North America is extremely strong in the life sciences, whereas contributions from Central & East Europe and West Asia are predominantly in the physical sciences. East & Southeast Asia are strong in chemistry. North & West Europe and Australasia & Pacific Islands split their contributions relatively evenly amongst these broad subject areas.

Research output by subject

The graphics on the map show the proportion each subject area contributes to a region's overall WFC*.



*Subject areas can overlap, so the total percentage may exceed 100%.

57,501

The total number of 2014 articles in the Nature Index.

North America
WFC: 19,425

The United States produced 38% of the total WFC in 2014, although it only places 10th in the world for research and development (R&D) funding as a percentage of gross domestic product (GDP).

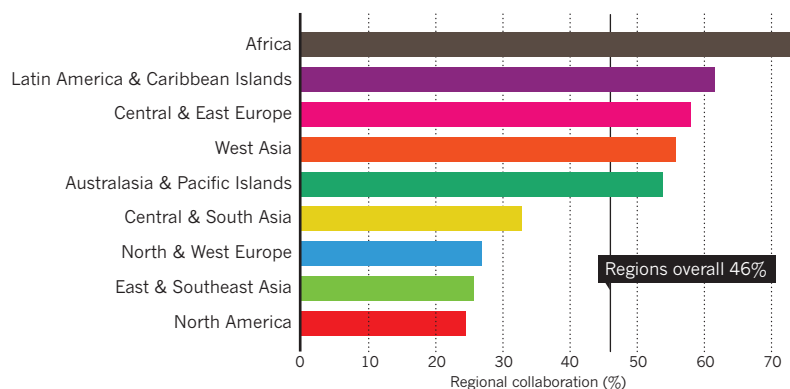
Germany came third globally for output in the Index with a 2014 WFC of 4,019.

Latin America & Caribbean Islands
WFC: 574

Although Brazil came 23rd in the world for WFC, it led that category for the Latin America & Caribbean Islands region, and it also invested the most in R&D as a percentage of GDP.

REGIONAL COLLABORATION PATTERNS

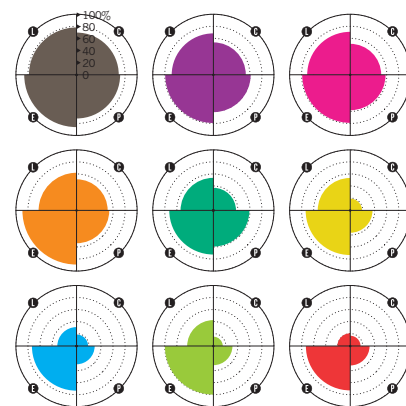
Most regions collaborate extensively with each other. African researchers are particularly active in forming connections with their counterparts in other regions, collaborating on over 70% of all their output in the Nature Index. The three heavy-weights — North & West Europe, East & Southeast Asia and North America — show the most regionally independent signature in their approach to collaboration.*



*Bars represent the proportion of a region's overall output in the Index (AC) stemming from collaborative efforts with other regions.

ENVIRONMENTAL COLLABORATIONS RULE

International collaboration rates differ not only across regions, but also across disciplines. In particular, researchers in the earth and environmental sciences reach out internationally.*



*Graphs represent the proportion of a region's overall output in the Index (AC) in each subject area stemming from international collaborative efforts.



Regions

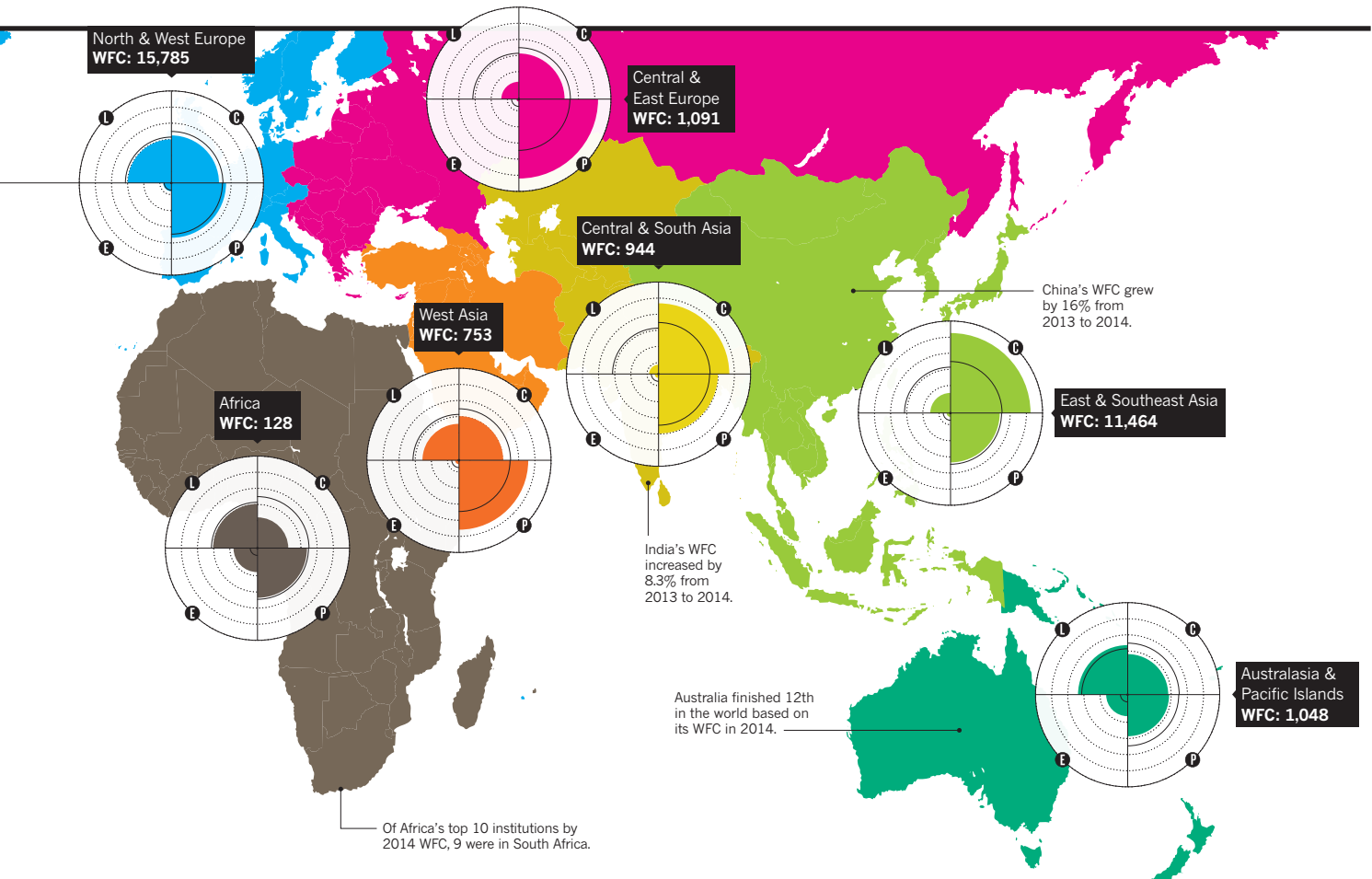
- North America
- Latin America & Caribbean Islands
- North & West Europe
- Africa
- Central & East Europe
- West Asia
- Central & South Asia
- East & Southeast Asia
- Australasia & Pacific Islands

Acronyms

AC: article count
(number of papers)

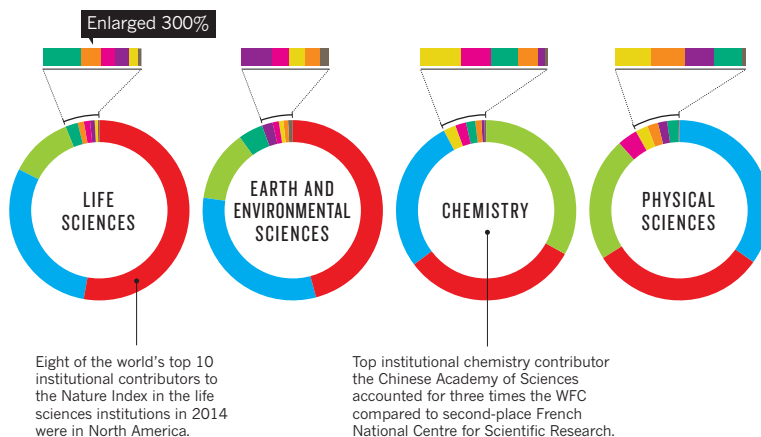
FC: fractional count
(apportions article count for each contributor affiliation)

WFC: weighted fractional count
(applies a weighting to FC to correct imbalance in number of astrophysics papers)



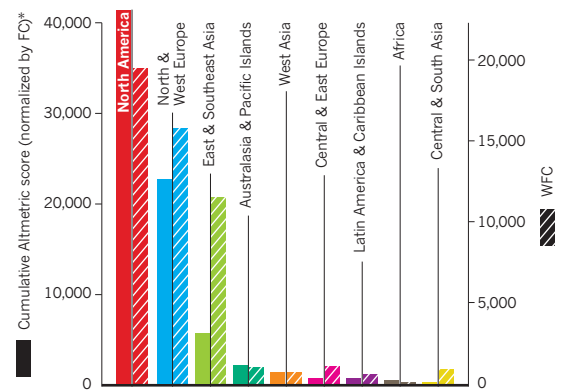
SPREADING THE SUBJECT SPECIALTIES

Each subject area in the Index shows a unique regional contribution pattern according to WFC. Three regions — North America, North & West Europe, and East & Southeast Asia — account for most of the WFCs across all disciplines.



GOING VIRAL

In general, a region's WFC correlates with its total Altmetric score. The exception is in East & Southeast Asia, where researchers might not publicize their work as well as scientists from other regions.



* Cumulative Altmetric scores were divided by FC for each region to account for the actual contribution of a region to a particular Altmetric score.

North America

This region includes lots of strong institutions — from government agencies to universities — but curtailed funding raises concerns for the future.

ARTICLE COUNT (AC): 28,378

FRACTIONAL COUNT (FC): 21,430

WEIGHTED FRACTIONAL COUNT (WFC): 19,425

North America remains the world's most dominant region for high-quality scientific output in the Nature Index, with a weighted fractional count (WFC) of nearly 19,500. The gap is getting narrower, however, between North America and East & Southeast Asia thanks to China, which is a distant second to the United States but with a rapidly increasing number of publications. Although the two countries that make up the North America region — the United States and Canada — enjoy substantial federal funding for scientific research, that source has been constrained in recent years and is not expected to grow significantly in the foreseeable future.

Almost half the region's output in the Index is in the life sciences, representing a greater share of total science output than in the rest of the world. In the United States, much life science research is financed by the National Institutes of Health (NIH), a government-funded agency. The NIH is the country's largest non-defence funder of research and the largest biomedical research agency in the world. The agency, however, has seen a reduction in purchasing power by a fifth over the last dozen years as budget increases have failed to keep pace with inflation. Canada, meanwhile, continues to place emphasis on life sciences through the Canadian Institute of Health Research. The government's most recent strategy for science and technology

innovation put life sciences and health as one of five priority areas, with particular focuses on neuroscience, ageing, regenerative medicine and biomedical engineering.

North America is one of the most self-sufficient regions when it comes to published papers, and its rates of collaboration are lower than the global aggregate in every subject area. Of all the North American articles that include researchers from more than one country, 11% are within the region, stemming from cooperation between the United States and Canada.

“WE’RE LEAVING GREAT STUFF ON THE CUTTING ROOM FLOOR, BECAUSE WE HAVE TO PRIORITIZE.”

The United States is the collaboration partner of choice for most of the world's countries. Both China and South Korea partner with US researchers for half of all their international collaborations. The United States is also the number one collaborator for Canada, as well as for several countries from every region.

Of the total WFC for North America, 4.5% came from articles published in either *Nature* or *Science*, a higher percentage than any other region except for Africa — but that continent's

4.7% arises from a WFC in those journals of only 6, while for North America the total is 870.

INTERNATIONAL CHALLENGER

The United States' WFC in the Nature Index is 17,936, a drop of 3.5% from the previous year. Although with only two years of data it's difficult to assess the significance of that change, its position as the lead country for high-quality research could soon be in jeopardy. The country with the second largest output in the Index is China, whose WFC of 6,037 is roughly a third of the US count. That number, however, is a 16% climb for China from 2013.

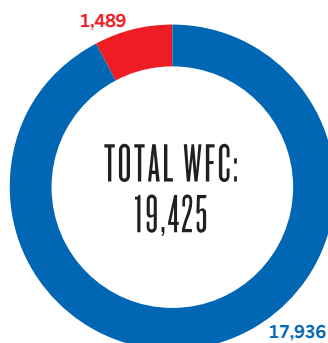
US National Science Foundation (NSF) senior analyst Carol Robbins says China is not the only contender experiencing meteoric growth. “The article output of developing countries has been growing faster than the European Union and the US since at least 2000,” Robbins says. But she cautions, “Growth in the developing world is going to look more rapid than growth in the developed world, because they're starting from a lower base.”

The United States is most productive in life sciences, which represents 44% of its 2014 output. But it is in chemistry and physical sciences, each accounting for nearly 30% of output, where the scientific giant enjoyed most international acclaim last year. The 2014 Nobel Prize in Chemistry, for example, for developing a super-resolution fluorescent microscope,

NORTH AMERICA ANALYSIS

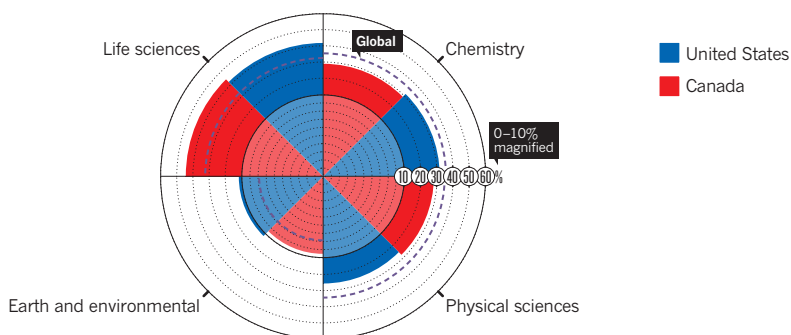
Countries' weighted fractional count (WFC)

Canada accounted for less than 8% of the region's WFC, leaving a lopsided advantage to the United States.



Relative subject area distribution

Both Canada and the United States focus on the life sciences, generating more than 40% of their outputs in this area.*



*Each slice represents the proportion each subject area contributes to a country's overall WFC. Subject areas can overlap, so the total percentage may exceed 100%.

went to Eric Betzig of Howard Hughes Medical Institute and William Moerner of Stanford University, along with Stefan Hell from Germany's Max Planck Society.

Even as its scientists produce award-winning results, US research spending continues to be curtailed, with steady erosion in federal funding for science since 2004, according to Matt Hourihan, director of the R&D Budget and Policy Program for the American Association for the Advancement of Science. Between 2010 and 2015, non-defence spending for research dropped by 5%, adjusted for inflation. And although President Barack Obama has proposed a 7% rise in spending for 2016, "that is a much bigger increase than Congress is likely to grant this year," Hourihan says.

Since the federal sequester cuts in March 2013, which imposed comprehensive reductions in federal spending, there's been a modest recovery in such expenditures, Hourihan says. He adds that spending is expected to grow only moderately until 2021. "The pool of funding from which science can draw is going to remain very tight for the next few years, unless Congress acts to change it," he says.

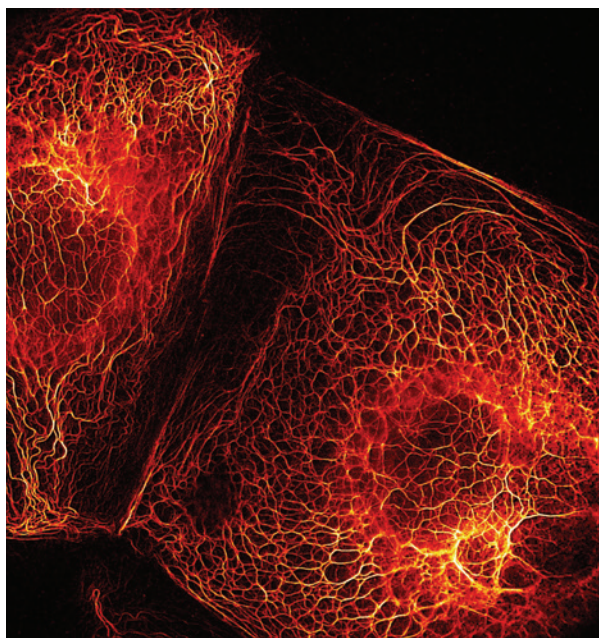
The NIH has had a turbulent couple of decades financially. Its budget doubled between 1998 and 2003 but has dropped by a fifth since then — though it bounced back from a 2013 low. With a little more money in its budget, the percentage of grant applications the agency approved rose somewhat to 18.1% in 2014 from 16.8% in 2013, according to NIH deputy director for extramural research Sally Rockey, although that doesn't compare to rates above 30% in the late 1990s and early 2000s. "We're leaving great stuff on the cutting room floor, because we have to prioritize," adds NIH principal deputy director Lawrence Tabak.

The long-term consequences of this budget

uncertainty are worrying, warns Shirley Tilghman, former president of Princeton University and a past participant in NIH advisory groups. The growth in NIH funding until 2003 encouraged many young people to enter the biomedical field, she says, but now there's not enough funding to support their research careers. "There are too many people chasing too little money in the US," she says.

Tilghman, along with three other luminaries — Bruce Alberts, former president of the

postdocs have been treated as a source of cheap labour for biomedical research, Tilghman says many of them don't manage to start their own lab until their late 30s. And the competition for scarce funding can make scientists more conservative in their thinking, she says, because they want to give funding agencies what they're expecting rather than propose a new idea whose outcome is uncertain. "Over time, the quality of science is going to go down because people are too scared to take big risks," she says.



Parallelized RESOLFT nanoscopy reveals the protein keratin in living cancer cells in amazing detail.

National Academy of Sciences, Marc Kirschner of the Harvard Medical School, and former director of the National Cancer Institute Harold Varmus — wrote a perspective in the *Proceedings of the National Academy of Sciences* last year calling on the country to revamp its biomedical research system. Tilghman argues in the paper that, for some years, graduate students and

CANADA'S EYE ON COMPETITION

Canada's WFC (1,489) is essentially unchanged from last year. That maintains its place as the country with the 7th largest WFC in the Index, way above its 37th place ranking in terms of population, according to data from the United Nations. Like the United States, Canada's output in the Nature Index is strongest in the life sciences, which accounts for about 40% of the country's total WFC. The nation's WFC of 33 in either *Nature* or *Science* is 2% of its WFC in 2014. Yet in Canada too there are worries about the nation's future competitiveness in the global research landscape, says Paul Dufour, an adjunct professor at the University of Ottawa's Institute for Science, Society, and Policy. "The state of science and technology innovation in this country is in decline," he says. Among his concerns is a fall in research investment. According to the Organization for Economic Co-Operation and Development (OECD), Canada's gross

domestic expenditure on research and development dropped as a percentage of GDP from 2.0% in 2001 to 1.6% in 2013, which is below the OECD average of 2.4%. "We're one of the lowest in the OECD and it's still dropping, so it's not a good picture over all," Dufour says.

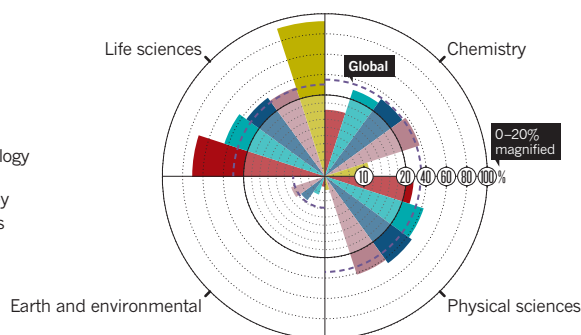
Canada weathered the recession of 2008–2009 fairly well due to a strong banking system,

ANDRIY CHMYROV/STEFAN HELL/MAX PLANCK INSTITUTE FOR BIOPHYSICAL CHEMISTRY

NORTH AMERICA ANALYSIS

Top 5 institutions' relative subject area distribution

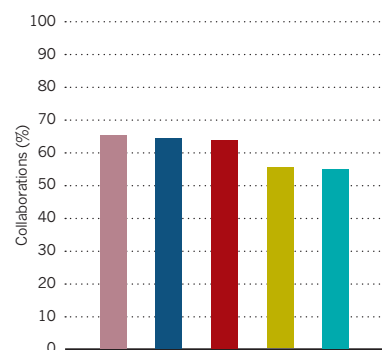
Harvard University, the region's leader by WFC, publishes about 70% of its output in the Index in life sciences.*



*Each slice represents the proportion each subject area contributes to an institution's overall WFC. Subject areas can overlap, so the total percentage may exceed 100%.

Top 5 institutions' collaborativeness

Over half of the work from researchers at the top institutions in North America stems from collaborative efforts with domestic and global counterparts.*



*Each bar represents the proportion of an institution's overall output in the index (AC) stemming from domestic and international collaborations.

Dufour says. Nevertheless, the Canadian government has emphasized austerity and has cut spending in all areas. The country's national statistical agency, Statistics Canada, estimated federal spending on science and technology would decline 5.4% in the fiscal year 2014–2015 to about US\$8.5 billion, continuing a downward slide since it peaked in 2010–2011. Prime Minister Stephen Harper's office, however, prefers to focus on a total of about US\$8.75 billion in new investments in science, technology and innovation since 2006. Its priority areas, besides health and life sciences, are environment and agriculture, energy and natural resources, information and communications technologies, and advanced manufacturing, ranging from aerospace and robotics to three-dimensional printing and nanotechnology.

One major government initiative is the Canadian High Arctic Research Station, costing around US\$113 million and billed to open in 2017. The country hopes that the station — above the Arctic Circle in Cambridge Bay, Nunavut — will attract international scientists and strengthen Canada's position in polar research.

In 2014, the government created the Canada First Research Excellence Fund. Starting with almost US\$40 million this year, the fund proposes to provide about US\$1.2 billion over the next decade to fund university research that creates “long-term economic advantages for Canada”, according to its mission statement. This funding effort has been controversial, however. In a December 2014 editorial, the *Toronto Star* suggested, “It's a significant investment fully undermined by a disastrous caveat: to access the funding, applicants will have to show that they have private-sector co-funders.” Such a focus on research with commercial applications means sacrificing the basic research that leads to future innovations, undermining Canadian science in the long run, the paper argued. And this is not the only sign that Canada's government wants closer ties between research and industry. The



This Canadian icebreaker takes scientists to study the polar environment, and in 2017 the country's High Arctic Research Station should open.

previous year, Canada's National Research Council had its mission refocused to support research that would help Canadian business be more competitive.

“YOU MUST DEMONSTRATE THAT YOU HAVE A WELL-KNOWN OR WELL-DEFINED MARKET OUTCOME.”

“You have to demonstrate that you have a well-known or well defined market outcome,” Dufour says of the new emphasis. “Some of the grass roots science community are quite vocal on the problems this may create.” For example, Evidence for Democracy is a non-profit group that formed in response to funding cuts, and is urging the government to return to a focus on more basic science.

TOP SCHOOL IMPACTS

US universities are well represented among the world's leading research institutions in the

Index, with Harvard, Stanford, the Massachusetts Institute of Technology (MIT) and the University of California, Berkeley all among the top 10 institutions by WFC. Canada's top school, the University of Toronto, is 21st.

Top US institution Harvard University, with a WFC of 865, has the second largest output overall in the Index — behind the Chinese Academy of Sciences, which has a WFC of 1,308. While the Chinese Academy's output improved by 8% over 2013, Harvard was up only 1.4% on the previous year. Nevertheless, this was in the face of declining income: Harvard's sponsored research budget dropped to US\$812 million in 2014, down US\$9 million from the year before. The decline was due to a 5% cut in federal awards, to US\$605 million, though that was partly offset by a 12% rise in contributions from foundations and businesses. The university has about 2,400 faculty members, plus 10,400 academic appointments in its affiliated teaching hospitals. There are approximately 6,700 undergraduates and 14,500 graduate and professional students.

The school's greatest strength is in the life sciences, which accounted for nearly three-quarters of its output. In fact, it's the Index's world leader in that field, with a WFC of 610, nearly double the 320 of the second-placed NIH. Harvard's life sciences output is boosted through its affiliation with more than a dozen leading research and teaching hospitals in the Boston area, including the Dana-Farber Cancer Institute and the Joslin Diabetes Center, as well as with independent research organizations such as the Whitehead Institute for Biomedical Research. For instance, researchers at the Broad Institute of MIT and Harvard contributed to Harvard's total with a December paper in *Nature Genetics*, “Comprehensive Variation Discovery in Single Human Genomes.”

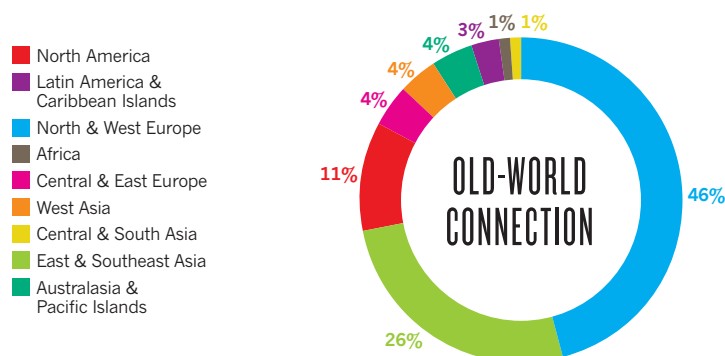
Harvard's WFC of 75 is also the highest of contributions to *Nature* and *Science*. The university is also in the top 10 for output in both physical sciences and chemistry, but comes in at 35th for earth and environmental sciences.

Stanford, with the second-highest output in

NORTH AMERICA ANALYSIS

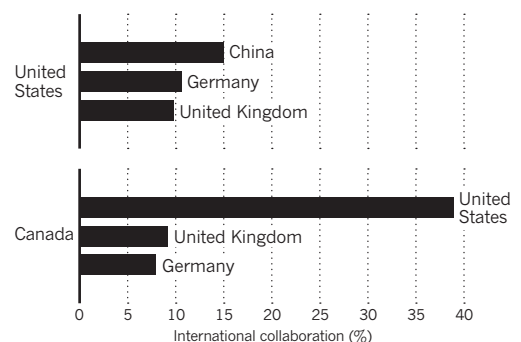
International collaborations

Scientists in North & West Europe make up nearly half of the collaborators with North American researchers.



Top 3 country collaborations

When Canadian scientists collaborate outside the country, it is with researchers from North America nearly 40% of the time.*



*Bars represent international collaboration rates between countries as a proportion of the total output (WFC) stemming from international collaborative efforts.



Stanford's SLAC relies on 284 microwave pulse generators in its particle accelerator, which is more than three kilometres long.

North America and fifth globally, had a WFC of 539, a drop of 2% from 2013. The school's sponsored research budget was US\$1.33 billion, down US\$21 million from the previous year. Approximately 82% of that support comes from the federal government, which actually increased its funding for most of the university's research; the major drop was caused by a \$37 million cut in funds for the SLAC National Accelerator Laboratory.

Despite its larger budget — mostly attributable to SLAC — Stanford is similarly sized to Harvard, with 2,118 faculty members in 2015,

7,018 undergraduates and 9,118 graduate students. At Stanford, life sciences and physical sciences each represent about 40% of its contributions, with chemistry covering about 30% and earth and environmental science 5%. (Nature Index assigns some articles to more than one field of science, so the totals don't come to 100%.) Stanford contributes heavily to the *Journal of High Energy Physics*, in part because of its work on the ATLAS detector at the Large Hadron Collider (LHC) in Switzerland. This journal published upwards of two dozen Stanford-authored papers on ATLAS-related work in 2014. But, despite its funding cut, SLAC shines as well. In a November paper in *Nature*, "High-Efficiency Acceleration of an Electron Beam in a Plasma Wakefield Accelerator," SLAC researchers showed how they might build a cheaper, more compact particle accelerator than the kilometres-long LHC. The paper garnered quite a bit of attention in news media, blogs and Twitter, according to Altmetric, which looks at the social-media impact of journal papers.

With the third highest WFC in the United States and sixth globally, MIT also made a splash in particle physics at the LHC. More than 50 MIT researchers and students were involved in a different LHC instrument, the compact muon solenoid, and helped confirm the discovery of the long-sought Higgs boson, which underpins why objects have mass. A June 22, 2014 paper, "Evidence for the Direct Decay of the 125 GeV Higgs Boson to Fermions," attributed to hundreds of researchers, including 31 at MIT, scored higher for public attention than any other paper ever in *Nature Physics*, according to Altmetric data.

MIT distributes its contributions fairly evenly — 42% in physical sciences, 37% in life sciences, and 34% in chemistry, though only 7% in earth and environmental sciences. That makes it much stronger than the country as a whole in physical sciences and chemistry. Its sponsored research budget of US\$1.28 billion includes US\$739 million in Department

of Defense funds for its defense research arm, Lincoln Laboratory.

The University of Toronto — with about 7,000 full-time faculty, 2,700 postdocs and research associates, 15,000 graduate students and a science budget of almost US\$1 billion — is Canada's largest research institution. Its WFC for 2014 rose 5% to 269. The country has two other schools in the top 100: McGill at 68 and the University of British Columbia at 70. Like Harvard, the University of Toronto has an affiliated network of several local hospitals, and its largest contribution is in life sciences, where it comes 9th worldwide.

SHARING SCIENCE, GOING BIG

Sharing the cost of research and working across disciplines is becoming common, as expansive and expensive projects such as the LHC draw on resources. "There's generally more collaboration, because of technology, because science is so complex," says the NSF's Hill.

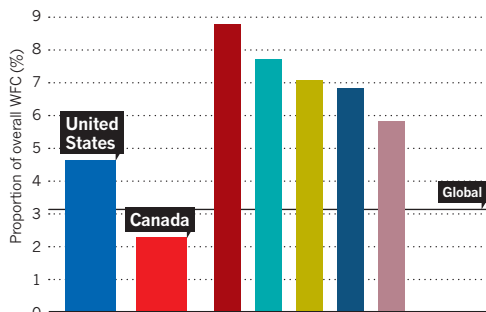
The NIH announced two large initiatives in 2014, both of which will bring together large numbers of people from different institutions. The Accelerating Medicines Partnership, which aims to develop new treatments for Alzheimer's disease, diabetes and autoimmune disorders, has a budget of US\$230 million over five years and will entail partnerships between NIH, pharmaceutical companies and non-profit groups. The Brain Research through Advancing Innovative Neurotechnologies (BRAIN) initiative seeks to derive a more complete understanding of the human brain. It received US\$46 million in 2014 to start a 12-year project that will involve more than 100 researchers from several countries.

Despite the promise of these bold projects, the NIH's Rockey still has worries over continued budgetary constraints. "At some point there's going to be diminishing returns, simply because we don't have the funds to keep up," she says. "We have every reason to be optimistic about the future scientifically. We just have to get our house in order." ■

NORTH AMERICA ANALYSIS

Contributions to Nature and Science

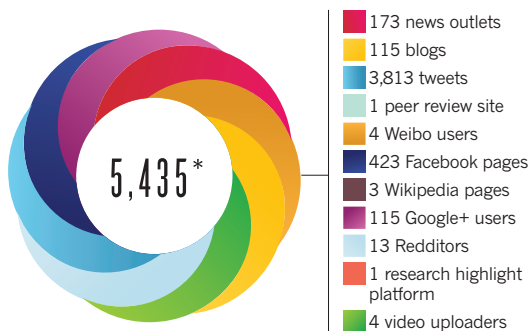
Harvard University surpasses the global level by more than 2.5 times in this metric of high-profile publishing.*



*Each bar represents an institution's or country's relative contribution to publications in *Nature* and *Science*, given as a proportion of its overall WFC.

Social impact

Not surprisingly, the world's number one Altmetric score in 2014 came from an article about social networking.*



*Altmetric score correct as of 21 May 2015. Experimental evidence of massive-scale emotional contagion through social networks. *Proceedings of the National Academy of Sciences*. DOI: 10.1073/pnas.1320040111.

North & West Europe

Strong spending and recruitment keep countries in this region near the top of the world's output in the Index, and scientists from universities collaborate more with their neighbours.

ARTICLE COUNT (AC): 25,137

FRACTIONAL COUNT (FC): 18,382

WEIGHTED FRACTIONAL COUNT (WFC): 15,785

North & West Europe accounted for about 30% of the publications in the Nature Index based on the weighted fractional count (WFC), second only to North America. Moreover, this region scored highly on the Index's WFC in all four categories: first in physical sciences, second in life sciences and earth and environmental sciences, and third in chemistry.

Germany (number 3 in the global Index) put in the region's strongest performance, edging the runner-up United Kingdom (number 4 globally) by nearly 25% according to WFC. In addition, Germany ran away with the region's leading WFCs in chemistry and physical sciences, topping the second-placed United Kingdom by about 40% in the former and 60% in the latter. But the UK led the region in the life sciences, according to the Index, with a WFC about 10% higher than Germany. And both the UK and France surpassed Germany in earth and environmental sciences.

PURCHASING PRESTIGE

Germany's scientific strength is cemented by consistently high research spending — more than US\$100 billion annually and the world's fourth highest. Data from the Organization for Economic Co-operation and Development (OECD) show Germany's public and private research spending as 2.9% of GDP in 2013, which is a full percentage point higher than

the European average. "We are aware that this is not the case in all European countries, and this is a clear competitive advantage not only in Europe but also in comparison to the US," says Rolf Zettl, managing director of the Helmholtz Association, Germany's largest publicly funded scientific research organization.

"THEY LIKE TO HAVE THAT EUROPEAN FUNDING EVEN IF IT COMES WITH A LOT OF RED TAPE."

Several European countries increased public research spending during the financial downturn that began in 2007. "By keeping up the activity level they helped mitigate the fall in business R&D expenditure," says Gernot Hutschenreiter, head of country innovation policy reviews at the OECD. However, he adds, "this buffering is now over and public expenditure is either stable or falling." Even the German government's pledged 3% annual increases from 2016 until 2020 are a reduction from the current 5%.

In the UK, R&D spending was only 1.6% of GDP in 2013 — considerably lower than Germany and also France, which spent 2.2%. Alex Halliday, vice-president of the UK's Royal

Society, says, "I think government does understand that we have to spend more money in the future, but it's quite a hard thing to do at the same time as you are having to make massive cuts elsewhere." Still, the quality of UK science remains high and it leads the region in WFC for papers published in *Nature* and *Science* with 128, or 3.9% of its total WFC — compared to the global aggregate of 3.1%.

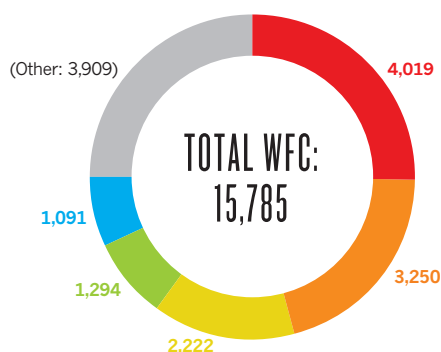
In part, Halliday attributes the UK's high-standard papers in the Index to its intensely competitive research auditing system, the Research Excellence Framework (REF), most recently published in 2014 and used to determine each university's funding allocation. Halliday, who returned to the United Kingdom after working in Switzerland and the United States, says, "I gradually became a convert because I began to see what it was achieving for the UK that other countries didn't have." He adds, "It has forced universities to think about how to build research strength in a very competitive way." UK excellence is often hampered by an ageing university infrastructure, and cannot compare to the kind of facilities available at the top universities in Switzerland, Halliday says.

Switzerland (4th in the region by WFC and 8th globally) spends around 2.9% of GDP on research, and generally outperforms relative to its small size; its 2014 WFC for *Nature* and *Science* papers was 44. The Netherlands (6th in the region, 14th globally) spent a lower percentage,

NORTH & WEST EUROPE ANALYSIS

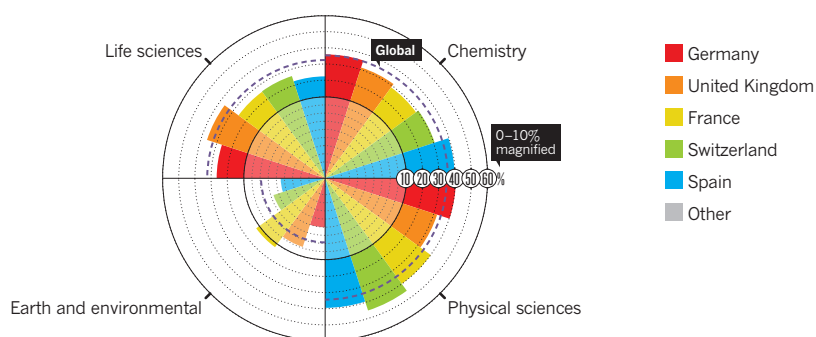
Countries' weighted fractional count (WFC)

Germany and the United Kingdom accounted for 46% of this region's output, and France made up another 15%.



Relative subject area distribution

Most of the top producers in this region published similar outputs in all categories except earth and environmental sciences.*



*Each slice represents the proportion each subject area contributes to a country's overall WFC. Subject areas can overlap, so the total percentage may exceed 100%.



Scientists supported by the French National Centre for Scientific Research (CNRS) explore subatomic physics.

1.98% of its GDP in 2013, but its WFC of 29 in *Nature* and *Science* ranks it in the top five. The country has concentrated funding on a small number of talented individuals, says molecular geneticist Hans Clevers, president of the Royal Netherlands Academy of Arts and Sciences. “There is a lot of emphasis on publication in top journals, but there are ongoing discussions asking if the country is emphasising the top 5% talent too much,” he says.

According to the Index, scientists in North & West Europe collaborate more with their immediate neighbours than any other region; 51% of all their international collaborations occurred within the region in 2014. When they do team up with researchers from further afield, it is usually with scientists in the United States. European Union (EU) funding partly explains the high collaboration level within the region. Although the EU research budget is only 5–7% of the total national budgets, Katrien Maes, chief policy officer of the League of European Research Universities, says universities see EU projects as a prestigious supplement to national funding. “They like to have that EU funding even if it is difficult to get and comes with a lot of red tape,” she says.

INSTITUTIONAL IMPACTS

By WFC rankings, all three top institutions in the Index for this region are national research organizations. The French National Centre for

Scientific Research (CNRS) takes the region’s top spot. Its overall WFC in the Nature Index is 762, which is third globally — behind the Chinese Academy of Sciences at 1,308 and Harvard University at 865. Regionally, Germany’s Max Planck Society and the Helmholtz Association of German Research Centres follow CNRS.

“MAX PLANCK LOOKS FOR THE SMARTEST SCIENTISTS AND PROVIDES THEM WITH PARADISE.”

CNRS employs more than 11,000 research staff with civil servant status and runs 10 fully funded labs. The 2014 annual budget of more than US\$3.5 billion represents a quarter of French public civilian research spending. Publications skew toward the physical sciences, with 41% in this field, compared to the global aggregate of about 35%. A 2014 OECD report called into question the “stultifying preeminence” of the CNRS in French research and labelled it a major handicap. The report noted slow reform of a bureaucratic system. “France is still in a transition and there is a kind of hybrid model now, which is very complex, and this creates difficulties,” says Hutschenreiter. Funding pressures are also an issue, and French

scientists protested a 1% cut to government’s 2015 research budget.

Nearly 30% of Germany’s overall WFC comes from papers published by scientists at the Max Planck Society and Helmholtz Association. The centres are run independently, with full scientific autonomy. The Max Planck Society consists of 83 facilities and in 2014 employed a total of 5,516 scientists, with an overall budget of more than US\$1.75 billion, coming jointly from federal and state budgets. Since its founding in 1948, the MPS has produced 18 Nobel Prize winners and this reflects the society’s ethos of researcher-centred excellence. “The Max Planck position is to look for the smartest and brightest scientists worldwide and provide them with paradise,” says Zettl. The Max Planck has 2,950 papers in the Nature Index, which represents at least half a paper per scientist. It shows particular strengths in physical sciences, with 46% of all its overall WFC in the Index in this area and 4.7% of its publications in *Nature* or *Science* — considerably higher than the 2.6% for the CNRS.

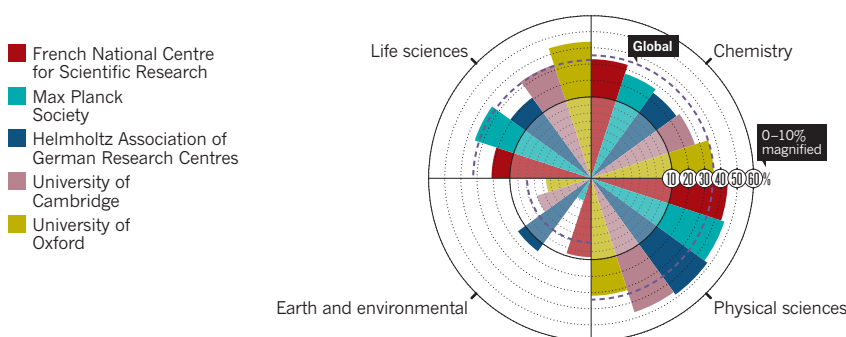
The newer and lesser-known Helmholtz Association was founded in 2001 from a collection of 18 independent research centres. The Helmholtz association has a WFC of 440, with 49% in the physical sciences — perhaps to be expected given its inclusion of Germany’s Deutsches Elektronen-Synchrotron (DESY) located in Hamburg and Zeuthen, near Berlin. As well as exploring particle physics, the facilities’ three large particle accelerators provide extremely powerful X-ray radiation used to study new materials and biomolecular processes. Helmholtz is also strong in earth and environmental sciences: 16% of its WFC is in these fields, almost double the global aggregate.

The Helmholtz Association provides programme-centred strategic research on pressing problems in energy, the environment, health and transport. Its nearly US\$3 billion 2015 budget comes mainly from the federal government with a 10% contribution from local states, plus more than US\$1 billion from

NORTH & WEST EUROPE ANALYSIS

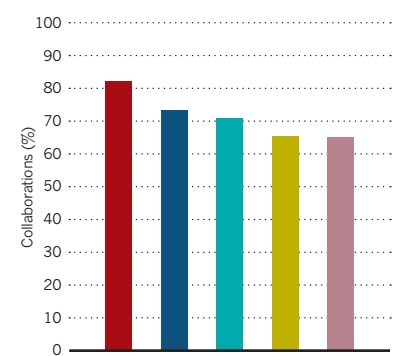
Top 5 institutions’ relative subject area distribution

The region’s top institution, the French Centre for Scientific Research, published 77% of its WFC in chemistry and physical sciences.*



Top 5 institutions’ collaborativeness

The percentage of collaboration by this region’s leading institutions resembled the order of output.*



additional research grants from other sources, such as EU programmes.

UK UNIVERSITIES EXCEL

For the rest of the region's top-10 institutions, the UK's university sector dominates, including the University of Cambridge, the University of Oxford, Imperial College London and University College London (UCL). Switzerland's top universities, the Swiss Federal Institutes of Technology in Zurich (ETH Zurich) and Lausanne (EPFL), take the other spots. Maes says the strength of these institutions is linked to their autonomy, particularly in relation to academic recruitment. "Research is a global competition and our universities are in the search for talent," she says.

Cambridge and Oxford are the oldest universities in the English-speaking world, established in 1209 and 1096, respectively. Based on the WFC of all institutions globally, Cambridge is ranked 9th in the Index and Oxford 11th, with WFCs of 403 and 356. Papers published in *Nature* and *Science* account for 5.0% of Oxford's WFC and 4.5% of Cambridge's — both significantly higher than the global aggregate of 3.1%.

The subject spread of Cambridge publications is close to the global aggregate with a slightly stronger performance in the physical sciences. One 2014 article in the Index came from Cambridge materials scientist, Jason Robinson, and colleagues. This article in *Nature Communications* describes a breakthrough in the field of spintronics, a technology that could help create super-fast computers, processing data using the electron property 'spin' rather than charge. The paper provides the first evidence that superconducting materials, which carry current without losing energy, can be made into data processing devices using a layered magnetic material containing the element holmium. Robinson says one of Cambridge's strengths is the sense of a collective way of working. He says, "When I first arrived there wasn't as much interaction between departments, but now I feel there is a lot of collaboration going on."



The University of Cambridge ranked ninth among the world's top institutions in the Nature Index.

"RESEARCH IS A GLOBAL COMPETITION AND OUR UNIVERSITIES ARE IN THE SEARCH FOR TALENT."

Oxford shows a stronger performance in the life sciences, with 43% of its WFC in this area, compared to a regional aggregate of the WFC of about 30%. Overall the university has the highest research income of any UK university. It has been particularly successful in bringing in funding for new research centres, particularly at the interface between physical sciences and biomedicine, such as Oxford's Institute for Biomedical Engineering, where engineers and clinicians work together to develop medical devices and technologies in areas including medical imaging and regenerative medicine. "That interface is going to generate new tools, new devices, new technology, new drugs, and

that's where we need to invest in the future," says Halliday. Oxford is also strong in bioinformatics and statistical genetics, illustrated by a *Nature Communication* in the Index, from a large interdisciplinary team led by Ian Tomlinson from Oxford's Wellcome Trust Centre for Human Genetics. The communication reports the whole genome sequencing of bladder cancers and uncovered genetic mutations that provide potential drug targets as well as markers for diagnosis. These results are part of a wider genomics collaboration, with the technology company Illumina, studying the genomes of 500 patients with hard-to-treat diseases.

Unlike most Swiss universities top institution ETH Zurich receives 80% of its budget of more than US\$1.6 billion from the federal government to support 5,000 scientific staff. ETH shows strength in physical science and chemistry, which make up about 40% and 37% of all publications. Although only 22% of its 2014 WFC was in life sciences, that is an increase from the 2013 level of 16%. In 2012 ETH opened a new department of health science and technology, which takes a systemic and multidisciplinary approach to health, from the molecular scale to social context.

ETH's strength in chemistry is not surprising given the county's Basel-based pharmaceutical industry, in particular, Roche, which is eighth in the region's institutions publishing in *Nature* and *Science*. In 2014, Roche outspent all other pharmaceutical companies with a global R&D budget of US\$9 billion, and is the only company represented in the top-10 of any region. The company has many collaborations with leading academic institutions, and it "strongly encourages our scientists to share their findings in both peer-reviewed publications and presentations at congresses," says John Reed, head of pharma research and early development.

This region's educational and research institutes and industry promise a strong output of scientific research for years to come. ■

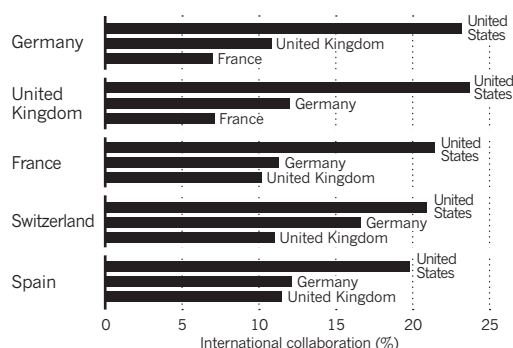
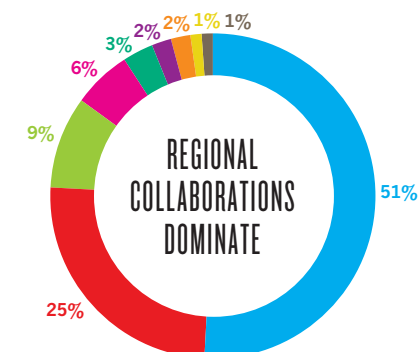
NORTH & WEST EUROPE ANALYSIS

International collaborations

When scientists in this region collaborate, it is usually with scientists from other countries in the region.

Top 3 country collaborations

When collaborating outside the region, scientists largely work with colleagues from the United States.*



*Bars represent international collaboration rates between countries as a proportion of the total output (WFC) stemming from international collaborative efforts.

East & Southeast Asia

While remaining strong in chemistry and physical sciences, buoyed by China's growing contribution, the region embarks on collaborations that could extend its reach.

ARTICLE COUNT (AC): 16,277

FRACTIONAL COUNT (FC): 12,092

WEIGHTED FRACTIONAL COUNT (WFC): 11,464

BASFE

East & Southeast Asia was the third largest regional contributor to the Index behind North America and North & West Europe. Its 2014 WFC of 11,464 is a 6% increase from 2013. China, the second-ranked country in the global Index, increased its WFC by 16% over 2013. In comparison, North America's WFC decreased by 4% and North & West Europe's dropped, too, but by less than 1%.

"China is growing much, much faster than the US," says Derek Hill, a science resources analyst at the National Science Foundation (NSF). "And China has been investing enormous resources in education and research and development."

Overall, the scientific output from East & Southeast Asia reflects the economic status of the region. The combined GDP of these countries makes up about 22% of the global GDP. Likewise, this region accounts for 22% of the Nature Index's weighted fractional count (WFC) for 2014. For comparison, North America accounts for about 24% of the world's GDP, yet it produces 38% of the Index's total WFC.

One area in which East & Southeast Asia dominates the Index is the output of chemistry. The region's chemistry WFC in 2014 of 6,062 makes up one-third of the global output in this field. Physical sciences represent the region's second highest area of publishing output in the



In Nanjing, China, BASF and Sinopec collaborate to increase the production of agricultural chemicals.

Index, but only reach about the global aggregate in terms of the percentage of the region's total WFC. The region's contributions to the Index in both life sciences and earth and environmental sciences are about half the equivalent proportions that those areas contribute to the global aggregate WFC. Among articles in the 2015 Index, scientists in East & Southeast Asia collaborate with scientists in other countries in about 25% of projects.

In earth and environmental sciences, though, the scientists in the region collaborate 80% of the time. All of the regions in the Index collaborate most in this subject category.

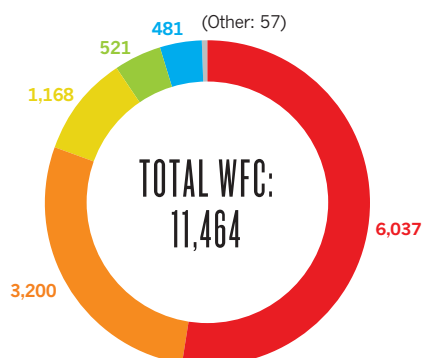
THE TRADITIONAL TOP THREE

China dominates East & Southeast Asia's Index performance: its WFC of 6,037 accounts for exactly half of the region's publishing output. Second-placed Japan, with a WFC

EAST & SOUTHEAST ASIA ANALYSIS

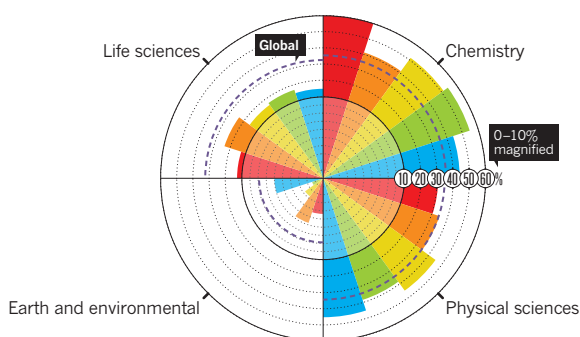
Countries' weighted fractional count (WFC)

In combination, China and Japan produced more than 80% of this region's contribution to the Index.



Relative subject area distribution

More than 80% of the publications from the Index explore chemistry or physical sciences.*



*Each slice represents the proportion each subject area contributes to a country's overall WFC. Subject areas can overlap, so the total percentage may exceed 100%.



BASF-YPC Company's low-density polyethylene plant produces 400,000 metric tons a year.

other leading countries in the region. Of Japan's WFC from 2014 articles in the Index, 41% and 35% come from chemistry and physical sciences. For South Korea, chemistry and physical sciences provide 51% and 46% of its WFC.

When scientists in East & Southeast Asia collaborate internationally, they tend to look to the west. In fact, 45% of collaborations are with scientists from North America. The second most likely source of collaborators, accounting for 28% of them, is North & West Europe. Other scientists from the same region only make up 18% of international collaborations, and other parts of Asia add only a few percent of the collaborators.

“CHINA WILL REMAIN THE DOMINANT GLOBAL FORCE FOR CHEMICALS BEYOND 2020.”

CUTTING-EDGE INSTITUTIONS

By far the region's top institutional contributor to the Index is the massive Chinese Academy of Science (CAS), which takes the number one spot in the world. Its WFC of 1,308 — up by 8.1% since 2013 — is more than 50% higher than second-placed Harvard's and accounts for 2.6% of the global output. Like China in general, CAS published strongly in chemistry and physical sciences, with WFCs of 771 and 413 leading the world in these disciplines. One example of CAS's physical sciences prowess can be found in a 2014 *Nature* article by two CAS researchers and 11 other authors. The paper shows that single-atom layers of graphene, as well as of hexagonal boron nitride, have unexpectedly high permeability to protons at room temperature. This permeability makes such monolayer crystals “promising candidates for use in many hydrogen-based technologies,” the authors conclude.

of 3,200, makes up another quarter. Third-placed South Korea was responsible for 10% of the region's WFC. Contributions from other countries split up the remaining 15%, with none of them providing even 5% of the output in the Index.

The top three country contributors to the Index from this region are very strong in high-quality chemistry and physical sciences research. Chemistry accounts for a whopping 60.3% of China's WFC; the global aggregate is 35.6%.

China's research in chemistry covers applied and basic science. In the March *Journal of the American Chemical Society*, for example, scientists from China's Wuhan University and

Central China Normal University described the synthesis and crystal structure of a non-linear optical material that resists damage from lasers. The Index articles for 2014 also include a January paper in *Inorganic Chemistry* in which scientists from China's Jiangsu University revealed new magnetic properties of iron compounds.

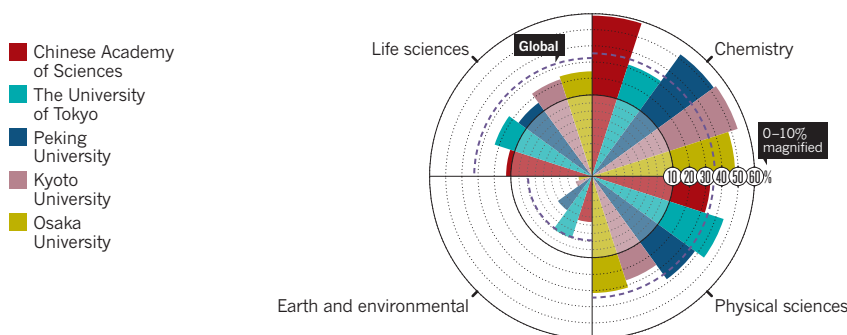
In addition to extensive publishing on chemistry in 2014 data in the Index, US-based IHS Chemical, which offers industry marketing information and technical expertise, says that Asia — especially China — “will remain the dominant global force for chemicals beyond 2020.”

Similar research concentrations exist in

EAST & SOUTHEAST ASIA ANALYSIS

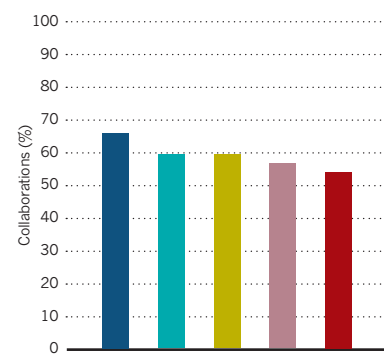
Top 5 institutions' relative subject area distribution

Chemistry articles made up more than half of this region's output, and the Chinese Academy of Sciences led this category globally.*



Top 5 institutions' collaborativeness

The Chinese Academy of Sciences published the most but collaborated the least among the leading institutions.*





Scientists at the Chinese Academy of Science, which has the highest institutional WFC in the Index, explore basic and applied science, including clinical research.

Japan's University of Tokyo came in second amongst the region's institutions. Its WFC of 456 placed it at number 7 globally. Like CAS, this university published largely on chemistry and physical sciences, with respective WFCs of 144 and 205.

Relatively speaking, this university puts more emphasis on the life sciences than CAS, with a WFC of 99. In addition, about 8% of the University of Tokyo's WFC goes to articles in earth and environmental sciences, which is about the proportion of the global aggregate WFC in this area.

For example, University of Tokyo earth scientist Masumoto Yukio and his colleagues reported in *Nature* in 2014 on the impact

of global warming in currents in the Indian Ocean. They noted that ongoing changes will continue to drive more extreme weather.

The region's number three institution, China's Peking University, generated a 2014 WFC of 292, and came in 17th globally. Like CAS and the University of Tokyo, Peking University focuses on chemistry and physical sciences.

In addition, this university relies on collaborations to expand its strengths in other areas. For example, Peking University Clinical Research Institute (PUCRI) maintains an ongoing collaboration with New York-based Medidata, which provides cloud-based, life science solutions.

Many companies in China, who still keep

track of clinical trials on paper, will be able to utilize Medidata's electronic systems. Takeru Yamamoto, Medidata's managing director of Asia-Pacific region, says, "Our goal remains to enhance the speed and operational efficiencies of clinical studies, so that we can enable life science companies to bring new therapies to patients more quickly — both from the local market and around the world."

"OUR GOAL REMAINS TO ENHANCE THE SPEED AND EFFICIENCIES OF CLINICAL STUDIES."

SPREADING EXPLORATIONS

China contributed 147 articles in *Nature* and *Science* in 2014 — the most for the region, just ahead of Japan with 137. Some of China's output that landed in these high-profile publications came from areas outside its typical focus on chemistry and physical sciences.

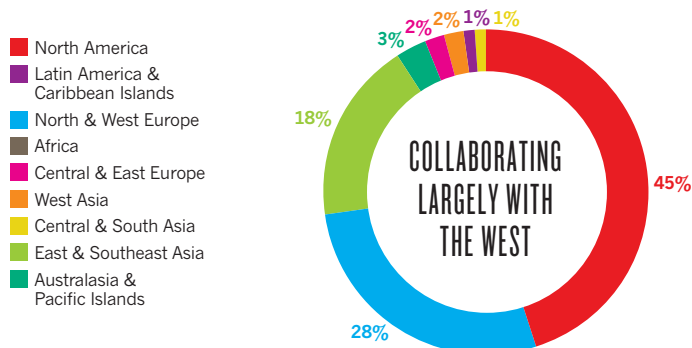
In the October *Nature*, for example, a group of researchers from various institutions in China and one in the United States, reported on the best methods of crop management to produce more food with fewer environmental consequences. In addition, some of these articles combine China's strength in chemistry with other areas. As an example, a July *Nature* article from researchers at the Chinese Academy of Sciences and the University of Science and Technology of China explored the biochemistry of lipids in search of clinical targets for fighting bacterial infection.

These researchers, as well as others across East & Southeast Asia, are thus using their foundational strength in chemical sciences to study not only that area but a host of related ones. Such work is fuelling the remarkably robust surge in the region's scientific research, as reflected in a rising WFC in the Index. ■

EAST & SOUTHEAST ASIA ANALYSIS

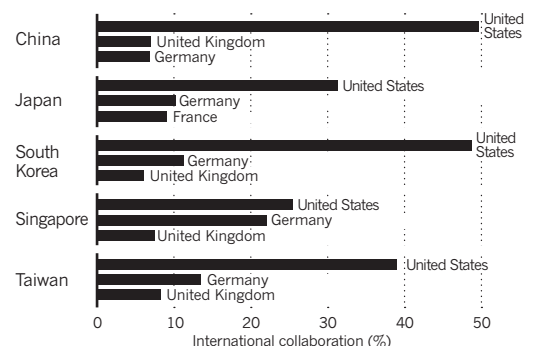
International collaborations

Nearly half of the region's collaborators work in North America, and more than a quarter come from North & West Europe.



Top 3 country collaborations

In China, Japan, South Korea and Taiwan, papers with US coauthors account for more than 30% of such international collaborations' WFC.*



*Bars represent international collaboration rates between countries as a proportion of the total output (WFC) stemming from international collaborative efforts.

Central & East Europe

Social change and economic stagnation create challenges for this region's biggest countries, but some of the smaller ones are shining.

ARTICLE COUNT (AC): 3,275

FRACTIONAL COUNT (FC): 1,377

WEIGHTED FRACTIONAL COUNT (WFC): 1,091

Change and upheaval were the two main forces at work in this region in 2014. To the south, Greek scientists hope for positive outcomes from the election of the new anti-austerity government. To the east, Russia's science is still in turmoil in the wake of economic sanctions, while its funding structure is undergoing reform. Despite this, the country still led the region in 2014 as measured by the Nature Index's weighted fractional count (WFC). Overall, as with last year's Index, the regional output is heavily dominated by the physical sciences, reflecting the emphasis placed on military and applied science by the former communist regimes, and the effects of ideology on life science research.

Maintaining second place in the region and 24th globally by WFC is Poland, the 7th largest economy in the European Union (EU), and one of its fastest growing. Poland comes second in the region (behind Russia) in physical sciences and chemistry WFCs and second in life sciences (after Hungary). Like other countries in the region, Poland also scores highly on collaborativeness; with 60% of its output coming from international collaborative efforts it far surpasses the United States (26%), Germany (47%) and the United Kingdom (50%) in forming international collaborations.

Poland is still working to reform its academic and research institutions, and to increase the economic impact of its scientific efforts. To

these ends, three key policy developments have taken place in the past year, says Maciej Żylicz, president of the not-for-profit Foundation for Polish Science. The first is a drive to improve research quality, by changing how institutions will be assessed. "The system is very flat at the moment," says Żylicz. "Poland would like to give more money to the best institutions." As of January 2015, the government is making its funding

"UNIVERSITIES CANNOT COVER ALL NEEDS WITHOUT WORLDWIDE NETWORKING."

decisions based entirely on performance.

The second big development is opening up Poland's R&D infrastructure to make it more international. That entails attracting students from abroad, changing the law to make it easier to appoint foreign nationals to academic posts and making the appointment process more open to competition. Thirdly, the government is trying to forge links between science and business, with a new law being passed that offers firms tax breaks to invest in R&D. The private sector currently accounts for about a third of Poland's R&D effort, says Żylicz. "If we can achieve 50:50, this will be a big achievement."

According to Eurostat, the EU's statistical office, Poland's 2013 R&D spend remained static at US\$3.66 billion, which represents a slight fall as a percentage of GDP from 0.9% in 2012 to 0.87% in 2013, one of the lowest in the EU. The government is, however, committed to raising this to 2% of GDP by 2020, says Żylicz. This means it will have to boost spending by between 10 and 15% per year; the increase for 2015 will be 10%. "We are on a good track," says Żylicz. Funding is also being directed to help Polish scientists compile grant applications for Horizon 2020, the EU's research and innovation programme that will offer nearly US\$85 billion of funding between 2014 and 2020.

CHECKING FUNDING SHORTFALLS

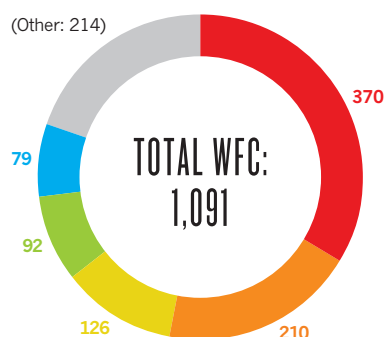
Third in the region, and 27th globally is the Czech Republic, whose 2014 WFC was 6.7% higher than in 2013. Like several of its neighbours, the Czech Republic's output is dominated by physics and chemistry — with 38.1% and 48.2% of its WFC — and these results reflect the country's historical strengths in these fields.

In 2013, the Czech Republic spent US\$3.2 billion on R&D, or 1.91% of its GDP, a slight increase over the 1.88% of 2012. This reflects a general stagnation that has taken place since 2010. The period between 2000 and 2009 was a golden era for Czech science, when the government increased funding by about 10%

CENTRAL & EAST EUROPE ANALYSIS

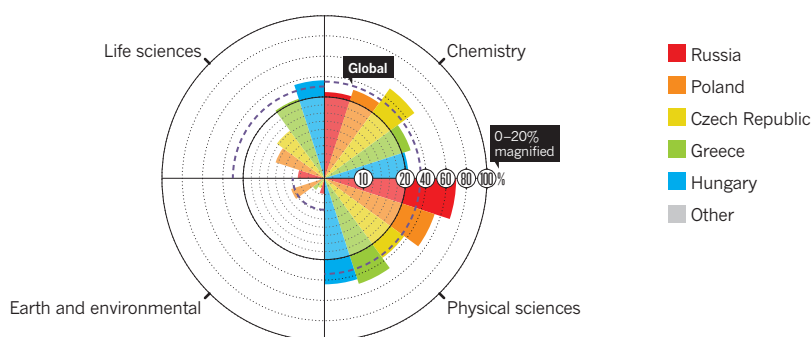
Countries' weighted fractional count (WFC)

The combined publications from Russia and Poland in the Index made up 53% of the region's output.



Relative subject area distribution

Research in the physical sciences is on the forefront of this region's top countries.*



*Each slice represents the proportion each subject area contributes to a country's overall WFC. Subject areas can overlap, so the total percentage may exceed 100%.

each year, says Václav Hořejší, director of the Institute of Molecular Genetics in Prague, and one of five scientists advising the Czech Prime Minister on science and higher education policy. Since then, although the government has maintained an annual spend of about US\$1.07 billion, this represents a decrease in real terms. Worst affected is the Czech Academy of Sciences, whose funding has fallen by some 10% from its 2009 level, says Hořejší.

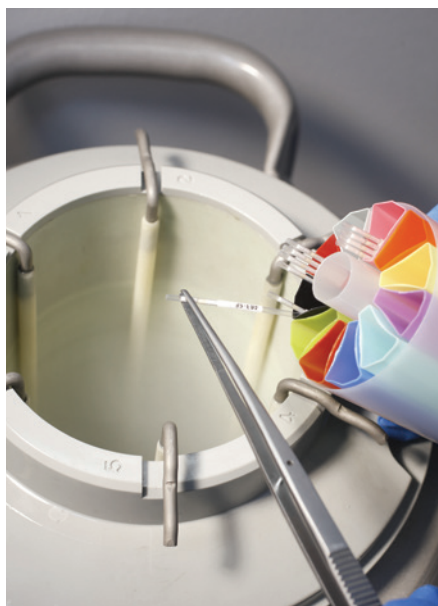
The government-funding shortfall is currently being offset by money from EU regional development funds. From 2007 to 2015, US\$2.13 billion has been invested, mainly in building new research facilities. These include six European centres of excellence and 40 regional centres for research and development. One example is BIOCEV, the Biotechnology and Biomedicine Centre of the Academy of Sciences and Charles University in Vestec. Set to open in September 2015, it will house 400 researchers and five state-of-the-art core facilities. “This is a large-scale activity that will probably greatly change the basic landscape of Czech science,” says Hořejší. The future support and sustainability of these new research infrastructures remains under discussion.

SMALL BUT STRONG

Estonia, with only 1.3 million people, punches above its weight in science. Its WFC for 2014 was 22, an increase of 68% compared with 2013. This is one of the largest WFC increases in the region.

In 2014, Estonia led the region in the proportion of its output published in *Nature* and *Science* — 5% of its WFC, compared to the global aggregate of 3.1%. This included a study in *Nature* about interacting genes in humans. Russia had more papers in these journals (33), but that represented only 1.2% of its WFC. Estonia published 12 articles in *Nature* and *Science* in 2014, the same number as its larger neighbours Poland (12 papers, 0.6% WFC) and Hungary (12 papers, 2.0% WFC).

Estonia is often held up as an example of how



Cryogenic facilities at BIOCEV in the Czech Republic provide cell-line storage for biomedical research.

shrewd planning, tough reform and a robust R&D political framework can transform a country's science base. In the early 1990s, Estonia rearranged its whole research system according to the western model, with its new funding system emphasizing research excellence and competition. In 2001, the country set up a Centres of Excellence in Research programme to promote productivity and international competitiveness, which established 22 centres over successive phases.

The government continues to prioritize R&D funding, says Indrek Reimand, Deputy Secretary for Higher Education and Research at Estonia's Ministry of Education and Research. In 2013, Estonia spent 1.73% of its GDP on R&D. While this is lower than the EU average of 2.2%, government R&D spending tripled between 2001 and 2007, and then doubled between 2007 and 2013, making its R&D spending growth one of the fastest in the world,

says Reimand. Over the past decade, Estonia has also invested heavily in its science infrastructure, refurbishing labs and buildings, and between 2007 and 2013 invested some US\$426 million of EU structural funds in R&D capacity. A quarter of the funding was earmarked for human resource development, such as doctoral training and schemes to promote transnational mobility for researchers and students.

INSTITUTIONS MOVING UP

For individual institutions, the Nature Index reveals that scientists at the University of Tartu coauthored 10 of Estonia's 12 *Nature* and *Science* papers. Several of these involved large, international genomics projects. This reflects the university's policy of developing collaboration partners to create an internationally competitive research infrastructure in genomics and biotechnology, says Marco Kirm, vice rector for Research at the University of Tartu. A cornerstone of this effort is the Geenivaramu, the Estonian Biobank, which is a comprehensive collection of genetic and health information covering 5% of the country's population. It draws collaborators from around the world, such as those involved in identifying genes associated with common diseases. “Universities cannot cover all needs — to have people with advanced knowledge — without worldwide networking,” Kirm says.

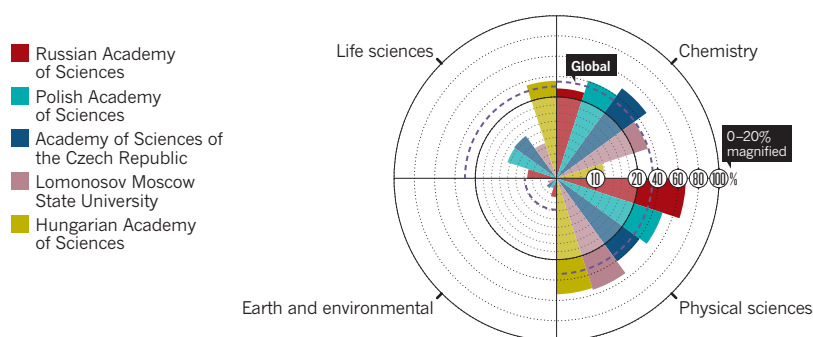
The Academy of Sciences of the Czech Republic, which incorporates 54 research institutes, comes third in the region (after the Russian Academy of Science and the Polish Academy of Science). Its output is heavily skewed toward chemistry (47.6% WFC) and physics (40.2%). Among this region's top institutions, the Hungarian Academy of Sciences puts most emphasis on the life sciences, which accounts for 36.4% of its WFC.

Some commentators see the region catching up with world leaders. Hořejší says, “I think some of our best research institutions are now fully comparable to the good ones in Western Europe.” ■

CENTRAL & EAST EUROPE ANALYSIS

Top 5 institutions' relative subject area distribution

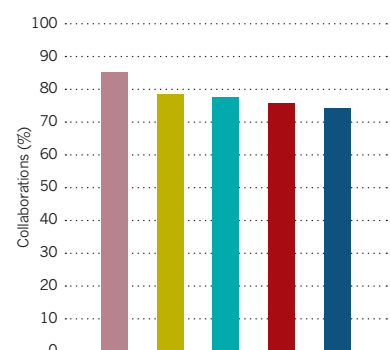
Despite the region's predominant focus on the physical sciences, the Hungarian Academy of Sciences kept its eye on the life sciences, devoting 36% of its overall output to this field.*



*Each slice represents the proportion each subject area contributes to an institution's overall WFC. Subject areas can overlap, so the total percentage may exceed 100%.

Top 5 institutions' collaborativeness

Although Russia's Lomonosov Moscow State University is only the region's fourth highest producer, it collaborates the most.*



*Each bar represents the proportion of an institution's overall output in the Index (AC) stemming from domestic and international collaborations.

Australasia & Pacific Islands

Research is dominated by heavyweights Australia and New Zealand but shifts in science policy on both sides of the Tasman Sea are creating uncertainty about the future.

ARTICLE COUNT (AC): 2,705

FRACTIONAL COUNT (FC): 1,249

WEIGHTED FRACTIONAL COUNT (WFC): 1,048

This vast region dotted with small, developing island states that stretch from the Indian Ocean to Hawaii and down to Antarctica is dominated by the giant landmass of Australia alongside New Zealand. With great variation in landscapes, strong agricultural industries and increasing vulnerability to climate change, these countries have naturally shown a particular focus on earth and environmental sciences. At the same time, life sciences are also an area of strength, well served by government support from Australia and New Zealand, and increasingly a field in which there is cross-border collaboration.

With the largest populations, economies and scientific communities, Australia and New Zealand are the region's ranking leaders in the Nature Index, at 12 and 31 in the world, based on weighted fractional count (WFC) for 2014. Meanwhile, among their smaller island neighbours, where science education and infrastructure remains under-developed, Papua New Guinea has dropped from 91 to 108, Fiji sits at 123, and Tonga at 137. More data will be required to analyse any temporal trends.

Across the region there is ongoing concern about policy changes shifting the emphasis towards input for outcome — allocating research funding on the basis of anticipated impact.

The ramifications are particularly great for

young researchers who some fear are being compelled to choose whether to devote themselves to applied or blue-sky research too early in their careers.

SUCCESS IN SPECIALIZATION

Australia is the region's best Index performer, achieving small increases in both its total article count (AC), up 3% from 2013, and in its weighted fractional count (WFC), up 2%. In contrast, the region's WFC decreased by 1.6% from 2013 data in the Index.

“WE ARE ABOUT TO TAKE EVERYTHING WE HAVE BUILT UP OVER A DECADE AND CRUSH IT.”

This improvement came during a year of uncertainty over science policy, for much of which the country did not have a science minister, and government spending on research and development fell to its lowest level as a proportion of total spending since the early 1980s.

After an outcry and name-calling — including scientists being branded “precious petals” by one minister — the portfolio of minister for science was reinstated days before Christmas and a new Commonwealth Science Council,

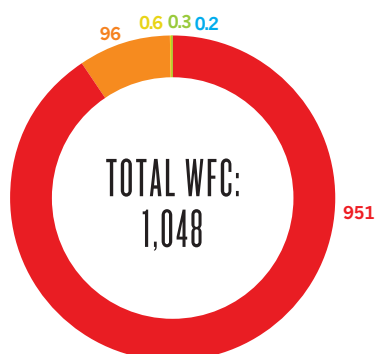
comprising leaders from science academia and industry, was formed to advise the government on science and technology. However, funding for major science infrastructure — including the world-class Australian Synchrotron relied upon for important Australian and New Zealand research in fields as diverse as biomedicine and defence — was kept on hold until well into 2015. “We are about to take everything we have built up over a decade and crush it,” says Australian National University’s Nobel Prize winning astronomer Brian Schmidt of the shortfalls for the country’s science. As recently as February 2014, Schmidt had contributed to a paper published in *Nature* identifying the oldest-known star in the galaxy — a discovery made possible only through the infrastructure-funding scheme. After strong ongoing protest the scheme was extended in the 2015/16 budget. To the dismay of many, however, the additional money to extend the scheme was taken from higher education research funding and is likely to affect the capacity for many university based scientists to continue using the facilities.

In this Index, all but one of the region's top institutions are Australian, but there has been some movement in their rankings. The University of Queensland has maintained its leading position with a WFC of 109, followed by Monash University (103), the University of New South Wales (UNSW; 88) and the Australian

AUSTRALASIA & PACIFIC ISLANDS ANALYSIS

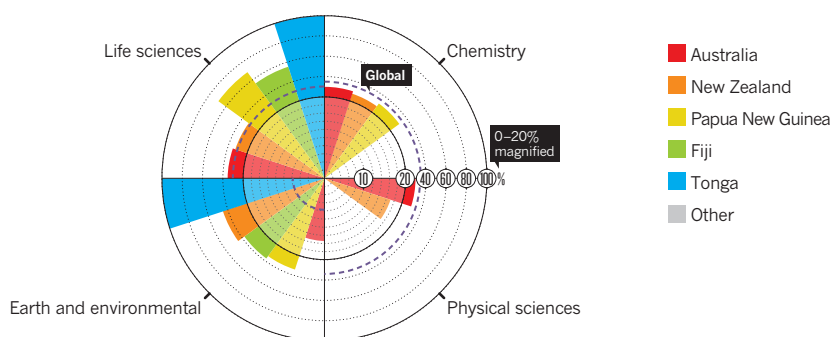
Countries weighted fractional count (WFC)

Australia produced 91% of this region's Index output, and New Zealand provided nearly all of the rest.



Relative subject area distribution

Tonga's seemingly strong focus in earth and environmental sciences and life sciences came from one article attributed to both categories.*



*Each slice represents the proportion each subject area contributes to a country's overall WFC. Subject areas can overlap, so the total percentage may exceed 100%.

National University (ANU; 87). Looking at the total number of publications from each institution, the University of Sydney has slipped from the top spot it held in 2013 Index data, with the ANU achieving 498, to the University of Sydney's 492 and the University of Melbourne's 478. The country's government research organization, the CSIRO, was the only non-university to reach the region's top 10.

Australia's strongest field for publication output is the life sciences, where the country ranks 9th globally. Among the country's institutions, the University of Queensland and University of Melbourne lead strongly in life sciences publications. Their focus is an example of the emerging specialization of the leading institutions in response to increasingly competitive funding regimes.

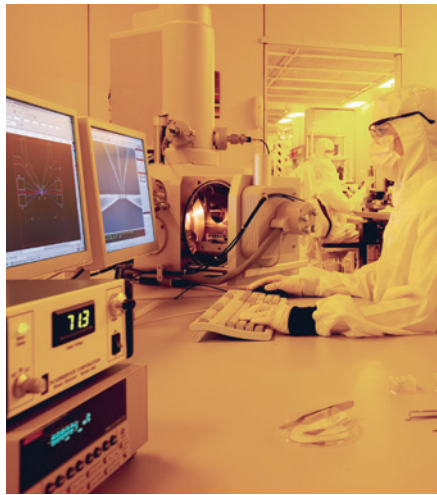
UNSW, by contrast, has established itself as a force in the physical sciences, which account for 46% of the university's publications in the Index. In particular, UNSW has established itself as a hub for quantum computing. "When you have that strength, you can then recruit the best people in the world to come here," says dean of science, Merlin Crossley.

In chemistry, Australia's Monash University produced the highest 2014 WFC in the region, and it also ranked 100th among institutions globally for total WFC.

Crossley expresses apprehension about the direction that research and funding are taking — in particular threatened changes to the country's strong fellowship programmes. There are good government grant provisions for senior researchers, he says. "But for junior researchers, I think it is very tough."

GHOST OF POLICIES PAST

Some of the challenges facing Australian research — uncertain funding and a loss of priority for government — echo those that affected science in New Zealand between 2010 and 2012. For this period, a ministry of science was deemed unnecessary, funding rounds were put on hold for 12 months, and changes were



Electron beam lithography plays a part in developing quantum computers at the University of New South Wales.

made to grants and funding processes that benefitted senior rather than junior researchers. Some scientists attribute New Zealand's fall in the ranking to these shifts. "The kinds of changes that you see are probably not relatable to changes that happened in the last 12 months. We're looking at the impact of the changes in our science sector that happened about five years ago," says president of the New Zealand Association of Scientists, Nicola Gaston.

New Zealand's WFC fell 19% from the 2013 level, pushing it from 28 to 31 in the global rankings. Gaston says that while government funding for New Zealand science has been increasing, the recent results suggest that the emphasis on linking input with outcomes and industry partnership undermines the pursuit of scientific excellence. "There were a lot of concerning things in the last five years and we are now seeing the consequences of those changes," Gaston says. The leading New Zealand institution in the Index, the University of Otago in Dunedin, is among the region's top 10 institutions and has moved up 30 places (to

406) in the global top 500. After Otago comes the University of Auckland (481), Victoria University of Wellington (687) and the University of Canterbury (890).

Thanks to strong funding from government and industry, New Zealand's greatest research strength is in the earth and environmental sciences, where the country ranks 16th globally; these fields account for 37% of the country's WFC. One of the most widely discussed recent pieces of New Zealand-led Antarctic research is an investigation of the effects of waves on sea ice published in *Nature* in May 2014. Led by hydrodynamics scientist Alison Kohout at the National Institute of Water and Atmospheric Sciences, the researchers found that the impact of large waves extends further into an ice shelf than previously thought, potentially affecting stability hundreds of kilometres from the ice edge. This implies that storms and the waves generated therein may play an important role in shaping the extent of sea-ice.

BIG STRIDES FOR SMALL COUNTRIES

Beyond Australia and New Zealand the numbers for research publications are small, but with a similar focus on life sciences and earth and environmental sciences. Among the stand-outs, the government-affiliated Papua New Guinea (PNG) Institute of Medical Research contributed to two of the six Index publications linked to PNG. One paper that looked at complex genetic mechanisms behind immunity to malaria may lead to future treatments.

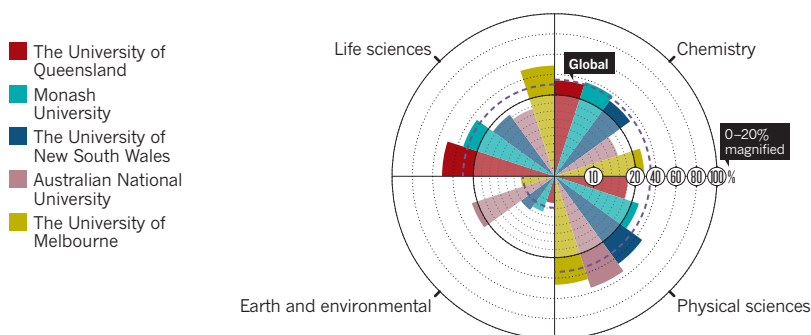
In Fiji, the University of the South Pacific is the only institution whose work features in this year's Index with contributions to two major papers in 2014 — one looking at sea salinity and temperature, and the other at diseased coral.

Scientists and politicians in both Australia and New Zealand are making concerted efforts to increase collaboration with research powerhouse, China. In the face of such changeable fortunes for local science, these links are likely to provide growing support for Australasia & the Pacific Islands. ■

AUSTRALASIA & PACIFIC ISLANDS ANALYSIS

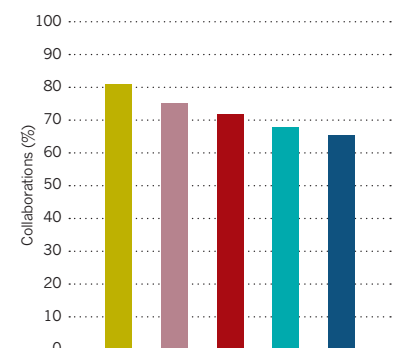
Top 5 institutions' relative subject area distribution

More than half of the University of Queensland's articles addressed issues in the life sciences.*



Top 5 institutions' collaborativeness

The University of Melbourne's scientists collaborated on about 80% of its articles.*



West Asia

International projects — including an advanced particle accelerator and educational facilities — bolster this region's focus on chemistry and physical sciences.

ARTICLE COUNT (AC): 1,927

FRACTIONAL COUNT (FC): 853

WEIGHTED FRACTIONAL COUNT (WFC): 753

This is a region divided. Ongoing conflict has stopped some countries from sponsoring the development of science or maintaining safe facilities for researchers — but not all. A number of nations, notably Israel and Turkey, have made inroads into supporting growth of their scientific communities or are adopting plans to do so.

Israel remains the region's leading scientific country and the only nation in the Index to break into the global top 20 based on weighted fractional count (WFC). Israel's WFC of 492 was significantly higher than both Turkey, second in the region with 79, and Saudi Arabia at 76. This success has been driven in part by high spending levels on R&D, which in Israel is 3.9% of GDP — second only to South Korea, according to 2014 figures by United Nations Educational, Scientific and Cultural Organization (UNESCO).

Israel's R&D spending is even driving high-tech work. In 2014, for example, an international team — led by Israeli scientists — reported in *Nature Nanotechnology* on a new DNA-based structure that might be used in electronics. Although this work remains in its early stages, the authors concluded: "Our results pave a way towards the implementation of DNA-based programmable circuits for molecular electronics."

Israel's Weizmann Institute is the top institution in the region with a WFC of 143, slightly below its 2013 figure. It has a relatively evenly spread publication count across disciplines

— producing the highest outputs in life sciences and physical sciences, followed by chemistry. Globally this institute is 64th based on WFC, and it is 21st on the Index's list of institutions around the world for WFC in *Nature* and *Science*.

However, despite these impressive statistics, research at Weizmann — and indeed within the country as a whole — is lacking in one key area. "While Israel invests significantly in R&D, particularly in information and communication technologies, the investments in biotech might be lagging behind," says Michal Neeman, vice

"YOU CAN'T JUST IMPORT RESEARCH BY HIRING A FEW EXPATRIATES WHO ARE WORLD RENOWNED."

president of the Weizmann Institute. The institute is working on filling in these gaps with its recently established Nancy and Stephen Grand Israel National Centre for Personalized Medicine. Created in 2013 with US\$150 million in donations, according to Neeman, the centre aims to lead Israel's research in genomics, protein profiling, bioinformatics and drug discovery. Its steering committee comprises leaders from several universities in Israel, which helps facilitate research collaborations across institutions.

Overall, Weizmann lags behind the region in collaboration. Whilst around half of its articles are the result of collaborative efforts, other institutions in the region are even more prolific in establishing research networks to drive publications.

BIG SPENDERS STILL COLLABORATE

Other countries in the region are also making significant R&D investments. Turkey's investment has grown every year since 1995, and is now just under 1% of GDP. Since 2000, Turkey also has developed national science, technology and innovation policies, including the establishment of the Turkish Research Area (TARAL) in 2004. This provides a forum for the country's stakeholders in research and innovation, including public agencies, universities, non-governmental organizations and the private sector. Such investments and policies appear to be paying off: the number of researchers employed and papers published are both on the rise. In this Index, Turkey ranked 36, having overtaken Iran and Saudi Arabia.

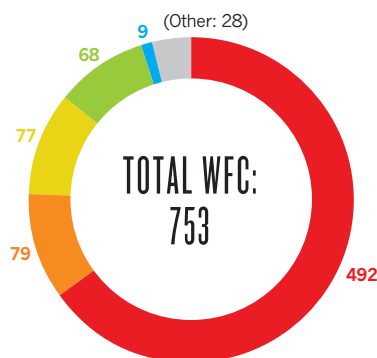
To further extend Turkey's science capabilities, the government encourages international collaboration — to this end the Scientific and Technological Research Council of Turkey (TÜBİTAK) provides fellowships for foreign PhD students and postdoctoral scientists.

Strong research output requires more than big investments. Saudi Arabia has poured billions into new universities, particularly with

WEST ASIA ANALYSIS

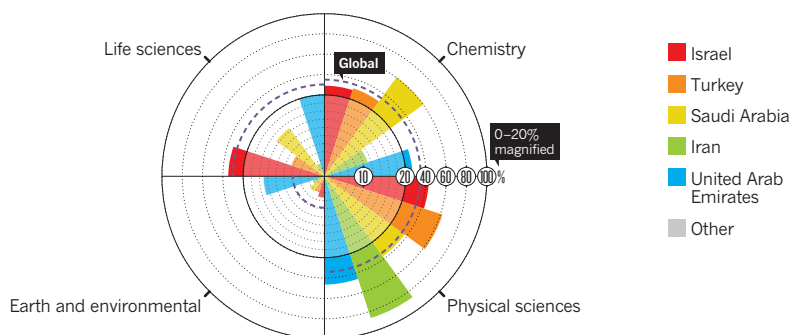
Countries' weighted fractional count (WFC)

Region-leader Israel contributed 65% of the output, and Turkey, Saudi Arabia and Iran added around 10% each.



Relative subject area distribution

Four of the top five countries published at least 40% of their Index articles in the physical sciences.*



*Each slice represents the proportion each subject area contributes to a country's overall WFC. Subject areas can overlap, so the total percentage may exceed 100%.

the 2009 opening of King Abdullah University of Science and Technology (KAUST), which is believed to have a US\$15 billion endowment, and has attracted top talent for research. From 2012 KAUST has increased its article output in the Nature Index by 40%. Given its more moderate increase in WFC over the same time period, it seems that KAUST researchers are actively contributing more to collaborative papers than working in isolation.

Performance in the Nature Index is also greatly dependent on collaboration — and this is where the Arab states are doing well. Saudi Arabia reaches out extensively to other countries for scientific collaboration, with 79% of its output being the result of international collaborations. Israel and Turkey collaborated internationally on 46% and 59% of their papers, respectively, showing that scientists in Saudi Arabia collaborate much more than their colleagues in neighbouring countries. This high collaboration rate, however, may be due in part to the practice at some universities — although not KAUST, which opposes such an approach — of bringing in foreign researchers for a short amount of time to add a local affiliation to papers.

Even higher international collaboration rates apply to other wealthy Gulf countries that have invested in higher education, such as the United Arab Emirates (UAE) and Qatar. Both countries host campuses for foreign institutions, including New York University, Weill Cornell Medical College, Northwestern University and Paris-Sorbonne. The UAE's AC is 4.3 times its FC, while Qatar's is 5.8 times larger, supported by significant scientific collaborations.

Collaborations can help stimulate organic improvement of science by educating home-grown researchers. Leaders in the region understand the value of educating a scientific workforce. "Building [an] education system and stimulating research must be entrenched within society," says Khaled Toukan, the chairman of the Jordan Atomic Energy Commission and the country's former minister for Higher Education and Scientific Research. "You can't just import



These brown magnets will focus the electron beam in the SESAME particle accelerator in Jordan.

it by hiring a few expatriates who are world renowned and they sit and publish papers."

Jordan lacks the bountiful energy resources enjoyed by other countries in the region including Saudi Arabia, the UAE and Qatar, which allow them to super-charge their research budgets. Instead, the country — which is yet to break into the top 100 — is having to slowly build its scientific community from the bottom up, a process that will probably require working with other countries. To build its first reactor for nuclear research, for example, Jordan's Board of Commissioners of the Energy and Mineral Resources Regulatory Commission sought the help of the Korea Institute of Nuclear Safety. Korean experts will help to build and run the facility, expected to be operational in 2016 at the Jordan University of Science and Technology in Irbid.

ACCELERATING INTERNATIONAL SCIENCE

Two big projects in Jordan should help improve national and international collaboration, Toukan says. Two 1,000-megawatt nuclear reactors are to be constructed in the northern part of the country through a US\$10 billion partnership with Russia, and the Synchrotron-light for Experimental Science and Applications in the Middle East (SESAME) in Allan, Jordan will be the first particle accelerator in the region.

SESAME's leaders hoped to get the facility online by the end of 2015. But a severe

snowstorm in December 2013 caused the roof of the experimental hall at SESAME to cave in, which set the project back by a year. A new roof has been built and construction has resumed. The plan now is to have two beam lines ready by the end of 2016, one for hard X-rays — those with the highest energy — and one for infrared spectromicroscopy. With these lines, researchers hope to investigate, for example, cells and viruses and make breakthroughs in medicine.

The SESAME site certainly won't be among the largest particle accelerators in the world. Its storage ring is only 133 metres in circumference — compared to 1,500 metres for SPring 8 in Japan — but it will be able to accommodate several experiments at a time when all of its 25 beam lines are functioning.

SESAME is an ambitious project on many levels. Launched by UNESCO, with oversight from CERN, it is receiving input and support from some of the top scientific leaders in countries including Germany, France and Italy. But its primary aim is to serve researchers in the region who come from areas with deeply divided politics, including Egypt, Iran, Israel, Palestine, Turkey, Bahrain, Pakistan and Jordan.

"This is a positive [move], where rather than destroying each other, people are working together to promote science for peace, harmony and positive contribution to the modern world," says Toukan.

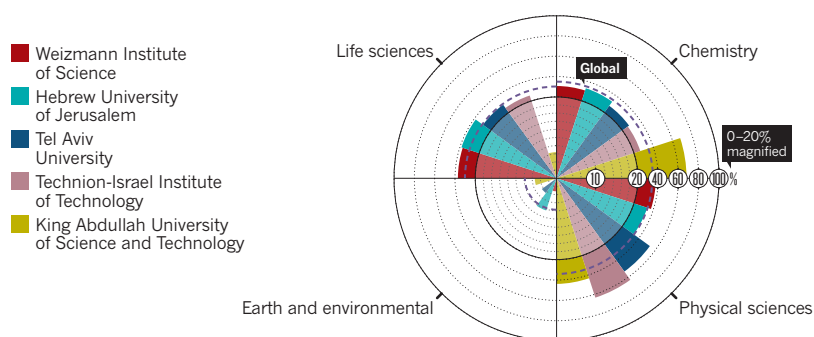
The hope is that SESAME can help alleviate persistent drawbacks for the region, including brain-drain, a lack of collaboration among researchers and low numbers of published papers. The laboratory could become a home for researchers considering going abroad or it might even lure back scientists who have already left. And with all the applications of synchrotrons, it could bring together researchers who would have otherwise never interacted.

"To survive in a global market, you really have to build industry," Toukan says. "And the only way to do it is through advanced scientific research and development, which the countries in this region realize now." ■

WEST ASIA ANALYSIS

Top 5 institutions' relative subject area distribution

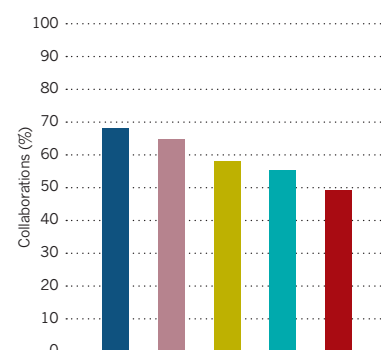
Israel's Weizmann Institute of Science led the region, and it published about equally in life and physical sciences.*



*Each slice represents the proportion each subject area contributes to an institution's overall WFC. Subject areas can overlap, so the total percentage may exceed 100%.

Top 5 institutions' collaborativeness

Among the top five, the Weizmann Institute of Science published the most but collaborated the least.*



*Each bar represents the proportion of an institution's overall output in the Index (AC) stemming from domestic and international collaborations.

Central & South Asia

India's dominance continues in this region, but its future funding is tenuous, while neighbouring smaller countries face more fundamental obstacles to scientific success.

ARTICLE COUNT (AC): 1,574

FRACTIONAL COUNT (FC): 1,057

WEIGHTED FRACTIONAL COUNT (WFC): 944

The countries of Central & South Asia have spent the last decade building their science profiles by expanding their community of researchers. Nonetheless, this region finishes 6th out of 9 in this Nature Index, based on its 2014 weighted fractional count (WFC) of 944. Most of the region's publications in the Index focus heavily on chemistry or physical sciences (47.7% and 40.9% of the region's total WFC, respectively), leaving little capacity for work in life and earth and environmental sciences.

Looking at the reasons, it seems that trends in researcher mobility may play a role in keeping the region from producing more work published in the top journals. Brain drain, for instance, is a big problem for countries in the region — an exodus of top talent that benefits countries at the top of the scientific pyramid leaves other nations bereft of leading researchers. Gail Joseph, a researcher at North Carolina Agriculture and Technology State University, says, "I see so many Indians here [in the US] who are excellent researchers. They feel more appreciated here, plus the infrastructure and technology [are] much more advanced abroad."

While the lure of international institutions is a factor, scientists in the region do not regularly team up with researchers from other countries. With 33% of articles arising from international collaborative efforts, scientists in Central & South Asia collaborate on fewer projects than

the regional aggregate of the WFC for the Index (46%). When researchers in this region do collaborate internationally, it is with scientists from North & West Europe (44% of international collaborations) and North America (30%). "The trend is for countries in the region to work more with the West than building regional networks," says Ravi Silva, director of the Advanced Technology Institute at the University of Surrey in the United Kingdom.

"I SEE SO MANY INDIAN RESEARCHERS WHO FEEL MORE APPRECIATED IN THE UNITED STATES."

The lack of collaborations within the region could be explained by one local philosophy. "Our emphasis has been growing the talent in India," says physicist Ajay Sood at the Indian Institute of Science (IISc) in Bengaluru. "We have a very low percentage of people coming from other countries, almost negligible." Nonetheless, India performs reasonably well on the global level.

INDIA'S DOMINANCE

India ranks 13th globally in terms of WFC and is by far this region's leader in science in the

Index, contributing 97.6% of Central & South Asia's WFC in 2014. For instance, India's 2014 WFC includes an article in *Nature Genetics* on heart disease in children, which reveals possible targets for therapies related to mutations in the *RAF1* gene.

Despite such clearly valuable research and India's WFC increasing by 8.3% from 2013 to 2014, some experts question the impact of India's publications.

Improving the quality of India's published papers will require more spending on research. Funding is divided into national laboratories that receive block grants and universities that compete for grants. Since there are more scientists in colleges and universities, they are competing for funds and working with limited resources. Moreover, Indian National Science Academy vice president S. C. Lakhota calls the funding competition "lengthy and painful for active researchers."

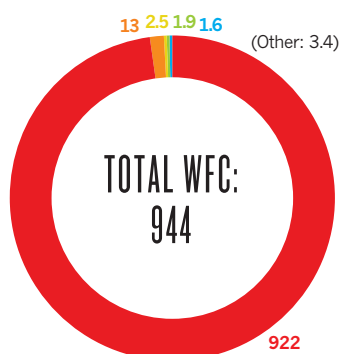
Consequently, the universities face challenges in attracting good scientists. Graduate students and young scientists are drawn more to research institutions than to universities, says Lakhota. This trend, he says, leads to "spiraling inequity in quality of resources and manpower." "Nearly all of the traditional teaching institutions suffer from lack of a critical mass of quality researchers and teachers."

Despite this precarious state of funding, Sood's IISc has top quality equipment, and it

CENTRAL & SOUTH ASIA ANALYSIS

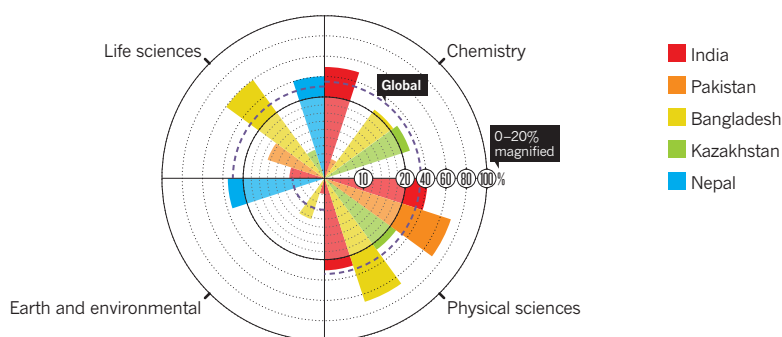
Countries' weighted fractional count (WFC)

The most dominant leader in any region, India produced 98% of the Index articles from Central & South Asia.



Relative subject area distribution

The countries in this region demonstrated some of the most diverse publishing, such as Pakistan's focus on physical sciences.*



*Each slice represents the proportion each subject area contributes to a country's overall WFC. Subject areas can overlap, so the total percentage may exceed 100%.

has attracted good researchers. Its WFC of 94 places it third among institutions in the region and 118th in the world. Other top research organizations include the Indian Institutes of Technology (IITs), which are spread across the country and which, in aggregate, ranks 51st in the world and 1st in the region with a WFC of 168. Reflecting India's focus on chemistry, IITs is one of the top institutions in the Index for chemistry worldwide, ranking 24th with a WFC of 107 — up 43% compared to its WFC in 2013.

Similar to the IITs, India's Council of Scientific and Industrial Research (CSIR), which ranks 72nd in the world with a WFC of 129, has dozens of labs and centres across India. It, too, is a key player in chemistry, being one of the top 30 institutions in the Index for this discipline with a WFC of 90. Unlike the IITs, CSIR falls into the category of a national lab, which guarantees block grants from the government.

ABOVE AND BEYOND

Looking only at international journals and funding doesn't tell the whole story, however. The success of India's Mars Orbiter Mission — which entered the Mars atmosphere in September and was recently reported to be so fuel efficient that the mission will last six months longer than originally planned — has been a major point of pride throughout the scientific community and the country in general. "It is a tremendous achievement at very low cost and successful at its very first attempt," says Venkatesh Narayanamurti, dean of Harvard University's School of Engineering and Applied Sciences. He calls the mission India's "single biggest accomplishment." Narayanamurti also highlighted another scientific accomplishment for India that will have a strong impact on technological capabilities: the development of the country's first regional GPS system, which is expected to be completed in 2015.

Despite these achievements, some researchers are disappointed that funding for research hasn't increased as they had hoped it would with the new government of Prime Minister



This launch put India's Mars Orbiter in the planet's atmosphere in September 2014.

Narendra Modi, who took office in 2014. Facing a slowdown in the economy, the Modi administration has failed in two budgets to boost R&D spending above 1% of the GDP. The funding increase of 4% was below-inflation and not enough to satisfy researchers.

"There is an apprehension in the Indian scientific community that from this year onward the past increase in funding will not continue and may actually turn into severe cuts for the basic sciences," says Kavita Dorai, a physicist at the Indian Institute of Science Education & Research Mohali in Punjab. "If this happens, it will have far-reaching consequences for both the scientific community and for the nation."

LAGGING BEHIND

The region's clear runner-up is Pakistan, which ranks 53rd in the world with a WFC of 13, down 29% compared to 2013. It has a sizable community of researchers approaching 53,000 — or about 295 researchers per million citizens — but it has yet to get a single university into the Index's top 10 institutions of the region. Similar to its neighbours, Pakistan's publication output leans heavily toward the physical sciences.

Even though Pakistan lags behind India in scholarly output, it has had some notable successes. In mid-December, Pakistan celebrated

the country's admittance as an associate member of CERN, the European Organization for Nuclear Research — a status not yet attained by regional rival India.

Pakistan's government is also moving forward with its initiative to close the gap between academia and industry in an attempt to boost the country's economy. The government has now supported the opening of 38 Offices of Research, Innovation and Commercialization (ORICs) in universities around the country since the initiative began in 2011. Aliya Rehman, director of the University of Karachi's ORIC, notes there is some resistance to these collaborations from both industry and academia. She recently conducted a survey that found that while hundreds of patents have been awarded to researchers at the University of Karachi, none of them have yet been commercialised. Rehman says this is due to lack of initiative and roadblocks in the process. "They do their research and it just goes in their cupboards," she said. One promising collaboration she is working on will link research being done on Pakistani seaweed with a company that has been manufacturing herbal medicine and cosmetics using imported seaweed.

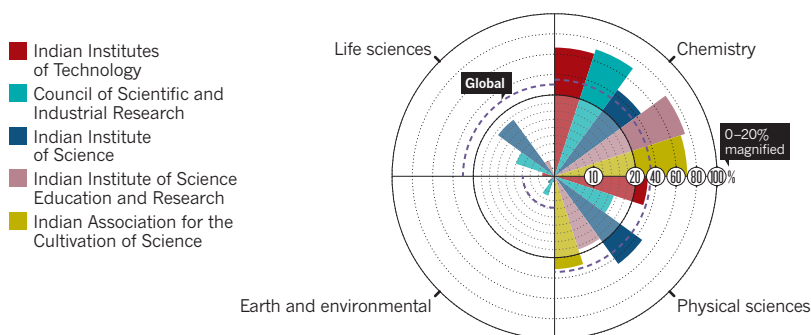
Still, Pakistani researchers face many barriers that are causing many of the brightest to seek opportunities elsewhere, says Rehman. "You have no idea how difficult it is to do research in Pakistan." She points to the funding mechanism in particular. "The funding agencies are very slow to process the project applications and by the time the funding comes, the work has been done in some other part of the world," she says.

Exacerbating the situation, some countries in Central & South Asia are still facing obstacles that scientists in developed nations cannot even imagine. In Pakistan, for example, Rehman points to electricity shortages and political instability as major impediments to research, sometimes closing down the universities for days. "It is an extremely difficult position and that is why a lot of people are leaving," she says. ■

CENTRAL & SOUTH ASIA ANALYSIS

Top 5 institutions' relative subject area distribution

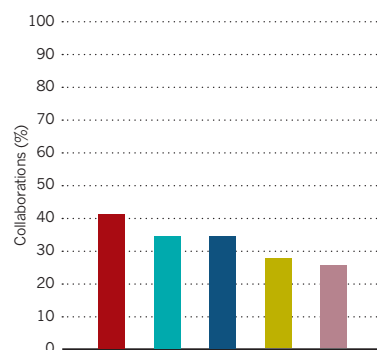
Since the top five institutions came from India, they reflected the country's emphasis on chemistry.*



*Each slice represents the proportion each subject area contributes to an institution's overall WFC. Subject areas can overlap, so the total percentage may exceed 100%.

Top 5 institutions' collaborativeness

Compared to top institutions in other regions, Indian institutions are more self-contained and collaborate far less.*



*Each bar represents the proportion of an institution's overall output in the Index (AC) stemming from domestic and international collaborations.

Latin America & Caribbean Islands

There is scope for improvement with the volume and quality of research in this region, but some innovative programmes for study abroad might improve future publications.

ARTICLE COUNT (AC): 2,249

FRACTIONAL COUNT (FC): 864

WEIGHTED FRACTIONAL COUNT (WFC): 574

Brazilian economist Antônio Delfim Netto, one of the government officials credited with the country's rapid economic development during the 1970s, famously argued: "One needs to wait for the cake to rise before cutting any slices." That is, a country should not try to redistribute wealth without a preceding phase of vigorous economic growth. If one applies Delfim Netto's maxim to Latin American science, it is clear that the cake has risen — there are almost seven times more papers published by Brazilian scientists in indexed journals, for instance, than 20 years ago, according to the Scimago/SCOPUS database, which started decades before the Nature Index — but this hasn't made it very competitive in the Index. The growth in absolute numbers is still not enough to place countries in Latin America and the Caribbean Islands among the world's leading scientific communities, according to the Nature Index.

Based on the Nature Index's 2014 weighted fractional count (WFC), Brazil produced the region's highest output and is 23rd globally with a 2014 WFC of 237. Behind Brazil, Argentina, Chile and Mexico came in 30th, 32nd and 34th in the global Index. Physical sciences account for 55.4% of the region's WFC.

Brazil puts the most emphasis on scientific research of all countries in the region — spending 1.3% of its GDP on R&D, followed by Mexico at 0.5% of its GDP. Among the four top countries,

Chile provides the least funding for research — about 0.36% of its GDP (which is also by far the lowest of the four in absolute terms, because it also has the lowest GDP) — but its WFC (95) is barely lower than Argentina's (99).

In this region, public funding is much more important than partnerships with the private sector, and scientists rarely become entrepreneurs. Despite this, some government promises for increased support have not been realized. For example, scientometrist Francisco Collazo-Reyes of Mexico's National Polytechnic Institute says, "The winning tickets in the last several presidential campaigns here have several times promised to raise funding to 1% of GDP, but this hasn't materialized so far."

**"ONE NEEDS TO
WAIT FOR THE CAKE TO
RISE BEFORE CUTTING
ANY SLICES."**

COLLABORATING ON COMMODITIES

The pattern of international collaborations in Latin America resembles that of North America. Both regions lean toward research partners in North & West Europe. In fact, 47% of Latin American and 49% of North American international collaborations involve scientists

from these areas. Latin American scientists also collaborate often with their neighbours to the north: 28% of Latin American international collaborative work is done with US and Canadian scientists.

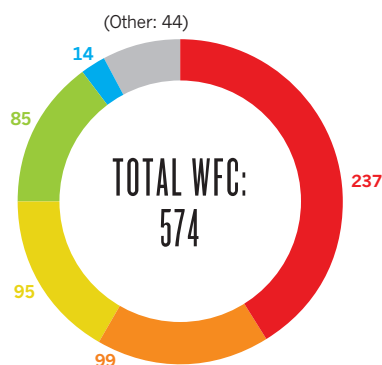
Much of Latin America's economic growth in the past couple of decades has been fuelled by Chinese demand for commodities. For example, China imports Brazilian and Argentinean soybeans and Brazilian iron ore. Latin American research centres, however, still seem largely oblivious to the potential of Asian science. Only 4% of international collaborations by scientists from Latin America and the Caribbean Islands include colleagues from East & Southeast Asia.

On average, though, scientists in Latin America and the Caribbean Islands collaborate more often internationally than scientists around the world. In addition, its scientists collaborate significantly with others in North America and Europe. For instance, four researchers from Brazil — plus others from France, Italy, Spain, the United States and Russia — published a 2014 *Nature Biotechnology* article on the sequencing of citrus. The research itself even added to this article's international flavour, since it explored the phylogeny of plants that started to be domesticated thousands of years ago in Southeast Asia. "Advances in citrus genomics should soon allow the identification of the somatic mutations that, with their ancient genetic backgrounds, underlie the

LATIN AMERICA & CARIBBEAN ISLANDS ANALYSIS

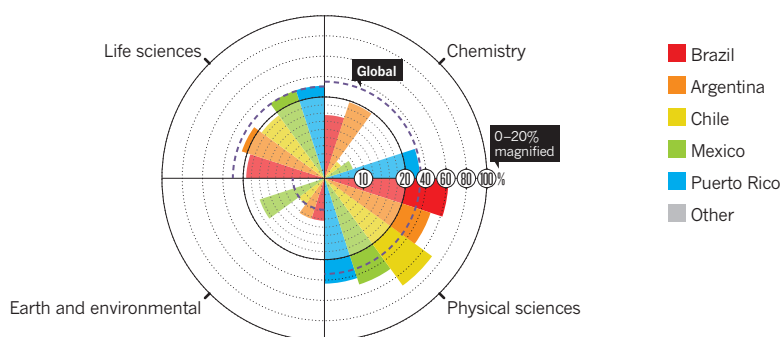
Countries' weighted fractional count (WFC)

Brazil supplied over 40% of the articles in the Index, and Argentina, Chile and Mexico each produced roughly 15%.



Relative subject area distribution

Physical sciences dramatically dominated the publishing, where all of the top five countries focused at least 40% of their output here.*



*Each slice represents the proportion each subject area contributes to a country's overall WFC. Subject areas can overlap, so the total percentage may exceed 100%.

diversity of citrus colour, flavour and aroma in modern cultivars,” the authors concluded.

But citrus is far from the only type of agricultural product that is driving Brazilian science. Indeed, although Brazil grows more than 700,000 hectares of orange trees, it plants more than 10 times that much in sugar cane. In fact, Brazil is the world leader in producing sugar-cane ethanol, which has become an attractive alternative fuel for vehicles. In 2014, according to Bloomberg, Brazil's state-development bank, Banco Nacional de Desenvolvimento Economico e Social, invested US\$843.5 million to increase the productivity of turning sugar cane into ethanol.

SIZE MATTERS

Publicly funded universities that, by North American and European standards, have huge numbers of students and staff, are responsible for most of the research in Latin America and the Caribbean. The two Latin American institutions with the highest WFCs are Brazil's University of São Paulo (USP), with 100,000 undergraduate and graduate students and 6,000 faculty, and the National Autonomous University of Mexico, with more than 300,000 students and about 37,000 academic staff.

Rogério Mugnaini, a scientometrist at USP, argues that institutions of such size are bound to perform in a relatively irregular way when it comes to publishing research. He says, “They will certainly have a number of groups in a position of international leadership, but also a very long tail of researchers that don't perform so well.”

As a result, he says, the overall performance of these gargantuan institutions suffers. None of the leading institutions in Latin America is among the top 200 in the world based on the Index's WFC.

Research strength in Latin America tends to be much more geographically concentrated than in other regions. Brazil, for example, has four institutions in the region's top 10, and three — USP, São Paulo State University and



This processing factory in Valparaíso, Brazil, turns sugar cane into ethanol for fuel.

the State University of Campinas — are in São Paulo State; the other top-10 institution, the Federal University of Rio de Janeiro, is in the adjacent state of Rio de Janeiro. About half of Brazil's science output comes from São Paulo, although a 2014 *Nature Genetics* article on the human hookworm's genome included a Brazilian author from Minas Gerais.

Both Chile and Argentina have two institutions in the regions' top 10, and the University of Puerto Rico, the sole representative of this US territory, is also among the top 10.

For Chile, says Atilio Bustos-González of the Scimago Research Group at Adolfo Ibáñez University in Viña del Mar, Chile, one of the main challenges is how to increase the output of quality science in research centres outside of Santiago.

REACHING FOR RECRUITMENT

To increase the international relevance of Latin American science, governments are creating programmes to fund scholarships overseas. The most ambitious and controversial so far is Brazil's Science Without Borders, which

started in 2011. Its initial aim was to send about 100,000 young scholars — mostly undergraduates, plus 15,000 doctoral candidates and 6,500 post-docs — to institutions abroad. President Dilma Rousseff pledged to double that number during her re-election campaign in 2014.

The initiative has been criticized for lax selection criteria and implementation. For example, some undergraduates have been accepted despite having little command of the language of the country to which they were headed, and there are no clear rules to monitor their activities abroad.

The ease with which some students have managed to spend most of their time traveling has led critics to call the initiative “Tourism Without Borders.”

“The focus on undergraduates has attracted a lot of scepticism about the long-term effects of the programme in Brazilian science,” says Mugnaini.

On a more modest scale, the Chilean Ministry of Education has since 2008 awarded Becas Chile (Chile Scholarships) for masters students, doctoral candidates and post-docs.

Those who receive the scholarships sign an agreement to return to Chile after the end of their fellowship. “The first PhDs of Becas Chile are starting to return, and that is bound to generate an increase in the country's scientific output,” predicts Bustos-González.

The hope is that programmes like Science Without Borders and Becas Chile will give Latin American researchers a chance to interact with scientists from countries with higher WFCs and attract foreign scientists to Latin America.

The Brazilian programme, for example, is offering 2,000 fellowships for “special visiting researchers” who are willing to spend at least a month each year in Brazil for a three-year period.

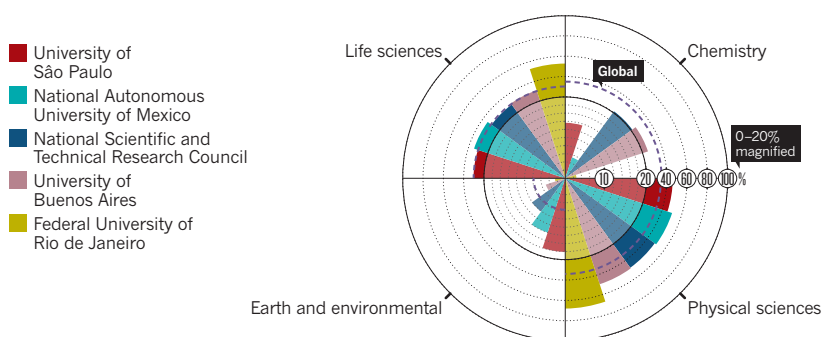
Increasing the cooperation with first-world scientists might improve quality in publications from Latin America & Caribbean Islands. ■

PAULO WHITAKER/REUTERS/CORBIS

LATIN AMERICA & CARIBBEAN ISLANDS ANALYSIS

Top 5 institutions' relative subject area distribution

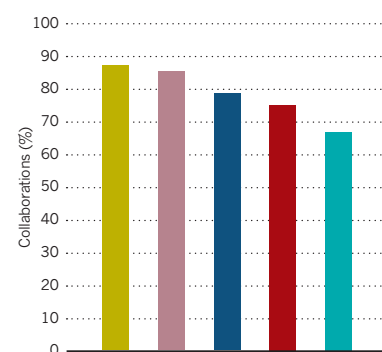
In a region largely focused on physical sciences, the National Autonomous University of Mexico generated more than 40% of its Index articles in the life sciences.*



*Each slice represents the proportion each subject area contributes to an institution's overall WFC. Subject areas can overlap, so the total percentage may exceed 100%.

Top 5 institutions' collaborativeness

Four of the top five institutions used international collaborators on more than 70% of their 2014 Index articles.*



*Each bar represents the proportion of an institution's overall output in the Index (AC) stemming from domestic and international collaborations.

Africa

Public health demands might drive advances in research, but scientists, working against the odds, must also strive to publish in global journals.

ARTICLE COUNT (AC): 651
FRACTIONAL COUNT (FC): 172
WEIGHTED FRACTIONAL COUNT (WFC): 128

In scientific publishing, Africa trails far behind the rest of the world, and economic factors explain some of its shortcomings. Although Africa is home to nearly 15% of the world's population, this region only produced 0.25% of the 2014 weighted fractional count (WFC) in the Nature Index. South Africa, which accounted for 64% of the region's 2014 WFC, spent only US\$2.8 billion on R&D (0.76% of its GDP). By comparison, the United States spent US\$466 billion (2.70% of GDP), and generated a WFC of 17,937. Africa's poor publishing record in the Index is down to more than economics.

In many cases, African scientists publish in journals that are not counted by the Index. "Many of the scientists we work with in Africa are publishing quite often, but most often their work is being published in much more local, regional or continental journals or ones with very specific topic areas," says Nina Dudnik, founder of the US-based nonprofit, Seeding Labs, which provides used equipment and training to scientists in developing countries in Africa and elsewhere. She cites one colleague in Ghana with 73 publications — virtually all of them in narrowly focused or regional publications that are not in the Index, such as *Food Research International* and the *Journal of the Ghana Science Association*. "Often scientists do not know the right way to pitch their research to a major journal," says Dudnik.

Most of Africa barely registers on the Index. Behind South Africa, Egypt contributes 11% of the region's 2014 WFC. Kenya, Algeria and Tunisia provide another 4%, 3.5% and 2%. Nine out of ten of Africa's top institutions by WFC are in South Africa, with the only exception being the Mpala Research Centre in Kenya.

**"SOMETIMES IT'S
NOT JUST LACKING
CUTTING-EDGE
EQUIPMENT, BUT ANY
EQUIPMENT AT ALL."**

PUBLIC HEALTH'S IMPACT

While Africa gets most of its WFC from physical sciences, efforts are under way to broaden the region's research scope. In particular, recent public-health challenges might drive more research in life sciences. For example, the Ebola epidemic — the worst ever recorded — has taken more than 10,000 lives, according to the US Centers for Disease Control and Prevention (CDC). This outbreak spurred the One Health research programme at the Southern African Centre for Surveillance of Infectious Diseases to assemble a multi-national team of

African researchers in Johannesburg to study strategies for controlling the virus, with funding from the Wellcome Trust. In Tanzania, The Zanzibar Research Agenda 2015–2020 calls for a range of health initiatives that will require research, such as exploring the potential to apply nanomedicine — nanometer-scale technology used in medical applications — to early detection of diseases, as well as diagnosis and follow-up on the impact of treatments.

Africa makes some effort to publish articles in the life sciences, which receives the second highest emphasis based on its percentage of the region's total WFC. In Index data for 2014, only two regions — North America and Australasia & Pacific Islands — placed more emphasis on life sciences.

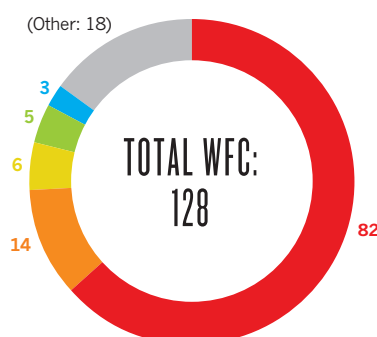
Like other developing regions, Africa could drive more life sciences research through clinical trials. According to Judy Coates, scientific and regulatory affairs manager at the Innovative Pharmaceutical Association South Africa in Johannesburg, her country has experienced a stable annual investment in clinical trials of about US\$200–250 million in recent years. A study by her organization, however, shows that this figure could grow to about US\$400 million if South Africa's pharmaceutical regulator, the Medicines Control Council, could improve the ability for companies to run trials with fewer delays.

Even with a relatively consistent investment

AFRICA ANALYSIS

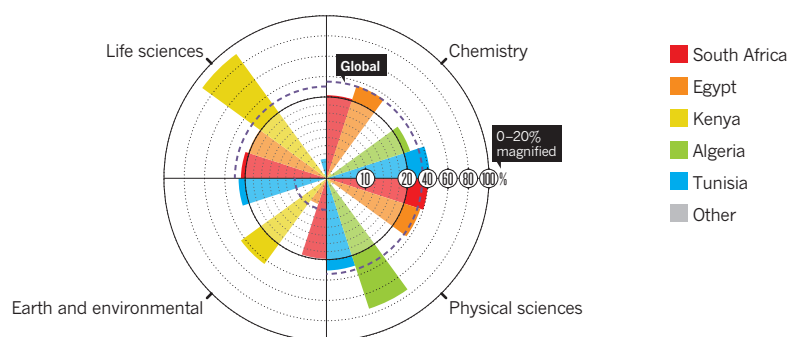
Countries' weighted fractional count (WFC)

South Africa and Egypt contributed 75% of the region's articles in the Index.



Relative subject area distribution

Although 91% of Kenya's Index articles explore life sciences, this came from a WFC of only 6.*



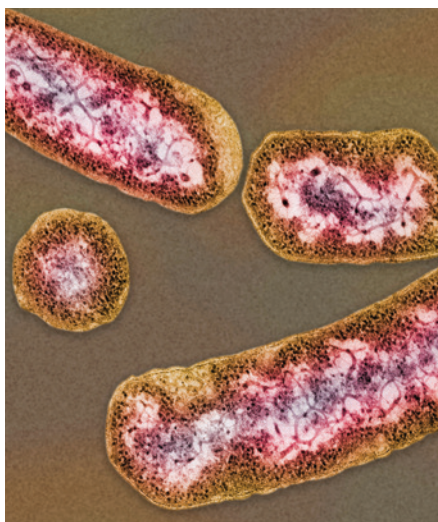
*Each slice represents the proportion each subject area contributes to a country's overall WFC. Subject areas can overlap, so the total percentage may exceed 100%.

in clinical trials in South Africa, the overall region's share of the global market is declining. A recent study by US-based Quintiles found, for example, a 9.1% decrease in sub-Saharan Africa's share of the global clinical-trial market from 2010 to 2012. In fact, most of that fall was in South Africa, where the share of the world market for clinical trials dropped by 7.9%. The experts at Quintiles speculated that sub-Saharan Africa could be losing some of the niche market in clinical trials, such as ones for malaria, which has been a driver in the past.

Still, scientists in the region study the local diseases. In 2014, for instance, a scientist from The Gambia was one of the dozen authors on a *Nature Communications* article about artemisinin combinations for treating malaria. Originally, this drug came from sweet wormwood (*Artemisia annua*), which is a herb used in traditional Chinese medicine, but now it can be mass-produced in genetically modified yeast. This study showed the value of doing research in Africa, because the authors concluded: "We find that a locally optimized treatment policy can be highly cost effective for reducing clinical malaria burden."

In addition, the healthcare industry can invest in Africa beyond clinical trials. For the pharmaceutical industry overall, "the companies are more involved in Africa since it is a growth market, and they are using numerous mechanisms, including investing in research infrastructure as well as initiating projects," says Dries Oelofse, business development manager at H3-D, a drug development centre at the University of Cape Town. For example, UK-based GSK funded a US\$6 million grant for African researchers to study non-communicable diseases in the region.

Despite Africa's small output compared to the rest of the world — or perhaps in some ways because of it — the region leads a significant metric in the Index. In the percentage of a region's WFC published in *Nature* or *Science*, Africa's 4.7% is the highest, surpassing second place North America (4.5%). Granted, that's



Prevotella bacteria in the gut of Hadza hunter-gatherers enhance the ability to digest plant material.

only about six publications for Africa (versus 870 for North America), but this is still an important metric.

COLLABORATION KING

Africa led the world in collaborations in 2014 articles in the Index. Overall, more than 70% of Africa's output comes from work done with scientists from other countries. This makes Africa the most internationally collaborative of all regions in the Index. On average, regions only collaborated internationally on 46% of their articles. Africa collaborated most in the earth and environmental sciences (85%) and the life sciences (80%). It collaborated less in the physical sciences (73%) and chemistry (69%). All but a few percent of those collaborators are with countries outside Africa. The region that African scientists most frequently work with is North & West Europe. This research bond arises in part from programmes that encourage collaborations between African scientists and those in the United Kingdom. For example, the Leverhulme Trust in

the United Kingdom offers funding up to about US\$750,000 over five years for some research projects.

Even when collaborating with scientists outside of the region, the research can make use of African resources. A 2014 *Nature Communications* article on the gut microbiome of Tanzania's Hadza hunter-gatherers included one author from the country, and the research explored how bacteria might have co-evolved with this human population. The results suggest that specific bacterial species and combinations impact how these people gain nutrition from even very fibrous plants.

To achieve more success in international publishing for Africa overall, though, the scientists need modern tools. A lack of advanced equipment limits high-profile publishing. As Dudnik explains, "Researchers using equipment that is not the Western gold standard have to work harder to demonstrate the validity of their results." That surely reduces Africa's impact.

In 2014, for example, Dudnik wrote in *The Wall Street Journal* about the US Centers for Disease Control and Prevention establishing a laboratory in a hospital in Uganda to test blood samples for Ebola in 2000. "Yet 14 years later," Dudnik wrote, "that lab is gone and no institution in the region has the equipment required to test for Ebola or other prevalent diseases including yellow fever, hepatitis, Marburg virus or HIV." So sometimes it is not just lacking cutting-edge equipment, but lacking any useful equipment at all.

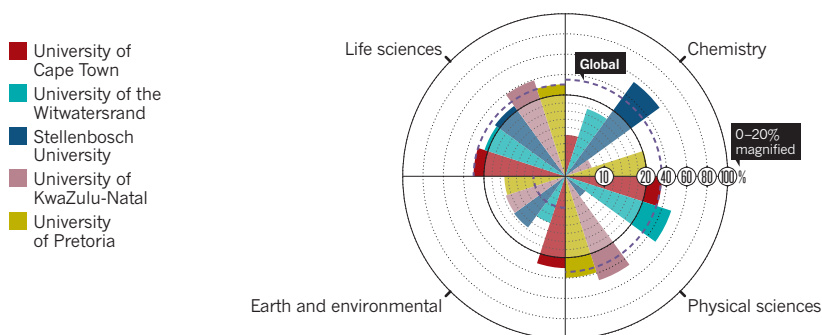
"Ultimately," says Dudnik, "the scientific output of African researchers receives less attention, reaches a smaller audience and is under-catalogued by global indices." By looking to international publications as potential outlets whenever possible, scientists in this region could start to work their way into the global world of science.

Spreading that trend across all of Africa, however, will take time, improved laboratory equipment and increased funding. ■

AFRICA ANALYSIS

Top 5 institutions' relative subject area distribution

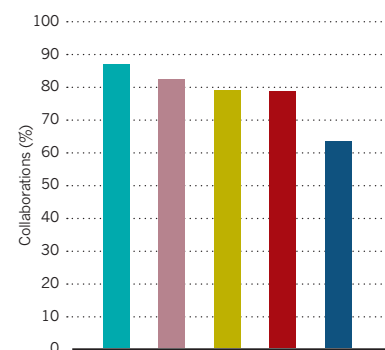
All of the top five institutions in the region were in South Africa, and they published, on average, across the range of categories.*



*Each slice represents the proportion each subject area contributes to an institution's overall WFC. Subject areas can overlap, so the total percentage may exceed 100%.

Top 5 institutions' collaborativeness

African scientists collaborated more than any region in the world, and the top five institutions followed this trend.*



*Each bar represents the proportion of an institution's overall output in the index (AC) stemming from domestic and international collaborations.

A guide to the Nature Index

A description of the terminology and methodology used in this supplement, and a guide to the functionality available free online at natureindex.com.

The Nature Index is a database of author affiliations and institutional relationships, used to track contributions to articles published in a group of highly selective science journals that have been chosen by an independent group of active researchers.

Data in the Nature Index are updated monthly, with the most recent 12 months of data made available under a Creative Commons license at natureindex.com.

The Nature Index provides absolute counts of high-quality publication productivity at the institutional and national level, and as such is one indicator of high-quality research output across the globe.

The database is compiled by Nature Publishing Group (NPG) in collaboration with sister company Digital Science.

The current journals tracked by the Nature Index will be reviewed again in 2015, and from 2016, coverage will be extended to include the clinical sciences.

NATURE INDEX METRICS

There are three measures provided by the Nature Index to track affiliation data. The simplest is the article count (AC). A country or institution is given an AC of 1 for each article that has at least one author from that country or institution. This is the case whether an article has one or a hundred authors, and it means that the same article can contribute to the AC of multiple countries or institutions.

To get a better sense of a country or institution's contribution to an article, and to remove the possibility of double-counting of articles, the Nature Index uses the fractional count (FC). FC takes into account the relative contribution of each author to an article.

The total FC available per paper is 1, and this is shared between all authors under the assumption that each contributed equally. For instance, a paper with 10 authors means that each author receives an FC of 0.1. For authors who have worked with joint affiliations, the individual FC is then split equally between each affiliation.

The third measure used is the weighted fractional count (WFC), which applies a weighting to the FC to adjust for the over-

Users of natureindex.com can search for specific institutions or countries and generate their own reports, ordered by article count (AC), fractional count (FC) or weighted fractional count (WFC).

Each query will return a profile page that lists the country or institution's recent research outputs, from which it is possible to drill down for more information. For example, articles can be displayed by journal, and then by article title. As in the supplement, research outputs are organized by subject area. The profile page also lists the institution or country's top collaborators, as well as its relationship with other research organizations.

representation of papers from astronomy and astrophysics.

The four journals in these disciplines publish about 50% of all papers in international journals in this field — approximately five-times the equivalent figures for other fields. Therefore, although the data for astronomy and astrophysics are compiled in exactly the same way as for all other disciplines, articles from these journals are assigned one-fifth the weight of other articles (i.e. the FC is multiplied by 0.2 to derive the WFC).

The total FC or WFC for an institution is derived by summing the FC or WFC for individual authors.

The process is similar for countries, although complicated by the fact that some institutions have overseas labs that will be counted towards the host country totals. What's more, there is

great variability in the way authors present their affiliations. Every effort is made to count affiliations consistently, and with the background of reasonable assumptions.

For more information on how the affiliation information is processed and counted, please see the frequently asked questions at natureindex.com.

THE SUPPLEMENT

Nature Index 2015 Global is based on a snapshot of data from natureindex.com, covering articles published between 1 January and 31 December 2014.

Most analyses within the supplement use the WFC as the primary metric, as it provides a more even basis for comparison, and in determining the relative contribution of each country/institution. ■

NATUREINDEX.COM

A global indicator of high-quality research

Institution name

Country

Research

Collaboration

Relationships

1 January 2014 - 31 December 2014

Region: Global
Subject/journal group: All

The table to the right includes counts of all research outputs for Institution name published between 1 January 2014 - 31 December 2014 which are tracked by the Nature Index.

Below, the same research outputs are grouped by subject. Click on the subject to drill-down into a list of articles organized by journal, and then by title.

Note: Articles may be assigned to more than one subject area.

AC	FC	WFC
1221	598.04	558.30

Outputs by subject



Subject	AC	FC	WFC
Chemistry	276	179.1	179.11
Earth & Environmental Sciences	95	42.73	42.73
Life Sciences	439	231.50	231.50
Physical Sciences	652	284.48	244.74

Return to institution outputs

Nature Index tables

The Index's leading countries and institutions for high-quality science, ordered by weighted fractional count (WFC) for 2014. Also shown are the total number of articles, and the change in WFC from 2013. Articles are from the 68 natural science journals that comprise the Nature Index (see Guide to the Nature Index, page S30).

TOP 100 COUNTRIES

2014	COUNTRY	WFC	ARTICLE COUNT	2013 WFC	2013-2014 CHANGE IN WFC
1	United States	17,936.51	26,638	18,581.10	-3.5%
2	China	6,037.22	8,641	5,204.06	16.0%
3	Germany	4,018.73	8,582	4,073.53	-1.3%
4	United Kingdom	3,249.72	7,592	3,271.65	-0.7%
5	Japan	3,200.43	4,976	3,365.50	-4.9%
6	France	2,221.95	5,243	2,232.59	-0.5%
7	Canada	1,488.90	3,226	1,480.64	0.6%
8	Switzerland	1,293.75	2,715	1,169.17	10.7%
9	South Korea	1,167.66	1,969	1,150.07	1.5%
10	Spain	1,090.72	2,897	1,177.00	-7.3%
11	Italy	1,046.98	3,052	1,078.08	-2.9%
12	Australia	951.22	2,497	932.86	2.0%
13	India	921.77	1,484	850.97	8.3%
14	Netherlands	757.33	2,189	759.47	-0.3%
15	Singapore	520.62	873	483.20	7.7%
16	Sweden	514.55	1,407	496.38	3.7%
17	Israel	492.44	1,012	473.15	4.1%
18	Taiwan	481.47	888	543.18	-11.4%
19	Russia	370.18	1,147	344.26	7.5%
20	Belgium	348.91	1,082	327.23	6.6%
21	Denmark	321.26	1,036	296.85	8.2%
22	Austria	318.98	856	279.97	13.9%
23	Brazil	237.01	715	233.69	1.4%
24	Poland	209.69	686	216.55	-3.2%
25	Finland	194.97	590	191.87	1.6%
26	Norway	149.81	415	122.42	22.4%
27	Czech Republic	126.33	372	118.43	6.7%
28	Portugal	117.45	416	123.53	-4.9%
29	Ireland	113.91	331	116.73	-2.4%
30	Argentina	98.58	321	105.55	-6.6%
31	New Zealand	95.69	275	117.58	-18.6%
32	Chile	95.13	857	75.43	26.1%
33	Greece	91.77	320	90.15	1.8%
34	Mexico	84.60	391	77.08	9.7%
35	South Africa	81.67	418	81.62	0.1%
36	Turkey	79.24	237	59.07	34.1%
37	Hungary	78.52	278	54.92	43.0%
38	Saudi Arabia	76.63	384	76.64	0.0%
39	Iran	67.87	147	58.55	15.9%
40	Ukraine	37.06	173	28.58	29.7%
41	Slovenia	36.36	106	43.20	-15.8%
42	Thailand	22.69	93	25.69	-11.7%

2014	COUNTRY	WFC	ARTICLE COUNT	2013 WFC	2013-2014 CHANGE IN WFC
43	Estonia	22.31	92	13.27	68.1%
44	Romania	21.41	79	17.47	22.6%
45	Croatia	17.56	102	21.86	-19.7%
46	Serbia	17.00	55	13.95	21.9%
47	Lithuania	16.85	58	11.26	49.7%
48	Malaysia	15.81	54	14.14	11.8%
49	Egypt	14.32	87	12.04	18.9%
50	Slovakia	14.16	64	12.57	12.6%
51	Puerto Rico	13.66	38	11.24	21.6%
52	Iceland	12.87	65	13.90	-7.4%
53	Pakistan	12.83	42	18.03	-28.8%
54	Cyprus	10.95	28	8.90	23.1%
55	Luxembourg	10.94	35	10.55	3.7%
56	Uruguay	9.55	22	5.21	83.5%
57	United Arab Emirates	9.37	49	7.08	32.2%
58	Colombia	9.36	56	9.45	-1.0%
59	Panama	8.84	32	6.61	33.9%
60	Bulgaria	8.59	63	9.49	-9.5%
61	Armenia	8.38	30	7.98	5.0%
62	Vietnam	7.53	29	8.23	-8.4%
63	Belarus	6.15	22	3.95	55.9%
64	Indonesia	5.92	30	4.28	38.4%
65	Kenya	5.64	25	5.36	5.2%
66	Qatar	4.98	35	3.96	25.6%
67	Peru	4.92	29	4.22	16.6%
68	Algeria	4.65	22	1.10	322.5%
69	Georgia	4.15	27	2.45	69.6%
70	Costa Rica	3.50	25	1.49	134.6%
71	Lebanon	3.08	14	3.34	-7.9%
72	Tunisia	2.75	13	2.84	-2.8%
73	Ecuador	2.48	19	2.48	0.1%
74	Bangladesh	2.45	14	2.28	7.7%
75	Venezuela	2.40	27	1.83	31.2%
76	Morocco	2.37	18	3.46	-31.4%
77	Latvia	2.18	12	3.18	-31.4%
78	Cuba	2.03	9	4.86	-58.2%
79	Oman	2.00	8	1.29	54.8%
80	Kazakhstan	1.93	9	2.85	-32.2%
81	Philippines	1.82	16	3.33	-45.4%
82	Moldova	1.68	10	3.35	-49.8%
83	Nepal	1.64	8	0.82	99.4%
84	Benin	1.62	6	0.37	341.4%
85	Uganda	1.61	11	0.29	452.6%
86	Mongolia	1.37	5	0.62	119.1%
87	Malta	1.30	5	0.46	179.4%
88	Senegal	1.17	4	0.56	110.1%
89	Cameroon	1.16	8	0.81	42.9%
90	Uzbekistan	1.16	10	0.17	576.6%
91	Bolivia	1.05	9	0.48	120.2%
92	Mali	1.00	3	0.19	415.5%
93	Macedonia	1.00	6	0.26	290.5%
94	Kuwait	0.95	7	3.17	-70.0%
95	Namibia	0.95	4	0.09	988.5%
96	Burkina Faso	0.93	4	0.05	1,944.6%
97	Azerbaijan	0.92	5	0.56	63.0%
98	Iraq	0.84	12	0.74	13.8%
99	Sri Lanka	0.83	8	0.70	18.6%
100	Kyrgyzstan	0.81	2	0.81	-0.2%

TOP 200 INSTITUTIONS

2014	INSTITUTION	COUNTRY	WFC	ARTICLE COUNT	2013 WFC	2013-2014 CHANGE IN WFC
1	Chinese Academy of Sciences (CAS)	China	1,307.74	3,124	1,209.37	8.1%
2	Harvard University	United States	865.09	2,615	852.85	1.4%
3	French National Centre for Scientific Research (CNRS)	France	761.48	4,907	719.07	5.9%
4	Max Planck Society	Germany	648.86	2,950	727.32	-10.8%
5	Stanford University (SU)	United States	538.57	1,265	550.20	-2.1%
6	Massachusetts Institute of Technology (MIT)	United States	501.38	1,483	507.17	-1.1%
7	The University of Tokyo (UTokyo)	Japan	456.23	1,251	472.88	-3.5%
8	Helmholtz Association of German Research Centres (Helmholtz)	Germany	440.09	1,629	422.02	4.3%
9	University of Cambridge	United Kingdom	403.11	1,384	401.39	0.4%
10	University of California Berkeley (UC Berkeley)	United States	365.55	1,236	362.16	0.9%
11	University of Oxford	United Kingdom	355.99	1,179	382.41	-6.9%
12	Swiss Federal Institute of Technology Zurich (ETH Zurich)	Switzerland	347.29	978	275.31	26.1%
13	National Institutes of Health (NIH)	United States	342.43	771	391.02	-12.4%
14	University of California, San Diego (UC San Diego)	United States	334.34	832	344.80	-3.0%
15	Yale University	United States	303.63	896	289.56	4.9%
16	University of Michigan (U-M)	United States	298.80	855	344.95	-13.4%
17	Peking University (PKU)	China	291.57	937	275.46	5.8%
18	Kyoto University	Japan	286.15	716	313.51	-8.7%
19	The University of Texas at Austin (UT Austin)	United States	274.17	629	246.84	11.1%
20	California Institute of Technology (Caltech)	United States	270.83	1199	280.77	-3.5%
21	University of Toronto (U of T)	Canada	268.61	829	256.09	4.9%
22	University of California Los Angeles (UCLA)	United States	260.59	744	286.64	-9.1%
23	University of Washington (UW)	United States	259.61	766	248.89	4.3%
24	Northwestern University (NU)	United States	259.33	586	298.02	-13.0%
25	Columbia University in the City of New York (CU)	United States	258.13	851	257.32	0.3%
26	University of Pennsylvania (Penn)	United States	252.97	589	295.67	-14.4%
27	Spanish National Research Council (CSIC)	Spain	242.90	1846	240.00	1.2%
28	University of Wisconsin-Madison (UW Madison)	United States	232.81	654	251.98	-7.6%
29	Swiss Federal Institute of Technology in Lausanne (EPFL)	Switzerland	232.70	687	207.58	12.1%
30	The Johns Hopkins University (JHU)	United States	226.16	783	223.91	1.0%
31	Cornell University	United States	226.04	689	247.53	-8.7%
32	Osaka University	Japan	218.77	555	219.88	-0.5%
33	The University of Chicago (UChicago)	United States	208.64	724	190.48	9.5%
34	Princeton University	United States	207.12	680	230.61	-10.2%
35	University of Illinois at Urbana Champaign (UIUC)	United States	206.36	551	229.86	-10.2%
36	Tsinghua University (TH)	China	205.58	611	195.00	5.4%
37	Nanjing University (NJU)	China	202.30	474	196.00	3.2%
38	University of California Santa Barbara (UCSB)	United States	201.06	552	196.04	2.6%
39	Imperial College London (ICL)	United Kingdom	200.52	727	185.01	8.4%
40	Nanyang Technological University (NTU)	Singapore	199.86	371	187.38	6.7%
41	University of Science and Technology of China (USTC)	China	191.75	541	175.73	9.1%
42	National University of Singapore (NUS)	Singapore	190.30	465	191.76	-0.8%
43	Zhejiang University (ZJU)	China	188.48	352	150.42	25.3%
44	University of California San Francisco (UCSF)	United States	188.02	446	221.76	-15.2%
45	University College London (UCL)	United Kingdom	185.66	799	183.78	1.0%
46	Tohoku University	Japan	178.14	426	189.32	-5.9%
47	University of North Carolina at Chapel Hill (UNC)	United States	177.36	387	170.63	3.9%
48	Russian Academy of Sciences (RAS)	Russia	171.47	910	165.96	3.3%
49	Pennsylvania State University (Penn State)	United States	171.14	587	185.84	-7.9%

2014	INSTITUTION	COUNTRY	WFC	ARTICLE COUNT	2013 WFC	2013-2014 CHANGE IN WFC
50	University of California Davis (UC Davis)	United States	169.69	478	183.16	-7.4%
51	Indian Institutes of Technology (IITs)	India	168.18	288	128.43	30.9%
52	Duke University	United States	167.60	501	173.44	-3.4%
53	Fudan University	China	162.59	344	129.22	25.8%
54	University of Maryland, College Park (UMCP)	United States	162.48	740	161.78	0.4%
55	Washington University in St. Louis (WUSTL)	United States	161.42	379	173.04	-6.7%
56	Lawrence Berkeley National Laboratory (LBNL)	United States	161.03	781	153.57	4.9%
57	Seoul National University (SNU)	South Korea	160.31	429	158.14	1.4%
58	University of Minnesota (UMN)	United States	158.05	491	178.08	-11.2%
59	Ludwig Maximilian University of Munich (LMU)	Germany	157.57	627	154.25	2.2%
60	Rutgers, The State University of New Jersey (RU)	United States	148.48	455	154.02	-3.6%
61	RIKEN	Japan	144.43	497	165.96	-13.0%
62	New York University (NYU)	United States	144.08	431	139.91	3.0%
63	University of Colorado Boulder (CU-Boulder)	United States	143.58	553	152.16	-5.6%
64	Weizmann Institute of Science (WIS)	Israel	142.96	296	150.96	-5.3%
65	The Ohio State University (OSU)	United States	142.01	555	142.91	-0.6%
66	The University of Manchester (UoM)	United Kingdom	141.03	565	125.06	12.8%
67	The Scripps Research Institute (TSRI)	United States	134.75	288	178.38	-24.5%
68	McGill University	Canada	133.57	468	136.55	-2.2%
69	National Research Council (CNR)	Italy	130.31	504	150.02	-13.1%
70	The University of British Columbia (UBC)	Canada	130.25	463	130.64	-0.3%
71	University of California Irvine (UCI)	United States	130.13	405	147.32	-11.7%
72	Council of Scientific and Industrial Research (CSIR)	India	128.64	196	115.24	11.6%
73	Texas A&M University (TAMU)	United States	128.34	394	147.32	-12.9%
74	Leibniz Association	Germany	128.11	540	117.56	9.0%
75	Tokyo Institute of Technology (Tokyo Tech)	Japan	127.23	331	105.59	20.5%
76	University of Bristol (UoB)	United Kingdom	125.73	399	109.62	14.7%
77	Nagoya University	Japan	125.28	432	132.97	-5.8%
78	University of Copenhagen (UCPH)	Denmark	124.84	615	117.29	6.4%
79	Purdue University	United States	123.37	349	112.74	9.4%
80	University of Pittsburgh (Pitt)	United States	122.10	380	148.22	-17.6%
81	Technical University Munich (TUM)	Germany	121.39	477	125.21	-3.1%
82	Vanderbilt University (VU)	United States	121.38	368	101.83	19.2%
83	The University of Texas Southwestern Medical Center (UT Southwestern Medical Center)	United States	117.93	229	124.11	-5.0%
84	Korea Advanced Institute of Science and Technology (KAIST)	South Korea	116.39	228	103.03	13.0%
85	Argonne National Laboratory (ANL)	United States	113.69	475	113.74	0.0%
86	Atomic Energy and Alternative Energies Commission (CEA)	France	112.95	1080	138.71	-18.6%
87	The University of Edinburgh	United Kingdom	112.04	796	110.44	1.4%
88	Indiana University (IU)	United States	111.67	354	119.17	-6.3%
89	University of Southern California (USC)	United States	111.59	270	127.44	-12.4%
90	Heidelberg University (Uni Heidelberg)	Germany	111.39	631	105.66	5.4%
91	University of Geneva (UNIGE)	Switzerland	111.18	446	108.07	2.9%
92	The University of Queensland (UQ)	Australia	108.83	392	94.78	14.8%
93	Georgia Institute of Technology (Georgia Tech)	United States	108.31	267	137.43	-21.2%
94	Emory University	United States	107.54	239	108.36	-0.8%
95	National Taiwan University (NTU)	Taiwan	107.49	299	102.57	4.8%
96	University of Florida (UF)	United States	106.90	414	105.28	1.5%
97	Shanghai Jiao Tong University (SJTU)	China	106.84	282	96.01	11.3%
98	Lanzhou University (LZU)	China	106.31	176	69.71	52.5%
99	University of Utah (Utah)	United States	105.95	282	113.06	-6.3%
100	Monash University	Australia	103.11	382	94.89	8.7%

2014	INSTITUTION	COUNTRY	WFC	ARTICLE COUNT	2013 WFC	2013-2014 CHANGE IN WFC
101	Los Alamos National Laboratory (LANL)	United States	102.26	375	115.64	-11.6%
102	University of Münster (WWU)	Germany	101.94	221	94.17	8.2%
103	Jilin University (JLU)	China	101.87	184	97.72	4.2%
104	University of Zurich (UZH)	Switzerland	101.37	422	104.36	-2.9%
105	National Institute for Material Science (NIMS)	Japan	100.71	240	81.79	23.1%
106	Pierre and Marie Curie University (UPMC)	France	100.44	1,372	96.46	4.1%
107	Agency for Science, Technology and Research (A*STAR)	Singapore	100.33	284	81.62	22.9%
108	Hokkaido University (HU)	Japan	100.03	234	105.93	-5.6%
109	Utrecht University (UU)	Netherlands	99.89	475	111.50	-10.4%
110	Kyushu University	Japan	98.31	275	84.56	16.3%
111	Rice University	United States	97.96	275	82.53	18.7%
112	University of Alberta (U of A)	Canada	97.78	295	101.74	-3.9%
113	University of Göttingen	Germany	97.69	369	98.58	-0.9%
114	Hebrew University of Jerusalem (HUJI)	Israel	95.18	245	91.30	4.3%
115	University of California Riverside (UCR)	United States	94.82	279	77.71	22.0%
116	University of Groningen (RUG)	Netherlands	94.80	425	74.72	26.9%
117	University of Würzburg	Germany	93.86	260	95.03	-1.2%
118	Indian Institute of Science (IISc)	India	93.72	149	83.64	12.0%
119	Nankai University (NKU)	China	93.09	222	113.52	-18.0%
120	Xiamen University (XMU)	China	92.73	204	76.02	22.0%
121	National Institute of Standards and Technology (NIST)	United States	92.54	329	88.53	4.5%
122	University of Rochester (UR)	United States	92.34	291	104.73	-11.8%
123	Boston University (BU)	United States	92.14	389	99.12	-7.0%
124	University of Basel	Switzerland	90.89	251	87.67	3.7%
125	Wuhan University (WHU)	China	90.67	154	98.80	-8.2%
126	Sichuan University (SCU)	China	89.44	167	76.83	16.4%
127	University of Leuven (KU Leuven)	Belgium	88.93	393	91.46	-2.8%
128	National Aeronautics and Space Administration (NASA)	United States	88.79	1,006	94.01	-5.6%
129	Memorial Sloan-Kettering Cancer Center (MSKCC)	United States	88.29	217	75.15	17.5%
130	University of New South Wales (UNSW)	Australia	88.11	277	69.81	26.2%
131	University of Chinese Academy of Sciences (UCAS)	China	88.05	516	71.24	23.6%
132	Sun Yat-sen University (SYSU)	China	87.87	191	79.43	10.6%
133	The University of Arizona (UA)	United States	87.57	522	78.02	12.2%
134	Australian National University (ANU)	Australia	87.16	498	93.53	-6.8%
135	Tel Aviv University (TAU)	Israel	86.99	318	78.16	11.3%
136	Soochow University	China	86.12	158	65.31	31.9%
137	Baylor College of Medicine (BCM)	United States	85.63	213	76.15	12.5%
138	Aarhus University (AU)	Denmark	85.28	294	77.35	10.3%
139	University of Erlangen-Nuremberg (FAU)	Germany	84.46	248	84.55	-0.1%
140	Oak Ridge National Laboratory (ORNL)	United States	84.36	269	86.77	-2.8%
141	Brown University	United States	83.87	245	71.51	17.3%
142	Humboldt University of Berlin (HU Berlin)	Germany	83.71	356	76.98	8.7%
143	The University of Melbourne (UniMelb)	Australia	82.60	478	89.76	-8.0%
144	Academia Sinica	Taiwan	81.82	476	80.21	2.0%
145	U.S. Department of Energy (DOE)	United States	81.44	173	74.77	8.9%
146	The University of Virginia (UVA)	United States	81.39	319	77.87	4.5%
147	Lund University (LU)	Sweden	81.10	328	72.99	11.1%
148	East China Normal University (ECNU)	China	80.63	144	65.56	23.0%
149	National Institute for Health and Medical Research (INSERM)	France	80.44	654	70.08	14.8%
150	University of Bonn (Uni Bonn)	Germany	80.37	464	78.01	3.0%

2014	INSTITUTION	COUNTRY	WFC	ARTICLE COUNT	2013 WFC	2013-2014 CHANGE IN WFC
151	Arizona State University (ASU)	United States	79.94	255	80.58	-0.8%
152	The University of Sydney (USYD)	Australia	79.89	492	95.14	-16.0%
153	University of Southampton (Soton)	United Kingdom	79.04	315	85.53	-7.6%
154	Technion-Israel Institute of Technology (IIT)	Israel	78.91	231	67.90	16.2%
155	University of Montreal	Canada	78.01	327	68.73	13.5%
156	Stony Brook University (SBU)	United States	77.80	302	78.79	-1.3%
157	Brookhaven National Laboratory (BNL)	United States	77.63	323	67.83	14.4%
158	University of Freiburg	Germany	77.39	282	72.75	6.4%
159	Uppsala University (UU)	Sweden	76.75	351	80.05	-4.1%
160	Durham University	United Kingdom	76.61	386	84.05	-8.8%
161	The University of Nottingham (UoN)	United Kingdom	76.54	236	74.17	3.2%
162	University of Hamburg (UHH)	Germany	76.48	361	83.82	-8.8%
163	Indian Institute of Science Education and Research (IISER)	India	75.88	106	58.72	29.2%
164	RWTH Aachen University (RWTH Aachen)	Germany	75.57	255	87.18	-13.3%
165	Case Western Reserve University (CWRU)	United States	75.33	201	76.24	-1.2%
166	Joseph Fourier University (UJF)	France	74.84	682	69.43	7.8%
167	Leiden University	Netherlands	73.69	482	73.08	0.8%
168	Hong Kong University of Science and Technology (HKUST)	China	73.59	133	54.60	34.8%
169	Hunan University (HNU)	China	73.23	105	54.57	34.2%
170	Iowa State University (ISU)	United States	72.56	208	78.91	-8.0%
171	Medical Research Council (MRC)	United Kingdom	71.76	470	67.17	6.8%
172	The University of Hong Kong (HKU)	China	71.75	185	71.38	0.5%
173	Radboud University Nijmegen (RU)	Netherlands	71.73	461	63.38	13.2%
174	University of Waterloo	Canada	71.02	199	61.22	16.0%
175	Yonsei University	South Korea	71.02	201	61.62	15.3%
176	Karolinska Institute (KI)	Sweden	70.88	234	59.23	19.7%
177	University of Massachusetts Medical School (UMMS)	United States	70.59	143	72.00	-2.0%
178	Pohang University of Science and Technology (POSTECH)	South Korea	70.38	151	70.00	0.5%
179	University of Notre Dame	United States	70.37	258	86.33	-18.5%
180	University of Cologne (UoC)	Germany	69.90	235	57.15	22.3%
181	University of California Santa Cruz (UCSC)	United States	69.85	537	58.03	20.4%
182	National Institute of Advanced Industrial Science and Technology (AIST)	Japan	69.79	185	79.48	-12.2%
183	University of Warwick (Warwick)	United Kingdom	69.68	392	61.07	14.1%
184	King's College London (KCL)	United Kingdom	69.57	239	71.59	-2.8%
185	The Rockefeller University	United States	69.55	207	82.62	-15.8%
186	University of Barcelona (UB)	Spain	68.98	608	72.14	-4.4%
187	Xi'an Jiaotong University (XJTU)	China	67.98	167	42.98	58.2%
188	Stockholm University	Sweden	67.67	416	71.69	-5.6%
189	East China University of Science and Technology (ECUST)	China	67.48	119	56.75	18.9%
190	University of Sheffield	United Kingdom	66.68	266	67.59	-1.3%
191	University of Tübingen	Germany	66.65	279	77.43	-13.9%
192	University of Amsterdam (UvA)	Netherlands	66.56	532	60.41	10.2%
193	University of Paris Sud (Paris 11)	France	65.88	611	72.33	-8.9%
194	University of Glasgow	United Kingdom	65.30	539	66.48	-1.8%
195	National Tsing Hua University (NTHU)	Taiwan	65.28	171	66.23	-1.4%
196	University of Ottawa (uOttawa)	Canada	64.43	147	59.20	8.8%
197	The University of Texas MD Anderson Cancer Center	United States	64.21	178	65.99	-2.7%
198	Icahn School of Medicine at Mount Sinai (ISMMS)	United States	64.14	200	53.91	19.0%
199	University of Regensburg (UR)	Germany	63.91	131	53.73	18.9%
200	Technische Universität Berlin (TU Berlin)	Germany	63.52	141	55.40	14.7%

TOP INSTITUTIONS: LIFE SCIENCES

2014	INSTITUTION	COUNTRY	WFC	ARTICLE COUNT	2013 WFC	2013-2014 CHANGE IN WFC
1	Harvard University	United States	610.16	1,363	587.65	3.8%
2	National Institutes of Health (NIH)	United States	320.93	728	369.99	-13.3%
3	Stanford University (SU)	United States	226.07	465	245.14	-7.8%
4	Max Planck Society	Germany	225.42	707	216.73	4.0%
5	Massachusetts Institute of Technology (MIT)	United States	182.86	578	183.17	-0.2%
6	Yale University	United States	179.07	400	189.31	-5.4%
7	University of California San Francisco (UCSF)	United States	177.02	418	211.77	-16.4%
8	University of California, San Diego (UC San Diego)	United States	168.43	390	182.69	-7.8%
9	University of Toronto (U of T)	Canada	157.03	381	128.58	22.1%
10	Chinese Academy of Sciences (CAS)	China	155.22	420	147.94	4.9%
11	French National Centre for Scientific Research (CNRS)	France	155.06	972	145.94	6.2%
12	University of Oxford	United Kingdom	152.07	420	147.83	2.9%
13	The Johns Hopkins University (JHU)	United States	146.19	333	140.18	4.3%
14	Columbia University in the City of New York (CU)	United States	142.53	368	127.22	12.0%
15	University of Pennsylvania (Penn)	United States	141.62	320	175.58	-19.3%
16	University of Michigan (U-M)	United States	133.65	304	143.00	-6.5%
17	University of Cambridge	United Kingdom	133.57	399	155.77	-14.3%
18	University of Washington (UW)	United States	125.90	339	137.32	-8.3%
19	University of California Los Angeles (UCLA)	United States	123.06	313	126.98	-3.1%
20	University of California Berkeley (UC Berkeley)	United States	121.51	300	126.58	-4.0%
21	Washington University in St. Louis (WUSTL)	United States	121.40	279	137.34	-11.6%
22	Cornell University	United States	113.45	346	140.95	-19.5%
23	Duke University	United States	112.08	320	113.86	-1.6%
24	University College London (UCL)	United Kingdom	106.93	331	115.85	-7.7%
25	The University of Texas Southwestern Medical Center (UT Southwestern Medical Center)	United States	104.98	211	107.98	-2.8%
26	The University of Tokyo (UTokyo)	Japan	99.33	262	112.60	-11.8%
27	New York University (NYU)	United States	99.21	238	92.73	7.0%
28	University of North Carolina at Chapel Hill (UNC)	United States	97.89	240	93.85	4.3%
29	The University of Chicago (UChicago)	United States	94.05	234	93.92	0.1%
30	University of Wisconsin-Madison (UW Madison)	United States	92.41	182	87.38	5.8%
31	Helmholtz Association of German Research Centres (Helmholtz)	Germany	90.06	432	85.65	5.2%
32	Baylor College of Medicine (BCM)	United States	84.40	210	74.30	13.6%
33	Vanderbilt University (VU)	United States	80.27	196	74.80	7.3%
34	University of California Davis (UC Davis)	United States	79.61	194	90.61	-12.1%
35	Memorial Sloan-Kettering Cancer Center (MSKCC)	United States	77.02	194	68.47	12.5%
36	Swiss Federal Institute of Technology Zurich (ETH Zurich)	Switzerland	76.08	207	46.48	63.7%
37	Northwestern University (NU)	United States	75.07	172	91.03	-17.5%
38	Emory University	United States	74.39	181	66.89	11.2%
39	University of Pittsburgh (Pitt)	United States	73.58	180	81.12	-9.3%
40	National Institute for Health and Medical Research (INSERM)	France	71.33	575	62.47	14.2%
41	The Scripps Research Institute (TSRI)	United States	71.09	193	95.51	-25.6%
42	McGill University	Canada	71.03	208	78.78	-9.8%
43	Rutgers, The State University of New Jersey (RU)	United States	71.00	163	61.90	14.7%
44	University of Massachusetts Medical School (UMMS)	United States	66.97	137	69.40	-3.5%
45	Spanish National Research Council (CSIC)	Spain	66.91	295	62.94	6.3%
46	The Rockefeller University	United States	66.68	146	77.26	-13.7%
47	Karolinska Institute (KI)	Sweden	65.96	222	55.50	18.8%
48	Imperial College London (ICL)	United Kingdom	65.08	244	54.58	19.2%
49	The University of British Columbia (UBC)	Canada	64.55	175	53.90	19.8%
50	Icahn School of Medicine at Mount Sinai (ISMMS)	United States	63.95	198	52.10	22.8%

TOP INSTITUTIONS: EARTH & ENVIRONMENTAL SCIENCES

2014	INSTITUTION	COUNTRY	WFC	ARTICLE COUNT	2013 WFC	2013-2014 CHANGE IN WFC
1	Chinese Academy of Sciences (CAS)	China	74.88	192	77.12	-2.9%
2	French National Centre for Scientific Research (CNRS)	France	74.14	479	56.92	30.2%
3	Helmholtz Association of German Research Centres (Helmholtz)	Germany	68.96	205	63.81	8.1%
4	University of California, San Diego (UC San Diego)	United States	54.32	131	47.45	14.5%
5	National Aeronautics and Space Administration (NASA)	United States	52.68	200	57.95	-9.1%
6	National Oceanic and Atmospheric Administration (NOAA)	United States	50.32	165	59.91	-16.0%
7	California Institute of Technology (Caltech)	United States	50.17	156	50.91	-1.5%
8	University of Washington (UW)	United States	49.12	111	42.34	16.0%
9	Swiss Federal Institute of Technology Zurich (ETH Zurich)	Switzerland	41.69	119	33.17	25.7%
10	Woods Hole Oceanographic Institution (WHOI)	United States	41.31	107	31.00	33.3%
11	U.S. Geological Survey (USGS)	United States	38.62	104	39.76	-2.9%
12	The University of Texas at Austin (UT Austin)	United States	37.58	83	21.11	78.0%
13	Massachusetts Institute of Technology (MIT)	United States	37.09	100	20.62	79.8%
14	University of Colorado Boulder (CU-Boulder)	United States	36.78	132	44.08	-16.6%
15	The University of Tokyo (UTokyo)	Japan	36.65	85	37.33	-1.8%
16	Columbia University in the City of New York (CU)	United States	32.65	105	41.25	-20.8%
17	Pennsylvania State University (Penn State)	United States	32.14	66	20.15	59.5%
18	University of California Berkeley (UC Berkeley)	United States	30.95	91	22.97	34.8%
19	University of Cambridge	United Kingdom	28.08	75	18.75	49.7%
20	National Center for Atmospheric Research (NCAR)	United States	25.08	81	25.37	-1.2%
21	Stanford University (SU)	United States	24.65	64	32.09	-23.2%
22	University of Hawaii at Manoa (UH Manoa)	United States	23.86	75	28.04	-14.9%
23	Utrecht University (UU)	Netherlands	23.00	59	21.31	8.0%
24	University of California Davis (UC Davis)	United States	22.96	59	16.60	38.3%
25	Japan Agency for Marine-Earth Science and Technology (JAMSTEC)	Japan	22.61	71	28.62	-21.0%
26	University of Maryland, College Park (UMCP)	United States	22.51	86	15.96	41.1%
27	Princeton University	United States	22.41	72	20.74	8.1%
28	Institute of Research for Development (IRD)	France	22.18	265	16.82	31.8%
29	Spanish National Research Council (CSIC)	Spain	22.02	97	18.56	18.6%
30	Yale University	United States	21.88	52	17.51	25.0%
31	Australian National University (ANU)	Australia	20.98	70	18.55	13.1%
32	University of Bristol (UoB)	United Kingdom	20.51	57	17.84	15.0%
33	University of Wisconsin-Madison (UW Madison)	United States	20.22	64	24.37	-17.0%
34	University of Oxford	United Kingdom	20.05	77	33.87	-40.8%
35	Harvard University	United States	19.46	61	32.26	-39.7%
36	University of California Los Angeles (UCLA)	United States	19.05	54	20.81	-8.5%
37	Max Planck Society	Germany	18.91	86	23.81	-20.6%
38	Oregon State University (OSU)	United States	18.91	50	19.77	-4.4%
39	The University of Arizona (UA)	United States	18.19	56	15.43	17.9%
40	University of Bremen	Germany	18.17	52	9.65	88.4%
41	University of Toronto (U of T)	Canada	18.16	43	12.10	50.1%
42	National Institute of Geophysics and Volcanology (INGV)	Italy	17.95	41	18.73	-4.2%
43	Brown University	United States	17.95	43	8.59	108.9%
44	University of Minnesota (UMN)	United States	17.93	57	15.15	18.4%
45	Colorado State University (CSU)	United States	17.51	47	17.98	-2.6%
46	The Commonwealth Scientific and Industrial Research Organisation (CSIRO)	Australia	17.34	63	16.92	2.4%
47	Paris Diderot University (Paris 7)	France	17.07	83	8.17	108.9%
48	University of Florida (UF)	United States	16.88	44	16.78	0.6%
49	University of Miami (UM)	United States	16.25	35	10.15	60.1%
50	U.S. Department of Energy (DOE)	United States	16.04	47	16.44	-2.4%

TOP INSTITUTIONS: CHEMISTRY

2014	INSTITUTION	COUNTRY	WFC	ARTICLE COUNT	2013 WFC	2013-2014 CHANGE IN WFC
1	Chinese Academy of Sciences (CAS)	China	771.24	1,396	681.87	13.1%
2	French National Centre for Scientific Research (CNRS)	France	251.51	921	227.97	10.3%
3	Max Planck Society	Germany	184.21	425	202.85	-9.2%
4	Massachusetts Institute of Technology (MIT)	United States	169.74	274	164.75	3.0%
5	Stanford University (SU)	United States	159.72	254	145.69	9.6%
6	Peking University (PKU)	China	151.32	366	142.68	6.1%
7	Kyoto University	Japan	151.26	237	157.12	-3.7%
8	The University of Tokyo (UTokyo)	Japan	143.72	228	159.48	-9.9%
9	Nanyang Technological University (NTU)	Singapore	143.06	217	123.90	15.5%
10	Harvard University	United States	141.23	256	143.52	-1.6%
11	University of California Berkeley (UC Berkeley)	United States	140.86	289	131.56	7.1%
12	Northwestern University (NU)	United States	136.36	211	152.92	-10.8%
13	Swiss Federal Institute of Technology Zurich (ETH Zurich)	Switzerland	127.29	217	102.80	23.8%
14	University of Oxford	United Kingdom	126.10	202	119.39	5.6%
15	Zhejiang University (ZJU)	China	125.25	178	86.42	44.9%
16	Nanjing University (NJU)	China	120.32	207	117.34	2.5%
17	Swiss Federal Institute of Technology in Lausanne (EPFL)	Switzerland	116.01	219	80.35	44.4%
18	Fudan University	China	114.02	186	80.10	42.3%
19	The University of Texas at Austin (UT Austin)	United States	112.69	161	109.67	2.7%
20	University of Cambridge	United Kingdom	110.12	186	105.84	4.0%
21	University of Illinois at Urbana Champaign (UIUC)	United States	108.91	191	115.67	-5.8%
22	Helmholtz Association of German Research Centres (Helmholtz)	Germany	108.35	302	91.62	18.3%
23	University of Science and Technology of China (USTC)	China	108.19	223	93.78	15.4%
24	Indian Institutes of Technology (IITs)	India	106.58	141	74.77	42.6%
25	Osaka University	Japan	105.69	171	106.33	-0.6%
26	Tsinghua University (TH)	China	101.79	201	92.06	10.6%
27	University of Wisconsin-Madison (UW Madison)	United States	96.53	139	105.23	-8.3%
28	National University of Singapore (NUS)	Singapore	93.39	177	83.81	11.4%
29	California Institute of Technology (Caltech)	United States	92.35	144	107.31	-13.9%
30	Council of Scientific and Industrial Research (CSIR)	India	90.40	117	79.46	13.8%
31	Lawrence Berkeley National Laboratory (LBNL)	United States	85.03	248	74.57	14.0%
32	Lanzhou University (LZU)	China	84.31	118	50.35	67.5%
33	University of California Santa Barbara (UCSB)	United States	83.37	137	62.14	34.2%
34	University of Pennsylvania (Penn)	United States	82.19	124	80.23	2.4%
35	Tohoku University	Japan	81.32	138	62.89	29.3%
36	The Scripps Research Institute (TSRI)	United States	79.61	130	101.52	-21.6%
37	University of California, San Diego (UC San Diego)	United States	79.07	134	78.52	0.7%
38	Jilin University (JLU)	China	77.57	128	73.88	5.0%
39	University of California Los Angeles (UCLA)	United States	75.45	134	87.43	-13.7%
40	University of North Carolina at Chapel Hill (UNC)	United States	74.34	101	75.09	-1.0%
41	The University of Manchester (UoM)	United Kingdom	73.82	132	53.06	39.1%
42	Imperial College London (ICL)	United Kingdom	73.20	126	62.12	17.8%
43	Korea Advanced Institute of Science and Technology (KAIST)	South Korea	73.03	133	56.93	28.3%
44	University of Michigan (U-M)	United States	72.80	112	92.32	-21.1%
45	Xiamen University (XMU)	China	71.25	138	59.87	19.0%
46	Ludwig Maximilian University of Munich (LMU)	Germany	71.20	130	55.22	28.9%
47	Yale University	United States	71.10	122	46.80	51.9%
48	Sichuan University (SCU)	China	70.75	98	68.45	3.4%
49	University of Toronto (U of T)	Canada	69.01	120	85.42	-19.2%
50	Seoul National University (SNU)	South Korea	68.64	111	70.70	-2.9%

TOP INSTITUTIONS: PHYSICAL SCIENCES

2014	INSTITUTION	COUNTRY	WFC	ARTICLE COUNT	2013 WFC	2013-2014 CHANGE IN WFC
1	Chinese Academy of Sciences (CAS)	China	413.44	1,376	406.86	1.6%
2	French National Centre for Scientific Research (CNRS)	France	333.36	2,812	335.41	-0.6%
3	Max Planck Society	Germany	300.72	1,948	353.91	-15.0%
4	Stanford University (SU)	United States	221.86	652	211.18	5.1%
5	Helmholtz Association of German Research Centres (Helmholtz)	Germany	213.14	819	217.24	-1.9%
6	Massachusetts Institute of Technology (MIT)	United States	212.29	718	226.42	-6.2%
7	The University of Tokyo (UTokyo)	Japan	204.65	737	193.50	5.8%
8	Harvard University	United States	200.80	1,149	191.30	5.0%
9	University of Cambridge	United Kingdom	187.59	839	170.15	10.3%
10	University of California Berkeley (UC Berkeley)	United States	149.28	735	135.57	10.1%
11	Swiss Federal Institute of Technology Zurich (ETH Zurich)	Switzerland	140.09	520	132.35	5.8%
12	University of California Santa Barbara (UCSB)	United States	115.63	377	120.80	-4.3%
13	University of Oxford	United Kingdom	113.00	594	126.23	-10.5%
14	University of Michigan (U-M)	United States	112.36	464	121.38	-7.4%
15	Peking University (PKU)	China	111.97	454	105.09	6.6%
16	Russian Academy of Sciences (RAS)	Russia	111.96	724	109.38	2.4%
17	Spanish National Research Council (CSIC)	Spain	108.99	1,281	98.40	10.8%
18	Swiss Federal Institute of Technology in Lausanne (EPFL)	Switzerland	104.69	401	102.90	1.7%
19	Princeton University	United States	102.49	469	114.36	-10.4%
20	The University of Texas at Austin (UT Austin)	United States	98.37	330	98.67	-0.3%
21	Tsinghua University (TH)	China	98.25	363	87.94	11.7%
22	California Institute of Technology (Caltech)	United States	95.56	839	100.29	-4.7%
23	University of Maryland, College Park (UMCP)	United States	90.92	542	96.06	-5.4%
24	University of Illinois at Urbana-Champaign (UIUC)	United States	86.99	297	111.83	-22.2%
25	Lawrence Berkeley National Laboratory (LBNL)	United States	86.75	514	76.52	13.4%
26	University of California Los Angeles (UCLA)	United States	81.40	314	97.72	-16.7%
27	National University of Singapore (NUS)	Singapore	80.80	171	88.74	-8.9%
28	Kyoto University	Japan	77.15	330	91.02	-15.2%
29	Los Alamos National Laboratory (LANL)	United States	76.30	289	84.24	-9.4%
30	National Research Council (CNR)	Italy	75.80	282	93.70	-19.1%
31	Tohoku University	Japan	75.65	211	96.92	-22.0%
32	The University of Chicago (UChicago)	United States	75.47	392	63.01	19.8%
33	University of Science and Technology of China (USTC)	China	74.91	301	71.40	4.9%
34	University of California, San Diego (UC San Diego)	United States	74.21	259	73.71	0.7%
35	Nanyang Technological University (NTU)	Singapore	72.88	141	71.87	1.4%
36	Seoul National University (SNU)	South Korea	72.34	242	66.08	9.5%
37	Imperial College London (ICL)	United Kingdom	71.34	370	79.35	-10.1%
38	Northwestern University (NU)	United States	71.33	239	91.07	-21.7%
39	Pennsylvania State University (Penn State)	United States	68.96	369	77.44	-10.9%
40	Cornell University	United States	68.66	265	73.02	-6.0%
41	National Institute of Standards and Technology (NIST)	United States	68.50	254	67.83	1.0%
42	Nanjing University (NJU)	China	68.43	233	64.94	5.4%
43	National Institute for Material Science (NIMS)	Japan	68.14	166	43.97	55.0%
44	Osaka University	Japan	67.71	245	62.61	8.1%
45	Yale University	United States	66.85	382	60.96	9.7%
46	University of Colorado Boulder (CU-Boulder)	United States	66.06	338	55.85	18.3%
47	Atomic Energy and Alternative Energies Commission (CEA)	France	65.66	765	91.23	-28.0%
48	Argonne National Laboratory (ANL)	United States	63.52	313	70.93	-10.4%
49	Columbia University in the City of New York (CU)	United States	61.89	351	74.99	-17.5%
50	Korea Advanced Institute of Science and Technology (KAIST)	South Korea	58.92	103	49.76	18.4%

TOP INSTITUTIONS IN NATURE AND SCIENCE JOURNALS

2014	INSTITUTION	COUNTRY	WFC	ARTICLE COUNT	2013 WFC	2013-2014 CHANGE IN WFC
1	Harvard University	United States	75.39	210	76.41	-1.3%
2	Stanford University (SU)	United States	41.44	103	38.30	8.2%
3	Massachusetts Institute of Technology (MIT)	United States	34.13	123	45.59	-25.1%
4	Max Planck Society	Germany	30.40	120	32.87	-7.5%
5	National Institutes of Health (NIH)	United States	24.04	69	27.57	-12.8%
6	University of California Berkeley (UC Berkeley)	United States	21.35	95	21.58	-1.1%
7	University of Washington (UW)	United States	20.63	63	14.49	42.3%
8	University of California, San Diego (UC San Diego)	United States	20.29	54	17.83	13.9%
9	Yale University	United States	20.16	56	17.04	18.3%
10	French National Centre for Scientific Research (CNRS)	France	19.46	166	15.12	28.7%
11	California Institute of Technology (Caltech)	United States	18.61	62	12.73	46.2%
12	University of Cambridge	United Kingdom	18.12	82	20.69	-12.4%
13	University of California San Francisco (UCSF)	United States	17.96	48	24.04	-25.3%
14	University of Oxford	United Kingdom	17.79	60	13.84	28.5%
15	Columbia University in the City of New York (CU)	United States	17.45	64	19.75	-11.6%
16	Helmholtz Association of German Research Centres (Helmholtz)	Germany	16.66	80	10.95	52.1%
17	The Scripps Research Institute (TSRI)	United States	14.18	35	18.43	-23.1%
18	The University of Tokyo (UTokyo)	Japan	13.21	44	15.55	-15.1%
19	Chinese Academy of Sciences (CAS)	China	13.11	58	18.71	-29.9%
20	University of Michigan (U-M)	United States	13.04	44	9.36	39.3%
21	Weizmann Institute of Science (WIS)	Israel	12.91	22	6.67	93.5%
22	Swiss Federal Institute of Technology Zurich (ETH Zurich)	Switzerland	12.74	43	13.98	-8.9%
23	Princeton University	United States	12.29	32	13.50	-9.0%
24	The University of Texas at Austin (UT Austin)	United States	12.20	40	4.60	165.3%
25	Cornell University	United States	11.83	55	13.31	-11.1%
26	The Johns Hopkins University (JHU)	United States	11.82	39	12.33	-4.1%
27	Washington University in St. Louis (WUSTL)	United States	11.40	40	8.41	35.6%
28	Medical Research Council (MRC)	United Kingdom	11.34	24	9.29	22.0%
29	University of Wisconsin-Madison (UW Madison)	United States	11.14	35	3.16	252.1%
30	Memorial Sloan-Kettering Cancer Center (MSKCC)	United States	10.81	29	5.08	112.9%
31	New York University (NYU)	United States	10.54	25	10.55	-0.1%
32	University of California Los Angeles (UCLA)	United States	10.35	41	12.75	-18.8%
33	The University of Texas Southwestern Medical Center (UT Southwestern Medical Center)	United States	9.88	20	11.79	-16.2%
34	The University of Chicago (UChicago)	United States	9.33	47	11.75	-20.6%
35	F. Hoffmann-La Roche Ltd	Switzerland	9.18	20	2.58	255.9%
36	The Rockefeller University	United States	9.14	20	11.45	-20.2%
37	University of Pennsylvania (Penn)	United States	9.01	30	10.23	-11.9%
38	Lawrence Berkeley National Laboratory (LBNL)	United States	9.00	52	5.97	50.7%
39	University of California Santa Cruz (UCSC)	United States	8.93	37	4.54	96.6%
40	University of Toronto (U of T)	Canada	8.64	38	15.70	-44.9%
41	Duke University	United States	8.55	33	7.14	19.8%
42	University of Maryland, College Park (UMCP)	United States	8.49	40	5.21	63.1%
43	Kyoto University	Japan	7.44	25	7.48	-0.5%
44	University of Copenhagen (UCPH)	Denmark	7.43	50	5.11	45.6%
45	RIKEN	Japan	7.33	32	9.62	-23.8%
46	University of California Davis (UC Davis)	United States	7.13	29	8.06	-11.6%
47	University College London (UCL)	United Kingdom	7.10	41	7.69	-7.6%
48	Pennsylvania State University (Penn State)	United States	7.01	25	6.26	11.9%
49	University of Zurich (UZH)	Switzerland	6.70	19	4.81	39.1%
50	Peking University (PKU)	China	6.48	28	4.10	58.0%

Weighted fractional count (WFC) for each institution is shown to two decimal places only. When two or more institutions have the same WFC, their positions are determined by the thousandth place (or beyond).

These results are based on the most recent data available as of 11 September 2014. Owing to continual refinements of the data, the figures in the database are liable to change and might differ to those printed in the supplements.